

Composite Construction in Steel and Concrete VII

Proceedings
of the Seventh
International
Conference
on Composite
Construction
in Steel and
Concrete



ASCE

EDITED BY
Mark Bradford, Ph.D., D.Sc., P.E.
Brian Uy, Ph.D., P.E.



STRUCTURAL
ENGINEERING
INSTITUTE

COMPOSITE CONSTRUCTION IN STEEL AND CONCRETE VII

PROCEEDINGS OF THE 2013 INTERNATIONAL CONFERENCE ON
COMPOSITE CONSTRUCTION IN STEEL AND CONCRETE

July 28-31, 2013
North Queensland, Australia

SPONSORED BY
Centre for Infrastructure Engineering and Safety
The University of New South Wales, Sydney, Australia

The Structural Engineering Institute
of the American Society of Civil Engineers

EDITED BY
Mark Bradford, Ph.D., D.Sc., P.E.
Brian Uy, Ph.D., P.E.

ASCE



STRUCTURAL
ENGINEERING
INSTITUTE

Published by the American Society of Civil Engineers

Published by American Society of Civil Engineers
1801 Alexander Bell Drive
Reston, Virginia, 20191-4382
www.asce.org/publications | ascelibrary.org

Any statements expressed in these materials are those of the individual authors and do not necessarily represent the views of ASCE, which takes no responsibility for any statement made herein. No reference made in this publication to any specific method, product, process, or service constitutes or implies an endorsement, recommendation, or warranty thereof by ASCE. The materials are for general information only and do not represent a standard of ASCE, nor are they intended as a reference in purchase specifications, contracts, regulations, statutes, or any other legal document. ASCE makes no representation or warranty of any kind, whether express or implied, concerning the accuracy, completeness, suitability, or utility of any information, apparatus, product, or process discussed in this publication, and assumes no liability therefor. The information contained in these materials should not be used without first securing competent advice with respect to its suitability for any general or specific application. Anyone utilizing such information assumes all liability arising from such use, including but not limited to infringement of any patent or patents.

ASCE and American Society of Civil Engineers—Registered in U.S. Patent and Trademark Office.

Photocopies and permissions. Permission to photocopy or reproduce material from ASCE publications can be requested by sending an e-mail to permissions@asce.org or by locating a title in ASCE's Civil Engineering Database (<http://cedb.asce.org>) or ASCE Library (<http://ascelibrary.org>) and using the “Permissions” link.

Errata: Errata, if any, can be found at <http://dx.doi.org/10.1061/9780784479735>

Copyright © 2016 by the American Society of Civil Engineers.
All Rights Reserved.
ISBN 978-0-7844-7973-5 (PDF)
Manufactured in the United States of America.

Front cover: Brian Uy, University of South Wales

Preface

These proceedings summarize the state-of-the-art in composite construction worldwide, as presented at an international conference on Composite Construction in Steel and Concrete held at Palm Cove in North Queensland (Australia) in July 2013. This is the seventh in a series of conferences on this topic organized by the United Engineering Foundation (and now Engineering Conferences International) aimed at assessing and synthesizing the most recent advances in research and practice in the area of composite steel-concrete construction. This conference was preceded by those held in Henniker, New Hampshire, USA (1987), Potosi, Missouri, USA (1992), Irsee, Germany (1996), Banff, Canada (2000), Kruger National Park, South Africa (2004) and Devil's Thumb Ranch, Colorado, USA (2008).

The papers contained in this volume cover a wide variety of topics, including composite bridges, composite slabs, shear connectors, composite columns, innovative composite structural systems, fire and seismic resistance of composite structural systems and practical applications. Sixty participants from fifteen countries participated in four days of presentations, panel and informal discussions dealing with all aspects of composite construction. The conference was organized and chaired by Professor Mark Bradford and Professor Brian Uy from The University of New South Wales, Sydney, Australia.

The papers in the proceedings were peer reviewed as per the guidelines used for the *Journal of Structural Engineering*, ASCE and are eligible for all ASCE awards and are open for discussion in the *Journal of Structural Engineering*, ASCE. The review process was administered by the proceeding editors, who would like to thank all the reviewers for their prompt and useful responses. The publication of the proceedings was supported by the Technical Activities Division of the Structural Engineering Institute (SEI), ASCE and assisted very ably by Professor Roberto Leon of Virginia Tech.

The support of the ASCE (SEI) and Centre for Infrastructure Engineering and Safety is also gratefully acknowledged. This conference would not have been possible without their support and funding.

Finally, the Editors would like to thank Mrs Rachel Stoddart, Dr Brendan Kirkland, Dr Vipulkumar Patel and the administrative staff of the Centre for Infrastructure Engineering and Safety for all their work in preparing the final draft of the proceedings. Without their contributions these proceedings would not have been possible.

Professor Mark Bradford and Professor Brian Uy
Australia, September 2015

Acknowledgments

Local Organizing Committee

Professor Mark Bradford, The University of New South Wales, Co-Chair
 Professor Brian Uy, The University of New South Wales, Co-Chair
 Mr John Brown, BOSFA
 Professor Keith Crews, University of Technology Sydney
 Dr Emre Erkmen, University of Technology Sydney
 Mr Alex Filonov, BlueScope Lysaght
 Professor Ian Gilbert, The University of New South Wales
 Associate Professor Muhammad Hadi, University of Wollongong
 Dr Ehab Hamed, The University of New South Wales
 Dr Amin Heidarpour, Monash University
 Dr Peter Key, Australian Steel Institute
 Dr Olivia Mirza, University of Western Sydney
 Professor Deric Oehlers, University of Adelaide
 Professor Yong-Lin Pi, The University of New South Wales
 Associate Professor Gianluca Ranzi, University of Sydney
 Dr Hamid Ronagh, University of Queensland
 Professor Scott Smith, Southern Cross University
 Professor Zhong Tao, University of Western Sydney
 Dr Hamid Valipour, The University of New South Wales
 Associate Professor Zora Vrcelj, Victoria University

International Scientific Committee

Dr Oreste Bursi, University of Trento, Trento, Italy
 Dr W. Samuel Easterling, Virginia Tech, Blacksburg, VA, USA
 Dr Mario Fontana, ETH, Zürich, Switzerland
 Professor Jerome F. Hajjar, Northeastern University, Boston, MA, USA
 Dr Kent Harries, University of Pittsburgh, Pittsburgh, PA, USA
 Dr James Harris, J. R. Harris & Co., Denver, CO, USA
 Dr Toko Hitaka, University of Kyoto, Kyoto, Japan
 Professor Ulrike Kuhlmann, University of Stuttgart, Stuttgart, Germany
 Dr Wolfgang Kurz, University of Kaiserslautern, Kaiserslautern, Germany
 Professor Dennis Lam, University of Bradford, Bradford, UK
 Professor Roberto T. Leon, Virginia Tech, Blacksburg, VA, USA
 Dr Gian Andrea Rassati, University of Cincinnati, Cincinnati, OH, USA
 Professor Bahram Shahrooz, University of California – Berkeley, USA
 Dr Robert Tremblay, Ecole Polytechnique, Montreal, Canada
 Professor K. C. Tsai, NCREC, Taipei, Taiwan
 Professor Yan Xiao, University of Southern California, Los Angeles, CA, USA

Financial Support

Centre for Infrastructure Engineering and Safety, University of New South Wales
 The Structural Engineering Institute of the American Society of Engineers



Contents

Keynote Paper

U.S. Composite Design Codes: A Personal View of the Influence of Composite Construction Conferences	1
Roberto T. Leon	

Bridges and Columns

New Langensand Bridge in Lucerne, Switzerland: Evolutionary System of a Composite Structure	13
Gabriele Guscetti, Claudio Pirazzi, Jérôme Pochat, and Reto Cantieni	
Welding and Properties of the Lamellar Flange Weld Joint for Modern Bridge Construction	27
Jaroslav Koukal, Martin Sondel, and Drahomir Schwarz	
Design Temperature Load Spectrum for the Fatigue Verification of Composite Bridges with Integral Abutments	36
Daniel Pak and Markus Feldmann	
The Squash Load of Concrete-Filled Tubular Sections	51
In-Kyu Jeung and Young-Bong Kwon	
Analyses of Through-Diaphragm Connections to CFT Columns	62
Liping Kang, Roberto T. Leon, and Xilin Lu	
Slab Effects on Beam-Column Subassemblies—Beam Strength and Elongation Issues	77
Gregory MacRae, Michael Hobbs, Des Bull, Tushar Chaudhari, Roberto Leon, Charles Clifton, and Geoff Chase	
Problems in Determining the Buckling Loads of Slender Full-Scale Concrete-Filled Tube Specimens	93
Tiziano Perea, Roberto T. Leon, Mark D. Denavit, and Jerome F. Hajjar	
Experimental Investigation on New Ring-Beam Connections for a Concrete-Filled Tubular Column and RC Beam	108
Wei Wang, Yiyi Chen, and Wanqi Li	

Composite Beams

Flexural Strength of High-Strength Steel-Concrete Composite Beams with Varying Steel Grades	120
Huiyong Ban and Mark A. Bradford	
Deformation-Based Design of Composite Beams.....	131
Leroy Gardner, Merih Kucukler, and Lorenzo Macorini	
Long-Term Deflection of Timber-Concrete Composite Beams in Cyclic Humidity Conditions in Bending.....	146
M. Hailu, R. Shrestha, and K. Crews	
CoSFB—Composite Slim-Floor Beam: Experimental Test Campaign and Evaluation	158
Oliver Hechler, Matthias Braun, Renata Obiala, Ulrike Kuhlmann, Florian Eggert, and Gunter Hauf	
Environmental Factors Affecting the Dynamic Response of Composite Steel-Concrete Beams	173
I. E. J. Henderson, B. Uy, X. Q. Zhu, and O. Mirza	
Vibration Performance of Composite Floors Using Slim Floor Beams.....	185
Stephen Hicks and Simo Peltonen	
Numerical Investigation of the Behaviour of Steel Beams in Steel-Concrete Composite Frames.....	199
Naveed Iqbal, Marko Pavlovic, Milan Veljkovic, Tim Heistermann, Fernanda Lopes, Aldina Santiago, and Luís Simões da Silva	
Behavior of a CFT Truss Girder with Precast Decks under Negative Bending Moment.....	214
In-Gyu Kim, Young-Jin Kim, Hyun-Chul Oh, Hyang-Wook Ma, and Chul-Hun Chung	
Behaviour and Design of Composite Beams Subjected to Combined Bending and Axial Forces	226
G. Vasdravellis, B. Uy, E. L. Tan, and B. Kirkland	
Nonlinear Finite Element Analysis and Design of Composite Beams Subjected to Shear and Bending	240
G. Vasdravellis and B. Uy	
Nominal Flexural Strength of Conventional or Hybrid Composite Girders.....	254
S. G. Youn and D. Bae	

Footfall-Induced Vibration in Longspan Composite Steel Beams Used in Two Projects at the University of Auckland.....	266
V. N. Patel and R. J. Built	

Composite Beams and Composite Joints

Innovative Aspects of Composite Construction in the New Leadenhall Building.....	288
John Stehle, Andy Butler, Mike Banfi, Rob Livesey, and Julie Bregulla	

Experimental Assessment of Ferritic Stainless Steel Composite Slabs.....	300
K. A. Cashell and N. R. Baddoo	

Case Study: Composite Construction for FLAT Slabs with Integrated Building Services.....	314
Thomas Friedrich, Juergen Schnell, and Wolfgang Kurz	

Progressive Collapse Analysis of Steel-Concrete Composite Frames with Floor Slab Actions.....	328
S. Jeyarajan, J. Y. Richard Liew, and C. G. Koh	

Resource-Efficient Design of Components for Office Buildings in Steel Composite Construction.....	342
Richard Stroetmann and Christine Podgorski	

FE Modelling of Sustainable Semi-Rigid Flush End Plate Composite Joints with Deconstructable Bolted Shear Connectors	356
A. Ataei and M. A. Bradford	

Experimental Tests of Composite Joints Subjected to Hogging and Sagging Bending Moments	375
Wioleta Barcewicz and Marian A. Gizejowski	

Composite Joints under M-N at Elevated Temperatures: Experimental Investigations and Analytical Models	387
J.-F. Demonceau, C. Haremza, J.-P. Jaspart, A. Santiago, and L. Simões da Silva	

Evaluation of the Mechanical Properties of Steel and Polypropylene Fibre-Reinforced Concrete Used in Beam Column Joints.....	401
Nassim Ghosni, Bijan Samali, and Hamid Valipour	

Analyses of the Rotational Capacity of Composite Connections for Plastic Design	408
Oliver Hechler, Christoph Odenbreit, and Jean-Pierre Jaspart	

Modelling of Semi-Rigid Joints in Steel-Concrete Composite Frames.....	422
S. Jeyarajan, J. Y. Richard Liew, and C. G. Koh	

Dynamics, Fire, and Seismic

Experiments on a Continuous Composite Truss Bridge with Concrete-Filled Lower Chords	438
Choong-Eon Kim, Hea-Young Ahn, Pil-Goo Lee, and Chang-Su Shim	

Sustainable Composite Beam Behaviour with Deconstructable Bolted Shear Connectors.....	445
Michael S. S. Lee and Mark A. Bradford	

Effect of Polyvinyl Alcohol (PVA) Fibre on the Dynamic Properties of Concrete Containing Fly Ash	456
A. Noushini, B. Samali, and K. Vessalas	

Fire Resistance Tests of Concrete-Filled Stainless Steel Tubular Columns.....	468
Mohamed Ghannam, Zhong Tao, and Tian Yi Song	

Static Loading Test of Precast CES Shear Walls with Different Shear Span Ratios.....	479
Tomoya Matsui and Hiroshi Kuramoto	

The Development of a Steel Fuse Coupling Beam for Coupled Core Wall Systems	494
Steven J. Mitchell, Gian A. Rassati, and Bahram M. Shahrooz	

Fire Tests of Concrete-Filled Circular Hollow Section Columns with a Solid Steel Core	508
M. Neuenschwander, M. Knobloch, and M. Fontana	

An Investigation on the Interface Shear Resistance of Twinwall Units for Tank Structures	522
J. S. Rana, C. Arya, J. Stehle, C. Crook, A. McFarlane, and T. Bennett	

Seismic Behavior of Steel-Concrete Composite Frame Structures and Design Practice in the United States.....	534
Mark D. Denavit, Jerome F. Hajjar, Tiziano Perea, and Roberto T. Leon	

Simulated Portfolio for the Seismic Risk Assessment of Composite Structures	548
A. Mühlhausen and U. E. Dorka	

Shear Connection

Shear-Bond Behaviour of Steel-Fibre Reinforced Concrete (SFRC) Composite Slabs with Deep Trapezoidal Decking: Experimental Study	561
Fairul Abas, Mark A. Bradford, Stephen J. Foster, and R. Ian Gilbert	
Analysis of Near to Free Surface Located Concrete Dowels in Composite Structures.....	581
J. Gajda and W. Kurz	
Composite Dowels as Shear Connectors for Composite Beams—Background to a New German Technical Approval.....	593
Karsten Kathage, Markus Feldmann, Maik Kopp, Daniel Pak, Max Gündel, Josef Hegger, and Joerg Gallwoszus	
Adhesives as a Permanent Shear Connection for Composite Beams.....	607
Marcus Kludka and Wolfgang Kurz	
Behaviour of Demountable Shear Connectors in Steel-Concrete Composite Beams.....	618
Dennis Lam, Xianghe Dai, and Eleonora Saveri	
Steel-Concrete Connections by Adhesion, Interlocking, and Friction for Composite Bridges under Cyclic Loading.....	632
Jean-Paul Lebet and Dimitrios Papastergiou	
The Effect of Carbon Nanotubes on the Headed Stud Shear Connectors for Composite Steel-Concrete Beams under Elevated Temperatures	648
Olivia Mirza, Kathryn Wilkins, Zhong Tao, and Brian Uy	
Predictive Models for the Stiffness of Vertical Screws as Shear Connection in Timber-Concrete Composite Floors.....	661
F. Moshiri, R. Shrestha, and K. Crews	
Numerical Study on the Behaviour of Composite Steel-Concrete Beams Utilising Innovative Blind Bolts	676
I. S. Wijesiri Pathirana, B. Uy, O. Mirza, and X. Q. Zhu	
Headed Shear Studs versus High-Strength Bolts in Prefabricated Composite Decks.....	687
Marko Pavlović, Milan Spremić, Zlatko Marković, and Milan Veljković	
Design Codes on Stud Shear Connectors for New Details	703
Chang-Su Shim and Dong-Wook Kim	

Slabs

Ultimate Strength of Continuous Composite Concrete Slabs.....	712
Alireza Gholamhoseini, Ian Gilbert, and Mark Bradford	
Evaluation of the Shear Force Behaviour of Composite Slabs.....	731
Simon Hartmeyer and Wolfgang Kurz	
Performance of Composite Slabs with Profiled Sheeting Using High-Strength Steel	744
Stephen Hicks, Audsley Jones, and Andrew Pennington	
Composite Slab Crack Widths Considering Shrinkage and Gravity Loading	754
Amir Khanlou, Gregory MacRae, Allan Scott, Stephen Hicks, Charles Clifton, Roberto Leon, and Alireza Gholamhoseini	
Longitudinal Shear Capacity of Composite Slabs—In Situ Tests on Slabs in Use for 35 Years and a Historic Review of Design Methods, Research, and Development.....	763
Markus Knobloch and Mario Fontana	
A Push Test Study on the Behavior of Post-Tensioned Composite Steel-Concrete Slabs	779
Mohammad M. Rana, Brian Uy, and Olivia Mirza	

**U.S. Composite Design Codes:
A Personal View of the Influence of Composite Construction Conferences**

Roberto T. Leon
Virginia Tech, Blacksburg, VA. E-mail: rleon@vt.edu

Abstract

Over 25 years have gone by since the first Composite Construction in Steel and Concrete Conference was organized in Henniker, New Hampshire (USA), and this seventh conference presents a great opportunity to assess the impact that this series of conferences has had on American composite construction codes. The intent of this paper is to provide a brief history of both modern composite member design provisions in the USA and how this conference series influenced their development. The latter include important direct impacts on the design provisions for shear studs, composite columns, and serviceability provisions, among others. Looking forward, the paper also gives some preliminary results on provisions for the determination of the equivalent stiffness of simply supported beams to be proposed for the 2016 edition of the AISC specification. It is written as a personal reflection and is not intended to represent the points of view of any of the organizations mentioned.

INTRODUCTION

The first Engineering Foundation Conference on Composite Steel and Concrete Structures was held at Western New England College in Henniker, New Hampshire (USA) on June 7-12, 1987. The Engineering Foundation conferences were an atypical American engineering event, as it consisted of morning and evening technical sessions, with the afternoon and late evenings dedicated to improvised, small group discussions on topics of interest to participants. The format encouraged open technical exchanges, while fostering the development of personal relationships. This first conference became the occasion for many of the most prolific composite construction users and researchers to meet and develop lifelong professional and social ties.

This first conference (CC I), and its six repetitions since, led to very close ties between the composite construction research communities in the USA, Europe, Canada, Australia and Japan and to fruitful collaborations between code writing committees in those regions. Figure 1 shows the location of the conferences, including its two predecessors focused on seismic

Table 1 - Conference participation

Year	Attendees	Countries	Papers
1987	96	17	63
1992	91	15	68
1996	100	18	72
2000	101	22	85
2004	80	18	70
2008	85	22	63

design, which had been held in Tokyo (CC -01) and Seattle (CC 0). Table 1 briefly summarizes the participation and contributions at the first seven conferences.

The first conference was organized primarily through the efforts of Dr. I. M. Viest (Viest, 2006) and Mr. Walter P. Moore, the past chairs of the composite construction committees for the American Institute of Steel Construction (AISC) and the American Society of Civil Engineers (ASCE), respectively. The conference came at a crucial point in the history of the development of modern design provisions for

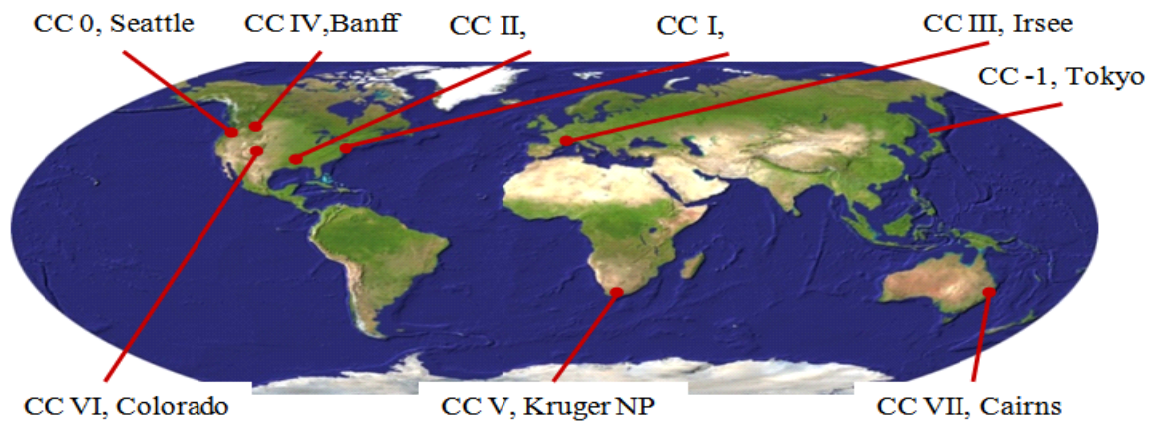


Figure 1 - Locations of Composite Construction in Steel and Concrete Conferences.

composite construction as both high rises utilizing this type of construction were beginning to be used in areas with high winds (**Figure 2**) and modern codes were being introduced.

In 1986 in the USA, AISC had issued its first version of a limit states (Load and Resistance Factor Design or LRFD) Specification, including its first set of provisions for the design of composite columns (AISC, 1986). The AISC Specification had included the design of encased composite beam and slab members since its 1936 edition, and had incorporated modern composite beams in its 1961 edition. On the other hand, design provisions for composite columns had been present only in the reinforced concrete design codes since the 1920s (ACI Committee on Building Regulations, 1910).

The design of composite columns within an American steel design specification was not considered until the seminal work of the Structural Stability Research Council Task Group 20 (Task Group 20, 1979). This group



Figure 2- Composite perimeter frame
(Houston, TX, early 1980s. © WPMoore)

published the first design rules for composite columns consonant with the existing steel column design curve and its associated stability provisions. From 1986, the AISC Specification has become the preeminent design guide for composite members in the USA (Hansell, 1978). For a complete history of American composite construction design provisions, the reader is referred to excellent articles by Furlong (Furlong 2012a,b).

Within a similar timeframe, across the Atlantic, CEN had published the first draft of the Eurocode 4 (CEN, 2009) in 1984, and work on the document was still ongoing under the leadership of J. Stark (Stark, 1998). The Henniker conference thus became one of the first venues in which the similarities and differences between the American and European codes in terms of the technical bases and aims of the documents, as well as their development processes, were widely discussed.

In the USA, the ASIC TC-5 Composite Construction subcommittee that developed the 1986 provisions was very small and dominated by very experienced multi-story building designers whose primary concerns were simplicity and transparency in the design rules and preservation of great design freedom for the structural engineer. Thus the approach was to keep strength design provisions to a minimum, to what has come to be known as “enabling legislation” language, and to explicitly exclude any provisions that would limit design flexibility, for example any specific limit for serviceability criteria. A number of important design issues are addressed in the Commentary to the Specification, which has no legal standing but is read carefully by designers as this is the primary source of background information on the code provisions. This approach was consonant with the desires of composite building designers who specialized in high-rise construction and the development of innovative structural schemes. In addition, it is consistent with the USA tradition that codes are developed by industry associations and not constrained in any way by government interference.

The aims and processes in the USA were in stark contrast to the EC4 development, where a much larger, younger and diverse group led by academics was tasked with developing a much more comprehensive, and some would say prescriptive, set of design rules. The EC4 development was also more constrained because it had to fit within a much larger and prescribed format not only for building codes but also for European normatives. As a young participant at the Henniker Conference, the author came away with the distinct impression that the initial drafts of EC4 could be considered revolutionary in that they went back to fundamental mechanics and rigorous reliability principles, while the American codes remained comparatively simplistic and more rooted in experimental data. A particularly memorable paper for the author was that on partial interaction by Robinson and Naraine (Robinson, 1988), which derived the sixth order differential equations for the case of partial interaction with uplift. The synthesis of this paper showed when uplift effects were important and was an excellent example of the uniform great quality and impact of all the papers at the first Conference. These characteristics remain the guiding principle for papers accepted at the Conferences.

The offline discussions that took place in Henniker regarding the scope and content of design codes were passionate and enlightening. The technical differences ranged

from small, as for the case of strength design of composite beams, to extreme, as was the case for composite decks and shear stud capacities. The lucid discussions between the leaders of the American and European groups led the author, and some of his American colleagues in attendance, to decide that there had to be some better middle ground. This view appeared to be shared by the large and strong Australian contingent present at that initial conference, and led to a long-term and fruitful American collaboration with the group at the University of Sydney led by Dr. R. Bridge.

In the last 20 years, the younger American group has taken over the reins of ASIC TC5 and implemented many of the EC 4, Canadian and Australian technical concepts into the AISC specification. This paper briefly summarizes some of the recent changes in the American codes that have had direct influence from the discussions that took place in the seven conferences on Composite Construction in Steel and Concrete held since 1987.

Contrary to the “pure” steel and reinforced/prestressed concrete codes where little American-European cross-pollination seems to have occurred, perhaps with the exception of truss models and anchorage to concrete, this paper intends to show that the conferences have had a permanent and important role in the development of composite construction provisions in the USA.

STRENGTH DESIGN OF COMPOSITE FLOORS

Design provisions for horizontal members can be roughly subdivided into three parts: design of the slab-deck system, design of the connectors (often shear studs) and the design of the concrete and steel portions of the beam. Although the Composite Conferences have always included a number of lively presentations on slabs and deck systems, the design of those components in the USA has been outside the purview of the AISC Specification. Initially those were based on an ASCE standard (ASCE 3-91, 1991) and lately on a new SDI specification (SDI, 2011). Therefore, this paper will not cover those aspects and the interested reader is referred to (Daniels, 1997) and (Abdullah, 2011) for more details on how this topic has been influenced by the Conferences. This discussion will limit itself to the latter two topics: composite beams and shear connectors.

Leon (Leon, 2001) identified a number of the areas in which the existing ultimate strength AISC specification needed improvement or clarifications. The first strength topic noted in that paper, and one that differentiates the American approach from the rest of the world, deals with the lack of a specific check for yielding of the steel beam under construction loads in the AISC specification. Although an explicit check is not included, this limit state was eliminated in the 1986 AISC Specification through the use of appropriate load factors (1.2 for both dead and construction loads) and resistance factors (0.85 for the steel portion of a composite beams and not the 0.9 usual for steel beams), calibrated to a fairly large construction load of 1.34 kPa including the load factor. In addition, the designer was required to include any additional load due to ponding of the concrete in the design of the steel beam. The problem was that many designers were unaware of these assumptions and were using significantly lower construction loads and load factors, and not accounting for

ponding. As with many situations of this type, the solution was to include detailed commentary language in the 2005 AISC Specification edition discussing the issue and alerting designers to the assumptions. In addition, the commentary warned designers as to the requirement of considering the effect of cambering, which will also affect the ponding calculations.

A much larger problem, and one that had been widely discussed since the first Conference, was the strength values for shear studs under different loading and geometry constraints (Easterling, 1993). The American specification had always assumed a design value based on the concrete strength and capped by the ultimate strength in tension of the stud. Those values were based primarily on pushout tests that did not separate the contributions of different force transfer mechanisms and all relevant testing parameters. The values in the AISC Specification were known to be high, particularly with respect to studs in a “weak” position (Rambo-Roddenberry, 2002). Although there had not been any documented failures, or even problems, with the use of these values, the extensive discussion at the Conferences with European and Australian colleagues led AISC TC5 to the decision that there was irrefutable evidence (Johnson, 1997) that the values should be adjusted. In a two-step process, through the 2000 and 2005 editions, the AISC stud strengths have been adjusted downward, although they still remain slightly higher than those used by other specifications. This is in spite of the fact that the American specification does not require transverse reinforcement below the head of the stud as other codes do (Kemp, 1997), another important difference that remains unresolved.

Leon (Leon, 2001) also cited three other important strength criteria in which the American specification differed substantially from similar documents:

- Horizontal shear in the slab: Current AISC LRFD provisions do not include a check on the horizontal shear strength of the slab. For the case of girders with decks with narrow troughs or thin slabs, shear strength of the slab may govern the design. Although the configuration of USA decks tends to preclude this mode of failure, it is important that it be checked if the force in the slab is large. This is an issue that is now discussed in the AISC Commentary as a result of the discussions at the conferences.
- Rotational capacity of hinging zones: Another area where American codes differ from other international design guides is in the area of required, or probably more accurately “implied,” rotational capacity. Use of plastic design principles and redistribution is predicated on the capacity of the system to deform through very large rotations, as is the use of low amounts of shear connection. The American codes are generally silent on this issue as only a 10% redistribution is commonly used, and that can be achieved by almost any section with reasonable bracing and local buckling limits.
- Minimum amount of interaction required: Currently there is no lower bound in the AISC specification, although its available design aids limit interaction to 25%. Current American practice leads to economic designs at low degrees of interaction (25%-35%), well below those of most other codes. This item has been discussed by TC5 extensively over the past three years, and it is likely that in the

2016 AISC edition minimum values of interaction will be specified. The changes are being made not because failures have been observed, but because consistency between design models and design provisions is desirable.

STRENGTH DESIGN OF COMPOSITE COLUMNS

At the first Conference, the author was introduced to the simple and elegant Eurocode formulation for composite column section strength (Roik, 1992). By the early 1990s, it was clear that the 1986 AISC provisions for composite columns were less reliable than the code intended (Lundberg, 1996). There were multiple reasons for this, including the decision to treat composite columns as a variation of a steel one, without regard to the volumetric ratio, confinement, initial imperfections, residual stresses and long-term effects. A concerted effort through the next 10 years (Leon, 2007) resulted in improved provisions in the 2005 AISC Specification (Leon, 2008) that mirror the Eurocode sectional strength provisions and remove many of the inconsistencies between AISC and ACI sectional strength provisions. This is a case where the American specification directly borrowed from European ones.

Stability considerations are another area where extensive interactions at the Conferences with European and particularly Australian researchers led to extensive changes in the American steel code. Beginning with the concepts of nominal loads to capture stability effects that were discussed at the Conferences, an ASCE committee composed of American and Australian researchers planted the seeds for the adoption of the current AISC Direct Design method (Length, 1997). These discussions have led to extensive research on the best equivalent rigidity values, particularly for slender sections (Perea, 2014), with revisions in both the 2010 and 2016 editions to the original equations proposed in the 2005 AISC Specification (Denavit, 2015). These research efforts testify both to the robustness of composite columns and the accuracy of current analytical models. Figure 3 shows a comparison for Perea's tests (Perea, 2014) of cyclic biaxial strengths measured (dots) vs. the proposed interaction surface.

As a follow-up to the large changes in the AISC Specification for composite columns introduced in 2005, including significant relaxation of the local buckling requirements for tubes, the latest AISC Specification has also been considerably expanded to permit the use of non-compact and slender steel sections in concrete-filled tubes (Lai, 2014). It is expected that with the 2016 version, the AISC Specifications will have the most modern and flexible design provisions for composite columns.

An issue that will remain unresolved in the American codes even in the 2016 editions is how to handle stiffness reductions due to long-term effects. Although the American reinforced concrete design provisions have long had a substantial reduction on stiffness if large permanent loads are present, the AISC ones have never incorporated such provisions. Changes in construction practice and materials have considerably reduced the impact of creep and shrinkage in the last 25 years, and there is scant experimental data on which to base modern provisions.

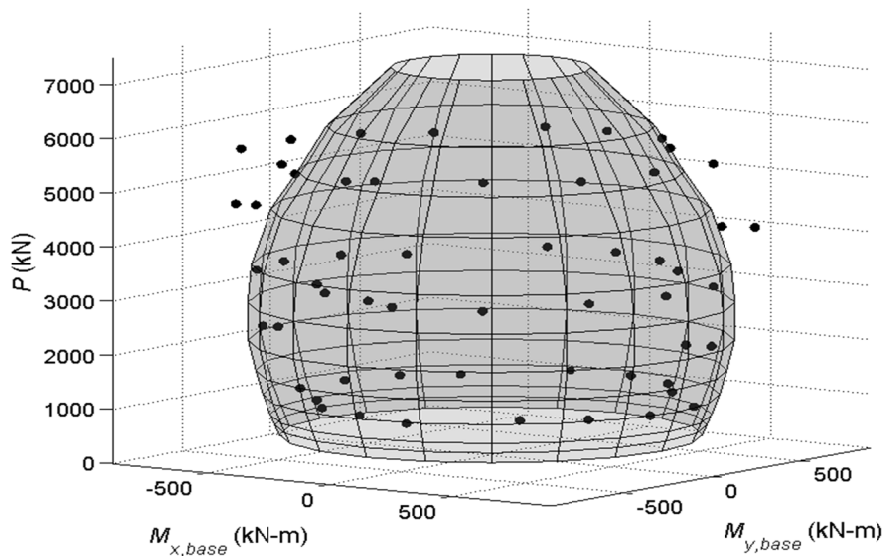


Figure 3 - Strengths measured during large-scale concrete-filled tube beam-column tests.

SEISMIC DESIGN

Seismic design provisions in the USA originated with an effort by the Building Seismic Safety (BSSC) in the early 1990's and culminated with the publication of the proposed provisions as Part II of the AISC Seismic Provisions (AISC, 1997). The work was heavily influenced by the interaction with Japanese researchers at the Conferences and its predecessor meeting (Roeder, 1985), as well as by the 1994 Northridge earthquake and its effects. This effort was led by Dr. Viest and included some of the most capable and well-known designers of composite structures in the USA. This work culminated not only in the publication of design provisions, but also the publication of a seminal book on composite construction for buildings in the USA (Viest, et al., 1997). In an interesting reversal of the influences noted previously, it appears to the author that the sections for composite construction in Eurocode 8 have borrowed considerably from American sources.

SERVICEABILITY

As noted earlier, American Specifications do not contain specific limits for serviceability limit states. This does not mean that serviceability criteria are not considered, only that the designer is free to set whatever limits are appropriate. Chapter L of the AISC Specification requires designers to consider all types of serviceability conditions, including the effect of creep and shrinkage on composite floor systems beginning with the 2005 edition. This requirement was introduced through the use of a "User Note" in the Specification, another innovation in the 2005 edition. "User notes" are non-mandatory clauses included to provide guidance within the Specification. In general, they are meant either to highlight issue that designers must account for or simple shortcuts in design that accelerate the design process. The

introduction of the long-term effects is considered by the author a victory as such provisions had been routinely dismissed in the past by the Specification Committee.

Another area where the American and European provisions diverge is in the calculation of the moment of inertia for composite beams. The 2005 and 2010 AISC Specification Commentary Section I3 provides three methods to calculate moment of inertia of composite beam: equivalent moment of inertia, lower bound moment of inertia and effective moment of inertia. For fully composite beams, the equivalent moment of inertia, I_{equiv} , is the transformed moment of inertia calculated utilizing the modular ratio (E_s/E_c) and elastic analysis. From short-term deflection tests, the effective moment of inertia, I_{eff} , has been found to range from 70% to 85% percent of that calculated based on I_{equiv} . Therefore, for realistic deflection calculations, it is recommended that I_{eff} be taken as $0.75I_{equiv}$. The Commentary does not favor one of the procedures, which in some cases can give very different results.

The effective moment of inertia for cases where elastic properties of partially composite beams are needed, which may be approximated by:

$$I_{eff} = I_s + \sqrt{\frac{\sum Q_n}{C_{f2}}} (I_{tr} - I_s) \quad (\text{Eq. 1})$$

where I_s is the moment of inertia for the structural steel section, I_{tr} is the moment of inertia for the fully composite uncracked transformed section, $\sum Q_n$ is the strength of shear connectors between points of maximum and zero moment, and C_{f2} is the compression force in concrete slab for fully composite beam, the smaller of $F_y A_s$ and $0.85 A_c f_c$.

The Lower Bound moment of inertia (I_{LB}) is an alternative of equivalent moment of inertia, and is based on the section properties at ultimate. Thus, contradictorily, an ultimate strength force distribution is used to calculate an elastic property. There were two reasons for suggesting this approach: (a) the location of the neutral axis could be calculated as part of the computations for ultimate strength (see Eq. 2 which is needed to calculate the ultimate strength by Eq. 3) and (b) the differences in the calculated moments of inertia by either the lower bound or the equivalent moment of inertia approach gave similar results (within 15%) for a large range of typical cross sections. The I_{LB} is calculated as follows

$$Y_{ENA} = [A_s d_3 + (\sum Q_n / F_y)(2d_3 + d_1)] / (A_s + (\sum Q_n / f_y)(2d_3 + d_1 - Y_{ENA}))^2 \quad (\text{Eq. 2})$$

$$I_{lb} = I_s + A_s (Y_{ENA} - d_3)^2 + \left(\frac{\sum Q_n}{f_y} \right) (2 \cdot d_3 + d_1 - Y_{ENA})^2 \quad (\text{Eq. 3})$$

where d_1 is the distance from the centroid of the longitudinal slab reinforcement to the top of the steel section, and d_3 is the distance from the centroid of the concrete force to the top of the steel section.

The reasons for having three methods in the AISC Commentary are historical and confusing, so an effort has been recently undertaken to develop a more rational

approach or to select a single technique to recommend to designers. A database of 122 tests for which reasonably clear load-deflection, material properties, dimensions and other important data could be found was developed. Figure 4 shows the distribution of degree of composite action ($n = \Sigma Q_n / \min(F_y A_s, 0.85 A_c f'_c)$) vs. the beam depths; it is obvious that much of the data is for very shallow beams, and that any scale effects may not be properly reflected for many of the much deeper composite beams in use today.

Since in most cases the tests were to verify ultimate strength, initial elastic stiffness are seldom reported. For most cases the load-deflection curves were enlarged and the slope to 40% of ultimate approximated by hand methods (Zhao, 2013). It is recognized that this introduces both aleatoric and epistemic errors into the data set. The error was estimated at about $\pm 10\%$ and was considered acceptable as the intent is to differentiate between different approaches for design and not to develop a well-calibrated analysis procedure.

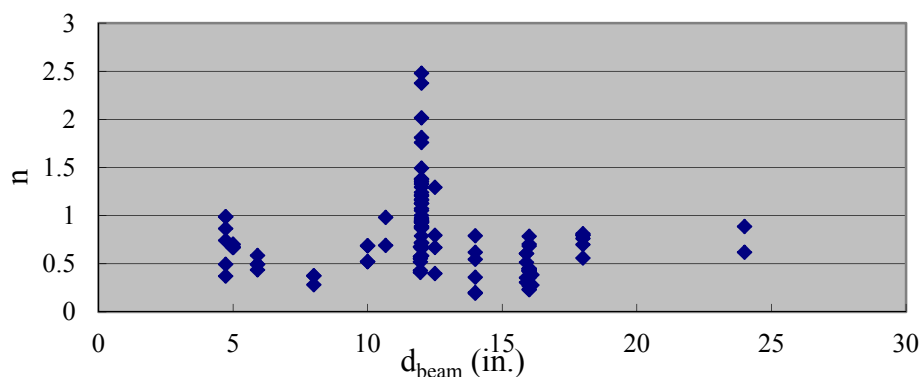


Figure 4 - Degree of composite action (n) vs. beam depth for beams in database.

Five methods for computing deflections were examined: the conventional AISC effective and lower bound approaches described above, the Newmark method (Newmark, 1951), the Cosenza-Mazzolani method (Cosenza, 1993) and Eurocode method (CEN, 2009). The Newmark method was considered as the more “exact” approach for beams with partial interaction, while the Cosenza-Mazzolani method was taken as a simplified European approach for comparison. Figure 5 shows a typical comparison of the results. As expected the lower bound approach provides a very conservative result. The Cosenza-Mazzolani one overestimated the stiffness, with the Newmark approach providing the best match, followed by the I_{eff} and the Eurocode. The overall results are summarized in Table 2, which shows the measured to predicted ratios and their standard deviations.

For the AISC formulas, comparisons indicate that the approach using an equivalent moment of inertia, I_{equiv} , results in a prediction of the deflections roughly equivalent to the average (50%) deflection for the 122 tests that were examined. On the other hand, the use of the I_{LB} corresponds roughly to the mean plus one standard deviation (84%). Based on these results, the use of the I_{LB} approach is considered as the best approach to live load deflection calculations for composite beams.

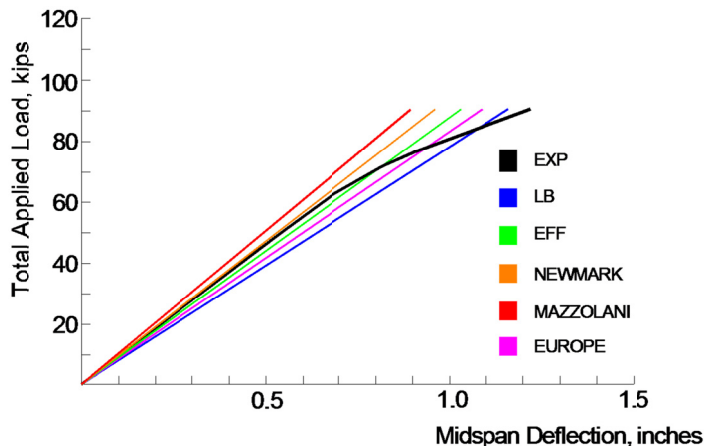


Figure 5 - Comparison of different methods for calculating composite beam initial stiffness.

Table 2 - Summary of comparisons of elastic stiffness of simply-supported composite beams

Calculation method	Mean	Standard deviation
Lower Bound	1.09	0.19
Effective	1.00	0.16
Newmark	0.99	0.15
Cosenza-Mazzolani	0.93	0.15
Eurocode	1.04	0.17

It is interesting to note that while many of the tests were supposed to mimic a distributed load, the best correlations were found when the tests were segregated by the number of point loads being used to model the distributed load. In fact, for specimens with four or more point loads, which correspond loosely to a uniformly distributed load, the best predictions were given by the Cosenza-Mazzolani approach. While better fits were found by doing multiple regression analyses, the formulas obtained did not correlate well with the physical models and thus were abandoned.

SUMMARY

This paper presents a brief personal reflection on the great influence of the Composite Construction in Steel and Concrete Conference series on the American design provisions. Beyond the purely technical matters, however, the series had a profound influence on the author's approach to research and his professional relationships. The Conferences have been an integral part of his professional life. As mentioned in the oral presentation in Cairns, the reason for traveling a long ways was both to renew and strengthen the personal acquaintances as well as to steal whatever new valuable ideas were brought to the conference by unsuspecting participants.

REFERENCES

- Abdullah, R., and Easterling, W.S. "Elemental Bending Tests and Modeling of Shear Bond in Composite Slabs." *Composite Construction in Steel and Concrete VI*. Reston, VA: ASCE, 2011. 138-150.
- ACI Committee on Building Regulations. "Standard Building Regulations for the use of Reinforced Concrete." 1910.
- AISC. *Seismic Provisions for Structural Steel Buildings*. Chicago, IL: AISC, 1997.
- AISC. *Specification for Structural Steel Buildings - Load and Resistance Factor Design*. Chicago: AISC, 1986.
- ASCE. *Composite Construction in Steel and Concrete*. Ed. D.L. Buckner and I.M. and Viest. New York: ASCE, 1988.
- ASCE 3-91. *Standard for the Structural Design of Composite Slabs (with Comentary)*. New York, NY: ASCE, 1991.
- CEN. EN 1994-1-1: *Design of Composite Steel and Concrete Structures - Part 1.1: General Rules and Rules for Buildings*. Brussels, 2009.
- Cosenza, E. and Mazzolani, S. "Linear Elastic Aanlysis of Composite Beams with Deformable Connectors: Exact Solutions and Differential Result (in Italian)." *First Italian Workshop on Composite Construction*. 1993. 1-15.
- Daniels, B.J. and Easterling, W.S. "Shortcomings in Composite Slab Design." *Composite Construction in Steel and Concrete II*. New York, NY: ASCE, 1997. 370-379.
- Denavit, M., Hajjar, J.F., Perea, T., and Leon, R.T. "Stability Analysis and Design of Composite Structures." *J. of Structural Engineering* (2015): (under review).
- Easterling, S.W., Giibings, D.R., and Murray, T.H. "Strength of Shear Studs in Steel Deck on Composite Beams and Joists." *AISC Engineering Journal* (1993): 44-55.
- Furlong, R.W. "Design Rules for Steel-Concrete Composite Columns: 1910 to 1963." *Concrete International* February 2012: 41-47.
- Furlong, R.W. "Design Rules for Steel-Concrete Composite Columns: 1971 to 2011." *Concrete International* April 2012: 61-66.
- Hansell, W.C., Galambos, T.V., Ravindra, M.K., and Viest, I.M. "Composite Beam Criteria in LRFD." *J. of the Structural Div., ASCE* 104.9 (1978): 1409-1426.
- Johnson, R.P., and Yuan, H.,. "Shear Resistance of Stud Connectors with Profiled Sheeting." *Composite Construction – Conventional and Innovative*. Zurich (CH): IABSE, 1997. 555-560.
- Kemp, A.R., Trincherro, P.E. "Horizontal Shear Failures Around Connectors Used With Steel Decking." *Composite Construction in Steel and Concrete III*. New York: ASCE, 1997. 104-118.
- Lai, Z., Varma, A. H., and Zhang K. "Noncompact and slender rectangular CFT members: Experimental database, analysis, and design." *J. of Constructional Steel resaerch* 101 (2014): 455-468.
- Length, ASCE Task Committee on Effective. *Effective Length and Notional Load Approaches for Assessing Frame Stability: Implication for American Steel Design*. New york: ASCE, 1997.

- Leon, R. T., Kim, D. K., and Hajjar, J. F. "Limit State Response of Composite Columns and Beam-Columns: Part I: Formulation of Design Provisions for the 2005 AISC Specification." *AISC Engineering Journal* 44.4 (2007): 341-357.
- Leon, R.T. "A Critical Review of Current LRFD Provisions for Composite Members." *Proceedings of the Annual Technical Session, Structural Stability Research Council*. Gainesville, FL: U. of Florida, 2001. 189-208.
- Leon, R.T. and Hajjar, J.F. "Limit State response of Composite Columns and Beam-Columns – Part 2: Application of Design Provisions for the 2005 AISC Specification." *AISC Engineering Journal* 45.1 (2008): 21-46.
- Leon, R.T., D.K. Kim and J.F. and Hajjar. "Limit State Response of Composite Columns and Beam-Columns - Part 1: Formulation of Provisions for the 2005 AISC Specification." *AISC Engineering Journal* 44.4 (2007): 341-358.
- Lundberg, J.E., and Galambos, T.V. " Load and Resistance Factor Design of Composite Columns." *Structural Safety* 18.2/3 (1996): 167-177.
- Newmark, N.M., C.P. Siess and I.M. and Viest. "Tests and Analyses of Composite Beams with Incomplete Interaction." *Proc. of the Society for Experimental Stress Analysis* 9.1 (1951).
- Perea, T., Leon, R. T., Hajjar, J. F., and Denavit, M. D. "Full-Scale Tests of Slender Concrete-Filled Steel Tubes: Interaction Behavior." *Journal of Structural Engineering* 140.9 (2014).
- Rambo-Roddenberry, M., et al. "Performance and Strength of Welded Shear Studs." *Composite Construction in Steel and Concrete*. Reston, VA, 2002. 458-469.
- Robinson, H. and Naraine, S.K. "Slip and Uplift Effects in Composite Beams." *Composite Construction in Steel and Concrete*. New York, NY: ASCE, 1988. 487-497.
- Roeder, C.W. *Composite and Mixed Construction*. New York: ASCE, 1985.
- Roik, K. and Bergmann, R. "Composite Columns." Harding, J. E., and Bjorhovde, R. (eds.). *Constructional Steel Design: An International Guide*. London: Elsevier Science Publishers, 1992.
- SDI. ANSI/SDI C-2011: Composite Steel Floor Deck-Slabs . Glenshaw, PA: Steel Deck Institute, 2011.
- Stark, J. "Eurocode 4: A European Code for Composite Construction." *Composite Construction in Steel and Concrete*. ASCE, New York, 1998. 37-49.
- Stark, J. "European Standards for Composite Construction." *Composite Construction in Steel and Concrete IV*. Reston, VA, ASCE, 2002. 828-839.
- Task Group 20, SSRC. "A Specification for the Design of Steel-Concrete Composite Columns." *AISC Engineering Journal* 16.4 (1979).
- Viest, I.M. *An Immigrant's Story*. Bloomington, IN: Xlibris, 2006.
- Viest, I.M., et al. *Composite Construction: Design for Buildings*. New York: McGraw-Hill, 1997.
- Zhao, H. Load-Deflection Behavior of Simply Supported Composite Beams in the Elastic Range. M.S. Report. Blacksburg: Virginia Tech, 2013.

New Langensand Bridge in Lucerne, Switzerland: Evolutionary System of a Composite Structure

Gabriele Guscetti¹; Claudio Pirazzi¹; Jérôme Pochat¹; and Reto Cantieni²

¹Ingeni SA, CH-1227 Carouge, Switzerland. E-mail: gabriele.guscetti@ingeni.ch

²rci dynamics, Structural Dynamics Consultants, CH-8600 Duebendorf, Switzerland.

E-mail: reto.cantieni@rcidynamics.ch

Abstract

The urban development of the city of Lucerne required the replacement of the existing Langensand road bridge by one designed according to modern standards of urban mobility. The bridge's shape is the result of a synthesis between function, construction method, structure, and the urban context (extremely dense environment and several complex constraints). The bridge crosses 79.7m with one single span girder over 11 railway lines. Its composite structure has an extreme slenderness of about $L/37$. The paper describes the advantages and problems of a steel-concrete composite construction especially in regard to its structural system, and the evolution during the construction phases, and to its slender and flexible structure. The paper will compare and highlight the theoretical approach (hypothesis and numerical models for static and dynamic actions) with the results of in situ tests for the two principal states of the structure: firstly, the half bridge and secondly, the final connected bridge.

INTRODUCTION

The Langensand Bridge, located in the city of Lucerne in Switzerland, crosses over a very dense rail network near the central station and links the centre of the city with a new quarter which is being highly developed (Figures 1 and 2). Its location is very strategic; the bridge is taken every day by over 20000 vehicles of which are 1000 public transport buses. Moreover, 1200 trains pass under the bridge every day.



Fig. 1 - City of Lucerne, urban context



Fig. 2 - New Langensand bridge

Therefore, the development of the city required replacing an obsolete concrete bridge dating from 1938 which no longer met the increasing needs of pedestrian and bike mobility as well as road and rail traffic (Figure 3). The project of the new bridge is the result of an international competition in 2004 that our company, Ingeni structural engineering, won with the Swiss architects Brauen and Wälchli. The construction work started in 2008 and finished at the end of 2009. The bridge was put in service at the beginning of 2010. In 2011, this construction work received the Swiss Steel Award.

Due to its strategic location and the development of the mobility needs, the demands of the client were strict and clear. Firstly, it was required to keep the exact same location of the existing bridge. Secondly, the capacity needed to be doubled in terms of pedestrian, bicycle and road traffic (Figure 4). Thirdly, the new bridge had to cross the eleven tracks without any supports over a span of 80 m. And finally, the construction could under no circumstances interrupt the rail and road traffic. In addition there were numerous restrictions to continually guarantee the safety of users and workers.



Fig. 3 - Existing old bridge

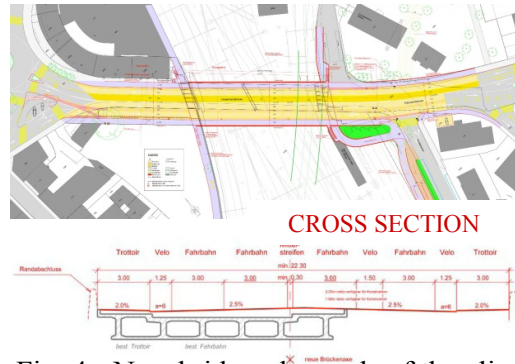


Fig. 4 - New bridge: demands of the client plan view and cross section

DESIGN

The former bridge was a concrete structure made from multi-box girders (Figure 5). It was important to understand this structural system in order to take advantage of it during the building stages where, in this project, it would be progressively dismantled to allow for the new construction. The requirements of the competition led to the placement of temporary propping in some areas between the railroad tracks and allowed the construction company to organise the site installation in the two adjacent areas (Figure 6).

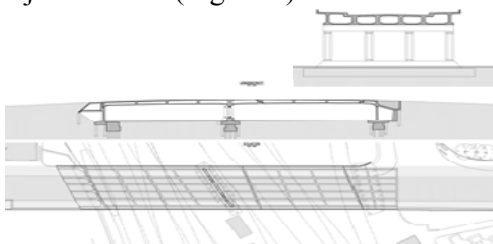


Fig. 5 - Concrete structure of the former and bridge

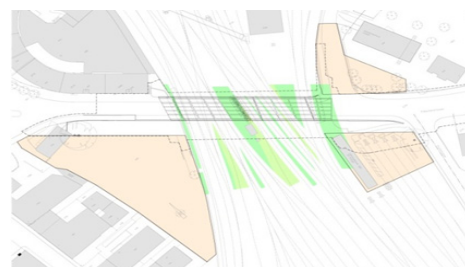


Fig. 6 - Available areas for work site temporary propping

Thus, the demands and constraints were very exacting and the context of the site very complex and dense with constant flux to manage. This notion of flux guided initial reflections around the design of the bridge (Figure 7). Moreover, the goal was to have a simple clean design in complete contrast to the complexity of the world of the trains below all in harmony with the surrounding area of the city.

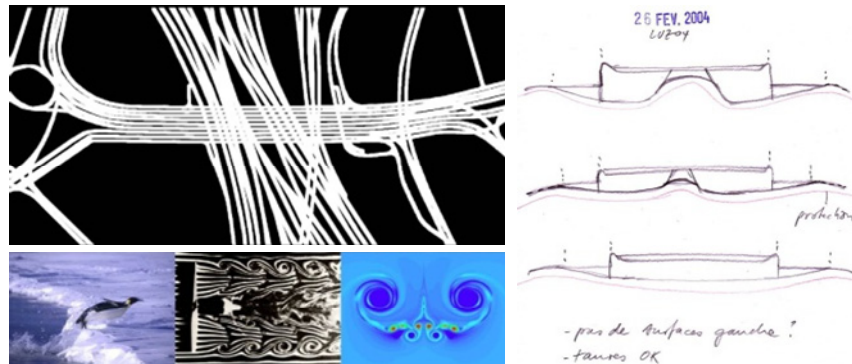


Fig. 7 - Notion of flux, design drafts

From a formal point of view, the project is the result of a synthesis between functionality, construction methods, structural behaviour and the urban context which it fits into. The chosen shape is defined by the space between the line of the limit of the free area required by the railway company and the longitudinal profile of the road. This profile is given by the maximal slopes allowed and its minimal vertical radius (Figure 8). In this way, the bridge is inserted between these limits very precisely.



Fig. 8 - Profile constraints and shape of the bridge

The resulting shape follows the movement of the bending moments of a simple beam with the maximal height at mid-span. Based on this principle, the outcome was a simple beam structure with a span of 79.7m and the maximal height of 2.6m. On the bearings the height is only 1.2m (Figure 9). This gives a very slender bridge with a ratio - length by height - of about 37. Such slenderness makes the bridge sensitive to deflections and vibrations. The cross section was imagined in terms of functional and constructive considerations (Figure 10). For functional purposes, the road from the pedestrian walkway and bike line was separated. This gave a curved longitudinal profile for the former and a flatter profile for the latter. Constructively, a particular composite structural system was chosen which is composed of two steel box girders covered by a concrete slab.

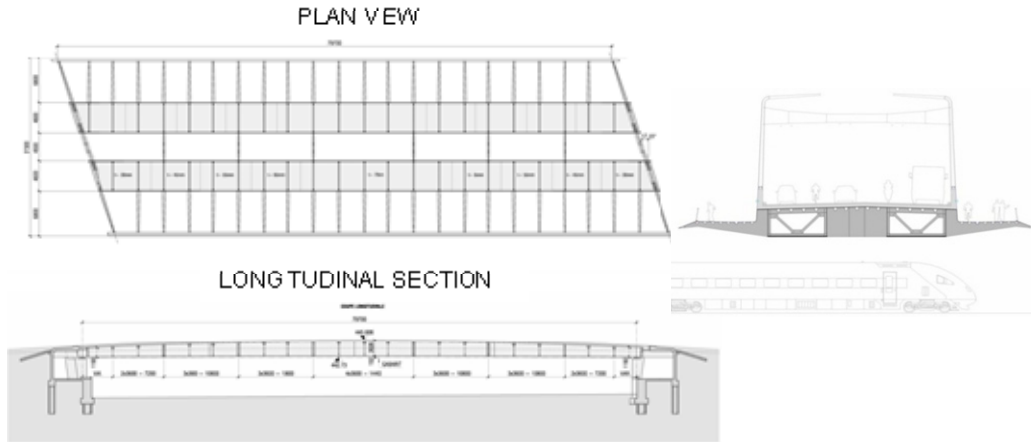


Fig. 9 - Plan view and longitudinal section

Fig. 10 - Cross section

This particular cross section allowed for the bridge to be built up in two half parts enabling each part to be structurally autonomous and functional during the working phases. The two steel boxes were launched over the railway tracks with an interval of about one year so as to never stop the road and rail traffic as required by the client. In the plan view (Figure 9), for geometrical reasons, the longitudinal axis of the bridge can't be placed perpendicular to the direction of the railways. Therefore, the bearings of the bridge are at an angle of about 17 degrees. This feature as well as the high torsion rigidity of the box girder, makes an important difference to the support reactions. A special process adjustment was necessary using lifting and measuring pot bearings. Six diaphragms link the two box girders to finally obtain the complete structure of the bridge with, naturally, better behaviour than each single girder. A series of cantilever beams with an impressive span of 6.8m and spaced out over 3.6m, are laterally fixed to the girders to support the pedestrian walkway and bike lane. Actually, the geometry of the bridge is quite complex. Along the bridge axis, each cross section is different from the one next to it. Figure 11 shows different cross sections in the middle of the bridge with and without a diaphragm and another one at the abutment. Furthermore, the manufacturing and the assembly on site (completely made by welding) were complex due to the limits of transportation and the methods and stages of construction (Figure 12). In particular, the box girder (4.6m wide) was manufactured in two parts in a "C" shape, each of a length of about 20m, and then welded together on site.

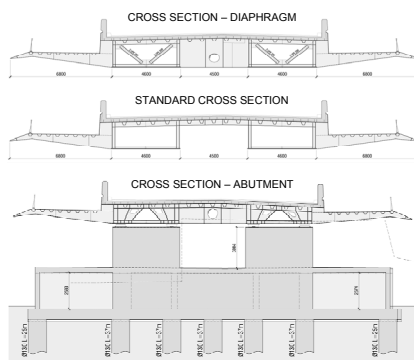


Fig. 11 - Different cross sections

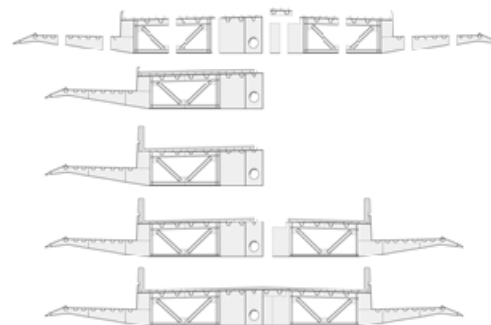


Fig. 12 - Manufacturing and assembly diagram

The concrete slab was added after the launching and, due to the use of the steel orthotropic deck, no concrete form was required. Not only do the steel deck and its cantilever part have a structural function but they create a clear and safe separation between the bridge site and the railway tracks below. In this way, all the work could be carried out without incident. The steel box girders, associated with the 24cm thick concrete slab, work as a composite structure. This composite behaviour also exists in the longitudinal way for the overall system as well as locally for the concentrated loads. The layer of concrete slab considerably increases the flexional rigidity by about 40% more than the steel section alone. To minimise the maintenance of the bridge during its life cycle, we used weathering steel for all the construction. The exposed upper parts of the cantilever are protected by paint and asphalt.

CONSTRUCTION STAGES

The guiding principle of construction was one of the most important elements which influenced the design and the constructive choices of the bridge. During the construction process we had different situations to deal with, in chronological order as follows:

1. one half of the steel bridge under construction and beside it the existing bridge partially dismantled, but still in use
2. one half of the composite bridge in use and the existing bridge being dismantled
3. one half of the composite bridge in use and the second half of the steel bridge under construction
4. one half of the composite bridge in use and the second half of the composite bridge under construction
5. the complete composite bridge in use made by joining together the two halves.

This method of building in two parts and then joining them together as one was applied to all the elements of the construction: foundation piles, abutments, bearings, expansion joints, waterproofing, road surface, finishing and equipment. The limited space of the construction site prevented us from assembling the entire half bridge before launching it over the railway as one piece. Thus, each half steel bridge was launched in four phases by 20m lengths (Figure 13). A complete phase (assembling, welding and launching) lasted three weeks. In view of the intensity of the rail traffic, the launching was carried out during the night, at a speed of about 8 to 10 meters per hour.

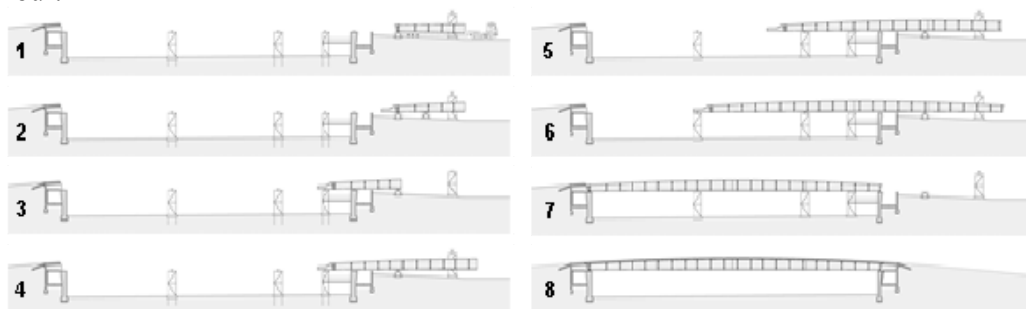


Fig. 13 - Launching phases

NUMERICAL MODELS

In its completed state, the bridge looks deceptively simple, but its clean appearance hides the technical issues had to be solved. One of the most challenging problems of this structure is its flexibility due to its great slenderness. This makes it susceptible to large deflections as shown in Figure 14. The total deflection between the initial cambered geometry, given at manufacturing in the shop, until the serviceability limit state, during the life cycle, is about 800mm. This value represents a significant ratio of one hundredth (1/100) of the span. Moreover, the total deflection is a sum of successive deflections in relation to the history of construction where the structure progressively evolves from a half steel bridge to a complete composite bridge.

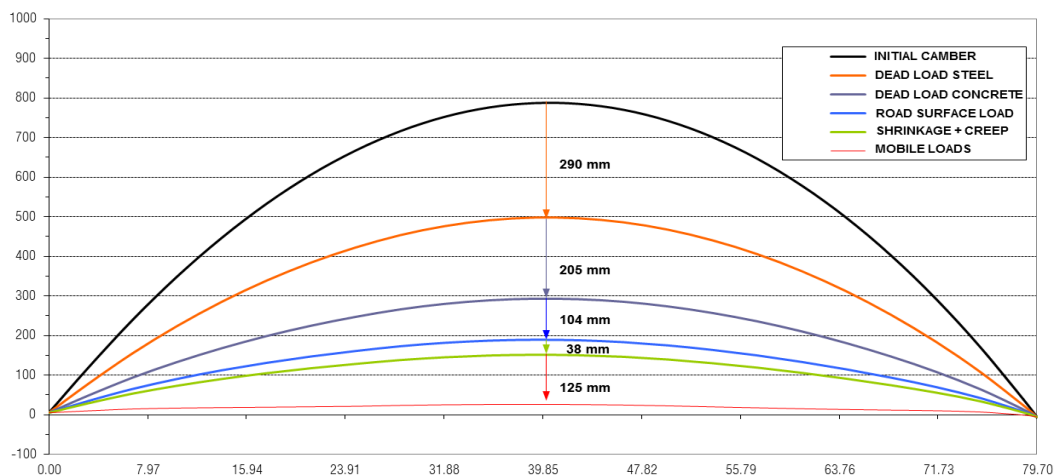


Fig. 14 - Camber and deflections of the half bridge

As a result, it was imperative that the numerical model be as close as possible to the real behaviour of the structure, in particular, to be able to manage the joining of the two half composite bridges. This final operation was, without a doubt, the most delicate phase of the construction. Therefore, to have complete mastery of the structural behaviour, different numerical models were used (Figure 15). From the simplest finite element model, (FEM) using bar elements, to the most sophisticated model using shell elements. All of these models followed the sequence of construction stages and the evolution of the structural system. This process of modelling provided much information about the sensitivity of some design parameters and finally allowed for design at the ultimate and the serviceability limit states. Above all, this process defined, in a most reliable way, the evolution of the deflections and thus the camber of the steel structure for manufacturing.

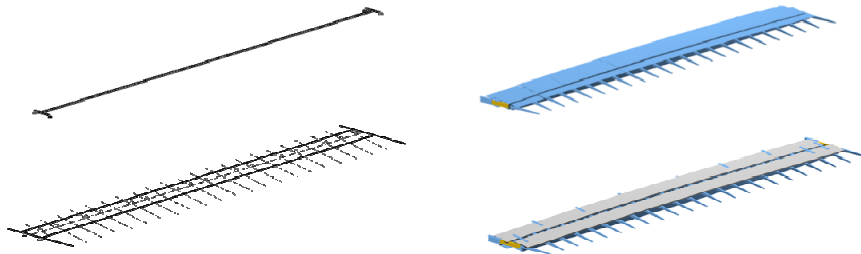


Fig. 15 - Finite element models

As mentioned above, in the design stage, the solution to launch a steel bridge with a complete orthotropic deck was selected (Figure 16). This was essentially for security reasons regarding the railway but not only. This steel structure allowed the engineers to keep the deflections (due to its dead weight and that of the concrete slab) under control. Actually, in this phase, the steel structure worked as a simple beam with a span of 80m. Temporary supports were not possible due to the extremely poor soil conditions (lakeside deposit) and the impossibility of boring or driving foundation piles between the railway tracks. Therefore, the risk of significant soil packing was too high.

The composite behaviour of the longitudinal system is well known. In order to evaluate the local structural behaviour of the steel deck under concentrated traffic loads, the composite orthotropic deck was modelled with finite elements, using the program Axis VM. In order to optimize computing capacity, only a symmetric part of the orthotropic deck was taken into account, considering structural continuity by appropriate boundary conditions (Figure 17). The steel structure was modelled by 2D shell- and 1D rib-elements and the concrete layer by 2D shell elements. For the shear studs as structural connection between both layers, linear spring elements were used. The sensitivity of the system was analysed by varying both, elastic modulus of the concrete and the spring constant. The calculation showed that the steel sheet is capable to assume at the same time the stresses of the longitudinal system and those due to the local concentrated loads. As a result, the bottom layer of reinforcement bars was not put on.



Fig. 16 - Steel deck

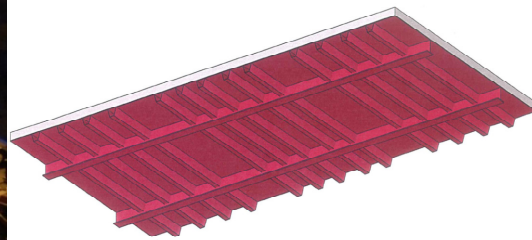


Fig. 17 - FEM of the composite deck

During the construction process, the geometry of the structure was regularly checked. A good correlation between the numerical model and the final construction was observed. A maximal difference of 35mm was measured (Figure 18). As a result, the position of the two half bridges was very close to the theoretical values. In the design stage, to be sure to join them, the engineers planned to adjust the two parts of the bridge using hydraulic jacks. They estimated any corrections to be plus or minus 50mm. For different practical reasons, the two parts were adjusted ballasting the second half bridge with tanks filled with water. In that way, the joining operation was carried out perfectly.

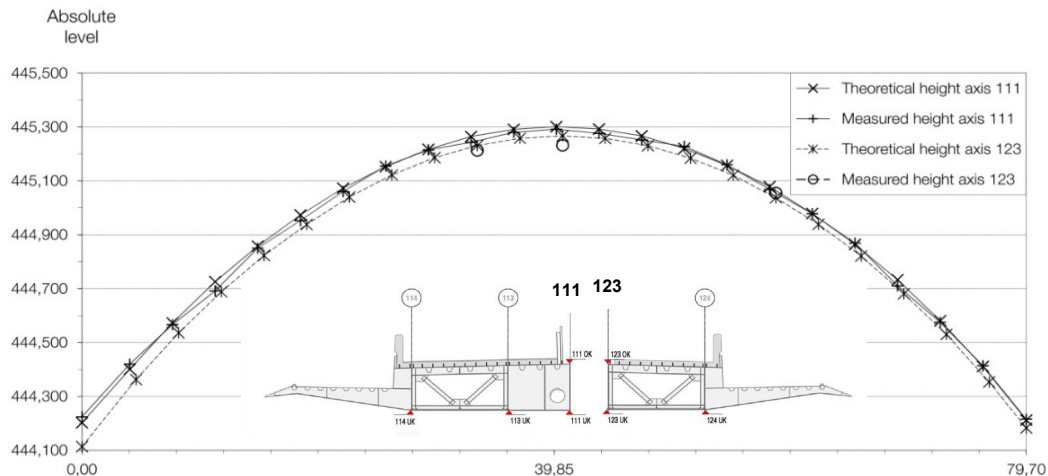


Fig. 18 - Geometry check at the linking axes 111 and 123

Before putting into service the first half bridge and the completed bridge, static load tests were made by the Ecole Polytechnique Fédérale de Lausanne (EPFL) [Goulet and all]. Several load cases were carried out to test the flexional and the torsional response of the structure. The results of the load tests confirmed that the behaviour of the structure conforms to values of the numerical model. The measurements were systematically lower than the calculated values of an average of 10%. This was for the two tests, the half bridge and the final bridge. This result was especially important because the reserve of the deflection under the mobile load action is very small. For the serviceability limit state, a deflection of 125mm was calculated with a reserve of 25mm of the limit of the free area required by the railway company. Therefore, the bridge has one bigger reserve of deflection that is a positive aspect.

APPROACH OF DYNAMIC PROBLEMS

It is possible that the slenderness of this bridge made it sensitive to dynamic problems especially because there is a mixed usage of vehicles and pedestrians (on cantilevered walkways of 6.8m). In the design stage, this problem was approached with a very simple solution based on a model of a spring submitted to a force of two times 100kN, which is representative of a weight of a truck's rear axle. An overrun of the limit acceleration of 0.8m/s^2 was detected for a specific position of two trucks in phase with the half bridge. The risk to have perceptible accelerations was accepted in this temporary phase. For the completed bridge, the same simple model showed that the behaviour would be better never overrunning the acceleration limits. Nevertheless, the engineers decided to reserve space and the corresponding weight (about 40t) in the box girders to install Tuned Mass Dampers (TMD's). They also decided to do extensive dynamic tests on the half bridge to anticipate the behaviour of the completed bridge in order to decide whether or not to install the TMD's. Reto Cantieni, RCI Dynamic, structural dynamics consultants, co-author of the paper, did this analysis and tests.

CONSIDERING DYNAMIC PROBLEMS IN THE DESIGN STAGE

The question of whether or not pedestrians walking on the cantilevers would be annoyed by traffic vibrations had already arisen at the design stage of the bridge. To answer this question, some knowledge of dynamic wheel loads produced by heavy vehicles is required as well as some knowledge of natural bridge vibration modes. The latter does not only include natural frequencies, but also mode shapes. Significant bridge response can be expected if the frequencies of wheel loads and bridge are identical and, in addition, only if the related bridge mode shape is optimum. A mode shape is optimum if its shape is similar to the quasi-static deflection shape generated by the vehicle as it crosses the bridge. Heavy vehicles' dynamic wheel loads appear in two frequency ranges: body bounce vibrations, $f = 1 \dots 3.5$ Hz, axle hop vibrations, $f = 7 \dots 15$ Hz [Cantieni and Krebs 1999]. Moving pedestrians are most susceptible to vibrations in the $f = 4 \dots 8$ Hz range [ISO 1997]. Based on the bridge model used in the design stage, the fundamental bridge mode in vertical bending was estimated at $f = 0.91$ Hz. The second mode could be expected at $f \approx 3.6$ Hz. The first transverse bending mode was estimated at $f = 5.63$ Hz. The risk of being confronted with significant problems was rated as being not too large. From the vertical bending modes, the first had an uncritically low frequency and the second a suboptimal shape (node in the bridge mid-point). However, some risk resulting from transverse vertical bending modes could not be excluded. An analytical evaluation of such modes requires a very detailed bridge FEM. This was not available. Therefore, the recommendation was to make subsequent installation of TMD's (Tuned Mass Dampers) easily possible.

DYNAMICS CHARACTERISTICS OF THE HALF BRIDGE

Ambient vibration technology was used to identify the dynamic characteristics of the new half bridge completed in December 2008. This technology is very well suited to identify a structure with an 80m span and many railway lines underneath. Further excitation was provided through the road traffic crossing the adjacent old existing bridge. There was no traffic on the new half bridge itself. Instrumentation included 15 DOF's (Degrees Of Freedom) per setup. Six of them were located in two 3D-reference points. Another six covered two 3D- and another three 1D- rovers. Of the four measurement lines indicated in Figure 19, two were instrumented 1D and two 3D (Figures 20 and 21). The sensors were of the 10 V/g PCB ceramic-type linear down to $f = 0.2$ Hz, the frontend was an LMS Pimento. The sampling rate was chosen to $sR = 100$ Hz, the length of the time window to $T = 1'800$ s. To cover the whole set of 104 DOF's, 12 setups were required; the total testing time was 8 hours at a temperature of close to freezing. The Artemis Software suite EFDD (Enhanced Frequency Domain Decomposition) technology was used to extract the bridge's modal parameters. Some of the 17 bridge natural modes identified in the $f = 1.22 \dots 23.7$ Hz range are presented in Figure 22 [Cantieni 2010].

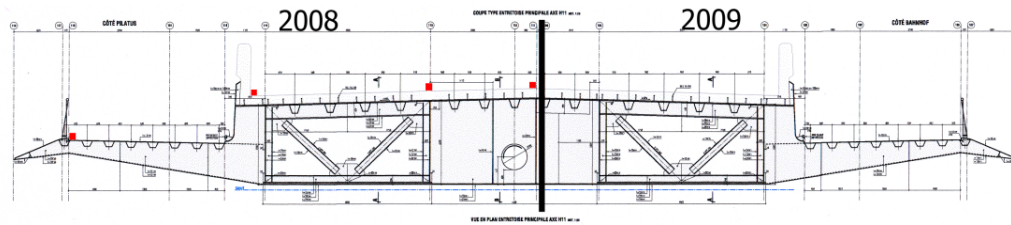


Fig. 19 - The four measurement point lines used on the 2008 completed bridge half are indicated with red squares.

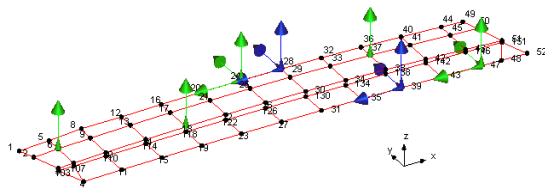


Fig. 20 - Instrumentation for setup 2. Blue: Reference DOF's, Green: Roving DOF's

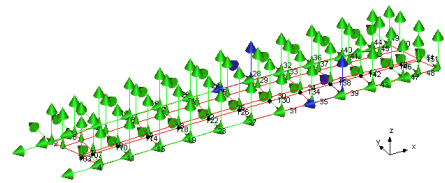


Fig. 21 - All 52 measurement points, 104 DOF's, measured

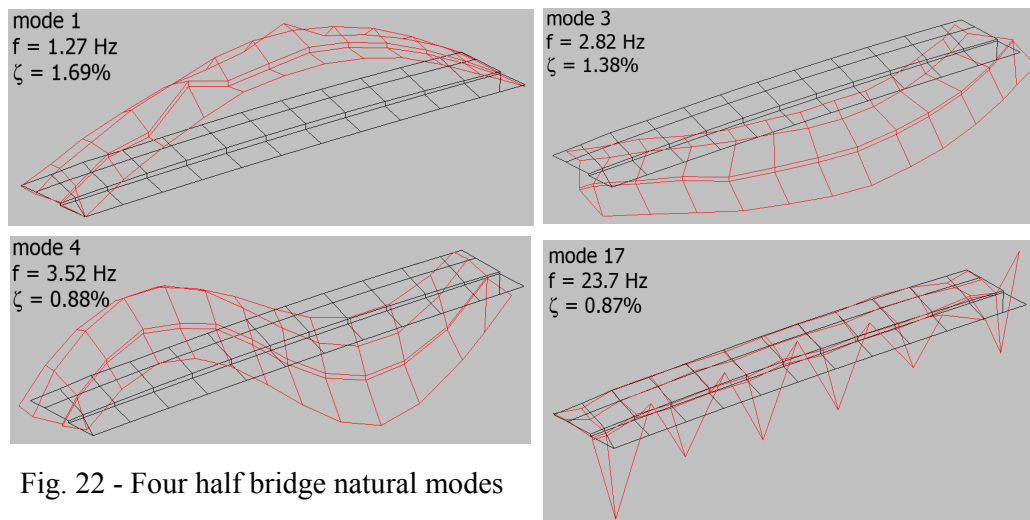


Fig. 22 - Four half bridge natural modes

DYNAMIC LOAD TESTING OF THE HALF BRIDGE

A comprehensive dynamic load testing schedule was performed the day after the ambient vibration tests ([Cantiene 2010]). Test vehicles included a steel-suspended 35-kN 4-axle truck, an air-suspended 35 kN 4 axle-truck as well as an air-suspended 3-axle bus (Figure 23). These vehicles crossed the bridge on a regular schedule. Further information on the influence of a vehicle's suspension can be gathered from [Cantiene, Krebs, Heywood 2000]. It can be mentioned here that the reference cited is the final report on a joint OECD test program between EMPA and the Queensland University of Technology with performing dynamic load tests using various vehicles in Switzerland as well as in Australia.



Fig. 23 - Two of the vehicles used for the dynamic load tests. Tests with crossing a 25 and a 50 mm-plank were also performed

Accelerations were measured at three points of the walkway cantilever. For passages without a plank on the pavement, a maximum value $a = 0.8 \text{ m/s}^2$ was not surpassed. With the plank, the maximum acceleration reached $a = 2.5 \dots 2.65 \text{ m/s}^2$. As, according to the literature ([Bachmann 1995]), a value of $a = 0.5 \dots 1.0 \text{ m/s}^2$ is rated as acceptable. As a result, the bridge owner decided to refrain from planning installation of TMD's. We however suggested keeping the pavement's evenness under control. Heavy vehicles' dynamic wheel loads are significantly dependent on this parameter. From analyzing the measured cantilever accelerations it became clear that the high frequency axle hop vibrations strongly influence the cantilever dynamic response. This is illustrated in Figure 24 where the body bounce excited vibrations reach $a = 0.20 \text{ m/s}^2$ whereas axle hop excited vibrations lead to the maximum registered value $a = 0.79 \text{ m/s}^2$. More details to this can be taken from [Cantiene 2010].

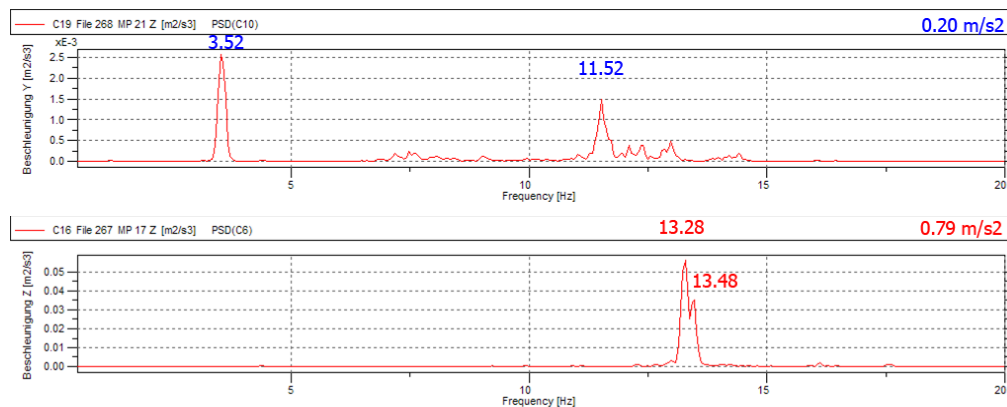


Fig. 24 - Acceleration frequency spectra measured under the passage of a heavy vehicle

DYNAMICS CHARACTERISTICS OF THE COMPLETED BRIDGE

In May 2012 a non-comprehensive ambient vibration test was performed on the completed bridge. Instrumentation included: one 3D- and one 1D- sensor located at a

cantilever tip were used as a reference and a rover respectively (Figure 25). All other parameters and signal processing features were kept as those having been used in December 2008.

It is naturally not possible to identify a bridge natural mode shape with using 7 DOF's in the same way as with using 104 DOF's. However, knowing the detailed results (frequencies and shapes) of the half bridge, some basic results gathered for the completed bridge could easily be verified (Figure 26). It also becomes clear from Figure 27 that the completed bridge is slightly less rigid than the half bridge.

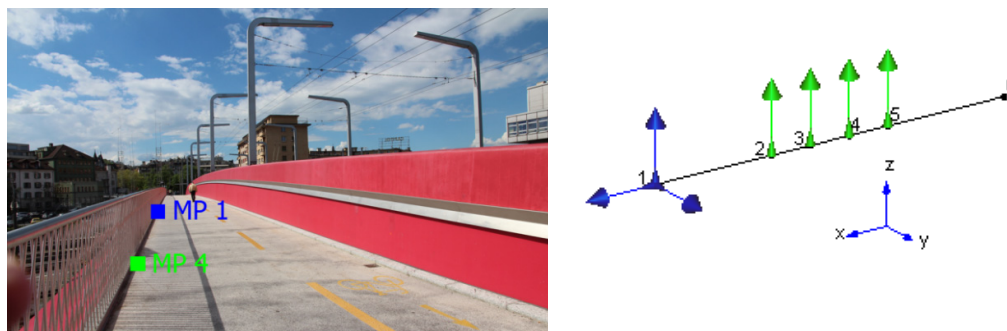


Fig. 25 - The 3D-reference point MP 1 close to mid-span, the 1D-rover moved over the bridge half span from MP 2 to MP 5. Point 6 is located at the abutment

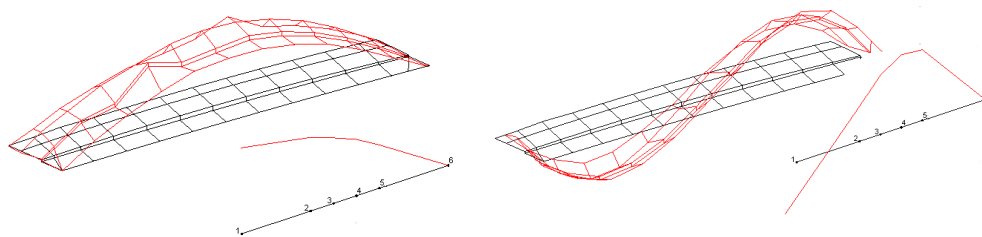


Fig. 26 - Shape of modes 1 and 4 for the half (top) and the completed (bottom) bridges (numbers see Fig. 27)

Table 1 - Comparison of some results of identification of the half bridge (LS 2, 2008) and the completed bridge (LS 3, 2012)

Mode LS 2	Frequency [Hz]	Damping [%]	Shape LS 2	Mode LS 3	Frequency [Hz]	f LS 3/f LS 2
1	1.266	1.69	long. bending 1	1	1.147	0.91
2	2.583	1.62	transv.bending1	2	2.258	0.87
3	2.824	1.38	transv.bending2			
4	3.525	0.88	long. bending 2	4	3.479	0.99

CANTILEVER DYNAMIC BEHAVIOR OF THE COMPLETED BRIDGE

The signals acquired from the ambient vibration test as discussed above could of course also be processed using simple FFT (Fast Fourier Transform) methodology. The difference to the dynamic loading tests on the half bridge as discussed earlier is

the loading procedure. On the half bridge, we had single heavy vehicles crossing the bridge in a relatively short amount of time. For the completed bridge we analysed signals of a 30 minutes length with a wide variety of vehicles crossing the bridge in both directions. In addition, there was pedestrian and bicycle traffic on the cantilever. The maximum acceleration amplitude at the cantilever tip, $a = 0.71 \text{ m/s}^2$, was measured during a jogger's passage. For traffic excitation the maximum amplitude did not cross $a = 0.42 \text{ m/s}^2$. And: It can very nicely be seen from the spectrum presented in Figure 28 that, indeed, the cantilever response concentrates on the two frequency ranges excited by heavy vehicles: body bounce at $f = 1 \dots 3.5 \text{ Hz}$ and axle hop at $f = 7 \dots 15 \text{ Hz}$. And: Almost all of the peaks shown in Figure 28 can directly be related to bridge natural modes. Dynamically speaking: the new Langensand Bridge is a cross-over between a beam and a wing. At the same time its beam-type vertical bending behaviour and its wing-type transverse bending behaviour are excited by traffic and are both significantly influencing the final response at the wing tips. For a highway bridge, this is quite unusual.

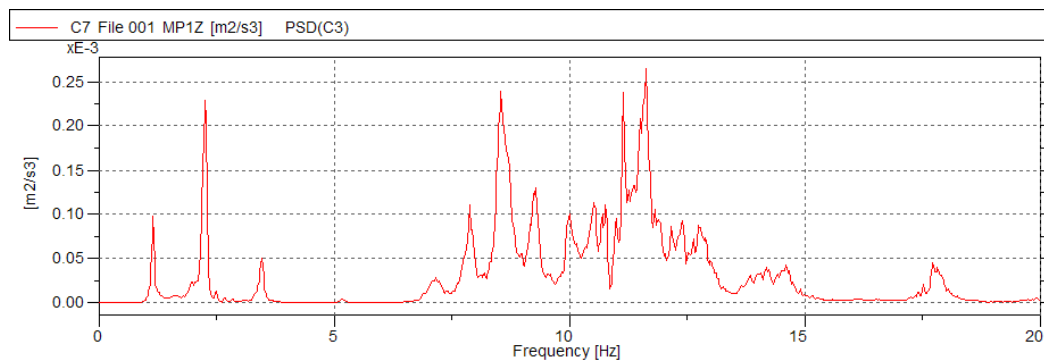


Fig. 27 - Vertical acceleration frequency spectrum measured at approximately mid-span

CONCLUSION

The design of the Langensand Bridge in Lucerne represents a minimal shape defined by strict constraints and needs. The result is a significant slender structure ($L/37$) susceptible to substantial deflections and dynamic effects further complicated by the interaction between road traffic and pedestrians. The concept is based on a special composite structure capable of adapting itself to the different phases of the construction which were required by the demands in terms of the upkeep of the road and the railway traffic without omitting the safety problems of the users and the exploitation of this transport network. Several FEM's were used to keep under control the various situations of the deflections during the history of the bridge's construction. Geometrical controls and static load tests showed that FEM's and real behaviour were much close. The difference was inferior to 10% which is an excellent result; in reality the structure is more rigid than the model. Consequently, the delicate link between the two half bridges was realised without significant complications or setbacks. The dynamic behaviour was approached with a simple model that showed the sensitivity of the structure. Thus, we decided to check the first phase of the construction with comprehensive dynamic tests on the half bridge in order to predict the final behaviour of the completed bridge. These tests of the half bridge plus a final

test of the completed bridge showed that the interaction of traffic loads and pedestrians didn't generate excessive accelerations for pedestrians on the tip of the cantilevered walkway. The values are lower than the acceptable value of 0.8m/s^2 . This project shows that a clear concept accompanied by a strong numerical modelling capable of analysing the several parameters influencing behaviour, enables the realisation of complex structures. This approach has to be completed with in situ tests to compare results and adjust, if necessary, the following phases of the construction. For this complex structure, we were able to adapt the delicate phase of joining the two half bridges to obtain the completed bridge.



Fig. 28 - New Langensand bridge in Lucerne Switzerland

REFERENCES

- Bachmann, H., ed., (1995). "Vibration Problems in Structures", *Practical Guidelines*. Birkhaeuser Verlag Basel, Boston, Berlin, ISBN 3-7643-5148-9.
- Cantieni, R., Krebs, W. (1999). "Analysis of Dynamic Wheel Load Signals in the Frequency Domain. Heavy Vehicles Systems", *a Special Series of the International Journal of Vehicle Design*, Vol. 6, Nos. 1-4, pp. 287-309.
- Cantieni, R. Krebs, W., Heywood, R. (2000). OECD IR 6 DIVINE Project: "Dynamic Interaction between Vehicle and Infrastructure Experiment". *Element 6, Bridge Research – Final Report*. EMPA Test Report No. 153'031, ISBN 3-905594-05-6.
- Cantieni, R. (2010). "Traffic Excited Vibrations Acting on Pedestrians Using a Highway Bridge". *Proc. 28th International Modal Analysis Conference (IMAC)*, Jacksonville, Florida, February 1-4, 2010, paper #210 on CD.
- Goulet J-A., Kripakaran P., Smith I. F.C., (2009). "Langensand Bridge in Lucerne", *Results from phase 1 static load tests*, Ecole Polytechnique Fédérale de Lausanne.
- "Mechanical vibration and shock - Evaluation of human exposure to whole-body vibration". ISO 2631-1:1997(E).

Welding and Properties of the Lamellar Flange Weld Joint for Modern Bridge Construction

Jaroslav Koukal^{1,2}; Martin Sondel^{1,2}; and Drahomir Schwarz^{1,2}

¹Czech Welding Institute Ltd., 17. Listopadu 2172/15, 70833 Ostrava, Czech Republic.
E-mail: jaroslav.koukal@csuostrava.eu; martin.sondel@csuostrava.eu;
drahomir.schwarz@csuostrava.eu

²VSB-Technical Univ. of Ostrava, 17. Listopadu 2172/15, 70833 Ostrava, Czech Republic.

Abstract

This paper describes the welding procedure qualification of the multilayer “lamellar” flange for modern bridge construction made in the Czech Republic. The fine-grained structural steel was used for construction and welding qualification. Weldability of this steel grade is briefly mentioned. Technological and proposed welding processes including weld joint preparation are described. FCAW welding in the overhead position is carried out by the seamless flux cored wire and SAW welding using solid wire in the flat position is applied. All required tests on the multilayer weld joint including tensile test, bend test, hardness distribution, impact test, and macroscopic evaluation are investigated. All test results are in good agreement with EN ISO 15614-1 standard requirements. Based on the satisfactory results, the proposed welding procedure for the multilayer flange weld joint can be qualified.

1 INTRODUCTION

Development and erection of the new modern bridge steel structures are more influenced by technical requirements for structure design and material savings which are possible due to the recent computer technique. Multilayer flanges with several plates combined, so called lamellar flange, have been used for top flange of the bridge structure. Samples and different kinds of the multilayer plates and their welded joints are presented in Figure 1.

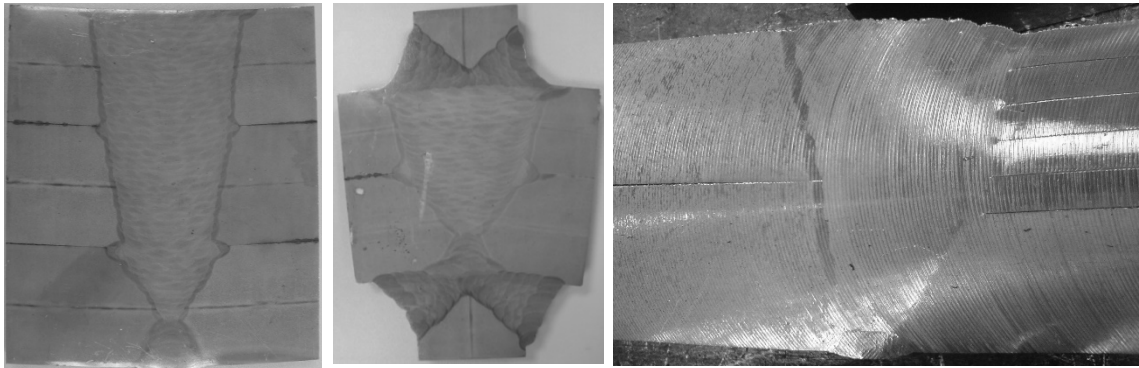


Figure 1. Welded joint samples of multilayer flanges.

Butt weld joint of the multilayer flange is only simple defined in EN ISO 1708-2 standard mainly with respect to the minimal weld penetration size for “V” sealing butt weld performed between plates. It is necessary to suggest the suitable technological procedure for welding and range of destructive and nondestructive testing for welding procedure qualification. Paper describe welding process and procedure qualification of the multilayer flange according to the EN ISO 15614-1 standard on the in site condition.

2 MODERN BRIDGE STRUCTURE USED IN PRAGUE

Construction coupled composite bridge was started in the fall of 2007. Its structure was completed in late 2009. The bridge was put into trial service together with a southwest ring road around the Prague in September 20th 2010.

Bridge of the total length of 461 m passes through the valley height 65 m in curves with a radius of 747.5 m, transverse slope of 4.0% and a constant longitudinal gradient of 2.4%. The total width of the bridge is a variable from 34.28 to 37.105 meters with two driving directions separated by barriers, bilateral official functions walkways with railings, completed on one side of a noise barrier.

The supporting structure is continuous with five sections with spans of 70.0 + 79.8 + 99.3 + 93.8 m + 80.5 m, while in the field with the largest span is strut frame with axial distance of 157.1 m. The beam is hinge supported on the pillars and abutments in other fields. Beam total length of 425.10 m is coupled to concrete and has a chamber cross-section with inclined walls. Oblique props strut frame are made of concrete. General view on the bridge is presented in the Figure 2.



Figure 2. General view on the coupled steel-concrete bridge over the Lochkov Valley.

The steel part of the bridge support structure forms an open cross section with inclined walls the height approximately 3.9 to 4.5 m, the bottom width of 11.0 m and the upper flanges of width 1.5 to 2.4 m. The main beam is extended by two external and one internal spar, which is supported by tubular struts. The upper flange of the main beam and the longitudinal members are connected by four GEWI rods of diameter 40 mm and are provided with studs for coupling with the deck slab, Figure 3.



Figure 3. Bridge steel chamber with plate flanges.

The steel structure is made of S355 steel. S355J2 + N steel was used for plates thickness up to 35 mm, S355K2 + N steel for plates thickness up to 50 mm and S355NL + N steel for thicker plates. Longitudinal walls reinforcement and bottom band of trapezoidal cross-section are made of the S355J2C + N steel and tubular steel struts of the S355J2H steel. The top flange thickness greater than 110 mm are made from two

plates called lamellar flange. Limiting the maximum used plate thickness was based on the EN 1993-1-10 requirement on prevent of brittle fracture. Lamellar flanges are designed over the supports P2, P4 and P5 in the negative bending moments. The maximum thickness of lamellar flange is 190 mm (plate thickness of 100 mm and 90 mm)

3 BASE MATERIAL FOR MULTILAYER FLANGE WELDING PROCEDURE QUALIFICATION

Fine grained micro-alloyed steel S355NL grade according to the EN 10027-1 with thickness of 190 (180) mm was used for design and welding procedure qualification. Weld joint preparation with respect to the welding in on site condition is presented in Figure 4.

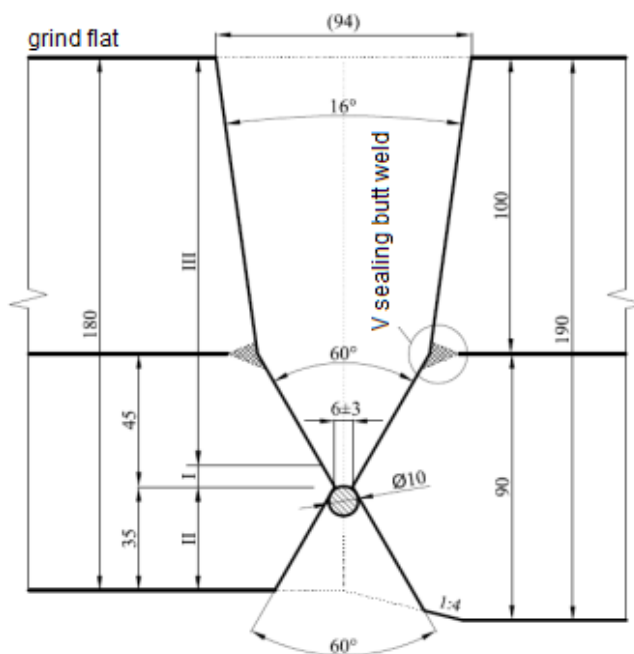


Figure 4. Weld joint preparation for multilayer flange.

Standardized the base mechanical properties and the chemical composition of the used S355NL steel are presented in Tables 1 and 2.

Table 1. The base mechanical properties of the S355NL steel.

Steel grade	R_m (MPa) +20°C	R_e (MPa) +20°C	A_5 (%) +20°C	KV (J) at -40°C
S355NL	470-630	≥ 315	~ 22	longitudinal: 34 transverse: 20

Table 2. Chemical composition of the S355NL steel.

Chemical composition (wt. %)						
C	Si	Mn	P	S	Al	Cr
≤0.018	≤0.50	0.90-1.65	≤0.03	≤0.025	≥0.02	≤0.30
Cu	Mo	N	Nb	Ni	Ti	V
≤0.35	≤0.10	≤0.015	≤0.05	≤0.50	≤0.03	≤0.12

The object of the welding procedure qualification of the multilayer flange presented in Figure 2 was only the main, both sides V butt weld joint, which is welded in site on the bridge construction. V sealing butt weld joint, see Fig. IV, was prepared, welded and checked in bridge production plant and was not subjected to the welding procedure qualification. The base material of S355NL steel belongs to the 1.2 steel group according to the TNI CEN ISO/TR 15608:2008 standard.

4 WELDABILITY OF THE MICRO-ALLOYED FINE GRAINED STEELS

Modern micro-alloyed fine grained steels are produced by using of the suitable chemical composition and different kinds of heat treatment. The aim is to achieve both high mechanical properties, resistance to the brittle fracture and good weldability of the steel. Palates and semi-products are most often produced by controlled rolling in combination with heat treatment which pointing out Al, Ti, Nb and V micro-alloying elements on material properties.

The attention should be mainly given to the influence of the base material chemical composition, welded thickness, hydrogen content in the weld metal, heat input and residual stresses at welding for ensuring the high quality of the fine grained steel welded joints.

Preheating and post heating make it possible to decrease cooling rate at welding which has significant influence on final mechanical, physical and chemical properties of the fine grained steel welded joints. Preheat temperature is determined based on the chemical composition of the steel with respect to welded thickness. Interpass temperature is corresponding to the preheat temperature (Max. +50°C) because the yield strength in the heat affected zone (HAZ) of the base material can be decreased at high interpass temperatures.

The main technological procedure for welding fine grained steels should be suggested in this way so that the HAZ was not significantly influenced by welding process. It is recommended to welding with low penetrated filler material, low electrode diameter, low amperage and with higher welding speed with up to 10 kJ·cm⁻¹ heat input. It is also necessary to use the welding consumables and technological procedures ensuring low hydrogen content in the weld metal at welding fine grained steels.

5 CONSUMABLES USED FOR WELDING MULTILAYER FLANGE

The following welding methods and consumables were used for welding multilayer flange test specimen:

- Welding of the root area “I” (see Fig. II) was carried out by FCAW method (Flux cored seamless electrode Nittetsu SM-3A, according to the EN ISO 17632-A: T 42 4 Z M 3 H5 with M21 shielding gas according to the EN ISO 14175 standard) in the PA (ISO 6947) flat welding position. Ceramic backing of 10 mm in diameter was used.
- Welding of the area “II” (see Fig. II) was carried out by FCAW method (Flux cored seamless welded electrode Nittetsu SF-3AM, according to the EN ISO 17632-A: T 46 4 Z P M 2 H5 with M21 shielding gas according to the EN ISO 14175 standard) in the PE (ISO 6947) overhead welding position.
- Welding of the area “III” (see Fig. II) was carried out by SAW method (Wire ESAB OK Autrod 12.22, according to the EN 756: S2Si + ESAB OK Flux 10.72 flux according to the EN 760: SA AB 1 57 AC H5) in the PA (ISO 6947) flat welding position.

Used Nittetsu filler materials are seamless continuously welded flux cored electrodes which ensuring high stable welding arc and good operational properties. These electrodes used for important welded steel structures also ensuring very low hydrogen content in the welded metal which its typical value is 3 ml/100g of welded metal.

6 WELDING AND PROPERTIES EVALUATION OF THE MULTILAYER FLANGE

Testing weld joint of 1000 mm length and 600 mm width was prepared for mechanical properties evaluation. With respect to the possible distortion and in order to simulate the real toughness of the welded bridge steel structure, the testing specimen was positioned and welded into the preparation made from HEB 1000 profile as can be seen in Figure 5.

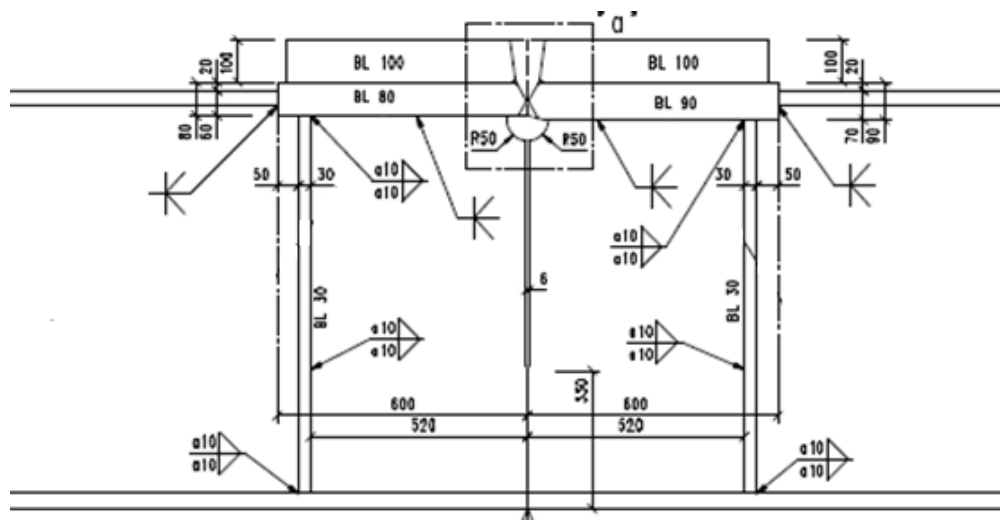


Figure 5. Schematically positioned testing specimen in the preparation made of the HEB 1000.

Both weld surfaces were grinded to flat after finishing of the all welding works and applied post heating. Welded joint of the multilayer flange could be now nondestructive tested using magnetic particle inspection according to the EN ISO 17638 and ultrasonic inspection according to the EN ISO 17640. Ultrasonic testing requires knowledge and experiences with multilayer flanges testing.

Mechanical properties and metallography examination of the testing multilayer flange were performed according to the EN ISO 15614-1 standard. Mechanical properties were evaluated according to the transverse tensile tests, impact toughness tests of the weld metal and HAZ at -40°C and hardness measurements. Positions and number of the impact toughness testing specimens were suggested in accordance to the EN ISO 15614-1 standard and took into account all the used welding methods and filler materials. All results from mechanical testing are summarized in the following Table 3.

Table 3. Performed tests on the multilayer flange.

Performed mechanical tests	EN ISO 15614-1 requirement	Test result (average)
Tensile test	Min. 470 (MPa)	Min. 550 (MPa)
Side bend test at 180°	Max. length of crack shall be less than 3 mm	No cracks on 4 specimens
Impact toughness test at -40°C	Min. 20J	Min. 60J (FCAW weld metal)
Hardness measurement	Max. 380 HV10	Max. value 290 HV10

Detail of the bend test specimen and bend test procedure is shown in Figure 6.

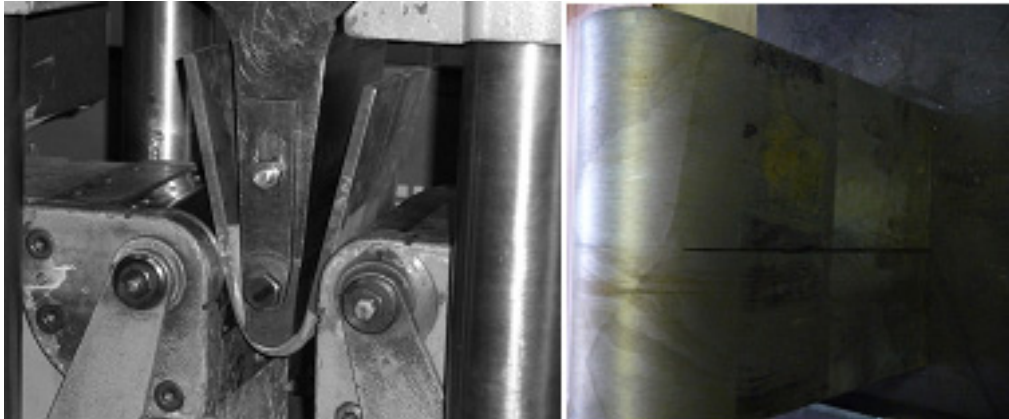


Figure 6. Bend test 180° of the multilayer flange.

Macrostructure examination was performed according to the EN 1321 standard and evaluation was performed according to the EN ISO 5817 standard for the B quality grade. Figure 7 presents macrostructure of the welded multilayer flange.

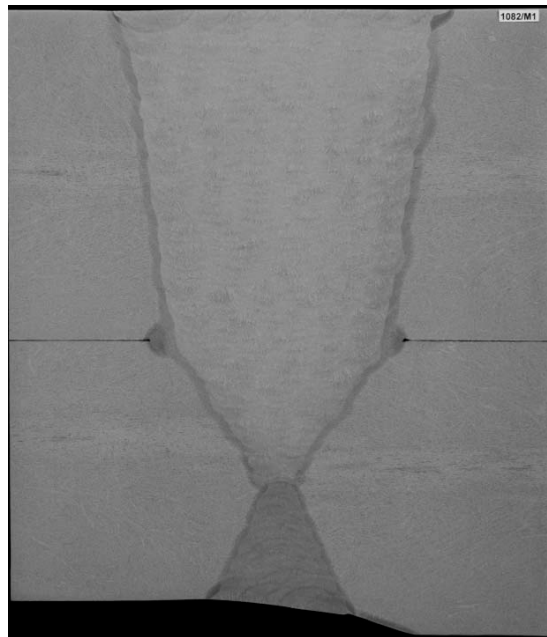


Figure 7. Macrostructure of the multilayer flange.

Results of the all mechanical tests performed on the welded multilayer flange specimen fulfill all requirements for the base material. There were identified no unallowable defects on the test specimen by metallography examination.

7 CONCLUSION

Welding procedure qualification tests were used for evaluation of the technological and welding procedure on the multilayer flange welded joint. Test results evaluated according to the EN ISO 15614-1 standard clearly proved that suggested technology and also welding consumables used for S355NL base material fulfill all requirements for welded joint. It is important to suggest proper size of the test specimen including toughness simulation in order to get near the real welding conditions of the bridge steel structure.

REFERENCES

- Koukal, J., Schwarz, D., and Hajdik, J. (2009). *“Materials and their weldability”*. Ostrava, Czech Welding Institute, Lt.D., VSB-TU Ostrava, 241p.
- Pilous, V. (19990). *“High strengths microalloyed fine grained steels and their weldability”*. Plzen, 35p.
- EN ISO 15641-1 (2004). Specification and qualification of welding procedures for metallic materials - Welding procedure test- Part 1: Arc and gas welding of steels and arc welding of nickel and nickel alloys.

Design Temperature Load Spectrum for the Fatigue Verification of Composite Bridges with Integral Abutments

Daniel Pak¹ and Markus Feldmann²

¹Dr.-Ing., RWTH Aachen Univ., Institute of Steel Construction, 52074 Aachen, Germany. E-mail: pak@stb.rwth-aachen.de

²Prof. Dr.-Ing., RWTH Aachen Univ., Institute of Steel Construction, 52074 Aachen, Germany. E-mail: feldmann@stb.rwth-aachen.de

Abstract

For (low cycle) fatigue design of steel foundation piles of composite bridges with integral abutments, not only traffic loads but also temperature loads as well have to be considered. Regarding this temperature fatigue load case, no specific rules and recommendations are given in EN 1991-2 (Eurocode 1: Actions on structures - Part 2: Traffic loads on bridges). The current paper proposes a simplified temperature load spectrum, to be used for (low cycle) fatigue design of constructional steel members of composite bridges with integral abutments. Therefore, effective bridge temperature hydrographs (100 year period) are derived by means of FE-calculations for various locations based on actual weather data. They are converted into pile strain hydrographs, taking into consideration residual strains and plastic deformations. The calculations are verified by laboratory low cycle fatigue tests and monitoring results. Finally, a design temperature load spectrum is proposed, based on classified temperature variations.

INTRODUCTION

In many countries composite bridges with integral abutments are already an alternative to well-established concrete bridge solutions, in particular if an economic, robust and light solution is aimed at [Feldmann and Pak 2009] [Feldmann et al. 2011]. For fatigue design of steel foundation piles of these bridges according to [EN 1993-1-9:2005 2009], frame effects have to be considered. Therefore, not only traffic loads but temperature loads as well have to be considered. Especially in case of long bridges and stiff soils, plastifications may occur in the steel piles which need to be considered for low cycle fatigue verification [Nilsson et al. 2008] [Pétursson et al. 2011]. The general approach proposed in this paper is shown in Figure 1.

By an idealisation of the elastically bedded beam by an equivalent cantilever (*B*) (equivalent cantilever method [Greimann et al. 1987]) the strains relevant for design caused by elongation and contraction of the superstructure (*A*) are determined (*C*), whereas residual strains are considered as well. Finally, the strains are classified by means of a Rainflow analysis and analysed according to [EN 1993-1-9: 2005 2009].

To accelerate that approach it needs to be simplified in a way where residual stresses / strains are neglected. This way the effective bridge temperatures, causing pile deformations, can be classified directly; afterwards the classified deformations can be transferred into classified strains, the load history does not need to be taken into consideration explicitly. The reliability and validity of this procedure is confirmed in the following.

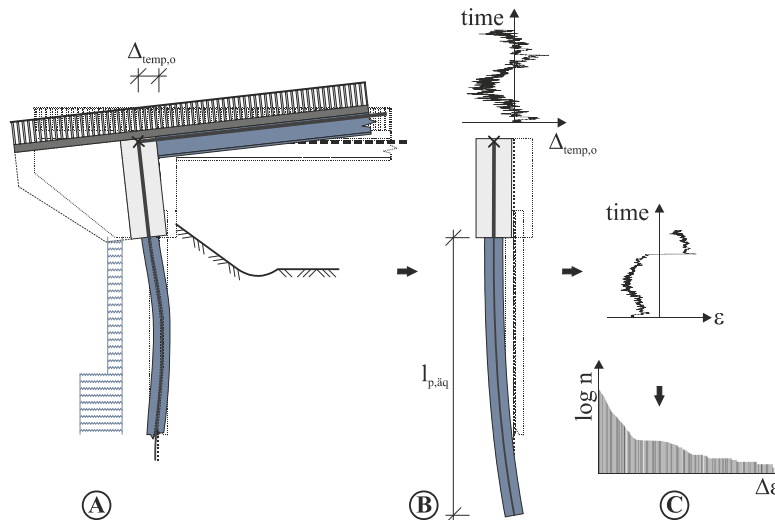


Figure 1. Determination of pile strains $\Delta\varepsilon$.

Furthermore the influence of self-weight (permanent axial load) and traffic load (alternating axial load) on the strains in the pile is examined. It can be shown that these axial loads do not need to be combined explicitly with the deformation controlled loads due to temperature variations but can be considered separately.

Finally an approach for the determination of an artificial temperature load spectrum as input for the fatigue design is developed. The applicability of that approach is shown by means of sample calculations.

DETERMINATION OF STRAIN SPECTRUM CONSIDERING LOAD HISTORY

Pile strains at the connection between pile and abutment, caused by a horizontal deformation of the superstructure (elongation and contraction due to temperature), are determined according to the following consecutive steps (Figure 2, method I):

1. calculation of the effective bridge temperature (EBT) hydrograph for a given cross section by means of a Finite Element calculation, based on:
 - a. ambient temperature hydrograph (temperature load)
 - b. global radiation hydrograph (radiation load)
 - c. wind speed hydrograph (thermal coefficient)

- at the structure’s actual location (time period chosen: 50 years, time step: $\Delta t = 2$ h);
2. transformation of the EBT hydrograph into a deformation hydrograph (axial deformation of the superstructure, elongation and contraction);
 3. reduction of the deformation hydrograph (local extremes);
 4. consideration of the foundation piles (elastically bedded beam) by means of an equivalent cantilever according to [Greimann et al. 1987];
 5. application of the deformations (3.) to the equivalent cantilever (4.);
 6. determination of the strain hydrograph for the pile’s cross section relevant for design (pile-abutment connection), based on the deformation hydrograph;
 7. strain classification by means of an adequate classification method;
 8. damage accumulation according to Palmgren-Miner (see following chapter).

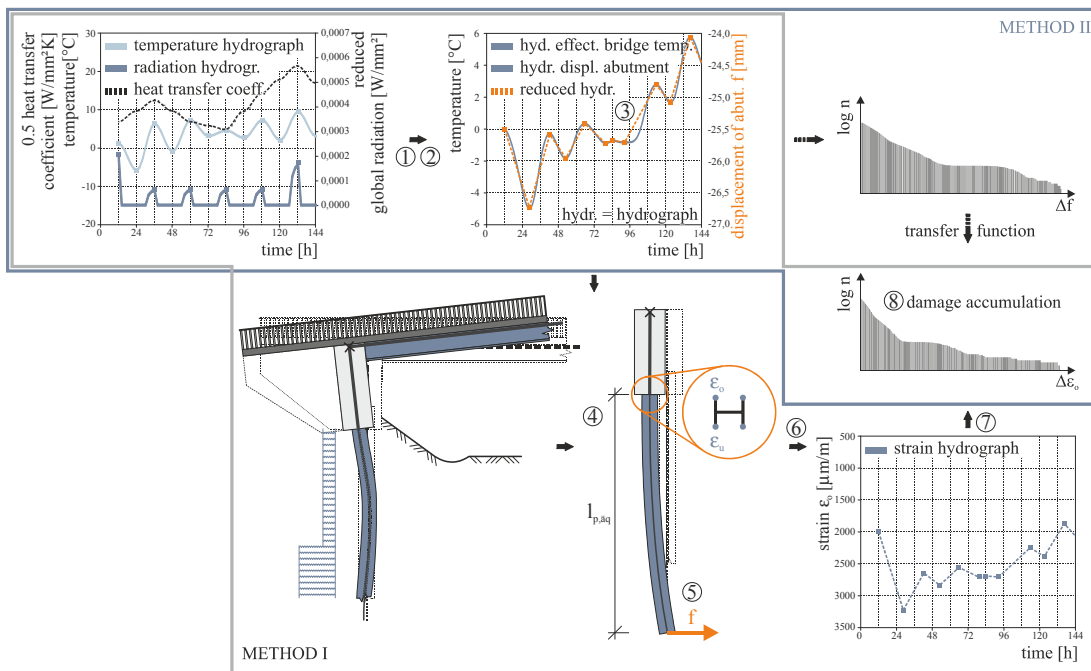


Figure 2. Determination of strain spectrum.

As long as the piles’ cross section is not subjected to plastic deformations, the deformation hydrograph can be transferred directly into a strain hydrograph by means of a linear admittance function (method II). The time consuming steps (5.) and (6.) can be skipped, as both curves are mathematically similar. To show that this simplification can be adopted for long bridges causing plastic deformations of the piles as well, both methods are compared in the following for a specific bridge structure.

Step 1-3: The calculation of the effective bridge temperature (EBT) is performed for the cross section of the bridge “Entenpfuhl”, monitored within the scope of the European research project INTAB [Feldmann et al. 2010]. In a first step,

a finite element model is calibrated by means of temperature monitoring data (1 year). In a second step, the model is used for generation of EBTs for a time period of 50 years (1950-1999) based on real weather data. These EBTs are transferred into bridge elongations / movements of the abutments, whereas rotations due to non-uniform temperature distribution over the superstructure’s height are disregarded.

Step 4/5: The horizontal abutment movements are applied to an equivalent cantilever, based on the equivalent cantilever method proposed by [Greimann et al. 1987]). Here the uniformly bedded pile is replaced by an equivalent cantilever; the determination of the cantilever’s length is based on the static equivalency to be granted. To generate an equivalent fixed-end moment, the following equation is proposed [Greimann et al. 1987]:

$$l_{p,\ddot{a}q} = l_c \sqrt{\frac{128(l_u/l_c)^4 + 128\sqrt{2}(l_u/l_c)^3 + 96(l_u/l_c)^2 + 24\sqrt{2}(l_u/l_c) + 6}{128(l_u/l_c)^2 + 64\sqrt{2}(l_u/l_c) + 16}} - l_u$$

$$l_c = 4 \cdot R = 4 \cdot 4 \sqrt{\frac{E_p I_p}{k_{e,h}}}, l_u : \text{abutment height}$$

In the way the approach is adopted here, abutment rotations are disregarded, as bridge elongations are applied to the cantilever directly. To validate the applicability of this simplification, the fixed end moment cycles ΔM determined according to this approach are compared to the moments in the pile-abutment connection calculated by means of a complete finite element model (including abutment rotations and earth pressure variations) (Figure 3).

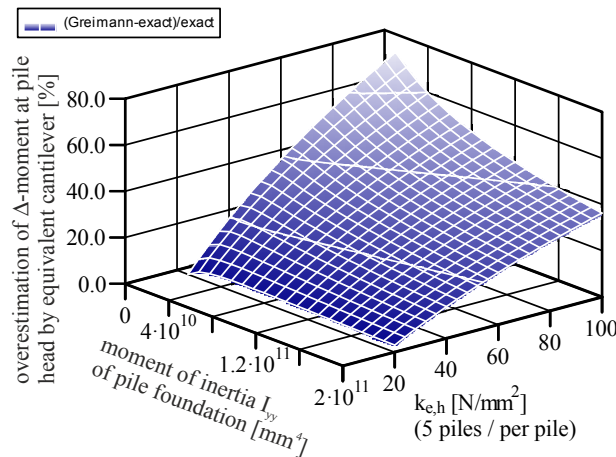


Figure 3. Deviation of maximum bending moment cycle ΔM at the pile-abutment connection (approach based on [Greimann et al. 1987]) compared to exact calculation.

For the given configuration of superstructure and abutments, the approach proposed by Greimann results in conservative results. If the soil stiffness is low (low modulus of subgrade reaction $k_{e,h}$) the results are nearly exact. With increasing soil

stiffness the moment cycles ΔM are increasingly overestimated, which conservatively leads to higher strains in the piles.

Step 6: Based on the equivalent cantilever approach, a computer program is written to allow for a time-efficient determination of resulting strain hydrographs at the pile-abutment connection, taking into consideration plastic deformations and residual strains (method I). The program is calibrated by comparing the results to strains determined by means of a conventional FE tool (MARC/Mentat). Furthermore both programs are calibrated to static and cyclic tests performed within the scope of the European research project RFCS INTAB [Feldmann et al. 2010] where pile strains were determined as well as fatigue life was checked for HP piles loaded about their weak axis. The program settings are given in Table 1.

Table 1. Program / system settings.

	MARC/Mentat	own program
element type	thin-walled 3D 2-node beam element including warping (type 79)	thin-walled 3D 2-node beam elem., plane sections remain plane
element parameter	11 stress points per segment, 5 layers over cross section height	100 div. over cross section height with constant strains / stresses
system parameter	500 beam elements	
material law	elastic-ideal plastic (without strain hardening) van-Mises yield criterion, $f_y = 355 \text{ N/mm}^2$	
further calc. parameters	small deformations, no 2 nd order effects	

For the determination of strain hydrographs according to method II (disregarding residual strains) normalized functions are derived to transform the deformation cycles Δf into resulting strain cycles $\Delta \varepsilon$ directly. These functions and the relevant coefficients for the determination of strains in the outer fibre for HP-profiles loaded about the weak axis are given in [Pak 2012].

Step 7: The resulting strains derived by both methods are classified by means of a Rainflow analysis according to [Clormann 1986].

A comparison of the accumulated cycles according to both methods (Figure 4) shows that a classification of the deformation cycles, followed by an analytical conversion into strain cycles, is possible and precise. Due to the non-linear correlation between deformations and strains, the width of the strain classes increases with increasing strain amplitudes.

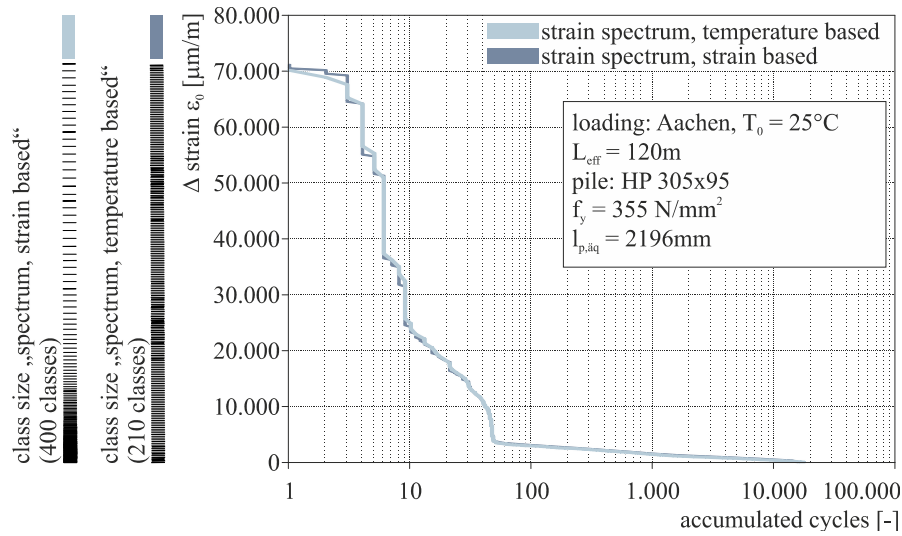


Figure 4. Accumulated strain spectrum based on strain / temperature cycles.

Furthermore it can be proven that constant strains in the pile (e.g. caused by self-weight of the superstructure, here: $N=500\text{ kN}$) can be neglected within the scope of a fatigue calculation, as long as influence of mean strain is disregarded in the final design check (Figure 5).

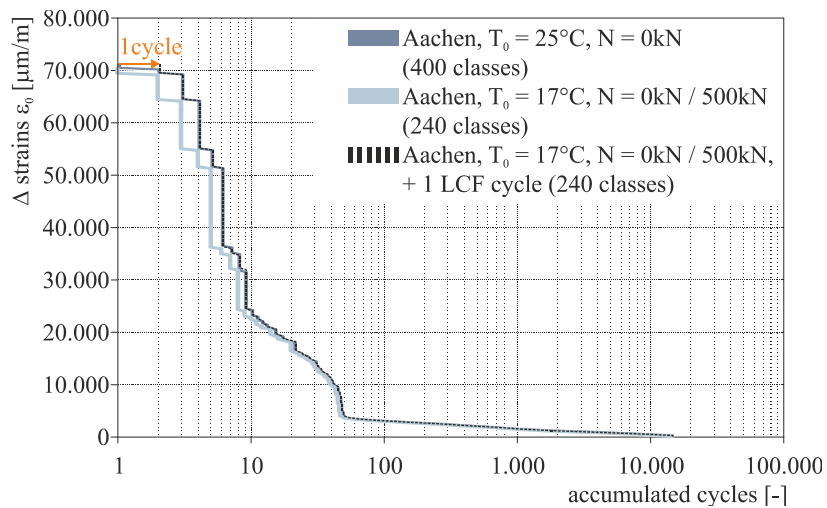


Figure 5. Accumulated strain spectrum for different construction temperatures T_0 / constant axial forces N (S355).

Moreover it can be observed that construction temperature T_0 has no influence on the strain spectrum and therefore can be neglected. A comparative calculation for two different construction temperatures ($T_0=17^\circ\text{C}$, $T_0=25^\circ\text{C}$), followed by a classification of strain cycles, reveals that only one additional high cycle is added to the strain spectrum. This high cycle is caused by the fact that the strain- and stress free condition is assigned to a temperature of $T_{start}=0^\circ\text{C}$. By shifting the summation curve by a single low cycle fatigue strain cycle, it becomes congruent with the $T_0=25^\circ\text{C}$ summation curve (Figure 5). In reality this load cycle does not occur.

Therefore it can be concluded, that a given (artificial) temperature load spectrum can be transferred directly into a strain spectrum; constant normal forces as well as construction temperature may be disregarded. Formulas and related coefficients for the determination of strains in the outer fibre for HP-profiles bended about their weak axis, based on given lateral deformations, are proposed in [Pak 2012]. In the following chapters, an adequate temperature load spectrum is proposed; the accumulated damage caused by this spectrum is compared to the damage caused by temperature load spectra based on actual weather data. Therefore the underlying concept of damage accumulation based of elastic as well as plastic strains is described first (Step 8).

DAMAGE ACCUMULATION BASED ON A GIVEN STRAIN SPECTRUM

For the determination of fatigue life, strain Wöhler curves according to [Coffin 1954], [Manson 1965] and [Morrow, 1965] are used. They are consisting of a plastic as well as an elastic part, which form in good approximation straight lines in double logarithmic scales (Figure 6) [Radaj and Vormwald 2007] [Haibach 2006].

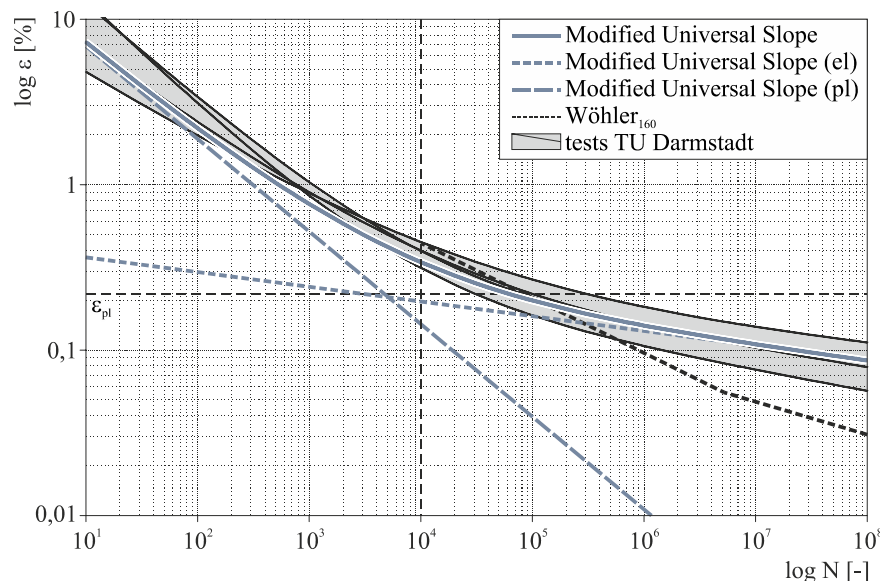


Figure 6. Strain Wöhler curves acc. to the “Modified Universal Slope Equation” with elastic and plastic part, based on INTAB material values as well as tests at TU Darmstadt.

The curves can be expressed as [Radaj and Vormwald 2007]:

$$\varepsilon_A = \varepsilon_{Ael} + \varepsilon_{Apl} = \frac{\sigma'_f}{E} (2N)^b + \varepsilon'_f (2N)^c$$

Here σ'_f refers to the fatigue strength coefficient, ε'_f to the fatigue ductility coefficient, b to the fatigue strength exponent, c to the fatigue ductility exponent, E

to the Young's modulus and N to the number of cycles to failure [Radaj and Vormwald 2007].

For determination of these parameters, estimation formulas are given in [Haibach 2006], which are based on the work of [Muralidharan and Manson, 1988] („Modified Universal Slopes Equation“). The parameters calculated by means of these formulas for the scope of this study are given in Table 2. They are based on material tests performed within the scope of the research project RFCS INTAB [Feldmann et al. 2010] (Table 3, position B).

For comparison purposes strain Wöhler curves determined by [Technische Universität Darmstadt] based on tests at a comparable steel *S460* are given in Figure 6 as well. They form an envelope, including the strain Wöhler curve based on the identified material values.

Table 2. Estimation formulas for parameters of strain Wöhler curves for metallic materials acc. to [Muralidharan and Manson, 1988] („Modified Universal Slopes Equation“).

parameter	estimation formula	value
σ'_f	$\sigma'_f = 0.623 \cdot R_m^{0.832} \cdot E^{0.168}$	1007.03
ε'_f	$\varepsilon'_f = 0.0196 \cdot D^{0.156} \cdot (R_m/E)^{-0.53}$	0.3677
B	$b = -0.09$	-0.09
C	$c = -0.56$	-0.56
D	$D = -\ln(1-Z)$ (Z = reduction in area)	0.3397

Table 3. Material properties *S460*, determined in the INTAB project.

Profile	position	steel grade	f_y	$f_u (=R_m)$	$A (=Z)$
		[-]	[N/mm ²]	[N/mm ²]	[%]
HP 305x95	<i>B</i>	S460	496	605	28.8
	<i>H</i>	S460	460	599	27.2

For fatigue life calculation a linear damage accumulation is performed according to Palmgren and Miner, where the total life to failure is estimated by a linear accumulation of the proportion of life which is consumed by strain reversal at each strain magnitude. Failure occurs if the sum of damage D complies with the Wöhler curve. Order as well as interaction effects are disregarded [Radaj and Vormwald 2007].

The Miner's rule is given by equation

$$D = \sum_i \Delta D_i \stackrel{!}{\leq} 1, 0, \Delta D_i = n_i / N_i$$

whereas N_i stands for the number of cycles to failure of a constant strain cycle $\Delta\varepsilon_i$ according to Wöhler's curve. n_i stands for the number of contributing cycles with

the strain amplitude $\Delta\varepsilon_i$ in the period under consideration, which are determined by means of the Rainflow method. Here the algorithm proposed by [Clormann 1986] is used.

To check the procedure, the strain hydrographs are determined for the tests performed within the scope of the INTAB project according to method I and method II. The accumulated damages D are compared to accumulated damages based on the actual strain measurements (Table 4). During testing, specimen “1” collapsed after 100 large and 36,500 small load cycles due to low cycle fatigue failure. The crack developed from the outer edge of the profile’s flange at the connection between steel profile and concrete.

Table 4. Accumulated damage D of the INTAB test specimen “1” at the pile – concrete block connection / at the position of the strain gauge based on measurements and calculations.

position	strain spectrum		accumulated damage D , specim. “1”
clamped support ($x=0\text{mm}$)	method I	(calculated)	0.832
	method II	(calculated)	0.834
strain gauge ($x=40\text{mm}$)	test	(measured)	0.637
	method I	(calculated)	0.618
	method II	(calculated)	0.620

The calculated accumulated damages D (Table 4) lead to the following conclusions:

1. Based on the crack which developed during the test, the dimension of calculated accumulated damage ($D=0.83$) at the connection between profile and concrete block ($x=0\text{mm}$) is reasonable.
2. Method I and method II lead to the same result. The equivalence of both methods can be shown again. It can be proven that a complex computation of strains including the exact load history is not necessary.
3. A comparison of the accumulated damage at position $x=40\text{mm}$ (strain gauge) according to method I or method II to the accumulated damage based on measured strains provides evidence of the applicability of method I as well as of the correct implementation into the computer program.

TEMPERATURE FATIGUE LOAD SPECTRUM FOR DESIGN

For practical use of the fatigue concept as described above, an adequate design fatigue temperature load spectrum is needed. [EN 1991-2:2003 2010] specifies the maximum variation in temperature for design $T_{e,max}-T_{e,min}$ for different bridge types. Further notes for setting up a fatigue load spectrum are not given. Other codes such as AASHTO [AASHTO 1996] do not consider fatigue in integral abutment bridges as well [Razmi 2012]. For establishing a load spectrum for low

cycle fatigue tests, [Arsoy 2002] suggests that the amplitude of a daily temperature cycle can be conservatively represented by 25% of the amplitude of a yearly temperature cycle. In the following this assumption is checked and adjusted.

Therefore the cross section of the bridge “Entenpfuhl” monitored within the scope of the INTAB research project [Feldmann et al. 2010] is investigated by means of a finite element model, which is loaded with different weather loads. For determination of the EBT, weather data from the cities of Hamburg, Aachen and Augsburg between 1950 and 1999 is used.

Table 5. Examples for accumulated damages at bridge “Entenpfuhl” with different assumed temperature hydrographs / different locations (100 years).

	temperature hydrograph of bridge site / model	EBT _{min} EBT _{max}	period	$\Delta\varepsilon_{max}$	$2n_i$	accumulated damage $2D$	
					(100 years)	(100 years)	total
	[-]	[°C]	[-]	[%]	$\Delta\varepsilon < 2\varepsilon_{pl}$	$\Delta\varepsilon > 2\varepsilon_{pl}$	
	C1	C2	C3	C4	C5	C6	C7
R1	Hamburg	-19.4 / 37.7 $\Delta=57.1$	01.01.1950- 31.12.1999	1.34	35,484 92	0.017 0.090	0.107
R2	Aachen	-17.9 / 42.7 $\Delta=60.6$	01.01.1950- 31.12.1999	1.70	35,286 92	0.015 0.115	0.145
R3	Augsburg	-26.7 / 44.2 $\Delta=70.9$	01.01.1950- 31.12.1999	4.18	35,408 94	0.043 0.202	0.245
R4	model acc. to Arsoy	-20.0 / 41.0 $\Delta=61.0$	50 years	1.75	36,500 100	0.526 0.740	1.266
R5	proposal for „Central Europe“	-20.0 / 41.0 $\Delta=61.0$	50 years	1.75	36,372 100	0.061 0.214	0.275

The resulting effective bridge temperature (EBT) hydrographs are classified by means of the Rainflow method and transformed into classified strains based on method II.

For strain determination, the following boundary system specifications are chosen:

1. $\Delta\delta = \Delta T \cdot \alpha_T \cdot L_{eff} = \Delta T \cdot 1,2 \cdot 10^{-5} [1/K] \cdot 120 [m]$ (deformation applied to equivalent cantilever)
2. $l_{p,äq} = 2196 [mm]$ (length of equivalent cantilever)
3. material parameters for HP 305x95 as given in Table 2 and Table 3

The resulting accumulated damage D is summarized for the different bridge sites in Table 5. The analysis confirms the educated guess that the 100 distinctive yearly temperature cycles can be separated from the “small” daily temperature cycles (Table 5, column C5). However an application of one maximum cycle per year,

based on the maximum variation in temperature for design $T_{e,max}-T_{e,min}$ as given by [EN 1991-2:2003 2010] proves to be too conservative (Table 5, row R4, column C6).

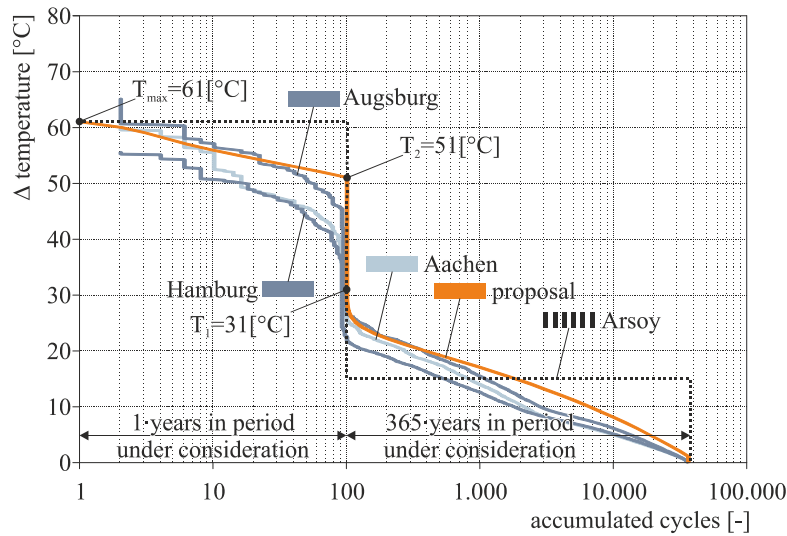


Figure 7. Accumulated temperature spectrum for different bridge locations (100 years).

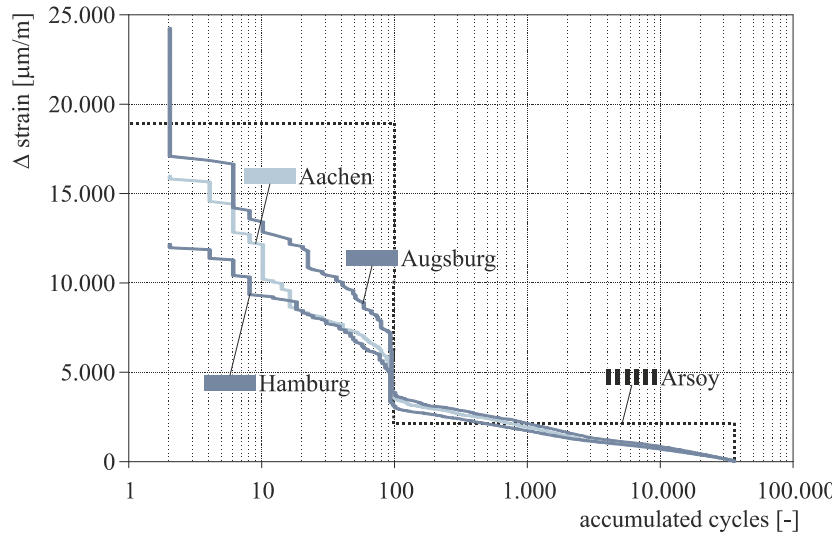


Figure 8. Accumulated strain spectrum for different bridge locations (100 years, $f_y=496\text{N/mm}^2$).

Furthermore Arsoy’s approach, representing the amplitude of a daily temperature cycle by 25% of the amplitude of a yearly temperature cycle [Arsoy 2002] is too conservative for the locations considered here (Table 5, row R4, column C6). This can be concluded from the accumulated strain spectra given in Figure 8 as well. Based on the accumulated temperature spectra (Figure 7) a design approach for the determination of a design fatigue temperature load spectrum is introduced (Table 6).

Table 6. Design approach for a design fatigue temperature load spectrum.

ΔT_i [°C]	cycle n_i [-]	note
1	$\frac{1}{a} \cdot (T_1 - \Delta T_i)^4$	choose a depending on T_1 and T_i a way, that $\sum n_i (0 < \Delta T_i \leq T_1) =$ 365 · years in period under consideration
...		
T_1		
T_2	$\frac{1}{b} \cdot (T_{max} - \Delta T_i)^4 + 1$	choose b depending on T_{max} and T_i a way, that $\sum n_i (T_2 < \Delta T_i \leq T_{max}) =$ 1 · years in period under consideration
...		
T_{max}		

For a period under consideration of 100 years and $T_{e,max} - T_{e,min} = 61^\circ\text{C}$ according to [EN 1991-2:2003 2010], the following parameters are proposed (see Figure 7):

$$a = 145 [-] \quad b = 285 [-] \quad T_1 = 31 [^\circ\text{C}] \quad T_2 = 51 [^\circ\text{C}] \quad T_{max} = 61 [^\circ\text{C}]$$

The damage D calculated by means of a linear damage accumulation based on this temperature spectrum is given in (Table 5, row R5). For a final validation of the proposed procedure, further investigations for different cross sections and additional locations, followed by statistical evaluations, are necessary.

OUTLOOK: STRAIN SPECTRUM UNDER CONSIDERATION OF ALTERNATING, FORCE-CONTROLLED AXIAL LOAD

To study the influence of an additional force-controlled axial loading caused by traffic loads on the superstructure, the strains in the cross section are calculated for the following cases:

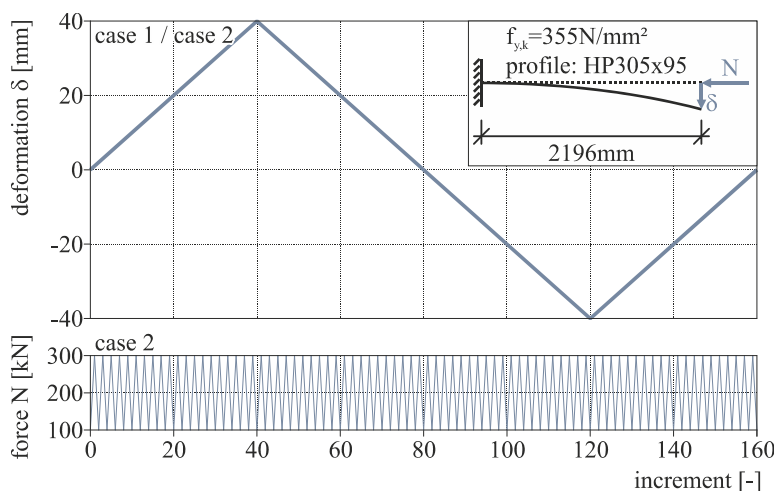


Figure 9. Cantilever loaded by single and combined actions: deformation and alternating normal force (160 increments).

- case 1: single action, deformation δ : displacement controlled deformation δ acting on equivalent cantilever perpendicular to pile's axis (Figure 9, top);
- case 2: combined action, deformation δ and normal force N : displacement controlled deformation δ acting perpendicular to pile's axis as well as force controlled normal force N acting in direction of pile's axis (Figure 9, top+bottom).

The resulting edge strains in the cross sections close to the pile-abutment connection caused by single loading (case 1) and combined loading (case 2) respectively are compared in Figure 10 (1st order theory).

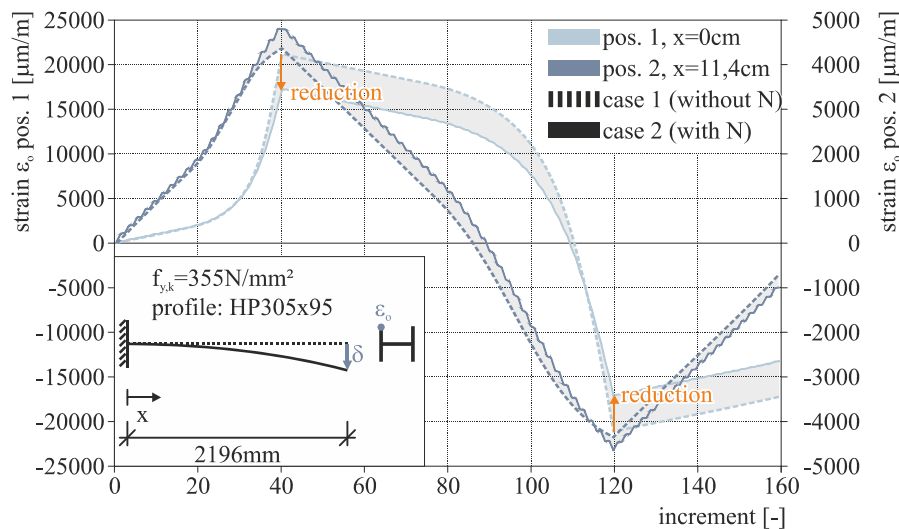


Figure 10. Change of strain distribution caused by an alternation axial force in section “Pos. 1, $x=0\text{cm}$ ” and “Pos 2, $x=11.4\text{cm}$ ”.

A comparison of the strain curve progression shows that the additional alternating normal force reduces the peak strains at the pile-abutment connection (“Pos 1”, left ordinate). This is caused by the fact that the plastic zone is widened, which comes along with an increase of strains in cross section “Pos 2” (right ordinate). The widening of the plastic zone results in stress redistribution, which leads to a reduction of stress and strain peaks in the critical cross section (“Pos 1”). This positive effect is neglected for low cycle fatigue verification if traffic loading is evaluated separately. However, as long as a simple concept for combining these effects is not at hand, a separate evaluation should be performed, as this approach is always conservative.

CONCLUSION AND OUTLOOK

For determination of a (low cycle) fatigue design temperature load spectrum, formulas are proposed based on investigations on bridges at 3 different locations in Germany. This temperature load spectrum can be transformed directly into a strain

spectrum, disregarding the actual load history (method II). Therefore, the movements of the abutments are applied to an equivalent cantilever. For the bridges investigated within the scope of this study this procedure is always safe-sided and nearly exact for weak soils. A consideration of load history is not necessary, which simplifies the design significantly.

Constant axial loading can be neglected. However the influence of these loads in case of a second-order-theory design needs to be checked. In that case, the load bearing by pile friction needs to be considered.

Alternating traffic loads, which are applied additionally, lead to a reduction of the maximum plastic strains developing in the pile. This phenomenon needs to be confirmed by tests. If the underlying theory can be approved, this reduction should be taken into consideration for design, e.g. by a reduction of the plastic stress amplitude in the load collective. This implies the determination of a safety concept for combined temperature and traffic actions, whereas traffic actions have to be applied as partly favorable.

The temperature induced variation of earth pressure has to be considered for the determination of load collectives as well.

ACKNOWLEDGEMENT

Acknowledgement goes to the Research Fund for Coal and Steel (RFCS) for the financial support within the scope of the INTAB / INTAB⁺ research projects as well as DAAD (German Academic Exchange Service) for a contribution towards travel expenses for attending the “CCVII – Composite Construction VII” conference.

REFERENCES

- AASHTO (1996). *A Standard Specifications for Highway Bridges*. 16th edition, American Association of State Highway and Transportation Officials, Washington, DC, p. 677.
- Arsoy, S. (2000). *Experimental and Analytical Investigations of Piles and Abutments of Integral Bridges*. Dissertation. Blackburg: Virginia Polytechnic Institute and State University.
- Clormann, U. H. (1986). Rainflow-HCM - *Ein Zählverfahren für Betriebsfestigkeitsnachweise auf werkstoffmechanischer Grundlage*. Stahlbau, 55(3), Berlin (D): Ernst & Sohn, pp. 65-71.
- Coffin, L. (1954). *A study of the effects of cyclic thermal stresses on a ductile metal*. Trans. ASME, 76(6), pp. 931-950.
- EN 1991-2:2003 (2010). *Eurocode 1: Actions on structures - Part 2: Traffic loads on bridges*. Brussels: European Committee for Standardization.
- EN 1993-1-9:2005 (2009). *Eurocode 3: Design of steel structures - Part 1-9: Fatigue*. Brussels: European Committee for Standardization.

- Feldmann, M., Pak, D (2009). *Zu Verbundbrücken mit integralen Widerlagern*, Stahlbau, 78(12), Berlin (D): Ernst & Sohn, pp.907-915, DOI: 10.1002/stab.200910106
- Feldmann, M., Naumes, J., Pak, D., Veljkovic, M., Nilsson, M., Eriksen, J., et al. (2010). *Economic and durable design of composite bridges with integral abutments*. Final Report EUR24224. Luxembourg (L): European Commission, Research Fund for Coal and Steel Unit (RFCS).
- Feldmann, M., Pak, D., Hechler, O., Martin, P.-O. (2011). *A Methodology for Modelling the Integral Abutment Behaviour of Non-Symmetrically Loaded Bridges*. Structural Engineering International, 21(3), pp. 311-319, DOI: 10.2749/101686611X13049248219962
- Greimann, L., Abendroth, R., Johnson, R., & Ebner, P. (1987). *Pile Design and Tests for Integral Abutment Bridges*. Iowa: Iowa Department of Transportation.
- Haibach, E. (2006). *Betriebsfestigkeit - Verfahren und Daten zur Bauteilberechnung*. Berlin, Heidelberg, New York: Springer Verlag.
- Manson, S. (1965). *Fatigue: a complex subject - some simple approximations*. Experimental Mechanics, 5(7), pp. 193-226.
- Morrow, J. (1965). *Cyclic plastic strain energy and fatigue of metals*. Publisher: A. S. Materials. ASTM STP (378), pp. 45-87.
- Muralidharan, U., Manson, S. (1988). *A modified universal slope equation for estimation of fatigue characterisation of materials*. J. of Eng. Materials and Technology, 110, pp. 55-58.
- Nilsson, M., Eriksen, J., Veljkovic, M. (2008). *Towards a better understanding of behaviour of bridges with integral abutments*. Composite construction in steel and concrete VI, proceedings, Leon, R. T. (ed.). Reston: American Society of Civil Engineers, pp. 717-727.
- Pak, D (2012). *Zu Stahl- Verbundbrücken mit integralen Widerlagern*. Dissertation, Schriftenreihe Stahlbau - RWTH Aachen 74. Aachen: Shaker.
- Pétursson, H., Collin, P., Andersson, J., Veljkovic, M. (2011). *Monitoring of a Swedish integral abutment bridge*. Structural Engineering International. 21(2), pp. 175-180
- Radaj, D., Vormwald, M. (2007). *Ermüdungsfestigkeit - Grundlagen für Ingenieure (Vol. 3)*. Berlin, Heidelberg, New York: Springer Verlag.
- Razmi, J. (2012). *Thermo-mechanical fatigue of steel piles in integral abutment bridges*. Dissertation, Faculty of the Graduate School of the University of Maryland, College Park.
- Technische Universität Darmstadt. (no date). *Materials Data for cyclic loading*. Publisher: F. W. Institut für Stahlbau und Werkstoffmechanik. Downloaded at 2011/08/01 via <http://www.wm.bauing.tu-darmstadt.de/mat-db>.

The Squash Load of Concrete-Filled Tubular Sections

In-Kyu Jeung¹ and Young-Bong Kwon²

¹Dept. of Civil Engineering, Yeungnam Univ., Daehakro 280, Gyongsan, Republic of Korea. E-mail: zy41122@naver.com

²Dept. of Civil Engineering, Yeungnam Univ., Daehakro 280, Gyongsan, Republic of Korea. E-mail: ybkwon@ynu.ac.kr

Abstract

This paper describes the squash load of concrete-filled tubular (CFT) section columns with or without local buckling based on the compression test results. Local buckling of non-compact and slender steel sections is accounted for in the limiting stress formula specified for the steel skin of CFT columns in a similar manner to the AISC specifications. Simple squash load formulae for CFT stub columns for the direct strength method have been proposed to account for post local buckling strength of slender steel skin and enhanced concrete compressive strength due to the confining effect by the steel skin. The squash loads predicted by the proposed strength formula were compared with available test results and those predicted by the AISC specifications and Eurocode4. The comparison confirmed that the squash load formula proposed could predict the squash load of CFT columns conservatively.

INTRODUCTION

The attractive way to solve the local instability and the low ductility of thin hollow steel tubes is filling them with concrete. The concrete-filled tubular (CFT) composite sections are being widely used as columns of high-rise buildings and bridge piers in recent years. Since the steel skin confines the filled-in concrete tri-axially and the concrete resists against the inward deformation of steel skin, both steel and concrete contribute to the strength enhancement of the CFT columns. The CFT columns are susceptible to local buckling of the steel skin, which in many cases is a slender or non-compact element. The post-local-buckling strength of the steel skin and the concrete compressive strength due to tri-axial confinement by the locally buckled steel skin, both of which contribute to the ultimate strength of CFT columns, need to be estimated accurately to predict the ultimate strength of CFT columns reasonably. The confining effect of a steel skin can increase the concrete compressive strength beyond $0.85F_c$. However, since micro-cracking can reduce the tri-axial effect, Chen and Atusta (1991) and Bradford (1991) have conservatively suggested that the effective strength of concrete in a steel casing should not exceed $0.85F_c$. However, the Eurocode4 (2004) has the provision where $1.0F_c$ can replace $0.85F_c$ for the concrete-filled hollow sections and some additional amount of strengths can be considered for circular composite tubes, and the AISC specifications (2010) applies $0.85F_c$ as the limit for rectangular compact steel sections and $0.95F_c$ for circular compact steel sections $0.7F_c$ for slender steel skin.

Simple squash load formula for the steel skin of CFT columns was developed to account for the local buckling stress and the post-local-buckling strength reserve. While the post-local-buckling strength reserve for the steel skin may be accounted for in the current design specifications such as AASHTO specifications (2007), AISC specifications (2005), Eurocode4 (2004) by the Effective Width Method, the strength formula for the Direct Strength Method proposed does not need to compute the effective area of the steel skin and uses the gross area of the steel skin. The strength formula uses the elastic local buckling stress of the steel skin, which can be computed by a rigorous analysis program or theoretical equations, and the ultimate strength formula based on the various test results. A design compressive strength formula for the filled-in concrete is also proposed to account for the strength ratio of the steel skin and filled-in concrete and the local buckling stress of the steel skin. The formula proposed can consequently account for the increase in compressive strength of the filled-in concrete due to the confining effect of the steel skin against the outward deformation of filled-in concrete. The design strengths of circular and rectangular CFT columns predicted by the proposed strength formulae were compared with the current specifications and previous test results.

PROPOSED SQUASH LOAD FOR CFT STUB COLUMNS

Even if the magnitude of the concrete compressive strength is slightly differently defined in the current specifications such as AISC (2005), AASHTO LRFD (2007) and Eurocode4 (2004), the ultimate strength capacity or the squash load of a concrete-filled composite stub column is generally given by

$$P_0 = F_y A_s + K_c F_c A_c \quad (1)$$

where F_y = steel yield stress; A_s = steel area; F_c = concrete compressive strength; A_c = concrete area and the factor K_c is differently taken as 0.7, 0.85, 0.95 or 1.0 according to the type of composite column, the width-to-thickness of steel skin and the shape of the cross section.

For the concrete-encased composite sections and the concrete-filled composite sections of low diameter-to thickness (D/t) ratio for circular shapes and low width-to-thickness (b/t) ratio for rectangular shapes, the current specifications can reasonably be used. However, since a thin steel skin of higher width-to-thickness ratio is generally used for the circular and rectangular CFT sections, local buckling in the steel skin should be considered in the prediction of the ultimate strength of CFT columns. Up to now, the effective width method has been a unique way to account for the local buckling of the steel skin. However, since the effective width of the section specified is generally dependent on the stress level, its calculation should be conducted repeatedly by the trial-error method. Moreover, since the effective width formulae in current design specifications have not been developed and are generally the same as those for steel sections, the effective width for the steel skin of CFT sections specified in the current specifications may be too conservative. To overcome this problem, the squash load of CFT stub columns can be expressed by Eq. (2).

$$P_u = F_{sd} \cdot A_s + f_{dc} \cdot A_c \quad (2)$$

Where F_{sd} = steel design strength; A_s = steel area; f_{dc} = concrete design strength; A_c = concrete area. The portion of the reinforcement steel bar area is omitted in Eq. (2) for simplicity in compression.

Substituting the test ultimate load P_{\max} for P_u in Eq. (2), the design strength of the steel skin F_{sd} generalized by the nominal yield stress can be given by

$$F_{sd} / F_y = \frac{P_{\max} - K_c F_c A_c}{F_y A_s} \quad (3)$$

Once calibrated to the previous test results, the design strength formulae can be expressed in a simple direct strength method. Since the local buckling stress of steel skins is generally increased by filled-in concrete, the design strength formulae proposed for welded steel section columns can be adopted conservatively for the design strength curves for the steel skin of CFT columns.

The design strength formula of steel sections can be adopted conservatively for the composite columns (Kwon et al 2007; Kwon et al. 2011). The design strength formula of a steel skin of rectangular concrete-filled composite columns is expressed in terms of stress by

$$F_{sd} / F_y = 1.0 \quad \text{for } \lambda \leq 0.816 \quad (4a)$$

$$F_{sd} / F_y = \frac{1.0}{\lambda} - \frac{0.15}{\lambda^2} \quad \text{for } 0.816 < \lambda \quad (4b)$$

Where

$$\lambda = \sqrt{F_y / F_{cr1}} \quad (4c)$$

The elastic local buckling stress F_{cr1} can be computed by rigorous computer programs or theoretical local buckling stress. The theoretical elastic local buckling stress formula given in Eq. (5) can be used for square sections and rectangular sections of equal width sub-panels.

$$F_{cr1} = \frac{4\pi^2 E}{12(1-\nu^2)} \left(\frac{t}{b} \right)^2 \quad (5)$$

Similarly, the design strength curves for a steel skin of circular concrete-filled composite columns is given

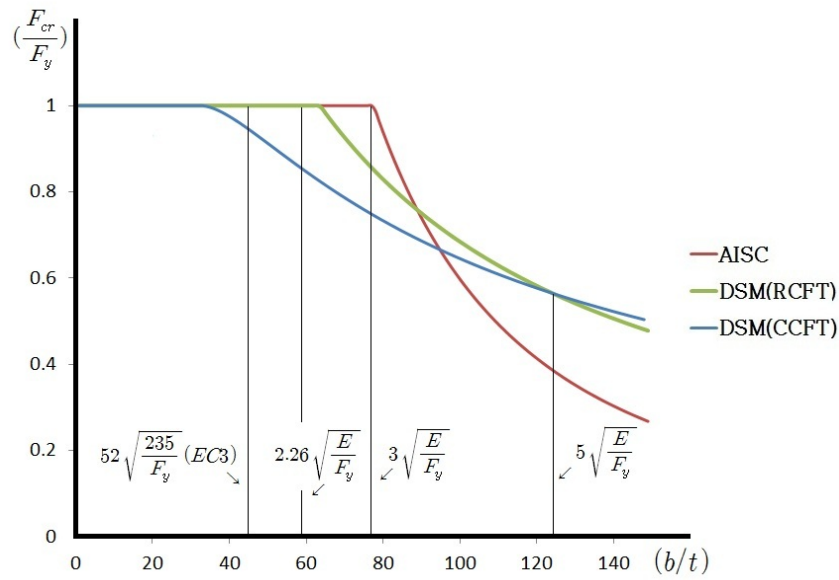
$$F_{sd} / F_y = 1.0 \quad \text{for } \lambda \leq 0.420 \quad (6a)$$

$$F_{sd} / F_y = \frac{1.0}{\lambda^{0.8}} - \frac{0.25}{\lambda^{1.6}} \quad \text{for } 0.420 < \lambda \quad (6b)$$

The theoretical elastic local buckling stress formula given in Eq. (7) can be used for circular sections.

$$F_{cr1} = \frac{2E}{\sqrt{3(1-\nu^2)}} \left(\frac{t}{D} \right) \quad (7)$$

Strength curve Eq. 4(a), (4b) and 6(a), 6b) are compared with the design strength curve specified in the AISC specifications (2010) in Figs. 1(a) and 1(b). To draw Figures 1(a) and 1(b), nominal steel and concrete strengths were assumed as 240 MPa and 24 MPa, respectively, Poisson’s ratio 0.3 and Young’s modulus 205,000MPa. As shown in Figure 2(a), steel design strength curve in the elastic buckling range for rectangular and circular sections is slightly higher than that in the AISC. However, near the slender section limit $3.0\sqrt{E/F_y}$ in the AISC specifications, the strength curve in AISC is slightly higher than proposed strength curve.



(a) Rectangular sections

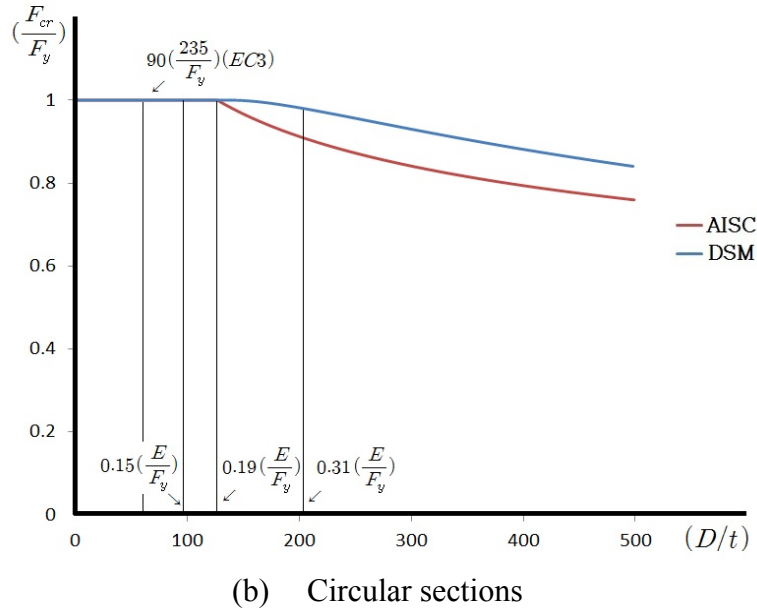


Figure 1. Comparison of steel design strength curve and AISC

Concrete design strength for both rectangular and circular CFT sections in Eq. (2) is given by

$$f_{cd} = K_c f_c \tag{8}$$

where f_c is a nominal concrete compressive strength. The factor for concrete design strength K_c is mainly dependent on the confining effect provided by the steel skin against filled-in concrete. The confining effect of the steel skin may differ according to the steel contribution ratio for ultimate strength and the local buckling strength of the steel skin of CFT columns. To account for the confining effect provided by a steel skin, the factor K_c can be proposed as

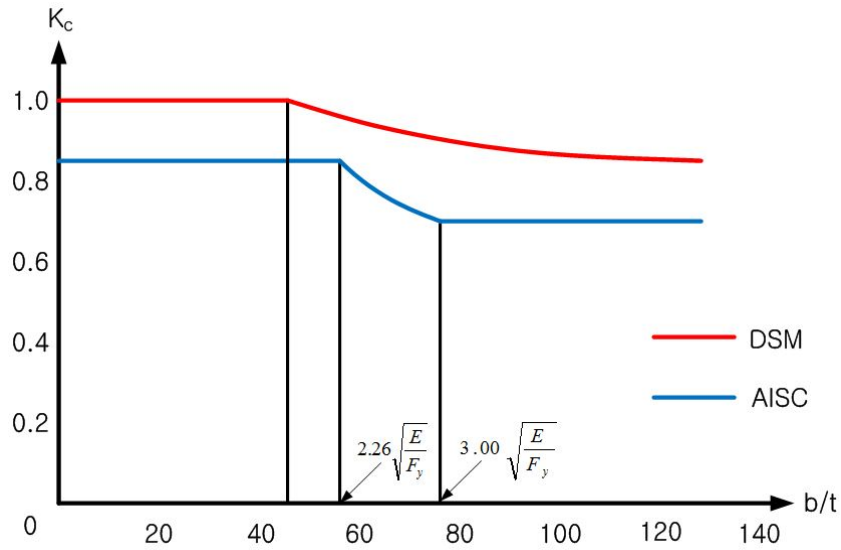
$$0.85 \leq K_c = 0.85(1 + 0.045 \sqrt{\delta} \frac{F_{sd}}{F_c}) \leq 1.0 \tag{9a}$$

where the steel contribution ratio for ultimate strength is

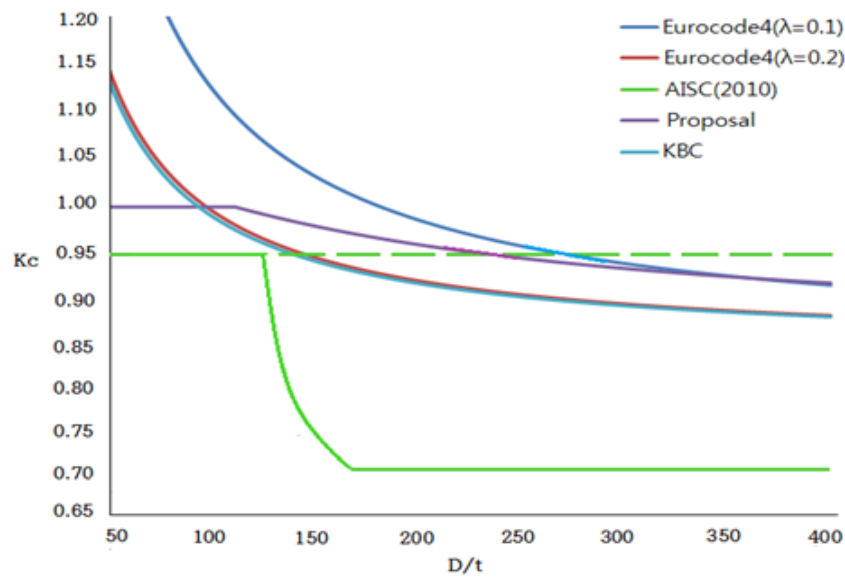
$$\delta = F_y A_s / (F_y A_s + F_c A_c) \tag{9b}$$

The factor K_c is compared with that the AISC specifications (2010) in Figures 2(a) and 2(b). As shown in Figure 2(a), the value of K_c is taken as 0.85 for rectangular compact sections and 0.7 for slender sections and nonlinearly interpolated values for non-compact sections in the AISC specifications (2010), which are quite different from

those in the previous AISC specifications (2005). As shown in Figure 2(b), the factor K_c proposed for circular sections is slightly higher than that in the AISC specifications (2010) but is well coincident with that in EC4 with $\lambda = 0.1 \sim 0.2$. The value of K_c is 0.95 for circular compact sections and 0.7 for slender sections and nonlinearly interpolated values for non-compact sections.



(a) Rectangular sections

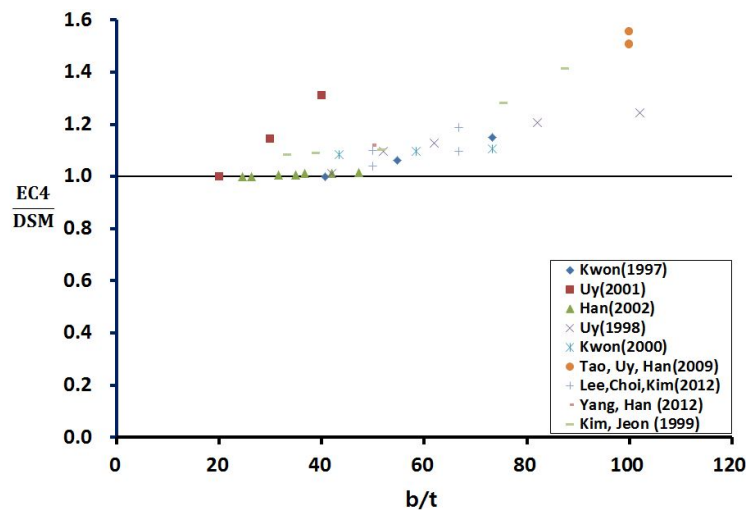


(b) Circular sections

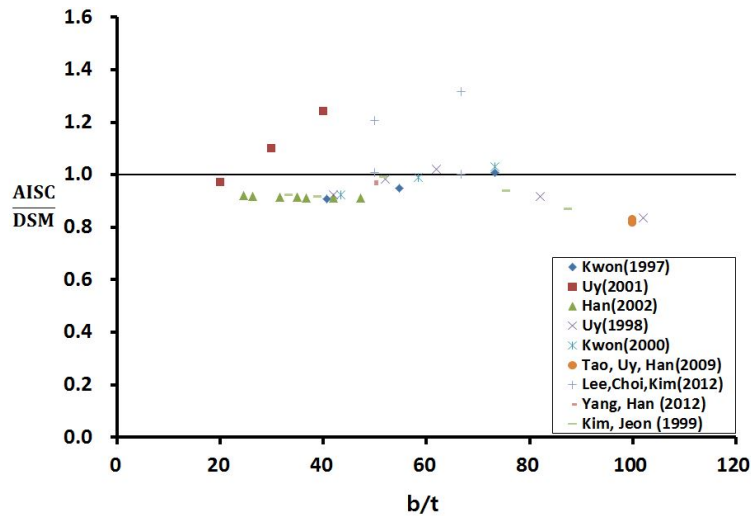
Figure 2. Comparison of proposed K_c , AISC and EC4

COMPARISON OF PROPOSED DSM, CURRENT SPECIFICATIONS AND TESTS

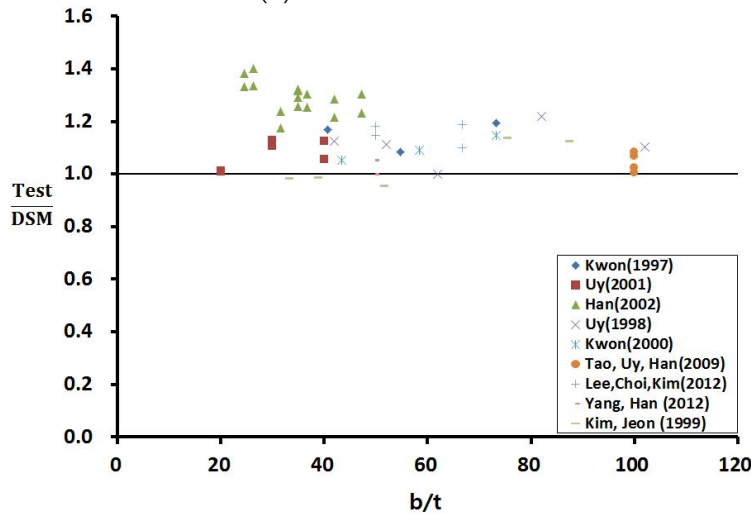
The squash loads predicted by the proposed Eq. (2) are compared with available test results in literature (Song 1997, Kwon 2001, Tao 2009, Lee 2012, Yang 2012, Uy 1998 & 2001, Han 2002, Kim 1999) and those estimated by the AISC specifications (2010) and EC4 (2004) in Figures 3(a)-(c) for rectangular sections. Referring to the comparison in Figure 3(a), EC4 predicted higher strengths than the DSM especially for the sections of larger width-to-thickness ratios which were beyond the maximum limit $52\sqrt{235/F_y}$ in EC4. It is due to that EC4 allows the local buckling of the slender steel skin exceeding the limitations in width-to-thickness ratio but do not provide how to account for it clearly, while the DSM can account for the post-local buckling of steel skins. The AISC specifications allow the use of slender sections and predicted lower strengths than the DSM for all test sections. As shown in Fig. 3(c), the DSM produces reasonable squash loads for all the test sections of diameter-to-thickness ratios between 20 and 110 in comparison with test results. The reliability analysis results shows that the mean and coefficient of variation of values for P_{test}/P_{DSM} of the rectangular CFT sections tested are 1.15 and 0.228, respectively. For comparison, those of P_{test}/P_{AISC} are 1.22 and 0.252. Conclusively, it can be concluded that the DSM can predict reasonable design strength for rectangular CFT columns.



(a) DSM and EC4



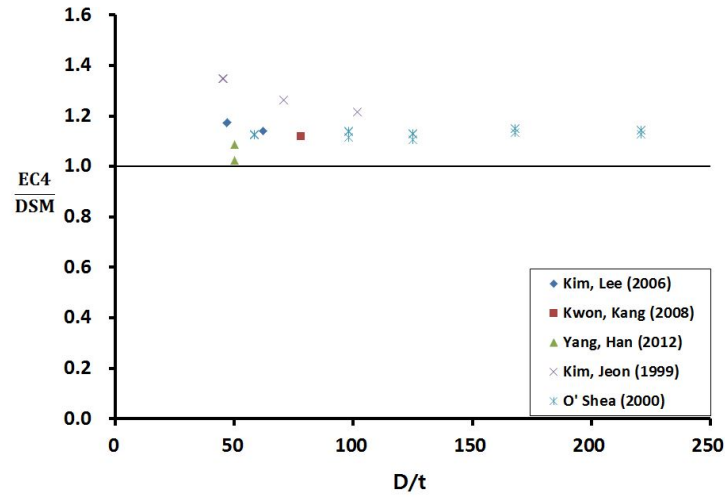
(b) DSM and AISC



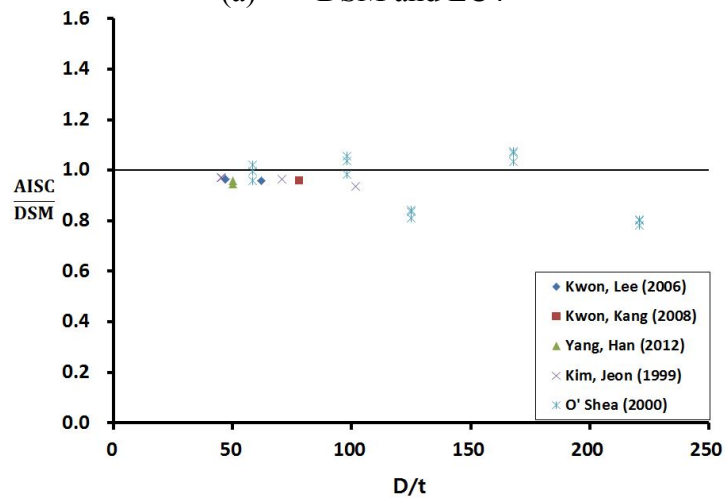
(c) DSM and tests

Figure 3. Comparison of DSM, AISC, EC4 and tests for rectangular CFT sections

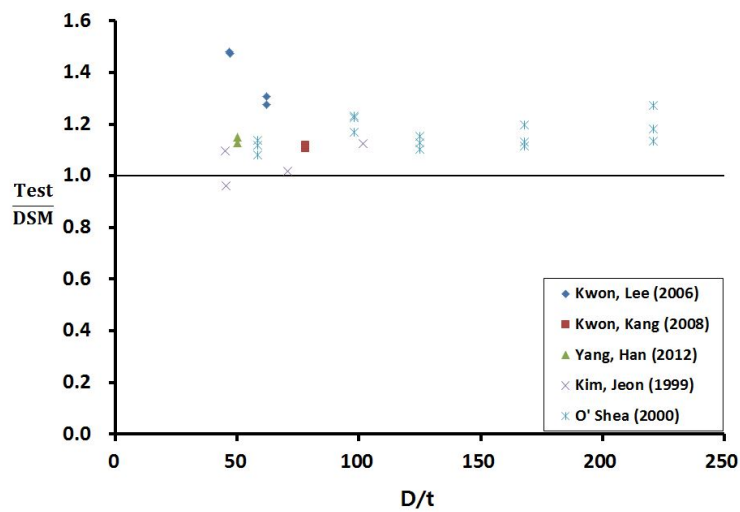
The squash loads predicted by the proposed Eq. (2) for circular CFT columns are compared with test results in literature (Kwon 2006, Yang 2012, Kim 1999, O’Shea 2000) and those estimated by the AISC specifications (2010) and EC4 (2004) in Figures 4(a)-(c). Referring to the comparison in Figure 4(a), EC4 predicted slightly higher strength than the DSM for all sections. However, AISC specifications predicted lower strengths than DSM for most test sections. However, in the case of slender steel skin, the strength predicted by the AISC specifications is slightly higher than the DSM. As shown in Figure 4(c), the proposed strength formula predicts the squash load quite reasonably. The reliability analysis results shows that the mean and coefficient of variation of values for P_{test}/P_{DSM} of the circular CFT sections tested are 1.21 and 0.128, respectively. Therefore, it can be concluded that the DSM can predict reasonable design strength for rectangular CFT columns.



(a) DSM and EC4



(b) DSM and AISC



(c) DSM and tests

Figure 4. Comparison of DSM, AISC, EC4 and tests for circular CFT sections

CONCLUSIONS

A simple squash load formula for concrete-filled tubular (CFT) stub columns was proposed. For the design strength of the steel skin of CFT stub columns which undergo local buckling, simple strength formulae for the Direct Strength Method were adopted. The design strength of filled-in concrete was also proposed to account for varying confinement effect due to the strength ratio between steel skin and filled-in concrete, and the local buckling stress of the steel skin. The squash load formula proposed can predict the ultimate strength of CFT stub columns conservatively. The squash load of CFT columns predicted by AISC specifications (2010), Eurocode4 (2004) and the proposed strength formulae for the DSM were in good agreement with the test results of CFT columns of comparatively low width-to-thickness ratios. However, in the case of rectangular CFT columns of width-to-thickness ratios beyond the limitation in the EC4, EC4 predicted non-conservative strengths for the rectangular CFT columns in comparison with the test results. The AISC specifications predicted more conservative strength than the DSM. However, the ultimate strength predicted by the DSM proposed showed good agreement with tests results of CFT columns with either low or high width-to-thickness ratios. Therefore, it is concluded that the proposed squash load formula can predict the ultimate strength for the CFT columns reasonably. However, the strength formulae should be calibrated further against various test results for the CFT columns of comparatively large width-to-thickness ratios for practical use.

ACKNOWLEDGEMENT

This research was supported by the 2013 R & D fund of KICTEP commissioned by Ministry of Land, Infrastructure and Transport of Korea (Rep.).

REFERENCES

- American Institution of Steel Construction (AISC) (2010). Specification for Steel Structural Buildings, Chicago, Il, USA.
- Bradford M. A. (1991). "Design of short concrete-filled RHS sections", *Civil Engineering Transactions*, Institution of Engineers, Australia, Vol. CE33, No. 3, pp189-194.
- Chen W. F. and Atsuta T. (1991). Theory of Beam-ColumnA-Volume 1: In-plane Behavior and Design, McGraw-Hill, New York.
- European Committee for Standardisation (ECS), Eurocode 4, (2004). Design of Composite Steel and Concrete Structures, Part 1-1: General rules and rules for buildings, Brussels, Belgium.
- Han L. H. (2002). "Tests on stub columns of concrete-filled RHS sections", *Journal of Constructional Steel Research*, Volume 58, Issue 3, pp353-372.
- Kim J. H. and Jeon S. H. (1999). "An Experimental Study on the ultimate strength of concrete-filled stub columns", *Journal of Steel Structures* (in Korean), Korean Society of Steel Construction, Vol. 11, No. 5, pp495-506.
- Korean Association of Highway and Transportation Officials (2005). Korea Highway Bridge Design Specifications, Seoul, Korea.

- Korean Association of Building and House Officials (2005), Korean Building Codes, Seoul, Korea.
- Kwon Y. B., Um C. S., Song J.Y. (2001). An Experimental Study on the Structural Behavior of Welded Steel Box Piers, *Journal of Structural Engineering*, KSCE, Vol.2 No. 6-A, pp837-848. (in Korean)
- Kwon Y. B., Seo S. J. and Kang D. W. (2011), "Prediction of the squash loads of concrete-filled tubular section columns with local buckling, *Thin-Walled Structures*, Vol.49, pp85-93.
- Kwon Y. B., Kim N. G. and Hancock G. J. (2007). "Compression Tests of Welded Section Columns Undergoing Buckling Interaction, *Thin-Walled Structures*, Vol.63, pp 1590-1602.
- Lee J. H. and Kwon Y. B. (2007). "The ultimate strength of concrete-filled steel composite columns", *Proceedings, IABSE2007, Weimar*, pp500-501.
- Song J. Y. and Kwon Y. B. (1997). "An Experimental Study on the ultimate strength of concrete-filled rectangular stub columns", *Journal of Korean Society of Civil Engineering*, Vol. 17, No. 1-4, 1997, pp607-615 (in Korean).
- O'Shea M. D. and Bridge R. Q. (2000). "Design of Circular Thin-Walled Concrete Filled Steel Tubes", *Journal of Structural Engineering*, Vol. 126, No.10-12, pp.1295-1303.
- Uy B. (1998). "Local and post-local buckling of concrete filled steel welded box columns", *Journal of Constructional Steel Research*, Volume 47, Issue 1-2, pp.47-72.
- Uy B. (2001). "Strength of short concrete filled high strength steel box columns", *Journal of Constructional Steel Research*, Volume 57, Issue 2, pp.113-134.

Analyses of Through-Diaphragm Connections to CFT Columns

Liping Kang¹; Roberto T. Leon²; and Xilin Lu³

¹State Key Laboratory of Disaster Reduction in Civil Engineering, Tongji Univ., Shanghai 200092, PRC (corresponding author). E-mail: kangliping2013@gmail.com

²The Via Dept. of Civil and Environmental Engineering, Virginia Tech, Blacksburg, VA 24061. E-mail: rleon@vt.edu

³State Key Laboratory of Disaster Reduction in Civil Engineering, Tongji Univ., Shanghai 200092, PRC. E-mail: lxlst@tongji.edu.cn

Abstract

Available theoretical equations for the shear capacity of composite joints vary in their assumptions for the shear deformation mechanisms and give different equations for calculating its shear strength. This paper discusses previously proposed equations for joint shear capacity, and suggests recommendations for obtaining more accurate predictions. Finite element analyses of through diaphragm connections to CFT columns were carried out in ABAQUS. ABAQUS results and theoretical estimations of the shear capacities were then used to define the properties of a rotational spring in a joint element in OpenSEES representing the shear deformation behavior of the joint. The OpenSEES and ABAQUS results were validated with experimental results from the literature. The results show that: (1) the steel tube flanges and not diaphragms dominate the shear deformation of the joint; and (2) the global behavior of the connection is very sensitive to shear capacity of the joint in joint yielding case.

1. INTRODUCTION

Composite connections between steel beams and concrete filled steel tube (CFT) columns with internal diaphragms, external diaphragms and through diaphragms are recommended in the Chinese design specifications CECS 159:2004 (CECS, 2004), because of their superior seismic performance during experimental studies. Connections with internal diaphragms are common in the US and Japan because of easy fabrication and lower amount of welding involved. However, welds at the beam-joint connection showed brittle fracture in the 1994 Northridge earthquake (Youssef, Bonowitz et al. 1995) for connections to steel I-shapes due to poor on-site welding quality (Lu, Li et al. 2005) and local stress concentrations (Popov, Yang et al. 1998). Similar behavior occurred in Japan during the 1995 Kyoto earthquake in connections to tube sections. On the other hand, connections with external diaphragms have the advantages of large stiffness and ease of fabrication; however, researchers have found that the local yielding of the external diaphragms may prevent development of the full design capacity of the connections (Zhou 2004). Connections with through diaphragms are the preferred connection type in Japan (Elremaily and Azizinamini 2001, Lu, Li et al. 2005); this may due to its efficient capability to

achieve the required strength, stiffness, and ductility for a moment resisting connection.

In a typical through diaphragm connections, steel tube columns are divided into three pieces: upper columns, lower columns and columns in joint area, and then each column section is welded to the through diaphragm by full penetration groove welds or fillet welds (Elremaily and Azizinamini 2001). This column tree is usually finished in factories with well controlled environment; thus the weld quality is easier to guarantee. Beam flanges are welded to through diaphragms with full penetration groove welds (Figure 1) and the beam webs are bolted/welded to the shop welded plates on the steel tube. In the joint, the moment from the beam is transferred to the column by through diaphragms. The shear force is transferred to the column through bolt connections or welds. Previous studies (Morino, Kawaguchi et al. 1993, Elremaily and Azizinamini 2001, Xu and Nie 2011) showed that connections with through diaphragms have superior seismic performance. However, careful welding and inspection is needed because of large amount of welding involved in the joint area (Elremaily and Azizinamini 2001).

The Chinese specification (Association 2004) provides equations to calculate the shear capacity of joints based on previous research on internal diaphragm connections by Lu. Lu's research (Lu, Yu et al. 2000) assumes that two internal diaphragms and their welds, two steel tube webs and the concrete in the joint area work together to resist the shear force in the joint and their contributions can be added algebraically. Zhou (Zhou 2004) gives a different assumption for the behavioral mechanism of the joint: two steel tube flanges and two internal diaphragms compose a "steel frame", and two steel tube webs act as a "shear wall". The "steel frame", "shear wall" and the concrete in the joint area act together to resist the shear force. However, the Japanese code on composite connections assumes that only two steel tube webs and the concrete in the joint work together to resist the shear force in the joint and gives very simple equations for the shear capacity of the joint (AIJ 1991).

The shear force-deformation relation of the joint is the key in analyzing the connection behavior and quantifying building drift. However, no guidance is included in the Chinese specification as to how to calculate the contribution of shear deformation of the joint to the overall drift. Wu et al. (Wu, Chung et al. 2007), Nie et al. (Nie and Qin 2007) and Fukumoto et al. (Fukumoto and Morita 2005) have studied the shear force-deformation relationship for the panel zone. The equation proposed by Nie et al. (Nie and Qin 2007) gives a good estimation of the elastic stiffness of the joint, but the estimated unloading stiffness and energy dissipation capacity do not match well many experimental results (Nie and Qin 2007). The equation proposed by Fukumoto et al. (Fukumoto and Morita 2005) gives satisfactory estimation of the joint up to the concrete ultimate strength; however, the equation tends to underestimate the shear capacity if the concrete reaches its ultimate strength (Fukumoto and Morita 2005). Wu's equation (Wu, Chung et al. 2007) is based on data from bolted joints to concrete-filled tubes. It assumes that the shear force in the joint causes shear deformation to two steel tube webs and flexural deformation to two steel tube flanges. The writers believes that the shear deformation mechanism of Wu et al. (Wu, Chung et al. 2007) is reasonable and easy to understand. However, this

method was derived for bolted connections and research is needed to validate its application to welded connections.

The purpose of this paper is to model the joint behavior between CFT columns and steel beams with through diaphragms using advanced tools, and study shear force-deformation behavior as a first step in the development of a comprehensive joint model describing the cyclic behavior of the joint. The damage mechanism under cyclic loads will be discussed and associated nonlinear damage relations will be introduced.

2. ABAQUS ANALYSES OF THE CONNECTIONS

Two finite element analysis models of connections (SCP and SCC, Table 1) between steel beams and square CFT columns with through diaphragms were developed in ABAQUS. Both models were validated with experimental data of two dimensional connections available from Morino's test (Morino, Kawaguchi et al. 1993). Both column ends are pinned, with axial force (15% of the squash load) applied on the column top and lateral forces acted on both beam ends. The difference between SCP and SCC connection is the steel tube in the joint: a square steel tube 125x4.5 with steel yield strength $f_y = 368.5 \text{ N/mm}^2$ was used in the SCP connection, so the joint yielded in the test. A welded steel plate PL-9 with steel yield strength $f_y = 368.5 \text{ N/mm}^2$, was used in the SCC connection, so that the column yielded in the test. The beams stayed elastic during the entire load history for both connections. This study will investigate the effect of the steel tube in the joint area on the shear capacity of the connection. Monotonic analyses in ABAQUS were compared to the cyclic analyses in the test; this is reasonable as the specimens show stable hysteresis characteristic and little deterioration with cycling.

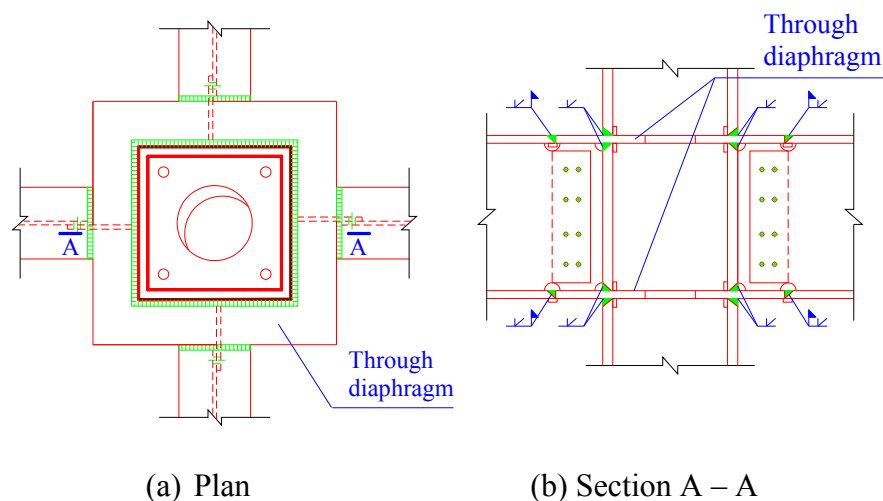


Figure 1. Connections with through diaphragms suggested in Chinese code (CECS 2004)

Table 1. Specimen details of SCP and SCC connections

Specimen	Column		Beam		Joint		
	Square steel tube $h_c \times t$ (mm)	Steel yield strength (N/mm ²)	Concrete compressive strength (N/mm ²)	Section $h_b \times b_f \times t_w \times t_f$ (mm)	Steel yield strength (N/mm ²)	Sect-ion	Steel yield strength (N/mm ²)
SCP	125x6	356.7	16.06	250x125x6x9	368.5	125x4.5	338.1
SCC	125x6	356.7	15.76	250x125x6x9	368.5	PL-9	368.5

2.1 ABAQUS Model

Half of the model was created in ABAQUS with symmetrical boundary conditions (Figure 2), in order to save computational memory and time. The steel tube column is modeled as three parts and each part is tied to the diaphragm. Beam flanges are continuous through the joint (diaphragms), while the webs are interrupted by the steel tube. Three dimensional eight node brick elements with full integration and incompatible modes (C3D8I) were adopted for all the parts above. A finer meshing was used in the joint area in order to capture the complex stress distribution.

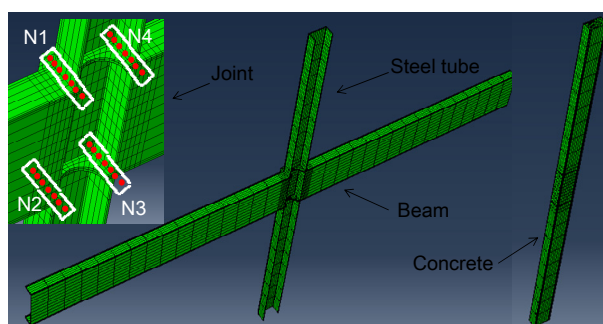


Figure 2. ABAQUS model of SCP connection

2.2 ABAQUS Results

Stress Distribution: ABAQUS results for SCP and SCC connections are shown in Figures 3 and 4. The concrete in the whole area of the joint shows severe plastic strains in the SCP connection, while the concrete column close to the joint presents large compressive strains in the SCC connection (Figure 3). The steel tube web in the joint area shows a high stress concentration for the SCP connection; however, only the steel tube close to the joint yields in the SCC connection (Figure 4). The strain distribution for the two connections shows that the SCP connection yields at the joint while the SCC connection yields at the column end. The thicker steel tube in the joint area with higher steel strength than the steel tube columns results in higher joint shear strength and stiffness, transferring the stress concentration to the columns.

Shear Capacity: ABAQUS results for the SCP and SCC connections are compared to the test results in Figures 5-6. The model is loaded only in the positive direction; for comparison purposes, a symmetrical curve is shown in the negative direction. The ABAQUS model of the SCP connection gives a good estimate of the stiffness, while the strength estimation from the model is about 10% lower (Figure 5(a)) in the positive direction than in the test. Unsymmetrical behavior in the test may be due to initial imperfections in the specimens. The ABAQUS model of the SCC connection gives a good estimate of both shear capacity and stiffness (Figure 6(a)). The column yields in the model, while it stays in elastic in the test for the SCP connection (Figure 5(b)). The larger strain in the column from the ABAQUS analysis can be explained by the fact that the value from the model is measured right at the end of the steel section, which is the location of the largest stress under this loading condition, while the value from the test is measured by the strain gauge located close to the end of the column, but not at the location of the largest strain. The ABAQUS model of the SCP connection gives a close estimate of the joint shear strain compared to the test results (Figure 5(c)). The ABAQUS results for the steel tube strain and joint shear strain are in good agreement for the SCC connection (Figure 6(b) and (c)).

Shear deformation of the joint: ABAQUS results are shown in Figures 7-8. The α deformation in the figure represent the angle change of the steel tube flanges in the loading process; the β deformation represent the angle change of the diaphragms; the γ deformation is the shear deformation of the joint, which is the subtraction of the α and β deformation. It can be seen that the β deformation component is about 20% of the α deformation component in the SCP connection, leading to relatively large shear deformation γ (Figure 7(a)). In the SCC connection, the β deformation component is around 90% of the α deformation component, resulting in very small shear deformation γ (Figure 7(b)). Shear force-deformation relations for the joints are shown in Figure 8. The joint yields in the SCP connection (Figure 8(a)), while it stays in elastic in the SCC connection (Figure 8(b)). This is because the steel tube in the joint of the SCC connection is two times in thickness and has a higher steel strength than that in the SCP connection, resulting in higher shear stiffness, higher shear strength, and smaller shear deformation in the joint

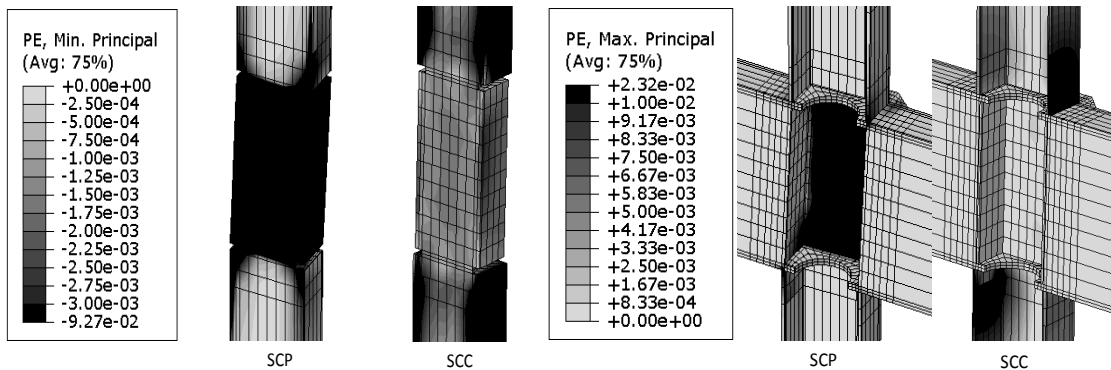


Figure 3. Minimum principal plastic strain of the concrete

Figure 4. Maximum principal plastic strain of the steel

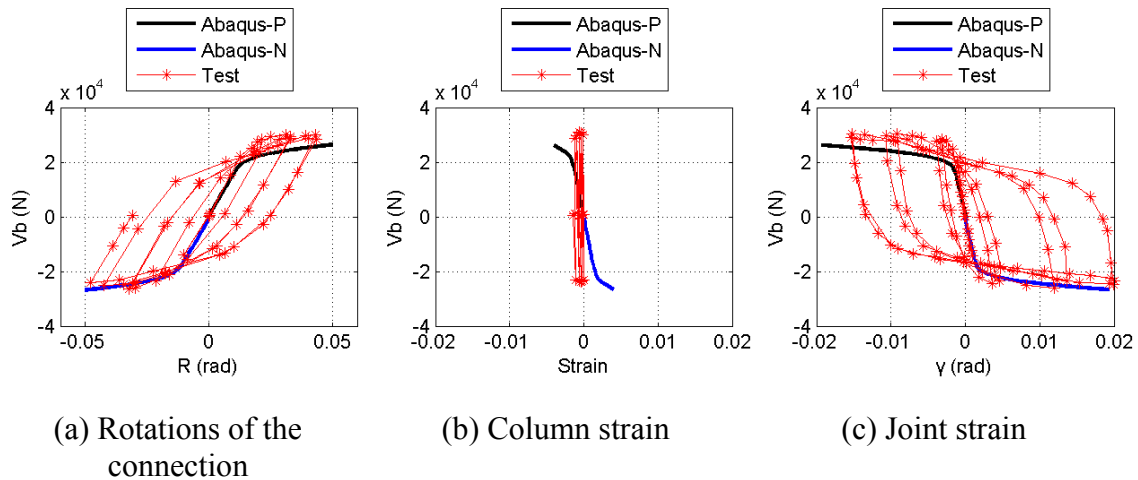


Figure 5. ABAQUS simulation results of the SCP connection

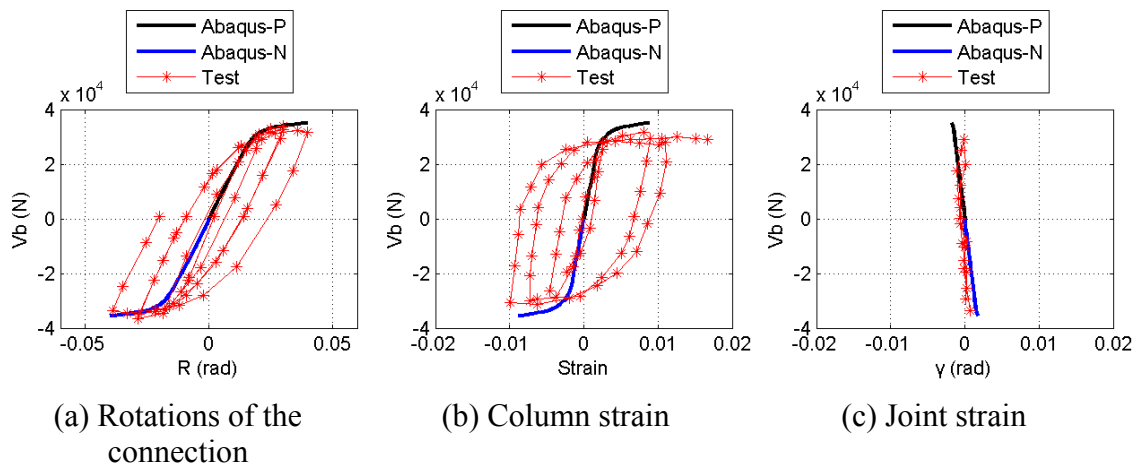


Figure 6. ABAQUS simulation results of the SCC connection

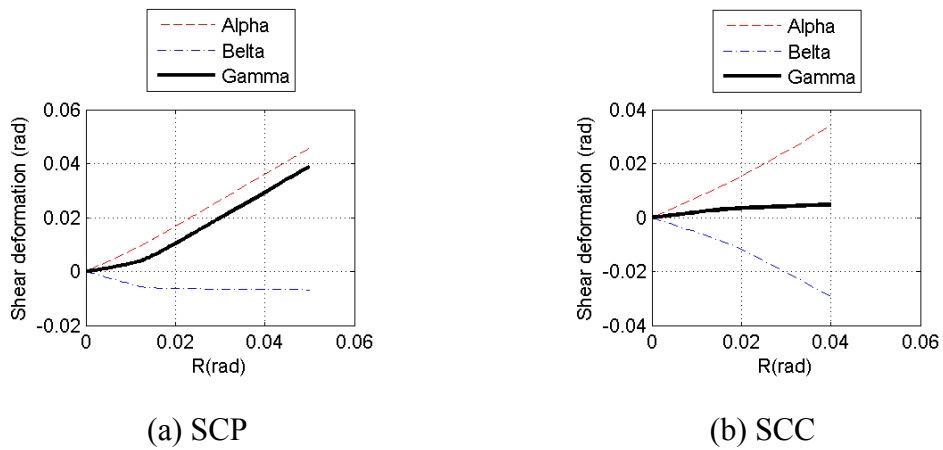


Figure 7. Shear deformations of the joint

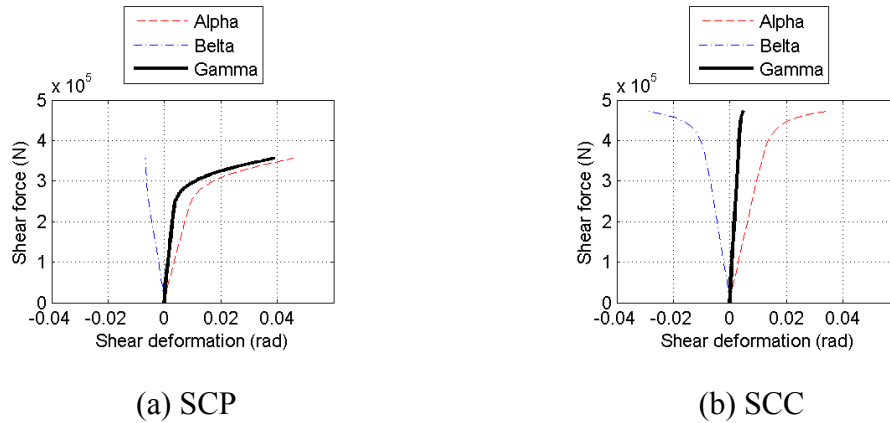


Figure 8. Shear force-deformation relations of the joint

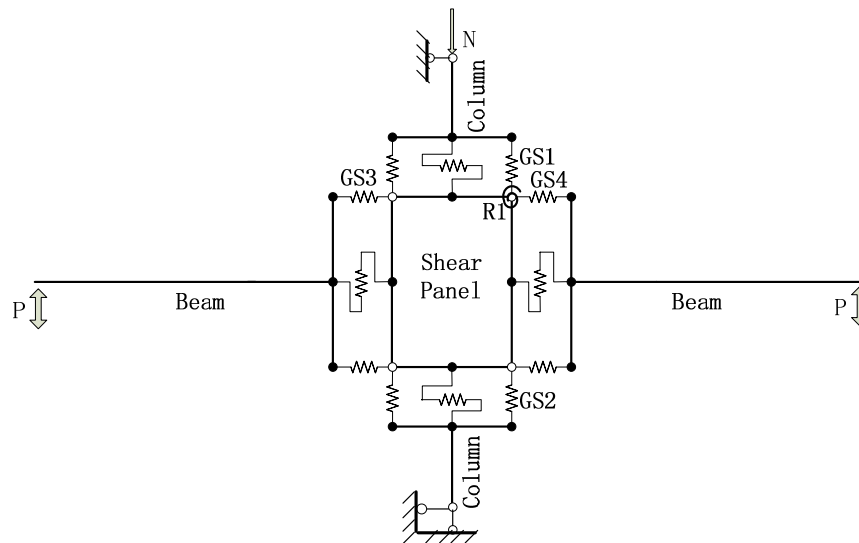


Figure 9. OpenSEES model of the connection

3. OPENSEES ANALYSIS OF THE CONNECTIONS

In this section, the shear capacity from different theories discussed in the Introduction are calculated and compared to the ABAQUS analyses. Then, analysis models are created in OpenSEES to analyze the effect of the shear force-deformation relation of the joint on the overall behavior of the joint and the connection (Figure 9). The OpenSEES model utilizes “NonlinearBeamColumn” fiber elements for both the column and the beam. In the joint, zero length translational springs are used to simulate the column-joint and beam-joint connections, and a zero length rotational spring is used to represent the shear mechanism in the shear panel zone. An “Elastic” material with high stiffness (1.0×10^{10} N/m) is used for the springs at column-joint connections (GS1 and GS2), and beam-joint connections (GS1 and GS2) to simulate perfect welded connections. A “steel02” material is used for the shear force-shear deformation curve of the rotational spring in the joint (R1); this relationship is

obtained from the ABAQUS analyses or Wu's equation and then is transformed into a moment-rotation relationship.

3.1 Shear capacities from available theories

Estimated shear capacities of the SCP and SCC connections are shown in Table 2. All the values are divided by 7.22×10^5 for convenient comparison; this is the shear capacity of the joint in for the SCC connection calculated from CECS equations. The authors believe that the welds should not be considered in CECS equation because the welds and the steel tube webs working in series; the shear capacity should be the lower one of the two – not the summation of the two. The estimated shear capacity of the panel zone without the weld contribution is also listed in the table (see CECS-m). The welds contribution for the shear strength in CECS equation has a significant effect on the total shear strength of the joint. From Table 2, it is seen that while the total shear capacity of the joint is comparable from different theories, the contribution from each component (steel tube webs, steel tube flanges, internal diaphragms, and the concrete) is different. Shear capacities of the joint are compared to the ABAQUS estimations in Figure 10. The CECS equation gives highest shear strength estimation for the SCP connection, and that from AIJ and Zhou are close. Wu's equation gives a close estimation of the stiffness to the ABAQUS analyses, but the estimated strength is the lowest of all the theories (Figure 10(a)). The estimated shear strength of the joint in SCC connection from AIJ, Zhou and Wu are close, but is smaller than CECS estimation. Wu's equation also gives close estimation of the stiffness for the SCC connection (Figure 10(b)).

Table 2. Shear capacity of the SCP and SCC connections.

Specimens	Theories	Steel tube webs	Steel tube flanges/internal diaphragms	Concrete	Joint
SCP	AIJ	0.305		0.102	0.407
	CECS	0.428	0.024 ^a	0.046	0.498
	CECS-m	0.124	0.024 ^a	0.046	0.194
	Zhou	0.278	0.003 ^b	0.117	0.399
	Wu	0.283	0.003 ^b	0.058	0.363
SCC	AIJ	0.662		0.084	0.747
	CECS	0.066	0.024 ^a	0.046	1.000
	CECS-m	0.269	0.024 ^a	0.046	0.338
	Zhou	0.562	0.014 ^b	0.094	0.670
	Wu	0.566	0.014 ^b	0.051	0.651

Note: ^a contribution from internal diaphragms; ^b contribution from steel tube flanges.

3.2 Shear capacity from ABAQUS analyses

Shear force-deformation relations for the joint were obtained from ABAQUS analyses, transformed to moment-rotation ($M-\theta$) relations, and these $M-\theta$ relations were then used to define an equivalent rotational spring (R1) in the panel zone representing the shear deformation in the OpenSEES model. In order to simplify the analysis, a bi-linear relationship for the shear force-deformation relations was adopted. The OpenSEES model of the SCP connection gives a close estimation to the shear force acting on beam ends (Figure 11(a)), strain in the steel tube (Figure 11(b)), and shear strain in the joint (Figure 11(c)). The OpenSEES results of the SCC connection are in good agreement with the test results for the shear force applied at beam ends (Figure 12(a)), shear strain in the joint (Figure 12(c)). However, the steel tube strain from OpenSEES is bigger than both ABAQUS and the test results for the SCC connection (Figure 12(b)). A small strain hardening ratio for the steel tube may cause larger plastic deformation in the steel tube. However, it appears that the OpenSEES model gives a good simulation of the connections with through diaphragms, with either column yields or joint yields case.

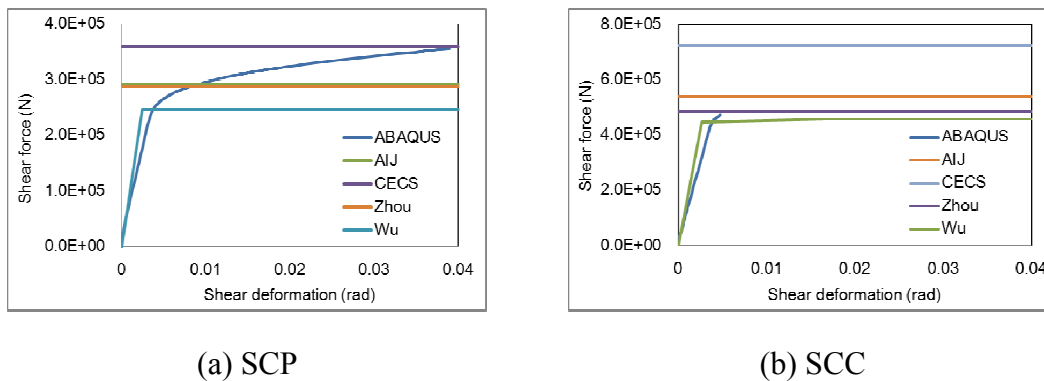


Figure 10. Shear force-deformation relations of the joint

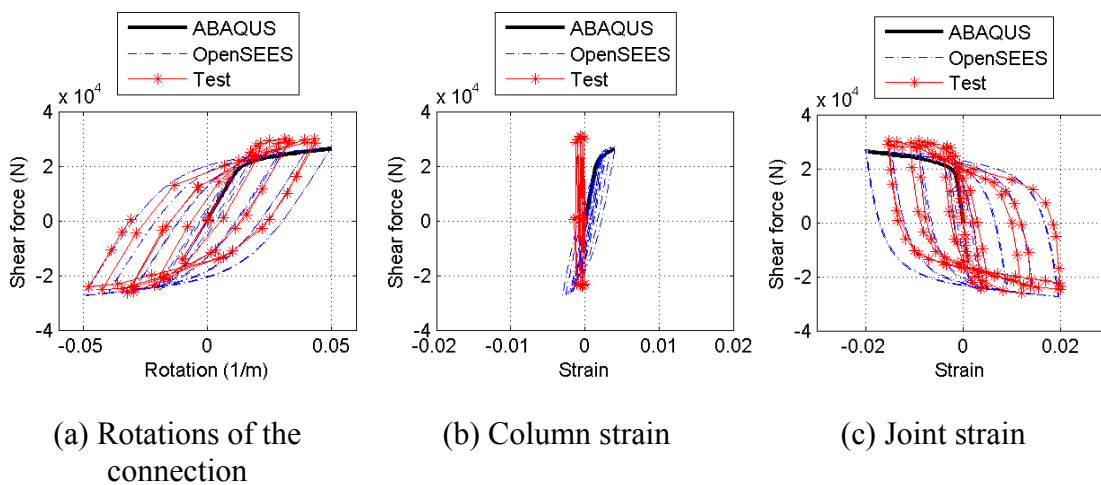


Figure 11. Results of the SCP connection with joint capacity from ABAQUS analyses

3.3 Shear capacity from Wu's equation

An OpenSEES model was established with joint behavior derived from Wu's equation. The model of the SCP connection gives close simulation of the stiffness, while the shear strength is underestimated by 30% (Figure 13(a)). Wu's equation gives a close estimation of the column strain (Figure 13(b)) and shear strain in the joint (Figure 13(c)). The joint of the SCP connection was designed to yield, and the joint behavior dominated the connection behavior. Simulated results of the SCC connection are in good agreement with the test results with respect to shear strength and stiffness of the connection (Figure 14(a)), shear strain of the joint (Figure 14(c)). The estimated strain of the column changes to the positive direction in the OpenSEES analysis (Figure 14(b)); this may be due to loss of stability, especially after column reaches to its yield strength. The column was designed to yield in the SCC connection and thus the column behavior dominates the connection behavior.

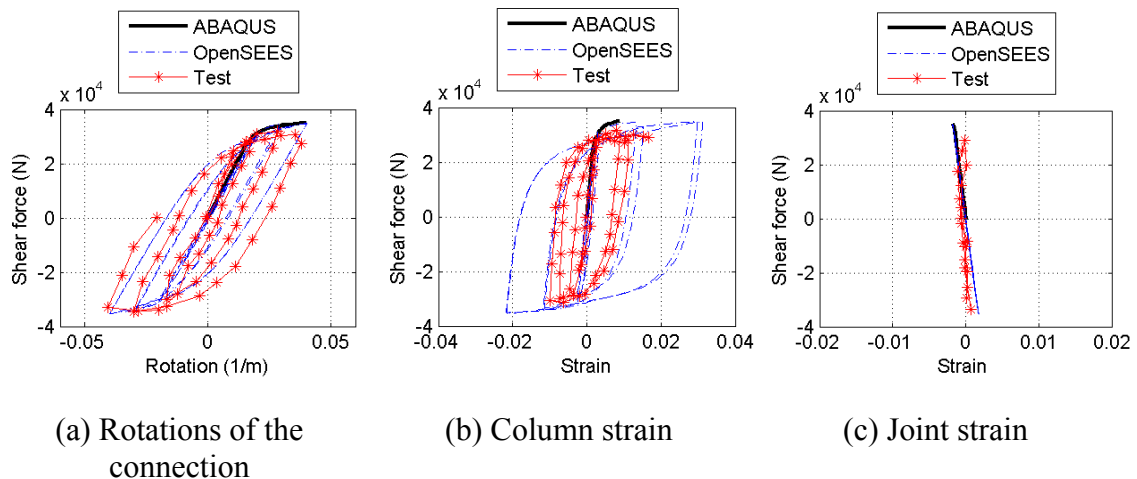


Figure 12. Results of the SCC connection with joint capacity from ABAQUS analyses

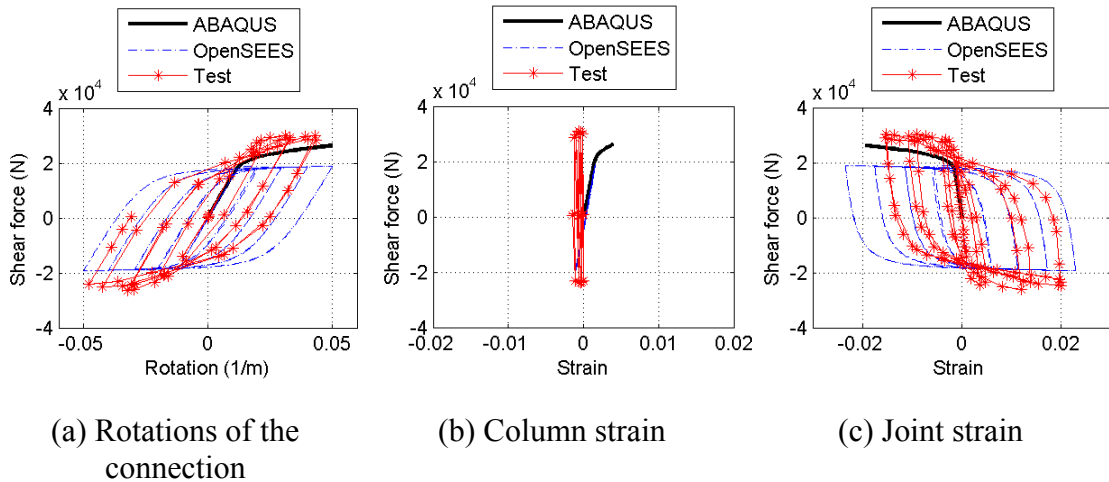


Figure 13. Results of the SCP connection with joint capacity from Wu's equation

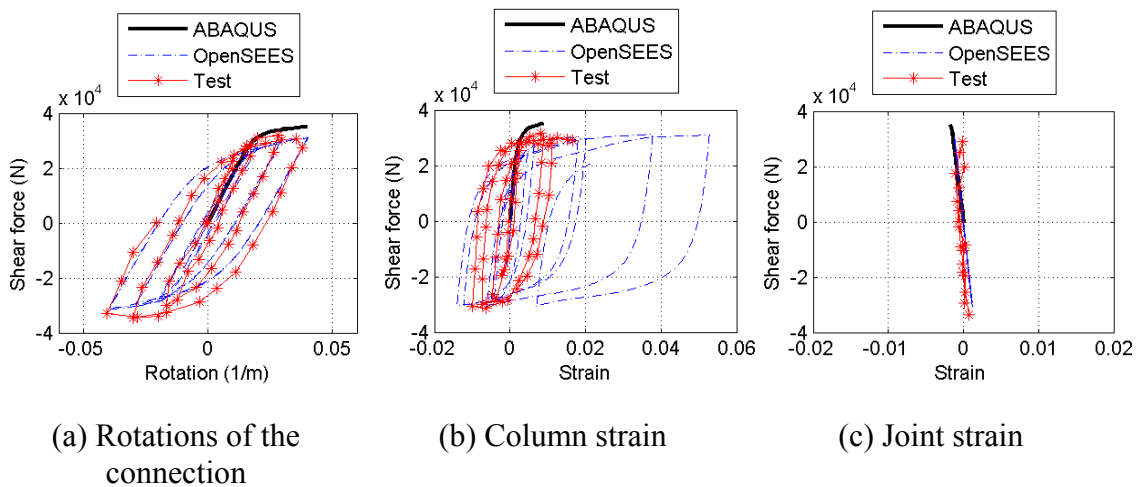


Figure 14. Results of the SCC connection with joint capacity from Wu's equation

Comparison of the OpenSEES models for both the SCP and SCC connections with the joint behavior obtained from ABAQUS or Wu's equation shows that: (1) different shear force-deformation relationships of the joints lead to different joint behavior and different overall connection behavior in the OpenSEES analyses; (2) the OpenSEES model with joint behavior obtained from ABAQUS analyses gives good estimation on the joint behavior and leads to reasonable estimation on the overall strength and stiffness of the connection; (3) the OpenSEES model with joint behavior obtained from Wu's equation gives a good estimation on the stiffness of the joint but underestimate the strength of the joint; and (4) the effect of the shear force-deformation relationship on the total behavior is more significant for the SCP connection compared to the SCC connection; the joint behavior controls the SCP

connection behavior while the concrete and steel tube behavior controls the SCC connection behavior.

4. DISCUSSIONS OF THE JOINT BEHAVIOR

Shear deformation mechanism: The shear capacity equation suggested in CECS assumes that when the joint reaches its yield strength, the two diaphragms and steel tube webs yield. However, this deformation mechanism may not occur because the diaphragms are highly restrained by the concrete and steel tube in the joint area; diaphragms may not be free to deform as assumed. Wu's equation assumes that the steel tube webs, steel tube flanges and the concrete work together to resist the shear force in the joint. When the joint reaches its yield strength, four plastic hinges occur in the steel tube flanges; the diaphragms have no contribution to the joint shear strength.

From the ABAQUS results (Figure 7), it can be seen that the deformation in the steel tube flanges (α) dominates the shear deformation of the SCP connection, while deformation of diaphragms (β) is much smaller, resulting in a significant shear deformation of the joint (γ deformation). The analysis shows that the steel tube flanges rather than the diaphragms contribute to the shear strength of the joint. The deformation assumption in the CECS equation is not applicable for the SCP connection. Even though the diaphragms thickness of the SCC connection is the same as the SCP connection, the shear strength of the SCC connection (4.7×10^5) is around 1.8 times of that of SCP connection (2.6×10^5). Meanwhile, the stiffness of the SCC connection is much higher than that of the SCP connection (Figure 8). The analysis implies that the thickness of the steel tube rather than the thickness of the diaphragm has a significant effect on the shear strength of the joint.

Effect of axial force ratio: From analyses in section 4.1, it can be seen that Wu's assumption on shear deformation mechanism is more appropriate than that from CECS for the connections analyzed. However, a notable disadvantage of Wu's equation is that it does not consider effect of axial force ratio on the shear capacity of the steel tube. The axial force ratio for both SCP and SCC connections is 0.15. To assess the effect of axial force, the shear capacities were recalculated with the consideration of the axial force effect. It is found that the estimated shear capacities are quite close to the results without axial force ratio. Thus, the effect of axial force ratio is negligible for both connections because the axial forces are small.

Effect of strain hardening ratio of the steel tube: Previous research shows that the steel tube has undergone significant strain hardening because of the high restraint from columns and beams. However, the calculated strain hardening ratio from Wu's equation is only 0.0008 for these joints. To assess the influence of strain hardening, a strain hardening ratio of 0.01, 0.03, and 0.05 was used for the shear capacity of the connection. It is found that the strain hardening ratio of the panel zone has a significant effect on the behavior of the panel zone strain, column strain, and the post yielding stiffness of the connection. A higher strain hardening ratio leads to higher

post yield stiffness of the joint, smaller shear deformation of the joint, and larger column strain. OpenSEES results with strain hardening ratio 0.01 for the joint are close to the ABAQUS results, which give reasonable estimations for the shear strength of the connection, column strain and panel zone strain when compared to the test results, as shown in Figure 15. The shear strength of the joint is increased by 25% ((from 248kN to 310kN)), leading to 23.5% increase (from 19.06kN to 23.54kN) in the shear strength of the connection.

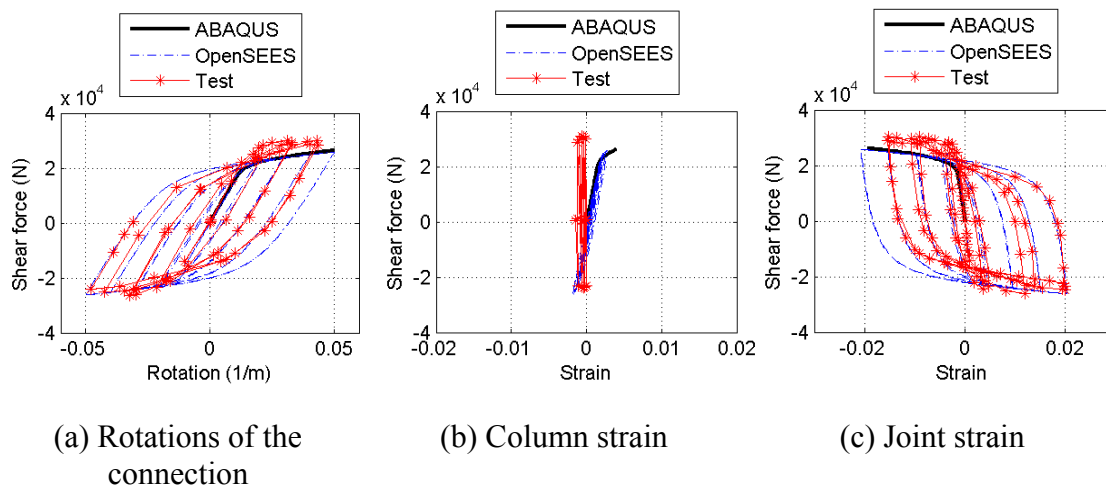


Figure 15. Results of the SCP connection with joint capacity from Wu's equation (strain hardening ratio of the rotational spring: 0.01)

5. CONCLUSIONS

Finite element analyses were conducted in ABAQUS to investigate damage behavior of through diaphragm connections to CFT columns, with experimental validation obtained from test in the literature that included column and joint yielding scenarios. The ABAQUS results show that:

1. The steel tube has a significant influence on the yielding mechanism of the joint. Yielding location is transferred from the joint to other weaker elements (column for the SCC connection) when a thicker steel tube and/or higher steel strength is used in the joint.
2. The deformation of the steel tube flanges in the joint area rather than that of diaphragms dominates the shear deformation of the joint.

Shear force-deformation relations for the joint are obtained from ABAQUS analyses were compared to the shear capacities calculated from existing models. While the joint shear strength is comparable among these theories, the contribution of each component is very different. Wu's equation gives a close estimation of the stiffness compared to ABAQUS results; however the estimated shear strength of the joint is the lowest among these theories.

OpenSEES analyses on these connections were then conducted with the joint behavior obtained from ABAQUS or Wu's estimation. The results show that:

1. The joint behavior in the OpenSEES analyses is very sensitive to the shear force-deformation relationship assumed.
2. The OpenSEES model with joint behavior from ABAQUS analyses models the connections well when compared to test results.
3. The OpenSEES model with joint behavior from Wu's equation gives contrasting results. In the case of joint yielding, a lower estimation of the shear capacity leads directly to a lower shear strength of the connection. In the case of column yielding, the model gives good results both with respect to shear strength and stiffness of the connection.

Possible influencing factors of the shear capacity of the joint were then analyzed. The axial force ratio has a negligible effect on the shear strength of the joint analyzed at low levels of axial force, such as those used in the calibration studies. However, the strain hardening ratio of the steel material has a significant effect on the joint behavior.

REFERENCES

- AIJ (1991). Standard for Structural Calculation of Steel Reinforced Concrete Structures. Architectural Institute of Japan.
- CECS (2004). Technical Specification for Structures with Concrete-filled Rectangular Steel Tube Members. China Engineering Construction Standardization Association, Beijing, China. (in Chinese).
- Elremaily, A. and A. Azizinamini (2001). "Design provisions for connections between steel beams and concrete filled tube columns." *Journal of Constructional Steel Research*, **57**(9), 971-996.
- Fukumoto, T. and K. Morita (2005). "Elastoplastic Behavior of Panel Zone in Steel Beam-to-Concrete Filled Steel Tube Column Moment Connections." *Journal of Structural Engineering*, **131**(12), 1841-1853.
- Lu, Xilin, Xueping Li and Yong Yu (2005). "Design Method of Connections Between CFRT Column and Steel Beams." *Building Structures*, **35**(1), 7-10. (in Chinese).
- Lu, Xilin, Yong Yu, T. Kiyoshi and S. Satoshi (2000). "Experimental Study on the Seismic Behavior in the Connection Between CFRT Column and Steel Beam." *Structural Engineering and Mechanics*, **9**(4), 365-374.
- Morino, S., J. Kawaguchi, C. Yasuzaki and S. Kanazawa (1993). Behavior of Concrete-Filled Steel Tubular Three-Dimensional Subassemblages. Engineering Foundation Conference, ASCE, 726-741.
- Nie, Jianguo and Kai Qin (2007). "Research on Shear Performance of Concrete-filled Square Steel Tubular Column Connections." *Journal of Building Structures*, **28**(4), 8-17. (in Chinese).
- Popov, E. P., T. S. Yang and S. P. Chane (1998). "Design of steel MRF connections before and after 1994 northridge earth-quake." *Engineering Structures*, **20**(12), 1030-1038.

- Wu, L.-Y., L.-L. Chung, S.-F. Tsai, C.-F. Lu and G.-L. Huang (2007). "Seismic Behavior of Bidirectional Bolted Connections for CFT Columns and H-beams." *Engineering Structures*, **29**(3), 395-407.
- Xu, Guigen and Jianguo Nie (2011). "Experimental study of connections of concrete-filled square steel tubular columns with continuous diaphragms." *China Civil Engineering Journal*, **44**(8), 25-32. (in Chinese).
- Youssef, N. F. G., D. Bonowitz and J. L. Gross (1995). A survey of steel moment-resisting frame buildings affected by the 1994 Northridge earthquake. National Institute of Standards and Technology, US Department of Commerce.
- Zhou, Tianhua (2004). "Study on Seismic Behavior and Load-carrying Capacity of Concrete-filled Square Tubular Column to Steel Beam Connection." Ph.D., Xi'an University of Architecture and Technology, Xi'an, China. (in Chinese).

Slab Effects on Beam-Column Subassemblies— Beam Strength and Elongation Issues

Gregory MacRae¹; Michael Hobbs²; Des Bull³; Tushar Chaudhari⁴; Roberto Leon⁵;
Charles Clifton⁶; and Geoff Chase⁷

¹Dept. of Civil and Natural Resources Engineering, Univ. of Canterbury, Private Bag 4800, Christchurch 8140, New Zealand. E-mail: gregory.macrae@canterbury.ac.nz

²Batchelar McDougall Consulting, Level 3, Three35 East, Lincoln Rd., Addington, Christchurch 8024, New Zealand. E-mail: michael@bmconsult.co.nz

³Dept. of Civil and Natural Resources Engineering, Univ. of Canterbury, Private Bag 4800, Christchurch 8140, New Zealand. E-mail: des.bull@pg.canterbury.ac.nz

⁴Dept. of Civil and Natural Resources Engineering, Univ. of Canterbury, Private Bag 4800, Christchurch 8140, New Zealand. E-mail: tushar.chaudhari@pg.canterbury.ac.nz

⁵Dept. of Civil and Environmental Engineering, Virginia Tech, Blacksberg, VA 24061. E-mail: rleon@vt.edu

⁶Dept. of Civil and Environmental Engineering, Univ. of Auckland, Auckland 1010, New Zealand. E-mail: c.clifton@auckland.ac.nz

⁷Dept. of Mechanical Engineering, Univ. of Canterbury, Private Bag 4800, Christchurch 8140, New Zealand. E-mail: geoff.chase@canterbury.ac.nz

Abstract

This paper describes the effect of composite slabs in increasing beam strength and its implications for design. It also discusses the “beam-growth” phenomena, which can detrimentally influence the performance of a frame with reinforced concrete or precast concrete beams, and its impact on steel beams with RC slabs. From the subassembly testing conducted the slab increased the beam strength by around 40%. However, the slab could not maintain strength at large drifts without degradation with transverse or longitudinal decking placed around the columns. This indicates that while transverse or longitudinal slabs should not be considered in design to size the beam, they should be considered in the beam overstrength calculations for the design of other members. Also, both rational considerations and experimental results indicate that beam growth effects tend to be small for composite steel beams because the steel beams are able to yield in both tension and compression.

INTRODUCTION

Slabs are commonly used in buildings around the world but are seldom considered explicitly in their seismic design. In most countries the effect of the slab is not considered at the beam ends at all. In New Zealand, slab effects are not considered determining beam end moment resistance, but they are considered when determining the overstrength from the beam/slab to determine column and panel zone demands. This NZ approach is more conservative than that internationally. It could be more economical if the slab effect could either be (i) fully ignored, or (ii) considered to size the beam as well as the column/panel zone. However, for either of these options to be used, experimental evidence, considering the possibility of secondary effects such as change in demands due to beam growth, is required.

It may be seen from the above discussion that there is a need for experimental testing so that models may be developed which would allow us to detail, and consider appropriately, the slab effect on the demands and capacities.

This paper seeks to address this need by seeking answers to the following questions:

- 1) What are the particular issues with slabs in MRFs?
- 2) What is the reliable strength in traditional construction?
- 3) Can methods be developed to stop slab degradation?
- 4) What is the beam elongation in presence of the slab?

SLAB ISSUES

A. Slab Effects on Subassembly Strength and Degradation

Steel beams in buildings in seismic regions generally support a floor slab. While the effects of this slab are generally ignored in specifications around the world, New Zealand design specifications require the slab effect to be considered in capacity design to determine column sizes. It was hypothesized that:

- a) For isolated/separated slabs, slab effects should not be considered in beam strength design to resist the lateral forces or in overstrength design, but axial force effects on the beam from the slab may be significant.
- b) For slabs which are full depth for a significant distance (say equal to the beam depth) from the column face, a strut-and-tie approach is used to reinforce that area, and which has sufficient confinement, then the slab effect could be considered both in beam strength design to resist the lateral forces and in overstrength design.
- c) For slabs which are placed in contact with the column face, but without special attention to design and detailing, that the current NZ design approach should be continued to be used where the slab effect is not considered for beam strength design to resist the lateral forces, but it is considered in overstrength design.

Cases (a) and (c) above are self-explanatory. The means of providing the reliable strength through large deformations in (b) is consistent with NZS 3404 Clause 13.4.11.3.3(b) for composite beams expected to sustain large seismic demands which states the slab should be reinforced and confined so that the steel beam can reach a maximum tensile strain of 24 times the yield strain before developing the nominal compression capacity of the concrete and compression reinforcement. Here the maximum compressive concrete strain reached is not permitted to be any more than 0.004. References regarding possible means of achieving this are given in the commentary to this clause, but it is not known if this option has ever been used in practice. There also similar to recommendations by AISC (2010) for partially restrained composite members for a full depth reinforced slab, but there is no specific confining requirement. Some means of providing the strut-and-tie and confinement effects are discussed below.

i) A strut and tie mechanism

A slab strut-and-tie mechanism is necessary in order to resist the force applied by the column to the slab. Such a mechanism is shown by Umarani et al. [2008] for a reinforced concrete column as shown in Figure 1. Here, the concrete provides the compressive diagonal struts as the column tries to push the slab on either side of the column apart, and the longitudinal and transverse steel (provided by well anchored rebar or continuous decking) provide tension. The reason for the pushing of the slab apart is described in the beam-elongation section below.

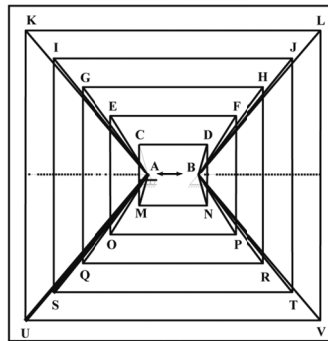


Figure 1. Strut and Tie Mechanism for Slab-Column Interaction
[Umarani et al. 2007]

ii) Prevention of slab shear/spalling failure

When the column pushes against the slab, the slab will only carry the load if it the concrete does not lose strength through an axial stress, shear stress or spalling failure.

A typical slab is confined on three sides – below and on the two sides. There is generally no confinement on the top, so the stress and strain associated with the initiation of spalling can be conservatively considered to be the unconfined concrete

crushing strength f'_c and $\epsilon_c = 0.002$ respectively. As a result of this, two possible ways to determine the likelihood of spalling are given below.

The likelihood of spalling can be assessed simply from **strength considerations**. The force on the slab may be as great as that caused by axial yielding of the beams, which is $\Sigma A_s f_y$, where A_s is the area of the steel beam cross-section and F_y is the steel yield stress. It may be slightly less than this as a result of axial forces being carried in the beams, and as a result of sharing of force between the outside of the column and that carried on the inner flange. If the beam axial yield force is greater than $A_c f'_c$, then there is a possibility of yielding. Here A_c is the area of the concrete slab bearing on the outside of one of the column flanges and f'_c is the compressive cylinder strength of the concrete at the time of testing.

Alternatively, the likelihood of spalling can be understood from **strain compatibility considerations** as follows. Unconfined concrete stress-strain curves indicate the unconfined stress of the concrete reaching the crushing strength f'_c which occurs at a concrete strain of about 0.002. The displacement imposed at the top of the concrete, Δ_c , may be estimated as the inelastic rotation of the plastic hinge multiplied by the distance from the neutral axis to the top of the concrete slab. The position of the neutral axis may be found from standard methods allowing for composite action. The strain in the slab may conservatively be estimated as the displacement divided by the length over which this strain occurs. In standard NZ design, the slab is disconnected from the beam over a distance of 1.5 times the depth of the steel beam ($1.5d$) from the column face. At the end of this length, $1.5d$, the slab is connected by shear studs which can deform. If they are conservatively assumed to be rigid, then the strain, ϵ , is $\Delta_c / (1.5d)$. If this is less than 0.002, then there is little likelihood of spalling failure.

The deformation capacity of the subassembly and slab may be increased by increasing the strain capacity within the concrete slab, through confinement of the top of the slab. One way it could be accomplished is by placing a plate over the top of the slab and tying it down as shown in Figure 2. Note that the tie-downs do not go through the beam member, as this is subjected to severe inelastic deformations and any hole or discontinuity in this plastic hinge region could lead to failure.

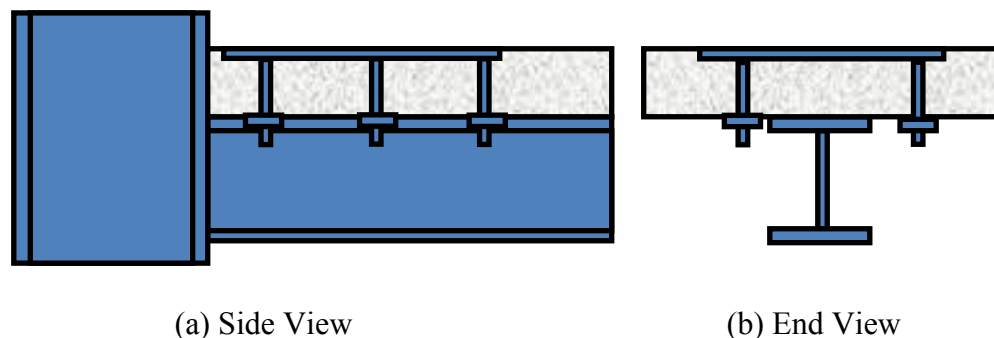


Figure 2. Slab Confinement with a Plate

Another way of providing confinement involves placing a steel cage in the slab placed in front of the column in a region of full-depth slab around the column as shown in Figure 3. This has the advantage of not only confinement of the concrete, but it also works as part of the truss mechanism with longitudinal steel. (The longitudinal and transverse steel is not shown in Figure 3a and transverse steel is not shown in Figure 3b). This concept was also advanced in Section 13.3.5 of the HERA Design Guides Volume 2 (referenced from NZS 3404 : C13.4.11).

Both of these configurations are being considered as part of the research program of Tushar Chaudhari at the University of Canterbury.

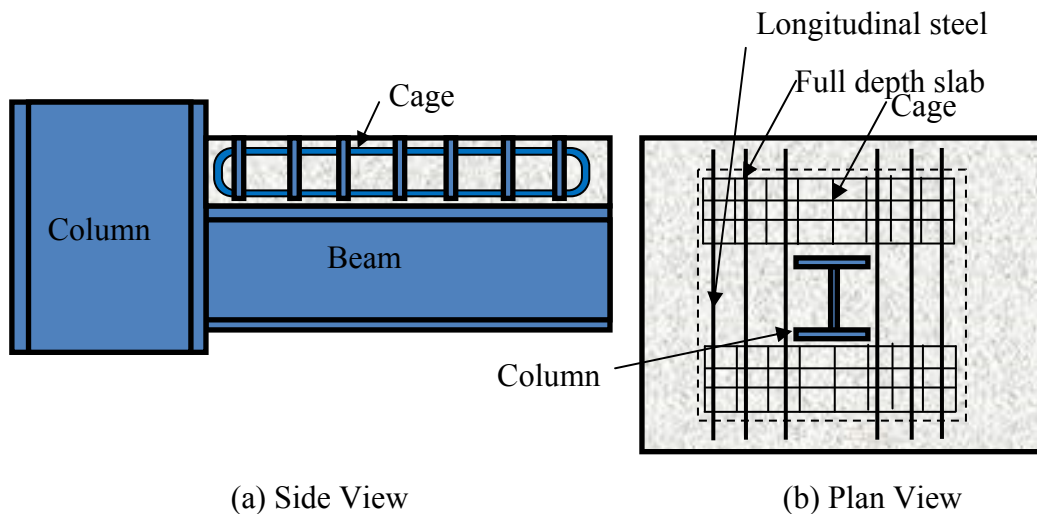


Figure 3. Slab Confinement with a Reinforcing Cage [Chaudhari]

B. Slab Effects on Beam Growth

Beam growth occurs in reinforced and prestressed concrete structures and full description of this phenomena is given by MacRae and Clifton (2013). It causes damage the slab and it can push columns apart causing additional demands on the steel frame. This is because the concrete structures carry load well in compression, but tend to crack/gap in tension. The situation for steel structures is quite different when the slab is separated from the column face to prevent contact during the lateral deformations as shown in Figures 4a and 4b. Here the top of the beam lengthens due to both elastic and plastic deformation. Similarly, the bottom of the slab shortens by the same amount so the theoretical beam growth, measured at the beam centerline, is approximately zero. During displacement in the reverse direction, the lengthening and shortening at the top and bottom of the column are recovered and the top and bottom shorten and lengthen respectively. Another way of stating it is that the neutral axis of the steel beams is at the steel beam centroid so there is unlikely to be any significant beam growth (or shortening) during all stages of testing until effects such as buckling become significant.

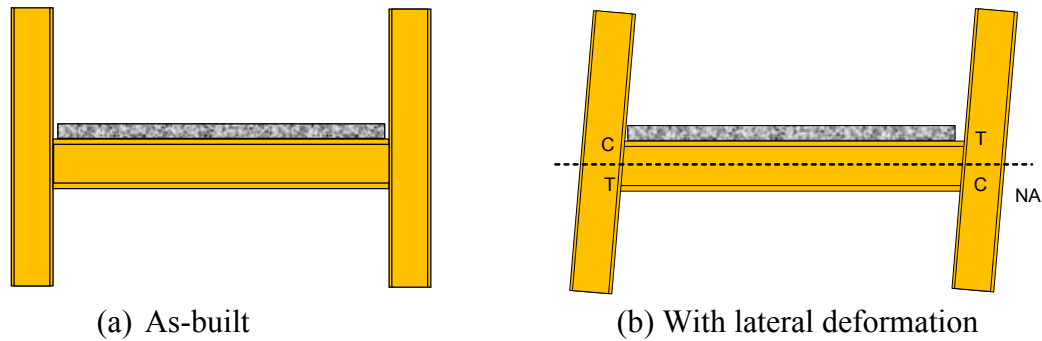


Figure 4. Steel Beam with Slab Separated from Column

If the slab touches the columns, and is strong in tension and compression, the neutral axis may be in the slab and the beam will yield axially in tension and compression as shown in Figure 5a. Since it is the elongating on the left hand side, and shortening on the right hand side, the net effect is that the columns remain the same distance apart and there is zero beam elongation.

If the slab is not strong, then the neutral axes at the different ends of the beam are at different heights as shown in Figure 5b. Here, the neutral axis due to flexure is on the right hand side is through the centre of the beam, while that on the left-hand side of the beam may be in the slab. This would imply more tension yielding at the centre of the beam than compression yielding and some net elongation. This elongation would be expected to be much less than that of a concrete beam where cracks/gaps open at both ends of the beam.

It should be noted that in the discussion above, the neutral axis position due to flexure is considered to be significant. It will also vary somewhat due to the horizontal axial force being transferred from the inertia forces of the beam and slab, through the connections at the end of the beam to the column and this may make some difference to the elongations discussed above.

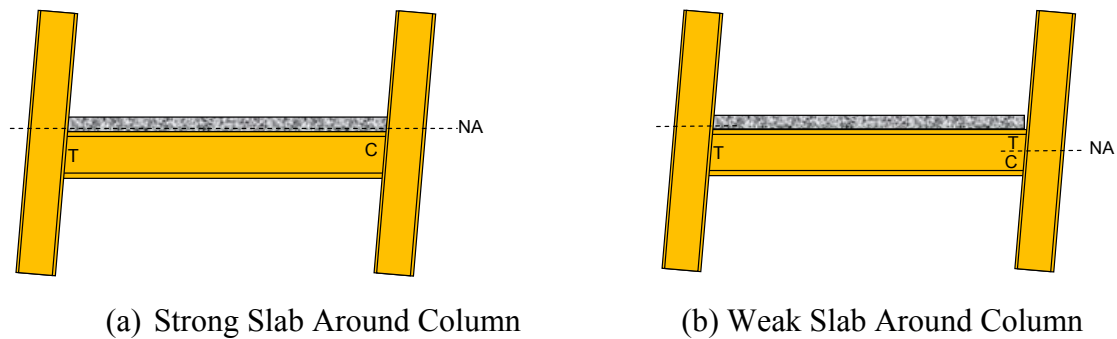


Figure 5. Deformation of Steel Beam with Different Strength Slabs

BEHAVIOUR OF TEST UNITS

A series of full scale beam-column-joint-slab subassembly tests were recently conducted at the University of Canterbury to quantify the effects of slabs under cyclic loading [Hobbs et al. 2013, Hobbs 2013]. Specimens tested have haunched moment end plate connections as shown in Figure 6. The height of the column between loading and reaction pins was 2.0m. The beams were two 3m 310UB32 sections connected to a 2m tall 310UC158 column using bolted moment-endplate connections. Panel zone doubler plates were used. All steel was specified to be Grade 300. The ends of the half beams were pinned to represent the point of inflection of the full length beam whilst the column was pinned at its base and a ram mount located 2m from the base pin centerline.

ComFlor 80 profiled sheet steel decking was used with a total slab depth of 150mm and slab dimensions of 6m by 3m. The decking was connected to the main beams with two 125mm×19mm diameter shear studs every 300mm. Where secondary beams were used one shear stud was provided every 300mm. No studs were placed over the length of beam 1.5 times the beam depth from the column face. Reinforcing steel provided included SE82 seismic mesh across the whole slab and 1.5m lengths of D10 bar centred across beams at approximately 100mm centres in the direction of the deck tray. Further reinforcing was provided around the column opening in the slab as per ComFlor recommendations (Corus 2005). The target strength for the concrete was 30MPa.

The units with different deck configurations are described in Table 1. The isolated unit was separated from the column by 25mm polystyrene glued to both sides of the column flanges, but it was still in contact with the web and the end of the haunch implying that the column was not fully isolated as shown in Figure 6. While isolated connections are simple to consider, axial forces from the slab through the beam onto the columns should also be considered in design. The transverse units had the deck placed transverse to the column. The outside of the column flanges beared against the full depth of concrete both sides with the distance to the beginning of the trough being about 30mm. In the full depth test unit, a square area of full depth slab was placed 300mm from the column making an area of approximately 910mm x 910mm which is in effect a “column capitol”. In this unit, extra reinforcing in the full depth portion of the slab was 2-D10's across each column face as recommended by Comflor. The schematic of the test setup is shown in Figure 7 and the test protocol as per Figure 8 [ACI, 2001].

Table 1. Unit Descriptions and Failure Mode

Slab Unit	Deck Tray Direction (to main beams)	Concrete Detailing	Behaviour
Isolated	Transverse	Separated from column	Beam buckling at 3.5% drift.
Transverse	Transverse	Poured upto column	Beam buckling at 2.5% drift. Slab spalling at 3.5% drift.
Longitudinal	Longitudinal	Poured upto column	Beam buckling at 2.5% drift. Slab spalling at 2.5% drift.
Full Depth	Transverse	Poured upto column, large full depth block	Beam buckling at 2.5% drift. Slab spalling between column flanges.

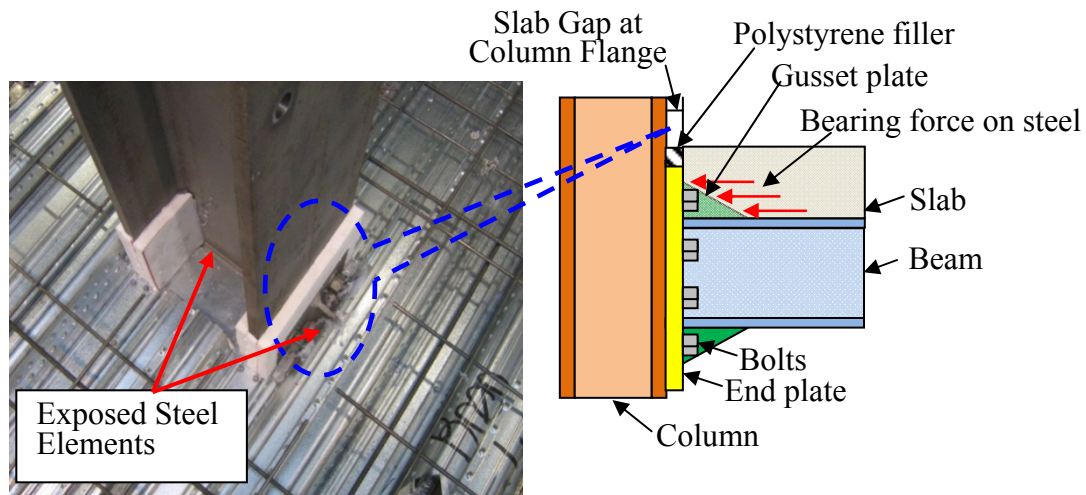


Figure 6. Partial Isolation

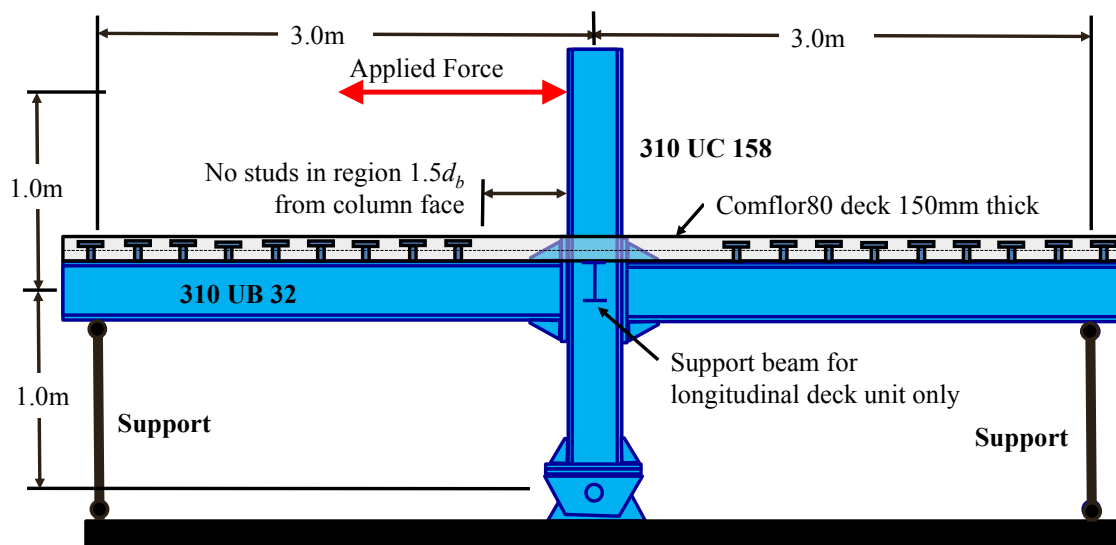


Figure 7. Beam and column setup for all tests.

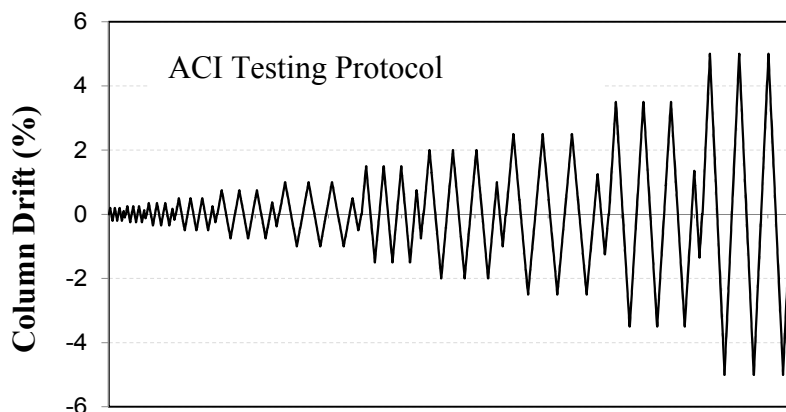


Figure 8. Test Regime (ACI, 2001)

In the tests, the column, panel zone and beam end connections remained essentially elastic. The unedited hysteretic behavior of the units is shown in Figure 9. It may be seen that the isolated column had the lowest lateral resistance. Lateral force resistances were increased by up to 40% due to the presence of the slab in contact with the column. The increase in strength was greater for decking running in longitudinal direction than in the transverse direction as a result of a more substantial full depth slab bearing on the column. However, at 100mm displacement (5% drift) all units had strength similar to that of the isolates unit as a result of strength degradation. This degradation in the unisolated connections generally occurred at drifts from 2.5% to 3.5% as a result of shear failure of the concrete between the flanges of the units shortly followed by spalling of the concrete. In the transverse unit, the deck failure mode

involved compression perpendicular to the ribs. For longitudinal floor, there was a longitudinal concrete shear failure at both edges of the trough of the profiled floor that was centred in the column. This extended over the full 3m of the beam length. In the isolated slab case, there was minimal damage to the slab because it was separated from the column. When full depth concrete was placed around the column, there was no significant cracking near the column but there was compressional concrete strain there. This resulted in lower strength at repeated cycles to the same displacement. In all cases with concrete around the column, there was a shear failure of the concrete between the column flanges at drift ratios greater than 3.5%.

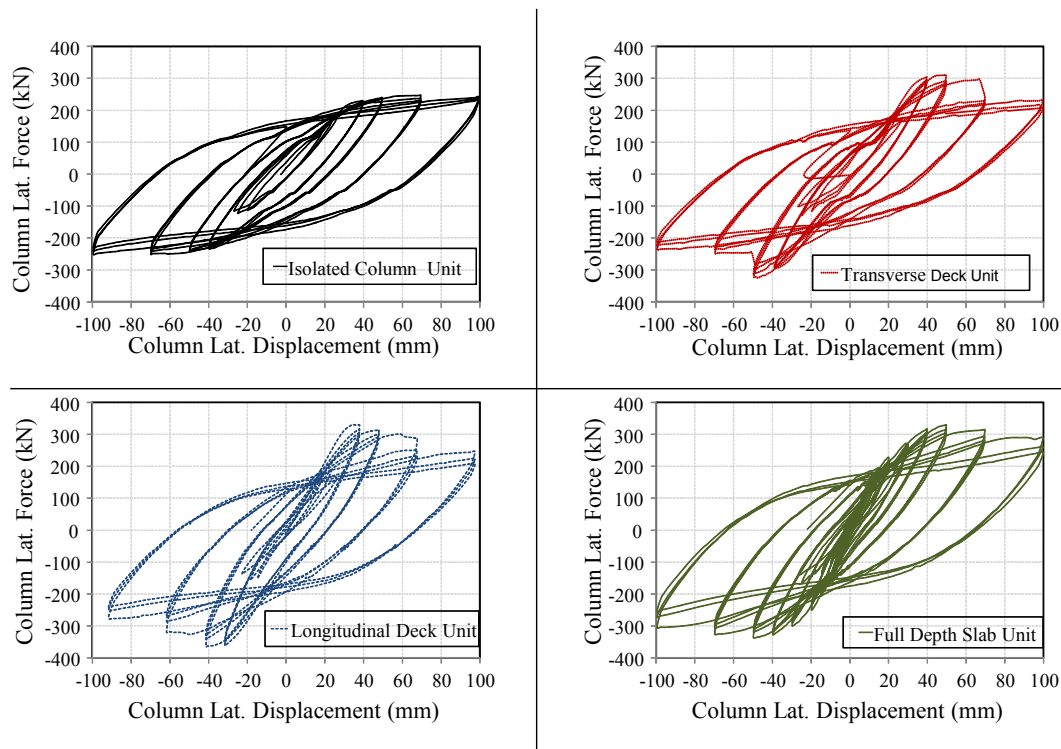


Figure 9. Subassembly Hysteresis Curves

From the discussion above, it may be seen that degradation occurred in both slabs with traditional longitudinal or transverse deck placement. While the degradation was less for the full depth slab unit, there was still significant strength degradation. For the envelope curve, the degradation was less than to 80% of the peak strength obtained even at the large drifts of 5% (i.e. column displacement of 100mm). This would make this configuration satisfactory according to many standard evaluation criteria. Also, with greater depth beams and similar depth slabs, the slab effect would likely be smaller so that it is likely to behave satisfactorily in these cases too. The need to specifically provide confinement of the slab around the column face is therefore not clear from these tests.

The comparison of the initial stiffness of the tested specimens are shown in Figure 10. The longitudinal slab assembly exhibits larger initial stiffness. Whereas in case of the partially isolated slab assembly, the increased initial stiffness indicates that although the slab was isolated from the column face, some contact still existed between the floor slab and the gusset plate, endplate and bolts heads as shown in Figure 6.

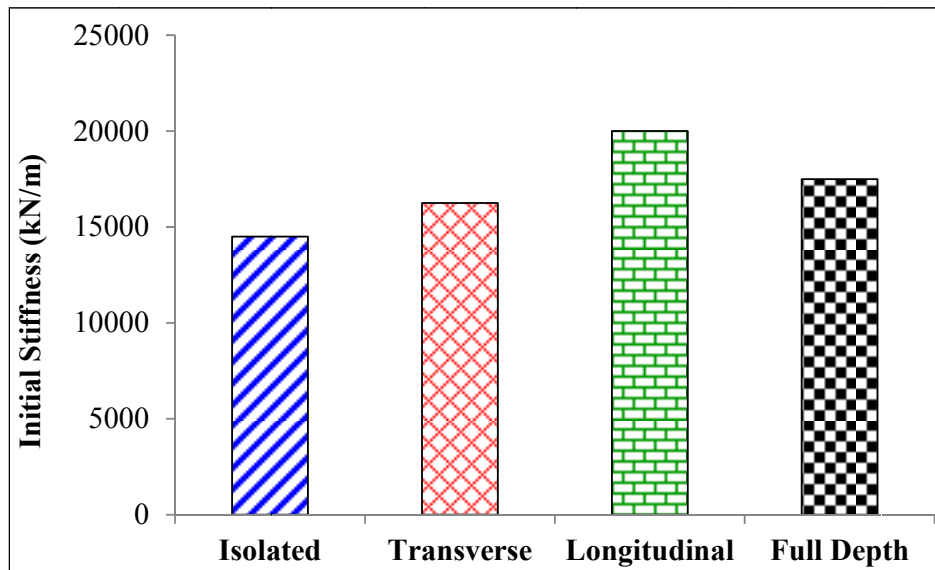
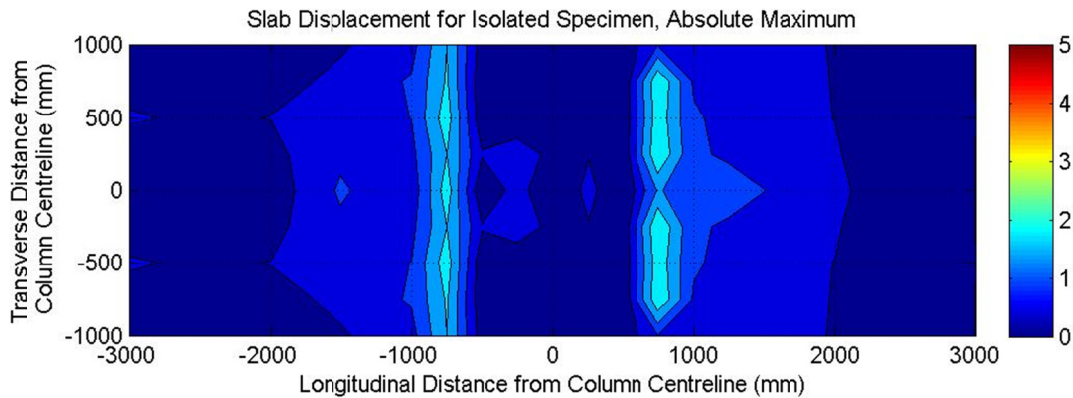


Figure 10. Comparison of Initial Stiffness

The gap opening of the slab in tested units are shown in Figure 11, in the form of an in-plane slab displacement of the slab surface, relative to its initial position. The maximum slab surface displacement (5.0mm) was observed in case of the longitudinal slab units, due to the large area of surface spalling.



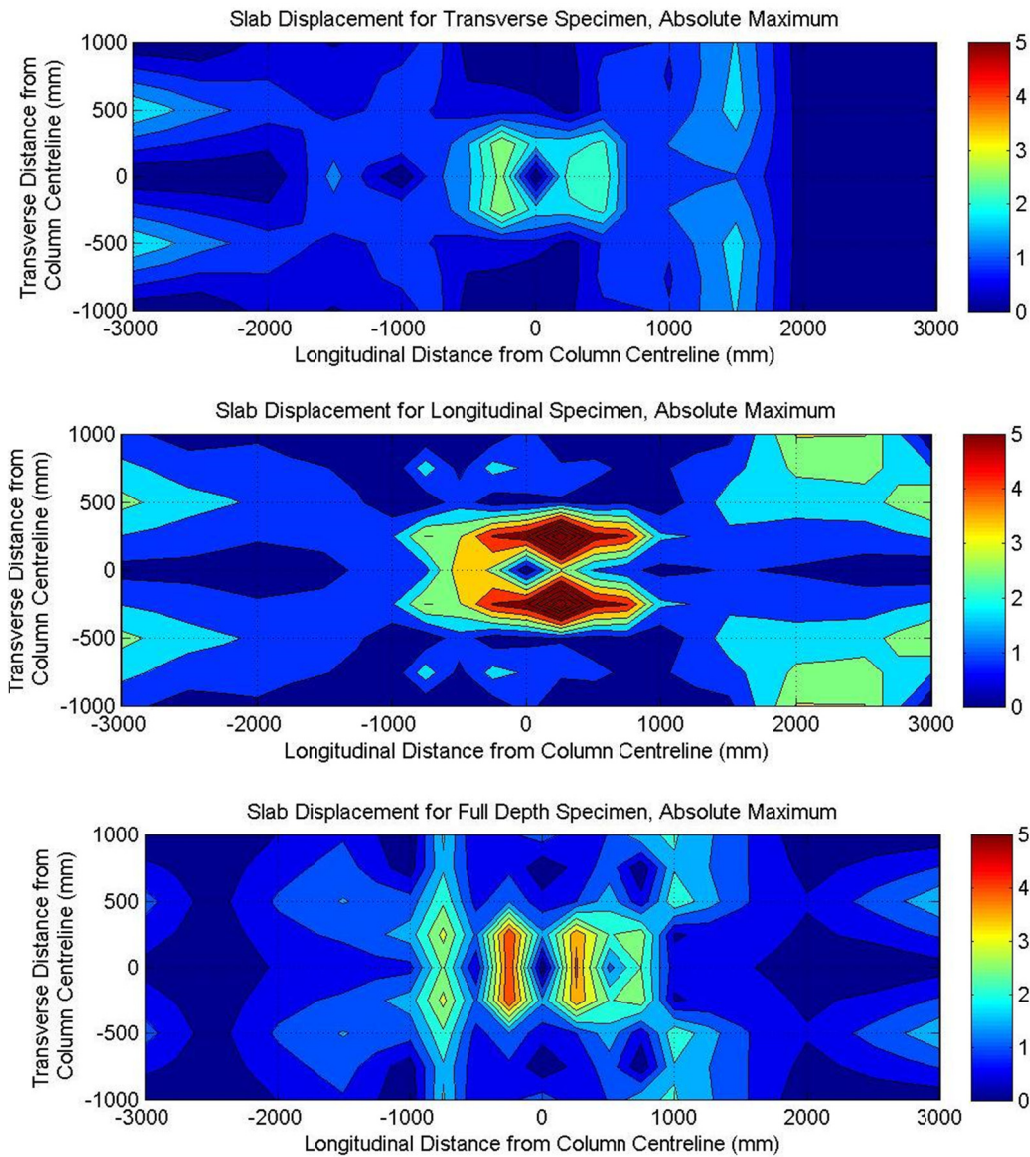
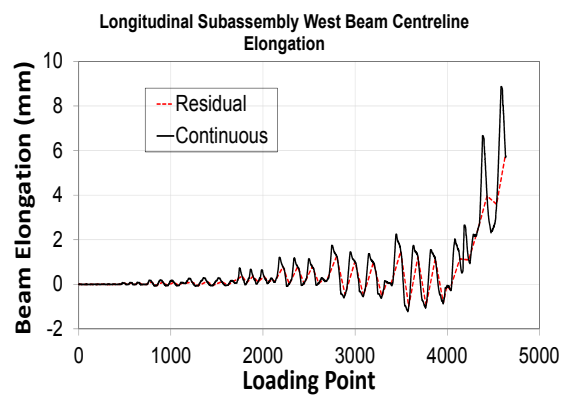
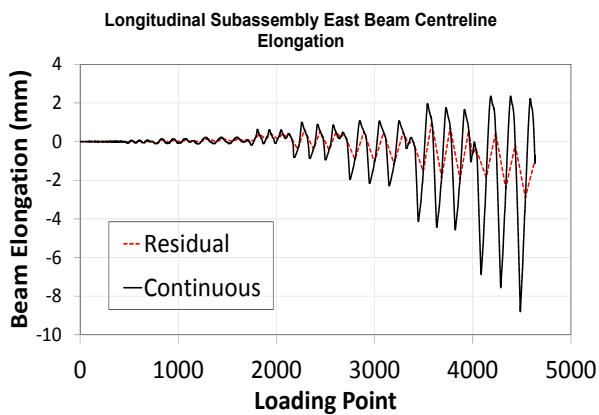
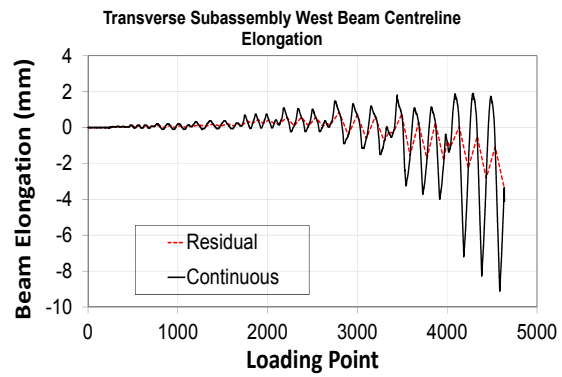
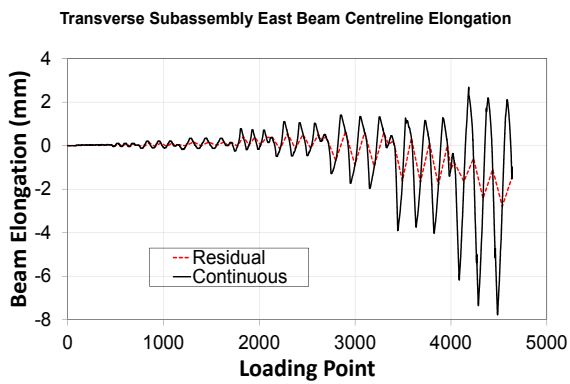
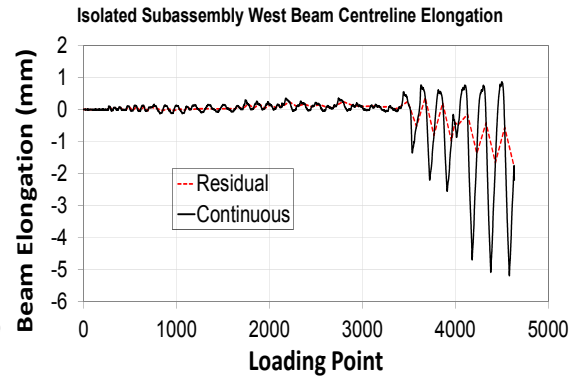
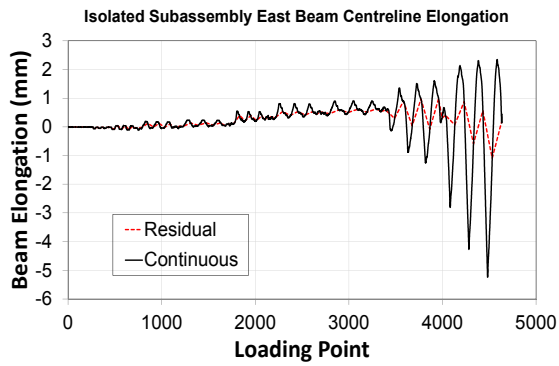


Figure 11. Maximum Slab Surface Displacements

The elongation experienced by the different beams is shown in Figure 12. The load points shown here are the same as those in Figure 8, and these are plotted at the same scale so it is possible to estimate the beam elongation at each level of displacement. The red line shown here is between the values of beam elongation only at the points of zero column displacement. If the neutral axis were expected to be at the top of the column flange, then the beam elongation at 4% drift, assuming 1% elastic frame drift, would be $(4\% - 1\%) \times 320\text{mm}/2 = 3.2\text{mm}$. At greater drifts, slightly greater displacements would be expected based on kinematics alone.



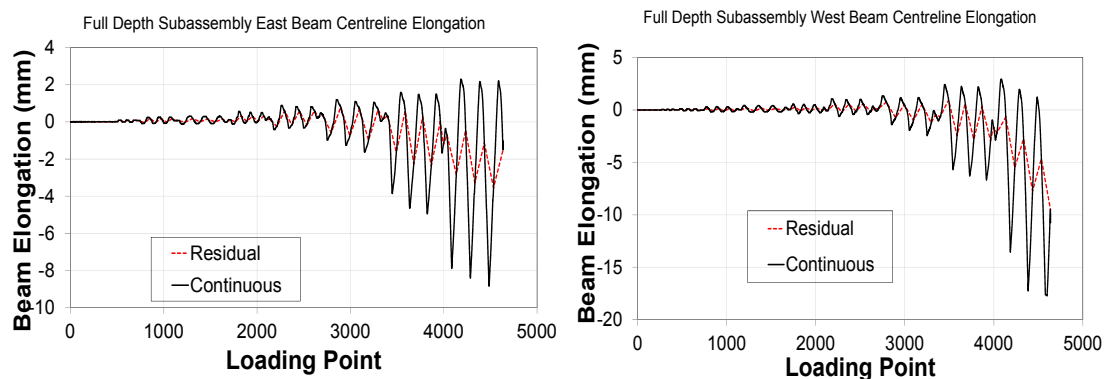


Figure 12. Beam Elongation During the Tests

The elongation shown here tends to be negative and it is likely a result of buckling of the beam and some spalling of the concrete at the slab/column interface. However, in case of the longitudinal slab assembly, the west beam did not exhibit a noticeable elongation under low drift cycles. At larger drifts cycles (3.5% and 5.0% drift) the bottom flange instruments mounting points fell within the buckled portion of the beam resulting in a skewed plot comparing to east beam as shown in Figure 10. Whereas in most of the units it is a similar magnitude to that from the kinematic considerations. Until the very last set of cycles, the absolute value of elongation at zero displacement, termed the residual displacement here, is generally less than about 1mm. This is small and it is likely to be smaller in a building with more realistic boundary conditions (such as other columns) which would resist the possibility of positive or negative beam elongation. It is not likely to adversely affect the structural response.

CONCLUSIONS

A series of tests were conducted to evaluate the effect of beam strength and beam elongation effects considering the presence of a slab. It was found that:

- 1) Slabs on steel beams may bear against the column increasing the strength of the beam and demands on the column and panel zone. However, compressive or shear failure of the slab may occur depending decking orientation. This can be accompanied with a shear failure of the concrete between the column flanges causing degradation in traditional construction.
- 2) For traditional construction, with the deck perpendicular to the frame and direction of loading, the moment resistance depends on the locations of the troughs relative to the column face. It is possible to obtain significant bearing resistance but spalling may also occur depending on the trough location. When the deck is parallel to the frame and direction of loading, a longitudinal shearing failure of the concrete in the trough at the interface with the topping occurred. While the strength of these tests was 31% more than that of the

partially isolated test, it degraded by about this amount after 2.5% drift for this configuration. The reliable strength of traditional construction with any possible configuration, where the troughs may be further or closer to the column, is therefore that of the beam alone.

- 3) The use of a full-depth reinforced slab immediately around the column provided a dependable moment capacity in the case studied of about 34% more than the partially isolated member. Also, partially isolating the column, by separating the slab from the column face, but not from the gusset plate, end-plate or bolt heads, still resulted in some spalling but little strength loss.
- 4) Beam elongation measurements showed that each beam tended to change in length by shortening up to about 1mm, or 2mm for both beams, during applied drifts up to 3.5%. With more realistic boundary conditions, this effect is expected to be less.

ACKNOWLEDGEMENTS

This work has been financed by the Ministry for Science and Innovation through the Natural Hazards Platform under the Composite Solutions project. Materials and manufacturing have been donated by Fletcher Steel, John Jones Steel and Tata Steel (ComFlor).

REFERENCES

- American Concrete Institution (ACI). (2001). "T1.1-01: Acceptance Criteria for Moment Frames Based on Structural Testing", Farmington Hills, Mich, USA.
- American Institute of Steel Construction (AISC). (2010), "AISC341-10 Seismic Provisions for Structural Steel Buildings", Chicago, IL.
- Corus New Zealand, (2005). ComFlor 80 Composite Floor Decking, Auckland, NZ.
- Heavy Engineering Research Association (HERA). (2003). "R4-100: Structural Steelwork Connections Guide, Part 1: Design Procedures", Manakau City, NZ.
- Hobbs M. (2013), "Slab Effects on Beam-Column Joints", Master of Engineering Thesis, Department of Civil and Natural Resources Engineering, University of Canterbury, Christchurch.
- Hobbs M., MacRae G. A., Bull D., Gunasekaran U., Clifton G. C., and Leon R (2013)., "Slab Column Interaction - Significant or Not?", Steel Innovations Conference, Steel Construction New Zealand, Wigram, Christchurch, 21-22 February, Paper 14.
- MacRae G. A and Clifton G. C. (2013), "Low Damage Steel Construction", Steel Innovations Conference, Steel Construction New Zealand, Wigram, Christchurch, 21-22 February, Paper 1.

- Standards New Zealand (1997). “NZS3404. Steel Structures Standard - Incorporating Amendment No.1 and Amendment No.2.” Wellington: Standards New Zealand.
- The HERA Report: R4-49. (1989). “New Zealand Steel Work Design Guide volume 2”. Auckland: HERA.
- Umarani C. and MacRae G. A. (2007). “A New Concept For Consideration Of Slab Effects On Building Seismic Performance”, Journal of Structural Engineering, Structural Engineering Research Centre, Chennai, India, No. 34-1, 25–32.

Problems in Determining the Buckling Loads of Slender Full-Scale Concrete-Filled Tube Specimens

Tiziano Perea¹; Roberto T. Leon²; Mark D. Denavit³; and Jerome F. Hajjar⁴

¹Universidad Autónoma Metropolitana, Departamento de Materiales, Mexico 02200. E-mail: tperea@azc.uam.mx

²Dept. of Civil and Environmental Engineering, Virginia Polytechnic Institute and State Univ., Blacksburg, VA 24061. E-mail: rleon@vt.edu

³Dept. of Civil and Environmental Engineering, Northeastern Univ., Boston, MA 02115. E-mail: mdenavit@sdlal.com

⁴Stanley D. Lindsey and Associates, 2300 Windy Ridge Parkway SE, Suite 200S, Atlanta, GA 30339. E-mail: JF.Hajjar@neu.edu

Abstract

This paper describes the methodology for post-processing experimental data related to the axial strength of slender full-scale concrete-filled tubes. Although utilizing a state-of-the-art testing system, the results obtained during testing needed to be corrected to account for the compliance, frictional forces, resolution and capacity limits of the testing system, as well as the initial imperfections of the specimens. A complex load protocol, aimed at determining the buckling load capacity of CFT columns, a set of points in the P-M interaction diagram of CFT beam-columns, and the torsional strength of CFT members, was used. This load protocol consisted of a set of load cases applied sequentially: (1) pure compression, (2) uniaxial and biaxial bending combined with different constant axial load levels, and (3) torsion with and without constant compression loading. Successful post-processing of the data required the application of different techniques to correct, filter and extrapolate the measured experimental response. In addition, these efforts required that behavior of the loading system be characterized through integration of data from different sensors and computational simulations using stiffness and displacements obtained directly from the test.

INTRODUCTION

A comprehensive experimental program that consisted in testing 18 full-scale and slender concrete-filled steel tube (CFT) specimens was conducted at the Multi-Axial Sub-assembly Testing (MAST) Laboratory at the University of Minnesota as part of a NEES project [Perea 2010]. The main objectives of this experimental program were to characterize the response of slender CFT beam-column to a complex load protocol, in order to verify and improve their modeling [Leon *et al.* 2009; Perea *et al.* 2010]. This modeling, in turn, was used to both verify current specifications and provide advanced analysis and design recommendations.

The Multi-Axial Sub-assembly Testing system (MAST), shown in Figure 1(a), consist of a stiff cruciform steel crosshead connected to the strong floor with four vertical actuators and connected to the L-shaped strong wall with two horizontal actuators in each wall. The eight actuators are connected at the ends using swivels with low-friction bearings. Each vertical actuator has a static load capacity of $\pm 1,468$ kN (± 330 kips) and ± 508 mm (± 20 inches) of piston stroke. In turn, each horizontal actuator has a load capacity of $\pm 1,957$ kN (± 440 kips) and ± 406 mm (± 16 inches) of piston stroke. Thus, the MAST system has the capability of controlling the top 6 degrees-of-freedom (DOFs) independently with a total capacity of $\pm 5,872$ kN ($\pm 1,320$ kips) in vertical force (F_z), $\pm 3,914$ kN (± 880 kips) in shear for each axis (F_x , F_y), and a maximum stroke of ± 508 mm (± 20 inches) and ± 406 mm (± 16 inches) respectively for both the horizontals and the vertical displacement.

The crosshead is driven by a servo-hydraulic control system (HCC) that converts digital input commands (displacement, force or mixed control) for the 6 DOFs at the crosshead center to control commands for each of the eight actuators. The control system is similar to those used in shake tables, but can shift control during testing from displacement to load and *vice versa* on any channel. This is particularly useful in controlling buckling tests as control can be shifted from load to displacement as the buckling begins. An important limit on the HCC is that most quantities can be theoretically controlled to 0.05% of full-scale. This is more than sufficient for axially and flexurally stiff specimens such as shear walls, but, as will be discussed later, was not sufficient to control some of the very flexurally weak specimens tested in this project. This research is particularly valuable because of the extreme slenderness of some of the specimens; current specifications have been calibrated to databases with few slender columns [Leon *et al.* 2005; Kim 2007].

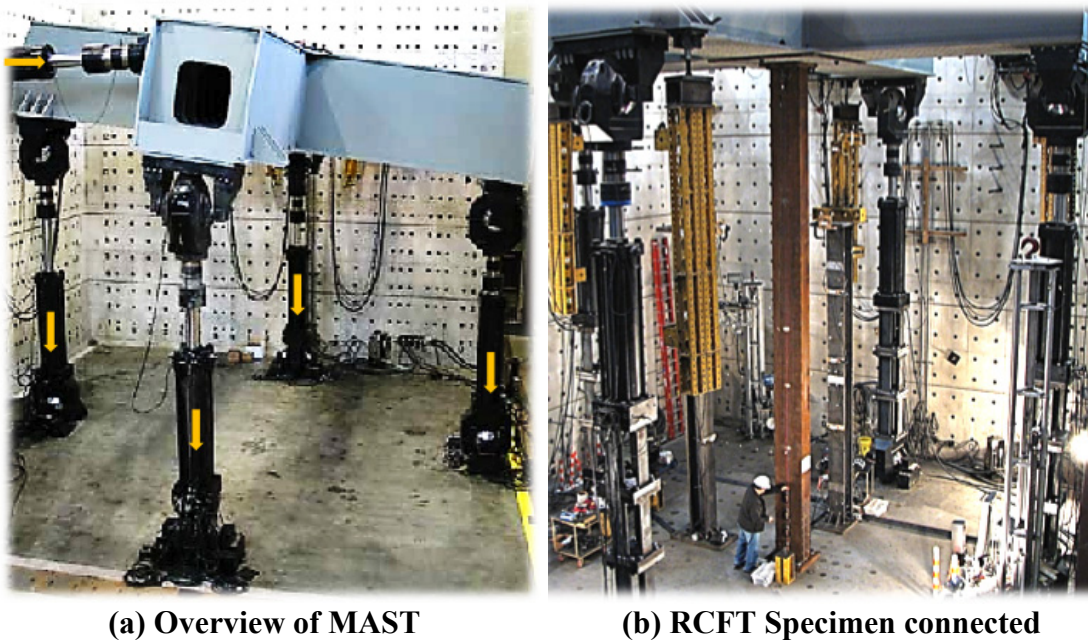


Figure 1 - Multi-Axial Sub-assembly Testing (MAST) system

A very careful and deliberate process was required to post-process values from the experiments so that they could be directly compared to design values. Some of the post-processing is inherent to the geometric and material uncertainties intrinsic in specimens used for buckling studies. However, there were other sources of potential errors that can be attributed to the system setup and control. To extract reliable values for comparison to current design provisions, it was necessary to address all these issues. How this was done is discussed in the following sections.

EXPERIMENTAL PROGRAM AND TEST SETUP

The specimens in the experimental program were selected to be both relatively slender in length and in width-to-thickness parameters. Few specimens with these attributes have been tested in prior research as noted in experimental databases [Leon *et al.* 2005; Kim 2007; Goode and Lam 2011]. In total, 18 full-scale CFT specimens were tested with variations in steel tube shape and size, length, and concrete strength. The test matrix is shown in Table 1 with nominal values and in Table 2 with measured values. The tests were labeled by a test number – shape – length – concrete strength convention; thus Specimen 8-Rw-18-12 corresponds to the eighth specimen in the series, with a Rectangular cross section loaded along its weak axis (or C# for Circular sections of # nominal diameter), with a length of 5.5 m. (or 18 ft.) and a nominal concrete strength of 83 MPa (or 12 ksi). An idea of the scale of the tests is given by the person standing at the bottom of Figure 1(b).

Table 1. Test matrix with nominal values

Section	Cross-Section	D/t	L = 5.5 m = 18 ft.		L = 7.9 m = 26 ft.	
			$f'_c = 5$ ksi = 34.5 MPa	$f'_c = 12$ ksi = 82.7 MPa	$f'_c = 5$ ksi = 34.5 MPa	$f'_c = 12$ ksi = 82.7 MPa
Circular	HSS141.3x3.4 (HSS5.563x0.134)	45	1-C5-18-5			18-C5-26-12
	HSS323.9x6.4 (HSS12.75x0.250)	55	2-C12-18-5	6-C12-18-12	10-C12-26-5	14-C12-26-12
	HSS508.0x6.4 (HSS20x0.250)	86	3-C20-18-5	7-C20-18-12	11-C20-26-5	15-C20-26-12
Rectangular	HSS508x305x7.9 (HSS20x12x ⁵ / ₁₆) <i>weak axis buckling</i>	67	4-Rw-18-5	8-Rw-18-12	12-Rw-26-5	16-Rw-26-12
	HSS508x305x7.9 (HSS20x12x ⁵ / ₁₆) <i>strong axis buckling</i>	67	5-Rs-18-5	9-Rs-18-12	13-Rs-26-5	17-Rs-26-12

Thick plates were welded to the ends of the specimens, with the bottom plate rigidly connected to the strong floor and the top plate rigidly connected the specimen to the crosshead as shown in Figure 1(b) and Figure 2(a). Through control of the crosshead DOFs, different end conditions could be simulated; most often a fixed-free ($K=2$) condition was enforced. Due to control issues, fixed-fixed ($K=0.5$) conditions were used in specimens 1-C5-18-5 [as shown in Figure 2(b)] and 18-C5-26-12. The axial strength of some of the specimens exceeded the vertical capacity of the system (5,872 kN or 1330 kips) and so a pure compression test was not possible in some of the

larger sections. All the specimens retained a large portion of their strength at the maximum displacement (406 mm or 16 in.) although they were often being held in an unstable configuration as the crosshead horizontal DOFs shifted to displacement control as buckling began.

Table 2. Test matrix with measured values

No.	Specimen Name	L (m)	HSS (mm)	F_y (MPa)	F_u (MPa)	E_s (GPa)	f_c' (MPa)	f_c (MPa)	f_t (MPa)	E_c (GPa)	λ -
1	1-C5-18-5(*)	5.50	141.3x3.4	383	487	194.0	37.9	37.9	7.6	27.6	0.90*
2	2-C12-18-5	5.50	323.9x6.4	337	446	199.2	37.9	38.6	7.6	27.6	1.55
3	3-C20-18-5	5.52	508.0x6.4	328	471	200.3	37.9	40.0	7.6	27.6	1.05
4	4-Rw-18-5	5.54	508x305x7.9	365	502	202.4	37.9	40.7	7.6	27.6	1.38
5	5-Rs-18-5	5.54	508x305x7.9	365	502	202.4	37.9	40.7	7.6	27.6	0.88
6	6-C12-18-12	5.50	323.9x6.4	337	446	199.2	87.6	91.0	11.4	41.9	1.90
7	7-C20-18-12	5.53	508.0x6.4	328	471	200.3	87.6	91.0	11.4	41.9	1.30
8	8-Rw-18-12	5.55	508x305x7.9	365	502	202.4	87.6	91.7	11.4	41.9	1.65
9	9-Rs-18-12	5.55	508x305x7.9	365	502	202.4	87.6	91.7	11.4	41.9	1.04
10	10-C12-26-5	7.95	323.9x6.4	335	470	200.2	50.3	54.5	4.1	34.5	2.38
11	11-C20-26-5	7.99	508.0x6.4	305	477	201.7	50.3	55.8	4.1	34.5	1.61
12	12-Rw-26-5	7.96	508x305x7.9	406	534	200.1	50.3	56.5	4.1	34.5	2.14
13	13-Rs-26-5	7.97	508x305x7.9	383	505	200.2	50.3	57.2	4.1	34.5	1.35
14	14-C12-26-12	7.96	323.9x6.4	383	461	198.3	79.3	80.0	5.2	40.0	2.72
15	15-C20-26-12	7.98	508.0x6.4	293	454	200.1	79.3	80.0	5.2	40.0	1.78
16	16-Rw-26-12	7.96	508x305x7.9	381	506	200.5	79.3	80.7	5.2	40.0	2.30
17	17-Rs-26-12	7.96	508x305x7.9	380	496	200.1	79.3	80.7	5.2	40.0	1.46
18	18-C5-26-12(*)	7.94	141.3x3.4	383	487	194.0	79.3	80.7	5.2	40.0	1.51*

Notes: L is the length; F_y , F_u and E_s are the yielding stress, the ultimate stress, and the Young's modulus of the HSS section, respectively; f_c' and f_c are the concrete strength at 28 days and at the day of testing, respectively; f_t and E_c are the tension strength and the Young's modulus of the concrete, respectively; λ is the slenderness parameter calculated as defined by AISC 360 (2010) generally based on $K=2$ (except (*), $K=0.5$).

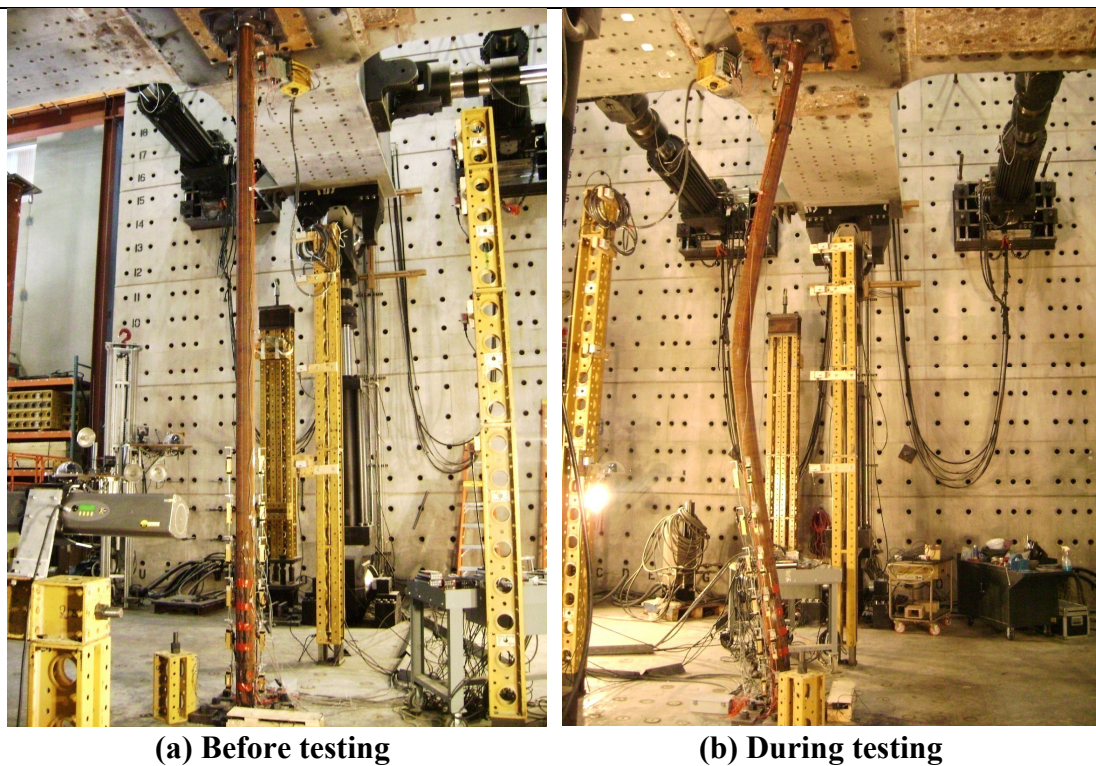


Figure 2. Specimen 1-C5-18-5

Instrumentation

The specimens were extensively instrumented to assess and quantify their behavior as carefully as possible. The wealth of information collected and its redundancy are crucial to the post-processing described later. The data recorded included outputs from:

- Built-in load cells and magnetostrictive linear position sensors from all eight actuators. Calculations of the resultant crosshead forces, external moments, and overall displacements and rotations associated with the horizontal and vertical axes were obtained from these sensors.
- Sets of three or four strain gages located at nine longitudinal sections, primarily near the bottom of the column, to monitor strains and calculate internal moments and curvatures. The majority of these gages were uniaxial and longitudinal, but at any given level at least one was a biaxial strain gage to allow monitoring of transverse (confinement) strains.
- Sets of three LVDTs for measuring relative displacements (elongation of shortening) located at six levels near the bottom of the specimen to monitor curvature and length changes indicative of local buckling at the critical section.
- String-pots distributed along the height for measuring lateral displacements and obtaining the displaced profile in both horizontal axes. These were located at four levels for the 5.5 m. (18 ft.) specimens, and 5 levels for the 7.9 m. (26 ft.) specimens.
- LED (light-emitting diode) semiconductors for measuring the position change of about 80 points near the bottom of the specimen. These measurements are captured by a Krypton system and were used primarily to monitor the growth of local buckling.
- Eight still cameras and eight video cameras distributed in 4 robotic towers were used to capture images and videos of the whole specimen and some local points of interest.
- Additional calculated channels were obtained from the measured data including: (a) moments at the base, and at different points along the specimen; (b) rotations and curvatures at different cross-sections; (c) evolution of the displaced shape of the column and deformations in selected segments; and (d) stresses at different positions through the cross-section and the specimen length.

All the data is currently archived in the NEES repository [NEES 2011].

Initial Geometry Surveys and Setup

As with any buckling experiment, characterizing the initial imperfections was a key goal of the project. Figure 3 shows typical deformation patterns for several of the specimens when they were first bolted to the reaction floor. The figure shows the global or interstory deformations (Δ), but the local or out-of-straightness deformations (δ) can also be obtained from the numerous intermediate measurements. All of these imperfections were included directly in the advanced analyses used to correct the data and were used as the initial coordinates for all lateral deformations measured during the test. Because of the difficulties in welding the thick end plates

exactly perpendicular to the specimens, several specimens (2, 3, and 7) appear to exceed the $\Delta < H/500$ conventionally required in construction, but appear to be almost straight ($\delta \approx 0$); specimen 1, the most slender one, actually shows the reverse ($\Delta \approx 0$ and large δ).

After these measurements were made, the top plate of the column was bolted to the MAST crosshead, resulting in parasitic forces. The crosshead then was moved until the system came back to the initial state of zero forces and moments. The final data taken during this process was named LC0 and became the baseline for all measurements.

Load protocol

The specimens were subjected to a variety of successive load histories, providing a wealth of data useful for developing design recommendations and calibration of advanced nonlinear computational models. The first load case (LC1) consisted of moving the crosshead with an incremental downward vertical displacement (Δ_z) and with free lateral translation (Δ) and free rotations (θ) controlled at the top. Since the base is rigidly connected to the strong floor and top DOF's are controlled as mentioned ($F=0$ and $M_1=0$), the full-scale specimen will behave as a slender fixed-free member with an effective length of K approximately equal to 2. Since the rigidity in the circular specimens is equal in any direction, both principal translations (Δ_x and Δ_y) and rotations (θ_x and θ_y) were controlled as free in the CCFTs ($K_x=K_y=2$). The rigidity is different in the two perpendicular directions in the case of the RCFTs, and so the Y-axis was kept fixed ($\Delta_y=\theta_y=0$) and only the X-axis was controlled free ($K_x=2, K_y=0.5$). For the weakest CCFT specimens (1C5-18-5, 18C5-26-12), the boundary conditions were set as fixed-fixed ($K=0.5$) in both directions in order to have a strength well above the resolution of the loading system. These axially stiff yet flexurally compliant CFT beam-column specimens were a unique challenge to control.

The second load case (LC2) subjected the specimens to combined axial compression and uniaxial bending. This was achieved with vertical force control at a specified load (P_i) and displacement control of the lateral DOFs. Again, most specimens were held in a fixed-free ($K=2$) configuration with bending moments at the crosshead were force controlled

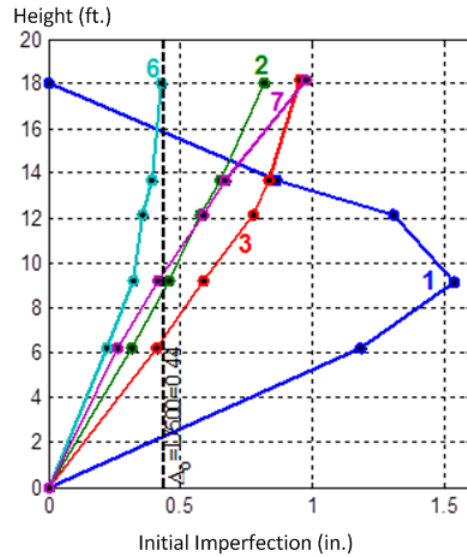


Figure 3. Initial configurations of some specimens (numbers refer to

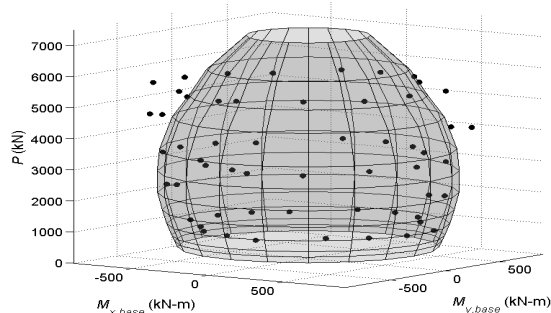


Figure 4. 3D interaction surface (analytical) and experimentally measured points (dots)

to zero [specimens 1-C5-18-5 and 18-C5-26-12 were held in a fixed-fixed ($K=1$) configuration]. The third load case (LC3) maintained the same control as the second load case, but subjected the specimen to combined axial compression and biaxial bending. Two axial load levels were used for LC2 and three different ones for LC3, resulting in a large number of triaxial load combinations that allowed the construction of a very complete interaction surface (Figure 4). Additional latter load cases were conducted, subjecting the specimens to torsion or alternate end conditions. Full details of the test program including these load cases and discussions on wet concrete effects are presented elsewhere [Perea 2010].

CORRECTIONS FOR ISSUES RELATED TO THE TEST SETUP

Because the data was used to assess the reliability of current American design provisions and because careful track had been kept of all aspects of the tests except residual stresses, it was of important to assess the impact of several testing factors on the overall results, as discussed below.

System compliance: According to the MAST manufacturers, the conversion process by the HCC accounts for all geometric nonlinearities. However, details of the algorithms used by the HCC are not public, and so the overall system compliance was not accurately known when the test series was planned. However, during analyses of the pilot test for this research project (1-C5-18-5), an incompatibility between the experimental and the predicted analytical axial deformations of the CFT specimens was noticed, as shown in Figure 5. Finite element analyses [French *et al.* 2004] modeling the crosshead under critical load conditions had indicated the presence of deformations that were not properly accounted by the HCC in the computation of the control commands (Figure 6). This required a correction when comparing experimental and analytical results since part of this measured experimental data corresponds to deformation developed in the system and part deformation in the specimens.

To determine the magnitude of the correction, an experimental determination of the crosshead relative vertical displacement with a specimen of known axial stiffness was performed [Gaulke *et al.* 2010] as part of this research. As seen in Figure 7, which shows a variation in crosshead deflections from about 2.5 mm (0.096 in) at the center to 5.1 mm (0.25 in) at the ends (± 3.2 m (± 10.5 ft) from center), the crosshead develops deflections that are not considered in the computed value by the controller (in this case $\Delta_z = 2.8$ mm (0.11 in)). Based on the measurements and analyses, all the data was corrected to reflect system compliance assuming that the behavior of the MAST was elastic throughout the load history.

Friction in the actuator clevises: The large vertical load actuators have very carefully machined bearings at the clevis pins to eliminate as much of the friction as possible. However, tests conducted without any specimens in place indicate that this friction is on the order of 8.34 kN (1,875 lbs) in force and 39.15 kN-m (28,875 lbs-ft) in moment (Figure 8) for the entire eight-actuator system.

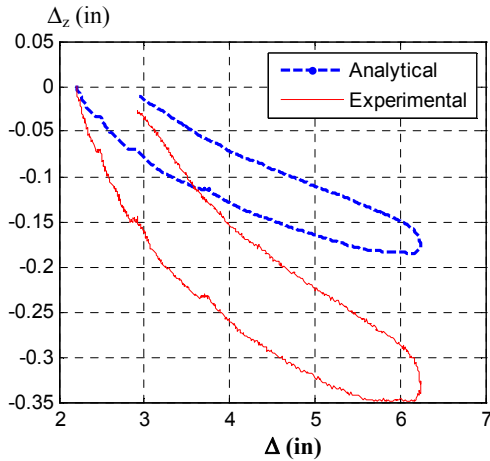


Figure 5. Experimental vs. analytical axial shortening (Δ_z)

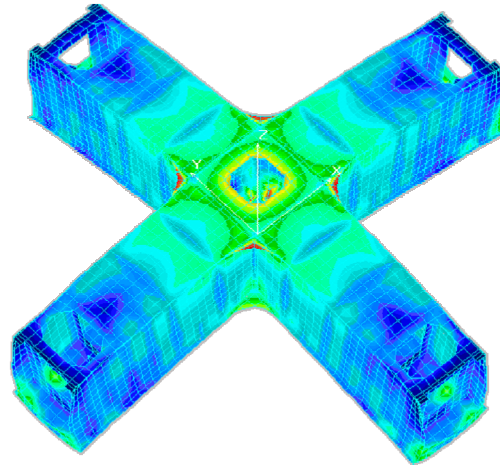


Figure 6. Crosshead deflections from FEA analysis [French *et al.* 2004]

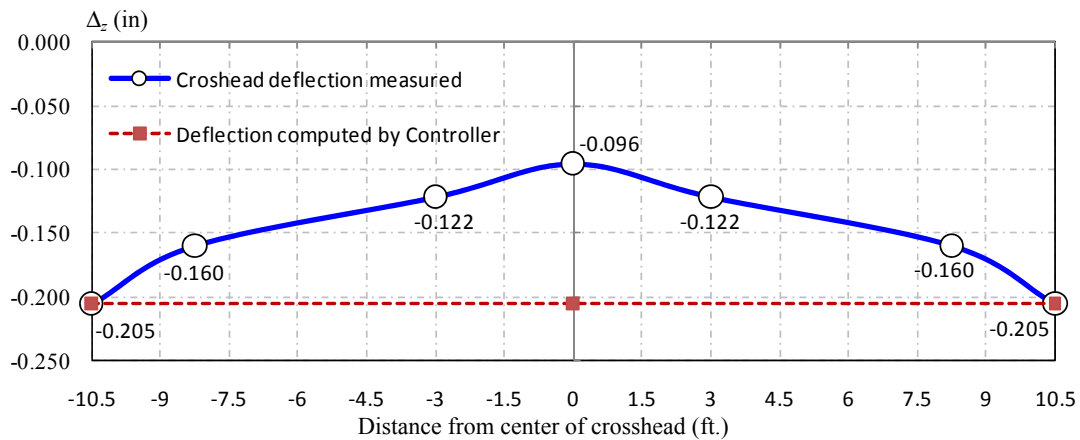


Figure 7. Crosshead deflections along the span from averaged measurements in compliance test

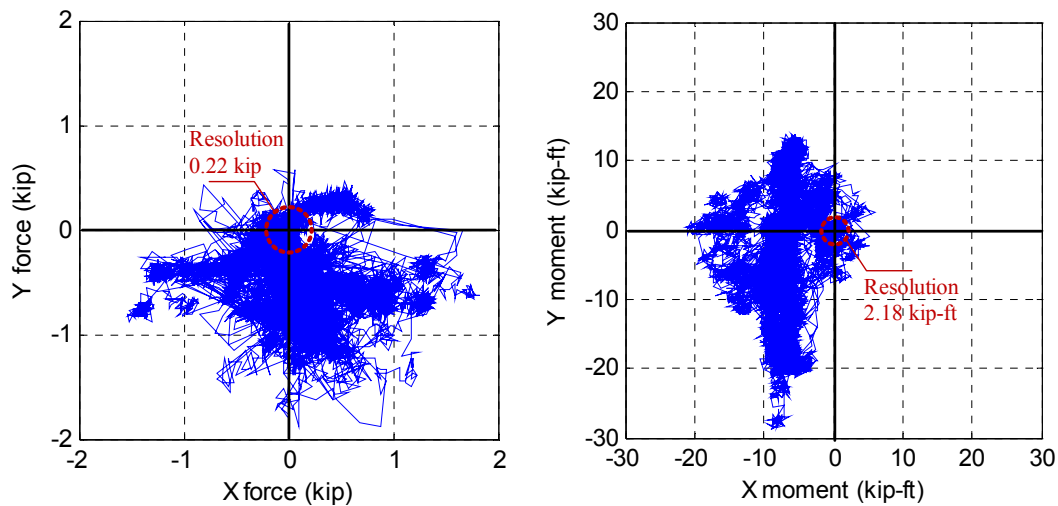


Figure 8. Computed top forces reported by the controller from the empty crosshead test

These values are small compared to the lateral load capacity of the system and would be negligible for specimens that are laterally stiff such as concrete or masonry walls. However, for slender column specimens, this level of restraint at the top represents a large proportion of their lateral resistance as they approach buckling. As soon as the load reverses from a peak, this friction needs to be overcome in order to move the specimen in the opposite direction. These spurious forces need to be removed when comparing analytical and experimental results. Figure 9(a) shows typical uncorrected results with the ideal imperfections, while Figures 9(b) and 9(c) show analyses with the measured imperfections and with the friction effects included to give an idea of the magnitude of this effect.

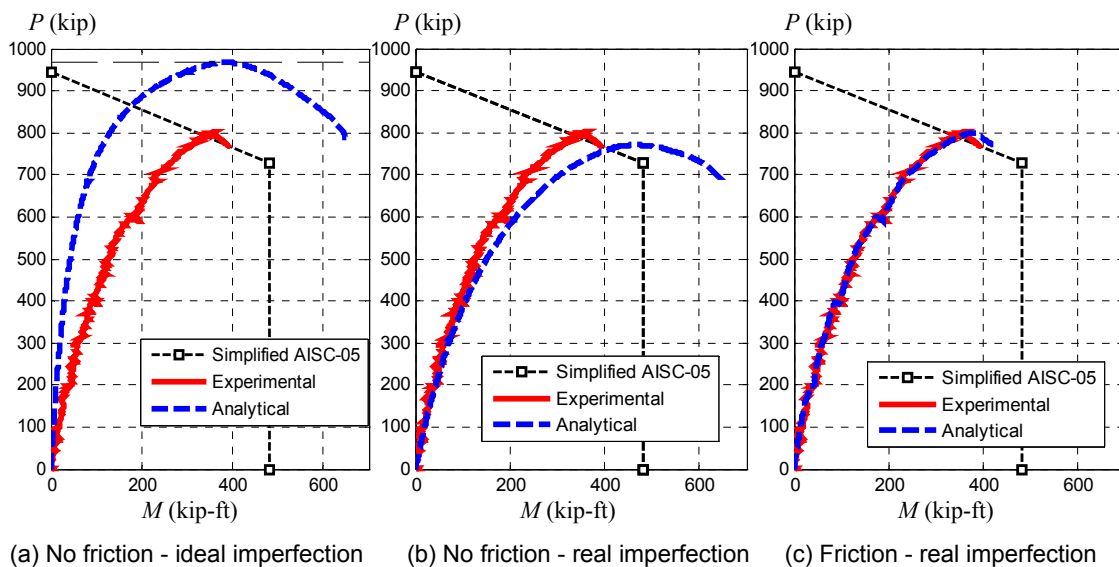


Figure 9. Effects of friction on test results

Lack of perfect control for the DOFs: As described before, the 6 DOF's at the top for the Specimens 2 to 17 were in vertical displacement control with horizontal forces (F_x , F_y) and top moments (M_x , M_y) in load control such that both forces and moment are kept at zero (fixed base and free top condition, or effective length $K=2$). However, as the system approached the idealized capacity as a fixed-free specimen, the controller began to impose extraneous forces in the opposite direction of motion, and thus increased the maximum load. These forces are probably the result of both the HCC using algorithms originally meant for shake tables, which intended to account for inertial forces in the system, and interactions between the 6 DOFs. These forces were negligible in the context of the quasi-static tests described herein. In addition, as shown in Figure 10(a) there was substantial force relaxation (dF) at the peaks, resulting in appreciable differences in the lateral force vs. displacement traces [Figure 10(b)] for some of the more flexible specimens. There was no simple way of accounting for these effects except by introducing into the analyses springs at the top of the column and calibrating their force-deformation relationship with the experimental results.

Limit on axial compressive capacity: As described earlier, the system is limited to a vertical axial capacity of 8572 kN (1320 kip). The buckling capacity of some

specimens, even when the large slenderness and imperfections are taken into account, exceeded the capacity of the crosshead. This implies that some alternate method of determining the axial capacity for these specimens was needed. In the literature [e.g., Horton *et al.* 1971], there are methodologies that aim to estimate the elastic buckling load based on the response [$P-\Delta$ curve as shown in Figure 11(a)] with a lower load, including those proposed by: (a) Southwell who noticed that the axial load (P) vs. lateral displacement ratio (P/Δ) keep a linear relationship; similarly, (b) Ayrton and Perry [$1/P$ vs. $1/\Delta$, illustrated in Figure 11(b)], and (c) Donnell (P vs. P/Δ). In this research, a more refined approach was used, based on the fact that, in either the elastic or the inelastic buckling ranges, the critical load is given when the tangent slope in the $P-\Delta$ curve reaches zero; thus, the axial force (P) vs. $P-\Delta$ tangent ($dP/d\Delta$) plot is proposed [Figure 11(c)] for the determination of the buckling load, including the geometric imperfection and the material non-linearities. Similar to the Donnell form [Figure 11(b)], where the secant $P-\Delta$ is used for the estimation of the Euler load (P_E), the critical load (P_n) from the tangent form is defined by its y-intercept or when the tangent becomes zero.

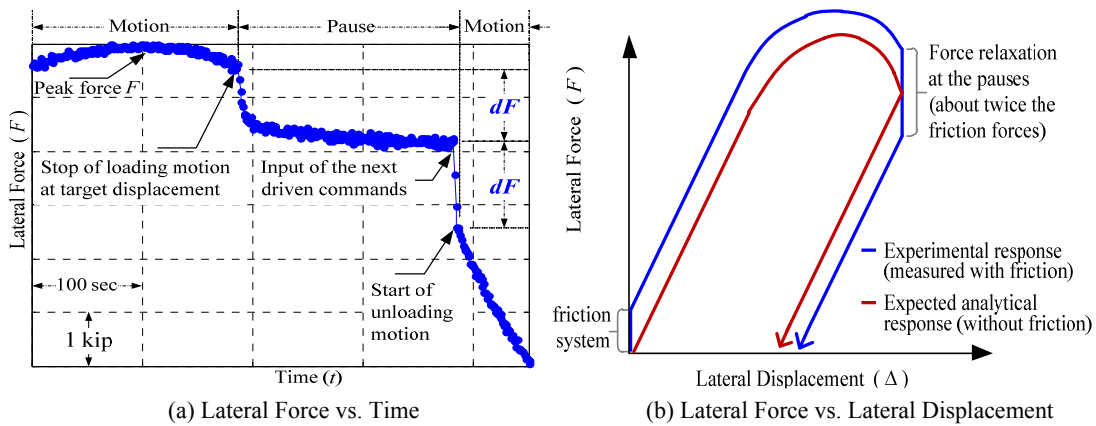


Figure 10. Force relaxation with time at the testing pauses (data for 4Rw-18-5)

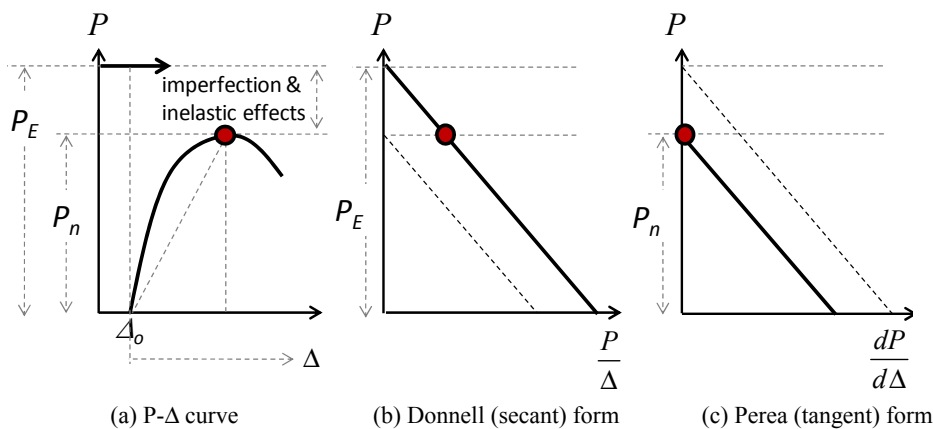


Figure 11 – Determination of buckling load for specimens that exceeded MAST axial capacity

CORRECTIONS FOR ISSUES RELATED TO THE SPECIMENS

Among the main reasons that explain differences between the experimental and the analytical maximum axial load capacities and are related to the specimens are:

Initial imperfections: The calculation of the critical load in the AISC (2010) assumes that the initial geometric imperfection will be lower than those limits and tolerances ($\Delta_0/L = 1/500 = 0.2\%$ or $\delta_0/L = 1/1000 = 0.1\%$) given by the Standards (i.e., ASTM A6 [ASTM 2013]; AISC 303 [AISC 2010b]; ACI-117 [ACI 2006]). Thus, design equations in the Specification were tuned and calibrated with geometric imperfection ratios within the tolerances ($\Delta_0/L = 1/750$ or $\delta_0/L = 1/1500$). As shown in Figure 3, the initial imperfections were exceeded in most specimens and, for some specimens the geometric imperfection was significantly larger. To address this problem, advanced analyses were carried out using OpenSees (2010) with a special version compiled by Denavit (2010) that, in addition to the standard OpenSees framework, includes comprehensive constitutive material models and robust 3D distributed-plasticity beam element formulations. These formulations were developed and calibrated by Tort and Hajjar (2007) for RCFTs and Denavit and Hajjar (2010) for CCFTs. Details of these models are given elsewhere in these proceedings [Denavit *et al.* 2013]. These analyses allowed the experimental results obtained with imperfections different from those assumed in the specification to be converted into results for the imperfections assumed in the specification.

Effective stiffness: The equivalent stiffness (EI_{eff}) as calculated in the AISC (2010) is an approximation of the “true” effective stiffness. Exact calculation of the EI_{eff} is not trivial since this parameter is highly dependent of the level of cracking and confinement in the concrete, the initial stress or strain field in the steel tube, and even the value of the compressive load in the element. Figure 12 shows typical data, with two experimental stiffnesses, one for the loading (EI_{expl}) and unloading portions (EI_{explU}). These values are compared to the EI_{eff} calculated from the Specification. Because of the non-linearity of large portions of the loading curve, particularly as the peaks were being reached, the unloading stiffness (EI_{explU}) is considered a better measure of the actual beam-column rigidity.

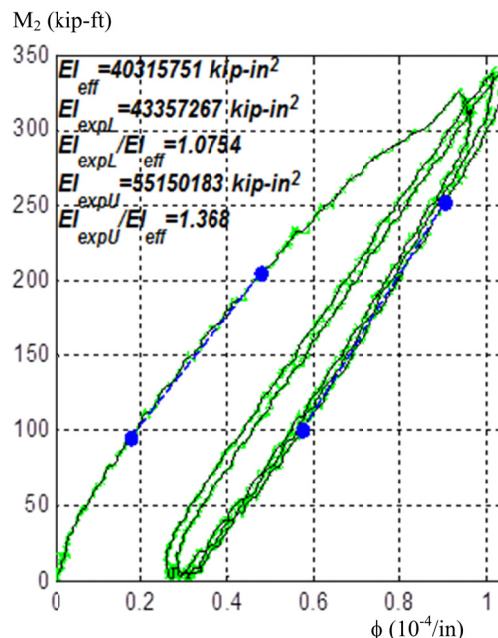


Figure 12. Extraction of stiffnesses for Specimen 3C20-18-5

Effective confinement in concrete: Even though the AISC equations give considerable credit to the circular sections due to confinement, differences were expected in the CFTs buckling capacity due to this parameter. The transverse strain gages indicated that this effect was limited to the areas where concrete crushing occurred and this effect was difficult to isolate from the local buckling occurring at the same critical sections. The effect of confinement appears to have been smaller as the slenderness increases, so linking this effect to slenderness, as is done in the Eurocode, appears to be a reasonable approach.

RESULTS

The large number of factors discussed required careful modeling using the OpenSees fiber models described previously. The buckling loads obtained from this set of computational analyses are summarized in Table 3 and Figure 13. In Table 3, the experimental values previously extracted from the raw and processed or adjusted data are also shown. In addition, this table shows the effective length factor (K), the slenderness parameter (λ) and the buckling load (P_n) that is obtained with the AISC (2010) Specifications. Very good agreement between the predicted and measured data is found when all of the factors described above are taken into account in the comparisons.

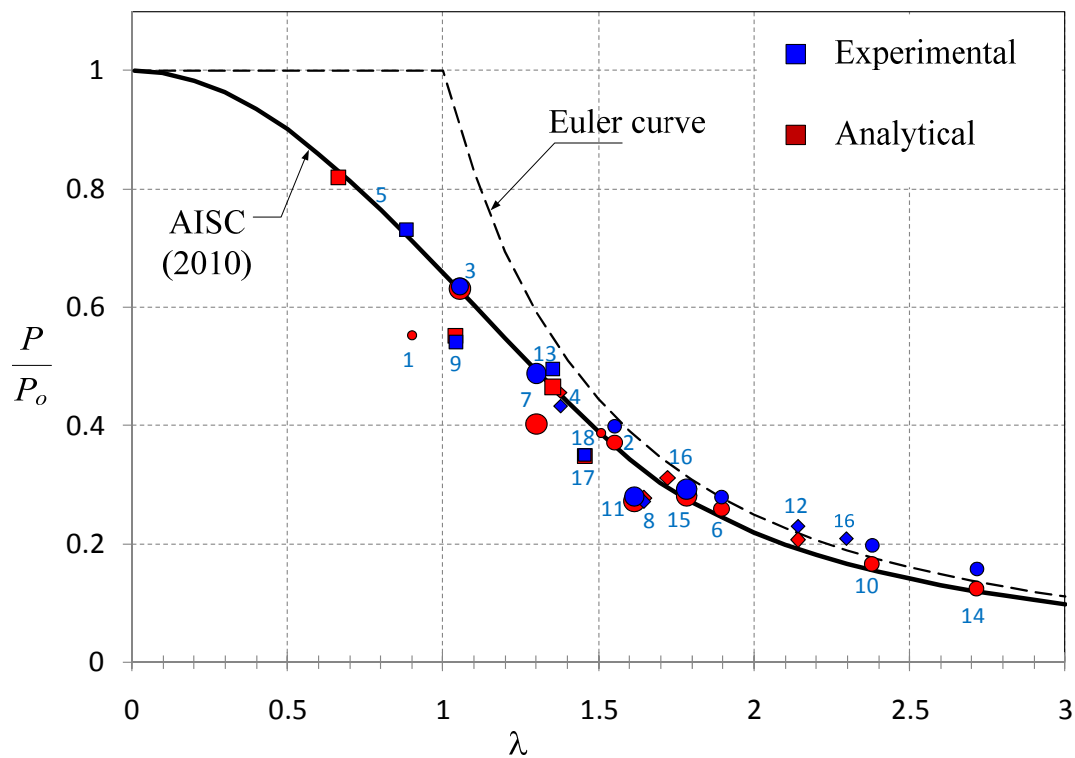


Figure 13. Comparison of axial capacities

Table 3. Buckling loads from computational analysis

Specimen	K	AISC (2010)		Maximum raw data	Adjusted critical load	Analytical critical load	ratio $E[P_n]/P_n$
		λ	P_n (kip)	P_{exp} (kip)	P_{cr} (kip)	$E[P_n]$ (kip)	
2C12-18-5	2.0	1.55	393	427	400 ^a	429.5	1.09
6C12-18-12	2.0	1.90	472	581	500 ^a	540.4	1.14
10C12-26-5	2.0	2.38	207	362	222 ^a	262.2	1.27
14C12-26-12	2.0	2.72	216	386	225 ^a	285.1	1.32
3C20-18-5	2.0	1.05	1469	1320 ⁺	1478 ^b	1486.7	1.01
7C20-18-12	2.0	1.30	2190	1320 ⁺	1791 ^b	2168.7	0.99
11C20-26-5	2.0	1.61	992	802	802	825.3	0.83
15C20-26-12	2.0	1.78	1080	1127	1100 ^a	1146.2	1.06
4Rw-18-5	2.0	1.38	939	1070	950 ^a	901.7	0.96
8Rw-18-12	2.0	1.65	1124	961	961	946.2	0.84
12Rw-26-5	2.0	2.14	501	791	540 ^a	601.1	1.20
16Rw-26-12	2.0	2.30	534	1140	1000 ^a	673.0	1.26
5Rs-18-5	2.0	0.88	1501	1320 ⁺	1705 ^b	1521.0	1.01
9Rs-18-12	2.0	1.04	2209	1320 ⁺	1918 ^b	1877.5	0.85
13Rs-26-5	2.0	1.35	1199	1320	1200 ^a	1275.9	1.06
17Rs-26-12	2.0	1.46	1323	1120	1120	1126.9	0.85

Notes: (+) MAST axial capacity reached before reaching buckling; (a) load given at the instant the controller added significant top forces a moments; (b) load from the tangent plot

CONCLUSIONS

Comparison of experimental data and code predictions for the nominal axial load capacity on CFT columns, one of the primary goals of this research, required careful attention and correction for both geometric and experimental setup issues. These difficulties included characterization of the effective flexural stiffness, large dispersion in initial out-of-straightness and out-of-plumbness, among others. The raw experimental data was adjusted and processed accordingly. Results from the processed data seem to be more consistent with the expected values than the raw experimental data.

ACKNOWLEDGEMENTS

The work described in this report is part of a NEESR project supported by the National Science Foundation under Grant No. CMMI-0619047, AISC, NEES, the Georgia Institute of Technology, and the University of Illinois at Urbana-Champaign. In-kind material and labor was provided by Atlas Tube Inc. and LeJeune Steel Co. Any opinions, findings, and conclusions expressed in this document are those of the authors and do not necessarily reflect the views of the National Science Foundation or other sponsors.

REFERENCES

- ACI (2006). *ACI 117-06: Specifications for Tolerances for Concrete Construction and Materials and Commentary*, American Concrete Institute (ACI), Farmington Hills, Michigan, USA.
- AISC (2010). *ANSI/AISC 360-10: Specification for Structural Steel Buildings*, American Institute of Steel Construction (AISC), Chicago, Illinois, USA.
- AISC (2010b). *AISC 303-10: Code of Standard Practices for Steel Buildings and Bridges*, American Institute of Steel Construction (AISC), Chicago, Illinois, USA.
- ASTM (2013). *ASTM A6, A6/A6M-13: Standard Specification for General Requirements for Rolled Structural Steel Bars, Plates, Shapes, and Sheet Piling*, American Society for Testing and Materials (ASTM), West Conshohocken, Pennsylvania, USA.
- Denavit, M. D., Hajjar, J. F., Perea, T., and Leon, R. T. (2010). "Cyclic evolution of damage and beam-column interaction strength of concrete-filled steel tube beam-columns", *9th US National and 10th Canadian Conference on Earthquake Engineering*, EERI, Oakland, California, USA.
- Denavit, M. D. and Hajjar, J. F. (2010). "Nonlinear seismic analysis of circular concrete-filled steel tube members and frames", *Report No. NSEL-023*, Newmark Structural Laboratory Report Series, ISSN 1940-9826. Department of Civil and Environmental Engineering, University of Illinois at Urbana-Champaign, Urbana, Illinois, USA.
- Goode, C. D. (2007). *ASCCS Database of Concrete-Filled Steel Tube Columns*. ASCCS.
- Gourley, B. C., Tort, C., Denavit, M. D., Schiller, P. H., and Hajjar, J. F. (2008). "A Synopsis of Studies of the Monotonic and Cyclic Behavior of Concrete-Filled Steel Tube Beam-Columns," *Report No. NSEL-008*, Newmark Structural Laboratory Report Series, ISSN 1940-9826. Department of Civil and Environmental Engineering, University of Illinois at Urbana-Champaign, Urbana, Illinois, USA.
- French, C. W., Schultz, A. E., Hajjar, J. F., Shield, C. K., Ernie, D. W., Dexter, R. J., Du, D. H. C., Olson, S. A., Daugherty, D. J., and Wan, C. P. (2004). "Multi-Axial Subassemblage Testing (MAST) System: Description and Capabilities" *Proceedings of the 13th World Conference on Earthquake Engineering*, IAEE, Vancouver, British Columbia, Canada.
- Gaulke, R. Kinsley, A. Bergson, P. (2010). Deformation test for the MAST crosshead, *MAST Internal Report*, NEES@UMN, University of Minnesota, Minneapolis, Minnesota, USA.
- Hajjar, J. F., French, C. W., Schultz, A. E., Shield, C. K., Ernie, D. W., Dexter, R. J., Du, D. H., and Bergson, P. M. (2002). "A system for multi-axial subassemblage testing (MAST): initial developments", *Proceedings of the*

- American Society of Civil Engineers Structures Congress*. April 4–6, 2002, 313–314. Denver, Colorado, USA.
- Horton, W. H., Cundari, F. L., and Johnson, R. W. (1971). “Applicability of the Southwell Plot to the Interpretation of Test Data Obtained from Stability Studies of Elastic Column and Plate Structures”. *Technical Report 69-32*. Stanford University. California, USA.
- Kim, D. K. (2007). “A Database For Composite Columns”, *M.S. Thesis, School of Civil and Environmental Engineering*, Georgia Institute of Technology, Atlanta, Georgia, USA.
- Leon, R. T., Aho, M. F., and Kim, D. K. (2005). “A database for encased and concrete-filled columns”. Georgia Institute of Technology, Atlanta, Georgia, USA.
- Leon, R., Perea, T., Hajjar, J., and Denavit, M. (2009). “Determination of buckling loads from triaxial load tests of slender concrete”, *Proceedings of the 3rd International Conference on Advances in Experimental Structural Engineering*, San Francisco, California, USA.
- NEES (2001). <http://nees.org/warehouse/project/440>.
- Perea, T. (2010). “Analytical and experimental study on slender concrete-filled steel tube columns and beam-columns”, *Ph.D. Thesis, School of Civil and Environmental Engineering*, Georgia Institute of Technology, Atlanta, Georgia, USA.
- Perea, T., Leon, R., Denavit, M., and Hajjar, J. (2010). “Experimental tests on cyclic beam-column interaction strength of concrete-filled steel tubes”, *Proceedings of the 9th US National and 10th Canadian Conference on Earthquake Engineering*, Toronto, Canada.

Experimental Investigation on New Ring-Beam Connections for a Concrete-Filled Tubular Column and RC Beam

Wei Wang¹; Yiyi Chen²; and Wanqi Li³

¹State Key Laboratory of Disaster Reduction in Civil Engineering, Tongji Univ., Shanghai 200092, China. E-mail: weiwang@tongji.edu.cn

²State Key Laboratory of Disaster Reduction in Civil Engineering, Tongji Univ., Shanghai 200092, China. E-mail: yiyichen@tongji.edu.cn

³College of Civil Engineering, Tongji Univ., Shanghai 200092, China. E-mail: lwqxyf631@hotmail.com

Abstract

This paper introduces a new type of connections—reinforced concrete (RC) ring beam joints between concrete-filled steel tubes (CFSTs) column and RC beam. In this connection, the continuous load transferring in the frame beams are achieved by the transitional ring beam encircling the CFST column. Bidirectional cyclic loading tests on four interior column joint specimens were conducted to evaluate the seismic performance of this new connection system and the influence of the reinforcement on the joint behavior. Test results indicated the multi-directional nature of the force system in the ring beam. RC ring beam should be designed against the combination of multi-directional forces including axial load, bending, torsion, and shear due to the interaction of ring beam and CFST column under external load. The connections with reasonable design were observed to have good ductility and suitable for seismic resistant application.

1. INTRODUCTION

The concept of confined concrete has been widely accepted and applied in structural engineering. Concrete filled steel tubes (CFSTs), as an economical type of column, have been developed for several decades due to their advantages over either pure steel or pure reinforced concrete (RC) columns (Roeder et al. 2010). In engineering practice, RC beams are frequently employed instead of steel beams in CFST column systems with the incentive to reduce cost. Therefore, the safety and economical design of CFST column-RC beam connections poses unique challenge that has not been addressed by traditional design standards.

Very limited research work exist on the connections between CFST columns and RC beams due to the difficulty to arrange the longitudinal steel bars in the beam and the transferring of moments and shear forces at the beam ends. A new through-beam connection for a CFST composite column and RC beams was proposed (Nie et al. 2008). Axial compression experiments on six specimens and reversed cyclic loading tests on three interior column specimens and three corner column specimens were conducted to evaluate the new beam-column system. An experimental investigation was carried out on a similar through-beam connection between concrete filled twin steel tube columns and RC beams (Zhang et al. 2012). Both experimental results showed that the effective confinement can be achieved by the stiffening ring, and an excellent axial bearing capacity can be obtained, as well as a good ductility and energy dissipation capacity. However, the steel tube is completely interrupted in these connections, leading to high material and labor cost along with complicated fabrication. Furthermore, little research is available on the seismic behavior of three-dimensional (3D) beam-to-column connections under the severe earthquake.

This paper introduced a new type of connection between CFST column and RC beam. The cyclic behavior of three-dimensional (3D) interior CFST column to RC beam subassemblies was experimentally investigated. Test results were presented and discussed on the hysteretic behavior of the connections subjected to bidirectional cyclic lateral loading.

2. EXPERIMENTAL PROGRAM

A new through-column connection for CFST column and RC beams is introduced. Due to the construction and manufacture efficiency, RC ring-beam joints are used, of which ribbed steel bars or square bars as outer shear connectors are welded around the periphery of the column in the joint region and RC ring beam is placed as a transition zone between frame beams and columns. In order to avoid the interruption of the steel tube in the connection zone, the steel reinforcing bars in the RC frame beam does not cross through the steel tube continuously, but are anchored into the aforementioned transitional RC ring beam in this area. The interaction between the RC ring beams and the CFST column with outer shear connectors equilibrates moments and shear forces from the beams.

Four specimens, named R-2-S, R-3-S, R-4-S and R-4-S-V6 were designed on a one-half size scale for prototype connections. The parameters include different longitudinal reinforcement ratios and stirrup reinforcement ratios for the ring beam as shown in Table 1, where As_{kt} and As_{kb} denote the longitudinal reinforcement of the frame beam at the top and bottom levels respectively; As_{ht} and As_{hb} denote the longitudinal reinforcement of the ring beam at the top and bottom levels respectively. The geometric dimensions and reinforcement arrangements are shown in Figure 1. The material properties of the used steel and concrete are summarized in Table 2.

Table 1. Specimens and test parameters

Specimens	Frame beams		Ring beams			Columns	Shear connectors
	$b_b \times h_b$	A_{skt}/A_{skb}	$b_r \times h_r$	A_{sht}/A_{shb}	Stirrups	$d_c \times t_c$	
R-2-S	250×500	4 Φ 22/4 Φ 20	250×500	2 Φ 22/2 Φ 20	Φ 12@100	350×9	3 \blacksquare 20
R-3-S	250×500	4 Φ 22/4 Φ 20	250×500	3 Φ 22/3 Φ 20	Φ 12@100	350×9	3 Φ 20
R-4-S	250×500	4 Φ 22/4 Φ 20	250×500	4 Φ 22/4 Φ 20	Φ 12@100	350×9	3 Φ 20
R-4-S-V6	250×500	4 Φ 22/4 Φ 20	250×500	4 Φ 22/4 Φ 20	Φ 6@100	350×9	3 Φ 20

Table 2. Material properties of steel and concrete used in the test

Components	Yield strength f_y (MPa)	Tensile strength f_u (MPa)	Elongation (%)	Compressive cube strength f_{cu} (MPa)
Tube column	464	632	32	-
Rebar- Φ 22	408	599	27	-
Rebar- Φ 20	407	597	29	-
Rebar- Φ 12	521	620	22	-
Rebar- Φ 6	456	572	22	-
Concrete(R-2-S)	-	-	-	67
Concrete(R-3-S)	-	-	-	44
Concrete(R-4-S)	-	-	-	45
Concrete(R-4-S-V6)	-	-	-	41

Specimens were tested in a purpose-built 3D testing system for beam-column connections (Wang et al. 2011) in the State Key Laboratory of Disaster Reduction in Civil Engineering, Tongji University. The schematic loading arrangement and test setup are shown in Figure 2. At the beginning, a constant compressive axial load of 1200kN was first applied at the top of the CFST column and maintained throughout the test. The alternately repeated vertical loads, P, were then synchronously applied at beam ends by servo actuators. Considering the maximum numbers and loading capacities of servo actuators which can be offered by the lab, this biaxial cyclic loading program assumes that the seismic load is input simultaneously in two directions, i.e. major loading direction along the west-east plane and minor loading direction along the north-south plane. The loading ratio of PWE in the west-east plane to PNS in the north-south plane is 1:0.75, which was realized by setting parallel connection of two sets of actuator pairs with different maximum loading capacities to the oil pump. The interstory drift was applied in each principal direction, with the resultant at 37° having a magnitude equal to the drift in principal direction multiplied by 1.25.

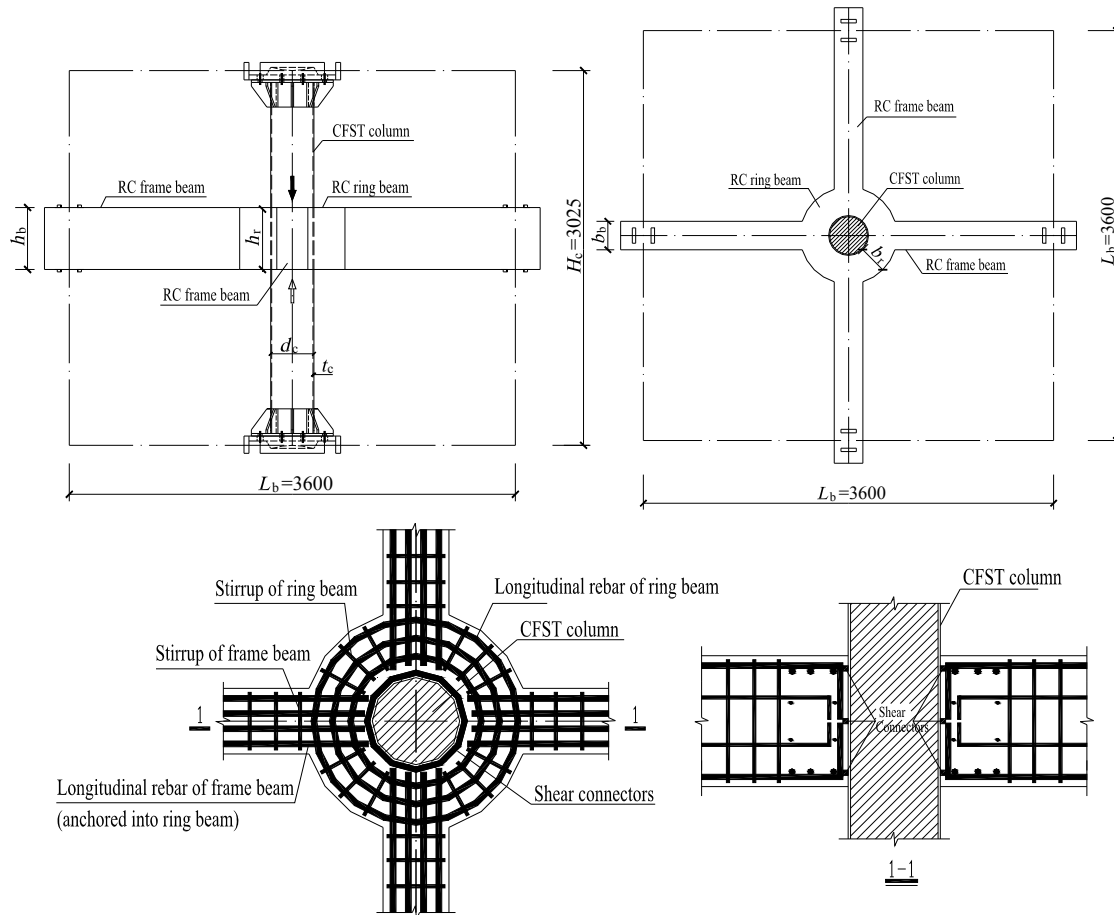


Fig. 1 Dimensions and reinforcement arrangement of specimens

The vertical force-displacement relationships at four beam ends can be equivalently expressed as the story shear force (P_c) versus story drift (Δ) relationship of a single column according to energy conservation principle (Wang et al. 2011). It makes the test results for 3D subassemblies more intercomparable. The axial strains at the steel reinforcement were also measured to investigate the load-strain histories on the ring beam. As shown in Figure 3(a), the strain gauge location is designated as S-X where X represent the angle measured clockwise from the 0-East axis. At each location, 4 strain gauges were attached to either the longitudinal reinforcement or the stirrups. At location S-0, S-90 and S180, four strain gauges were attached to the longitudinal reinforcement (Figure 3(b)). While at location S-17, S-73, S-107 and S-163, the four strain gauges were attached to the stirrups (Figure 3(c)).

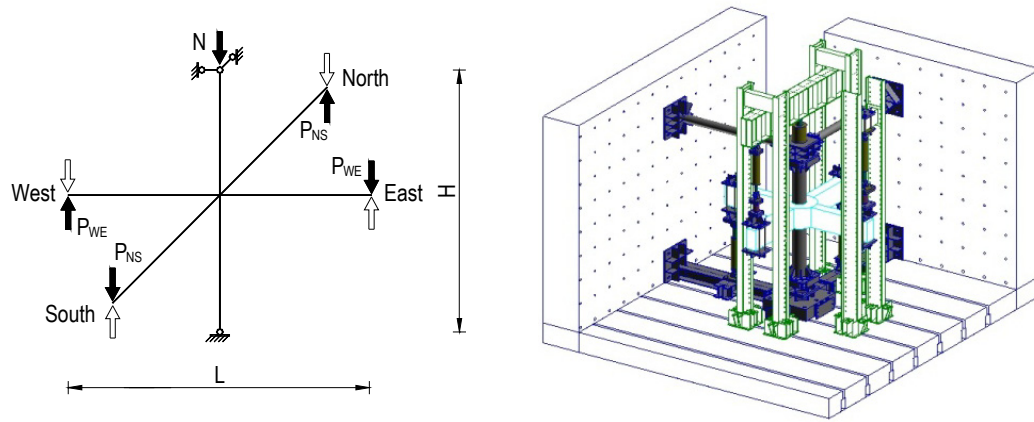
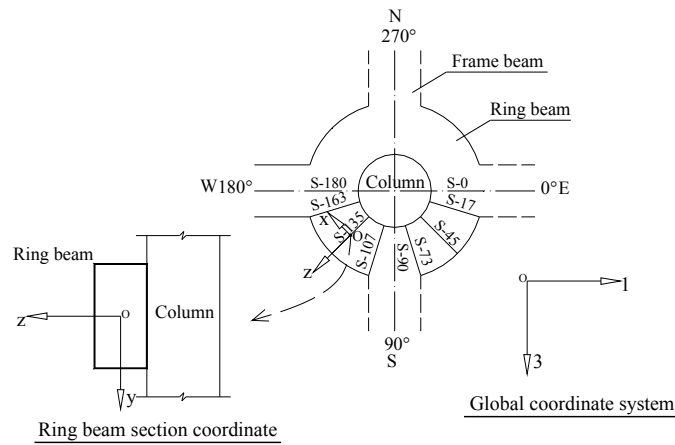
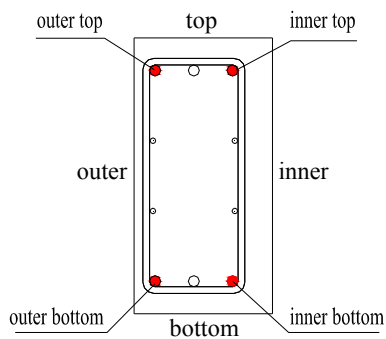


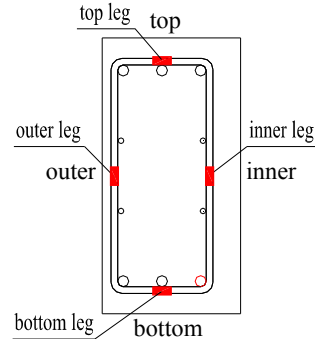
Fig. 2 Schematic loading arrangement and test setup



(a) Sectional view and coordinate system



(b) Longitudinal reinforcement



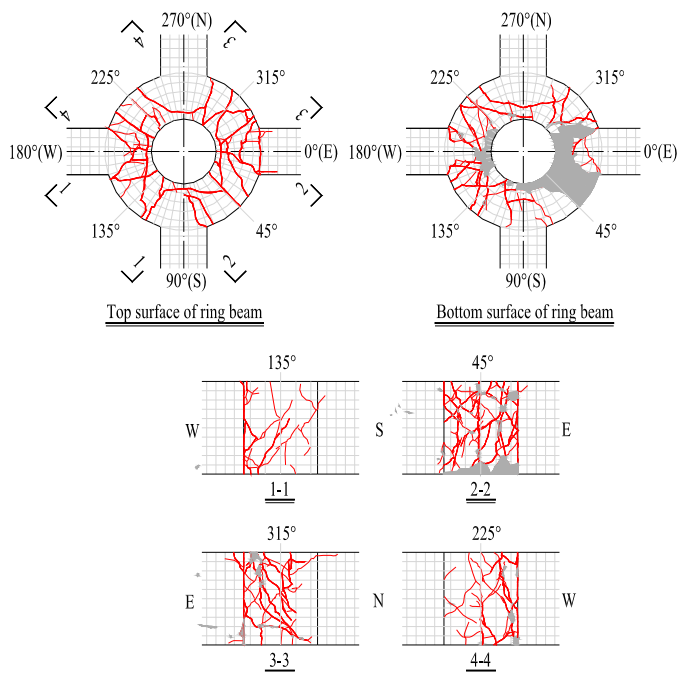
(c) stirrup

Fig. 3 Strain gauge locations of ring beam

3. EXPERIMENTAL RESULTS

3.1 Cracking pattern

A typical failure mode from specimen R-2-S is described in this section to illustrate the development of cracks in the RC ring beams. After the initial pre-load of 1200kN at the CFST column, there were no visible cracks in the ring beam. During the cyclic loading at the beam ends before rebar yielding, horizontal cracks perpendicular to the frame beam were observed at the junction between the frame beams along East and West direction and the ring beam. Radial cracks were observed at the 225o and 45o locations at the ring beam and diagonal cracks at 315o and 135o locations, which propagated at 30o to the radial direction. During the cyclic loading at the beam ends after rebar yielding, inverted “V” cracks were observed at the junction between the top/bottom of the ring beam and the frame beam. Horizontal cracks perpendicular to the frame beam were observed at the ring beam close to the column wall, extending to intersect with diagonal cracks in the side wall of the ring beam, finally forming a complete crack. As the loading increased, the crack width increased. In addition, concrete spalling could be found at the bottom of the ring beam first near 0o and 180o locations, then within the range from 23o to 90o locations. The final cracking pattern is shown in Figure 4. The crack distribution along the ring beam illustrates the multi-directional performance of the internal force condition in this type of joint.



Note: redline-cracks; shaded area-concrete spalls.

Fig. 4 Typical crack pattern of specimens after final loading

3.2 Hysteretic behavior

The equivalent column story shear versus story drift responses of the subassemblies from the major loading direction along west-east plane and minor loading direction along north-south plane are coupled and presented in Figure 5. The curves displayed pinching behavior. This was caused by the opening and closing of cracks during cyclic loading. The cracks appeared in the concrete were not closed when the applied load was zero which explain the early low rigidity in the initial stage. However, when the cracks were closed, a stable response was observed from the figure. The maximum loads and ductility ratios for each specimen are also summarised in Table 3. The ductility ratio is defined as the ratio of the displacement corresponding to the maximum load and the nominal yielding displacement. The capacity of joints to dissipate energy when subjected to seismic loads is as important as their strength or ductility in the evaluation process. The equivalent damping coefficient η_e for the maximum loading loop of the specimens is also given in Table 3. As can be seen from the comparison between four specimens, both the longitudinal reinforcements and stirrups are very crucial to enhance the load-carrying capacity and improve the ductility of the connection system.

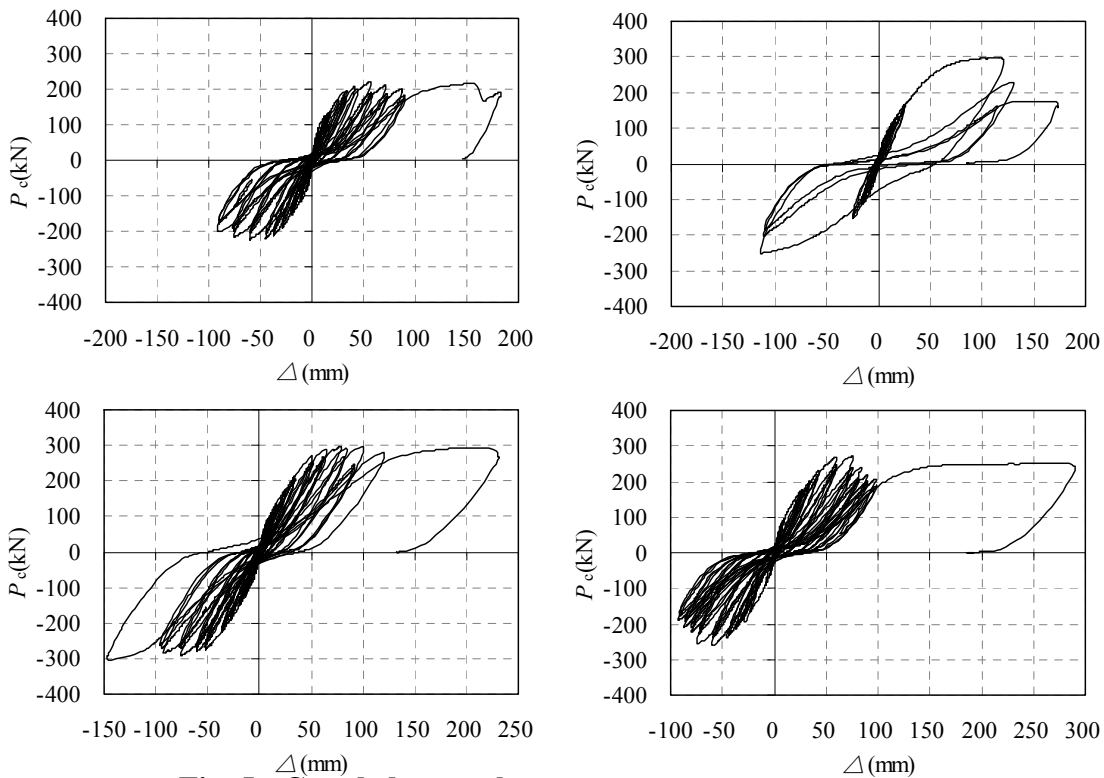


Fig. 5 Coupled story shear versus story drift responses

Table 3. Maximum load, ductility and energy dissipation capacity

Specimens	Maximum load (kN)	Ductility ratio	h_e
R-2-S	223	2.6	0.09
R-3-S	274	3.1	0.19
R-4-S	300	3.3	0.11
R-4-S-V6	266	2.0	0.08

3.3 Load-strain curves of ring beam reinforcement

Taking Specimen R-4-S for example, the equivalent column story shear-strain responses for longitudinal reinforcements and stirrups of the ring beam are shown in Figure 6 to 9.

Under cyclic loading, the load-strain curves of the longitudinal reinforcement and stirrups at S-135 location for each specimen illustrate symmetric “butterfly” shape (for example, as shown in Figure 6). The strain variation of the longitudinal reinforcement at the inner ring (Figure 6(b) and (d)) is greater than that at the outer ring (Figure 6(a) and (c)). The story shear-strain curves of the longitudinal reinforcements and stirrups at S-45 location illustrate asymmetric “butterfly” shape (Figure 7). While at locations of S-17, S73, S-107 and S-163, the story shear-strain curves of the stirrups (see Figure 8(c) and (d)) show asymmetric behavior. Whereas at S-0, S-90 and S-180, the story shear-strain curves of the longitudinal reinforcement illustrate asymmetry “butterfly” shape.

Through analysing the ring beam reinforcement behavior, the following observations can be made: (1) Within the ring beam range with adjacent frame beams subjected to opposite bending (e.g. S-135 location), the bending moment about the y-axis (M_y) is significant, while the moment direction is not affected by the external load and the inner surface of the ring beam is always under tension. The interaction between the ring beam inner surface and the outer wall of tubular column is weak. (2) Within the ring beam range with adjacent frame beams subjected to identical bending (e.g. S-45 location), the bending moment about the z-axis (M_z) is significant. The moment direction is affected by the external load and the interaction between the ring beam inner surface and the outer wall of tubular column is strong. (3) In the ring beam locations within the width of the frame beam (e.g. S-17, S-73, S-107, S-163, S-0, S-90 and S-180), the bending about the z-axis (M_z) is significant. The moment direction is affected by the external load and changes at different zones. The interaction between the ring beam inner surface and the outer wall of tubular column is strong.

The analysis of the crack development and reinforcement reveals the importance of the reinforcement arrangement on the force distribution within the ring beam. The loading protocol also affects the joint performance as the crack developments are multi-directional.

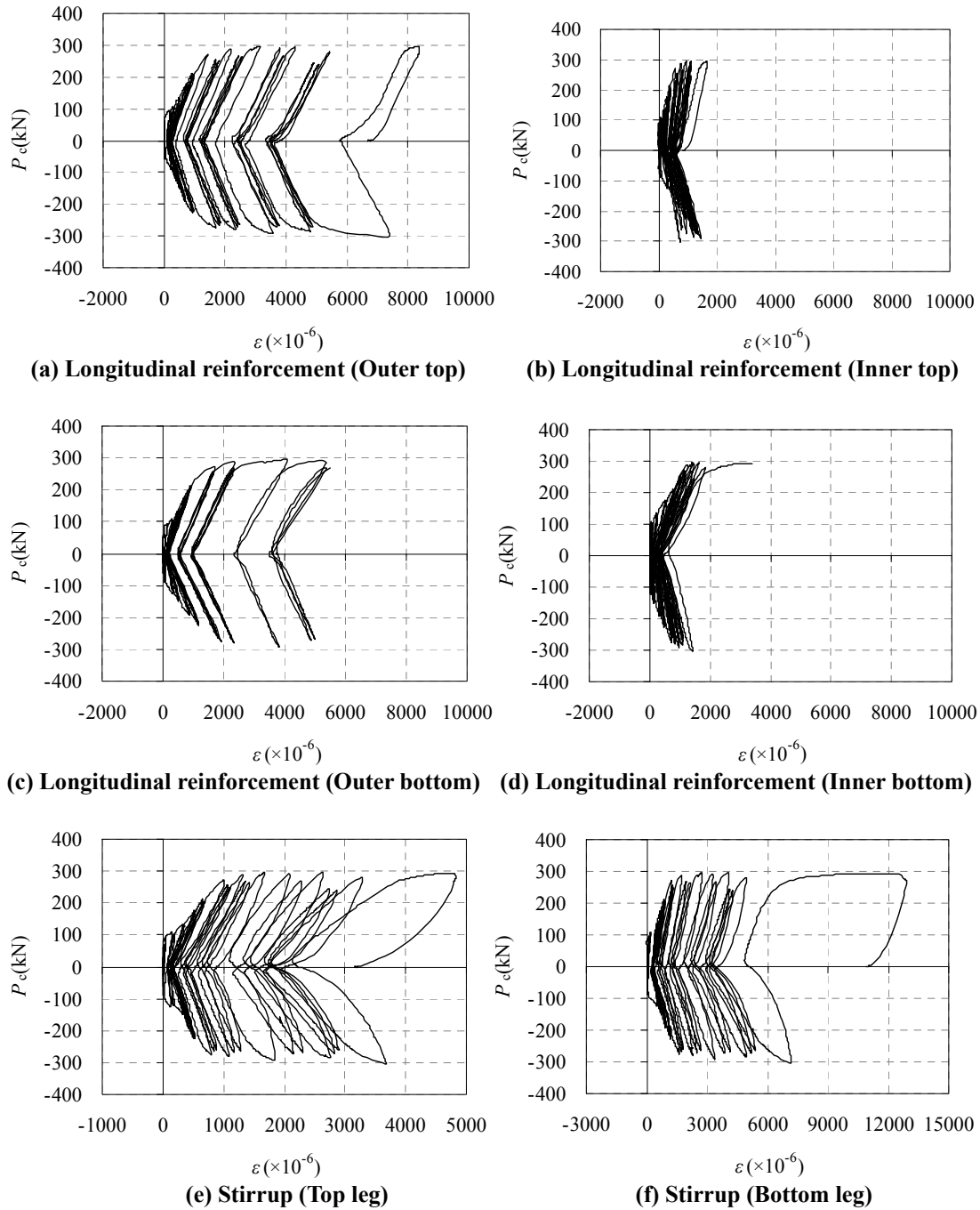


Fig. 6 Load-strain curves of reinforcement for specimen R-4-S at S-135 location

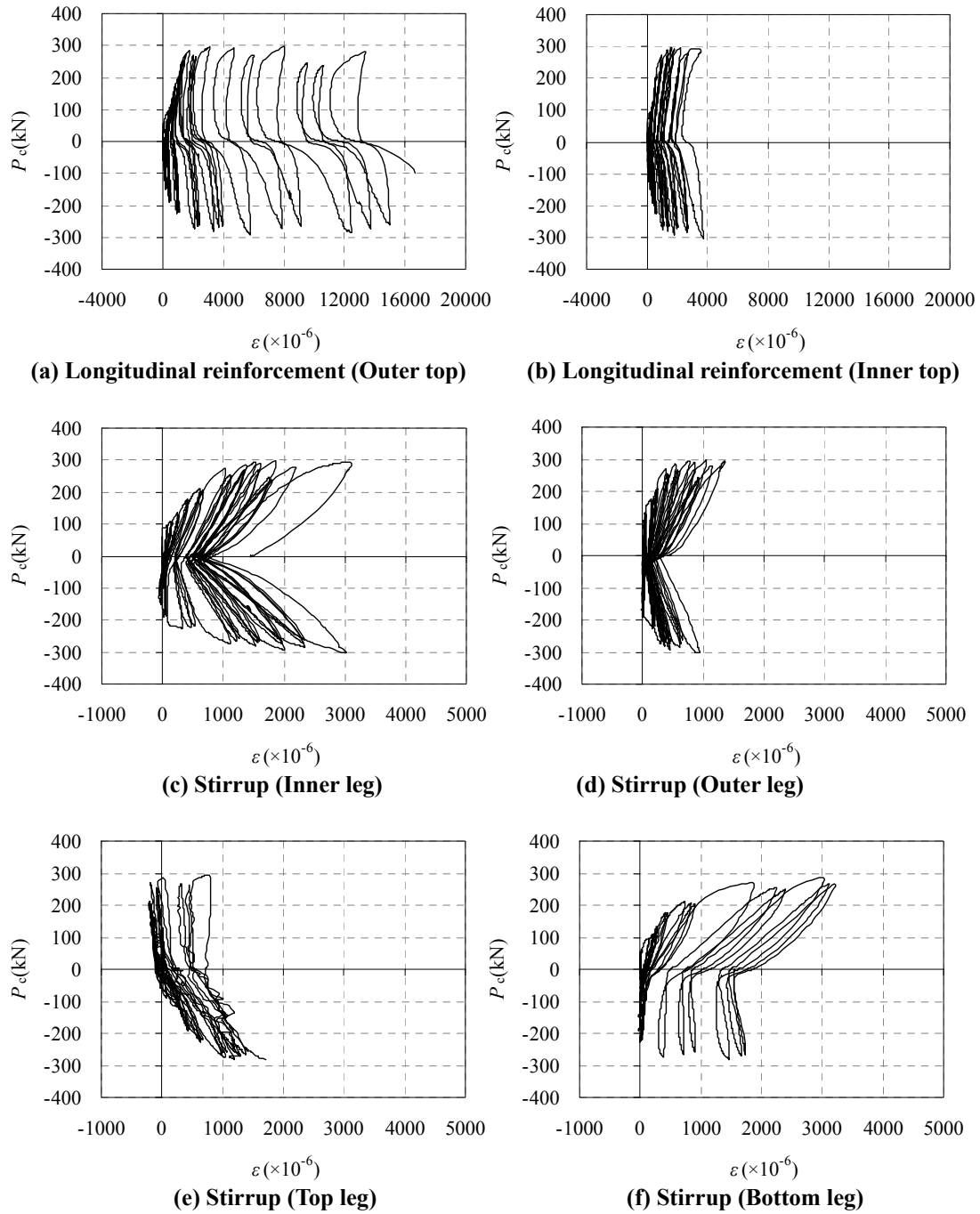


Fig. 7 Load-strain curves of reinforcement for specimen R-4-S at S-45 location

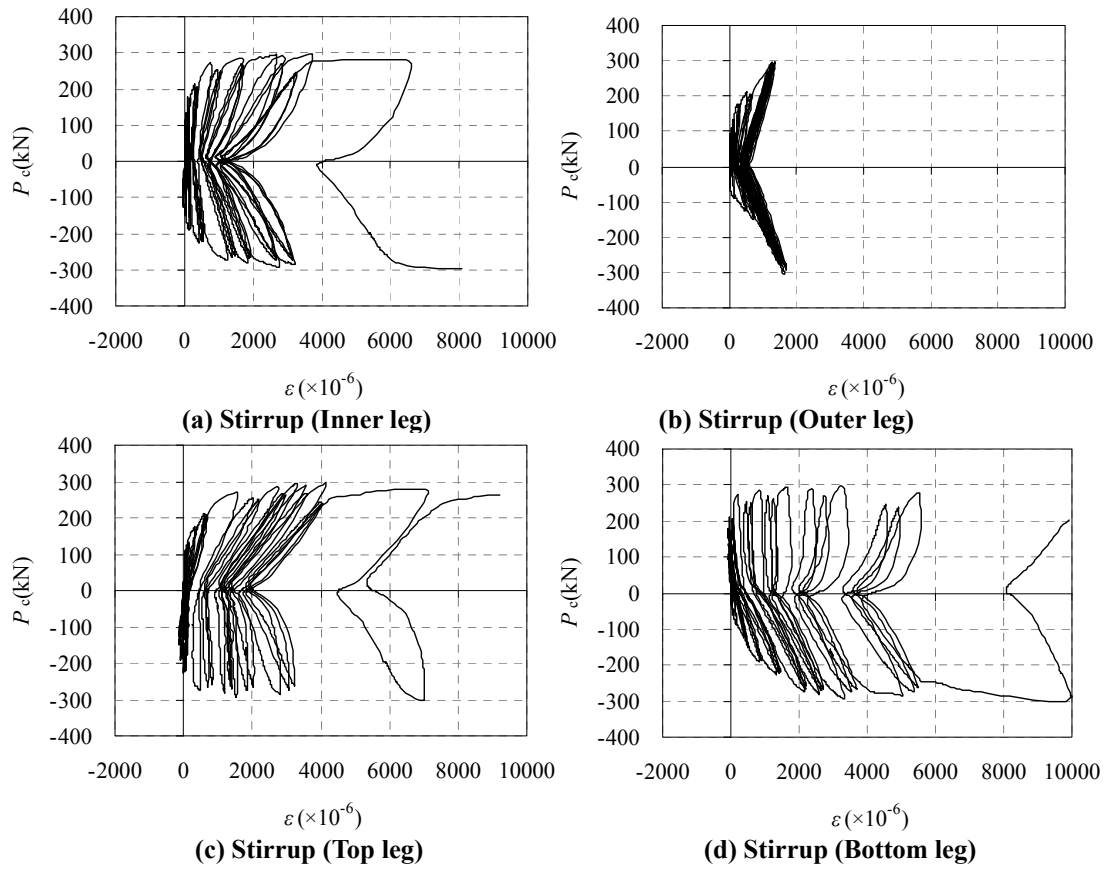


Fig. 8 Load-strain curves of reinforcement for specimen R-4-S at S-163 location

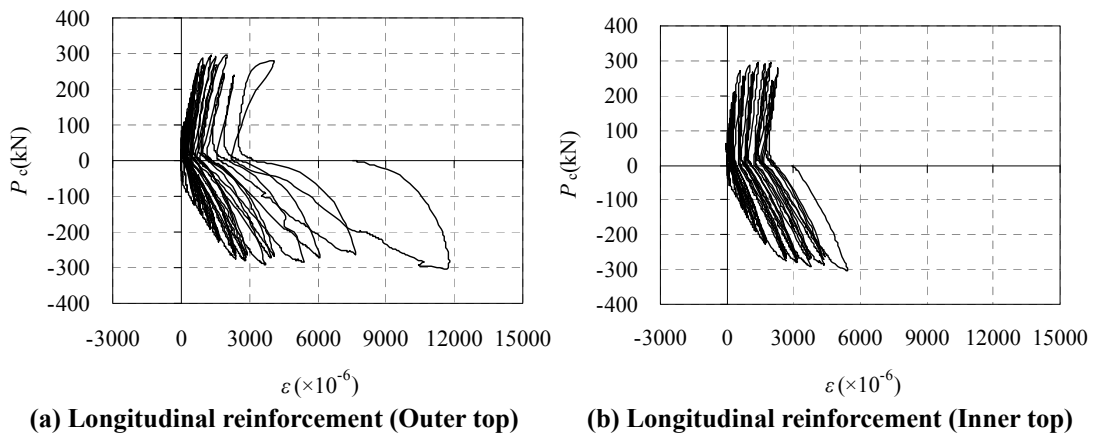


Fig. 9 Load-strain curves of reinforcement for specimen R-4-S at S-180 location

4. CONCLUSIONS

A new type of RC ring beam joints between CFST column and RC beam is introduced and the seismic behaviour was investigated based on bidirectional cyclic loading tests on four interior column joint specimens with 3D configuration. The main findings can be summarized as follows.

(1) Internal forces of ring beam are a consequence of the interaction of ring beam and CFST column under external load.

(2) The crack developed near the proximity of the ring beam under cyclic loading, illustrating the multi-directional nature of the force system in the ring beam.

(3) RC ring beam should be designed against the combination of multi-directional forces including axial load, bending, torsion and shear. The connections with reasonable design were observed to have good ductility and suitable for seismic resistant application.

Acknowledgements

The authors wish to kindly acknowledge the financial support from the National Science Foundation of China through Grant No. 51038008 and the State Key Laboratory of Disaster Reduction in Civil Engineering, Tongji University.

References

- Nie JG, Bai Y, Cai CS. (2008). "New connection system for confined concrete columns and beams. I: Experimental study." *Journal of Structural Engineering*, 134(12), 1789–1799.
- Roeder CW, Lehman DE, Bishop E. (2010). "Strength and stiffness of circular concrete filled tubes." *Journal of Structural Engineering*, 136(12), 1545-1553.
- Wang W, Chen YY, Li WQ, Leon RT. (2011). "Bidirectional seismic performance of steel beam to circular tubular column connections with outer diaphragm." *Earthquake Engineering and Structural Dynamics*, 40, 1063–1081.
- Zhang YF, Zhao JH, Cai CS. (2012). "Seismic behavior of ring beam joints between concrete-filled twin steel tubes columns and reinforced concrete beams." *Engineering Structures*, 39, 1–10.

Flexural Strength of High-Strength Steel-Concrete Composite Beams with Varying Steel Grades

Huiyong Ban¹ and Mark A. Bradford, Dist.M.ASCE²

¹Research Fellow, Centre for Infrastructure Engineering and Safety, School of Civil and Environmental Engineering, Univ. of New South Wales, Sydney, NSW 2052, Australia. E-mail: h.ban@unsw.edu.au

²Scientia Professor and Australian Laureate Fellow, Centre for Infrastructure Engineering and Safety, School of Civil and Environmental Engineering, Univ. of New South Wales, Sydney, NSW 2052, Australia. E-mail: m.bradford@unsw.edu.au

Abstract

In order to investigate the bending capacity of composite beams constructed with high strength steel (HSS) sections, a three-dimensional finite element model allowing for both material and geometric non-linearity is described and validated against previous experimental results. An extensive body of parametric studies incorporating selected steel grades and degrees of shear connection is further undertaken. The flexural strength of such composite beams are analysed, and the effects of the steel yield strength and cross-sectional residual stresses are elucidated. Based on a comparison with composite beams using conventional mild steel, it is found that the method of rigid plastic analysis that is normally utilised to design composite beams with mild steel sections somewhat overestimates the bending strength of composite beams with HSS. There is no significant difference in the strength of a composite beam when considering the cross-sectional residual stress. A reduction factor is proposed for the adaptation of rigid plastic analysis, from which the prediction of the bending strength of composite beams with HSS becomes more accurate. This research has the potential to promote the practical application of HSS in composite construction, which is more environmentally sustainable due to the better efficiency of material utilisation compared with composite beams with lower-strength mild steel.

Keywords: High strength steel; Composite beam; Finite element analysis; Partial shear connection; Strength; Residual stress.

INTRODUCTION

High strength steel (HSS), having a steel grade of larger than 460 MPa, is being utilised increasingly in contemporary building and bridge construction because of the development of suitable fabrication techniques, as well as in response to growing demands for advanced structural materials with higher strength (Pocock 2006). The application of HSS in infrastructure engineering can provide more efficient, economic and sustainable design solutions because of its increased yield strength and more resource efficient compared with conventional mild steel (IABSE 2005). Design solutions with frames that use HSS need less steel compared to their mild steel counterparts, and they are lighter so less expense is needed in providing safe and adequate foundations.

Previous investigations reported in the existing literature are devoted to the mechanical performance of bare steel structures fabricated from HSS (Shi *et al.* 2012a), such as the buckling behaviour of columns subjected to compression (Ban *et al.* 2012a, 2013a and b; McDermott 1969; Nishino *et al.* 1967; Rasmussen and Hancock 1992 and 1995; Shi *et al.* 2012b and c; and Usami and Fukumoto 1982), residual stress within hot-rolled and welded sections (Ban *et al.* 2012a, 2013c), the performance of connections (Girão Coelho and Bijlaard 2007; Puthli 2001; Shi *et al.* 2012), and others. It was concluded from this research that the structural behaviour of HSS is generally better compared to mild steel. The overall buckling behaviour of HSS columns, for instance, is significantly improved due to the less severe effects of residual stresses and geometric imperfections.

For flexural members constructed with HSS, Beg and Hladnik (1996) investigated experimentally the buckling behaviour of ten S690 HSS I-section beams, and proposed a slenderness limit for such members. Earls (1999) researched numerically the inelastic failure of HSLA80 (550 MPa) HSS I-shaped beams, and concluded that the effect of the cross-section compactness and bracing configuration was different to that for conventional mild steel beams. Gao *et al.* (2008) undertook an experimental program for HSS (745 MPa ~ 800 MPa) four-point loaded beams, and elucidated the effect of the width-to-thickness ratio of the component plates. Shinohara *et al.* (2012) studied the elastic behaviour of HSS (over 700 MPa) H-shaped beams under cyclic loading through several tests, and proposed a new limiting value for the plate slenderness ratio. Lee *et al.* (2013) carried out 15 HSS (HSB800 and HSA800) I-shaped beam tests to study the effect of the flange slenderness on the flexural strength and rotation capacity, which indicated that the strength was satisfactory but that the rotation capacity was reduced.

It is more beneficial to apply HSS in composite construction, specifically in composite beams because a major portion of the steel section is subjected to tension in a case of sagging moment, and so local buckling may not govern the failure of the beam. As a result, the increased-strength attribute of HSS can be utilised more effectively. Despite this advantage, surprisingly limited research has been reported on the behaviour of composite structures constructed with HSS. Uy and Sloane (1998) tested two 690

MPa HSS composite beams, and found that current design theory produced slightly unconservative results for the flexural strength. Bradford and Pi (2012) developed a finite composite beam element for the non-linear inelastic analysis of composite HSS and geopolymer concrete members. Despite its higher strength, compared with the conventional mild steel, HSS does have poorer performance with respect to its post-yield response, and therefore the bending behaviour of composite beams using HSS may differ from that with conventional mild steel. The present paper is devoted to a study of the flexural strength of HSS-concrete composite beams, and the effects of steel grade and residual stresses are also clarified.

FINITE ELEMENT MODEL

A three-dimensional finite element (FE) model was developed herein by employing the widely-used commercial program ABAQUS. Both the steel joist and concrete slab were modelled by using the shell element S4R, and the shear connector between these two components was simulated by the element CONN3D2. Figure 1 represents a typical meshed model, in which the thickness of the shell element is shown rendered.

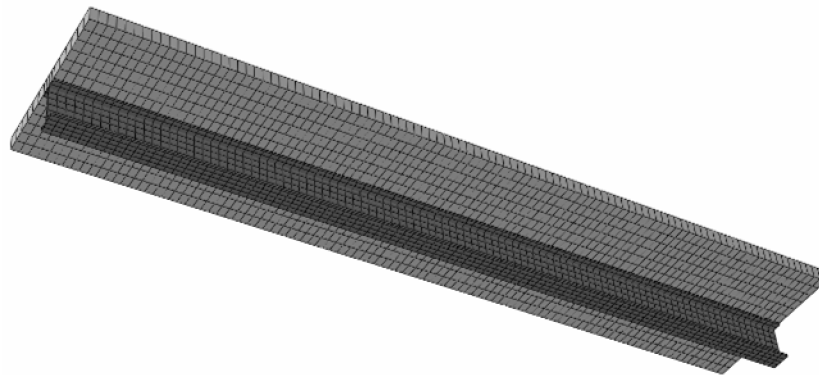


Figure 1. A typical finite element model for composite beam

The constitutive model for the steel material in the joist was simulated by using a multi-linear stress-strain relationship using von Mises' yielding criterion that allows for both the yield plateau and strain hardening, while an elastic perfectly-plastic model was adopted for the steel reinforcement embedded in the concrete slab. The non-linear stress-strain relation for concrete in compression was described by using the quadratic curve equation prescribed in Eurocode 2 (BSI 2004), and other parameters for specifying its material properties were also determined in accordance with Eurocode 2. The well-known load-slip model proposed by Ollgaard *et al.* (1971) was adopted for the shear connectors.

In order to verify the accuracy and reliability of this FE model, a large number of simply supported beams that were the same as those tested by Chapman and Balakrishnan (1964), Kwon *et al.* (2011) and Uy and Sloane (1998) were modelled. The test configurations, geometry of the specimens and material properties were all reported in detail in the corresponding literature, which are not repeated herein. The parameters for the constitutive models for steel, concrete and shear connectors were all determined based on relevant test results. Figure 2(a) describes a comparison between the computed results (P_{FEA}) obtained through the FE model and the test results (P_t) for the flexural strength of all specimens. Satisfactory agreement between these two groups of results can be observed, and the FE analysis results are on average 1.2% less than those obtained from the tests with a standard deviation of 0.055. In addition, a typical comparison between the load-deflection curves obtained from the FE model and the tests is shown in Figure 2(b), which indicates excellent agreement as well. As a consequence, the FE model developed herein is proven to be accurate and reliable for the prediction of flexural strength of composite beams with varying steel grades.

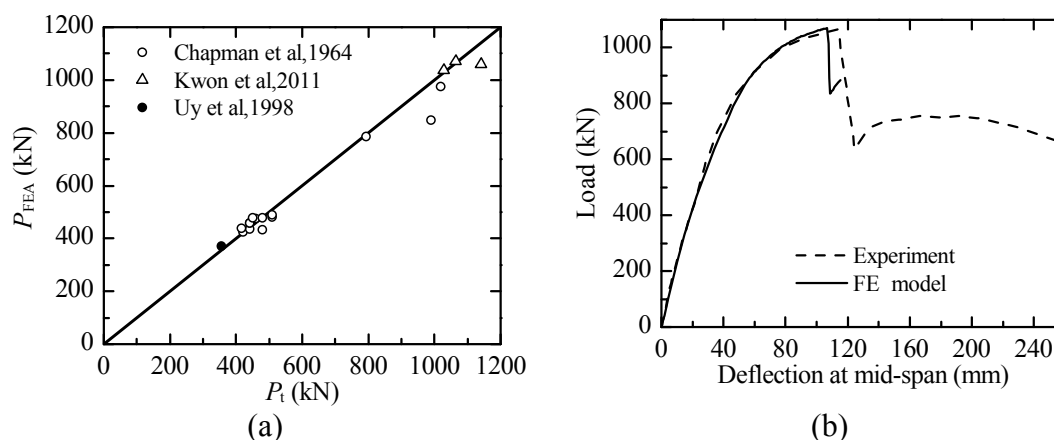


Figure 2. Comparison of FE analysis results with test results. (a) Flexural strength; (b) Load-deflection response

EFFECTS OF STEEL GRADE

To quantify the effects of the steel grade on the flexural strength of composite beams, eight simply supported beams subjected to single-point loading at the mid-span were analysed by using the validated FE model, incorporating one conventional mild steel (235 MPa) and three kinds of HSS (i.e. 460 MPa, 690 MPa and 960 MPa) joists. The corresponding concrete compressive strengths were 20 MPa, 35 MPa, 50 MPa and 60 MPa, respectively. Complete shear connection between the concrete slab component and steel joist was taken into account, and two degrees of shear connection were selected, i.e. 1.0 and 1.2. The material properties of steel were taken as the nominal values suggested by Ban *et al.* (2011), and for the concrete material the prescriptive

representation in Eurocode 2 was utilised. The sectional geometry of the steel joist was designed as $300 \times 150 \times 16 \times 12$ (mm) and the concrete slab was 1200 mm wide and 100 mm thick, with a span of 5500 mm.

Figure 3 shows a comparison between the flexural strength (M_{FEA}) obtained from the FE model and the values (M_n) computed based on rigid plastic analysis (Oehlers and Bradford 1995), and the same value of the yield strength was employed in these two calculation approaches for the same grade of HSS. It can be seen that the effect of the degree of shear connection for composite beams with complete shear connection is very slight, whilst the steel grade has a severe impact. The flexural strength (M_{FEA}) of 960 MPa HSS-concrete composite beams, for instance, is lower than the value obtained from rigid plastic analysis (M_n); as much as 9.5%. This percentage was 4.3% and 2.1% for 690 MPa and 460 MPa HSS composite beams respectively. As a consequence, the rigid plastic analysis that is commonly adopted in national standards overestimates the flexural strength of composite beams with HSS, and this conclusion is consistent with that obtained by Uy and Sloane (1998).

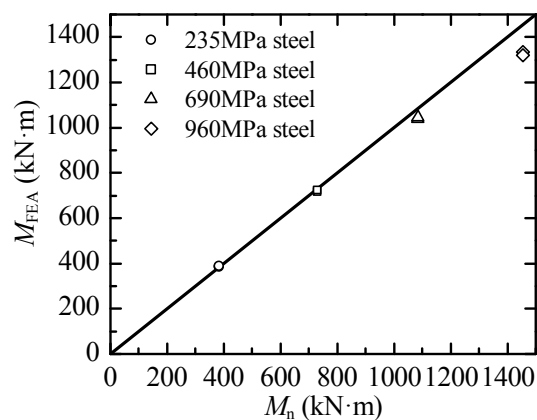


Figure 3. Comparison of flexural strengths obtained from FE model and rigid plastic analysis

Figure 4 shows a typical distribution of the stress along the sectional height for 690 MPa HSS composite beams when the peak load is being reached.

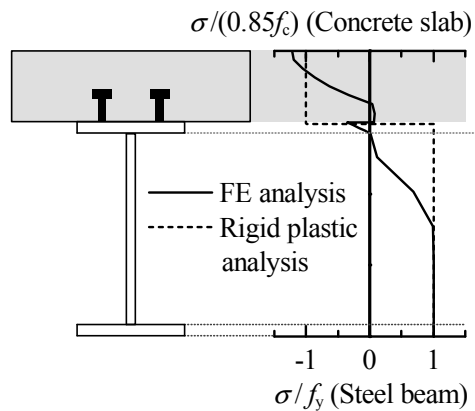


Figure 4. Stress distribution along the sectional height for 690 MPa HSS composite beam

From Figure 4 it is seen that the assumed rectangular yield stress block in rigid plastic analysis results in an over-estimation of the development of plasticity within the steel joist. One of the most important reasons is the poor plastic deformation possessed by HSS, and the other is the higher yield strain for HSS because of its increased yield strength but unchanged elastic modulus. The higher yield strain of HSS can lead to premature crushing of the concrete slab before the sufficient development of plasticity within steel joist, and the flexural strength is therefore lower than that in accordance with rigid plastic analysis.

EFFECTS OF PARTIAL SHEAR CONNECTION

To evaluate the effects of the degree of shear connection (β) on the flexural strength, 40 composite beams with varying steel grades (i.e. 235 MPa, 460 MPa, 690 MPa and 960 MPa) and degrees of shear connection ranging from 0.2 to 1.2 were analysed. Figure 5(a) illustrates the ratios of the flexural strengths obtained from the FE model to those obtained from rigid plastic analysis. It can be seen that an increase of either the degree of shear connection or the steel grade results in a more significant difference between the flexural strengths from the FE model and those from rigid plastic analysis.

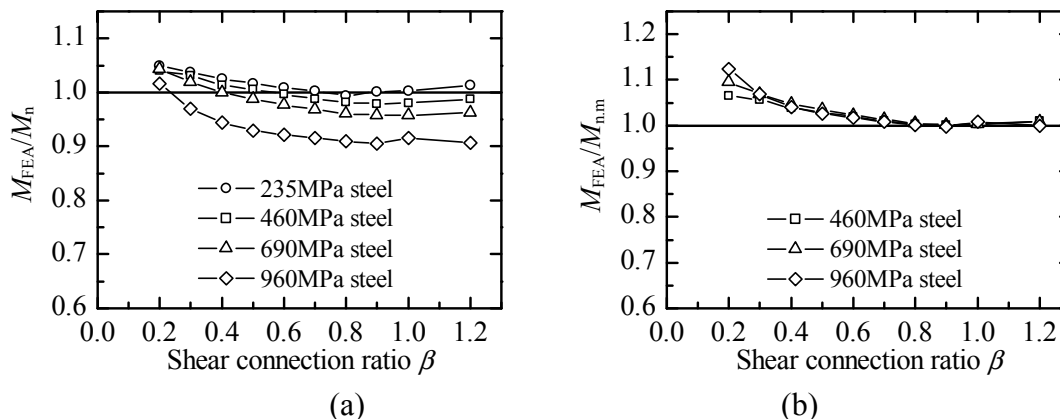


Figure 5. Comparison of flexural strengths from FE model and rigid plastic analysis with partial shear connection. (a) Conventional rigid plastic analysis; (b) Modified rigid plastic analysis

A reduction factor (α) for the steel strength is proposed herein to adopt conventional rigid plastic analysis, and which reflects the reduced development of plasticity in HSS as observed in the aforementioned FE analyses. Based on numerical investigations, Ban and Bradford (2013) proposed the value for α as

$$\alpha = 0.97 + 0.08f_{yG} - 0.18f_{yG}^2, \quad (1)$$

in which f_{yG} denotes the yield strength of the steel in units of GPa. For 235 MPa conventional mild steel, the value of α according to Equation (1) is 1.0. Figure 5(b) gives a comparison of the FE analysis results M_{FEA} with the values $M_{n,m}$ determined from rigid plastic analysis using the proposed factor α . It is seen that they have good agreement, particularly for composite beams with a degree of shear connection larger than 0.5.

EFFECTS OF RESIDUAL STRESS

For bare steel beams, there is normally no effect of the cross-sectional residual stresses on the flexural capacity, because the entire steel cross-section is yielded as its flexural capacity is attained. However, this plasticity may not develop through the full depth of a critical section of the steel joist in a composite beam, particularly composite beams constructed with HSS, as was noted previously in this paper. It is therefore of interest to quantify the effects of residual stresses on the flexural strength of composite beams. For this, 16 composite beams were analysed by using the validated FE model, allowing for four steel grades (235 MPa, 460 MPa, 690 MPa and 960 MPa), two degrees of shear connection (0.5 and 1.0) and two residual stress models (one is consistent with that reported by Ban *et al.* (2013a) and the other ignores the residual stress). Figure 6 shows a typical distribution of the von Mises stresses within a composite beam, from

which it is seen that the bottom flange and a major portion of web near the mid-span region is completely yielded. A comparison of the flexural strengths for composite beams with and without residual stresses is represented in Figure 7. It is indicated that these are very close to each other, with a maximum difference of only 1.4% for 960 MPa HSS composite beams. Hence, despite the limited development of plasticity for HSS in a composite beam, the effect of residual stress is very slight.

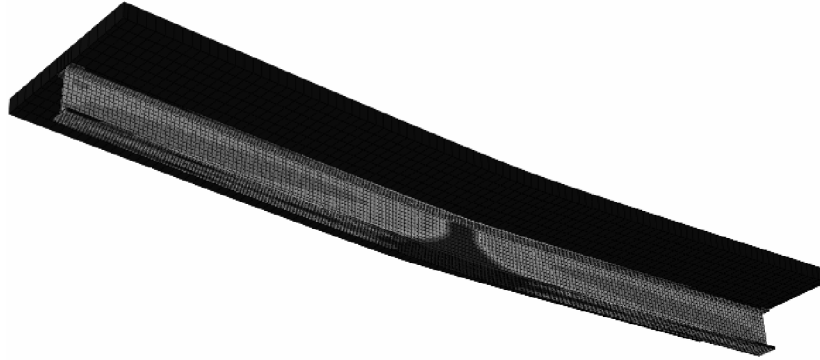


Figure 6. A typical distribution of von Mises stress within a composite beam allowing for residual stresses

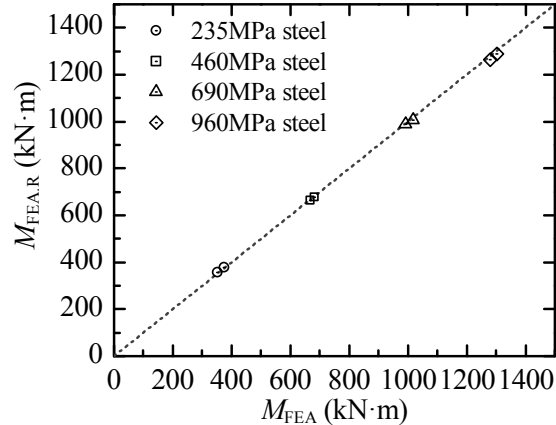


Figure 7. Comparison of flexural strengths for composite beams with and without residual stresses

CONCLUSIONS

A three-dimensional FE model incorporating both geometric and material non-linearity was described and validated against independent experimental investigations reported elsewhere in the literature. Based on a number of parametric analyses by using

this model, it was found that the development of plasticity for HSS within a composite beam was overestimated using conventional rigid plastic analysis, and which therefore will lead to unconservative results for the flexural strength of such members. This overestimation was shown to be more severe with an increase of the steel grade and with the degree of shear connection. A reduction factor for the steel strength was suggested so as to adapt rigid plastic analysis for HSS, which was shown to be more accurate for the prediction of the flexural strength of HSS composite beams. In addition, despite the limited development of plasticity for HSS within a composite beam, the effect of the residual stresses on the flexural strength was very slight.

It should be noted that the proposed amendment of Eurocode 4 herein is only applicable to composite beams using such HSS considered in this work. Despite a large number of parameters having been considered including various strengths of steel and concrete, partial and full interaction as well as residual stresses, more further investigations on the effects of loading patterns, cross-sectional geometries and usage of profiled steel decking for the slab are still in need, which may provide a more broad basis for verifying and improving the research findings obtained in this work.

Applying high strength and high performance structural materials is one of the trends in the development for contemporary infrastructure construction, and the present research contributes to the application of HSS in composite construction as a more sustainable design solution.

REFERENCES

- Ban H.Y., and Bradford M.A. (2013). "Flexural behaviour of composite beams with high strength steel." *Engineering Structures*, 56, 1130-1141.
- Ban H.Y., Shi G., Shi Y.J., and Wang Y.Q. (2011). "Research progress on the mechanical property of high strength structural steels." *Advanced Materials Research*, 250-253(1-4), 640-648.
- Ban H.Y., Shi G., Shi Y.J., and Wang Y.Q. (2012a). "Overall buckling behavior of 460MPa high strength steel columns: Experimental investigation and design method." *Journal of Constructional Steel Research*, 74, 140-150.
- Ban H.Y., Shi G., Shi Y.J., and Wang Y.Q. (2012b). "Residual stress tests of high-strength steel equal angles." *Journal of Structural Engineering*, ASCE, 138(12), 1446-1454.
- Ban H.Y., Shi G., Shi Y.J., and Bradford M.A. (2013a). "Experimental investigation of the overall buckling behaviour of 960 MPa high-strength steel columns." *Journal of Constructional Steel Research*, 88, 256-266.
- Ban H.Y., Shi G., Shi Y.J., and Wang Y.Q. (2013b). "Column buckling tests of 420 MPa high strength steel single equal angles." *International Journal of Structural Stability and Dynamics*, 13(2), 1250069.

- Ban H.Y., Shi G., Shi Y.J., and Wang Y.Q. (2013c). "Residual stress of 460 MPa high strength steel welded box section: Experimental investigation and modeling." *Thin-Walled Structures*, 64, 73-82.
- Beg D., and Hladnik L. (1996). "Slenderness limit of class 3 I cross-sections made of high strength steel." *Journal of Constructional Steel Research*, 38(8), 201-207.
- Bradford M.A., and Pi Y.L. (2012). "Nonlinear elastic-plastic analysis of composite members of high-strength steel and geopolymer concrete." *CMES: Computer Modeling in Engineering & Sciences*, 89(5), 387-414.
- British Standards Institution. (2004). *BS EN 1992-1-1: 2004 Eurocode 2: Design of Concrete Structures Part 1-1: General Rules and Rules for Buildings*, BSI, London.
- Chapman J.C., and Balakrishnan S. (1964). "Experiments on composite beams." *The Structural Engineer*, 42(11), 369-383.
- Earls C.J. (1999). "On the inelastic failure of high strength steel I-shaped beams." *Journal of Constructional Steel Research*, 49(1), 1-24.
- Gao L., Sun H.C., Jiang K.B., and Xu G.Y. (2008). "Load-carrying capacity of the high-strength steel thin-walled box-section beam." *Proceedings of the 10th International Symposium on Structural Engineering for Young Experts*, Changsha, China, 877-882.
- Girão Coelho A.M., and Bijlaard F.S.K. (2007). "Experimental behaviour of high strength steel end-plate connections." *Journal of Constructional Steel Research*, 63(9), 1228-1240.
- International Association for Bridge and Structural Engineering. (2005). *Use and Application of High-Performance Steels for Steel Structures*, IABSE, Zurich.
- Kwon G., Engelhardt M.D., and Klingner R.E. (2011). "Experimental behavior of bridge beams retrofitted with postinstalled shear connectors." *Journal of Bridge Engineering*, ASCE, 16(4), 536-545.
- Lee C.H., Han K.H., Uang C.M., Kim D.Y., Park C.H., and Kim J.H. (2013). "Flexural strength and rotation capacity of I-shaped beams fabricated from 800-MPa steel." *Journal of Structural Engineering*, ASCE, 139(6), 1043-1058.
- McDermott J.F. (1969). "Local plastic buckling of A514 steel members." *Journal of the Structural Division*, ASCE, 95(ST9), 1837-1850.
- Nishino F., Ueda Y., and Tall L. (1967). "Experimental investigation of the buckling of plates with residual stresses." *Test methods for compression members*, American Society for Testing and Materials. ASTM special technical publication, Philadelphia, PA, (419), 12-30.
- Oehlers D.J., and Bradford M.A. (1995). *Composite Steel and Concrete Structural Members: Fundamental Behaviour*, Pergamon, Oxford.
- Ollgaard J.G., Slutter R.J., and Fisher J.W. (1971). "Shear strength of stud connectors in lightweight and normal-weight concrete." *AISC Engineering Journal*, 8, 55-64.
- Pocock G. (2006). "High strength steel use in Australia, Japan and the US." *The Structural Engineer*, 84(21), 27-30.

- Puthli R., and Fleischer O. (2001). "Investigations on bolted connections for high strength steel members." *Journal of Constructional Steel Research*, 57(3), 313-326.
- Rasmussen K.J.R., and Hancock G.J. (1992). "Plate slenderness limits for high strength steel sections." *Journal of Constructional Steel Research*, 23(1), 73-96.
- Rasmussen K.J.R., and Hancock G.J. (1995). "Tests of high strength steel columns." *Journal of Constructional Steel Research*, 34(1), 27-52.
- Shi G., Ban H.Y., Shi Y.J., and Wang Y.Q. (2012a). "Progress in application and research of high strength steel structures." *Proceedings of the Twelfth International Symposium on Structural Engineering (Volume I)*, Wuhan, China, 583-586.
- Shi G., Ban H.Y., and Bijlaard F.S.K. (2012b). "Tests and numerical study of ultra-high strength steel columns with end restraints." *Journal of Constructional Steel Research*, 70, 236-247.
- Shi G., Liu Z., Ban H.Y., Zhang Y., Shi Y.J., and Wang Y.Q. (2012c). "Tests and finite element analysis on the local buckling of 420 MPa steel equal angle columns under axial compression." *Steel and Composite Structures*, 12(1), 31-51.
- Shi Y.J., Pan B., Shi G., and Wang Y.Q. (2012). "Investigation on bolted connection of high strength steel tension splices under static shear." *Proceedings of the 6th International Symposium on Steel Structures (ISSS-2011)*, Seoul, Korea, 1012-1018.
- Shinohara T., Suekuni R., and Lkarashi K. (2012). "Cyclic behavior of high strength steel H-shaped beam." *Applied Mechanics and Materials*, 174-177, 159-165.
- Usami T., and Fukumoto Y. (1982). "Local and overall buckling of welded box columns." *Journal of the Structural Division*, ASCE, 108(ST3), 525-542.
- Uy B., and Sloane R.J. (1998). "Behaviour of composite tee beams constructed with high strength steel." *Journal of Constructional Steel Research*, 46(1), 203-204.

Deformation-Based Design of Composite Beams

Leroy Gardner¹; Merih Kucukler²; and Lorenzo Macorini³

¹Dept. of Civil and Environmental Engineering, Imperial College London, London SW7 2AZ, U.K. E-mail: Leroy.gardner@imperial.ac.uk

²Dept. of Civil and Environmental Engineering, Imperial College London, London SW7 2AZ, U.K. E-mail: Merih.kucukler10@imperial.ac.uk

³Dept. of Civil and Environmental Engineering, Imperial College London, London SW7 2AZ, U.K. E-mail: L.macorini@imperial.ac.uk

Abstract

Current design specifications for steel and composite structures generally assume elastic-plastic or rigid-plastic material behaviour, which means that the beneficial influence of strain hardening is neglected. This assumption may lead to overly conservative strength predictions particularly for stocky bare steel sections and composite beams subjected to sagging bending. The continuous strength method (CSM) is a deformation based design approach that allows for strain hardening in the design of metallic cross-sections. Although the method has been successfully applied to bare steel, stainless steel and aluminium alloy cross-sections, use of the CSM for steel-concrete composite structural components, which may considerably benefit from strain hardening, has not been extensively studied. Thus, the primary purpose of this study is to extend the application of the CSM to composite structures, with an emphasis on simply supported beams subjected to sagging bending.

1. INTRODUCTION

Although largely disregarded in design codes, strain hardening may considerably increase the strength of structural components provided the elements are not susceptible to instability effects or such effects are adequately suppressed. Thus, consideration of strain hardening may lead to more efficient design. The continuous strength method (CSM) is a deformation based design approach that accounts for strain hardening. Originally developed for stainless steel structural elements (Gardner and Nethercot, 2004; Ashraf et al., 2008; Afshan and Gardner, 2013), which exhibit a high degree of strain hardening, application of the method has also been extended to structural carbon steel (Gardner, 2008; Gardner et al., 2011) and aluminium alloy members (Ashraf and Young, 2011). For bare metallic elements, the continuous strength method requires the determination of the deformation capacity of the cross-section, as limited by local buckling. In lieu of placing the cross-sections into discrete behavioural classes, which is the approach that is traditionally adopted in design codes, the continuous strength method assigns a limiting strain to a cross-section. This limiting strain is controlled by the slenderness of the cross-section and is used, in conjunction with a simple strain hardening material model, to determine the resistance of a structural element.

Composite steel-concrete construction attempts to use the combined merits of the two materials to achieve more efficient structural solutions. Simply supported composite beams subjected to sagging bending, where the concrete is largely in compression and the steel is in tension, offers the opportunity to exploit the full capacity of both materials. Similar to those for bare steelwork, current design codes for composite structures, including Eurocode 4 (EN 1994-1-1, 2004), generally neglect strain hardening and use simple material models for the determination of the plastic bending moment resistance of composite beams. The potential benefit of strain hardening on the sagging bending moment resistance of simply supported composite beams has been reported in previous experimental and numerical studies (Ansourian, 1982; Chung and Chan, 2010), thus suggesting that failure to account for strain hardening in design codes may lead to somewhat conservative results. The results of analytical and numerical studies performed to investigate the effect of strain hardening on the sagging bending moment capacity of composite beams are reported in this study. Simple expressions to calculate the bending capacity of composite beams with full shear connection, allowing for the influence of strain hardening, are derived. The proposed design expressions are compared with experimental and numerical results to demonstrate the accuracy and benefits of their application. The behaviour of composite beams under sagging bending moment with partial shear connection is also investigated by means of finite element modelling and an indicative design approach is outlined. Finally, the response of continuous composite beams, featuring regions of hogging bending moments and with the possibility of moment redistribution is discussed.

2. APPLICATION OF THE CONTINUOUS STRENGTH METHOD TO COMPOSITE BEAMS WITH FULL SHEAR CONNECTION

The bending resistance of composite beams with full shear connection can be derived by means of simple equilibrium considerations in conjunction with suitable material laws - see Figure 1. Considering various geometric and material properties for the composite section, seven design scenarios, featuring different neutral axis locations and points of initiation of yielding, can be identified (Kucukler, 2011). Herein, an analytical expression for the bending resistance, incorporating strain hardening, is derived considering only one scenario, that being where the neutral axis lies within the concrete, and the steel section has fully yielded, as shown in Figure 1, in which h_c is the depth of the concrete flange, h_a is the depth of the steel section, f_{cd} is the design concrete (cylinder) compressive strength and $\epsilon_{csm,c}$ and $\epsilon_{csm,a}$ are the outer fibre concrete and steel strains respectively.

The deformation capacity of the cross-section will typically be limited by either crushing of the concrete or tensile ductility of the structural steel for composite beams with full shear connection. The capacity of the shear studs should also be verified, with existing design provisions remaining applicable. In this study, the maximum outer fibre concrete strain has been limited to the crushing strain of the concrete ϵ_{cu} (i.e. $\epsilon_{csm,c} = \epsilon_{cu} = 0.0035$), while the maximum outer fibre strain in the steel $\epsilon_{a,max}$ has been limited to $15\epsilon_y$ where ϵ_y is the yield strain.

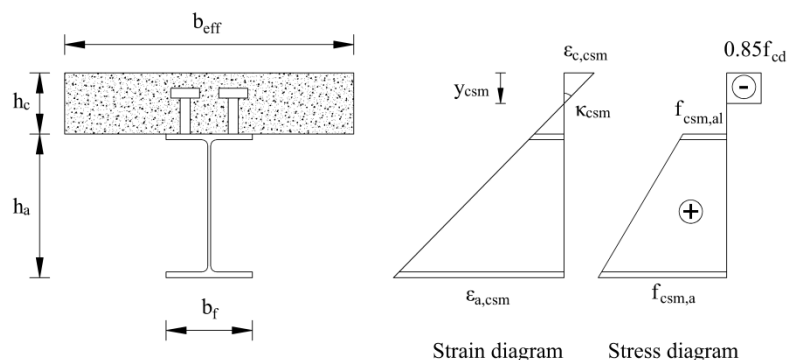


Fig. 1 - Strain and stress distributions for a composite beam with full shear connection

The following material laws are assumed in the analytical model: the stress-strain relationship for the structural steel is represented by the strain hardening material response of Figure 2 (EN 1993-1-5, 2005) in which E is the Young's modulus, E_{sh} is the slope of the strain hardening region and f_y is the yield strength of the steel, while the concrete material behaviour is assumed to be rigid plastic, with plasticity occurring at a stress level of $0.85f_{cd}$. These material models are used to evaluate stress values from the strain distribution.

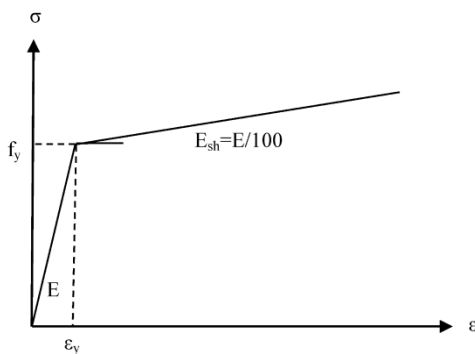


Fig. 2 - CSM material model for structural steel with strain hardening

The position of the neutral axis at failure initially needs to be determined so as to calculate the bending capacity. Since the neutral axis shifts under increasing curvature, its location at failure depends on the failure mode, either concrete crushing or reaching of the steel ductility limit ($\epsilon_{csm,a} = 15\epsilon_y$). The general relationship between curvature κ and neutral axis position y_{csm} (measured from the outer concrete fibre) is provided by Equation 1, where A_a is the cross-sectional area of the steel section and b_{eff} is the effective width of the concrete slab.

$$\kappa = \frac{0.85f_{cd}b_{eff}y_{csm} - A_a(f_y - E_{sh}\epsilon_y)}{E_{sh}A_a(h_c + h_a/2 - y_{csm})} \quad (1)$$

The position of the neutral axis y_{csm} is given by Equation 2, where the coefficients B, C and D are given by Equations 3-7.

$$By_{csm}^2 + Cy_{csm} + D = 0 \quad (2)$$

For the concrete crushing failure mode, the neutral axis position at failure $y_{csm,c}$ is found by employing coefficients B_c , C_c and D_c while for failure governed by the steel ductility limit, the neutral axis at failure $y_{csm,a}$ is found using coefficients B_a , C_a and D_a , with the subscripts 'c' and 'a' denoting concrete and steel respectively.

$$B_c = B_a = 0.85f_{cd}b_{eff} \quad (3)$$

$$C_c = \{(\epsilon_y + 0.0035)E_{sh} - f_y\}A_a \quad (4)$$

$$C_a = \{-0.85f_{cd}b_{eff}(h_c + h_a) - (f_y - 14E_{sh}\epsilon_y)A_a\} \quad (5)$$

$$D_c = -0.0035E_{sh}A_a(h_c + h_a/2) \quad (6)$$

$$D_a = (f_y - E_{sh}\epsilon_y)A_a(h_c + h_a) + 15\epsilon_y E_{sh}A_a(h_c + h_a/2) \quad (7)$$

To ascertain the governing failure mode, $y_{csm,c}$ and $y_{csm,a}$ may be substituted into Equations 8 and 9 respectively whereby the limiting curvatures κ_{csm} for concrete ($\kappa_{csm,c}$) and steel ($\kappa_{csm,a}$) failure can be determined. Note that $\kappa_{csm,c}$ and $\kappa_{csm,a}$ represent reaching the limiting strain at the outer concrete and steel fibres respectively. The governing failure mode is defined by the lower of $\kappa_{csm,c}$ and $\kappa_{csm,a}$.

$$\kappa_{csm,c} = \frac{\epsilon_{cu}}{y_{csm,c}} = \frac{0.0035}{y_{csm,c}} \quad (8)$$

$$\kappa_{csm,a} = \frac{15\epsilon_y}{h_c + h_a - y_{csm,a}} \quad (9)$$

Having determined the governing values of y_{csm} and κ_{csm} (i.e. either $y_{csm,c}$ and $\kappa_{csm,c}$ for a concrete governed failure or $y_{csm,a}$ and $\kappa_{csm,a}$ for a steel governed failure), the outer fibre stresses in the steel section at failure (see Figure 1) can be found from Equations 10 and 11:

$$f_{\text{csm,a}} = f_y + E_{\text{sh}} \left\{ \kappa_{\text{csm}} (h_c + h_a - y_{\text{csm}}) - \varepsilon_y \right\} \quad (10)$$

$$f_{\text{csm,al}} = f_y + E_{\text{sh}} \left\{ \kappa_{\text{csm}} (h_c - y_{\text{csm}}) - \varepsilon_y \right\} \quad (11)$$

The moment capacity of the composite section, allowing for strain hardening, can finally be calculated by means of Equation 12:

$$M_{\text{csm,c}} = f_{\text{csm}} A_a \left(h_c + \frac{h_a}{2} - \frac{y_{\text{csm}}}{2} \right) - \frac{(f_{\text{csm,a}} - f_{\text{csm,al}})}{2} A_a \left(h_c + \frac{h_a}{3} - \frac{y_{\text{csm}}}{2} \right) \quad (12)$$

The above proposals were validated numerically and compared with a series of experimental results collected from the literature (Chapman and Balakrishnan, 1964; Ansourian, 1982; Nie et al., 2004) on composite beams with full shear connection. The comparisons, shown in Table 1, have been made on the basis of measured geometric and material properties, with all partial factors set to unity. It may be seen that the proposed method, accounting for strain hardening, provides a more accurate prediction of test capacity than the current approach given in EN 1994-1-1 (2004).

Table 1 - Comparison of moment capacities from test results on composite beams with shear connection with those predicted by EN 1994-1-1 (EC4) and the CSM

No. of tests = 15	$M_{\text{EC}}/M_{\text{test}}$	$M_{\text{csm}}/M_{\text{test}}$	$M_{\text{csm}}/M_{\text{EC}}$
Mean	0.93	0.98	1.05
COV	0.064	0.052	-

3. APPLICATION OF THE CONTINUOUS STRENGTH METHOD TO COMPOSITE BEAMS WITH PARTIAL SHEAR CONNECTION

The behaviour of composite beams with partial shear connection is more complex than that for the case of full shear connection. This is due to the deformability and finite resistance of the shear connectors, which lead to a more complex arrangement of internal forces in the composite section, and two distinct neutral axes, as shown in Figure 3. Thus, the contribution of strain hardening to the cross-section moment capacity cannot be calculated using the simple analytical approach described in Section 2. However, using finite element models in conjunction with suitable nonlinear relationships for the constituent materials and shear connection, the load-deformation response and collapse load of composite beams with partial shear connection can be predicted with a high degree of accuracy (Gattesco, 1999; Zona et al., 2011). A similar approach was adopted herein using the finite element programme ABAQUS (2010). The steel beam and concrete slab were modelled using quadratic beam elements (B22), while the connection between the two components (i.e. the behaviour of the shear studs) was represented using rigid

links and nonlinear springs, as shown in Figure 4. The ability of 2D models to simulate the 3D response of composite beams have been demonstrated in several previous studies (Salari et al., 1998, Queiroz et al., 2009).

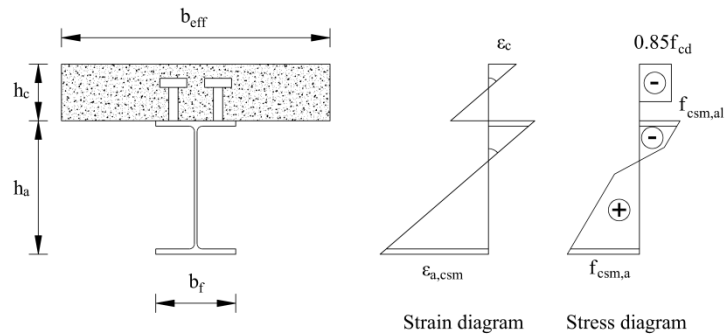


Fig. 3 - Strain and stress distribution diagrams for a composite beam with partial shear connection

For the purpose of validating the finite element models, the obtained results were compared against those from existing experimental and numerical studies (Chapman and Balakrishnan, 1964; Queiroz et al., 2007; Queiroz et al., 2009). The comparisons, which are reported in Gardner et al. (2013), show good agreement between the results of the present FE models and those reported in the literature, indicating the ability of the models to capture accurately the true response of composite beams with partial shear connection.

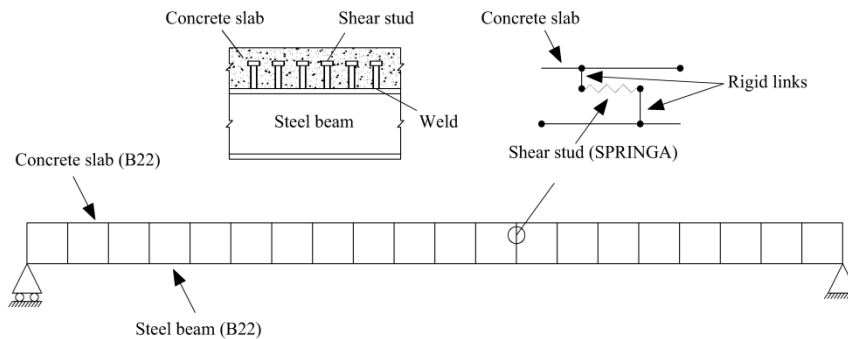


Fig. 4 - Components of finite element model of a composite beam with partial shear connection

The adopted material stress-strain models for the steel (Figure 1) and concrete (Figure 5) were taken from EN 1993-1-5 (2005) and EN 1992-1-1 (2004), respectively, where the following symbols are used: E_{cm} is the mean value of the secant modulus of elasticity of concrete, f_{cm} is the mean value of concrete cylinder compressive strength, f_{ctm} is the mean value of axial tensile strength, ϵ_{c1} is the compressive strain in the concrete at the peak stress f_{cm} , ϵ_{cu1} is the ultimate compressive strain in the concrete. The recommendations of Johnson and Molenstra

(1991), using Curve A and a maximum slip $s_{\max} = 6$ mm were followed for the shear studs. The load-slip relationship is shown in Figure 6, where P is the load applied to the shear stud and P_d is the design shear resistance of the shear stud. Failure was signified when the designated maximum strains in either of the materials were reached: $\epsilon_{cu} = 0.0035$ for the concrete and $\epsilon_{a,\max} = 15\epsilon_y$ for the steel or when the maximum allowable slip in the shear studs, defined as $s_{\max} = 6$ mm, was reached.

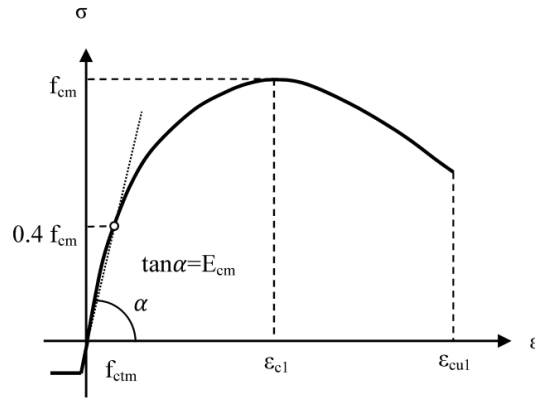


Fig. 5 - Concrete material model employed in FE study

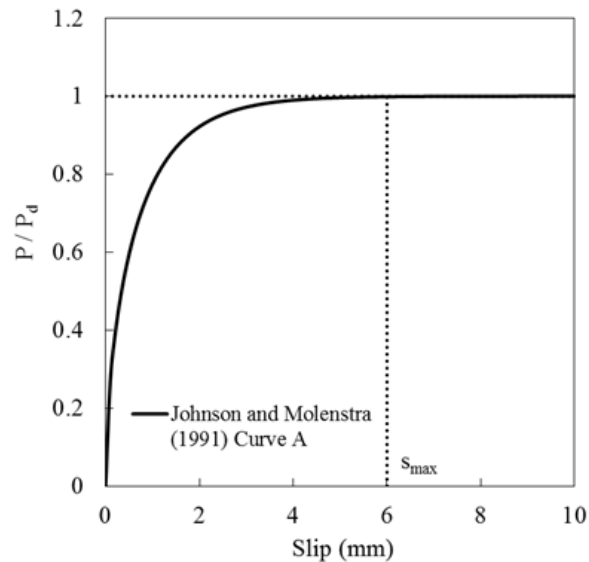


Fig. 6 – Load-slip relationship for shear studs (Johnson and Molenstra, 1991)

A series of simply-supported composite beams loaded by a point load at mid-span were analysed, providing structural performance data for a range of varying parameters. Various steel profiles, concrete slabs and levels of shear connection were considered, while the material properties, S355 steel ($f_y = 355$ N/mm²) and C30 concrete ($E_{cm} = 33$ kN/mm², $f_{cm} = 38$ N/mm², $f_{ctm} = 2.9$ N/mm², $\epsilon_{c1} = 0.0022$, $\epsilon_{cul} = 0.0035$) remained constant. Results for a UB 457×152×60 steel profile with a 3000 mm wide and 125 mm thick concrete slab and varying degrees of shear connection, $0 < \eta \leq 1.4$, are illustrated by Figure 7(a), where $\eta = N_c/N_{c,f}$ with N_c being the design

value of the compressive normal force within the concrete flange and $N_{c,f}$ being the design value of the compressive normal force within the concrete flange with full shear connection. The ratio between the ultimate bending resistance M_{max} obtained through the FE models and plastic bending moment resistance $M_{pl,c}$ determined through the Eurocode 4 provisions for beams with full shear connection is plotted on the vertical axis and the degree of shear connection η is given on the horizontal axis in the figure. Two sets of results are illustrated with and without considering strain hardening in the figure, which are compared against the plastic bending resistance for partial shear connection calculated according to the equilibrium and the interpolation method provided in Eurocode 4.

The influence of strain hardening on the response of composite beams with partial shear connection may be assessed by comparing the results of the FE models with the two different material models shown in Figure 7a. The results indicate that for low levels of shear connection, the influence of strain hardening is small, while for higher degrees of shear connection, strain hardening may increase the bending moment resistance by up to about 15 %. The FE results without strain hardening fall below the resistance calculated through the equilibrium method of Eurocode 4 for intermediate to high degrees of shear connection. This suggests that although it is neglected in the calculation, strain hardening is required to attain the full bending resistance of composite sections in the presence of partial shear connection. The FE results suggest that the sagging bending capacity of simply-supported beams can be enhanced through a more systematic approach to the use of strain hardening in composite design.

Based on the numerical results, a tentative approach to determine the sagging bending capacity of composite beams with partial shear connection, but accounting for strain hardening, is proposed. The approach proposed herein uses the CSM bending resistance of the bare steel section M_{csm} which is outlined in Section 4 for $\eta = 0$ and the CSM bending resistance for the composite section with full shear connection $M_{csm,c}$, described in Section 2 for $\eta \geq 1.4$, in conjunction with an interpolation function for intermediate degrees of shear connection. Note that the use of $\eta = 1.4$ is based on the FE results that indicated a degree of shear connection equal to 1.4 times that deemed necessary to provide full shear connection in Eurocode 4 is required in order to achieve the bending resistance with strain hardening $M_{csm,c}$, derived in Section 2. A total of 71 parametric FE results are shown in Figure 7b, together with an indicative interpolation function generated by regression analysis. For the range of parameters considered, which were described earlier in this section, the interpolation function may be seen to provide an accurate match to the numerical data, indicating that the described approach may be used to predict the ultimate capacity of composite beams with partial shear connection allowing for strain hardening. Clearly a wider range of parameters and loading types need to be considered before the method is suitable for use in practice, but the present study has demonstrated the validity of the proposed approach.

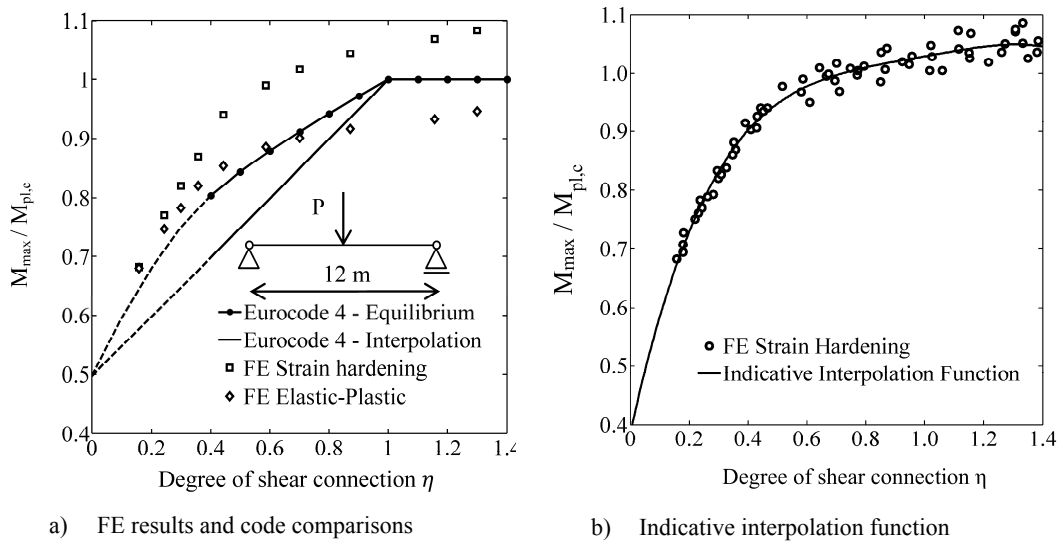


Fig. 7 - Finite element results, code comparisons and the outline CSM approach for bending capacities in the case of partial shear connection

4. APPLICATION OF THE CONTINUOUS STRENGTH METHOD TO BARE STEEL ELEMENTS

For composite beams under hogging bending moments, consideration must be given to the possibility of buckling of the steel elements in compression. This has been previously considered in the context of bare steel elements in compression and bending, and the key aspects are summarised herein, with a focus on local buckling. Susceptibility to local buckling of the cross-section is assessed through the cross-section slenderness $\bar{\lambda}_p$, determined from Equation (13):

$$\bar{\lambda}_p = (f_y / \sigma_{cr})^{0.5} \tag{13}$$

in which f_y is the material yield strength and σ_{cr} is elastic critical buckling stress of the cross-section or its most slender constituent plate element. Following the CSM design approach, the deformation capacity ϵ_{csm} (i.e. the limiting strain) of the cross-section may subsequently be determined from Equation (14) for $\bar{\lambda}_p \leq 0.68$.

$$\frac{\epsilon_{csm}}{\epsilon_y} = \frac{0.25}{\bar{\lambda}_p^{3.6}} \quad \text{but} \quad \frac{\epsilon_{csm}}{\epsilon_y} \leq 15 \tag{14}$$

where $\epsilon_y = f_y / E$ is the yield strain of the material. Since the capacity of the cross-sections where $\bar{\lambda}_p > 0.68$ will be below the yield load (or moment) with no benefit from strain hardening, the CSM does not apply to such cross-sections. Existing methods, such as the effective width (EN 1993-1-5, 2005) or direct strength methods (Schafer, 2008), can be used for the determination of capacity of these sections.

After ascertaining the limiting strain, the cross-section resistance, under any loading condition, may be determined with reference to the strain hardening material model. The CSM employs an elastic, linear hardening material model (see Figure 2) with, for structural steel, a strain hardening slope $E_{sh}=E/100$ where E is the Young's modulus and a maximum allowable strain of $15\varepsilon_y$, which corresponds to the minimum ductility requirements set out in EN 1993-1-1 (2005).

In pure compression, there is a uniform strain distribution and cross-section resistance can simply be calculated by means of Equation (15).

$$N_{csm} = \frac{Af_{csm}}{\gamma_{M0}} \quad (15)$$

where A is the cross-sectional area (previously termed A_a in the context of composite construction), γ_{M0} is a partial safety factor for cross-section resistance with a recommended value of unity for steel elements and f_{csm} is given, from the elastic, linear hardening material model shown in Figure 2, by:

$$f_{csm} = f_y + E_{sh}\varepsilon_y \left(\frac{\varepsilon_{csm}}{\varepsilon_y} - 1 \right) \quad (16)$$

Cross-section resistance in bending $M_{csm,Rd}$ is given by Equation (17) for bending about the major (y-y) axis and Equation (18) for bending about the minor (z-z) axis (Gardner et al., 2011), in which W_{pl} is the plastic section modulus, W_{el} is the elastic section modulus, y and z refer to the major and minor axes, respectively, and α is a coefficient dependent on section type with $\alpha = 2.0$ for square and rectangular hollow sections (SHS and RHS) and $\alpha = 1.2$ for I-shaped sections.

$$M_{y,csm,Rd} = \frac{W_{pl,y}f_y}{\gamma_{M0}} \left[1 + \frac{E_{sh}}{E} \frac{W_{el,y}}{W_{pl,y}} \left(\frac{\varepsilon_{csm}}{\varepsilon_y} - 1 \right) - \left(1 - \frac{W_{el,y}}{W_{pl,y}} \right) / \left(\frac{\varepsilon_{csm}}{\varepsilon_y} \right)^2 \right] \quad (17)$$

$$M_{z,csm,Rd} = \frac{W_{pl,z}f_y}{\gamma_{M0}} \left[1 + \frac{E_{sh}}{E} \frac{W_{el,z}}{W_{pl,z}} \left(\frac{\varepsilon_{csm}}{\varepsilon_y} - 1 \right) - \left(1 - \frac{W_{el,z}}{W_{pl,z}} \right) / \left(\frac{\varepsilon_{csm}}{\varepsilon_y} \right)^\alpha \right] \quad (18)$$

Table 2 - Comparison between the CSM, Eurocode and test results for compression and bending resistances of steel, stainless steel and aluminium alloy cross-sections

Material		Compression resistance		Bending resistance	
		N_{EC}/N_{test}	N_{csm}/N_{test}	M_{EC}/M_{test}	M_{csm}/M_{test}
Steel	No. of tests	74		88	
	Mean	0.89	0.95	0.87	0.92
	COV	0.11	0.078	0.076	0.069
Stainless steel	No. of tests	85		63	
	Mean	0.81	0.95	0.74	0.89
	COV	0.084	0.077	0.099	0.083
Aluminium alloy	No. of tests	189		70	
	Mean	0.91	0.97	0.85	0.98
	COV	0.12	0.083	0.10	0.093

Comparisons between the above design expressions and test data on steel (Gardner et al., 2011), stainless steel (Afshan and Gardner, 2013) and aluminium alloy cross-sections (Su et al., 2012a, 2012b) are summarised in Table 2. All comparisons are made on the basis of measured geometric and material properties and with partial factors set equal to unity. Results obtained from the respective current European design standards, namely EN 1993-1-1 (2005), EN 1993-1-4 (2006) and EN 1999-1-1 (2007) are also shown. In all cases, the results suggest that the CSM provides a more accurate prediction of observed physical behaviour over current design approaches, through rational deformation based design and systematic exploitation of strain hardening. Despite the increased strength determined through the CSM, an increase in the partial safety factors may not be required owing to the reduced variability (COV) of the model predictions in comparison with the experimental results – see Table 1. The use of the same partial safety factors has been verified in the case of stainless steel (Afshan and Gardner, 2013), and the above design proposals are currently under consideration for inclusion in the European and North American design standards for stainless steel.

5. APPLICATION OF THE CONTINUOUS STRENGTH METHOD TO COMPOSITE BEAMS SUBJECTED TO HOGGING BENDING

In continuous composite beams, the steel sections will experience compressive loading in the hogging regions and will thus be susceptible to local buckling. The behaviour in such regions will be similar to that described in the previous section this paper. When designing continuous composite beams, the use of a deformation based approach, such as the CSM allows not only a realistic prediction of the ultimate bending capacity under sagging and hogging moments but also an

accurate evaluation of the collapse load. This is attained when a mechanism is formed or the ultimate rotational capacity of the beam at the proximity of one of the internal supports or fixed ends is reached, while the largest sagging moment is lower than the sagging bending resistance.

In general, a procedure similar to that detailed in Section 4 can be followed for calculating hogging bending moment capacity. In this case, the reinforced concrete slab is in tension and much of the steel profile is in compression. Since the contribution of concrete in tension is usually disregarded, concrete tensile strength being negligible Figure (5), the tensile resistance of the slab is largely provided by the steel reinforcement. The deformation capacity of the composite cross-section is controlled by the ductility of steel reinforcement embedded in cracked concrete and the deformation capacity of structural steel. This, according to the CSM, can be obtained from Equation (14), which allows for local buckling.

In typical continuous composite beams, the bending moment demand obtained from elastic analysis is larger at the internal support than at mid-span, while the moment capacity of the composite cross-section is usually lower at the interior supports than in the regions of sagging bending moment. Thus, large deformations under hogging moment giving rise to significant redistribution of bending moment from interior supports to mid-span are usually required to attain plastic collapse and exploit the full capacity of the composite cross-section at mid-span. Previous research (Kemp and Nethercot, 2011) has shown that an accurate evaluation of maximum rotational capacity limited by local buckling in the steel profile is critical for a realistic prediction of the collapse load, while rigid plastic analysis and the moment redistribution method do not always lead to a safe design (Gattesco et al., 2010), even for beams with a Class 1 composite cross-section (Eurocode 4). In this respect, the use of the CSM incorporated into a detailed FE description (Section 3) represents an effective alternative, as it enables an accurate evaluation of the maximum deformation in the component materials and connection device thus obtaining a realistic prediction of the collapse load for a continuous beam. Further research is underway on this topic.

6. CONCLUSIONS

The continuous strength method (CSM) is a deformation based design approach that allows for strain hardening in the design of metallic cross-sections. Although its application has been studied for bare steel, stainless steel and aluminium alloy cross-sections, the use the CSM for steel-concrete composite structural components, which may considerably benefit from strain hardening, has not been extensively investigated. In this study, the CSM is extended to composite beams under sagging bending moment, where the influence of the strain hardening has been found previously to be significant. For the case of full shear connection, explicit analytical expressions which incorporate the influence of strain hardening and two failure criteria (concrete crushing and exceeding of a steel ductility limit) have been derived. The predictions are compared against fifteen collected test results from the literature, suggesting that the CSM offers more accurate and less scattered predictions than current codified approaches. A finite element model, which was validated

against experimental and numerical studies from the literature, has been employed to generate structural performance data for the case of partial shear connection. An indicative interpolation function predicting capacity for varying degrees of shear connection is established by means of the numerical data. Finally, application of the CSM to the composite beams subjected to hogging bending is also discussed. Future work will be directed towards consideration of a wider variety of design scenarios, more comparisons with test data and reliability analyses to establish a consistent design methodology that can be used in the design of steel-concrete composite structures.

REFERENCES

- Abaqus (2010). Version 6.10. Reference Manual, Simulia, Dassault Systemes.
- Ansourian, P., (1982). Plastic Rotation of Composite Beams. *Journal of the Structural Division, ASCE*, 108(3), 643-659.
- Aribert, J. M. (1997) Analyse et formulation pratique de l'influence de la nuance de l'acier du profilé sur le degré minimum de connexion partielle d'une poutre mixte. *Construction Métallique*, 3, 39-55
- Ashraf, M., Gardner, L. and Nethercot, D. A. (2008). Structural stainless steel design: Resistance based on deformation capacity. *Journal of Structural Engineering-ASCE*. 134(3), 402-411.
- Ashraf, M. and Young, B. (2011). Design formulations for non-welded and welded aluminium columns using Continuous Strength Method. *Engineering Structures*. 33(12), 3197-3207.
- Afshan, S. and Gardner, L. (2013). The continuous strength method for structural stainless steel design. *Thin-Walled Structures*. 68, 42-49.
- Chapman, J. and Balakrishnan, S., (1964). Experiments on composite beams. *The Structural Engineer*. 42(11), 369-383.
- Chung, K. F. and Chan, C. (2010). A Numerical investigation into the effect of strain hardening on the structural behaviour of simply supported composite beams. *Proceedings of the 9th Pacific Structural Steel Conference*. 19th-22nd October, 2010, Beijing, China. pp. 988-993.
- EN 1992-1-1 (2004). Eurocode 2: Design of concrete structures - Part 1.1: General rules and rules for buildings. European Committee for Standardization (CEN).
- EN 1993-1-1 (2005). Eurocode 3: Design of steel structures - Part 1.1: General rules and rules for buildings. European Committee for Standardization (CEN).
- EN 1993-1-4. (2006). Eurocode 3: Design of steel structures - Part 1.4: General rules - Supplementary rules for stainless steel. CEN.
- EN 1993-1-5 (2005). Eurocode 3: Design of steel structures – Part 1.5: Plated structural elements. European Committee for Standardization (CEN).
- EN 1994-1-1 (2004). Eurocode 4: Design of composite steel and concrete structures - Part 1.1: General Rules and Rules for Buildings. European Committee for Standardization (CEN).
- EN 1999-1-1 (2007). Eurocode 9: Design of aluminium structures - Part 1.1: General structural rules. European Committee for Standardization (CEN).

- Gardner, L. (2008). The Continuous Strength Method. *Proceedings of the Institution of Civil Engineers - Structures and Buildings*. 161(3), 127-133.
- Gardner, L. and Nethercot, D. A. (2004). Stainless steel structural design: A new approach. *The Structural Engineer*. 82(21), 21-28.
- Gardner, L., Wang, F. and Liew, A. (2011). Influence of strain hardening on the behavior and design of steel structures. *International Journal of Structural Stability and Dynamics*. 11(5), 855-875.
- Gardner, L., Macorini L. and Kucukler M. (2013). The Continuous Strength Method for steel and composite design. *Proceedings of the Institution of Civil Engineers - Structures and Buildings*. 166(8), 434-443.
- Gattesco, N. (1999). Analytical modeling of nonlinear behavior of composite beams with deformable connection. *Journal of Constructional Steel Research*, 52(2), 195-218.
- Gattesco, N., Macorini, L., and Fragiaco, M. (2010). Moment Redistribution in Continuous Steel-Concrete Composite Beams with Compact Cross Section. *Journal of Structural Engineering-ASCE*, 136(2), 193-202.
- Johnson, R. and Molenstra, N. (1991). Partial shear connection in composite beams for buildings. *Proceedings of the Institution of Civil Engineers: Part 2*. 91(1), 679-704.
- Kemp, A. R. and Nethercot D. A. (2001). Required and available rotations in continuous composite beams with semi-rigid connections. *Journal of Constructional Steel Research*, 57(4), 375-400.
- Kucukler, M. (2011). Influence of strain hardening on sagging bending moment resistance of composite beams with full or partial shear connections. MSc. Dissertation, Imperial College London.
- Nie, J., Xiao, Y. and Chen, L. (2004). Experimental studies on shear strength of steel-concrete composite beams. *Journal of Structural Engineering, ASCE*. 130(8), 1206-1213.
- Queiroz, F., Queiroz, G. and Nethercot, D. (2009). Two-dimensional FE model for evaluation of composite beams, I: Formulation and validation. *Journal of Constructional Steel Research*. 65(6), 1055-1062.
- Queiroz, F., Vellasco, P. and Nethercot, D. (2007). Finite element modelling of composite beams with full and partial shear connection. *Journal of Constructional Steel Research*. 63(4), 505-521.
- Salari, M.R., Spacone, E., Shing, P.B., and Frangopol, D.M. (1998). Nonlinear analysis of composite beams with deformable shear connectors. *Journal of Structural Engineering-ASCE*, 124(10), 1148-1158.
- Schafer, B. W. (2008). Review: The direct strength method of cold-formed steel member design. *Journal of Constructional Steel Research*. 64(7-8), 766-778.
- Su, M. N., Young, B. and Gardner, L. (2012). Compression tests of aluminium alloy cross-sections. *Proceedings of the 14th International Symposium on Tubular Structures*. Edited by Gardner, L. 12th-14th September, 2012, London, UK. 501-508.

- Su, M. N., Young, B. and Gardner, L. (2012). Bending tests of aluminium alloy cross-sections. Proceedings of the 14th International Symposium on Tubular Structures. Edited by Gardner, L. 12th-14th September, 2012, London, UK. 509-516.
- Zona, A. and Ranzi, G. (2011). Finite element models for nonlinear analysis of steel-concrete composite beams with partial interaction in combined bending and shear. *Finite Elements in Analysis and Design*. 47(2), 98-118.

Long-Term Deflection of Timber-Concrete Composite Beams in Cyclic Humidity Conditions in Bending

M. Hailu¹; R. Shrestha²; and K. Crews³

¹Center for Built Infrastructure Research, Faculty of Engineering and IT, Univ. of Technology, Sydney, P.O. Box 123, Broadway 2009, NSW, Australia. E-mail: Mulugheta.Hailu@uts.edu.au

²Lecturer, Centre for Built Infrastructure Research, Faculty of Engineering and IT, Univ. of Technology, Sydney, P.O. Box 123, Broadway 2009, NSW, Australia. E-mail: Rijun.Shrestha-1@eng.uts.edu.au

³Professor of Structural Engineering, Centre for Built Infrastructure Research, Faculty of Engineering and IT, Univ. of Technology, Sydney, P.O. Box 123, Broadway 2009, NSW, Australia. E-mail: keith.Crews@uts.edu.au

Abstract

A laboratory investigation to determine the long-term behaviour of Timber-Concrete Composite (TCC) beams was started from August 2010 at the University of Technology, Sydney. The test was conducted on four six-meter-span TCC beams; this paper reports the results to-date for only two beams. The materials used are laminated veneer lumber (LVL) for the joists and 32 MPa concrete for the flanges. From the start of the test (August 2010), the specimens have been under sustained loads of (1.7kPa) whilst the environmental conditions have been cyclically alternated between normal and very humid conditions (typical cycle duration is six to eight weeks) and the temperature remains quasi constant (22 °C). During the test, the mid-span deflection, moisture content of the timber beams and relative humidity of the air are continuously monitored. The investigation is still continuing and this paper reports the results of the experimental investigation for the last two and half years.

1 INTRODUCTION

Timber-concrete composite (TCC) floor system is a construction technique where by the concrete is placed on top of the timber joist and connected with shear connectors such that timber and concrete work as a composite element and are essentially in tension and compression, respectively. The three components of TCC floors; timber, concrete and connection, are characterized by different time dependent behaviour. This behaviour is affected by, the stress level, moisture content, temperature and relative humidity of air. Concrete is characterized by significant creep and shrinkage phenomena, timber by creep, mechano-sorptive and shrinkage/swelling (Ahmadi 1993, Armstrong 1960, 1961 & 1972, Brebbia 1991, Toratti 1993, Bou Said 2004, Ceccotti 2006, Epmeier 2007), and connection by creep and mechano-sorptive effect. Due to complexity of the composite action, a series of experimental tests is desirable in order to investigate the behaviour of the composite structures. There are hardly available literatures on long-term deflection of TCC

beams under cyclic humidity conditions but a few long-term tests performed on TCC structures so far are reported in (Ahmadi 1993, Brebbia 1991, Bou Said 2004, Ceccotti 2006, Fragiaco 2007, Grantham 2004, Hailu 2012, Meierhofer 1993).

Yeoh (2010) tested three 8 meters T-section TCC floor beams with three types of connectors in uncontrolled, unheated indoor environment, classified as service class 3 as per Euro code 5. The test result showed largest creep coefficients for plate connection and least with rectangular notch connection. The long-term deflection for beams with normal concrete was larger than the beams with low shrinkage concrete.

Ceccotti (2006) tested a 6 m span TCC floor system with glue in connection in outdoor unsheltered well ventilated conditions and protected from direct radiation from the sun. The test lasted for five years and it was classified as service class 3 as per Euro code 5. The maximum average deflection monitored throughout the test was 3.36 mm, which was almost four times the instantaneous elastic deflection and is well below the limiting value $L/300$ as per the Euro code 5 (2008).

Bou Said (2004) monitored a composite beam with glue-in mechanical connectors loaded in sheltered outdoor conditions for 2 years. The short term deflection estimated using Euro code 5 was exceeded and it also exceeded the long-term deflection limits.

Grantham et al. (2004) reported results on a full-scale long-term test performed on a timber floor strengthened with SFS screws and lightweight aggregate concrete.

Meierhofer (1998) conducted a long-term bending test on a 4 m span beam with SFS screw connectors under relatively unfavourable conditions: outside under roof, i.e. the specimens were fully exposed to the natural temperature changes and wetting cycles which provide to be a very dominating influence. The creep factor after one year varied between 2 and 4.

Ahmadi (1993) tested a simply supported 3.9 m long TCC slab loaded with a full sustained live load of 2 kN/m^2 for 140 days. The ultimate long-term deflection under this 100 % sustained live load was within acceptable limits set by the building codes AITC and ACI 318-89 and the relative dimensional changes in the timber joists due to variations of humidity and temperature caused cracks in the concrete.

Brebbia et al. (1991) conducted long-term experimental investigation on a 4 m span TCC beam with gang-nail connector type for about two years and the final deflection was about 4 times that of the no-slip theory and about 2.5 times the actual value under short term load.

The present research work aims to obtain detailed experimental result about the long-term deflection of the composite beams subjected to sustained loads for about two and half years. Particular attention is devoted to behaviour of the beams in cyclic humidity conditions.

2 EXPERIMENTAL PROGRAM

Two TCC beams with identical geometry, each with a clear span of 5.8 m, are currently being tested under long-term test in the civil engineering structures laboratory at University of Technology Sydney which was started on 04-August-2010, 200 days after the concrete pour.

2.1 CHARACTERISTICS OF THE COMPOSITE BEAMS

The top slab is made of a normal weight concrete with commercial strength of 32 MPa, the test results for the concrete compressive strength after 28, 56 and 91 days were 39.5, 44.3 and 50.3 MPa, respectively. The mean drying shrinkage was 800 micro strains at 28 days. A standard reinforcing mesh of 7 mm diameter normal strength reinforcement bars at 200 mm spacing was provided in the concrete slab to prevent shrinkage cracks. Figure 1, shows typical cross-section of the beams under investigation.

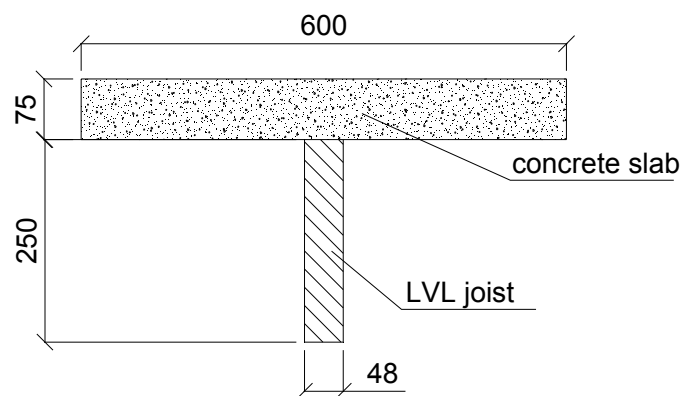


Figure 1. Cross-section of the TCC beam (Typical) (measured in mm).

The joists are made of 250 x 48 mm laminated veneer lumber (LVL). The mean modulus of elasticity and characteristic bending strength of the LVL was 12.3 GPa and 48 MPa, respectively. Two types of shear connector configurations were used in the beams. The first beam, B_6N, had six bird's-mouth notch connections (Figure 2). The second beam, referred to as B_SFS, was constructed with a pair of SFS screws at $\pm 45^\circ$ angles (Figure 2) and with a spacing of 300 mm between pairs of screws. Series of push-out tests were conducted (Khorsandnia et al. 2012) to determine the slip modulus of the connectors and the results are tabulated below in Table 1. Layout of the connectors along the span of each of the tested beams is shown in Figure 3.

Table 1. Type of connector and slip modulus.

Specimen	Type of connector	Slip modulus, K_{sls} , (kN/mm)	Characteristic strength, Q_k , (kN)
B-6N	bird-mouth notch with coach screw	36.9	59.5
B-SFS	SFS screw	54.9	32.6

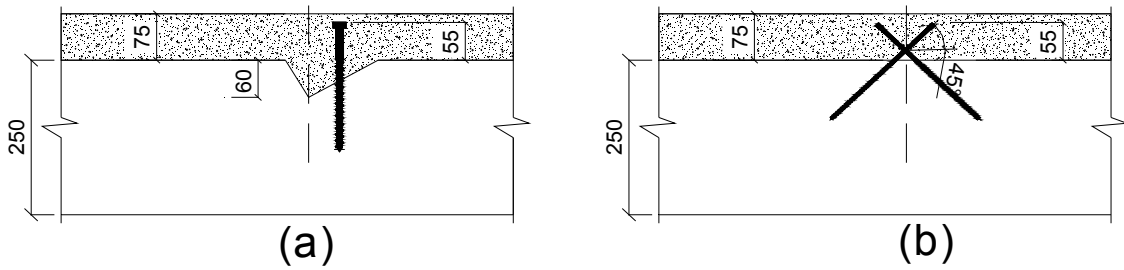


Figure 2. (a) Birds mouth with Ø16 mm coach screw and (b) SFS screw connections.

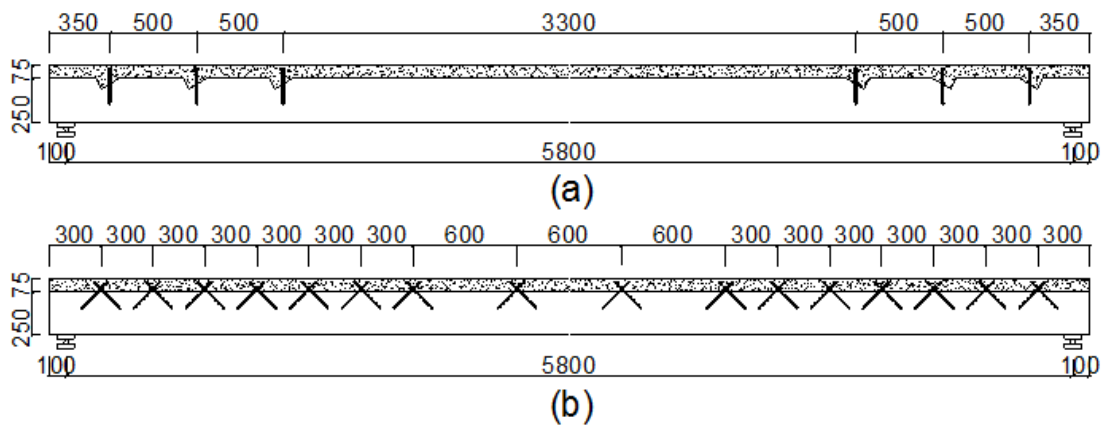


Figure 3. (a) Beam B-6N and (b) Beam B-SFS.

A short term static test was done to determine the bending stiffness of the composite beams before they were subjected to a long-term test conditions. The results are shown in Table 2, where “EI” refers to the tested effective stiffness of the composite beams.

Table 2. TCC beams bending stiffness.

Specimen	Stiffness, (kN/m)	EI (10^{12} Nmm ²)
B_6N	1254	4.34
B_SFS	1323	4.60

2.2 LONG-TERM TEST

2.2.1 TEST SET-UP AND INSTRUMENTATION

Figure 4, shows the long-term test set up. The beams were loaded with equally spaced lead bars (Figure 5) which were arranged such that the bars apply a uniformly distributed load of 1.05kN/m (1.7kPa). The load level is such that no plasticity in any material is expected to occur immediately after the loads have been applied. A ratio of up to 20 % of the failure load including the self-weight is what could be expected to be present on timber concrete composite floors under normal use. The air humidity was artificially accentuated using a humidifier positioned to apply uniform water vapour to the fog-room. The fog-room is made air-tight to avoid loss of humidity during the wet conditions.

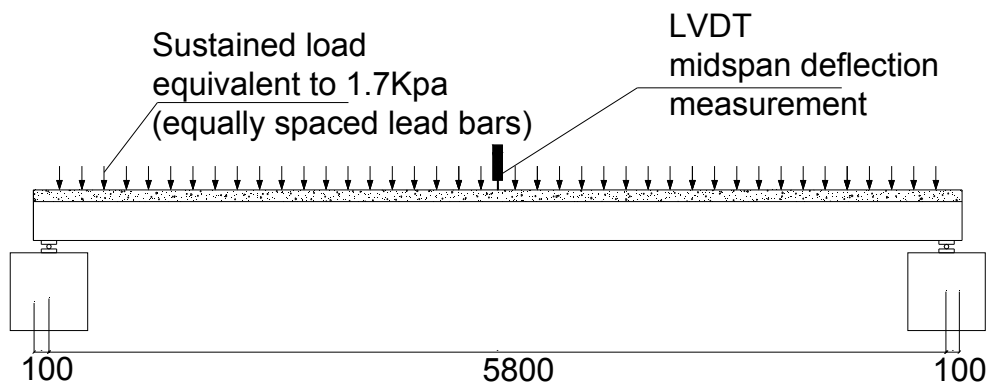


Figure 4. Test set up (measured in mm).

The quantities that have been monitored are mid-span deflection using LVDTs (Linear Voltage Displacement Transducers) with a range ± 25 mm, relative humidity and temperature of the room using climate loggers and moisture content of the timber using small timber blocks placed beneath the TCC beams.



Figure 5. Beams under quasi-permanent loads (lead bars).

The instantaneous elastic mid-span deflections immediately after the application of the loads are shown in Table 3.

Table 3. Instantaneous elastic mid-span deflection.

Specimen	Instantaneous elastic deflection (mm)
B-6N	4.39
B-SFS	4.17

2.2.2 ENVIRONMENTAL CONDITIONS

The relative humidity (RH) and temperature of the room are measured regularly every hour. The changes in RH, moisture content and temperature are shown in Figure 6, for the last two and half years. The test is on-going.

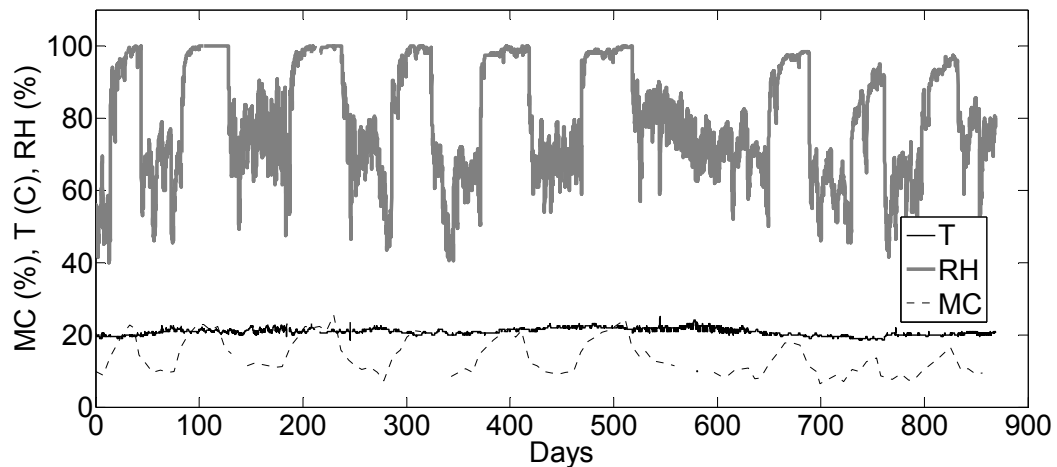


Figure 6. Changes in relative humidity, moisture content and temperature.

This environmental condition, based on Euro code 5, can be assigned to service class 3; it is characterized by moisture content in the material corresponding to a temperature of 20°C and relative humidity of the surrounding air exceeding 85%.

2.2.3 MOISTURE CONTENT

To monitor the variation of moisture content in LVL joists, separate moisture content samples with 100x100x45 mm sizes cut from same batch of LVL were kept beneath the TCC beams and the changes in the level of moisture are measured regularly every week. The test samples for the moisture content are shown in Figure 7.

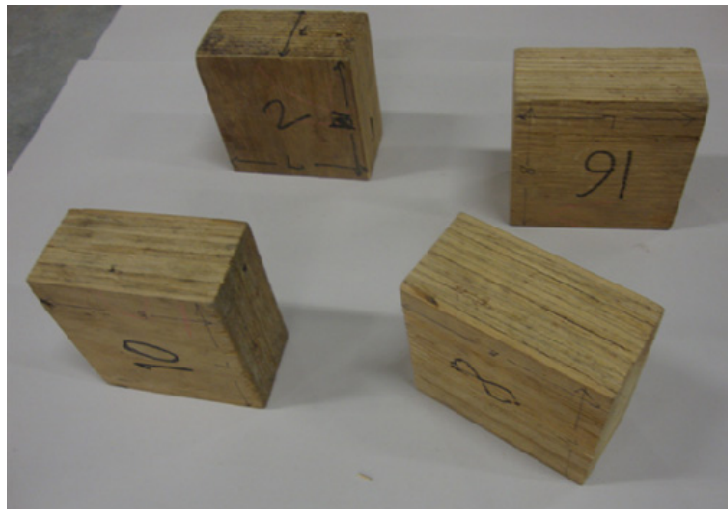


Figure 7. LVL MC Test samples.

The oven-dry method as described in AS/NZ 1080.1:1997 is used in moisture content measurement and the moisture content obtained from the test samples was

around 9 % at the start of the test and increased to above 20 % after the humidifier was operated. It is observed from the result that it takes at least two weeks for the moisture content samples to attain 10 % moisture content increment.

2.2.4 LONG-TERM DEFLECTION

The mid-span deflection was measured every minute during loading of the specimen for the initial 24 hours and every hour for the remaining of the long-term test. Figure 8, shows the mid-span deflection, moisture content versus time of the TCC beams.

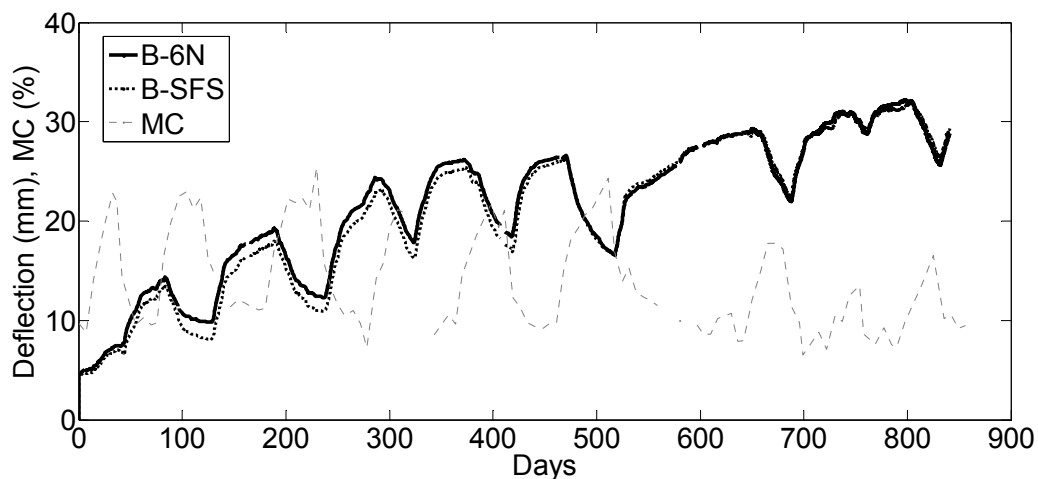


Figure 8. Mid-span deflection, moisture content versus time.

The specimens were loaded when the humidity chamber was at normal room environmental conditions which will be referred as dry state here onwards. Despite the instantaneous elastic deflection due to the applied loads very little additional deflection due to creep occurred. After, approximately one week water vapour was admitted, and the deflection increased in both the beams (Figure 8), this period referred as wet period is the first absorption period in the test, and the beams responded with increase in their deflections. In this wet period the air humidifier was used to increase and maintain the air humidity approximately at 100 %, this was then followed by dry period. The humidity chamber was opened and an air fan was used to increase the ventilation. During this period (desorption) the deflection in both the beams increased sharply with the deflection reaching more than twice their instantaneous deflections. When the humidity chamber kept at this state the rate of deflection increase slows down tending to reach some limiting values.

The beams were then again exposed to the wet period by admitting water vapour to the chamber, the deflection in the beams suddenly changes direction and started to recover and the recovery continues as the air humidity was maintained at high RH levels. This procedure was repeated every four to six week except in some instances the duration may be longer due to instrument malfunction or other reasons.

The length of the humidity cycle is four to six weeks and is monitored using the moisture content measurements on the moisture content samples

The results of the long-term investigation indicates that the long-term deflection of the TCC beams is accelerated due to the variation in air humidity in the humidity chamber and most of the change in deflection occurs within period during which moisture content cycle changes, and is more pronounced during a period when the humidity changes from wet to dry (Figure 9). The moisture content of the beams under load, cycled from dry to wet and back to dry again; the deformation also followed a cyclic pattern i.e. the beam deflections fluctuated in response to the cyclic air humidity of the chamber. However the recovery in each cycle is only partial and the total amount of creep is very large as shown in Figure 9. It should be noted that creep increased during drying and decreased during the wetting cycle with the exception of the initial wetting when creep increased.

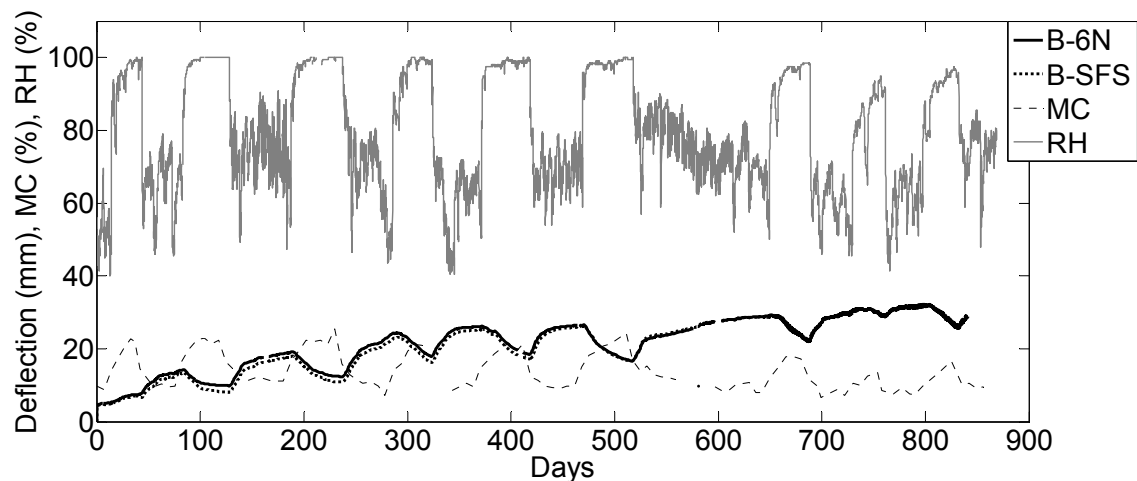


Figure 9. A comprehensive plot of deflection, RH% and MC %.

Three distinct behaviours were observed in the long-term test of these beams;

- increase in RH & MC followed by an increase in deflection in the first one week (first adsorption)
- decrease in RH and MC followed by an increase in deflection in all dry periods (desorption)
- increase in RH and MC followed by decrease in deflection (local recovery) in all wet periods (adsorptions)

The significant MC variation may have contributed to the high creep and deflection. The findings from this test show that it is not just the level of the moisture content that affects creep deflections. The rate of change, number and length of the cycles have a pronounced effect on the deflections, with rapid changes in moisture content (air humidity) producing more severe creep under bending loads also reported in Yeoh (2013). The rapid response to the change in MC is pronounced when the humid cycle changes from wet to dry, during this transition the moisture leaves the surfaces at a faster rate than from the middle cross section of the LVL, causing a faster

reaction from the beams. During the dry period the deflection increased faster initially and then followed by a very slow rate when the environment is maintained in the dry conditions and showing tendency to flatten at some point. However, this is not the case when the humidity changes from dry to wet.

The following observation has been reported by several researchers (Capretti & Cecotti, 1996, Kenel & Meierhofe 1998, Lukaswezkas, 2009 and Yeoh 2009); When TCC beam is exposed to naturally varying environmental conditions in bending, an increase in the ambient relative humidity of the air causes an increase in timber moisture content, which promotes elongation of the timber beam, but this is prevented by the concrete slab. The overall effect is, therefore, a downward deflection, and self-equilibrated stress distribution over the composite cross-section. However, it needs to be emphasised that in semi-controlled environmental conditions characterized by moisture cycling; except the first cycle in all other cycles, increase in air humidity causes an increase in timber moisture content, which causes recovery of deflection while in the contrary a decrease in air humidity causes loss of moisture from the timber, which causes a rapid increase in the deflection of the TCC beams. Although there are hardly available literatures on the long-term experimental investigations on TCC beams subjected to cyclic humidity conditions in bending, this behaviour has been reported as typical creep behaviour of wood in bending (Armstrong 1960, Gibson 1996, Hearmon 1964, and Toratti 1993). Toratti (1993) explained the oscillation of the creep curves (the alternate increase of deflection and recovery of deflection) is the shrinkage strain of wood, since the shrinkage is of much higher in magnitude perpendicular to the cell wall, this would result in higher shrinkage values when wood is compressed and less when tensioned as compared to unstressed state. Based on this explanation it can be argued that the effect of drying shrinkage of concrete is not significant enough to reverse the situation.

The creep mechanism is worst for long span structural composite beams where the stiffness of the floors is much more dependent on the composite action between the concrete and the timber joists. It was confirmed by several authors that the long-term behaviour of TCC is significantly influenced by the variation of the MC, concrete creep and the various interaction of shrinkage and creep, shrinkage and swelling of the LVL, and creep of the connection system, contributes a significant additional deflection in TCC floor structures.

Both the beams (B-6N and B-SFS) have attained most of the deflection with in one and half years, as was also found out by several researches that most of the deflection developed during the first one and half to two years, after which the deflection tends to either plateaus or to increase much more slowly (Cecotti et al. 2006, Yeoh 2013). However, the deflection from these beams is showing a distinct increase throughout the period, with minimal reduction in the rate of deflection increase to the end of this reporting period. Similar finding was also reported in Kenel et al. (1998).

The changes in temperature also are found to significantly affect the long-term deflection of the TCC beams. Generally a reduction in temperature causes a shortening of both the concrete slab and, to a lesser extent, the timber beam. The overall effect is then a downwards deflection (Lukaswezka 2009). Yeoh (2013) also reported a low temperature and high RH, increased the MC of the LVL and

consequently caused the deflection to increase whilst higher temperatures and low MC, reduced the deflection. In this investigation the temperature of the humidity chamber remained quasi-constant (20 ± 2 °C) with little or no variation in temperature throughout the test period. Hence, the influence of the temperature is either none or negligible to be observed in this test.

CONCLUSIONS

This paper reports the results of an experimental test performed on two 5.8 m clear span TCC beams with two different type of connection. The beams were under a sustained load in sheltered indoor conditions and subjected to cyclic humidity condition. The most important quantities such as mid-span deflection, moisture content, relative humidity and temperature of the environment were continuously monitored through-out the test.

The conclusions made are (i) the relative humidity monitored during the long-term test varied from 45 % to 100 % while the timber moisture content fluctuated in the range of 7 % to 20 % and temperature remained quasi constant (21 °C ± 1), (ii) cycling the humidity has accelerated the creep response of the beams and induced very high deflection about seven times their initial deflection, (iii) the mid-span deflection markedly augmented with in two years of the long-term test, with a final value well above the limits usually adopted by national regulations.

ACKNOWLEDGEMENT

This experimental research work has been carried out by means of the financial supports of Structural Timber Innovation Company (STIC). Which is gratefully acknowledged.

REFERENCES

- Ahmadi, B. H. and Saka, M. P. (1993). 'Behaviour of composite TCC floor' *Journal of Structural Engineering*, vol. 119, no. 11, pp. 3111-30
- Armstrong, L. D. and Kingston, R. S. T. (1960). 'Effect of moisture changes on creep in wood' *Nature*, 185 (4716), 862-863.
- Armstrong, L. D. and Christensen, G. N. (1961). 'Influence of moisture changes on deformation of wood under stress' *Nature*, 191 (4791), 869-870.
- Armstrong, L. D. and Grossman, P. U. A. (1972). 'The behaviour of Particle board and hard board beams during Moisture cycling', *Wood Science and Technology*, vol. 6, p. 9.
- Brebbia, C. A., Dominguez, J., Escrig, F. (1991). 'Structural Repair and Maintenance of Historical Buildings II' Vol.1 General Studies, Materials and Analysis, Proceedings of the Second International Conference, held in Seville, Spain, 14-16 May.
- Bou Said, E., Jullien, J. F. and Ceccotti, A. (2004). 'Long term modelling of timber-concrete composite structures in variable climates', paper presented to the 8th WCTE, Lahti, Finland, June 2004.

- Ceccotti, A., Fragiaco, M. and Giordano, S. (2006). 'Long-term and collapse tests on a timber concrete composite beam with glued in connection', *Materials and Structures*, 2006, p. 10.
- Epmeier, H., Johansson, M., Kliger, R. and Westin, M. (2007). "Bending creep performance of modified timber, Holz Roh- Werkst.
- Frangiaco, M. (2006). 'Long-term behaviour of timber-concrete composite beams. I: finite element modelling and validation', *Struc Eng*, vol. 132(1), pp. 13-22.
- Frangiaco, M., Amadio, C. and Macorini L. (2007). 'Short- and Long-term performance of the "Tecnaria" stud connector for timber-concrete composite beams', *Materials and Structures RILEM* 40(10), vol. 40, no. 10, p. 13.
- Frangiaco, M. and Ceccotti, A. (2004). 'A simplified Approach for Long-Term Evaluation of Timber-Concrete Composite Beams', 8th WCTE, vol. 2, Lahti, Finland, pp. 537-42.
- Gibson, E. J. (1965). 'Creep of wood: Role of water and effect of a changing moisture content', *Nature*, no. 4980.
- Gowda, C., Kortessmaa, M., Ranta-Maunus, A. (1996). 'Long term creep tests on timber beams in heated and non-heated environment', Espoo, vol. VTT Publications 278, p. 35.
- Grantham, R., Fragiaco, M., Nogarol, C., Zidaric, I. and Amadio, C. (2004). 'Potential upgrade of timber frame buildings in the UK using timber-concrete composites', In 8th World Conference on Timber Engineering WCTE, 2: 59-64.
- Hailu, M., Gerber, C., Shrestha, R., Crews, K. (2012). 'Long-term behaviour of Timber-Concrete-Composite beams', in '12th WCTE', Proceedings of the World Conference on Timber Engineering, New Zealand, Auckland.
- Hearmon, R. P., J. (1964). 'Moisture content changes and creep of wood', *Forest products*, p. 2.
- Kenel, A. & Meierhofer, U. (1998). Long-term performance of timber-concrete composite structural elements, Report.No. 115/39, EMPA, Dübendorf, Switzerland, in German.
- Khorsandnia, N., Hamid, R., Crews, K. (2012). 'Experimental and analytical investigation of short-term behaviour of LVL-concrete composite connections and beams', *Journal of Construction and Building Materials*, 37(2012) 229-238.
- Lukaszewska, E., Fragiaco, M. & Johansson, H. (2010). 'Laboratory Tests and Numerical Analyses of Prefabricated Timber-Concrete Composite Floors', *Journal of Structural Engineering*, vol. 136, no. 1, pp. 46-55.
- Meierhofer, A. U. (1993). 'Tests on Timber Concrete Composite structural elements 'International council for building research studies and documentation, working commission W18 – Timber Structures, CIB-W18/ 2-7-5.
- Toratti, T. (1993). 'Long term deflection of timber beams', *Rakenteiden Mekaniikka*, vol. 26 No 3 1993, pp. 19-28.
- Yeoh, D. F., and Deam, B. (2010). 'Long-term behaviour of LVL-concrete composite connection and beams under sustained loads', unpublished, University of Canterbury.

CoSFB—Composite Slim-Floor Beam: Experimental Test Campaign and Evaluation

Oliver Hechler¹; Matthias Braun¹; Renata Obiala¹;
Ulrike Kuhlmann²; Florian Eggert²; and Gunter Hauf²

¹ArcelorMittal Commercial Sections S.A. and Research and Development, rue de Luxembourg 66, L-4221 Esch-sur-Alzette, Luxembourg. E-mail: Sections.Tecom@arcelormittal.com

²Institute of Structural Design, Univ. of Stuttgart, Pfaffenwaldring 7, D-70569 Stuttgart, Germany. E-mail: sekretariat@ke.uni-stuttgart.de

Abstract

The composite slim-floor beam (CoSFB) solution is based on the development of an innovative composite connection. This connection is achieved by arranging reinforcement bars through the web of the slim-floor beam, hardly adding to complexity in fabrication or costs. By this technology, an economic and efficient method to activate the full effective width of the concrete chord (EN1994-1-2) for slim-floor beams has been innovated. In order to structurally assess the system, push-out tests, shear beam and long beam tests with focus on structural, vibration and deformation behavior of the CoSFB have been performed. Their evaluations show an increase of the load bearing capacity by 100% and of the stiffness by 150%, compared to non-composite slim-floor beams. The shear connection provided sufficient resistance with a ductile load-deformation behavior. This paper presents the experimental results, their evaluation, and their comparison to existing design approaches of reinforcement bars as shear connectors.

INTRODUCTION

A stylistic device of modern architecture is the combination of transparent structural envelopes with column free ground floor design. Next to the implicit flexibility of these objects for sustainable conversion of use, the possibility to easily upgrade the services for multifunctional living is advised. Slim-floor construction combines the advantages of prefabricated slab elements with steel-framed construction and lead to economic building solutions fulfilling the above specified demands [Hechler and Braun 2010]. Slim-floor construction is characterized by the integration of a steel beam into the slab, see Figure 1. The steel section consists of a hot rolled beam with a supporting plate welded below the lower flange. To facilitate the erection, the width of this plate is larger than the flange of the hot rolled section, so that slab elements are easily placed on it. The slim-floor beam (SFB) can be combined with any kind of slab system. Fully or partially prefabricated concrete slab elements perfectly suit with the SFB; a safe and quick erection is assured.

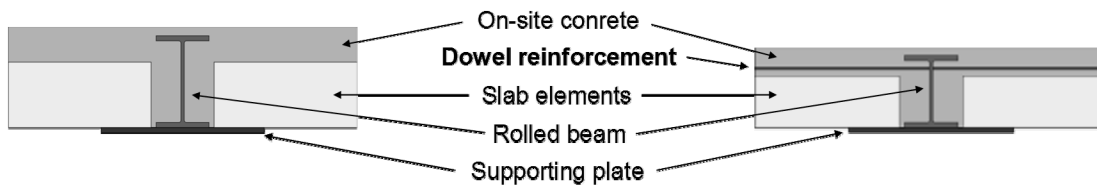


Fig. 1 - Standard slim-floor beam (SFB)

Fig. 2 - Typical CoSFB-section

Slim-floor construction enables low construction height of the floors; consequently either the total height of the building is decreased for fixed quantity of floors (leading to e.g. less façade area) or the total quantity of floors may be increased for a fixed building height (interesting for cities with limited height for buildings). The technical installations (e.g. heating and cooling devices) are installed easily and flexible due to the absence of down standing beams. Therefore structural and service design are independent processes in the designing phase. However, because of the low beam height, the design of an SFB is generally governed by the stiffness of the system and thus, spans are limited to approximately 7m, see Figure 15.

Therefore the goal has been formulated to enlarge the span range of slim-floor systems without an increase in construction height and satisfying all requirements on the slim-floor system and beams imposed by the ultimate and serviceability limit states, including vibration comfort. This technical challenging objective has been accomplished by Braun and Hechler [Braun et al. 2009] with realizing a composite action between steel beam and in-situ concrete due to an innovative shear connection, therefore activating the concrete slab as compression chord in longitudinal direction with its effective width. The resulting economic and sustainable structural solution offers the possibility to realize slim-floor beam spans up to 14m with an assumed slim-floor beam distance of 10m and a construction height of only 40cm. The major advantage however is the integrated fire resistance met without any additional measures up to the European fire resistance rating R90 (R120) [“R90”: maintaining the load bearing function during 90min of European standard fire exposure]. This has been documented with the help of numerical analyses.

The technical challenge of this innovation is to be seen in the shear connection, realized in this configuration for the first time. It is based on the composite dowel concept and consists of a drilled hole through the web of the rolled beam and a reinforcement bar guided through this hole to allow for shear transmission and prevention of cracking of the concrete in shear planes, see Figure 2 and Figure 3.



Fig. 3 - Bar through web of section

The use of concrete dowels has been motivated by the design of apertures plates with holes and related work on their bearing capacity ([Leonhardt et al.1987],

[Wurzer 1997], [Zapfe 2001]). However major differences to existing design are to be found in the geometrical boundaries of the composite dowel in the CoSFB application. As the dowel is confined between the steel flanges of the rolled profiles, only local failure mechanism are supposed to occur. Though, it is unknown whether the flanges allow for load distribution and transfer from concrete into the steel profile. Further block failure of the dowel must be avoided. Experience for this particular case has been drafted from the design of filler beam bridges which do work with similar geometrical boundaries in composite action, although the design of this action is based on empirical knowledge.

Consequently it has been decided to further investigate in

- the global behaviour of the composite slim-floor beam with special focus on the shear force capacity, effective width of the concrete chord, the deflection and vibration behavior by 2 shear beam tests and 2 long-span beam tests and
- the shear connection characteristics of the concrete dowels in the composite slim-floor beams by 27 Push-Out Tests.

This research campaign is presented in this contribution.

EXPERIMENTAL INVESTIGATIONS IN THE GLOBAL BEHAVIOUR OF COMPOSITE SLIM-FLOOR BEAMS (BEAM TESTS)

To investigate in the global behaviour of the composite slim-floor beam two shear beam tests and two beam tests were performed [Kuhlmann et al. 2009], see also Table 1. Focus has been to analyze the shear force capacity, activated effective width of the concrete chord, the deflection and vibration behaviour as well as the overall structural behavior of composite slim-floor beams.

Table 1 – Overview of beam test programme and test results

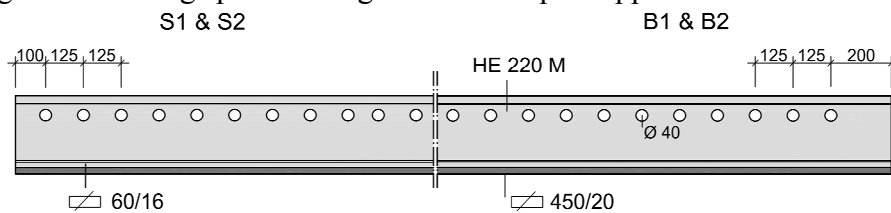
Typ	Geometry L x B [m]	Type	β [%]	Aim	P_j [kN]
S1	4.0 x 2.5 m	Single span girder	100	Shear force capacity, structural behaviour (bearing capacity, effective width of concrete chord)	1881.8
S2			50		1688.5
B1	8.0 x 2.5 m	Single span girder	100	Structural behaviour (bearing capacity, effective width of concrete chord), deflection behaviour, vibration analysis	944.8
B2			100		953.3

The short-span shear beam tests (S1, S2) have been designed to check the transferability of test results from push-out tests to beam behavior. One short-span test was designed with $\beta = 100\%$ shear connection (S1); the second (S2) was designed with $\beta = 50\%$ shear connection, once to produce possible shear connection or shear block failure and secondly, to later have the possibility to conclude on the behavior of the CoSFB system with partial shear connection in case the concrete dowel provides sufficient ductility. Each shear beam spans 4m from hinged support to hinged support. Both were 4-point-bending tests (see Figure 4 and Figure 5).



Fig. 4 – Bending (left photo) and shear (right photo) beam tests at Stuttgart

Shear beam S1, with a full shear connection, had concrete dowels at each 125mm. Shear beam S2, with a partial shear connection, had the same distance of concrete dowels, however half of the dowels have been closed by silicone to prevent their action (see Figure 5). To investigate in the overall structural behavior (load bearing and deformation behavior) two long span girders (B1, B2) were tested in a 4-point bending test. The long span bending tests are simple supported beams with 8m span.



For shear beam S2 half of the holes were filled with silicone.

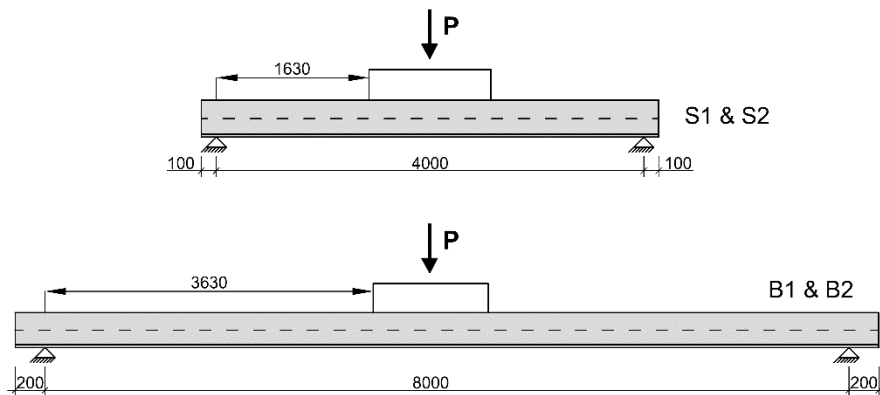


Fig. 5 – Beam test specimens [mm]: S1 & S2 l = 4200mm, span 4000mm; B1 & B2 l = 8400mm, span 8000mm

As the effective width of the concrete chord plays an important role for the bearing capacity of the composite section, the concrete slab width of the test girders was selected as 2.50m. Figure 6 shows the section of the investigated slim-floor girder. The tests were executed deflection controlled. During testing, the jacking force, deflections at $\frac{1}{4}$ span length and mid-span as well as the slip in these location and the supports by deflection measurement devices, the strains in the reinforcement bars of the concrete dowels as well as the stirrups by strain gauges and the strains in

the concrete over the width of the concrete chord by strain transducers had continuously recorded during testing.

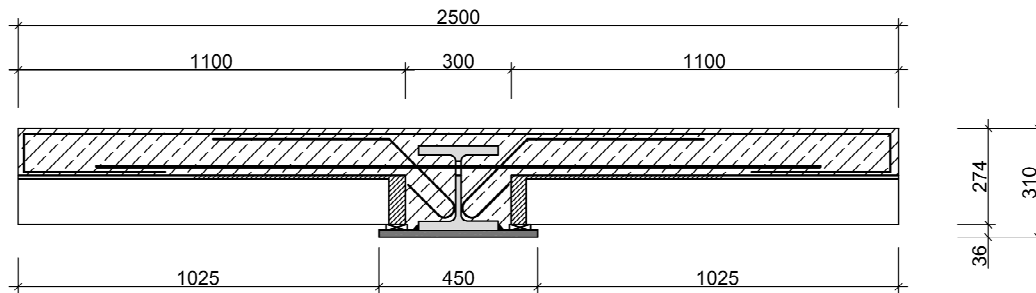


Fig. 6 – Beam test section: S1 & S2, B1 & B2

TEST RESULTS AND EVALUATION FOR THE GLOBAL BEHAVIOUR OF COMPOSITE SLIM-FLOOR BEAMS – LONG-SPAN BEAM TESTS

Both girder beam tests B1 & B2 showed a very ductile behavior and a large deformation behavior at ultimate limit state (Figure 7). Test girder B1 attained a maximum load of 944.8kN and test girder B2 a maximum load of 953.3kN. Both test girders failed due to a bending failure in the concrete compression zone. Near the load pads (bearing of the load distribution girder) the concrete constricted, concrete blocks started to spall mechanically. A comparison of the calculative bearing capacity and the experimental capacity clearly shows a full composite action between the steel girder section and the concrete chord.

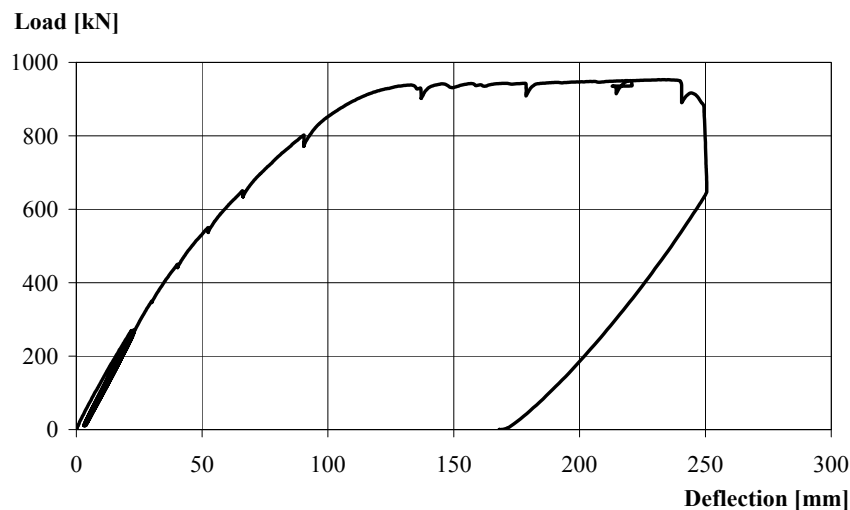


Fig. 7 – Load-deflection curve - test girder B2

Based on the strain distribution, determined from the results of strain transducer on the concrete chord at mid-span, the effective width of the concrete chord at mid-span was recalculated. According to DIN EN 1994 the effective width is calculated to 1.0m; the test results however clearly show a full activation of the concrete chord over the whole slab width, see Figure 8.

The evaluation of the strain records for the transverse reinforcement shows, that all reinforcement bars of the concrete dowels have exceeded the yielding point before ultimate failure of the girder test specimens. At a load of 75% of the ultimate load the reinforcement of the concrete dowel reached the yielding strength. Therefore composite action has been achieved by the concrete dowels and they provide a high and ductile capacity of the shear joint. Due to the longitudinal shear force in the concrete, the stirrups were activated but without exceeding the yielding strength. Therefore it is recommended to foresee stirrups in final design to prevent block failure of the composite joint.

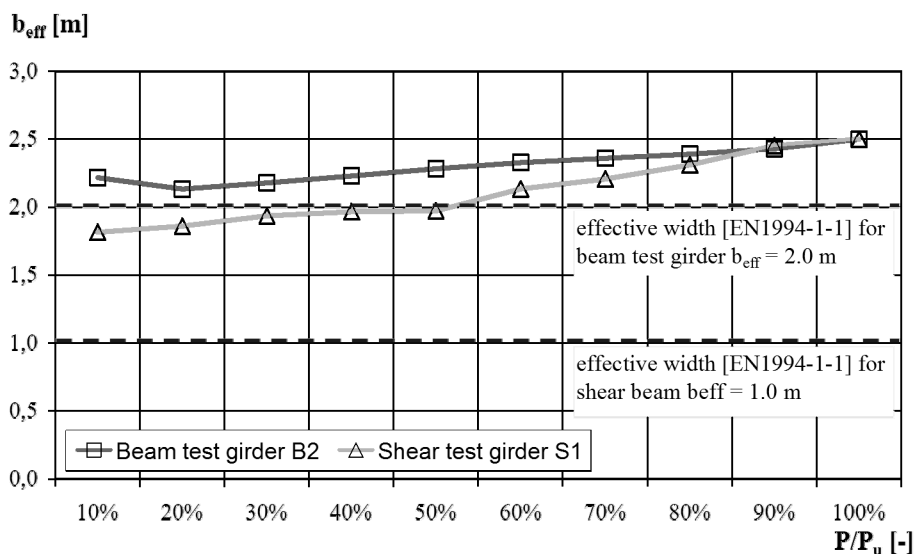


Fig. 8 – Effective width at mid-span (calculated from compressive concrete stresses)

EVALUATION FOR THE GLOBAL BEHAVIOUR OF COMPOSITE SLIM-FLOOR BEAMS – VIBRATION TESTS

To check the stiffness at serviceability limit state level, the natural frequency of one long-span beam was measured. Two measurement campaigns were carried out. The first was executed for the un-cracked, unloaded, composite section, before the start of ULS testing. The second was performed for the cracked composite section. For these measurements ULS testing has been stopped at the load level corresponding to a deflection of $L/300$ and unloaded for the measurements. The measured natural frequencies for the 2 conditions are given in Table 2. The derived stiffness confirmed for full activation of the effective width and full shear connection.

Table 2 - Measured natural frequencies (nf)

Condition	1 st nf [Hz]	2 nd nf [Hz]
Un-cracked	8.84	30.62
Cracked after preloading	8.69	30.13

TEST RESULTS AND EVALUATION FOR THE GLOBAL BEHAVIOUR OF COMPOSITE SLIM-FLOOR BEAMS – SHEAR BEAM TESTS

The shear test girder S1 with a span of 4.0 m reached a maximum load of 1881.8kN (corresponds to ultimate bending moment of 1529kNm). The girder deflection at the ultimate state limit was 142mm at mid-span, for the serviceability (50% of the ultimate load) 16mm. The load-deflection curve is given in Figure 9.

Despite the length of the shear force charge (1.63m), the girder failed due to bending with failure of the concrete compressive strength (Figure 9). As for the long-span beam tests, first, concrete blocks spalled near the load bearing pad and increased in transverse girder direction. Further slant cracks were monitored on the top side of the concrete plate in direction towards the girder supports, a typical shear crack behavior.

For shear beam test S2, with 50% shear connection, the maximum load capacity was 1688.5kN (corr. bending moment of 1371kNm) with a mid-span deflection of 152.3mm. The deflection at serviceability (50% of the ultimate limit state) was about 15.4mm, see Figure 10. The minor difference regarding the maximum jack force and the maximum moment respectively indicates that the composite joint of the partial connected shear beam did not fail. Also shear beam test S2 failed due to failure of the concrete compr. strength in mid-span. It has to be remarked, that additional load components as friction and clamping effects may result in an increase in resistance of the concrete dowels in the beam tests.

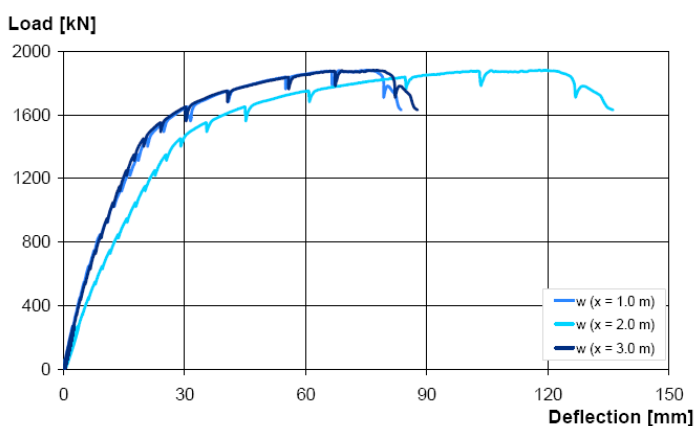


Fig. 9 – Load-deflection curve shear-beam test S1 (full shear connection)

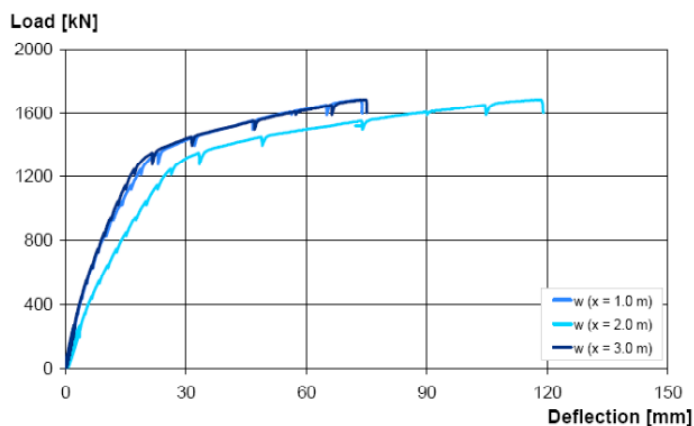


Fig. 10 – Load-deflection curve of shear beam S2 (partial shear connection)

EXPERIMENTAL INVESTIGATIONS OF SHEAR CONNECTION (PUSH-OUT TESTS)

To investigate in the shear connection characteristics and capacity of the concrete dowels in the composite slim-floor beams a total of 6 push-out tests in 2009 [Kuhlmann et al. 2010] and 21 push-out tests in 2011 [Kuhlmann et al. 2012] were planned and performed. In this test campaign the following parameters have been varied to check their influence on the shear connection, see also Table 3:

- concrete compression strength (cylindric concrete compression strength f_{ck} and corresponding tensile concrete strength f_{ctm} ,
- the web thickness of the steel beam section t_{web} ,
- the diameter of the hole in the slim-floor beams' web \varnothing_d ,
- the diameter of the reinforcement bar through the web hole \varnothing_r .

The concrete class has been varied from C20/25 to C50/60, to cover the common application range in building construction. The cross section of the test specimens are shown in Figure 11. For the reference tests the steel section was based on a HE220M (S355M) profile with the addition of a welded bottom flange 450x20mm ($t_{web} = 15.5\text{mm}$). For the tests on the thinner web thickness (2-1a and 2-1b) the steel section HE240A (S355M) has been chosen ($t_{web} = 7.5\text{mm}$). The concrete dowels were based on drilled holes with a diameter of $\varnothing_d = 40\text{mm}$ at 125mm distance each but has been changed to a diameter of $\varnothing_d = 25\text{mm}$ for test series 2-2a. In test series 2-3 the web holes were filled with silicone to exclude concrete in this location around the penetrating reinforcement bar. Through each dowel a reinforcement bar with diameter $\varnothing_r = 12\text{mm}$ was placed. To check the influence of the bar diameter it has been changed to $\varnothing_r = 25\text{mm}$ for series 2-2b.

The slab thickness was in total 27.4cm supported by cams of 16mm for the beam tests, thus the concrete topping over the beam was 50mm. In test P1 stirrups were inserted at the edges to connect the chamber concrete with the in-situ concrete of the deck layer (the series P1 has shown, that these stirrups are not required and therefore they have been omitted for the subsequent series). The slab consisted of a COFRADAL200[®] deck [Arval] with a height of 14cm as lost formwork and second phases a concrete chord of 13.4cm.

Each half of the push-out tests has 5 holes (dowels) positioned in the steel web (see Figure 11). Hence, each push-out test had 10 concrete dowels in sum (see Figure 12).

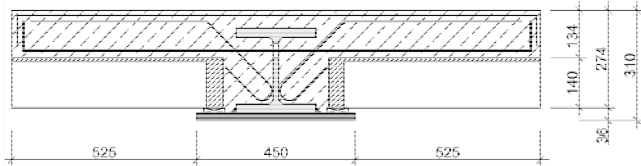
The tests have been performed deflection controlled. Regularly the loading has been stopped and kept constant for approximately 5min to cover the influence of the short-term relaxation. During testing, the jacking force P_j , slip and inclination by deflection measurement devices and strains at the reinforcement bar at selected locations have continuously been recorded.

Table 3 – Overview of push-out test programme and test results

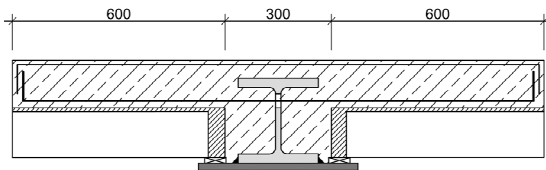
	Series	No. of tests	Beam Section	t_{web} [mm]	\varnothing_d [mm]	\varnothing_r [mm]	f_{ck} [N/mm ²]	f_{ctm} [N/mm ²]	P_j [kN]	$0.92P_j$ [kN]
2009	P1	3	HE220M	15.5	40	12	34.0	2.2	2167	1994
	P2	3	HE220M	15.5	40	12	39.4	-	2282	2099
2011	1a	3	HE220M	15.5	40	12	26.7	4.1	1963	1806
	1b	3	HE220M	15.5	40	12	55.1	5.1	1654	1522
	2-1a	3	HE240A	7.5	40	12	29.5	4.0	1728	1590
	2-1b	3	HE240A	7.5	40	12	58.2	5.3	1591	1464
	2-2a	3	HE220M	15.5	25	12	32.7	4.4	2029	1867
	2-2b	3	HE220M	15.5	40	25	40.0	4.7	3978	3659
	2-3	3	HE220M	15.5	40*	12	38.3	4.7	1416*	1303*

* web holes filled with silicone

Push-out section: P1:



Push-out section: P2, 1a to 2-3:



Steel girder for push-out tests:

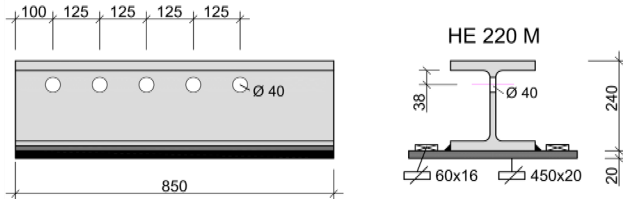


Fig. 11 – Push-out test specimens (2-1a & 2-1b with HE240 A) [mm]



Fig. 12 – Push-out test at Stuttgart

RESULTS AND EVALUATION FOR THE SHEAR CONNECTION (PUSH-OUT TESTS)

All push-out tests showed a ductile behaviour and reached a slip deformation in the shear joint $>6\text{mm}$, as required for ductile composite action acc. to [DIN EN 1994].

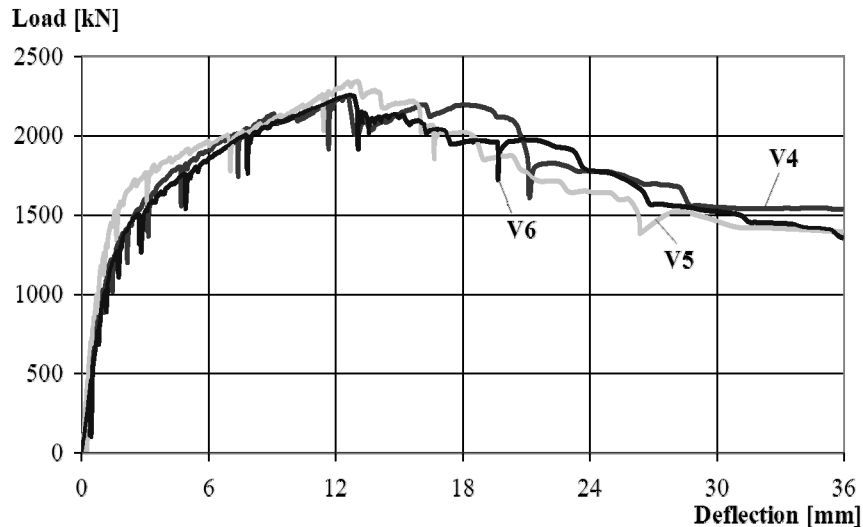


Fig. 13 – Static load-deflection curves of P2 (test V4-V6)

All test with a reinforcement diameter of $\varnothing_r = 12\text{mm}$ failed due to failure of the concrete dowel reinforcement without any shear block failure. The test with diameter $\varnothing_r = 25\text{mm}$ failed due to cracking of the specimens footing before failure of the shear connection. In Table 3 the shear connection capacity is given for short term loading (P_j) as well as after short term relaxation ($0.92 P_j$). The influence of the short term relaxation has been estimated to approximately 6-10%. A typical load-deflection diagram for the concrete dowels in the CoSFB configuration is given in Figure 13 showing a high initial stiffness and a ductile behavior with maximum bearing capacity at high deflection values.

Due to the tests the following results were identified experimentally; the relations have been derived for the shear capacity including the short-term relaxation:

- The shear stud capacity is hardly influenced by the concrete strength up to approximately $f_{ck} = 45\text{N/mm}^2$ (max. -12% for selected tests). For higher strength concrete with $f_{ck} > 45\text{N/mm}^2$ a drop in shear capacity has to be noted (approx. -25%);
- This dependency for high strength concrete is recognized as well for smaller web thicknesses (HE240A) and therefore depends on the concrete strength only independently from the steel girder web thickness;
- The influence of the web thickness appears in general only in a small range - with a reduction of the web thickness about 50%, the bearing capacity reduces only about 12% for low strength and just 4% for higher strength concrete;

- The tests with a smaller web hole diameter \varnothing_d have shown a lower shear capacity, however with -9% to an insignificant level;
- The influence of the reinforcement bar (diameter) seems to be decisive in design for the bearing capacity. The doubling of the diameter (which means a quadruplicating of the cross-sectional-area) results in a significant increase in bearing capacity; the final resistance could not be determined due to failure of the test specimens' concrete footing;
- The infill of concrete in the web hole around the reinforcement bar has a great influence on the bearing capacity of the concrete dowel shear connection. If the concrete filling in the hole is prevented, the maximum load is reduced by a third with highly increased slip at ultimate bearing capacity level.

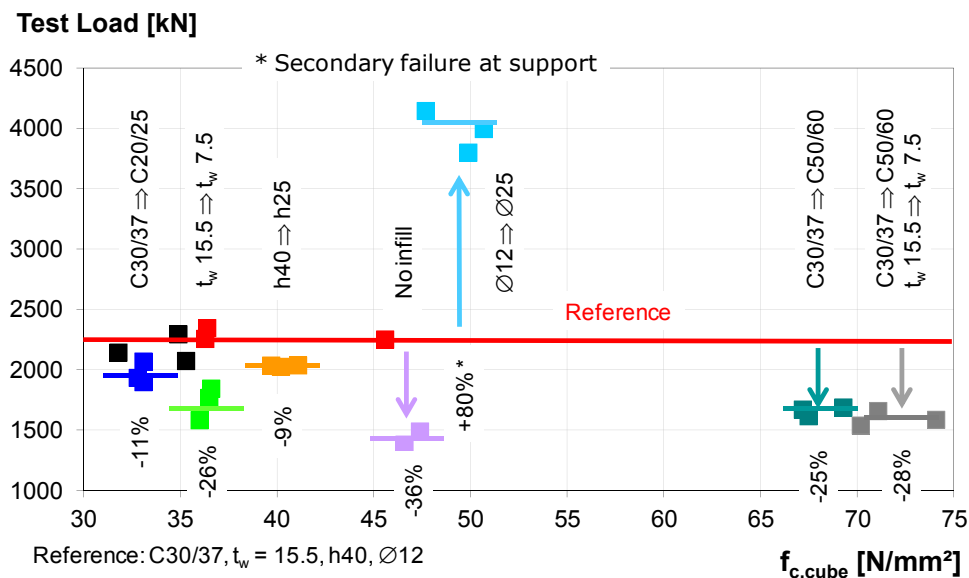


Fig. 14 – Influence of tested parameters on the bearing capacity

The shear connection capacity over the concrete strength for all test series is summarized in Figure 14 and the relation of the each bearing capacity to the reference series is given.

The tests clearly showed the high performance and bearing capacity of the reinforcement bar as shear connector through the steel girder web (concrete dowel). Hereby the capacity mainly depends on the reinforcement bar. A large ductility, far larger than the 6mm criteria imposed by the Eurocode, is also to be noted. Shear block failure has not been observed.

COMPARISON OF PUSH-OUT TEST RESULTS TO EXISTING DESIGN APPROACHES

In the frame of the test results analyses the experimentally derived shear capacities P_{exp} have been compared to various design approaches in literature. The shearing criterion by Zapfe [Zapfe 2001] for concrete dowels deeply embedded in concrete seems hereby the best fitting one. Therefore the experimentally determined load capacities P_{exp} have been compared to calculated capacities P_{th} by [Zapfe 2001]. For this comparison, the characteristic concrete tension strength f_{ctk} and the Youngs' modulus of the concrete E_{cm} have been calculated according to the Eurocode from the measured f_{ck} . For the reinforcement E_s has been assumed to be 210000 N/mm².

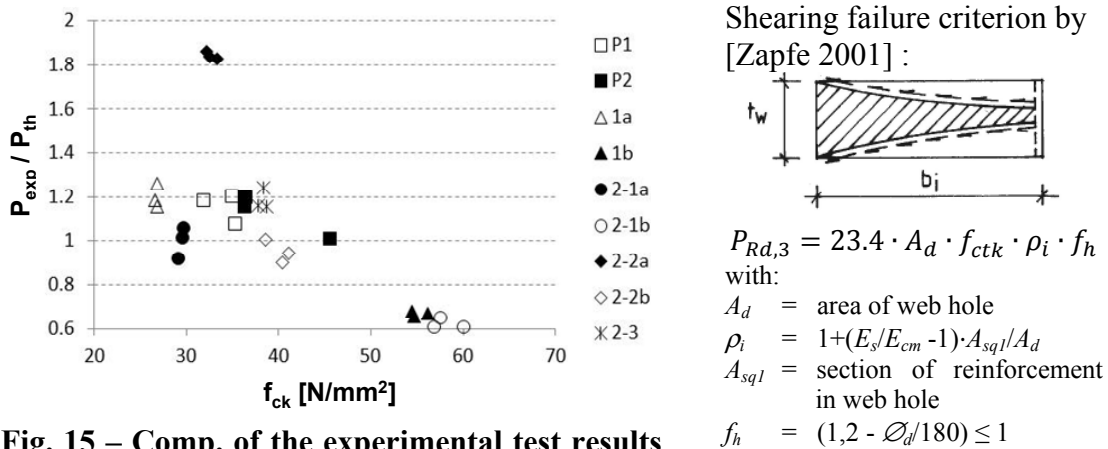


Fig. 15 – Comp. of the experimental test results P_{exp} to calculated values P_{th} acc. to [Zapfe 2001]

From the comparison, see Figure 15, it is concluded that the linear dependency of this criterion from the tension strength f_{ctm} cannot be confirmed for the CoSFB configuration, see especially P_{exp}/P_{th} for series 1b and 2-1b. Further the influence of the reinforcement diameter is not reflected appropriately, see P_{exp}/P_{th} for series 2-2a. Therefore a new design model is to be developed.

POTENTIAL OF THE NEW SLAB SYSTEM

As demonstrated, CoSFB and Cofradal200® floor systems have an excellent overall performance: high load bearing capacity and stiffness, ductility and robustness. Further, the combination of composite and slim-floor construction by using an innovative horizontal shear connection leads to efficient material use, hence to a sustainable construction [Braun et. al. 2011], and to an economic solution. For the total costs for an erected CoSFB + Cofradal200® less than 125€/m² can be achieved. It should be outlined, that these costs cover material, fabrication, transport and erection costs. Additional costs for fire resistance and/or acoustical and thermal insulation are inexistent. Thanks to the use of a horizontal shear connection, the composite action is activated without increasing the slab height.

The average slenderness ratio (beam span / height) of the CoSFB is around 35. This leads to slender constructions in combination with large spans. CoSFB spans of 12m (beam distance up to 10m) and a construction height of only 35cm can be realized. The typical weight of the CoSFB is around 20kg/m^2 .

More than 40 million square meters of floors are built in central Europe per year (figure of 2009, non-residential buildings). Most of them are constructed with a standard $8\text{m} \times 8\text{m}$ grid, mainly because of cost reasons. This contribution presents a solution with which grids of $14\text{m} \times 10\text{m}$ are realizable without a significant cost increase, see Fig. 16. Therefore the customer demand is not only met but extended.

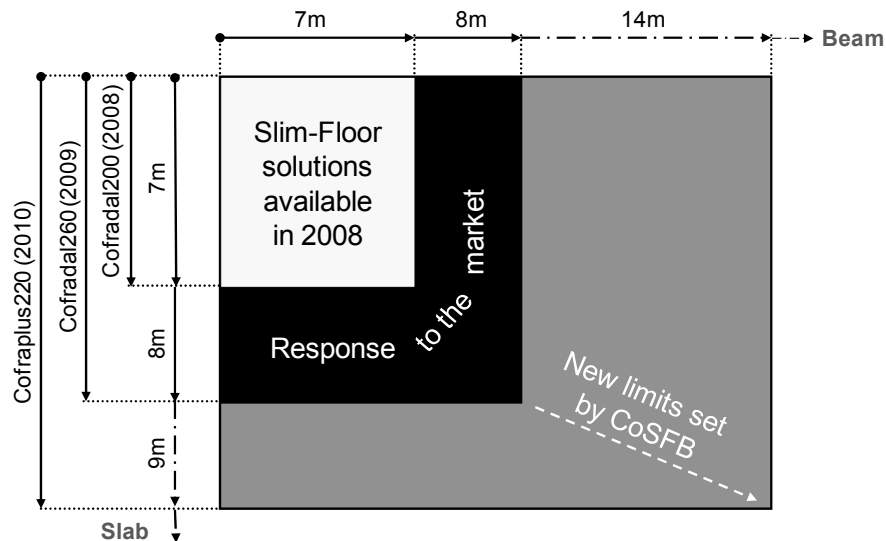


Fig. 16 – Economic floor solutions

SUMMARY AND CONCLUSIONS

This contribution outlines the potential and the testing of concrete dowels and their application for slim-floor construction. Sufficient load bearing capacity and ductile behavior of this innovative shear connection has been proven for slim-floor beams configurations. Thus the concrete dowels can be distributed equidistant, partial shear connection can be designed. Further the beam tests have shown an activation of the concrete chord even larger than the effective width according to Eurocode 4 [DIN EN1994-1-1]. Therefore it is concluded that based on the described test results, that the full plastic design of CoSFBs in accordance with EN is possible. Design values for the shear connection will be soon available in a General Technical Approval to be published by DIBT [DIBT 2013]; detailed information on the bearing mechanism and design guidance will be published [Braun]. Hereby the effect of dropping bearing resistance of the shear connection with increase in concrete strength will be covered.

ACKNOWLEDGEMENTS

The authors wish to express their deep gratitude to the representatives of ArcelorMittal Arval Floor Systems (France) for their inspiring cooperation.

REFERENCES

- [Braun et al. 2011] M. Braun, O. Hechler, G. Hauf & U. Kuhlmann: Embodied energy optimization by innovative structural systems. Final Conference of the COST Action C25: Sustainability of Constructions – Towards a better built environment (Innsbruck), 2011.
- [Braun et al. 2009] M. Braun, O. Hechler, V. Birarda: 140 m² Column Free Space due to Innovative Composite Slim Floor Design. 9th International Conference on Steel Concrete Composite and Hybrid Structures(ASCCS2009) (Leeds, UK), 2009
- [Braun] Braun, M.: On the design and application of composite slim-floor beams in construction. Dissertation, in preparation.
- [DIBt 2013] DIBt: Technical approval for CoSFB composite shear connection, Deutsches Institut für Bautechnik, Berlin, in preparation.
- [DIN EN1994-1-1] DIN EN 1994-1-1: Design of composite steel and concrete structures - General rules and rules for buildings; December, 2010.
- [Hechler & Braun 2010] O. Hechler, M. Braun: New Structural Concepts in High-Rise Building. Highrise towers and tall buildings 2010. Design and Construction of Safe and Sustainable Highrise Structures. International Conference at the Technische Universität München. Overseas Publishers Association 2000, April 2010.
- [Kuhlmann et al. 2010] U. Kuhlmann, G. Hauf, M. Konrad. Push-out and girder tests for the determination of the bending capacity and longitudinal shear capacity of Composite Slim-Floor girder with COFRADAL200® deck elements, internal report ArcelorMittal, March 2010.
- [Kuhlmann et al. 2012] U. Kuhlmann, G. Hauf, F. Eggert. Push-Out Tests for the Determination of the longitudinal Shear Capacity of Composite Slim-Floor Beams, 2nd internal report ArcelorMittal, 2012.
- [Leonhardt et al. 1987] Leonhardt, R. et. al.: Neues vorteilhaftes Verbundmittel für Stahlverbundtragwerke mit hoher Dauerfestigkeit, Beton- und Stahlbetonbau, S.325-331, 1987.
- [Wurzer 1997] Wurzer, O.: Zur Tragfähigkeit von Betondübel, Dissertation am Institut für Konstruktiven Ingenieurbau, Universität der Bundeswehr, München, 1997.

- [Zapfe 2001] Zapfe, C.: Trag- und Verformungsverhalten von Verbundträgern mit Betondübeln zur Übertragung der Längsschubkräfte, Dissertation am Institut für Konstruktiven Ingenieurbau, Universität der Bundeswehr, München, 2001.
- [ARVAL] ArcelorMittal Construction Benelux: Arval COFRADAL200[®].

Environmental Factors Affecting the Dynamic Response of Composite Steel-Concrete Beams

I. E. J. Henderson¹; B. Uy¹; X. Q. Zhu²; and O. Mirza²

¹Centre for Infrastructure Engineering and Safety, Univ. of New South Wales, NSW 2052, Australia. E-mail: I.Henderson@student.unsw.edu.au; B.Uy@unsw.edu.au

²School of Computing, Engineering and Mathematics, Univ. of Western Sydney, Penrith, NSW 2751, Australia. E-mail: xinqun.zhu@uws.edu.au; O.Mirza@uws.edu.au

Abstract

This paper presents a long term experimental study to quantify changes in dynamic response due to a long term loading and varying temperature effects. The experimental study is set up for one year. Two types of blind bolt connectors were used as shear connection systems in steel-concrete composite beams alongside a welded shear stud system and a non composite beam. Two questions are answered; firstly, do composite steel-concrete composite beams experience a change in frequency and/or mode shape due to environmental factors. Secondly, for identical specimens, does the type of shear connection system used change the extent to which environmental factors affect the frequency of the specimens. The results indicated that the dynamic behaviour is affected by both the load and changes in environmental factors over the course of the year as expected. The extent of the effect is dependent on which type of shear connector is used.

INTRODUCTION

Of the nearly 5000 bridges in New South Wales, about 17% are more than 50 years old. Most of these existing bridges are considered structurally deficient by modern standards for the loads they are required to carry. These bridges will have to be replaced or strengthened by utilising post installed shear connection systems or other similar means. Before retrofitting or strengthening existing structures, the condition of the structure should be assessed and the damage condition determined.

The process of implementing a damage detection and characterization strategy for engineering structures is referred to as structural health monitoring (SHM). The term damage can be defined as changes to the material and/or geometric properties of these structures, including changes to the boundary conditions and system connectivity, which adversely affect the system's performance (Farrar & Worden 2007). The incentives behind research into SHM are increased safety and the obvious financial incentives of detecting damage and taking remedial action as early as possible. The civil engineering community has studied vibration-based damage assessment of bridge structures and buildings since the early 1980's. These days several bridges globally have structural health monitoring systems in place. Ko & Ni (2005) cite no less than 18 articles based on different examples of long term monitoring systems implemented on bridges throughout the world. However, as Farrar & Worden (2006) state, environmental and operating condition variability

presents significant challenges to the bridge monitoring application. Kullaa (2011) postulates 4 possible analysis avenues under uncertain environmental conditions. The easiest of these is to quantify damage only using those variables which are insensitive to changes in environmental factors such as the modal assurance criterion (MAC), and coordinate modal assurance criterion (COMAC). A more difficult solution path is to quantify and establish a relationship between the environmental factors and the response variable of interest. Research on the effects of environmental factors on SHM schemes vary in scope from the full scale bridge approaches demonstrated by Farrar et al (2000), Sohn (2007), and Moser & Moaveni (2013) through to a purely numerical approach such as Deraemaeker et al. (2006, 2008). The simple approach of a single or double span beam experimental series for the express purpose of evaluating the impact of environmental factors on dynamic responses is less well covered. One such paper is put forward by Xia et al. (2006). They have shown for a steel reinforced concrete slab that frequencies decrease while the damping ratios increase consistently with the increase of temperature and humidity. However, mode shapes are insensitive to environmental changes. Kim et al. (2007) conducted a similar experimental study on a steel plate with twin girder span and came to the conclusion that structures can be effected by environmental factors and that detection of simulated damage using Frequency Response Function (FRF) methods are also affected. In this paper the effect of environmental factors on the frequency response of steel-concrete composite beams under the serviceability load condition and with different shear connection systems will be investigated. Two points will be addressed. Firstly do steel-concrete composite beams experience the same effects as those expressed by Xia et al. (2006) or Kim et al. (2007). Secondly, for identical test specimens under the same environmental conditions do the types of shear connectors used change how the specimen is affected by environmental conditions.

TEST SPECIMENS

The test series comprised of four specimens. Three composite steel-concrete beams with different types of shear connectors were designed with partial shear connection. Two types of blind bolt and a conventional welded stud were used as the shear connectors. A fourth non composite beam was used for comparison. Each beam was supported at both ends with a 6m span. The steel beams were universal steel beam sections of 460UB 74.6. The concrete slab was 150mm thick with a 1m wide. Figure 1 shows the top view of one of the beams. Figure 2 shows the three different types of shear connectors. Figure 2 (a) shows a 100mm M20 8.8 bolt, known as B1, which is the blind bolt one. The bolt has a folding washer mechanism that allows the bolt to be secured from the bolt head side using a special tool. Figure 2 (b) and (c) show the second blind bolt type (B2) in both closed and open configurations. It works by having a section that spreads open when the bolt is secured. Figure 2 (d) shows the conventional shear stud that is being tested as a comparison to B1 and B2. The shear stud connected beam will be referred to as SS from here on and the non-composite beam will be referred to as NC.

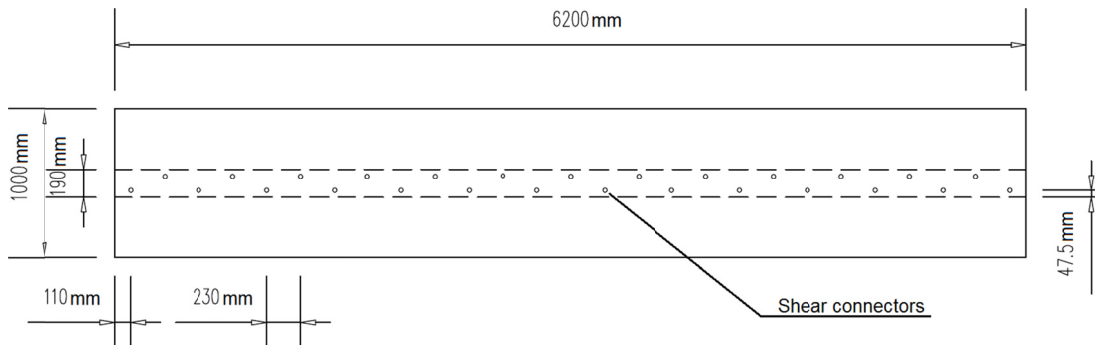


Figure 1. Shear connector layout and general beam dimensions

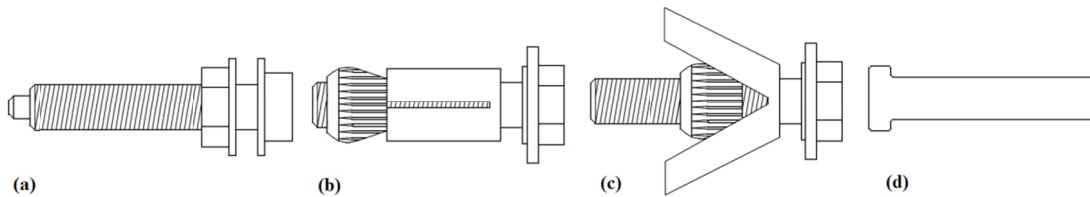


Figure 2. Different types of shear connectors.

All three shear connected beams will be compared to the non composite beam of the same dimensions. These four beams are simply supported with a six metre span and subjected to a serviceability load of 8.33kN/m. This loading is comprised of the dead load, 4.33kN/m, and an additional 4kN/m which is provided by the steel plates. The load on the beam is comprised of 16 steel plates per beam located as shown in Figure 3.

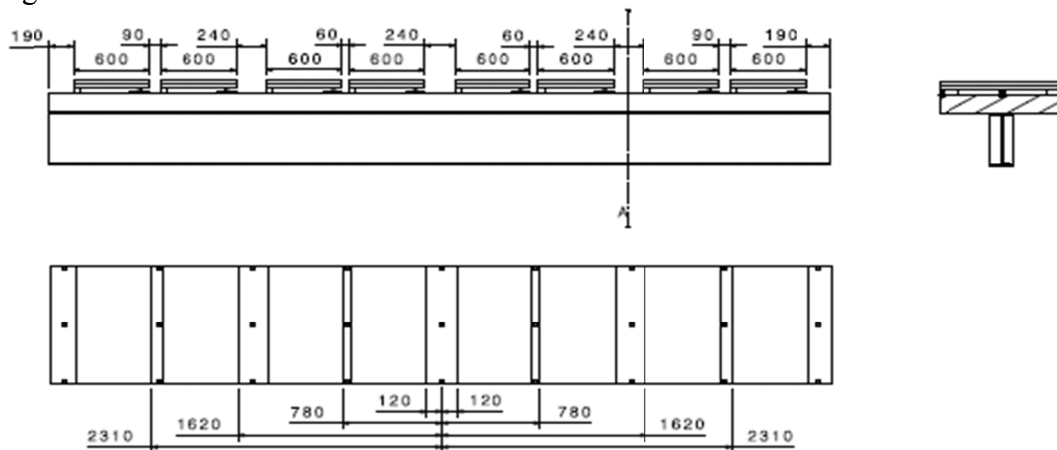


Figure 3. Long term experimental setup (dimensions in mm).

Each steel plate is 1000x600x32mm and weighs 150kg to give the total loading of 2400kg. The plates are stacked in two layers each stack is supported on two rollers on one side and two blocks on the other. The placements of the loads have been chosen to allow enough space for DEMEC gauges at the 1/4, 1/2, and 3/4 span locations and placement of accelerometers.

EXPERIMENTAL PROCEDURE

A total of thirty six accelerometers divided into four sets are being utilised. The accelerometer placement is indicated in Figure 4. Positions 15, 25, 35, and 45 are central to the length of the specimen. The other accelerometers are located at 750mm intervals from the central positions. The hammer location is marked by a cross. This location was chosen to not be too close to any individual accelerometer and also to not be on a node of the first few modes. Its location is 200mm inset from the edge and 1800mm from centre of the beam.

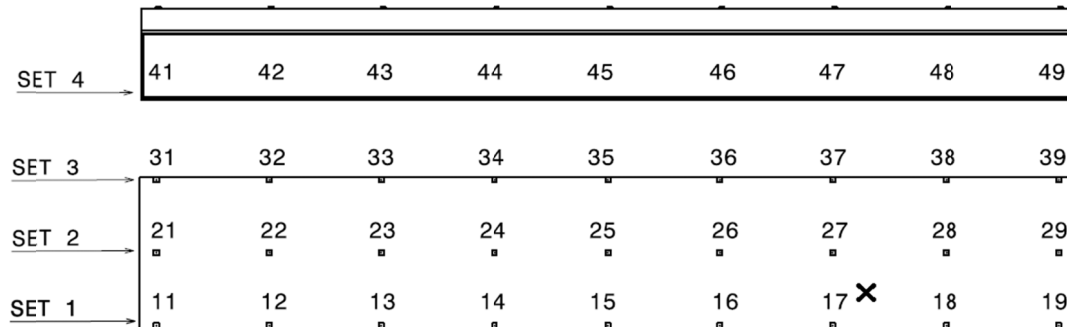


Figure 4. Accelerometer and hammer locations and numbering convention.

Figures 5 and 6 show the B2 specimen with and without the loading plates in place. The accelerometers can be clearly seen in Figure 5. In Figure 6 it can be seen that the loading plates cover the entire top surface of the specimen. Due to this the impact location is on the underside of the concrete beam. This does not affect the results as the direction of the input can be accounted for during analysis.



Figure 5. B2 specimen in situ with accelerometers

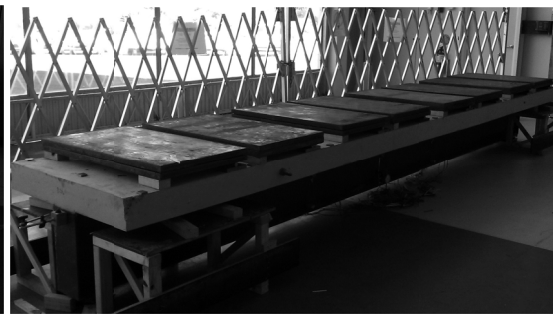


Figure 6. B2 specimen in situ with steel loading plates

The response from all thirty six locations was measured simultaneously using a multi-channel data logging system. Each test was repeated six times these were averaged in the frequency domain using Equation 1.

$$T_{xy}(f) = \frac{1}{n} \sum_1^n \frac{P_{xy}(f)}{P_{xx}(f)} \quad (1)$$

Where T_{xy} is the average estimated transfer function of the systems (FRF), P_{xy} is the cross power spectral density and P_{xx} is the power spectral density. Subscript x denotes input, subscript y denotes output, and n is the number of experimental results to be averaged together. The four specimens were kept for one year. The temperature, humidity, ambient vibration response, impulse input vibration response, central deflection, and strain at the quarter, mid, and three quarter span locations were measured once a week. However, only the temperature and vibration response will be discussed herein.

RESULTS & DISCUSSIONS

Before the mass is placed on the specimens the frequencies of the specimens were measured. An example of the B2 beam is given here. The fundamental mode of the B2 specimen was 22.43 Hz. Once the loading plates were put into place the frequency response of the beam changed immediately to 16.09 Hz. Over the following four days the frequency was measured on a daily basis. To minimise the effect of temperature on the specimens over this period the measurements were taken at the same time of day. As the beam settled under the influence of the load the frequency of the fundamental mode increased again. There are several interdependent factors forming the complex behaviour which causes this. However, a large contribution to this phenomenon could be caused by the deflection of the beam. Over the course of the first four days the measured deflection at the central locations increased thus increasing the curvature of the specimens. This increase in curvature could be responsible for the increase in frequency experienced after placement of the load. The first fifteen measurements after the placement of the load for the B2 specimen are shown in Figure 7.

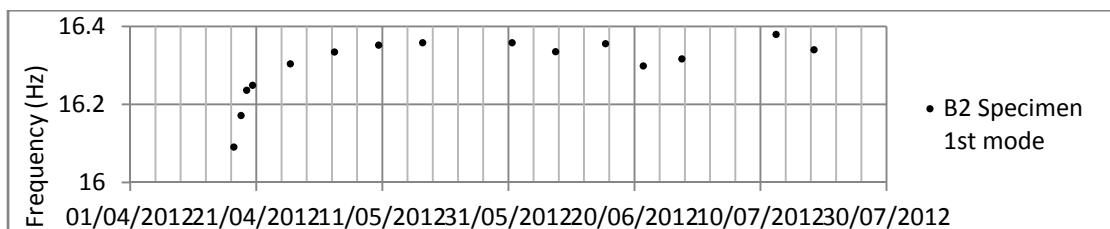


Figure 7. 1st mode frequency of the B2 specimen vs time.

The first four measurements can be seen as outliers to the dataset which as a whole sits roughly between 16.3 and 16.4 Hz. The first measurement that falls within the 16.3 and 16.4 Hz band was taken on the 26/04/2012. After this date any change in frequency could be seen as being due to environmental factors. This measurement period was the subject of a statistical analysis presented later. Prior to the load being placed on the specimens the frequency response was recorded and modal parameters are shown in Table 1 from the test dates 12th and 13th of March 2012. One year later the load was removed and the initial experiment repeated on the 04th to the 18th of March 2013. The modal parameters of all four specimens are shown in Table 2. By comparing Tables 1 and 2 it can be seen that there is an observed difference in the frequency of the specimens in the prior and post loading condition.

Table 1. Modal parameters of all specimens prior to loading.

Mode	NC		SS		B1		B2	
	f (Hz)	ζ (%)	f (Hz)	ζ (%)	f (Hz)	ζ (%)	f Hz	ζ (%)
B ₁	21.977	1.96	23.259	1.92	22.954	2.06	22.419	1.71
T ₁	61.627	0.45	66.176	0.42	64.363	0.39	66.671	0.41
B ₂	89.835	6.23	98.120	2.60	98.051	3.90	93.722	0.72
T ₂	120.40	0.40	127.99	0.42	126.66	0.38	128.60	0.38
B ₃	133.84	2.81	159.43	2.10	153.19	2.81	149.15	1.13
T ₃	186.78	0.46	195.56	0.36	192.43	0.37	195.57	0.37
B ₄	177.29	2.97	227.07	1.19	224.85	0.86	223.09	0.71
T ₄	254.88	0.47	264.83	0.37	262.31	0.38	265.81	0.39
B ₅	225.46	1.83	301.86	0.21	298.46	0.43	297.42	0.22
T ₅	326.55	0.08	337.69	0.35	335.45	0.36	341.55	0.34
B ₆	290.12	1.31	378.34	0.45	373.96	0.43	373.83	0.16
T ₆	405.86	0.65	416.61	0.33	413.40	0.45	419.90	0.31
B ₇	360.88	0.39	459.15	0.37	454.30	0.36	460.97	0.40
T ₇	--	--	493.29	0.48	497.24	0.49	491.06	0.40

Table 2. Modal parameters of all specimens post loading.

Mode	NC		SS		B1		B2	
	f (Hz)	ζ (%)	f (Hz)	ζ (%)	f (Hz)	ζ (%)	f Hz	ζ (%)
B ₁	20.552	1.26	24.022	0.61	22.934	0.71	23.549	0.65
T ₁	58.777	0.51	64.570	0.45	63.864	0.51	64.748	0.49
B ₂	71.539	1.42	90.882	2.28	86.089	1.10	89.400	1.12
T ₂	118.02	0.53	125.55	0.39	124.44	0.39	126.01	0.37
B ₃	77.785	2.42	144.04	1.09	140.99	1.40	135.38	1.77
T ₃	181.92	0.81	191.6	0.43	188.13	0.46	192.07	0.47
B ₄	--	--	214.99	0.53	216.55	0.44	215.69	0.47
T ₄	248.30	0.50	259.06	0.41	256.18	0.46	260.52	0.39
B ₅	152.01	2.68	286.06	0.47	295.01	0.56	291.80	0.39
T ₅	321.29	0.77	331.0	0.44	327.97	0.42	333.39	0.35
B ₆	198.80	0.72	360.86	0.49	370.71	0.47	361.81	0.44
T ₆	397.87	0.99	409.08	0.46	405.07	0.46	409.60	0.43
B ₇	--	--	439.20	0.24	451.87	1.14	444.66	0.44
T ₇	--	--	495.97	0.50	491.52	0.29	497.33	0.63

In general the frequency of the specimens is reduced whilst the damping ratios remain much the same for higher modes whilst being reduced for lower bending modes. Also, the bending modes are more greatly affected than the torsional modes. Assuming no damage occurred to the specimens during the course of the experiment the difference in modal properties of the specimens are most likely due to the long term loading and to a lesser extent the ageing of the concrete. As this long term test was conducted with a load it is important to check that the load didn't cause

any damage to the specimen during the course of the year. If damage was accrued during the year than an investigation into the effect of environmental change in temperature on the frequency of the specimens would be invalidated as the overall condition of the specimens could not be considered constant. The mode shapes can be used to find out if the observed difference in frequency of the prior and post loading condition is due to local or global changes in specimen properties. With nine accelerometers in each of the four sets it is possible to visualise the first seven bending modes and the first seven torsional modes. Figure 8 shows the first fourteen modes of the B1 beam prior to the load being applied and plotted directly from the modal analysis of the experimental result.

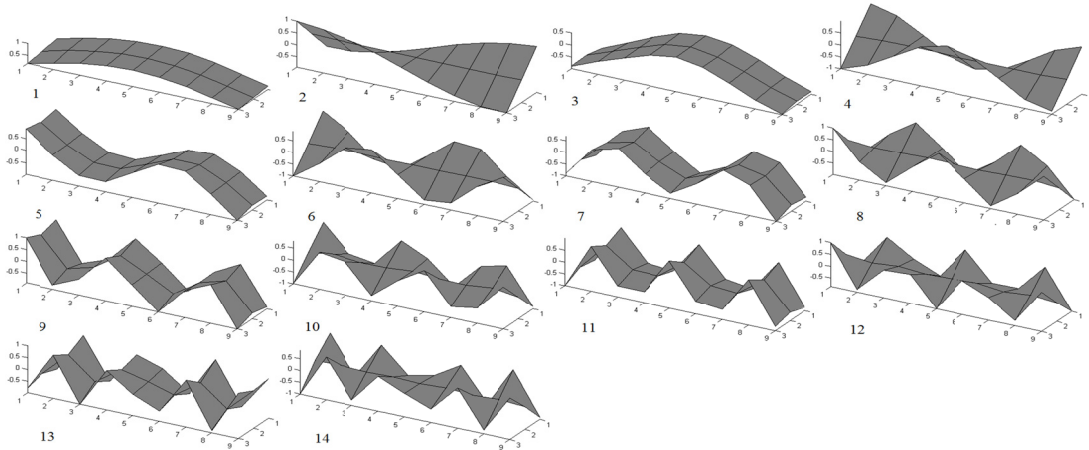


Figure 8. First 14 modes, B1 specimen prior to loading.

In order to compare the mode shapes gained, the modal assurance criterion (MAC) and coordinate modal assurance criterion (COMAC) were used. Equation (2) shows how the MAC values are calculated (Allemang, 2003).

$$MAC_{cdr} = \frac{|\{\psi_{dr}\}^H \{\psi_{cr}\}|^2}{\{\psi_{dr}\}^H \{\psi_{dr}\} \{\psi_{cr}\}^H \{\psi_{cr}\}} \quad (2)$$

Where ψ_{qr} is the modal coefficient for degree-of-freedom q , mode r , $\{\psi\}^H$ is the complex conjugate transpose (Hermitian) of $\{\psi\}$, and $\{\psi_r\}$ is the modal vector for mode r . The COMAC value gives an indication of the contribution of each degree of freedom to the MAC for a given mode pair (Allemang, 2003). High values of COMAC indicate high correlation and low values show areas of little correlation. Equation (3) shows how the COMAC is calculated (Allemang, 2003).

$$COMAC_q = \frac{\sum_{r=1}^L |\psi_{qr} \Phi_{qr}|^2}{\sum_{r=1}^L \psi_{qr} \psi_{qr}^* \sum_{r=1}^L \Phi_{qr} \Phi_{qr}^*} \quad (3)$$

Where L is the number of matching pairs of modal vectors and A^* is the complex conjugate of A . The MAC and COMAC values were calculated in the Matlab environment by exploiting the modal vector calculated by the Matlab package

used to analyse the raw experimental data. The MAC and COMAC values based on the first fourteen modes of each specimen in the prior and post loading condition were calculated. From this it was seen that the mode shapes had not significantly changed over the course of the year. As an example, Figure 9 shows the MAC and COMAC of the B1 specimen. The COMAC has been inverted so that 0 indicates no change. The numbers on the x and y axis of the COMAC represent the number of spline interpolation points use on longitudinal (x), and transverse (y), splines. These are necessary as the response was measured at only 27 locations which are all that practicality would allow. By using a spline interpolation the COMAC can be calculated at any number of points. In this case that number is $21 \times 61 = 1281$ points. More points can be used to build a finer image however the computational expense increases significantly for very little gain in resolution after a certain point.

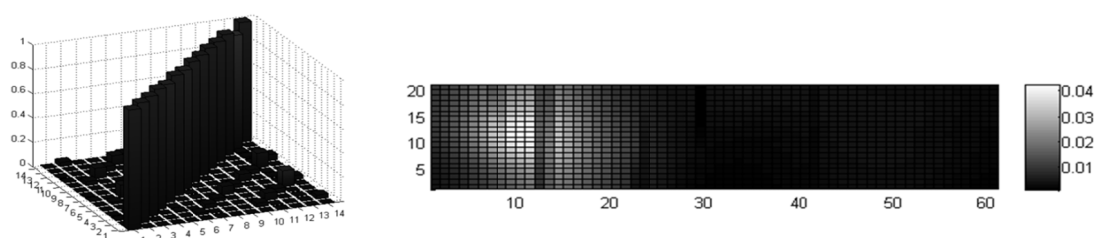


Figure 9. MAC & COMAC of the B1 specimen.

Over the course of the year the temperature and humidity were recorded each time the dynamic response was measured. Figure 10 shows a graph of how the temperature and humidity changed over the course of the year.

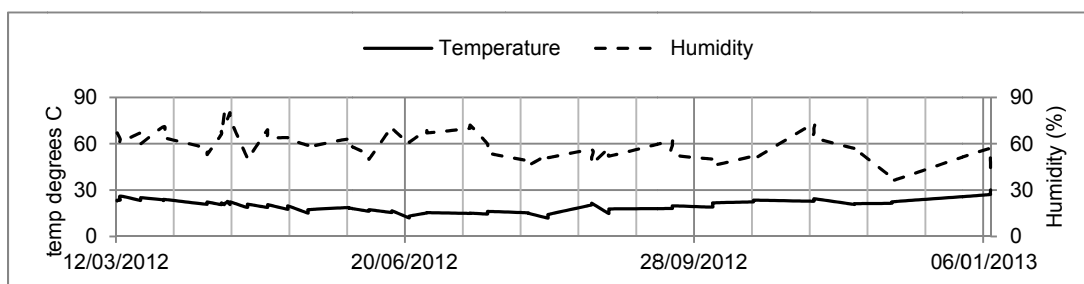


Figure 10. Temperature and humidity variation with time.

The vertical axis has units of both degrees Celsius for the temperature and percentage for the humidity. The nearly vertical sections of the curves are due to multiple readings being taken on each day of testing. The temperature and humidity ranges experienced by the specimens over the course of test period were $11.9 - 30.1^{\circ}\text{C}$ and $36 - 81\%$ respectively. The effect of humidity is more complex than the effect of temperature (Xia et al., 2006). Due to this the effect of humidity will be left as an area for further study and not covered here. The temperature effect studied here is really a combined effect of temperature and humidity however as the two cannot be easily separated and the temperature is the dominant effect the combined effect of temperature and humidity will be referred to from here on in as the temperature effect. To analyse the effect of temperature on the frequency response of the

specimens the data excluding the four data points representing the settling of the loading underwent a bivariate analysis. Figures 11-16 show the percentage change in frequency versus temperature, and the MAC value versus temperature, of the fundamental mode for each of the three shear connected specimens. A linear regression line along with 95% interval lines for a two sided t distribution of $(n - 2)$ degrees of freedom were fitted to each data set.

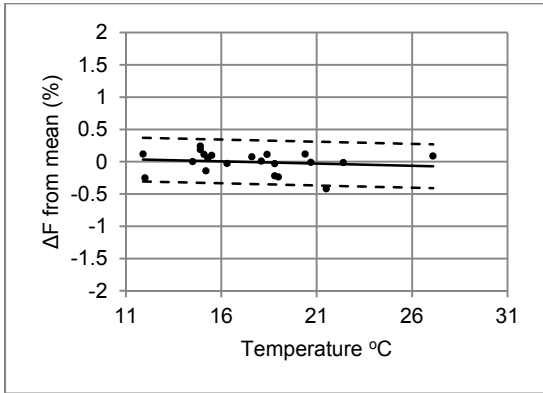


Figure 11. B2 1st bending mode

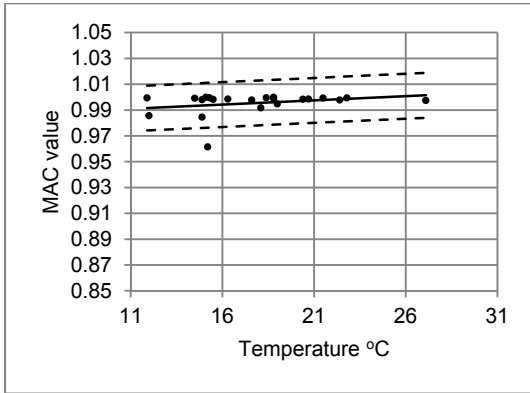


Figure 12. B2 1st bending mode MAC

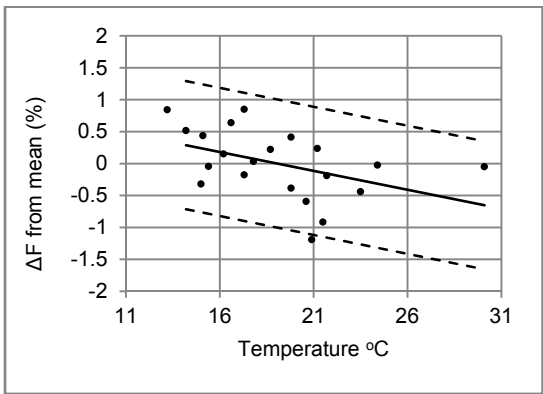


Figure 13. SS 1st bending mode

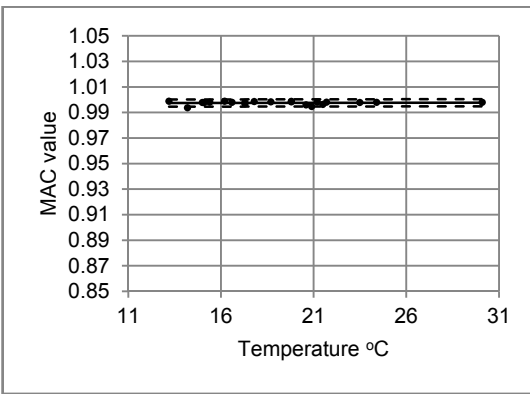


Figure 14. SS 1st bending mode MAC

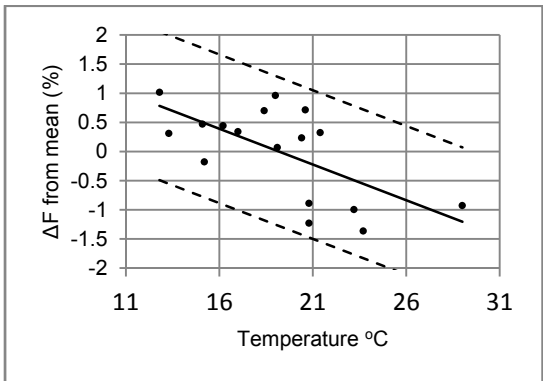


Figure 15. B1 1st bending mode

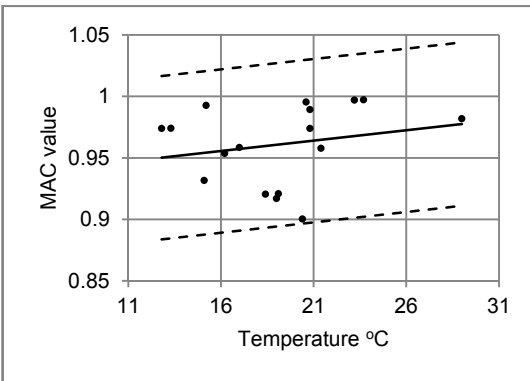


Figure 16. B1 1st bending mode MAC

Xia et al (2006) showed that for a reinforced concrete slab over a small temperature range the effect of temperature can be corrected by applying a scheme derived from Clough and Penzien (1993) and Adams et al (1978). Whilst this is true for a concrete slab the effect of the shear connection system used must be taken into consideration for steel-concrete composite beams. Comparing Figures 11, 13, and 15 it is clear to see that the difference in slope of the linear trend line is significant. As all the specimens are identical with the exception of the shear connector type used it must be the case that the shear connector type has an impact on how greatly a steel-concrete composite beam is affected by temperature. As such, correction schemes not accounting for difference in shear connector would have to be calculated on a case by case basis. Figures 12, 14, and 16 show the MAC values corresponding to the data in Figures 11, 13, and 15. Generally these MAC values show no change with temperature. Xia et al. (2006) also found that environmental factors had no appreciable effect on the MAC value of their test specimen. This makes sense as environmental factors effect global rather than local beam properties whereas mode shapes are sensitive to local changes in beam properties. The same analysis was also conducted on selected higher modes, first torsional mode, third bending mode, and sixth bending mode. Looking at the temperature effect on the frequency of higher modes it is clear that for the modes tested the change in temperature effects all tested modes equally on a percentage basis. As an example the first torsional mode of the SS specimen is shown in Figures 17 and 18. Comparing the slope of the trend line in Figure 17 to the slope of the trend line in Figure 13 it can be seen that the change in temperature affects these two modes similarly.

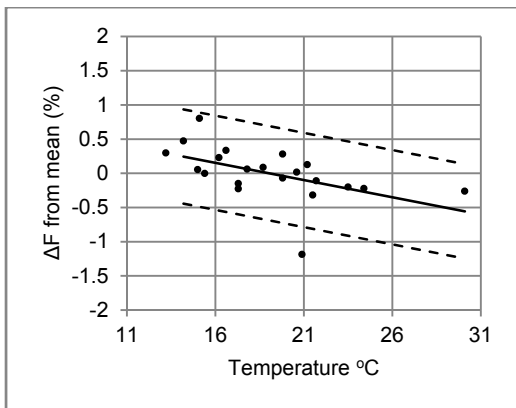


Figure 17. SS 1st torsional mode

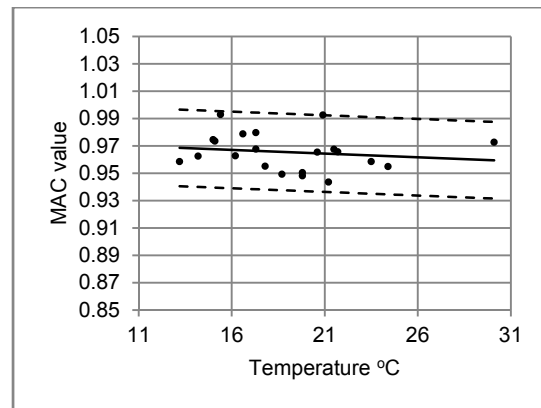


Figure 18. SS 1st torsional mode MAC

The R^2 values of the frequency vs temperature plots in Figures 11, 13, 15, and 17 range from 0.2 to 0.4. This is about half the values gained by Xia et al. (2006). However, this doesn't necessarily mean that there is no relationship between temperature and the frequency. Colton and Bower (2002) state that R^2 is reflecting variation solely obtained from the sampled data. Therefore unmeasured variables which also affect the sampled data become sources of error. R^2 can be low while meaningful relationships exist. Although establishing acceptable levels for R^2 across applications is inappropriate, Colton and Bower (2002). It is still generally held that an R^2 of 0.2 to 0.5 shows a moderate linear relationship. The loading plates introduce

a significant measure of uncertainty to the frequency response of the specimens due to the interaction of the plates with each other and the upper surface of the concrete slab. This is the probable course of the reduction in R^2 values of the temperature versus frequency plots. Further investigation into this phenomenon will be conducted at a later date. The R^2 values of the MAC plots range from 0.001-0.04. Even allowing for some extra variance in the data due to the presence of the loading plates it must be concluded that no significant relationship exists between the temperature and the mode shape.

CONCLUSION

The results show that the dynamic behaviour of the specimens is affected by both the load and changes in environmental factors over the course of the year as expected. The temperature shows a moderate linear relationship with the frequency change of the specimens over the temperature range experienced during the course of testing. To directly address the two key points outlined earlier. Firstly, the steel-concrete composite beams do experience similar effects due to environmental factors as those experienced in the experimental studies of Xia et al (2006) and Kim, Park, & Lee (2007). Secondly the type of shear connection used affects the extent to which the frequency is changed by environmental factors. This is an important conclusion as it shows that structures of identical geometry and materials can have a varied response under the same environmental conditions. The implication of this is that correction schemes for environmental factors need to encompass more than material properties to accurately represent observed behaviours. Or, correction schemes need to be developed on a case by case basis. Further work to isolate the effect of the loading and to incorporate other test data such as humidity, strain, and deflection will have to be conducted before any correction scheme is proposed.

REFERENCES

- Adams, R.D., Cawley, P., Pye, C.J. & Stone, B.J., (1978) A vibration technique for non-destructively assessing the integrity of structures. *Journal of mechanical Engineering Science*. Vol. 20, pp. 93-100
- Allemang, R.J. (2003). The model assurance criterion (MAC): twenty years of use and abuse, *Sounds and Vibration*. Vol.37, pp. 14-21
- Clough, R.W. & Penzien, J. (1993) *Dynamics of structure*. 2nd ed., New York, McGraw Hill.
- Colton, J.A. & Bower, K.M. (2002) Some misconceptions about R^2 , *International Society of Six Sigma Professionals EXTRAOrdinary Sence*, Vol. 3, pp. 20-32.
- Devore, J. & Farnum, N., (2005), *Applied Statistics for Engineers and Scientists Second Edition*. Duxbury Thomson Brookes/Cole
- Deraemaeker, A., Preumont, A, & Kullaa, J. (2006) Modelling and removal of environmental effects for vibration based SHM using spatial Filtering and factor analysis, *Conference & exposition on structural dynamics IMAC.XXIV*.

- Deraemaeker, A., Reynders, E., De Roeck, G. & Kullaa, J. (2008) Vibration-based structural health monitoring using output-only measurements under changing environment. *Mechanical Systems and Signal Processing* Vol. 22, pp. 34–56
- Farrar, C.R., Cornwell, P.J., Doebling, S.W. & Prime, M.B., (2000) Structural health monitoring studies of the Alamosa canyon and I-40 bridges. *Los Alamos National Laboratory report LA-13635-MS,2000*.
- Farrar, C.R. & Worden, K., (2007) An introduction to structural health monitoring. *Phil. Trans. R. Soc. A* Vol. 365, pp. 303–315
- Kim, J. T., Park, J. H. & Lee, B. J. (2007), “Vibration-based damage monitoring in model plate-girder bridges under uncertain temperature conditions.”, *Engineering Structures* , Vol. 29, pp. 1354–1365.
- Ko, J.M.& Ni, Y.Q., (2005), Technology developments in structural health monitoring of large scale bridges. *Engineering Structures* Vol. 27, pp. 1715-1725.
- Kullaa, J., (2011) Distinguishing between sensor fault, structural damage, and environmental operational effects in structural health monitoring. *Mechanical Systems and Signal Processing*. Vol. 25, pp. 2976-2989
- Mirza, O., Zhu, X. & Uy, B. (2011). Retrofitting/strengthening strategy for existing bridges using blind bolts as shear connectors. *Proceedings of the 4th Australian Small Bridges Conference*, Melbourne, Australia.
- Moser, P. & Moaveni, B. (2013) Environmental Effects on the Identified Natural Frequencies of the Dowling Hall Footbridge. *Experimental techniques* vol. 37, pp. 15-26
- Sohn, H. (2007) Effects of Environmental and Operational Variability on Structural Health Monitoring. *Phil. Trans. R. Soc. A*. Vol. 365, pp. 539-560
- Xia, Y., Hao, H., Zanardo, G. & Deeks, A. (2006), Long term vibration monitoring of an RC slab: Temperature and humidity effect. *Engineering Structures*, Vol. 28, pp. 441-452.

Vibration Performance of Composite Floors Using Slim Floor Beams

Stephen Hicks¹ and Simo Peltonen²

¹General Manager Structural Systems, Heavy Engineering Research Association, P.O. Box 76-134, Manukau, Auckland 2241, New Zealand. E-mail: stephen.hicks@hera.org.nz

²R&D Director, Composite Structures, Peikko Group Corporation, Voimakatu 3, P.O. Box 104, 15101 Lahti, Finland. E-mail: simo.peltonen@peikko.com

Abstract

Deltabeam is a hollow slim floor beam made from welded steel plates with regular web penetrations. Due to the long spanning capabilities of this product, the Deltabeam technology has recently been used in a prestigious shopping centre in the UK. As the floor would be subject to continuous walking activities the main contractor, Bovis Lend Lease, was concerned with occupant-induced vibrations. This paper presents the results from vibration tests conducted by the University of Sheffield, which can be compared directly with the requirements given in ISO 10137. Through extending the scope of the test results by numerical modelling and applying the design rules given in SCI P354, a methodology has been developed to estimate the vibration performance for this floor type and is presented.

INTRODUCTION

Serviceability issues relating to the vibration response of steel-framed floors are frequently becoming the governing design criteria because: long slender spans can be readily achieved; the natural frequencies can be low; the construction is relatively light in weight; and the level of damping is generally low. The highly publicised vibration serviceability problem with the Millennium Bridge in London (Dallard *et al.*, 2001) has focused designer's attention to issues related to human acceptance of vibration.

In the interests of providing harmonized design guidance for floor vibrations, two major European research projects were undertaken (European Commission Directorate-General for Research and Innovation, 2006; European Commission Directorate-General for Research and Innovation, 2010). Through the JRC-ECCS cooperation agreement, the results from this work led to the development of a JRC-Scientific and Technical Report (Feldmann *et al.*, 2009), which presents a simplified design method that is amenable to hand calculations. However, the simple design method is only confined to dynamic actions from walking activities (i.e. dancing and jumping are not included). Moreover, in a similar way as AISC/CISC Design Guide 11 (Murray *et al.*, 1997), the methodology can be difficult to apply when eigenmodes other than the first mode are excited by the activity or several modes are excited simultaneously and for floors that do not possess a rectangular plan form.

The Steel Construction Institute (SCI) Publication 354 (Smith *et al.*, 2007) was developed from these European research projects and provides two design methodologies: the general design method, which is based on modal superposition and is similar to the method given for reinforced concrete construction (Willford *et al.*, 2006); and the simplified design method, which was developed from considering the results from parametric studies of steel-framed floors using the general design method. Although developed on a completely different basis, the simplified design method is of a similar form to that given by AISC/CISC Design Guide 11.

HUMAN PERCEPTION OF VIBRATION

Many modern standards describe the severity of human exposure to vibration in terms of acceleration. To ensure that the measure of the vibration is not influenced by one unrepresentative peak in the response, it is often preferred to express the severity of the vibrations in terms of an average measure. The measure in greatest use is the frequency-weighted root-mean-square (rms) value, which is given by the following equation.

$$a_{w,rms} = \left(\frac{1}{T} \int_0^T a_w(t)^2 dt \right)^{1/2} \quad (1)$$

where $a_w(t)$ is the frequency-weighted acceleration as a function of time (expressed in m/s^2) and T is the period under consideration and, for vibrations with occasional shocks and transient vibration (i.e. walking activities).

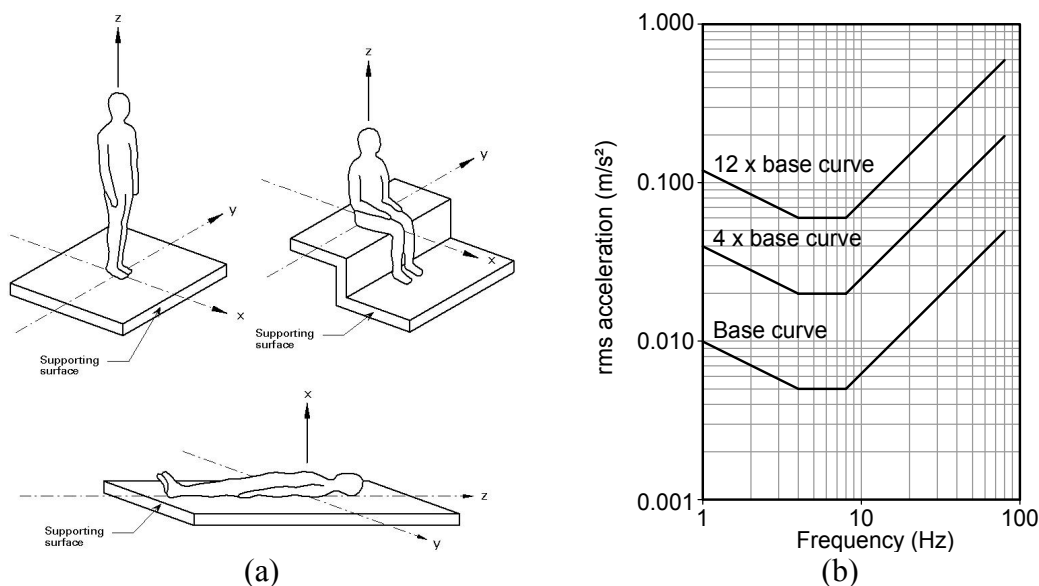


Figure 1 (a) ISO 2631-1 directions of basicentric coordinate systems for vibrations influencing humans (b) ISO 10137 building vibration curves for z-axis vibrations

The perception of vibrations depends on the direction of incidence to the human body. To account for this, most modern standards such as ISO 2631-1 (International Organization for Standardization, 1997) use the ‘basicentric’ coordinate system shown in Figure 1(a) (N.B. the z-axis corresponds to the direction of the human spine). The threshold of human perception is defined by a ‘base value’ which, for continuous vibrations, is given as an rms acceleration of: 5×10^{-3} m/s² in the z-axis direction; and 3.57×10^{-3} m/s² in the x- and y-axis direction. However, acceptable vibration levels vary with the frequency of the motion and, as a consequence of this, it is necessary to filter the acceleration. The appropriate filters or frequency weighting parameters, are given in ISO 2631-1 for situations where the critical vibration direction is specified according to the directions in Figure 1(a), or ISO 2631-2 (International Organization for Standardization, 2003) if the critical direction is unknown. The base curves in ISO 10137 (International Organization for Standardization, 2007) are derived from dividing the base values by the appropriate frequency weighting parameter. For example, the base curve for z-axis vibrations shown in Figure 1(b) is based on an environment where vision/hand control is critical, which corresponds to the W_g frequency weighting curve given in BS 6841 (British Standards Institution, 1987) whose asymptotic approximation is given by:

$$\left. \begin{aligned} W_g &= 0.5\sqrt{f} \text{ for } 3 \text{ Hz} \leq f < 4 \text{ Hz} \\ W_g &= 1.0 \text{ for } 4 \text{ Hz} \leq f < 8 \text{ Hz} \\ W_g &= \frac{8}{f} \text{ for } f \geq 8 \text{ Hz} \end{aligned} \right\} \quad (2)$$

ISO 10137 covers many vibration environments in buildings. To achieve this wide coverage, limits of satisfactory vibration magnitude are expressed in relation to the base curve and a series of multiplying factors whose magnitude are dependent on the building environment (see Table 1). The multiplying factors in Table 1 are based on continuous vibrations and correspond to a ‘low probability of adverse comment’ (according to ISO 10137, continuous vibrations are those with a duration of more than 30 minutes per 24 hours).

The base curve for continuous vibrations in the z-axis, together with a range of typical factored curves for different building environments, is shown in Figure 1(b). Each line in Figure 1(b) represents a constant level of human reaction known as an isoperceptibility line: the area above a line corresponds to an unacceptable human reaction in the corresponding environment. In practice, base curves are rarely used because they relate to only a single frequency response. Instead, measured or calculated accelerations are attenuated by the frequency weighting parameter appropriate to the frequency under consideration (e.g. Equation (2)).

Table 1 Multiplying factors used in several countries to specify satisfactory magnitudes of building vibration with respect to human response according to ISO 10137.

Place	Time	Multiplying factors to base curve for 16h day 8h night	
		Continuous vibration	Impulsive vibration excitation with several occurrences per day
Critical working areas (e.g., some hospital operating theatres, some precision laboratories, etc.)	Day	1	1
	Night	1	1
Residential (e.g. flats, homes, hospitals)	Day	2 to 4	30 to 90
	Night	1.4	1.4 to 20
Quiet office, open plan	Day	2	60 to 128
	Night	2	60 to 128
General office (e.g. schools, offices)	Day	4	60 to 128
	Night	4	60 to 128
Workshops	Day	8	90 to 128
	Night	8	90 to 128

To facilitate comparisons of test measurements with the required multiplying factors presented in Table 1, the ‘response factor’ is calculated, which is defined as the measured frequency-weighted acceleration divided by the appropriate base value. The response factor should be less than, or equal to, the limiting multiplying factor for the particular floor type (see Table 1). For z-axis vibrations, the response factor is given by:

$$\text{Response factor} = \frac{a_{w,rms}}{5 \times 10^{-3}} \quad (3)$$

Generally, walking activities are not continuous; by their very nature they are intermittent. For intermittent vibrations, a cumulative measure of the response has been found to be more reliable in determining perceptive tolerance levels (Griffin, 1996). In these cases ISO 10137 gives vibration dose values (VDVs), which describe the perception levels due to occasional short-duration vibrations. This allows the vibration levels to be higher than the thresholds for continuous vibrations given in Table 1 as long as the occurrence is rare. The recommended levels of VDVs for residential buildings are presented in Table 2. The general expression for calculating VDVs is given by:

$$VDV = \left(\int_0^T a_w(t)^4 dt \right)^{1/4} \quad (4)$$

where VDV is the vibration dose value (in $\text{m/s}^{1.75}$), $a_w(t)$ is the weighted acceleration (in m/s^2) and T is the total period of the day during which vibration may occur (in seconds).

Table 2 Vibration Dose Values ($\text{m/s}^{1.75}$) above which various degrees of adverse comments may be expected in residential buildings according to ISO 10137

Place	Low probability of adverse comments	Adverse comments possible	Adverse comments probable
Residential buildings 16h day	0.2 to 0.4	0.4 to 0.8	0.8 to 1.6
Residential buildings 8h day	0.13	0.26	0.51

DRAKE'S CIRCUS SHOPPING CENTRE

The Drake's Circus Shopping Centre in Plymouth is a multi-storey shopping centre offering 60,800 m^2 of retail space. The scheme is arranged over two principal trading levels, with the upper level having the addition of mezzanine floors. Beneath the trading floors a multi-storey car park provides 1270 spaces. This project was one of the UK's first large-scale application of the Deltabeam system which, *inter alia*, enabled the project to be completed 3-months faster than if conventional construction methods had been used. Deltabeam is a proprietary steel-concrete composite slim floor beam produced by Peikko Group, which is made from welded steel plates with regularly spaced circular web penetrations (see Figure 2). The beam is filled with concrete, which acts compositely with either pre-cast hollow core, composite, or thin shell slabs. The shear connection is developed through concrete dowel action at the circular web penetrations. The Deltabeam system possesses a fire rating of up to 120 minutes without the need for additional applied fire protection.

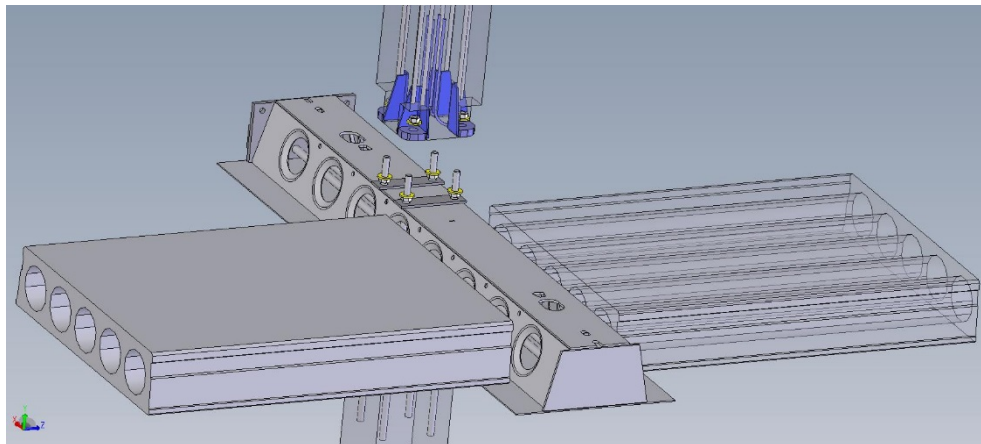


Figure 2 Steel-concrete composite Deltabeam

Due to the long-span slender floors on the Drake’s Circus project, concerns were expressed at the possibility of vibrations occasioned by walking activities causing annoyance to the occupants of the building. In response to these concerns, it was decided to conduct vibration testing on the floor. The floor consists of a 75 mm deep structural topping applied to 400 mm and 320 mm deep precast concrete hollow core units in the car parks and retail areas, respectively. The precast units are, in turn, supported by Deltabeams. The three principal floor areas that were considered worthy of investigation were: the Level 1 Car Park and Retail Area (10 m span hollow core units supported by 8 m span 320 mm deep D32-400 Deltabeams); and the Level 2 Car Park (16 m span hollow core units supported by 10 m span 400 mm deep D40-500 Deltabeams). The general arrangement of the three test areas are presented in Figure 3.

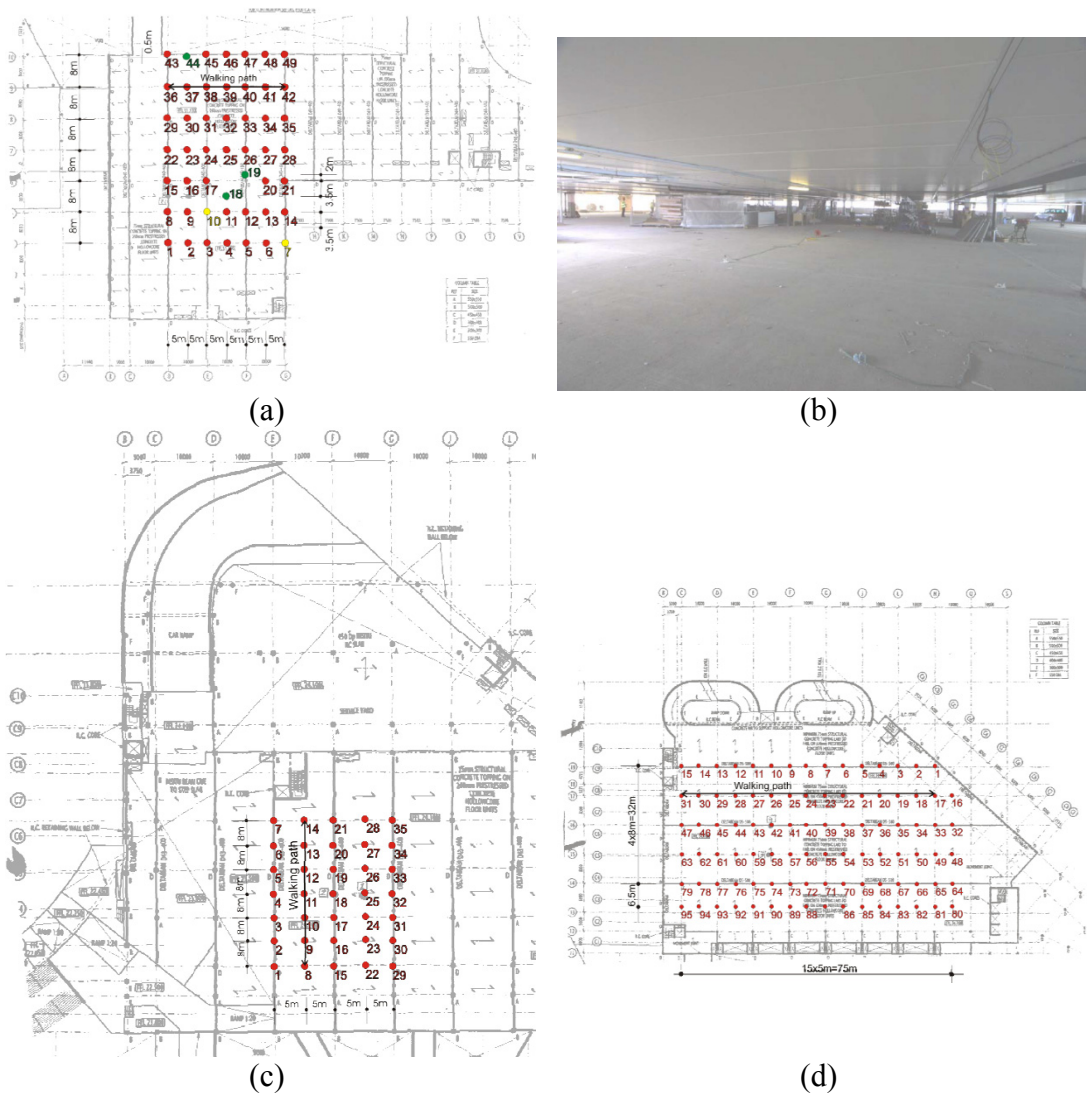


Figure 3 (a) Plan of Level 1 Car Park (b) Level 1 Car Park floor during testing (c) Plan of Retail Area (d) Plan of Level 2 Car Park

IN SITU VIBRATION TESTING

In situ testing was conducted on the areas shown in Figure 3 to: experimentally estimate the modal properties of the floors (i.e. natural frequencies, modal damping ratios and mode shapes); and to measure the accelerations of the floors due to a single person engaged in walking activities, to enable comparisons to be made with the acceptability criteria given in ISO 10137 (see Table 1). The numbered test grids shown in Figure 3(a), (c) and (d) were used to evaluate the mode shapes of the floor to identify the antinode positions (i.e. the maximum point of response) in order to plan the critical paths for the subsequent walking tests.

MODAL PROPERTIES OF THE FLOORS

The measured modal properties from Multi-Input Multi-Output (MIMO) shaker tests on the three floor areas are presented in Table 3.

Table 3 Modal properties for first six modes of vibration of the floors

Mode	Level 1 Car Park		Retail Area		Level 2 Car Park	
	Frequency (Hz)	Damping, ζ	Frequency (Hz)	Damping, ζ	Frequency (Hz)	Damping, ζ
1	6.0	1.7%	8.9	2.5%	4.96	1.40%
2	8.1	2.2%	8.9	0.8%	5.11	1.00%
3	8.3	1.3%	10.3	1.3%	5.50	1.10%
4	8.7	1.6%	11.0	2.7%	5.77	1.70%
5	8.8	1.4%	12.1	2.8%	5.81	1.80%
6	8.9	1.3%	12.5	1.3%	5.82	1.55%

As can be seen from Table 3, in all cases the frequencies to the modes of vibration were very closely spaced. This is primarily due to the bending stiffness of the floor being concentrated in one direction (this behaviour has also been observed by the first author on long-span floors using cellular beams). As a consequence of this, it is possible for several modes to be excited simultaneously from walking activities. This behaviour is not considered by either the JRC-Scientific and Technical Report or the AISC/CISC Design Guide 11.

In unfurnished 'bare-construction' structures SCI P354 recommends a damping value $\zeta = 1.1\%$. As can be seen from Table 3, the measured values were higher than this value and the first mode damping averaged at 1.9%, which supports the use of the SCI design recommendations for this type of construction.

MEASUREMENTS OF DYNAMIC RESPONSE DUE TO WALKING

A set of walking tests were carried out for each floor area. Two male participants were used JMWB (47-years old; 85 kg; 182 cm) and EPC (28-years old; 95 kg; 178 cm). The walking path was chosen to be as close to the antinode positions. For each subject five tests were carried out at 40 seconds each to controlled pace frequencies

of 1.6, 1.8, 2.0, 2.2 and 2.4 Hz (which correspond to the design range of pace frequencies given in SCI P354). All measured acceleration time histories were weighted according to the W_g curve (see Equation (2)) and the weighted rms acceleration $a_{w,rms}$ was taken as the maximum value using an integration time of 1-second (Equation (1)). To enable comparisons to be made directly with the Multiplying Factors given in Table 1, the results were converted to Response Factors using Equation (3). Finally, to maximize the value of the tests, VDV's were also evaluated using Equation (4). The highest responses measured from the walking tests are presented in Table 4.

Table 4 Maximum floor responses measured from walking tests

Floor	Walking path on Figure 3	TP with max response	Walker	Pace frequency (Hz)	$a_{w,rms}$ (m/s ²)	Response Factor	VDV (m/s ^{1.75})
Level 1 Car Park	TP36-42	39	EPC	2.2	0.0088	1.77	0.0013
Retail Area	TP08-14	11	EPC	2.4	0.0140	2.79	0.0029
Level 2 Car Park	TP17-31	30	EPC	2.1	0.0112	2.24	0.0017

Although no specific guidance is given in ISO 10137 for multiplying factors in retail environments, it is commonly accepted in the UK that the limit should not be set lower than that for a general office (Smith *et al.*, 2007); this equates to a multiplying factor of 4.0. As the measured maximum floor response factor is 2.79 for a 95 kg individual, the floor may be considered to be acceptable for a retail environment. It is interesting to note that the AISC/CISC Design Guide 11 permits a much higher multiplying factor of 20. However, the present authors are uncertain of the correlation between the human acceptance of vibrations with actual floors that delivers this level of response.

PERFORMANCE OF SCI P354 METHODOLOGY COMPARED WITH TEST MEASUREMENTS

To investigate the performance of the SCI P354 general method, the test measurements were compared with the results from finite element (FE) models that had been constructed according to the recommendations given in that design guide. Figure 4 shows frequency against mode number for both the tests and the FE models of each of the floors. Clearly, there is a good fit for both of the car park levels, but there is some discrepancy for the Retail Area. It is thought that the discrepancy may be caused by extra stiffness contributed from the columns. However, given that the difference between the measured frequency and the predicted frequency has little effect on the response, the FE models were not refined.

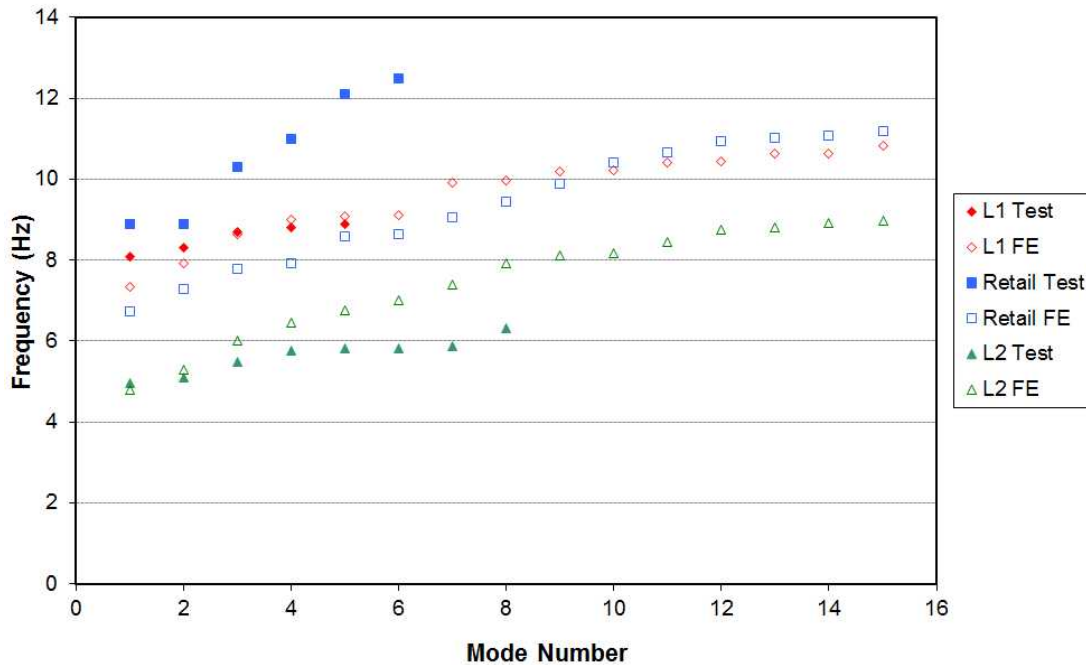
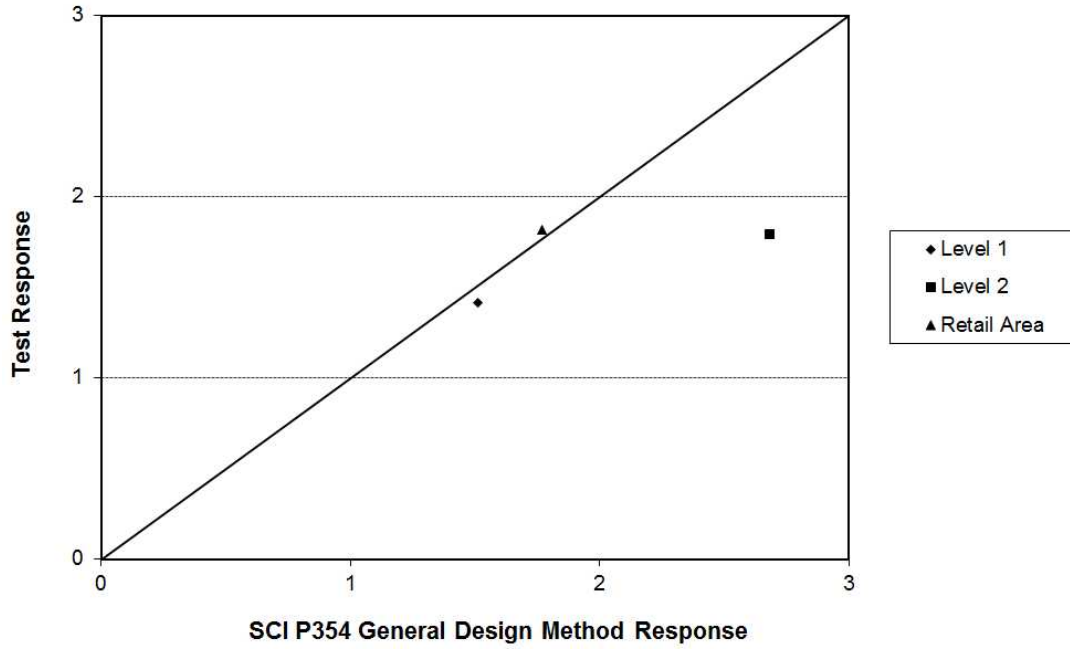


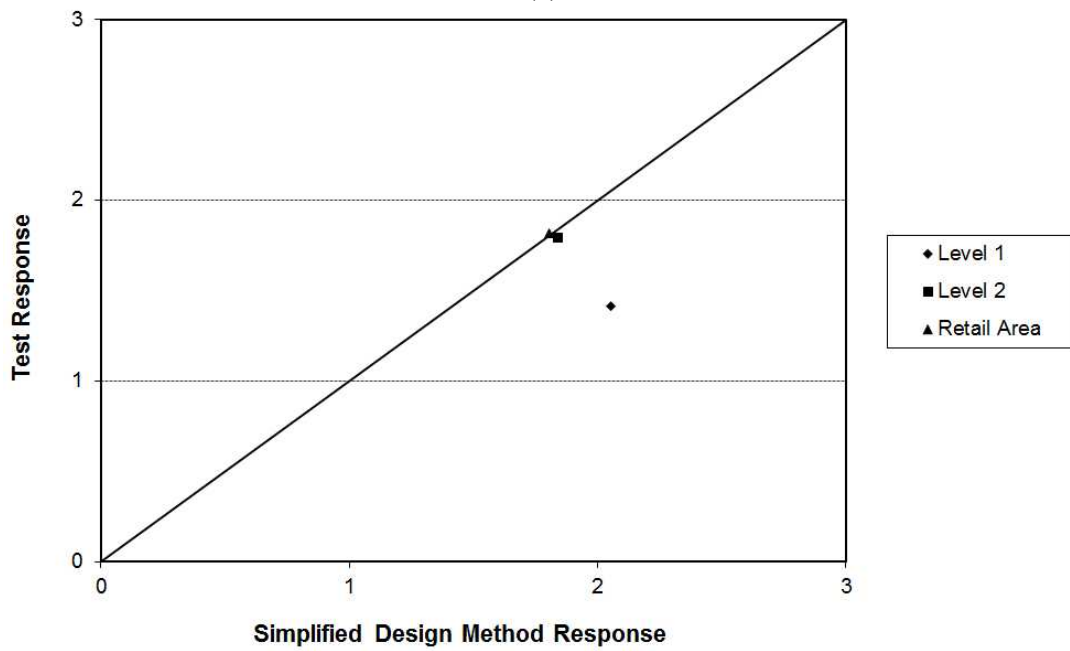
Figure 4 Comparison of measured frequencies with predictions made from finite element analyses

The FE models of the three floors predict fundamental frequencies of less than 10 Hz which, according to SCI P354, means that the floors must be considered to be capable of responding both resonantly (i.e. the response builds-up over time) and transiently (i.e. the floor responds to each footfall independently). Both cases were assessed for each floor and the worst response result taken as the prediction of floor response.

In international design guides, the mass of an ‘average person’ is normally taken as 76 kg. For the purposes of comparisons made in this section, the response factors were normalised to this mass, which resulted in corrected response factors of 1.42, 1.82 and 1.79 for the Level 1 Car Park, Retail Area and Level 1 Car Park, respectively. From a modal superposition of the test results according to the general design method given in SCI P354, response factors were predicted for the three floors (see Figure 5(a)). In every case the steady-state response dominated. Figure 5(a) indicates an unusually high level of fit, and implies that the general design method is valid for this floor type. Based on the mode shapes, it is possible to get an appreciation of the area of the floor participating in the vibration. The mode shapes determined in the testing were found to match those found in the finite element modelling very well and were used to develop the proposed simplified design method presented in the next section.



(a)



(b)

Figure 5 Comparison of measured response factor with that predicted using (a) the SCI P354 general design method (b) the proposed simplified design method

PROPOSED SIMPLIFIED DESIGN METHOD FOR COMPOSITE FLOORS USING DELTABEAM SLIM FLOOR BEAMS

Given the good correlation between the predictions using the SCI P354 general method and the measurements made on the floor of Drake's Circus, it was possible to develop a simplified design method that is appropriate to floors using Deltabeams. The scope of the simplified design method is limited to the following conditions:

- Construction using Deltabeams with precast concrete units and an in-situ structural topping of at least 75 mm.
- The span of the slab should be greater than the span of the beams between columns.
- The fundamental frequency of the floor is between 3 Hz and 10 Hz.

In other circumstances, the general design method given in SCI P354 may be used.

FLOOR LOADING

The loading used to calculate the frequency and response of the floor should be taken as the load equivalent to the self-weight and other permanent loads, plus a frequent variable action factor ψ_1 times the imposed load (which represents the imposed loads that may be reasonably assumed to be permanent during building use from, *inter alia*, office furniture, filing cabinets, etc.). From measurements made on office floors (Hicks *et al.*, 2003), it is recommended that $\psi_1 = 0.1$ unless it is known that the imposed loads that will be present in service are likely to be higher or lower.

FUNDAMENTAL FREQUENCY

The first mode, or fundamental, frequency of the floor can be determined from:

$$\delta_s = \frac{5mgL_{slab}^4}{384EI_{slab}} \times 10^3; \delta_b = \left(\frac{5mgL_{slab}L_{beam}^4}{384EI_{beam}} + \frac{mgL_{slab}^4}{384EI_{slab}} \right) \times 10^3 \quad (5)$$

$$f_0 = \frac{18}{\sqrt{\max(\delta_s, \delta_b)}}$$

where m is the distributed floor loading as described above (kg/m^2), g is the acceleration due to gravity ($=9.81 \text{ m/s}^2$), L_{slab} is the span of the slab (m), L_{beam} is the span of the beam (m), EI_{slab} is the stiffness of the slab (Nm^2/m) and EI_{beam} is the stiffness of the beam (Nm^2)

(N.B the second moment of area of the cross-section should be based on the uncracked concrete properties, with an effective breadth of 1 m in addition to the concrete enclosed in the section. The dynamic elastic modulus of $E_{conc} = 38 \text{ kN/mm}^2$ should be used for normal weight concrete, or $E_{conc} = 22 \text{ kN/mm}^2$ for lightweight concrete).

MODAL MASS

The modal mass can be determined from:

$$M = \frac{L_x L_y m}{4} \quad (6)$$

where m is the distributed floor loading, as defined above (kg/m^2), L_x and L_y are the dimensions in metres of the rectangular floor area that can be considered to participate in the motion (usually the area where the span of the slab between supporting beams is identical). Examples of the floor areas that may be considered are given in Figure 6.

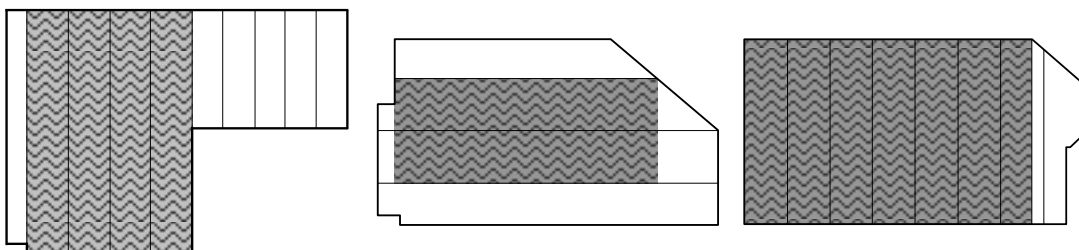


Figure 6 Examples of the rectangular floor area on different building arrangements that can be considered to participate in the motion and define L_x and L_y

FLOOR RESPONSE

The response of the floor can be determined from:

$$a_{w,rms} = \frac{0.15Q}{2\sqrt{2} M \zeta} W \quad (7)$$

$$R = \frac{a_{w,rms}}{5 \times 10^{-3}}$$

where: Q is the static force exerted by a person, normally taken as 746 N ($76 \text{ kg} \times 9.81 \text{ m/s}^2$), M is the modal mass (kg), ζ is the critical damping ratio which, according to SCI P354, can be taken as 1.1% for bare floors and 3.0% for fully finished and fitted-out floors and W is the weighting factor from ISO 2631-1, ISO 2631-2 or SCI P354 (for z-axis vibrations, and environments where vision/hand control is critical, Equation (2) may be used) based on the fundamental frequency of the floor.

ACCEPTABILITY CRITERIA

The floor response calculated from Equation (7) should be less than, or equal to, the recommended Multiplying Factors given in ISO 10137, SCI P354 or other design guidance.

To demonstrate the performance of the simplified design method, the response of the three test floors was predicted using the equations presented above. As can be seen from Figure 5(b), the proposed method compares favourably with the measurements and can therefore be used with confidence.

CONCLUSIONS

Vibrations in steel-concrete composite floors are not a new phenomenon. Indeed, the first guidelines for considering this serviceability limit state were developed over 30 years ago. However, as slender floors are increasingly being constructed, it is essential that a serviceability assessment of the floor vibration from walking activities be fully considered at the design stage.

Based on the measurements made on the floor of the Drake's Circus Shopping Centre, the Deltabeam floor performs very well in comparison to standard methods of construction by producing responses which are lower than half those that would be expected from traditional composite construction. Although no specific guidance is given in ISO 10137 for multiplying factors in retail environments, it is commonly accepted in the UK that a multiplying factor of 4.0 is appropriate. As the measured maximum floor response factor is 2.79 for a 95 kg individual, the floor may be considered acceptable for this environment.

The measured floor frequencies were very closely spaced. This is primarily due to the bending stiffness of the floor being concentrated in one direction and has been observed on other long-span floors. As a consequence of this, it is possible for several modes to be excited simultaneously. Neither the JRC-Scientific and Technical Report or the AISC/CISC Design Guide 11 considers this behaviour.

The SCI P354 general design method compared very well with the measurements. A simplified design method for this form of construction is proposed, which is amenable to hand calculations, and is shown to compare favourably with the measurements.

ACKNOWLEDGEMENTS

The authors would like to thank Prof. Alex Pavic of Exeter University (formerly Sheffield University), Prof. Paul Reynolds and Prof. John Brownjohn of Sheffield University, whom were responsible for the testing. Also thanks go to Andy Smith of Grubb Engineering Corporation (formerly SCI), who was responsible for the finite element modelling and response analysis.

REFERENCES

- British Standards Institution (1987). BS 6841 Measurement and evaluation of human exposure to whole-body mechanical vibration and repeated shock, BSI, London.
- Dallard, P., Fitzpatrick, A.J., Flint, A., Le Bourva, S., Low, A., Ridsdill-Smith, R.M. & Willford, M. (2001). "The London Millennium Footbridge." *The Structural Engineer*, 79(22), 17-33.
- European Commission Directorate-General for Research and Innovation (2006). *Final report of ECSC project: Generalisation of criteria for floor vibrations for industrial, office, residential and public building and gymnastic halls*, EUR 21972, <http://bookshop.europa.eu/>, 344.
- European Commission Directorate-General for Research and Innovation (2010). *Final report of RFCS project: Human-induced vibration of steel structures (HiVoss)*, EUR 24183, <http://bookshop.europa.eu/>, 20.
- Feldmann, M., Heinemeyer, C., Butz, C., Caetano, E., Cunha, Á., Galanti, F., Goldack, A., Hechler, O., Hicks, S., Keil, A., Lukic, M., Obiala, R., Schlaich, M., Sedlacek, G., Smith, A. and Waarts, P. (2009) "Design of floor structures for human induced vibrations", *JRC-ECCS Publication*, EUR 24084, JRC 55118, 64.
- Griffin, M.J. (1996) "Handbook of human vibration", Academic Press Ltd, London, 988.
- Hicks, S.J., Brozzetti, J., Rémy, B. and Lawson, R.M. (2003). "Dimensionnement des Planchers Mixtes Acier Béton vis-à-vis des Vibrations." *Construction Métallique*, No. 1, 3-31.
- International Organization for Standardization (1997). ISO 2631-1 *Mechanical vibration and shock – Evaluation of human exposure to whole-body vibration - Part 1: General requirements*, ISO, Geneva.
- International Organization for Standardization (2003). ISO 2631-2 *Mechanical vibration and shock – Evaluation of human exposure to whole-body vibration - Part 2: Continuous and shock-induced vibration in buildings (1 to 80 Hz)*, ISO, Geneva.
- International Organization for Standardization (2007). ISO 10137 *Bases for design of structures – Serviceability of buildings against vibration*, ISO, Geneva
- Murray, T.M., Allen, D.E. & Ungar, E.E. (1997). "Floor Vibrations Due to Human Activity." *AISC/CISC Steel Design Guide Series 11*, American Institute of Steel Construction, Chicago, 69.
- Smith, A.L., Hicks, S.J. and Devine, P.J. (2007). "Design of Floors for Vibration: A New Approach." *SCI Publication 354*, Ascot, 124.
- Willford, M.R. & Young, P. (2006). "A Design Guide for Footfall Induced Vibration of Structures." *Cement and Concrete Industry Publication (CCIP) 16*, Camberley, 82.

Numerical Investigation of the Behaviour of Steel Beams in Steel-Concrete Composite Frames

Naveed Iqbal¹; Marko Pavlovic^{1,*}; Milan Veljkovic¹; Tim Heistermann¹; Fernanda Lopes²; Aldina Santiago²; and Luís Simões da Silva²

¹Dept. of Civil Engineering, Univ. of Belgrade, Serbia; presently, Division of Structural and Construction Engineering, Luleå Univ. of Technology, Luleå SE-97187, Sweden. E-mail: naveed.iqbal@ltu.se; marko@imk.grf.bg.ac.rs; milan.veljkovic@ltu.se; tim.heistermann@ltu.se

²ISISE – Dept. of Civil Engineering, Univ. of Coimbra, Coimbra 3030-788, Portugal. E-mail: fernanda@dec.uc.pt; aldina@dec.uc.pt; luisss@dec.uc.pt

Abstract

The methods proposed by the design codes for single member design in fire situation assume that these members are isolated in their response. The real response of structural members such as beams is, however, more complex due to thermal expansion and the presence of restraints against this expansion by the surrounding structure. It is therefore imperative to study the response of structure at high temperature in a way which includes its interaction with its surroundings such as in a full-scale fire test and in numerical analysis. This paper focuses on the numerical investigation of steel beams, with a concrete slab and connected to concrete filled tubular (CFT) columns through reverse channel connections. The finite element software ABAQUS has been used in this study. The aim of the investigation is to study the behaviour of the composite steel-concrete beam exposed to increasing temperature in fire.

1. INTRODUCTION

The conventional method for analyzing the design strength of a structural member has been the ‘‘standard fire test’’. In the standard fire test an isolated structural member such as a beam or a column is subjected to increasing temperature according to a temperature-vs-time relationship based on the ISO 834 standard fire curve. The drawback of a standard fire test is that it is not representative of the real behaviour of a structural member exposed to fire in a framed structure due to two reasons; It does not consider the interaction of a member with its surrounding structure during fire exposure and also that the standard fire is not representative of a natural fire [Wald et al 2006]. The interaction with the surrounding structure through the connections can have both beneficial and adverse impact on the robustness of the overall structure with respect to its resistance to fire. The redistribution of the load taking place at high temperature from the heated parts to the colder parts of the structure adds to this robustness. On the contrary failure of the connection region for example during the cooling phase might cause a sudden failure.

One way to study the restrained response of a steel beam to fire is to study the behaviour of a sub-frame assembly consisting of a steel beam supported by columns at each end exposed to fire as shown in Figure 1 [Lopes et al 2013]. The test setup is in the form of a ‘rugby goalpost’ where the columns provide the required restraints to the beam during its exposure to high temperature. Lopes et al performed a series of tests on the sub-frame setup to study the behaviour of reverse channel connections with respect to restrained thermal expansion of the beam, its yielding or buckling and at the catenary stage [Lopes et al 2013].

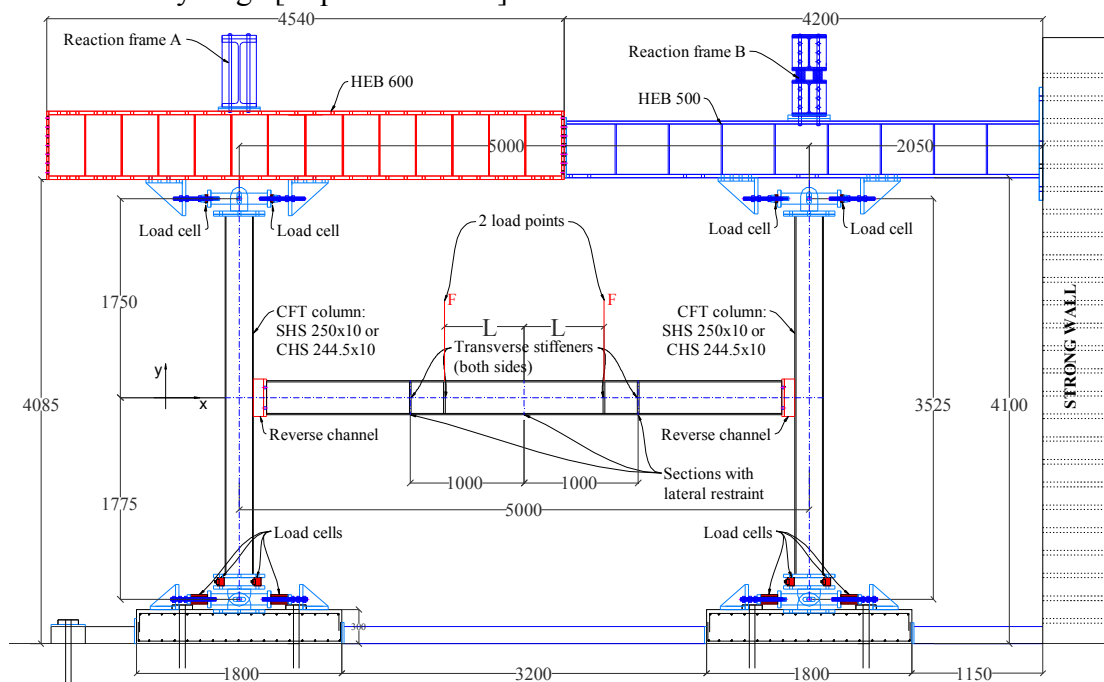


Fig. 1: Sub-frame test setup [Lopes et al 2013].

Full scale fire tests on building are very rare due to the cost and complexity involved in carrying out such tests. A series of tests carried out on steel framed building at the Cardington facility of the Building Research Establishment (BRE) provided a unique opportunity for studying the real behaviour of real structures and their components exposed to fire. Results from Cardington tests have been extensively used for validation of numerical models. In the tests it was observed that in the regions near the connections, the beams underwent local buckling of the bottom flange and web of the beam. The local buckling happens due to the thermal expansion of the beam under axially restrained conditions. The upper flange, due to the restraint from the concrete slab, did not undergo any buckling. The buckling of the bottom flange releases the hogging moment at the supports and thus enables the beam to behave as a simply supported beam, which subsequently allows for large deflection in the beam [Wald et al 2006].

Establishing simplified design procedures that can predict the restrained behaviour of steel beams in fire are very important as design tools. Yin and Wang have proposed one such analytical procedure which can be used to predict the behaviour of a restrained steel beam under the wide range of temperature starting from the initial heating to the catenary stage at very high temperatures [Yin and

Wang, 2005]. It is very important to determine if the proposed method is able to predict the restrained behaviour of beam satisfactorily and the way to ascertain this could be to compare test results or validated finite element model results to the results from the proposed hand calculation procedure. The following sections will provide details of the hand calculation procedure as well as the comparison between the results obtained from the hand calculation procedure and those from finite element models of sub-frames.

2. Analytical Model

The analytical model used here for comparison to FEM has been proposed by Yin and Wang in their publications [Yin and Wang 2005]. The detailed model is not presented here but its general concept is described as follows. The method is intended to describe the behaviour of a steel beam, which is axially and rotationally restrained at the supports, at elevated temperatures. The beam axial force and the midspan deflection, as a function of increasing temperature, are the parameters measured from this model. The general trend of the variation of the axial force in the beam with respect to increasing temperature can be seen from Figure 2. The variation of the axial force with respect to increasing temperature can be divided into three distinct phases described as follows:

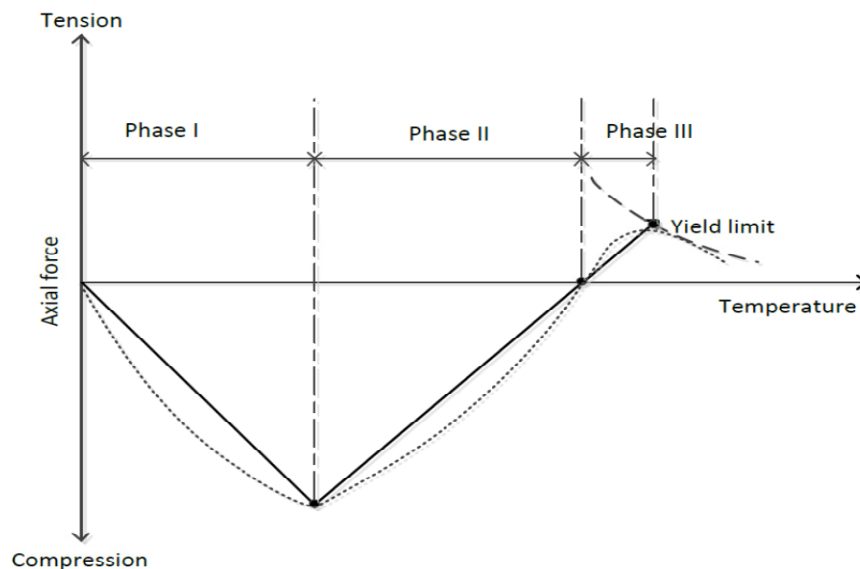


Fig. 2: Axial force variation with respect to increasing temperature.

Phase I:

As the beam is exposed to increasing temperature, initially the thermal expansion of the beam will be restrained by the surrounding structure. This restrained thermal expansion will produce compressive force in the beam whose magnitude will depend on the level of the stiffness of axial restraint. The compressive force in the beam will continue to increase until the beam cross sectional yield limit is reached under the combined effect of the bending moment due to applied loading and the

axial compressive force due to restrained thermal expansion. For a slender beam, however, the beam will undergo flexural buckling before the yield limit is reached.

Phase II:

When the beams capacity is reached in compression, it starts exhibiting vertical deflection at an increasing rate. The vertical deflection of the beam introduces contraction of the beam at the ends, which compensates for some of the thermal expansion. This results in the reduction of the compressive force in the beam and goes on decreasing with the increasing vertical deflection until a limit is reached i.e. the beam contraction becomes equal to its thermal expansion. At this point the axial force in the beam is equal to zero and the temperature of the beam corresponds to the conventional critical temperature i.e. the temperature at which the bending moment resistance of the beam is equal to the bending moment due to applied loading.

Phase III:

Beyond the conventional limiting temperature the beam will not be able to resist the applied loading through flexural resistance alone. The catenary action in the beam will provide the additional resisting mechanism as the axial force in the beam now becomes tensile. The vertical deflection of the beam now starts to increase at a very high rate as the flexural resistance of the beam is reduced significantly and the bending moment resistance is offered by the product of the resisting tensile axial force at the connections and the midspan deflection. The axial force continues to increase until a limit is reached which is imposed by either the capacity of the connection components to the axial force or the yield of the beam cross section in tension.

The hand calculation procedure presented above has been validated against finite element model results using the sub-frame model, which provides simultaneously flexible axial and rotational restraint to the beam in a detailed study [Iqbal 2013]. Results from that study have also been used here for comparison as discussed below.

3. Finite Element Model (FEM)

3.1 Test setup and mesh

The sub-frame setup is shown in Figure 1, which consists of a steel beam supported by a concrete filled tubular (CFT) column at each end. The connection between the steel beam and the CFT column consist of a channel section whose legs are welded to the face of the column section and the web is bolted to the endplate of the steel beam as shown in Figure 3. The dimensions of the different components of the sub-frame setups used in the fire tests and then for validation of the FE-models are provided in Table 1.

The model is created using finite element software ABAQUS. All parts of the sub-frame are modelled using 3D reduced integration solid elements C3D8R. The

concrete slab on top of the steel beam is introduced later in the model, which is modelled by using four node shell elements S4R.

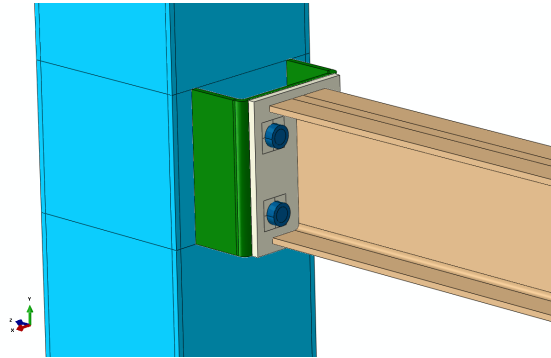


Fig. 3: The connection region between steel beam and the CFT column.

Table 1. Dimensions of the Sub-frame components

Setup	Column	Beam	Connection	Beam span [m]
1	SHS 250x8	UB 178x102 x19	UK SHS 180x42.7	2
2	SHS 250x10	IPE300	U200x90x10	5
3	SHS 250x10	IPE300	U200x90x8	5
4	SHS 250x10	IPE300	U200x90x12	5

3.2 Temperature application

The temperature is applied to the beam by assigning it as a predefined field to the different regions. In the initial step the 20°C temperature is applied to the whole model which is then increased in the ‘heating’ step according to an amplitude curve defining the temperature vs. time relationship. The temperature gradient through the depth of the beam is defined by means of splitting the beam into two zones i.e. the top zone (top flange) and the bottom zone (bottom flange plus web) and applying different temperature to them separately as shown in Figure 4. The temperature of the top zone will be slightly lower than the bottom zone due to the heat sink effect of the concrete slab. According to EN 1994-1-2 the temperature of the web can be taken as equal to that of the bottom flange if the height of the beam does not exceed 500 mm, which holds true for the given beam dimensions and therefore using same temperature for the web and the bottom flange is not without justification [Hanus F. 2010].

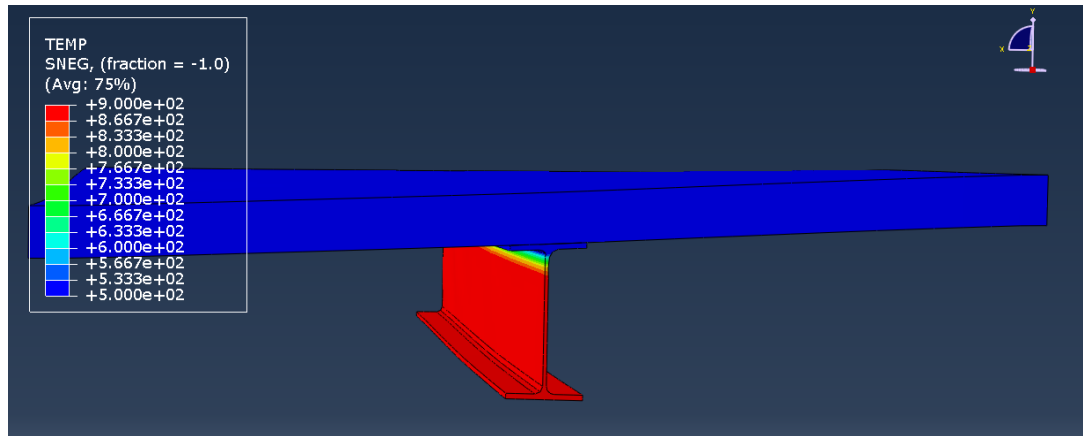


Fig. 4: Temperature gradient through the web of the beam as a predefined field.

3.3 Analysis procedure

The FE-analysis of the sub-frame model without the slab was performed using the ABAQUS implicit solver. The convergence problems due to material softening at very high temperatures are taken care of by introducing artificial damping in the model through ‘dissipated energy fraction’ option in ABAQUS. Introducing the concrete slab on top of the steel beam in the model produced convergence problems, which are then solved by performing a quasi-static analysis using the dynamic explicit solver. Variable non-uniform mass scaling with a target time increment of 5e-6 sec was used. Duration of load application step was set to last for 1.0 sec, while heating step, with thermal action lasted for 4.0 sec.

3.4 Validation of FE-Model

The finite element models of the sub-frames are validated against the laboratory fire tests conducted on the list of sub-frame setups shown in Table 1. The parameters that are compared between the fire tests and the FE-models include the maximum compressive force, the maximum tensile force and the maximum midspan deflection in the beam. These parameters are measured as a function of increasing temperature for both fire tests and FE-analysis. The results shown in Figure 5 to Figure 6 show the comparison between the two [Iqbal 2013].

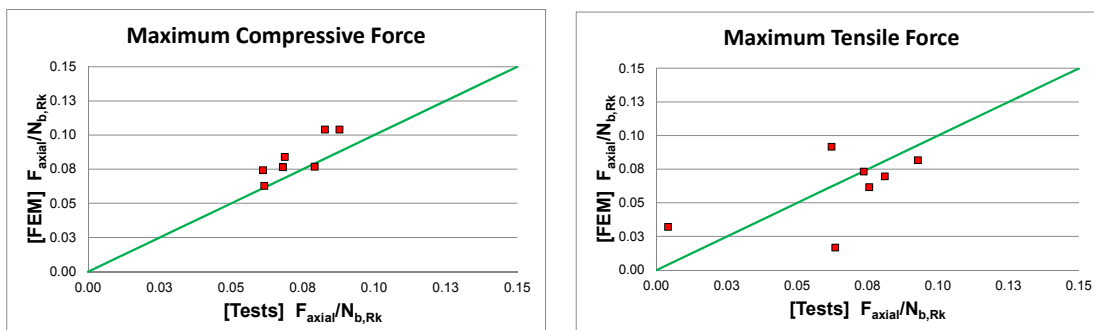


Fig. 5: Comparison between Tests and FEM (Maximum tensile and compressive force).

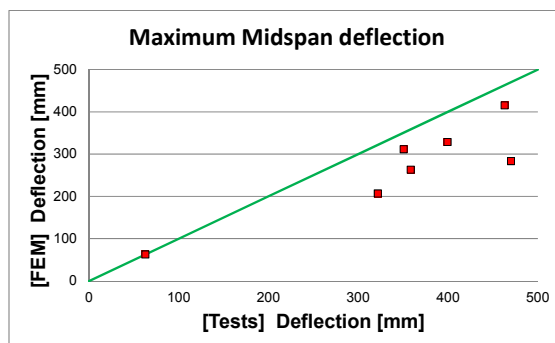


Fig. 6: Comparison between Tests and FEM (Midspan deflection).

The results show that maximum compressive force in the beam is very closely matched between the tests and the FE-analysis. The maximum tensile force exhibits comparatively more scattered results for the comparison between the tests and FE-analysis. The midspan deflection is seen to be higher in the tests than the FE-models which could be attributed to the generally stiff behaviour of the FE-model.

3.5 FE-Model with concrete slab

In a real structural frame a composite steel beam is always supporting a concrete deck and the interaction between them is usually through steel studs welded on the top surface of the top flange of the steel beam and embedded into the concrete deck. These studs transmit the longitudinal shear at the interface between the steel beam and concrete deck. The interaction between the concrete deck and the steel beam will produce a composite action in the beam, which might produce a response of the beam in fire that is very different than a steel beam without concrete deck.

The concrete deck is added to the sub-frame model as a shell using S4R elements whose reference surface (chosen as the 'Bottom surface' in the shell offset) coincides with the top surface of the beam top flange. Figure 7 shows the concrete deck on the top flange of a sub-frame model with its rendered thickness. The model also shows a beam on the opposite side of the column, which is introduced to model the continuity of the slab at the connection region.

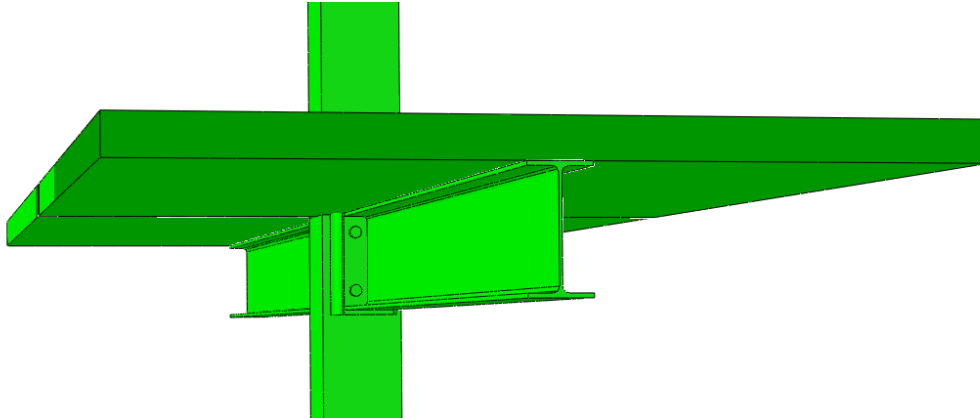


Fig. 7: FE-Model of the sub-frame with the concrete deck as a shell.

Symmetry boundary conditions are applied along the longitudinal edges of the slab, which means that similar parallel sub-frames are present. At the cross sectional edges symmetry boundary conditions are again used since only half the sub-frame is modeled utilizing the symmetry with respect to the midspan of the beam. The other boundary of the concrete slab is located in the adjacent compartment which could either be fire compartment or not which makes it unclear what will happen there. The interaction between the top flange of the beam and the concrete deck is modeled by using a tie constraint at the interface, which would model full interaction and not consider any reduction in stiffness due to slipping of the studs. The reinforcement bars are entered into the concrete deck by defining the ‘Rebar layers’ as part of the shell section properties. The diameter of each bar is 6mm with 200 mm spacing between adjacent bars and applied in both long and short directions of the slab.

4. Results

4.1 Without concrete slab (FEM vs. HCM)

A steel beam without a concrete slab is expected to be at uniform temperature through the span and the cross section since the heat sink effect of the concrete slab is absent and steel itself has very good heat conduction properties. Figure 8 shows how the axial force in the beam changes as a function of changing temperature for setup 1 from Table 1 and uniform temperature distribution. The comparison between the proposed hand calculation procedure described above and the FE-analysis in Figure 8 shows how closely the hand calculation procedure is able to predict the axial force in the beam.

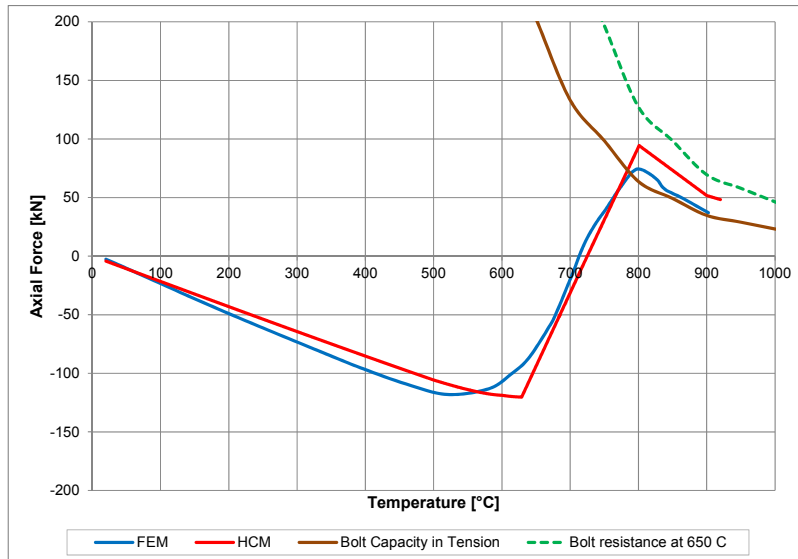


Fig. 8: Axial force in the beam as a function of temperature (HCM vs FEM).

The limit on the maximum catenary force in the beam is imposed by the capacity of the beam in tension. In reality however the connection components will impose the limit on the beam capacity as can be seen from Figure 8 the resistance of the bolts in tension is reached earlier than the cross section of the beam could undergo yielding under tension. Protecting the connection region will, however, increase their capacity in tension due to a lower temperature and thus prevent connection failure.

A concrete slab present at the top flange of the beam will impact the temperature distribution through the beam cross section due to the heat sink effect brought about by it. The temperature gradient depends on the height of the beam cross section and as was discussed in Section 3.2 the temperature in the bottom flange and the web can be considered as the same according to Eurocode. The reduced temperature will only be in the top flange of the beam which is in contact with the concrete slab. Setup 4 with a beam in the opposite direction of the column is used for comparison between the hand calculation procedure and finite element results for a slightly lower temperature of the top flange than the web and bottom flange. This example is shown to see the effect of the temperature distribution alone without the composite effect due to the presence of the concrete slab. Figure 9 shows the variation of the axial force in the beam with temperature.

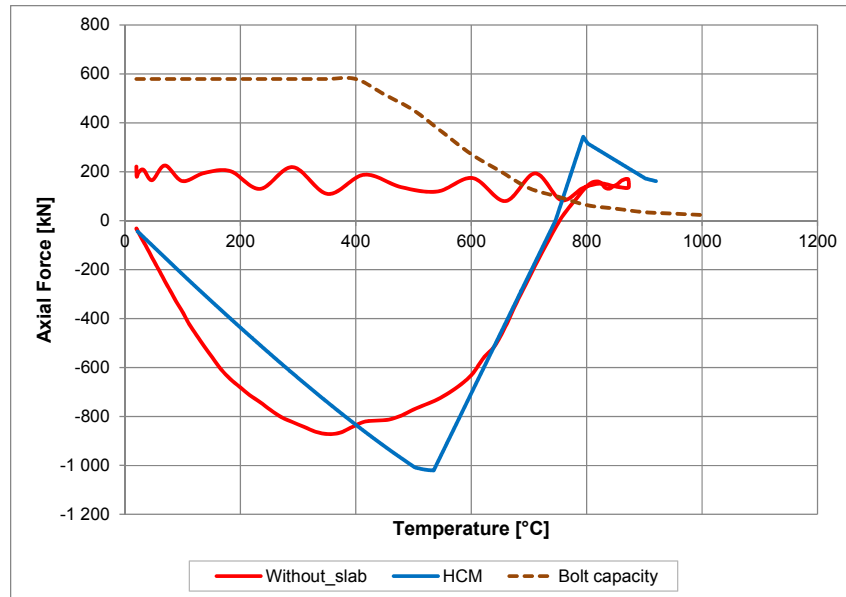


Fig. 9: Axial force in the beam as a function of temperature (HCM vs FEM).

The maximum compressive force in the beam is slightly overestimated by the hand calculation procedure which is conservative. FE results for the cooling phase shows that the tensile force is increasing in the beam due to contraction. It can be seen that at 20°C the level of the tensile force in the beam is around 200 kN. Once again the important thing to consider would be the level of strains in the bolts and they are able to resist these tensile strains. Figure 10 shows the deformed shape of the connection components at maximum catenary stage. The level of strains is well beyond the limit and therefore the upper row of bolts has already failed at this of the catenary force in the beam. In the uniform temperature case the plastic hinge is formed in the beam near the connection, which releases the hogging moment from acting on the connection region.

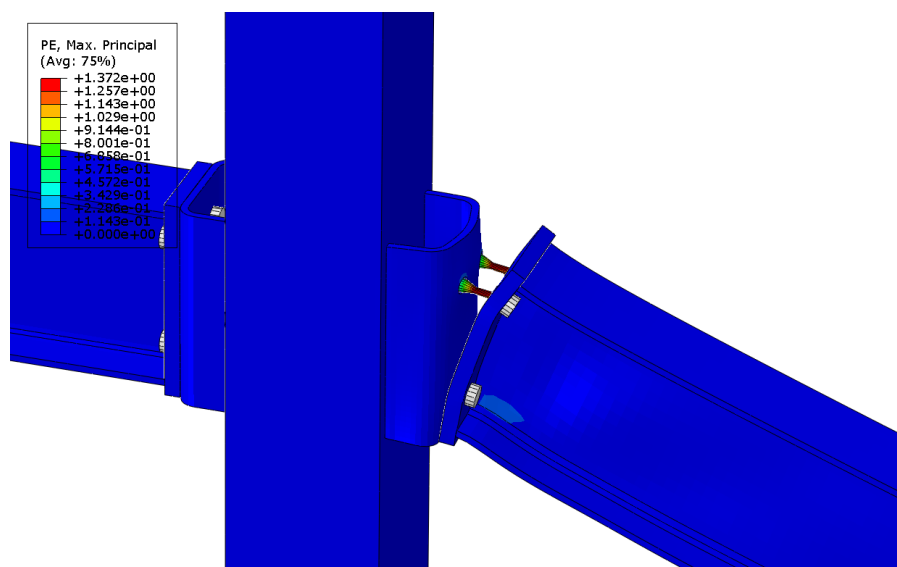


Fig. 10: Deformed shape of the connection region at maximum catenary force.

4.2 With concrete slab (comparison with the beam without slab)

Adding the concrete deck on the top flange which is constrained to it through tie constraints will induce a composite action in the beam. The beam is expected to behave in a much stiff manner than it was without the concrete deck. Initially as the temperature increases the lower part of the steel beam (web and bottom flange) being at a much higher temperature compared to the top flange and the slab will undergo considerable expansion. This differential expansion will induce tensile stresses in the slab as shown in Figure 11 which will exceed the tensile cracking strain already around 150°C.

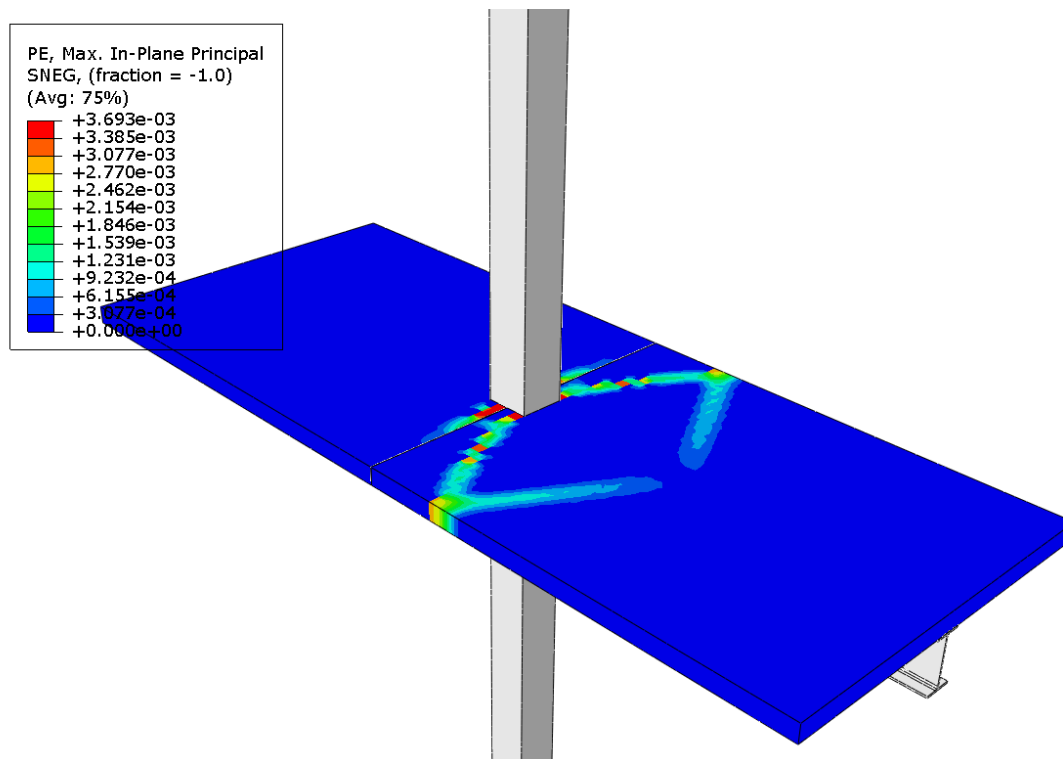


Fig. 11: Maximum In-plane Plastic Strains in the concrete deck.

The variation of the axial force and the vertical midspan deflection in the composite beam as a function of the temperature is shown in Figure 13 and Figure 14 respectively. The axial force in the beam is seen to be exclusively compressive and no catenary action is observed in the beam. As the beam starts to cool down from its maximum temperature of 900°C the compressive force is seen to decrease. The maximum deflection observed in the beam is very small (around 30 mm) and as the beam cools down a reverse bowing is observed which causes the beam to bend in the opposite direction. The connection components are observed to be not subjected to very large forces in this case as they were in the case of no concrete deck.

The behaviour of the composite beam can be attributed to the very stiff interaction between the concrete deck and the top flange of the beam. It is understood that the steel beam will have very low stiffness at temperatures in excess of 600°C at

which stage the beam normally starts to transit into the catenary phase. Figure 12 shows the stress distribution the steel beams at around 140°C before the concrete in the composite beam cracks. The steel beam in the composite section has no compressive stresses yet at this stage which could be attributed to its interaction with concrete deck which resists its thermal expansion. In a real situation the behaviour of the slab would be more like a membrane action. The other important aspect need to be considered here is that the interaction between the top flange and the concrete deck is also very stiff whereas in reality this interaction will take place through studs welded to the top flange and embedded into the concrete deck. This interaction will have a finite stiffness and not the full interaction considered here in the given situation.

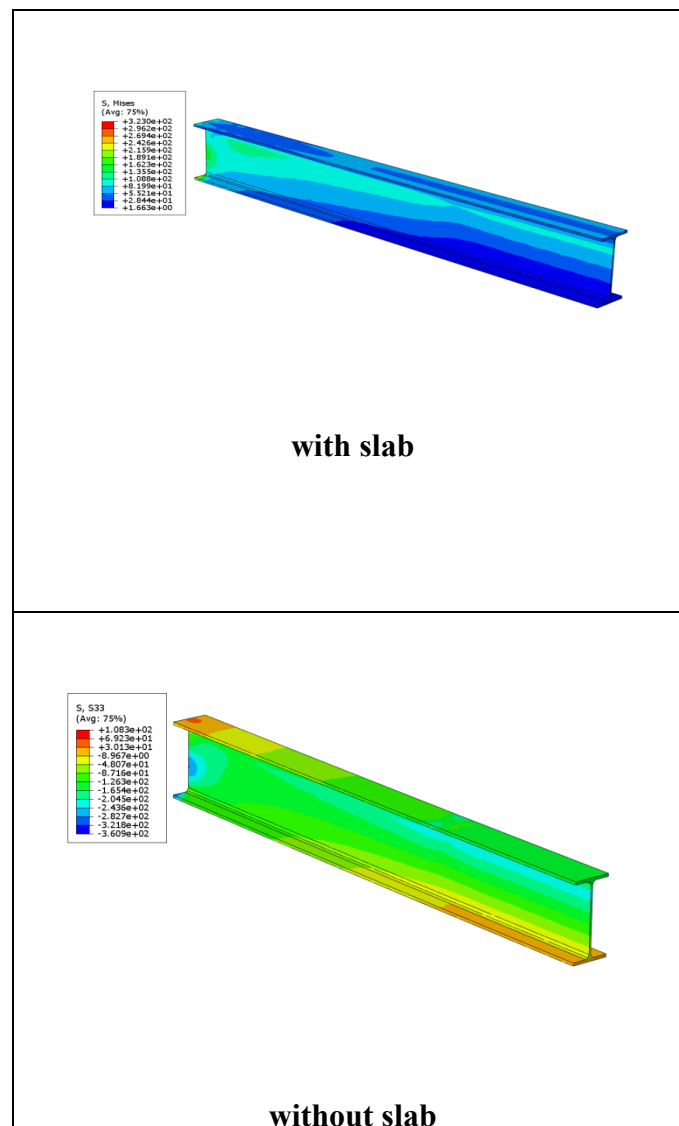


Fig. 12: Longitudinal stresses in the steel beams at 140°C .

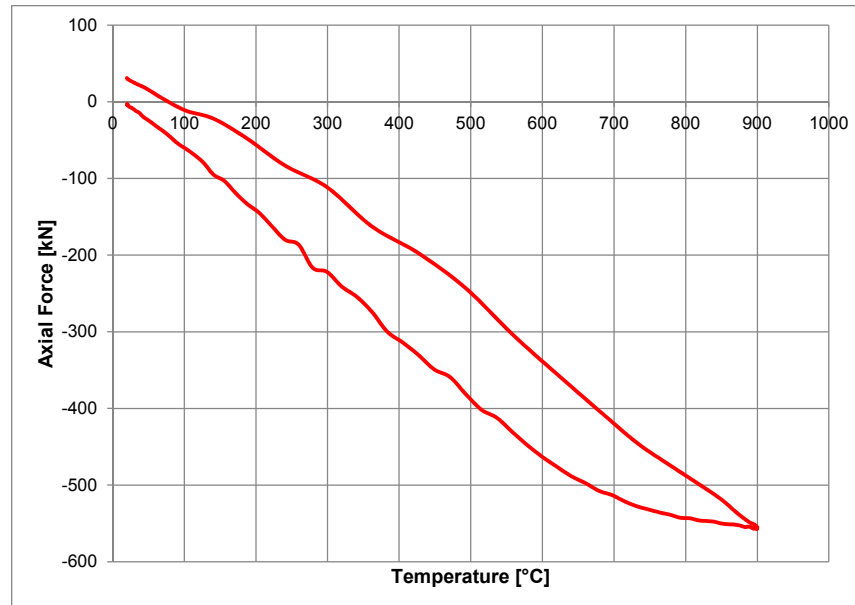


Fig. 13: Axial force vs. temperature.

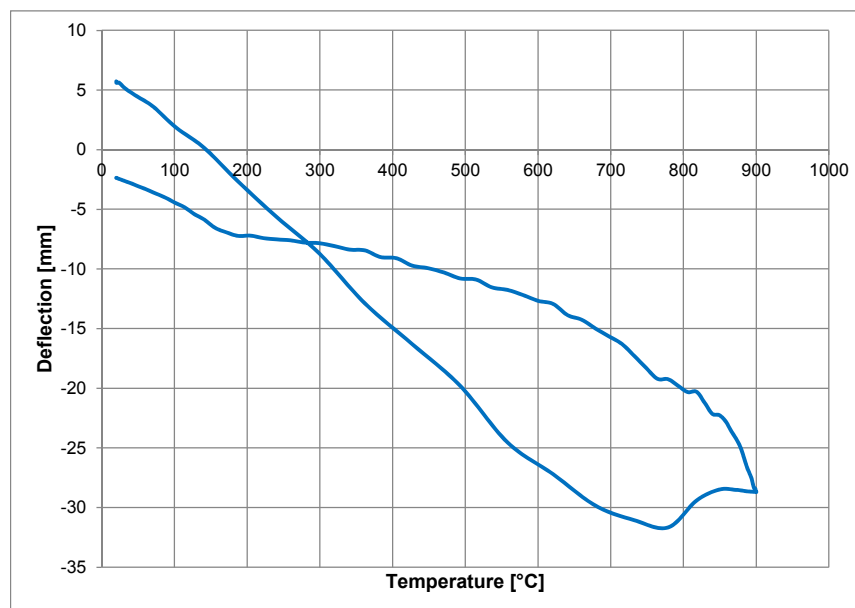


Fig. 14: Midspan deflection vs. temperature.

5. Conclusions

This paper presents a comparison between proposed hand calculations procedure and the finite element results. This is done by using the finite element models validated against test data, as the validation examples [Iqbal 2013]. For the sake of comparison each model is subjected to uniform temperature and temperature gradient through the depth of the cross section each separately loaded with 0.4 and 0.6 times the cross sectional bending moment capacity of the beam at ambient temperature. The supports consisting of the reverse channel connection and supporting columns provide finite axial and rotational restraint stiffness to the beam,

which is taken into account in the improved hand calculation method [Iqbal 2013]. The results show that such hand calculation procedure can predict the beam behaviour with sufficient accuracy especially in the case of uniform temperature distribution.

At the maximum catenary force in the steel beam it has been observed that the level of strains produced in the top bolt row are in excess of 20%, which are enough to cause their rupture. This indicates that the limit to the maximum catenary (tensile force) in the beam is limited by the capacity of the connection components (in this case bolts). It is therefore very important to determine if the capacity of the connection components is enough to withstand these forces to prevent sudden failure (especially in the case of bolt failure).

The concrete deck addition to the top flange of the beam has shown that the behaviour of the beam, in the particular example considered, becomes very stiff due to the presence of composite action between the steel beam and the concrete deck. Maximum deflection in the steel beam at 750°C (critical temperature) is 200 mm whereas for the composite beam it is only around 30 mm. The level of axial force at the same temperature is almost zero for the steel beam without slab whereas for the composite beam the axial force is around 500 kN compressive force. It is however important that for accurate modeling of the composite action, which is much closer to real composite beam behaviour, the slab is modeled with membrane action in the transverse direction and also that the interaction between the top flange and concrete deck by realistically modeled by modeling the studs with finite strength and stiffness.

ACKNOWLEDGMENTS

The research that produced these results was supported by funding from the European Community's Research Fund for Coal and Steel (RFCS) under grant agreement n° RFSRCT-

2009-00021. Acknowledgements are also gratefully due to the European Regional Development Fund (NSS – Nordic Safety and Security).

REFERENCES

- Wald, F., da Silva, L. S., Moore, D. B., Lennon, T., Chladna, M., Santiago, A., Benes, M., Borges, L., *Experimental behaviour of a steel structure under natural fire*, Fire Safety Journal, vol. 41, 2006, p. 509 – 522
- Lopes, F., Aldina, S., da Silva, L. S., da Silva, J. G. S., Iqbal, N., Veljkovic, M., *Full-scale Fire Tests on Composite sub-frames with reverse channel connections to CFT columns*, Composite Constructions VII, 2013
- Iqbal, N., *Restrained behaviour of beams in a steel frame exposed to fire*, Licentiate thesis, Luleå University of Technology (LTU), 2013
- Yin, Y. Z., Wang, Y. C., *Analysis of catenary action in steel beams using a simplified hand calculation method, Part 1: theory and validation for uniform temperature distribution*, Journal of Constructional Steel Research, Vol. 61, 2005, p. 183 – 211

- Yin, Y. Z., Wang, Y. C., Analysis of catenary action in steel beams using a simplified hand calculation method, Part 2: theory and validation for non-uniform temperature distribution, *Journal of Constructional Steel Research*, Vol. 61, 2005, p. 213 – 234
- Hanus, F., Analysis of simple connections in steel structures subjected to natural fires, PhD thesis, Faculty of Applied Sciences, University of Liege, 2010

Behavior of a CFT Truss Girder with Precast Decks under Negative Bending Moment

In-Gyu Kim¹; Young-Jin Kim²; Hyun-Chul Oh³; Hyang-Wook Ma⁴; and Chul-Hun Chung⁵

¹Daewoo Institute of Construction Technology, Suwon 440-210, Korea. E-mail: ingyu.kim@daewooenc.com

²Daewoo Institute of Construction Technology, Suwon 440-210, Korea. E-mail: youngjin.kim@daewooenc.com

³Daewoo Institute of Construction Technology, Suwon 440-210, Korea. E-mail: hyunchul.oh@daewooenc.com

⁴Daewoo Institute of Construction Technology, Suwon 440-210, Korea. E-mail: hyangwook.ma@daewooenc.com

⁵Dankook Univ., Youngin 448-701, Korea. E-mail: chchung5@dankook.ac.kr

Abstract

For the fast construction of bridges, it is necessary to design bridges as light and modular superstructures. For this purpose, a new composite bridge constructed by segmental method is suggested, which consists of concrete filled steel tubular girders and prefabricated concrete decks (Kim 2010). This paper presents a study of the structural behavior of the proposed CFT truss girder at a continuous under negative bending moment. A numerical analysis is performed to verify the structural behaviors of CFT truss girder in continuous support. Based on the results of a numerical analysis, a model with a continuous composite member shape is fabricated and static tests are conducted.

1. INTRODUCTION

As the deterioration of public infrastructures and cost saving for the construction of public infrastructure business becomes an issue, the topics of rapid construction methods for economic feasibility, durability and maintenance of civil structures have become a major challenge. New technology, research and development related to these subjects have been furthered in response to this growing challenge. From the point of view of cost saving and upgrading construction efficiency, interest in composite construction, which referred to as compound structure or hybrid structure, has increased in order to address that need. At this point, composite and compound bridge types using concrete filled steel tube (hereinafter referred to as "CFT"), have maximized the advantages of each main materials, concrete and steel, in construction. Furthermore, CFT bridges have an excellent appearance, are economical, lightweight, and efficient to maintain, leading to various studies being conducted.

Pre-fabricated types of truss girder bridge systems, which are designed to improve the construction of CFT bridges, will be introduced in this study. For the construction of pre-fabricated CFT girder bridges, separate segments were

manufactured in a factory to improve the workability of filling process in the CFT truss girder bridges. Each segment was filled with concrete at the factory, then transferred to the work site and erected for concrete filling in order to perform effectively. Each segment joint is constructed with bolts or welded in-situ. In addition, truss girders enhance the overall appearance of bridges through spatial openness. The CFT truss girder bridges have less sight obstacles than existing types, such as steel-box bridges, and they have approximately 50m of pier span length and 2.5m of girder height, which are equal to steel-box girder bridges. Bridge decks can accommodate cast-in-place concrete decks or precast decks, regardless of the upper chord curvature. The CFT truss girder bridges are light-weight and have an excellent see-through view, as shown in Figure 1.



Figure 1. Perspective Image of a CFT truss girder bridge.

2. RESEARCH AND DEVELOPMENT OF THE CFT TRUSS GIRDER BRIDGE

2.1 Overview of the construction method and development contents

Pre-fabricated CFT girder bridges in the shape of truss using CFT have excellent axial rigidity and can save more steel quantity than steel-box girder bridges. Upper and lower chords of truss girders are compound sections of CFT, and the vertical and diagonal chords consist of hollow steel tube. However, existing CFT truss girder bridges have been built in the work place with steel tubes, and then filled with concrete. Therefore, its drawbacks include increased construction cost due to a long construction period and a high-pressure concrete filling method which ensure to attain adequate filling. In order to overcome these drawbacks, The steel tubes are manufactured as a unit segment to fill CFT with concrete in advance at the factory in pre-fabricated CFT girder bridge construction method. And then the segments are only assembled in-situ. Therefore, it can shorten the construction period and is capable of more cost savings than existing bridge methods. The key point of this method is the joint of each segment. In particular, the joint method (welding, bolting etc.) and shape of joint are very significant factors in this bridge system. Authors have conducted numerical and experimental validations numerous times and based on these validations, authors have completed the pre-fabricated CFT truss girder bridge. From the initial stage of this study, various types of experiments have been

done to complete the pre-fabricated CFT girder bridge systems. First of all, as shown in Figure 2, a 4-points bending test measure the pure internal force of CFT



Figure 2. 4-Points bending test on CFT.

As a result of the 4-points tests on CFTs, the efficiency of the concrete filling process for single CFT has increased and rapid internal force, caused by initial defects, has been prevented. This means that induced stress on the concrete had been exposed to bending and compression force at the same time, but, due to constrained effect by concrete, internal force has increased through the buckling-prevention-effect on steel tubes. In other words, when CFTs were used as simple beams, CFT had an effect of preventing rapid reduction in internal force.

Many studies on the bending performance of truss girders have been conducted. Experiments on CFT truss girders have been performed as shown in Figure 3. A CFT truss girder is usually comprised of chords and braces. The chords and braces are jointed together with combination of fillet weld and butt weld. CFT truss girder which has a straight upper chord and an arched lower chord is suggested. Upper and lower chords are concrete filled tubes, and braces are circular hollow section (CHS) tubes as illustrated in Figure 3. Two specimens with 20 meter length and different heights are manufactured for the test of constructability and behaviors. Each specimen consists of three prefabricated segments and four bolted joints to be assembled together. As a result of the tests, the upper chords are under compression except top sections at the ends. Due to arching action of the lower chords with fixed end conditions rotationally, the arched lower chords are subjected to compressive stress at the ends and tensile stress at the center.



Figure 3. Test of the single CFT truss girder.

Pre-fabricated CFT and girders have curvature because the adjoining area on bridge decks have a section of cylindrical shaped steel tubing so they have an unstable upper working space compared to regular bridge structures such as steel-box girder bridges and steel plate girder bridges. This unstable upper working space reduces construction performance and stability performance while combining decks and girders through shear studs. Therefore, as shown in Figure 4, authors achieved a higher degree of construction performance and stability performance by designing separate upper shapes. Furthermore, separate studies are being conducted to secure the performance of operating equipment when setting studs and are currently installing equal and unequal angles for concrete pouring on decks. These developments can be applied to both concrete-in-place decks and precast concrete decks.

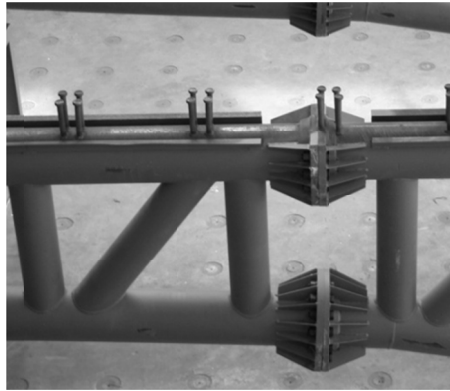


Figure 4. Shape of upper chord for binding precast concrete decks.

For an evaluation of the overall behavior of CFT bridges, authors have produced a bridge model test that spans 20m in length and has a width of 3.6m. This model was subject to static and fatigue tests as shown in Figure 5 and 6. For static tests, using 2 actuators of 1,000kN each, authors applied a load to the model as shown in Figure 5. For fatigue tests, authors applied a load of 96kN on the model and then repeatedly applied the load over 2,000,000 times.

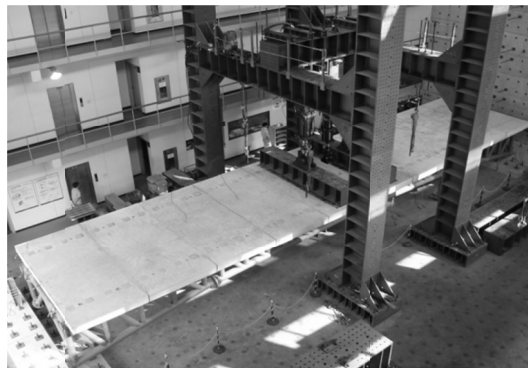


Figure 5. Static test on CFT models.

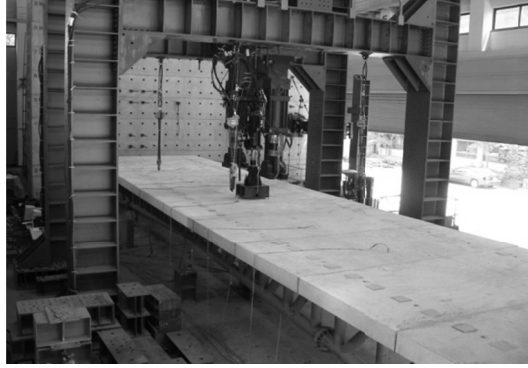


Figure 6. Fatigue test on CFT models.

Due to the constraint effect of the arched lower chords, the arched lower chords are under tension at the center and compression at the ends. This result means that CFT truss bridge with arched lower chords is highly efficient and available for the short and medium bridges. The load capacity of CFT girder bridges under elastic condition is approximately three times greater than the design load based on FEM analytical method, 432kN. Because the maximum tensile strain at the center is greater than the maximum compressive strain at the end, the load capacity of the suggested CFT girder bridge is governed by the section at the center of the arched lower chords. Slippage between upper chords and decks is not observed until the strain hardening of the chords during the test. After completing the test, the filled concrete and the steel tubes are not separated at the center of the chords. This can be regarded as the ductile behavior of the suggested CFT truss girder bridge.

3. BEHAVIOR EVALUATION OF PRE-FABRICATED CFT GIRDER UNDER NEGATIVE BENDING MOMENTS ON CONTINUOUS SUPPORT POINTS

3.1 Overview

As discussed earlier, a study on single spans with pre-fabricated CFT truss girders has been progressing up to the present time. However, for continuous spans of CFT truss girders, authors needed to validate the moment of negative bending for the continuous supporting points. Authors examined various types of supporting points in the case of continuous spans for pre-fabricated CFT trusses. Supporting points are various in types, which are shown in Figure 7, and are based on combined shapes with top of the pier. Figure 7(a) is a continuous type of with upper and lower chords embedded in the coping points of the pier. Figure 7(b) is a continuous type with only the lower chords embedded in the coping points of the pier. Figure 7(c) is a normal continuous girder type using bridge seats without embedding into the coping points of the pier. Each type has its strengths and weaknesses, and its behavioral characteristics and functional ability are determined according to the span shape and girder height employed.

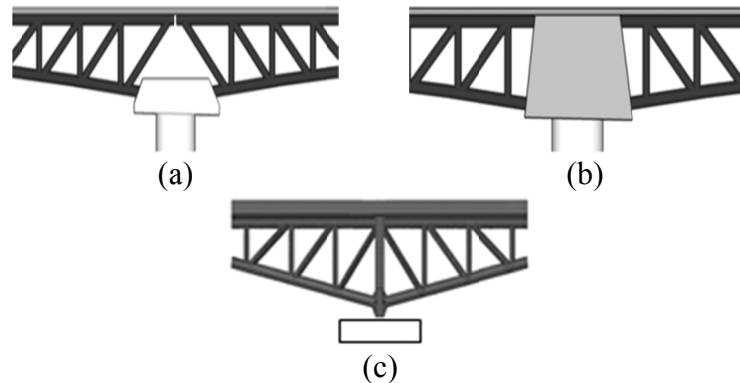


Figure 7. Types of truss based on combined methods of CFT upper and lower chords and coping points of piers, (a) Lower chords embedded in coping (b)Upper and lower chords embedded in coping (c)Bridge bearing on coping.

In Figure 7(a) and 7(b), due to the embedded chords the weight on the center of the spans can be reduced and, based on the shapes of the lower chords at the supporting points, the effect of negative bending moment will be reduced. Therefore, effective truss girder shapes can be made with a largely increased effect of axial force. However, due to temperature loads, in the case of bridges with long supporting spans, the stress on the span sections increased, contrary to what was demonstrated previously. Considering the temperature load on continuous bridges with bridge seats on the coping points of piers which are free from temperature stress, they are more effective in long-supporting-span girder bridges. For the lower chords, arch-shaped bridges are desirable, but they are difficult to manufacture and have little arch-shape effect in the case of long-supporting-span bridges, and therefore, both of straight upper chord and straight lower chord have been shown to be more realistic.

In Figure 7(c), through the examination of a the moment of negative bending on pre-fabricated CFT truss girders, authors checked and confirmed the behavior of the upper chords, lower chords and diagonal chords on the continuous supporting points.

Basic drawings of specimen were designed through finite element analysis method. For an analysis, authors applied loads with total of 480kN –120kN each as shown in Figure 8. As a result of the analysis, the axial force, which is the primary force applied to the specimen, and the diagram at the time of application are shown in Figure 9 and their values are included in Table 1.

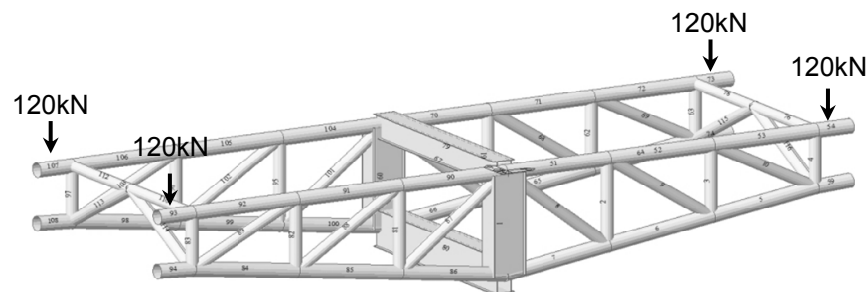


Figure 8. Loading of negative bending moment on continuous supporting points of CFT truss girder bridges test model.

Table 1. Axial force and moment values of finite element analysis Results.

	Upper chords	Lower chords	Remarks
Maximum axial force	56.91kN	-72.52kN	
Maximum moment force	33.78kNm	29.42kNm	

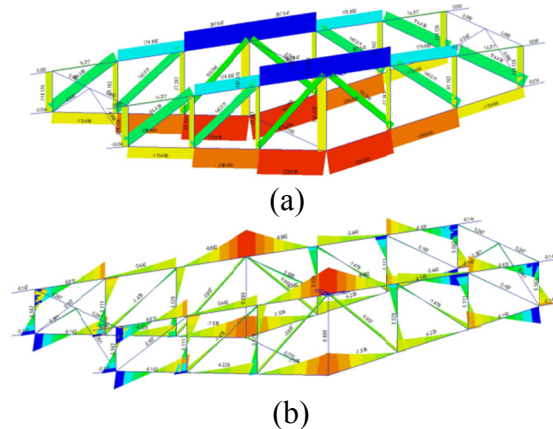


Figure 9. Finite element analysis results of continuous supporting points of CFT truss girder bridges test model: (a) Axial force diagram; (b) Moment force diagram.

The specification of the experiment specimens are shown in Table 2 and the shapes are in Figure 10. Compression strength of filling concrete was 35Mpa. Yield stress of steel was 240Mpa and allowable stress was 140Mpa. The thickness of diaphragms was 8mm.

Table 2. Description of experiment specimen.

Chord	Diameter(mm)	216.3
	Thickness(mm)	8.0
Brace	Diameter(mm)	165.2
	Thickness(mm)	7.0

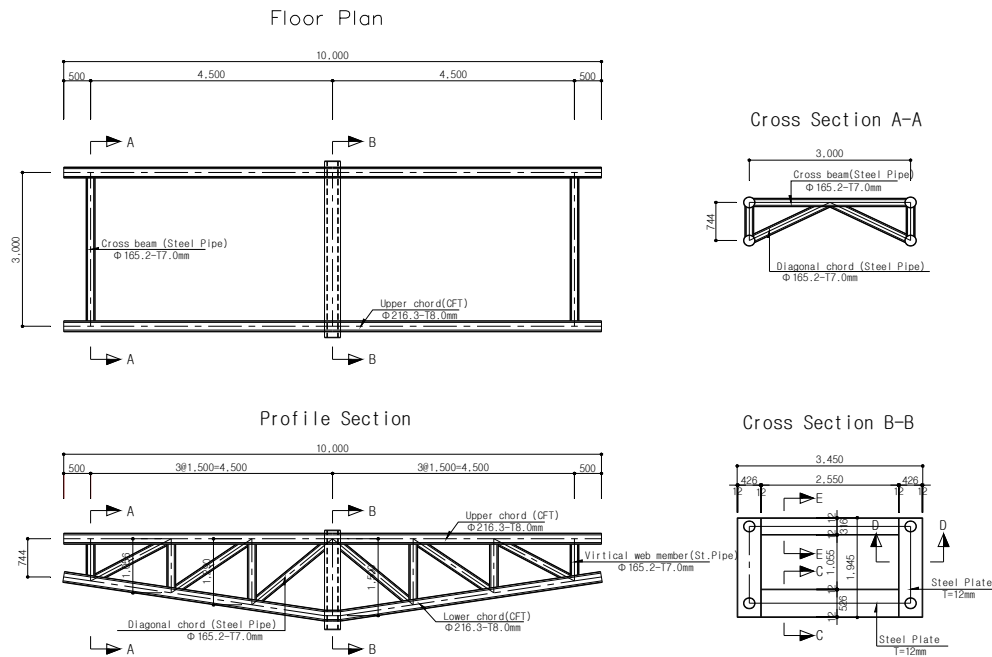


Figure 10. Experiment specimens for negative bending moment onto continuous supporting points of CFT.

3.2 Specimen and test set-up

An experimental model to test the continuous supporting points of CFT truss girder bridges was manufactured in a factory with a single steel truss with a length of 10m and a width of 3.0m. It was filled with concrete for upper and lower chords. The process is shown in Figure 11. Bridge decks were combined with precast concrete decks. The size of a deck was 2.0m in length and 3.6m in width and a total of 5 deck panels were made. Authors have introduced a compressed force of 7MPa for the deck through internal tendons to integrate with decks.

In order to measure gauges were attached in multiple locations as shown as Figure 12. A total of 120 gauges were attached to measure the steel strain and the deflection of cantilever sections and 1/4 length sections of the spans were measured through LVDTs. Concrete strain gauges were also attached on the deck floors. Five steel strain gauges are mounted on the top, S1, S2, S3 and the bottom of each chord which are divided by the same angle as shown as Figure 12(a) and 11(b).

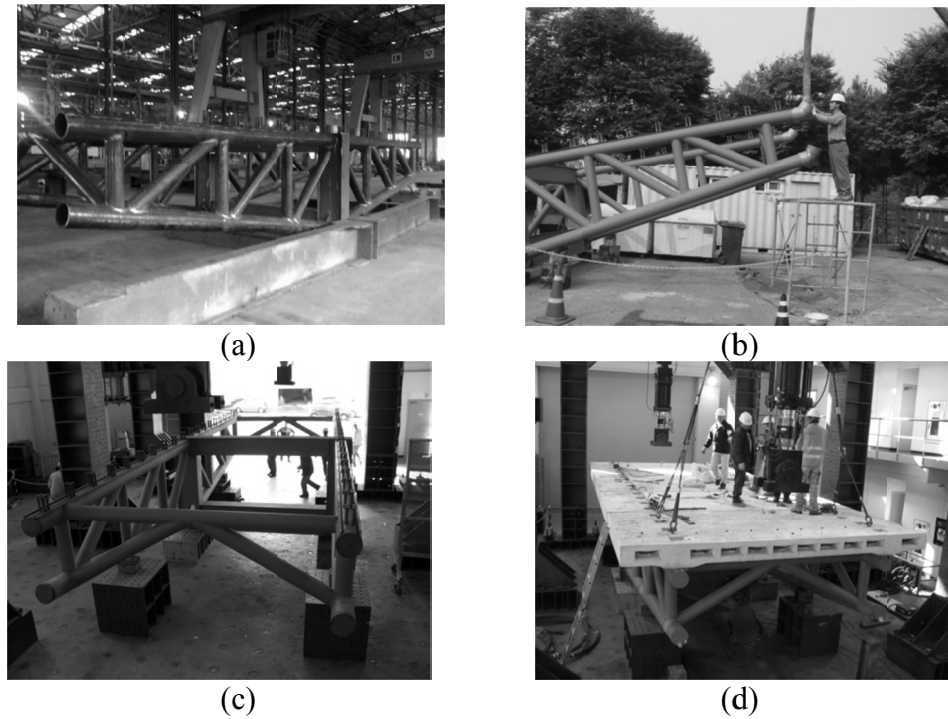


Figure 11. Manufacturing process of the experimental model for the testing of continuous supporting points of CFT truss girder bridges: (a) Production of girder; (b) Filling concrete into steel tube; (c) Setting girders; (d) Combining precast deck.

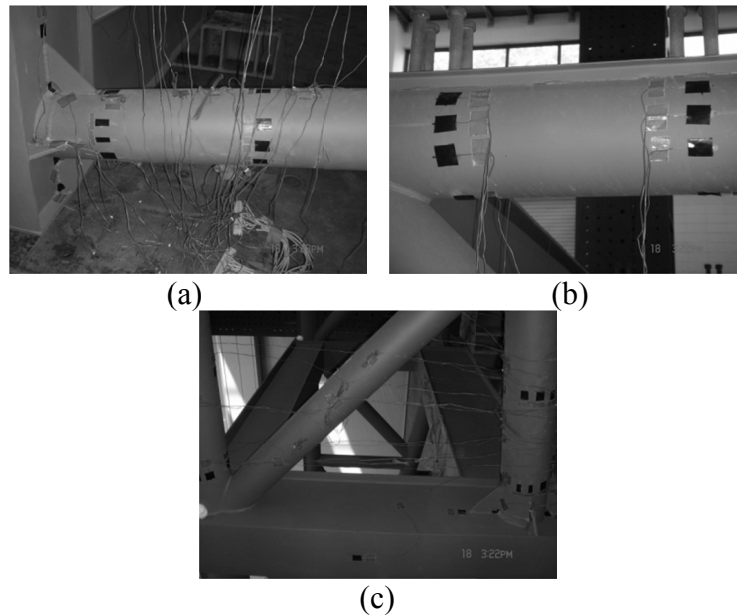


Figure 12. Locations of the strain gauges: (a) Lower chords at the center points; (b) Upper chord at 1/4 length points; (c) Diagonal chord.

3.3 Experiment results

The experiment on the continuous supporting points was conducted twice. First, authors conducted a negative bending moment experiment on the CFT truss girders of the experimental specimen. At this time, the loads applied to experiment specimens were controlled to move within a range of their elastic behavior. The second experiment was conducted after combining precast decks on CFT truss chords. The applied load was about 800kN in the case of non-combined decks and, after combining the decks, a load of up to 3600kN was applied resulting in the destruction of the specimen.

Test results are as shown as in Figure 13 and 14, for continuous supporting points of CFT truss without combining decks and Figure 15 and 16 show test results for continuous supporting points of CFT truss with prestressed, precast decks.

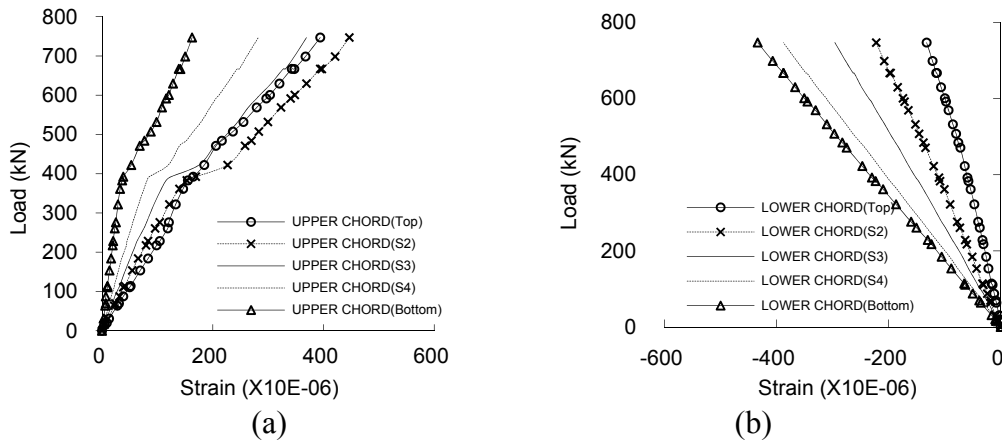


Figure 13. Strain curves of upper and lower chords at the center: (a) upper chords; (b) lower chords.

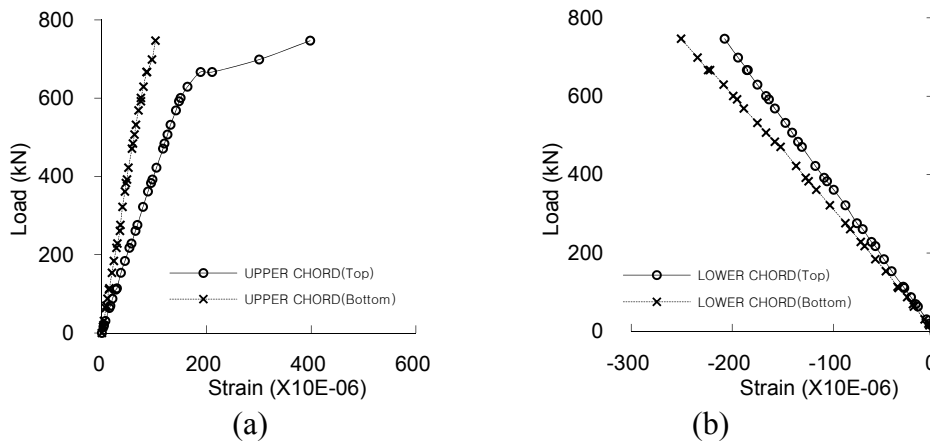


Figure 14. Strain curves of upper and lower chords at 1/4 length points: (a) upper chords; (b) lower chords.

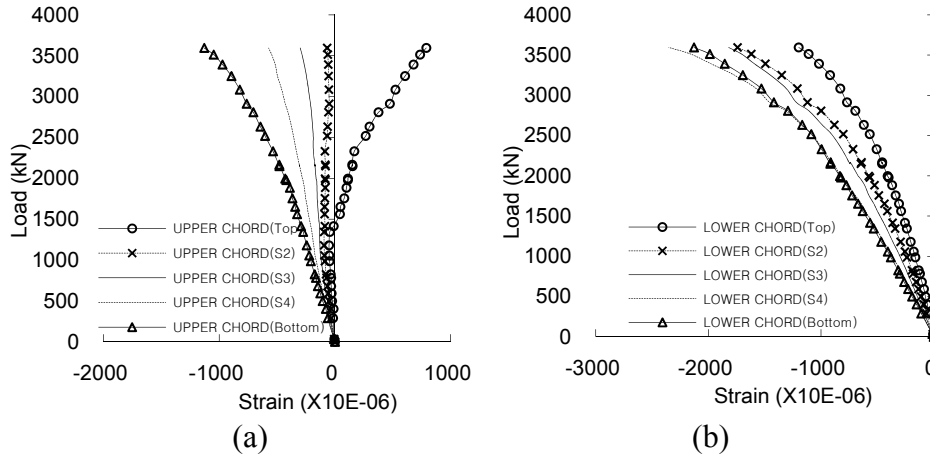


Figure 15. Strain curves of upper and lower chords at the center: (a) upper chords; (b) lower chords.

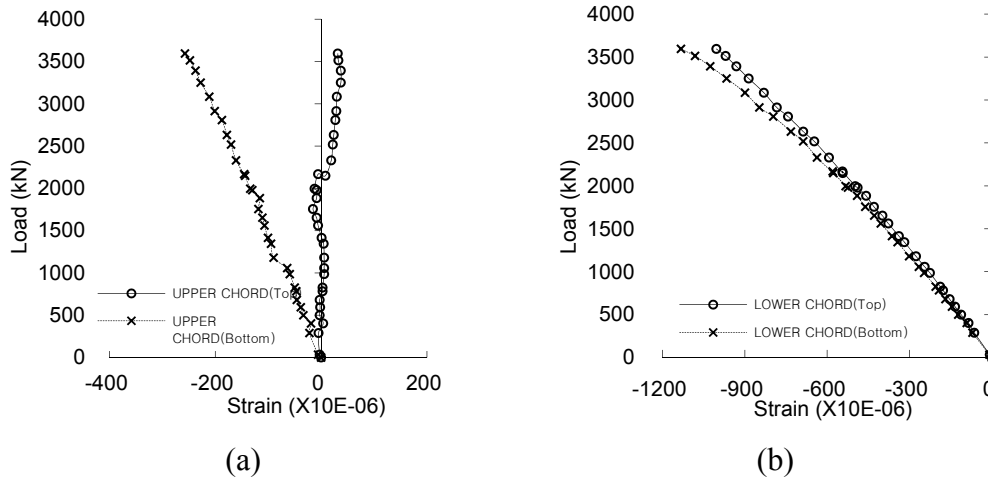


Figure 16. Strain curves of upper and lower chords at 1/4 length points: (a) upper chords; (b) lower chords.

The authors are planning to proceed with the analytical study on nonlinear materials using three-dimensional SOLID elements for further experiments on experiment specimens of continuous bridges with truss girder combined with precast concrete decks as well as the evaluation of the behavior of specimens used in experiments. Through analytical study, the authors will review the nonlinear behavior of the specimens in experiments and then compare and examine them using their experiment values.

4. CONCLUSION

The CFT truss girder bridge is a combined bridge technology that secures safety and economic feasibility. The method maximizes the structural mechanics and structural merits of the truss shape. A CFT truss girder bridge has an excellent appearance and see-through view, and can be manufactured simply and reduces many of the reinforcing members necessary for the fabrication of steel bridges. It has huge merits with regard to efficiency of installation, due to minimal costs associated with

steel tube manufacturing at a factory. The pre-fabricated CFT truss girder bridge, which strengthens the merits of the CFT truss girder and enhances constructability, can be applicable to all kinds of bridges up to 100m in span length due to it having a girder segment without limitation that can span the length of bridges. Especially by applying it on middle and long spans of over 50m, it can save more than 20% of steel parts used in construction and it also provides a cost saving of more than 10% of the construction cost. In addition to relatively short spans of 20m – 60m in length, CFT truss girder bridges are expected to be an alternative solution for acquiring economic feasibility, construction performance and safety for long spans of more than 60m, which are very limited and harder to adapt to regular steel bridges.

REFERENCES

- American Concrete Institute (2002). *Building code requirements for reinforced concrete*(ACI, 318-02) and *Commentary* (ACI 318R-02).
- Elchalakani, M., Zhao, X. L. and Grzebieta, R. H. (2001). “Concrete-filled circular steel tubes subjected to pure bending.” *Journal of Constructional Steel Research*, 57(11): 1141-1168.
- Gho, W.M. and Liu, D. (2004). “Flexural behaviour of high-strength rectangular concrete filled steel hollow sections.” *Journal of Constructional Steel Research*, 60(11): 1681-1696.
- Han, L.H. (2004). “Flexural Behaviour of Concrete-Filled Steel Tubes.” *Journal of Constructional Steel Research*, 60(2): 313-337.
- Lu, Y.Q. and Kennedy, D. J. (1994). “The flexural behaviour of concrete filled hollow structural sections.” *Can. J. Civil Eng*, 21(1): 111-130.
- Wheeler, A.T. (2000). “Thin-walled steel tube filled with high strength concrete in bending.” *Engineering Foundation Conferences*, Composite Construction IV, Banff, Alberta, Canada.

Behaviour and Design of Composite Beams Subjected to Combined Bending and Axial Forces

G. Vasdravellis, M.ASCE¹; B. Uy, M.ASCE²; E. L. Tan³; and B. Kirkland²

¹Institute for Infrastructure and Environment, Heriot-Watt Univ., Edinburgh EH14 4AS, U.K. E-mail: g.vasdravellis@hw.ac.uk

²Centre for Infrastructure Engineering and Safety, Univ. of New South Wales, Sydney, NSW 2052, Australia. E-mail: b.uy@unsw.edu.au; b.kirkland@unsw.edu.au

³Institute for Infrastructure Engineering, Univ. of Western Sydney, Locked Bag 1797, Penrith, NSW 2751, Australia. E-mail: e.tan@uws.edu.au

Abstract

Steel-concrete composite beams can often be subjected to combined bending and high axial forces. However, the moment-axial force interaction in composite beams is not covered by the current codes of practice. An experimental investigation comprising twenty-four full-scale tests was conducted recently in the University of Western Sydney, aiming to investigate the behaviour and ultimate strength of composite beams under bending and axial forces. Nonlinear finite element simulations and parametric studies complemented the tests. It was found that the moment capacity of a composite beam is reduced in most situations under simultaneous axial loading. Partial shear connection does not alter the shape of the interaction curve, but it affects the ductility of the beam and the amount of axial load transferred to the slab. Based on the experimental and numerical results, simplified design rules are proposed to account for the effect of axial loads on the bending capacity of composite beams.

INTRODUCTION

Composite construction of steel and concrete is a popular structural method due to its numerous advantages against conventional solutions. The optimal combination of the properties of the two most popular construction materials, i.e. steel and concrete, results in structures that are both safe and economic. Composite action between the steel beam and the reinforced concrete slab, which is commonly achieved through the welding of shear studs to the top flange of the beam, results in significant reduction of beam deflections, enabling the use of smaller steel sections compared with bare steel systems.

In engineering practice, there are situations where composite beams are subjected to combined actions, e.g. simultaneous action of positive or negative bending and axial tension or compression. Such examples include: a) in floor beams where the axial force can either be as part of a specific bracing system or where the beam acts as part of a diaphragm; b) high-rise frames where the effects of wind loading become significant and can impose large axial forces on the beams of the

building; c) structures where inclined members are used, e.g. stadia beams or inclined parking ramp approaches; and d) bridges, where inclination and traffic loads may introduce large axial forces on the supporting beams.

Current structural codes, e.g. Eurocode 4, AISC 360-10 and AS2327-1, do not provide specific rules for the design of composite beams under combined axial forces and bending moments; they refer to rules established for bare steel sections. Since the behaviour of a composite beam differs substantially from that of a bare steel section, the moment-axial load interaction of composite beams still deserves further investigation. Despite the large amount of available experimental data on the flexural behaviour of composite beams, experimental data on the behaviour of composite beams under combined loading is rather limited. Previous research works on composite beams under combined actions include those by Uy and Bradford (1993), Uy (1996), Nie et al. (2009), Tan and Uy (2009), Baskar and Shanmugam (2003), Uy and Tuem (2006).

The effects of axial tension on the sagging and hogging moment regions of composite beams were studied in Vasdravellis et al. 2012a and 2012b. In this work, the ultimate strength of composite beams subjected to combined actions was investigated by experimental tests, rigid plastic sectional analyses and extensive finite element simulations. Interaction curves were established and simple design rules were proposed for use in practice. Composite beams under the effects of axial compression and negative bending were studied in Vasdravellis et al. 2012c. Simplified design rules and detailing at the regions of continuous supports were proposed for the more efficient design of continuous composite beams. This paper summarizes the main experimental results, the numerical analyses, and the proposed design models for composite beams under combined bending and axial force. The preliminary results on the axial compression – positive bending interaction are also presented.

EXPERIMENTAL PROGRAM

The relevant geometry and details of the reinforcement and shear studs are shown in Fig. 1. All specimens were constructed with a 600mm-wide and 120mm-deep concrete slab connected to a UB203x133x30 universal beam section. The beam-to-slab connection was achieved through 19mm-diameter, 100mm-long headed shear studs welded in a single line along the centre of the top flange of the steel beam. Specimens tested under positive bending had partial shear connection equal to about 0.6 and specimens tested under negative bending had full shear connection. Longitudinal and transverse reinforcement was placed in the concrete slab in the arrangement shown in Fig. 1.

Two 10mm-thick web stiffeners were welded between the beam flanges at the point of the vertical load application to prevent premature web buckling due to the concentrated midspan load. In addition, specimens subjected to compression were reinforced by using a series of web and flange stiffeners at the two ends of the beam (see Fig. 1). This configuration aimed to avoid local failure due to large stress concentration at the points of the axial load application and allowed for the high compressive loads to be partly transferred to the composite cross section at the

midspan. Lateral bracing was placed along the length of the beams subjected to negative bending to eliminate the possibility of lateral-torsional buckling failure mode. The lateral bracing consisted of steel rectangular members anchored on the edges of the concrete slab and welded on the bottom (compressive) flange of the steel beam.

Material property tests

Both concrete and steel material property tests were performed to obtain the actual strength of the materials. Concrete tests consisted of standard cylinder compressive tests and flexural splitting tests. The latter aimed to determine the tensile strength of the concrete. The cylinders were 200mm high with a diameter of 100mm, while the flexural tests were performed on 100x100x400mm specimens. The mean compressive strength of concrete was 24 MPa and the mean tensile stress was 2.8 MPa. Tensile tests were also conducted on coupons cut out from the flange and web of the steel beams as well as the reinforcing bars. The mean values of the yield stresses were 365 and 388 MPa for the flange and the web, respectively.

The load-slip characteristics of the shear studs were evaluated by conducting three push-out tests for each loading combination. The push-out specimens were constructed using shear studs and concrete from the same batches as those used to form the steel-concrete composite beams in the main experimental series. Each of the push-out specimens were tested following the testing procedure described in Eurocode 4 [2]. The resulting load-slip curves showed that the average capacity of one shear stud is about 110kN, while the maximum slip achieved during the tests varied from 8 to 14mm (Vasdravellis et al. 2012b).

Experimental setup

A combination of load actuators was used to produce simultaneous bending and axial forces in the composite beam specimens. The vertical load was applied with the use of a 1000kN-capacity hydraulic actuator with a usable stroke of 250mm. To apply positive bending the beam was positioned with the slab above the steel beam, and to apply negative bending the beam was positioned with the slab underneath the steel beam. Fig. 1 shows the test setup for negative bending application. The axial load was applied using four 800kN-capacity hydraulic actuators placed in parallel. Therefore, this system was capable of applying a maximum 3200kN tensile or compressive axial load with a 200mm usable stroke. The axial compressive load was transferred to the composite beam section by the use of a plate which was welded to the steel beam section and a triangular spreader plate of equal width as the beam flange, i.e. 134mm, as schematically shown in the test setup of Fig.1. In this way the loaded area was the area of the steel beam plus a portion of the slab area equal to the width of the spreader plate times the depth of the slab. The tensile load was transferred through the steel beam section.

Instrumentation

A combination of LVDTs and strain gauges was deployed to record the relevant parameters and to obtain the experimental behaviour of the beams. An automatic data acquisition system was used to automatically record data from all measuring devices including load cells, strain gauges and LVDTs throughout the test. Strain gauges were used to measure strains of the steel beam and reinforcing bars. Strain gauges were located in sets of seven through each cross-section with one set at midspan and one set at each quarter point, as shown in Fig. 1. LVDTs were used to measure the deflection of the beam. These were placed at the midspan and at the quarter points. The connector slip and interface slip were also measured by LVDTs. The slip was measured at the ends, quarter points and midpoint.

Test procedure

One pure bending and one pure axial load test was performed initially for each of the four experimental series. Subsequently, five tests were conducted for each of the bending – axial force combinations. The vertical loading was applied in incremental steps in the order of 10% of the theoretical design strength of the composite section. To obtain different levels of axial force, the increments of applied axial load were varied. Both loads were increased until either material failure occurred or the maximum stroke of either of the load actuators was reached.

The resulting moment in each tested beam was calculated taking into account the equilibrium of the external forces acting on it. The following equation was used to calculate the ultimate bending moment:

$$M = \frac{P_V L}{4} + P_H e - M_{sw} \quad (1)$$

where P_V is the vertical force applied at the centre of the beam, P_H is the horizontal force, M_{sw} is the moment due to the beam's self-weight and e is the eccentricity between the location of the load application pin and the plastic neutral axis of the composite beam. The eccentricity was estimated by:

$$e = \left(D_c + t_f + \frac{d_w}{2} \right) - y_c + \delta \quad (2)$$

where D_c is the slab thickness; t_f is the flange thickness; d_w is the height of the web; y_c is the depth of the plastic neutral axis (PNA), measured from the top of the slab; and δ is the measured vertical deflection at the midspan.

EXPERIMENTAL RESULTS

A detailed description of the experimental results can be found in Vasdravellis et al. (2012a, 2012b, 2012c). A brief summary of the complete moment – axial force interaction is provided herein. Fig. 2 presents the complete moment –axial force

interaction diagram resulting from the four series of tests, i.e. positive bending and tension, positive bending and compression, negative bending and tension, and negative bending and compression. The results of the FEM analyses, described in the next section, are superimposed to the experimental data points. In all combinations the moment is reduced with increasing the applied axial load. Typical experimental failures of the specimens included slab compressive failure under positive bending, steel beam flange local buckling under negative bending, steel global buckling under axial compression, and shear connection failure under high axial compression/tension in the specimens designed with partial interaction. These failure modes are illustrated in Fig. 3. An important outcome of the experiments concerning compressive axial force is that a large amount of compression can be transferred from the steel beam to the concrete slab through the shear connection system if adequate reinforcement is provided at the ends of the steel beam. A set of plates welded to the beam flange and web, as shown in Fig. 1, can provide this feature.

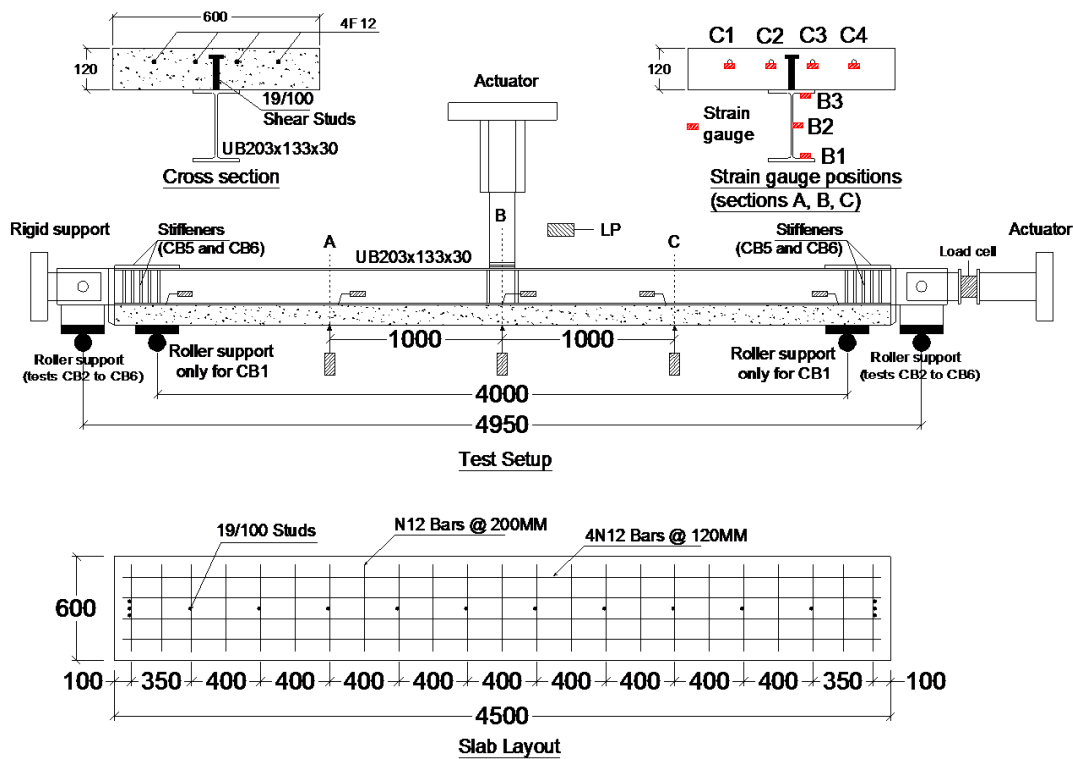


Figure 1. The tests setup for negative bending moment.

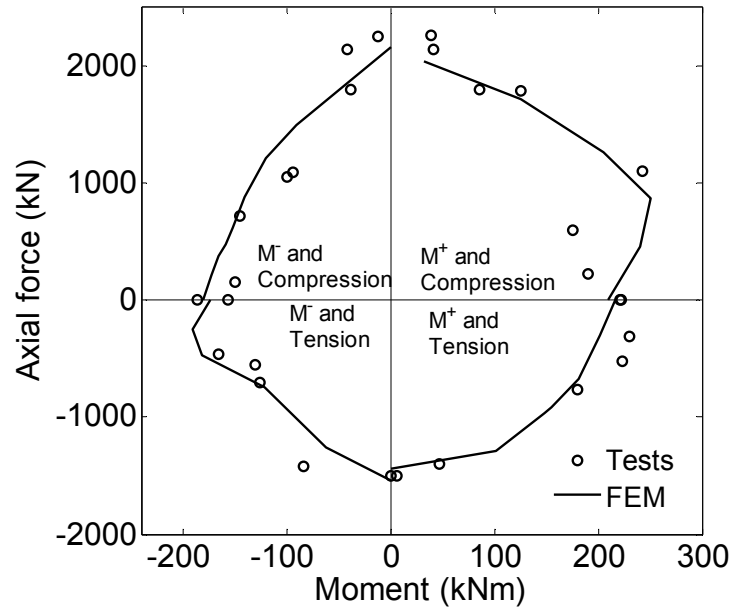
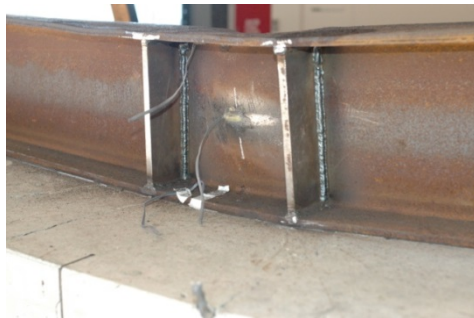
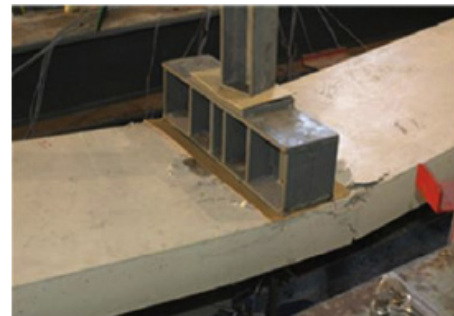


Figure 2. Complete moment–axial force interaction curve from tests and FEM analyses.



a)



b)



c)



d)

Figure 3. Experimental failure modes: a) local buckling of steel beam flange and web; b) compressive failure of slab; c) stud failure; and d) buckling due to high axial compression.

THEORETICAL ANALYSES

Rigid plastic analysis

An analytical calculation of the composite beam capacities was conducted by means of rigid plastic analysis (RPA). Under negative bending, only the steel parts (reinforcement bars and steel beam section) of the composite section were considered to contribute to the section capacity, while the concrete in tension was neglected. To determine combined capacities, the plastic neutral axis is assumed to lie in several points within the section height and the resulting moment and axial compression are summed taking as centre of rotation the plastic centroid of the composite section. For comparison purposes with the experimental values, no partial safety factors were assumed and the average yield strengths resulted from the material tests were used in the calculation of the internal forces. In all situations, results have shown that RPA can be safely used for the calculation of the ultimate combined strength of composite beams, since it provides a conservative figure when the nominal values of the materials' strength are used. The interaction points provided by the RPA were in general consistent with those derived from tests and the FEM analyses.

Finite element model

A nonlinear three-dimensional finite element model was constructed to simulate the tests on the composite beams. The model relies on the use of the commercial software Abaqus (Dassault Systems 2010).

The concrete slab was modelled using eight-node linear hexahedral solid elements with reduced integration, namely C3D8R in ABAQUS, while the steel beam was modelled with eight-node elements with incompatible modes (C3D8I). The main reason for using different elements is that the elements with incompatible modes are more efficient to capture local instabilities such as flange and/or web buckling without the need to introduce imperfections in the model. The reinforcing rebars were modelled as two-node three-dimensional linear truss elements, T3D2. The lateral bracing was modelled indirectly by applying boundary conditions which prevent lateral displacement at the same points on the beam compression flange as the fly bracings were located in the tests. Due to the symmetrical geometry and loading, only half of the beam was modelled, while appropriate boundary conditions were applied to the plane of symmetry. An overview of the mesh and a schematic representation of the various modelling assumptions are depicted in Fig. 4.

To model the reinforcement in the slab the embedded element technique was employed. The embedded element technique in ABAQUS is used to specify an element or a group of elements that lie embedded in a group of host elements whose response will be used to constrain the translational degrees of freedom of the embedded nodes. In the present case, the truss elements representing the reinforcement are the embedded region while the concrete slab is the host region. Using this technique, it is assumed that perfect bond exists between the rebars and the surrounding concrete. Contact interaction was applied to the beam-slab interface which did not allow separation of the surfaces after contact. The node-to-surface

contact with small sliding was used while the "hard" contact without friction was specified as the contact property.

The true stress-strain relations obtained from material tests were converted into piecewise linear curves and used to model the steel material for the beam and the reinforcing bars. Elastic-plastic material with isotropic hardening law was used as the constitutive law for all the steel parts of the model.

The concrete material stress-strain relationship was calibrated according to the values obtained from the concrete cylinder and splitting tests. The stress-strain curve for compression followed the formula proposed by Carreira and Chu (1985) while the tensile behaviour is assumed to be linear up to the uniaxial tensile stress provided by the material test. The stress-strain law used is plotted in Fig. 5a. The post-failure behaviour for direct straining across cracks is modelled using the tension-stiffening option and determining a linear relation until stress is zero at a strain value of 0.05. This value is used to avoid numerical instabilities in the computational procedure while accuracy is not affected considerably. There are two plastic models available in ABAQUS for modelling the concrete behaviour. In the present analysis the damaged plasticity model was preferred over the smeared cracked model. This model provides a general capability for the analysis of concrete structures under static or dynamic and monotonic or cyclic loading based on a damaged plasticity algorithm. Compared to the companion model (smeared crack model), it models concrete behaviour more realistically but it is computationally more expensive. Nevertheless, this model was chosen for monotonic loading due to its numerical efficiency when full inelastic response has to be captured.

A discrete spring model representation of shear studs is chosen to simulate the slip in the slab-beam interface. The nonlinear spring element SPRING2 was adopted to connect a beam flange node with a slab node at the interface at the same positions where studs were welded to the specimen, as schematically shown in Fig. The force slip law for the spring element is derived by the standard push-out tests on 19mm-diameter shear studs. A piecewise linear curve was fitted to the experimental diagram and defined as the force-slip law for the springs, as shown in Fig. 5d.

The vertical load was applied as an imposed displacement on the top of the beam flange, while the axial load was applied as an edge pressure on the steel beam section. The axial load direction was kept constantly horizontal, i.e. it did not follow the rotation of the edge, in order to be consistent with the experimental loading procedure. The analysis consisted of two steps. In the first step the contact interactions were established, ensuring that numerical problems due to contact formulation will not be encountered during the next steps, while in the second step the vertical and the axial loads were applied simultaneously, following the experimental procedure. The static nonlinear solution algorithm with adaptive stabilisation as a fraction of dissipated energy was employed to solve for the nonlinear response of the composite beams. Finite element analysis with concrete elements in tension may result in convergence problems. To avoid these, the discontinuous analysis option was also used in the general solution control options.

The behaviour of the finite element model and the failure modes at the ultimate deformation of the composite beams were monitored during the FEM analyses through the establishment of specific failure criteria which were defined

corresponding to the ultimate strength of the various section components. In particular, failure of the composite beam in the simulation was identified by one of the following situations: a) flange or web buckling, b) reinforcement fracture, and c) shear connection failure. While local instabilities can be captured accurately using the large displacement nonlinear analysis option in ABAQUS, the second and third conditions should be identified by monitoring some specific response quantities. The strain of the reinforcing bars and the relative displacements in the nonlinear springs representing the studs were monitored during the analysis. An excessive strain in the rebars reaching the experimental rupture values should indicate a reinforcement fracture, while a measured slip near or above the failure slip of the push-out tests was a criterion for shear connection failure. Finally, a ductile failure mode was defined when none of the above criteria was met and the analysis was ended by numerical problems due to excessive cracking of concrete in tension, while the ultimate load achieved was easily identified by the load-deflection curve.

FEM model validation

The experimental tests were reproduced using the developed FEM model. The FEM model was able to predict the combined strength of the composite beams with good accuracy. The model was assessed by comparing the structural behaviour of the tested beams with that of the model in terms of force – deflection curves, slip evolution in the slab - beam interface, axial force – displacement response, and strain evolution in the steel beam. Fig. 5 shows typical comparisons which demonstrate good agreement between the experimental and numerical responses.

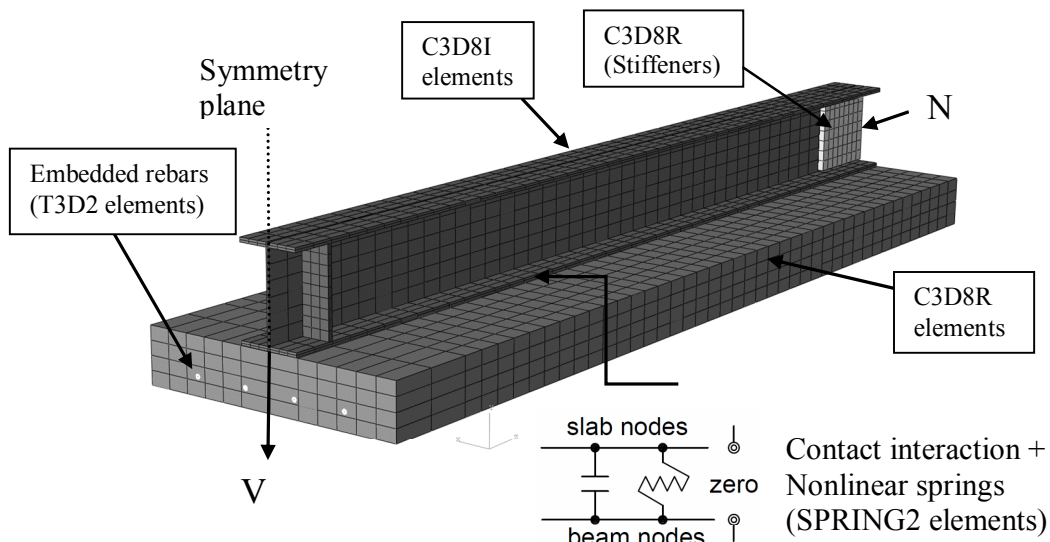


Figure 4. Details of the finite element mesh used for modelling the composite beams for the negative bending case.

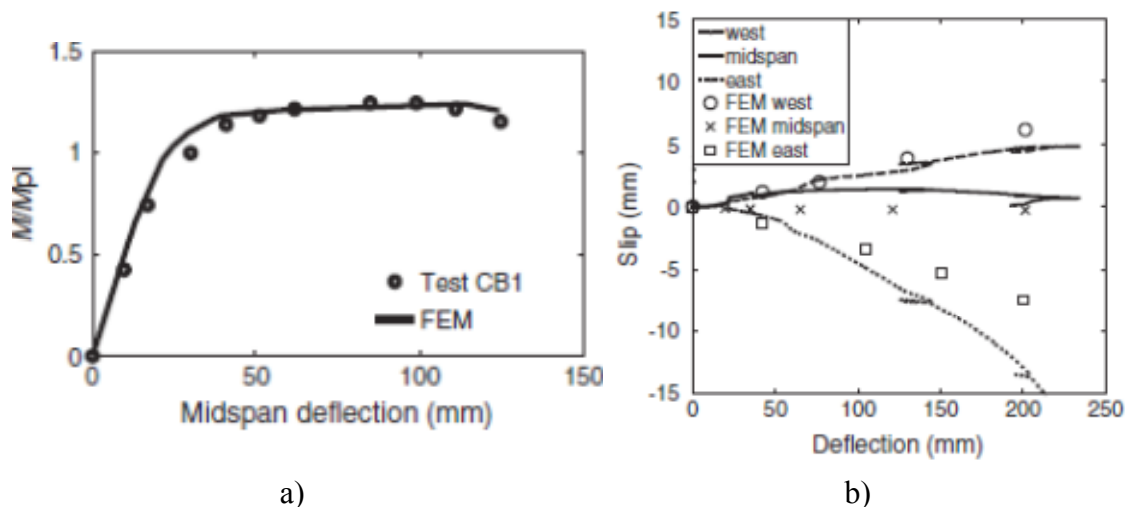


Figure 5. Experimental versus numerical response comparison: a) negative moment – midspan deflection; and b) slip evolution under positive bending.

PARAMETRIC ANALYSES

The validated FEM model was used to conduct an extensive parametric study on composite beams subjected to combined bending and axial force. A wide range of composite beam section commonly used in buildings was studied. The results of the parametric analyses generally confirmed the experimentally derived interactions. Both full and various degrees of partial interaction were studied. The shape of the interaction was not affected in most situations when the composite beam had partial shear connection. More details of the parametric analyses are provided in Vasdravellis et al. (2012a, 2012b, 2012c). Regression analysis of the numerical results allowed the derivation of simplified design equations for use in practice.

PROPOSED DESIGN MODELS

Based on the experimental and numerical results simplified equations are proposed for the design of composite beams subjected to any combination of positive or negative bending moment and axial tension or compression. In the following equations, M_u and N_u represent the bending and axial resistances of a composite section, respectively, calculated according to the current structural codes (e.g. Eurocode 4):

a) Composite beams under negative bending and compression (Fig. 6a):

$$\frac{M}{M_u} + \frac{N}{N_u} \leq 1.0 \quad (3)$$

According to this formula, the hogging moment resistance of a composite beam is reduced with the presence of compression forces following a linear

relationship. Although the interaction diagrams from the parametric analyses indicated that in some cases the reduction in moment capacity is delayed (Vasdravellis et al. 2012a), a linear reduction is proposed for a reasonably conservative design, which also conforms with the experimental output. The proposed design formula assumes that adequate lateral restraint is provided to the compression flange so that flexural or distortional buckling is excluded as failure mode. In addition, longitudinal stiffeners according to the design details proposed in Vasdravellis et al. (2012c) is recommended to be welded to the steel beam web at the internal support regions of continuous composite beams to ensure that web local buckling is delayed and adequate rotation capacity for plastic structural analysis is available.

b) Composite beams under negative bending and tension (Fig. 6c):

$$\frac{N}{N_U} + 0.8 \frac{M}{M_U} = 1, \text{ for } N > 0.20N_U \quad (4)$$

$$M = M_U, \quad \text{for } N \leq 0.20N_U \quad (5)$$

According to this formula, the bending capacity at the hogging moment regions of composite beams is not reduced when an axial tensile force up to 20% of the axial strength is applied in the beam, and it reduces linearly to zero when larger values of axial force are present.

c) Composite beams under positive bending and tension (Fig. 6d)

$$\frac{M}{M_U} + 0.6 \frac{N}{N_U} = 1.0 \quad (6)$$

where M_u is the plastic resistance of a composite beam to bending, according to structural code provisions (including the associated safety factors for materials), and N_u is the plastic resistance of the steel section to axial tensile loading, e.g. the steel reinforcement in the slab is neglected under an axial force acting in the steel section. According to this equation, the moment capacity of a composite section is reduced linearly until the 40% of the M_u by increasing the axial tensile force acting on the steel section. It has to be pointed out, however, that in practice it is very rare for a beam to be subjected to tensile axial forces greater than the 30%-40% of its axial capacity; however, it was judged as necessary to study the whole range of axial force percentages in order to complete the interaction diagram and have a full picture on the behaviour of composite beams under combined actions.

d) Composite beams under positive bending and compression (Fig. 6b):

$$\frac{N}{N_U} + 0.75 \frac{M}{M_U} = 1, \text{ for } N > 0.25N_U \quad (7)$$

$$M = M_U, \quad \text{for } N \leq 0.25N_U \quad (8)$$

This design equation is currently based on analysis of the experimental section only. The initial analyses indicated that the bending capacity at the sagging moment regions of composite beams is not reduced when a low compressive force (up to 25-30% of the axial strength) is applied to the beam, while it deteriorates considerably when larger values of axial force are present. Moreover, Fig. 5b shows that there is rather different behaviour of the composite section when full and partial shear connection is used. Extensive parametric analyses, aiming to clarify this behaviour, are on course.

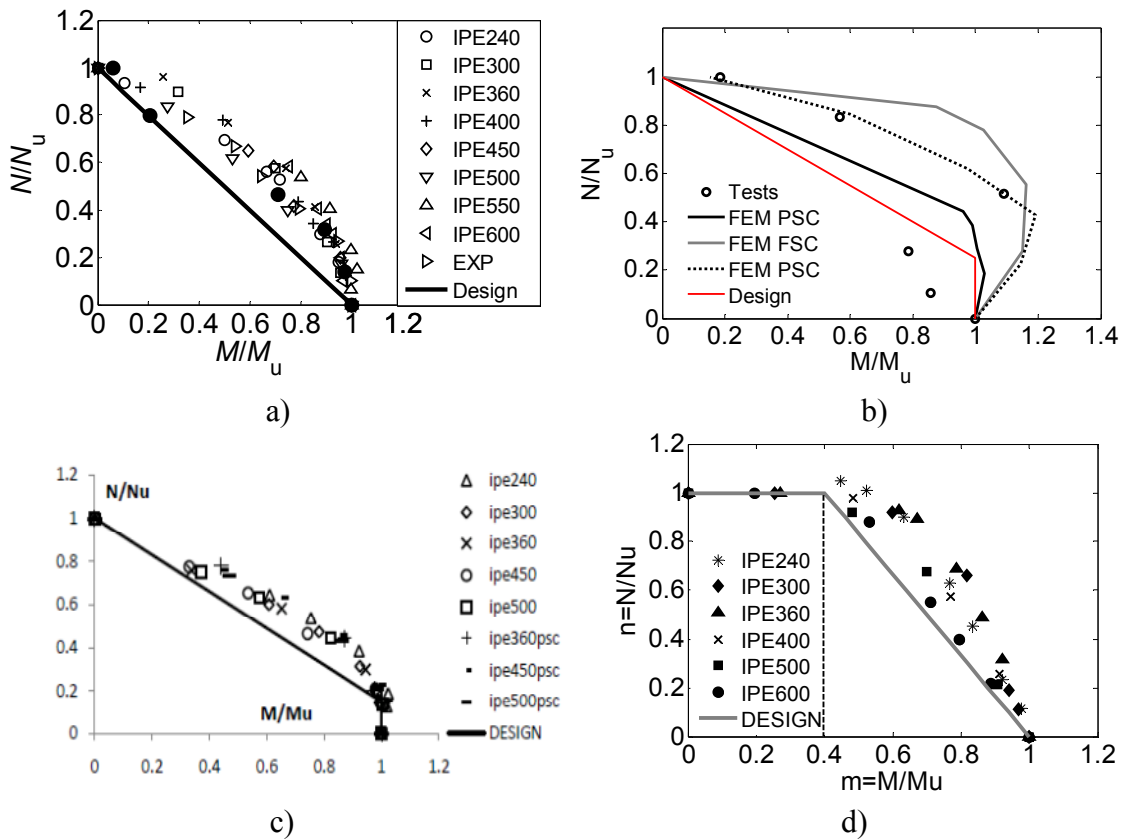


Figure 6. Results of parametric analyses and proposed design equations for composite beams under combined bending and axial force.

CONCLUSIONS

The ultimate strength of steel-concrete composite beams under the combined effects of axial compression or tension and positive or negative bending was investigated through a large experimental programme comprising twenty-four full-scale tests on composite beams prototypes. The beams were tested up to collapse and

the reduction of the moment capacity due to the presence of an axial force was identified. A finite element model was also constructed to complement the experimental findings. The model was assessed against the experimental data and found capable to predict the structural behaviour of composite beams under combined actions with good accuracy. Extensive parametric studies were conducted using the validated numerical model and simplified design rules were proposed. The main conclusions from this research are:

- Experimental testing and numerical simulations demonstrated that the bending moment capacity of a composite beam is significantly deteriorated under the simultaneous action of an axial compressive or tensile force.
- In order to transfer substantial compressive forces in a composite beam without experiencing premature buckling of the steel section, reinforcing the flanges and the web with additional steel plates locally at the edges is recommended.
- Rigid plastic analysis can be conservatively used for the design of composite beams under combined bending and axial force.
- The developed three-dimensional nonlinear finite element model can be used as a tool for the assessment of the nonlinear behaviour and the ultimate failure modes of composite beams under combined negative or positive bending and axial compression or tension.
- Simplified design models for the moment – axial force interaction in composite beams are proposed for use in practice.

REFERENCES

- AISC 360-10. Specification for structural steel buildings. Chicago (IL, USA): American Institute of Steel Construction; 2010.
- Baskar, K. and Shanmugam, N.E. (2003). “Steel-concrete composite plate girders subject to combined shear and bending.” *Journal of Constructional Steel Research*; 59(4): 531-57.
- Carreira, D.J. and Chu, K.H. (1985). “Stress-strain relationship for plain concrete in compression.” *ACI Journal Proceedings*; 82(11): 797-804
- Dassault Systems (2010). Abaqus Theory Manual. Dassault Systèmes Simulia Corp., Providence, RI, USA
- Eurocode 4 (2004). Design of composite steel and concrete structures. London (UK): British Standards Institution.
- Nie, J., Tang, L., Cai, C.S. (2009). “Performance of steel-concrete composite beams under combined bending and torsion.” *Journal of Structural Engineering*; 135(9): 1048-57.
- Standards Australia (2004). Composite structures Part 1: Simply supported beams. AS 2327.1-2004. Sydney (Australia).
- Tan, E.L. and Uy, B. (2009). “Experimental study on straight composite beams subjected to combined flexure and torsion.” *Journal of Constructional Steel Research*; 65(4): 784-93.

- Uy, B. and Tuem, H.S. (2006). "Behaviour and design of composite steel-concrete beams under combined actions." *Eighth International Conference on Steel-Concrete Composite and Hybrid Structures (ICSCCS 2006)*, Harbin, China: 286-91.
- Uy, B. and Bradford, M.A. (1993). "Cross-sectional deformation of prestressed composite tee-beams." *Structural Engineering Review*; 5(1): 63-70.
- Uy, B. (1996). "Long term behaviour of composite steel-concrete beams prestressed with high strength steel tendons". *Advances in Steel Structures (ICASS '96)*: 419-24.
- Vasdravellis, G., Uy, B., Tan, E.L. and Kirkland, B. (2012a). "The effects of axial tension on the hogging-moment regions of composite beams." *Journal of Constructional Steel Research*; 68 (1): 20-33.
- Vasdravellis, G., Uy, B., Tan, E.L. and Kirkland, B. (2012b). "The effects of axial tension on the sagging-moment regions of composite beams." *Journal of Constructional Steel Research*; 72, pp. 240-253.
- Vasdravellis, G., Uy, B., Tan, E.L. and Kirkland, B. (2012c). "Behaviour and design of composite beams subjected to negative bending and compression". *Journal of Constructional Steel Research*, 79, pp. 34-47.
- Vasdravellis, G., Uy, B., Tan, E.L., Kirkland, B. (2015). "Behaviour and design of composite beams subjected to sagging bending and axial compression". *Journal of Constructional Steel Research*; DOI: 10.1016/j.jcsr.2015.03.010.

Nonlinear Finite Element Analysis and Design of Composite Beams Subjected to Shear and Bending

G. Vasdravellis, M.ASCE¹; and B. Uy, M.ASCE²

¹Institute for Infrastructure and Environment, Heriot-Watt Univ., Edinburgh EH14 4AS, U.K. E-mail: g.vasdravellis@hw.ac.uk

²Centre for Infrastructure Engineering and Safety, Univ. of New South Wales, Sydney, NSW 2052, Australia. E-mail: b.uy@unsw.edu.au

Abstract

The shear strength and the moment-shear interaction in steel-concrete composite beams was previously evaluated by the authors through an experimental program comprised of fourteen tests on simply-supported composite beams. In this paper, a nonlinear finite element model is developed to simulate the behavior of the experimental section. The model was assessed in terms of the ultimate strength and the failure modes of the composite beams under shear and bending and found to be accurate in capturing the nonlinear response of the specimens. The numerical model was then used to carry out an extensive parametric study on the various factors that influence the shear strength of a composite beam. These factors include the slab thickness, the slab width, and the reinforcement ratio. Based on the results of the numerical study, design models are proposed for the calculation of the shear strength and the shear-moment interaction in composite beams.

INTRODUCTION

Composite construction of steel and concrete is the most efficient structural system for buildings and bridges due to the numerous advantages that it provides compared with other structural solutions (Uy and Liew, 2002). There are practical situations where steel-concrete composite beams can be subjected to combined bending and significant shear forces; some representative examples include transfer beams in high-rise buildings, beams in industrial buildings supporting concentrated loads from operating machinery and beams acting as shear links in eccentrically braced frames. Plastic limit analysis of gravity-resisting members can result in increased shear that should be taken into account in the design (Bruneau et al., 2011). However, current structural provisions concerned with the design of composite structures, such as the Eurocode 4 (BSI, 2004), the AS 2327.1 (Standards Australia, 2003) and the AISC 360-10 (American Institute of Steel Construction, 2010), do not provide explicit design methods for the calculation of the composite shear strength and do not address the interaction between bending and shear in composite beams; they refer the designer to the corresponding structural steel provisions. As a result, composite beams are currently designed against shear loading by neglecting the contribution of the concrete slab, i.e. it is assumed that the shear loading is resisted by the web of the steel beam alone. This assumption can be conservative especially

when the slab is in compression (Johnson, 2012) and may lead to uneconomical design. Eurocode 4 refers to the rules given in the parts 1-1 and 1-5 of Eurocode 3 (BSI, 2005, 2003), relevant to the design of steel members. When the section is compact, the shear resistance is equal to the plastic shear capacity of the web:

$$V_{pl,Rd} = 0.6A_v f_{yw} \quad (1)$$

where A_v is the shear area of the steel beam and f_{yw} the yield strength of the steel of the web. The same approach is followed by the AISC 360-10 and AS2327.1 standards. The reduced moment capacity of a steel-concrete composite section is taken into account in Eurocode 4 when the acting shear is higher than half the $V_{pl,Rd}$. The design moment resistance is then calculated using a reduced design steel strength in the shear area of the steel beam, equal to $(1-\rho)f_{yw}$, where:

$$\rho = \left(\frac{2V}{V_{pl,Rd}} - 1 \right)^2 \quad (2)$$

and V is the design shear force. For a design shear force equal to $V_{pl,Rd}$, the code assumes that the available moment resistance is equal to that provided by the flanges of the steel section only.

There is limited experimental data on composite beams under combined actions. Most of the past research is concerned with the shear strength of composite girders, where the girder consists of slender plates, rather than compact composite beams. Prior works concerning shear behavior of composite beams include those of Johnson and Willmington 1972; Nie et al. 2004; and Liang et al. 2004, 2005. The behavior of composite girders was extensively investigated by Baskar and Shanmugam 2003; Shanmugam and Baskar 2003; and Sherafati et al. 2011.

The work presented herein is part of a research program aiming to investigate the ultimate strength of composite beams under combined actions. Previous research by the authors investigated the behavior and design of composite beams under combined bending and axial forces (Vasdravellis et al. 2012a, 2012b, 2012c). The shear strength and moment-shear interaction in simply-supported compact composite beams was experimentally investigated by the authors (Vasdravellis and Uy 2014). Fourteen simply-supported composite beams were tested under combined bending and shear. A test on a bare steel section under high shear served as a reference beam for direct comparison with the corresponding composite beam. Beams with partial shear connection and with shear reinforcement in the concrete slab were also tested. The tests aimed to assess the contribution of the concrete slab to the ultimate shear capacity of a composite section and to ascertain a moment-shear interaction law for composite beams subjected to combined positive bending and shear forces. This paper focuses on the implementation of a nonlinear finite element model (FEM) aiming to complement the experimental results. The accuracy of the model is assessed against the experimental results and the validated model is subsequently used to extend the experimental findings to a wider range of sections and to study the effects of various parameters on the shear strength of composite beams. A semi-

empirical design model is proposed for a more efficient design of composite beams in regions with high shear forces.

EXPERIMENTAL PROGRAM

Details of the experimental investigation can be found in Vasdravellis and Uy 2012 and 2013. A brief summary of the main experimental results is outlined here to facilitate reading of this paper. Table 1 summarizes the test matrix. The clear spans of the composite beams ranged from 0.8 m to 5.5 m. Different shear-to-moment ratios, denoted as η (units: m^{-1}), were realized. A shorter span increases the value of η , and as η increases the shear force becomes more important. The η ratios are reported in Table 1.

The tested composite beams consisted of an 150 mm-deep and 1200 mm-wide solid concrete slab section connected to a 360UB45 steel beam section (equivalent to an IPE330 or a W10x39 steel section). Full shear connection was provided in specimens CBMV-1 to 10, 13 and 14. Specimens CBMV-11 and CBMV-12 were identical to beams CBMV-5 and 8 with span lengths 2.8 and 1.2 m, respectively, except that they were designed to achieve partial shear connection. The degree of shear connection, β , in each beam is reported in Table 1.

Each beam was tested until the ultimate collapse conditions were met. Cracking of concrete and the sequence of failures in each composite beam specimen were carefully recorded during the experimental process. Once the maximum applied load had been achieved, the test was continued until at least a 10% drop of the reaction force was recorded. The shear and moment developed in each beam in association with the value of η , and the experimental shear – moment interaction diagram, were of particular interest.

EXPERIMENTAL RESULTS

Typical experimental failures are shown in Fig. 1. Beams CBMV-1 to 6 failed in flexural mode (Fig. 1a), while beams CBMV-6 to 10 experienced shear-governed failures consisting of slab shear cracking (Fig. 1b) and beam web diagonal buckling (Fig. 1c). Table 1 reports the percentage ratio of the moment achieved in each specimen, denoted as M_u , to the ultimate moment achieved by the beam CBMV-1, denoted as $M_{u,f}$, and the percentage ratio of the shear achieved in each specimen, V_u , to the shear strength of specimen CBMV-10, denoted as $V_{u,s}$.

The experimental force – deflection and moment - deflection responses are plotted in Figs. 2a and b, respectively. The results show that the ultimate load sustained by each beam increases as the span decreases: V_u ranged from 238 kN in beam CBMV-1 to 892 kN in beam CBMV-10. $M_{u,f}$ is equal to 655 kNm. In beams CBMV-1 to 6 no reduction in M_u due to the presence of shear force is observed (see Table 1). M_u in the short specimens (CBMV-7 to 10) is significantly reduced as the shear force increases, assuming values equal to 82, 73, 65, and 55 % of $M_{u,f}$, respectively. Fig. 3 shows the reduction of the moment capacity of the composite beams as a function of the ratio $V_u/V_{u,s}$ and the ratio $V_u/V_{pl,Rd}$. The interaction diagram demonstrates that the moment capacity of a composite beam starts to decrease when

the applied shear is greater than the 60% of the ultimate shear capacity of the composite section. In addition, it is shown that the bending capacity of the composite section is not reduced before the applied shear reaches the shear strength of the steel section, indicating a high degree of conservatism in the current codes' approach.

Table 1. Test matrix and ultimate strengths of specimens

Specimen	Span length (m)	η (m^{-1})	β	V_u^1	M_u^2	$M_u/M_{u,f}^3$ (%)	$V_u/V_{u,s}^4$ (%)
CBMV-1	5.5	0.36	1.3	238	655	100	27
CBMV-2	4	0.50	1.2	337	674	103	38
CBMV-3	3.2	0.63	1.2	427	684	104	48
CBMV-4	3.0	0.67	1.0	465	697	106	52
CBMV-5	2.8	0.71	1.0	498	697	106	56
CBMV-6	2.6	0.77	0.9	524	681	104	59
CBMV-7	1.4	1.43	1.0	767	537	82	86
CBMV-8	1.2	1.67	1.1	798	479	73	89
CBMV-9	1.0	2.00	1.2	854	427	65	95
CBMV-10	0.8	2.50	1.6	892	357	55	100
CBMV-11	2.8	0.71	0.6	447	625	95	50
CBMV-12	1.2	1.67	0.5	750	450	68	84
CBMV-13	2.8	0.71	1.0	503	697	106	56
CBMV-14	1.2	1.67	1.1	809	479	73	91
BS1	0.8	2.50	-	538	215	-	-

¹Ultimate shear achieved by each specimen; ²Ultimate moment achieved by each specimen; ³Ultimate moment of specimen CBMV-1; ⁴Ultimate shear strength of specimen CBMV-10

Fig. 4 shows the force-deflection curves of the BS-1 and CBMV-10 specimens along with the prediction of the shear strength of the steel beam according to the procedure of Eurocode 3 (BSI, 2005). The shear strength of the steel beam is calculated as 460 kN and compares well with the experimental yield strength equal to 470 kN. The maximum shear strength of BS-1 reached 538 kN, significantly lower than the maximum shear strength of 892 kN achieved by CBMV-10, indicating the high degree of conservatism of the current code provisions in calculating the shear resistance of a composite section. The contribution of the slab to the ultimate shear strength of the beam is evaluated by subtracting the maximum shear of the BS-1 specimen from the maximum shear of the CBMV-10 specimen, resulting in 354 kN or 40% contribution. The experiments showed that the concrete slab of a fully shear connected composite beam contributes significantly to the shear strength of the composite section. Taking the contribution of the slab into account can result in a more efficient design of composite structures.

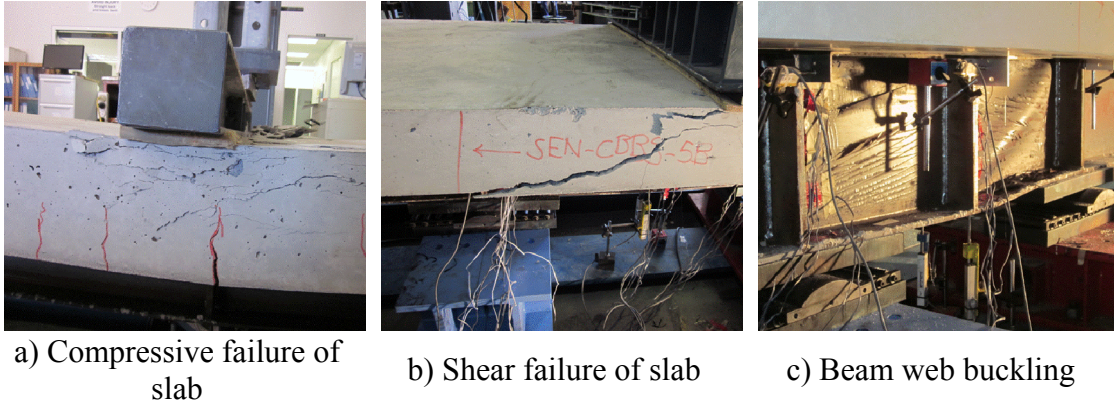


Figure 1. Typical failure modes of the tested composite beams

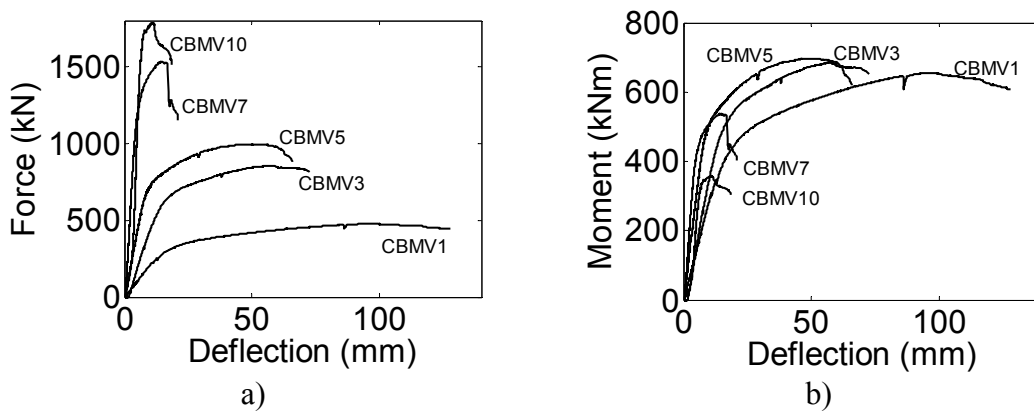


Figure 2. a) Force versus midspan deflection; and b) moment versus midspan deflection experimental curves.

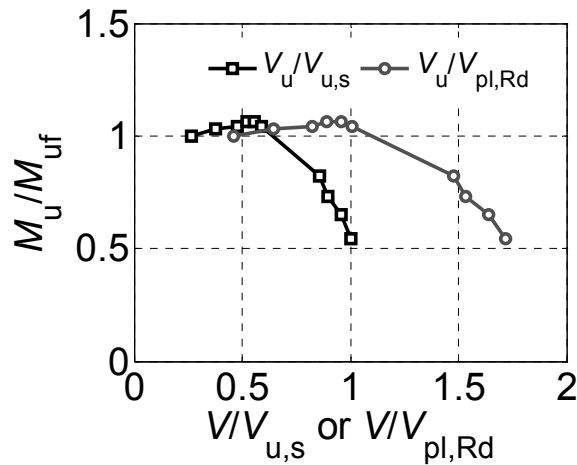


Figure 3. Reduction of the moment capacity of the experimental composite beam as a function of $V_u/V_{u,s}$ and $V_u/V_{pl,Rd}$.

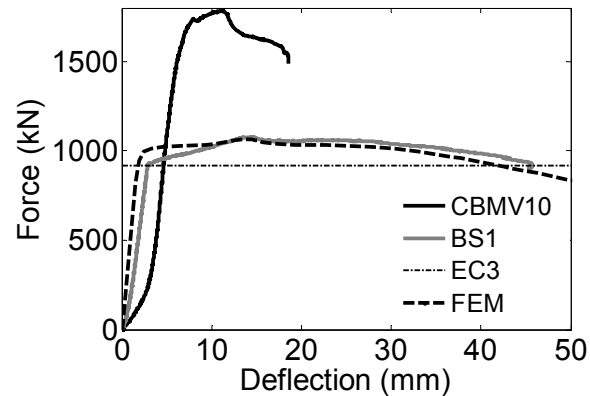


Figure 4. Load-deflection responses of specimens CBMV-10 and BS-1, and Eurocode 3 and FEM model predictions

FINITE ELEMENT MODEL

A FEM model of the experimental specimens was developed using the commercial software Abaqus (Dassault Systemes, 2012). The concrete slab, steel beam and stiffeners were modeled using the four-node shell element with reduced integration and finite membrane strains. The slab reinforcement was modeled as smeared in two directions within the shell elements of the concrete slab. The simulation used the same boundary conditions and loading arrangement as in the experimental program. The stress-strain relationships obtained from the coupon tests were used as input for the steel material definition. Structural steel was modeled as elastic-plastic material with isotropic hardening. The compressive uniaxial stress-strain law of concrete followed the formula proposed by Carreira and Chu (1985) up to the maximum stress f'_c . A perfectly plastic plateau was then specified until the crushing strain equal to 0.004 followed by a softening part. The tensile behaviour of concrete was assumed to be linear up to the uniaxial tensile stress equal to $f_t = f'_c/10$. The post-failure behaviour for direct straining across cracks was modeled using the tension-stiffening option and determining a linear relation until stress is zero at a strain value of 0.035. The damaged plasticity model was used to define the behavior of concrete in the model (Dassault Systemes, 2012).

The shear studs were modeled using the connector element “Cartesian” and connecting a node of the top beam flange with the corresponding node of the slab mid-surface. An elastic-plastic force-slip behavior was specified along the longitudinal direction of the beam, according to the experimental behaviour from pushout tests reported in Vasdravellis et al. (2012a).

A buckling analysis was first performed to specify the buckling modes of the short composite beams. The first buckling mode generated in Abaqus is consistent with the web buckling failures observed in the tests. A static nonlinear analysis was then conducted with the first buckling mode specified as initial imperfection to the model. The buckling mode was scaled to produce a transverse to the web initial imperfection equal to $\min\{D_{\text{beam}}/200; L_s/200\}$ where D_{beam} is the beam height and L_s the shear span, as specified in Eurocode 3: Part 1-5 (BSI, 2003).

Typical experimental and numerical force-deflection curves are compared in Fig. 5. The FEM model predicts the force-deflection response of both the flexural and the short beams with good accuracy. The average error of the FEM model for all the composite beams is 2.74% with standard deviation 2.21%, which is considered an acceptable correlation. The ultimate deformation modes of the FEM models for the shortest beams are shown in Figs. 6(a) and (b) and are consistent with the experimental ones. Fig. 4 shows that the initial stiffness, ultimate strength, and post-buckling behavior of the bare steel specimen BS-1 are predicted accurately by the FEM model. Therefore, the developed FEM model can be reliably used for the prediction of the shear strength of compact composite beams.

The validated FEM model was used to analyse the experimental beam under simply supported conditions with either concentrated force or uniform loading and confirmed that the shear strength was not affected by the experimental setup used for this study.

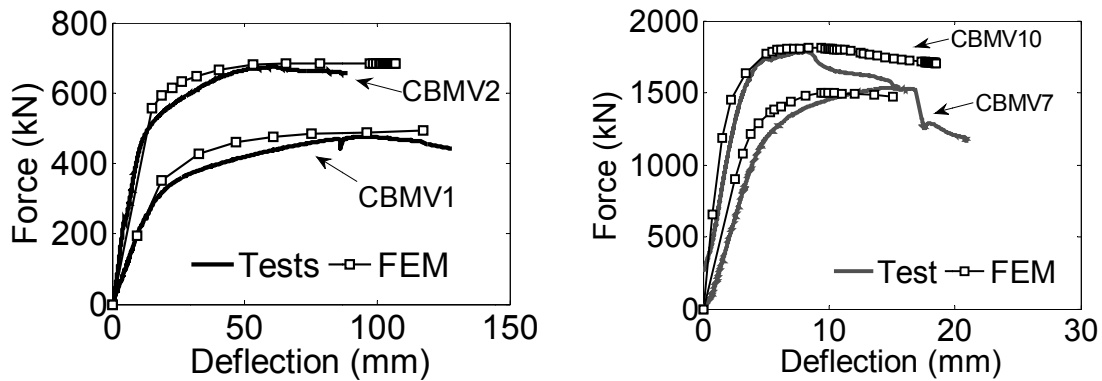


Figure 5. Comparison of force-deflection curves obtained from the tests and the FEM model: long (flexural) beams (left); and short beams (right).

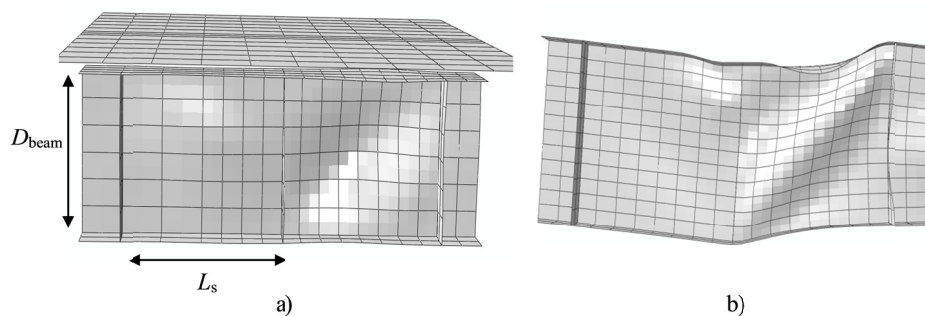


Figure 6. Failure modes predicted by the FEM model: a) composite beam CBMV-10; and b) bare steel specimen BS-1.

PARAMETRIC ANALYSES

A wide range of practical composite beams were designed for the parametric analysis. The steel sections considered are (equivalent sections are given in parenthesis): IPE300 (W310x165x44.5), IPE360 (W360x170x58), IPE400 (W410x180x67), IPE450 (W460x190x74), IPE500 (W530x210x82) and IPE600 (W610x230x125). The yield strength is 300 MPa and all sections are compact. The corresponding effective width of the slab was calculated according to Eurocode 4. Each composite beam is simply-supported and loaded with a midspan imposed displacement. The moment-shear interaction diagram was constructed for each beam by reducing the initial span of each section to produce increasing shear/moment ratios. The shortest shear span was assumed to be equal to the steel beam height. It was found that the shear strength of the composite beam was not increased by further reducing the shear span, thus the shortest beams defined the ultimate composite shear strength. The parameters studied are: the slab depth, slab width, longitudinal reinforcement ratio, and the degree of shear connection. From these parameters, slab width and longitudinal reinforcement ratio were found to have negligible effect on the shear strength of the composite beam. Thus, the results of the rest of the parameters are presented next. The slab depth slenderness ratio, defined as $\lambda_{sd}=D_{slab}/D_{beam}$, where D_{slab} is the slab depth, is introduced to measure the effect of slab depth in a consistent way.

Moment-shear interaction diagram

The moment-shear interaction diagram resulting from the analyses of the parametric beams is plotted in non-dimensional form in Fig. 7 along with the experimental interaction points. The reduction in moment capacity of the parametric beams due to high shear follows the same trend observed in the experimental tests. The numerical analyses confirm the experimental outcome that the moment resistance of a composite beam is reduced when the applied shear is greater than 60% of the shear strength of the composite section.

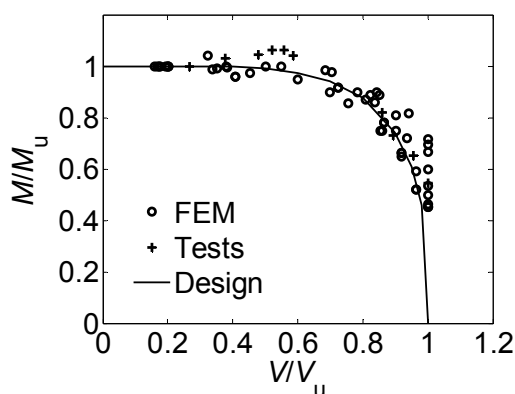


Figure 7. Moment-shear interaction diagram resulting from the parametric analyses and the tests, and superimposed design curve

Effect of the slab depth on the shear strength of composite beams

Fig. 8a plots the shear strength of the parametric beams as a function of λ_{sd} . The slab depth values range from 100 mm to 200 mm with a step of 20 mm; in practice, however, the lower values are most commonly used for composite floor systems. The width was equal to the corresponding effective width. The shear strength variation is plotted as ratio $V_{comp}/V_{0,sd}$, where V_{comp} is the shear strength of a composite beam and $V_{0,sd}$ is the shear strength of the composite beam with slab depth equal to 100 mm. The shear strength of a composite beam is significantly increased by increasing the slab depth. In addition, the increase is larger when λ_{sd} is larger, i.e. in composite beams with shallower steel sections than in those with deeper ones. Fig. 8b plots the percentage contribution of the slab shear strength, V_{slab} , to V_{comp} as function of the ratio λ_{sd} . V_{slab} was calculated subtracting the shear resisted by the steel beam in the FEM model from the total shear. It is shown that the contribution of V_{slab} to V_{comp} ranges from 16 to 60%, depending on the ratio λ_{sd} of the section. For values $\lambda_{sd} \approx 0.4$, as in the experimental section, the contribution ranges from 41 to 50%, which is in agreement with the experimental evidence of this study. A similar contribution of the concrete slab was found in the study by Nie et al. (2004) for their specific sections.

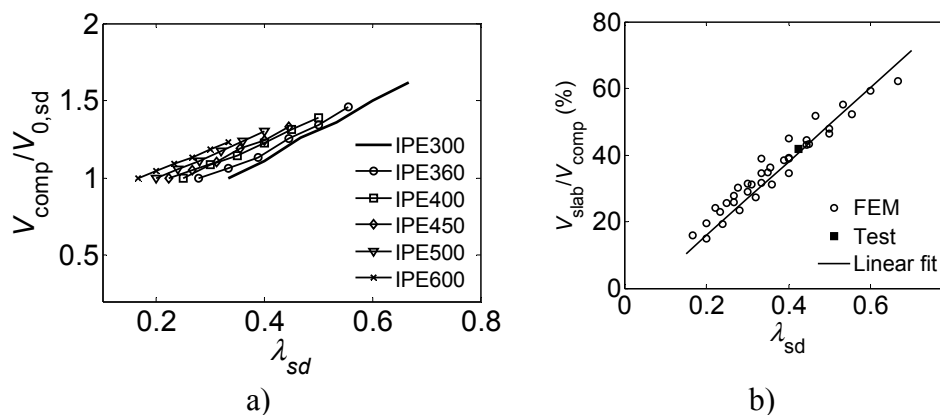
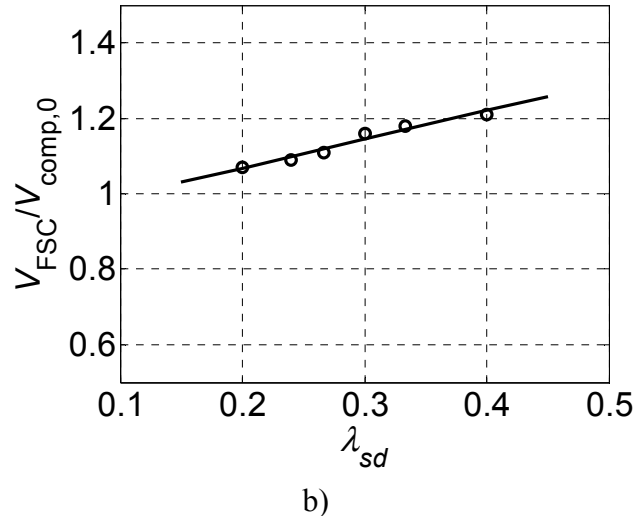


Figure 8. Effect of slab depth on the shear strength of composite beams: a) as ratio $V_{comp}/V_{0,sd}$; and b) as percentage contribution of V_{slab} to the total shear strength

Effect of the degree of shear connection on the shear strength of composite beams

The shortest parametric beams were analyzed using different degrees of shear connection. β values ranged from $\beta=0.1$, i.e. practically no shear connection between the slab and the beam, to $\beta=2$, i.e. a shear connection twice as full. It was found that the shear strength for β values greater than one is not affected. Partial shear connection, however, considerably affects the shear strength of a composite beam. A higher value of β increases the shear capacity and the increase level is greater in beams with larger λ_{sd} . Fig. 9 plots the ratio $V_{FSC}/V_{comp,0}$, where V_{FSC} is the shear

strength of a composite beam with $\beta = 1$ and $V_{\text{comp},0}$ is the shear strength of a composite beam with no shear connection between the slab and the beam, as function of λ_{sd} . A best fit line is superimposed to the data points. It is shown that there is an almost linear relationship between the gain in shear strength and the ratio λ_{sd} .



b)
Figure 9. Effect of the degree of shear connection on the shear strength of composite beams

PROPOSED DESIGN PROCEDURE FOR COMPOSITE BEAMS UNDER BENDING AND SHEAR

Based on the experimental results and the parametric analyses, a design model for calculating the reduced moment capacity of a composite beam in regions of high shear is proposed. The moment-shear interaction in steel-concrete composite beams is calculated according to equation (3):

$$\left(\frac{M}{M_{\text{Rd}}}\right)^3 + \left(\frac{V}{V_{\text{comp}}}\right)^6 = 1 \quad (3)$$

where M_{Rd} is the positive design moment resistance of the composite section, calculated according to the provisions of the relevant standards, and V_{comp} is the shear strength of the composite section. Fig. 7 shows that there is good fit between the proposed equation and the interaction points resulting from the experiments and the parametric analyses of a wide range of composite sections. According to this formula, the reduction of the moment capacity starts when the applied shear is greater than approximately 60% of V_{comp} .

To develop a design model for the calculation of the shear strength of a composite beam, it is assumed that the shear strength of a composite section consists of the individual contributions of the shear capacity of the steel beam alone, $V_{\text{pl,Rd}}$, and the concrete slab, V_{slab} , i.e.:

$$V_{\text{comp}} = V_{\text{pl,Rd}} + V_{\text{slab}} \quad (4)$$

In Eq. (4) $V_{\text{pl,Rd}}$ is the shear strength of the steel beam alone and calculated according to Eq. (1) for compact steel sections. V_{slab} accounts for the effects of both the shear strength of concrete slab and the shear connection between the slab and the beam. Eq. (4) assumes full shear connection for the composite beam; thus, the effects of the composite action are implicitly accounted for in the proposed formula. For simplicity, a formula similar to the one provided in ACI 318-11 (American Concrete Institute, 2011) for the shear strength of concrete section without shear reinforcement is proposed. Regression analysis of the parametric data showed that there is an almost linear relationship between the ratio λ_{sd} and the term $V_{\text{slab}}/(b_f D_{\text{slab}})^{0.7} (f'_c)^{1/2}$, as shown in Fig. 10, where b_f is the width of the beam's top flange. Thus, the shear strength of the concrete slab is proposed to be calculated by:

$$\begin{aligned} V_{\text{slab}} \\ = \varphi_s f(\lambda_{\text{sd}}) (b_f D_{\text{slab}})^{0.7} \sqrt{f'_c} \end{aligned} \quad (5)$$

where φ_s is a safety factor and $f(\lambda_{\text{sd}})$ is a function of the slab slenderness ratio given by:

$$f(\lambda_{\text{sd}}) = 110 \lambda_{\text{sd}} + 13 \quad (6)$$

The units in Eq. 5 are in N and mm. $f(\lambda_{\text{sd}})$ is superimposed to the numerical results in Fig. 10. The ratios of the composite shear strength calculated using the FEM model to the values provided by the design model have mean value 0.98 and standard deviation 0.03. The corresponding values associated with the calculation of V_{slab} are 0.97 and 0.11. Therefore, it is suggested that φ_s should be equal to 0.80 to provide a safety margin. The inclusion of appropriate safety factors for the materials will produce an even more conservative design. Further analyses with different f'_c values produced results that are predicted accurately by the design model.

For the calculation of the shear strength of a partially connected composite beam, $V_{\text{comp},\beta}$, both the degree of shear connection and the ratio λ_{sd} are accounted for. The following design procedure is proposed to calculate the $V_{\text{comp},\beta}$:

1. Calculate the ratio λ_{sd} of the section.
2. Calculate the shear strength of a composite beam with full shear connection, V_{comp} , according to Eqs. (4) to (6).
3. From the graph of Fig. 9 calculate the shear strength of a composite beam with no shear connection, $V_{\text{comp},0}$, for the specific λ_{sd} value.
4. The shear strength of the composite beam with any degree of shear connection, $V_{\text{comp},\beta}$, can be computed using linear interpolation between the values V_{comp} and $V_{\text{comp},0}$, since the relation of the moment reduction is a linear function of β , as shown in Fig. 9a.

The proposed model is believed to be valid under the range of applications where: a) compact composite beams are subjected to positive (sagging) bending moment and shear; b) punching shear failure is not the governing failure mode, although structural codes provide sufficient design guidance to prevent this failure

mode if necessary; c) the composite beam is subjected to both concentrated loads and UDL; however, vertical stiffeners are placed below the concentrated load; and d) B_{eff} is assumed to be greater than three times the steel beam depth.

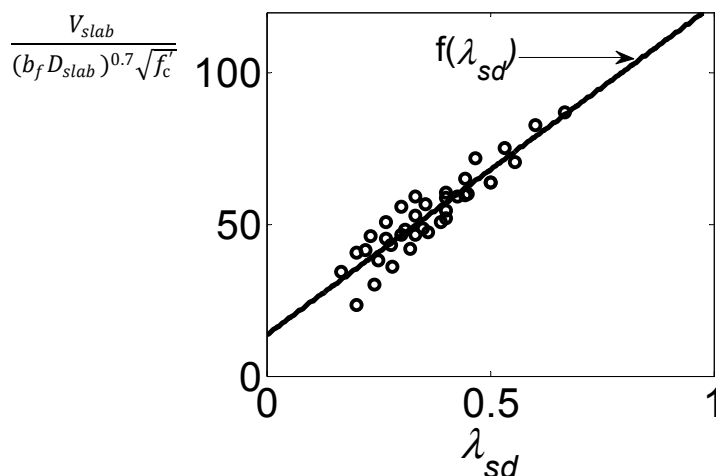


Figure 10. Scatter of data points relating λ_{sd} with the shear strength of slab, and linear best-fit line used in the design.

CONCLUSIONS

This paper presented an experimental and numerical study on the shear strength and moment-shear interaction in simply-supported composite beams. Based on the experimental and numerical results the following conclusions can be drawn:

The results presented in this work showed that the moment capacity of a composite beam starts to decrease when subjected to shear force exceeding the 60% of the shear strength of the composite section or the 100% of the shear strength of the steel beam.

The experiments showed that use of partial shear connection reduces the shear strength, but increases the ultimate deformation capacity of a composite beam under high shear force.

The use of inclined rebars as shear reinforcement prevents the sudden shear failure of the slab, slightly increases the shear strength of a composite beam, and significantly enhances its ductility.

The experimental and numerical results demonstrated a high level of conservatism in the current code provisions for both the calculation of the composite shear strength and the reduction in moment capacity due to shear. A more efficient design of composite beams can be achieved when the contributions of the slab and the composite action are taken into account. The results of the numerical analyses showed that this contribution ranges from 16 to 60%, depending on the ratio λ_{sd} (defined as slab depth/beam depth) of the section.

The parametric analyses have shown that the most important factors that affect the shear strength of a composite beam are the slab depth and the degree of shear connection, while the slab width and the longitudinal reinforcement ratio have limited influence on the shear strength.

The shear strength of a composite beam is significantly enhanced by increasing the slab depth; however, this increase is less for deeper sections, with lower λ_{sd} values. Moreover, the contribution of the slab is a linear function of the ratio λ_{sd} of the section.

A higher degree of shear connection increases the shear capacity of a composite beam, and the increase level is higher in beams with larger λ_{sd} values. In addition, there is a linear relationship between the gain in strength and the ratio λ_{sd} , as well as the gain in strength and the degree of shear connection.

A semi-empirical design model for the more accurate calculation of the shear strength and moment-shear interaction in simply-supported composite beams is proposed based on regression analysis of the experimental and parametric results.

ACKNOWLEDGEMENTS

The experimental work described herein was funded by the Australian Research Council (ARC) Discovery Project DP0879734. The authors would like to thank all the technical staff of the Structures Laboratory of the University of Western Sydney for their precious assistance on the preparation and execution of the experimental program.

REFERENCES

- American Concrete Institute (2011). ACI 318-11: Building code requirements for structural concrete. ACI Committee 318, Structural Building Code.
- American Institute of Steel Construction (2010). ANSI/AISC 360-10: Specification for structural steel buildings. Chicago, Illinois, 60601-1802.
- Baskar, K. and Shanmugam, N.E. (2003). "Steel-concrete composite plate girders subject to combined shear and bending". *J. Constr. Steel Res.*, 59(4), 531-557.
- British Standards Institution (2002). Eurocode 1: Actions on structures. Part 1-1: General actions: Densities, self-weight, imposed loads for buildings. BS EN 1991-1-1: 2002.
- British Standards Institution (2003). Eurocode 3: Design of steel structures. Part 1-5: Plated structural elements. BS EN 1993-1-5: 2003.
- British Standards Institution (2004). Eurocode 4: Design of composite steel and concrete structures. Part 1-1: General rules and rules for buildings. BS EN 1994-1-1: 2004.
- British Standards Institution (2005). Eurocode 3: Design of steel structures. Part 1-1: General rules and rules for buildings. BS EN 1993-1-1: 2005.
- Carreira, D.J. and Chu, K.H. (1985). "Stress-strain relationship for plain concrete in compression". *ACI Journal Proc.*, 82(11), 797-804.
- Dassault Systèmes (2012). Abaqus user's manual, version 6.12. Dassault Systèmes Simulia Corp., Providence, RI, USA.
- Johnson, R.P. and Willmington, R.T. (1972). "Vertical shear in continuous composite beams". *Proc. of the Institution of Civil Engineers*, 53(2), 189-205.

- Liang, Q.Q., Uy, B., Bradford, M., and Ronagh, H. (2005). "Strength analysis of steel-concrete composite beams in combined bending and shear". *J. Struct. Eng.*, 131(10), 1593-1600.
- Liang, Q.Q., Uy, B., Bradford, M., and Ronagh, H. (2004). "Ultimate strength of continuous composite beams in combined bending and shear". *J. Constr. Steel Res.*, 60(8), 1109-1128.
- Nie, J., Xiao, Y. and Chen, L. (2004). "Experimental studies on shear strength of steel-concrete composite beams" *J. Struct. Eng.*, 130(8), 1206-1213.
- Shanmugam, N.E. and Baskar, K. (2003). "Steel-concrete composite plate girders subject to shear loading". *J. Struct. Eng.*, 129(9), 1230-1242.
- Sharefati, A., Farimani, R., and Azizimanini, A. (2011). "Effect of concrete slab on shear capacity of composite plate girders under positive moment". *J. Bridge. Eng.*, in press: doi:10.1061/(ASCE)BE.1943-5592.0000319.
- Standards Australia (1998). AS4100: Steel structures. Standards Australia International Ltd., Sydney.
- Standards Australia (2003). AS2327.1: Composite structures. Part 1: Simply supported beams. Standards Australia International Ltd., Sydney.
- Uy, B. and Liew, J.Y.R. (2002). Composite steel-concrete structures, Chapter 51, Civil Engineering Handbook, (edited by W.F. Chen and J.Y. Richard Liew). CRC Press, Boca Raton.
- Vasdravellis G., Uy B., Tan E.L., Kirkland B. (2012a). "Behaviour and design of composite beams subjected to negative bending and compression". *J. Constr. Steel Res.*, 79, pp. 34-47.
- Vasdravellis G., Uy B., Tan E.L. and Kirkland B. (2012b). "The effects of axial tension on the sagging-moment regions of composite beams". *J. Constr. Steel Res.*, 72, pp. 240-253.
- Vasdravellis G., Uy B., Tan E.L., Kirkland B. (2012c). "The effects of axial tension on the hogging-moment regions of composite beams". *J. Constr. Steel Res.*, 68 (1), pp. 20-33.
- Vasdravellis G., Uy B. (2014). "Shear strength and moment - shear interaction in steel-concrete composite beams". *J. Struct. Eng. (ASCE)*; 140 (11).
- Vasdravellis G., Uy B., Tan E.L., Kirkland B. (2015). "Behaviour and design of composite beams subjected to sagging bending and axial compression". *J. Constr. Steel Res.*; DOI: 10.1016/j.jcsr.2015.03.010.

Nominal Flexural Strength of Conventional or Hybrid Composite Girders

S. G. Youn¹ and D. Bae²

¹Dept. of Civil Engineering, Seoul National Univ. of Science and Technology, 232 Gongneung-ro, Nowon-gu, Seoul 139-743, Korea. E-mail: sgyoun@seoultech.ac.kr

²Dept. of Civil and Environmental Engineering, Kookmin Univ., 77 Jeongneung-ro, Seongbuk-gu, Seoul 136-702, Korea. E-mail: dbbae@kookmin.ac.kr

Abstract

This paper contains a parametric study for the development of the nominal flexural strength of conventional composite girders and hybrid composite girders using HSB high-performance steels in positive bending region. The flexural strength and the ductility of a wide range of conventional or hybrid composite girders are calculated using moment-curvature analysis, and the plastic moment of each section is obtained using simple plastic theory. For developing new design equations, the obtained flexural strength and the ductility of conventional or hybrid composite girders are compared to the previous research work and the current AASHTO LRFD's design equations. The comparison results show that there are considerable differences in flexural strength distribution between the conventional composite girders and the hybrid composite girders. It was also observed that in case of the hybrid composite girders, until considerably high ductility parameter, the flexural strength is not smaller than the plastic moment. Based on the results of parametric study, new design equations are proposed for predicting the nominal flexural strength of conventional or hybrid composite sections.

INTRODUCTION

Currently the Ministry of Land, Infrastructure and Transport (MOLIT) of the Korean Government has a plan for developing new design code system for infrastructure. The design regulations related to steel-concrete composite structures are distributed in the steel design codes (KSSC, 2008) or the concrete design codes (KCI, 2012) and thus, there is a need to develop new design codes just for steel-concrete composite structures separately. A national research project is running to develop new capacity based design codes on steel-concrete composite structures based on limit state design concepts. The termination of the research project is expected for the period 2011-2014. This project has an additional purpose for including high-performance steel and high-performance concrete in the design codes for steel and concrete composite construction. The research results related to high-performance materials conducted by the Korea Bridge Design & Engineering Center (KBRC, kbrc.snu.ac.kr) established by 2004 are included in the new design codes. The ultimate flexural strength of conventional composite girders or hybrid composite girders at sagging and hogging bending regions was also a research topic in KBRC (Ryu et al., 2005; Youn et al., 2008).

The high-performance steels of HSB600 and HSB800 have developed by a steel company POSCO in Korea (Lee et al., 2007). The HSB steels have higher performance characteristics, such as yield and tensile strength, weldability, cold formability, than those of conventional structural steels, such as SM400, SM490, SM520, etc. The minimum yield strength (0.2% proof stress) of HSB600 and HSB800 is 450 MPa and 690 MPa, respectively, and the minimum tensile strength of HSB600 and HSB800 is 600 MPa and 800 MPa, respectively. HSB Steels do not have an obvious yield point and perfect plastic region before strain hardening process in the stress-strain curves as shown in Fig. 1. These steels are included in the steel bridge design codes in 2012 (MOLIT, 2012).

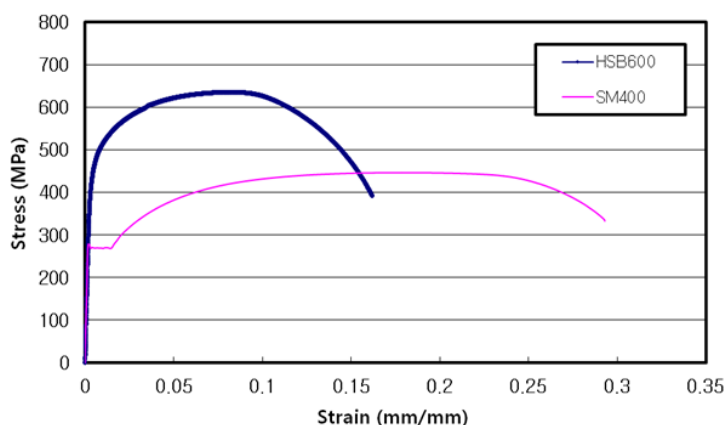


Fig. 1 Stress-strain curves of SM400 and HSB600

The high strength concrete is also included in the concrete bridge design codes in 2012 (MOCT). The maximum compressive strength of concrete is limited to 70 MPa. The stress-strain curves of concrete are also introduced for nonlinear analysis or design of the concrete structures. Fig. 2 shows the stress-strain curves for design of the concrete structures. The ultimate compressive strain of concrete is a fixed value of 0.0033 mm/mm for concrete with the strength up to 40 MPa concrete and 0.003 mm/mm for 70 MPa concrete. The ultimate concrete strain between 40 MPa and 70 MPa concrete can be determined by linear interpolation. In case of steel-concrete composite columns 100MPa high-performance concrete can be applied.

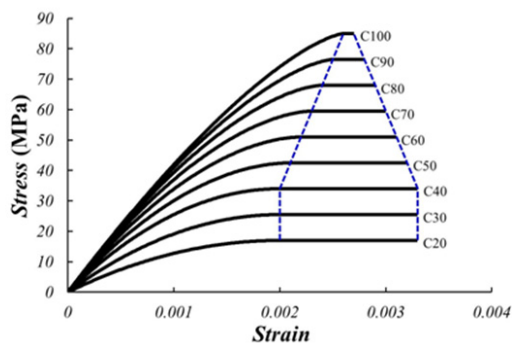


Fig. 2 Stress-strain curves of concrete

The ultimate flexural strength of composite girders at sagging bending is influenced by the material characteristics of steels and concrete. The cross-section details of composite girders also influence on the ductility and the ultimate flexural capacity of composite girders. The moment capacity of composite sections in sagging bending may be determined by simple plastic theory. The simple plastic theory requires composite sections to be ductile to show sufficient rotation and moment capacity greater than plastic moment. For brittle composite sections, the moment capacity is governed by premature concrete crushing and thus, the bending resistance should be reduced for ensuring additional safety margin. In the codes of AASHTO LRFD (2007) and Eurocode 4 (2005), strength reduction factors and ductility requirements are also introduced.

In composite bridges, steel girders may be designed by homogeneous sections (conventional composite girder) or hybrid sections (hybrid composite girder). In hybrid composite girders in sagging bending region HSB steels may be used only at the tension flange because the tension flange contributes most of the ultimate flexural strength to the hybrid composite girders. The minimum compressive strength of the cast-in-place concrete for bridge deck is 27 MPa. For precast concrete bridge decks 35 MPa may be used for post-tensioning. Different from composite columns of concrete filled steel tube columns or steel reinforced concrete columns, transverse cracks caused by hydration heat should be considered when high strength concrete applies in the cast-in-place concrete bridge decks. In addition the empirical design method based on the fatigue strength of concrete decks applies in Korea. This method adapts the minimum thickness of concrete bridge deck of 240 mm and the longitudinal reinforcement ratio, 0.006 at sagging bending region and 0.015 at hogging bending region. If high strength concrete applies at cast-in-place concrete decks, transverse cracks may be expected at early curing stage and these cracks affect the serviceability and the durability of concrete bridge decks.

In order to develop new design equations for predicting the nominal flexural strength of conventional composite girders and hybrid composite girders, the ultimate moment capacity and the ductility of a wide range of composite sections are investigated by using moment-curvature analyses and simple plastic theory.

STRENGTH REDUCTION FACTOR

For the safety of brittle composite sections, the ultimate moment capacity of composite girders should be reduced to introduce additional safety margin. In the AASHTO LRFD (2007), the nominal flexural strength at the ductility limit, $D_p / D_t = 0.42$, is regulated to $0.78 M_p$ for conventional composite girders. D_t represents the total height of composite section and D_p is the depth of plastic neutral axis in composite section. The lower boundary values of the ultimate moment capacity at $D_p / D_t = 0.42$ are close to $0.96 M_p$ as shown in Fig. 3. It means the addition safety margin is 1.23 for $0.96 M_p$ or 1.28 for the plastic moment M_p as shown in Fig. 4 (Youn et al., 2013). These values of 1.23 and 1.28 are related to the research results conducted by Ansourian (1982) and Wittry (1993).

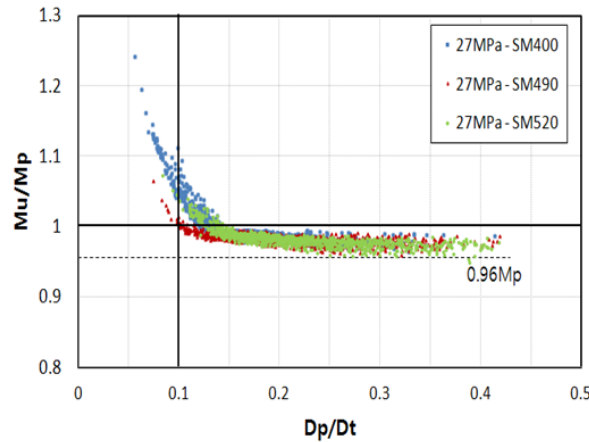


Fig. 3 Normalized moment capacity M_u / M_p of conventional composite girders

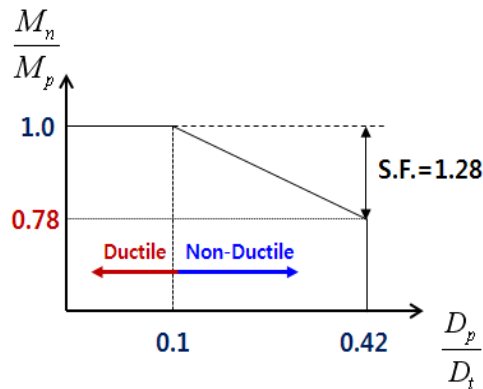


Fig. 4 Relationship between ductility parameter and moment capacity in the AASHTO LRFD (2007)

Wittry assumed the ultimate moment capacity of brittle composite girders linearly decreases from the plastic moment M_p to the yield moment M_y as the ratio of D_p / D' changes from 1 to 5 and proposed new design equation for brittle composite sections with additional strength reduction factor $\phi=0.85$ at $D_p / D' = 5$ as shown in Eq. 1 and Fig. 5.

$$M_n = \frac{5M_p - \phi M_y}{4} + \frac{\phi M_y - M_p}{4} \left(\frac{D_p}{D'} \right), \quad 1 \leq D_p / D' \leq 5 \quad (1)$$

where D' is the depth of maximum plastic neutral axis for ductile conventional composite girders proposed by Wittry. D' is $0.7(D_t / 7.5)$ for 345 MPa composite section and $0.9(D_t / 7.5)$ for 250 MPa composite section.

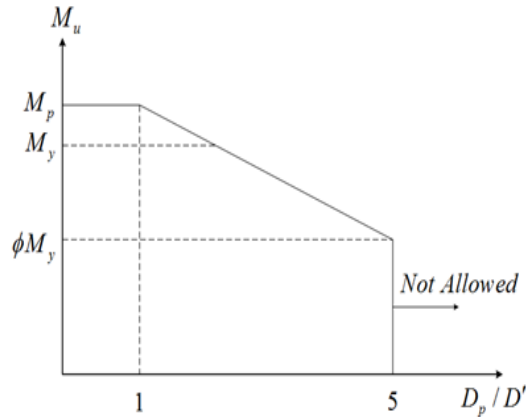


Fig. 5 Wittry's proposal for strength prediction

When the ductility limit $D_p / D' = 5$ in Wittry's equation is used, the actual ductility limit changes with varied steel grades and the ultimate curvature of cross-section at the ductility limit is not same to that at the ductility limit $D_p / D_t = 0.42$. Furthermore the ultimate moment capacity of brittle composite sections does not linearly decreases from the plastic moment to the yield moment as the ductility ratio D_p / D' changes and also the steel grade changes as shown in Fig. 6 and Fig. 7 (Youn et al., 2013).

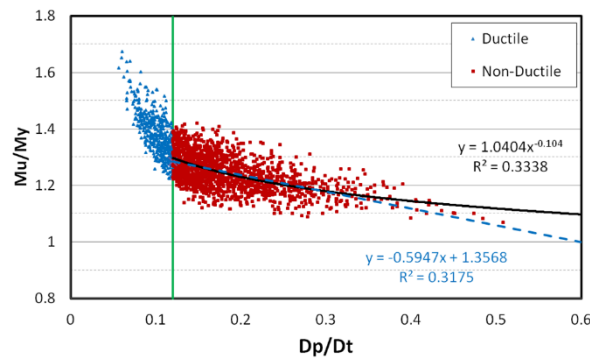


Fig. 6 Curve Fit of Non-ductile Composite Girders with SM400 Steel

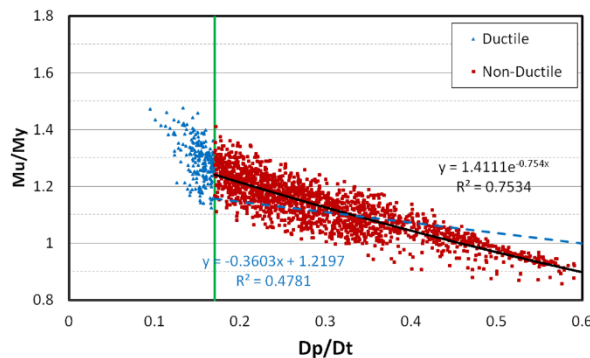


Fig. 7 Curve Fit of Non-ductile Composite Girders with HSB600 Steel

The values of M_u / M_y at $D_p / D_t = 0.42$ are summarized in Table 1. Therefore there are some needs to change the addition safety margin of 1.23 for $0.96 M_p$ or 1.28 for the plastic moment for consistency to varied steel grades.

Table 1 M_u / M_y at $D_p / D_t = 0.42$

	SM400	SM490	SM520	Average	HSB600	HSB800
M_u / M_y	1.139	1.099	1.063	1.100	1.028	0.889

Concrete stress-strain model presented in the Comité Européen du Béton (1991) is applied as shown in Eq. 2 and material properties of steels are summarized in Table 2.

$$f_c = \frac{0.85 f_{ck} (a - 206,600 \epsilon_c) \epsilon_c}{1 + b \epsilon_c} \quad (2)$$

where, $a = 39,000(0.85 f_{ck} + 7.0)^{-0.953}$

$$b = 65,600(0.85 f_{ck} + 10.0)^{-1.085} - 860$$

Table 2 Material properties of steels

Property	SM400	SM490	SM520	HSB600	HSB800
Yield strength (MPa)	240	320	360	450	690
Tensile strength (MPa)	400	490	520	600	800
Yield strain (mm/mm)	0.00117	0.00157	0.00175	0.00221	0.00336
Strain-hardening strain (mm/mm)	0.016	0.020	0.015	0.00221	0.00336
Elastic modulus (MPa)	205,000	205,000	205,000	205,000	205,000
Modulus of strain-hardening region (MPa)	4,800	3,800	4500	4,455	3,222

MODIFIED WITTRY'S EQUATION

The nominal flexural strength of brittle composite girders shown in the equation (1) is modified to obtain new strength equation as a function of the ductility parameter D_p / D_t . For example, as shown in Eq. 3, a modified strength equation for composite sections with SM400 steel can be obtained as same as the process of Wittry's equation (see Eq. 1).

$$M_n = \frac{0.42M_p - 0.12\phi 1.139M_y}{0.30} + \frac{\phi 1.139M_y - M_p}{0.30} \left(\frac{D_p}{D_t} \right), \quad 0.12 \leq D_p / D_t \leq 0.42 \quad (3)$$

Fig. 8 shows the comparison of the ultimate flexural capacity and Eq. 3 of a wide range of brittle composite sections to obtain safety factor at the ductility limit $D_p / D_t = 0.42$. From the Fig. 8 the safety factor of 1.18 can be obtained at the ductility limit, $D_p / D_t = 0.42$ (Youn et al., 2013).

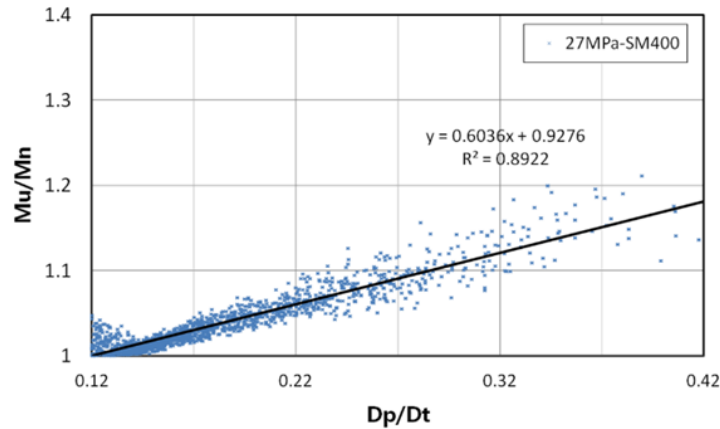


Fig. 8 Safety factor for brittle composite girders with SM400 Steel

For conventional composite sections with SM490 and SM520, safety factors at the ductility limit $D_p / D_t = 0.42$ are very close to 1.18. Using the safety factor ϕ of 1.18, the predicting equation for nominal flexural strength can be developed as show in Eq. 4 and Eq. 5. Fig. 9 shows the comparison of the proposed new design equation and the predicting strength equation in the AASHTO LRFD (2007). From the Fig. 9 it can be found that the safety factor at $D_p / D_t = 0.42$ is 1.18 for the plastic moment and 1.13 for $0.96 M_p$.

$$D_p / D_t \leq 0.1 : \quad M_n = M_p \quad (4)$$

$$0.1 \leq D_p / D_t \leq 0.42, \quad M_n = M_p \left(1.047 - 0.47 \frac{D_p}{D_t} \right) \quad (5)$$

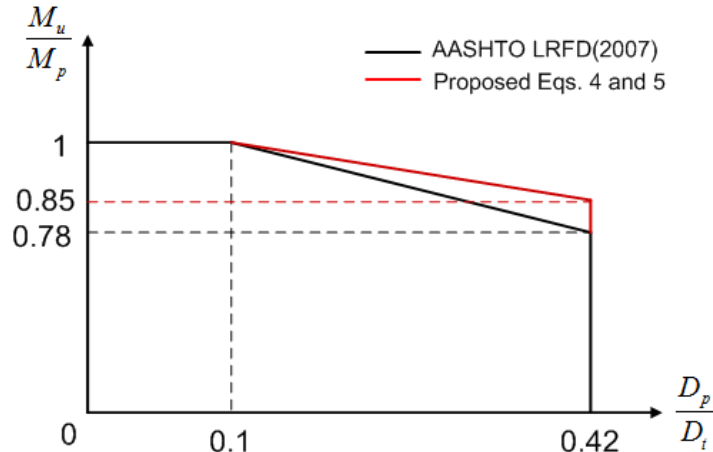


Fig. 9 Comparison of Proposed Equation and AASHTO LRFD's Strength Prediction

For conventional composite sections with HSB600 or HSB800, Wittry's method is not compatible for developing strength equations because M_u / M_n does not show linear distribution as shown in Fig. 10. Therefore in cases of HSB600 or HSB800 the safety factor of 1.13 for the ultimate moment capacity is directly used for developing new design equations as shown in Eq. 6 and Eq. 7. Fig. 11 show the proposed strength reduction factors for conventional composite girders with HSB600 and HSB800.

For conventional composite section with HSB600 ;

$$0.1 \leq D_p / D_t \leq 0.42, \quad M_n = M_p \left(1.056 - 0.56 \frac{D_p}{D_t} \right) \tag{6}$$

For conventional composite section with HSB800 ;

$$0.1 \leq D_p / D_t \leq 0.42, \quad M_n = M_p \left(1.091 - 0.91 \frac{D_p}{D_t} \right) \tag{7}$$

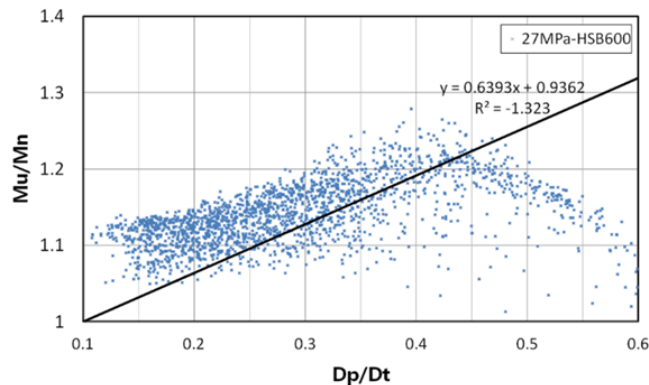


Fig. 10 Safety Factor for Non-ductile Composite Girders with HSB600 Steel

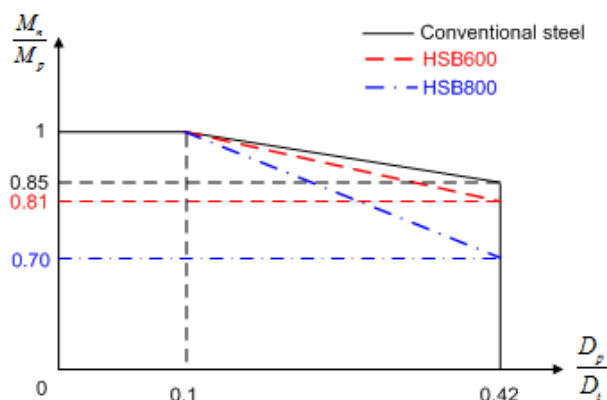


Fig. 11 Proposed Strength Equations of Conventional Composite Girders with HSB Steels

HYBRID COMPOSITE GIRDER

Hybrid composite girders can be applied in steel and concrete composite bridges and simple plastic theory also can be applied to calculate the collapse load of simple-supported or continuous composite girders. Ductile hybrid composite sections are to be ductile to show that the ultimate moment capacity is greater than its plastic moment as shown in Fig. 12 (Youn, 2013).

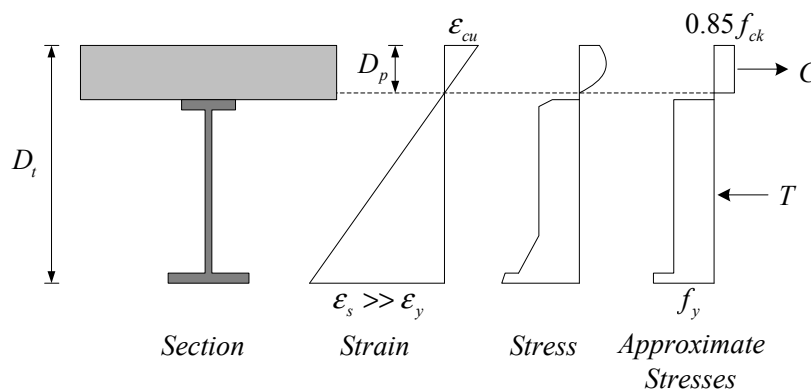


Fig. 12 Stress and strain distribution of hybrid composite section

For brittle hybrid composite sections, the ultimate moment capacity should be also reduced to obtain additional safety margin as same as that of conventional composite sections. In addition previous experimental tests conducted by Youn et al. (2008) suggest that the ultimate moment capacity of hybrid composite sections using HSB600 is greater than the predicting equations for the nominal flexural strength in the AASHTO LRFD (2007).

Fig. 13 shows the normalized ultimate moment capacity of a wide range of hybrid composite sections with 27 MPa concrete deck according to the ductility parameter D_p / D^* . D^* represents the depth of maximum plastic neutral axis in the AASHTO bridge design codes (2000) and $D^* = D_t / 7.5$. The normalized ultimate

moment capacity of hybrid composite sections is quite higher than the plastic moment M_p up to high ductility parameter D_p / D^* and thus, there are some needs to change the value of ductility parameter for classifying ductile or brittle hybrid composite sections. In addition it can be found that the ultimate moment capacity converges $0.96 M_p$ at $D_p / D_t = 0.42$ similar to that of conventional composite sections.

Ansourian (1982) proposed the minimum ductility parameter $\chi = 1.4$ is required for applying simple plastic theory to calculate the collapse load of simple-supported or continuous composite beams in sagging bending regions. This is same to the value of ductility parameter $D_p / D_t = 0.143$. It means the ductility parameter $D_p / D_t = 0.143$ can be adapted for the criteria for classifying ductile or non-ductile hybrid composite section in plastic design. Rotation capacity of the hybrid composite section is not less than that of the conventional composite sections, because rotation capacity is proportioned to the ultimate curvature of composite sections and the ultimate curvature depends on the ductility parameter of D_p / D_t . Therefore the additional safety margin for brittle hybrid composite sections can be introduced by dividing the ultimate moment capacity with the safety factor. The safety factor increases linearly from 1.0 at $D_p / D_t = 0.143$ to 1.13 at $D_p / D_t = 0.42$.

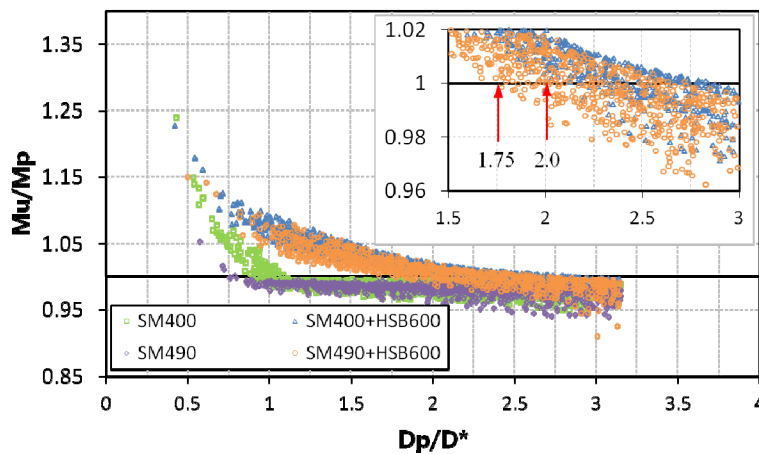


Fig. 13 Effect of hybrid steel combinations on ultimate moment capacity

For examples, the nominal flexural strength of hybrid composite sections with HSB600 can be proposed by using the safety factor of 1.13 at $D_p / D_t = 0.42$ (Youn, 2013) as follows ;

For SM400+HSB600 hybrid composite sections;

$$D_p / D_t \leq 0.1 : M_n = 1.08M_p \tag{8}$$

$$0.1 \leq D_p / D_t \leq 0.42 : M_n = 1.08M_p (1.067 - 0.67 \frac{D_p}{D_t}) \tag{9}$$

For SM490+HSB600 hybrid composite sections;

$$D_p / D_t \leq 0.1 : \quad M_n = 1.06M_p \quad (10)$$

$$0.1 \leq D_p / D_t \leq 0.42 : \quad M_n = 1.06M_p \left(1.062 - 0.62 \frac{D_p}{D_t}\right) \quad (11)$$

where, M_p is the plastic moment of the hybrid composite sections with HSB600 high-performance steel at tension flange only.

In the previous equations, the maximum nominal flexural strength of $1.08M_p$ and $1.06M_p$ can be changed to the plastic moment M_p , and also the criteria of the ductility parameter for dividing ductile girders or brittle girders also can be changed from $D_p / D_t = 0.1$ to $D_p / D_t = 0.15$. In addition, steel combinations of hybrid composite sections can be changed and thus, it is considered that regulating predicting equations for each several hybrid composite section is not compatible to introduce in the design codes of steel and concrete composite structures. The research program is still running in order to propose simple predicting equations for calculating the nominal flexural strength of hybrid composite sections with HSB600 and HSB800.

SUMMARY AND CONCLUSIONS

In October 2011, the Korean Government has started a research project to develop the new design code for steel and concrete composite structures based on limit state design concepts. In 2013, the Korean Government starts to change the current Korean codes system to a set of new design codes system for whole infrastructures. This system will be similar to the Eurocodes's system. This paper presents a parametric study for the development of the nominal flexural strength of conventional composite girders and hybrid composite girders using HSB high-performance steels. In order to introduce HSB steels in the new steel and concrete design codes, the ultimate flexural strength and the ductility of a wide range of brittle composite girders are calculated by using moment-curvature analyses. The results of this research project for developing new design codes for steel-concrete composite structures are expected to the part of new design codes system.

ACKNOWLEDGEMENT

This research was supported by a grant from the R&D Policy and Infrastructure Development Program (11 technical standardization 09-01-Development of capacity based design codes on steel-concrete composite structures) funded by the Ministry of Land, Infrastructure and Transport (MOLIT) of the Korean Government.

REFERENCES

- AASHTO. (2000), LRFD bridge design specifications, 2nd Ed., Washington, D.C.
- AASHTO. (2007), LRFD bridge design specifications, 4th Ed., Washington, D.C.
- Ansourian, P. (1982), "Plastic Rotation of Composite Beams," *Journal of Structural Division*, ASCE, Vol. 108, No. ST3, pp. 643-659.
- Comite Euro-International du Beton (CEB) (1991), CEB-FIP Model Code 1990, Thomas Telford, Lausanne, Switzerland.
- Eurocode 4 (2005), Design of Composite Steel and Concrete Structures, Part 2. General rules and rules for bridges. ENV 1994-2:2005.
- Korea Concrete Institute (KCI), (2012), Design specifications for concrete structures, KCI, Korea (in Korean)
- Korean Society of Steel Construction (KSSC), (2008), Design specifications for steel structures, KSSC, Korea (in Korean)
- Lee, J. K., Yoon, T. Y., Choi, J. L., and Cho, J. Y. (2007), "Development and commercialization of high performance steel for bridges(HSB600)," *Proceedings of the Korea Society of Steel Construction*, KSSC, pp. 103-107.
- Ministry of Construction and Transportation (MOCT), (2012), Design specifications for highway bridges – Limit State Design (in Korean), MOCT, Korea.
- Ryu, H. K., Lee, P. G., Shim, C. S., Yoon, S. G., and Chang, S. P., (2005), "Bending capacity of continuous composite hybrid beams," *Proceedings of The International Conference on Advanced Materials for Construction of Bridges, Buildings IV*, 2005
- Wittry, D. M. (1993), "An Analysis Study of the Ductility of Steel-Concrete Composite Sections." MS thesis, Univ. of Texas-Austin, Austin, Tex.
- Youn, S. G., (2013), "Revaluation of Nominal Flexural Strength of Composite Girders in Positive Bending Region," *Journal of Korean Society of Steel Construction*, Vol. 25, No. 2, pp.165-178. (in Korean)
- Youn, S. G., (2013), "Nominal Moment Capacity of Hybrid Composite Sections using HSB600 High-Performance Steel," *International Journal of Steel Structures*, Vol. 13, No. 2, pp.1-10.
- Youn, S. G., Bae, D., and Kim, Y. J., (2008), "Ultimate Flexural Strength of Hybrid Composite Girders Using High-Performance Steel of HSB600 at Sagging Bending," *Proceedings of the 2008 Composite Construction in Steel and Concrete VI*, ASCE, Colorado, pp. 680-690.

Footfall-Induced Vibration in Longspan Composite Steel Beams Used in Two Projects at the University of Auckland

V. N. Patel¹ and R. J. Built²

¹Associate, Beca Ltd., P.O. Box 6345, Wellesley St., Auckland 1141, New Zealand. E-mail: vijay.patel@beca.com

²Senior Technical Director, Beca Ltd., P.O. Box 6345, Wellesley St., Auckland 1141, New Zealand. E-mail: richard.built@beca.com

Abstract

Floor vibration due to human activity has become increasingly recognized by structural engineers, architects, and building owners as an inherent issue in long-span steel framed floor systems. In the past, attention was primarily focused on strength and deflection serviceability limits. However, as designers seek to push the limits on structural spans, grid spacings and adopt light-weight, low damping structural steelwork floor systems, more detailed consideration is required of the design tools and processes available to analyze and predict the vibration performance of floor systems. Selection from published criteria of an “acceptable” vibration limit is sometimes possible depending upon the intended use of the space and the availability of manufacturers’ data for any vibration sensitive equipment. Building owners and user groups often have little understanding or quantitative “feel” for what performance the proposed “acceptable vibration limit” actually represents. The theoretical predication of vibration performance against actual measured performance can sometimes vary significantly. This can lead to dispute post-construction as to whether the floor has an “acceptable” level of vibration. Post construction remediation of a space that is deemed to be “too lively” is often difficult, therefore, it is important that the vibration design criteria proposed are discussed and agreed and the limits of theoretical predications of vibration performance are clearly understood by all parties at the outset. Beca Ltd (Beca) are currently in the process of designing two projects at the University of Auckland, utilizing long-span partial-composite cellular steel beams. Both buildings will utilize existing structural frame layouts and foundations. As the new structure is to be built on the existing foundations, there is a necessity to keep it as lightweight as possible. The question of vibration sensitivity has been raised as a potential issue as both buildings contain research laboratories. An in-depth investigation has been conducted into the factors affecting vibration performance in order to give the client and user groups confidence that footfall induced vibration will not be an issue with the proposed floor structure.

1. Introduction

Client requirements, coupled with architectural and cost constraints, have demanded new buildings to provide large uninterrupted floor spaces, which are fast to construct with a high degree of adaptability for building services. In response to these issues, Engineers have pushed the limits on column and beam grid spacings. Where

previously strength and serviceability deflections governed design, it is increasingly the dynamic performance of floors which require increased consideration. The use of high strength light-weight cellular steel beams and composite metal-deck floor systems has reduced construction costs through lighter loads imposed on foundations and reduced craneage requirements. A range of software, including finite element (FE) tools, are now available to design composite long-span floor systems providing consideration of both strength and vibration issues.

Beca are currently designing two projects at the University of Auckland (UoA) which comprise long-span partial-composite cellular steel beams and metal-deck floors. The two buildings are to be used for postgraduate research and teaching spaces, as well as office and laboratory areas. Due to the nature of the intended use, there is a need to minimise footfall induced floor vibration effects on occupants and laboratory equipment.

This paper outlines: the fundamental principles of vibration and factors to be considered during design, provides an outline of the two UoA projects, reviews the analysis and acceptance criteria adopted for the projects and summarises the on-site testing and validation of the analysis tools used.

2. Fundamental Principles of Vibration

To better understand the effect of footfall induced vibration on composite floor systems, it is necessary to understand the principles of vibration.

2.1 Frequency

The natural frequency of a system, given in hertz, Hz (cycles per second), is a measure of the rate at which the system vibrates¹. When a cyclic force (e.g. walking) is applied to a structure, it will begin to vibrate. If the cyclic force is applied continuously, the motion of the structure will reach a steady-state (constant amplitude and frequency).

For floors with a frequency of less than 8Hz, resonance can occur from one of the first four harmonic components of walking activity coinciding with the natural frequency of the floor. This is known as resonant excitation. Conversely, for floors with a sufficiently 'high frequency' (such that the first four harmonic components of the walking activity do not cause resonance), the response is dominated by a train of impulses corresponding to the heel impacts; which is known as impulsive excitation.

2.2 Modal mass

A mode of vibration is characterised by a modal (natural) frequency and a mode shape. Each mode is independent of the other modes. All modes have different frequencies and different mode shapes. The modal mass of a system is a measure of how much mass is involved in the particular mode shape. A large modal mass will require a lot of energy to excite the mode. Systems with larger modal masses will therefore be less affected by footfall induced vibration.

2.3 Excitation

The forcing function from a walking activity is assumed to be perfectly sinusoidal, for the purpose of analysis. The excitation imposed to a floor is affected by the pace frequency, the length of walking path, and the location of the walking activity (excitation) relative to the receiver.

The pace frequency, f_p , used for design falls into the range¹: $1.8\text{Hz} \leq f_p \leq 2.2\text{Hz}$

The excitation point and response point should be chosen to produce the maximum response of the floor. In most cases, the maximum response will be when excitation and receiver are at the point of maximum modal displacement.

2.4 Response

Calculation of floor vibration response considers the mass, stiffness and damping properties of the structure, and by applying an appropriate excitation function². For low frequency floors, both the steady state response and transient response need to be checked, as the higher frequencies of the floor may result in the transient response being greater than the steady state³. For high frequency floors only the transient response needs to be checked.

The Response factor of a floor is the ratio between the calculated weighted RMS (root-mean-square) acceleration, and the base value given in BS6472⁴. This standard covers many vibration environments in buildings. Limits of satisfactory vibration magnitude are expressed in relation to a frequency-weighted 'base curve' and a series of multiplying response factors. A Response factor of 1 ($R = 1$) is the level of vibration that can just be perceived by humans. $R=2$ is twice as much as can just be felt (etc).

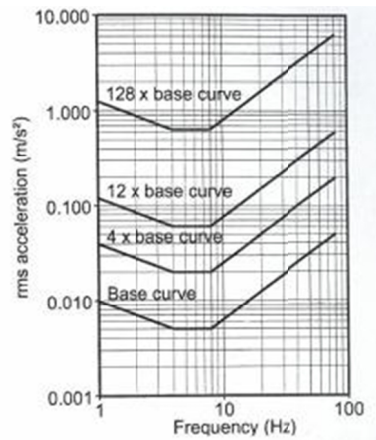


Figure 1. Building Vibration Curves For z-axis Vibrations⁴

2.5 Damping

Damping describes the amount of energy dissipation that occurs when a structure vibrates. With higher levels of damping, more energy is dissipated as sound and heat, which in turn, leads to lower levels of structural vibration⁵. The fact that no system will oscillate indefinitely without an applied load, shows that all structures contain some level of inherent damping. When calculating vibration responses, it is important to use a realistic estimate of structural damping. Experience with floors of similar construction will provide a more accurate estimate of the likely amount of damping that may be achieved. Guidance on design damping values can be found in section 4.3

3. University of Auckland Projects

3.1 University of Auckland – Science Centre Building B302

The proposed new 13 storey Science Centre Tower is located on the corner of Symonds Street and Wellesley Street East on the University of Auckland Central City Campus. The new structure is located on the site of an existing 3 storey building and will utilise the existing building grid set-out and foundations. As the new structure is to be built on the existing foundations, there is a necessity to keep it as light as possible.

The new structure is a steel braced frame building utilising Buckling Restrained Braces (BRB's). The gravity structure consists of steel welded I-section columns, supporting tapered steel primary beams spanning 6.4m, partial-composite long-span cellular secondary beams at 3.2m centres spanning 13.4m and 14.8m, with a 140mm-thick composite reinforced-concrete metal decking. The cellular beams are 800mm deep with 500mm diameter penetrations at regular centres, to allow for services reticulation. These beams have been designed as partial-composite members as a layer of visco-elastic material has been used over half the beam-span to provide additional damping to the floor system.

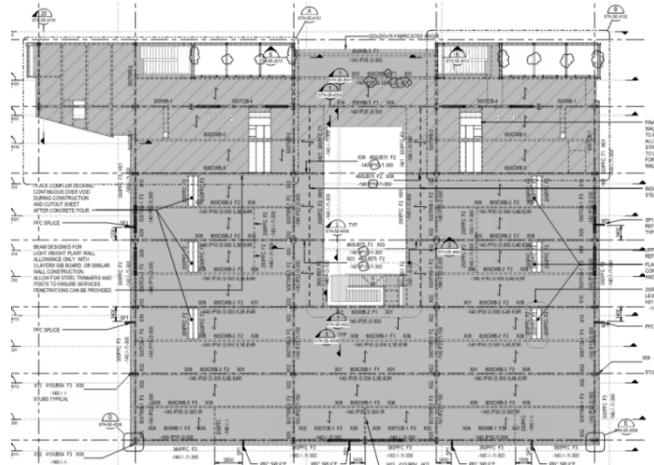


Figure 2. UoA Science Centre Building B302

3.2 University of Auckland – Faculty of Engineering Extension – B403/B404

The Faculty of Engineering is located on the corner of Grafton Road and Symonds Street on the University of Auckland Central City Campus. The existing School of Engineering Buildings B403 and B404 are four level reinforced concrete structures. The proposed extension comprises an additional six new lightweight stories to be built above the existing.

The proposed structure is an exoskeletal steel frame with BRB bracing, erected on the outside of the existing building envelope supporting the vertical and lateral loads of the new floors above. The gravity structure consists of steel primary beams spanning 6.2m, with partial-composite long-span cellular secondary beams at 3.1m centres spanning 12.2m and 13.4m, with a 140-thick composite reinforced-concrete metal decking. Like the proposed Science Centre Tower, the cellular beams have been designed as partial-composite members, as a layer of visco-elastic material has been used over half the span to provide additional damping to the floor system.

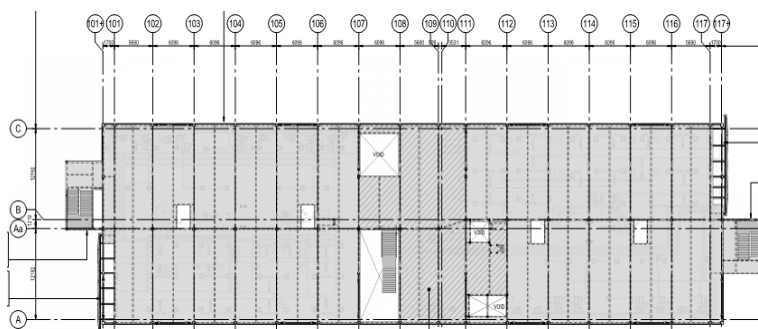


Figure 3. UoA Engineering School Building

4. Design Assumptions / Considerations for Science Centre Building B302

Vibration issues arising from using long-span composite steel beams can often be minimised and mitigated, if the resulting issues are identified early in the design process. Early identification of factors contributing to a lively floor enables the Design Team to consider mitigation measures that can be easily incorporated into the design development.

The following items were encountered and considered during the design of the University of Auckland Science Centre project:

4.1 Floor Span and Structural Set-Out

The frequency of a floor system is directly related to its stiffness and mass. The stiffness of the structure is inversely related to its span (EI/L). Therefore, as the span of the floor or supporting beams increase, the stiffness decreases, creating a livelier floor. By providing a floor system and supporting structure that is not too slender for the required spans, vibration characteristics of the system can be controlled.

The University has a requirement to provide large clear-span spaces free of columns, to maximise efficiency of interior room layouts, and provide flexibility for future space planning layout changes to meet changing User Group needs. The existing building structural layout with columns at a grid spacing of 6.2m by 13.4m and 14.8m, provides architecturally efficient space planning and enables re-use of existing building foundations; but led to an inherently flexible structural system using steel structure.

Alternative grid options with additional columns, to reduce beam spans and stiffen the floor system, were investigated at an early stage. The alternative grid layouts resulted in a cheaper structure solution, with better vibration performance, however, the University decided that the reduction in space planning flexibility associated with these alternative layouts out-weighted the reduced cost and improved vibration performance.

Floor penetrations and atrium voids create areas of structural discontinuity, but are aesthetically pleasing. There are three main atrium void configurations up the height of the building. The vibration performance of the floor adjacent to the voids is found to be more sensitive than areas away from the voids. Special consideration of the vibration response of cantilevered balcony slabs and backspan beams at the atriums was required.

4.2 Floor Mass (Modal Mass Participation)

The amount of mass associated with a floor plate affects its vibration response. The mass used in the vibration analysis needs to accurately represent the mass actually present. For vibration assessment, the un-factored self-weight of the structure, plus super-imposed dead loads of items actually present (such as ceilings, floor covering, services etc.), plus a nominal allowance for imposed live loads is to be made, a value of 10% of live load can be assumed to be present, but may vary from building to building..

Adding mass to the floor system can reduce vibration response. For the Science Centre, the structure needs to be kept as light as possible so as not to overload the retained existing foundations, from the additional 10 floor levels. A 140-thick ComFlor60 profile metal decking was adopted given its long-span capability, and low mass properties. The unit weight of 140mm-thick Comfloor60 decking is 2.46kPa, while a conventional 140mm thick slab is 3.36kPa.

4.3 Damping

The amount of damping assessed to be provided in the end state can considerably affect the final results of the vibration analysis. Guidelines are provided for the amount of damping that a given structural system and fit-out may provide; see Table 1, extracted from P354¹, below:

Table 1. Critical Damping Ratios for Various Floor Types¹

ζ	Floor finishes
0.5%	for fully welded steel structures, e.g. staircases
1.1%	for completely bare floors or floors where only a small amount of furnishings are present.
3.0%	for fully fitted out and furnished floors in normal use.
4.5%	for a floor where the designer is confident that partitions will be appropriately located to interrupt the relevant mode(s) of vibration (i.e. the partition lines are perpendicular to the main vibrating elements of the critical mode shape).

However, the actual amount of damping present may vary during the life of the building. The additional damping provided by fit-out (such as services, partitions, suspended ceilings, furniture and fixtures) may be reduced by future fit-out changes.

On the University projects, the level of damping provided by the base structure and limited architectural finishes was assumed to be 2%. To provide a long-term dependable level of damping, a viscoelastic layer (*Resotec*) was provided between the cellular beams top flange and concrete slab. The *Resotec* provides an additional 2% damping, regardless of the level of internal fit-out. The damping values of *Resotec* were provided by the supplier, as designed by Arup Consulting Engineers, and was tested using Oasys Compos software, where the *Resotec* was modelled and damping values recorded. The 'Base Case' for the vibration analysis of the structure therefore assumed a total of 4% damping.

4.4 Support/Restraint Conditions

For the purposes of floor vibration response, the beams can be assumed to be fixed-end restrained at interior supports, even if a nominal structural pin connection is provided, as the strains in the floor system induced during vibration are not large enough to overcome the frictional forces in the joints.

Vertical restraint is also applied to the floor by the façade connections at each floor slab around the perimeter of the building and balustrading around the perimeter of the atriums. Sensitivity of this assumption was checked by modelling the façade elements and the balustrades in a Finite Element (FE) model. Pinned vertical supports were modelled for these elements.

4.5 Effect of Partitions

Internal partitions provide a mechanism to interrupt the vibration response of a floor. The partitions can behave in one of two ways, depending on their detailing and connectivity. An internal partition wall that spans from a given floor to the floor above, with direct connection, will connect the floor slabs together and act to reduce vibration by mobilising the mass of both floors. An internal partition that does not connect directly to the floor above, but rather stops at the suspended ceiling will increase the damping to the floor.

To demonstrate what the system can achieve (as a minimum), a bare floor has been analysed, and this is considered as the 'Base Case'. This would be applicable, should open-plan layouts of the floor be required. A case modelling the variable effect of partitions proposed was considered and it was found that the partition walls significantly improved the floor vibration response.

4.6 Excitation

The response of a floor system differs across its width. Nodal lines form at stiff areas such as column and beam lines, and these areas will be less responsive than areas in the middle of the slab and beam. The excitation point and response point will generally produce the maximum effect when they are in the same location. In reality, these two points are not always going to coincide.

By considering the location, length and continuity of corridors and walking paths, the effect of the response generated can be controlled. The longer the walking path, the higher the dose of vibration that will be transmitted to other floor areas. By breaking up the walking paths or corridors into discrete lengths, the duration of continuous walking activity will reduce, and the dose of vibration will consequently decrease.

SCI P354¹ recommends that the 'average' mass for a human being, and hence, the assumed mass for the applied footfall source, is 76kg. This document also recommends a walking frequency of 1.8-2.2Hz to be used during design; these excitation masses and frequencies were used in the analysis of the University of Auckland projects.

The floors have been independently checked for footfall induced floor vibration, and for vibration response from mechanical plant. Mechanical plant is to be appropriately isolated, either on isolation bearing pads or positioned in areas where it will not cause adverse effect to the building occupants.

4.7 Composite Beam Action

Structural steel beams supporting metal deck floor slabs have the ability for the steel beams to be constructed composite with the concrete floor slab through shear stud connection. This composite shear stud connection significantly increases the stiffness of the support beam, improving the vibration characteristics of the floor system.

Composite design of long-span steel beams is generally required to provide a cost-effective solution to withstand ULS loads for strength and SLS loads for deflection. Although, when minimising the size of the steel beam for strength, this may give rise to susceptibility to dynamic loading, such as footfall induced vibration.

Once vibration is taken into account, there may be a need to increase the minimum beam size to provide additional stiffness. During Preliminary Design of the floor systems, it was found they were relatively lively using an 800mm deep composite cellular beam with 140mm thick ComFlor60 metal decking, if a minimum 2% damping was assumed.

Given that satisfactory vibration performance was not able to be obtained with 2% damping, it was decided to provide additional damping using a visco-elastic material inserted between the slab and steel beam. A proprietary visco-elastic product called *Resotec*, produced in the United Kingdom, developed by Arup Group, and distributed by Richard Lees Steel Decking, was selected. This product is capable of achieving an additional 2% damping when placed over the outer quarter spans of the steel beams. Shear studs are omitted from the Resotec regions and only provided over the middle half of the beam span providing full composite connection over the maximum moment region. The beam is then classified as exhibiting partial composite action, where the degree of composite action can be determined.

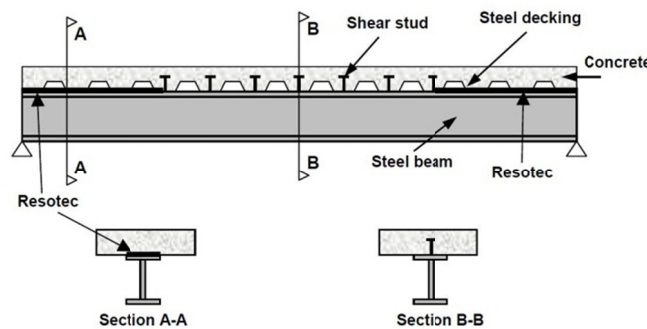


Figure 4. Partially Composite Beam with Resotec Visco-Elastic Layer

4.8 Acceptance Criteria

Consultation with the Client and User Groups of the building has been undertaken to ascertain the required vibration characteristics of the various areas within the building. For example, vibration requirements for a laboratory research space are more stringent than those for an academic office or post-graduate write-up space. Similarly, increased vibration response can be accepted in “active” areas such as public foyers and lobby areas.

To provide a reference datum of the amount of vibration currently experienced and deemed acceptable, various spaces within existing buildings was subject to vibration testing. Testing of existing spaces included measuring modal properties from various dynamic excitations, and data logging of background vibration levels over a 48 hour period. This provided baseline “acceptance criteria” based on existing normal usage, with a reference that was meaningful to the Client and User Groups.

The acceptance criteria finally adopted, as noted in Section 5.2, were based on a combination of the desires of the Client and User Groups, measurement of the vibration response of existing spaces, and guidance from industry documentation such as BS6472⁴, SCI P354¹, ASHRAE 2003⁶ and ISO2631⁷ and published data for various items of research equipment.

4.9 Architectural Considerations

Space planning can affect how much of an issue vibration may be. The distribution of corridors, corridor lengths and relativity of excitation to receptors, will determine the effect of a given walking path. If these walking paths are confined to stiffer areas of floors, such as beam lines and/or columns, then the effect of the walking path can be minimised. The location of receptors to machinery or plant can also determine the effect of a continuous source of vibration. If all plant is confined to say the roof level plant room or basement, and typically there is no human occupancy or the floor is a slab on grade (in the case of the basement), then the effect of this plant will be minimised.

Specific users of a building may have the need to be situated in areas of low response, due to the nature of their work or the equipment they use. If this is the case, rather than trying to employ a solution across the whole floor plate, or even the entire building, it may be possible to situate them in a location that does not respond as much as other areas e.g. on a slab on grade, over a nodal zone, or away from sources or locations of excitation.

4.10 Post Construction Changes

Remedial action once a floor is in service is often challenging and expensive. It may be easier to reconfigure floors, move people or equipment away from vibration sources or walking paths, or alter the timing of the vibration activity, rather than look for intrusive solutions.

If the floor configuration is not able to be altered, then there may be a need to change the response of the floor system. This may be achieved by adding mass to the floor, which is not usually very effective and may affect other structural elements, increasing the stiffness of the floor support members by stiffening beam elements, adding additional columns, providing stiffeners under the floor slab, providing partition wall systems to lower deflections, provide damping mechanisms such as tuned mass dampers or specialist damping materials, or isolating vibration sources by using isolation pads under mechanical plant (etc).

5. Acceptance Criteria for University of Auckland Projects

5.1 Guidelines on Acceptability Limits

Correlation of the physical movement of a floor under excitation to a corresponding acceptance limit is hard to determine. The acceptability of movement is based on human perception, and can be subject to an individual's interpretation, unless quantitative values are assigned. As perception and discomfort can vary between humans, current standards propose criteria that will attract a 'low probability' of adverse comment. Research has been carried out to assess the effect of human response to vibration, and is captured in a number of international standards. Documents such as BS 6472:1992, BS 6841, ISO 10137, ISO 2631-1 and ISO 2631-2, cover many environments, and look to express the limits of satisfactory vibration magnitude in relation to a frequency-weighted 'base curve' and series of multiplying factors.

The base curves for vibration represent the threshold of human perception, defined by a 'base value', which is given as a Root Mean Square (RMS) acceleration of $5 \times 10^{-3} \text{ ms}^{-2}$ for z-axis vibrations and $3.57 \times 10^{-3} \text{ ms}^{-2}$ for x- and y-axis vibrations⁸; see directions of vibration and base curves in figures 5 and 6 below. The base value of acceleration that can be perceived depends on the direction of incidence to the human body, where the z-axis corresponds to the direction of the human spine. As noted above, the x- or y-axis vibration is more easily perceived (has a lower base value for perception). Each of the base curves are increased by a multiplication factor (or Response Factor) depending on the minimum vibration perception deemed to be appropriate for a given environment.

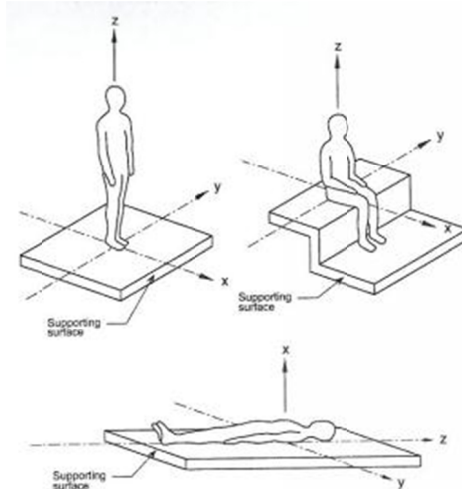


Figure 5. Directions of Vibration Defined in ISO 2631⁷ and BS 6472⁴

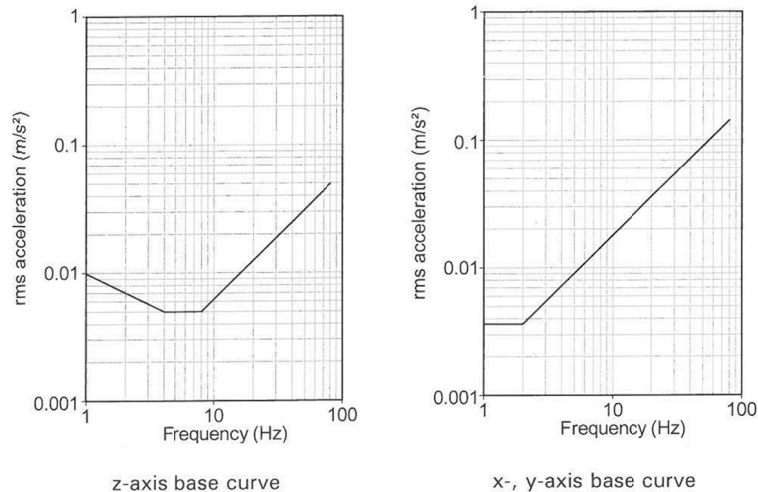


Figure 6. Base Curves for Perception of Vibration, taken from BS 6472⁴

5.2 Adopted Acceptance Criteria

The following tables indicate the proposed acceptance criteria that were established through consultation with the Client and User Groups, and rationalisation based on testing carried out in occupied spaces. This criterion has been established to attract a 'low probability' of adverse comment during use of the various spaces in the building. Vibration sensitive machines have been positioned on stiffer parts of the floor, and may have independent isolators, to prevent adverse effect. Mechanical plant that could cause adverse excitation will be isolated and/or positioned in the basement or plant levels to minimise effects.

Table 2. University of Auckland Science Centre Adopted Vibration Criteria

Description of Use / Occupancy of Area BBN Curve [Note 1]	Suggested "Target" Response factor "R"	Suggested Theoretical predicted "R" (Max peak) [Note 2]
Mechanical Plant Space / Plantroom	8	10
Public Circulation Area (no long term seating)	6	7.5
Atrium Meeting / Break-out Spaces. Seating with nearby walking movements	5	6.5
Academic Office	4	5
PGR Office / Write-up Space	4	5
Computer Laboratory / Teaching Space	4	5
General Post-Grad Research Laboratory Space	4	5
"Sensitive locations" within building e.g. Sensitive equipment zones in Research Laboratory Space	2	2.5

Notes:

1. BBN Classification from “The Control of Vibration in Buildings” – BBN Laboratories, Cambridge MA, 1988 by C.Gordon.
2. Beca estimate of “target” for Max. Peak values predicted by OASYS GSA Finite Element Program (assumed 25% increase on ISO2631 criteria).

6. Vibration Analysis of B302

6.1 Footfall Induced Vibration Modelling used on B302 Science Centre

Dynamic response of the floor structure was highlighted as an issue at the early stages of the project, due to the grid spacing of columns and lightweight structure proposed. As the design progressed it became apparent that dynamic response was going to significantly influence the design of the gravity floor support system. A greater degree of certainty of performance and level of analysis was therefore required.

Preliminary design of the structure was first analysed using the proprietary Fabsec and CellBeam software programs. This was verified using the Hera NZ Floor Vibration Analysis Program version 2 Microsoft Excel Spreadsheet and a hand-check using the guidance of SCI P354¹. This confirmed that a more in-depth analysis was required, and a Finite Element (FE) model was created using Oasys GSA⁹ Software, to model the floor plates in 3D.

Vibration analysis was completed under the guidance of SCI Publication P354, 2007. Two different methods of analysis were evaluated, with the first being a conservative hand-calculation estimate. It was found that the peak response of the floor system was in excess of the prescribed maximum for the given workspace.

The P354 refined approach is to assess the floor system using Finite Element (FE) modelling. FE modelling takes a continuous structure and breaks it up into a number of discrete elements. The relationship between these elements are then determined using methods for multi-degree-of-freedom discrete systems. Oasys GSA software⁹, developed by Arup, was used to model the floor system. Three typical levels of the Science Centre Tower were assessed; Levels 2, 5 and 7 (the other floors are similar in nature to these). Floor vibration was measured in terms of a Response Factor, R. Response evaluated in Oasys GSA reported values were then evaluated as peak, average and point values. The peak value represents the absolute maximum response factor of the floor given its chosen parameters. The average response factor represents a mean peak value across the floor. The point value evaluates a chosen point on the floor which is the same location for each output, used to compare the response to the variables evaluated.

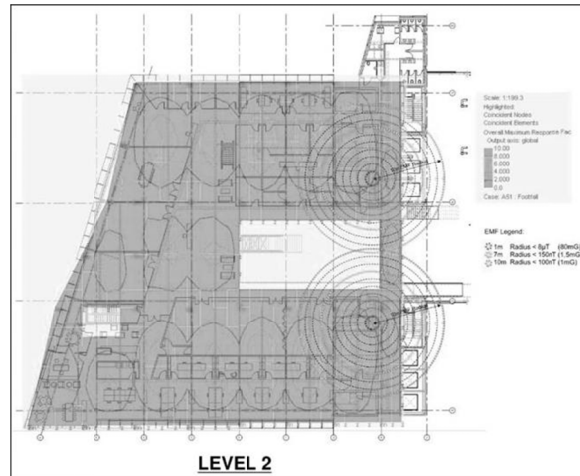


Figure 7. Typical Base case plot for Level 2

6.2 Variables used during modelling and their effect

A ‘Base Case’ was established for each floor, which had an assumed “worst-case” damping value of 4% for a bare floor. The 4% comprised a 2% allowance for the floor system itself (reinforced concrete, reinforced steel deck system, and steel beams) with no partitions or furniture, and 2% accounting for the *Resotec* visco-elastic damping layer provided. As outlined in Section 4.4, façade restraint to the perimeter of the structure and balustrade restraint to the atrium areas was applied. From this base case, a number of independent and concurrent variables were examined to determine their effect on vibration performance.

The following variables were assessed:

6.2.1 Floor Beam Stiffeners

Tertiary 200UB floor stiffeners were placed perpendicular to the castellated beams at mid-span, to mobilise more mass at the location of maximum response. This had a positive effect on reducing the floor response by an R factor of about 0.3 to 0.4. This solution was incorporated into the design to provide acceptable response at atrium areas.

6.2.2 Increased Damping

An increased level of damping of 5% and 6% was analysed to evaluate the effectiveness of an inaccuracy in the estimate of the actual damping available. The level of damping that may be available could increase in a number of ways, including, the actual inherent damping from the floor system, from furnishings, fixtures and services, or from superior performance from the visco-elastic material (*Resotec*) to that assumed.

From test results from the AUT-WG building (which has a floor system similar to the proposed new structure), it was found that the damping from a bare floor was 2.2%. This provided validation to the estimated 2%. From the proposed

architectural layouts, furnishings are indicated in all areas, and there is no current requirement for whole-floor open plan spaces. The presence of fixtures and furnishings could potentially increase the damping available by 1 to 2% from the minimum 4% base case assumption.

6.2.3 Internal Partition Walls

As noted in Section 4.5, internal partitions can have a positive effect by significantly reducing floor vibration response. Sensitivity analysis led us to model the internal partition walls, by creating an element with the same effective stiffness as a 100mm wide timber stud wall with a single layer of gib-board either side. This was deemed appropriate over a blanket increase in damping value applied to the whole floor. An allowance for doorways was made, by not modelling partitions at these locations. Modelling partition walls reduced the floor response to vibration by a reduction in R factor of 2 to 4, depending on the extent of partition and base level of damping assumed. The Client was advised that this improved response might be lost should open plan office layouts be adopted in the future or the full height corridor walls be removed.

6.2.4 Deeper Secondary Beams

Use of a deeper castellated beam was analysed to determine the cost-effectiveness and change in dynamic response. A 900mm deep member was designed and modelled, in lieu of the 800mm deep sections. It was found that the reduction in response was minor with an R value reduction of only 0.1.

6.2.5 Increased Floor Slab Mass

An increase in modal mass has been proven to reduce floor vibration response. A 140Comflor60 deck was assumed as the 'Base Case' floor system. It was found that by changing the floor slab system to a 140-flat deck profile, a 25% increase in slab mass can be achieved. The increased modal mass reduced the floor vibration response, with a reduction of $R=2.6$. However, the cost associated with increased floor mass is not just the cost of the concrete itself. The additional demand placed on beams, columns, foundations and lateral bracing system meant that this solution was not deemed acceptable.

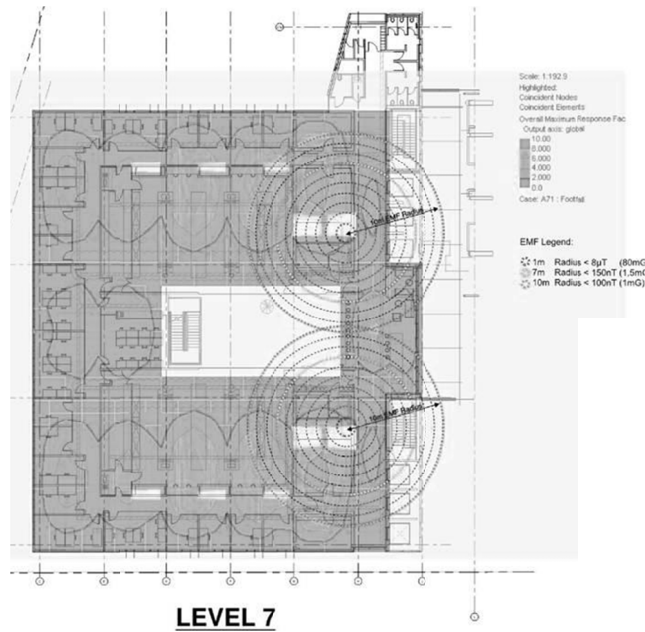


Figure 8. UoA B302 Partitions Modeled, Resotec, 4% Damping

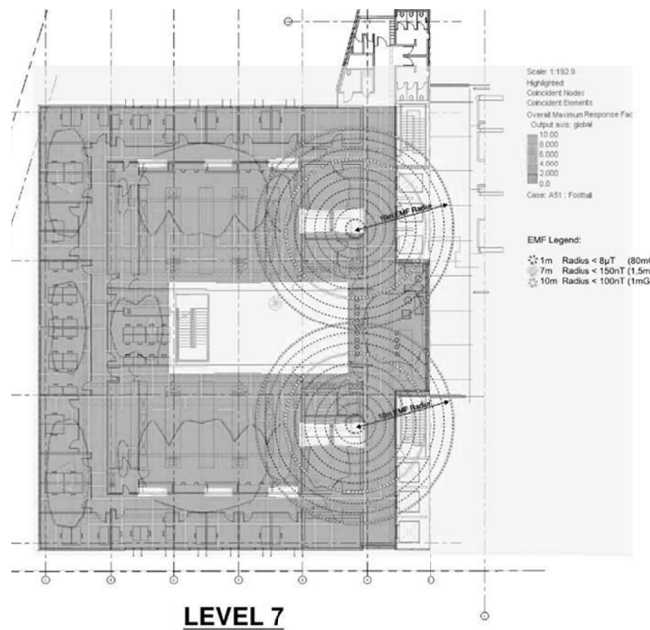


Figure 9. UoA B302 Base Case, No Partitions, Resotec, 4% Damping

6.2.6 Other factors

Other factors to be considered include:

Location of excitation has been assumed to be in the worst place for a

receiver placed anywhere on the floor. There are defined walking paths, dictated by the corridors and furniture layouts, and this beneficial effect has not been taken account of in the general analysis, but was used when considering the performance of localised specialist areas.

The nature of footfall induced vibration is that the excitation is intermittent. In the FE models created, excitation has been considered as continuous, and therefore the maximum response experienced by a receiver would be sporadic, rather than constant. This may affect the users perception of vibration, and as a result, the users may be more accepting of occasional higher vibration response.

6.3 Viscoelastic Damping Layer

As noted above the use of viscoelastic materials is a simple method of increasing the damping properties of a slab at the time of construction. *Resotec* is an example of a commercially available product. The Resotec system improves the dynamic performance of composite floors by dissipating energy through shearing of the viscoelastic damping layer during low-level vibrations¹⁰. Viscoelastic materials used in this application are up to 3mm thick, consisting of the polymer sandwiched in between two thin steel plates. At the location of application, composite connection is lost between the steel beam and reinforced concrete, as there can be no direct connection between the two surfaces to allow the viscoelastic layer to undergo shear deformation.

6.4 Vibration Dose Values [VDV's]

The nature of footfall induced floor vibration is that the excitation is not likely to be continuous, but rather, intermittent¹¹. A cumulative measure of this intermittent response can be calculated and benchmarked against the acceptable tolerance level. The Vibration Dose Value (VDV) measures the level of human perception due to specified occasional vibrations for short durations e.g. a person or a group of people walking down a hallway.

The analysis of VDV for the Science Centre assumed a peak response factor for continuous vibration of $R=9.4$, which is the highest resulting response factor from the analysed 'Base Case'. The analysis results showed that in order to achieve a low probability of adverse comment, any hallway in the building should not be traversed more than 111 times in an hour by an individual person, or group of people. Given the current architectural layout and building usage, this is unlikely to occur.

7. On-Site Testing and Validation of Theoretical Analysis of University of Auckland Projects

To determine floor vibration acceptance criteria and to validate the theoretical analysis of the new floors, it was decided to test and analyse several existing floors which were either; of the same construction as the proposed new floor system, or, were floors housing similar users to the intended use. The purpose of the testing was for the Client to be able to physically experience the vibration response of various

floors so they could have a physical understanding of the different “R” values.

Nine floors across four buildings were tested, providing a representative sample for the proposed structure and end use of the new Science Centre and Engineering School buildings. The four buildings tested were:

- The existing B301 Chemistry Research Building, occupied by staff and students that would end up in the new B302 building. This provided an ability to benchmark the vibration response and damping achieved in their existing work areas. The structure is a reinforced concrete frame supporting precast concrete floors. Floor spans and frame centres at 6m to 8m are considerably less than the new B302 building.
- The UoA School of Engineering Buildings 403/404, again, occupied by staff and students that would end up in the new building extension. The existing structure is reinforced concrete frames supporting precast concrete floors, which has a different vibration response to the proposed new steel frame structure.
- The UoA Property Services Building which is a 1980’s era building constructed from steel beams and composite metal decking. The Client occupies this building and considers the floors to be “fairly lively”. The purpose of testing was to compare the actual performance of these existing floors to the predicted performance of the B302 Science Centre which has significantly larger floor spans.
- The Auckland University of Technology WG Building, which has a structural layout similar to the proposed new buildings. These similarities include: steel beam spans, composite floor construction, steel beam spacing and the use of cellular beams. This building has a mixed office and circulation type usage, which is similar to some areas of the proposed Science Centre building. Due to the similar nature of the structure this provided the Client the ability to see and feel what a similar end product could potentially be like. Testing was aimed at analyzing the level of vibrations felt, and damping achieved on a floor with similar structure to the proposed new buildings. Different levels of fit-out and furnishing on each of the three levels gave a representative result of the different damping that is achievable.

7.1 Vibration Testing and Data Logging

Vibration testing was undertaken to provide information in relation to the dynamic performance of each slab, to quantify the modal properties of the structure, and to measure the response of the slab to a person walking on the floor. These properties were required to assess the inherent properties of the structure, to understand the environment that the Users are currently used to, to establish the actual amount of damping that may be achieved out of the structure, and to give the Client the ability to quantify what a physical floor vibration and proposed acceptance limit response value actually correspond to.

Each floor was subject to a combination of up to three different types of tests, depending on the desired results:

- Accelerations under normal operating conditions
- Accelerations under controlled walking
- Dynamic testing, in order to determine the level of damping and their natural frequencies

Damping of the modes, modal frequencies, and critical walking frequencies likely to induce resonance were calculated. A controlled walking test was undertaken, using a metronome to set the gait and an accelerometer to record the time history of the walk. Where required, vibration data loggers were placed for a period of 48 hours, to measure accelerations experienced under normal operating conditions. The data was extracted and plotted, and a response factor for the given use of the space was calculated.

7.2 Theoretical vs. Measured Floor Vibration Results

An FE model of the AUT-WG floor plates tested was created to determine the correlation between analytical prediction and measured floor vibration results.

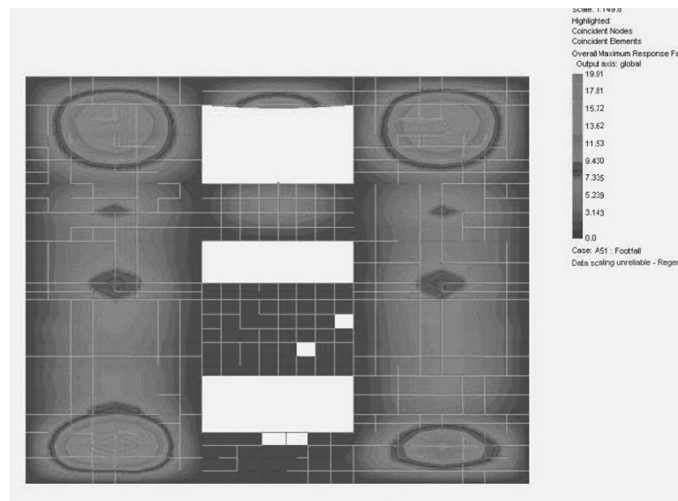


Figure 10. AUT-WG FE Model output

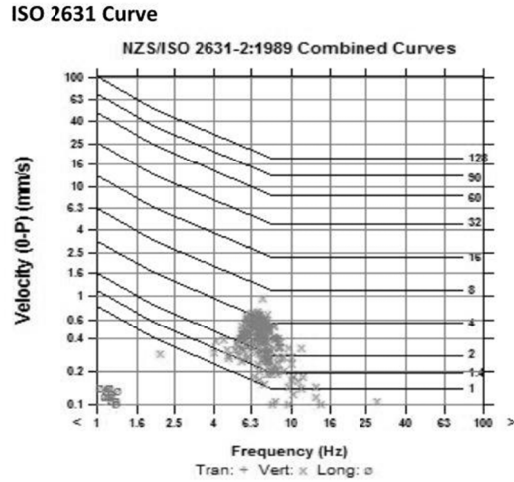


Figure 11. AUT-WG Testing Response output

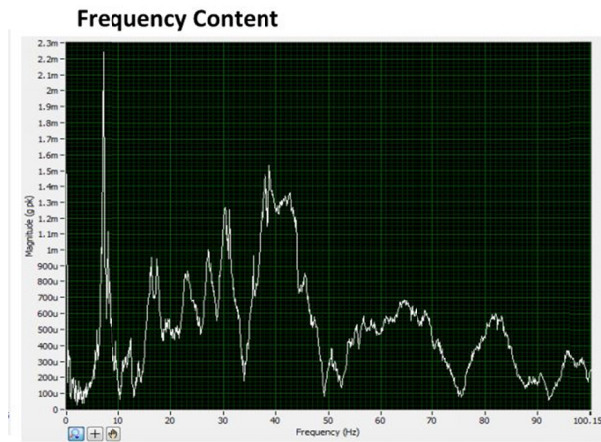


Figure 12. AUT-WG Testing Frequency output



Figure 13. AUT-WG Measurement location photo

Assumptions made in the OASYS GSA model included columns and walls fixed at mid-height between the floor of concern and the floor above and below. Major penetrations modeled, including penetrations for lifts, stairs, escalators and service risers. Restraints for façades, balustrades and atrium walls have been used and all other items have been considered as variables. The variables which were found to provide the greatest amount of effect on the overall response of the floor is the provision of full-height and partial-height partitions, and floor damping.

The OASYS GSA analytical models of AUT indicated a maximum vibration response value of $R=19.9$. This compares to measured response values in the range of $R= 10$ to $R = 6$. There is a poor correlation between the measured response values and the analytical prediction.

The discrepancy between analytical and measured results can be attributed to a variety of factors, including;

- Variations in analytical modeling assumptions such as “effective” span of floor beams, effect of partitions, damping, restraint conditions, stiffness assumptions of supporting elements, variation between analytical 76kg walker excitation force and pace frequency compared to actual etc.
- Excitation of the slab during on site testing may not have the receiver in the worst place for the given excitation, but rather a convenient location for testing. Oasys GSA excites the slab from all locations across the floor plate and provides a contour plot of response values, which gives the maximum response value for each receiver location with the excitation (walker) in the worst place. The analytical model therefore provides a floor response corresponding to a worst case location for the receiver (occupant) at each location for the worst case walking path in the critical location. The site measured walking path and position of receiver may not correspond to the above “worst” case.
- Damping reported by site measurements is specific to a mode, while Oasys GSA evaluates all modes of vibration.
- Various levels of construction material were scattered over the floors during on-site measurement, which may affect the mode shapes and provide varied levels of damping during testing.

References

- Allen, D. and Murray, T., Design criterion for vibrations due to walking, American Institute of Steel Construction Engineering Journal, Fourth Quarter, 1993
- BS 6472-1: 2008, Guide to evaluation of human exposure to vibration in buildings. Vibration sources other than blasting, British Standards Institute; 2008
- Gendreau, M., Mechanical and footfall vibration impact to healthcare facilities: criterion and design strategies based on research case studies, ASHRAE, 2003
- Hicks, S. and Devine, P., Vibration characteristics of modern composite floor systems, Pacific Steel Conference 2007, Steel Structure in Natural Hazards, Wairakei, New Zealand, 13-16 March 2007 Conference Paper Submission
- Hicks, S. and Smith, A., Design of floor structures against human-induced vibrations, Steel Construction, Vol. 4 issue No. 2, 2011

ISO 2631-1:1997, Mechanical vibration and shock – Evaluation of human exposure to whole-body vibration – Part 1: General requirements, International Organisation for Standardisation, 2005

<http://www.oasys-software.com/>

Pearce, A. and Cross. J., Structural vibrations – a discussion of modern methods, The Structural Engineer, Vol. 21 issue No. 12; June 2011

Saidi, I. et al, 2006, Floor vibrations due to human excitation – damping perspective, Earthquake Engineering in Australia, Canberra 24-26 November 2006 Conference Paper Submission

Smith, A., Hicks, S. and Devine, P., Design of floors for vibration – a new approach, P354, The Steel Construction Institute, 2007

Willford, M. et al, 2006, A constrained layer damping system for composite floors”, The Structural Engineer, Vol. 84 issue No. 4; February 2006

Innovative Aspects of Composite Construction in the New Leadenhall Building

John Stehle¹; Andy Butler¹; Mike Banfi²; Rob Livesey²; and Julie Bregulla³

¹Laing O'Rourke, Engineering Excellence Group, Dartford DA2 6SN, U.K. E-mail: jstehle@laingorourke.com; anbutler@laingorourke.com

²Arup, London W1T 4BQ, U.K. E-mail: mike.banfi@arup.com; rob.livesey@arup.com

³BRE, Watford WD25 9XX, U.K. E-mail: bregullaj@bre.co.uk

Abstract

The Leadenhall Building will add a very distinctive shape to the London skyline. The external steel megaframe is one of the most visible parts of the building but the composite floors also include innovative features. The analysis for footfall vibration and the design of the floor beams for axial force used new approaches but the most significant innovation was the use of precast planks to span between the steel beams. The connection between the planks and the steel beams was developed partly in response to the specific challenges encountered on this project. Continuity between the planks for negative bending and in-plane shear was provided by the use of bars with threaded couplers and ducts cast into the planks. To transfer the shear between the slabs and the beams, a tab connection was used. A series of tests was carried out to establish the properties of the connection and validate the system. Results are presented in this paper.

DESIGN

General

The design of the Leadenhall building is iconic and unique in its geometry, as can be seen in Figure 1 below. At ground level the majority of the area of the building will become a public space and the first full floor is at level 5. This is the largest floorplate and measures approximately 2000 square metres net internal. Above this the floorplate reduces linearly with building height. To achieve the slope, steel beams and concrete plank elements are re-arranged at every level near the South face. Where this re-arrangement does not occur, the structural grid can be considered to be 16m by 10.5m between Mega-columns, which poses a challenge with regards to the strict vibration criteria imposed by the client (Response factor generally <4).

The external Megaframe structure, which nodes out every 7th level, provides the overall building stability, while between Megalevels, K-bracing in the North-East and North-West corners of the main building provides stability to intermediate floors. The floors are subject to significant diaphragm forces due to restraint of internal columns and the sloping columns on the south façade.

The floor beams are fabricated plate girders with holes in the webs to allow integration of services. The bottom flange is typically larger than the top.

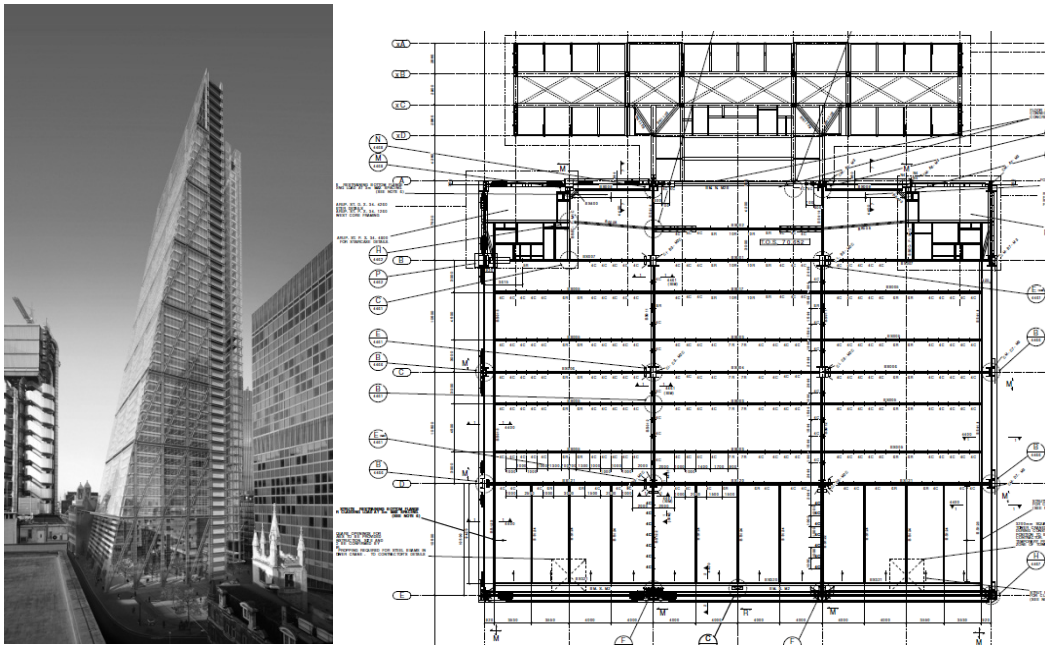


Fig.1 - The Leadenhall Building design, architectural image (left), sample structural floor plan (right)

The precast plank system

The development of the precast plank system started while the project was being tendered. In fact foundations for the building had already been installed under an earlier contract. So any solution could not weigh more than the original slab design. Also the solution could not compromise the program and hence there was no opportunity to revisit many design decisions and the basic beam layout and beam sizes had to be accepted. Therefore the system is basically 150mm deep precast planks typically span up to 4.5m between steel beams, with which they act compositely. This depth matches the original solution and to keep the weight the same lightweight concrete was used and the thickness reduced over part of the width in the middle of the span. The provision of channels in the soffit also ensured an equally utilitarian functionality to enable the fixing of services and suspended ceilings with ease.

The key to the system is the detail at the joint between the units on top of the steel beam. The connection [patent pending, publication number GB 2495319, 2013] is shown in Fig. . This has to deal with flexure and diaphragm forces in the slab and provide the shear connection between steel and concrete necessary for composite action. A dowel bar with a female coupling device is precast in to the plank on one side of the joint (right side in detail A below), while a loose dowel bar with a male thread is pre-loaded in the corrugated void former in the plank on the other side of the joint (left side in detail A). Once both planks have been installed the loose bar is slid across and screwed into final position. Once the coupling is checked and signed off, the void former and joint is fully concreted with a high strength flowable grout.

At edge beams a traditional detail was used with pockets left in the planks that fitted over studs on the beam.

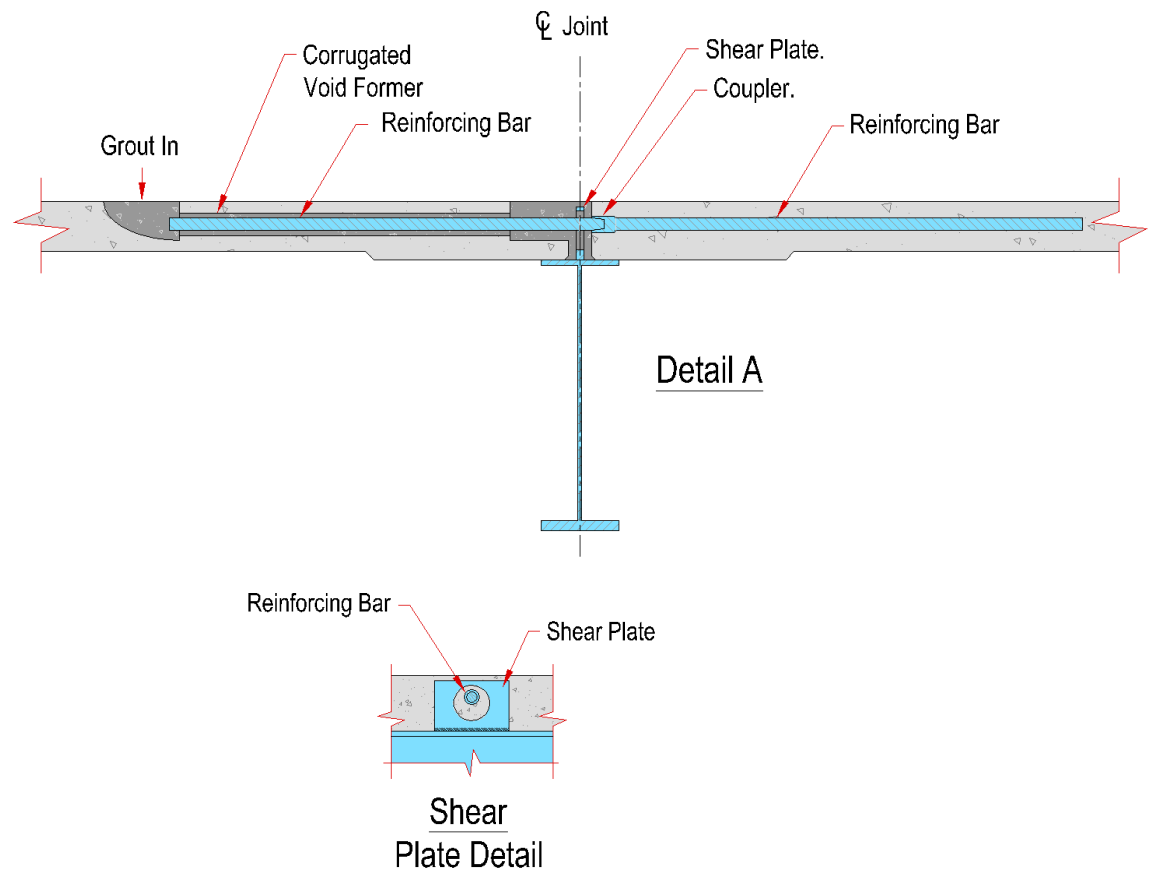


Fig. 2- Connection details

The slab was designed using normal code rules but taking into account that the self weight was applied before the joint over the beam was completed. Deflections had to match those predicted for the original scheme and were calculated taking account of the staged loading, creep and shrinkage. Concrete Society technical note 59 [Concrete Society 2004] was used to assess the influence of cracking.

Although the shear connection between the slab and steel beam has some similarities to the Perfobond connection developed by Leonhardt Andrä and Harre [Leonhardt et al 1987] the differences were such that no reliable predictions of the resistance could be made and testing was required to allow the design to proceed.

Response to footfall vibration

The relatively long span of the beams meant that the response to footfall vibration had to be considered. Adequate response was demonstrated by analysis using the methods set out in CCIP 016 [Willford and Young 2006]. The analysis was done on a floor by floor basis but this was complicated as the tapering shape meant each floor was different. Routines were set up whereby analysis models for each floor could be extracted from the engineering model of the whole frame. The models were then automatically analysed and plots of response factors produced. This analysis was

carried out on the original slab design i.e. lightweight concrete on trapezoidal composite metal deck. As the precast concrete planks have different properties to the metal deck slab the floors were re-analysed for the new precast scheme.

Beams subject to Axial Force

As mentioned above there are significant diaphragm forces in the floors. These lead to large forces in the composite beams and these needed to be considered in design. A methodology was developed to carry out the assessment of the beams. The basis of the methodology was described by Banfi [Banfi 2008] but has been developed since then. The assessment is based on typical guidance in SCI publication P355 [Lawson and Hicks 2011] for beams subject to vertical load but adjusted to take into account the axial force. This involved consideration of the effect of the axial load on:

- Overall stability of the beam
- Stability of the bottom flange
- Stability of the tees at openings in the web of the beams
- Forces in the studs
- The acceptable level of partial interaction.

The methodology was developed for the slab on metal deck and adjusted for the as-built slab. The main adjustment was in the resistance and spacing of the shear connection.

TESTING OF THE PRECAST SLAB SYSTEM

As well as assessing the resistance of the shear connection, the series of tests conducted at BRE looked at; the pull-out strength of bar grouted in plank, buildability, overall system strength and dynamic performance.

The tests for connection resistance were conducted as shown below. A total of 9 were conducted to give appropriate design parameters for a range of loading and geometry conditions. The tests showed the resistance expected and very ductile behaviour (Figure 5 and 6). The results were assessed in accordance with EN1994-1-1 [BSI 2004] and EN1990 [BSI 2002].

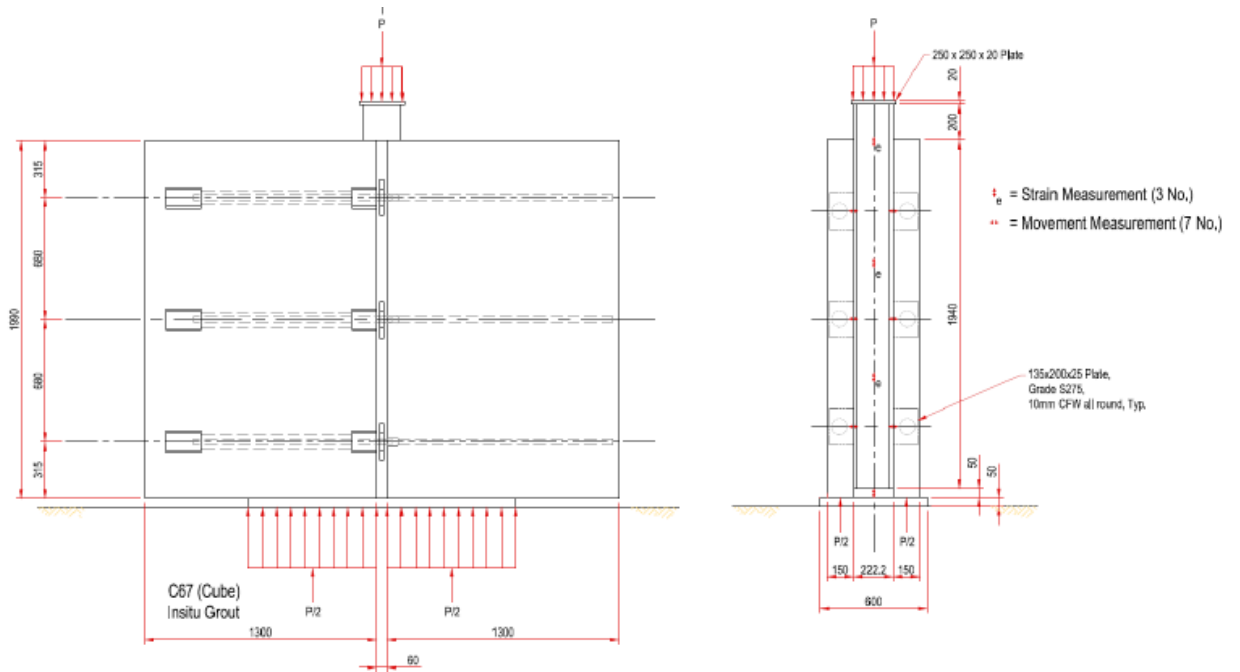


Fig. 3 - Connection shear strength test configuration



Fig. 4 - Photo of connection shear strength test at BRE



Fig. 5 - Post-test examination of shear connection plate

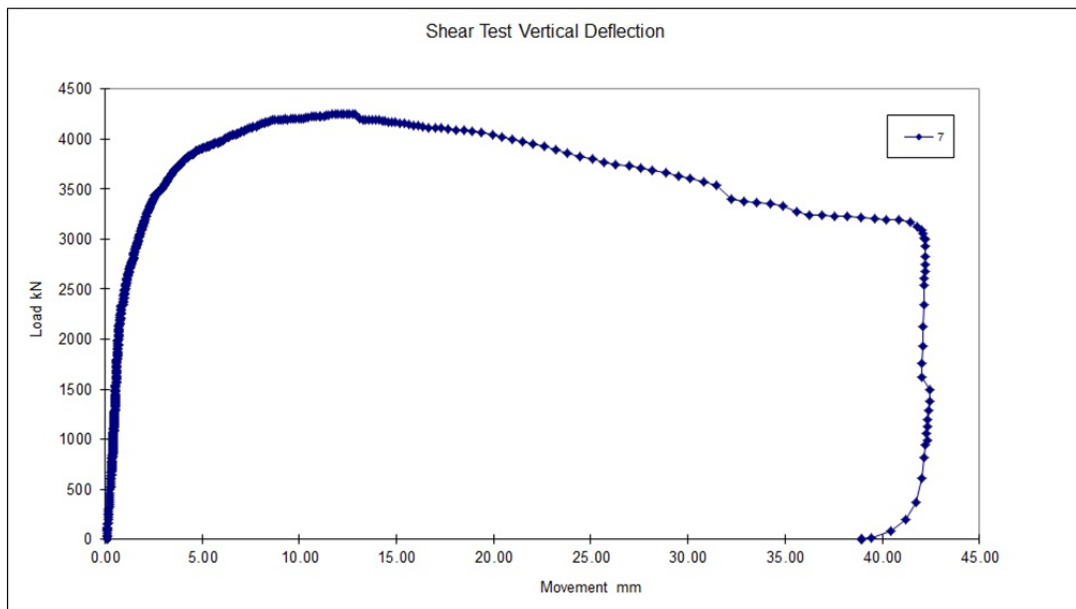


Fig. 6 - Load displacement graph for one of the shear tests

A 16m by 10.5m ‘typical’ bay was erected in BRE’s laboratory for buildability, overall load testing and dynamic assessments. Prior to erection, a digital engineering model was used for manufacturing and assembly purposes (Figures 7 to 11).

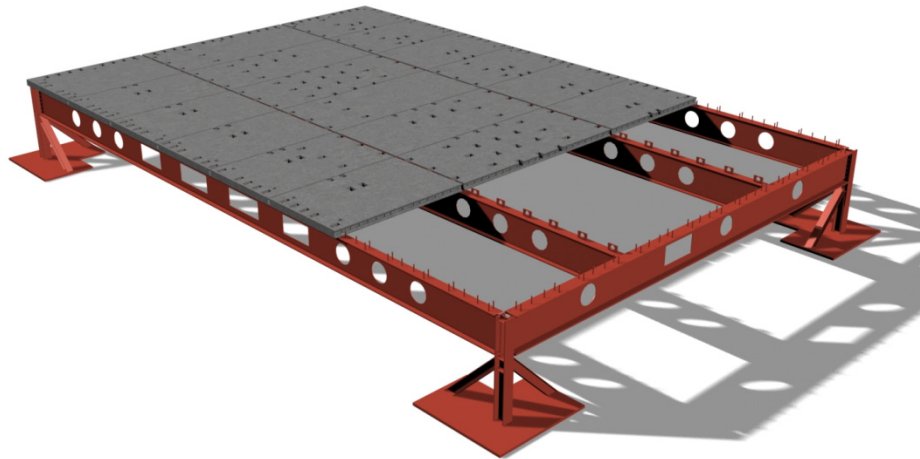


Fig. 7 - Digital engineering model of the test bay

With regards to buildability, it soon became apparent that control of the temporary stability of the steel beams would be a real issue for the project. This could be dealt with by increasing the width of the top flange of the steel beam. However, as the steel had already been ordered for the project, a simple temporary propping solution was developed.

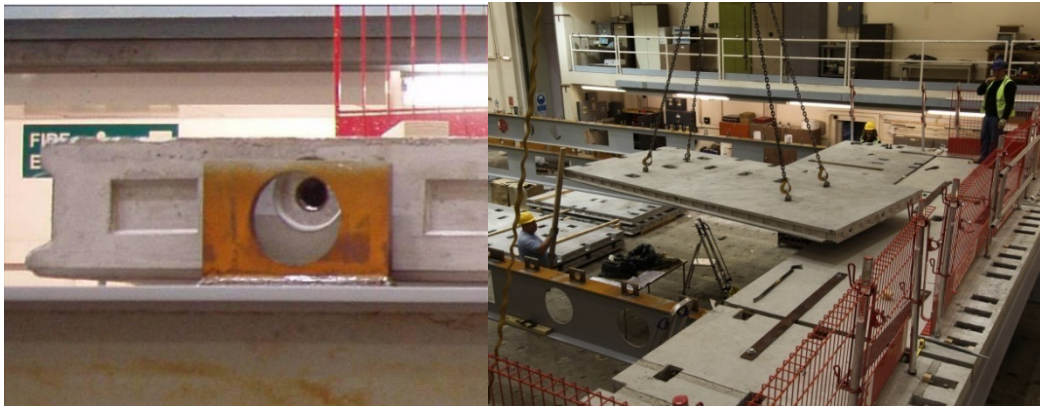


Fig. 8- Erection in progress in the laboratory at BRE

With regards to overall strength, the floor was loaded to ‘ultimate’ design load conditions as shown below. Even under such loading, the floor responded almost elastically, with the majority of deformation fully recovered, and no significant residual cracks were observed.

A range of dynamic tests were conducted, including footfall, pacing and rotary shaking to give information on the performance characteristics of the floor system with respect to design for the project.

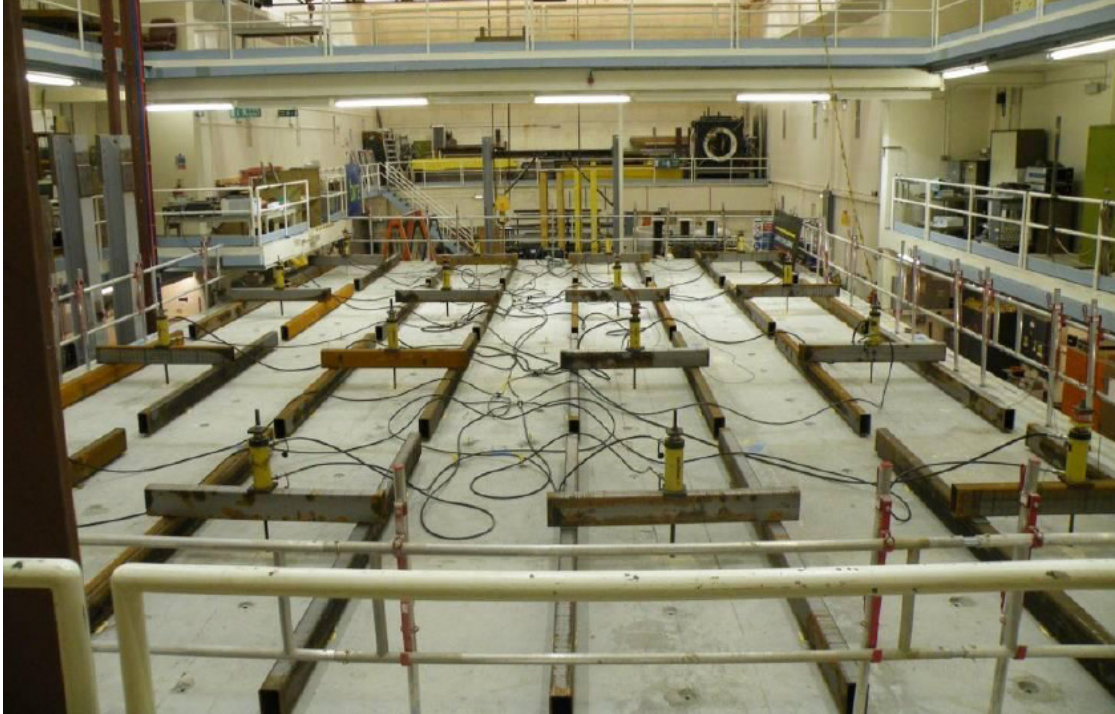


Fig. 9 - Loading arrangement on floor



Fig. 10 - Beam deflection under 'ultimate' design load



Fig. 11 - Dynamic testing under 'pacing' load (left), rotary shaker (right)

MANUFACTURE OF THE PRECAST SLABS

The precast plank elements were manufactured by Explore Manufacturing Limited (a Laing O'Rourke group company) at its state-of-the-art facility near Worksop in the East Midlands. As part of the manufacturing process was innovative for Explore, a regular dialogue and evolution of the design system took place at a frenetic pace, which made for a great learning experience for all involved. An early evolution of the design involved a structurally ribbed soffit, but this was replaced by a coffered soffit in order to simplify formwork and reinforcement cages. Reinforcement cages were continually reviewed and optimised to maximize the use of automated bent meshes and minimise labour content (Figure 12). Also, samples were produced to ensure an appropriate quality of surface finish and demonstrate an ability to cast dowel bars in correct positions so that the elements could be confidently connected on site (Figure 13).

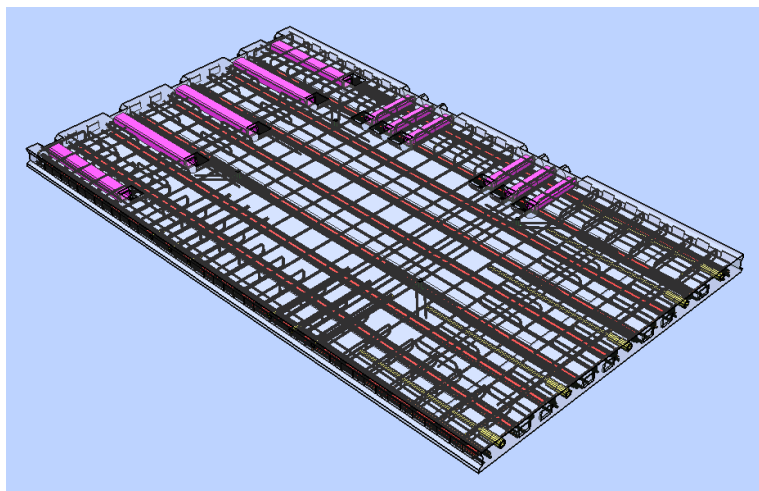


Fig. 12 - Use of digital engineering to enable optimised reinforcement cage



Fig. 13 - Manufacturing trials demonstrating quality of finish (left) and connectivity (right)

ASSEMBLY

The precast planks were assembled on site by Expanded Limited, a Laing O'Rourke group company. Each plank, weighing about 2 tonnes, was installed in position by a very small team of operatives who only had to screw the dowel bars together and grout up the connections. The dry construction enables very quick access to erection activity overhead as can be seen below where an access device is already located on the slab prior to grouting.

Edge protection sockets, lifting points and façade fixings are pre-installed in the elements, minimising the amount of onsite work and work at height. The plank system allowed a very fast rate of construction, up to 700 square metres per day with one crane and minimal labour, as can be seen in Figure 14.

A combination of steel and precast concrete was also used for the construction of the North Core. Here the planks are raised up above the main framework and do not act compositely. However this was an excellent example of prefabrication. Table units one storey high were fabricated with the precast planks, horizontal services and the temporary edge protection and were installed in one lift (Figure 15).



Fig. 14 - Plank assembly at the work-front



Fig. 15 - North core module, delivered as one unit (steel table, precast planks, horizontal services and edge protection)

Conclusions

A new method for lightweight concrete floors in composite action has been demonstrated through testing to be a reliable construction technique and has proven through practice its ability to deliver high quality construction in a fast, clean and efficient manner (Figure 16).



Fig. 16 - View of structural soffit

ACKNOWLEDGEMENTS

The authors would like to thank the Leadenhall Development Company Limited for the opportunity to build such a building and their willingness to accept the change of floor system. They would also like to thank the many colleagues in Laing O'Rourke, Arup, BRE and the rest of the supply chain who contributed to the successful construction of the floors at the Leadenhall development.

References

- Banfi, M., Composite beams with web openings subject to axial load. Eurosteel 2008.
- (1) BRITISH STANDARDS INSTITUTION. BSEN1990 2002. Eurocode- Basis of structural design. BSI, 2002.
- (2) BRITISH STANDARDS INSTITUTION. BSEN1994-1-1: 2004. Eurocode 4: Design of composite steel and concrete structures. Part 1. General rules and rules for buildings. BSI, 2004.
- Concrete Society, Influence of tension stiffening on deflection of reinforced concrete structures. Concrete Society, 2004.
- Lawson, R.M., and Hicks, S.J., Design of composite Beams with large web openings. SCI P355, SCI, 2011.
- Leonhardt F., Andrä, W., Andrä H-P. and Harre W.; Neues, vorteilhaftes Verbundmittel für Stahlverbund-Tragwerke mit hoher Dauerfestigkeit. Beton und Stahlbetonbau 12/1987.
- Willford, M.R. and Young, P., A design guide for footfall induced vibration of structures. CCIP 016, Concrete Centre 2006.
- GB 2495319, Patent application no. GB 2495319, Floor Construction, 10th April 2013, Stehle, J., Laing O'Rourke Plc.

Experimental Assessment of Ferritic Stainless Steel Composite Slabs

K. A. Cashell¹ and N. R. Baddoo²

¹Dept. of Mechanical, Aerospace and Civil Engineering, Brunel Univ., London UB8 3PH, U.K. E-mail: katherine.cashell@brunel.ac.uk

²Steel Construction Institute, Ascot, Berkshire SL5 7QN, U.K. E-mail: n.baddoo@steel-sci.com

Abstract

This paper describes investigations into the structural behaviour of ferritic stainless steel floor decking in composite construction. Although commonly used in the automotive and industrial sectors, structural applications of ferritic stainless steels are rare owing to a relative lack of knowledge, performance data, and design guidance. These materials display considerably better atmospheric corrosion resistance than carbon steels, as well as having good ductility, formability and excellent impact resistance. As part of a wider investigation into the use of ferritic stainless steels in structural applications, an experimental study has been undertaken to assess the viability of using these materials for the profiled decking in composite floors. The shear connection behaviour between the steel beams and the composite slab is clearly critical and this is influenced by the through-deck welding process of the shear connectors. The practicality of this welding technique is assessed and described in this paper. Furthermore, the results of a series of push tests are presented. These enable the resistance of the shear connectors to be established and compared with the strengths specified in EN 1994-1-1 for composite slabs using galvanized steel decking.

INTRODUCTION

Ferritic stainless steels are low cost, price-stable, corrosion-resistant materials which are widely used in the automotive and domestic appliance sectors. They are a family of 'utility' stainless steels which display considerably better atmospheric corrosion resistance than carbon steels, as well as having good ductility, formability and excellent impact resistance. Nevertheless, structural applications are scarce owing to a lack of suitable information and design guidance. It is in this context that a major collaborative project is underway in Europe entitled Structural Applications of Ferritic Stainless Steels (or SAFSS). The principal aim of this study is to develop the information needed for comprehensive structural design guidance to be included in relevant parts of the Eurocodes and other accompanying standards/guidance. Although the research has general applicability to the use of ferritic stainless steel, there is a particular focus on trusses and space frame structures as well as exposed decking in composite floor systems, the latter of which is relevant to the current paper.

Steel-concrete composite construction is a popular choice amongst engineers and designers as it represents a very efficient use of materials, providing quick, cost effective and sustainable construction (Simms and Hughes, 2011). Typical ingredients include steel decking, slab reinforcement, shear connectors, structural steel section and the concrete slab, as shown in Figure 1. The use of steel-concrete composite floor slabs is well established and the design approach is presented in Eurocode 4 (EN 1994-1-1, 2004). It is estimated that the European market size for decking in composite floor systems is 60-80,000 tonnes per annum. However, the use of stainless steel for the decking has not been explored in any great detail, although it offers two distinct advantages over galvanized steel, which may be favourable in certain circumstances:

- i. Corrosion resistance – this may be important in applications with exposed decking or in other sensitive environmental conditions, e.g. during the construction stage, or in a car park.
- ii. Thermal capacity – it has been shown that the thermal mass in floor slabs can be used to regulate temperatures in the structure thereby reducing the need for additional cooling and heating measures (Barnard and Ogden, 2006; Kendrick and Wang, 2007). This is optimized by using profiled slabs as the exposed area is greater than in flat slabs and also by having an exposed metal deck to allow good convective and radiative heating/cooling. Whilst the thermal performance of galvanised and stainless steel has not been shown to differ significantly, stainless steel is more likely to be exposed as it provides a more attractive appearance.

Ferritic stainless steels can offer a cost-effective solution in composite floors. However, before this technology can be further developed, it is necessary to satisfy the required structural performance of composite slabs using profiled decking rolled from ferritic stainless strip steel. Apart from the SAFSS project, no other research programme looking at the use of stainless steel in composite floor systems is known to the authors.

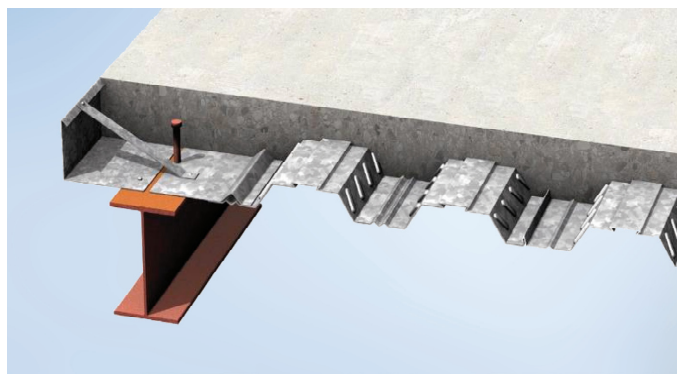


Figure 1. Steel-concrete composite construction (image available from the SCI)

Historically, the performance of shear connectors has been established using small-scale push test specimens, where a small number of shear studs are embedded in a concrete section and welded to a steel section which is then loaded whilst the concrete section is held in position. This type of test is described in Eurocode 4

(2004) and the essence of the test has remained unchanged since the 1930's (Hicks, 2007). However, it is important to note that the validity of these tests has come into question in recent years as comparisons have shown that the specimens have lower resistances and ductility than composite beams with the same material properties, cross-section and decking geometry (e.g. Rambo-Roddenberry, 2002; Bradford et al., 2006; Hicks, 2007). The reason for this lies in the loading and restraint conditions of the push tests, which are different to those experienced in a composite beam. In particular, the vertical forces and negative bending in the slab at the line of the shear connectors are currently ignored.

Nevertheless, a cost-effective and straight-forward alternative to the standard push test has yet to be developed and introduced in design guidance (although it is currently being investigated in a major European project entitled "Development of improved shear connection rules in composite beams" which is being coordinated by the Steel Construction Institute and funded by the Research Fund for Coal and Steel), and therefore the tests adopted in this programme are as specified in Eurocode 4. It is acknowledged that the push tests may not give the full impression of the composite performance but they can still give a useful insight into the most salient parameters and provide a basis for comparison with other materials. A primary objective of this study is to gain an insight into the effect of different shear connection arrangements on the composite performance.

This paper provides a background to the SAFSS project, followed by a brief description of ferritic stainless steel. Thereafter, a discussion on composite behaviour will be given as well as a description of the experimental investigation into the composite performance of ferritic stainless steel-concrete composite slabs. A series of 8 push composite tests has been completed at Brunel University in order to assess the shear connection behaviour and these will be discussed together with the findings from the through-deck welding trials. More detailed discussion is available elsewhere (Cashell and Baddoo, 2014).

SAFSS PROJECT

The SAFSS project is a 3-year collaborative project which commenced in mid-2010 with a view to increasing the structural use of ferritic stainless steels. The project is largely funded by the European Union Research Fund for Coal and Steel (RFCS) with additional support from Aperam, AcerInox and Outokumpu Stainless Oy and is being coordinated by the Steel Construction Institute. The project has been divided into eight separate work packages with various partners working on each. The work packages (WP's) include studies into: (WP1) Mechanical properties; (WP2) Structural performance of light gauge members; (WP3) Structural performance of steel decking in composite floor systems; (WP4) Structural performance at high temperatures; (WP5) Structural performance of welded connections; (WP6) Structural performance of bolted and screwed connections; (WP7) Corrosion resistance; and (WP8) Design guidance and implementation into the Eurocodes. The study discussed in this paper is relevant to WP3.

FERRITIC STAINLESS STEELS

Ferritic stainless steels do not contain significant quantities of nickel and are therefore cheaper and relatively price-stable compared with austenitic stainless steels. Ferritics also differ from the more commonly-used austenitic stainless steels in that they have higher mechanical strengths (approximately 250-330 N/mm² 0.2% proof strength), are magnetic, have lower thermal expansion, higher thermal conductivity and are easier to cut and work.

The mechanical and physical properties of ferritics make them suitable for use in composite floor slabs where an attractive metallic surface finish is desirable. Unlike galvanised steel, ferritic stainless steels have a naturally occurring corrosion resistant surface layer so there is no requirement for applying protective surface layers and no remedial work or corrosion risk at cut edges in most normal applications. Furthermore, ferritics are easy to recycle compared to galvanised steel where the zinc from the galvanised coating must be removed prior to re-melting the steel.

Three of the 'traditional' ferritic grades are covered in the American SEI/AISI Specification for design of cold-formed stainless steel structural members (SEI/AISI, 2002) for thicknesses up to 3.8 mm. The South African (South African Bureau of Standards, 1997) and Australian/New Zealand (Standards Australia Standards New Zealand, 2001) structural stainless steel standards take similar approaches. The Eurocode for structural stainless steel, EN 1993-1-4 (2006) states it is applicable to three traditional ferritic grades (grades 1.4003, 1.4016 and 1.4512), however, the guidance is almost exclusively derived from work on austenitic and duplex stainless steels and in many cases ferritic-specific guidance is missing. EN 1993-1-4 refers to a number of clauses in other parts of Eurocode 3 such as EN 1993-1-2 (2005), 1-8 (2005), 1-9 (2005) and 1-10 (2005) which have not been validated for ferritic stainless steels. One exception is that EN 1993-1-2 (2005) includes data on one ferritic grade.

COMPOSITE BEHAVIOUR

In composite structures, the applied loads are transferred between the floor slab and the beams through shear connectors which are embedded in the concrete slab and welded to the steel beam. The capacity of these studs is typically established experimentally through push tests, although there are shortcomings to this approach, as presented earlier in this paper. International design standards such as Eurocode 4 (EN 1994-1-1, 2004) provide theoretical models for predicting the shear resistance of the shear studs.

The Eurocode 4 theoretical model is presented in Sections 6.6.3.1 and 6.6.4.2 of the code. When stud connectors are welded within ribs of profiled steel decking, their resistance is reduced compared with their resistance in a solid slab. To account for this, Eurocode 4 applies an empirically-derived reduction factor (k_t) which is multiplied to the design resistance for a shear stud in a solid slab (P_{Rd}) to give the final shear stud resistance (referred to as $P_{Rd,rib}$ hereafter). However, it is noteworthy that Eurocode 4 provides no guidance as to how the standard solid slab specimen

should be adjusted when decking is present, which has given rise to a large degree of scatter in test results (Hicks, 2007).

The reduction factor k_t is defined as:

$$k_t = \frac{0.7}{\sqrt{n_r}} \frac{b_0}{h_p} \left(\frac{h_{sc}}{h_p} - 1 \right) \quad \text{but } k_t \leq 0.85 \text{ for studs welded through profiled steel sheeting}$$

and $k_t \leq 0.75$ for profiled sheeting with holes. (1)

where:

- b_0 = the width of a trapezoidal rib at mid-height of the profile;
- n_r = is the number of stud connectors in one rib at a beam intersection,
- h_p = the height of the steel sheeting measured to the shoulder of the profile;
- h_{sc} = the as-welded height of the stud, but not greater than $h_p + 75$ mm.

P_{Rd} is defined as being the lesser of two values calculated using Equation (6.18) and (6.19) in Eurocode 4 for steel and concrete failure, respectively. Equation (6.18) determines the resistance based on the strength of the steel, presented here as Equation (2):

$$P_{Rd} = \frac{0.8f_u \pi d^2 / 4}{\gamma_V} \quad (2)$$

where:

- f_u the specified ultimate tensile strength of the material of the stud but not greater than 450 N/mm^2 for a profiled slab;
- d the diameter of the shear connectors;
- γ_V the partial factor.

Equation (6.19) in Eurocode 4 determines the resistance based on the strength of the concrete, presented here as Equation (3):

$$P_{Rd} = \frac{0.29\alpha d^2 \sqrt{f_{ck} E_{cm}}}{\gamma_V} \quad (3)$$

where:

- α a function of the dimensions of the deck and shear connectors;
- f_{ck} the characteristic cylinder strength of the concrete;
- E_{cm} the secant modulus of elasticity of the concrete.

Annex B in Eurocode 4 states that the characteristic slip capacity δ_{uk} should be taken as the maximum slip capacity of a specimen δ_u reduced by 10%, where δ_u is the slip corresponding to the characteristic load level (P_{Rk}). In Clause 6.6.1.1(5) of that standard, a shear connector is defined as ductile if the characteristic slip capacity is at least 6 mm, and the minimum degree of shear connection rules in the standard are calibrated for this ductility.

EXPERIMENTAL PROGRAMME

The primary objective of the laboratory experiments is to gain a greater understanding of the composite performance of slab specimens using ferritic stainless steel decking by completing a series of standard push tests. A number of parameters can affect the load-slip characteristics between the steel and the concrete, such as the way that the stud is welded to the steel section, continuity of the decking and the strength of the concrete. The focus in these tests is to ensure that the composite performance of specimens using ferritic decking is, at least, as good as that when galvanised decking is used and also to investigate the effect of different construction arrangements.

Prior to undertaking the main experimental programme, which consists of 8 push tests, it was important to conduct welding trials in order to verify the practicality of the through-deck welding technique commonly used in the UK. The welding trials were completed at Hare Decking Ltd (formerly Richard Lees Steel Decking) in the UK, where 19 mm carbon steel shear studs were welded through ferritic stainless steel sheeting to the structural steel beams using the same technique as used for regular galvanised steel decking (Figure 2). Once welded into position, they were subjected to the standard tests performed on welded shear studs in construction, i.e. the ring and bend tests (Figure 3); all welds passed these tests. Importance was given to subjecting the ferritic specimens to the same standard of testing as is commonly used on-site for galvanised decking.



Figure 2. Through deck welding

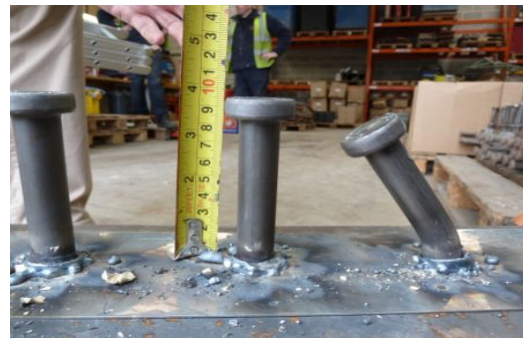


Figure 3. Bend test and 'left after weld height'

Further observations from the trials were that the welds were very satisfactory and all welds were found to have good collars and to be of correct 'left after weld height', i.e. 95 mm 'left after weld height' for a shear stud which was originally 100 mm in height, as shown in Figure 3. Based on the results of these trials, it can be deduced that there is no greater risk using ferritic decking than using galvanised decking from the welding perspective. Once the welding trials were completed with satisfactory results, the push test specimens were prepared at the same location.

Push tests

A total of 8 push tests were completed at Brunel University, all of which used Arcelor Mittal Cofraplus 60 decks (as shown in Figure 4) with a thickness of 0.8 mm in grade 1.4003 ferritic stainless steel. The tests were completed in accordance with EN1994-1-1 Annex B, differing slightly in that the code describes a flat concrete slab without steel decking whereas the test specimens were profiled with ferritic stainless steel sheeting. Structural tees were used rather than universal column sections to enable both sides of the specimen to be cast at the same time, thus ensuring consistent concrete properties within each specimen. The general construction of the test specimens is shown in Figure 5. Anti-cracking mesh (A193) was included in each specimen as shown in the diagram. There were 2 shear studs in each individual slab for all tests, thus resulting in 4 shear studs per test.

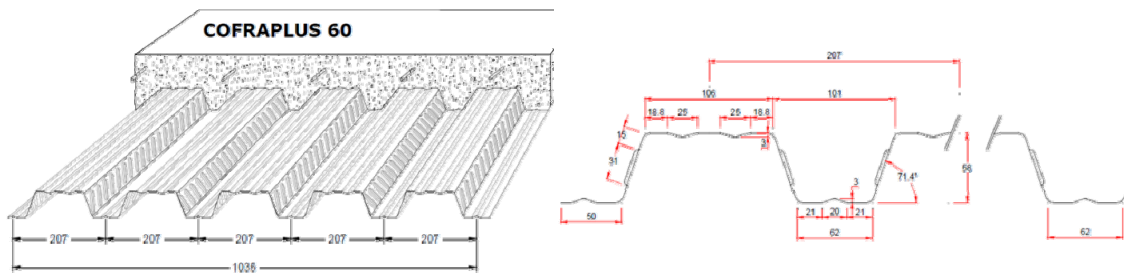


Figure 4. Cofraplus 60 decking

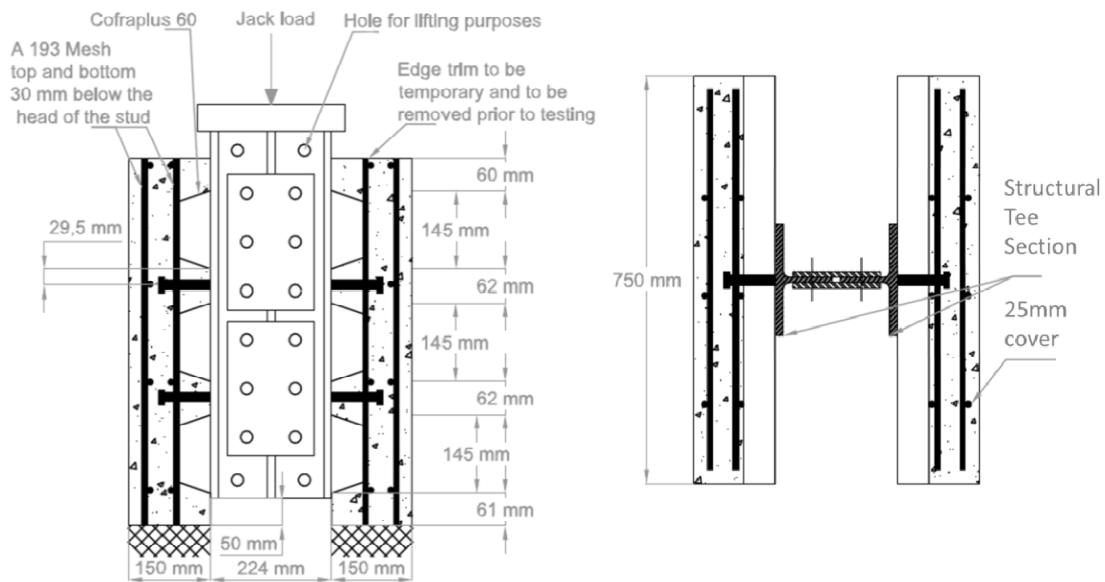


Figure 5. Test specimen

Whilst through-deck welding is popular in the UK, other parts of Europe typically use studs welded directly to the steel beam and decking with pre-punched holes. Both of these scenarios were examined in the current programme with three identical specimens of each category tested. The decking was rolled with a central stiffener in the centre of the trough which had to be hammered flat local to the stud position in the through-deck welded specimens to ensure direct electrical contact through the components as well as the integrity of a homogeneous weld. There was insufficient space to offset the shear stud. In order to ensure that this process did not affect the integrity of the weld, the two remaining tests in the programme had shear studs welded to the steel beam through a narrow strip (100 mm wide) of flat ferritic stainless steel sheeting with the same material properties as the profiled sheeting. A profiled sheet with pre-punched holes was then placed over the studs. The test programme is summarised in Table 1.

Table 1. Push-out test programme

Series :	Number of tests:	Details	Shape of slab	Continuity of deck beyond weld?	Through-deck welded?
1	2	Studs welded through narrow flat sheet	Profiled	No	Yes
2	3	Studs welded through continuous profiled deck	Profiled	Yes	Yes
3	3	No through-deck welding	Profiled	No	No

In each case the test specimens were loaded to failure by applying a hydraulic jack to a plate on top of the steel tees. Load was transferred to the concrete through the shear studs. In accordance with EN 1994-1-1, the load was first applied in increments up to 40% of the expected failure load and then cycled 25 times between 5% and 40% of the expected failure load. In each test, following the cycles, the load and displacement were gradually increased until failure occurred, typically by concrete pull-out, which was accompanied by a significant reduction in load capacity. The longitudinal slip between each composite slab and the steel section was measured continuously using displacement transducers, as was the lateral displacement of the slabs.

Results

Load-slip relationships for Series 1, 2 and 3 are presented in Figures 6-8 respectively whilst the Figure 9 is an image of a specimen after testing. A summary of all the experimental data is presented in Table 2, where f_{ck} refers to the compressive cylinder strength of the concrete on the day of testing (taken as the average of three cylinders), P_f is the failure load observed in the tests and P_{Rk} is the characteristic resistance per stud equal to 90% of P_f divided by the number studs (4 in this case), as defined in Eurocode 4 Annex B (EN 1994-1-1, 2004). δ_u is the slip

corresponding to P_{Rk} whereas δ_{uk} is the characteristic slip equal to δ_u reduced by 10%. $P_{Rd,rib}$ is the design resistance as described previously. The yield (f_y) and ultimate (f_u) strengths of the ferritic decking were 326 N/mm^2 and 480 N/mm^2 , respectively, based on taking the average of 4 tensile test coupons. On the other hand, the yield and ultimate strengths of the shear studs were 446 N/mm^2 and 488 N/mm^2 , respectively.

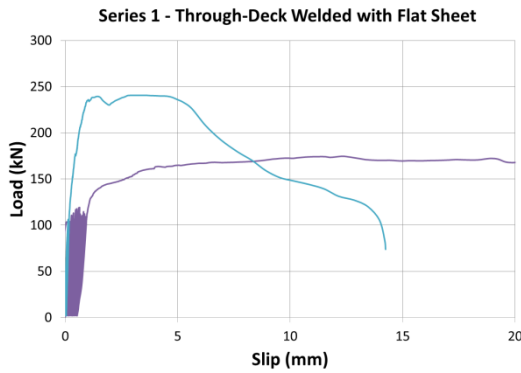


Figure 6. Load-slip curves for Series 1

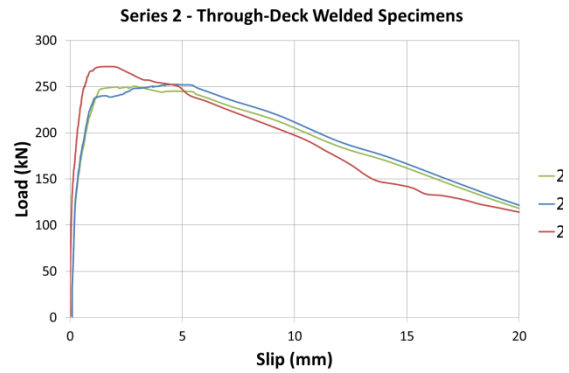


Figure 7. Load-slip curves for Series 2

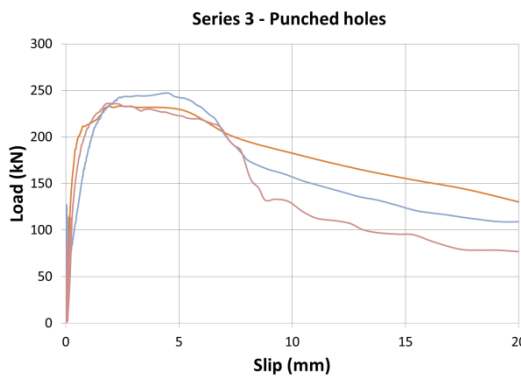


Figure 8. Load-slip curves for Series 3

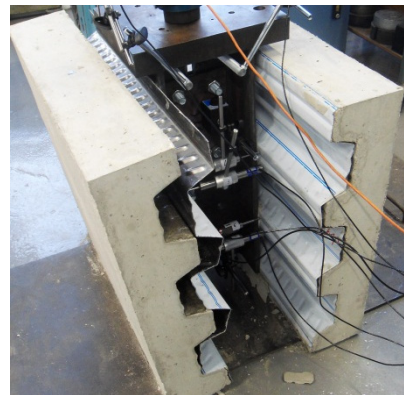


Figure 9. Failed specimen after testing

Table 2. Results of push tests

Specimen	f_{ck} (N/mm^2)	$P_{f,total}$ (kN)	P_{Rk} (kN)	δ_u (mm)	δ_{uk} (mm)	$P_{Rd,rib}$ (kN)	$P_{Rk}/P_{Rd,rib}$
1-A	35.82	174.66	43.66	22.07	19.86	64.07	0.69
1-B	44.44	234.70	58.68	6.43	5.78	64.07	0.92
2-A	30.05	249.72	62.43	7.67	6.90	64.07	0.98
2-B	41.26	245.19	61.30	9.62	8.66	64.07	0.96
2-C	34.29	270.93	67.73	5.61	5.05	64.07	1.06
3-A	37.54	231.66	57.92	6.77	6.09	64.07	0.91
3-B	29.59	244.20	61.05	6.58	5.92	64.07	0.96
3-C	39.25	232.40	58.10	6.87	6.18	64.07	0.91

Observations and analysis

During the 25 cycles between 5% and 40% of the expected failure load, the specimens remained in good condition with no visible cracks, although concrete movement could be heard. At about 80-90% of the peak load and a slip of around 1 mm, visible delamination occurred between the concrete slab and the decking. With the addition of more load, the concrete began to visibly and audibly crack. Failure was typically accompanied by a notable drop in the load-carrying capacity of the specimen.

All of the specimens demonstrated concrete pull-out failure around the shear connectors although one stud was found to have sheared off in Specimen 3-C. It is impossible to know exactly when this happened although it is likely that it was after the concrete had failed as the displacement increased. After each test, the concrete slab was removed from the profiled sheeting, which was very easy as no bond remained. Figure 10 shows Specimen 3-A without the steel deck where the evidence of concrete pull-out can be seen, whereas the steel deck from this test is presented in Figure 11, showing the remaining concrete around the shear stud.

Concrete pull-out failure occurs when the concrete surface fails due to tension occurring across the failure surface. It has been shown that standard push-tests are dominated by failure of the concrete around the shear connectors, as was observed in these tests, rather than shearing of the shear connector itself (Smith, 2009). The typical failure surface for single shear connectors is a cone of concrete starting underneath the head of the shear connector and growing in diameter down the length of the shear connector, although the shape is restricted by the shape of the decking (see Figure 11). However, this type of failure would be less likely to occur in a real composite member which is loaded in bending and, for this reason, many researchers have added a lateral load to the test specimens (e.g. Easterling *et al.*, 1993; Rambo-Roddenberry, 2002; Bradford *et al.*, 2006; Smith, 2009; Smith and Couchman, 2010).



Figure 10. Failed specimen – concrete



Figure 11. Failed specimen - decking

As stated previously, all of the slabs behaved very similarly, regardless of the construction form and all failed in an identical manner. As expected, the Series 2 specimens which were through-deck welded and offered continuity of the steel sheeting demonstrated higher load and slip capacities. Also, during the unloading

stage of the load-slip response, these slabs were more ductile than the specimens with punched holes. The combination of the through-deck welded shear studs and the continuous steel sheeting enhanced the bond strength and consequently the load and slip capacity of the slab. Previous studies have shown that composite specimens with pre-punched holes (i.e. Series 3) offer the advantage of producing more reliable and better stud welds with fewer failures (Ernst et al., 2009), but there was no issue with the through-deck welded studs in this test programme.

It is noteworthy that the response of Specimen 1-A was quite different to the other slabs in that it had a considerably lower load resistance, much greater slip capacity and the shape of overall load-slip relationship was quite dissimilar to the other tests (refer to Figure 6). This is due to experimental error at the time of casting. This was the first specimen to be cast in this programme and the concrete mixture was quite 'lumpy' and inconsistent. Although it was of acceptable strength on test day ($f_{ck} = 35.82 \text{ N/mm}^2$), it is thought that the texture and consistency of the concrete affected the bond between the deck and the slab thereby causing this test to behave uncharacteristically. The concrete mixture probably added to the mechanical interlock between the slab and the decking allowing more slippage to occur without a loss in bond strength.

COMPARISON BETWEEN THEORETICAL AND EXPERIMENTAL RESULTS

Using the equations presented earlier in this paper, the reduction factor (k_t) for the Cofraplus 60 decks used in these tests is found to equal 0.63. The design strength ($P_{Rd,rib}$) for each of the test specimens is presented in Table 2, together with the ratio of the test resistance to the design resistance. The ratio of $P_{Rk}/P_{Rd,rib}$ varied between 0.91 for Specimens 3-A and 3-C and 1.06 for Specimen 2-C. It is clear that this ratio is higher for Series 2 relative to Series 3 showing that the through-deck welded shear connectors offer slightly greater shear resistance. In general, given that the design resistance $P_{Rd,rib}$ values in Table 2 do not include safety (γ) factors, having a 'test to design' ratio of around 1 is as expected.

The ductility of the specimens was reasonable with all of the δ_{uk} values being around the 6 mm value required by the Eurocode in order to justify the assumption of ideal plastic behaviour of the shear connection. As stated before, it has been shown that these types of push tests give lower strength and slip resistances than composite beam specimens. Hicks (2007) showed that studs in beam tests out-performed those in push tests both in terms of resistance and ductility, by 46% and 269% respectively. In particular, it has been shown that push test specimens which fail by concrete pull-out as occurred in these tests give brittle failure and low strengths (Johnson and Yuan, 1998).

There is no data in the literature for equivalent tests using galvanised steel decks. However, Bradford *et al.* (2006) reported some tests which were conducted in a similar manner (i.e. no lateral force applied) and used galvanized decking with a very similar profile shape to the Cofraplus 60. These tests appeared to show very limited ductility (δ_{uk} values significantly below 6 mm) which the authors attributed to the test arrangement causing premature failure. A new test procedure was proposed

wherein a normal force is applied to the specimen in addition to the longitudinal force in order to prevent concrete pull-out failure and unrealistically low ductility.

On this basis, it is reasonable to deduce that specimens with ferritic stainless steel decking behave at least as well as slabs with galvanised decking and therefore conform to the current requirements of the Eurocode specification.

CONCLUSIONS

This paper has described a series of push tests which were completed as part of a wider project looking at structural applications of ferritic stainless steels (SAFSS). An overview of the project was given followed by an introduction to ferritic stainless steel, including their relevant properties for structural use. One potential application for ferritics is for decking in composite construction and, towards this end, a series of push tests were conducted in order to determine the suitability of these materials for this application and the results presented herein.

The methodology, results and analysis of the push tests were presented, and it was concluded that the resistance of shear connectors is comparable with the resistance given in Eurocode 4 (EN 1994-1-1, 2004) for galvanised decking both when through-deck welded and when directly welded to the steel section through pre-cut holes in the deck. All of the tests failed in the same manner which was through concrete pull-out, regardless of the construction form used. The results also showed that there is sufficient ductility to use the current minimum shear connection rules in Eurocode 4 for headed stud shear connectors.

It is accepted that the method of testing is not ideal as it creates internal forces which are different to those that occur in composite members under bending forces. However, as a starting point, it is important to complete the tests in accordance with the Eurocode so that comparisons with existing design equations can be made. Further work is required in order to numerically analyse the push test specimens so that the effect of the loading conditions can be quantified and further understood. Specific recommendations or modifications to the Eurocodes have not been proposed as further analysis is required, including a direct comparison with the performance of galvanised steel under identical conditions.

ACKNOWLEDGEMENTS

The research leading to these results has received funding from the European Community's Research Fund for Coal and Steel (RFCS) under Grant Agreement no. RFSR-CT-2010-00026, Structural Applications of Ferritic Stainless Steels. The authors would also like to thank the technical staff of the structures laboratories at Brunel University, particularly Malcolm Austen and Keith Withers, for their assistance with the experimental work as well as Zainab Adigun, Olayinka Oladiran and Seyed Ghaffar for their contribution to the specimen preparation and testing.

REFERENCES

- Barnard, N and Ogden, R (1996). "The thermal capacity of steel frame buildings." Seminar Paper available from the Steel Construction Institute, UK
- Bradford M.A., Filonov A. and Hogan T.J. (2006). "Push testing procedure for composite beams with deep trapezoidal slabs." *Proceedings of the Eleventh international conference on metal structures*, Rzeszow, Poland.
- Bradford M.A., Pi Y.-L., Uy B. (2008). "Ductility of composite beams with trapezoidal composite slabs." *Proceedings of the Sixth International Conference on Composite Construction in Steel and Concrete*, Colorado, USA, pp. 151-158.
- Cashell K.A. and Baddoo N.R. (2014). "Ferritic stainless steels in structural applications." *Thin-Walled Structures*, 83, 169- 181
- Easterling, W. S., Gibbings, D. R., and Murray, T. M. (1993). "Strength of Shear Studs in Steel Deck on Composite Beams and Joists." *Engineering Journal, AISC*, 30(2), 44-55.
- EN 1992-1-1 (2004). "Eurocode 2—Design of concrete structures - Part 1-1: General rules and rules for buildings." CEN, Brussels, Belgium.
- EN 1993-1-2 (2005). "Eurocode 3—Design of steel structures, Part 1-2: General rules — Structural fire design." CEN, Brussels, Belgium.
- EN 1993-1-4 (2006). "Eurocode 3—Design of steel structures: Part 1-4: General rules — Supplementary rules for stainless steels." CEN, Brussels, Belgium.
- EN 1993-1-8 (2005). "Eurocode 3—Design of steel structures, Part 1-8: Design of joints." European Committee for Standardisation. CEN, Brussels, Belgium.
- EN 1993-1-9 (2005). "Eurocode 3—Design of steel structures, Part 1-9: Fatigue." CEN, Brussels, Belgium.
- EN 1993-1-10 (2005). "Eurocode 3—Design of Steel Structures- Part 1-10: Material toughness and through-thickness properties." CEN, Brussels, Belgium.
- EN 1994-1-1 (2004). "Eurocode 4.—Design of composite steel and concrete structures Part 1-1: General rules and rules for buildings." CEN, Brussels, Belgium.
- Ernst S., Bridge R. and Wheeler A. (2009). "Push-out tests and a new approach for the design of secondary composite beam shear connections." *Journal of Constructional Steel Research*, 65, 44-53.
- Hicks S. (2007). "Strength and ductility of headed stud connectors welded in modern profiled steel sheeting." *The Structural Engineer*, 85(10), 32-38
- Johnson R.P. and Yuan H. (1998). "Models and design rules for stud shear connectors in troughs of profiled sheeting." *Proceedings of the Institution of Civil Engineers Structures and Buildings*, 128, 252-263.
- Kendrik C. and Wang X (2007). "Thermal mass in new build UK housing: a comparison of structural systems in a future weather scenario." Report to the Steel Construction Institute, UK.
- Rambo-Roddenberry M. (2002). "Behavior and strength of welded stud shear connectors", PhD Thesis, Virginia Polytechnic Institute and State University.

- SEI/ASCE (2002). "Specification for the Design of Cold-Formed Stainless Steel Structural Members." SEI/ASCE 8-02.
- Simms W.I. and Hughes A.F. (2011). "Composite Design of steel framed buildings - In accordance with Eurocodes and the UK National Annexes." Steel Construction Institute (SCI), Ascot, UK.
- Smith A.L. (2009). "Effect of key variables on shear connector performance using new push rig." SCI Report RT1236, Ascot, UK.
- Smith A.L. and Couchman G.H. (2010). "Strength and ductility of headed stud shear connectors in profiled steel sheeting." *Journal of Constructional Steel Research*, 66, 748-754.
- South African Bureau of Standards (1997). "Code of Practise, Structural Use of Steel, Part 4: The Design of Cold-formed Stainless Steel Structural Members." SABS 0162-4:1997.
- Standards Australia Standards New Zealand (2001). "Cold-formed stainless steel structures." AS/NZS 4673:2001.

Case Study: Composite Construction for FLAT Slabs with Integrated Building Services

Thomas Friedrich¹; Juergen Schnell²; and Wolfgang Kurz³

¹Dipl.-Ing. TH, Domostatik GmbH, Cusanusstraße 23, D-54470 Bernkastel-Kues, Germany. E-mail: th.friedrich@domostatik.com

²Prof. Dr.-Ing., Kaiserslautern Univ. of Technology, Paul-Ehrlich-Straße, Gebäude 14, Raum 515, D-67663 Kaiserslautern, Germany. E-mail: jschnell@rhrk.uni-kl.de

³Prof. Dr.-Ing., Kaiserslautern Univ. of Technology, Paul-Ehrlich-Straße 14 - Raum 14/511, D-67663 Kaiserslautern, Germany. E-mail: wolfgang.kurz@bauing.uni-kl.de

Abstract

About 10 years ago, the idea arose of developing a new flat slab type with integrated building services. The first idea concentrated on a pre-fabricated slab element with a sandwich cross section. The open space (hollow space) between the two outer shells of the sandwich is available for various installation devices. It was also necessary to provide appropriately large openings in the web members joining the two outer shells. In order to provide the necessary strength around the large openings, a steel plate was embedded within the concrete web element. Appropriate composite connecting means were additionally needed to provide bonding capacity to the respective outer shells of the sandwich. In order to satisfy these requirements for the bonding devices, two independent solution proposals were offered. The web members were additionally pre-stressed, in order to reduce the absolute values of the shear stresses. In order to optimize the bonding element, two variants were tested. Different projects were built with the new composite element.

1. Introduction: Sandwich cross-section for structural elements with integrated building services

In 2003 the idea was conceived to use a sandwich cross-section with a construction height equal to that of conventional flat slabs that they would replace. Since flat slabs are currently manufactured with precast slab elements with in-situ structural concrete topping, the thought was logical to precast the elements with a modified cross-section. There were several reasons for making use of the cross-sectional form of a precast slab for manufacturing a flat slab in the form of a sandwich.

One reason for this change was the idea to integrate at the same time the components of building services in the loadbearing structure. If the original requirements called for optimising the performance of a thermo-active element so

that it would achieve exclusive climatizing of the building, the remaining components of the building services were then also to be integrated into the cross-section in the course of development work (Figure 1).

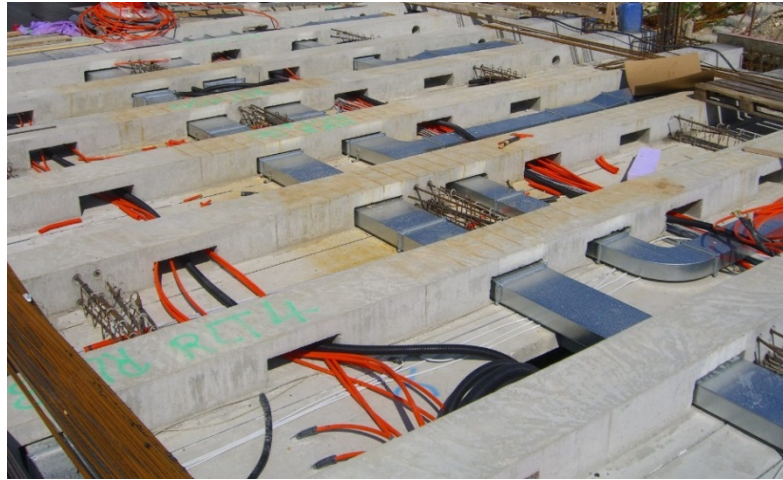


Figure 1. Ribbed slabs with openings for the integrated service lines

The sandwich cross-section presented itself as the ideal means for meeting these requirements. Separation of the cross-section into several layers enables a marked increase in thermo-active performance, since in this way only the individual very thin shells have to be provided with service lines.

Thanks to the low concrete mass, supplemented by arrangement of the pipes near the surface, not only a considerable increase in performance could be achieved, but the responsiveness of the overall system was moreover clearly enhanced as well. This made it possible for the first time to boost the activation of the element, until now limited in its performance, to a higher level – with the result that the rooms can be completely climate-controlled with this system alone.

The separation of the two shells, moreover, created a largely free interspace between the two shells that could be used for accommodating the integrated service lines (Figure 2).



Figure 2. View into the hollow floor space with service line cross-sections

If the demand for integrated building services was of primary concern, the sandwich cross-section with its low self-weight positively affected the loadbearing structure as well. From the standpoint of structural engineering, the dimensions of the two shells can be reduced to a minimum. Because the loading of conventional building structures requires only low compression zones ($x/d < 0.10$), the shell can, as a general rule, be reduced to a structural minimum to absorb the compression zone. The dimensioning of the shell to absorb the tension zone must satisfy the requirements for corrosion protection of the installed reinforcement and, at the same time, provide sufficient room for integrating the pipelines for cooling and heating. Low dimensions of the two shells result in lower weights. And the lower weights also give rise to lower stress and strain. This reduction of self-weights, in turn, opened up the objective of floors with wider spans: the reason being that broken-down cross-sections can be economically realized only in such a manner. Floors with wide spans and low weight, again, make prestressed reinforcement economically attractive: low self-weight offers two-fold advantages in that not only lower deflection forces are needed, but also, due to lower loading, in that less reinforcement is required. A reduction in self-weight – for example by 50% with the construction height being equal – results in equal savings in the prestressing reinforcement.

At the same time it became evident that floor elements of this kind can be manufactured only as precast construction. That again means that the building services as well must be prefabricated and integrated in the precast plant. Craftsmanship-oriented construction methods lose in this way their previous image: and what has been demonstrated by the automobile industry for a long time already will in future also apply to building – i.e., increasingly widespread industrialized production in an enclosed factory, independent of the weather. This brings additional advantages as well as a marked increase in manufactured quality and time savings for installation at the construction site.

The two separated shells must be interconnected for structural reasons in discrete places to enable them to absorb the shear forces in addition to exhibiting the required flexural tensile strength. This can in turn be ideally achieved with linear ribs placed in the direction of span. The ribs, however, restrict the possibilities for installing the piping within the hollow space of the floors. The aim is to install the piping not only parallel to the ribs, but also vertically to them. For this reason it must be possible to lead the piping through the ribs. Openings in the ribs are therefore obligatory.

2. Manufacture of the slabs with sandwich cross-section – initial designs

Once the sandwich cross-sections had been identified as the central element of the innovative floor slabs, it was necessary to ensure economical production.

The thought logically arose to approach manufacture of the elements in a way similar to production of double walls: i.e., to effectively connect the two shells with each other. This, however, immediately gave rise to the question of stability and corrosion of the rebars of the lattice girder when not cast into the concrete, as is customary with double walls.

A possible approach to solving this task was to encase the rebars in such a way as to provide the rather thin-diameter bars with sufficient stability and protect them at the same time from corrosion. This requirement is automatically met by providing an encasing rib. But this leads to the difficulty of arranging the openings for the pipes. Accordingly, the initial tests concentrated on a specific encasing for the diagonals bar with fibre concrete (Figure 3).



Figure 3. Concrete truss comprised of lattice girders and encased diagonals

Neither the manufacture nor the loadbearing capacity achieved in the initial tests was convincing. Consequently, continuous ribs were concreted in place with the adjusted lattice girders – into which the individual pipes were embedded as openings between the diagonals. However, owing to the dimensions of the slabs with slight thickness, only openings with small diameters (< 100 mm diameter) were feasible, since the diagonal arrangement of the bars of the lattice girders restricted free access.

3. Large web openings require a composite construction, with sheet steel as ribbed reinforcement

Due to the large spans and the resulting greater floor thicknesses, the hollow space became larger as well, so that the dimensions of the openings also had to be adjusted. Lattice girders as reinforcing elements could not be used due to their height and loadbearing capacity, and when stirrups are used as shear reinforcement, the dimensions of the openings are restricted to small dimensions due to the load-transfer model. The installed service ducts require openings which match the height of the hollow space and which have a width equalling to 2 to 3 times that of the height of the hollow space. Dimensions of that order could not be realized with the structural capabilities of reinforced concrete. The alternative is a composite construction in the form of continuous metal plate installed in the web. The surrounding concrete absorbs the compressive forces and the metal plate, the tensile forces of the truss for absorbing the shear force. The desired dimensions for the openings could then be arranged in the metal plate strips. With these, the opening was then framed with the metal plate and the remaining dimensions and the material thickness of the plate were sufficiently dimensioned to be able to absorb the forces that occurred around the opening (Figure 4).

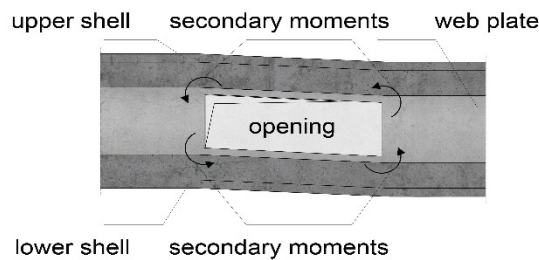


Figure 4a. Shear loading around the web openings

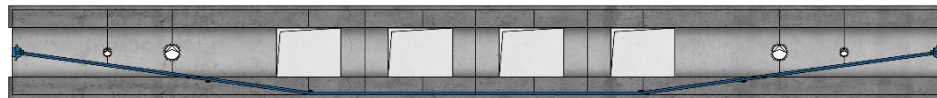


Figure 4b. Ribbed girder with large openings and installed prestressing steel; span to depth ratio $l/d \leq 30$

However, for the plate installed in the rib, sufficient bonding with the two shells was essential. Owing to the very thin shells of the sandwich cross-section, the dimensions for establishing the bond were very restricted. Only the arrangement of the horizontal headed studs could be accommodated in the thin shell.

The first applications of the innovative floor slabs were implemented with this solution (Figure 5). This design, however, involved considerable complexity in manufacturing the steel plate with the two rows of headed studs affixed to both sides of the plate. The small dimensions around the headed studs, moreover, led to structural problems in arranging the reinforcement layers in the individual concrete shells. The concrete of the rib surrounding the rib web plate was supplemented with stirrups. The individual ribs were additionally pretensioned to reduce shear loading. Using this method, the first projects were able to be successfully implemented (Figure 6).



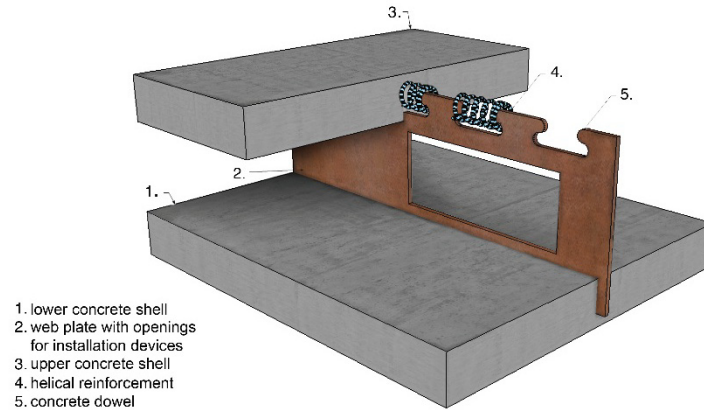
Figure 5. Web plates built into the ribs with cross section



Figure 6. Floor element with sandwich cross section

4. Composite construction using concrete dowels with concentrated transfer of forces achieved with helical reinforcement

Due to the considerable complexity involved with the arrangement of the horizontal headed studs, an alternative means for establishing the bond between concrete and steel was sought and found with implementation of the concrete dowels that were directly integrated in the web plate. With their design, it was possible to solve the spatial problems within the slender concrete shell, since now the relevant sheet plate edges together with the specially shaped geometry of the concrete dowels could be integrated into the individual concrete shells. The shape of the individual dowels is cut out to match the desired openings by laser beam during manufacture (Figure 7). In designing the geometry of the concrete dowels, previous experience gained was drawn upon. However, during design of the geometry it quickly emerged that the dowels, designed like a tooth, would act on the surrounding concrete like a blade. Analogously to the structural designs with prestressed concrete, where great forces are transmitted into very small areas in the concrete, installation of local reinforcement in the form of a strategic arrangement of a helical reinforcement became evident as a logical solution. It is known that peripheral confinement of concrete results not only in corresponding increase in force absorption, but at the same time in an increase in deformation capacity (Figure 8). Simultaneous increase in compressive strength is in this way accompanied by ductile loadbearing behaviour. This is a beneficial material property that is highly desirable in composite structural design.



**Figure 7a. Integrated web plate with large openings:
Bond via horizontal headed studs**

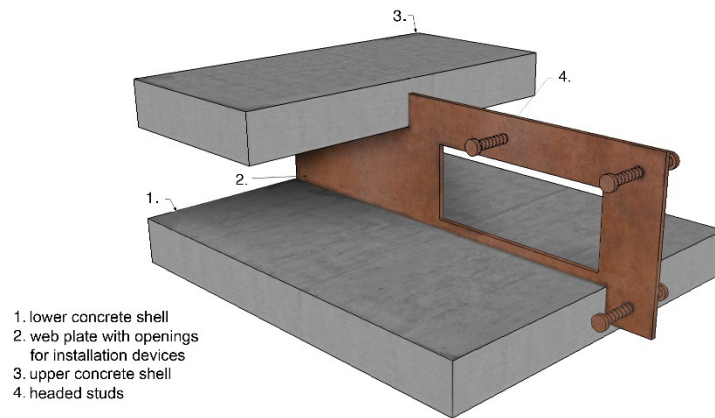


**Figure 7b. Integrated web plate with large openings:
Bond via helically reinforced concrete dowels**

Tests performed on concrete dowels with and without helical reinforcement show the effect achieved in the form of an increase in loadbearing capacity. To assess the effect of the concrete dowels, their behaviour during push-out tests and pull-out tests is of significance.

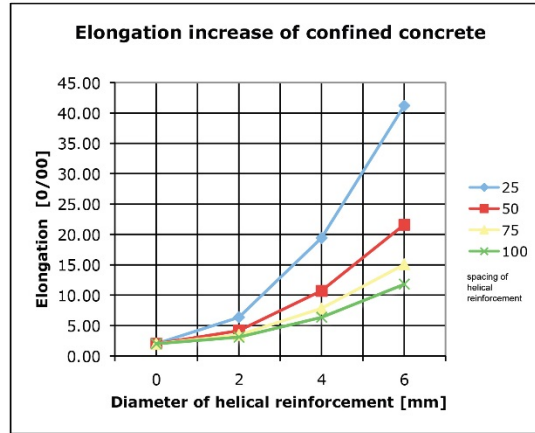


Figure 8a. Behaviour of peripherally confined concrete with helical reinforcement: Increase in compressive strength”

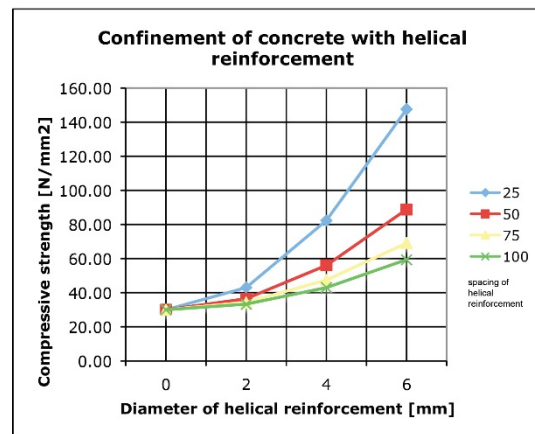


Figure 8b. Behaviour of peripherally confined concrete with helical reinforcement: Increase in ductility and simultaneous increase in elongation

The interaction of these two effects will then also demonstrate the increase that can be attained through helical reinforcement for the concrete dowels (Figure 9).

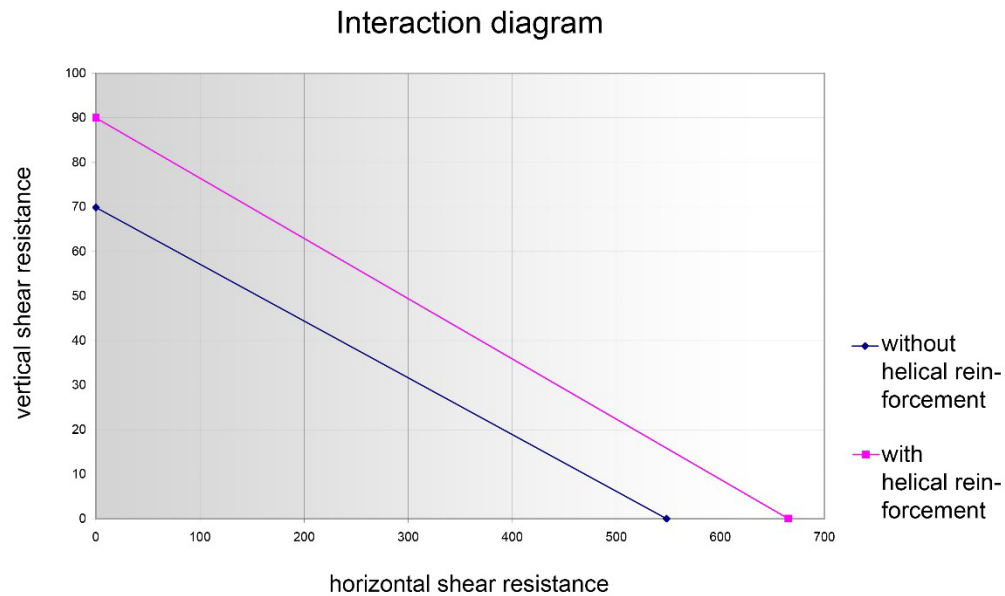


Figure 9. Interaction diagram – pull-out tests versus push-out tests with concrete dowels with and without helical reinforcement

5. Large-scale test on a composite girder with helically reinforced concrete dowels

The above-mentioned individual tests showed the possibilities for increasing the loadbearing capacity with innovative connectors in the form of helically reinforced concrete dowels. In connection with the desired large-size blockouts in the webs, the task was now to test the loadbearing capacity of the system. For this purpose, an experimental girder consisting of a long slab element with sandwich cross-section was manufactured. The reinforcement of the web was achieved with the metal plate with the desired openings and the connectors in the form of concrete dowels for joining both the compression and the tension zones. Encasing the web plate for fire resistance was provided with concrete for the rib. Additional provision also took place of prestressing (unbonded mono strand pretensioning) for the web, as implemented until now. This relieves the sandwich cross-section both under bending and shear forces. The latter is particularly effective in forming the larger web openings. The cable geometry chosen in the form of a trapezoid enables the arrangement of the blockouts over large areas of the girder. Only in the area of the support – where the tensioning cables rise from the lower edge of the web to the centre of the cross-section, and where the shear forces gain their maximum value – are the openings restricted to smaller dimensions. The experimental girder was manufactured in the precast plant, the same as the other precast elements (Figure 10). The large-scale experiment established the deflection, the cracks, and in particular the local deformations around the openings. The final result showed that the resistance values taken over from small-scale testing were sufficient for designing the entire system, since the loadbearing capacity of the system clearly exceeded the precalculated value (Figure 11).



Figure 10. Manufacture of the experimental girder with web plate and the helically reinforced connector including prestressing reinforcement

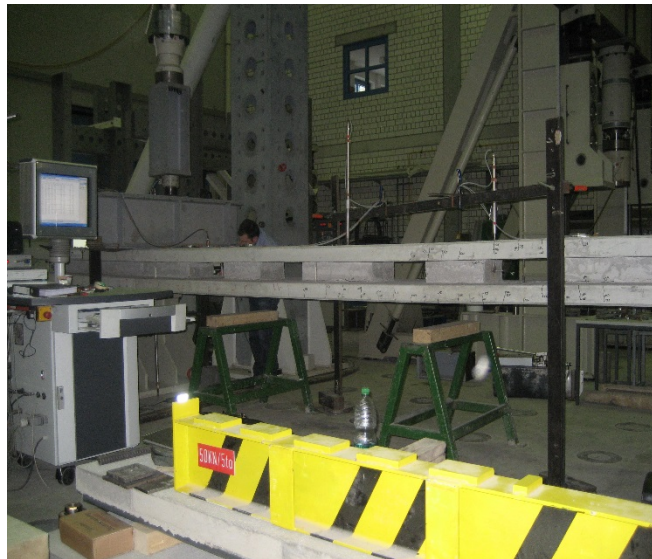


Figure 11. Load tests performed on a metal plate strip with sandwich cross-section and the larger web openings

The small-scale tests performed on the connectors and the results of the large-scale test then served as basis for implementing concrete construction projects using the new connectors. Since this method is at this time not standardized in Germany, individual construction projects must be tested on a case-to-case basis and their feasibility assessed based on these tests.

6. Specific implementation of the new composite construction method on a current project

The client was convinced of the possibilities of the prefabricated sandwich floor when commissioning the construction of his office and laboratory buildings. Cooling and heating with the floor, while making use of the large spans alone had already been a strong argument. Utilization of the hollow space of the floor for accommodating the entire ventilation and for the electric and IT wiring was exactly what he wanted. In this way, a raised floor would no longer be needed and the flooring could be directly applied to the concrete surface. The individual floor areas were then completely planned with the prefabricated floor slabs. Only two interior columns were arranged over a surface of 20 x 20 m. The individual floor slabs merge with a flush prestressed beam in in-situ concrete that spans from façade to façade over the two columns. The area of approx. 400 m² was covered with a total of 16 slabs measuring 2.50 x 10 m. The individual slabs consist of two individual shells connected to each other only via the two ribs (Figure 12). The inserted ribs were designed as composite construction. The metal plates are provided with large web openings at regular intervals and incorporate the two concrete shells with the helically reinforced concrete dowels (Figure 13).

The hollow space of the sandwich floor slab has a height of 20 cm and accommodates the arrangement of central cable ducts with branching off pipelines, including volume flow control (Fig. 2). The inspection openings arranged above the upper shell provide access to the ventilation ducts whenever needed. The cable trays for testing the electricity and IT systems are also installed in the hollow space.



Figure 12. Manufacture of the hollow slabs with the webs reinforced with metal plate and the helically reinforced connector



Figure 13. Web plate with the helically reinforced connector for use in the slab rib

The floor plates, including the integrated building services, are completely manufactured in the precast plant. Following their erection at the construction site, however, the plates must be connected with each other and the integrated piping. With the erection of the plates as structural elements, the share of the building services is already installed in horizontal connection (Figure 14). Only the connection to the ducts running vertically remains to be supplemented climate control facilities installed above the floor ensure a comfortable indoor climate that, for even more comfort, is supplemented by acoustic absorbers that are integrated in the lower shell of the floor.

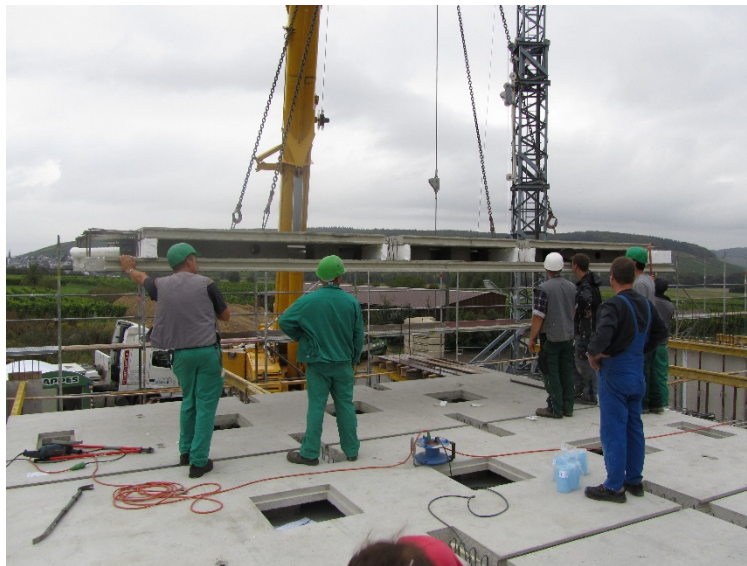


Figure 14. Assembly of the hollow slabs

7. Modification of the geometry of the metal plate for the composite construction – a future development

The experience gained with implementation of the present solution in the precast plant enabled gaining more knowledge on optimisation of construction of the steel plate. A plate placed at the opening provides greater resistance to the absorption of shear force and secondary moments when designed as double-T cross-sections (analogous to a rolled profile). In that case, the concrete dowels will then be arranged in the flanges of the profile. Even better suited for the geometry adjusted to the spatial conditions of these thin concrete shells are 3-dimensionally formed plates whose geometry results from edging this material. In advance, a laser beam cuts all openings and blockouts out of an appropriate metal strip. This procedure has the great advantage that openings for a subsequent arrangement of shear reinforcement for the thin concrete shells can be provided as well. Only then will individual sections of the plate be folded up towards the side. In this way, a web plate with moulded-on flanges is in effect created whose geometry optimally matches the very cramped spatial conditions (Figure 15). Metal-plate processing machines are today able to cut out of a metal plate strip of appropriate thickness any desired geometry and subsequently fold up the plates to form the three-dimensional geometry. In this way it is also possible to optimally adapt the shape and the dimensions for the concrete dowel to the anticipated loadings.

8. Tried and tested floor system

This development over the last 10 years has gone through many stages to end in a technologically mature floor system that has been successfully implemented (Figure 16). There are several aspects that make the system successful. Aside from the structural aspects such as low weight and the large span that can consequently be achieved, are the advantages of the integrated building services. A prefabricated loadbearing element with the described building-utilities properties has many advantages. Coordination among the consultants takes place in the first planning stage and is moreover reduced to the specifications for the system. Industrialized production of the precast elements protected from adverse weather conditions makes the manufacture of complex geometries (e.g., the sandwich cross-section) possible and with markedly higher precision than elements cast in-situ. The work on the construction site is then restricted purely to assembly.

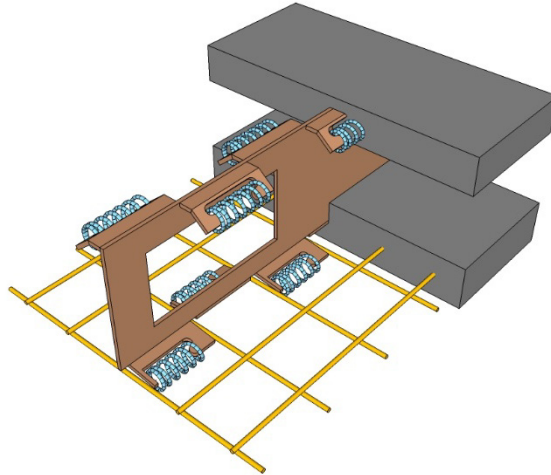


Figure 15. Optimised geometry of the web plate, taking into consideration such boundary conditions as web openings and assembly of transverse and helical reinforcement



Figure 16. Placing large floor elements with integrated service lines on construction side

REFERENCES

- Abramski, M.; Friedrich, T; Kurz, W.; Schnell, J.: New prestressed composite slab system for buildings with Multiple HVACR Installations, Composite Construction in Steel and Concrete VI, 6h International Conference, Colorado, USA, 2008
- Abramski, M.; Friedrich, T; Kurz, W.; Schnell, Tragwirkung von Betondübeln für Sandwich-Verbunddecken mit großen Öffnungen, Stahlbau (2010) Heft 4, S.248 – 258
- Abramski, M.; Friedrich, T; Kurz, W.; Schnell, J.: Innovative Shear Connector for a new Prestressed Concrete Slab System for Buildings with Multiple HVACR Installations, ASCE, 2010
- Friedrich, T.: Economical and innovative solutions with precast Concrete ICCX Oceania, Sydney march 2009

Progressive Collapse Analysis of Steel-Concrete Composite Frames with Floor Slab Actions

S. Jeyarajan^{1,*}; J. Y. Richard Liew²; and C. G. Koh³

Dept. of Civil and Environmental Engineering, National Univ. of Singapore, 1 Engineering Dr. 2, Singapore 117576. E-mail: a0016508@nus.edu.sg¹; ceeljy@nus.edu.sg²; cgkoh@nus.edu.sg³

Abstract

This paper proposes a simplified slab model, which can be easily incorporated in the commercial software ABAQUS for collapse analysis of 3-D composite building frames. The proposed model avoids complex geometric modelling of metal deck profile and requires less computational time for analysing large building frame. Verification studies have been carried by comparing the results with established experimental and numerical data available from the literature. The proposed slab model was applied to a three dimensional 9-storey building frame and the results are compared with the model without the floor slabs. Numerical results show that incorporation of slabs in the model reduces the beam deflection by as much as 50%. As one of the failure criteria for the progressive collapse is related to limiting beam deflection, the present of slabs tends to reduce the beam deflection and enhance the robustness of the building against progressive collapse.

1.0 INTRODUCTION

Robustness and progressive collapse analyses of building structures have been performed over the last two decades, but mostly on skeleton frames or on plane frame (2D) without the present of floor slab. This is because detailed modelling of non-linear behaviour of steel-concrete composite slab is rather tedious and involved other structural components including interaction between floor beams and slab and beam to column joint behaviour. A full non-linear analysis requires much computational time to capture the non-linear interaction between each composite slab and beam components ([Alashker et al. 2011]). Therefore most collapse analyses consider only the skeleton frames excluding the floor slab. However, floor slab is a vital part of the building and some researchers show that it contributes considerably to the resistance of progressive collapse. Remarkable studies include the contribution by [Sadek et al. 2008], [Kwasniewsk 2010], [Fu 2009] and [Alashker, et al. 2011], who have incorporated the composite slab in the progressive collapse analysis with few simplifications. Researchers have been concerned about analysis time and complexity of geometric modelling for the large scale 3-D detailed building frame investigation. This paper proposes a simplified slab modelling approach which can be easily incorporated in the commercial software ABAQUS for 3-D composite buildings frame analysis. The proposed models avoid complicated geometric modelling of metal deck profile and reduce the computational time for analysing large building framework.

2.0 NUMERICAL STUDIES

2.1 Numerical models of composite frame components

2.1.1 Proposed simplified composite slab model

A simplified composite slab model is proposed to avoid complicated geometry modelling of profile composite slab and to reduce the computational time required for analysing 3D large scale framework. Profile metal deck is represented by rebars in longitudinal direction based on equivalent area and second moment of area of the respective web and flange plates of the metal deck. Profile concrete is converted into equivalent uniform concrete section and it is modelled using four-node homogeneous shell element with reduced integration (S4R). Rebar is defined using rebar definition through ABAQUS library.

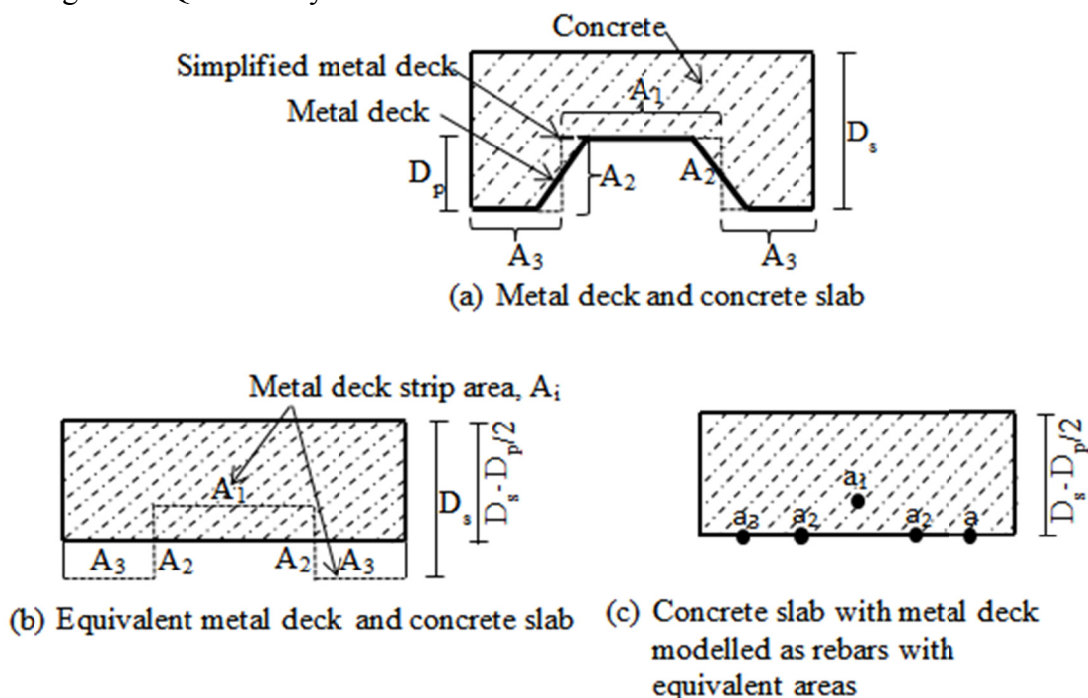


Figure 1. Proposed simplified model for composite slab

The proposed simplified model for composite slab is shown in Figure 1. The profile concrete in the composite slab as shown in Figure 1a is converted into an equivalent concrete slab with uniform thickness, $D_s - D_p/2$, as shown in Figure 1b. Metal deck strip areas A_1 , A_2 and A_3 are calculated by multiplying the deck thickness by its strip length. Then equivalent area of rebar, a_i for each metal deck strip area, A_i is computed by equating their second moment of area (I). Concrete top face is considered here as reference surface to calculate the equivalent area of rebar. The second moment of area of metal deck about its centroid axis is negligibly small due to the smaller metal deck thickness compared to the slab thickness. The rebar area becomes, $a_1 = A_1$, $a_2 = A_2$ and $a_3 = A_3 \times D_s^2 / ((D_s - D_p/2)^2)$. Therefore the profile composite slab shall be converted into equivalent uniform concrete section using the proposed simplified slab model and thus the slab could be model using shell element

and the rebar could be represented by rebar option in ABAQUS. The simplified slab model is proposed based on the assumptions that (1) slip between the concrete and metal deck is neglected. [Izzuddin et al. 2013] suggested that slip between concrete slab and metal deck will not significantly affect the global response of the frame, (2) stiffness of metal deck in the orthogonal direction is negligible and can be ignored, (3) inelastic behaviour of each composite slab element (concrete, metal deck and rebar) can be defined their respective material stress-strain relationship and small error due to the change of depth of bottom deck area A_3 is negligible. This model is different from that used by [Alashker, et al. 2011] who assumed that the rebar area = 50% of metal deck area and that rebar area was defined at the centreline of the slab, and (4) embossment on the metal decking is not taken into consideration in calculating the area and second moment of area of deck.

2.1.2 *Beam and column*

Steel beams and columns are modelled using B31-two-node linear beam elements. Interaction between beam and slab is defined by tie constrain to represent the composite action between the concrete slab and steel beam. Partial composite action, slip between studs and concrete are not considered. Partial interaction in composite beams was found to have negligible effects on the global response of 3-D frames [Izzuddin, et al. 2013]. In addition, local buckling of members is not considered, which can be avoided by using steel sections with at least Class 3 cross section.

2.1.3 *Joints*

A simplified joint model is adopted to reduce the computational cost of 3-D building frame analysis. Composite joint is modelled by a six degree of freedom (DOF) non-linear connector. The connector behaviour is represented by axial force-displacement and moment-rotation relationships. These relationships can be established using Eurocode 3-1-8 and Eurocode 4-1-1 component model approach ([BSEN1993-1-8 2005],[BSEN1994-1-1 2004]). Figure 2 shows that the joint components (Figure 2a) are represented by the simplified joint model in ABAQUS (Figure 2b). As shown in Figure 2a, axial springs are used to represent the joint component for slab under tension, bolt in shear, beam web in bearing and fin-plate in bearing, etc. Eurocode 3-1-8 and Eurocode 4-1-1 component model is used to calculate the stiffness and resistance of each axial spring connector. The connectors in a joint are then assembled using two rigid bars and then analysed using the finite element analysis software, ABAQUS, subject to axial force and moment as shown in Figure 2c. The joint's moment-rotation ($M-\theta$) and axial force-displacement ($F-d$) relationships can be calculated. Finally, these relations are represented by axial and rotational connector in the analysis of the frame with semi-rigid joint, as shown in Figure 2d. The frame analysis assumes zero joint size and neglect the effect of panel zone shear deformation in the beam to column joints ([da Silva et al. 2008]). It is also assumed that the axial force has no significant influence on the moment resistance of joint and axial force moment coupling effect has been ignored due to the

lack of guidance available in the literature. The details of the simplified composite joint model and verification studies are given by [Jeyarajan et al. 2013]. Simplified joint model is shown in Figure 2.

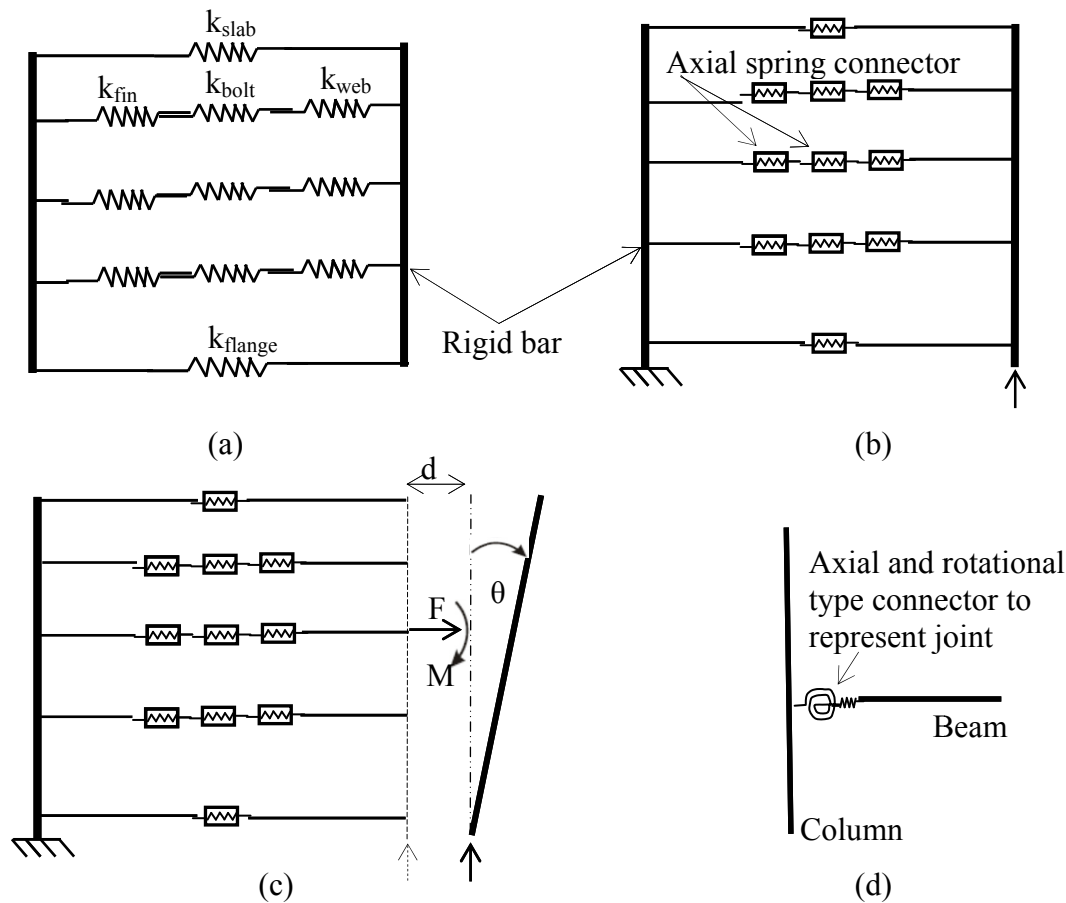


Figure 2. Model for fin-plate joint (a) Eurocode 3 component model (b) ABAQUS model (c) force deformation relationship of joint (d) joint representation in frame analysis

2.2 Verification studies

2.2.1 Numerical study of composite slab bending test

Composite slab tested by [Easterling and Abdullah 2009] is referred to verify the proposed simplified composite slab model. Schematic test model is shown in Figure 3. Material properties and test detail shall be found in [Easterling and Abdullah 2009].

Numerical results are summarized in Figures 4 to 6. ABAQUS explicit dynamic analysis is used to predict composite slab response. Load is slowly applied by means of smooth amplitude function to ensure a quasi-static loading using dynamic explicit procedure. Different loading rates have tried and the reasonable loading rate is chosen. Dynamic fluctuation of the load displacement curve is still

observed in the ABAQUS analysis. There is considerable deviation in the numerical result compared the experimental results. Accumulation of error is due to the simplification in the proposed slab model and usage of Eurocode 2 (EC2) concrete model instead of given data. Material definition adopted in the reference literature is rather difficult. Therefore concrete damage plasticity model is used to define both compression and tensile behaviour of concrete at once in ABAQUS. On the other hand detailed modelling of non-linear behaviour of composite slab is rather tedious and involved other structural components including interaction between steel deck/rebar and concrete slab. A full non-linear analysis requires much computational time to capture the non-linear interaction between concrete slab and steel components. The proposed slab model avoids complex geometric modelling of metal deck profile and requires less computational time for analysing large building framework. Overall, proposed slab model is reasonably predicting the complex composite slab behaviour.

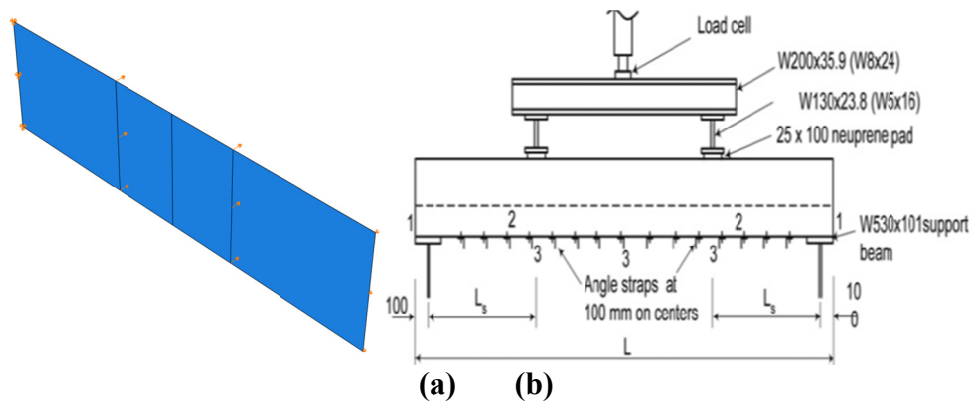


Figure 3. (a) Simplified slab model in ABAQUS CAE (b) test setup [Easterling and Abdullah 2009]

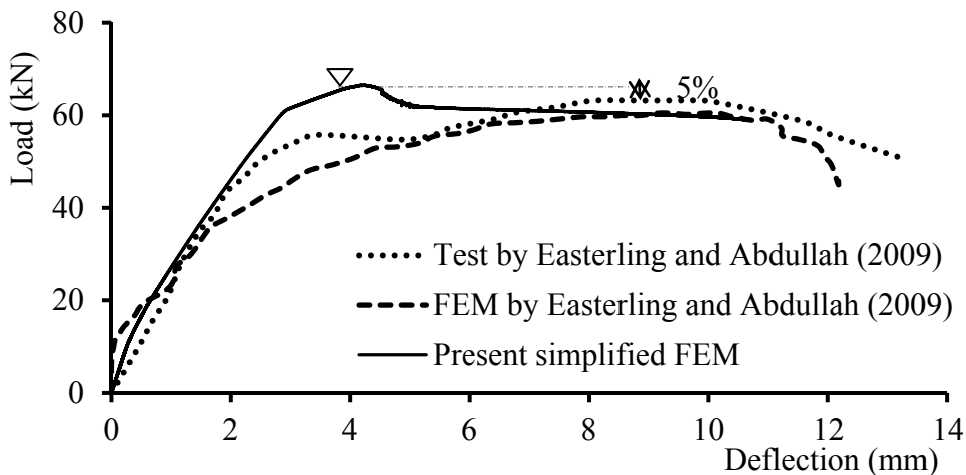


Figure 4. Load-mid span deflection for specimen S5

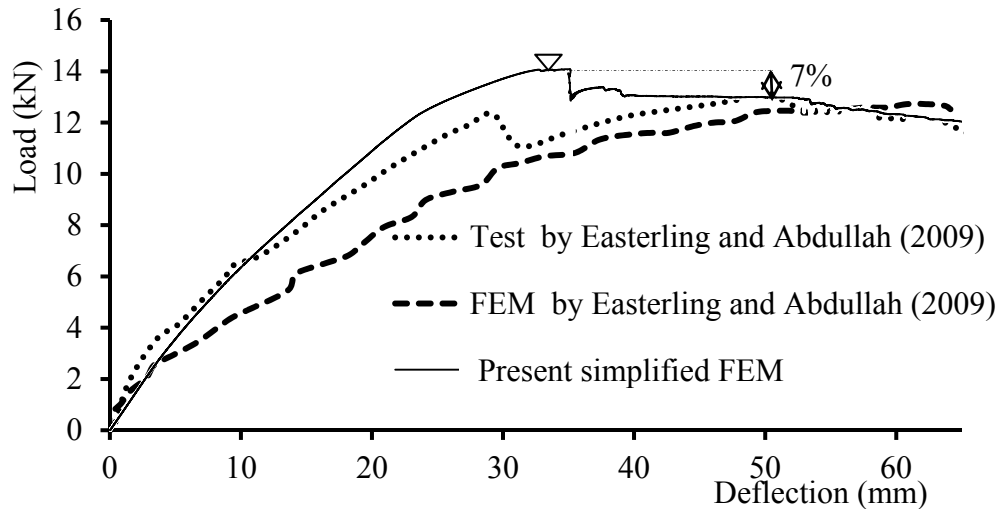


Figure 5. Load-mid span deflection for specimen S8

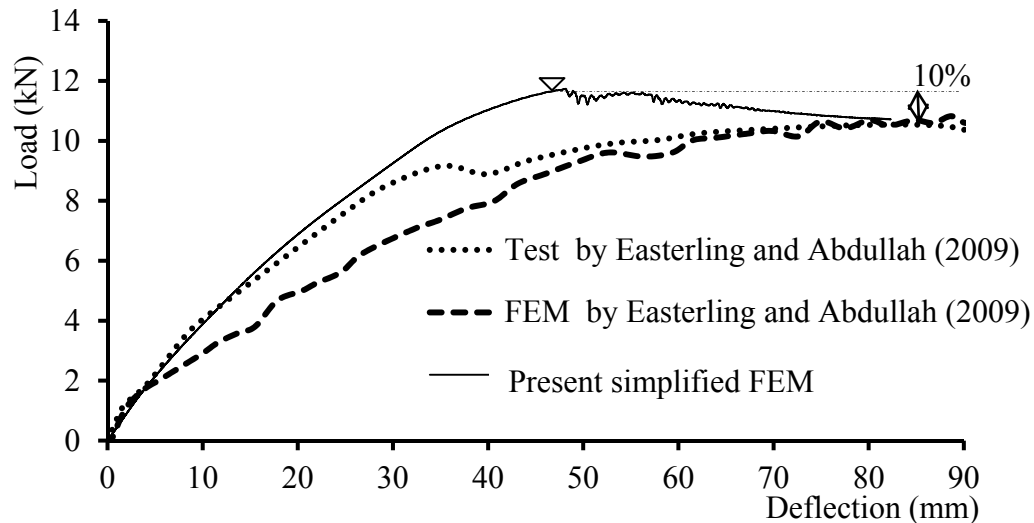


Figure 6. Load-mid span deflection for specimen S9

2.2.2 Numerical study of composite beam behaviour under flexural load

Tests carried out on composite beam by [Ranzi et al. 2009] are referred to for the numerical study of composite beam response under flexural load. 130 mm thick, 2000 mm wide composite slab is connected with 8050mm length Australian standard 360UB44 beam (CB1) and 410UB54 beam (CB2). One stud is welded in each trough for CB1 and two studs are welded in each trough for CB2. Studs are of 19 mm diameter and, after welding, have a height of 115 mm above the steel deck. Beam CB1 is tested at a concrete age of 20 days, and reloaded at 27 days. CB2 is tested at a concrete age of 22 days. Schematic detail is shown in Figure 7. The beams are tested by applying 16 point loads, which is represented with strip line load in numerical model. Material properties and test detail shall be found in [Ranzi, et al. 2009].

Numerical results are summarized in Figures 8 and 9. In detailed model, (1) profiled deck embossment is avoided (2) studs are simplified as wire element and

embedded into the concrete, which leads to avoid the slip between stud and surrounding concrete (3) head of the stud is not modelled. Even though there is significant deviation, overall behaviour is predicted reasonably. Proposed slab model is preferred to incorporate in the 3D building analysis since the proposed model avoids complex geometric modelling of metal deck profile and reduce the computational time for analysing large building framework.

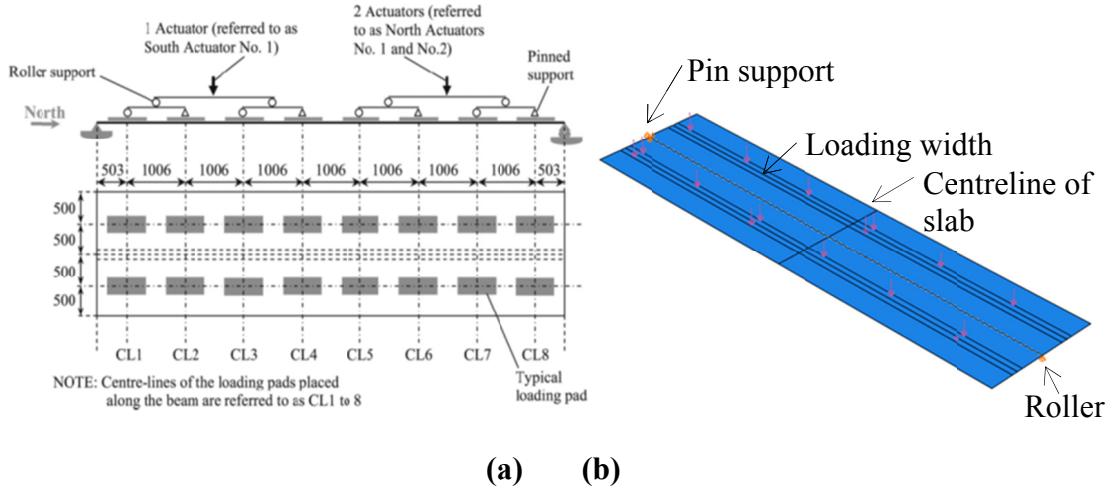


Figure 7. (a) Test setup [Ranzi, et al. 2009](b) simplified slab model in ABAQUS

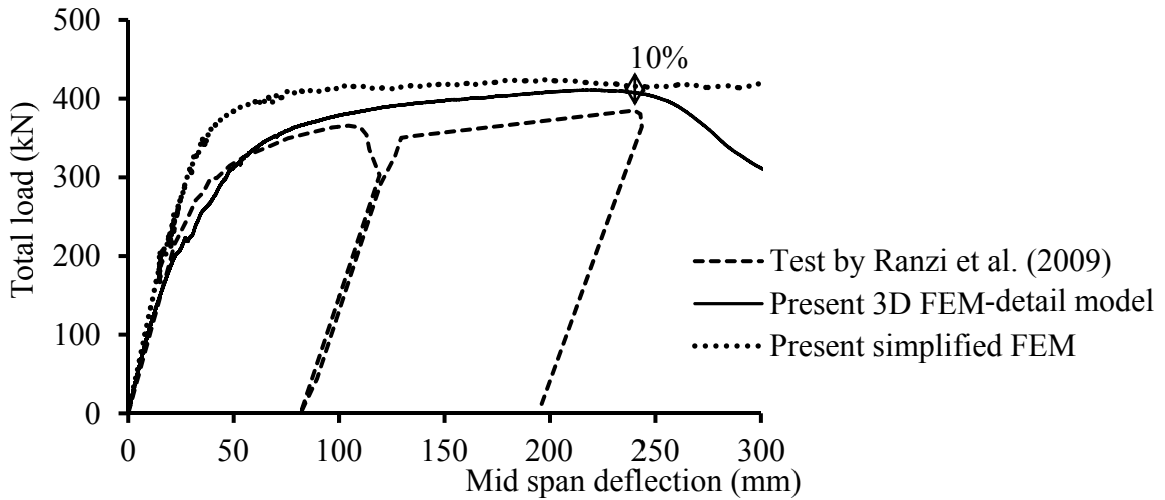


Figure 8. Total applied load – mid span deflection of beam CB1

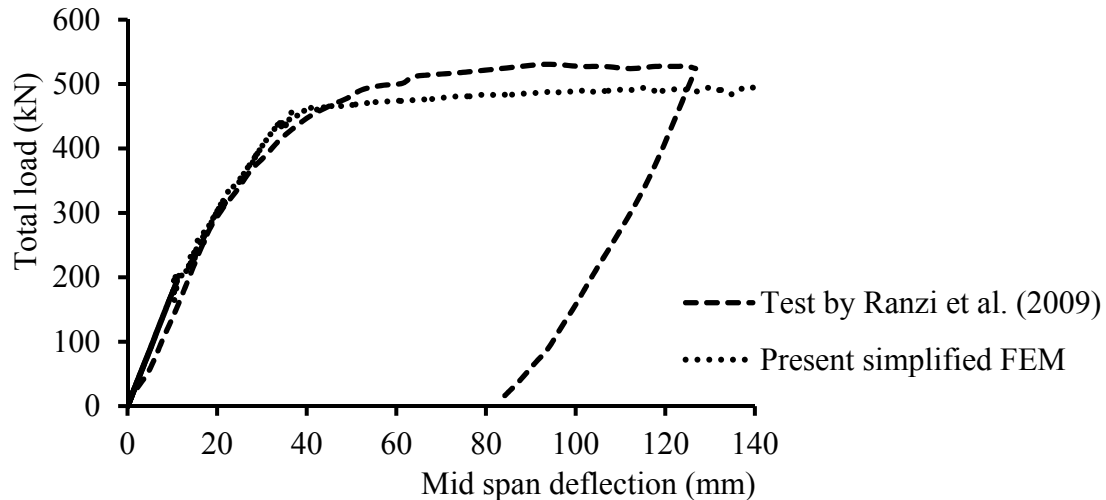


Figure 9. Total applied load – mid span deflection of beam CB2

2.2.3 Numerical studies of composite frame response under column loss

Progressive collapse analysis on nine-storey steel moment-resisting frame by [Marjanishvili and Agnew 2006] is referred for the numerical study using alternate path approach. Based on the simplified numerical modelling approaches mentioned above, nine-storey steel moment-resisting skeleton building frame is validated numerically against similar work done by [Marjanishvili and Agnew 2006] using commercially available software ABAQUS. Nine-storey building frame is shown in Figure 10. Linear static (LS), linear dynamic (LD) and non-linear dynamic (ND) analyses are performed using General Services Administration progressive collapse guidelines [GSA 2003]. One ground floor primary column support is instantly removed to simulate the column loss scenario. Frame consist six bays in the longitudinal direction at 8.25m space and three in the transverse direction at 9.75m space. Main girders are W21 x 57 and secondary beams are W16x31. Floor-to-floor height is 4.3 m. Ground to the 5th floor columns are W14x159 and 6th floor to roof are W14x 90. Live load of 1.9kPa and dead load due to the self-weight of 90mm uniform concrete slab are applied. Perimeter wall weight of 19.7kN/m at every floor, except roof level is allowed. All the secondary beams are pin–pin connected with main beams. Perimeter frames and internal main frames are moment resistant frames. Material properties shall be found in [Marjanishvili and Agnew 2006].

Then (1) uniform thickness of 90mm slab (RC) (2) 120mm comflor60 deck is added in skeleton model to study the slab contribution in progressive collapse design. RC slab is reinforced with nominal bottom reinforcement of R6@ 300 c/c both-way with cover of 25mm. LS, LD and ND analysis are performed with instantaneous gravity load application and instantaneous column removal cases for progressive collapse analysis. Moment frame maximum beam deflections are summarized in Tables 1 and 2. Maximum deflection of frame is occurred at the column removed location. Different mesh sizes are taken into consideration and uniform mesh size of 450mm is reported in this paper. Result shows that instantaneous gravity load application is conservative dynamic effect representation than the member removal

scenario. Ground floor column removal is simulated by removing its support at step 2 in ABAQUS. Step 1 is used to load the structure gradually and maintain the load to represent the service life of the building.

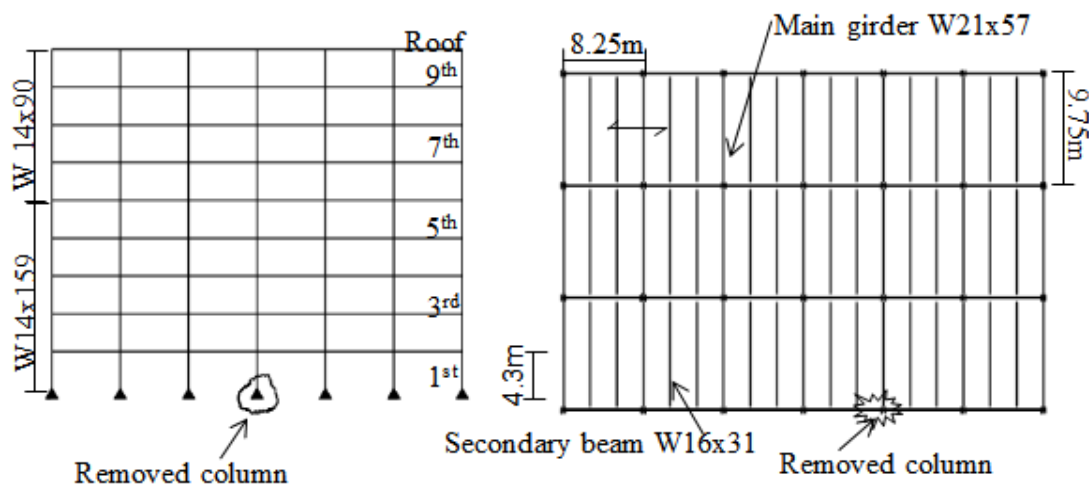


Figure 10. Elevation and plan view of the building frame

Table 1. Slab contribution on deflections for moment frame perimeter column removal

	Deflecti on_skele ton frame (mm)	Deflection_ frame with 90mm slab (mm)	Deflection_ frame with 120mm comflor60 (mm)	Slab contribution for 90mm slab (%)	Remarks
LS	166.8	82.1	75.5	50.78	
LD	188.6	-	-	-	Instant load
	162.8	65.8	59.6	59.58	Support removal
ND	286.7	-	-	-	Instant load
	225.3	78.1	70.2	65.34	Support removal

Table 2. Slab contribution on deflections for moment frame corner column removal

	Deflection_ skeleton frame (mm)	Deflection_ frame with 90mm slab (mm)	Slab contribution (%)	Remarks
LS	249.8	120.4	51.80	Support removal
LD	227.6	98.3	56.81	Support removal
ND	308.3	120.9	60.78	Support removal

Then diagonal braces (CHS 200x8mm) are added at two corners of the above mentioned frame. All joints are considered as pin to study the simple braced frame

response under instant column loss. One ground floor perimeter and corner column supports are instantly removed once at a time to simulate the ground floor column loss scenario. Schematic views of simple braced frame are shown in Figure 11. Maximum beam deflections of simple braced frames are summarized in Tables 3 and 4. Frame deflection-time relationship for perimeter column (PC) and corner column (CC) loss are shown in Figures 12 to 15.

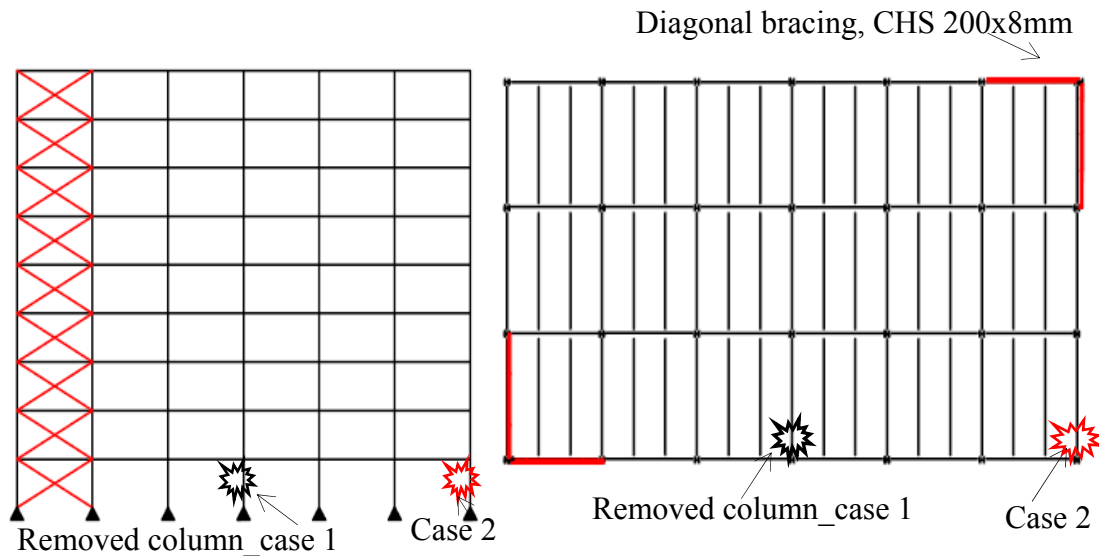


Figure 11. Elevations and plan view of simple braced frame

Table 3. Maximum deflection of simple braced frame due to perimeter column removal

	Skeleton frame	Deflection _ 90mm slab (mm)	Deflection_ comflor60 (mm)
LS	Collapsed	402.3	384.7
LD	Collapsed	379.4	359.3
ND	Collapsed	482.7	440

Table 4. Maximum deflection of simple braced frame due to corner column removal

	Skeleton frame	Deflection _ frame with 90mm slab
LS	Collapsed	1427.4
LD	Collapsed	1274.4
ND	Collapsed	Collapsed

Numerical results show that the simple braced frame deflections are much higher than the moment frame deflection. [Marjanishvili and Agnew 2006] assumed that the joints were not failed (fixed joint and pin joint). Even though frame is not collapsed for such large deformations, concrete strain exceeds the limit of 0.0031 for

all above cases in braced frame. Plastic strain of concrete is monitored at each step to predict the failure since failure criteria is not defined in this verification study. However it is ease to define the failure criteria in ABAQUS. Local buckling of beam and column are not considered in the simplified numerical model. It could be avoided by choosing the steel section within Class-3 cross section. Results show that loss of a column in simple braced frame may cause to severe damage on building or may cause to catastrophic progressive collapse. The use of skeleton frame in the progressive collapse (or large deflection) analysis should be avoided. Because skeleton frame model does not provide the real scenario in term of forces and deflection compared to the frame with slab model. Slab reduces the frame deflection as much as 50% compared to the skeleton frame and thus slab contributes favourably to resist progressive collapse. Results clearly show that loss of corner column in a building is critical than the loss of a perimeter column.

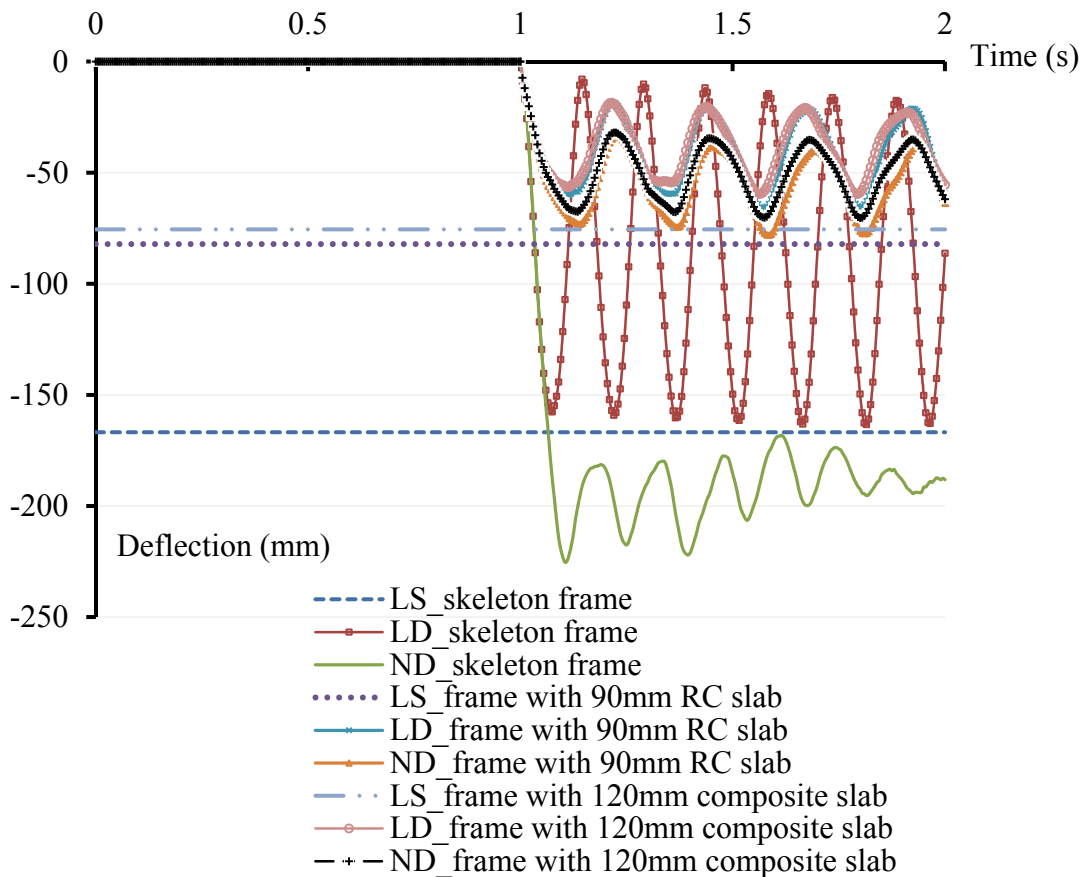


Figure 12. Moment frame deflections for perimeter column removal

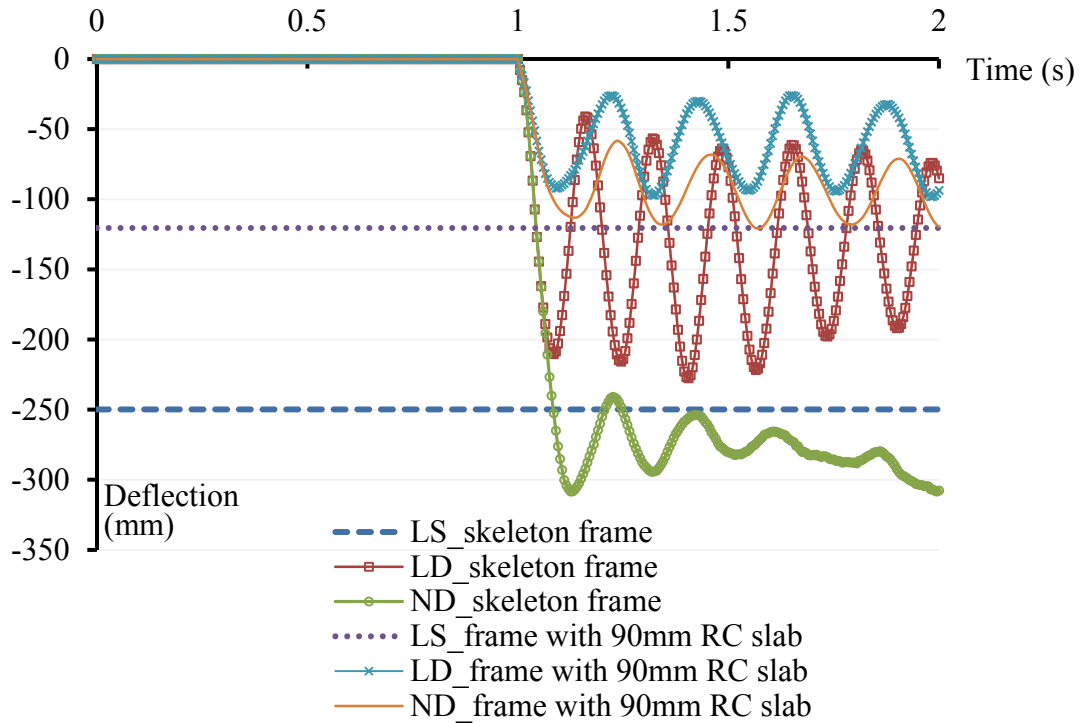


Figure 13. Moment frame deflections for corner column removal

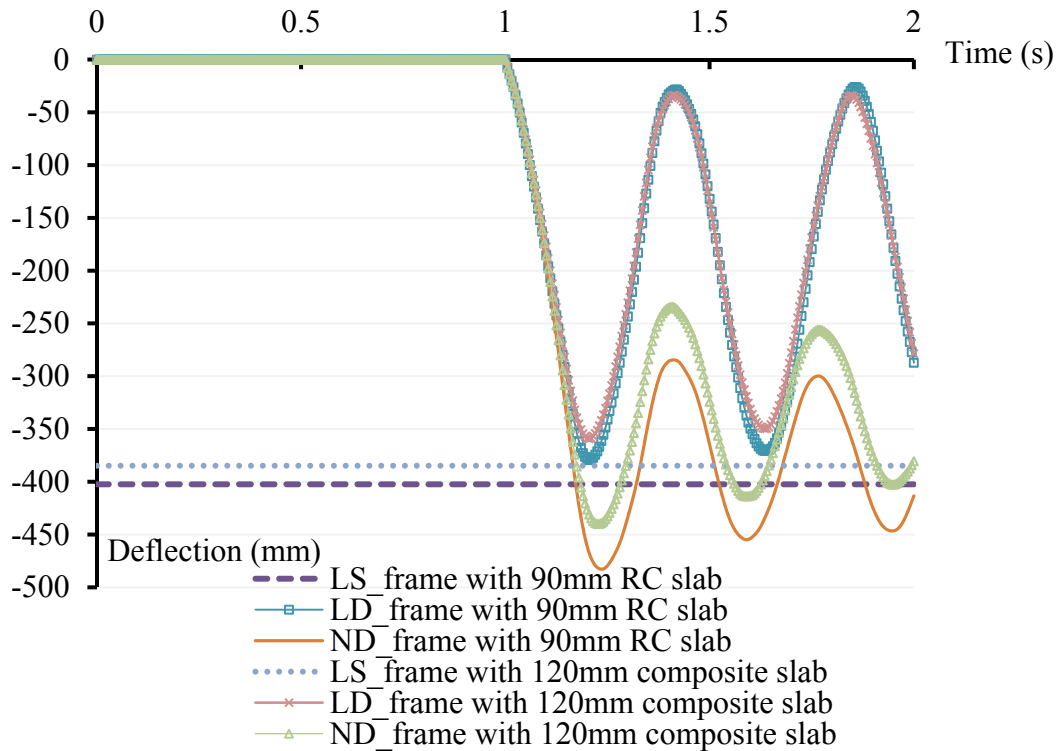


Figure 14. Braced frame deflections for perimeter column removal

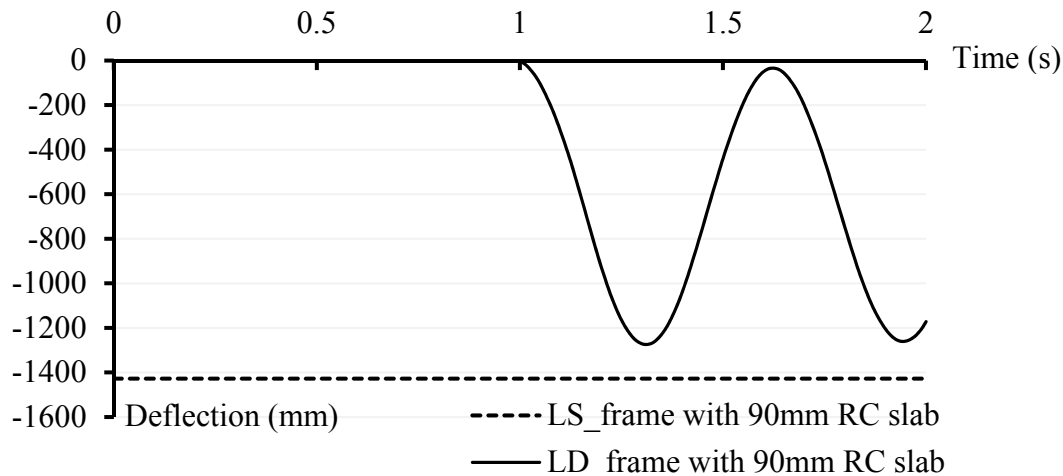


Figure 15. Braced frame deflections for corner column removal

3.0 CONCLUSIONS

A simplified composite slab model and a composite semi-rigid joint model based on Eurocodes using non-linear connector have been proposed to analyse 3D composite building frame. The proposed slab model avoids complex geometric modelling of metal deck profile and improves the computational time for analysing large building frame. Inclusion of the simplified slab model in the analysis of composite building frame is relatively simple. It predicts the building frame responses accurately compared to the skeleton frame model. Also slab reduces the beam deflection as much as 50% compared to the skeleton frame in the progressive collapse alternate load path analysis. Therefore presence of slab contributes favourably to resisting progressive collapse. Analysis results show that simple braced frame with simple joints (pin) are susceptible to progressive collapse compared to the moment resisting frame, which has higher redundancy to re-distribute the load. The use of skeleton frame in the progressive collapse (or large deflection) analysis should be avoided. Because skeleton frame model does not provide the real scenario in term of forces and deflection compared to the frame with slab model. Loss of corner column in a building is critical than the loss of a perimeter column due to the floor slab influence.

The proposed joint model also will avoid detailed finite element modelling of joint components and leads to overall improvement in computational efficiency of analysing large building frames. The incorporation of semi-rigid joint model in 3D frame analysis tends to produce more realistic estimate of frame behaviour compare to model using pin or rigid joints.

REFERENCES

- Alashker, Y., Li, H. and El-Tawil, S. 2011. "Approximations in Progressive Collapse Modeling". *Journal of Structural Engineering* 137, 914-924.
- BSEN1993-1-8 2005. Eurocode 3: Design of steel structures. In *Part 1-8: Design of joints* European Committee for Standardization.

- BSEN1994-1-1 2004. Eurocode 4: Design of composite steel and concrete structures. In *Part 1-1: General rules and rules for buildings* European Committee for Standardization.
- da Silva, J.G.S., de Lima, L.R.O., da S. Vellasco, P.C.G., de Andrade, S.A.L. and de Castro, R.A. 2008. "Nonlinear dynamic analysis of steel portal frames with semi-rigid connections". *Engineering Structures* 30, 2566-2579.
- Easterling, W.S. and Abdullah, R. 2009. "New evaluation and modeling procedure for horizontal shear bond in composite slabs". *Journal of Constructional Steel Research* 65, 891-899.
- Fu, F. 2009. "Progressive collapse analysis of high-rise building with 3-D finite element modeling method". *Journal of Constructional Steel Research* 65, 1269-1278.
- GSA 2003. GSA Guidelines for Progressive Collapse Analysis U.S. General Services Administration, USA.
- Izzuddin, B.A., Jahromi, H.Z. and Vlassis, A.G. 2013. "Modelling approaches for robustness assessment of multi-storey steel-composite buildings". *Engineering Structures* 51, 278-294.
- Jeyarajan, S., Liew, J.Y.R. and Koh, C.G. 2013. Modelling of semi rigid joint in composite frames. In *Composite Construction VII*, Queensland, Australia.
- Kwasniewsk, L. 2010. "Nonlinear dynamic simulations of progressive collapse for a multistory building". *Engineering Structures* 32, 1223-1235.
- Marjanishvili, S. and Agnew, E. 2006. "Comparison of various procedures for progressive collapse analysis". *Journal of Performance of Constructed Facilities-ASCE* 20, 365-374.
- Ranzi, G., Bradford, M.A., Ansourian, P., Filonov, A., Rasmussen, K.J.R., Hogan, T.J. and Uy, B. 2009. "Full-scale tests on composite steel-concrete beams with steel trapezoidal decking". *Journal of Constructional Steel Research* 65, 1490-1506.
- Sadek, F., EI-Tawil, S. and Lew, H.S. 2008. "Robustness of Composite Floor Systems with Shear Connections". *Journal of Structural Engineering* 134, 1717-1725.

Resource-Efficient Design of Components for Office Buildings in Steel Composite Construction

Richard Stroetmann and Christine Podgorski

Prof. Dr., Technische Universität Dresden, Dresden 01062, Germany. E-mail: stahlbau@tu-dresden.de

Abstract

The issue of sustainability is becoming increasingly important in all industries. Above all, the construction industry is affected by a high use of materials and a large amount of waste. Therefore, a large contribution to sustainability can be already made by a specific choice of designs and materials in the design phase of buildings. Within the scope of the German FOSTA research project P881 “Sustainable office buildings in steel composite construction” recommendations and planning tools for slabs and columns in consideration of structural and technical as well as economic and ecological requirements will be created. In this paper, the requirement profiles of floor systems are given. After an introduction to the environmental and economic performance, the possibilities of an environmentally compliant design for structural components are discussed. This includes the optimisation of static, ecological, and economical aspects. Furthermore, concepts for the increase of resource efficiency are demonstrated.

1 INTRODUCTION

The demographic change and the growing awareness of sustainability are examples of changing social conditions, which affect the user requirements of office buildings. Resource conservation, recyclability, life cycle costs and conservation of value, even under changing property conditions, are increasingly the focus of planning.

From the very first, the structural system of the building is of great importance. Column positions and stiffening walls determine the spatial possibilities and allow different flexibility of the floor layout, or restrict it. Besides their static function, the structural system often adopts other functions. For example, it serves as a thermal mass accumulator in order to generate a more comfortable climate. Based on the requirements and the presetting of the building and its structural design, media lines for air conditioning as well as electricity, telecommunications and water supplies are integrated into the building design and the necessary adjustments are conducted [Stroetmann et al. 2014].

2 REQUIREMENTS FOR STRUCTURAL SYSTEMS

Diverse technical and formation requirements for the structural system arise from the geometry and the different functions of an office building. Therefore, for

example, column grids, technical building services and design demands of underground parking, conference rooms and offices differ from each other. For the appearance of foyers and conference rooms, the shape of a ceiling or the design of a column and its surface are very important.

Taking into account different usage scenarios over the life cycle of a building, appropriate attention to the structural system and the finishes are to be provided (e.g. the use of flexible partition systems) to allow changes of use with low-order conversion and short interruptions.

From the requirements of the building and the specifications for the facade and column grids, the conditions and design parameters for the structural system arise such as the spans of slabs and beams, floor-to-floor heights, live and additional dead loads, arrangements for fire protection, the design of components and spaces for services. For this purpose, suitable construction systems and components as well as design principles should be selected with sustainability in mind.

3 FLOOR SYSTEMS

For office buildings, steel-concrete composite structures are used in many technologically highly-developed countries, particularly in inner-city locations. Advantages of this construction type are, amongst others, the high degree of prefabrication, the low-weight construction conditions, the rational economic construction, and the extensive independence of the weather conditions. According to the structural design of the floor systems, there is a distinction of two basic design principles: floor systems with downstand beams as composite beams and slim-floor-systems with integrated floor beams (Figure 1).

At low-to-medium spans (grid up to approximately 11 x 8 m), the use of slim floors with integrated steel beams is possible. Advantages of this construction type are low construction heights and installation freedom. This has a positive effect on the floor-to-floor heights and thus also on the facades and the volume of the building that has to be heated.

For larger spans downstand beams are suitable, which allow for a free floor layout. Common lengths for secondary beams are between 6 and 15 m, for primary beams 6 to 12 m. Therefore, it is possible to span over established widths of offices buildings (double sequence systems) without columns. The spacing of the secondary beam determines the span of the slab, which is often between 2.5 and 4.0 m. Rolled and welded I-sections are used as floor beams. The slab is made of in-situ concrete, precast concrete with concrete infill as well as half precast concrete or profiled sheeting with structural concrete topping. The latter option has the advantage that the profiled sheetings replace the formwork and they can be considered as reinforcement if the geometry is appropriate and end anchorage is used. Furthermore, the profiled sheetings can be placed by hand due to the low weight and be used to attach suspended ceilings and service distribution.

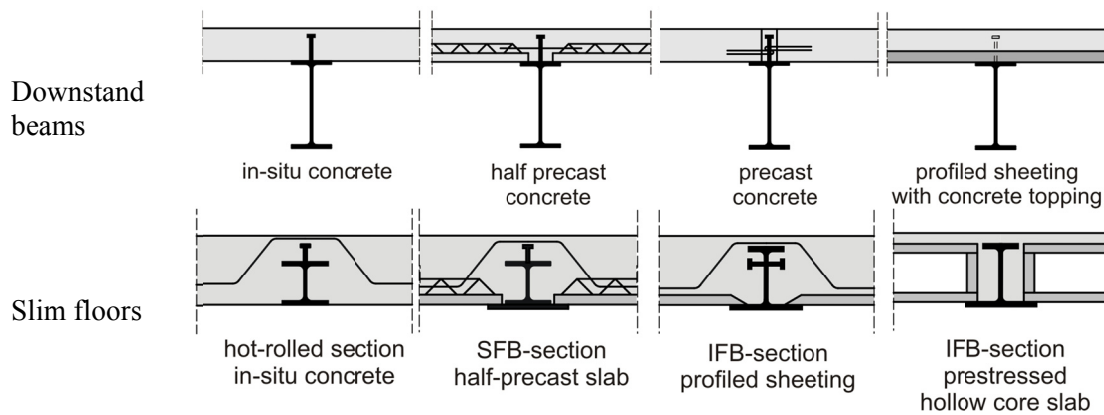


Figure 1. Downstand and slim floor beams with different slab types

4 SYSTEM SELECTION AND REQUIREMENTS FOR STRUCTURAL DESIGN

Depending on the choice of placing inner columns or not, preferred variants for floor systems can be derived. Besides the free span, further criteria for the selection of the system are the construction height (from which the floor-to-floor height depends), demands for services and the design of the floor soffit.

Figure 2 shows a floor plan with different variants for the arrangement of columns and beams. The first floor panel (left) shows the column-free span in transverse direction of the building with composite beams being supported by each facade column. If the supports are located at a greater distance, edge beams are needed that brace the beam (second floor panel). The same applies if an inner row of columns is placed (panel 3 and 4). The positioning of these supports is generally asymmetric with the axis of the partition walls at the central corridor if, for example, conventional cellular offices are arranged. The shorter spans allow the economic use of slim-floor systems. To limit deformations and crack widths in the concrete slabs, to increase the modal masses of vibrating elements (due to human-induced vibrations) and to optimize the use of materials, the floor beams and downstand beams are implemented as continuous beams. This is possible with moderate effort by the arrangement of supporting reinforcement in the structural concrete topping and contact pieces for carrying the compressive force into the bottom flange of the composite beam.

For floor systems and columns the load bearing capacity and serviceability needs to be proved. Within the scope of project P881 the checks are based on Eurocodes EN 1990 to EN 1994. For the ultimate limit state the resistance of the section, stability (buckling of columns and lateral torsional buckling of beams, as far as necessary), shear connection and the transferring of the shear force needs to be verified. The serviceability limit state considers the deflection and crack control as well as the restriction of human-induced vibrations.

To increase the material efficiency, the use of higher strength steel is recommended. With increasing slenderness of the components the effect of deformations and vibrations increases. Eurocode 3 and 4 do not specify according limits.

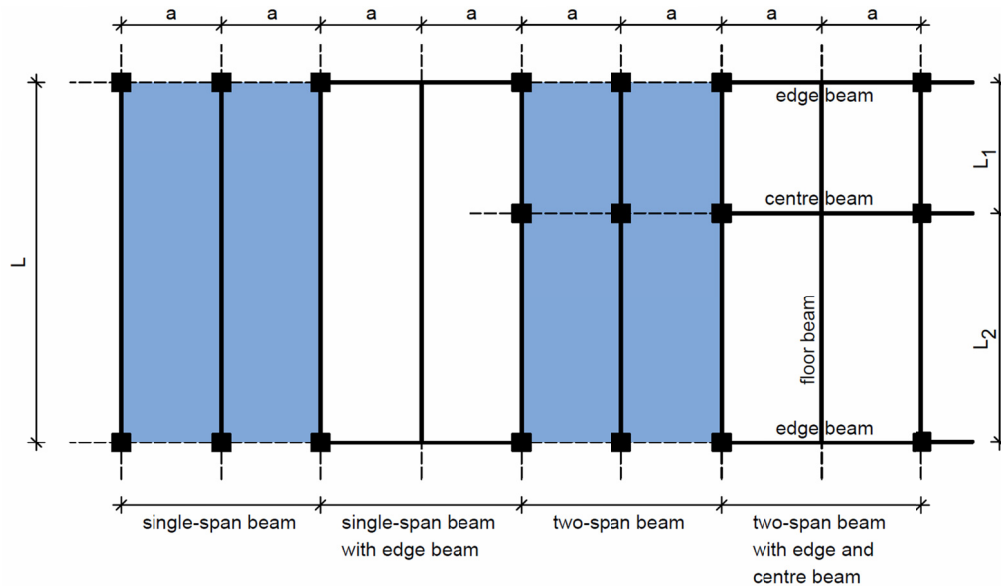


Figure 2. Configuration of downstand beams as single and two-span beams

In Eurocode 2, recommended values are given for the deflection limit of beams, slabs and cantilevers. Concerning the following parametric studies, a deflection limit of $1/250$ of the span is used and installation of services after 28 days is assumed. The deformations of the composite beams are determined assuming that the weight of the slab is carried by the steel beam. If necessary, the steel beam is cambered for the loads resulting from self-weight and services, 30 % of the live load, as well as for the deformation part caused by shrinkage and creep.

Besides the deflections, the vibration behaviour is analysed. Vibrations in office and administrative buildings are caused by people walking. The vibration behaviour can become the controlling load case if the ratio between stiffness and mass distribution is low and the system has only a slight damping [Maier 2005]. The OS-RMS method from [HIVOSS 2008] provides a design guide, which is used to establish a criterion for acceptable vibrations for the convenience of the user and for the prediction of human-induced floor vibrations, taking into account the use of the building. Using the dynamic properties of the floor, such as natural frequency, modal mass and damping, the OS-RMS value (OS=One Step, RMS=Root Mean Square) is determined. In determining damping, building materials, use, and services are considered.

5 ASSESSMENT OF SUSTAINABILITY

5.1 GENERAL

In the context of the current AIF research project P881 environmental, economic and socio-cultural and functional properties of office buildings will be investigated and tools for a sustainable design will be developed. With the social criteria, needs of the various stakeholders (users, owners, etc.) are considered. These include efficient workplaces as well as functionality and design of the building. With the help of scenario analysis for future uses, changing requirements are considered in

the design process of office buildings. Furthermore, tools are developed for the economic assessment of flexibility based on the life cycle.

Based on the grids of the building, the floor layout, and the floor-to-floor heights from a previous design process, a quantitative comparison of construction systems can be made, not only in consideration of functional properties, but also of the environmental and economic performance.

5.2 ENVIRONMENTAL PERFORMANCE

The environmental performance of a building, construction systems, or components is evaluated by the life cycle assessment (LCA). This method helps to identify the opportunities to improve and develop materials, products, construction methods, and building structures. EN ISO 14040 [2009] describes the principles and framework of LCA, EN ISO 14044 [2010] contains requirements and guidelines for generating the LCA. The LCA studies involve four phases; see [EN ISO 14044, 2010]. In the first phase of the study, the scope including the system boundaries and the level of detail is defined. The definitions depend on the subject and the intended use of the study. The second stage is the life cycle inventory analysis phase (LCI), in which all input and output data regarding the system being studied are summed up. It involves the data, which are necessary to meet the goals of the study. The third phase is the life cycle impact assessment (LCIA) with the purpose to provide additional information for the valuation and assessment of the results of the LCI and its environmental significance. LCA data with similar environmental impact are combined to impact categories.

LCA studies involve four phases; see [EN ISO 14044, 2010]. In the first phase of the study, the scope including the system boundaries and the level of detail is defined. The definitions depend on the subject and the intended use of the study. The second stage is the life cycle inventory analysis phase (LCI), in which all input and output data regarding the system being studied are summed up. It involves the data, which are necessary to meet the goals of the study. The third phase is the life cycle impact assessment (LCIA) with the purpose to provide additional information for the valuation and assessment of the results of the LCI and its environmental significance. LCA data with similar environmental impact are combined to impact categories.

Table 1 contains impact categories provided by the “Assessment System for Sustainable Building” [BNB 2011] which are currently used for the environmental performance of office buildings. In the fourth phase, the results of phase 2 and 3 are summarised as a base for conclusions, recommendations, decisions and evaluations. Based on LCI and LCIA, auxiliary variables are used, such as the ecological quality of BNB [2011] and DGNB [2012], in which the weighted environmental impacts are summarised. The procedure is not scientifically justified and is not intended in EN ISO 14044. The data collection of each criterion is about the life cycle of a building (Figure 3). This includes the product stage, construction process, use and end of life stage as well as the benefits and loads from reuse, recovery and recycling at end of the life cycle.

Table 1. Criteria of environmental performance und factors of relevance [BNB 2011]

Ecological Quality	Criteria	max. Points	Factors of Relevance
Effects on Global and Local Environment	Global Warming Potential (GWP)	100	3
	Ozone Depletion Potential (ODP)	100	1
	Photochemical Ozone Creation Potential (POCP)	100	1
	Acidification Potential (AP)	100	1
	Eutrophication Potential (EP)	100	1
	Risks to the Local Environment	100	3
	Sustainable Logging / Wood	100	1
Demand of Resources	Primary Energy Demand Not Renewable (PE_{nre})	100	3
	Total Primary Demand (PE_{tot}) and Amount of (PE_{re})	100+50	2
	Fresh Water Demand and Quantity of Wastewater	100	2
	Demand of Space	100	2

The environmental indicators for various building materials and products are provided in databases (e. g. [Oekobau.dat 2013]) and environmental product declarations (EPD). However, in general only the data of the product stage as well as the benefits and loads at the end of the life cycle are collected. The information of the remaining modules is not yet available. An estimate is partly possible by calculating the construction management processes.

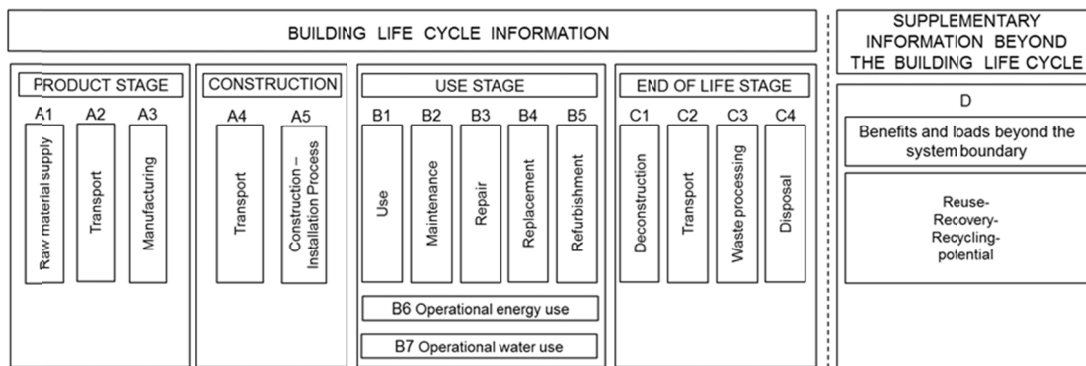


Figure 3. Stages of the building life cycle according to EN 15978

Table 2. Selected ecological indicators for various construction materials

Materials	PE_{tot} [MJ/kg]	GWP [kg CO ₂ -eqv./kg]	Life Cycle Modules	Source
Concrete C30/37	0.573	0.091	A, B1, C1-C3, D	Ökobau.dat 2013
Reinforcement	12.35	0.764	A1-A3, D	Ökobau.dat 2013
Profile steel	11.52	0.776	A1-A3, D	EPD BFS 2013
Profiled sheeting	18.34	1.00	A1-A3, C4, D	IFBS 2013
Prestressed hollow core slab	1.496	0.159	A1-A3, C1, D	BRESPA 2013

In Table 2, the Total Primary Energy Demand and the Global Warming Potential for 1 kg of the respective construction material are listed and compared with the specification of the life cycle modules. For Western European quality steels an EPD was created, which considers the strength classes S235 to S960 in the integral over the produced tonnage of the participating companies and their ecological impact. Currently, ecological indicators for concrete are available for the concrete grades from C20/25 to C50/60 according to EN 1992-1-1 [EC 2 2011]. The used EPD for prestressed hollow core concrete slabs [BRESPA 2013] considers concrete grade C45/55. With increasing concrete grade, the effects on the global environment and the demand of resources increase. This results from higher cement content and higher cement strength classes. In addition to the used masses, the transport distances of the construction products and the impacts of crane hours for installation of the construction elements need to be considered.

In the assessment systems for office buildings of BNB and DGNB reference values are used for the impact analysis (LCIA). Relating to this, target and limit values are defined. Hence, a grading by points is possible. Subsequently, the ecological indicators are weighted by relevance factors to summarise them to a degree of fulfilment for the ecological quality. For a comparative assessment for the optimisation of construction components and systems, it is necessary to determine target and limit values for relevant solutions. With this, the quality of each solution can be classified. By using factors of relevance, the degree of fulfilment can be defined subsequently in accordance with BNB and DGNB. The approach is shown in Figure 4 in the context of research project P881.

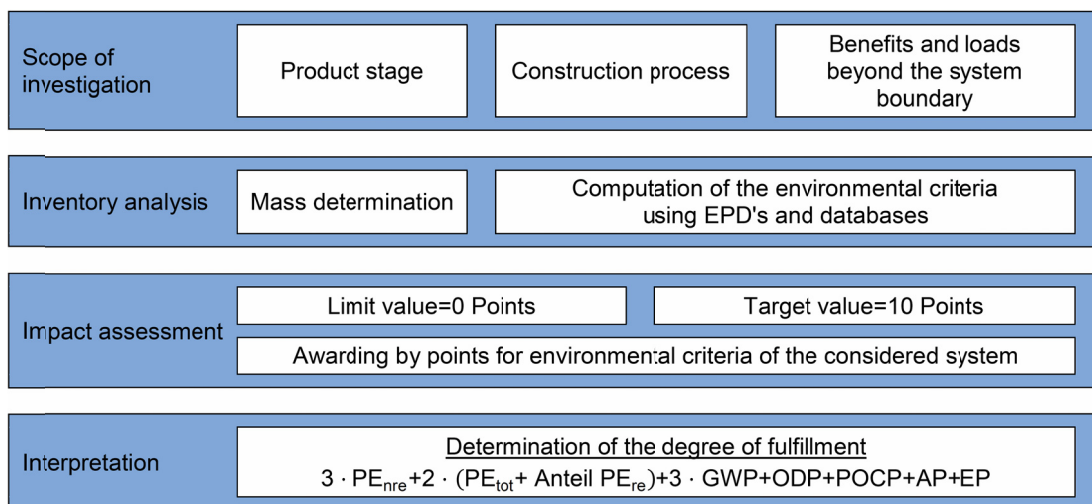


Figure 4. LCA in context of the research project P881

5.3 ECONOMIC PERFORMANCE

The economic performance contains the building-related life cycle costs (LCC, costs for construction, operating, maintenance, replacement, revenues and recycling) as well as the value stability of the building. For the evaluation and comparison of columns and floor systems in office buildings, the material, manufacturing,

construction, maintenance, and disposal costs are considered in project P881. Possible effects on the cost of facade, services, operating, and earthworks are not investigated. Prices of building materials, performance values for production, construction, and wages are liable to undergo regional, temporal, and economic fluctuations.

Table 3 shows a compilation of prices and work processes that have been summarized on the basis of research and experience of construction companies in Germany. The performance values highly depend on the training of the personnel. For example, the performance value of laying profiled sheeting's amounts, depending on experience of the staff, between 0.4 and 0.6 h/m². In the following chapters the costs are presented as relation values in percent. Thus, absolute changes in material costs and performance values are avoided in the representation, so that the significance remains for same ratio values.

The manufacturing costs can be reduced by resource-efficient design of the structure. In many cases, material savings for steel structures can be achieved through increases in strength. The moderate price differences to normal-strength steels can often be offset by corresponding reductions in mass [Stroetmann 2011]. The lower transport and erection weight, as well as the welded volumes in the shop fabrication, also has a positive impact on construction time. Costs for provision of building site facilities reduce and the building can be used earlier. Recurring component dimensions and connecting constructions also support the rapid construction progress.

Table 3. Material prices and working processes

Materials		Prices	Additional processes
Concrete	C20/25	113 €/m ³	Casting
	C25/30	116 €/m ³	
	C30/37	121 €/m ³	
Reinforcement		580 €/t	Laying
Profile steel (basic price)	S235	600 €/t	Cutting, corrosion protection, welding, cambering, drilling, laying
	S355	635 €/t	
	S460	685 €/t	
Studs		2 €/item	Welding
Profiled sheeting		15 €/m ²	Laying, fixing
Half-precast slab (h=50 mm)		7.5 €/m ²	Laying by crane
Precast slab		68-115 €/m ²	Laying by crane
Prestressed hollow core slab		50-70 €/m ²	Laying by crane
Formwork		2.03 €/m ²	Positioning
Supports		4.25 €/item	Positioning

6 SUSTAINABLE EXAMINATION OF FLOOR SYSTEMS

6.1 GENERAL

In the following paragraphs, the optimisation of floor systems is presented and explained for selected examples and criteria. In consideration of the previous explanations, the constructions are investigated according to the ecological and economic performance.

6.2 CONCRETE SLAB AND PROFILED SHEETINGS

Figure 5 shows the results of the investigation for in-situ concrete and profile sheeted slabs. Static systems are calculated as continuous beams with spans of 2.40 m to 8.40 m in increments of 1.20 m. For design, the concrete grades C20/25 and C30/37 as well as the profile sheeting Cofrastra 40 t=0.75 mm are considered [Deutsches Institut für Bautechnik 2007]. The graphs on the left are showing that, as expected, the slab thickness and the mass of concrete and reinforcement increase with the span. The minimum height of 100 mm is decisive for profiled sheeting slabs to a span of approximately 3.60 m. Due to the advantageous inner lever arm, the construction height and the mass of concrete are lower in comparison to the reinforced concrete slabs. The reinforcement in profiled sheeting slabs is required to cover the hogging moment and as structural reinforcement for transverse load distribution and crack control. The profiled sheeting is considered as bottom reinforcement, formwork and support during construction. To limit the deflection during construction to 1/180 of the span, supports are used.

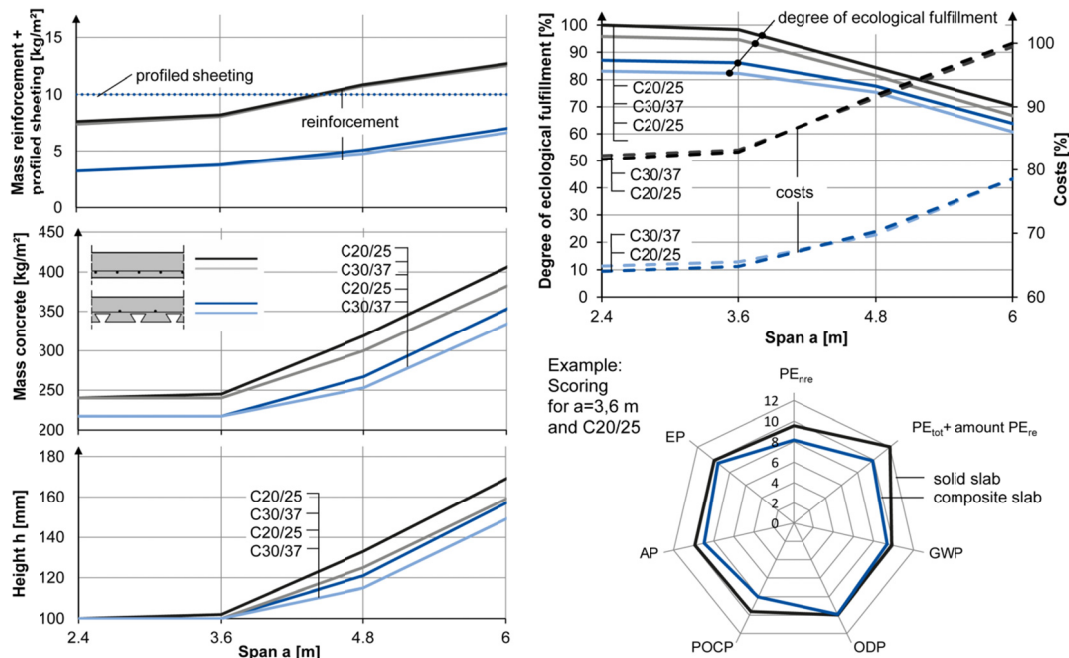


Figure 5. Comparison of in-situ concrete and profiled sheeting slabs for continuous beams with a load of 3 kN/m² for different concrete grades

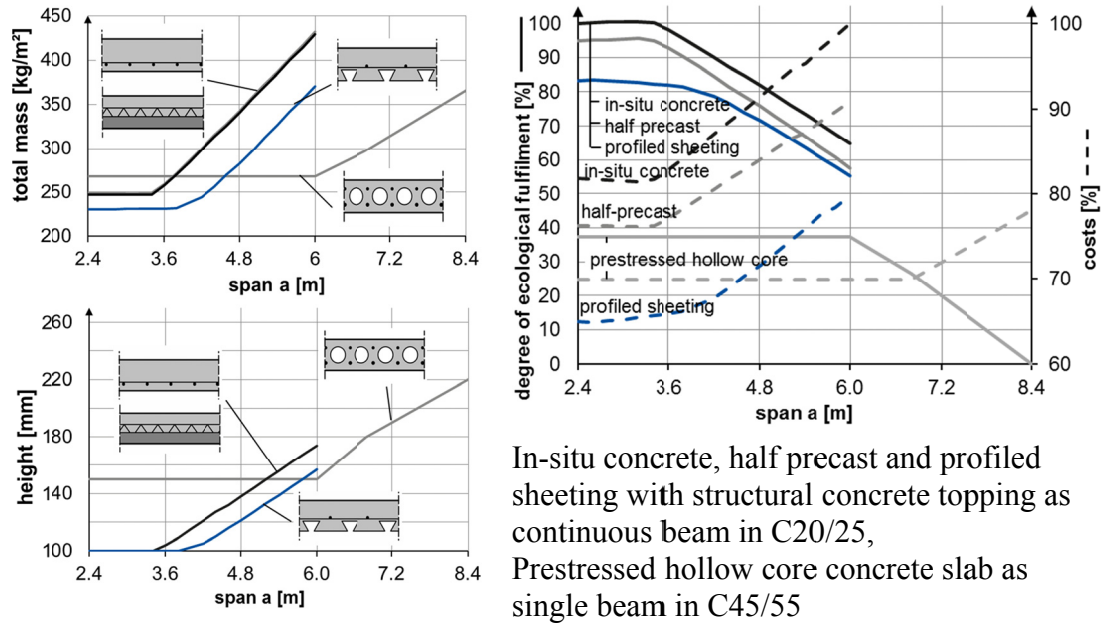


Figure 6. Comparison of different slab types according to degree of ecological fulfillment and costs

The reinforced concrete slabs induce slightly better results according to the LCA in Figure 5. Although their slab thickness is higher than for profiled sheeting slabs, the savings in concrete and reinforcement are compensated by the ecological input and output data of the galvanised profiled sheeting. Due to lack of ecological data, the formwork is not considered for reinforced concrete slabs. In environmental terms both slab types are almost equivalent. Despite the reduction in slab thickness by using higher concrete grades, the material savings are compensated due to the disadvantageous ecological data of C30/37 in comparison to C20/25. This conclusion does not apply to shorter spans (Figure 5). The costs of materials and processes for formwork and supports are considered. The savings of the formwork and the rapid construction of profiled sheeting slabs is significant (Figure 5).

In practice, instead of in-situ concrete slabs, half precast or precast slabs are used because the effort of formwork on the construction site is reduced to a minimum. Due to transport, installation and loads of placing concrete a higher ratio of reinforcement is necessary. According to the environmental performance the half precast slab is to prefer, in comparison to profiled sheeting slab, for spans higher than 4.80 m (see Figure 6).

As mentioned in paragraph 3, prestressed hollow core concrete slabs are used only for large spans (approx. 6 to 12 m). This corresponds to the mass balance, the environmental and economic performance. According to the data of the environmental product declaration [BRESPA 2013] prestressed hollow core slabs are classified disadvantageous in comparison the other considered floor systems.

6.3 COMPOSITE FLOOR WITH DOWNSTAND BEAM

The analyses in the previous paragraph ensue that spans up to 4 m are favourable with regard to ecology and economy. The consequence for the floor system is that the steel beams are arranged in a narrow grid. In Figure 7 the construction height and the total mass (slab and beam) are assessed for various distances of the beam and building depth as well as for in-situ concrete and profiled sheeting slabs. The composite beams are calculated as two span beams with a column at 4.80 m (corresponding to the room depth of a cellular office). Therefore, two unequal spans L_1 and L_2 ensue. With increasing distance of the beams, the construction height, the total mass and the masses of the reinforcement are increasing, while the mass of the steel profile per square metre decreases. For the grids of 2.4 m and 3.6 m the total mass is almost equal because of the identical slab thickness and the dominant mass of concrete.

In Figure 7, the ecological degree of fulfilment and the costs for composite floor systems with various distances of beams are presented. From the charts, it is clear that the slightly higher mass for a beam distance of 3.6 m in comparison to 2.4 m can be compensated, and this is the favourable option according to the environmental performance. For the determination of costs, cutting, corrosion protection, and installation of the steel profile are considered. These costs increase with the increasing number of steel beams (=small distance of beams) so that higher material costs are compensated for the steel profile. In paragraph 6.2 it was determined that the material savings for slabs with higher concrete grades, due to higher cement strength classes and content, do not have a positive effect in ecological terms. The same is true for higher concrete grades for composite beams. However, the mass of rolled steel can be reduced by the use of higher strength steels if the ultimate limit state is decisive for dimensioning.

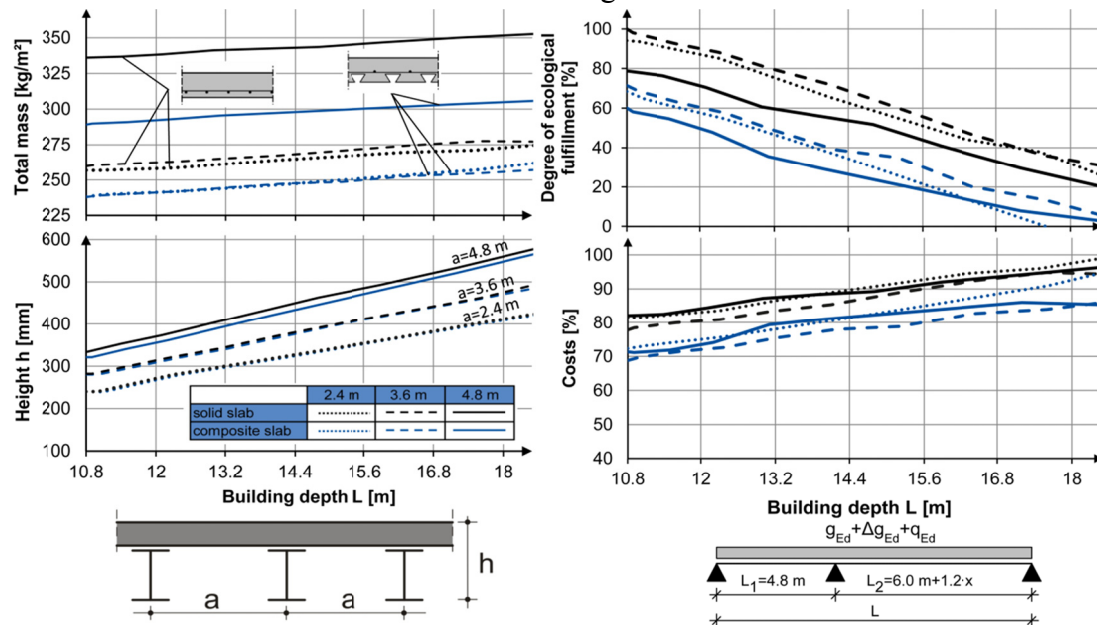


Figure 7. Comparison of masses, construction height, ecological performance and costs for composite floors for various distances of the beams (S355) and different slab types

From Figure 8, it is apparent that the material savings attained by using S460 in comparison to S235 have a positive effect on the ecological performance and costs. The influence of the deflection check on the dimensioning of the composite floor can be reduced or even become insignificant if advantageous continuous beams, instead of single span beams, are designed and/or if the beams are cambered for dead loads or, if needed, for a percentage of the live loads. In the calculation of the relevant deformations for the facade or partitions, the time of the installation of these elements is of importance because of the creep and shrinkage. Only the parts are relevant that occur after the installation.

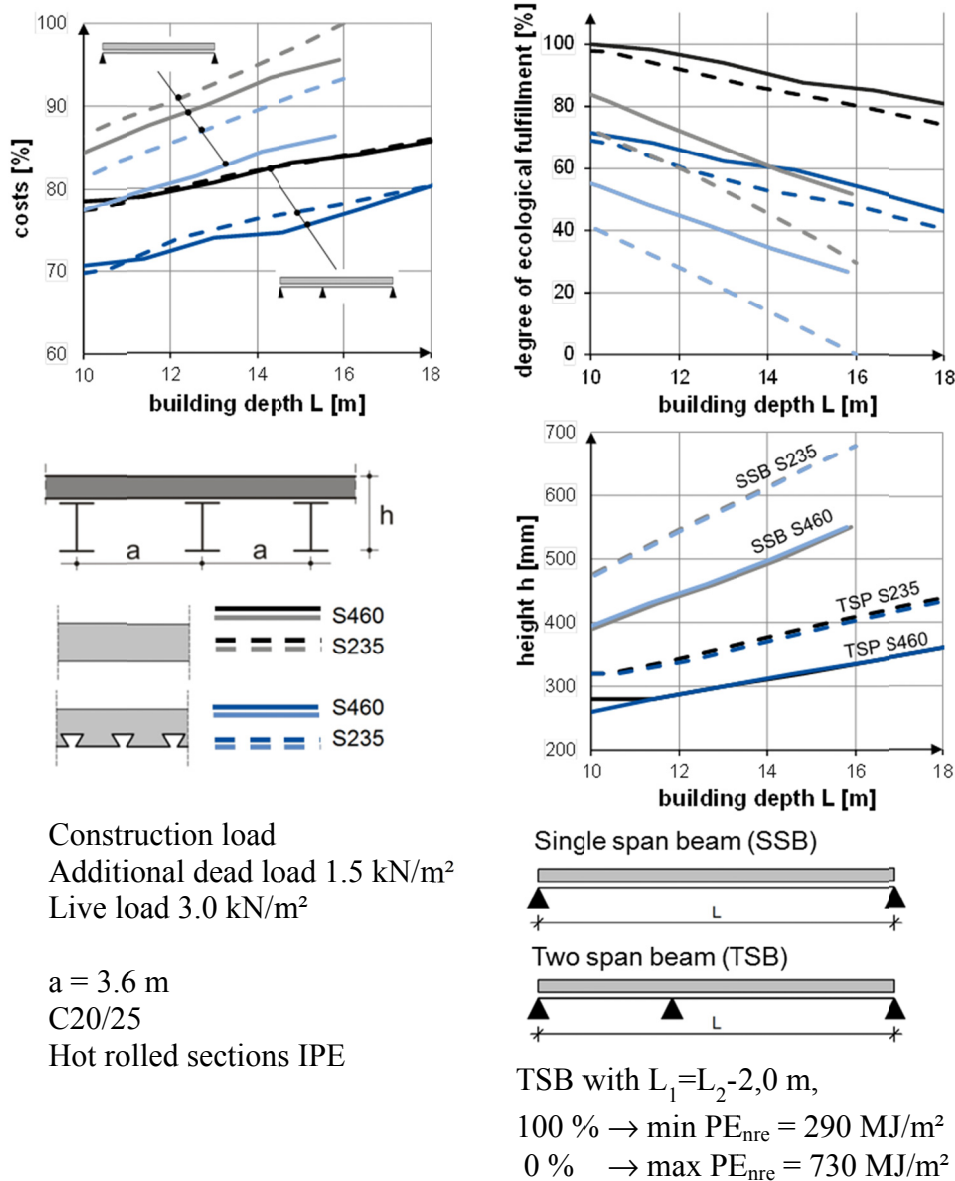


Figure 8. Composite beams as single- and two-span beam in S235 and S460

Another possibility is the selection of the steel section and the use of welded sections. These allow optimising the proportions (height, area, plate thickness) of the cross section. The production costs of welded sections are generally higher than for rolled sections. In case of recurring grids and a large number of beams, the additional labour can be reduced significantly through mass production and automation of processes (e.g. automatic welding machine for connecting webs with flanges), so that the effort can be worthwhile for appropriate projects.

7 CONCLUDING REMARKS

Resource-efficient construction begins in the early design phase. Elementary decisions are made with regard to building floor plans, column grids and floor-to-floor heights. In the life cycle of the office buildings changes in use through changing office organisation forms (size of usage units, position of partition walls, vertical development, fire compartment), changing services and further influences can be important for the assessment of sustainability. Besides the effort of conversion, the time of non-use, temporary relocation of the users and the resulting economic consequences as well as the conservation of value and the ability to bring the building to the market are of importance. Not least, the ergonomics of an office building are significant for the productivity of the people working in the building. However, this is difficult to quantify.

The sustainability of office buildings in steel and steel composite constructions is the subject of the FOSTA research project P881, which will be completed at the end of 2014. The results are provided, besides the project report, in the form of a planning guide and a software tool for sustainable planning [Stroetmann et al. 2014].

8 REFERENCES

- Arcelor Mittal, „Bemessungshilfe zum Nachweis von Deckenschwingungen“, www.arcelormittal.com/sections.
- Assessment System for Sustainable Buildings (BNB) (2011). „Bewertungssystem Nachhaltiges Bauen (BNB) 2011_1: Gewichtung und Bedeutungsfaktoren“, www.nachhaltigesbauen.de.
- BRESPA – Decken (2013). DGNB-Navigator – Produktdatenblatt <http://www.dw-systembau.de>.
- Deutsches Institut für Bautechnik (2007). „Allgemeine bauaufsichtliche Zulassung – COFRASTRA Verbunddecken“, Antragsteller Arcelor Mittal Construction Deutschland.
- Eisele, J. , Staniek, B. (2005). „Bürobau Atlas“, Verlag Georg D.W. Callwey GmbH & Co. KG, Darmstadt.
- EN 1991-1-1 (2010). Eurocode 1: Actions on structures – Part 1-1: General actions - Densities, self-weight, imposed loads for buildings.
- EN 1992-1-1 (2011). Eurocode 2: Design of concrete structures – Part 1-1: General rules and rules for buildings.
- EN ISO 14040 (2009). Environmental management – Life cycle assessment – Principles and framework.

- EN ISO 14044 (2010). Environmental management – Life cycle assessment – Requirements and guidelines.
- EPD-BFS-20130094-IBG1-DE (2013). „Umwelt-Produktdeklaration – Baustähle: Offene Walzprofile und Grobbleche“, Institut für Bauen und Umwelt e.V., bauforumstahl.
- EPD-IFBS (2013). „Umwelt-Produktdeklaration – Profiltafeln aus Stahl für Dach-, Wand- und Deckenkonstruktionen“, Institut Bauen und Umwelt e.V.
- German Sustainable Building Council (DGNB) (2012). „Neubau Büro- und Verwaltungsgebäude“, *Handbuch für nachhaltiges Bauen*.
- Maier, C. (2005). „Großversuch zum Einfluss nichttragender Ausbauelemente auf das Schwingungsverhalten weitgespannter Verbundträgerdecken“, Eigenverlag FG Statik und Dynamik der TU Darmstadt, Darmstadt.
- Ökobau.dat (2013), <http://www.nachhaltigesbauen.de/oekobaudat/>.
- RWTH Aachen et al. (2008). „Human induced Vibrations of Steel Structures (HIVOSS), Schwingungsbemessung von Decken – Leitfaden“.
- Stroetmann, R. (2011). „High strength steel for improvement of sustainability“, Eurosteel 2011, August 31 – September 2, Budapest, Hungary.
- Stroetmann R., Mensinger M., Eisele, J., Feldmann, M., Linghan, V., Zink, K., Podgorski, C., Huang, L., Trautmann, B., Pyschny, D., Kokot, K., Baudach, T. (2014). Ganzheitliche Planung nachhaltiger Bürogebäude in Stahl- und Stahlverbundbauweise: *Stahlbau* 83, Heft 7, Verlag Ernst & Sohn, pp 429 – 440.

FE Modelling of Sustainable Semi-Rigid Flush End Plate Composite Joints with Deconstructable Bolted Shear Connectors

A. Ataei¹ and M. A. Bradford²

Centre for Infrastructure Engineering and Safety, School of Civil and Environmental Engineering, Univ. of New South Wales, Sydney, NSW 2052, Australia. E-mail: a.ataei@unsw.edu.au¹; m.bradford@unsw.edu.au²

Abstract

Composite construction is a popular and effective method of construction, exploiting the strengths of both reinforced concrete and structural steel in building construction in a complementary fashion. Within paradigms related to minimisation of emissions and maximisation of product recycling, these composite systems are problematic on a number of fronts. Firstly, common and traditional composite systems utilise ordinary portland cement, which is known to be a very large contributor to atmospheric CO₂ emissions. Secondly, for typical construction practices for steel-concrete composite systems, casting of the concrete onto profiled steel decking and conventional reinforcement placing are undertaken on-site, which is time consuming and labour intensive, and which can increase the cost of construction. Thirdly, composite action between the steel beam and the concrete slab is usually achieved by using headed shear studs. The headed shear studs connect these two elements permanently, which leads to much waste at the end of the service life of the building when it is demolished. This paper models a sustainable semi-rigid beam-to-column composite blind bolted connection with deconstructable bolted shear connectors using ABAQUS finite element (FE) software. In this “green” system, precast geopolymer concrete (GPC) slabs are attached compositely to the steel beam via pretensioned bolted shear connectors and the composite beam is connected to GPC-filled square columns using blind bolts. Non-linear material properties and non-linear geometric effects are considered in the simulation of a connection in hogging bending. Based on the FE modelling, using pretensioned bolts as shear connectors with GPC can improve the behaviour of semi-rigid flush end plate composite joints in terms of ductility and load capacity. Moreover, the behaviour of the bolted shear connectors should be considered in composite joint design as being very different to headed stud connectors.

Keywords: Composite connections; FE modelling; Geopolymer concrete; Partial interaction; Blind bolting.

INTRODUCTION

Concrete and structural steel are the two most widely used materials in the construction industry. Whenever these materials are used individually, they are limited by the weaknesses of concrete to resist tensile stresses and by the propensity of structural steel sections to buckle prematurely under compressive stresses. When

they are combined in so-called composite construction, the merits of these two materials can be exploited optimally, and the efficiency of composite construction can be increased significantly where the concrete is utilised appropriately for compression predominantly and the structural steel for tension predominantly.

Ordinary Portland cement (OPC) in concrete, one of the main components of composite members, results in the atmospheric emission of very large amounts of CO₂. Davidovits (1994) pointed out that the production of one tonne of OPC produces approximately one tonne of CO₂, contributing some 65% of anthropogenic CO₂ emissions, and the demand for OPC has been increasing significantly over the years. Moreover, climate changes due to global warming from anthropogenic emissions have become a major concern and several attempts have been conducted to reduce the use of OPC in concrete in many nations.

GPC which commonly utilises fly ash as a by-product of coal-burning power stations as the binder, is a viable replacement for OPC. These concretes are also known to possess small shrinkage deformations as well as having superior durability (Ng 2011). However, it appears that on-site batching and finishing is harder to undertake than that for conventional concretes, and so precast GPC components are ideal a replacement for conventional OPC concretes in composite framed building structures.

Combining precast GPC slabs with steel elements by using a deconstructable shear connection may solve the problems and concerns associated with dismantling and recycling traditional composite structures. Pre-tensioned high strength bolts installed through holes in precast GPC slabs into pre-drilled holes in the steel beam produce a composite flooring system that can be deconstructed at the end of life of the structure (Bradford and Pi 2012a,b, 2013; Rowe and Bradford 2013; Ataei and Bradford 2013; Lee and Bradford 2013). Marshall *et al.* (1971) appear to be the first researchers to have reported the use of bolted shear connection, but the context of the usage is not clear. Twelve push tests using high strength bolts as shear connectors were carried out and reported by Dallam (1968). In these set of tests, the bolts were embedded in the concrete slab and pre-tensioned by the turn-of-nut method after the concrete had aged 28 days. He pointed out that high strength bolts displayed a higher capacity and ultimate strength than stud shear connectors. Six full-scale simply supported composite beams with high-strength bolted shear connectors were tested by Dallam and Harpster (1968). Based on this, they concluded that pre-tensioned high strength bolts provide a very rigid connection between the steel beam and concrete slab at service loads, and a reserve capacity sufficient to develop the ultimate moment capacity of the fully composite section is present. Dedic and Klaiber (1984) conducted several tests on the retrofitting of existing bridge girders by using post-installed high strength bolts under static loading. Hungerford (2004) and Schaap (2004) conducted several direct shear tests to investigate the behaviour of 19 mm diameter post-installed shear connectors. Based on experimental work, Kayir (2006) proposed an equation to predict the ultimate strength of pre-tensioned bolted shear connectors. A series of test was conducted on three types of 22-mm diameter post-installed shear connectors under static and fatigue loading by Kwon *et al.* (2010). It was concluded that bolted shear connectors exhibited significantly higher fatigue strength than stud shear connectors. Five full-scale non-composite beams were

constructed to investigate the retrofitting of the bridge beams by Kwon *et al.* (2011). The reinforced concrete slabs were attached compositely to the steel girder via post-installed connectors in four beams. It was concluded that the strength and stiffness of the non-composite bridge girder can be improved significantly. These studies did not focus on deconstructability and, moreover, no research appears to have been reported on the modelling of sustainable semi-rigid flush end plate composite joints with deconstructable bolted shear connectors.

In order to provide a robust and efficient means for modelling sustainable semi-rigid beam-to-column composite blind bolted connections with deconstructable bolted shear connectors, the present paper presents a three-dimensional modelling using ABAQUS software. The modelling is benchmarked firstly against the extensive testing of connections with blind bolting reported by Loh *et al.* (2006), and then shear stud load-slip relationship data are replaced by the strength and the stiffness characteristics of the pre-tensioned bolted shear connectors determined from push tests conducted by Lee and Bradford (2013). The modelling is shown to provide an efficacious technique for conducting parametric studies, so as to develop design guidance in this novel application in composite construction.

FINITE ELEMENT MODEL

MATERIAL PROPERTIES

For the ABAQUS modelling, the actual stress-strain curves determined by Loh *et al.* (2006) were used for the shear connectors, steel beam, reinforcement, profiled sheeting and blind bolts. The points defining the relationship between the stress and strain of the materials adopted in the FE modelling are given in Table 1.

Table 1(a): Material properties for reinforcement bars.

Strain ($\times 10^3 \mu\epsilon$)	0	3	15	50	110	155
Stress (MPa)	0	600	600	680	680	500

Table 1(b): Material properties for profiled sheeting.

Strain ($\times 10^3 \mu\epsilon$)	0	2.75	60
Stress (MPa)	0	550	550

Table 1(c): Material properties for blind bolts.

Strain ($\times 10^3 \mu\epsilon$)	0	5	40	90	160
Stress (MPa)	0	980	1040	900	580

Table 1(d): Material properties for shear connectors.

Strain ($\times 10^3 \mu\epsilon$)	0	2	50	150	220
Stress (MPa)	0	450	520	500	420

Table 1(e): Material properties for steel beams and columns.

Strain ($\times 10^3 \mu\epsilon$)	0	1.75	13	70	150
Stress (MPa)	0	400	400	485	515

Concrete in compression and tension was represented using the damaged plasticity model in ABAQUS. For concrete in compression, the curve of Carreira

and Chu (1985) was used, for which the stress-strain relationship is linear when the stress is less than $0.35f_c$, and

$$\sigma_c = \frac{f_c \gamma (\varepsilon / \varepsilon_c)}{\gamma - 1 + (\varepsilon / \varepsilon_c)^\gamma} \quad (1)$$

thereafter, in which

$$\gamma = (f_c / 32.4)^3 + 1.55 \quad (2)$$

$\varepsilon_c = 0.002$, f_c is the mean cylinder compressive strength and is in units of MPa. For OPC, the values of the cylinder compressive strength, the Young's modulus and the Poisson's ratio adopted are 17.5 MPa, 21 GPa and 0.2 respectively, while for GPC, the values of the cylinder compressive strength, the Young's modulus and the Poisson's ratio adopted are 40 MPa, 30 GPa and 0.2 respectively.

For concrete in tension, the stress-strain relationship is linear until concrete cracking, after which the concrete is assumed to be perfectly plastic. Ataei and Bradford (2013) pointed out that the post-peak part of the stress-strain relationship for tensile concrete has negligible effect on the moment-rotation response of composite beam-to-column connections. This simplistic model circumvents several difficulties that are encountered in FE modelling of these members and improves the rate of convergence, as vindicated with the close agreement between the numerical model and the tests of Loh *et al.* (2006).

The main modes of failure identified in the analysis of the composite joint were concrete crushing (compressive failure), fracture of the reinforcement, fracture of the stud shear connectors and bolts and local buckling of the beam compression flange. The following criteria were adopted to determine the onset of each failure mode:

- The strain corresponding to onset of concrete crushing (compressive failure) was taken as $\varepsilon_{cu} = 0.005$.
- Fracture of blind bolts occurs at the ultimate strain ($\varepsilon_u = 0.1$) obtained from the tensile test conducted by Loh *et al.* (2006).
- Fracture of the stud shear connectors occurs at the ultimate slip ($s_u = 10$ mm) obtained from the push-out tests conducted by Loh *et al.* (2006) and Tan and Uy (2009).

ELEMENT TYPE

Three-dimensional solid elements were used to model the bare and composite connections. 8-node solid elements with reduced integration (C3D8R) were used to mesh and simulate all components, except for the steel reinforcing bars. These elements lead to more precise and reasonable results and they avoid the shear locking difficulties encountered using other elements such as C3D8I. For the reinforcing bars, a two-node linear truss element (T3D2) was chosen. A typical FE model of a composite joint is shown in Figure 1 (a).

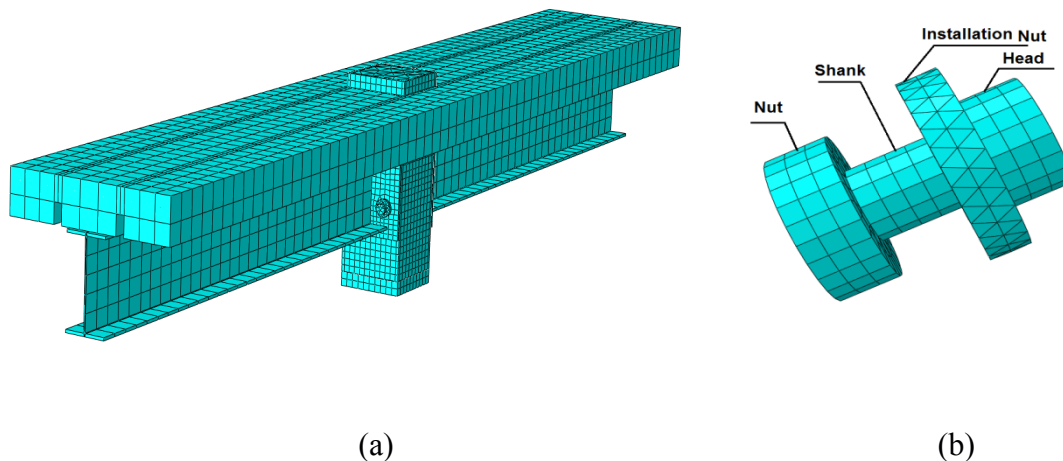


Figure 1: Representation of FE mesh for (a) composite joint (b) bolt.

MODELLING BLIND BOLTS AND SHEAR CONNECTORS

In the present research, the load-slip response obtained from the push tests with GPC slabs was used and converted into a piecewise-linear load-slip relationship for the FE modelling. The shear studs in the tests were replaced by springs and load-slip curves were applied to model the shear stud connectors.

Most previous researchers appear to have modelled blind bolts with axial and shear springs, with the axial and shear forces carried by these springs being defined based on the shear and tensile strengths of the bolts, with the pretension being neglected. ABAQUS provides an option that allows for the pretension being included simply, in which the bolt is divided lengthwise into two, defining a surface on which the pretension is applied. The pretension is then applied in the bolts using the “bolt load” module, and this option was used in the present study. Figure 1 (b) illustrates the meshing of blind bolt. All components were modelled, except the threads on the shank and ledges. The head and nut of the bolts were assumed to connect completely to the shank.

LOAD APPLICATION

The loading was applied in two steps. First, the pretension was applied to the blind bolts and the joints were then loaded, at which state the bolts were subjected to the pretension. Mirza and Uy (2011) have pointed out that Riks’ technique is needed to capture any unloading in the non-linear analysis, and so the GENERAL method and modified RIKS method were used for the first step and second step respectively. A static concentrated load was applied at the centre of the CFST column, as was done in the tests.

In FE modelling, correct representations of the boundary conditions are essential since slightly different boundary conditions can produce significantly

different results. For the simulation in this paper, the boundary conditions were taken as being exactly the same as in the tests, with the column being allowed to move in the vertical direction and with the flanking ends of the beams having roller supports.

CONTACT MODELLING

One of the most important aspects of FE modelling is simulation of the contact interaction between components. There are various materials in composite connections which interact with each other, and the results of the FE analysis depend on the accurate modelling of the contact interaction between these materials. The interactions between these materials were treated in ABAQUS in the following way.

Experiments reported elsewhere show there is no separation between the head of the bolt and the flush end plate in a composite connection, and also between the nut of the bolt and the inner face of the steel column. Therefore, the TIE option was used for connecting these components which leads to their having the same displacements. The TIE option was also used for the steel beam and flush end plate because of the welding of these two components together.

In order to simulate the interaction between the top flange of the steel beam and the lower part of the profiled steel sheeting, surface-to-surface contact interaction with a coefficient of friction of 0.1 was adopted, in which the top flange and the profiled sheeting were considered as master and slave surfaces respectively. The same interaction was used to model the interaction between the profiled sheeting and the lower part of the concrete slab. Because the headed stud connectors are through-welded to the top flange, the TIE option was used.

Modelling the interface between the concrete slab and shear stud connectors is one of the main issues in the FE modelling of the composite beam and joint. As noted earlier, in this research the strength and the stiffness characteristics of the pre-tensioned bolted shear connectors determined from the push tests are used for modelling of the connection between the concrete slab nodes and steel flange nodes, and so an axial connector model was used to model the interface slip. These connectors were located at the same positions where studs were welded or bolts were placed on the specimen. A schematic diagram of the axial connector model is shown in Figure 2. Reinforcement was also embedded into the slab, with the slab being the host region and the bars being an embedded region. This technique connects these two different components and prevents slip between them. Interaction of the concrete and inner faces of the steel tubular column was simulated as a surface-to-surface contact interaction with a coefficient of friction of 0.25.

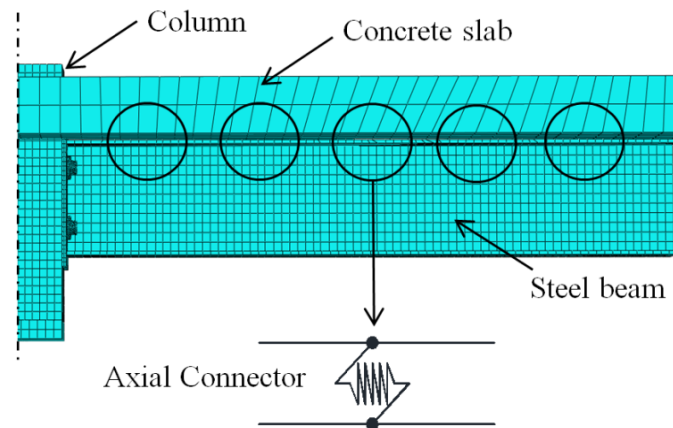


Figure 2: Axial connector model for CJ1

COMPARISON OF TESTS AND FE MODEL

In this research, the test results obtained by Loh *et al.* (2006) were used to validate the FE model. Loh *et al.* (2006) presented a comprehensive set of experiments on composite connections. In this work, one non-composite (SJ6) and five semi-rigid composite beam to column connections (CJ1- CJ5) were tested under symmetric loading, with the composite beams being connected to the tubular columns using blind bolts. Two rows of M20 Grade 8.8 blind bolts attached flush end plates to the columns, and to which the steel beams were connected. Composite action was achieved between the steel beam and concrete slab by stud shear connectors welded through the profiled steel decking. The tests were designed to simulate an internal composite beam-to-column connection typical of a low-rise building system. In the tests, the variables were the degree of shear connection, the shear stud spacing and the area of reinforcement. Tables 2 and 3 summarise the dimensions and components in the experimental programme.

Table 2: Variables in the tests of Loh *et al.* (2006).

	CJ1	CJ2	CJ3	CJ4	CJ5
Reo. bars	4 ϕ 16	4 ϕ 16	4 ϕ 16	2 ϕ 16	6 ϕ 16
Reo. ratio	1.30%	1.30%	1.30%	0.65%	1.90%
a (mm)*	100	140	300	140	100
b (mm)*	265	480	800	480	160

* a = distance of first connector from column face

b = stud spacing

Table 3: Constants in tests of Loh et al. (2006).

Property	Value
Slab thickness (mm)	120
Slab width (mm)	515
Profiled sheeting	Lysaght Bondek
Column	200×200×9
Steel beam	250 UB 25.7
End plate thickness (mm)	10
Blind bolt	Hollow-Bolt M20
Stud shear connectors	19×100 mm

Loh *et al.* (2006) also conducted three push tests to define the load-slip characteristics of shear stud connectors. Fig. 3 (a) shows the results of these tests and a piecewise linear force-slip relationship was used as the force-slip law for the springs. The points defining the relationship between the load and slip of bolted shear connectors adopted in the FE modelling are given in Table 4.

Table 4: Load-slip relationship for stud shear connectors.

Load (kN)	0	100	100	75
Slip (mm)	0	1	7	15

Lee and Bradford (2013) conducted a set of push tests on bolted shear connectors with precast GPC slabs. In this work, five push tests were undertaken to obtain the load-slip characteristics of this new method of connection, where the GPC precast concrete slabs are connected compositely to the steel beam using pretensioned high-strength bolts. Table 5 summarises the dimensions and components of the three push tests of this experimental programme.

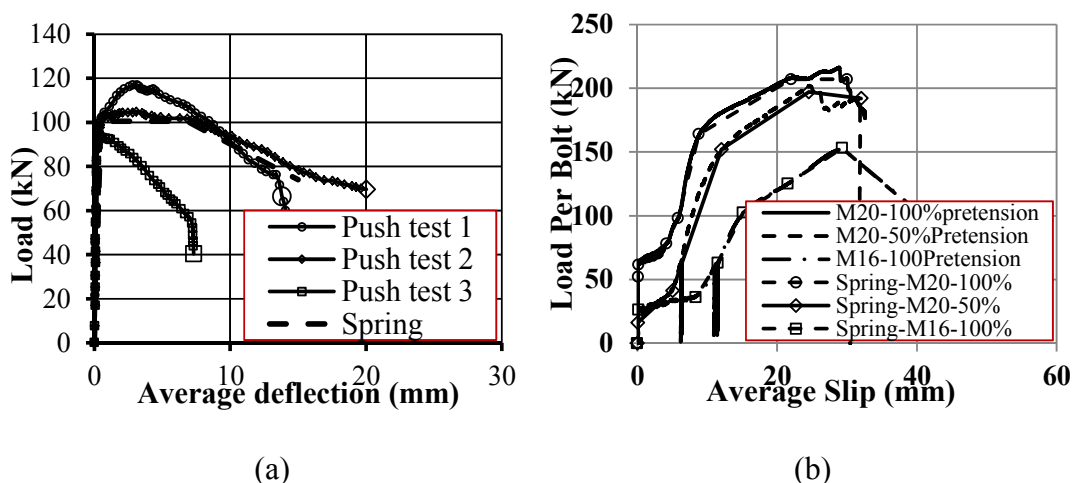


Figure 3: Load-slip relationship for (a) shear stud connectors and spring, (b) Bolted shear connectors and spring.

Table 5: Variables in tests of Lee and Bradford (2013).

	PT1	PT2	PT3
Bolt diameter (mm)	20	20	16
Hole diameter (mm)	24	28	24
GPC Strength (MPa)	40	40	40
Pretension per bolt (kN)	145	80	95
Clearance (mm)	4	4	8

The load-slip relationship for the three push tests is shown in Figure 3 (b). The points defining the relationship between the load and slip of the bolted shear connectors adopted in the FE modelling are given in Table 6.

Table 6(a): Load-slip relationship for bolted shear connectors (M20 bolts with 100% pretension).

Load (kN)	0	52	61	78	98	164	207	207
Slip (mm)	0	0.1	0.2	4.2	5.8	8.8	22	30

Table 6(b): Load-slip relationship for bolted shear connectors (M20 bolts with 50% pretension).

Load (kN)	0	16	41	152	197	192
Slip (mm)	0	0.04	5	12	24.5	32

Table 6(c): Load-slip relationship for bolted shear connectors (M16 bolts with 100% pretension).

Load (kN)	0	26	36	63	102	125	153	97.3
Slip (mm)	0	0.17	8.4	11.5	15	21.5	29.3	41.2

A most important consideration for a FE model is its validation with physical tests. In order to achieve this, the results of the ABAQUS-based FE modelling are compared herein with the experimental results of Loh *et al.* (2006). In this comparison, the load versus deflection response was modelled, and the results are given in Figures 4(a) to 4(e) for the five composite connections tested and in Figure 4(f) for the connection with a bare steel beam. It can be seen that the agreement is very good for much of the range of the response.

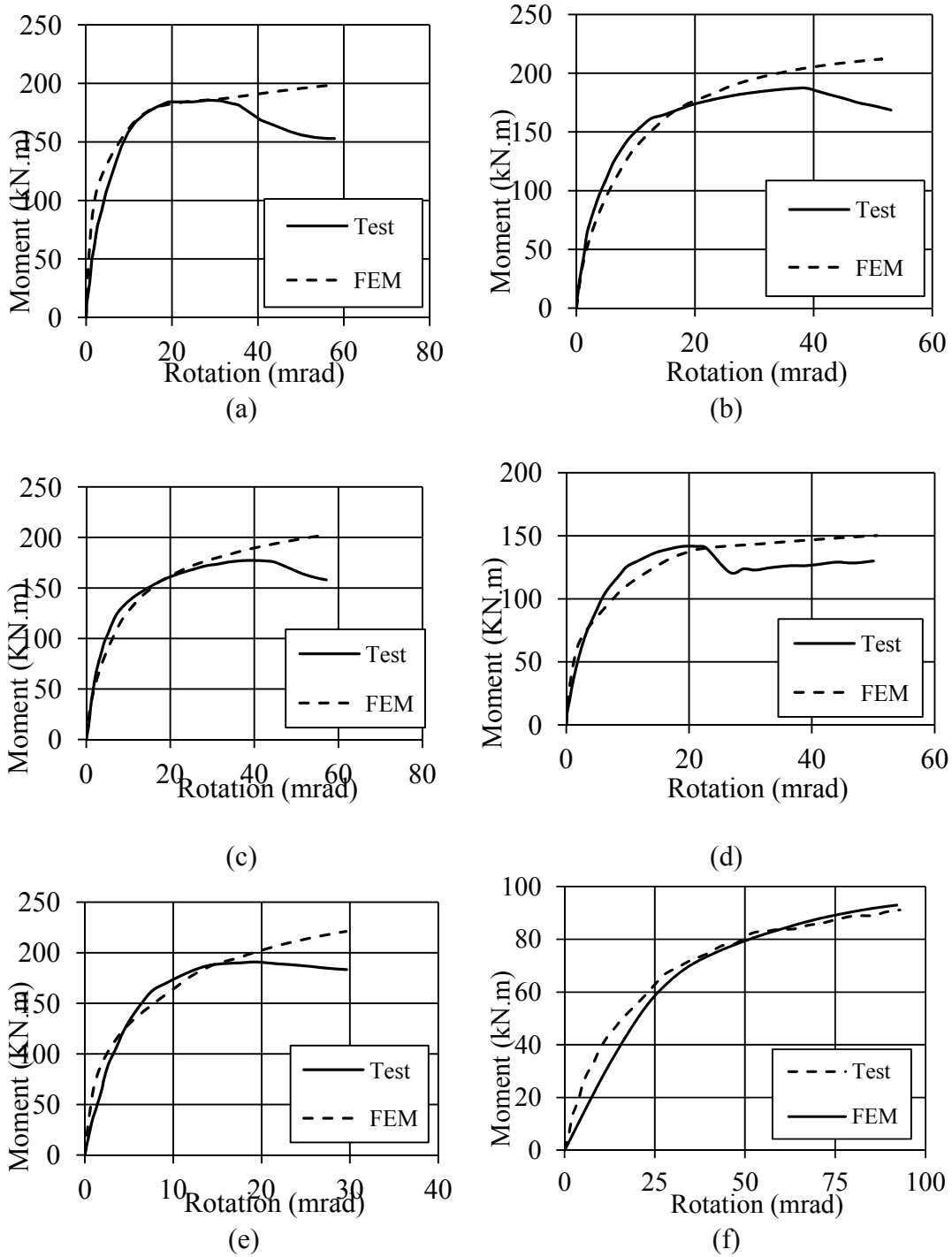


Figure 4: Comparisons of load-deflection response for FE model and tests: (a) CJ1 (b) CJ2 (c) CJ3 (d) CJ4 (e) CJ5 and (f) CJ6.

FE MODELLING OF DECONSTRUCTABLE JOINTS

GENERAL

The FE modelling of a semi-rigid beam-to-column composite blind bolted connection conducted and validated against the experiments conducted by Loh *et al.* (2006) was used to develop a FE model for a deconstructable composite joint. As noted earlier, the compressive strength of the concrete in these tests was on the order of 17.5 MPa, which is relatively low. Therefore, in order to investigate the effect of the compressive strength of the GPC and also the bolted shear connectors on the behaviour of semi-rigid flush end plate composite joints, two series of FE models were conducted including the semi-rigid flush end plate composite joints with bolted shear connector and OPC, which had the same concrete compressive strength as Loh *et al.*'s tests, and semi-rigid flush end plate composite joints with bolted shear connectors and GPC, which had 40 MPa compressive strength.

For the first series of FE models, the load-slip input characteristics for the spring, which represent the shear studs, were replaced by the strength and the stiffness characteristics of the pre-tensioned bolted shear connectors obtained from the push tests conducted by Lee and Bradford (2013).

For the second series of FE models, the load-slip input characteristics for the springs and the concrete properties were replaced by the strength and stiffness characteristics of the pre-tensioned bolted shear connectors and GPC material properties respectively. In the following sub-sections, the behaviour of the stud and bolted shear connectors are described and then the load-deflection response of the 5 composite specimens for two series of FE models are explained in detail.

COMPARISON OF STUD AND BOLTED SHEAR CONNECTORS

One of the main components that may influence the behaviour of a composite joint is the type of the shear connector. In this part, the results of push tests with two types of shear connectors (studs and bolted shear connectors) are explained. Figure 5 shows the load-slip relationship for bolted and stud shear connectors.

As shown in Figure 5, for stud shear connectors there are two distinctive stages, that involve a region of full interaction and then a region of almost no interaction. The composite action between the concrete slab and steel beam is produced by the bearing of the concrete and studs. However bolted shear connectors can be seen to have three distinctive stages, that involve a region of full shear interaction, a region of zero shear interaction and a region of partial shear interaction. In these bolted connectors at the first and third stages of interaction, composite action is produced by interface friction due to the pretension load and by bearing of the concrete and bolts respectively.

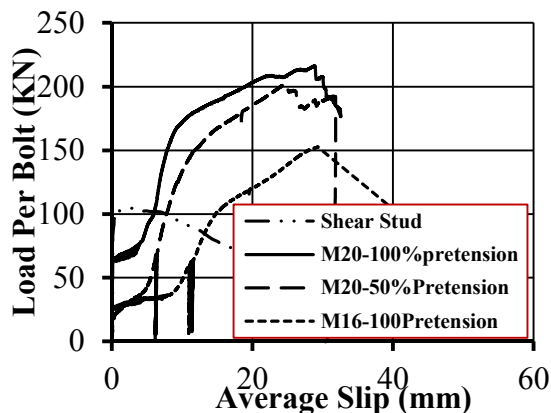


Figure 5: Load-slip relationship for bolted and stud shear connectors.

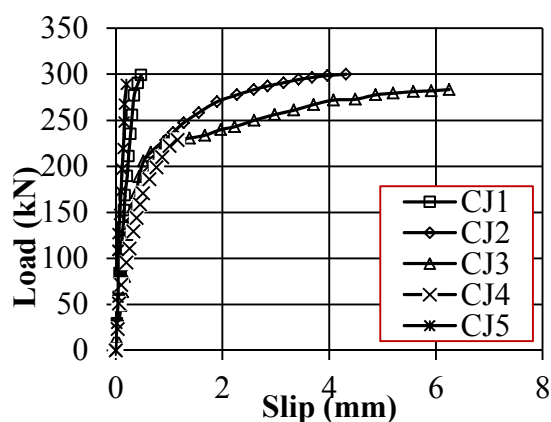


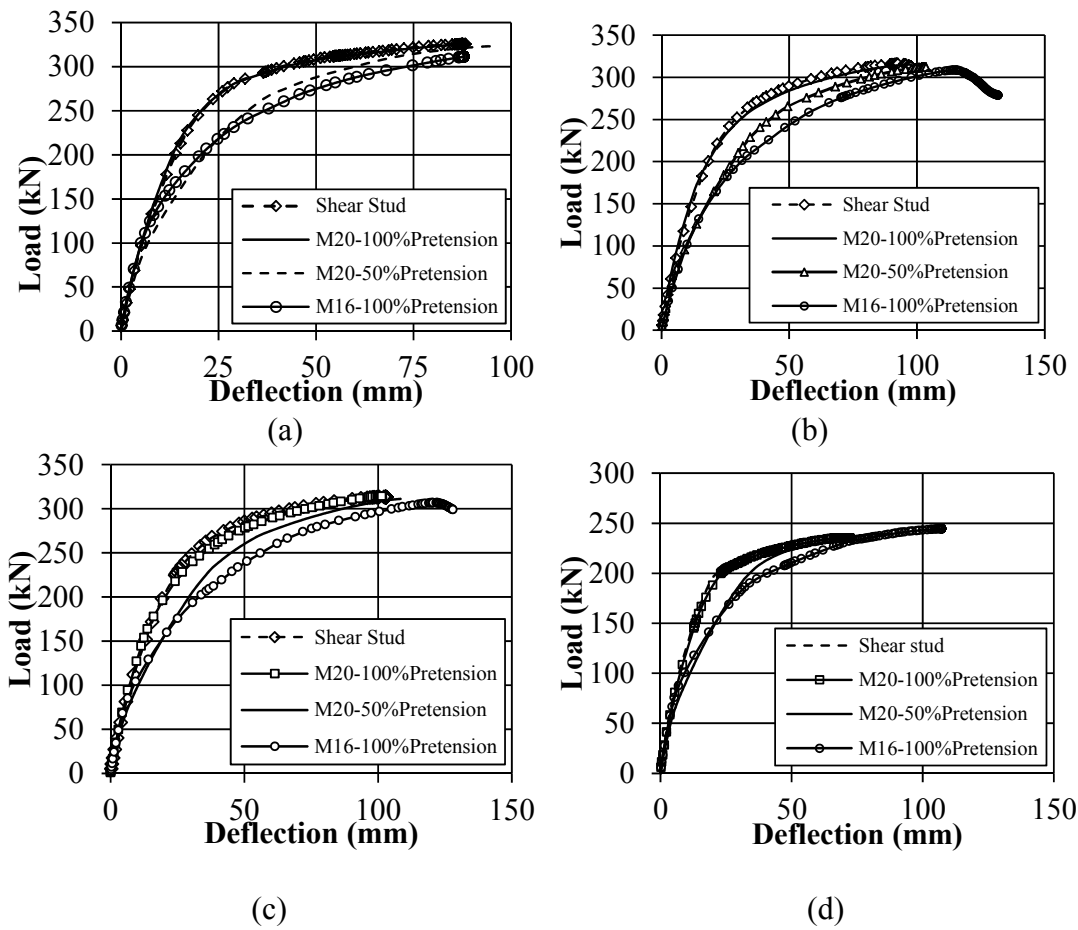
Figure 6: Load-slip relationship for shear connectors (Loh et al. 2006)

Figure 5 shows that the load and deflection capacities of the bolted shear connectors are much higher than for stud shear connectors. The first slip for the stud connector starts at around 100 kN, while the first slip for the bolted shear connector with an M20 bolt with 100% pretension, an M20 bolt with 50% pretension and an M16 bolt with 100% pretension commence at about 25 kN, 30 kN and 60 kN respectively, which means that at the first stage the studs are stiffer than the bolts. However, after bearing of the bolts in the concrete slabs, the shear strength of the bolts increases significantly compared with studs. The values of slip are almost the same as the clearance between the bolts and hole in the GPC slab.

Figure 6 shows the load-slip response for the five composite joint specimens. It can be seen that the ultimate slip of the stud shear connector for these five specimens is between 0 and 5 mm. A comparison of Figs. 5 and 6 shows that, unlike a stud shear connector, most of the shear strength of the bolted shear connectors is in the third stage, when the slip of the bolts exceeds 5 mm significantly. Therefore, the size of the hole in bolted shear connectors and the hole clearance are very important and should be considered during the designing of a connection, otherwise the strength capacity of the connectors is not properly considered in composite joints.

EFFECTS OF BOLTED SHEAR CONNECTORS

In order to investigate the effects of the bolted shear connectors in this part, only the load-slip input characteristics for the spring, which represent the shear studs and used in the validated model in Section 3, were replaced by the strength and the stiffness characteristics of the pretensioned bolted shear connectors obtained from the push tests of Lee and Bradford (2013). In order to achieve this, the results for the ABAQUS-based FE modelling with bolted shear connectors are compared with the FE modelling results of composite joints with shear studs herein. In this comparison, the load versus deflection response was determined, and the results are given in Figures 7(a) to 7(e) for the five composite connections tested.



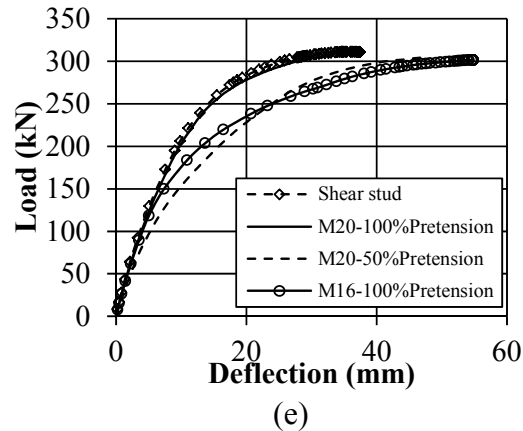


Figure 7: Comparison of deconstructable and conventional composite joints: (a) CJ1 (b) CJ2 (c) CJ3 (d) CJ4 and (e) CJ5

The load versus deflection response for joints with M20 8·8 bolts and 100% of the minimum pretension load (M20-100% pretension), M20 8·8 bolts and 50% of the minimum pretension load (M20-50% pretension) and M16 bolts 8·8 and 100% of the pretension load (M16-100% pretension) were modelled and compared with the joints with stud shear connectors, and the results are also given in Figures 7(a) to 7(e) for the five composite connections tested. For the M20-100% pretension joint, the load versus deflection response for the five composite joints is almost the same as those with stud shear connectors. It is difficult to conclude that an increase in the strength of the shear connectors caused a slight differences in the load-deflection relationship and does not affect the behaviour of the composite joints, since the behaviour and the mode of failure for the semi-rigid end plate composite joints depends on the geometric and material properties of the joints. In these specific cases, using stronger shear connectors does not have significant effect on the behaviour of composite joints. Bonilla Rocha *et al.* (2012) pointed out that the ultimate strength of the studs does not have any influence on the connection capacity. The mode of failure was local buckling of the beam flange caused by the compression, as was shown in the experimental results. Figure 8 shows the mode of failure and local buckling of the joint CJ5 using M20 bolts and 100% pretension.

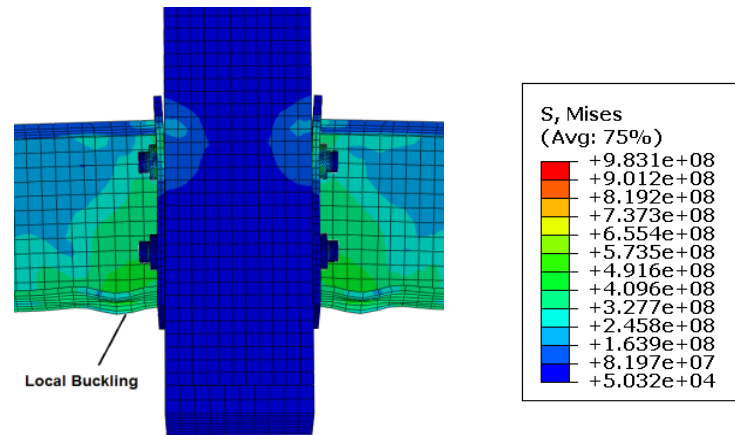


Figure 8: Local buckling of flange in joint CJ5.

The load versus deflection response for joints with M20-50% pretension was also modelled, and the results are given in Figures 7(a) to 7(e) for the five composite connections tested. As shown in these figures, the load capacity of the joints is almost the same as those of composite joints with shear studs, but they failed with significantly more mid-span deflection, so that composite joints with bolted shear connectors are more ductile than joints with stud shear connectors. Moreover, it can be seen that the initial stiffness of the joints with M20-50% pretension bolted shear connectors for the five composite joints are smaller than those with stud shear connectors. This is may be because the load-slip characteristics of the bolted shear connectors are completely different to those for stud shear connectors. This leads to a higher initial stiffness for a composite joint with stud shear connectors, but when the bolts start to bear on the concrete slab and steel beam the bolted shear connector is much stiffer than a shear stud. It can also be seen that the failure mode of the composite joint is characterised by a higher mid-span deflection than a joint with stud shear connectors.

The load versus deflection response for joints with M16-100% pretension was also modelled, and the results are also given in Figures 7(a) to 7(e) for the five composite connections tested. As shown also in these figures, the load capacities of the joints are almost the same as those for the composite joints with shear studs. Again, the joints failed with much more mid-span deflection than their shear stud counterparts, indicating significantly more ductility. For these joints, their initial stiffnesses are smaller than those with stud shear connectors.

Comparisons of the load-deflection curves in Figures 7(a) to 7(e) for the five composite joints with the same bolted shear connectors (M20 bolts) but with different pretension loads shows that the pretension load in the bolt shear connectors affects the behaviour of the joints. It can be seen that a 50% decrease in the pretension force in the bolts causes an increase between 7% and 45% in the ductility of joint without any decrease in the load capacity for joints CJ1-CJ4 and CJ5 respectively.

Comparisons of the load-deflection curves in Figures 7(a) to 7(e) for the five composite joints with different sized bolts shows that, generally, the joints with M20-100% pretension bolts are stiffer than those with M16-100% pretension bolts. The initial stiffness of the joints with different bolts is the same. This may be because in

the initial part of the response the friction force created by the pretension load at the interface resists the slip and there is full interaction between the beam and slab. It can also be seen that when the loading on the joint increases, the deflection of the joint with M16 bolts is much more than that with M20 bolts. This is to be expected, as the frictional load in the composite joint with M16 bolts, which has 95 kN pretension force, is overcome sooner than composite joint with M20 bolts, which has 145 kN pretension force.

EFFECTS OF BOTH BOLTED SHEAR CONNECTORS AND GPC

In order to investigate the effect of both the bolted shear connectors and GPC, in which the concrete compressive strength of 40 MPa is higher than that used in the tests of Loh *et al.* (2006), the load-slip input characteristics for the spring and the concrete properties were replaced by the strength and the stiffness characteristics of the pre-tensioned bolted shear connectors and GPC properties. In order to achieve this, the results of the ABAQUS-based FE modelling with bolted shear connectors are compared herein with the FE modelling results of composite joints with shear studs. For this comparison, the load versus deflection response was modelled, and the results are given in Figures 9(a) to 9(e) for the five composite connections tested. These figures show that the ductility of most joints is improved, except for joint CJ5 whose ductility is limited by local buckling of the steel compressive flange.

It can be seen that an increase in the compressive strength of concrete causes an increase of between 5% and 15% in the load capacity of the composite joints for CJ1-CJ5. However, the ductility of composite joints CJ2, CJ2 and CJ5 decreases due to their premature failure.

CONCLUSIONS

This paper has described a numerical modelling of semi-rigid composite beam connections using blind bolting, GPC and bolted shear connectors. This type of structural system falls within a class of low-carbon deconstructable building frames. Firstly, the procedure was benchmarked against the extensive testing of connections with blind bolting reported elsewhere, and the shear stud load-slip relationship data was replaced by the strength and the stiffness characteristics of pretensioned bolted shear connectors determined from some push tests also reported elsewhere. Non-linear material characteristics and non-linear geometric behaviour was considered in the modelling. Comparisons of composite joints with stud and bolted shear connectors showed that using the bolted shear connectors instead of stud shear connectors can improve the behaviour of semi-rigid flush end plate composite joints in terms of ductility. Since the behaviour of pretensioned bolted shear connectors is completely different to stud shear connectors, their behaviour should be considered during the design of composite connections.

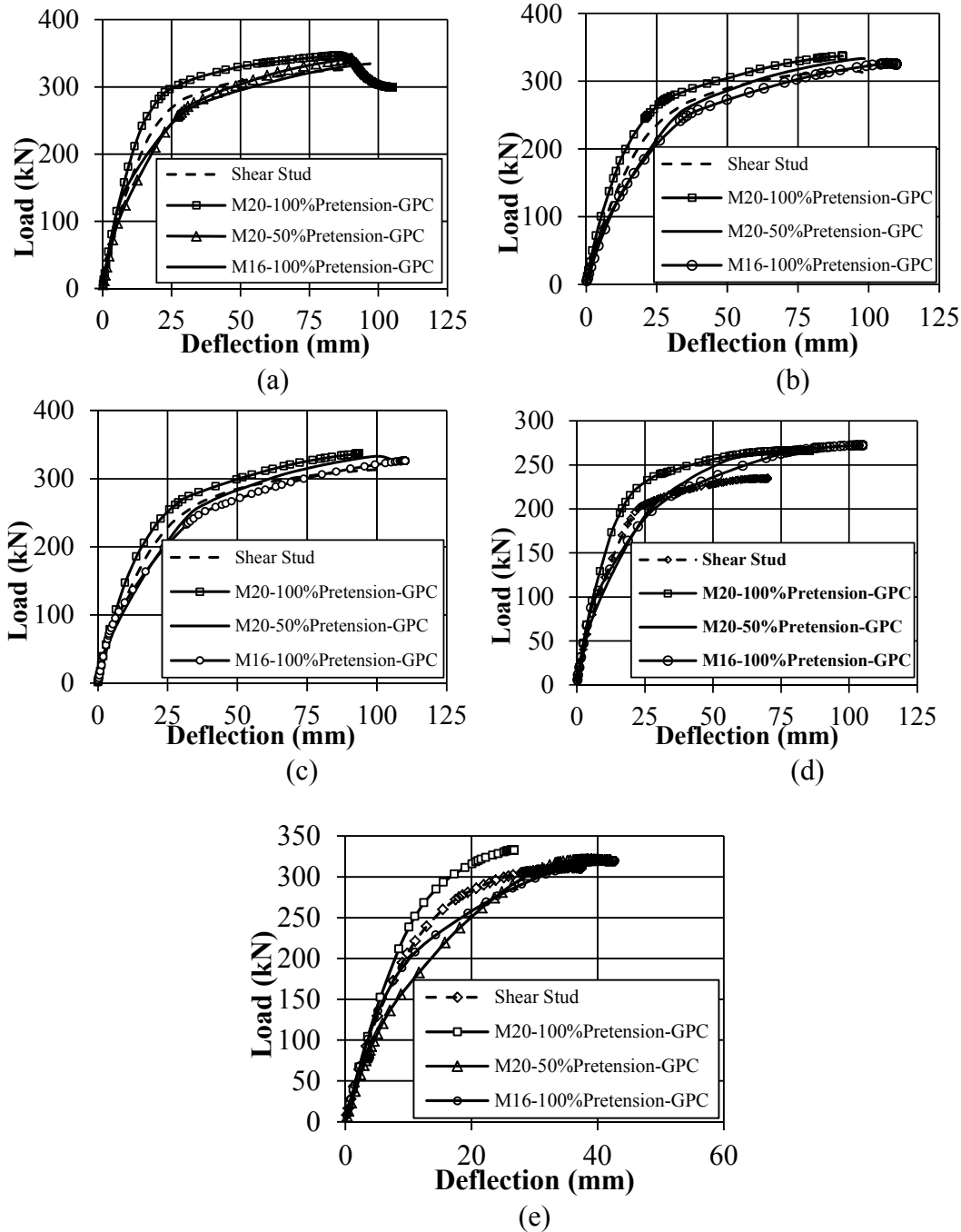


Figure 9: Comparison of deconstructable and conventional composite joints considering GPC.

ACKNOWLEDGEMENTS

The work reported in this paper was undertaken with the financial support of the Australian Research Council through an Australian Laureate Fellowship (FL100100063) awarded to the second author.

REFERENCES

- Ataei A. and Bradford M.A. (2013) FE modelling of semi-rigid flush end plate joints with concrete-filled steel tubular columns. *5th International Conference on Structural Engineering, Mechanics and Computation*, Cape Town, South Africa.
- Bonilla Rocha J.D., Arrizabalaga E.M., Larrua Quevedo R. and Recarey Morfa C.A. (2012) Behavior and strength of welded stud shear connectors in composite beam. *Revista Facultad de Ingeniería Universidad de Antioquia* 63: 93-104 (in English).
- Bradford M.A. and Pi Y.-L. (2012a) Numerical modelling of deconstructable composite beams with bolted shear connectors. *Conference on Numerical Modeling Strategies for Sustainable Concrete Structures*, Aix-en-Provence, France, II-2, 1-8.
- Bradford M.A. and Pi Y.-L. (2012b) Numerical modelling of composite steel-concrete beams for life-cycle deconstructability. *1st International Conference on Performance-Based and Life-Cycle Structural Engineering*, Hong Kong, 102-109.
- Bradford M.A. and Pi Y.-L. (2013) Nonlinear elastic-plastic analysis of composite members of high-strength steel and geopolymer concrete. *Computer Modeling in Engineering and Sciences* 2320: 1-27.
- Carreira D.J. and Ku K.H. (1985) Stress-strain relationship for plain concrete in compression. *ACI Structural Journal* 82: 797-804.
- Dallam L.N. (1968) Pushout tests with high strength bolt shear connectors. Report for Missouri State Highway Department, Department of Civil Engineering, University of Missouri-Columbia, Missouri.
- Dallam L.N. and Harpster J.L. (1968) Composite beam tests with high-strength bolt shear connectors. Report for Missouri State Highway Department, Department of Civil Engineering, University of Missouri-Columbia, Missouri.
- Davidovits J. (1994) High-alkali cements for 21st century concretes. In: *Concrete Technology, Past Present and Future*, P. Kumar Metha (ed.), ACI SP-144, 383-397.
- Dedic D.J. and Klaiber F.W. (1984) High-strength bolts as shear connectors in rehabilitation work. *Concrete International* 1984: 41-46.
- Hungerford B.E. (2004) Methods to develop composite action in non-composite bridge floor systems: Part II. M.S. Thesis. Department of Civil, Architectural and Environmental Engineering, University of Texas at Austin, Texas.
- Kayir H. (2006) Methods to develop composite action in non-composite bridge floor systems: Fatigue behaviour of post-installed shear connectors. MS thesis. Department of Civil, Architectural and Environmental Engineering, University of Texas at Austin, Texas.
- Kwon G., Engelhardt, M.D. and Klinger, R.E. (2010) Behavior of post-installed shear connectors under static and fatigue loading. *Journal of Constructional Steel Research* 66: 532-541.

- Kwon G., Engelhardt, M.D. and Klinger, R.E. (2011) Experimental behavior of bridge beams retrofitted with post-installed shear connectors. *Journal of Bridge Engineering, ASCE* 16: 536-545.
- Lee S.S.M. and Bradford M.A. (2013) Sustainable composite beams with deconstructable shear connectors. *5th International Conference on Structural Engineering, Mechanics and Computation*, Cape Town, South Africa.
- Loh H.Y., Uy B. and Bradford M.A. (2006) The effects of partial shear connection in composite flush end plate joints. Part I - experimental study. *Journal of Constructional Steel Research* 62: 232-246.
- Marshall W.T., Nelson H.M. and Banerjee, H.K. (1971) An experimental study of the use of high-strength friction-grip bolts as shear connectors in composite beams. *The Structural Engineer* 49: 171-178.
- Mirza O. and Uy B. (2011) Behaviour of composite beam-column flush end-plate connections subjected to low-probability, high-consequence loading. *Engineering Structures* 33: 642-662.
- Ng T.S. (2011) An investigation into the development of high performance geopolymer concrete. PhD Thesis, The University New South Wales, Sydney, Australia.
- Rowe M. and Bradford M.A. (2013) Partial shear interaction in deconstructable composite steel-concrete composite beams with bolted shear connectors. *International Conference on Design, Fabrication and Economy of Welded Structures*, Miskolc, Hungary, 585-590.
- Schaap B.A. (2004) Methods to develop composite action in non-composite bridge floor systems: Part I. M.S. thesis. Department of Civil, Architectural and Environmental Engineering, University of Texas at Austin, Texas.

Experimental Tests of Composite Joints Subjected to Hogging and Sagging Bending Moments

Wioleta Barcewicz¹ and Marian A. Gizejowski²

Faculty of Civil Engineering, Warsaw Univ. of Technology, Armii Ludowej 16, 00-637 Warsaw, Poland.

¹E-mail: w.barcewicz@il.pw.edu.pl

²E-mail: m.gizejowski@il.pw.edu.pl

Abstract

Experimental investigations on the behaviour of composite steel-concrete beam-to-column joints are presented. The undertaken subject is related to the design of multi-storey buildings that are not only subjected to common actions including persistent design situations, but that could also be exposed to accidental situations (such as explosion, fire, or impact) resulting in local damage to the structure. At this stage of the investigations, two separate experimental arrangements are considered, which allow the behaviour of joints under negative (hogging) and positive (sagging) bending moments to be modelled. The aim of the experimental tests is the observation of possible failure modes of the joints and a comparison of results expressed in terms of joint moment-rotation characteristics. Analysis of the joint properties for different load situations would ultimately allow for the formulation of recommendations for engineering practice.

INTRODUCTION

In the modern approach to structural design, according to current codes of practice, engineers are advised to take into account the requirements of structural robustness, and to increase structural integrity and stability in order to prevent the occurrence of progressive or disproportionate collapses. This can be related to unforeseen or unidentified events that destroy locally only a limited volume of building structure, therefore they do not lead either to the progressive collapse of entire structures or local failure of disproportionate extent to the cause of damage.

For example, when damage results in the loss of resistance of only one column of a building framework, it is associated with excessive, but limited, deformations of the residual substructure hanging over the damaged column. In order to ensure the structural robustness, some guidelines are given in Eurocodes in relation to unidentified accidental actions.

In the design strategy adopted in (EN 1991-1-7), a column of a single storey may fail as a result of an unforeseen event, but not being able to resist loads it ensures the development of an alternative load path and the formation of a new equilibrium of the deteriorated (or residual) structural system. The residual structural system is able to develop a catenary action in order to limit the extent of failure. Therefore, structural engineers are advised to ensure robustness by redundancy for providing an alternative load path potential, by local resistance of key structural components, or by

adequate connectivity for ensuring structural continuity when the structure is being transformed from its original state to the final residual state. One of the possible ways to consider an increase in structural continuity is to keep the balance between the joint ductility and strength of those joints that are considered to be critical structural components. This balance is possible, for example, by using semi-rigid joints, which may exhibit a sufficient level of stiffness and resistance, and simultaneously provide the deformability necessary in redistribution of internal forces from a damaged structural member to the adjacent members.

Research on structural robustness of steel and composite frameworks has been growing over the last two decades. A number of PhD theses dedicated to this topic have been completed, (Demonceau 2008), (Hai 2009) and (Saleh 2013) among others, as well as international programmes and research networks such as the European COST Action TU0601 “Robustness of Structures”, within which recent investigations have been presented, see (Kuhlman et al. 2009). In many publications, an exceptional event is modelled as the loss of a column in a building frame. In such event, the catenary effect appears and large tensile forces are present. Joints, which were previously subjected to hogging bending, are subjected to sagging bending after the column loss. This phenomena inspired the authors of the present paper to extend the experimental investigations on the semi-rigid composite steel-concrete joints under the negative bending moment, undertaken in (Barcewicz 2010). At this stage, experimental tests, conducted at the Warsaw University of Technology, concentrate on a comparison of the behaviour of joints subjected separately to bending moments of different signs (see Figure 1) but neglecting the effect of tensile forces. Further investigations are planned, including a sequential action of hogging and sagging bending with the presence of a tensile force.

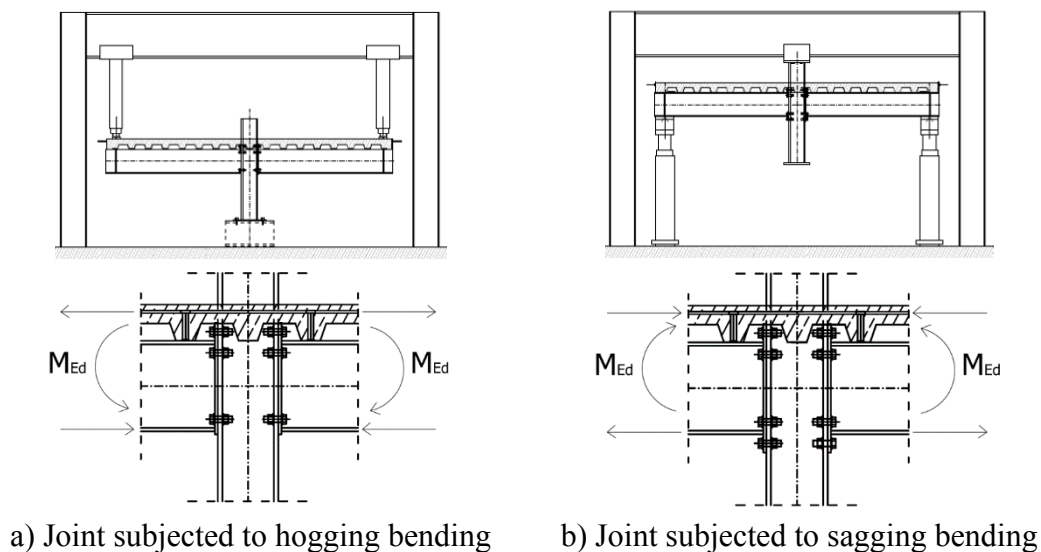


Figure 1. Experimental simulations of the behaviour of joints subjected to opposite moments.

The aim of the tests presented herein was the observation of the possible failure modes of the joints in different load configurations and a comparison of the results expressed in terms of joint moment-rotation characteristics.

DESCRIPTION OF THE SPECIMENS AND TEST RIG

The tested specimens consisted of isolated joints with bolted end-plate connections between the parts of a framed structure: beams (IPE300) and an unstiffened column (HEB200) made of steel grade S235JR, as well as a composite slab cast on the profiled sheeting (Cofraplus 60). The concrete class was of C25/30. Regarding the action of hogging bending, two types of slab were considered with reinforcement made of steel grade BSt500S: 6 #8 and 6 #12 mm, distributed inside the concrete slab of effective width equal to 800 mm. This gives ratios of the reinforcement area to the cross-sectional area of concrete above the steel ribs of 0.60% and 1.35%, respectively. In the specimen under sagging bending, only the latter reinforcement ratio was used. Composite action between the beams and the slab was provided by means of headed studs ($\phi 19$ mm x 100 mm). Details of the composite slab cast on the Cofraplus 60 profiled sheeting are shown in Figure 2.



a) Specimens before casting



b) Specimens during casting

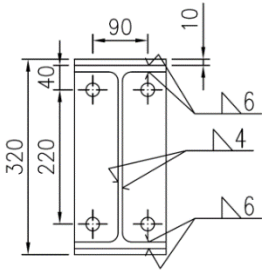
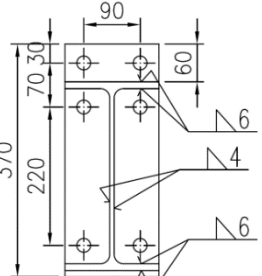
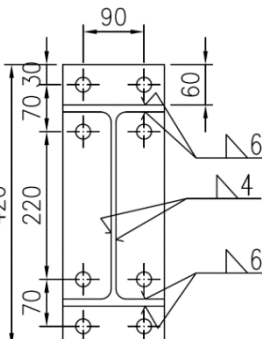
Figure 2. Preparation of the composite slab for the specimens.

For the joints considered herein, representing the group of semi-rigid joints, end-plates of thickness equal approximately to 50% of the bolt diameter were used. Bolts for the end-plate connections were M20 class 10.9. For comparison purposes, bare steel joints, shaped in the same way as the steel part of the composite joints, are also considered.

The specimens with isolated joints subjected to hogging bending moment were widely examined within the previous research of authors (Barcewicz 2010) and (Barcewicz and Gizejowski 2011). The range of the experimental investigations covered different types of specimens with flush and extended end-plates of the thickness 8-12 mm.

As the tests on the joints subjected to positive bending moments have been realized recently as pilot tests, the number and range of the specimens are limited only to two joints with extended end-plates of 10 mm thickness. One of them was bare steel and the second was composite steel-concrete. The summary limited to the joint detailing with end-plate thickness of 10 mm is presented in Table 1.

Table 1. Summary of specimen types.

Bending moment	End-plate dimensions	End-plate view	Reinforcement ratio	Specimen symbol
Hogging bending	10 x 150 x 320		0% (steel)	ES1
			0.60% (composite)	EZ1
			1.35% (composite)	EZ5
	10 x 150 x 370		0% (steel)	ES2
			0.60% (composite)	EZ2
			1.35% (composite)	EZ6
Sagging bending	10 x 150 x 420		0% (steel)	WS
			0.60% (composite)	-
			1.35% (composite)	WZ1

Expected differences in the behaviour of joints subjected to moments of opposite signs led to take into account a change in the shape of the end-plates (see Figure 1b). In the joints under hogging moment, the end-plate with the upper extension was used. However, the joints under sagging bending are shaped with end-plates extended at the top and the bottom of the joint. Otherwise the same geometry of the joint with the end-plate extended only from one edge could cause that such joints will behave under sagging moment analogically to the joints with the flush end-plate. This phenomenon is connected with the inverted location of the tension and compression zones of the joints and could significantly decrease the values of the initial stiffness and the moment resistance of such joints because of the smaller number of bolt-rows and the shorter distance between the furthest bolt-row to the centre of compression (the lever arm).

All specimens were subjected to static, monotonic loading until failure occurrence. A symmetrical arrangement was used to control the specimen behaviour

and any effect of imperfections that could cause column drift. Two independent hydraulic jacks were used to apply the same loads on each cantilever tip, at 1540 mm from the column face. The general view of the test rigs with the composite specimens in two load configurations are presented in Figure 3.



a) Hogging bending of the composite joint



b) Sagging bending of the composite joint

Figure 3. General view of the test rigs with the composite specimens in two load configurations

For the group of specimens under hogging bending (Figure 3a), loading was realized by pressing the composite slab from the top, and the loading process was fully force controlled. These specimens were supported from the bottom by the column base.

The specimens in sagging bending (Figure 3b) were hung to the rigid frame and the jacks pressed the lower beam flanges from the bottom. This loading process

was divided into two stages: in the elastic range it was force controlled, and later it was changed to being displacement controlled. This method is generally recommended since it allows evaluation of the full joint characteristic, including rotation capacity.

For all specimens, the joint rotation was measured by electronic inclinometers, located symmetrically in the web of each beam in the vicinity of the joint, at a distance of 100 mm from the column face and in the middle of the column web (for control of symmetry). Readings of the actual force in the jacks were provided by the hydraulic system.

BEHAVIOUR OF THE JOINTS SUBJECTED TO HOGGING BENDING

Due to the diversity of the specimens subjected to hogging bending, different failure modes could be observed and the influence of several effects could be examined: composite action effect, height of the end-plate effect (and the presence of the additional bolt-row), and reinforcement ratio effect.

Failure mode of the bare steel joints with flush and extended end-plates was a rupture in the fillet welds connecting the end-plate to the upper flange of the beam. This brittle failure was preceded by significant end-plate deformations in both flush and extended end-plates.

Tests of composite joints with a lower reinforcement ratio were terminated owing to a rupture in the reinforcing bars and the large cracking of concrete. A view of the cracked slabs of specimens EZ1 and EZ2 is shown in Figure 4.

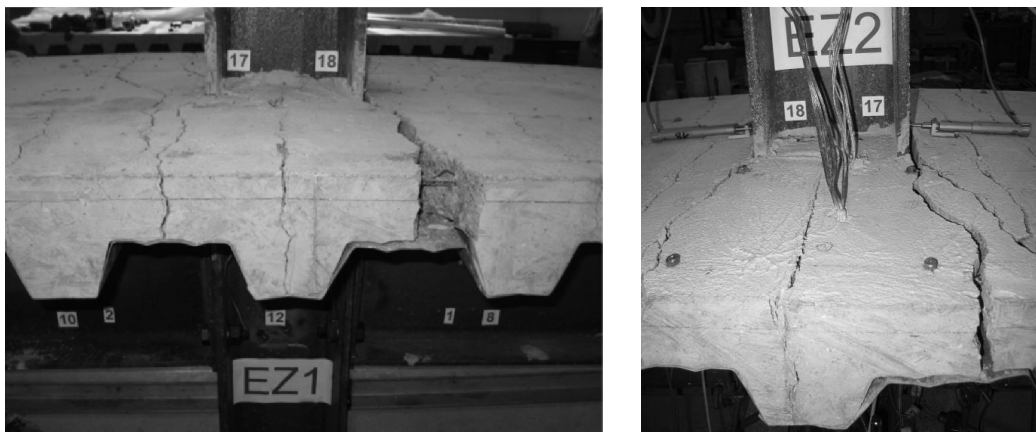


Figure 4. View of the cracked slabs of specimens EZ1 and EZ2

The failure of these specimens is located in the tension zone as shown in Figure 5a. Deformations of the end-plates in the composite specimens were also visible, as in the bare steel counterparts, but they were relatively smaller than those of the respective steel joints. On the other hand, failure of the composite joints with a higher reinforcement ratio was observed to appear in the compression zone. In this case, the source of failure was the yielding of the column web in compression, as presented in Figure 5b.

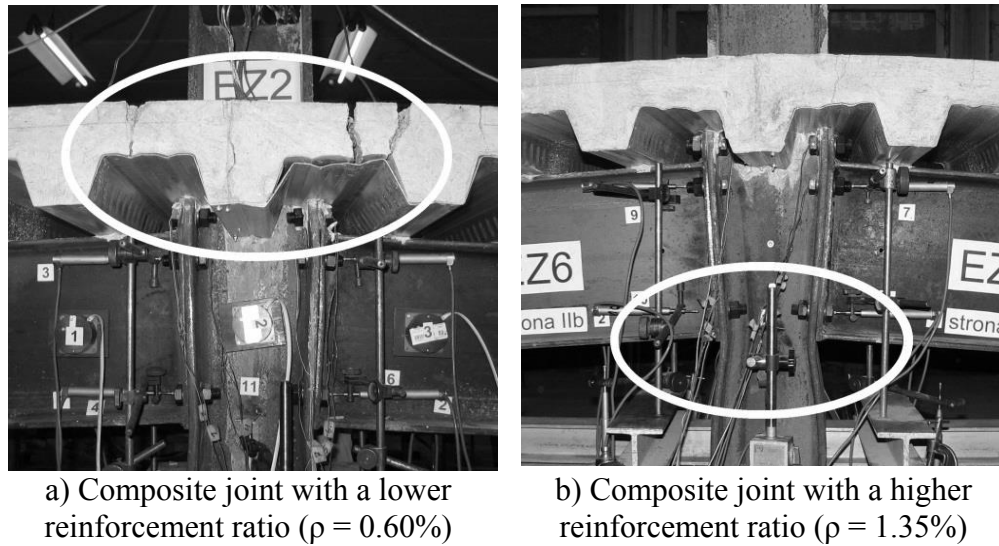


Figure 5. Failure modes of the composite joints subjected to the negative bending moment

Test results are expressed in the form of relationships between the bending moment applied to the joint and the joint rotation. The particular sets of $M-\phi$ curves (in Figure 6) are useful to explain the effect of the height of the end-plates as well as the influence of a composite action and reinforcement ratio on the overall behaviour of joints subjected to the hogging bending moment. Due to the force controlled loading system, the recorded measurements were possible until the maximum value of the applied load had been reached. Except for joint EZ6, in case of which instrumentation was removed slightly earlier, the possible readings of angles of rotation were associated with the ultimate moment resistances and equal to about 50 mrad in case of steel joints and 30 mrad for composite joints (independent of the type of end-plate and the amount of reinforcement).

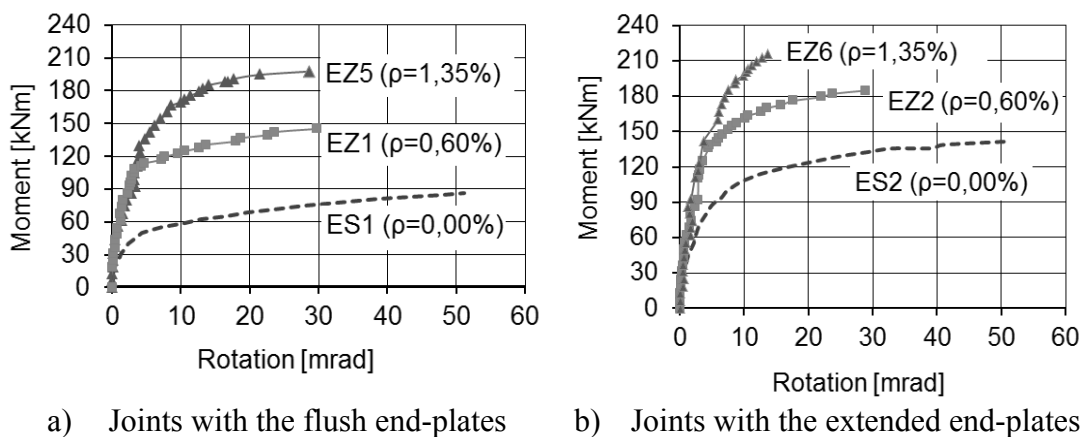


Figure 6. $M-\phi$ curves for the joints subjected to hogging bending

From the test results, it is clearly visible that the overall behaviour and finally the failure mode of composite joints subjected to hogging bending mostly depend on

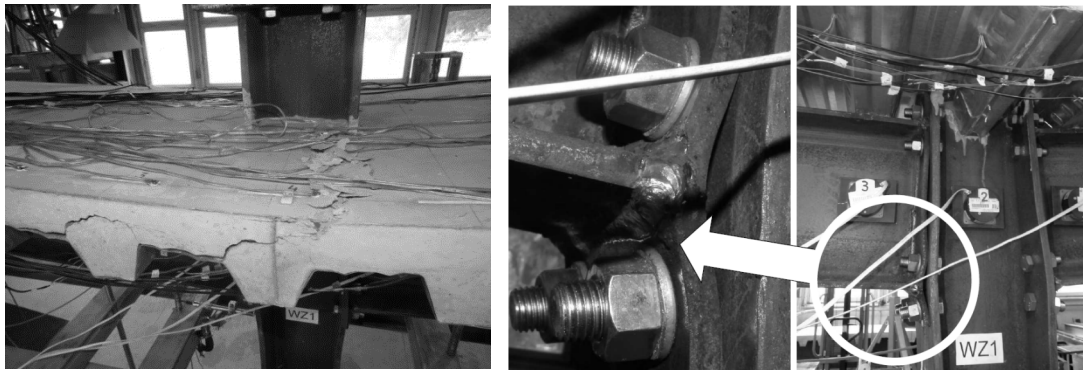
the reinforcement ratio. A detailed procedure of taking into account the effect of joint reinforcement ratio in the joint analytical model is proposed in (Barcewicz and Gizejowski 2011).

BEHAVIOUR OF THE JOINTS SUBJECTED TO SAGGING BENDING

In the case of the experimental tests, in which the specimens were subjected to sagging bending moments, only two joints: WS (as a counterpart of joint ES2) and WZ1 (as a counterpart of joint EZ6) were considered (see Table 1).

Failure mode of the bare steel joint WS was a fracture of the end-plate in the HAZ of the fillet welds connecting the end-plate to the lower flange of the beam. It was associated with large end-plate deformations at both sides of the column.

The source of composite joint WZ1 failure was the crushing of concrete. The view of the crushed composite slab is presented in Figure 7a. Plastic deformations of the bending column flanges and end-plates were also observed, increasing with the growth of the joint rotation. After the complete crushing of the slab, the steel part of the joint was damaged due to a rupture of the fillet weld connecting the end-plate to the bottom flange of the beam. It is presented in Figure 7b.



a) View of the crushed slab of composite joint WZ1

b) View of the steel part of composite joint WZ1

Figure 7. Failure modes of composite joint WZ1

Test results of the joints WS and WZ1 in terms of the $M-\phi$ curves are presented in the next chapter. Due to the utilization of the displacement controlled loading system, the readings of the joint rotation at failure were possible for these specimens.

COMPARISON OF THE TEST RESULTS

The $M-\phi$ curves of the joints subjected to hogging and sagging bending moments are compared in Figure 8. From the comparison presented in this figure, it is visible that the steel joint WS showed a slightly higher ultimate moment resistance than joint ES2, the same initial stiffness, and a larger rotation capacity. After the elastic range of the $M-\phi$ curve of joint ES2, stiffness degradation occurs more rapidly.

In the case of the composite joints, both of them reached almost the same ultimate moment resistance and similar initial stiffness.

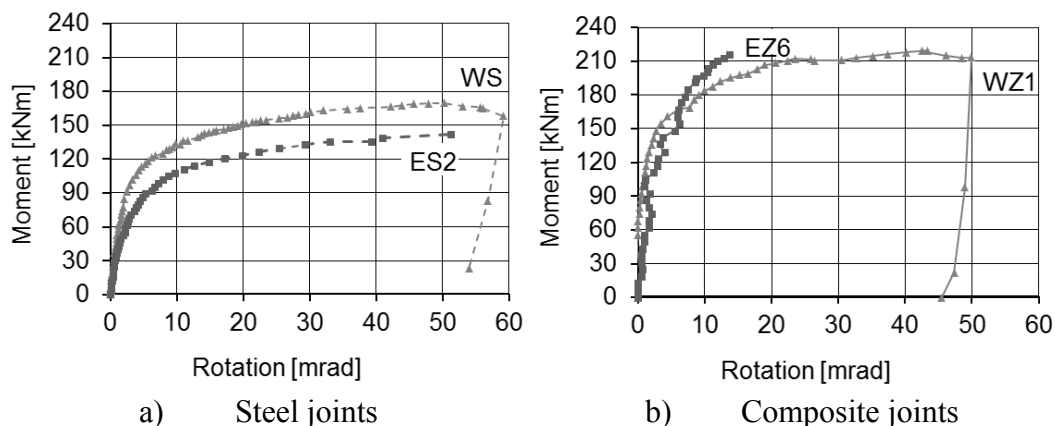


Figure 8. Comparison of the $M-\phi$ curves for the joints in hogging and sagging bending

The visible difference in ductility between the two $M-\phi$ curves of composite joints results from the lack of possibility of rotation capacity evaluation in the case of joint EZ6. This is due to the force controlled loading process applied in the experiment that resulted in the earlier termination of readings. Similar composite joint resistances are obtained under the condition that in the tension zone there is an extended end-plate with bolt rows on both sides of the flange, and regardless of whether in the compression zone the end-plate is extended or flush. The semi-rigid joints analysed herein as subjected to sagging bending demonstrated a good degree of ductility.

INFLUENCE OF THE SIGN OF BENDING MOMENT ON THE ANALYTICAL MODELLING OF JOINT PROPERTIES

Remarks taken from the previous chapters may be useful in the prediction of basic joint properties. The aim of this chapter is to show the differences in analytical determination of the design moment resistance and the initial stiffness in the case of the negative and positive bending moment.

The initial stage of analytical modelling of steel and composite joints, according to the component method implemented in (EN 1993-1-8) and (EN 1994-1-1), is the identification of active components, which could be a source of deformations and potential failure modes of the joints. These components are located in three different zones within a joint: tension, compression, and shear zone.

The shear zone covers the column web panel in shear. In the case of the experimental tests presented here, symmetrical double-sided joints with balanced moments allow the activity of this component to be neglected.

The position and activeness of the components in the tension and compression zones highly depend on the load configuration and joint detailing. In typical situations, where the joint is subjected to hogging bending moment, the components of the tension zone are situated in the upper part of the steel beam section and in the

slab, in which reinforcement is the active component, while the influence of cracked concrete is omitted. A list of the active components regarding the joints with end-plate connections, subjected to the negative moment, as well as the design procedure of determination of the design moment resistance and the initial stiffness are given in (EN 1993-1-8) and (EN 1994-1-1).

Regarding the composite beam-to-column joints subjected to sagging bending moments, there is no guidance in the Eurocodes. In such situation, the joint components of the tension zone are situated in the lower part of the steel beam section. However, the compression zone is located in the upper part of the joint, mostly in the slab, in which concrete plays the important role. This means that with respect to the component method, the new component is activated, namely: concrete slab in compression. The influence of this new component should be taken into account in terms of both resistance and stiffness replacing the previous component: longitudinal steel reinforcement in tension. Formulae for the new component characteristics are given in (Demonceau 2008).

Contrary to the joints subjected to hogging bending, where the centre of compression is assumed to be in the line with the centre of the bottom flange of the connected beam, the centre of compression of the joints under sagging bending is assumed to be at the middle of the height of the contributing part of the composite slab z . It may be computed by expressing the equilibrium of the load developing in the slab in compression with components in tension, and assuming a rectangular stress distribution in the concrete: $z = \sum F_{tr,Rd} / [b_{eff,conn} \cdot (0.85f_{ck}/\gamma_C)]$ and $z \leq h_{concrete}$, where:

$F_{tr,Rd}$ – the effective design tension resistance of bolt row r

f_{ck} – characteristic value of the cylinder compressive strength of concrete at 28 days (or on the day of testing in the case of the experimental investigations)

γ_C – partial factor for concrete

$h_{concrete}$ – the total height of concrete above the ribs (in the case of a composite slab)

$b_{eff,conn}$ – the width of concrete taken into account for this joint component, defined as: $b_{eff,conn} = b_c + 0.7h_c \leq b_{eff}$, where:

b_c – the width of the column flange

h_c – the depth of the column cross-section

b_{eff} – the effective width of the composite slab to be considered in the vicinity of the joint.

The results of the analytical modelling, according to Eurocode provisions and some additional developments presented in (Barcewicz and Gizejowski 2011), are compared with the experimental results in Table 2. The calculated values are based on the actual material properties. The joint initial stiffness $S_{j,ini,test}$ was determined for the linear part of the $M-\phi$ curve by means of the least squares method, while the values of the moment resistance $M_{j,R,test}$ are determined by the intersection point of the $M-\phi$ curve with the straight line representing the secant stiffness $S_{j,test}$ (Barcewicz and Gizejowski 2011). The comparison presented above shows good agreement between the predicted values of the initial stiffness and the joint moment resistance with the results determined experimentally.

Table 2. Comparison of the joint properties from the tests and the calculations

Joint properties	Hogging bending						Sagging bending	
	Flush end-plate connections			Extended end-plate connections			WS	WZ1
	ES1	EZ1	EZ5	ES2	EZ2	EZ6		
$S_{j,ini,test}$ [kNm/mrad]	22.63	46.91	56.29	44.44	66.89	78.19	50.51	80.63
$S_{j,ini,calc}$ [kNm/mrad]	21.62	39.22	51.07	52.33	65.87	75.10	52.27	73.93
$S_{j,ini,calc} / S_{j,ini,test}$	0.96	0.84	0.91	1.18	0.98	0.96	1.03	0.92
$M_{j,R,test}$ [kNm]	55.52	124.89	178.79	92.40	158.89	201.18	124.80	168.78
$M_{j,R,calc}$ [kNm]	49.40	128.31	181.29	82.75	161.67	194.70	91.90	137.64
$M_{j,R,calc} / M_{j,R,test}$	0.89	1.03	1.01	0.90	1.02	0.97	0.74	0.82

CONCLUDING REMARKS

In modern structural design processes, designers should take into consideration not only typical permanent situations, but care should also be paid to the accidental situations. Sometimes even a small change in the typical shaping of structures may be useful in order to allow the structure to resist a local overload or other accident events. One method for ensuring an increase in structural continuity is to keep the balance between the joint ductility and strength of the joints that are often considered to be critical structural components. This balance could be possible by using semi-rigid joints, which may exhibit a sufficient level of stiffness, resistance, and deformability, necessary in the redistribution of internal forces from a damaged structural member to the adjacent members.

In the present paper, symmetrical double-sided beam-to-column joints with bolted end-plate connections are dealt with. End-plates of thickness equal to half of the bolt diameter were used and, in the case of sagging bending, symmetrical extensions beyond both beam flanges. Regarding the bare steel joints in hogging bending, the height of the end-plate is important, whereas for the composite joints in the same situation, the most influenced parameter is the reinforcement ratio. For composite joints subjected to the positive moment, parameters of concrete (concrete class, thickness and, effective width of the slab) are crucial as well as a detailing of the bottom steel part of the composite joint in the tension zone. Joints with thin extended end-plates exhibit a good balance between strength and rotation capacity, which may allow an equilibrium state to be achieved in the case of a change in the sign of bending moment. Further investigations are needed to proof the good

behaviour of such joints within the interaction of bending and tension in the case of a more realistic simulation of an accidental event.

Experimental investigations are also needed to observe the joint behaviour in full scale multi-bay sub-frame testing when the specimen is subjected first to the application of service loads and then to the simulation of column removal scenario. Pilot testing of steel and composite sub-frames based on the same flush end-plate joint detailing as adopted herewith have been presented in (Kozłowski et al. 2011) and on the same double extended end-plate joint detailing in (Saleh 2013).

REFERENCES

- Barcewicz, W. (2010). *Stiffness, strength and rotation capacity of a certain class of joints in steel structures with composite slabs*, PhD thesis, Faculty of Civil Engineering, Warsaw University of Technology [in Polish], Warsaw.
- Barcewicz, W, Gizejowski, M.A. (2011). „Evaluation of M- ϕ characteristic of composite joints. Influence of the reinforcement ratio on the behaviour of steel-concrete joints”. In: Dunai, L, Ivanyi, M, Jarmai K, Kovacs N, Vigh L.G (eds.), *Eurosteel 2011, 6th European Conference on Steel and Composite Structures. Research – Design - Construction*. Proc. intern. Eurosteel conf., Budapest, 30 August – 2 September 2011.
- Demonceau, J-F. (2008). *Steel and composite building frames: sway response under conventional loading and development of membrane effects in beams further to an exceptional action*. PhD Thesis, Universite de Liege, Faculte de Sciences Appliquees. Annee Academique 2007-2008.
- EN 1991-1-7. *Eurocode 1: Actions on structures, Part 1-7: Accidental actions*.
- EN 1993-1-8. *Eurocode 3: Design of steel structures, Part 1-8: Design of joints*.
- EN 1994-1-1. *Eurocode 4: Design of composite steel and concrete structures, Part 1-1: General rules and rules for buildings*.
- Hai, L.N.N. (2009). *Structural response of steel and composite building frames further to impact leading to the loss of a column*. PhD Thesis, Universite de Liege, Faculte de Sciences Appliquees. Annee Academique 2008-2009.
- Kozłowski, A, Gizejowski, M, Slecza, L, Pisarek, Z, Saleh, B. (2011). „Experimental investigations of the joint behaviour – Robustness assessment of steel and steel-concrete composite frames”. In: Dunai, L, Ivanyi, M, Jarmai K, Kovacs N, Vigh L.G (eds.), *Eurosteel 2011, 6th European Conference on Steel and Composite Structures. Research – Design - Construction*. Proc. intern. Eurosteel conf., Budapest, 30 August – 2 September 2011.
- Kuhlmann, U., Rölle, L., Jaspert, J-P., Demonceau, J-F., Vassart, O., Weynand, K., Ziller C., Busse E., Lendering M., Zandonini R., Baldassino N. (2009). *Robust structures by joint ductility*. Final report, Office for Official Publications of the European Communities.
- Saleh, B.A.K. (2013). *Modelling of beam-to-column joints of steel concrete composite frames subjected to standard and extreme load combinations*. PhD thesis, Faculty of Civil Engineering, Warsaw University of Technology, Warsaw.

Composite Joints under M-N at Elevated Temperatures: Experimental Investigations and Analytical Models

J.-F. Demonceau¹; C. Haremza²; J.-P. Jaspart¹; A. Santiago²; and L. Simões da Silva²

¹Dept. of ArGEnCo, Liège Univ., Liège, Belgium. E-mail: jfdemonceau@ulg.ac.be; Jean-Pierre.Jaspart@ulg.ac.be

²ISISE – Dept. of Civil Engineering, Univ. of Coimbra, Coimbra, Portugal. E-mail: haremza@dec.uc.pt; aldina@dec.uc.pt; luisss@dec.uc.pt

Abstract

The Eurocodes recognise robustness as a way to ensure the structural integrity of a building frame subjected to an unforeseen event and therefore to avoid a so-called “progressive failure” mode in extreme loading situations. However, few practical guidelines exist nowadays which would allow a designer to design a structure accordingly. Within the European RFCS ROBUSTFIRE project, the behaviour of steel and composite car parks subjected to localised fire leading to a column loss was investigated. Under such a scenario, the beam-to-column joints play a key role in the global structural response. Indeed, these joints, initially loaded in bending, may be subjected to elevated temperatures and to combined axial load “N” and bending moment “M”. In this paper, a methodology to predict the mechanical response of bolted composite beam-to-column joints at elevated temperatures under M-N is presented and validated through comparison to experimental tests conducted at the University of Coimbra.

INTRODUCTION

The Eurocodes recognise robustness as a way to ensure the structural integrity of a building frame subjected to an unforeseen event (explosion, impact ...) and therefore to avoid a so-called “progressive failure” mode in extreme but exceptional loading situations. However few experience and practical guidelines exist nowadays which would allow a designer to design a structure accordingly.

Within the European RFCS ROBUSTFIRE project, the behaviour of steel and composite car parks subjected to localised fire leading to a column loss was investigated, and practical design guidelines were derived. To reach this goal, experimental, numerical and analytical developments were carried out.

Under such a scenario, the beam-to-column joints play a key role in the global structural response. Indeed, these joints, initially loaded in bending, may be subjected to elevated temperatures and to combined axial load “N” and bending moment “M”.

Within the above mentioned project, a methodology to predict the mechanical response of bolted composite beam-to-column joints at elevated temperatures under M-N is proposed; this methodology will be presented and discussed in the paper.

This methodology is based on an analytical method able to predict M-N resistance interaction curves for joints and which is in full agreement with the

Eurocode model recommended for the joint characterisation, i.e. the component method.

The validation of the proposed model through comparisons against experimental results obtained from six tests performed at the University of Coimbra on a composite steel-concrete beam-to-column frame under fire is introduced in the paper. The tested composite frame was subject to mechanical (bending and axial forces) and thermal actions (constant temperature equal to 500°C or 700°C). The objective of these tests was to observe the combined bending moment and axial loads in the heated joint when catenary action develops in the frame during the column loss due to a localized fire.

The paper will first summarise the conducted experimental test campaign and then present the developed analytical method, with its validation through comparisons of its predictions against experimental evidences.

EXPERIMENTAL TESTS

A total of seven beam-to-column sub-frames (see Figure 1) were tested at the University of Coimbra: one reference test at ambient temperature; five tests at 500°C or 700°C; and a demonstration test, for which the sub-frame was subject to an increase of the temperature up to the failure of the column. The effect of the axial restraint to beam coming from the unaffected part of the building was also studied. The six first tests that represent “theoretical” reference situations (Haremza et al., 2013) are used for the calibration.

Experimental program

A typical open car park structure was specially designed for the European ROBUSTFIRE project (Demonceau et al. 2013). From the studies performed on this common building, general design rules for such structures ensuring sufficient robustness under fire conditions can be obtained. The selected structure was a braced open car park building with eight floors of 3 m height, composite slabs, composite beams and steel columns. The tested sub-frame was selected from the fifth floor of this car park building; however, because of the laboratory dimensions, the beam length was reduced from 10 m in the real building to 3 m in the tested sub-frame. In this paper, the six tests performed under constant temperatures (tests 1 to 6) are presented and the obtained results are used to calibrate the proposed analytical model. The objective of these tests was to derive: i) the joint properties at 20°C, 500°C and 700°C (no axial restraint to the beam), and ii) the joint M-N curves at 500°C and 700°C under variable axial loads (full or actual beam axial restraints).

Sub-frame and testing setup

The sub-frame was defined by two unprotected composite beams IPE 550 steel cross-sections, grade S355, and one unprotected HEB 300 cross-section steel column, grade S460 (Figure 1). The hydraulic jack at the column top applied the

mechanical loading, whereas the hydraulic cylinder located at the column base simulated the progressive loss of the column.

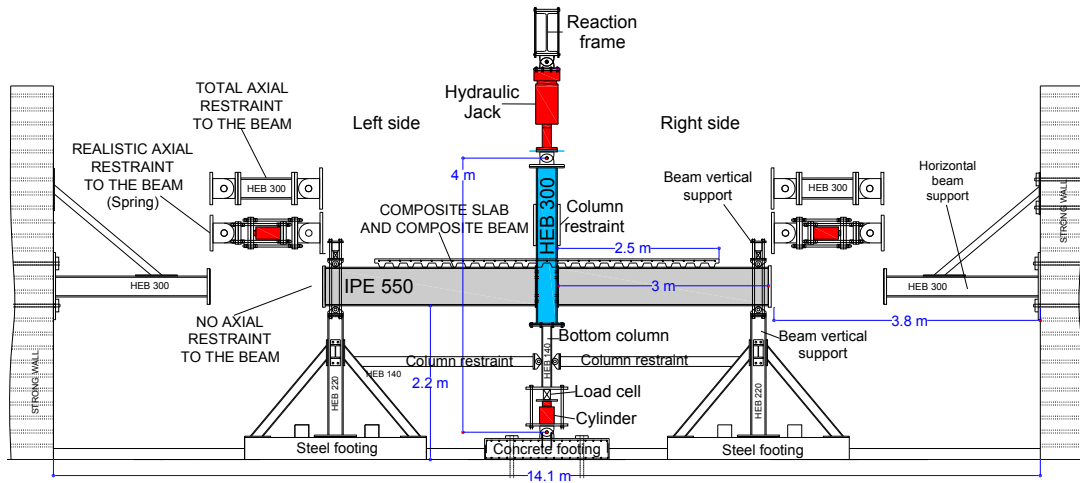


Figure 1. General layout, longitudinal view

The joint configuration is representative of usual joint typologies used in open composite steel-concrete car park structures (see Figure 2); bolts M30, grade 10.9, and a steel end-plate 15 mm thick, S355, were used (Demonceau et al., 2013; and Haremza et al., 2013). In order to ensure the composite behaviour of the beam-to-column joint, ten steel rebars of diameter 12 mm were placed in the composite slab (five at each side of the column). The composite slab (1 mm thick steel sheeting and reinforced concrete C25/30) had 900 mm width and 130 mm of total thickness. The steel beam was fully connected to the composite slab by 22 shear studs (Haremza et al., 2013).

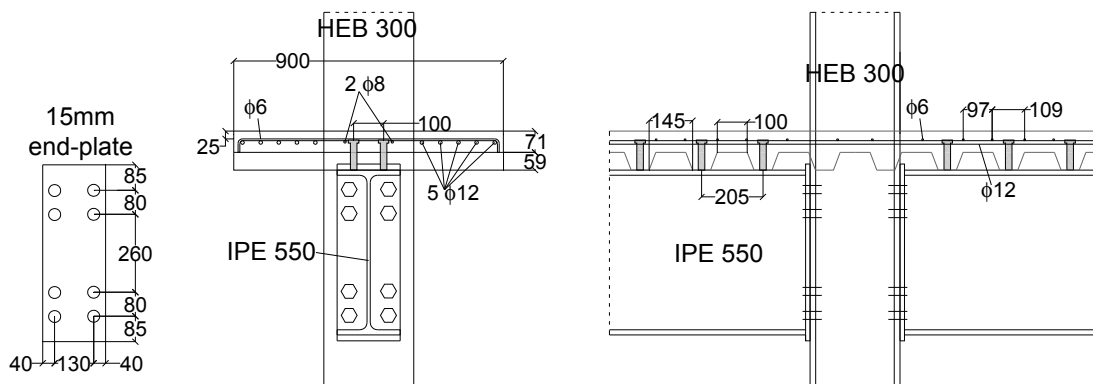


Figure 2. Configuration of the tested beam-to-column joints

Description of the loading sequence

Each test, from test 1 to test 6, was divided into 3 main steps (see Figure 3): step 1 - application of an initial hogging bending moment in the joint, step 2 - heating of the joint zone up to 500°C or 700°C (except for test 1 at 20°C), and step 3 -

simulation of the loss of the column and increase of the sagging bending moment up to the failure of the joint.

In step 1, the internal loads in the joint were simulated as in the real car park. A hogging bending moment equal to -450 kNm was applied to test 1 at ambient temperature. According to Eurocode 1 part 1.2 (EN 1991-1-2, 2002), effects of actions under fire may be deduced from those determined in normal temperature design, by calculating a reduction factor ψ_{fi} (53% in this case). The resulting hogging bending moment considered in tests under elevated temperatures was -236 kNm. During step 2, temperatures increased with a linear rate of 300°C/hour, up to the target temperature in the beam bottom flanges: 500°C for tests 2 and 4, and 700°C for tests 3, 5 and 6. Steel temperatures were increased using Flexible Ceramic Pad (FCP) heating elements (concrete was not heated). The heated zone was defined by a length of 0.6 m of the beam to each side of the joint, the bolts and 1 m of column (Haremza et al., 2013). Temperatures were kept constant throughout step 3, for which the progressive loss of the column was simulated. Then, the vertical load at the column top was increased in the downward direction, in order to increase the sagging bending moment in the joint and to reach the joint failure.

The effect of the beam axial restraint coming from the unaffected part of the building was studied, and three different restraints stiffness's were considered (Figure 3). When no restraint was applied (tests 1, 2 and 3), the beams were free to deform axially. For the total beam axial restraint (tests 4 and 5), a steel beam with profile HEB 300, linked from the end of the tested beams to strong walls was used (see Figure 1). The actual axial restraints to the beams (spring restraints in test 6) provided by the part of the building not directly subject to the fire were simulated using hydraulic cylinders, with a spring stiffness equal to 50 kN/mm. The total as well as the actual restraints at their extremities were pinned and allowed the rotation.

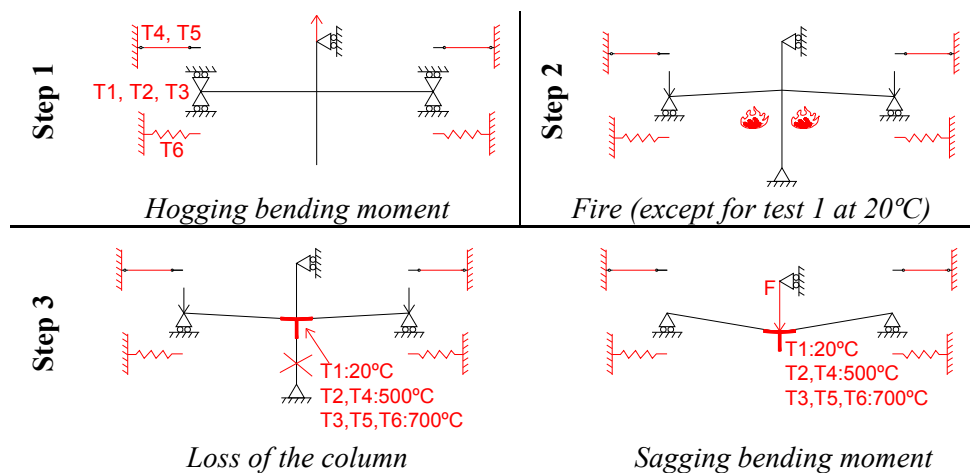


Figure 3. Outline of the tests 1 to 6

Material tests

For calibration of the proposed analytical model against the test results, material tests were performed to determine material properties of the steel joint components and concrete slab (Haremza et al., 2013). Mechanical properties of the

beam, the column and the end-plate were defined by steady-state tensile coupon tests performed at ambient and elevated temperatures (500°C and 700°C). Figure 4 presents the stress-strain curves from the tensile tests performed at 20°C, 500°C and 700°C: a) the flanges of the IPE 550 steel beam (S355J0 + M) and the end-plate (S355J2), and b) the flanges of the HEB 300 steel column (S460M). Each curve is compared with Eurocode curves (EN1993-1-2:2005); it can be observed that Eurocode provides secure results except for high strength steel S460 under 500°C.

Mechanical properties of the bolts M30, grade 10.9 were defined by steady-state tensile coupon tests at ambient and elevated temperatures (200°C, 400°C, 500°C, 600°C, 700°C and 800°C). Figure 5 presents the stress/strain curves for each temperature. Tests showed that yield and ultimate stresses increased at 200°C before decreasing at higher temperature (Haremza et al., 2013). The Young’s modulus decreased with temperature, and the ductility was significantly increased from 600°C.

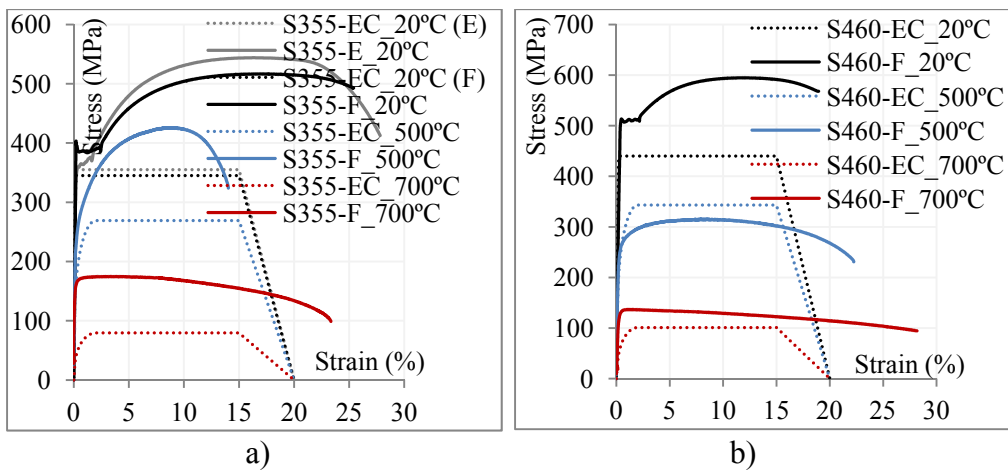


Figure 4. Comparisons of stress-strain curves obtained from Eurocode 3 part 1.2 (EC), and tests performed at 20°C, 500°C and 700°C for steel: a) S355J0 + M - IPE 550 (flange-F) and S355J2 from the end-plate (E); b) S460 - HEB 300 (flange-F)

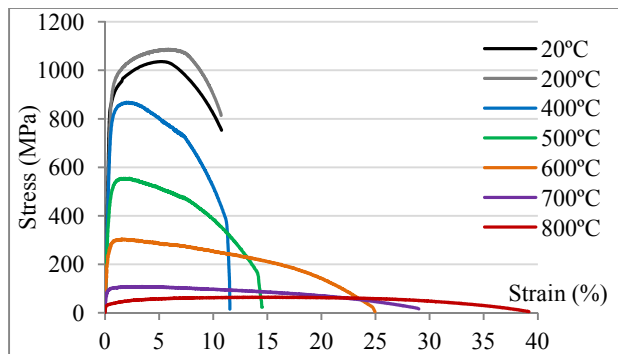


Figure 5. Stress-strain curves of bolts M30 10.9 at 20°C, 200°C, 400°C, 500°C, 600°C, 700°C & 800°C

Experimental test results

Temperature results

Tests 2 to 6 were performed under constant temperatures: bottom flanges reached 500°C in tests 2 and 4, and 700°C in tests 3, 5 and 6. Figure 6 depicts the temperature evolution during tests 2 and 6 - at 200 mm from the connection (in the bottom flange, web and top flange), at the column centre, in bolt row 4, and in the concrete rib in contact with the steel beam near the joint. The reduced beam web thickness allowed a faster temperature increase; because beams top flanges were shielding by the concrete slab and heated only by heat transfer, steel temperatures were much lower than the ones measured in the bottom flanges and webs (Haremza et al., 2013). In all the tests, concrete temperatures did not rise above 300°C.

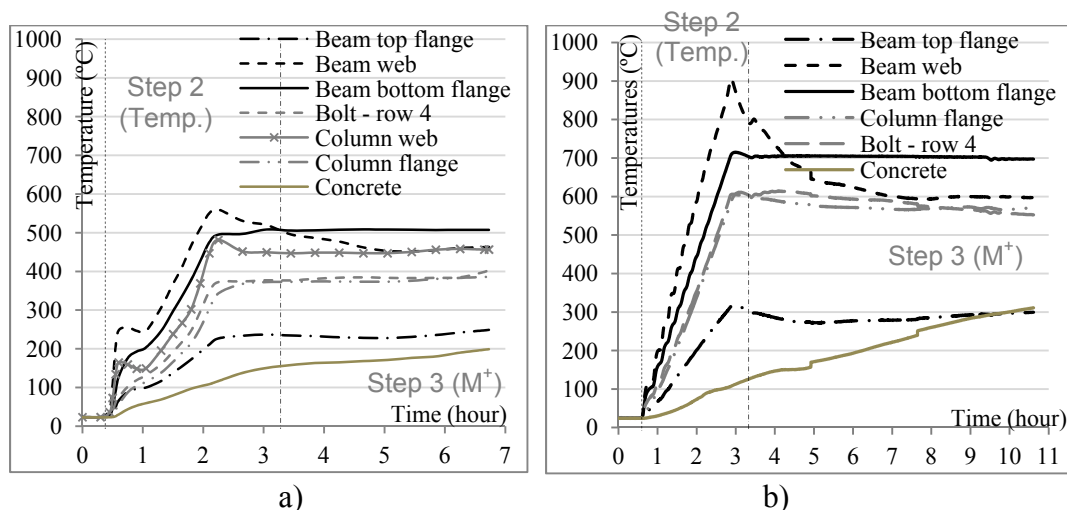


Figure 6. Evolution of the temperatures during a) test 2 at 500°C, b) test 6 at 700°C

Mechanical results and failure modes

Figure 7 depicts, for each test, the evolution of the bending moment versus a) the rotation of each connection, and b) the time. The joint rotation was estimated using the vertical displacements measured at: i) 1500 mm from the end-plate, and ii) at the column top. The reaction loads at the beams supports were used to calculate the bending moment.

In step 1, the initial hogging bending moment was applied: -501 kNm for reference test 1, and -236 kNm for tests 2 to 6. At the beginning of the heating phase (step 2), the column reaction load increased under thermal expansion effects and reached a maximum value: the minimum hogging bending moments reached around -500 kNm in tests 3, 5 and 6 (under 700°C), and around -357 kNm in tests 2 and 4 (under 500°C). Finally, this reaction load decreased because of the degradation of steel properties at elevated temperatures.

Under sagging bending moment (step 3), concrete crushing in compression was the first failure mode observed, due to the joint rotation and the resulting high compressive strain at the upper concrete surface. Bolts failures also happened later in

the bottom bolt rows in tests 1, 2 and 6, because of higher tensile forces under sagging bending moment (Haremza et al., 2013). The steel end-plates deformed in the bottom and centre part in all the tests, and showed a high ductility (Haremza et al., 2013); Figure 8 shows, as an example, the final deformations of test 6 (700°C and spring axial restraint).

The evolution of the bending moment at the joint versus the beam axial load is presented in Figure 9 for tests 4, 5 and 6. During the heating phase (step 2), due to the thermal expansions of beams, the beams ends moved in the outward direction, and compression loads were applied by the restraints. After the column loss (step 3), the axial restraints increased the compression loads because beams ends continued to move outwards.

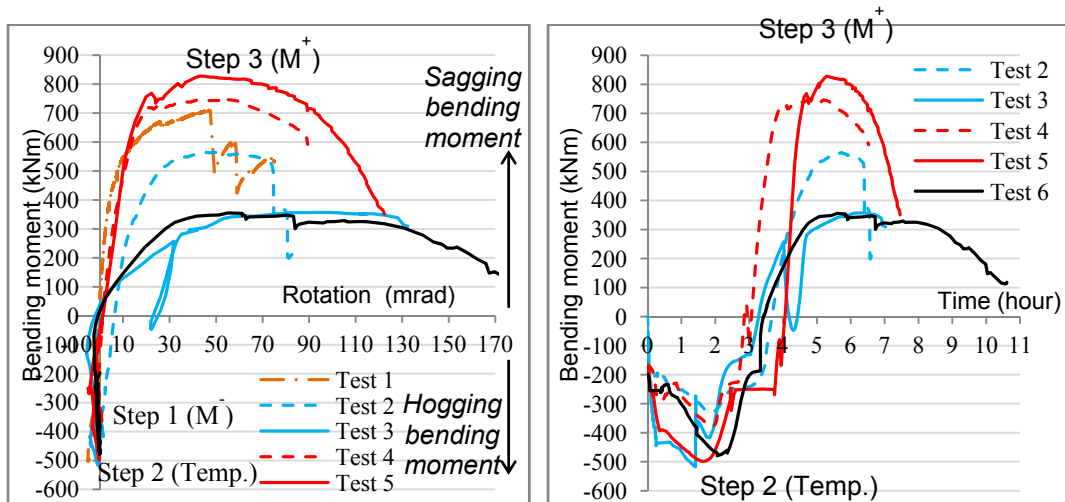


Figure 7. Joint bending moment versus a) rotation at the connection, b) time

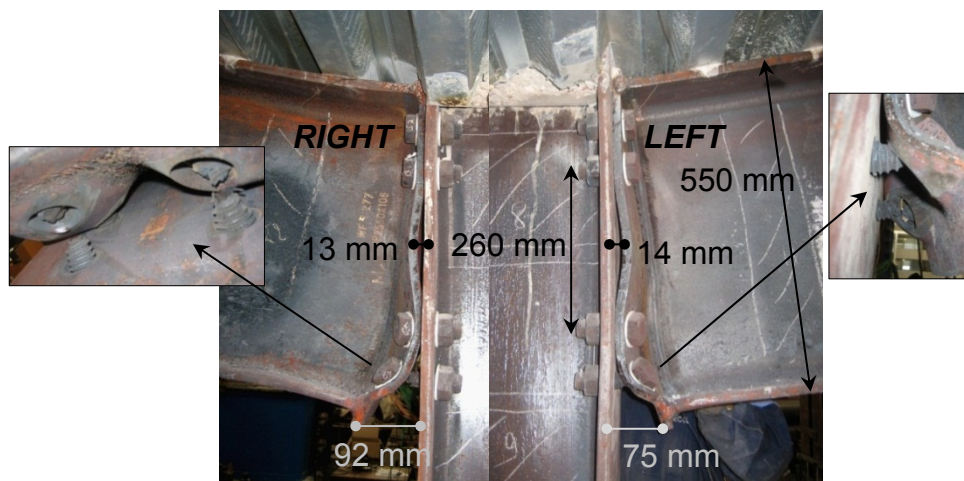


Figure 8. Deformations of the joint at the end of test 6 (700°C – spring axial restraint)

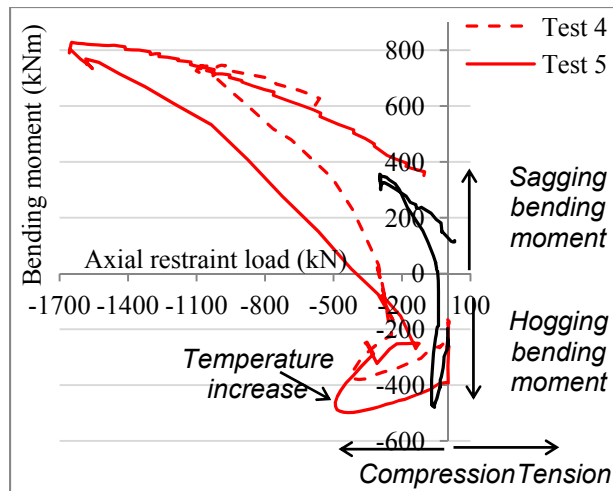


Figure 9. Joint bending moment versus axial loads at the joint

ANALYTICAL METHOD

This section presents an analytical method developed at the University of Liege to predict the resistance of steel or composite joints submitted to both an axial force and a bending moment at elevated temperature. The model was developed in Cerfontaine (2004) (see also Cerfontaine and Jaspart (2005)) for steel joints at ambient temperature. It was extended to composite joints in Demonceau (2008) (see also Demonceau and Jaspart (2010)), in which a formula giving the resistance of the “new” component “concrete slab in compression” was introduced. Within the Robustfire project, this model was extended to elevated temperature.

M-N interaction curve for joint resistance

When a joint is subjected to both bending moment and axial load, its resistance is represented by an interaction curve that can be evaluated following the procedure presented herein. The proposed analytical model is based on the component method (method recommended in the Eurocodes for the design of joints) and on the assumption that all components activated at failure are fully ductile, meaning a plastic redistribution of the forces is considered within the joint without any displacement limitations.

The joint is divided into different rows (Figure 10) that can be activated in tension (T) or in compression (C). The resistance of each row can be calculated using the component method (i.e. using the rules from Eurocode 3-1-8 (2005), Eurocode 4-1-1 (2004) or from Demonceau (2008) for the component “concrete slab in compression”), knowing that this resistance is given by the weakest component involved in the row. These rows are listed below for the considered joint, with the corresponding components:

- Row 1 (C): upper part of the slab in compression → concrete slab + column web
- Row 2 (T): slab reinforcement in tension

- Row 3 (C): lower part of the slab in compression → concrete slab + column web
- Row 4 (C): top flange in compression → beam flange and web + column web
- Row 5 (T): bolt row in tension → column flange + end-plate + bolts + beam web + column web
- Row 6 (T): bolt row in tension → column flange + end-plate + bolts + beam web + column web
- Row 7 (T): bolt row in tension → column flange + end-plate + bolts + beam web + column web
- Row 8 (T): bolt row in tension → column flange + end-plate + bolts + beam web + column web
- Row 9 (C): bottom flange in compression → beam flange and web + column web

For given bending moment and axial force, a row will be activated or not depending on the position of the neutral axis and whether the upper rows are in tension or in compression. In any case, the following equilibrium equations have to be fulfilled:

$$N = \sum_{\text{activated rows } i} F_i \quad (1)$$

$$M = \sum_{\text{activated rows } i} F_i \cdot h_i \quad (2)$$

Where:

- F_i is the force sustained by row i ; it is taken positive in tension.
- h_i is the distance from row i to the reference axis, positive for upper rows (the reference axis is arbitrary chosen at mid-height of the beam profile in Figure 10)

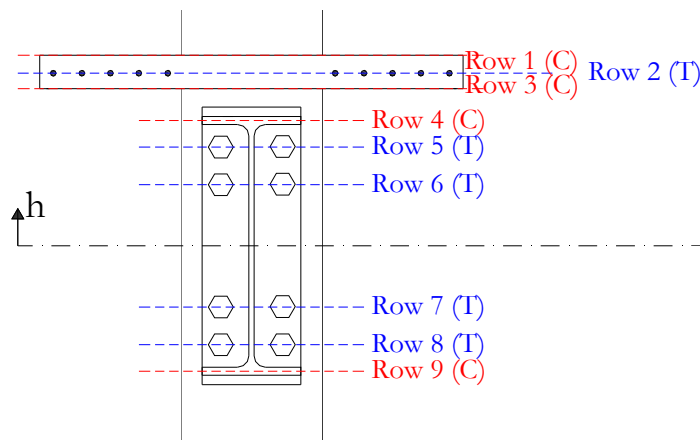


Figure 10. Rows and reference axis

Based on the previous considerations, the whole resistance curve can be established as follows. Considering first that the upper rows are in tension, the activated rows can easily be determined for any chosen position of the neutral axis (at the very top of the joint, between two successive rows or at the very bottom).

Knowing the activated rows, the corresponding loading (M,N) can be computed using the equilibrium equations given just above. Indeed, all activated rows are supposed to sustain a force equal to their resistance (plastic distribution) while the other ones sustain a force equal to zero. One particular point of the resistance diagram can thus be determined for each position of the neutral axis. The same can be done for lower rows in tension. Finally, the whole interaction curve is established. Figure 11 shows the nominal M-N resistance curve of the considered joint at ambient temperature and Figure 12 gives the position of the neutral axis corresponding to each particular point of the interaction curve.

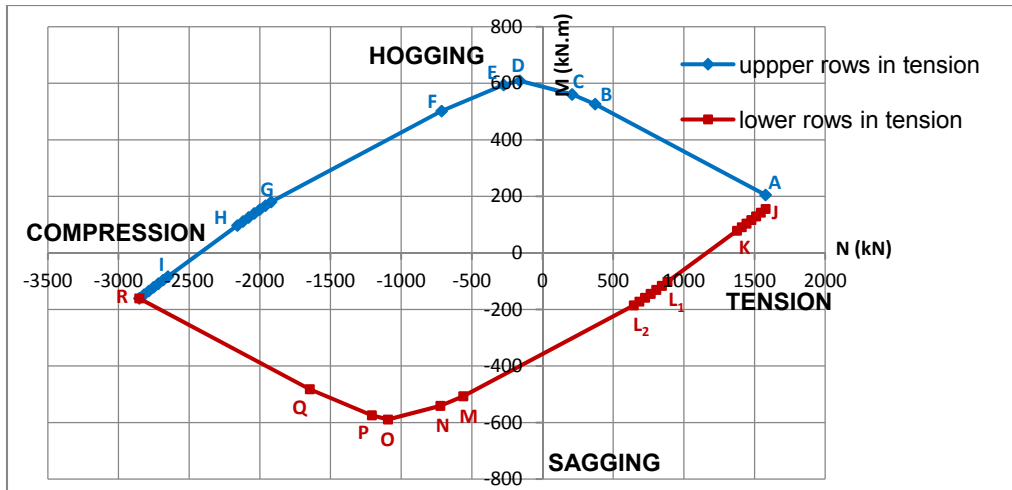


Figure 11. Nominal resistance curve at ambient temperature

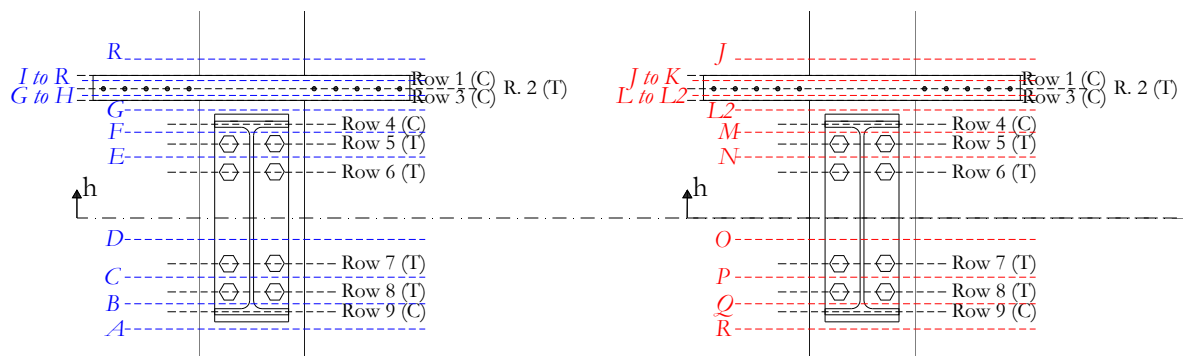


Figure 12. Position of the neutral axis for the particular points of the M-N resistance curve, for upper rows in tension (left) and for lower rows in tension (right)

The same procedure can be applied at elevated temperature provided the temperature distribution in the joint is known. Each component resistance is then simply evaluated based on the material resistance at its given temperature.

Validation of the analytical model against experimental tests

The aim of these analytical predictions is to be compared to the loading of the tested joints at failure. Consequently, the ultimate joint resistance should be predicted instead of the nominal resistance. That is why all safety factors were taken equal to 1,0 and the material ultimate resistances were considered instead of the yield resistances. The component temperatures were estimated based on the measurements made during the tests (they had to be extrapolated from the measure points which were not necessarily at the component locations).

The material resistances at elevated temperatures were evaluated based on the Eurocode rules and material tests when available (Haremza et al. 2013). The slab reinforcement remained at relatively low temperature during the tests and the ambient-temperature nominal resistance was thus considered (anyway, it is not activated under sagging moment). For concrete, the decrease in resistance with temperature was also given by the Eurocode but the ambient-temperature resistance was deduced from tests on concrete cubes at 20°C.

For each test, the loading M+N of the joint at failure has been identified. This loading corresponds to one particular point on a (M,N) diagram and can be compared to the analytically predicted M-N interaction resistance (based on the temperature distribution recorded at the moment the joint fails). As the temperature distribution during the tests was not exactly the same in the right and left joints, one analytical resistance curve was computed for each side.

Figure 13 and Figure 14 give examples of comparisons of the experimental resistances to the analytical predictions for Test 5 and Test 6 respectively (for the other tests, similar results are obtained (Haremza et al., 2012)).

For tests 4 and 5, two different analytical curves were predicted (see Figure 13). The first one is the normal one, in which the resistance of the component “concrete slab in compression” is computed considering a given effective width where the compression stresses mainly develop close to the contact zone between slab and column flange. As the slab was observed to be crushed along its whole width at the end of the tests, a second analytical curve was determined considering the whole width of the tested specimen slab as effective.

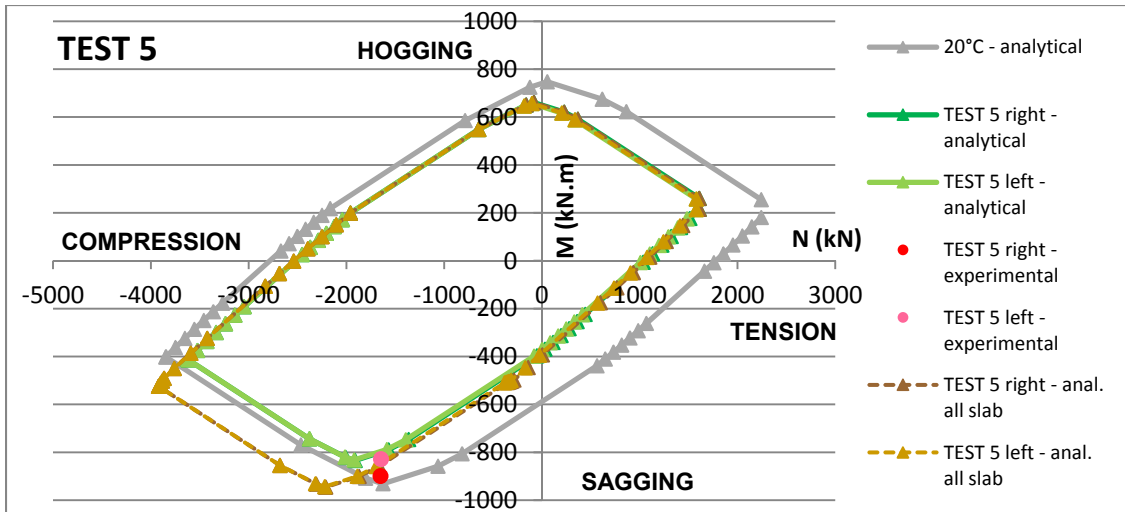


Figure 13. Comparison of the experimental resistances to the analytical curve for TEST 5

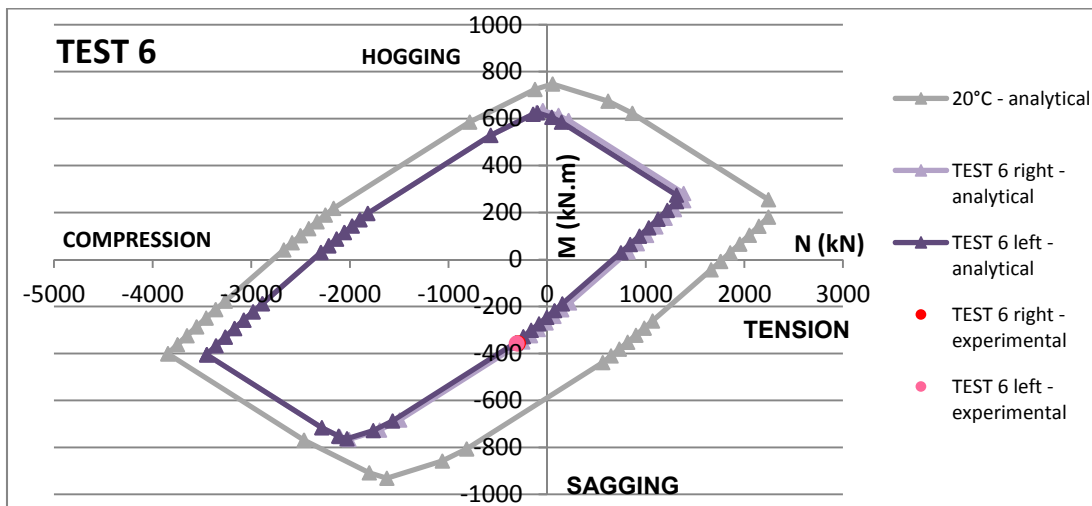


Figure 14. Comparison of the experimental resistances to the analytical curve for TEST 6

These comparisons show good agreement between experimental and analytical results, which validates the model predicting the M-N resistance curve for joints at elevated temperature.

CONCLUSIONS

Within this paper, investigations aiming at validating an analytical model to predict the M-N resistance of joints at elevated temperatures have been presented.

The proposed analytical model is based on the component method, method recommended in the Eurocodes for the characterisation of the joint mechanical properties. The comparisons of the analytical predictions to the experimental results have demonstrated the accuracy of the proposed method.

For the validation, the temperatures of the different joint components were extracted from the test measurements. In an actual design, the realisation of a 3D thermal analysis through an appropriate numerical tool is still needed. A perspective to the presented work is to propose one day a full analytical procedure, including the estimation of the component temperatures, in the image of what is already proposed for a specific joint configuration in Demonceau et al. (2009).

ACKNOWLEDGEMENTS

The research that produced these results was supported by funding from the European Community's Research Fund for Coal and Steel (RFCS) under grant agreement n° RFSR-CT-2008-00036, and also from Portuguese Foundation for Science and Technology (FCT) under the framework of the research project PTDC/ECM/110807/2009.

Material support provided by PECOL, FELIZ and MARTIFER are gratefully acknowledged.

REFERENCES

- Cerfontaine F. "Etude de l'interaction entre moment de flexion et effort normal dans les assemblages boulonnés". PhD thesis presented at the University of Liège. Belgium, 2004.
- Cerfontaine F. and Jaspart J.P. "Resistance of joints submitted to combined axial force and bending – Analytical procedures and comparison with laboratory tests". Eurosteel 2005 proceedings. Maastricht, The Netherlands, June 2005.
- Demonceau J.F. "Steel and composite building frames: sway response under conventional loading and development of membrane effects in beams further to an exceptional action". PhD thesis presented at the University of Liège. Belgium, 2008.
- Demonceau J.F., Hanus F., Jaspart J.P. and Franssen J.M. "Behaviour of single sided composite joints at room temperature and in case of fire after an earthquake", International Journal of Steel Structures, Vol. 9, pp 329-342, December 2009
- Demonceau J.F. and Jaspart J.P. "M-N interaction in beam-to-column joints – Development of a design model", SEMC 2010: The Fourth International Conference on Structural Engineering, Mechanics and Computation, Cape Town, South Africa, 6-8 September 2010.
- Demonceau J.F., Huvelle C., Comelieu L., Hoang L. V., Jaspart J.P., Fang C., et al. "Robustness of car parks against localised fire (Robustfire)", European Commission, Grant Agreement Number RFSR-CT-2008-00036, Final report, EUR 25864, 2013 (freely downloadable at <http://bookshop.europa.eu/>).
- EN 1991-1-2: 2002, "Eurocode 1: Actions on structures – Part 1-2: General actions – Actions on structures exposed to fire", European committee for standardization, November 2002.
- EN 1993-1-2: 2005, "Eurocode 3: Design of steel structures – Part 1-2: General rules – Structural fire design", European committee for standardization, April 2005.

- EN 1993-1-8: 2005, “Eurocode 3: Design of steel structures – Part 1-8: Design of joints”, European committee for standardization, May 2005.
- EN 1994-1-1: 2004, “Eurocode 4: Design of composite steel and concrete structures – Part 1-1: General rules and rules for buildings”, European committee for standardization, December 2005.
- Haremza C., Santiago A., Simoes da Silva L., Comelieu L. Hoang V. L., Demonceau J.F., Jaspart J.P., Fang C., Izzudin B., Elghazouli A., Nethercot D. and Obiala R. “Robustness of car parks against localised fire – Deliverable III”, European Commission, Grant Agreement Number RFSR-CT-2008-00036, 2012 (freely downloadable on <http://orbi.ulg.ac.be/handle/2268/126851>).
- Haremza C., Santiago A., Simões da Silva L. “Experimental behaviour of heated composite steel-concrete joints subject to variable bending moments and axial forces”, *Engineering Structures* 51, p150-165, 2013.

Evaluation of the Mechanical Properties of Steel and Polypropylene Fibre-Reinforced Concrete Used in Beam Column Joints

Nassim Ghosni¹; Bijan Samali²; and Hamid Valipour³

¹Ph.D. Candidate, Univ. of New South Wales, Sydney, NSW 2052, Australia. E-mail: n.ghosni@student.unsw.edu.au

²Institute and Program Director, Professor of Structural Engineering, Institute for Infrastructure Engineering, Univ. of Western Sydney, Australia. E-mail: b.samali@uws.edu.au

³Doctor of Structural Engineering, Univ. of New South Wales, Sydney, NSW 2052, Australia. E-mail: h.valipour@unsw.edu.au

Abstract

Investigations on improving characteristics of concrete structures utilizing Fibre Reinforced Concrete (FRC) have gained momentum in the last few decades. Using suitable fibres and additives in concrete to advance its performance is an important consideration in the construction industry. With regards to structural aspects of concrete, the important goal of this project is to improve the ductility of the concrete beam column joints, which helps eliminate or reduce the need for steel reinforcement. Fibres within the matrix, can bridge the cracks, which improves the performance of concrete matrix and results in a better stress bearing concrete material. This research project aims to investigate the effect of polypropylene (PP) and steel fibre volume percentage within the concrete on its mechanical properties. Concrete fresh properties as well as hardened properties have been tested and evaluated to work out the best fibre percentage to be added to concrete structure. From among the trial mix designs, five sets of FRC have been fully tested for the mechanical properties and also evaluated for the beam column concrete joint behaviour. Slump, mass per unit volume and air content have been tested to work out the fresh properties of concrete. 7 and 28-day compressive strength and also indirect tensile tests have been performed on the hardened concrete the results of which are presented in this paper. By using 0.5% by volume fraction of 30mm steel fibre, the indirect tensile strength of concrete has increased by 21%; however, when 1% of steel fibre has been utilized, about 45% increase has been observed. Furthermore, a sample of the joint test conducted will be presented in this work to illustrate the finite goal of this project.

INTRODUCTION

Concrete is inherently a brittle material with highly weak post peak behaviour. The higher the concrete strength, the steeper the trend of failure in the post peak behaviour of concrete will be (Swamy 1986). It is possible to improve the mechanical properties of concrete by adding steel fibres or some other types of fibre such as synthetic fibres. Fibres act as secondary reinforcement in the concrete structure to restrain crack propagation. Incorporation of these fibres can influence the behaviour of concrete and change the sudden failure trend in to a gradual failure with post peak

characteristic. Therefore, these fibres are likely to transform concrete from brittle in to a more ductile material. It has been shown (Qian & Stroeven 2000) that steel fibres can greatly influence the load bearing capacity in larger loads. In another research (Ghosni, Samali & Vessalas 2013), it has been discussed that in small loadings of structure where concrete material itself is in the tensile load bearing stage, PP fibres can significantly improve matrix properties.

Literature (Chanh 2004) shows that the workability of steel fibre reinforced concrete (SFRC) is significantly affected by the aspect ratio (l/d) of the steel fibres in the mix and SFRC's workability has found to decrease with the increase in aspect ratio of the steel fibres. With regards to hardened concrete properties, previous research explain that introducing a certain percentage of steel fibres to plain concrete does not alter the pre-peak compressive strength of concrete substantially (Fanella & Naaman 1985). However, (Song & Hwang 2004) reported that the compressive strength of high strength fibre reinforced concrete (HSFRC) increased with the addition of hooked-end steel fibres by 7.1% with a volume fraction (V_f) of 0.5%, 11.8% at 1.0% fraction, 15.3% at 1.5% fraction, and a drop to 12.9% at 2.0% fraction. It was concluded that 1.5% of volume fraction was the maximum improvement for the compressive strength in HSFRC. A 4.6% increase in compressive strength was observed by (Thomas & Ramaswamy 2007) for HSFRC with compressive strength of 85MPa and fibre volume fraction of 1.5% hooked-end steel fibres.

(Olivito & Zuccarello 2010) found that their results give no real convincing evidence that the addition of steel fibres had a significant effect on the compressive strength but it was observed that SFRC had changed its failure mode from brittle to a ductile failure. These results show signs that the steel fibres considerably increase the post-cracking ductility or energy absorption of the material.

Unlike compressive strength of SFRC, the addition of steel fibres in plain concrete increases the split tensile strength of the material. When hooked-end steel fibres with length (L_f) of 30mm and aspect ratio of 55 were used, the effect of the steel fibres varied across different concrete strengths. The increase of split tensile strength of SFRC with a fibre volume (V_f) of 1.5%, by 38.2% in normal-strength concrete (35 MPa), 41.2% in moderately high-strength concrete (65 MPa) and 38.5% in high-strength concrete (85 MPa) (Thomas & Ramaswamy 2007). Previous testing has been carried on the strength of high strength fibre reinforced concrete (HSFRC) through splitting tensile test. Song & Hwang (2004) found that when using hooked-end fibre with an average L_f of 35mm and aspect ratio of 64, the splitting tensile strength of HSFRC improved with the increase of volume fraction (test limited to a V_f of 2%). The splitting tensile strength of steel fibre reinforced concrete is strongly influenced by the number of fibres intersecting the failure plane and their orientation (Potrzebowski 1983).

Researches on PP fibres also report promising results with regards to concrete mechanical properties (Ghosni, Vessalas & Samali 2013). As regards to compressive strength, it has been reported (Mindess & Vondran 1988) that a 25% increase in compressive strength at 0.5 volume percentage of the polypropylene. In another research (Massoud, Abou-Zeid & Fahmy 2003), the role of polypropylene fibers is stated insignificant in differentiating compressive strength using the same fibre

volume. It is concluded that below the 0.1% volume percentage dosage rate, fibres have no statistically significant effect on the characteristics of the hardened concrete (Midwest-Research-Institute 1994).

In PP fibre mixes, workability of fresh concrete has been reported to be reduced (Bayasi & Zeng 1993). With 0.5% by volume of 12.7 mm and 19 mm PP fibres, slump test results showed 11.6% and 88.5% reduction, respectively. Other research works have also reported that fibre addition can affect concrete slump noticeably (Al-Tayyib et al. 1988; Pantazopoulou & Zanganeh 2001). By adding 0.4% by weight of PP fibres, a large reduction in compressive strength and also workability is reported (Barr & Newman 1985). According to Siddique et al. (Siddique, Khatib & Kaur 2008) PP fibers have a non-desirable effect on the air content of concrete. With the addition of PP fibers, air content of concrete has been reported to increase.

MATERIAL AND METHODOLOGY

Two types of fibre have been studied in this research; steel fibres and polypropylene fibre. It has been indicated in literature (Qian & Stroeven 2000) that different type and different length of fibres can perform differently in the concrete matrix. Softer fibres (PP fibres) control crack initiation and steel fibres, which are larger and stronger fibres, can control larger cracks. Hooked steel fibres (30 mm and 60 mm), PP fibre (65 mm), fibrillated PP fibre (19mm), monofilament PP fibre (18mm) have been introduced to the mix with 0.5% and 1% volume of the whole mix. Fibre characteristics are described in Table 1. Moreover, two control mixes, one with 100% PC (C) and one with 70% PC and 30% FA (CF) are tested and compared to FRC results . These mixes also include the addition of 30% fly ash (FA) for partial replacement of Portland cement (PC) and utilisation of manufactured coarse and fine sands to replace natural coarse and fine sand, respectively, to aim for producing a 'greener' concrete. Water ratio to cementitious material of the mix is fixed at 0.35 and a target slump of 80 ± 20 is set. Water used for concrete mix is drinking tap water.

In the fresh concrete properties tests all the procedures are followed according to Australian Standards. For freshly mixed concrete properties, AS 1012.3.1-1998 was used for the measurement procedures. Wet density and the air content were additionally determined in accordance with the test method requirements of AS 1012.5-1999 and AS 1012.4.2-1999, respectively. For vibration and compaction of concrete, the procedure listed in AS 1012.8.1-2000 is followed and all moulded test specimens were externally vibrated using a vibration table. Compressive strength testing was carried out after 28 and 56 days ageing. A universal testing machine applying axial loads on 100×200 mm cylinders were used.

Table 1: Fibre type and Characteristics

Fibre	Density [kg/m ³]	Diameter [mm]	Cut length [mm]	Aspect ratio	Tensile strength [MPa]
Fibrillated PP (PF)	910.0	0.055	19	345	~ 600
Monofilament PP (PM)	910.0	0.022	18	818	~ 600
Structural PP (PP)	905.0	0.850	65	75	250
Hooked Steel (SF30)	7800	0.750	30	40	1050
Hooked Steel (SF60)	7800	0.750	60	80	1225

MATERIAL TEST RESULTS AND DISCUSSIONS

Data from tests relating to the fresh properties of FRCs are presented in Table 2. The amount of High Range Water Reducer (HWR) used in each mix has been different as a slump of 80mm was targeted. Although a few of the mixes couldn't reach that slump, even with high amounts of HWR, most mix designs showed promising results in terms of fresh properties. Mass per unit volume of the concrete mixes has also been measured to have the volume density of the engineered concrete. Usually, the volume density of conventional concrete is approximately 2,400 to 2,500 kg/m³; this property is measured then to evaluate the effects of fibre and on concrete density and also use this value for further calculations.

Table 2: Fresh Properties

Mix ID	W/C	Slump [mm]	HWR [ml/ m ³]	AC [%]	Volume Density [Kg/m ³]
C	0.35	60	1317	0.8	2510
CF	0.35	75	1000	1.0	2450
PM0.5	0.35	60	1243	1.9	2380
PM1	0.35	55	1615	2.6	2290
PF0.5	0.35	80	1150	1.1	2380
PF1	0.35	65	1846	1.5	2290
PP1	0.35	45	3250	2.0	2418
SF30-0.5	0.35	90	1333	1.1	2470
SF30-1	0.35	60	2000	2.0	2490
SF60-0.5	0.35	90	2125	2.0	2490

Results of Table 2 show that in mixes where fibre is present, the amount of HWR needed to reach the target slump is generally higher. Therefore, it can be concluded that fibre addition decrease the workability of the mix. Furthermore, the amount of HWR needed for lower percentages of SFRCs is moderately lower than that of higher percentages. In general, the amount of HRW needed to be added to SFRC is slightly higher than that of PP FRC comparing the same volume percentage of fibre usage. The amount of HWR used in monofilament containing mixes was much higher than that of fibrillated fibres which show that monofilament PP fibres decrease the workability of the mix more than fibrillated PP fibres. Furthermore, visual inspection of the mixes showed that by adding HWR to monofilament FRCs, there is a risk of segregation before getting the desired slump especially in higher percentages. This is also true when 1% of longer steel fibres are added to the concrete mix. In mixes where PP fibres are present, a decrease in volume density is observed. This is most probably due to the lower volume density of PP fibres.

Results of tests under compressive load are illustrated in table 3. Regarding the effect of PP fibres on hardened properties of concrete some conclusions are presented. Considering the compressive strength properties it is observed that in PP FRCs, this parameter has slightly decreased, except for PM1 mix, whereas in SFRCs, the reverse is true. With regards to the indirect tensile tests, results show that both fibres help with enhancing the performance of concrete matrix except for monofilament PP fibre. Where 1% of 30 mm steel fibre is used in the concrete matrix, the splitting tensile strength has increased by about 182% which can considerably be beneficial to improve properties of concrete.

Table 3: Hardened Properties

Mix ID	28D Compressive Strength [MPa]	56D Compressive Strength [MPa]	28D Indirect Tensile [MPa]
C	73.0	76.5	4.5
CF	61.5	70.3	4.5
PM0.5	56.0	62.1	4.2
PM1	43.5	49.0	3.8
PF0.5	56.5	63.4	4.3
PF1	58.0	66.0	5.2
PP1	50.7	55.5	5.4
SF30-0.5	64.7	85.5	5.7
SF30-1	65.5	88.7	8.2
SF60-0.5	60.4	76.5	7.8

STRUCTURAL TEST RESULTS AND DISCUSSIONS

As mentioned before, the results of this study are incorporated in structural applications of concrete to enhance the ductile behaviour of concrete material. This can help with reducing the amount of steel reinforcement used in the structure. The fibres percentages and types with better performance in material characteristics are tested in reinforced beam under 4 point static, 3 point cyclic loads and also beam-column exterior joints. Comparative results of these applications are very promising. For example, where 1% fibrillated PP fibre has been incorporated; the ductility of concrete beam has almost doubled. The performance of this concrete under cyclic loadings applied to beam-column joints have yielded enhanced performance. Where fibres are added to concrete, the stirrups are eliminated in the joints. A sample of Load-deflection curve is presented in Figure 1. Two of the structural joints lack the typical stirrup as the reinforcement in the joint for the seismic design. It is observed that the performance of the structural element without stirrup but with fibres is comparable to that of a conventional joint with stirrups.

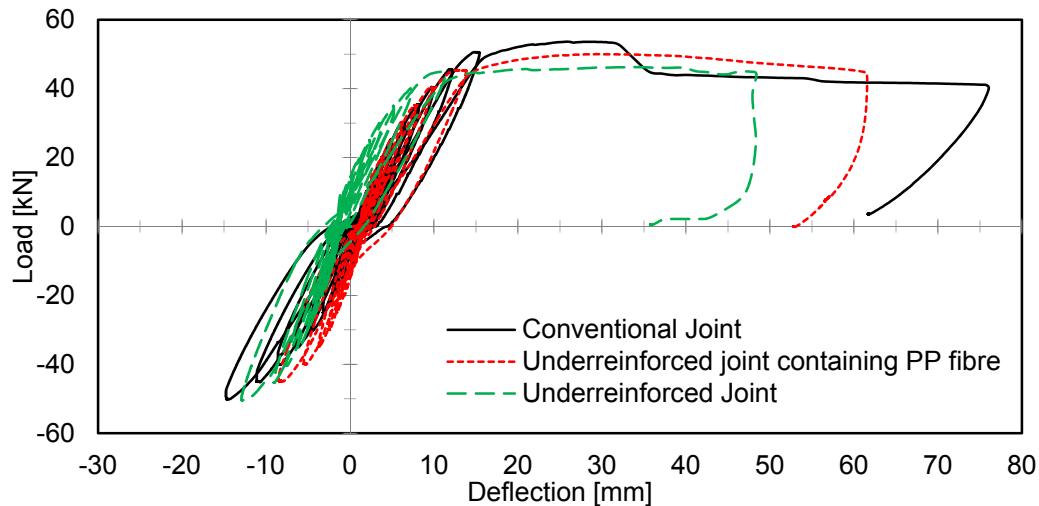


Figure 1: Exterior joint load deflection curves under cyclic loading

CONCLUSION

An efficient and thorough investigation on different aspects of PP FRC and SFRC is conducted in this project, the results of which are very promising in terms of both material and structural applications of concrete. This study also considers the effect of adding 30% FA in the concrete mix as a replacement of PC to help achieving greener concrete and environmentally friendly buildings with sustainability. PP and steel fibres were added to the mix by 0.5% and 1% of the volume of the mix. Two types of PP fibre and two types of steel fibre have been used and the results are compared.

The outcome of this research work can conclude that although adding fibres may affect the workability of concrete material but this can be managed by using HWR to maintain the desired slump. Adding PP fibres do not enhance the compressive strength of the mix but addition of steel fibres can noticeably change this property of concrete. Where 1% of 30 mm steel fibre is used, the compressive strength of FRC has increased.

Adding fibres to concrete used in structural joint show that the performance of under reinforced joint can be significantly maintained.

REFERENCES

- Al-Tayyib, A.J., Al-Zahrani, M.M., Rasheeduzzafar & Al-Sulaimani, G.J. 1988, 'Effect of polypropylene fiber reinforcement on the properties of fresh and hardened concrete in the Arabian Gulf environment', *Cement and Concrete Research*, vol. 18, no. 4, pp. 561-70.
- Askari, M., Markazi, A.H.D., 2012, 'A new evolving compact optimised Takagi-Sugeno fuzzy model and its application to nonlinear system identification', *International Journal of Systems Science*, Vol.43, no4, pp776-785.
- Barr, B. & Newman, P.D. 1985, 'Toughness of polypropylene fibre-reinforced concrete', *Composites*, vol. 16, no. 1, pp. 48-53.

- Bayasi, Z. & Zeng, J. 1993, 'Properties of Polypropylene Fiber Reinforced Concrete', *American Concrete Institute*, vol. 90, no. 6, pp. 605-10.
- Chanh, V. 2004, 'Steel fiber reinforced concrete', paper presented to the *Faculty of Civil Engineering Ho chi minh City university of Technology*.
- Fanella, D.A. & Naaman, A.E. 1985, 'Stress-strain properties of fiber reinforced mortar in compression', *Journal of the American Concrete Institute*, vol. 82, no. 4, pp. 475-83.
- Ghosni, N., Samali, B. & Vessalas, K. 2013, 'Energy Absorption And Flexural Toughness Evaluation of Fibre Reinforced Polymer Modified Concrete', paper presented to the *International Conference on Fracture Mechanics of Concrete and Concrete Structures, FRAMCOS 8, Spain, Toledo*.
- Ghosni, N., Vessalas, K. & Samali, B. 2013, 'Evaluation of fresh properties effect on the compressive strength of polypropylene fibre reinforced polymer modified concrete', *From Materials to Structures: Advancement through Innovation*.
- Massoud, Abou-Zeid & Fahmy 2003, '*POLYPROPLYNE FIBERS AND SILICA FUME CONCRETE FOR BRIDGE OVERLAYS*', *Submitted for Presentation and Publication In the 82nd Annual Meeting of the Transportation Research Board*.
- Midwest-Research-Institute 1994, *Emission Factor Documentation for AP-42 Section 11.6, Portland Cement Manufacturing*, vol. Final Report, U. S. Environmental Protection Agency Office of Air Quality Planning and Standards Emission Inventory Branch.
- Mindess, S. & Vondran, G. 1988, 'Properties of concrete reinforced with fibrillated polypropylene fibres under impact loading', *Cement and Concrete Research*, vol. 18, no. 1, pp. 109-15.
- Olivito, R.S. & Zuccarello, F.A. 2010, 'An experimental study on the tensile strength of steel fiber reinforced concrete', *Composites Part B: Engineering*, vol. 41, no. 3, pp. 246-55.
- Pantazopoulou, S.J. & Zanganeh, M. 2001, 'Triaxial Tests of Fiber-Reinforced Concrete', *Journal of Materials in Civil Engineering*, vol. 13, no. 5, pp. 340-8.
- Potrzebowski, J. 1983, 'The splitting test applied to steel fibre reinforced concrete', *International Journal of Cement Composites and Lightweight Concrete*, vol. 5, no. 1, pp. 49-53.
- Qian, C. & Stroeven, P. 2000, 'Fracture properties of concrete reinforced with steel-polypropylene hybrid fibres', *Cement and Concrete Composites*, vol. 22, no. 5, pp. 343-51.
- Siddique, R., Khatib, J. & Kaur, I. 2008, 'Use of recycled plastic in concrete: A review', *Waste Management*, vol. 28, no. 10, pp. 1835-52.
- Song, P.S. & Hwang, S. 2004, 'Mechanical properties of high-strength steel fiber-reinforced concrete', *Construction and Building Materials*, vol. 18, no. 9, pp. 669-73.
- Swamy, R. 1986, 'Properties of High Strength Concrete', *Cement , Concrete and Aggregate*, vol. 8, no. 1, p. 9.
- Thomas, J. & Ramaswamy, A. 2007, 'Mechanical Properties of Steel Fiber-Reinforced Concrete', *Journal of Materials in Civil Engineering*, vol. 19, no. 5, pp. 385-92.

Analyses of the Rotational Capacity of Composite Connections for Plastic Design

Oliver Hechler¹; Christoph Odenbreit¹; and Jean-Pierre Jaspart²

¹ArcelorMittal Chair of Steel and Façade Engineering, Univ. of Luxembourg, rue Richard Coudenhove-Kalergi 6, L-1359 Luxembourg-Kirchberg, Luxembourg.

E-mail: Christoph.Odenbreit@uni.lu

²Dept. of ArGEnCo, Liège Univ., MS²F Division, chemin des Chevreuils 3, 4000 Liège, Belgium. E-mail: Jean-Pierre.Jaspart@ulg.ac.be

Abstract

The demand for economic and eco-efficient solutions in construction industry is particularly enforcing efficient design and construction methods. The design of composite construction according to the plastic hinge theory in combination with semi-rigid joints provides one contemporary promising answer to these demands. This combination enables to mobilize almost all cross section and system reserves. However, the capability for redistribution of the bending moment from internal support to mid-span, to activate these system reserves, requires sufficient rotation capacity of the composite beam and, especially, the connections. This paper presents design guidance on plastic and robust design of composite beams with semi-rigid composite connections with special focus on the influence of the reinforcement (ratio, diameter and type). With the provision of an engineering logic, new opportunities to design elegant and slender structures are given to engineers in a simple way.

INTRODUCTION

In composite construction, as for steel construction, the economic execution of the connection between the steel beam and the column is of decisive importance regarding the efficiency of the total slab system. Costly welding and precision work have to be avoided. Generally, composite connections can be designed either fully-rigid, semi-rigid or pinned. Figure 1 shows typical designs for moment resisting composite connections.

The fully rigid connection, providing full strength, has to have at least the same bending capacity as the connected beam. This means, that the steel-part of the connection has to offer not less than the bending resistance of the connected steel beam itself.

The pinned connection is the simplest solution. However, rotation and crack width control at the connection is challenging and the resistance of the section in negative bending is lost.

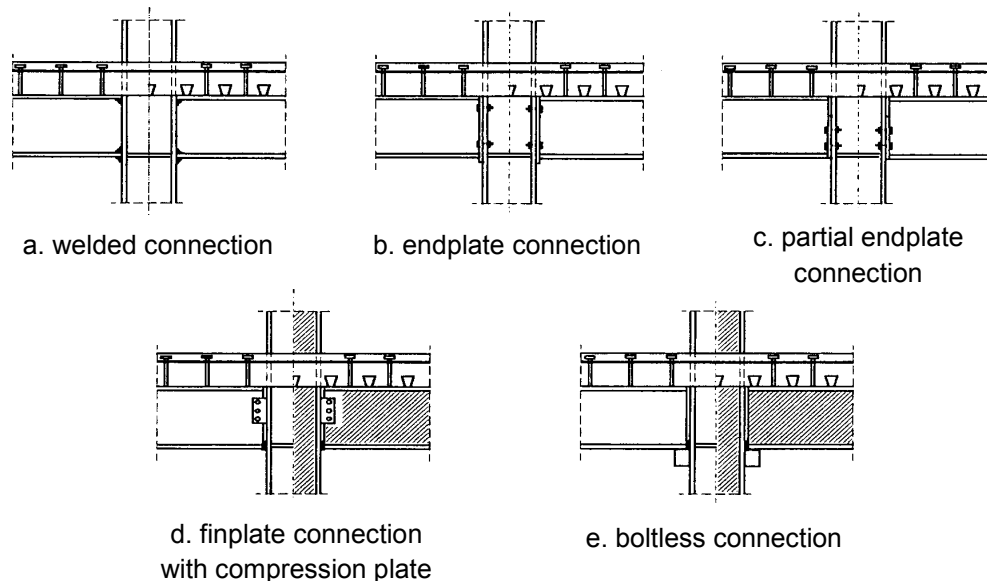


Fig. 1 – Types of composite connections [Odenbreit 2000]

The semi-rigid, partial strength, composite connection is an efficient and economic intermediate solution between fully rigid and pinned connections with following advantages:

- a) Compared to the pinned connection:
- An optimization of the beam section is possible due to the activation of an additional bending resistance in the connection;
 - The deflection in mid-span is reduced due to the restraint connection;
 - The crack width in the connection zone in the serviceability limit state is controlled (reinforcement design).
- b) Compared to the fully-rigid connection:
- Expensive construction details may be omitted (like e.g. stiffeners in the connections' steel part) due to the reduced negative bending moment resulting from redistribution of moment from connection to mid-span; the detailing and construction are simplified;
 - Less reinforcement is required for connection design.

Particularly the combination of semi-rigid joints and design with the plastic hinge theory bears a high potential to gain economic structures. Plastic hinges form generally at the supports where the composite connection is located. Therefore the bending resistance of the connection is reached before the bending resistance at mid-span is fully exploited. To activate this full moment capacity, redistribution of the moments from the support into the field is necessary. This redistribution of moments increases the rotation in the connection.

Investigations [Odenbreit 2000] showed, that beams with composite connections have the potential to reach their full plastic design capacity. However, the moment redistribution requires sufficient plastic rotation capacity in the connection. Thus, the relevant components of the connections have to be designed with enough ductile behaviour. One decisive component on the rotational capacity is

the ultimate strain capacity of the concrete chord in the negative bending moment area close to the column.

Designers generally lack information how to account for ductile behaviour and how to design semi-rigid connections. Therefore this paper presents guidance on the design of semi-rigid composite connections with special focus on the influence of the reinforcement (type and ratio) on its rotational capacity.

DESIGN OF SEMI-RIGID COMPOSITE CONNECTIONS

The general design approach is to account for the stiffness of the connection for the calculation of the internal forces and subsequently check whether the design loads are lower than the resistance envelope as well as whether the rotation due to the loads Φ_{Ed} is not exceeding the ultimate rotation Φ_u of the connection. Therefore an engineering logic has been prepared and its steps are listed in the following.

(1) The bending stiffness of the composite section in uncracked (EI_1) and cracked (EI_2) conditions as well as the plastic moment resistance at mid-span $M_{F,pl,Rd}$ need to be calculated, see Figure 2.

(2) The bi-linear spring with the rotation stiffness S_j [Eq. (3)], plastic moment resistance $M_{j,Rd}$ on the basis of Eurocode 3 [EN 1993-1-8, 2005] with consideration of the reinforcement and the ultimate rotation capacity Φ_u [Eq. (4)] are to be determined.

Semi-rigid, partial-strength connections should be accounted for in the structural analysis. Consistency is achieved by implementing a spring element in the structural system at the connection (see S_j in Figure 2) to account for the connections' stiffness. To consider the redistribution of moments, the calculation of the moment resistance capacity and related loading should be done according to step (3) and (4).

It is to be remarked, that the bi-linear curve in step (2), see Figure 3, is representing the non-linear rotational behaviour of the connection, see Figure 6, in a simplified way. This simplification has been validated by numerical investigations to be sufficiently exact for the determination of the displacements at serviceability limit state as well as the load-bearing capacities at ultimate limit state [Odenbreit 2000].

(3) The internal forces for the structural system, given in Figure 2, with EI_1 , EI_2 and the spring stiffness S_j [Eq. (3)] are to be calculated with a linear-elastic analysis using the design limit of the connection resistance $M_{j,pl,Rd}$. From this analysis the related loading q_{el} , the moment in mid-span $M_{F,el}$ and the connection rotation $\Phi_{j,el}$ are to be estimated.

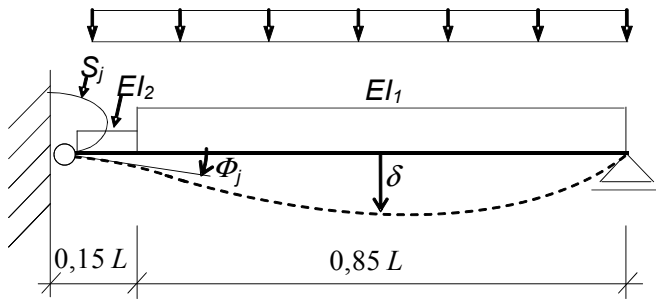


Fig. 2 – Consideration of the semi-rigid, partial strength connection in the structural system

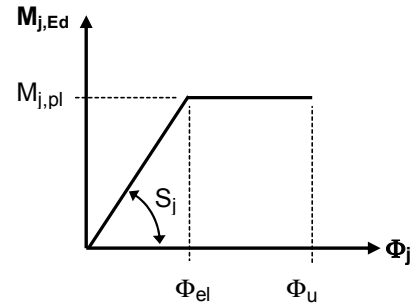


Fig. 3 – Bi-linear rotational curve of the connection for the static analysis

(4) In this step, the load will be increased from q_{el} to q_{pl} until $M_{F,pl,Rd}$ is reached to account for the redistribution of moment from support to mid-span after a plastic hinge has been formed at the connection, see Figure 4. Therefore the internal forces for the structural system given in Figure 2 with EI_1 , EI_2 and by neglecting the connection stiffness ($S_j = 0$) are calculated according to the plastic hinge theory with a limit of the resistance in mid-span of $\Delta M_F = M_{F,pl,Rd} - M_{F,el}$, the related loading q_{pl} and the connection rotation $\Phi_{j,pl}$ is so obtained.

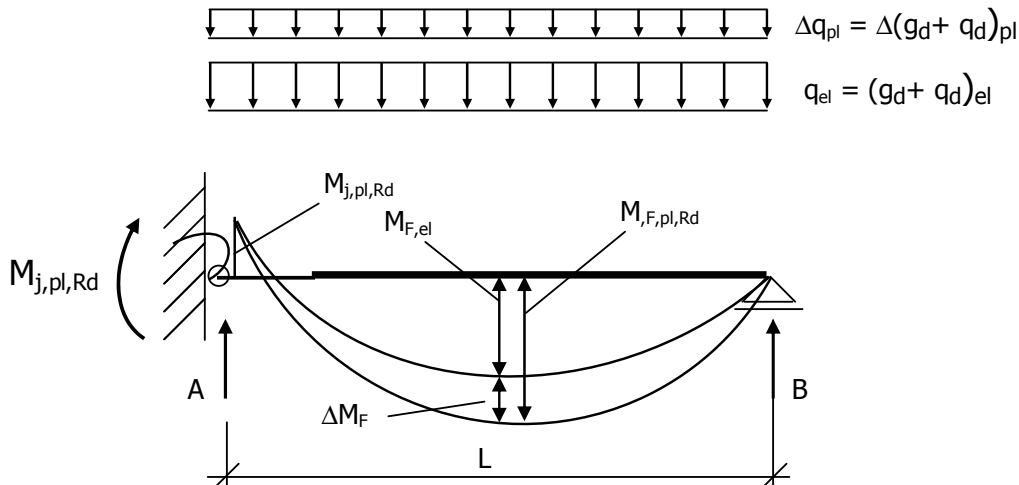


Fig. 4 – Illustration of the gain in design resistance from elastic analysis to plastic hinge theory for systems with semi-rigid connection

(5) Finally the following checks are to be performed to conclude the design:

$$q_{Ed} \leq q_{Rd} = q_{el} + q_{pl} \tag{1}$$

$$\Phi_{j,el} + \Phi_{j,pl} \leq \Phi_u \tag{2}$$

THE ROTATIONAL STIFFNESS

The rotational stiffness of the connection can be obtained through tests or by applying the component method given in Eurocode 3 [EN 1993-1-8, 2005]. In addition, investigations have been performed to obtain a relation between the stiffness S_j of the composite connection, see Figure 6, the stiffness EI_2 of the connected composite beam and the connection type. According to these ones, the following relation can be derived through the definition of a non-dimensional stiffness $s_{j,nd}$ [Odenbreit, 2000]:

$$S_j = \frac{s_{j,nd} \cdot EI_2}{L_j} \tag{3}$$

with S_j = stiffness of the joint according to Figure 3 to be implemented as spring stiffness in the static system given in Figure 2, EI_2 = bending stiffness of the composite beam in negative bending, L_j = length of the composite connection, see Figure 5 [Odenbreit 2000] and $s_{j,nd}$ = non-dimensional stiffness parameter of the connection.

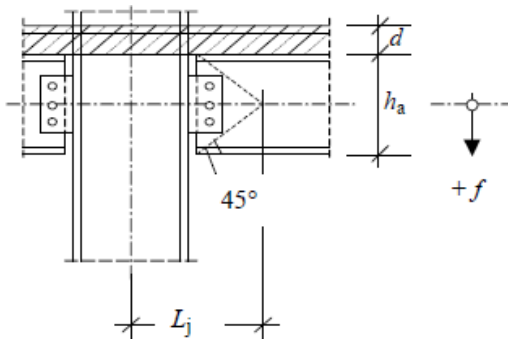


Fig. 5 – Definition: length of composite connection L_j [Odenbreit 2000]

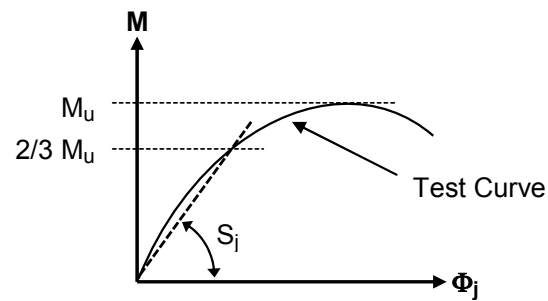


Fig. 6 – Definition: spring stiffness S_j from experimental data [Odenbreit 2000]

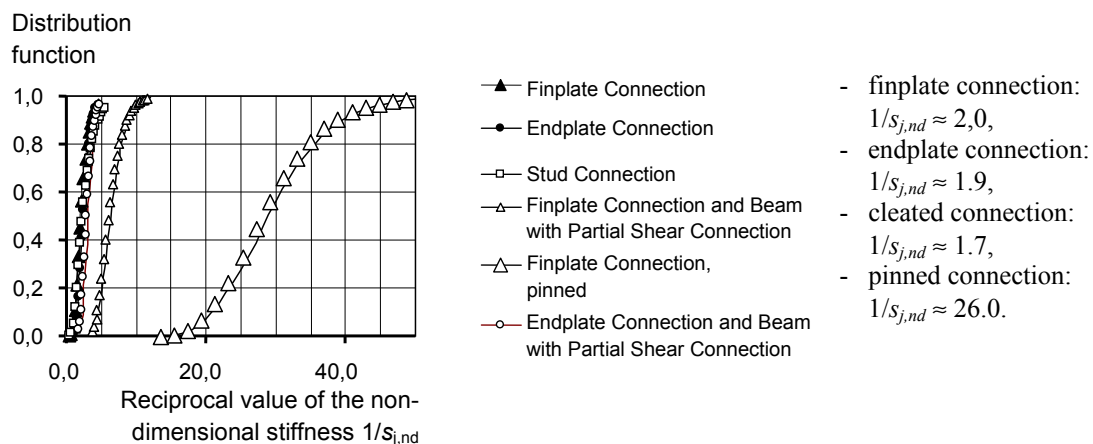


Fig. 7 – Distribution function of the non-dimensional stiffness $s_{j,nd}$ and determined values for standard connections

The non-dimensional stiffness $s_{j,nd}$ has been empirically derived from statistical evaluation of 56 tests on different composite connections. It corresponds to the stiffness of the connection at 2/3 of the connections' ultimate moment capacity M_u , see Figure 6, and has been derived from the rotation-moment curves [Odenbreit 2000]. The distribution function of $s_{j,nd}$ is presented in Figure 7 and specific values for standard connections are listed.

THE PLASTIC BENDING RESISTANCE OF THE CONNECTION AND THE ULTIMATE ROTATION CAPACITY

The plastic bending resistance $M_{j,pl}$ is e.g. determined with the help of the component method given in Eurocode 3 [EN 1993-1-8, 2005] and additional consideration of the reinforcement bars in the concrete chord. In principle, the lower flange of the steel beam at the connection has to take over the compression forces and the reinforcement in the concrete slab the tension forces. In addition, the semi-rigid, partial-strength composite connection has, because of its reduced bending resistance, to assure the redistribution of a substantial part of the bending moment towards mid-span. The reduced plastic bending resistance in the connection is to be kept constant during plastic rotation (between $\Phi(M_{j,pl})$ and Φ_u) in the plastic hinge, see Fig. 4.

The mentioned plastic rotation requires a considerable ductility in the connection. Brittle failure of any component must be avoided. To assure this ductility:

- The resistance of the steel plate must be lower than the shear resistance of the bolts,
- The bending resistance of the connection plate must be lower than the tension resistance of the bolts and
- The reinforcement in the concrete slab may not fail in a brittle way.

For the component "reinforced concrete in tension", the maximum rotation capacity Φ_u , which can be provided, may be assessed with the following equation:

$$\Phi_u = \frac{\varepsilon_u \cdot L_j}{h_j} \quad (4)$$

with L_j = length of the concrete component of the connection, h_j = height of the connection and ε_u = ultimate strain of the reinforced concrete.

The ultimate strain in the reinforcement can be derived by [Odenbreit 2000]:

$$\varepsilon_u = \varepsilon_{s,y} - \beta_t (\varepsilon_{sr2} - \varepsilon_{sr1}) + \delta \left(1 - \beta \frac{\sigma_{sr1}}{f_{tk}} \right) (\varepsilon_{s2} - \varepsilon_{s,y}) \quad (5)$$

with $\varepsilon_{s,y}$ = strain in the reinforcement at yield strength, $\beta_t = 0.25$ (for a permanent load and alternation of load), ε_{sr1} = strain in the reinforced concrete member, when the tension strength f_{ctm} of the concrete is reached, but the concrete is still uncracked, σ_{sr1} = stress in the reinforcement at the first crack ε_{sr2} = strain in the reinforcement in the crack, when the tension strength of the concrete f_{ctm} is slightly exceeded (ε_{sr2} roughly estimated to be 0.0001 [Odenbreit 2000]), δ = factor to consider the different types of ductility of the reinforcement, f_{tk} = tension strength of the reinforcement and

β = factor to distinguish between mesh and bar reinforcement. However, Equation (5) is yet not covering the influence of the bar diameter sufficiently and needs further investigations.

THE INFLUENCE OF THE REINFORCEMENT DIAMETER ON THE ROTATION CAPACITY

The rotational capacity of the connection is significantly influenced by the reinforcement design of the composite connection. The determination of the strain and the elongation of the component "reinforced concrete in tension", see Equation 5, considers the degree and type of reinforcement; namely the factor β distinguishes between mesh reinforcement ($\beta = 1.0$) and bar reinforcement ($\beta = 0.85$) [DIN 1045]. However tests showed [Odenbreit 2000], [Kindmann & Kathage 1994]), that this specification may not sufficient to account for the real behaviour of the connection and its dependency on the bar diameter has to be considered.

Therefore a test campaign has been performed at the University of Luxembourg [Hahn 2009] to check the influence of the reinforcement component on the design of composite connection with plastic hinge theory. The test setup and specimens for the connection assembly, see Figure 9, have been designed in reference to [Kindmann & Kathage 1994].

This configuration has been chosen so as the moment in the connection can be clearly divided into a compression and tension component. The compression component is directly transmitted horizontally into the lower flange of the connected beam; the tension component is exclusively taken over by the reinforcement in the concrete chord. The shear is directly transmitted via the end plate into a cleat and is therefore not interacting with the tension and compression components.

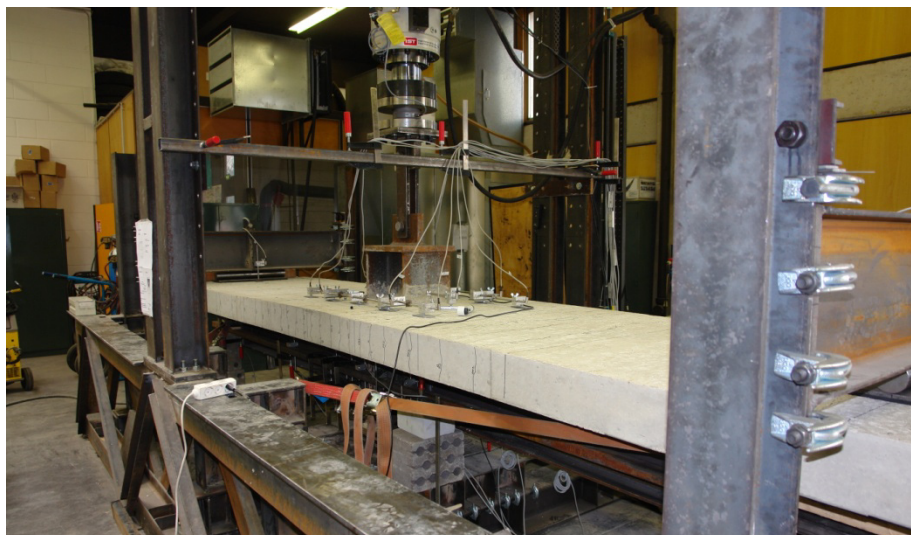


Fig. 8 – Test assembly at University of Luxembourg [Hahn 2009]

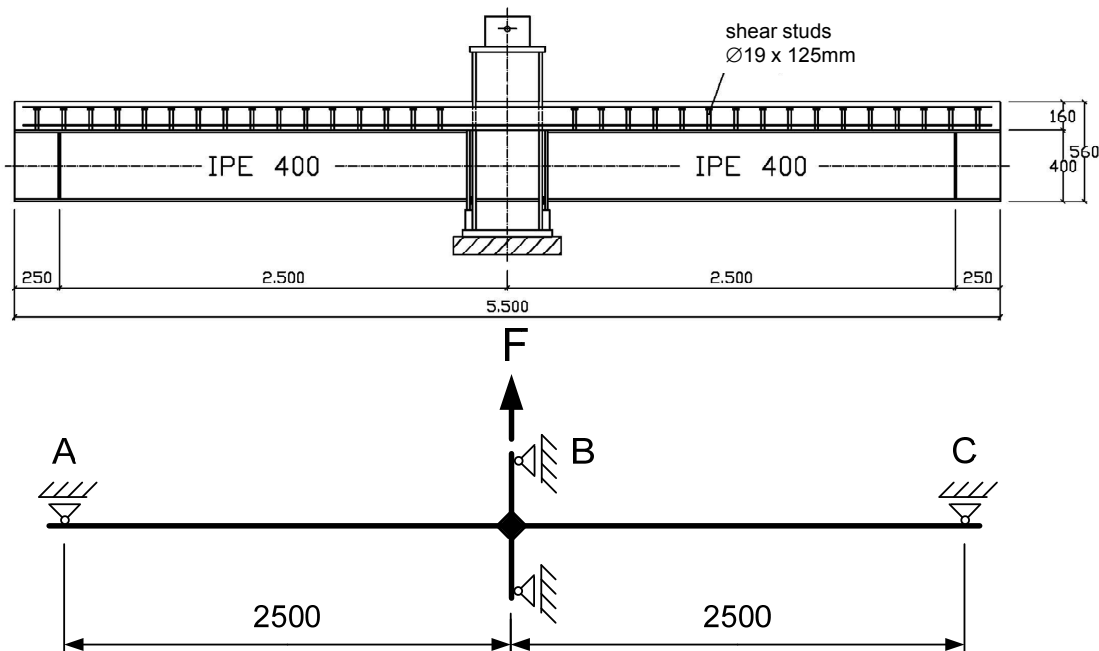


Fig. 9 – Test setup and static system [Hahn 2009]

For all tests, the constructional detailing of the connections has been kept identical but the diameter of the reinforcement bar has been varied. An overview on the test campaign is given in Table 1.

Table 1 – Overview of test programme

Test series specification	ρ_s [%]	Reinforcement (BSt 500)					
		$\varnothing = 8$ mm	$\varnothing = 10$ mm	$\varnothing = 12$ mm	R513	R589	Q513 + $\varnothing = 12$ mm
[Hahn 2009]	0.63	A-2					
	0.63				A-1		
	0.71			A-3			
	1.04	A-5					
	1.11						A-4
[Kindmann & Kathage 1994]	0.74		VT 2.1			VT 2.2	
	1.06			VT 1.1			
	1.41			VT 2.4			

For the connection design the steel compression component has been over-designed, to achieve a very stiff compression component which deformation is negligible for the estimation of the connections' rotation. The degree of shear connection between concrete chord and steel beam (studs $\varnothing 19$ mm) has been designed to be 100%. The compression members have been checked against stability failure.

The static system of the test setup is shown in Figure 9. The supports A and C are pinned supports and linked to the testing rig; the hydraulic jack is located at the support B and is pulling deflection controlled with a force F .

For each test, a pre-loading with 10 cycles of the load range from 5% to 40% of the ultimate load expected has been applied to loosen any bonding and exclude settlement of the testing frame. Subsequently the test has been loaded in small deflection increments until failure. To measure deflections, slip in the shear joint and rotations, 26 displacement transducers (W) and three inclinometers (I) have been used, see Figure 10.

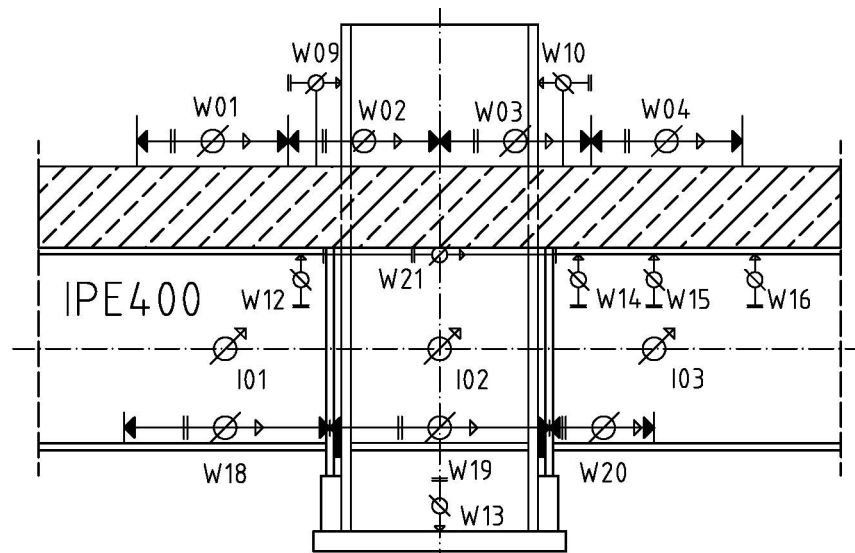


Fig. 10 – Measurement campaign for each test setup [Hahn 2009]

As planned, all tests failed due to tension failure of the reinforcement bars. In all tests the concrete showed a similar crack pattern with the crucial crack occurring at the location of the column flange, shown exemplarily for test A-5 in Figures 11 and 12. This crucial crack occurred always already after pre-loading, starting from the outer edge of the column flange and growing towards the edge of the concrete chord to the location of the first transversal reinforcement. Table 2 lists the results of the tests presented in this paper [Hahn 2009] as well as of previous test [Kindmann & Kathage 1994].



Fig. 11 – Side elevation of failed test specimen (Test A-5)



Fig. 12 – Top view on failed test specimen (Test A-5)

From the test it is to be concluded that:

- (1) an increase of the degree of reinforcement, without changing the reinforcement diameter and the overall connection assembly, leads to an increase in stiffness of the connection (concluded from comparing tests A-2 with A-5 [$\text{Ø}8$] as well as A-3 and VT 1.1 with VT 2.4 [$\text{Ø}12$], see Figure 13);
- (2) an increase of the degree of reinforcement, without changing the reinforcement diameter and the overall connection assembly, also the rotation capacity of the connection is increasing (concluded from the same comparison as above);
- (3) with increase of the reinforcement bar diameter and constant degree of reinforcement the rotational capacity of the connection is increased (concluded from the comparison of tests A-2 with VT 2.1 and A-3, see Figure 14);
- (4) the moment-rotation curves of Figure 15 show, that the application of a mesh-reinforcement reduces the ultimate rotation capacity of the joint; compare for example test A-1 with A-2. Even additional bar reinforcement is not able to compensate this deficit significantly, which is shown by the comparison of test A-4 with A-5.

Table 2 – Collection of test results

	Series	Reinforcement	ρ_s [%]	$M_{pl,cal}$ ^{***} [kNm]	$M_{pl,cal}$ ^{***} [kNm]	$M_{u,test} /$ $M_{pl,cal}$	Φ_{test} [mrad]	$S_{j,test}$ ^{****} [kNm/rad]	Failure
[Hahn 2009]	A-1	R 513	0.64	320.6	275.4	0.86	9.0	87847	R*
	A-2	Ø = 8 mm	0.63	364.9	363.3	1.00	22.1	76639	R
	A-3	Ø = 12 mm	0.71	402.1	416.0	1.03	45.7	81817	R
	A-4	Q 513 + Ø = 8 mm	1.11	595.4	557.9	0.94	14.9	78302	R
	A-5	Ø = 8 mm	1.04	582.5	582.5	1.00	43.8	88258	R
[Kindmann & Kathage 1994]	VT 1.1	Ø = 12 mm	1.06	538.0	595.0	1.11	67.7	88344	R/B**
	VT 2.1	Ø = 10 mm	0.74	382.0	425.0	1.11	36.0	88266	R
	VT 2.2	R 589	0.74	380.0	396.0	1.04	9.2	95652	R
	VT 2.4	Ø = 12 mm	1.41	659.0	770.0	1.17	70.6	322851	R/B

* Rupture of reinforcement *** acc. to [8] with material properties from testing

** Buckling of steel section **** acc. to [8]

As almost the whole rotation of the tested composite connections results from strains in the concrete chord, conclusion (1) is considered in Equation (3) (in the EI_2) and conclusion (2) is already accounted for in Equation (5) appropriately. However the increase in rotation capacity in dependency of the bar diameter as well as the decrease in reference to the type of reinforcement is not yet covered.

The increase in the rotation capacity due to the increase in bar diameter results from the following conditions:

- (1) the extreme negative bending moment is located at support, thus in the connection zone;
- (2) the connection is rotating around the contact area of lower flange of the steel beam with the support and therefore pulls locally away the concrete chord from the column;
- (3) due to the penetration of the column through the concrete chord, see Figures 11 and 12, the point of crack initiation for the concrete chord are predefined.

In the consequence the negative bending moment at the connection causes only very few major cracks at the beam end connection in the concrete. A larger reinforcement bar diameter leads directly to a higher crack opening potential due to the bigger anchorage length. Figure 14 shows, that the rotation capacities of the connections

A-2, VT2.1 and A-3 steadily increase with increasing bar diameter, even if the ratio of reinforcement is nearly kept the same. The same effect is shown by the comparison of curve A-5 with A-3 in Figure 15: Even if test A-3 has a significantly weaker connection with a smaller ratio of reinforcement than A-5, its ultimate rotation capacity is bigger. The reason for this enhanced rotation capacity lies in the bigger bar diameter.

This positive effect needs to be reflected by the review of factor β in Equation (5).

The negative effect of the application of meshes as longitudinal reinforcement is resulting from the restriction in anchorage length to the distance of the perpendicular welded reinforcement bars (mesh size) and therefore, the elongation length for the strains in the major cracks. In the consequence, the impact of the type of reinforcement is to be sustained in the review of the factor β in Equation (5).

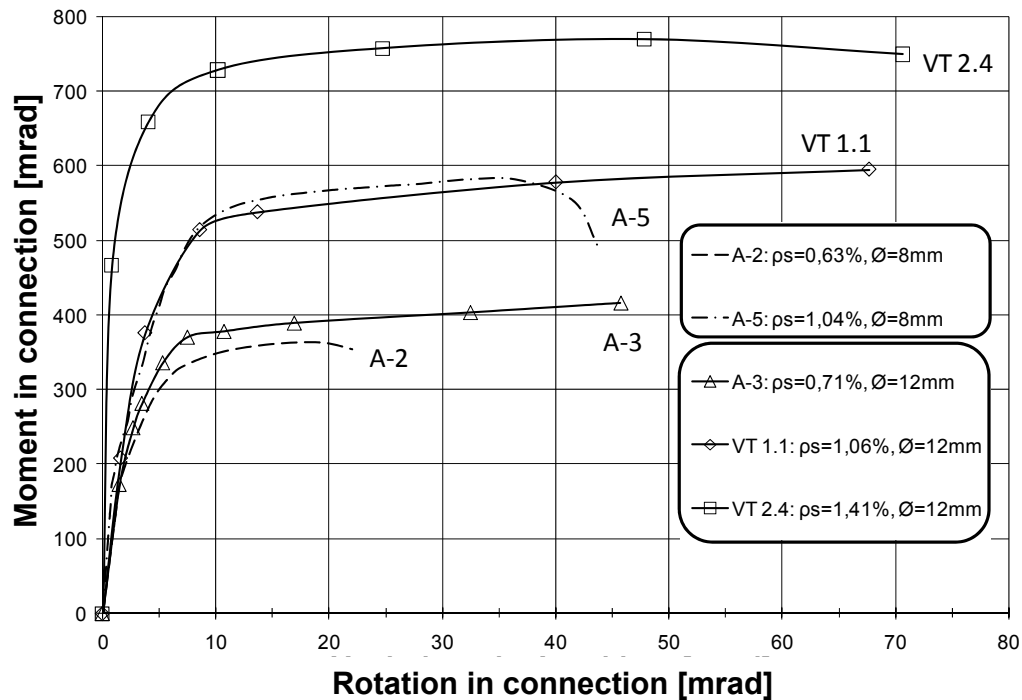


Fig. 13 – Comparison of the rotation-moment curves for tests with varying reinforcement ratio and constant reinforcement diameter

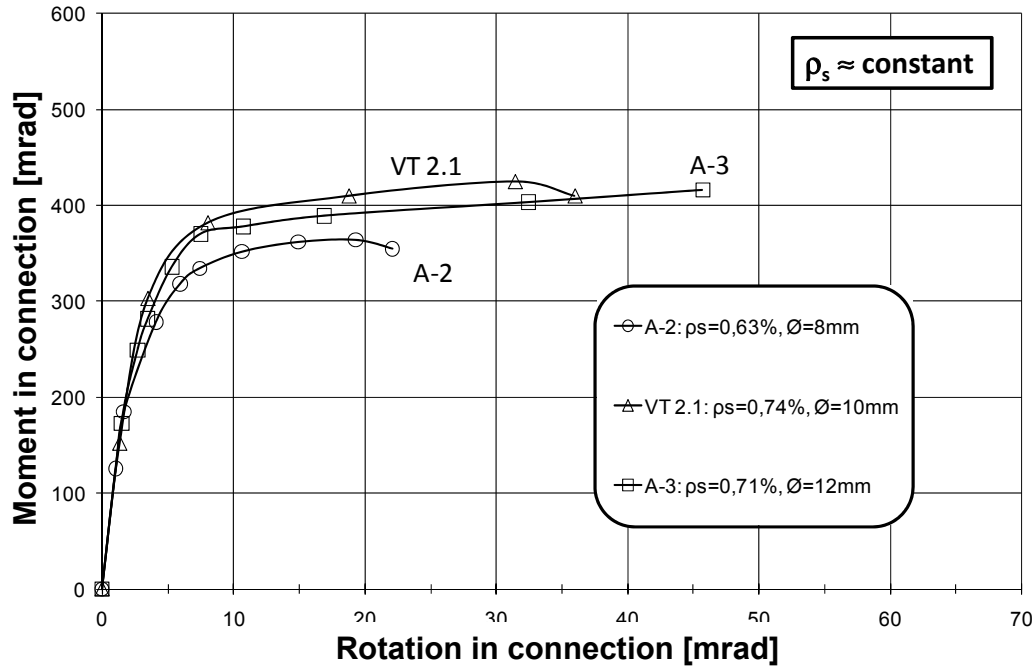


Fig. 14 – Comparison of the rotation-moment curves for tests with constant reinforcement ratio and varying reinforcement diameter

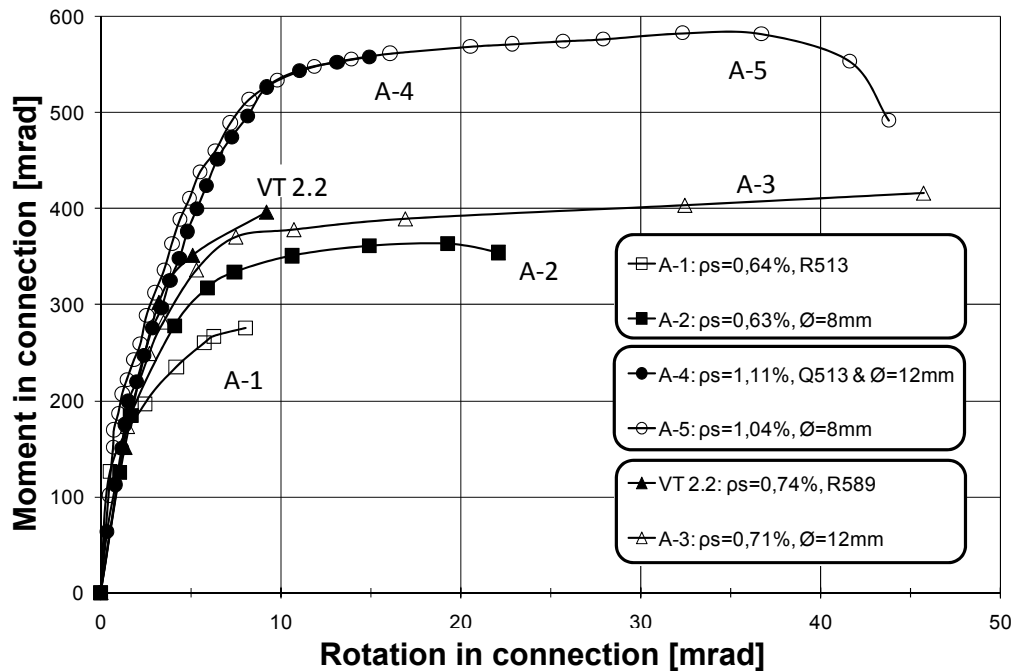


Fig. 15 – Comparison of the rotation-moment curves for tests with varying type of reinforcement (bar vs. mesh reinforcement)

CONCLUSIONS

This paper presented a design logic for the design of composite construction according to the plastic hinge theory in combination with semi-rigid joints. Design equations for all relevant parameters are explained and values, when relevant, are provided. Special focus has been put on the experimental analyses of the rotation capacity of composite connections required for the robust design of these kinds of structures. Hereby the significant influence of the reinforcement (ratio, diameter and type) on the rotation capacity has been demonstrated. Research potential how to account for this influence has been outlined.

The presented design logic is based on the evaluation of 9 self-conducted tests and on the evaluation of 74 tests on composite connections from all over Europe. The analysis of these tests and accompanying non-linear numerical investigations [Odenbreit 2000] proofed, that a simplified characterization of the non-linear behaviour of the connection by a bi-linear law is sufficiently exact to determine the displacements at serviceability limit state as well as the load-bearing capacity at ultimate limit state. Therefore a robust method has been presented to design efficient and thus economic structures in a simple way.

ACKNOWLEDGEMENTS

The authors wish to express their deep gratitude to the representatives of KöKO Köster & Co Bolzenschweisstechnik, Spannverbund Luxembourg S.A. and ArcelorMittal Global R&D (Esch, Luxembourg) for material supply and their inspiring cooperation and as well as to the Fonds National de la Recherche Luxembourg for their financial support.

REFERENCES

- DIN 1045: Beton und Stahlbeton, 1998
- EN 1993-1-8: Design of steel structures. Design of joints. 2009
- Hahn, C.: Zur Rotationskapazität von Verbundanschlüssen bei der Bemessung nach dem Fliessgelenkverfahren, PhD Thesis, University of Luxembourg, 2009.
- Kindmann, R., Kathage, K.: Experimentelle Untersuchungen zur Rotationskapazität von Verbundanschlüssen. Stahlbau, Vol. 63, No. 10, 1994
- Kreller, H.: Zum nichtlinearen Trag- und Verformungsverhalten von Stahlbetonstabtragwerken unter Last- und Zwangseinwirkung. Deutscher Ausschuß für Stahlbeton, Vol. 409, Beuth Verlag GmbH Berlin Köln, 1990.
- Odenbreit, C.: Zur Ermittlung der Tragfähigkeiten, der Steifigkeiten und der Schnittgrößen von Verbundträgern mit halbsteifen, teiltragfähigen Verbundanschlüssen, Dissertation, Technische Universität Kaiserslautern, 2000
- Odenbreit, C., Jaspert, J.-P., Hahn, C.: Untersuchungen über das Trag- und Dehnungsverhalten des Betongurtes bei Verbundanschlüssen, Stahlbau, Vol. 78, No. 1, 2009

Modelling of Semi-Rigid Joints in Steel-Concrete Composite Frames

S. Jeyarajan^{1,*}; J. Y. Richard Liew²; and C. G. Koh³

^{1,2,3}Dept. of Civil and Environmental Engineering, National Univ. of Singapore, 1 Engineering Dr. 2, Singapore 117576. E-mail: a0016508@nus.edu.sg¹; ceeljy@nus.edu.sg²; cgkoh@nus.edu.sg³

Abstract

This paper introduces a semi-rigid joint model to capture the composite beam-to-column joint behaviour so that the influence of joints on the building frame can be assessed precisely. The beam-to-column joint is modelled using a 6-degree of freedom non-linear connector. Depending on the joint type (e.g., simple, rigid or semi-rigid), connector load deformation behaviour can be represented by axial force-displacement relationship and moment-rotation relationship. This will avoid detailed finite element modelling of joint components to improve the computational efficiency of analysing large three-dimensional (3D) building frame. Analysis of 3D frame shows that the use of semi-rigid joint model predicts less beam deflection and higher load carrying capacity compared to pin-joint model. The incorporation of semi-rigid joint model in 3D frame analysis tends to produce more realistic estimate of frame behaviour compare to model using pin or rigid joints.

1.0 INTRODUCTION

Design engineers tend to avoid detailed modelling of composite joints in numerical analysis due to complexity of geometric modelling, insufficient guidelines, high computational cost and complicated interaction behaviours among the joint components. As a result, joints are generally simplified into pin or rigid. In reality these simplified assumptions may be inaccurate and uneconomic. They represent the limiting cases of the joint behaviour and lead to a wrong interpretation of the structural behaviour in terms of load resistance and structural responses. Researchers have proven that joint rigidity improves the robustness and redundancy of building frames. The Eurocodes provide sufficient details to realistically predict behaviour of steel and composite joints based on the component approach. As a result, component method is widely adopted for modelling semi-rigid joints in numerical frame analysis. However detailed joint component modelling in large scale frame is still time consuming due to complicated geometry modelling and high computational cost.

A wide range of steel and composite connections have been investigated over several decades to determine the axial force-displacement and moment-rotational characteristics and a vast number of experimental data on joints is currently available. Recently, several researchers have attempted to propose further simplification in

modelling semi-rigid joints for frame analysis. Some of the significant contributions include the work done by [Sadek et al. 2008], [Kwasniewski 2010], [Izzuddin et al. 2008; Izzuddin et al. 2008], [Zha et al. 2010] and [Alashker et al. 2011], who have incorporated simplified composite joint models in progressive collapse analysis of building frames. This paper introduces a semi-rigid joint model so that the behaviour of the composite joint can be captured accurately and their influence on the overall stability of framework can be assessed precisely. This avoids detailed finite element modelling of joint components and leads to overall improvement in computational efficiency of analysing large building frames.

2.0 NUMERICAL MODELLING OF COMPOSITE SLAB AND JOINTS

2.1 Composite joint model

A simplified joint model is proposed to reduce the computational cost of 3-D building frame analysis. Composite joint is represented by a six degree of freedom (DOF) non-linear connector. Depending on the joint type (e.g. simple, rigid or semi-rigid), connector behaviour can be represented by axial force-displacement and moment-rotation relationship. They are calculated using Eurocodes (EC3 and EC4). The procedure for joint modelling is given below. Figure 1 shows that the joint components (Figure 1a) are represented by the simplified joint model in ABAQUS (Figure 1b). As shown in Figure 1a, axial springs are used to represent the joint component for slab under tension, bolt in shear, beam web in bearing and fin-plate in bearing, etc. Eurocode 3-1-8 and Eurocode 4-1-1 component model is used to calculate the stiffness and resistance of each axial spring connector. The connectors in a joint are then assembled using two rigid bars and then analysed using the finite element analysis software, ABAQUS, subject to axial force and moment as shown in Figure 1c. The joint's moment-rotation (M- θ) and axial force-displacement (F-d) relationships can be calculated. Finally, these relations are represented by axial and rotational connector in the analysis of the frame with semi-rigid joint, as shown in Figure 1d. The frame analysis assumes zero joint size and neglect the effect of panel zone shear deformation in the beam to column joints (da Silva et al. 2008).

Eurocode 3 (EN 1993-1-8:2005) Cl 6.2.7.1 highlights that the component model for determining the design moment resistance, $M_{j,Ed}$, of a joint does not take account of any co-existing axial force in the connected member. The model should not be used if the axial force in the connected member exceeds 5% of the design plastic axial resistance of its cross section. It further mentioned that if the axial force N_{Ed} in the connected beam exceeds 5% of the design resistance, $N_{pl,Rd}$, the following conservative method may be used to account approximately for the axial force and moment interaction effect on the joint:

$$\frac{N_{j,Ed}}{N_{j,Rd}} + \frac{M_{j,Ed}}{M_{j,Rd}} \leq 1 \quad (1.0)$$

where, $N_{j,Rd}$ is the axial resistance of the joint by assuming no applied moment and $M_{jR,d}$ is the moment resistance of joint by assuming no applied axial force.

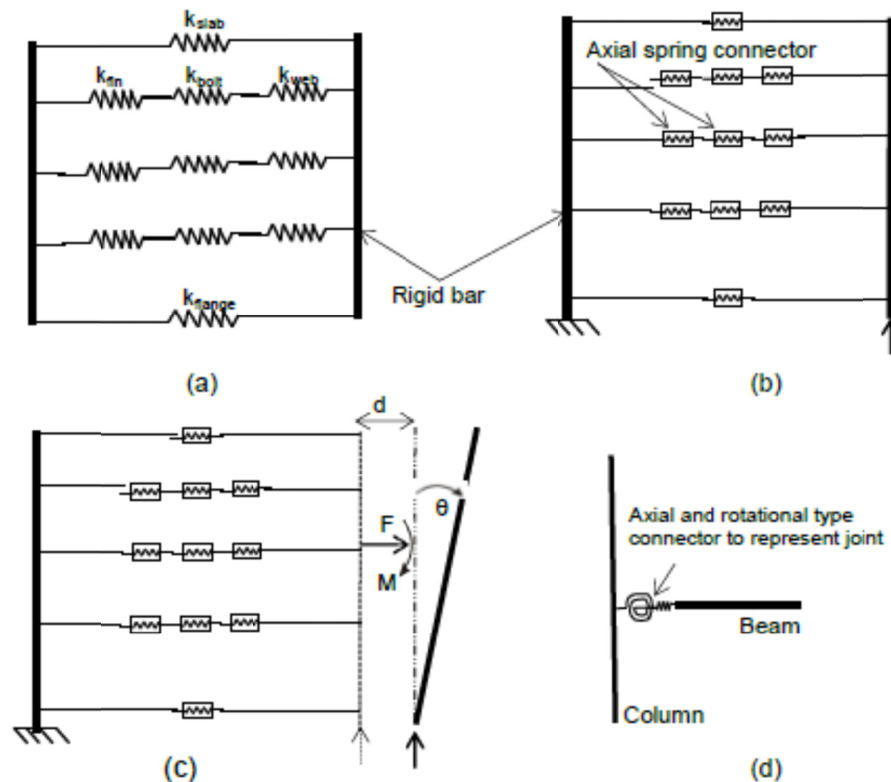
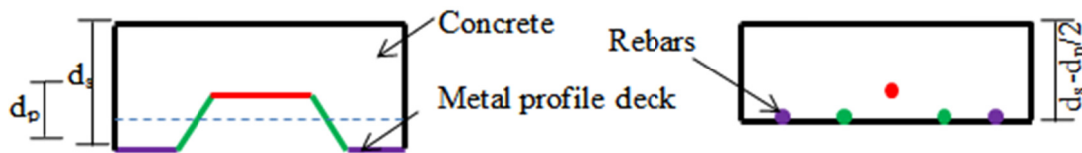


Figure 1. Model for fin-plate joint (a) Eurocode 3 component model (b) ABAQUS model (c) force deformation relationship of joint (d) joint representation in frame analysis

2.2 Composite slab

A simplified slab model is adopted to avoid complicated geometry modelling and to reduce the computational time for 3-D large scale frame analysis. Profile deck is represented by rebar in longitudinal direction based on equivalent area and second moment of area (I) of the respective web and flange plates of the metal deck. Profile concrete is converted into equivalent uniform concrete section and it is modelled using four-node homogeneous shell element with reduced integration (S4R). Rebar is defined using rebar definition through ABAQUS library. Simplified slab model is shown in Figure 2. The details of the proposed simplified slab model is given by [Jeyarajan et al. 2013].



(a) Composite slab with metal decking (b) Simplified composite slab model
Figure 2. Simplified slab model – deck strips converted into rebars

3.0 VERIFICATION STUDIES

3.1 Reinforced concrete two-way slab under flexural load

Test carried out on reinforced concrete slab by [Cervera et al. 1987] and [Nazem et al. 2009] is used to study the reinforced concrete two-way slab response subject to flexural load. A corner supported reinforced concrete (RC) slab, S1 is studied by comparing the numerical results with the experimental results. The slab is composed of two reinforcement meshes at both top and bottom. A concentrated load is applied at the centre of the slab, at point A, as depicted in Figure 3.3a. Only transverse deflections are restrained at the corner supports. Steel and concrete material properties are given in Tables 1 and 2. Figure 3b shows the comparisons between the test result and numerical result predicted using ABAQUS on the load versus mid-point deflection curve. The predicted load-deflection response is found to be in good agreement with the test result. It means numerical result predicts initial stiffness, maximum resistance and load-deflection relation of the slab very well. Four-node homogeneous shell element with reduced integration (S4R) is sufficient to predict the reinforced concrete slab behaviours.

Table 1. Equivalent reinforcement layer

	Top layers thickness (mm)		Bottom layers thickness (mm)	
	x-direction	y-direction	x-direction	y-direction
S1	0.193	0.193	0.397	0.397

Table 2. Material properties

<i>Concrete</i>	
Young's modulus	$E_c = 16400 \text{ N/mm}^2$
Poisson's ratio	$\nu = 0.15$
Maximum compressive strength	$f'_c = 43 \text{ N/mm}^2$
Maximum compressive strain	$\epsilon_{cu} = 0.0035$
Cracking tensile stress	$f'_t = 3 \text{ N/mm}^2$
<i>Steel</i>	
Young's modulus	$E_s = 201000 \text{ N/mm}^2$
Yield stress	$f_y = 670 \text{ N/mm}^2$

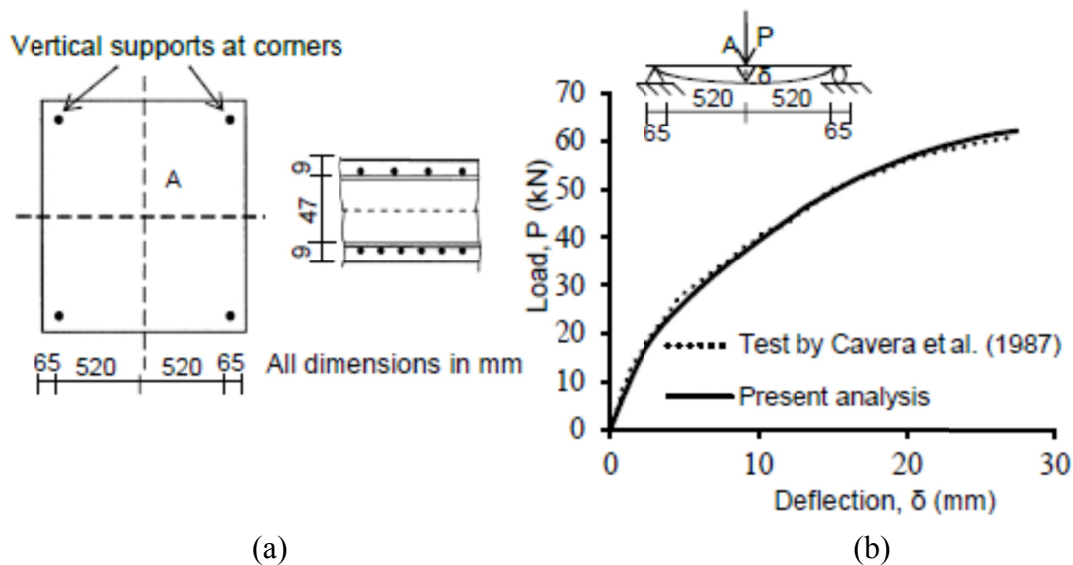
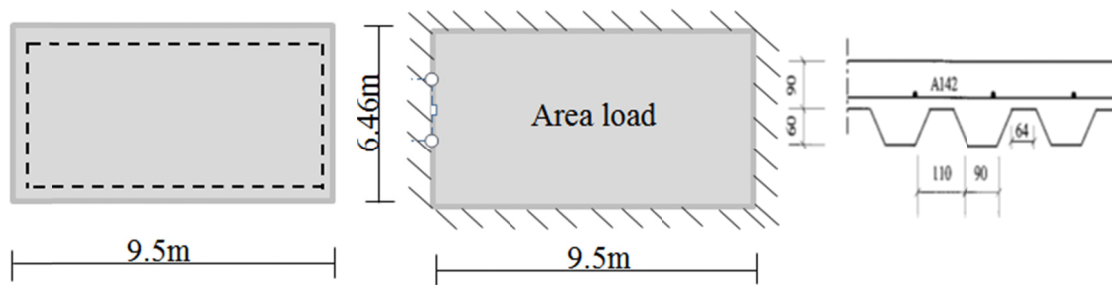


Figure 3. (a) RC slab details ([Nazem, et al. 2009]) (b) load-deflection curve for RC two-way slab

3.2 Large deflection behaviour of ribbed slab

Ribbed slab with dimensions of 9.5m x 6.46m was tested to failure under gradually applied uniformly distributed load by [Elghazouli and Izzuddin 2004]. Ribs of the slab are running along the short direction. Reinforcement mesh 142mm²/m with yield and maximum strength about 580 and 640N/mm² respectively were provided. Light weight concrete was used and its average concrete cube strength was 50N/mm². Steel deck was removed after concrete was cast to study the ribbed slab response under large deflection.



(a) Four edges simply supported slab (b) Fully restrained slab (c) Cross section of slab
 Figure 4. Plan and cross-section view of the ribbed slab ([Elghazouli and Izzuddin 2004])

Slabs with two boundary conditions, four edges simply supported against vertical displacement and four edges fully fixed against rotation and displacements were tested. The plan view and sectional view of the slab are shown in Figure 4. Test and FEM results from Elghazouli and Izzuddin (2004) are compared with the result obtained from the simplified numerical model as shown in Figures 5 and 6. FE mesh size is 100mm. Figure 5 shows the ribbed slab response under large deflection for slab edges simply supported against vertical displacement. Initial stiffness and maximum resistance of slab up to deflection of 25mm is reasonably well predicted the ribbed slab response. Catenary action can be observed beyond the deflection about 50mm. Even though there is deviation with literature overall ribbed slab response predicted reasonably well. The deviations among the ribbed slab Elghazouli and Izzuddin (2004) result and present analysis are occurred due to simplification in the proposed slab model and usage of simplified concrete material model (concrete damaged plasticity model is adopted using EC2: maximum tensile stress: 1N/mm^2 , Young modulus: 30000N/mm^2 , maximum compressive stress: 50N/mm^2), which concrete model does not consider the shear contribution of concrete in its resistance. The given material model in Elghazouli and Izzuddin (2004) is difficult to define in ABAQUS. Therefore shear contribution of concrete is conservatively avoided and only stress-strain relationship for compression and tension are defined for concrete using concrete damage plasticity model in ABAQUS.

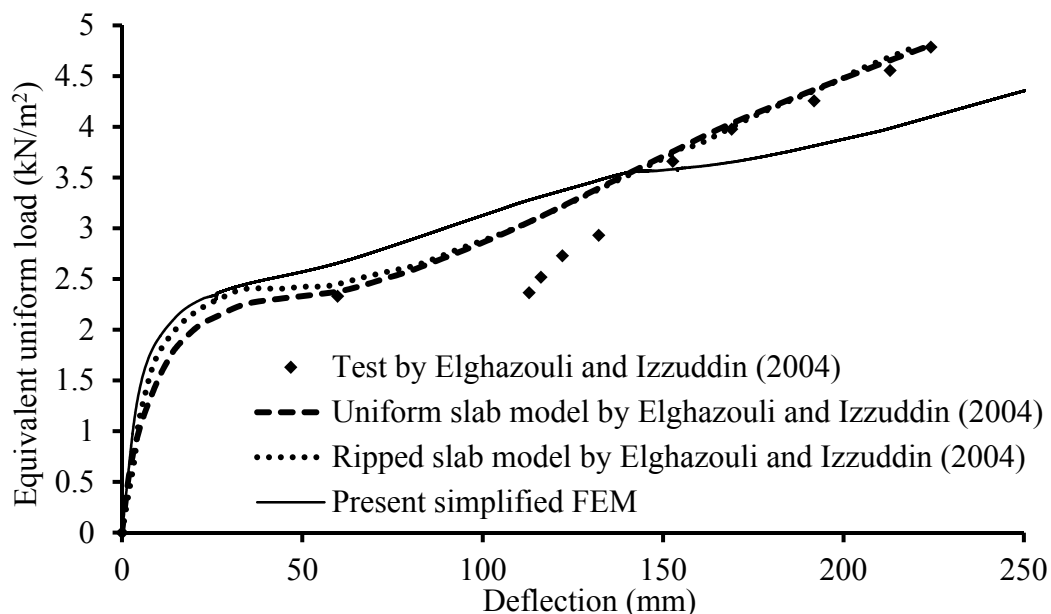


Figure 5. Load-maximum deflection relation for vertically supported slab

Figure 6 shows the ribbed slab response under large deflection for fully restrained slab (slab with four edges fixed against displacement and rotation). Initial

stiffness is reasonably predicted the ribbed slab response compared to the Elghazouli and Izzuddin (2004) FEM result. The simplified numerical analysis over predicts the maximum resistance by 10% due to the simplification in the proposed slab model. As shown in Figure 2, the proposed simplified slab concrete thickness is overestimated by half of the profile depth in the transverse direction of the profile ribs. This overestimated concrete thickness over-predicts the composite slab resistance of fully restrained slab because floor load is transferred herein both short span and long span directions. Generally flange concrete (continuous/top part of the ribbed slab concrete) is effective in carrying the load in transverse direction of profile rib. The overestimation of composite slab resistance using the proposed slab model shall not significantly affect the result in real scenario because one-way load transfer mechanism is typically observed in metal-deck composite floor slab. However, overall behaviours reasonably agree with the Elghazouli and Izzuddin (2004) test and numerical results. The proposed slab model is accurate enough in predicting the composite slab behaviour with less computational effort.

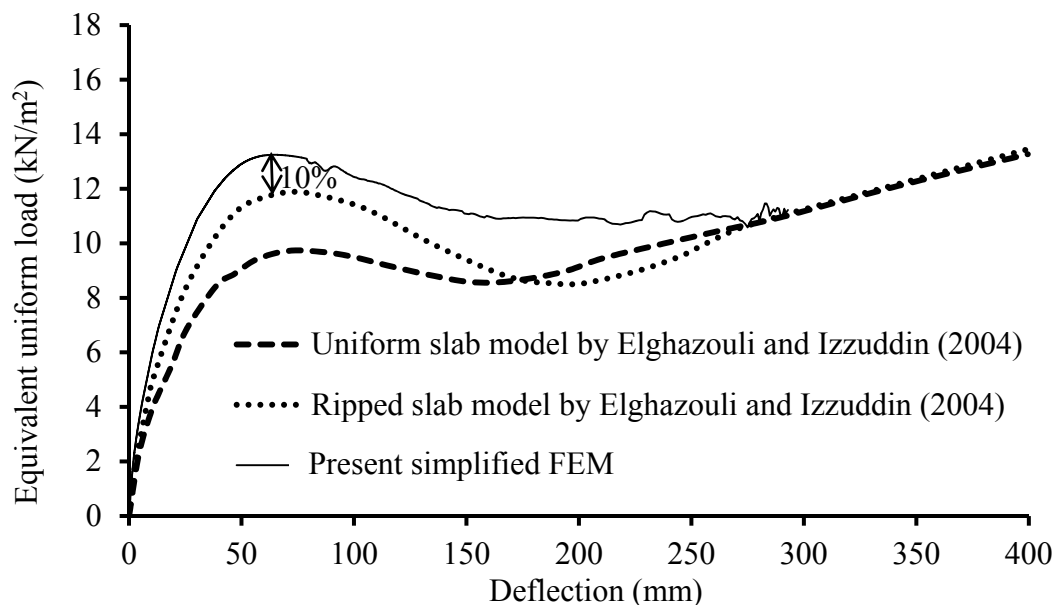


Figure 6. Load-maximum deflection relation for fully restrained slab

3.3 Numerical study of web-cleat connection

Web-cleat connection investigated by [Sadek, et al. 2008] is used to study the web-cleat response under flexural load. Two 6.1m span beams were connected with a column by web-cleat connection as shown in Figure 8b. The web-cleat connection details are shown in Figure 7. Column is pushed downward under displacement control until failure of the joint. Both beam ends are assigned with pin boundary conditions. ASTM A992 ($f_y = 344.8\text{MPa}$) structural steel was used for column and beam. The beam

size was W16x26 and column size was W14x74. ASTM A325 high strength bolt and ASTM A36 9.5mm thick web-bleat were used for web-bleat connection. Proposed joint model is adopted for column-to-beam joint. 'Slot-rotation' type connector is assigned between column and beam intersection to represent the joint in ABAQUS. FE mesh size is 25mm. Joint moment-rotation relationship is defined using test data, which test was done by [Sarraj et al. 2007]. Eurocodes are used to define the axial force-displacement relationship of web-bleat connection. FEM results from Sadek et al. (2008) are compared with the result obtained from the simplified numerical model as shown in Figure 3.18a. The vertical load-centre column displacement behaviour of the web-bleat beam-to-column connection is agreed well with those by [Sadek, et al. 2008]. Proposed joint model predicts the initial stiffness, maximum resistance, failure point (displacement) and the load-displacement response of semi-rigid joint precisely. The proposed joint model avoids detailed finite element modelling of joint components and improves the computational efficiency. The proposed joint model is accurate enough in predicting the joint response with less computational effort.

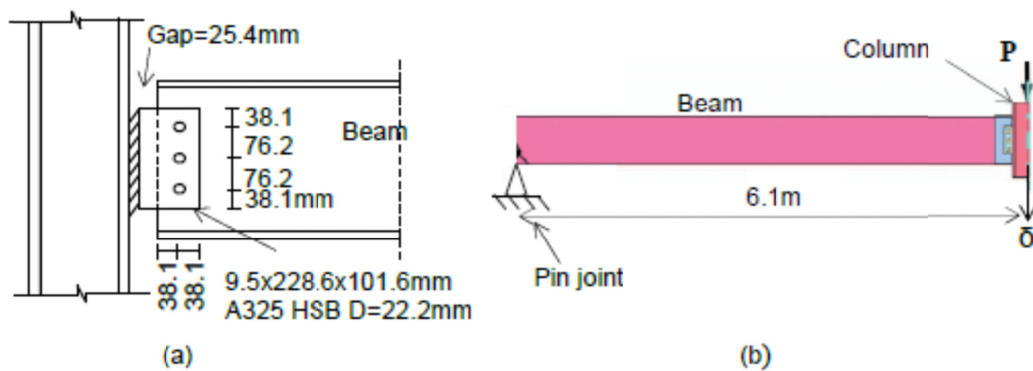


Figure 7. (a) Single plate web-bleat connection (b) test half model ([Sadek, et al. 2008])

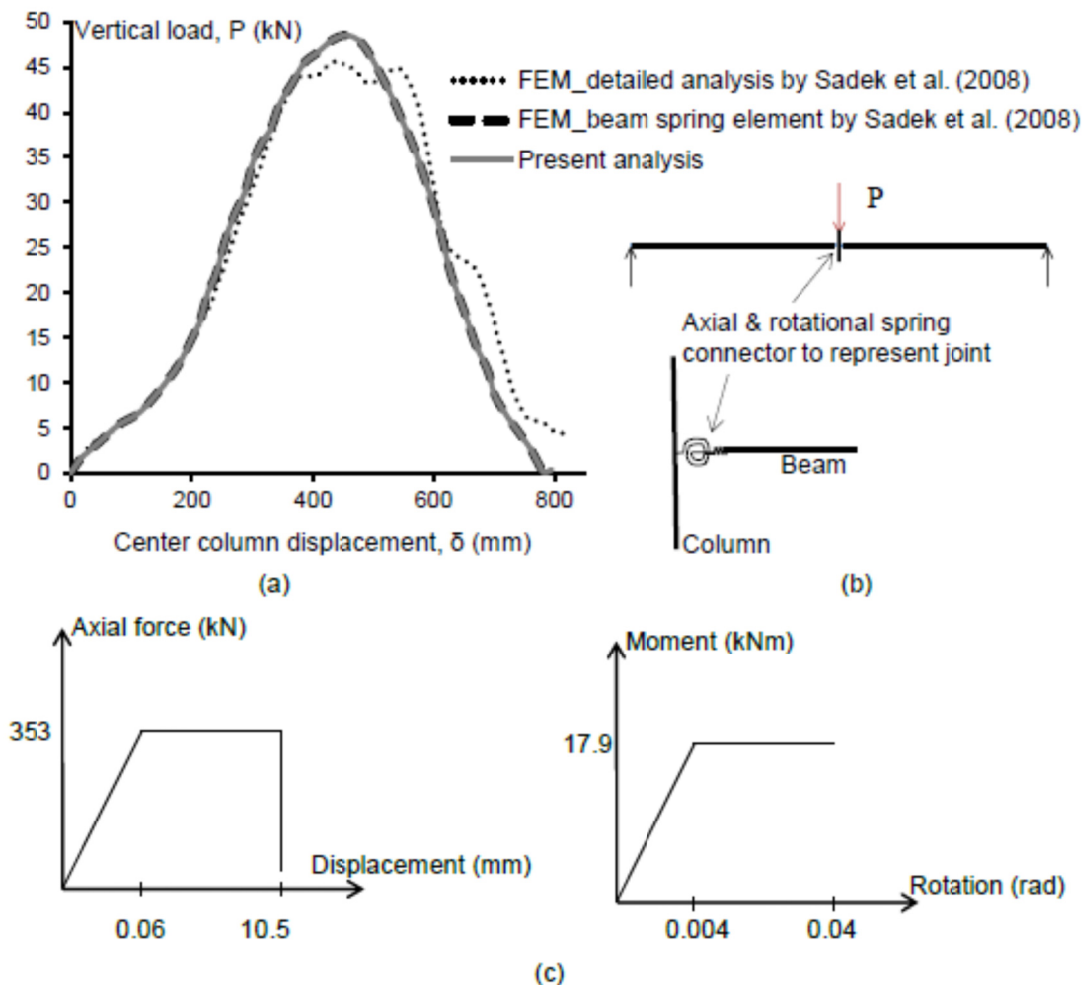


Figure 8. (a) Column vertical load-displacement (b) joint representation in FE analysis (c) axial force-displacement and moment-rotation relationship

3.4 Numerical study of end-plates joints

Composite end-plate connection tested by [Gizejowski et al. 2010] is referred to study the steel and composite semi-rigid joints behaviours under flexural load. Beam-to-column flush and extended end-plate steel and composite connection behaviours are investigated here. Typical flush end-plate connection details are shown in Figure 9 and Table 3. Material properties can be found in [Gizejowski, et al. 2010]. Test and FEM results from [Gizejowski, et al. 2010] are compared with the results obtained from the simplified numerical model. Load-displacement relationships for steel joint specimens (ES1, ES2 and ES4) and composite joint specimens (EZ1, EZ2 and EZ3) are shown in Figures 10 to 15.

FE mesh size is 50mm. In this verification study, non-linear moment-rotation relationship is defined using Gizejowski et al. (2010) test result to predict the joint load-displacement response precisely. ‘Join + rotation’ type connector element using ABAQUS is defined between column and beam joint to represent the column-to-beam joint with the assumption of joint will not deform axially. This assumption is only valid for small deflection/rotational deformation of joint. Non-linear static analysis is performed for steel joint. Load-displacement response of steel joints is agreed well with the test result. Initial rotational stiffness and maximum resistance of all joints are well predicting the test result.

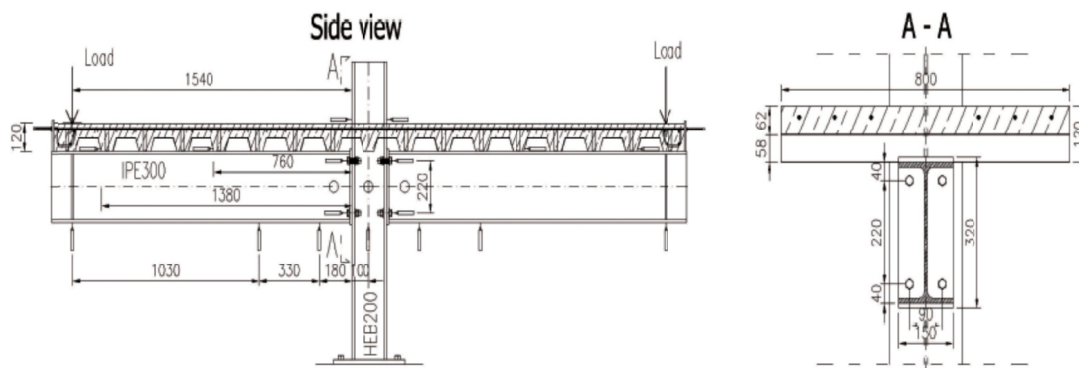


Figure 9. Schematic view of flush end-plate joint [Gizejowski, et al. 2010]

Table 3. Joint details

Joint symbol	Type of end-plate	End-plate thickness (mm)	Slab (C25/30) reinforcement
Steel joint, ES1	Flush	10	-
Steel joint, ES2	Extended	10	-
Steel joint, ES4	Flush	12	-
Composite joint, EZ1	Flush	10	6T8
Composite joint, EZ2	Extended	10	6T8
Composite joint, EZ3	Extended	8	6T8

Analysis results clearly show that the proposed joint model is capable to predict the initial rotational stiffness, maximum resistance and the load-displacement response accurately. For the composite joint, non-linear static and non-linear dynamic analyses are performed since ABAQUS is sensitive to concrete damage/crack and causing to abort (convergence problem occur). ABAQUS explicit dynamic analysis is performed to predict composite joint response. Load is slowly applied by means of smooth amplitude function to ensure a quasi-static loading using dynamic explicit procedure. Different loading rates have tried and the reasonable loading rate is chosen. Dynamic fluctuation in the load-displacement curve is still observed in the numerical results. However,

numerical results reasonably well agree with the test results. Present simplified numerical analysis predicts the composite joint initial rotational stiffness reasonably well compared to the test result. The maximum resistance of the joint also reasonably well predicts the test result. Present numerical analysis results using the simplified numerical model provide accurate results than the Gizejowski et al. (2010) FEM results. The proposed simplified joint model can be easily incorporated in the building frame model and improves the computational efficiency. The proposed joint model is accurate enough in predicting the composite joint behaviour with less computational effort.

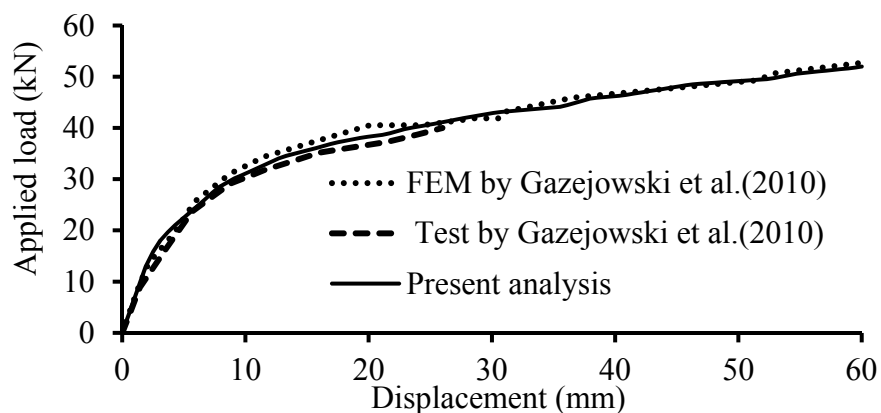


Figure 10. Load-displacement behaviour of steel joint ES1

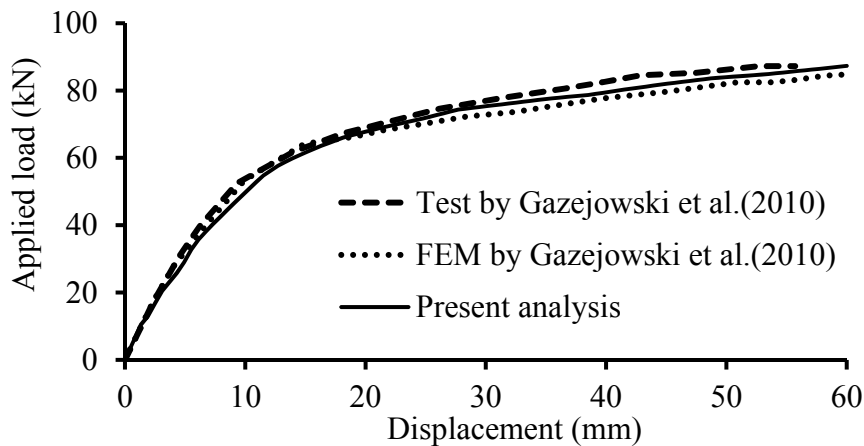


Figure 11. Load-displacement behaviour of steel joint ES2

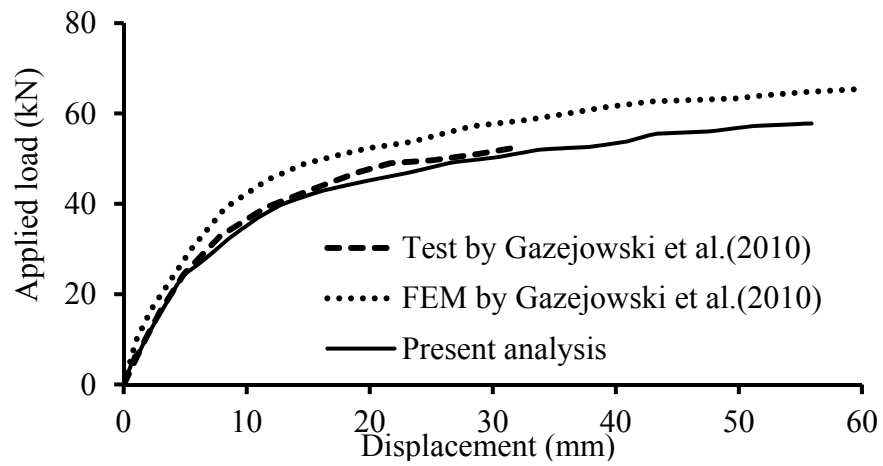


Figure 12. Load-displacement behaviour of steel joint ES4

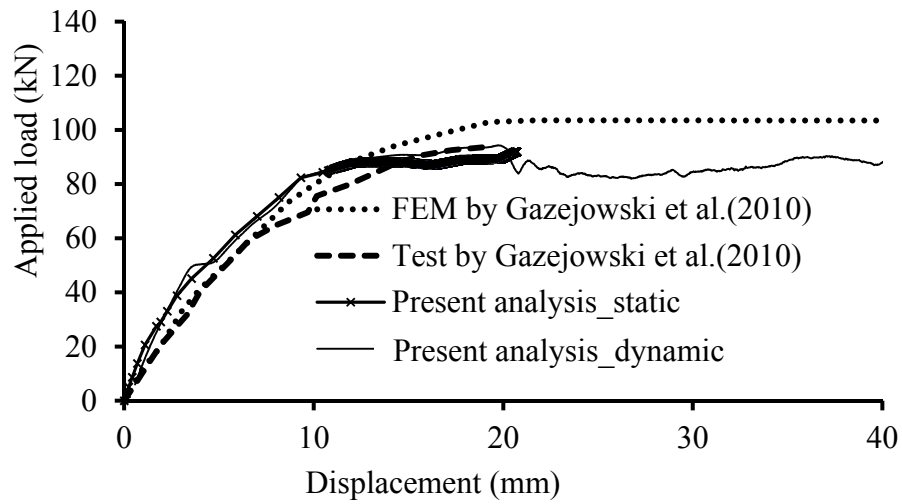


Figure 13. Load-displacement behaviour of composite joint EZ1

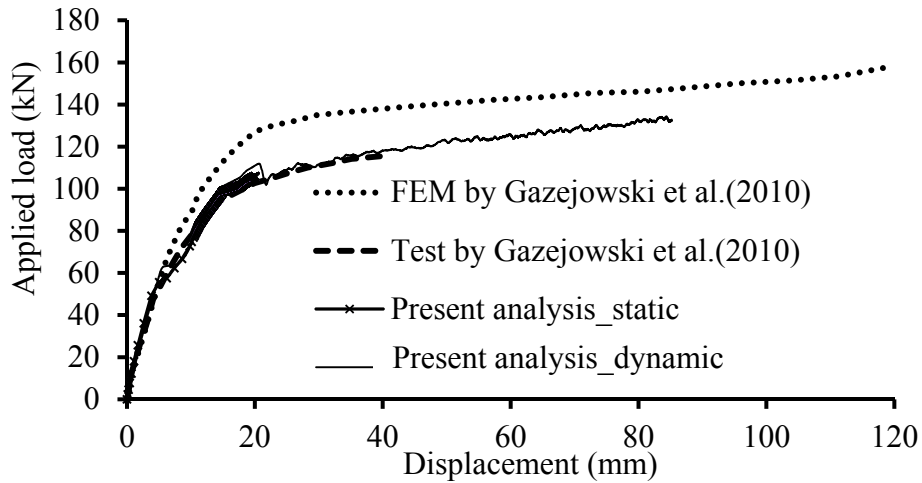


Figure 14. Load-displacement behaviour of composite joint EZ2

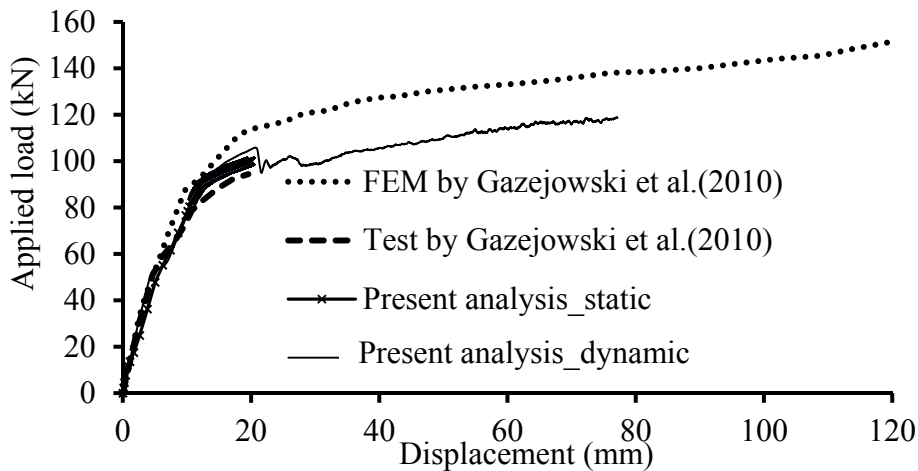


Figure 15. Load-displacement behaviour of composite joint EZ3

3.5 Numerical study of steel-concrete composite frame behaviour under flexural load

The two-storey frame experimental study by [Wang and Li 2007] is referred to for the numerical study of steel-concrete composite semi-rigid connection frame behaviours under flexural load. The beam-column connection consists of a flush end plate welded to the beam end and bolted to the column flange. Full scale composite frame is shown in Figure 16. All beams were loaded together incrementally until failure. Two concentrated loads were applied at all the beams at level-1. All beams were loaded together incrementally until failure. Following member sizes are used: steel columns = HW250x250x9x14; steel beams BB1 to BB4 = HW200x100x5.5x8; steel beams 1 to 4 = HW300x150x6.5x9; and beams 5 to 8 = HW200x100x5.5x8. Material properties and frame details can be found in [Wang and Li 2007].

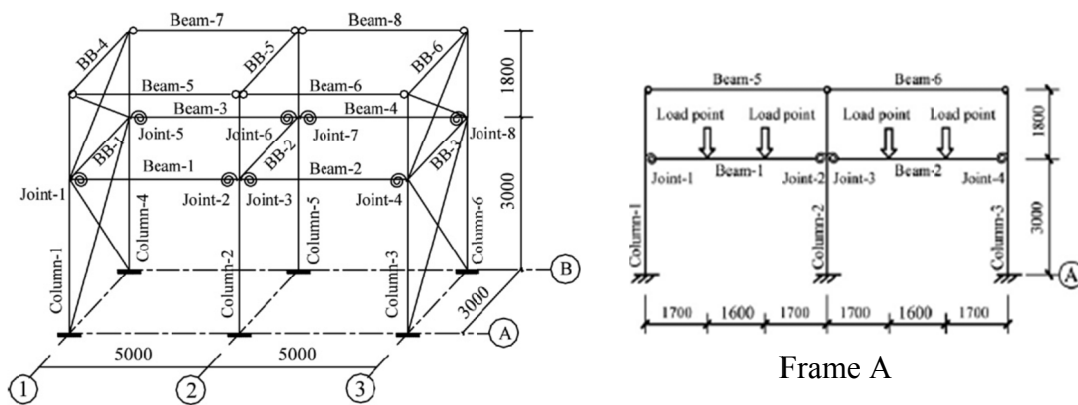


Figure 16. General details of investigated frame [Wang and Li 2007]

Material damage models (damage criteria) are not reported in Wang and Li (2007). Therefore material damage models are approximately defined for each composite frame components. The load-deflection response of Beam-1 with the material damage model is shown in Figure 17. ABAQUS explicit dynamic analysis is used here to predict the composite frame response. Load is slowly applied by means of smooth amplitude function to ensure a quasi-static loading using dynamic explicit procedure. Different loading rates have tried and the reasonable loading rate is chosen. Dynamic fluctuation in the load-deflection curve is still observed in the numerical results. However, numerical results reasonably well agree with test results. The proposed simplified composite joint model and composite slab models are adopted in this simplified numerical model. Semi-rigid end-plate connection composite frame response is reasonably predicted the test results. Numerical results are also compared with the UFC-DoD (Department of Defence-2009) and GSA (General Services Administration-2003) guideline's acceptance criteria. Maximum rotational limit for non-linear analysis is given in both abovementioned guidelines. Maximum allowable deflection limit is calculated using the given allowable rotational limit and then compared with the numerical analysis results. The DoD acceptance limit for non-linear analysis for partially restrained moment connection is 22.1 mm and GSA acceptance limit for non-linear analysis for partially restrained connection is 25.5 mm. Local buckling of steel section is avoided in the simplified numerical model, which can be avoided by using steel sections with at least Class 3 cross section.

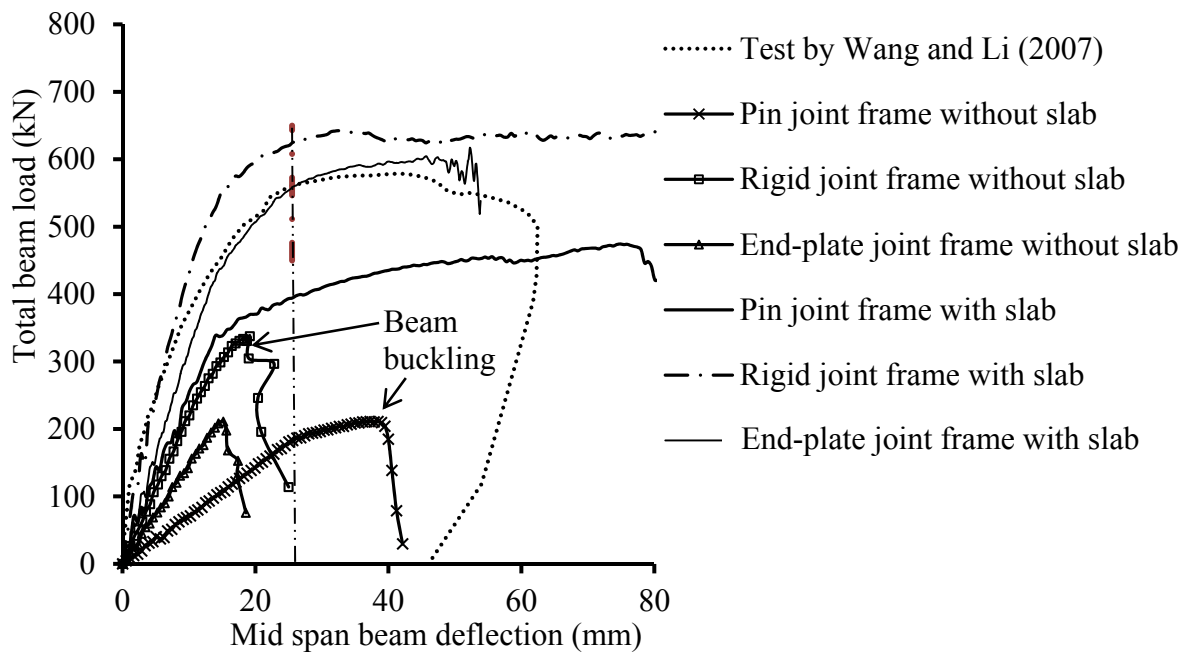


Figure 17. Load-deflection behaviour of Beam-1 with material damage model

In addition to the end-plate semi-rigid joint composite frame response, parametric study for pin and fix jointed skeleton frame (frame without floor slab) and frame with composite slab response also investigated to study the joint and slab contribution on building frame response. Analysis results conclude that, conventional simplifications such as skeleton frame or extreme cases of joint simplifications (pin, rigid) do not predict the real frame behaviour well. It also shows that the use of semi-rigid joint in composite frame enhances the building frame resistance compared to pin-joint building frame resistance. The building frame without floor slab under predicts the frame response and also the frame without floor slab becomes susceptible to buckling. The floor slab generally increase the frame resistance by 50% compared to the resistance of frame without slab. Therefore floor slab and joints are vital structural elements and they enhance the building frame response significantly. The proposed simplified slab and joint model can be easily incorporated in the building frame model and improve the computational efficiency.

4.0 CONCLUSIONS

A semi-rigid joint model based on Eurocode 3-1-8 component model using non-linear connector and a simplified composite slab model have been proposed to analyse 3D composite frame. The non-linear connector behaviour can be represented by axial force-displacement relationship and moment-rotation relationship. The proposed joint model will avoid detailed finite element modelling of joint components and leads to

overall improvement in computational efficiency of analysing large building frames. The incorporation of semi-rigid joint model in 3D frame analysis tends to produce more realistic estimate of frame behaviour compare to model using pin or rigid joints.

REFERENCES

- Alashker, Y., Li, H. and El-Tawil, S. 2011. "Approximations in Progressive Collapse Modeling". *Journal of Structural Engineering* 137, 914-924.
- Cervera, M., Hinton, E. and Hassan, O. 1987. "Nonlinear Analysis of Reinforced Concrete Plate and Sheel Structures Using 20-Noded Isoparametric Brick Elements". *Computers & Structures* 25, 845-869.
- Elghazouli, A.Y. and Izzuddin, B.A. 2004. "Realistic Modeling of Composite and Reinforced Concrete Floor Slab under Extreme Loading". *Journal of Structural Engineering* 130, 1895-1996.
- Gizejowski, M.A., Barcewicz, W. and Salah, W. 2010. "Finite Element Modeling of the Behaviour of a Certain Class of Composite Steel-Concrete Beam to Column Joints". *Archives of Civil Engineering, LVI LVI*, 19-55.
- Izzuddin, B.A., Vlassis, A.G., Elghazouli, A.Y. and Nethercot, D.A. 2008. "Progressive Collapse of Multi-Storey Buildings due to Sudden Column Loss-Part II: Application". *Engineering Structures* 30, 1424-1438.
- Izzuddin, B.A., Vlassis, A.G., Elghazouli, A.Y. and Nethercot, D.A. 2008. "Progressive collapse of multi-storey buildings due to sudden column loss - Part I: Simplified assessment framework". *Engineering Structures* 30, 1308-1318.
- Jeyarajan, S., Liew, J.Y.R. and Koh, C.G. 2013. Progressive collapse analysis of composite frames with floor slab actions. In *Composite Construction VII*, Queensland, Australia.
- Kwasniewski, L. 2010. "Nonlinear dynamic simulations of progressive collapse for a multistory building". *Engineering Structures* 32, 1223-1235.
- Nazem, M., Rahmani, I. and Pajand, M.R. 2009. "Nonlinear FE Analysis of Reinforced Concrete Structures Using a Tresca-Type Yield Surface". *Civil Engineering* 16, 512-519.
- Sadek, F., El-Tawil, S. and Lew, H.S. 2008. "Robustness of Composite Floor Systems with Shear Connections". *Journal of Structural Engineering* 134, 1717-1725.
- Sarraj, M., Burgess, I.W., Davison, J.B. and Plank, R.J. 2007. Finite element modelling of fin plate steel connections in Fire. In -, University of Sheffield, UK.
- Wang, J.-F. and Li, G.-Q. 2007. "Testing of semi-rigid steel-concrete composite frames subjected to vertical loads". *Engineering Structures* 29, 1903-1916.
- Zha, X., Ye, J. and Yu, M. 2010. "The influence of joints and composite floor slabs on effective tying of steel structures in preventing progressive collapse". *Journal of Constructional Steel Research* 66, 442-451.

Experiments on a Continuous Composite Truss Bridge with Concrete-Filled Lower Chords

Choong-Eon Kim¹; Hea-Young Ahn²; Pil-Goo Lee³; and Chang-Su Shim⁴

¹R&D Team, SamhyunPF, Seoul 138-859, Korea. E-mail: slmania@hanmail.net

²SamhyunPF, Seoul 138-859, Korea. E-mail: hh5528@nate.com

³Steel Structure Research Division, RIST, Incheon 406-840, Korea. E-mail: pg289@rist.re.kr

⁴Dept. of Civil and Environmental Engineering, Chung-Ang Univ., Seoul 156-756, Korea. E-mail: csshim@cau.ac.kr

Abstract

Concrete filled tubular structures have advantages to overcome stability of thin plates and to increase stiffness. A hybrid bridge combining common steel box girders and truss girders was suggested to increase the span length of steel-concrete composite bridges. In negative moment regions, a truss girder has lower chords of concrete filled rectangular steel box section to increase flexural stiffness. A bridge model with span length of 30m was fabricated and static tests were performed to assess the effect of composite chords on the flexural behavior of the girder. Depth of the girder varies from 2.0 m to 3.0 m. Significant reduction of stresses in lower steel chord was observed and measured deflections showed a good agreement with calculated values considering the contribution of infilled concrete. Cracking and crack width of the upper concrete slab were observed and indirect crack control by longitudinal reinforcing bars can be used for the design.

INTRODUCTION

There are many attempts to increase economy of long span bridges including double composite action (Kim and Shim 2009, Shim et al. 2011), hybrid section (Lee et al. 2005), truss beams (Shim and Kim, 2010) and corrugated steel webs. Double composite sections in negative moment regions increase flexural stiffness, and hybrid section using high strength steel enhances material usage. Truss section and corrugated webs are adopted to minimize deadweight of long span bridge girders. These improvements make composite bridges very competitive for spans between 40 to 100 m compared to concrete bridges.

Steel tubular structures have been widely used for their characteristics, such as pleasing appearance, light-weight, easy fabrication, and rapid erection. Concrete filled steel tube (CFT) not only raises the compressive strength and ultimate strain of confined concrete but also provides its flexural strength. The CFT was used for a lower flange subjected to compressive force (Uehira and Ito 2008). Shear connection for steel and concrete composite trusses were investigated by several researchers (Machacek and Cudejko 2009, 2011, Bouchair et al. 2012).

In this paper, a hybrid combination of steel box girder and composite truss section was proposed as presented in Fig. 1. Fabrication cost of the steel box girder is lower than that of truss section. For positive moment region, a typical steel box section was used and composite truss section using concrete filled lower chord members was designed for negative moment regions.

Design concepts of this new bridge type were verified by a bridge model test. A 30m long and 2.4m wide continuous composite truss bridge was fabricated to check constructability and fabrication error control. Static tests were performed to estimate global and local behavior and comparisons between design concepts and test results were provided in this paper.

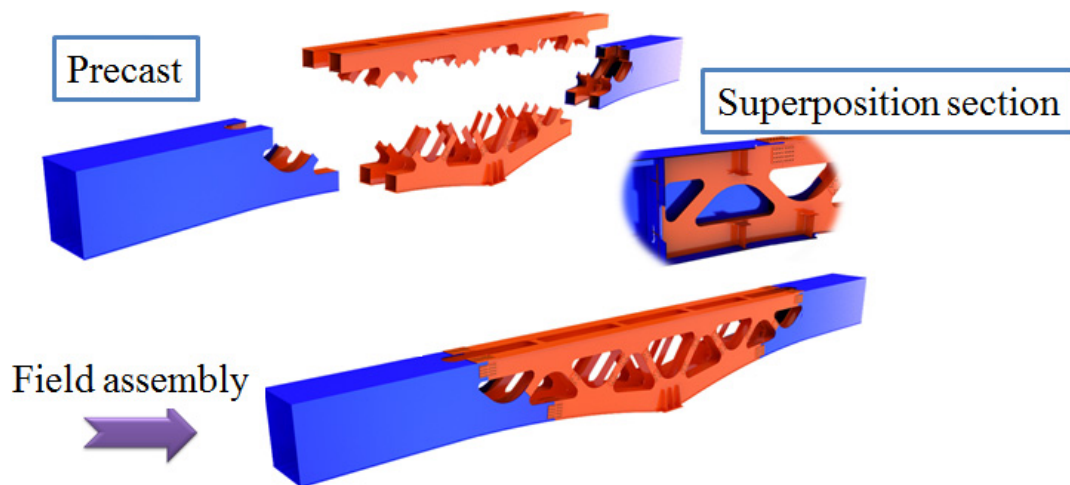


Figure 1 Continuous Composite Truss Bridge

EXPERIMENTAL PROGRAM

Main objectives of the experiment were to evaluate structural performance of composite truss structure in negative moment region. As shown in Fig. 2, a girder with 15m-15m length for negative moment section was designed to simulate 70m-70m two-span continuous bridges.

Three stages of construction were considered as presented in Fig. 3 and static loadings were applied to the ends of the girder at each stage to investigate flexural behavior of the girder. When the top slab concrete was hardened, the final loading was applied to observe cracking and inelastic behavior of the composite section in negative moment region. Deflections and strain of each section were measured.

The design compressive strength of concrete was 27MPa and 40MPa for the slab and bottom chord members, respectively. The confinement effect on the compressive strength of infilled concrete in the bottom chord members was not considered in the design of the bridge model. The yield strength of the chord member and secondary members were 320MPa and 215MPa, respectively. From the standard cylinder tests of concrete, average strength of concrete for the slab and lower chord was 28.3MPa and 42MPa, respectively.

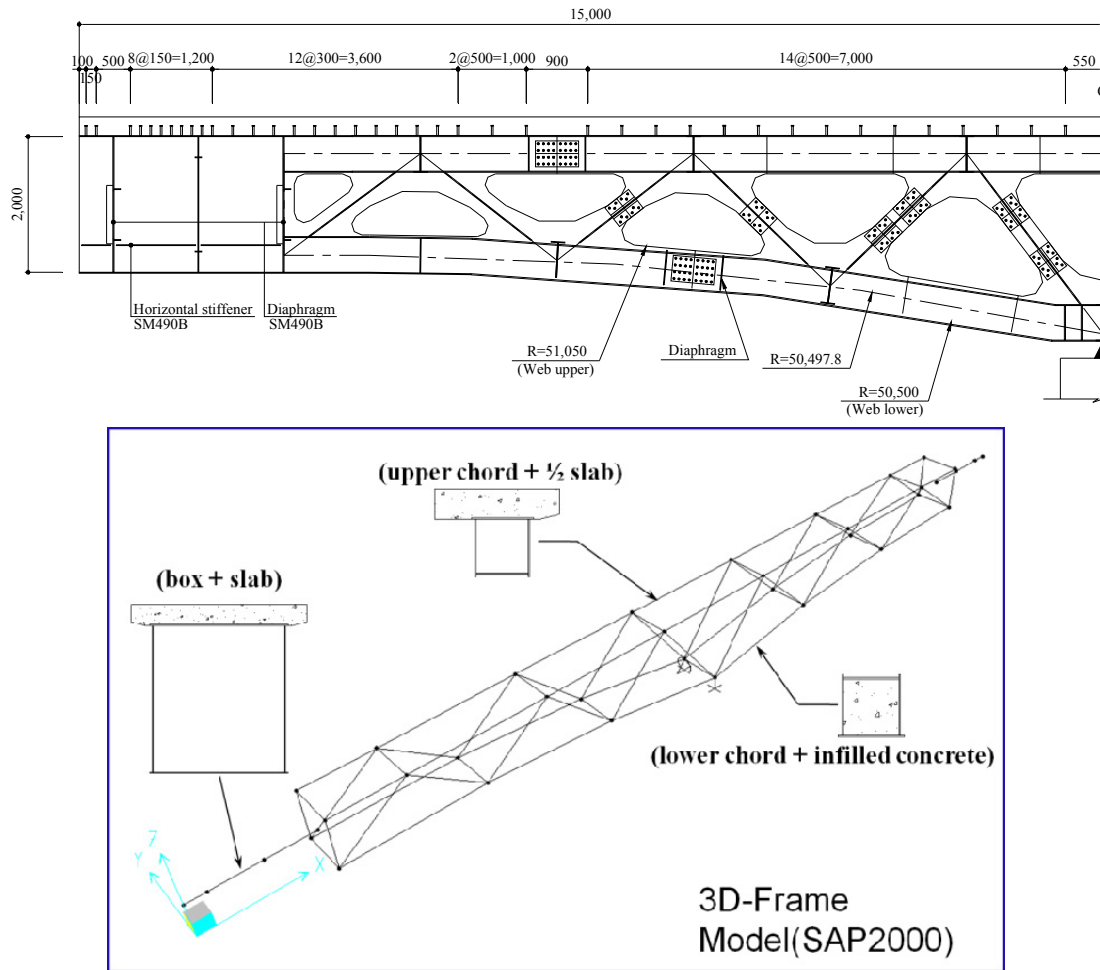


Figure 2 Test specimen and frame model

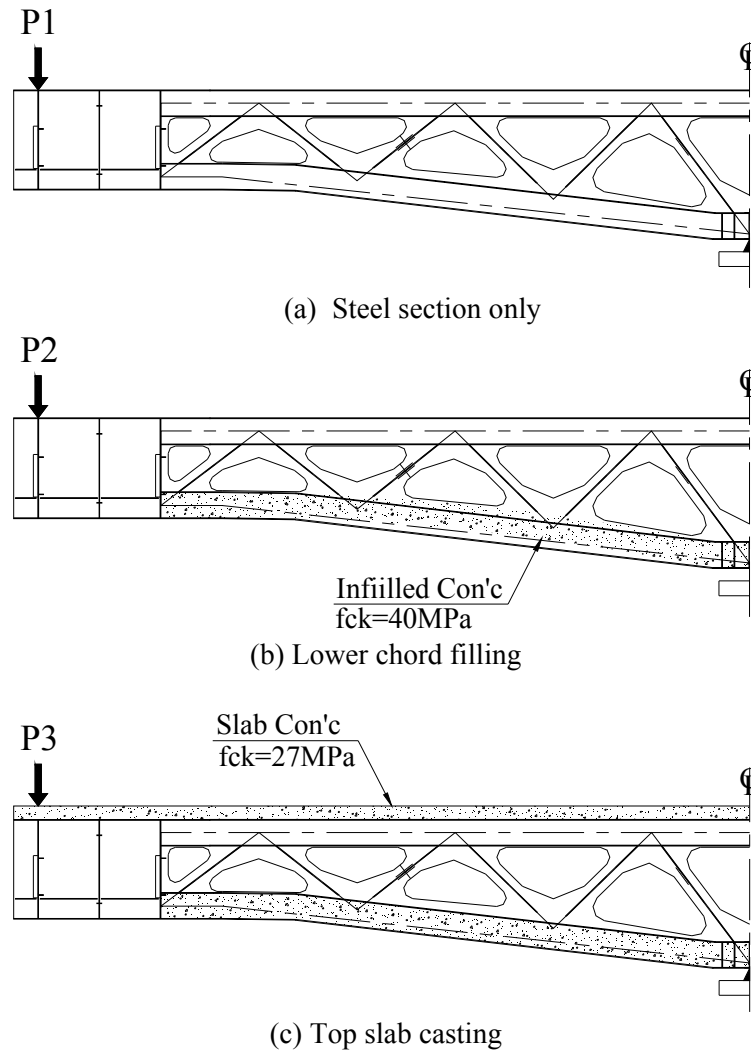
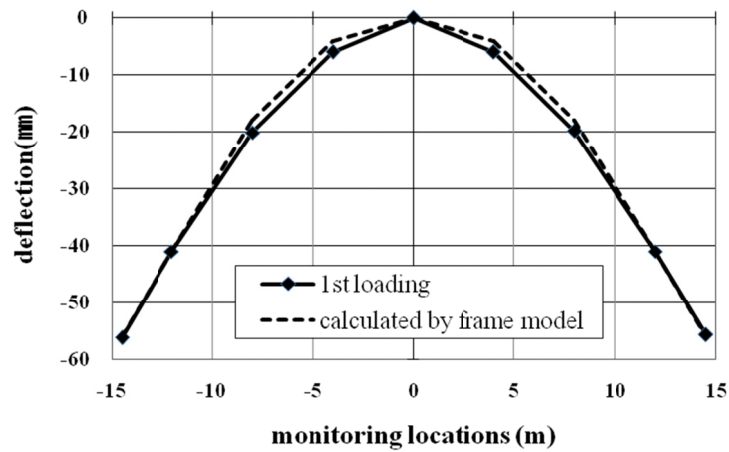


Figure 3 Test procedure

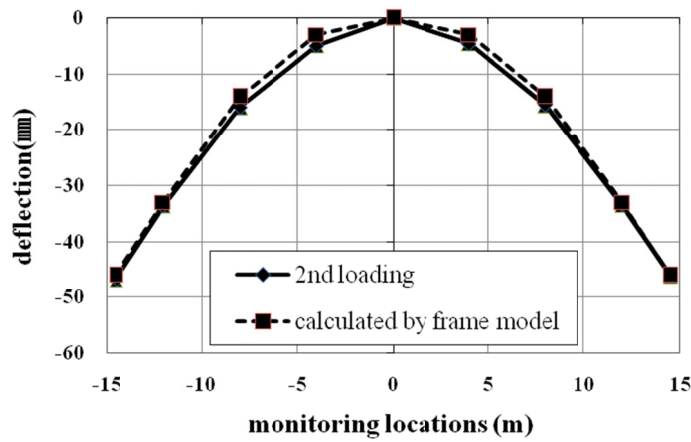
FLEXURAL BEHAVIOR OF COMPOSITE TRUSS GIRDER

Flexural stiffness of the girder was evaluated from the measured deflection values, which are presented in Fig. 4. Design values were obtained from FE analyses of frame models (Fig. 2). Comparisons showed the differences within 2% for the 1st loading and 2nd loading. By filling the lower chord, the flexural stiffness of the girder increased 18%. Concrete filled steel members for lower chord showed considerable enhancement of flexural stiffness.

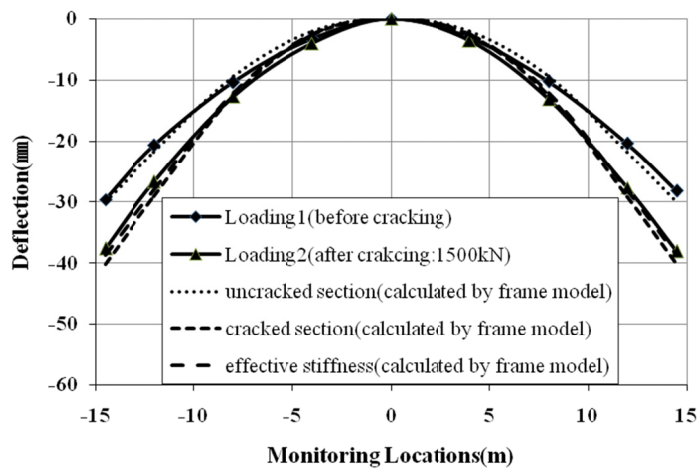
When concrete of the top slab was hardened, 3rd loading was applied to 300 kN, which is less than cracking load. The measured deflection showed the flexural stiffness of the composite girder agrees well to the calculated values assuming gross section of the concrete slab. When the loading was applied to 1500 kN, cracking at the slab was observed. The measured deflection showed that the calculated deflection assuming the gross section of the slab is smaller than the measured value. Deflection by neglecting the concrete section in tension gave conservative results. Therefore, it is necessary to consider tension stiffening effect for the evaluation of flexural stiffness of composite girder in negative moment region. This is important to design a long-span continuous bridge.



(a) 1st loading



(b) 2nd loading



(c) 3rd loading

Figure 4 Deflection

From the measured strains of top chord and lower chord members, concrete filling in the bottom chord members showed 10% decrease of stress in the top chord member when the strain values are compared at the same load level of each loading stage. In the design of the bottom chord, the composite action of the bottom chord decreases stress of the bottom chord member near the middle support by 50%. In the experiment, the decrease was 40% from the measured strain.

When 3rd loading was applied to 1900kN, cracking of the concrete slab was observed and recorded. Table 1 summarizes crack spacing and crack width. Design loading was 1500kN and the measured crack width was less than 0.1mm, which is reasonable considering the designed tensile reinforcements in the negative moment region. Fig. 5 shows cracking pattern of the slab. Maximum crack spacing was 287mm, which is similar to actual transverse cracking of concrete slab in composite bridges.

Table 1. Maximum crack spacing and crack width for each service load (unit: mm)

Location	Service load 1500 kN		Service load 1896kN	
	max. crack spacing	crack width	max. crack spacing	crack width
CW01		0.0910		0.1171
CW02		0.0663		0.0860
CW03	287	0.0798	287	0.1015
CW04		0.0598		0.0770
CW05		0.0319		0.0419

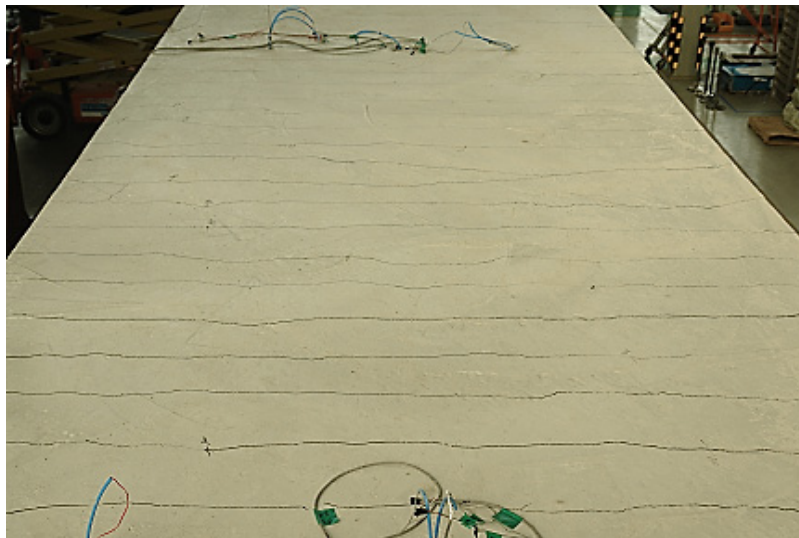


Figure 5 Cracking of concrete slab

CONCLUSIONS

For long-span composite bridges, a new concept combining steel box girder and double-composite truss girder was proposed. For positive moment regions, common steel box girder is used due to its lower fabrication cost. For negative moment region, the double composite action by filling concrete in lower chord members, which are mainly in

compression by dead loads, gives considerable increase of flexural stiffness for continuous bridges.

A bridge model was fabricated and static tests were performed to verify the design concepts and calculated values. Significant reduction of stresses in lower steel chord was observed and measure deflections showed a good agreement with calculated values considering the contribution of infilled concrete in lower chord members. Cracking and crack width of the upper concrete slab were observed and indirect crack control by longitudinal reinforcing bars can be used for the design.

ACKNOWLEDGMENTS

This research was supported by a grant(10 CTIP A04) from Construction Technology Innovation Program funded by the Ministry of Land, Infrastructure and Transport (MLIT) of the Korean Government.

REFERENCES

- Bouchair A., Bujnak J. and Duratna P. (2012), "Connection in Steel-Concrete Truss", *Procedia Engineering*, 40, 96-101.
- Kim H.H., Shim C.S. (2009), "Experimental investigation of double composite twin-girder railway bridges", *Journal of Constructional Steel Research*, 65(6), 1355-1366.
- Lee P.G., Shim C.S., Ryu H.K., Chang S.P. (2005), "Inelastic Behavior of Continuous composite beams with hybrid girder", *Eurosteel Conference on Steel and Composite Structures*, Maastricht, Netherland, 06. 08, 4621-4628.
- Machacek J. and Cudejko M. (2009), "Longitudinal shear in composite steel and concrete trusses", *Engineering Structures*, 31(6), 1313-1320.
- Machacek J. and Cudejko M. (2011), "Composite steel and concrete bridge trusses", *Engineering Structures*, 33(12), 3136-3142.
- Shim C.S., Whang J.W., Chung C.H., Lee P.G. (2011), "Design of Double Composite Bridges using High Strength Steel", *Procedia Engineering*, 14, 1825-1829.
- Shim C.S., Kim D.W. (2010), "Structural Performance of Composite Joints using Bent Studs", *International Journal of Steel Structures*, 10(1), 1-13.
- Uehira K., Ito S. (2008). "Recent Progress of Hybrid Structures and Its Design Methods in Japan", *EASEC-11, Building a Sustainable Environment*, Taipei, TAIWAN

Sustainable Composite Beam Behaviour with Deconstructable Bolted Shear Connectors

Michael S. S. Lee¹ and Mark A. Bradford²

¹Centre for Infrastructure Engineering and Safety, School of Civil and Environmental Engineering, Univ. of New South Wales, Sydney, NSW 2052, Australia. E-mail: s.s.lee@unsw.edu.au

²Centre for Infrastructure Engineering and Safety, School of Civil and Environmental Engineering, Univ. of New South Wales, Sydney, NSW 2052, Australia. E-mail: m.bradford@unsw.edu.au

Abstract

Composite structures using steel joists mechanically connected to concrete slabs serving as the flooring and decking systems are commonly used in buildings and bridges, respectively. The use of the state-of-art precast geopolymer concrete slabs coupled with innovative deconstructable pretensioned bolted shear connectors under service loads in a life-cycle composite beam design can reduce CO₂ emissions, thereby enhancing the sustainability in and recyclability of the construction industry. Most previous research has been conducted on composite beams with welded shear studs that cannot be deconstructed easily. A number of push tests are reported in the current study to establish the interface strength and stiffness characteristics of the bolted shear connectors. The application of the push test data in predicting complex full-scale composite beam behaviour with three distinctive regions that are delineated by the shear flow force at the interface, by the coefficient of friction at the interface and bolt pretension, and by the size of the clearance hole relative to the diameter of the bolt is explained. An initial theoretical investigation based on a simple mechanics-based “full-zero-full” shear interaction mechanism is presented and discussed.

INTRODUCTION

Composite structures using steel joists mechanically connected to concrete slabs are commonplace in buildings and bridges. Concrete is normally strong in compression but weak in tension, whilst steel in compression is prone to buckling effects, and so their symbiotic attributes in composite beams make the composite beam an efficient member. The mechanical shear connectors are designed to bring about composite action in these complementary materials to increase the strength, ductility and stiffness of composite beams above those of the individual materials themselves. Normally, the weakest component governs the strength of the composite structure. Ordinary Portland cement (OPC) has been used as a paste to produce concrete over a very long period. It is widely-known that OPC is a major contributor to anthropogenic greenhouse gas production, with large CO₂ emissions being associated with the manufacture of OPC, with one tonne

of OPC producing approximately one tonne of CO₂ [Davidovits 1994]. The use of geopolymer concrete (GPC) as a replacement for OPC is seen as one means of mitigating the excessive CO₂ emissions associated with OPC, and is a topic of current research in cementitious materials science. Fly ash is a waste material from coal burning power stations, and has been used as a source of geopolymer for GPC that is reported to exhibit comparable if not better material properties to OPC-based concrete [Hardjito *et al.* 2004]. However, GPC is not as readily batched on-site nor as workable by comparison to concrete based on OPC, and so its use in precast applications is an important research issue. The slab systems considered in this paper are precast GPC ones.

There are many types of mechanical shear connectors [Oehlers and Bradford 1995] as shown in Figure 1, but the most commonly used ones are the stud connectors normally welded to the top flanges of the steel joists before casting the concrete slabs [solid or profiled with steel sheeting] because they are economical and easy to install. Clearly the welding and casting of the concrete around headed stud connectors is highly problematic in formulating de-constructability and recycling technologies for composite beams. High-strength bolted steel shear connectors [Figures 1(b) and 1(h)] provide a viable alternative to headed connectors in terms of deconstructability. Despite this and despite the potential for retrofitting composite bridge beams whose studs have failed under fatigue loading, surprisingly little has been reported in the open literature on high-strength bolts as shear connectors.

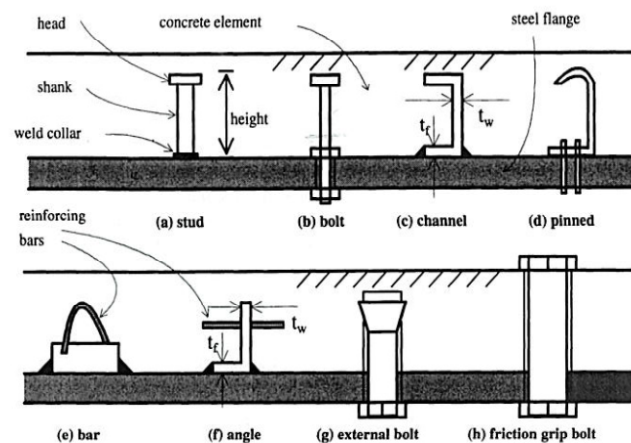


Figure 1. Mechanical shear connectors [Oehlers and Bradford 1995]

Most of the previous research of composite beams has been based on stud shear connectors for normal steel joists and with OPC slabs. Of the limited studies on bolted

shear connectors in composite steel-concrete beams, Dallam (1968) and Dallam and Harpster (1968) reported push tests and beam tests undertaken with bolts embedded in the concrete, Marshall *et al.* (1971) undertook tests on embedded and post-installed bolts and, more recently, Kwon *et al.* (2010) investigated the use of post-installed shear connectors under static and fatigue loading. However, none of those studies offered a complete understanding of the structural behaviour of these types of structures, nor did they consider the issues of deconstructability and sustainability. Therefore, more detailed investigations of the structural behaviour of bolted shear connectors, bolted steel joists and precast GPC slabs, all of which can be recycled at the life-end of a structure, is much-needed. The results of five initial push tests have been reported in detail elsewhere by the authors [Lee and Bradford 2013]. The potential of applying the push test data to predict the structural response of full-scale sustainable composite beams with deconstructable bolted shear connectors using a mechanics-based model [Rowe and Bradford 2013] is discussed and the full scale experimental program has also been reported in detail [Lee and Bradford 2013]. This paper reports the results of four additional push tests, and presents an initial theoretical investigation based on a simplified mechanics-based model. This understanding allows for a codified design approach.

SUMMARY OF PUSH TEST RESULTS

The results of five initial push tests confirmed one of the research hypotheses, in which there are three distinctive stages of the load-slip evolution of pre-tensioned bolted shear connectors: *viz.* a region of “full interaction”, a region of “zero interaction” and a region of “partial interaction”. These are delineated by the shear flow force at the interface, by the coefficient of friction at the interface and the bolt pretension, and by the size of the clearance hole relative to the diameter of the bolt shown in Figure 2 [Lee and Bradford 2013].

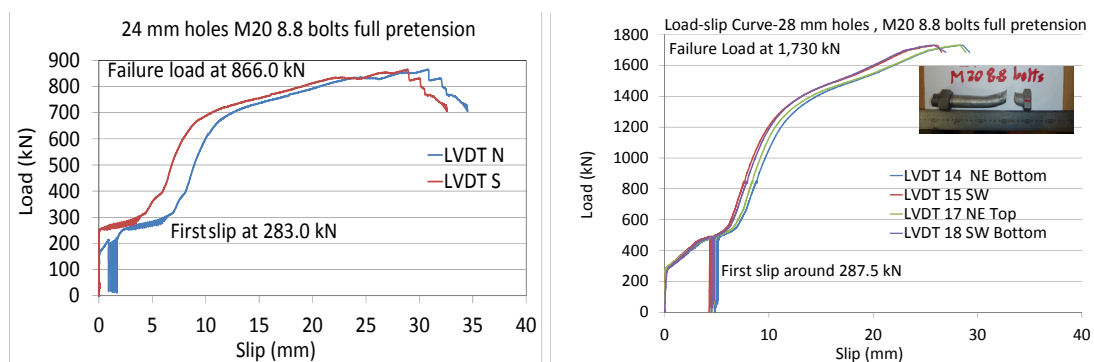


Figure 2. Load-slip evolution for typical single and double panel push tests

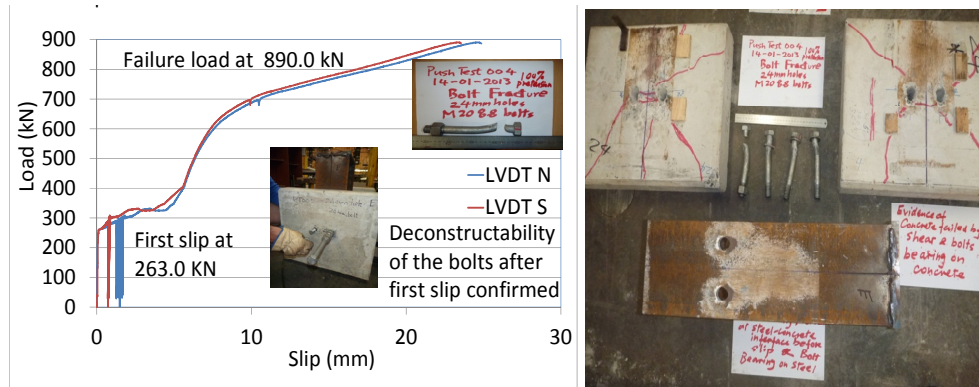


Figure 3. Push test 004 to confirm de-constructability of shear connectors

The double panel push test confirmed that the shear force could be transferred successfully across the panels which replicate a similar situation in realistic slabs. One of the push tests was also performed to confirm deconstructability of the shear connectors under service loads with a typical push test failure mode as shown in Figure 3. The bolts were unloaded and then pre-tensioned again and reloaded to failure. The key results of five initial push tests are summarised in Table 1.

Table 1. Key push test results

Test	P_{sp} (kN)	P_u (kN)	μ	s_b (mm)	s_u (mm)
001	283	866	0.49	4	30.8
002	80	808	0.25	6	25.8
003	100	609	0.26	8	31.5
004	263	890	0.45	4	24.8
005	288	1730	0.50	8	28.6

Legend: P_{sp} = load for first slip; P_u = ultimate load; μ = coefficient of friction; s_b = slip at first bearing; s_u = ultimate slip.

Four additional push tests (006-009) conducted to Eurocode 4 specifications (8 bolts being cycled 25 times between 5% and 40% of the estimated failure load) were carried out with concrete strength of 48 MPa at 90 days (a confirmatory compression test was carried out to confirm the strength which is comparable to that for the initial push tests at 90 days).

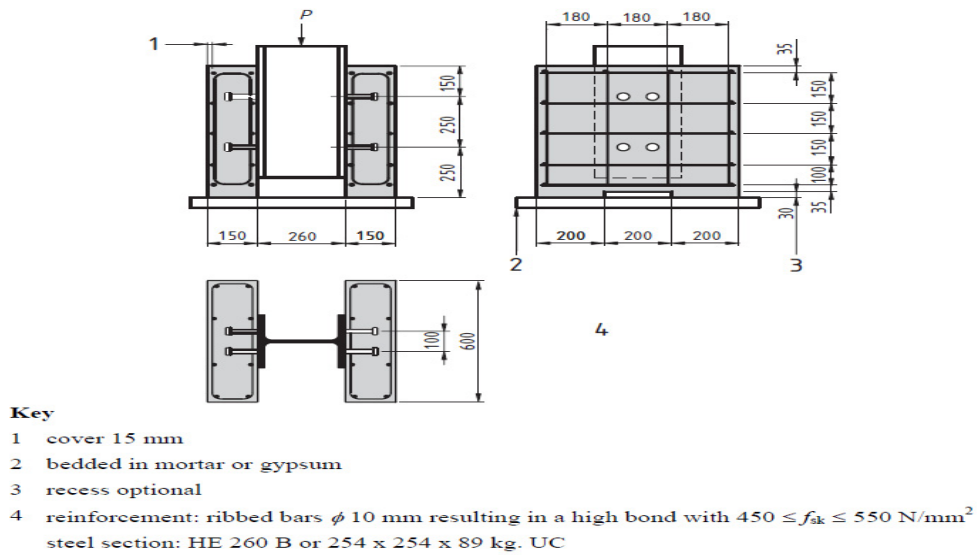


Figure 4. Dimensions of standard push test specimens with shear studs replaced bolts [Eurocode 4]

Push tests 006 and 007 were designed using eight M20 8·8 single nut bolts embedded in the two 600 × 600 × 150 mm thick GPC panels with 15 mm cover [Figure 1(b)] tightened manually. The pretension was calibrated as 130 kN. These two push tests are material tests for the full-scale control beam. Push tests 008 and 009 were designed using eight M20 8·8 bolts pretensioned to 145 kN using the calibrated electric wrench and squirter washers through eight 24 mm precast holes as per the five initial push tests except push test 002. The load-slip evolution of push tests 006 and 007 is presented in Figure 5.

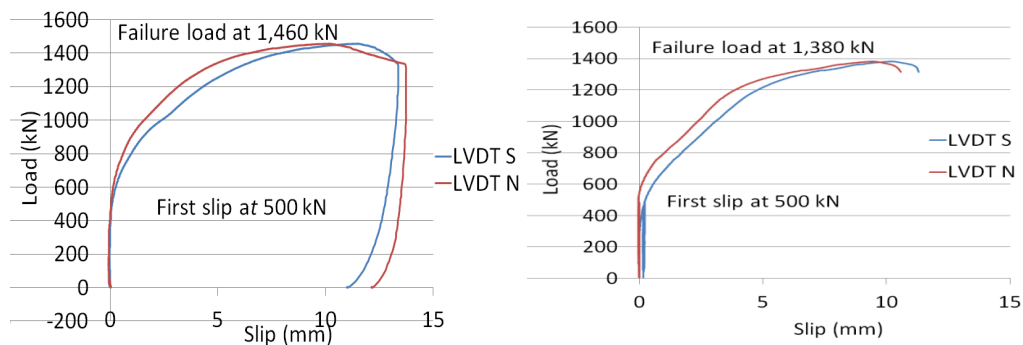


Figure 5. Load-slip evolution of push tests 006 and 007

The load-slip curves for the single nut bolts embedded in the GPC panels in Figure 5 show two rather than three distinctive stages of composite action at the steel-concrete interface. The reason is that the single nut bolts were embedded in the concrete

panels during the pre-casting process and therefore there is no hole clearances between the bolts and the surrounding GPC concrete. The first stage is of a frictional nature and once the friction is overcome, the bolts start to bear on the concrete. Push tests 006 and 007 recorded similar load of 500 kN at first slip and then a failure load of 1,460 kN and 1,380 kN respectively with a similar ultimate slip of around 10 mm (*cf.* 6 mm specified by EC4 to ensure ductile behaviour of composite beams). These results are comparable to those presented by Kwon *et al.* (2010) in terms of the general shape of the load-slip curves and the loads at first slip and at failure. Push test sample 006 appears to be somewhat less stiff than sample 007 during the second stage of the steel-concrete interface behaviour *i.e.* the bolts started to bear onto the concrete.

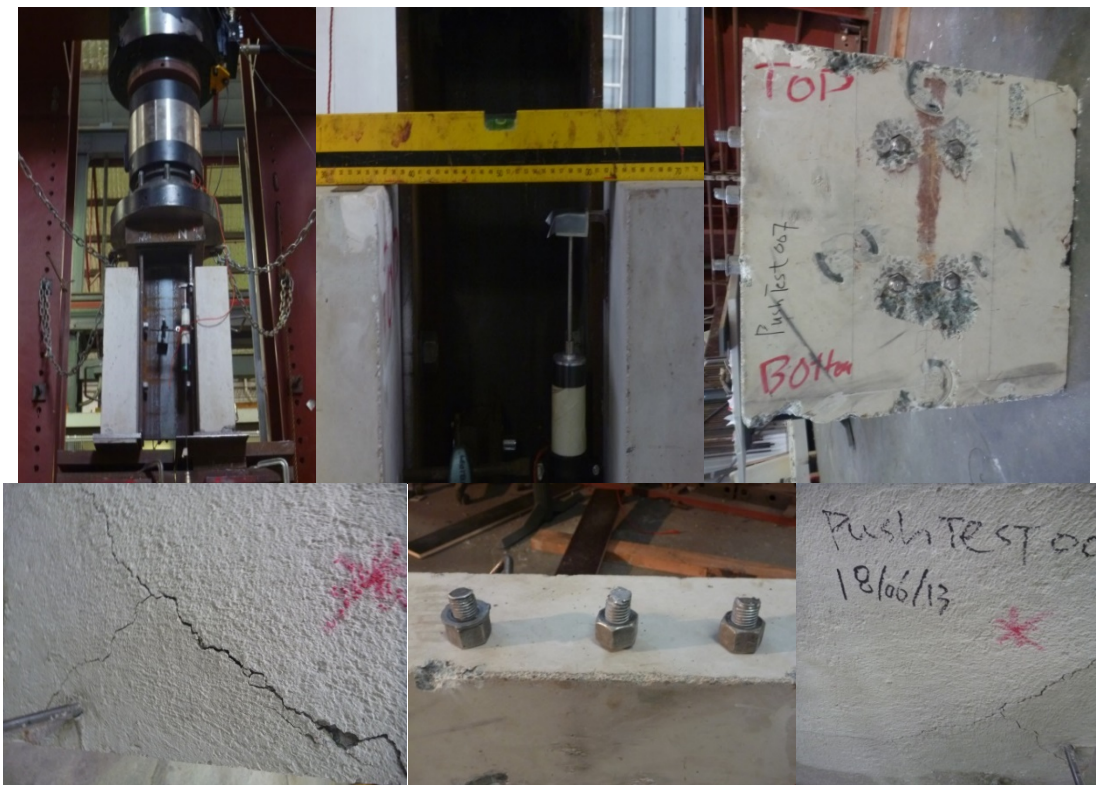


Figure 6. Test set up and failure mode for push tests 006 and 007

Both push tests failed by bolt fracture and concrete shear cracks as shown in Figure 6. There was also evidence of friction being overcome in the failed samples coupled with loud banging noise during the first stage of loading before the first slip. The load-slip curves of push tests 008 and 009 are shown in Figure 7. The general shape of the curves is similar to previous push test 005 with three distinctive stages of steel-concrete interface behaviour *i.e.* fully composite (held by friction), near non-composite [with 4 mm total slip clearance between the bolts and the surrounding GPC concrete as demonstrated in Figure 7] and then finally, partially composite as the bolts start to bear

onto the GPC concrete. Push tests 008 and 009 recorded a load of 560 kN and 585 kN at first slip and a failure load of 1,715 kN and 1,770 kN respectively. The ultimate slip at failure is in the order of 20 mm showing again very ductile behaviour of these types of shear connection. These test results are comparable to those of Kwon *et al.* (2010). One interesting observation is that the loads at first slip of push tests 008 and 009 (single panel with 8 bolts) appear to be twice that of previous push test 005 [double panels with 8 bolts]. This will be a subject of further investigation and it is likely that the bolts in these two tests start to slip more or less the same time giving a much higher load at first slip.

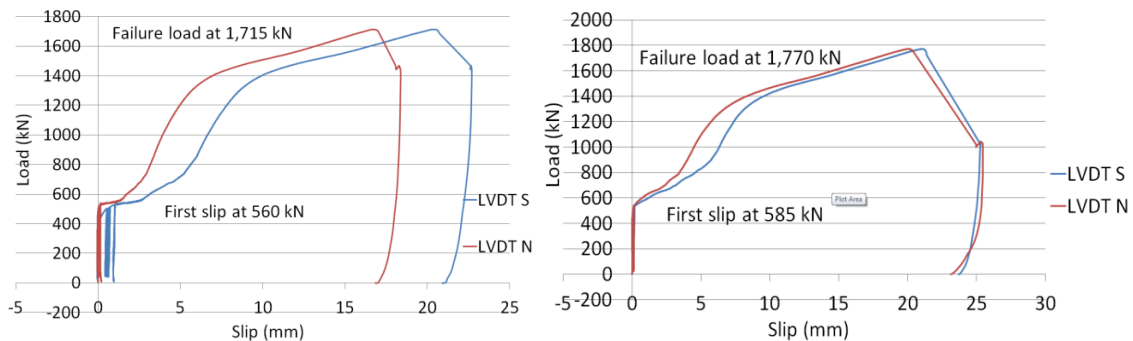


Figure. 7. Load-slip evolution of push tests 008 and 009



Figure. 8. Test set up and failure mode for push tests 008 and 009

The test set up and failure mode observed for push tests 008 and 009 are shown in Figure 8. Both push test specimens failed by bolt fracture with no apparent concrete shear cracks on the non-contact side of the GPC concrete panels and this could be due to the increased concrete strength of 48 MPa at 90 days.

QUASI-ELASTIC MECHANICS BASED MODEL

Framework of Theoretical Model: A theoretical model of the response of a beam with pretensioned bolted shear connectors at service loading can be developed, which uses the empirical results from the push testing [Rowe and Bradford 2013]. This is illustrated with reference to a simply-supported geometrically symmetrical beam of length $2L$, with the x origin at mid-span. Initially, the beam has full interaction because of the prestress provided by the bolts, which has a shear flow force capacity of $p = \mu nP/L$, where P is the prestress in each of the n bolts and μ is the coefficient of friction. When the shear flow force at the ends of the beam $\frac{1}{2}qLB/I$ reaches p , where B and I are the first and second moments of area, the bolts in that location start to slip, *i.e.* when $q = q_1 = 2pI/(LB)$. As q increases from q_1 , the bolts start to slip with a limiting value of s_b , being defined by the size of the total clearance between the bolts and the holes. When q reaches a value of q_2 , the bolts then start to bear on the concrete. This phenomenon of three regions will start to propagate from the end supports where the shear flow forces are a maximum towards the mid-span. These regions of different behaviour of shear connection are illustrated by the load-slip relationship shown in Figure 9. A beam-type finite element model [Ranzi *et al.* 2004] can be cast in an adaptive mode using geometric compatibility and equilibrium of forces. Typical values of k_1 , k_2 and k_3 for the pre-tensioned bolted shear connectors based on the initial push tests (4 bolts) are in the order of 0, 27,000 N/mm, 107,500 N/mm respectively. For the purpose of this paper, a simpler model of “near to full”-“near to zero”-“near to full” shear interaction [Rowe and Bradford 2013] was used to illustrate the concept and to predict the general load slip behaviour of the full scale composite beams with pretensioned bolted shear connectors having a span of $2L$ and simply supported under a uniformly distributed load q . For this model in Figure 9, $k_1 = k_3 \rightarrow \infty$ and $k_2 \rightarrow 0$.

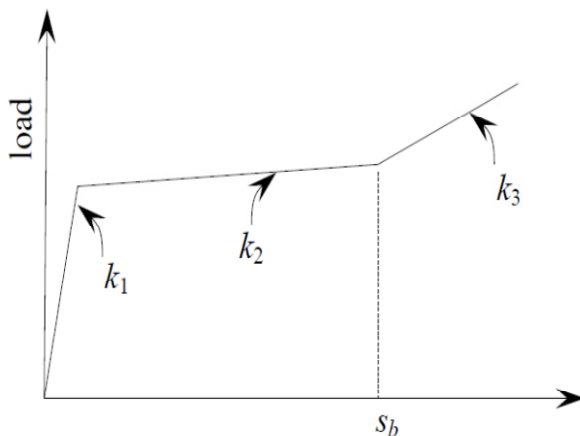


Figure. 9 - Idealised response in elastic range

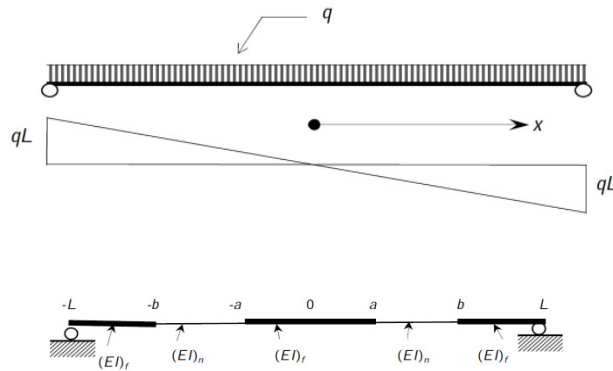


Figure. 10 - Simplified shear interaction model of composite beam with span length of 2L

Refinement of Theoretical Model: The equation for bending in the composite beam in Figure 10 under a uniformly distributed load q can be applied to the different regions, *i.e.* full interaction $(-a, a)$, zero interaction $(a, b) \cup (-a, -b)$ and full interaction $(b, L) \cup (-b, -L)$ of the composite beam shown in Fig. 10. The equation for bending is given as:

$$(EI)_{f,n} v'' = -M = \frac{q(x^2 - L^2)}{2}, \tag{1}$$

in which M is the bending moment, EI is the stiffness of the composite beam and the subscripts f and n indicate the region of the beam has either full or zero shear interaction respectively, v is the transverse deflection and v'' is the curvature. Equation (1) can be applied to three different regions of the composite beam shown in Figure 10. Applying the displacement and slope compatibility and static boundary conditions at $x = 0$, a (where first interface slip occurs), b (where first bearing on the holes occurs) and L produces, after some algebra,

$$\frac{v(0)}{\bar{v}(0)} = \left(\frac{1-n}{5}\right) \left[(3\alpha^3 - 4\alpha^2 - 6\alpha + 12)\alpha - (3\beta^3 - 4\beta^2 - 6\beta + 12)\beta \right] + 1, \tag{2}$$

where $\bar{v}(0) = \frac{5q(2L)^4}{384(EI)_f}$, $\alpha = \frac{a}{L}$, $\beta = \frac{b}{L}$, $n = \frac{(EI)_f}{(EI)_n}$.

For the domain (a, b) and noting that $s(a) = 0$ by definition, the slip $s(x)$ is:

$$s(x) = \frac{v'(x) - v'(a)}{h}, \quad (3)$$

where s is the slip deformation in domain (a, b) and h is the distance between the centroids of the two elements (the GPC concrete slab and the steel joist) of the composite beam. The location of the region of bearing can be determined using $x = b$, which produces the cubic equation

$$\beta^3 - 3\beta = \frac{6(EI)_n s_f}{qhL^3} + \alpha^3 - 3\alpha, \quad (4)$$

where the load at which bearing commences is defined in

$$q_2 = q_1 + \frac{6s_f(EI)_n}{hL^3(3\alpha - \alpha^3 - 2)}. \quad (5)$$

CONCLUSIONS

Additional push test data have been determined for composite beams with pre-tensioned high strength bolts as shear connectors with precast geopolymer concrete slabs, and added to the repository of five previous initial push test results. The potential of applying the push test data to predict the full scale beam behavior using a simplified quasi-elastic mechanic based composite beam model has been further refined to illustrate the concepts based on a “Full-Zero-Full” shear interaction model, proposed in earlier work.

ACKNOWLEDGEMENTS

The work in this paper was supported by the Australian Research Council through an Australian Laureate Fellowship. The support of the technical staff in the UNSW Heavy Structures Research Laboratory is acknowledged with thanks.

REFERENCES

- Dallam, L.N. (1968). Pushout tests with high strength bolt shear connectors. Report for Missouri State Highway Department, Department of Civil Engineering, University of Missouri – Columbia.
- Dallam, L.N. and Harpster, J.L. (1968). Composite beam tests with high-strength bolt shear connectors. Report for Missouri State Highway Department, Department of Civil Engineering, University of Missouri – Columbia.

- Davidovits, J. (1994.) High-alkali cements for 21st century concrete. In P. Kumar Metha (ed), ACI SP 144: 383-397. Detroit: American Concrete Institute.
- Hardjito, D., Wallah, S.E., Sumajouw, D.M.J. and Rangan, B.V. (2004). On the development of fly ash-based geopolymer concrete. *ACI Materials Journal*. 101(6), 467-472.
- Kwon, G., Engelhardt, M.D. and Klinger, R.E. (2010). Behavior of post-installed shear connectors under static and fatigue loading. *Journal of Constructional Steel Research*. 66, 532-541.
- Lee, S.S.M. and Bradford, M.A. (2013a). Sustainable composite beams with deconstructable bolted shear connectors. SEMC 2013: Proceedings of Fifth International Conference on Structural Engineering, Mechanics and Computation, Cape Town, South Africa.
- Lee, S.S.M. and Bradford, M.A. (2013b). Sustainable composite beam behaviour with deconstructable bolted shear connectors-Full scale experimental investigation. Concrete 2013, Gold Coast, Queensland, Australia.
- Marshall, W.T., Nelson, H.M. and Banerjee, H.K. (1971). An experimental study of the use of high-strength friction-grip bolts as shear connectors in composite beams. *The Structural Engineer*. 49(4),171-178.
- Oehlers, D.J. and Bradford, M.A. (1995). *Steel and Concrete Composite Structural Members: Fundamental Behaviour*. Pergamon, Oxford.
- Ranzi, G., Bradford, M.A. and Uy, B. 2004. A direct stiffness analysis of composite beams. *International Journal for Numerical Methods in Engineering*. 61(5), 657-672.
- Rowe, M. and Bradford, M.A. (2013). Partial shear interaction in deconstructable composite steel-concrete composite beams with bolted shear connectors. International Conference on Design, Fabrication and Economy of Welded Structures, Miskolc, Hungary, 585-590.

Effect of Polyvinyl Alcohol (PVA) Fibre on the Dynamic Properties of Concrete Containing Fly Ash

A. Noushini¹; B. Samali²; and K. Vessalas³

¹Centre for Infrastructure Engineering and Safety, School of Civil and Environmental Engineering, Univ. of New South Wales, Sydney, NSW 2052, Australia. E-mail: a.noushini@unsw.edu.au

²Institute for Infrastructure Engineering, Univ. of Western Sydney, Penrith, NSW 2751, Australia. E-mail: b.samali@uws.edu.au

³Centre for Build Infrastructure Research, School of Civil and Environmental Engineering, Univ. of Technology Sydney, P.O. Box 123, Broadway, NSW 2007, Australia. E-mail: kirk.vessalas@uts.edu.au

Abstract

The object of the present investigation is to study the effect of polyvinyl alcohol (PVA) fibres on dynamic properties of concrete containing fly ash as partial replacement for portland cement. Specimens of different concrete types, with variations in the length of fibers and proportioning, have been investigated to assess the performance of uncoated PVA fibre of two geometric lengths (6 and 12 mm) in concrete. Based on total concrete volume, 2 fibre fractions of 0.25 and 0.5%, were evaluated for their effect on damping ratio, fundamental frequency and dynamic modulus of elasticity of PVA fibre reinforced concretes (FRCs). From the results, it can be stated that although PVA fibre addition in low volume fractions used in this study significantly enhance the mechanical properties of FRC, it has no considerable effect on concrete material and RC beams dynamic characteristics.

1 INTRODUCTION

Vibrations in structures which is caused by dynamic loads (e.g. earthquakes or wind loads) vary in amplitude and frequency with excitation source, depending on structural type and applied load. There is no doubt that dynamic property of concrete material is of great significance to these structures, particularly in vibration control and noise mitigation.

Damping is defined as a process whereby vibrational energy is dissipated over a period of time (Smith 1988). To avoid resonance of a specific structure at typical modes, whether in material level or member and structural level, damping is helpful in reducing vibration and resonance (Amick & Monteiro 2005; Zheng et al. 2008).

Two main sources of damping are categorised as intrinsic damping which is basically provided by the structure and the material damping. The other damping is the supplementary damping created utilizing additional devices attached to the structure such as tuned mass dampers, sloshing dampers, viscous dampers, and friction devices. Concrete buildings are generally known to have damping ratios between 1% and 3% of critical damping. If it is possible to increase this percentage to 5% or more, dampers can be eliminated or reduced in some of the structures and save

a lot of energy and money. It is also investigated that by increasing the damping ratio of concrete to 10 or 15% the structure gains the capacity to dissipate the vibrating energy without needing any additional dampers (Jinping et al. 2008; Ou 2002).

Damping ratio is the main parameter representing the property of materials in vibration reduction (Zheng et al. 2008). Due to the number of variables that affect damping in a system, the most realistic way of determining damping of a material or structure is through laboratory investigations. Logarithmic decrement (δ) is one of the most popular parameters of measuring and calculating the damping properties of concrete. This parameter simply provides a measure of the rate of decay of oscillation and is used to find the damping ratio (ξ) of an underdamped system based on the assumption of viscous damping. The logarithmic decrement is defined as the natural logarithm of the ratio of any two successive positive amplitude peaks as shows in equation (1) (Chopra 1995).

$$\delta = \frac{1}{m} \ln \frac{U_n}{U_{n+m}} = \frac{2\pi\xi}{\sqrt{1-\xi^2}} \quad (1)$$

where U_n is the amplitude of n^{th} peak, U_{n+m} is the amplitude of a peak after m cycles and m is the number of cycles between the two successive positive peaks.

Since damping ratio is generally small in the case of concrete (<20%) (Menefy 2007), equation (1) can be further simplified to give a direct relationship between the δ and the ξ as follows;

$$\delta \approx 2\pi\xi \quad (2)$$

Thus, damping ratio (ξ) can be calculated as;

$$\xi = \frac{1}{2\pi m} \ln \frac{U_n}{U_{n+m}} \quad (3)$$

The first serious study on the damping behaviour of concrete was performed in 1940 by Thomson (Thomson 1940). In this investigation, it has been reported that the mechanical properties of concrete e.g. compressive strength and modulus of elasticity can be predicted through dynamic methods and damping measurements. Following the mentioned study, many research works have been carried out so far to explore the effect of various parameters (such as concrete composition, curing condition, moisture content, temperature, compressive strength and modulus of elasticity) on damping properties of concrete and concrete elements.

As a concrete specimen is excited dynamically, each element of the matrix absorbs a portion of the dynamic energy. The synthetic fibre itself, due to its viscoelastic energy dissipation character as a polymeric material, is able to absorb the energy inside itself (Sun et al. 1985). However, although fibres in synthetic FRC are viscoelastic and have damping ratios higher than concrete, the FRC composite is not a good viscoelastic material since it is usually provided by a low volume fraction of fibres. In such cases, adequate damping may not necessarily be produced due to the

hysteresis energy loss in matrix because of the strain cycling in the vicinities of fibre ends, nor from synthetic fibres (Yan et al. 2000a). It can take place due to fibre/matrix debonding which may occur under certain strain and stress conditions surrounding the fibres. This may cause energy loss under alternating loading. Concrete is considered a brittle material which contains micro cracks that may open and close during dynamic loading under flexure. These cracks may cause the matrix to rub on the fibre surface and results in energy loss during vibration (Yan et al. 2000a, 2000b) and accordingly higher damping ratio can be achieved for FRCs (Fu & Chung 1996; Nelson & Hancock 1979).

Fibres generally and synthetic fibres specifically are reported to enhance the dynamic properties of concrete by increasing the damping ratio of plain concrete (Yan et al. 2000a). Furthermore, it has been reported that damping ratio can be used as an indication of changing concrete mechanical characteristics e.g. flexural strength and ductility (Arivalagan & Kandasamy 2009).

In this study, the performance of using uncoated PVA fibre on damping properties of concrete has been investigated. PVA fibres of two geometric lengths, 6 and 12 mm, with volume fraction of 0.25% and 0.50% were utilised to prepare FRC mixes. Furthermore, a non-FRC mix (control) was also made to be used as reference point of this study. The compressive strength and modulus of elasticity (MOE) of concrete samples were also measured to evaluate the mechanical properties of FRC and control concrete. Furthermore, an impact resonant frequency test was also conducted over steel reinforced concrete (RC) beams incorporating PVA fibres, to assess the dynamic properties of the RC beams.

2 EXPERIMENTAL PROGRAM

2.1 *Materials*

Shrinkage limited Portland cement (PC) and fly ash (FA) were used as the binder for all concrete mixes. Shrinkage limited Portland cement was used in this study to minimise concrete drying shrinkage. The fineness of FA by 45 μm sieve was determined to be 94% passing (tested in accordance with AS 3581. 1-1998).

A maximum nominal size of 20 mm aggregate was used in all mixes. All aggregates used in mix design were sourced from Dunmore, Australia, which includes 50/50 blended fine/coarse manufactured sand and 10 mm and 20 mm crushed latite gravel. The grading of all aggregates complies with the Australian Standard; AS 2758.1 specifications and limits. All aggregate was prepared to saturated surface dry condition prior to batching.

Drinking grade tap water was used for all mixes after conditioning to room temperature (23 ± 2 °C). Furthermore, in order to improve the workability, a polycarboxylic-ether based high range water reducing admixture (HWR) was used. Non-coated polyvinyl alcohol fibre of 2 different geometries, 6 and 12 mm, with specifications mentioned in Table 1 with graphical illustration shown in Figure 1, were used in all FRC mixes.

Table 1. Properties of PVA fibres.

Specific gravity [g/cm ³]	Diameter [mm]	Thickness [dtex]	Cut length [mm]	Tensile strength [MPa]	Young's modulus [GPa]	Elongation [%]
1.29	0.014	1.8-2.3	6 and 12	1500	41.7	7

**Figure 1. PVA fibres; 6 mm fibres (left) 12 mm fibres (right).**

2.2 Mixing and samples preparations

Mixes were prepared to obtain characteristic compressive strength at 28 days (f'_c) of 60 MPa to conform to AS 3600 requirements as structural concrete (ranging from 20 MPa to 100 MPa) even after adding fibres which may cause strength reduction, along with a slump of 80 ± 20 mm. In order to obtain the desired slump, HWR dosage was varied. Details of the mix proportions for control concrete (no fibres) are presented in Table 2. Mix ingredients were all measured and added to the mix by weight. All FRCs also followed the same proportioning and only fibres were added to the mixture by 0.25% and 0.5% of volume fraction of the mix.

For non-FRC (control) mix, mixing was performed in accordance with AS 1012.2. However, for FRC mixes, due to the presence of fibres, the standard mixing regime suggested in Australian Standard for conventional concrete was modified. Accordingly, the mixing time was increased to 3 minutes to achieve a completely homogeneous concrete. Slump was taken to check the workability and, thereafter, freshly mixed concrete was placed into moulds and compacted using an external vibrating table. Curing of test specimens was carried out in accordance with AS 1012.8. Specimens were placed in a water tank after demoulding to be cured in lime-saturated water at a temperature of 20 ± 2 °C until the testing date.

Table 2. Mix proportions of reference concrete.

kg/m ³					Lit/m ³		Water/C*
Cement	Fly ash	Sand	10 mm aggregate	20 mm aggregate	Water	HWR	
301	129	635	390	700	151	1.215	0.35

* Cementitious materials

2.3 Testing methods

Uniaxial compression and modulus of elasticity (MOE) tests were performed on cylindrical specimens of 100×200 mm and 150×300 mm, respectively, at the age of 28 days in accordance with AS 1012.9 and AS 1012.17 specifications and method.

The impact resonance test was used to determine the resonant frequency of 75 × 100 × 400 mm prisms following the test method recommended in American Standard, ASTM C 215 (08), by applying a small load impulse and measuring the resulting acceleration through the specimen for different modes of vibration. To excite the normal modes of vibration, a small metal hammer (impactor) was used to manually apply a small load impulse to the specimen. The accelerometer attached to the specimen, was used to transform the resulting vibrations into electrical signals. The miniature accelerometer is assumed to have no influence on the resonance frequencies of the beam. The specification of impactor (hammer) and accelerometer are shown in Table 3.

Table 3. Impactor and accelerometer specifications.

Impactor (hammer)	
Model	PCB 086D05
Sensitivity (±15%)	0.23 mV/N
Measurement range	± 22,240 N pk
Resonant frequency	≥ 22 kHz
Non-linearity	≤ 1%
Accelerometer	
Model	PCB 356B08
Sensitivity (±10%)	10 mV/(m/s ²)
Measurement range	± 490 m/s ² pk
Frequency range (±5%)	0.5 – 5000 Hz
Frequency range (±10%)	0.3 – 6500 Hz
Resonant frequency	≥ 20 kHz
Broadband resolution	0.001 m/s ² rms
Non-linearity	≤ 1%
Transverse Sensitivity	≤ 5%
Weight	20 gm

Soft rubber supports were also used to permit the specimen to vibrate freely in each mode of vibrations. The schematic of test apparatus is shown in Figure 2. A computer based data acquisition system is used to record hammer force and acceleration response signals during the tests. Data processing, including Fast Fourier Transform (FFT) and Frequency Response Function (FRF) calculations were then executed using a specifically developed MATLAB programme. From recorded dynamic response time histories, using FFT, the auto spectrum of the given signal can be obtained and the FRF can be computed.

For each concrete type, impact resonance test was carried out at 14 and 28 days of ageing. For each age, 3 specimens of the same concrete were tested and since the test is non-destructive, same specimens were used for the next testing age. To provide more accurate results, at least 5 strikes were applied on each sample for each mode of vibration and the average was taken from the successive results.

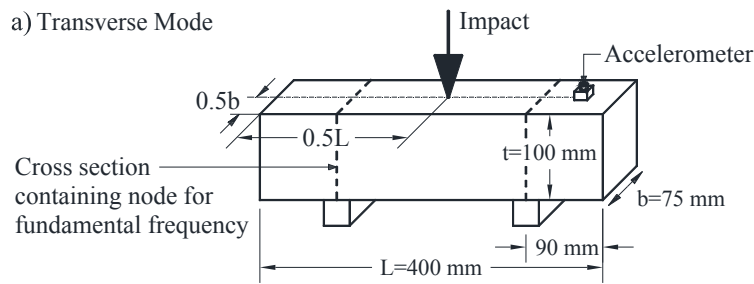


Figure 2. Typical impact resonance test set-up (locations of impact and accelerometer) for transverse mode of vibration (ASTM C 215 – 08).

Furthermore, impact resonant frequency test (hammer test) for transvers mode of vibration was also conducted over steel reinforced concrete (RC) beams incorporating PVA fibres, to assess the dynamic properties of the RC beams.

The RC beams used for this test were designed in accordance with AS 3600 (2009). All specimens were 1.9 m long with a span of 1.8 m and a depth of 200 mm (effective depth = 159 mm). A concrete cover of 25 mm was also applied for all beams. Figure 3 shows the beam geometry and the reinforcement details.

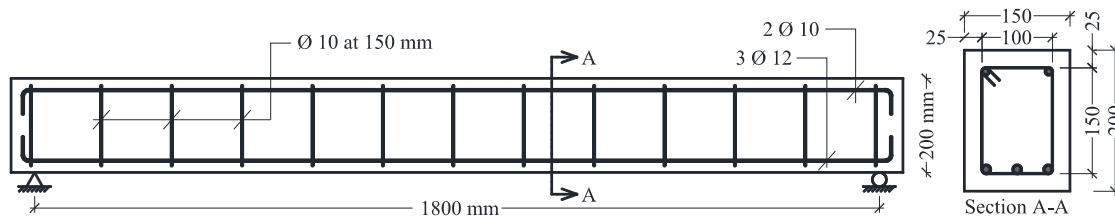


Figure 3. Schematic of RC beam.

All beams were provided with 10 mm diameter stirrups (Ø10) with a constant spacing of 150 mm (centre-to-centre) over the whole of their length in order to avoid shear failure and have a reinforcement ratio (ρ_s) of 1.42%. The reinforcement details are summarized in Table 4.

Table 4. Steel reinforcement arrangements.

Tension steel reinforcement			Compression steel reinforcement		
Diameter	No.	f_{sy} (nominal)	Diameter	No.	f_{sy} (nominal)
[mm]		[MPa]	[mm]		[MPa]
12	3	250	10	2	250

Beams were subjected to an impulsive load applied at mid-span to excite their higher transverse mode frequencies. The beam response to this impulsive load was captured by the means of 6 accelerometers mounted at different places of the beam as illustrated in Figure 4. The points to attach the accelerometers were; the one-fourth spans and mid span on top surface along the centreline of the beam, the one side at centre and at two face ends of the beam on top. The most important data captured,

which is the focus of this study, is corresponding to the mid span. To minimise errors and noise affecting the results, 5 hits were carried out for every strike location.

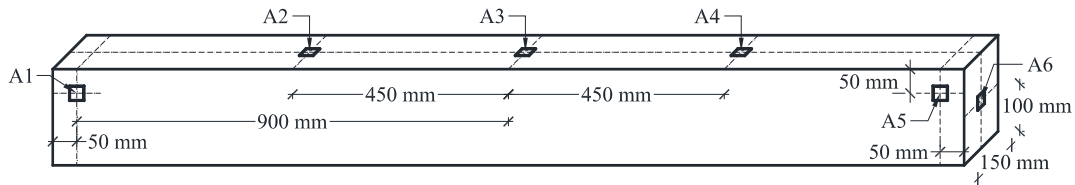


Figure 4. Accelerometers arrangement on RC beam.

The specification of impactor (hammer) and accelerometers are shown in Table 5.

Table 5. Hammers and accelerometers specifications.

Impactor (hammer)	
Model	PCB 086D20
Sensitivity ($\pm 15\%$)	0.23 mV/N
Measurement range	$\pm 22,240$ N pk
Resonant frequency	≥ 12 kHz
Non-linearity	$\leq 1\%$
Accelerometers	
Model	PCB 352C34
Sensitivity ($\pm 10\%$)	10.2 mV/(m/s ²)
Measurement range	± 490 m/s ² pk
Frequency range ($\pm 5\%$)	0.5 – 10000 Hz
Frequency range ($\pm 10\%$)	0.3 – 15000 Hz
Resonant frequency	≥ 50 kHz
Broadband resolution	0.0015 m/s ² rms
Non-linearity	$\leq 1\%$
Transverse Sensitivity	$\leq 5\%$
Weight	5.8 gm

From the test results, the fundamental (natural) frequencies were measured and acceleration-time history graphs were prepared. Acceleration-time history was used in order to calculate the damping ratio, following logarithmic decrement method as described previously. A sample acceleration-time history in free vibration is illustrated in Figure 5.

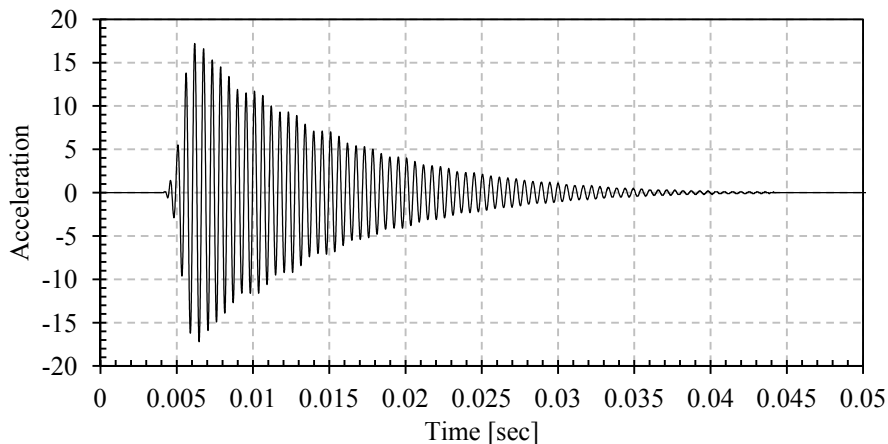


Figure 5. Sample PVA-FRC (6PVA-0.25%) acceleration-time history.

The dynamic modulus of elasticity (DMOE) can also be calculated from the fundamental transverse frequency, using the below mentioned equation;

$$DMOE_{transverse} = CMn^2 \quad (4)$$

where M is the mass of specimen in kg, n is the fundamental transverse frequency in Hz and C is a factor equal to 1122.6, calculated from table 1 of ASTM C 215-08.

3 RESULTS AND DISCUSSION

Table 6 presents the mechanical properties of FRCs and control concrete. By looking at the results, it can be noted that most PVA-FRCs have higher compressive strength at 28 days ($f_{c,28}$) compared to the control except for 12PVA-0.50% which includes 0.5% volume fraction of 12 mm fibres. It can also be observed that with a same fibre content shorter fibres act better than longer ones in terms of compressive strength and the optimum fibre volume fraction goes to 0.25% for both fibre lengths. In the case of concrete MOE, it can be noted that PVA fibres in low volume fractions used in this study do not significantly affect the modulus of elasticity. However, it is noted that within the FRCs incorporating the same fibre, 0.25% volume fraction shows higher $E_{c,28}$ and in a same fibre content longer fibres have lower $E_{c,28}$.

Table 6. Mechanical properties of different mixes at 28 days of age.

Mix Reference	Fibre length [mm]	V_f [%]	Compressive strength- $f_{c,28}$ [MPa \pm SD ¹]	Modulus of Elasticity- $E_{c,28}$ [GPa]
Control	-	-	60.0 \pm 3.2	39
6PVA-0.25%	6	0.250	67.0 \pm 3.2	40
6PVA-0.50%	6	0.500	61.5 \pm 2.5	38
12PVA-0.25%	12	0.250	64.5 \pm 3.2	39
12PVA-0.50%	12	0.500	58.5 \pm 2.8	36

¹SD: Standard deviation

From the result of the impact resonance frequency test, the material dynamic properties of FRCs and control concrete, including three primary characteristics; resonant (fundamental or natural) frequency, dynamic modulus of elasticity and damping ratio, are calculated for transverse modes of vibration. Figure 6 shows the damping ratio of control and FRCs in transverse mode of vibration at the age of 14 and 28 days. For each concrete mix design a number of 45 samples were recorded as damping ratio. These 45 samples were calculated from the acceleration-time history of 5 hammer strikes over 3 specimens. From each acceleration-time history, 3 damping ratios were calculated from 3 different parts of the graph, to minimise the measurements errors. To follow the same trend for calculating the damping ratios and minimising measurement errors, ' U_{n+m} ' was taken as half the value of ' U_n ' (refer to equation (3)). In Figure 6, the horizontal short dash mark, '—', indicates the average value of damping for each mix.

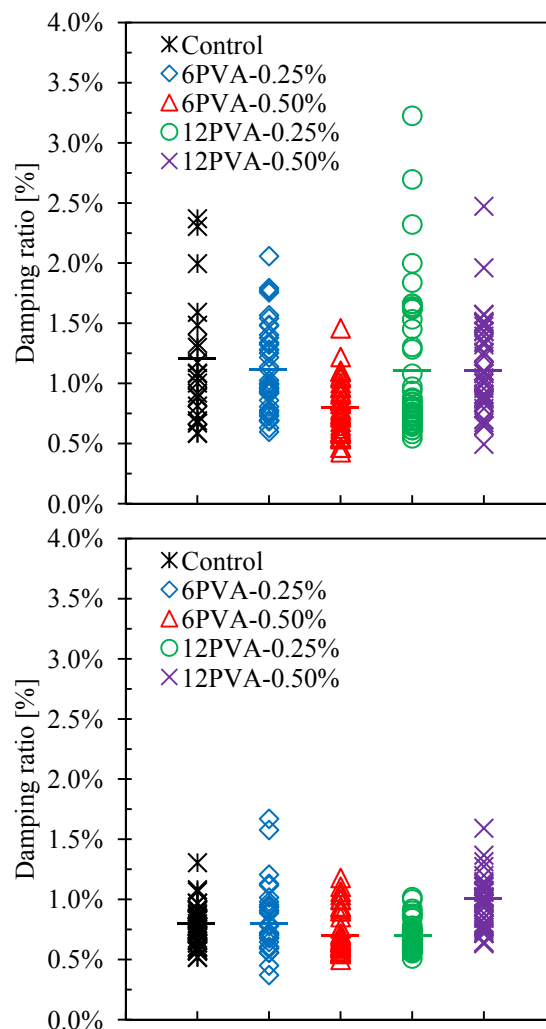


Figure 6. Damping ratio of FRCs versus control concrete in transverse mode at the age of; 14 days (left) 28 days (right).

It has been previously (Yan et al. 2000a) reported that concrete has damping ratios more than 0.5% which can be a reference point. Damping ratio of all concretes is observed to decrease by ageing which is in line with previous investigations (Amick & Monteiro 2006; Cole & Spooner 1965; Swamy & Rigby 1971; Yan et al. 2000a). According to the results, it can be seen that addition of PVA fibres in low volume fraction has no significant effect on concrete damping ratio. The results of all above calculations for transverse mode of vibration are summarised in Table 7.

Table 7. Dynamic properties of control and FRCs at transverse mode.

Mix Reference	Resonant frequency		Dynamic-MOE		Damping ratio (ξ)	
	[Hz \pm SD]		[GPa \pm SD]		[% \pm SD]	
	14 day	28 day	14 day	28 day	14 day	28 day
Control	2206 \pm 11	2245 \pm 10	40.2 \pm 0.4	41.5 \pm 0.4	1.2 \pm 0.5	0.8 \pm 0.2
6PVA-0.25%	2240 \pm 29	2260 \pm 37	41.5 \pm 1.1	42.0 \pm 1.4	1.1 \pm 0.4	0.8 \pm 0.3
6PVA-0.50%	2210 \pm 14	2240 \pm 7	40.5 \pm 0.5	41.5 \pm 0.3	0.8 \pm 0.2	0.7 \pm 0.2
12PVA-0.25%	2230 \pm 22	2240 \pm 12	41.0 \pm 0.8	41.5 \pm 0.4	1.1 \pm 0.6	0.7 \pm 0.1
12PVA-0.50%	2190 \pm 34	2220 \pm 37	39.5 \pm 1.3	40.5 \pm 1.4	1.1 \pm 0.4	1.0 \pm 0.2

Regarding the dynamic characteristics of RC beams, the beams natural frequencies for uncracked section are presented in Table 8. If a shift in natural frequency occurs in a system, it can be inferred that the system has undergone changes. The magnitude of the changes is also an indicator of the severity or state of the change experienced (Razak & Choi 2001).

Table 8. RC beams natural frequency of uncracked section for transverse mode.

Beam label	Natural frequency [Hz \pm SD]
B-Control	76.7 \pm 0.2
B-6PVA-0.25%	77.3 \pm 0.1
B-12PVA-0.50%	68.5 \pm 1.0

4 CONCLUSIONS

The effect of PVA fibre addition on damping characteristics of concrete has been investigated in the current study. Test results indicated that the compressive strength of concrete increases by fibre addition. However, it has been observed that PVA fibre addition in low volume fraction used in this study do not significantly affect the concrete modulus of elasticity, natural frequency and damping ratio. Furthermore, comparing 28-day dynamic-MOE with static chord MOE shows a similar trend. Dynamic-MOE results are slightly higher than that of static-MOE which complies with literature (Malhotra & Sivasundaram 2004).

5 REFERENCES

- Amick, H. & Monteiro, P.J.M. 2005, 'Modification of concrete damping properties for vibration control in technology facilities', Proceedings of SPIE - The International Society for Optical Engineering, vol. 5933, pp. 1-12.
- Amick, H. & Monteiro, P.J.M. 2006, 'Experimental determination of model damping in concrete beams', ACI material Journal, vol. 103, no. 3, pp. 153-60.
- Arivalagan & Kandasamy 2009, 'Energy Absorption Capacity of Composite Beams', Engineering Science and Technology Review, vol. 2, pp. 145-50.
- Chopra, A.K. 1995, Dynamics of Structures: Theory and Applications to Earthquake Engineering, Prentice Hall, New Jersey.
- Cole, D.G. & Spooner, D.C. 1965, 'The damping capacity of hardened cement paste and mortar in specimens vibrating at very low frequencies', Proceedings of American Society for Testing and Materials, pp. 661-7.
- Fu, X. & Chung, D.D.L. 1996, 'Vibration damping admixtures for cement', Cement and Concrete Research, vol. 26, no. 1, pp. 69-75.
- Jinping, O., Tiejun, L. & Jilong, L. 2008, 'Dynamic and Seismic property experiments of high damping concrete and its frame models', Jurnal of Wuhan university of technology-Mater.Si.Ed
- Malhotra, V.M. & Sivasundaram, V. 2004, 'Resonant Frequency Method', in, Handbook on Nondestructive Testing of Concrete, p. 384.
- Menefy, L. 2007, 'Investigation of reactive powder concrete and its damping characteristics when utilised in beam elements', Griffith University, Gold Coast.
- Nelson & Hancock 1979, 'Interfacial slip and damping in fibre reinforced composites', Journal of Materials Science, vol. 13, no. 3, pp. 2429-40.
- Ou, J.P. 2002, 'Smart Concrete Products and structural Systems', Control and Health monitoring of Structures, pp. 4-5.
- Razak, H.A. & Choi, F.C. 2001, 'The effect of corrosion on the natural frequency and modal damping of reinforced concrete beams', Engineering Structures, vol. 23, no. 9, pp. 1126-33.
- Smith, J.W. 1988, Vibration of Structures: Application in civil engineering design, Chapman and Hall, London.
- Sun, C.T., Chaturvedi, S.K. & Gibson, R.F. 1985, 'Internal damping of short-fiber reinforced polymer matrix composites', Computers & Structures, vol. 20, no. 3, pp. 391-400.
- Swamy, N. & Rigby, G. 1971, 'Dynamic properties of hardened paste, mortar and concrete', Materials and Structures, vol. 4, no. 1, pp. 13-40.
- Thomson, W.T. 1940, 'Measuring changes in physical properties of concrete by the dynamic method', vol. 40, proceeding of the American Society of Testing and Materials, pp. 1113-8.
- Yan, L., Jenkins, C.H. & Pendleton, R.L. 2000a, 'Polyolefin fiber-reinforced concrete composites: Part I. Damping and frequency characteristics', Cement and Concrete Research, vol. 30, no. 3, pp. 391-401.

- Yan, L., Jenkins, C.H. & Pendleton, R.L. 2000b, 'Polyolefin fiber-reinforced concrete composites: Part II. Damping and interface debonding', *Cement and Concrete Research*, vol. 30, no. 3, pp. 403-10.
- Zheng, L., Sharon Huo, X. & Yuan, Y. 2008, 'Experimental investigation on dynamic properties of rubberized concrete', *Construction and Building Materials*, vol. 22, no. 5, pp. 939-47.

Fire Resistance Tests of Concrete-Filled Stainless Steel Tubular Columns

Mohamed Ghannam¹; Zhong Tao²; and Tian Yi Song³

¹Institute for Infrastructure Engineering, Univ. of Western Sydney, Penrith, NSW 2751, Australia. E-mail: 17156947@student.uws.edu.au

²Institute for Infrastructure Engineering, Univ. of Western Sydney, Penrith, NSW 2751, Australia. E-mail: z.tao@uws.edu.au

³Institute for Infrastructure Engineering, Univ. of Western Sydney, Penrith, NSW 2751, Australia. E-mail: t.song@uws.edu.au

Abstract

This paper presents the fire resistance test results of 6 concrete filled stainless steel tubular (CFSST) columns. The influence of various parameters, including the cross-section type (circular and square), the load ratio (0.3, 0.45) and the presence of steel reinforcement (plain and reinforced concrete), were investigated. To capture the initial imperfections of the CFSST columns, a photogrammetry method was employed for the measurement prior to the fire testing. Fire tests were conducted on the CFSST columns under axial compression. The failure mode, temperature distribution, deformation, and fire resistance of the CFSST columns are presented and discussed.

Keywords: Concrete filled stainless steel tubes; Fire resistance; Deformation; Failure mode.

1. INTRODUCTION

Stainless steel has been used in the construction industry for many years as minor components, such as fixings, fasteners, and cladding. This can be seen in the Chrysler Building in USA and Lloyds Building in England. Due to the high cost of stainless steel (about 3-5 times the cost of carbon steel), its application in major structural components is still limited. But in recent years, the whole-life cost for a structure has become an important concern for engineers and property owners. Owing to the benefits of stainless steel, i.e. high corrosion resistance, easily maintained, extremely durable and high fire resistance, it is believed that this type of steel material will be increasingly used in civil engineering and construction (Tao et al., 2011, Uy et al., 2011). To overcome the shortcoming of adopting stainless steel induced by the high cost, a promising method is to use the stainless steel tube in composite structures, and one typical example is the concrete filled stainless steel tubular (CFFST) column (Uy et al., 2011).

Currently, extensive research have been done to investigate the behaviour of stainless steel members at ambient temperature, but the research on stainless steel members under high temperature or in fire is very limited (Gardner and Baddoo, 2006), especially for the CFSST columns. Renaud (2007) reported 7 fire tests of square CFSST columns. A numerical investigation was done using a model that was verified through the comparison with the test results, and a simplified calculation method was provided for the design of composite members with stainless steel in fire. Lee (2011) reported the post-fire results of two preloaded square CFSST columns, which were part of a series to investigate the bond strength between the stainless steel tube and concrete. More recently, Han et al. (2013) investigated the experimental behaviour of five full scale CFSST columns (3 square and 2 circular specimens) in fire. It was found that CFSST columns have much higher fire resistance compared to the normal concrete filled steel tubular (CFST) columns with carbon steel. Considering the scarce of fire tests on CFSST columns, a series of CFSST columns were tested in fire conditions by the authors recently. These test results are reported in this paper. The failure modes, temperature distribution, deformation and fire resistance of the test specimens were discussed.

2. EXPERIMENTAL PROGRAM

2.1 SPECIMEN PREPARATION

A total of 6 CFSST columns exposed to fire with initial axial loads were tested. Test parameters were cross section type (four circular columns and two square columns), nominal load level (0.3 and 0.45), and presence of steel reinforcement (plain and reinforced concrete). Table 1 shows the specimens details, where CT and ST in the specimen labels denote circular and square columns, respectively; t is the tube thickness; D is the overall diameter of a circular tube or width of a square column; L is the length of a column with the end plates; and n is the load level. The load level (n) was calculated according to Eq. (1).

$$n = P / (f_y A_s + f_c' A_c) \quad (1)$$

where P is the applied load, f_y is the 0.2% proof strength of stainless steel, A_s is the stainless steel tube area, f_c' is the cylinder compressive strength of concrete and A_c is the concrete core area.

Table 1 Specimens details

Specimen label	Steel reinforcement	Load ratio n	D (mm)	t (mm)	L (mm)	Stainless steel grade	$f'_{c,28}$ (N/mm ²)
CT01	–	0.31	196.2	2.95			
CT02	4Φ12	0.28	196.9				
CT03	–	0.48	195.6				
CT04	4Φ12	0.42	195.9		1870	EN 1.4031	40.3
ST01	–	0.31	200.4	4.00			
ST02	–	0.46	200.9				

Cold-formed tubes were used for circular specimens. The square tubes were fabricated by welding two U-shape cold formed plates. The inner radius of the square specimens at the corners is 7.5 mm. Top and bottom plates with a thickness of 20 mm were welded to the ends of a steel tube, and a 150 mm hole was drilled in the top plate for pouring concrete. Holes with a diameter of 2 mm were drilled into the surface of the tube where ceramic rods were to be attached, and these holes would act as references points in the later photogrammetry process for monitoring the deformation of the steel tube in fire.

2.2 MATERIAL PROPERTIES

Coupons were cut from the stainless steel tubes and tested for material properties at ambient temperature according to AS 1391 (2007). The average 0.2% proof strengths (f_y) for the circular and square tubes were 292.9 and 307.9 MPa, respectively; and the ultimate strengths (f_u) were 712.0 and 641.7 MPa, respectively.

Normal Portland cement and lime stone coarse aggregate were used. The concrete mix per m^3 was: Lime stone coarse aggregate 980 kg, Sand 875 kg, Cement 311.7 kg, Fly ash 96.7 kg, Water 156.9 kg, and 122RI water reducer 667 ml. Concrete cylinders were tested according to AS 1012.9 (1999). The average cylinder compressive strength $f'_{c,28}$ at 28 days was 40.3 MPa and the measured elastic modulus (E_c) was 33,500 MPa.

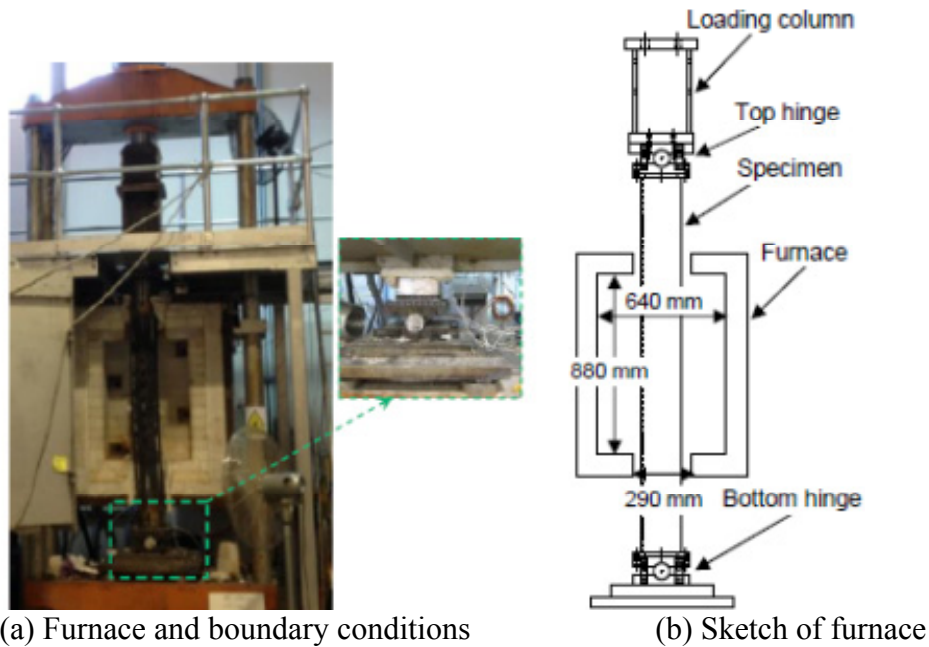
Four reinforcing bars with a diameter of 12 mm were provided for specimens CT02 and CT04. The average yield strength of the reinforcement (f_s) was 586.7 MPa, and the modulus of elasticity (E_s) was 198,200 MPa.

2.3 TESTING APPARATUS AND PROCEDURE

The fire tests were performed in a furnace in the Structures Lab at University of Western Sydney, Australia as indicated in Figure 1. The furnace chamber has a plan area of 640 mm in wide and 630 mm in depth, and a height of 880 mm. Since the column was installed passing through the furnace chamber, the height exposed to fire was therefore 880 mm for the column. The temperature inside the furnace is controlled by four burners, and the nominal maximum temperature that the furnace can reach is 800 °C. Five thermocouples were used to measure the temperatures inside the furnace.

The capacity of the loading jack is 2000 kN. The axial deformation of the specimen was determined by measuring the displacement of the jack. The specimens were installed in the furnace by bolts, and cylindrical hinges were used to provide hinged end condition as indicated in Figure 1. The thermocouples and displacement transducer were connected to a data logging system outside the furnace.

Prior to the fire testing, the axial load was applied onto the specimen. After the applied load reached the predetermined value, the load was kept constant and then the furnace temperature was increased gradually to a target temperature of 800 °C. This temperature was kept constant until the column failed.



(a) Furnace and boundary conditions

(b) Sketch of furnace

Figure 1. General View of the testing furnace.

2.4 MEASUREMENT OF INITIAL IMPERFECTIONS

Photogrammetry method was used to measure the stainless steel tube initial imperfections for all specimens. Australis program (Australis 7.34, 2011) was used in the photogrammetry process.

Using this method, the level of accuracy attained was determined within the program in light of an analysis of the convergence of individual retro reflective dots (points) in multiple images taken. The program measures the number of points that appear on successive photos for two or more images. Generally, the more points that are convergent across more images, the higher the level of accuracy attained. This is due to the final stages of image processing by the program that involve bundle triangulation. As such, the accuracy to which the location of an individual point is identified is related to the number of successful convergences utilized in the triangulation process through successive images that contain the same point. The levels of accuracy in each direction (X, Y, and Z) are attributable to the success of the triangulation associated with each direction and the overall accuracy is taken as the average of these three directional accuracies (Lee, 2011).

Australis program joined the images to form a single 3D image of the retro reflective dots that were applied to the test specimens. The coded targets as shown in Figure 2 were very important in the photogrammetry process as they provided unique reference points to aid in the linking of the images (Gillicuddy, 2011). To map the imperfections of the tubes, retro-reflective dots were arranged upon the outer surface at a spacing of 120 mm as shown in Figure 2.

A scaling bar (1000 mm long) was used for the calibration process of the camera, as the coded targets would not be sufficient to get the desired accuracy because of their small size (50 mm) compared to the column length (1870 mm).

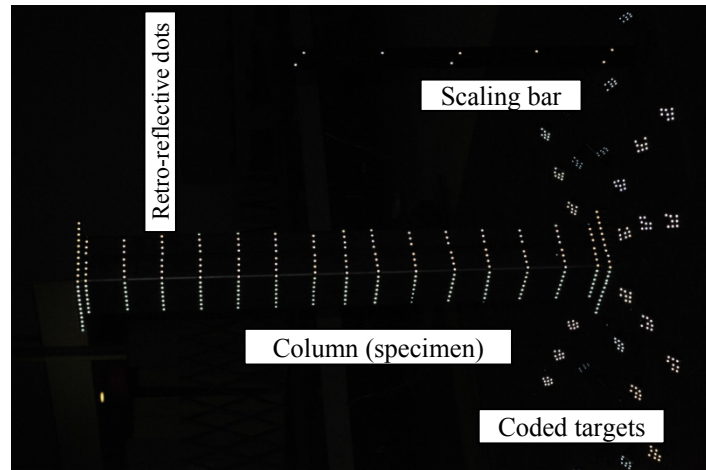


Figure 2. A point cloud indicating the measurement arrangement.

The camera was calibrated as per the guidelines set out in the User Manual for Australis (Australis 7.34, 2011). Camera calibration quality was achieved to a rating of 1.1 (good).

Once the camera was calibrated, the calibration parameters (camera resolution, focal length, principal point, distortion) were applied to the photos taken of the specimen in generation of the tube profile. Each specimen was photographed in both portrait and landscape views at approximately 120 positions in 360 degree circles around the specimens as per the *User Manual for Australis* (Australis 7.34, 2011). Figure 3(a) shows the position of the circles around the column where the photos were taken, and Figure 3(b) indicates the profile of a specimen and the camera positions as given by *Australis*.

To quantify the imperfections of a column, the centroids of measured sections with retro reflective dots had to be found. This was done by using Microsoft Excel based on the coordinates of the dots determined by Australis software. The X-axis of the specimen in the rotation plane was thus determined by connecting all the centroids, as shown in Figure 4. If a line is drawn from the centroid of the top section to that of the bottom section, the global imperfection along the whole column can be determined accordingly. In general, the maximum imperfections measured ranged from 0.2 to 1.3 mm. Figure 4 indicates the measured axis of a typical column. A sine curve with its peak equal to the maximum imperfection (0.77 mm) is shown in the same figure. For this specimen, a sinusoid can reasonably represent the distribution of initial imperfections. But for a few others, the initial imperfections distributed rather randomly along the length. The measured initial imperfections may be used in future finite element analysis.

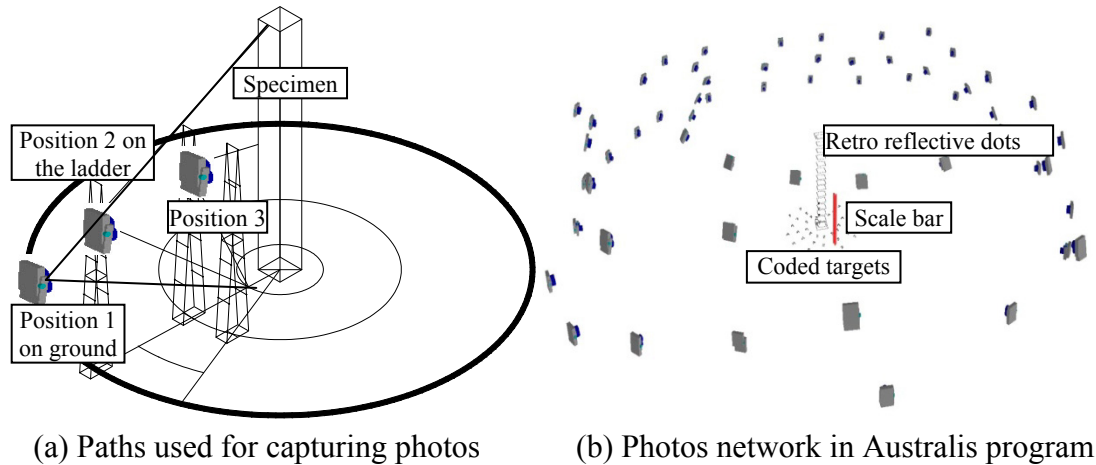


Figure 3. Camera positions in the network.

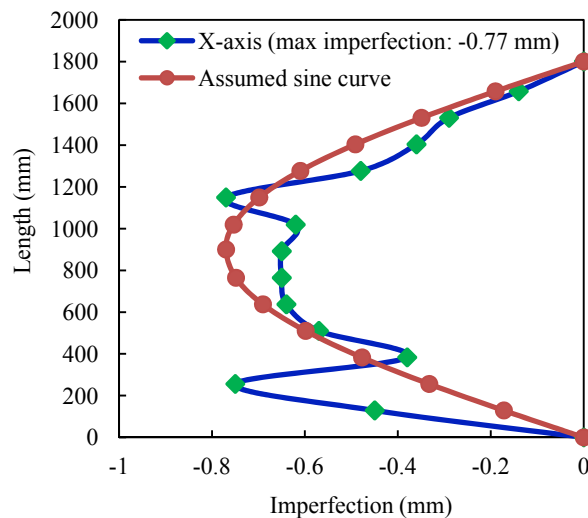
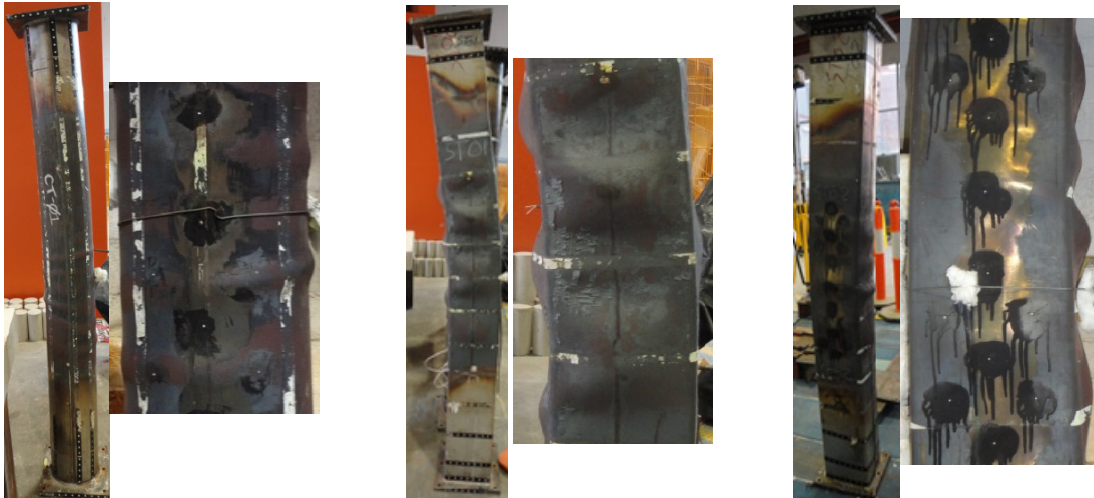


Figure 4. Distribution of initial imperfections for a typical specimen (CT01).

3. TEST RESULTS AND DISCUSSION

3.1 FAILURE MODES

Figure 5 shows the typical failure modes of CFSST columns. If compare the failure modes of specimen CT01 with that of specimen ST01, it can be found that the section type has a significant effect on the failure mode. For the circular column CT01 as shown in Figure 5(a), the column failed due to the overall buckling, and local buckling only occurred near the mid-height. In general, local buckling was not significant for this specimen. But for the square columns ST01 and ST02 shown in Figure 5(b) and (c), obvious local buckling occurred on the steel tube. It can also be found that the presence of the steel reinforcement had no obvious influence on the failure mode of CFSST columns.



(a) Circular specimen CT01 (b) Square specimen ST01 (c) Square specimen ST02
Figure 5. Typical failure modes of CFSST columns in fire.

3.2 TEMPERATURE VERSUS TIME CURVES

The temperatures of the CFSST column specimens were measured through three thermocouples, where two of them were attached to the stainless steel surface and embedded in the centre of the concrete core, respectively; and the third one located at 50 mm distance from the outer stainless steel surface. The positions of the thermocouples are indicated in Figure 6.

Figure 6(a) shows the temperature (T) versus time (t) curves for a typical specimen ST01, where the furnace temperature was the average temperature measured by thermocouples located in the furnace. For this specimen, the thermocouple at Point 2 in the concrete failed after 40 min fire exposure. But it is clear that the concrete temperature remained nearly stable within the time period between 40 and 80 min after the temperature exceeded 100 °C. This is explained as a result of evaporation of the free water and the beginning of release of the bond water, which consume more heat leading to a delay in the temperature rise of the concrete core. This phenomenon has been well documented by many other researchers.

A finite element (FE) model was proposed by Tao and Ghannam (2012) and Ghannam et al. (2012) to predict the heat transfer in CFSST columns, where shell elements were used for the steel tubes and solid elements were used for concrete core. The simulation was carried out by using ABAQUS program. This model is further used in this paper to predict the temperature development for current specimens in fire. Figure 6 shows a comparison between the test results and the predicted results. A good agreement between the test and predicted results was obtained.

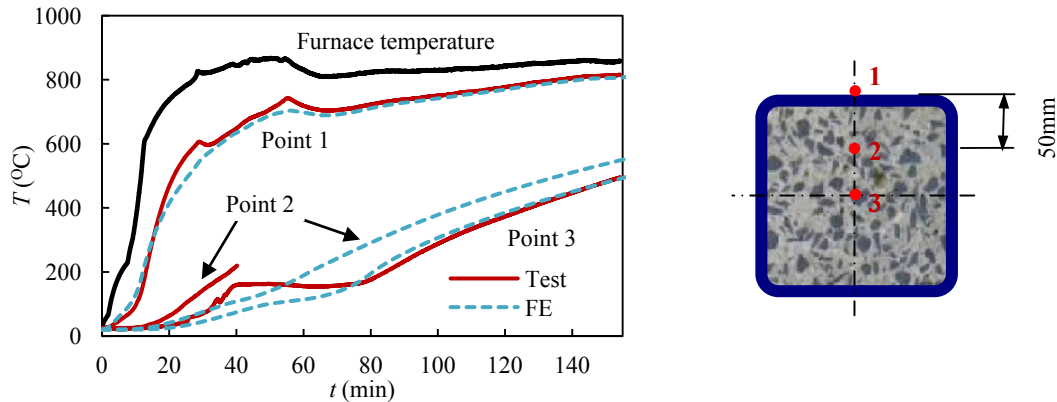


Figure 6. Temperature (T) versus time (t) curves of specimen ST01.

3.3 AXIAL DEFORMATION VERSUS TIME CURVES

Figure 7 illustrates the relation of axial deformation (Δ_c) versus time (t) for the column CT01. As can be seen, the curve can be divided into three stages. In the first stage, the column began to expand as a result of the thermal expansion of stainless steel and concrete. Then the column began to contract gradually in the second stage before a sudden contraction occurred in the third stage indicating the column failure. It is found that columns with a lower load level had higher expansion compared with those with a higher load level. Meanwhile, columns with reinforcement had higher expansion than those of specimens without reinforcement.

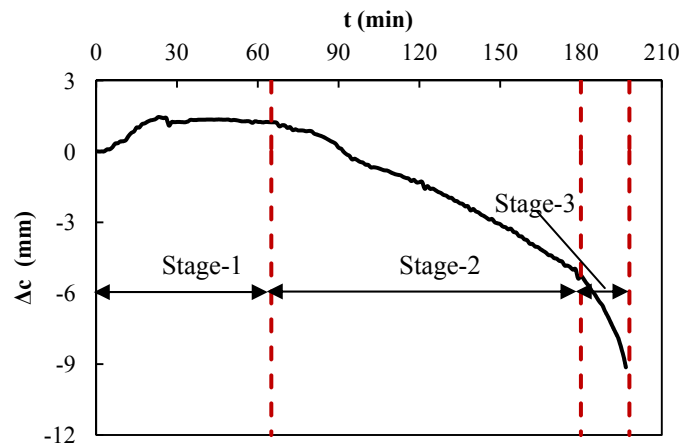


Figure 7. Axial deformation (Δ_c) versus time (t) relation for column CT01.

3.4 FIRE RESISTANCE

The fire resistance for CT01, CT02, CT03, CT04, ST01 and ST02 are 196.7, 173.9, 122.2, 143.1, 154.3 and 155.1 min respectively. For the fire resistance of columns, the criteria specified in ISO-834 (1999) was adopted, which is either the axial shortening exceeding $0.01H$ mm or the deformation rate exceeding $0.003H$ mm/min, where H is the length of the specimen in mm. During the testing, generally, the test was terminated due to the fact that the applied column load could not be kept

constant induced by the rapidly increased column deformation. Clearly, a fire rating over 2 hours was achieved for all columns.

Figure 8(a) and (b) shows the influence of the load level on circular columns filled with plain concrete and reinforced concrete, respectively. The fire resistance increased from 122.2 min for the column CT03 to 196.7 min for the column CT01, as the load level decreased from 0.48 to 0.31. The same trend is observed for the columns with steel reinforcement, where the fire resistance increased from 143.1 min for the column CT04 ($n=0.42$) to 173.9 min for the column CT02 ($n=0.28$). But for the two square columns ST01 ($n=0.31$) and ST02 ($n=0.46$), the fire resistance were 154.3 min and 155.1 min, respectively, which are almost the same. This may be attributed to the influence of initial imperfections, which were different for the two specimens and the influence of furnace temperatures. Specimens ST01 and ST02 were exposed to an average peak furnace temperatures of 860°C and 760°C respectively. As can be observed, the average furnace temperature of specimen ST02 was 100°C lower than that of specimen ST01.

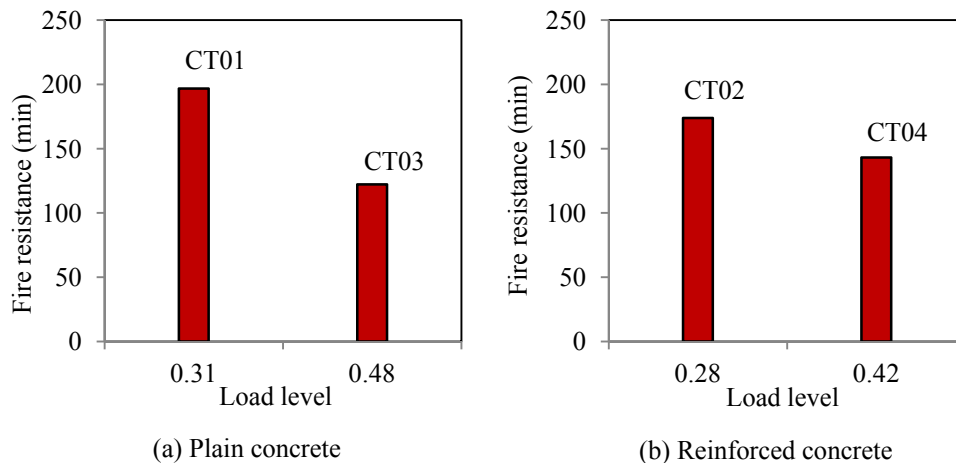


Figure 8. Influence of load level on the fire resistance of circular columns.

The influence of reinforcement is illustrated in Figure 9 for specimens with different nominal load levels. It is expected that the presence of steel reinforcement will increase the fire resistance of a column. This effect can be seen from the comparison between the fire resistance of column CT03 with plain concrete and that of CT04 with reinforced concrete. For CT03, the fire resistance is 122.2 min, whilst that for CT04 is 143.1 min with the presence of steel reinforcement. But this beneficial effect of steel reinforcement was not observed for the column CT02 when compared with the column CT01. The fire resistance for CT01 and CT02 are 196.7 and 173.9 min, respectively. Once again, this may be due to the influence of initial imperfections, which outweighed the beneficial effect provided by the steel reinforcement. It should be pointed out that the steel reinforcement ratio for CT02 was only 1.6%, and the strength contribution from the steel reinforcement might not be very significant.

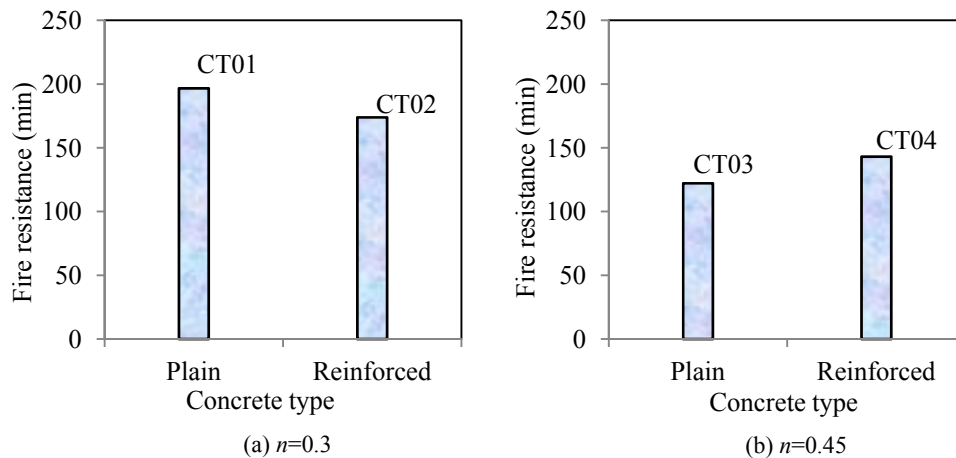


Figure 9. Influence of reinforcement on the fire resistance of circular columns.

4. CONCLUSIONS

Fire test results of 6 concrete filled stainless steel tubular columns were reported in this paper. Prior to the fire testing, a photogrammetry method was employed to measure the initial imperfections of these specimens. It was found that the maximum imperfections measured normally ranged from 0.2 to 1.3 mm, and the imperfections had a significant influence on the fire resistance of CFSST specimens. For circular columns, the fire resistance increased with an increase in the load level; but this trend was not observed in the two square columns. Steel reinforcement was provided in two circular specimens. Compared with the reference specimens, one had higher fire resistance but the other had lower fire resistance. Since the steel reinforcement ratio for the two specimens was not very high, the beneficial effect might be offset by the presence of large initial imperfections. In general, good fire resistance was achieved for all CFSST specimens. A fire rating over 2 hours was achieved for all of them without any fire protection.

The experimental work presented in this paper has provided a good basis for the development of finite element models. Ongoing research is being conducted by the authors to incorporate the measured imperfections into the finite element simulation.

5. ACKNOWLEDGEMENTS

This work is supported by the Australian Research Council (ARC) under its Future Fellowships Scheme (Project No: FT0991433). The financial support is gratefully acknowledged. The authors also would like to thank the technical staff for their laboratory assistance.

6. REFERENCES

- Australis V7.34 (2011). "User Manual Photometrix Pty Ltd." *PO Box 3023, Kew, Vic 3101, Australia, Version 7.34.*
- Gardner, L., and Baddoo, NR. (2006). "Fire testing and design of stainless steel structures." *Journal of Constructional Steel Research*, 62 (6), 532-543.
- Ghannam, M., Tao, Z., and Uy, B. (2012). "Heat transfer analysis of concrete-filled stainless steel columns exposed to fire" *Proceedings of the 10th International Conference on Advances in Steel Concrete Composite and Hybrid Structures, Singapore*. pp. 873-880.
- Gillicuddy, MB. (2011). "Methods to enhance the bond between the steel tube and the concrete in concrete-filled steel tubular columns." Honors thesis, School of Engineering, University of Western Sydney, Australia.
- Han, L.H., Chen, F., Liao, F.Y., Tao, Z., and Uy, B. (2013). "Fire performance of concrete filled stainless steel tubular columns." *Engineering Structures*, 56, 165-181.
- ISO 834-1. (1999). "Fire-resistance tests-Elements of building construction-Part 1: General requirements." *International Organization for Standardization, Geneva.*
- Lee, AD. (2011). "Bond between the stainless steel tube and concrete in concrete-filled stainless steel columns after fire exposure." Honours thesis, School of Engineering, University of Western Sydney, Australia.
- Renaud, C. (2007). "Stainless Steel in Fire-WP2: Composite members in fire" Final report SRI 07/110 - CR/PB.
- Standards Australia. (1999). AS 1012.9-1999: Methods of testing concrete - Determination of the compressive strength of concrete specimens."
- Standards Australia. (2007). "AS 1391-2007: Metallic materials - Tensile testing at ambient temperature."
- Tao, Z., and Ghannam, M. (2012). "Refined FE model to predict the temperature field within concrete-filled steel tubes" *Proceedings of the 7th International Conference on Advances in Steel Structure, Nanjing, China*. pp. 781-789.
- Tao, Z., Uy, B., Liao, F.Y., and Han, L.H. (2011). "Nonlinear analysis of concrete-filled square stainless steel stub columns under axial compression." *Journal of Constructional Steel Research*, 67 (11), 1719-1732.
- Uy, B., Tao, Z., and Han, L.H. (2011). "Behaviour of short and slender concrete-filled stainless steel tubular columns." *Journal of Constructional Steel Research*, 67 (3), 360-378.

Static Loading Test of Precast CES Shear Walls with Different Shear Span Ratios

Tomoya Matsui¹ and Hiroshi Kuramoto²

¹Dr. Eng., Dept. of Architecture and Civil Engineering, Toyohashi Univ. of Technology, Toyohashi 441-8580, Japan. E-mail: matsui@ace.tut.ac.jp

²Dr. Eng., Division of Global Architecture, Graduate School of Engineering, Osaka Univ., Suita 565-0871, Japan. E-mail: kuramoto@arch.eng.osaka-u.ac.jp

Abstract

In this study, static loading tests were conducted on concrete encased steel (CES) shear walls. One experimental variable was the construction method, using precast and integral construction specimens. Another variable was the shear span ratio, in which specimens were designed to fail either in shear or in flexure. This paper describes the test and investigates the failure mode, ultimate strength, and restoring force characteristics. Results showed that the maximum shear force resistances of precast walls were smaller than that of integral construction walls. Precast shear walls showed slip at the boundary of the wall panel and CES frame at a small level of drift angle, implying that the slip deformation affects shear strength resistance of precast shear walls. Further, it was found that the flexural strength CES shear walls can be evaluated using a method based on the Architectural Institute of Japan (AIJ) design standard for steel reinforced concrete (SRC) structures.

INTRODUCTION

Steel reinforced concrete (SRC) structures developed in Japan have good structural performance for resisting lateral forces imposed by wind and earthquakes, and have been adopted for medium-rise, high-rise, and super high-rise buildings. However, the number of SRC buildings being constructed has decreased since the 1990s, which may be attributed to the development of new structural engineering systems such as high-strength concrete structures or concrete-filled steel tube (CFT) structures. Nevertheless, SRC structures can provide better seismic performance in comparison with other structural systems. Hence, our aim was to develop a structural system with the same level of seismic performance as SRC structures with an easy construction method. We have conducted a continuing development study on composite

Concrete Encased steel (CES) structures, composed of steel and fiber reinforced concrete (FRC) as shown in Figure 1.

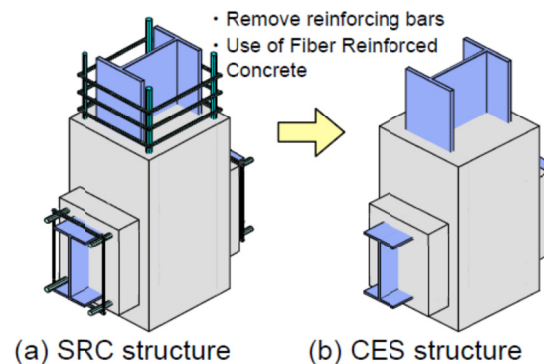


Figure 1. Composite concrete encased steel structural system

In experimental studies on CES columns [Fujimoto, et al. 2008], CES beam-column joints [Matsui, et al. 2008], and a two-bay, two-story CES frame [Fauzan, Kuramoto, et al. 2008], it was confirmed that the CES structural system showed stable restoring force characteristics and good seismic performance. Static loading tests were carried out on CES shear walls with different anchorage methods, using the CES frame and FRC wall panel [Suzuki, Matsui, et al. 2012]. The shear strength resistance of the specimen whose wall longitudinal reinforcement was anchored to the CES frame was almost the same as that of the specimen without the anchorage, while the flexural strength resistance of the specimen whose wall longitudinal reinforcement was anchored to the CES frame was 5 % greater than that of the specimen without the anchorage. These results confirmed that the effect of the anchorage condition of the wall longitudinal reinforcement on the shear and flexural strength of the CES shear wall is small. Moreover, it was found that the accumulative dissipated energy were not very different between specimens whose wall longitudinal reinforcement were not anchored to the CES frame and specimens whose wall longitudinal reinforcement were anchored to the CES frame. Therefore, our next step was to consider the applicability of the precast method with the view of making the construction method more efficient and labor-saving.

In this study, static loading tests were conducted on four CES shear walls. One experimental variable was the construction method, using precast and integral construction CES shear wall specimens. Another variable was the shear span ratio, in which specimens were designed to fail in shear failure mode or in flexural failure mode. This paper describes the test and investigates the failure mode, ultimate strength and restoring force characteristics. In addition, an evaluation method of the ultimate strength of CES shear walls is discussed.

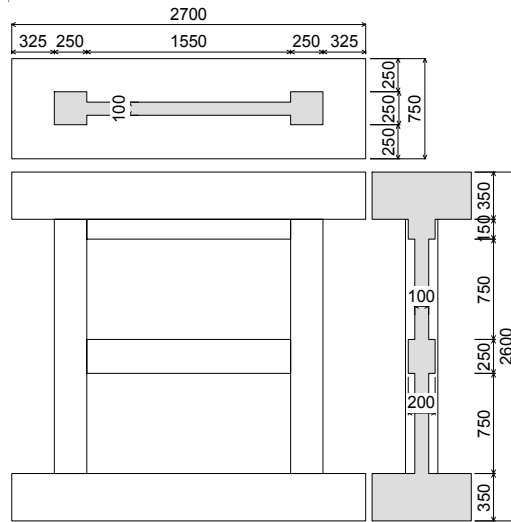


Figure 2. Specimen configuration

Table 1. Experimental variables

Specimen	Type of wall	Shear span ratio
CWDS	Integral construction	1.1
CWDF		1.65
CWPS	Precast	1.1
CWPF		1.65

Table 2. Specification of section

Specimen	CWDS CWDF	CWPS CWPF
Column	b×D	250×250 (mm)
	Steel	H-170×120×6×9 ($s_p=4.9\%$)
Beam	b×D	200×250 (mm)
	Steel	H-148×100×6×9 ($s_p=5.2\%$)
Wall	Thickness	100 (mm)
	Longitudinal bar	D6@75 zigzag ($w_p=0.42\%$)
	Transverse bar	D6@65 zigzag ($w_p=0.42\%$)

w_p : wall reinforcing ratio

D6 indicates deformed reinforcing bars with a nominal diameter of 6 mm

OUTLINE OF CES SHEAR WALL TESTS

Description of specimens

The specimens were designed to simulate the lower two story of a multi-story shear wall in a medium high-rise building and scaled to one-third of the prototype walls. Four specimens were prepared for this test. One experimental variable was the precast

and integral construction method for the shear wall specimen as shown in Table 1. Another variable was the shear span ratio, in which specimens were designed to fail in shear failure mode or in flexural failure mode. Specimens CWDS and CWDF were integral construction shear wall specimens, while specimens CWPS and CWPF were precast, dividing the FRC panel into two parts at each story. The shear span ratio was 1.1 for specimens CWDS and CWPS and 1.65 for specimens CWDF and CWPF. Specimen configuration and bar arrangements are shown Figure 2 and Figure 3 respectively, while the details of the specimen cross sections are given in Table 2. The column had a 250-mm square cross-section, while the beam section was 200 mm × 250 mm. The column span length was 1,800 mm and the wall thickness was 100 mm.

For specimen CWDS, the longitudinal and transverse wall reinforcing bars were not anchored to the CES frame and bent at a 180° hook in the wall panel, in order to simplify the anchoring method. The top and bottom of transverse wall reinforcing bars at a story were securely fixed to the steel web in the CES columns by welding, in order to fix the reinforcing bars to prevent falling of wall reinforcing bar or wall panel on work as shown Figure 3. For specimen CWPS, the CES frame was made first. Then, the precast wall panel was installed and the transverse reinforcing bars of the precast wall panel were welded. Non-shrink cement grout was injected into the spaces between the precast wall panel and the CES frame. In addition, the precast wall panel had shear cotters at the boundaries.

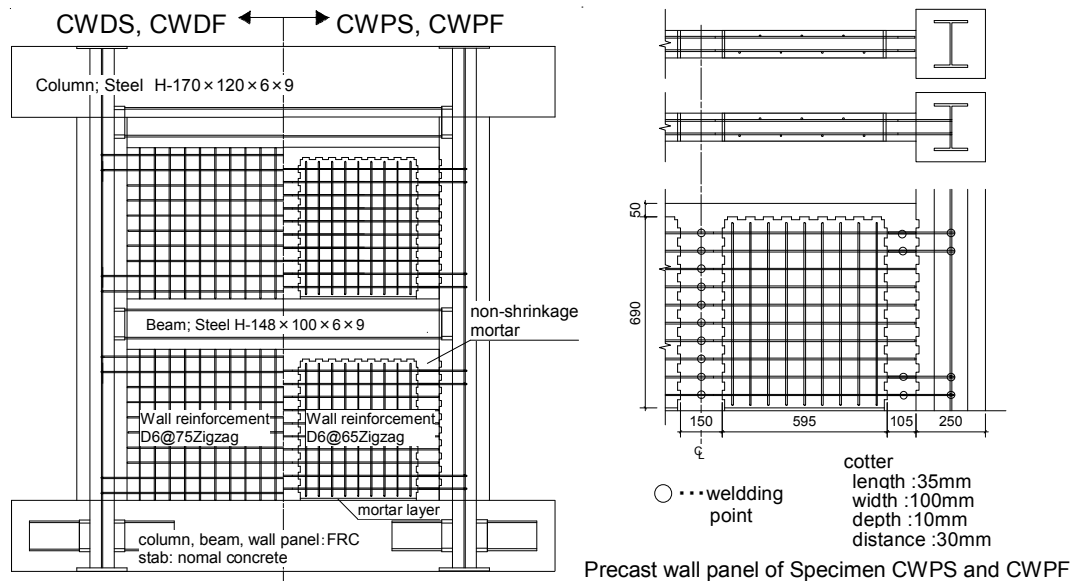


Figure 3. Bar arrangement

The material properties of the concrete, grout and steel used are shown in Tables 3, 4 and 5, respectively. Vinyon fibers with a diameter of 0.66 mm and a length of 30 mm were used for the FRC. The water–cement ratio was 60%, while the volumetric ratio of the fibers was 1.0%.

Table 3. Material properties of concrete **Table 5. Material properties of steel**

Specimen		σ_B (MPa)	E_c (GPa)	E_{c0} (μ)	Age (day)		Yield strength (MPa)	Tensile strength (MPa)	Elastic modulus (GPa)	
CWDS	1 story	30.3	22.1	2619	112	CWDS, CWPS	PL-6 column	300	422	197
	2 story	33.7	25.6	2337	106		PL-9 column	297	442	209
CWPS	1 story	29.0	23.0	2493	118		PL-6 beam	317	---	---
	2 story	33.8	24.7	2506	112		PL-9 beam	338	---	---
CWDF	1 story	35.1	24.8	2739	52		D6	396	518	192
	2 story	27.8	23.1	2419	47		PL-6 column	323	466	202
CWPF	1 story	35.1	26.3	2479	59	PL-9 column	326	425	197	
	2 story	27.4	21.3	2434	57	PL-6 beam	349	465	191	
						CWDF, CWPF	PL-9 beam	322	437	189
							D6	414	520	188

σ_B : Compressive strength, E_c : Elastic modulus,
 E_{c0} : Strain at compressive strength

Table 4. Material properties of grout

Specimen		σ_B (MPa)
CWPS	Grout layer (under wall panel)	29.6
	Non-shrink grout (vertical and transverse joint area)	92.5
CWPF	Grout layer (under wall panel)	39.5
	Non-shrink grout (vertical and transverse joint area)	77.4

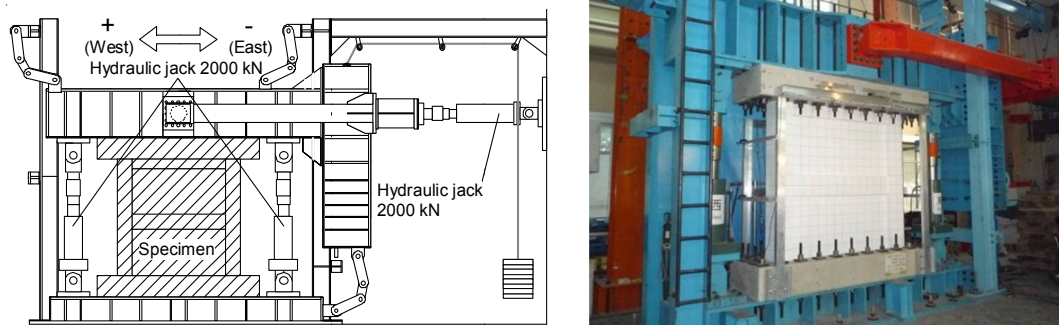


Figure 4. Loading apparatus

Loading program

Figure 4 shows the loading apparatus used. The wall specimens were loaded with horizontal cyclic shear forces using a hydraulic jack with a 2,000 kN capacity, while applying a constant axial force equivalent to the axial load ratio of boundary columns of 0.2, using two vertical manual jacks, each of which had a 2,000 kN capacity. During the testing, additional moment was also applied to the top of the specimens using vertical jacks to maintain the prescribed shear-span ratio of 1.1 or 1.65, using the following equation.

$$N_e = \frac{N_c}{2} - \frac{Q}{l}(h-a), \quad N_w = \frac{N_c}{2} + \frac{Q}{l}(h-a) \quad (1)$$

where N_e : axial force of east side jack

N_w : axial force of west side jack

N_c : constant axial force (specimens DS and PS were loaded with 1086kN, specimens CWDF and CWPF were loaded with 1230kN)

Q : shear force

l : distance between the two vertical jacks

h : assumed height of applied shear force

a : actual height of applied shear force.

The loading was conducted by controlling the relative wall drift angle, R , given by the ratio of the horizontal deformation, δ , to the height corresponding to the measuring point for the horizontal displacement at the top of the specimen, h_0 , (2,050 mm), i.e. $R = \delta / h_0$. The horizontal load sequence consisted of two cycles for each story drift angle.

Measurement Method

In the tests, the horizontal displacement was measured along with the longitudinal deformation of the column and partial deformation of the wall panel. The strains on the steel of the column and beam, and on selected longitudinal and horizontal bars of the wall, were measured using strain gages. Additionally, the widths of cracks were measured using a crack scale at each loading cycle.

TEST RESULTS

Failure mode

Figure 5 shows the cracking patterns of each specimen at the drift angle of 0.75×10^{-2} rad and after the final loading cycles. In specimen CWDS, shear cracks at the first story wall panel and flexural cracks at the boundary column occurred in the cycle of 6.25×10^{-4} rad. Then, slip was observed at the underside of beam in the cycle of 0.5×10^{-2} rad. Maximum shear force was reached at a drift angle of 0.75×10^{-2} rad, in which shear cracks spread to the upper corner of the first-story wall and the lower corner of the second-story wall. After maximum shear, shear cracks spread and compressive failure of concrete at the upper corner of the first-story wall and the lower corner of the second-story wall developed with increasing loading cycle. Concrete damage at the boundary column increased, and the loading finished at a drift angle of 5.0×10^{-2} rad.

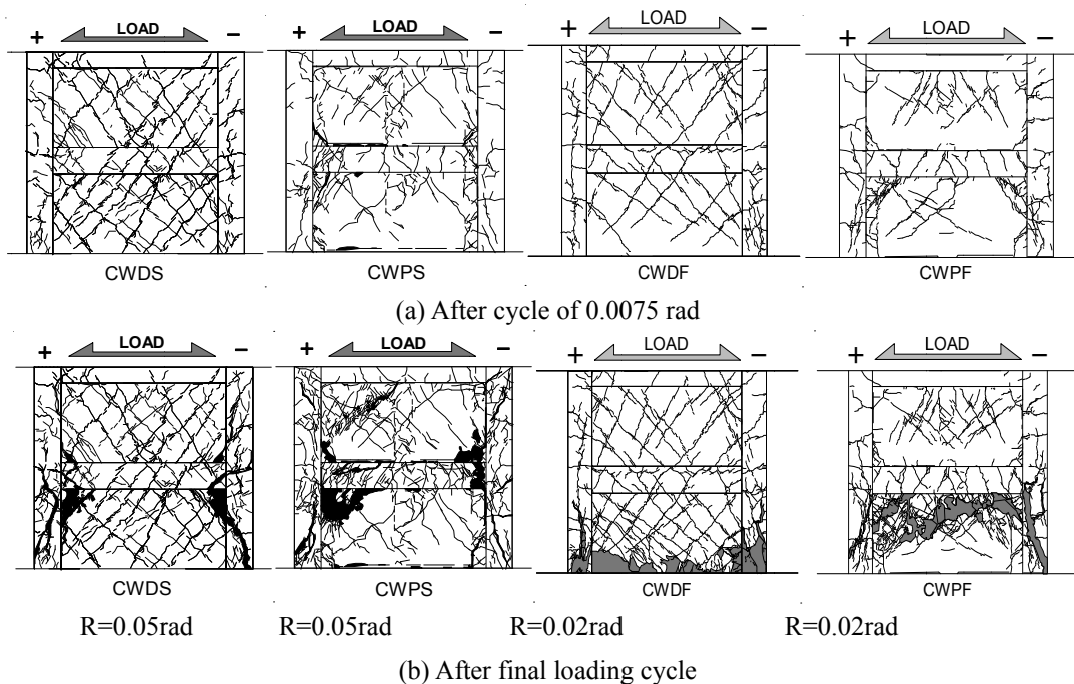


Figure 5. Cracking patterns



Figure 6. Damage of specimen CWPS at drift angle of -0.03rad



Figure 7. Fracture of steel beam of specimen CWPS (Observation after test)

For specimen CWPS, cracks at the area of the non-shrink grout and flexural cracks at the column occurred in the cycle of 6.25×10^{-4} rad. Then, slip was observed at the underside of beam and at the boundary of the column and grout in the cycle of 0.25×10^{-2} rad. Shear cracks spread at the upper corner of the first-story wall and the lower corner of the second-story wall in the cycle of 0.5×10^{-2} rad. After maximum shear force was reached at a drift angle of 1.5×10^{-2} rad, concrete damage at the column, beam and wall corner increased with increasing loading cycle. In addition, separation at the boundary of column and grout was severe as observed in Figure 6. The steel of the beam fractured at the end at a loading cycle of 5.0×10^{-2} rad as shown in Figure 7.

In specimen CWDF, flexural cracks at the boundary column occurred in the cycle of 0.125×10^{-2} rad, while shear cracks at the first-story wall panel occurred in the cycle of 0.25×10^{-2} rad. Maximum shear force was reached at a drift angle of 1.5×10^{-2} rad. After maximum shear force, compressive failure of concrete at the bottom of the column and the lower corner of the first-story wall panel developed with increasing loading cycle. There were significant damages at the bottom of the column and wall panel.

As for specimen CWPF, flexural cracks at the boundary column, shear cracks at the wall panel, and cracks at the area of the non-shrink grout occurred in the cycle of 0.125×10^{-2} rad. Then, slip was observed at the boundary of the beam and grout and at the boundary of the column and grout in the cycle of 0.25×10^{-2} rad. Shear cracks at the column occurred in the cycle of 0.5×10^{-2} rad. Maximum shear force was reached at a drift angle of 0.75×10^{-2} rad. Comparing the cracking patterns of specimens CWPF and CWDF in this loading cycle, there were less cracks in specimen CWPF than in specimen CWDF. After maximum shear force, shear cracks at the column and wall panel developed with increasing loading cycle. Damage at the upper wall panel was significant, with specimen CWPF failing in shear at the wall panel after yielding.

Hysteretic characteristics

Figure 8 shows the shear force versus drift angle relationships. Specimen CWDS recorded a maximum shear force of 1,204 kN at the drift angle of 0.75×10^{-2} rad. After that, shear forces decreased slowly with increasing concrete damage of the wall panel and column. On the other hand, specimen CWPS recorded a maximum shear force of 995 kN at the drift angle of 1.5×10^{-2} rad. The maximum shear force of specimen CWPS was about 20 percent less than that of specimen CWDS. After reaching maximum, specimen CWPS maintained its shear force until it showed strength deterioration at the drift angle of 3.5×10^{-2} rad when the steel at the end of the beam fractured. The restoring characteristics of specimen CWPS were different from that of specimen CWDS.

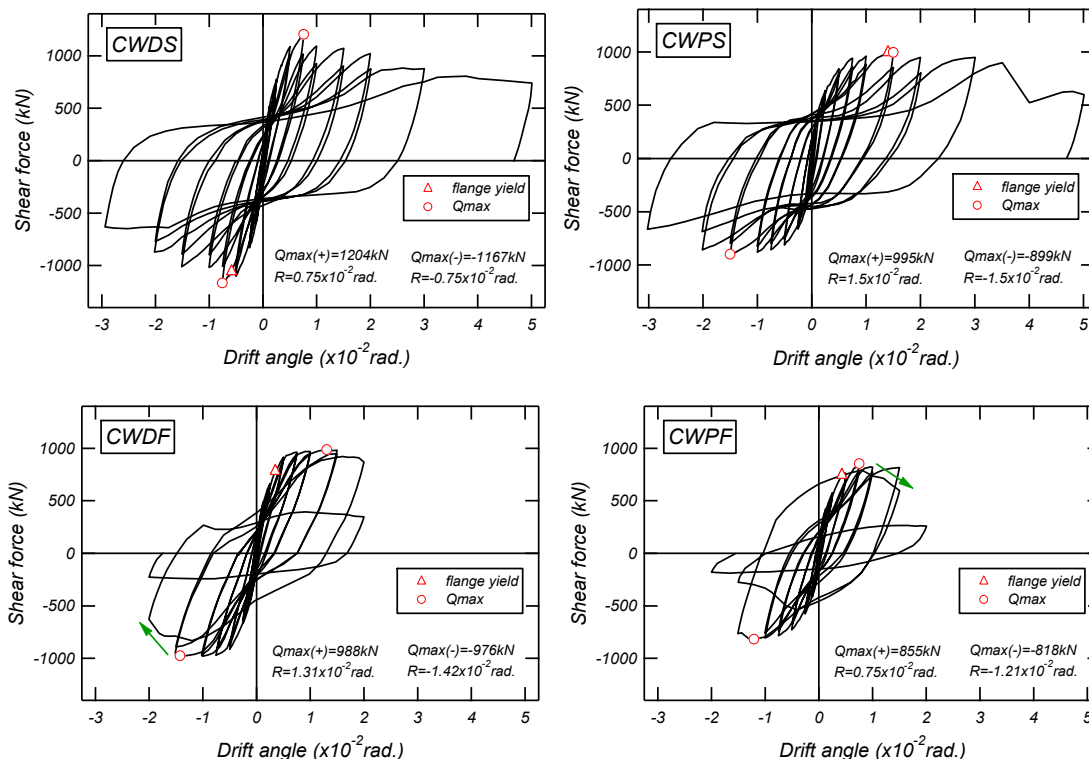


Figure 8. Shear force versus drift angle relationship

Specimen CWDF recorded a maximum shear force of 988 kN at the drift angle of 1.31×10^{-2} rad, while specimen CWPF recorded a maximum shear force of 855 kN at the drift angle of 0.75×10^{-2} rad. The maximum shear force of specimen CWPF, which was the precast shear wall, was about 10 percent less than that of specimen CWDF.

Furthermore, deformability was different between the two specimens. Looking at the loading cycle when the shear force decreased to about 80 percent of maximum (Figure 8, solid arrows), specimen CWDF was at the cycle of 2.0×10^{-2} rad, while specimen CWPF was at the cycle of 1.5×10^{-2} rad, respectively. The restoring characteristics of specimen CWPF, the precast shear wall, were different from that of specimen CWDF, the integral construction shear wall.

Slip at the boundary of wall panel and CES frame and elongation of the beam

Figure 9 shows the slip displacement at the boundary of the wall panel and CES frame at the peak of positive loading until the drift angle of 1.5×10^{-2} rad. Figure 10 shows the points where the displacements were measured.

Looking at the slip displacement at the boundary of the wall panel and beam, slip in specimen CWPS occurred at the drift angle of 0.25×10^{-2} rad, while slip in

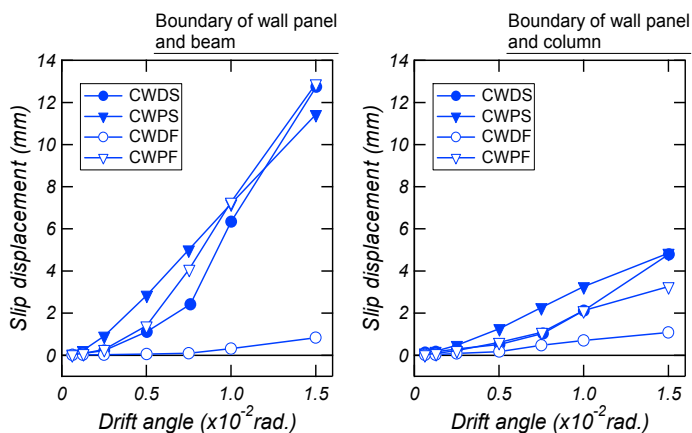


Figure 9. Slip displacement at the boundary of the wall panel and CES frame

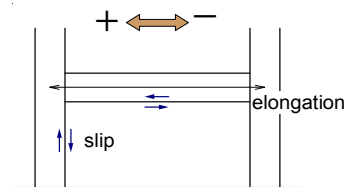


Figure 10. Measured points

specimen CWDS occurred at the drift angle of 0.5×10^{-2} rad. In addition, looking at the slip displacement between the wall panel and boundary column, slip of specimen CWPS was larger than that of specimen CWDS. It was found that the slip at the boundary of the wall panel and CES frame was more likely to occur in the precast specimen than in the integral construction specimen. Specimens CWDF and CWPF also showed the same tendency as specimens CWDS and CWPS. Specimen CWDF, in particular, had very small slip displacements.

Figure 11 shows the elongation of the beam at the peak of positive loading until a drift angle of 1.5×10^{-2} rad (positive sign represents elongation). The points where the displacements were measured are shown in Figure 10. It can be seen that the beam elongation of specimens CWDS, CWPS and CWPF, in which the wall panel finally failed in shear, increased steeply from a drift angle of 0.75×10^{-2} rad. Moreover, these elongations were larger than that of specimen CWDF, in which the bottom of the wall failed.

Deformation Components

Figure 12 shows the percentages of shear and bending deformation at the peak of positive loading cycle until the drift angle of 1.0×10^{-2} rad for all specimens. The bending deformation was calculated using the curvature obtained from the vertical displacements measured at the side column (Figure 13), while the shear deformation was calculated by subtracting the bending deformation from the total deformation.

For specimen CWDF, shear deformation was about 50% at the drift angle of 0.0625×10^{-2} rad, while the percentage of shear deformation decreased from about 40% to 50% in the succeeding loading cycles. As for specimen CWPF, which is a precast shear wall, shear deformation was also about 50% at the drift angle of 0.0625×10^{-2} rad.

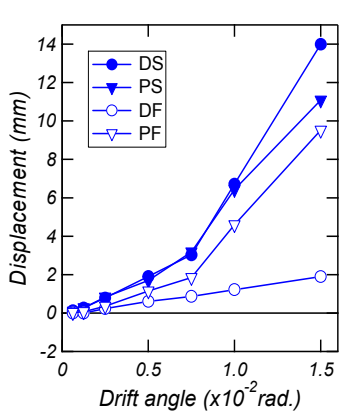


Figure 11. Elongation of beam

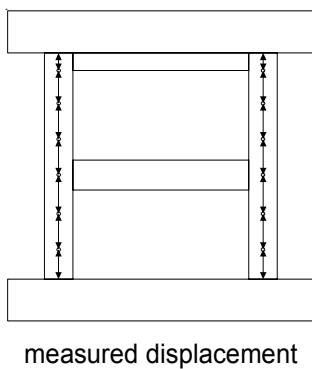


Figure 13. Measured displacement

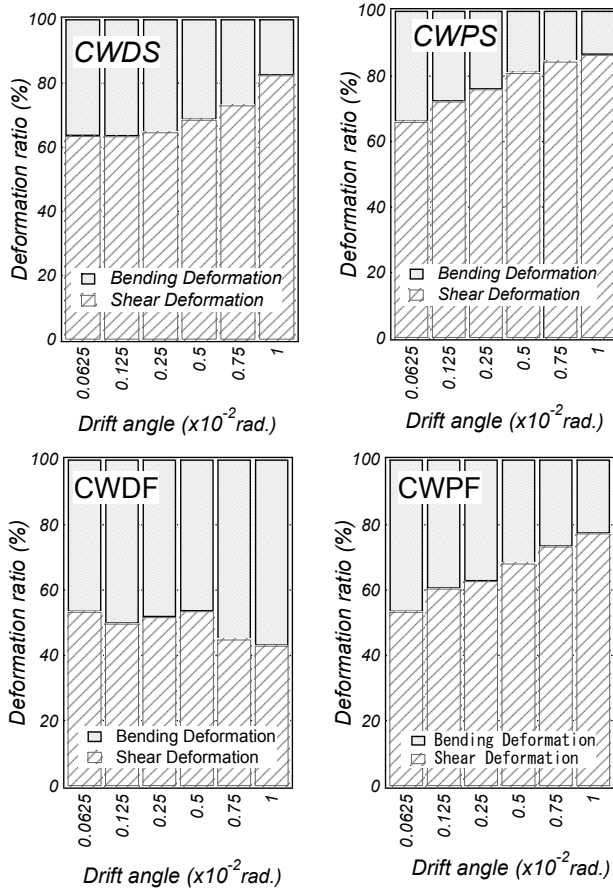


Figure 12. Percentage of deformation components

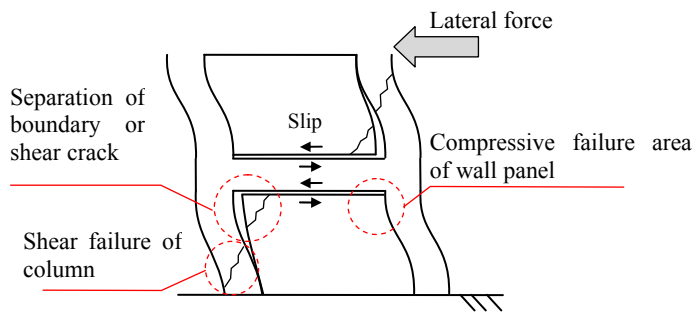


Figure 14. Deformation behavior of precast CES shear wall specimen

However, the shear deformation increased and bending deformation decreased with increasing drift angles. In the same way, the shear deformation of specimens CWDS and CWPS increased with increasing drift angles.

In the precast shear wall specimens, deformation and failure occur with increasing drift angles as shown in Figure 14. Because of separation at the boundary of

the wall panel and column or spreading of shear cracks at the wall panel corner, significant slip occurs at the boundary of the wall panel and beam. Furthermore, the column on the compressive side and the column on the tensile side and wall panel of the CES shear wall moves separately, with each member deforming individually.

STRENGTH EVALUATION

The calculation results of the ultimate strengths for all specimens are listed in Table 5. The value in parenthesis is the ratio of test result to calculated result. Flexural strength was calculated using Eq. (2), which omits the term for the reinforcing bars in the boundary column from an equation given in the "AIJ Standards for Structural Calculation of Steel Reinforced Concrete Structures" [Architectural Institute of Japan, 2001].

[Flexural strength]

$$Q_{mu} = \left(\frac{N}{2} + {}_{sCS}A \cdot {}_s\sigma_y + \frac{{}_mW A}{2} \cdot {}_w\sigma_y \right) \frac{{}_w l}{{}_w h} \quad (2)$$

where N : total axial force in the boundary columns (N)

${}_{sCS}A, {}_mW A$: cross section of the steel in the boundary column and the vertical reinforcement in the wall panel, respectively (mm^2)

${}_s\sigma_y, {}_w\sigma_y$: yield strengths of the steel in the boundary column and the vertical reinforcement in the wall panel, respectively (N/mm^2)

${}_w l$: distance between the centers of the boundary columns of the wall (mm)

${}_w h$: assumed height of the applied lateral force (mm).

[Shear strength by truss-arch equation]

$$Q_{su} = {}_w t \left\{ {}_w l_t \cdot {}_w p \cdot \sigma_{wh} \cdot \cot \phi + \tan \theta (1 - \beta) {}_w l_a \cdot v \cdot \frac{\sigma_B}{2} \right\} \quad (3)$$

$${}_w l_a = {}_w l + \frac{1}{\cos \theta} \sqrt{\frac{2 {}_{CS} M_U}{v \cdot \sigma_B \cdot {}_w t (1 - \beta)}} \quad (4)$$

$$\beta = \frac{2 {}_w p \sigma_{wh}}{v \sigma_B} \quad (5)$$

$$\tan \theta = \sqrt{\left(\frac{{}_w h}{{}_w l + D} \right)^2 + 1} - \frac{{}_w h}{{}_w l + D} \quad (6)$$

where ${}_w t$: thickness of wall

${}_w l_t$: equivalent wall length of truss mechanism (whole length of wall)

${}_w p$: wall lateral reinforcing ratio

σ_{wh} : yield strength of the lateral reinforcing bar (N/mm^2)

ϕ : angle of concrete strut of truss mechanism ($\cot \phi = 1$)

- θ : angle of concrete strut of arch mechanism
 v : effective coefficient of concrete
 σ_B : compressive strength of concrete (N/mm²)
 wl_a : equivalent wall length of arch mechanism
 ${}_{cs}M_U$: ultimate flexural moment of boundary column
 D : depth of boundary column.

Because it was observed that the steel flange of the beam yielded at the maximum shear force in the test, the shear strength was calculated by adding the lower steel flange of the beam to the transverse wall reinforcing bar of $w_p \cdot \sigma_{wh}$.

The ratios of measured strength to calculated flexural strength of specimens CWPF and CWDF are about 0.97 to 1.12 in Table 5, showing that the flexural strength of CES shear walls can be evaluated by Eq. (2).

For specimen CWDS, which showed shear failure, the ratio of measured strength to calculated shear strength is 0.99, which demonstrates that the calculated strength gives good correlation with the experimental results and that the shear strength of the CES shear wall can be evaluated by Eq. (3).

However, since the maximum shear forces of the precast wall specimens were smaller than that of integral construction shear wall specimens, and the slip displacement of precast wall specimens were larger than that of integral construction shear wall specimens, the equation for the shear strength of RC frame infilled walls was used to evaluate the strength [Japan Building Disaster Prevention Associate, 2001]. The calculation results for the precast specimen are shown in Table 6.

[Shear strength by RC infilled shear wall]

The shear strength is given by the smaller value of the following two equations,

$$Q_{su} = {}_w Q'_{su} + 2\alpha \cdot Q_c \quad (7-1)$$

$$Q_{su} = {}_f Q_j + {}_p Q_c + \alpha \cdot Q_c \quad (7-2)$$

where ${}_w Q'_{su}$: shear strength of infilled wall panel

${}_f Q_j$: frictional force under the beam

${}_p Q_c$: direct shear strength at the top of a column

Q_c : smaller value of the other column between the shear force at the yielding and shear strength

α : reduction factor in consideration of the deflection condition to allow for load bearing contribution of columns (= 1.0 in case of shear failure, = 0.7 in case of flexural failure). Also, friction coefficient is assumed to be 0.7.

Equation (7-1) is expressed as the sum of the strengths of the wall panel and the two boundary columns, while Eq. (7-2) is expressed as the sum of the frictional force between beam and wall panel, the direct shear strength at the top of a column and the strength of the other column. However, these evaluation methods are usually used

Table 5. Calculated strength of CES shear wall with flexural failure

Specimen		CWDS	CWPS	CWDF	CWPF
Maximum share in test: Q_{exp} (kN)		1204	995	988	855
Flexural strength: Q_{mu} (kN)		1161	1149	881 (1.12)	881 (0.97)
Shear strength: Q_{su} (kN)	Eq. (3)	1222 (0.99)	1202 (0.83)	1241	1241

*value in parenthesis is the ratio of test result to calculated result

Table 6. Calculated shear strength of precast CES shear wall

Specimen		CWPS	CWPF
Maximum share in test: Q_{exp} (kN)		995	855
Shear strength: Q_{su} (kN)	Eq. (7-1)	587 (1.69)	679 (1.26)
	Eq. (7-2)	973 (1.02)	1173 (0.73)

*value in parenthesis is the ratio of test result to calculated result

for RC frame infilled walls.

For specimens CWPF and CWPS, which are the precast shear walls, the ratios of the measured to calculated strength using Eq. (7-1) are 1.26 and 1.69 respectively. Hence, the equation underestimates the shear strength of the precast CES shear wall. Using Eq. (7-2), the ratio of the measured to calculated strength for specimen CWPS is 1.02, which shows good agreement between the calculated shear strength and experimental result. On the other hand, for specimen CWPF, although the maximum shear force did not reach the calculated strength, the calculated shear strength was larger than the calculated flexural strength. In this case, the strength of specimen CWPF is determined by the flexural strength. Therefore, Eq. (7-2) corresponds well to the strength of precast CES walls.

It must be noted that the discussion in this section is based on the limited number of specimens in this test and may not be generally applicable. Results may vary with changes in the wall configuration (such as a change in the wall thickness or in the cross-section of the column), or in the shear span. These results will have to be verified for other kinds of CES walls.

CONCLUSION

Static loading tests were conducted on shear walls with a simplified anchoring method for connecting the CES frame to the FRC wall panel, and which includes precast shear wall specimens. The failure mode, lateral load carrying capacity, and deformability of the CES shear walls were examined. The following conclusions can be drawn.

- 1) Specimens CWDS and CWPS showed shear failure of the wall panel.
- 2) Specimen CWDF showed flexural failure, while specimen CWPF, which has a precast shear wall, showed shear failure after yielding.
- 3) The maximum shear forces of the precast CES shear wall specimens were less than that of the integral construction CES shear wall specimens.
- 4) The differences in the maximum shear forces and failure modes between the precast CES shear wall specimens and the integral construction CES shear wall specimens may be attributed to the large slip displacements at the boundary of the wall panel and CES frame and the elongation of the beam on the precast CES shear wall.
- 5) The flexural strength of the CES shear wall specimens can be evaluated by using the equation in the AIJ design standard for SRC structures, while the shear strength of the integral construction CES shear wall specimen can be evaluated by the truss-arch equation.
- 6) The shear strength of the precast CES shear wall specimens can be evaluated by using equations for the shear strength of RC frame infilled wall conservatively. However, the stress transfer mechanisms and the evaluation methods will have to be examined further.

REFERENCES

- Architectural Institute of Japan, (2002), "Evaluation method and design of shear strength for Multi-story precast reinforced concrete structural walls" (in Japanese)
- Japan Building Disaster Prevention Associate, (2001), "Guidelines for Seismic Retrofit of Existing Reinforced Concrete Buildings Japanese version"
- Fauzan. Kuramoto, H. Matsui, T. and Taguchi, T. (2008). Test on 2-Bay 2-Story CES Frame Subjected to Lateral Load Reversals, *Proceedings of Fourteenth World Conference on Earthquake Engineering*. Paper No. 05-06-0063.
- Matsui, T. and Kuramoto, H. (2008). Stress Transferring Mechanism of Beam-Column Joints for Composite CES Structural System Subjected to Seismic Load. *Proceedings of Fourteenth World Conference on Earthquake Engineering*. Paper No. 05-06-0081.
- Fujimoto, T. Kuramoto, H. and Matsui, T. (2008). Seismic Performance of Columns and Beam-Column Joints in Composite CES Structural System. *Proceedings of Fourteenth World Conference on Earthquake Engineering*. Paper No. 05-06-0073
- Suzuki, S. Matsui, T. Kuramoto, H. (2012). A Fundamental Study on Structural Performance of CES Shear Walls with Different Anchorage Condition of Wall Reinforcing Bars. *Proceedings of fifteenth World Conference on Earthquake Engineering*.

The Development of a Steel Fuse Coupling Beam for Coupled Core Wall Systems

Steven J. Mitchell¹; Gian A. Rassati²; and Bahram M. Shahrooz³

¹LJB, Inc., 2500 Newmark Dr., Miamisburg, OH 45342. E-mail: SMitchell@ljbinc.com

²Dept. of Civil and Architectural Engineering and Construction Management, Univ. of Cincinnati, Cincinnati, OH 45221. E-mail: gian.rassati@uc.edu

³Dept. of Civil and Architectural Engineering and Construction Management, Univ. of Cincinnati, Cincinnati, OH 45221. E-mail: bahram.shahrooz@uc.edu

Abstract

Coupled core wall systems are being used in seismically active areas worldwide as an effective type of structural system for resisting earthquake demands. At the University of Cincinnati, the design evolution of an innovative type of steel coupling beam was investigated that provides a significant advantage for structures utilizing linked concrete walls. The concept of post-event reparability can be realized through the use of a steel coupling beam in which a weak-link, or ‘fuse’ section is induced at the center of the clear span of the beam. During extreme seismic events on a fused coupled core wall system, all inelastic response is focused onto the weak link while the elastic integrity of the surrounding embedded beams and walls is ensured by careful detailing. A code-compliant design procedure has been established that preserves the intended performance. Results and conclusions from the analytical modeling of a 20-story structure indicate that steel fuse coupling beams perform favorably in a seismic event. Data from experimental tests demonstrate the adequacy of the design procedure and show the performance under cyclic load demands.

INTRODUCTION AND PREVIOUS RESEARCH

A new generation of coupling beams has been developed and investigated for their application to the seismic design of structures. An innovative coupling beam consisting of a steel coupling beam with a replaceable mid-section has been studied in a past project [Fortney 2005]. This design concept is based on concentrating damage resulting from a seismic event in specially detailed components, which, after a seismic event, may be removed and replaced, returning the structure to a serviceable condition. When designed and detailed appropriately, coupling beams have been shown to perform closely to links in eccentrically braced frames, and this particular objective is analogous to replaceable links in such frames [Fortney et al. 2007].

By focusing damage onto the mid-sections of the coupling beams, the response of the overall system is such that reinforced concrete walls are prevented from undergoing inelastic behavior, which is desirable because damage in the walls is

either costly or impractical to repair. Steel coupling beams have been proven to show outstanding energy dissipation characteristics and ability to provide adequate lateral stiffness to coupled core wall (CCW) systems, while allowing reduced floor-to-floor heights. Previous testing of a steel coupling beam with a replaceable mid-section [Fortney 2005], designated herein as a steel fuse coupling beam (SFCB), found that this new system showed similar energy dissipation and stiffness characteristics to those of a continuous steel coupling beam. SFCBs consist of two relatively short beam stubs, embedded for most of their length into the reinforced concrete shear walls (herein referred to as the *embedded beams*), and of a short beam (the *fuse beam*), installed between the embedded beams. Consistent with the design criterion for links in eccentrically braced frames, the fuses in SFCBs are designed as shear-critical members, allowing energy dissipation primarily through shear yielding, which is generally a considerably more stable and ductile failure mechanism when compared to flexural-critical behavior in longer beams [El-Tawil et al. 2007].

STEEL FUSE COUPLING BEAM DESIGN METHODOLOGY

As part of the previous experimental testing of SFCBs, no code-compliant design procedure was developed. A complete design procedure has been generated and validated by means of large-scale experimentation, which included the proof-of-concept replacement of a damaged fuse with a new one and retesting of the specimen [Mitchell 2012]. The SFCB is designed utilizing built-up, doubly-symmetric I-shaped sections and bolted connections between fuse and embedded beams. Fillet welds are used to assemble the built-up sections. Figure 1 shows the layout for a steel fuse coupling beam.

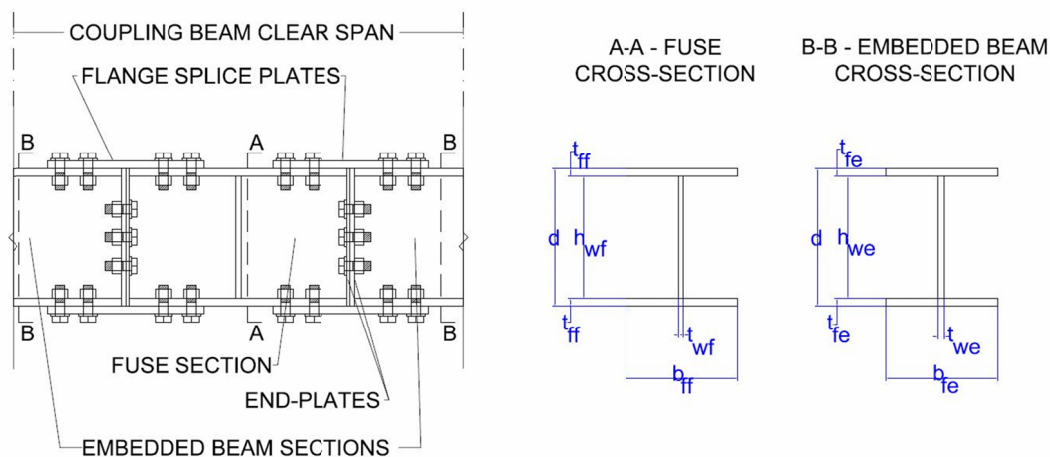


Fig. 1 - Assembly of a SFCB and dimensions to proportion

As mentioned above, all plasticity phenomena are forced to occur away from the faces of the reinforced concrete walls and are focused onto a replaceable fuse that dissipates energy in shear, a more favorable behavior than flexure. In the proposed SFCB systems, the mid-span fuse beam is designed first to resist the seismic effects

from the appropriate loading combination, as calculated from the system analysis. Subsequently, the amplified expected capacity of the fuse is used to proportion the surrounding elements of the coupling beam that are embedded within the wall piers, as well as the connections between the fuse and the embedded beams. Once the fuse is designed following appropriate procedures for conventional steel coupling beams, and following prescribed element aspect ratios to preclude element local buckling, Equation 1 may be used to determine the maximum expected shear capacity of the fuse. This is used in the demand Equations for the remainder of the SFCB design, and is therefore expressed relative to the capacity of the embedded beams.

$$(1) \quad V_{u,emb} = 1.1R_y V_{nf} = 1.1R_y (0.6F_{yf} h_{wf} t_{wf})$$

The fundamental performance objective of the proposed design methodology for a SFCB is to preserve the integrity of the embedded beam components under the demands of a design earthquake [Mitchell 2012]. Equation 1 accounts for the ratio of expected yield stress to the specified minimum yield stress of the fuse beam material, as well as an additional 10% to account for strain-hardening. Figure 2 presents a diagram of the forces transferred between the fuse and the embedded beams. It should be noted that the assumed rigid fixity of the SFCB is at the face of the wall pier, i.e. portions of the beam embedded within the reinforced concrete are assumed to be perfectly rigid.

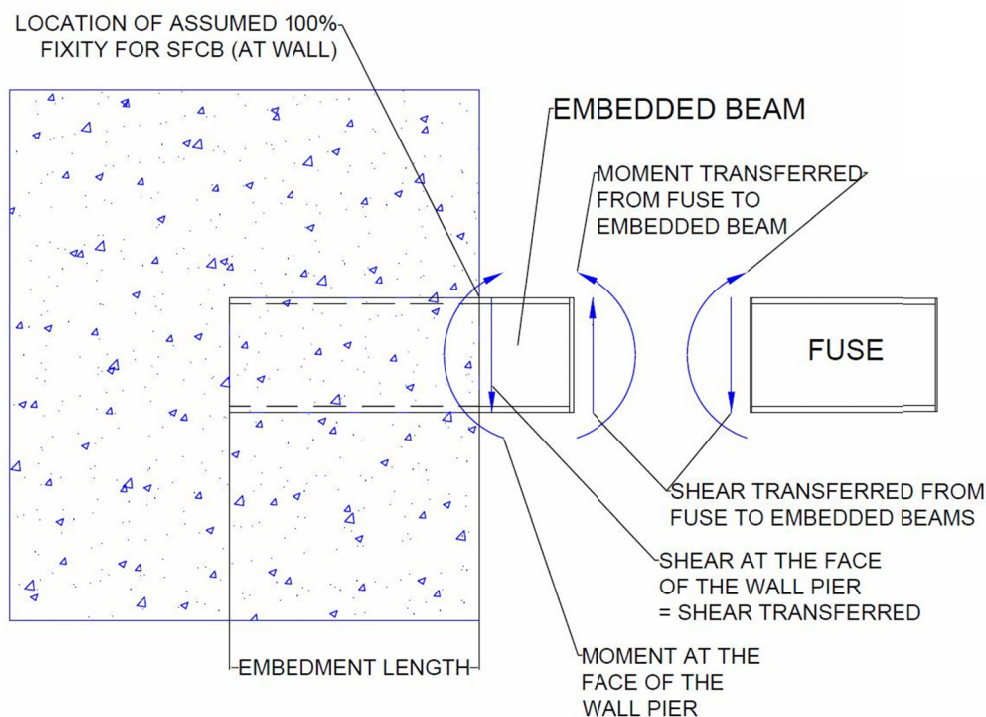


Fig. 2 - Transfer of forces within a SFCB

The design shear capacity of an embedded beam, calculated in Equation 2, must be greater than the expected shear transfer from the fuse to preserve the SFCB performance.

$$(2) \quad \phi V_{ne} = \phi(0.6F_{ye}h_w t_{we}) \geq V_{e,emb}$$

Maximum flexural demands on embedded beams are calculated at the face of the wall piers. These demands are functions of the expected fuse shear strength and the geometry of the coupling beams, and may be calculated using Equation 3.

$$(3) \quad M_{wall} = M_{u,emb} = (1.1R_{yf}V_{nf})\left(\frac{e}{2}\right) + (1.1R_{yf}V_{nf})(L_{emb})$$

where e is the length of the fuse and L_{emb} is the length of an embedded beam between the fuse and the face of the wall.

In order to preserve the integrity of the embedded beams with regard to flexure, design capacities are calculated considering the onset of yielding within any portion of the cross-section. This is accomplished by using the elastic section modulus to calculate the yield moment. Equation 4 must be satisfied for an adequate flexural design of embedded beams.

$$(4) \quad M_{ye} = F_{ye}S_e \geq M_{u,emb}$$

Bolted connections between the fuse and the embedded beams are designed as slip-critical connections in order to preserve a stable hysteretic response under repeated load-reversals. The remaining design considerations for SFCB components include (a) detailing embedment length into reinforced concrete walls, (b) auxiliary transfer reinforcement within the walls, and (c) appropriate end- and stiffener plate design and detailing. These requirements follow established procedures for conventional steel coupling beams.

PROTOTYPE BUILDING DESIGNED WITH SFCBS

The test specimens considered for large-scale experimentation as part of this research were selected and scaled down from a set of floors within a 20-story prototype structure designed with SFCBs. Moreover, this prototype structure provides a platform to globally investigate the seismic performance of coupled core walls utilizing SFCBs.

A single-bay, central core wall was chosen for the prototype structure, with two C-shaped walls linked with two SFCBs per floor. Floor-to-floor height was selected as 2.743 meters (9 feet), resulting in a 54.86 meter (180 foot) structure. The general layout for the core wall is presented in Figure 3. Code-approved loads were prescribed onto the prototype structure following the Equivalent Lateral Force Procedure [ASCE 7-10] and adequate SFCB designs were achieved at every level. The software package ETABS [CSI, 2010] was used at this stage in design, in which an elastic analysis was carried out on the structure.

In order to globally assess the nonlinear response of the structure, the software package RUAUMOKO [Carr, 2008] was used to carry out an adaptive pushover

analysis on an idealized, two-dimensional model of the structure. The wall piers were modeled at the corresponding centroids of their plan view layouts, and the coupling beams modeled at each floor represented the strength and stiffness values of two coupling beams. Wall piers were assumed fixed at their base. A schematic of the two-dimensional model generated for RUAUMOKO is presented in Figure 4.

CENTRAL CORE WALL GEOMETRY

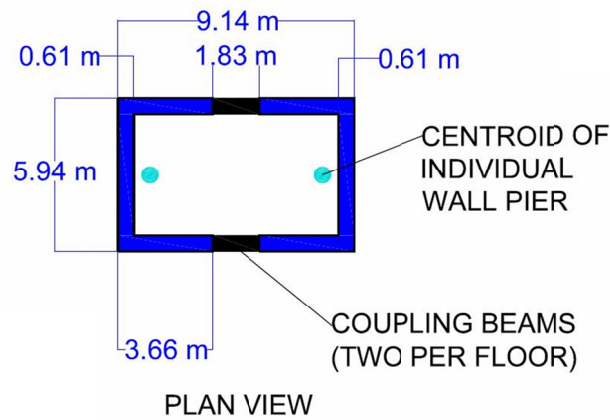


Fig. 3 - Plan view for the prototype structure core wall

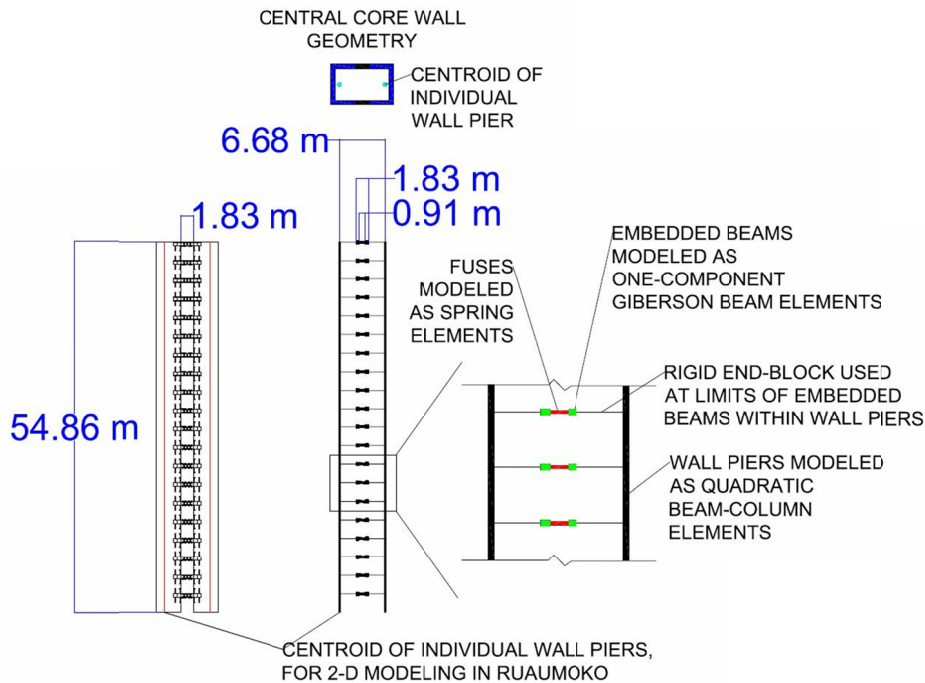


Fig. 4 – Prototype structure two-dimensional model

The adaptive pushover analysis was terminated at loading demands significantly larger than those generated using the Equivalent Lateral Force Procedure [ASCE 7-10]. The base shear resulting from the analysis is 20,328 kN, approximately 2.45 times larger than the base shear calculated using the Equivalent Lateral Force Procedure (8,296 kN). Building displacement limits and coupling beam rotation limits were all satisfied under this magnitude of loading.

STEEL FUSE COUPLING BEAM AND WALL PIER PERFORMANCE

Base shear (normalized with respect to the design base shear) versus roof drift (normalized with respect to the total height) is presented in Figure 5. Structure softening becomes more apparent as the progression of fuse yielding beyond first yield continues.

Strain hardening effects were incorporated into the post-elastic response of the fuses and embedded beams modeled in RUAUMOKO, utilizing data processed from the experiment discussed in this paper and reported in [Mitchell 2012] and from previous steel coupling beam experiments [Fortney 2005]. Fuse strengths were allowed to develop beyond the theoretical limit established in Equation 1.

Embedded beam shear yielding was found to be minimal at the end of the loading application, with only beams located in floors 4 and 13 indicating forces beyond expected yield values. In each case, the shear demand was 2% beyond yield. A full condition assessment for SFCB shear performance at the conclusion of loading is presented in Figure 6. This graph represents the demands at the concluding time step of loading normalized by the expected yield capacities of the fuses and embedded beams in shear.

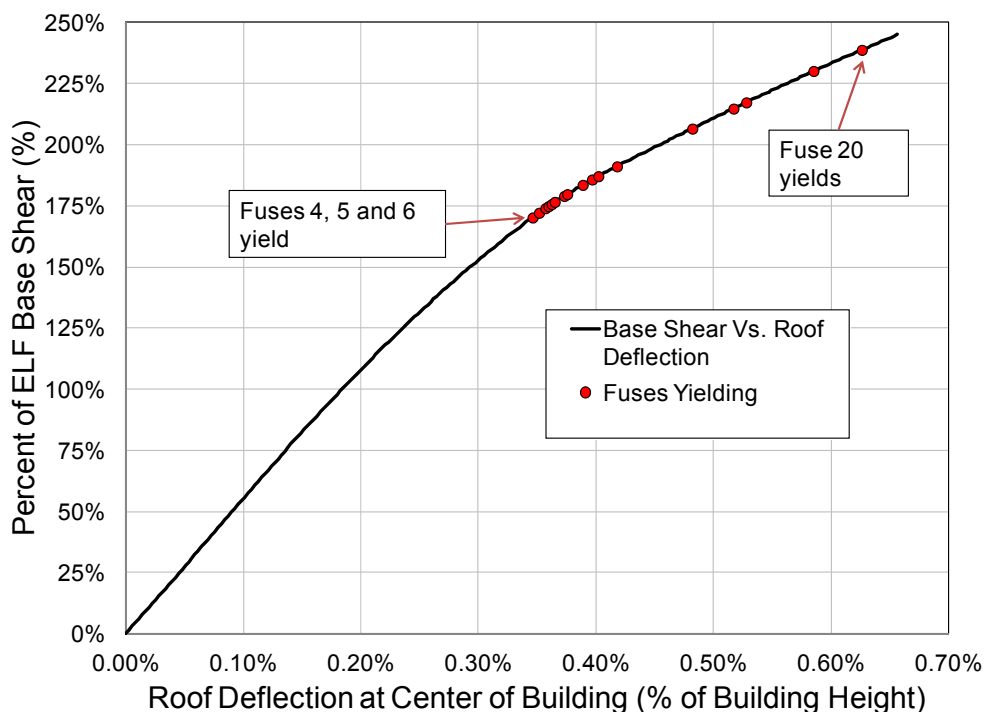


Fig. 5 – Normalized base shear vs. roof drift relationship

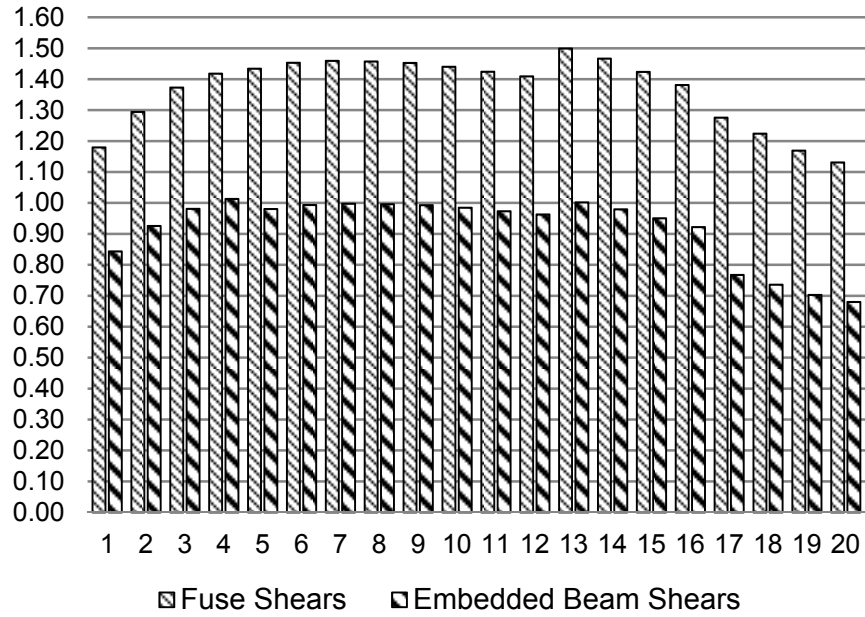


Fig. 6 – Demand/capacity ratios for SFCBs in shear, per floor

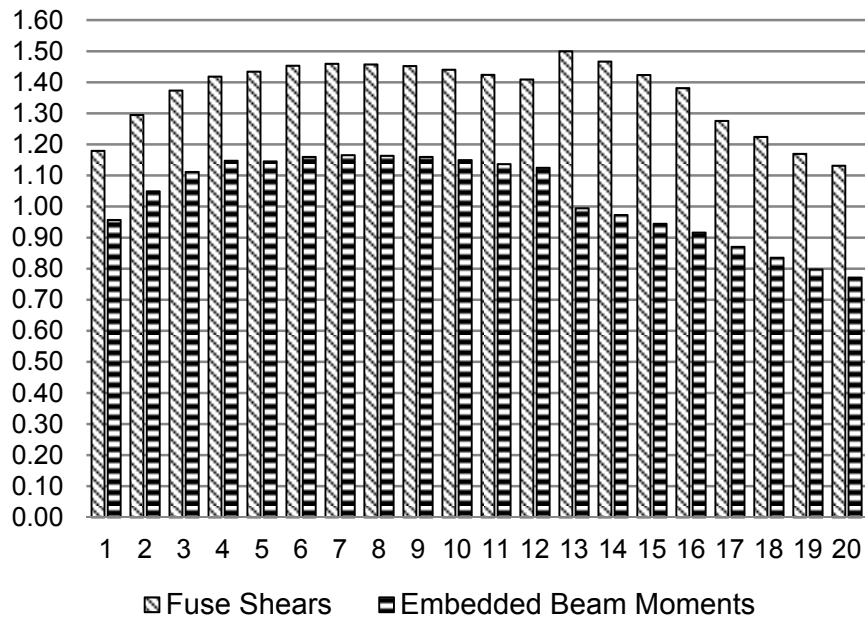


Fig. 7 – Demand/capacity ratios for fuses in shear and embedded beams in flexure

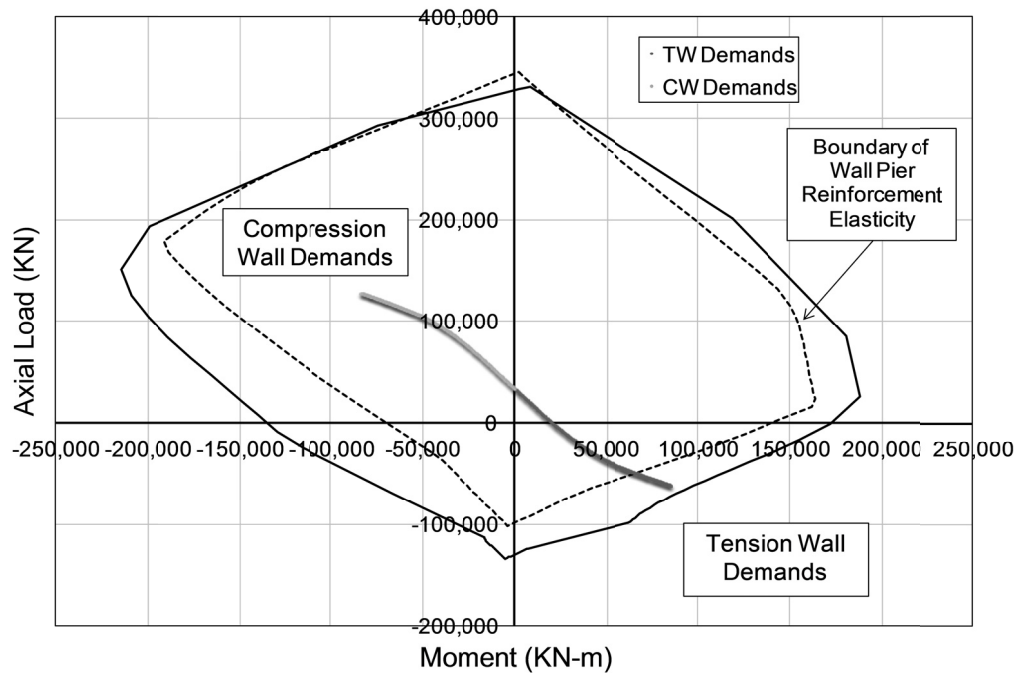


Fig. 8 – Wall pier performance at base of prototype structure

The flexural performance of the embedded beams was also evaluated using a similar procedure. Figure 7 compares the fuse shears demand ratios with the embedded beam flexural demand/expected capacity ratios. Demands exceeded available capacity in floors 2 through 12 by no more than 17%. Though not desirable, considered the magnitude of the pushover loading and the conservative approach taken in the calculation of yield moment capacities, this response is deemed acceptable.

In order to allow for the possible replacement of a damaged steel fuse after a seismic event, it is critical that the response of the shear walls be such that they remain mostly into the elastic range throughout the design event. In fact, excessive damage in wall piers would result in a permanent drift that would render replacement procedures of fuses difficult if not impossible. In order to determine the condition of the wall piers, axial force and bending moment couples were plotted against a capacity interaction diagram for each floor within the prototype structure. Demands were largest at the base of the structure, as expected. Figure 8 shows that the demands never reach the plastic interaction boundary, although they cross the elastic boundary, indicating some yielding has taken place. However, this is a consequence of the particular modeling approach for the fuse beam followed for the pushover analyses, which caused the fuse beams to harden beyond the expected shear strength (in some cases, 20% above that limit), therefore increasing the demands on the wall piers. With this in mind, the simulated response of the wall piers was deemed to be acceptable within the design hypotheses.

FULL-SCALE TESTING OF A STEEL FUSE COUPLING BEAM

The design procedure developed for SFCBs was validated experimentally by testing two wall pier segments joined by a steel fuse coupling beam, with the intent of (a) validating the design methodology, (b) demonstrating the post-event replacement concept for fuses, (c) obtaining performance data at various displacement levels, and (d) documenting modes of failure and damage progression within SFCBs. Two identical fuse sections were designed and fabricated in order to provide a replacement fuse to be installed after the first complete application of cyclic forces on the specimen. A half-scale SFCB specimen was designed from the grouping of floors in the prototype structure that experienced the heaviest demands resulting from lateral loading. Figure 9 presents the assembled SFCB specimen considered for experimental testing. The design procedure followed the methodology outlined previously.

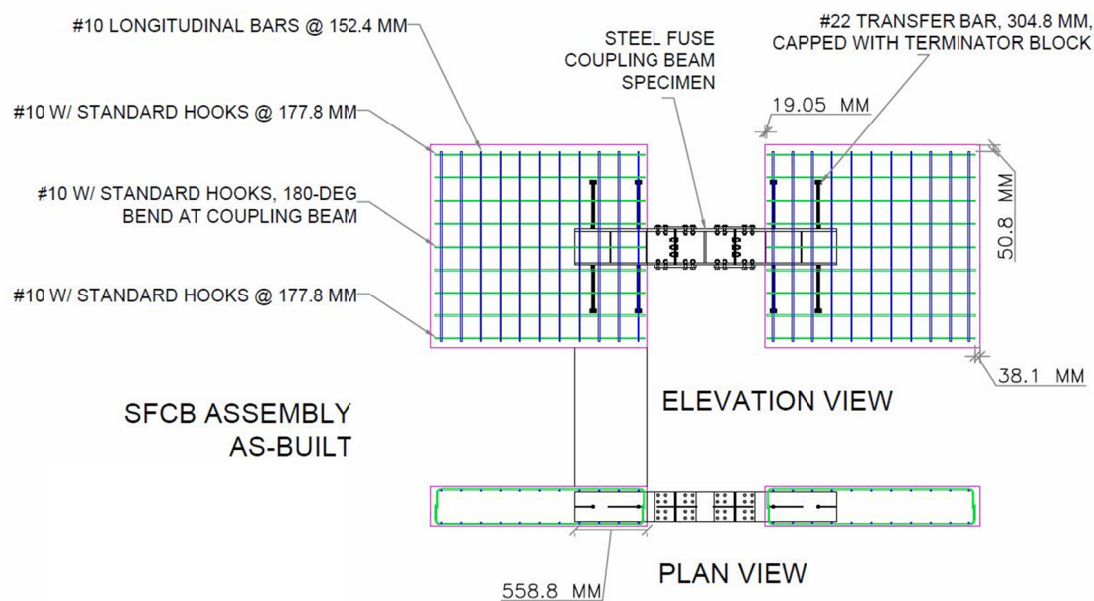


Fig. 9 – Specimen sub-assembly as-built of SFCB and reinforced concrete walls

A quasi-static loading history in the spirit of what is prescribed for qualification testing of shear links in Appendix K to the AISC Seismic Specification [ANSI/AISC 341-10] was applied to the specimen assembly using two servo-controlled hydraulic actuators in displacement control in a master/slave configuration. In addition to acquiring data from the actuators load cells and displacement transducers, numerous strain gauges and strain rosettes were installed at locations of interest to provide direct strain readings on the SFCB components.

The initial assembly was tested, referred to as Test 1, until the fuse element demonstrated yielding while the embedded beam elements remained essentially undamaged. Calculations considered measured material properties for steel, evaluated from material tension coupons provided through specimen fabrication. Loading for Test 1 was terminated at displacement cycles corresponding to a 2%

coupling beam chord rotation, at which point the shear force developed was 750 kN, approximately 35% beyond yield in the fuse and 1% beyond yield in the embedded beams. The hysteretic response of the specimen during Test 1 was stable with minimal stiffness degradation and no strength degradation. Applied force versus controlled coupling beam rotation is presented in Figure 10

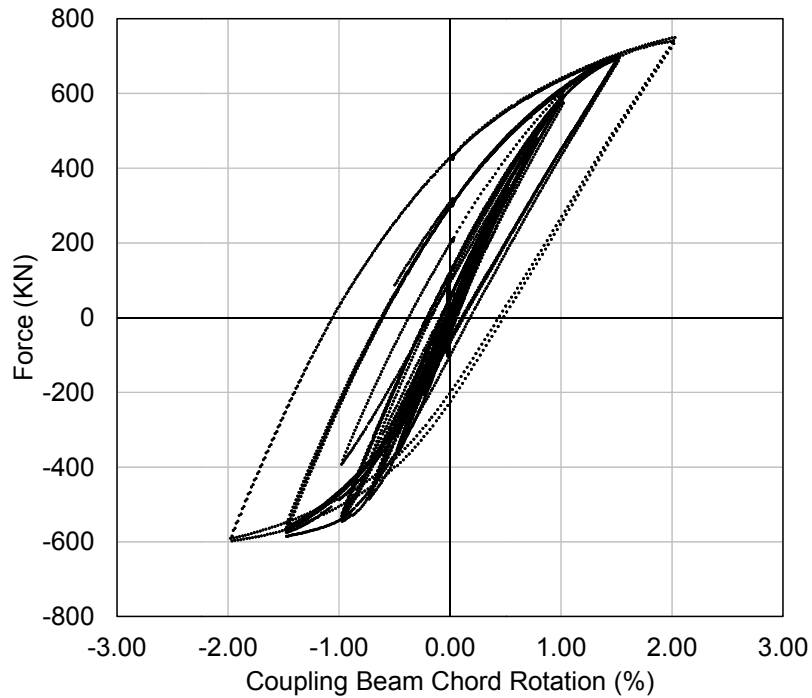


Fig. 10 – Beam chord rotation and corresponding force during SFCB Test 1



Fig. 11 – Damage noticed in plate components at the end of Test 2

The fuse installed and evaluated during Test 1 was disconnected and removed from the test assembly and all appropriate gauges were replaced. Once re-assembled, the repaired system was experimentally retested using the same testing protocol. Force-displacement relationships at the 2% chord rotation level in Test 2 were nearly identical to those of Test 1. Displacement demand was progressively increased past the 2% point, terminating at a displacement demand corresponding to 14% coupling beam chord rotation. At this point, the loading actuator had reached its full stroke. The most notable signs of damage in the SFCB components were double-curvature bending of the connecting end-plates and flange splice plates, shown in Figure 11.

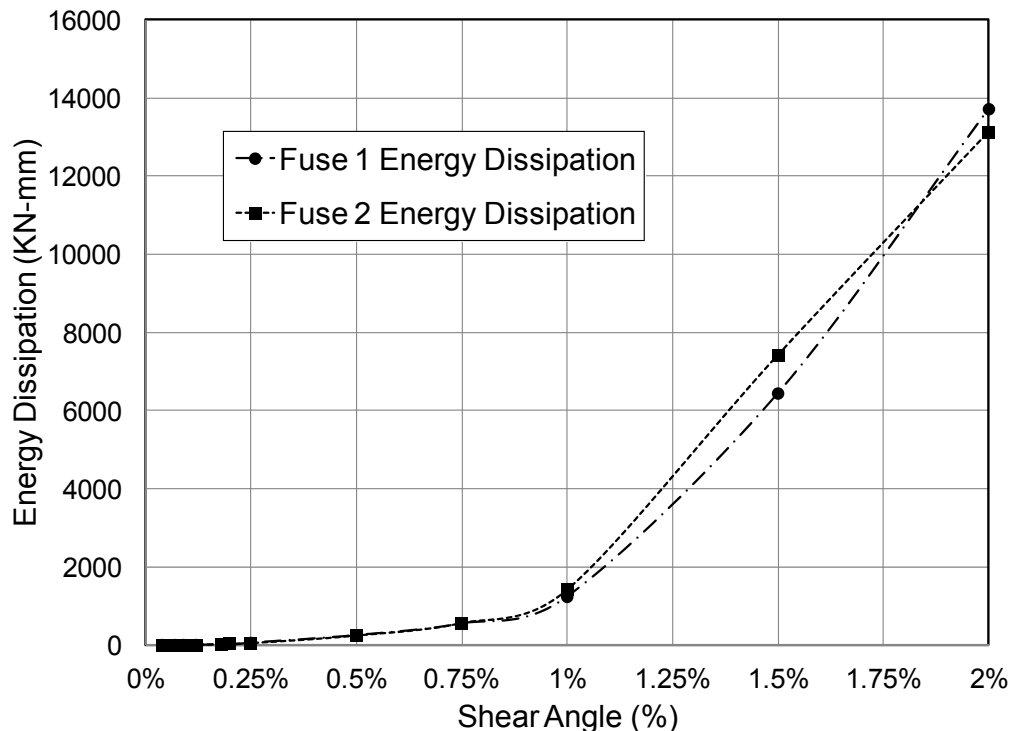


Fig. 12 – Plastic energy per cycle of loading, Test 1 and Test 2

COMPARISON BETWEEN ORIGINAL AND REPLACED SFCB SYSTEMS

The repaired system demonstrated remarkable strength and stiffness, as well as ductility up to the end of testing at a coupling beam chord rotation of 14%. The performance of the two specimens may be compared in terms of energy dissipation. Areas enclosed within each of the load-deflection hysteretic loops were calculated as a means to quantify the amount of energy dissipated in each cycle. These values are plotted in Figure 12 for each test with respect to the shear angle, approximately equal to the chord rotation. Insofar as energy dissipation capabilities, the repaired system was able to dissipate 2.75% more energy than the initial system.

The force-chord rotation response for the two tests, presented in Figure 13, shows how the original and the repaired system behave almost identically. Moreover, the stability of the hysteresis cycles at very large chord rotations is clearly

demonstrated. For the sake of clarity, the dashed box in Figure 13 includes Test 1 cycles, which are for all intents and purposes superimposed onto the Test 2 response.

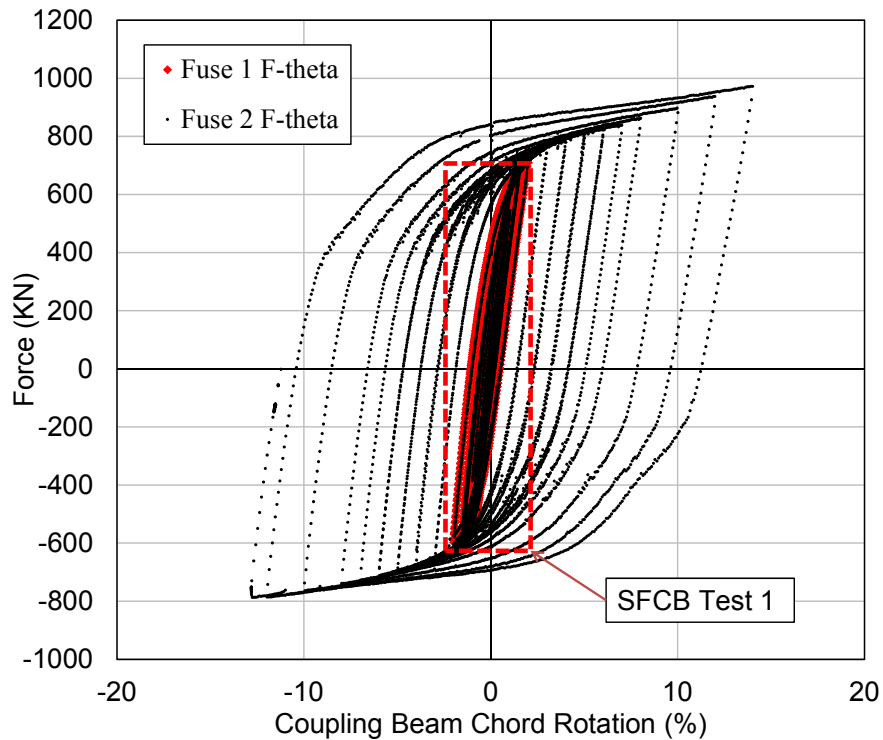


Fig. 13 – SFCB Test 1 and Test 2 hysteretic response

CONCLUSIONS

Several observations and conclusions can be drawn based on the analytical and experimental results presented in this paper. First, analyses of a 20-story analytical model indicate that SFCB systems can be designed so that fuses yield in shear while embedded beams remain essentially elastic in shear. However, flexural demands in a number of embedded beams indicated that the flexural yield capacity was exceeded. The relatively small exceedance was deemed to be acceptable given the conservative nature of using the moment capacity corresponding to the first yielding of the extreme fiber. Moreover, this exceedance did not occur until fuses in 75% of the floors had already yielded, indicating that large amounts of energy dissipation had already occurred. Also, wall piers were shown to respond with limited excursions in the inelastic range, indicating that fuses could be replaced with relative ease.

The code-compliant design procedure and methodology developed was validated through experimental testing of a SFCB sub-assembly. The hysteretic responses of the initial SFCB specimen and of specimen obtained by replacing the fuse were essentially the same, showing excellent stiffness, load carrying capacity, stability, and energy dissipation. There were no visible signs of impending failure or loss of ductility at the 14% coupling beam chord rotation cycle, when testing was stopped. The detailing of the fuse beam, and of the fuse beam-to-embedded beam

connection proved to be capable of providing outstanding ductility, with stable strength and stiffness even at large strain demands, showing a marked improvement with respect to previous research results [Fortney 2005].

Several strain gauges indicated the onset of localized yielding in the embedded beams at approximately first yield of the fuse. It was concluded that this local strain data may not necessarily represent the overall member response, especially when considering the uncertainties related to beam boundary conditions at the interfaces with the reinforced concrete walls as well as the to the boundary conditions of the specimen in the experiment.

NOTATION

F_{ye} = Specified yield strength of an embedded beam, MPa (ksi)

F_{yf} = Specified yield strength of a fuse beam, MPa (ksi)

L_{emb} = Length of an embedded beam, mm (in.)

$M_{u,emb} = M_{wall}$ = Moment in the coupling beam at the face of the wall pier, kN-m (kip-ft)

M_{ye} = Elastic moment capacity of an embedded beam, kN-m (kip-ft)

R_{yf} = Ratio of the expected yield stress to the specified minimum yield stress of a fuse beam

S_e = Elastic section modulus of an embedded beam, mm³ (in.³)

V_{nf} = Nominal shear strength of a fuse beam, kN (kips)

V_{ne} = Nominal shear strength of an embedded beam, kN (kips)

$V_{u,emb}$ = Shear demand of an embedded beam, kN (kips)

e = Length of the fuse, mm (in.)

h_{we} = Web height of an embedded beam, mm (in.)

h_{wf} = Web height of a fuse beam, mm (in.)

t_{we} = Web thickness of an embedded beam, mm (in.)

t_{wf} = Web thickness of the fuse, mm (in.)

ACKNOWLEDGMENTS

The work presented herein was funded by the National Science Foundation through grant CMMI-0653920.

REFERENCES

- ANSI-AISC 341-10 (2010) *Seismic Provisions for Structural Steel Buildings*, American Institute of Steel Construction, Chicago, IL
- ASCE7-10 (2010) *Minimum Design Loads for Buildings and Other Structures*, American Society of Civil Engineers, Reston, VA
- Carr A.J (2008), *RUAUMOKO manual and supplemental volumes*, University of Canterbury, Christchurch, New Zealand
- CSI Berkeley (2010) *CSI Analysis Reference Manual for SAP2000, ETABS, and SAFE*, Computers & Structures, Inc. Berkeley, CA

- El-Tawil S., Fortney P.J., Harries K.A., and Shahrooz B.M. (2007) *Recommendations for seismic design of hybrid coupled wall systems*" American Society of Civil Engineers, Reston VA
- Fortney P.J. (2005), *The Next Generation of Coupling Beams*, Doctoral dissertation, University of Cincinnati, Cincinnati, OH
- Fortney P.J., Shahrooz B.M., and Rassati G.A. (2007) "Large-scale testing of a replaceable 'fuse' steel coupling beam," *ASCE Journal of Structural Engineering*, 133(12):1801-1807
- Mitchell S.J. (2012) *The Development of a Steel Fuse Coupling Beam for Hybrid Coupled Wall Systems*, MS thesis, University of Cincinnati, Cincinnati, OH

Fire Tests of Concrete-Filled Circular Hollow Section Columns with a Solid Steel Core

M. Neuenschwander¹; M. Knobloch²; and M. Fontana³

¹Institute of Structural Engineering, ETH Zurich, Stefano-Franscini-Platz 5, 8093 Zurich, Switzerland. E-mail: neuenschwander@ibk.baug.ethz.ch

²Institute of Steel, Lightweight and Composite Structures, Ruhr Universität Bochum, Universitätsstrasse 150, 44801 Bochum. E-mail: stahlbau@ruhr-uni-bochum.de

³Institute of Structural Engineering, ETH Zurich, Stefano-Franscini-Platz 5, 8093 Zurich, Switzerland. E-mail: neuenschwander@ibk.baug.ethz.ch

Abstract

This paper presents the results of a fire testing program of four concrete filled circular hollow section columns with solid steel core. The structural fire behaviour is analysed by means of the recorded deformation–time as well as temperature–time course. Thereby it is shown, that after the temperature induced failure of the tube, the load is redistributed to the core. Depending on the pre-loading level, these columns can subsequently sustain the load with a bounded rate of deflection, until runaway failure occurs when the temperature induced stiffness degradation of the core sets in. A three-dimensional FEM model is validated with one of the fire tests and the influence of the support conditions, the eccentricity of the load and the input data of the constitutive model of the steel core are studied.

INTRODUCTION

Concrete-filled circular hollow section (CHS) columns with solid steel core consist of a steel tube, within which a solid round bar is concentrically placed and the void in-between is filled with concrete as illustrated in Figure 1. These columns offer a number of structural, economical and architectural advantages. On one hand their high load-bearing capacity at relatively high slenderness ratios makes them architecturally appealing, whereas from a structural engineering standpoint their performance when subjected to fire is exceptional: Their high overall fire resistance follows mainly from the fact that the temperature rise of the steel core is lagged by the concrete infill. The temperature-induced loss of stiffness and strength of this type of composite load-carrying element is delayed. In case of fire, the steel tube is heated quickly and gradually loses strength and stiffness. Consequently, its load-share is redistributed mainly to the steel core. The steel tube also reliably inhibits the spalling of the concrete.

The load-carrying behaviour in fire of concrete filled CHS columns with solid steel core has not been comprehensively analysed experimentally and numerically, neither are there simplified analytical engineering models to estimate the buckling strength at elevated temperatures. Most recently (Hanswille and Lippes 2008) performed at ambient temperature, five ultimate load tests of eccentrically loaded concrete-filled CHS columns with solid steel core and presented a FEM model for the

load-carrying behaviour. To the best of the authors' knowledge, apart from proprietary tests, only one fire test has been reported in literature by (Klingsch 1984). In terms of numerical studies on the fire behaviour of concrete-filled CHS columns with solid steel core (Neuenschwander, Knobloch and Fontana 2010, 2011, 2012) recently published a three-dimensional FEM model. In this paper the experimental study on four fire tests of concrete-filled CHS columns with solid steel core will be presented in the first section. The second section outlines the sensitivity of the FEM model on: (1) the material properties of the steel core and (2) the implementation of the end conditions of the column during the fire test, taking into account imperfections in the nominal boundary conditions



Figure 1. Concrete-filled CHS column with steel core.

EXPERIMENTAL STUDY

The experimental test program comprised of four ISO Standard fire tests with concrete-filled CHS columns with steel core, which were performed at the material test establishment of the Technical University of Brunswick in Germany. The test procedure consisted of two phases: In the first phase the axial load was applied and held constant and in the second phase the loaded column was exposed to an ISO Standard fire until failure. All of the columns were loaded with an eccentricity ensuring a determined direction of buckling failure. This section is divided into three parts, which describe: (1) the assembly of the test specimens, (2) the test setup and (3) the results.

Test Specimens

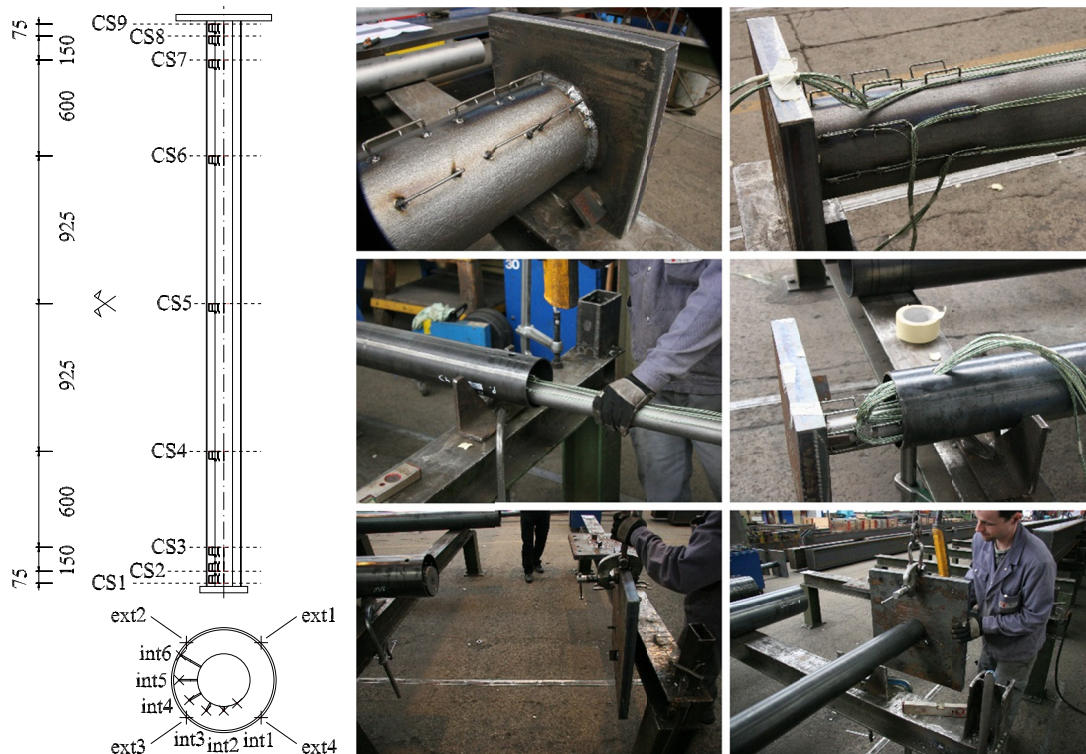
The steel grades used were S235 for the tubes and S355 for the cores. The concrete infill consisted of plain concrete of grade C25/30. Table 1 summarises the geometric properties of the specimens tested and indicates: (1) the outer diameter of

Table 1. Geometric properties of specimens tested.

<i>Specimen</i>	<i>D</i> [mm]	<i>L</i> [mm]	<i>t</i> [mm]	<i>D_{core}</i> [mm]	<i>t_c</i> [mm]	<i>t_p</i> [mm]
Sp1	133.0	3540	4.0	60	32.50	40
Sp2	219.1	3600	4.5	110	50.05	40
Sp3	219.1	3600	4.5	110	50.05	40
Sp4	219.1	3600	4.5	150	30.05	40

the entire composite column, D , (2) the column's length between the end-plates, L , (3) the tube wall thickness, t , (4) the diameter of the solid steel core, D_{core} , (5) the thickness of the concrete layer, t_c , and (6) the thickness of the end-plates, t_p .

Specimen 1, 2 and 4 were equipped with Type K thermocouples at nine different cross-sections (CS1 to CS9 in Figure 2) in order to capture non-uniformity in the temperature field in the longitudinal direction of the columns (cooling-effect of the supports sticking partially out of the furnace). At each of these measurement cross-sections thermocouples were placed at 10 mm spacing within the concrete layer, starting on the surface of the core (int1 in Figure 2) until reaching the inner side of the tube (int6 in Figure 2). On the outer surface of the tube four thermocouples (ext1 to ext4 in Figure 2) were positioned by means of metallic cable straps (stainless steel). High-temperature resisting insulation material was placed between the cable strap and the thermocouple to ensure, that the steel surface temperature was measured during the test. The thermocouples inside the concrete layer were fixed by means of wire on

**Figure 2. Temperature recording scheme and photos of the assembly procedure.**

small stirrups welded onto the core (Figure 2, photos top left and right). All the cables of the thermocouples were bundled and conducted outside of the column through the vapour-pressure relaxation drills at the bottom end (Figure 2, photo middle right).

In a first step of the assembly procedure the sand-blasted cores were carefully placed in the middle of the end-plates and fixed into position by means of a circumferential fillet joint. The stirrups for the thermocouples were then welded onto the core (Figure 2, photo top left). The second step consisted of placing the thermocouples and bundling their cables (Figure 2, photo top right). In the third step, the core now equipped with thermocouples, was inserted carefully into the tube and the bundled cables of the thermocouples were conducted out of the tube (Figure 2, photos middle left and right). In a fifth step, the top end-plate hanging on a crane was assembled by a bolted connection to the core (Figure 2, photo bottom left). The core therefore featured a concentric thread at its top face (Figure 1, photo bottom right). Once the bolted connection was established, the core and the end-plate could be lifted until the tube touched the two spacers on the end-plate, thus ensuring the concentric position of the tube (Figure 2, photo bottom right, however, one of the spacers is more clearly visible on the top left photo). This bolted connection was only temporary in order to ensure the coaxial position of the core during the placing of the concrete and was release after the curing time. In the last step, the tube was connected to both end-plates by circumferential fillet joints. The concrete was poured into the vertically positioned columns through one of the two holes in the top end-plate while the second hole served as an exhaust. A curing time of 35 days ensued, before the first fire test was performed.

Test Setup

Table 2 displays the properties of the four fire tests quoting: (1) the nominal boundary conditions, (2) the magnitude of the applied axial load, P_0 , (3) the eccentricity of the applied axial load, e , (4) the nominal elastic buckling length, L_{cr} , corresponding to the nominal boundary conditions and (5) the slenderness ratio, λ_K , at ambient temperature calculated with experimentally established mean values of the Young's modulus of steel and uncracked concrete.

Table 2. Properties of specimens tested.

<i>Specimen</i>	<i>End Conditions</i> [Bottom-Top]	P_0 [kN]	e [mm]	L_{cr} [mm]	λ_K [-]
Sp1	Pinned-Pinned	85	10	3540	1.397
Sp2	Pinned-Fixed	2000	10	2520	0.647
Sp3	Pinned-Fixed	1500	10	2520	0.647
Sp4	Pinned-Fixed	1900	10	2520	0.653

Figure 3 (top right) shows a transverse section (Source: Hass, Meyer-Ottens and Richter 1994) through the fire test rig at the material test establishment of the Technical University of Brunswick in Germany. The furnace chamber exhibits a square ground plot of 3.6 m, variable height in between of 3.6 m to 5.5 m and is equipped with six oil burners to run fire tests according to the ISO Standard fire. The

hydraulic jack is located underneath the furnace chamber and presses the column against the reaction beam (Figure 3, top right) situated above of the furnace chamber. A schematic representation of the test setup and the measurement equipment is shown in the diagram on the left in Figure 3. Nominally all the columns exhibited pinned end conditions at the bottom, which were realised with a rocker bearing as depicted in Figure 3 (bottom right). Pinned end conditions at the top (Spl only) were implemented in the same way, whereas fixed end conditions consisted simply of contact pressure between the top end-plate of the column and the bearing face of the structure relating to the reaction beam (Figure 3, photo top right). The rotational spring at the bottom stands for eventual imperfections in the rocker bearing, whereas the springs at the top account for the compliance of the reaction frame as a whole system. The nominal eccentricity of the applied load was controlled by additional end-plates with channels milled into for the rocker bearing (Figure 3, photo bottom right). These plates were positioned accordingly and fixed by welds before the column was built into the test rig. In addition to the displacement of the load jack, three other deformations of the specimen were recorded by means of displacement transducers at the locations shown

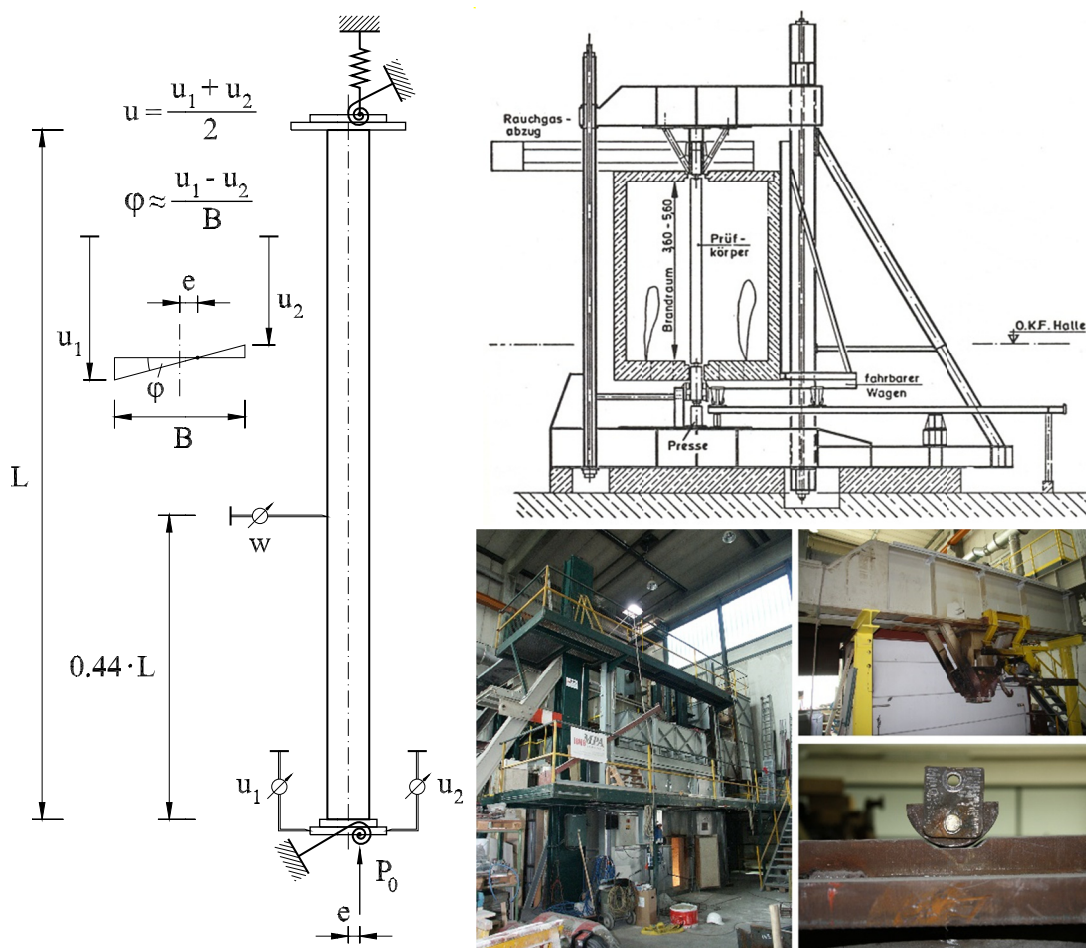


Figure 3. Test setup, photos and schematic of fire test rig at MPA in Brunswick, Germany (schematic reproduced with permission).

in Figure 3 (left): (1) the horizontal deflection, w , at a position slightly lower than the midspan of the column (fixed outlet in the furnace wall), (2) the axial displacement of the left edge of the end-plate, u_1 , and (3) the axial displacement of its right edge, u_2 . From the latter two the rotation in the hinge, ϕ , could be computed (Figure 3, left diagram) as well as the axial displacement, u , assuming a rigid end-plate. During all of the fire tests the temperature within the furnace was controlled continuously by six plate thermometers (according to EGOLF TR2, April 2000) positioned close to the test, these were positioned on two sides and at three different heights (Figure 1, left photo, small plates on rods sticking into the furnace chamber). In all the fire tests the deviation of the furnace temperature was within the tolerances required by the corresponding ISO Standard.

The material properties at elevated temperatures for the steel cores and tubes, as well as for the concrete used for the fire test specimens (Sp1 to Sp4) are recently established in an on-going research project at the Institute of Structural Engineering at ETH Zurich. Steady-state strain controlled tensile tests at elevated temperatures are performed with coupon specimens of the cores and the tubes. Figure 4 shows on the photo on the left the test equipment used, which is described in detail in [Knobloch, Pauli and Fontana 2013]. Additionally, Figure 4 shows example stress–strain curves at different elevated temperature-levels for the steel core and the tube used in specimen 4 (plots top right and bottom right). Four concrete compression tests at ambient temperature were performed 35 days after the concrete had been placed, at the

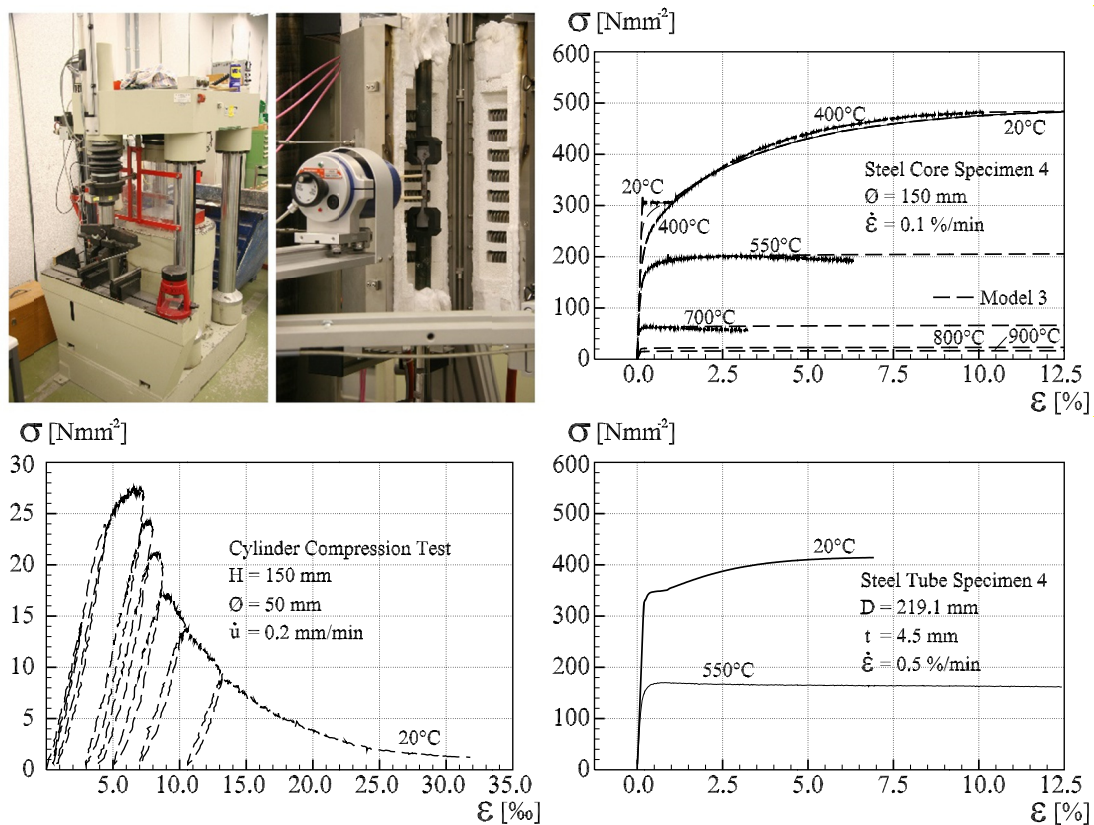


Figure 4. Material properties of steel core, steel tube and concrete.

time when the fire tests were performed. The mean value of the compression strength was $f_{cm}=27.1 \text{ Nmm}^{-2}$ and for the Young's modulus $E_{cm}=21'208 \text{ Nmm}^{-2}$. Figure 4 illustrates the test device used on the photo on the right as well as the stress–strain diagram of one of the tests (plot bottom left).

Results

Table 3 outlines the results of the four fire tests listing the failure time, t_f , at the prevailing pre-load level, P_0 . The computed values according to EN 1994-1-1 of: (1) the cross-sectional capacity, N_{pl} , (2) the slenderness ratio, λ_K , (3) the buckling strength, N_K , and (4) the ratio of the pre-load to the buckling strength, μ , are given. These values were calculated with the experimentally established mean values of the steel yield strength and the concrete compression strength, as well as with corresponding characteristic values.

Table 3 - Test results and computed buckling strength at ambient temperature.

<i>Test results</i>			<i>Calculations according to EN 1994 1-1</i>							
<i>Specimen</i>	<i>t_f</i> [min.]	<i>P₀</i> [kN]	<i>Actual mean values</i>				<i>Characteristic values</i>			
			<i>N_{pl}</i> [kN]	<i>λ_K</i> [-]	<i>N_K</i> [kN]	<i>μ</i> [-]	<i>N_{pl}</i> [kN]	<i>λ_K</i> [-]	<i>N_K</i> [kN]	<i>μ</i> [-]
Sp1	94	85	1686	1.473	545	0.16	1564	1.397	548	0.16
Sp2	24	2000	4642	0.688	3398	0.59	4431	0.660	3319	0.60
Sp3	169	1500	4642	0.688	3398	0.44	4431	0.660	3319	0.45
Sp4	178	1900	6912	0.674	5120	0.37	6704	0.658	5034	0.38

Figure 5 shows the temperature measurements of specimen 1 in the left column and of specimen 4 in the right column. In both columns each plot represents the data recorded at a specific cross-section along the specimen, starting at the bottom with CS1 up to the top till CS9, using the cross-section numbering introduced in the diagram of Figure 2. In every plot the recorded temperature–time curves of: (1) the surface of the core, θ_1 , (2) the measurement points within the concrete layer, θ_2 to θ_4 , and (3) the outside surface of the tube, θ_5 , are given.

First, the temperature–time curve of the steel core is analysed in detail, since the conceptual idea of this special type of composite column assumes a favourable influence of the concrete infill on the core's temperature–time behaviour. Therefore the plot in Figure 5 at the mid-span of specimen 1 (CS5) will be examined: It shows on one hand that steep temperature gradients are present in the concrete layer during the entire fire exposure, indicating that the concrete infill can reliably insulate the steel core. On the other hand a plateau can be observed in the core's temperature–time curve, extending approximately from 15 to 30 min. It reflects the energy consuming process of vaporisation of water in the concrete, and effectively lags the increase of the core's temperature. Similar observations can be made for specimen 4 in Figure 5.

Second, the degree of uniformity of the temperature field in the axial direction reached within the tested specimens is examined, since it is influenced by the thermal boundary conditions of the test setup. The photo in Figure 1 shows, how insulating

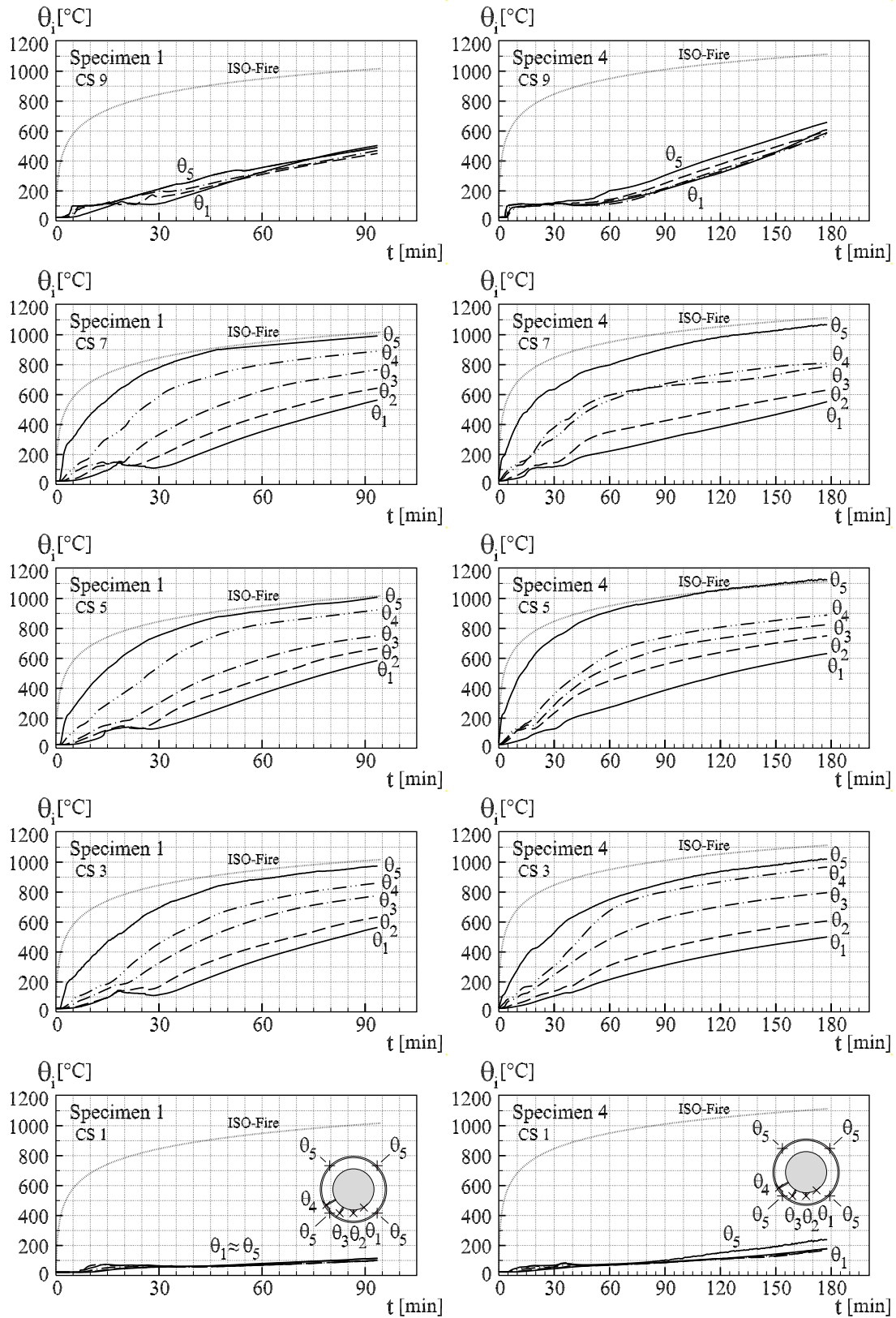


Figure 5. Temperature-time-curves specimen 1 and specimen 4.

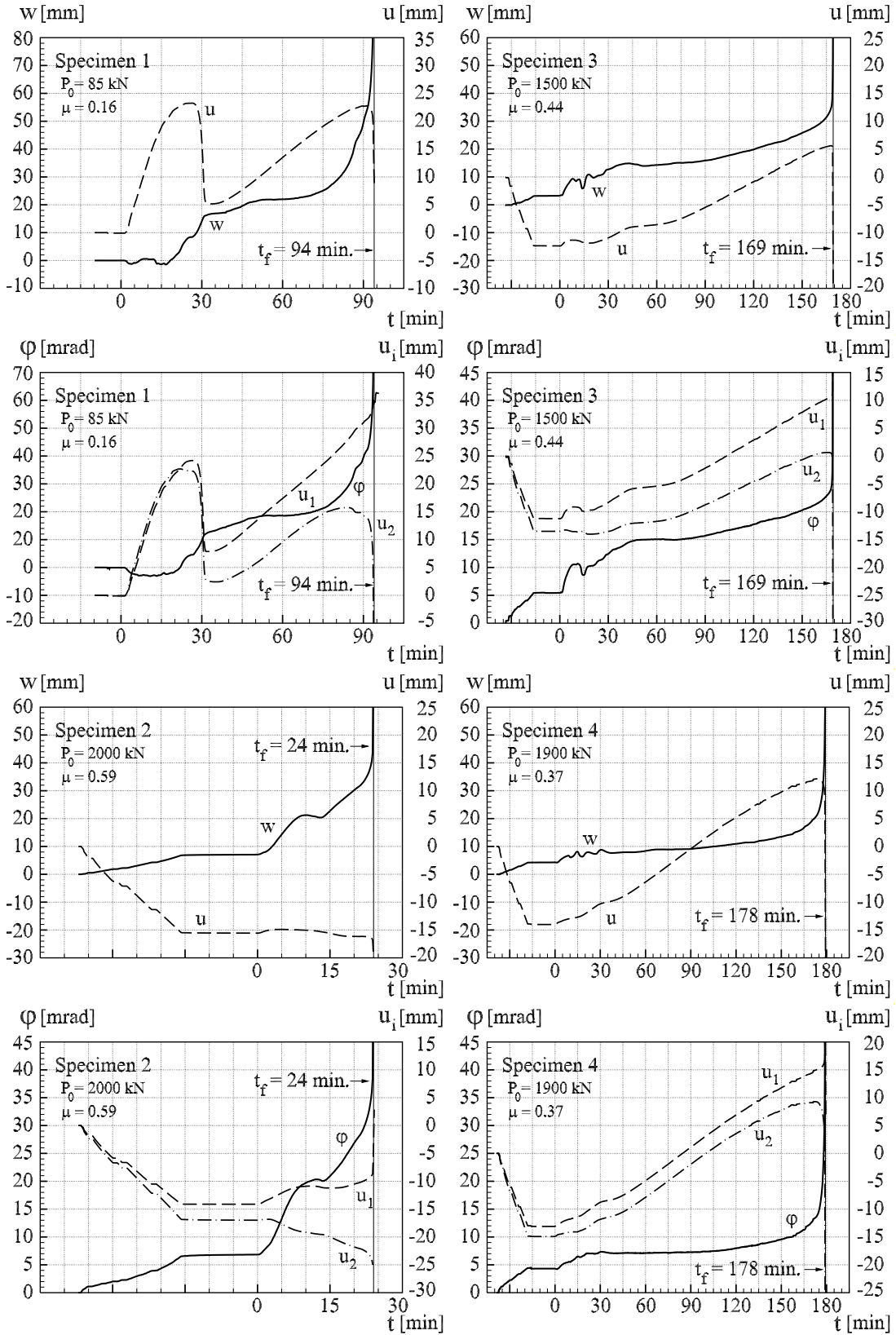


Figure 6. Deformation-time-curves specimen 1 to 4.

material had to be used at the top and bottom ends of the column, in order to protect the surrounding test equipment. However, realising the supports of the specimen inside the furnace is on the other hand beneficial for the overall accuracy of the test results. Accordingly, the results in Figure 5 show the typical flat gradient in the radial direction (θ_1 almost coinciding with θ_5) of a cross-section close to an iso-thermal boundary. Nevertheless, the uniformity of the measured temperature field over the rest of the specimen was satisfactory, as it can be observed by comparing the measurements of CS7 and CS3 (located at a distance of 225 mm from the end-plates) with those at midspan (CS5).

Figure 6 shows the recorded deformations of all specimens during the pre-loading phase and the fire test, which started at zero minutes. The results of each test are given as deformation–time curves in two different plots, indicating in the upper plot the midspan deflection, w , and the axial displacement, u , and in the lower plot the rotation of the end-plate, ϕ , and the axial displacement of the left and the right edges of the end-plate, u_1 , and, u_2 . The four specimens can be divided into stocky columns consisting of specimens 2 to 4 and one very slender column, specimen 1 according to their slenderness ratios (Table 2). Their characteristic load-carrying behaviour in fire is illustrated best by studying the results of specimen 1 given in its upper plot of Figure 6. At the beginning of the fire exposure the temperature increases almost only within the tube. Due to the thermal expansion, the tube therefore tends to displace the top end-plate away from the concrete and the steel core until the load is carried alone by the tube. This phenomenon can be observed in the upper plot of specimen 1 in Figure 6, where, u , starts increasing rapidly after 2 minutes of fire exposure. With increasing temperature, the proportionality limit of the steel tube decreases, and at some point the stresses in the tube (due to the pre-loading) exceed it. This is accompanied by a loss of stiffness, which leads to an increase in the midspan deflection and the onset of local tube buckling. Both can be observed in Figure 6, where, w , starts increasing after 17 minutes while simultaneously the rate of, u , slows down. Subsequently, the tube collapses by local buckling at 27 minutes, which can be seen



Figure 7. Specimens 1 and 4 after testing with details of buckled tube.

in Figure 6 by the abrupt decrease of, u . Additionally, local buckling was observed on the specimen after the test (Figure 7, photo left and top right). After the collapse of the tube the force closure is re-established between the end-plate and both the steel core and the concrete. Consequently the midspan deflection stabilises and the column enters a second phase, extending from 30 to 75 minutes, during which the stiffness of the steel core determines the load-carrying behaviour. Finally, the column fails with a runaway failure, when the temperature induced loss of stiffness of the core sets in. In the case of the stocky specimens, showing a higher pre-load ratio, μ , the stresses in the tube are much higher. Therefore the overstressing of the tube takes place earlier and the tube only slightly shifts away the end-plate as with specimen 3 or not at all as with specimens 2 and 4 (corresponding, u , in Figure 6). However, the loss of stiffness of the tube led as well in all these cases to an increase of the midspan deflection, followed by (except for specimen 2) a stable second phase when the core was fully activated and determined the load-carrying behaviour until failure. In the case of specimen 2, which featured the highest load ratio, increased P delta effects inhibited attaining a stable second phase.

NUMERICAL STUDY

A numerical study was performed with the three-dimensional FEM model described in detail in [Neuenschwander, Knobloch and Fontana 2012] using ABAQUS Standard. In order to capture any influence due to the non-uniformity of the temperature field, the measured temperatures were used as input to the model. The following constitutive relations were implemented: (1) for the steel core the stress–strain relationships determined from tensile tests at temperature levels of 400°C, 550°C, 700°C and at ambient temperature (Figure 4, upper right plot), (2) for the tube, with temperatures exceeding 300°C, a model based on the Ramberg–Osgood model and, for temperatures below, the model according to EN 1993-1-2 with modifications in order to fit with the measured stress–strain relationship at ambient temperature (Figure 4, lower right plot) and (3) for the concrete the model according to EN 1992-1-2 without modifications.

First, the numerical study consisted of a calibration process with respect to the deformation–time curves of specimen 4. Therefore the influence of eventual deviations from the nominal boundary conditions during the test were analysed and subsequently, adjusted boundary conditions were developed. The results of this calibration process are given in Figure 8 (upper left plot) showing the model's responses for the four studied different boundary conditions, BC1 to BC4. BC1 corresponds to the nominal boundary conditions except for the axial spring, which models the compliance of the test rig. Its stiffness was obtained by deducing from the measured axial displacement at the end of the pre-loading phase, the computed axial shortening of the column, which yielded $k_{axial}=118.5$ kN/mm. Still, the mid-span displacement after application of the pre-load was much smaller in the model compared to the test, indicating that there was some compliance in the nominally fixed upper end-condition. As an upper bound of this compliance, the pinned-pinned end-condition (BC2) was simulated. Introducing a rotational spring representing the

compliance of the nominally fixed upper end of the column led to BC3. The stiffness of the rotational spring was assessed

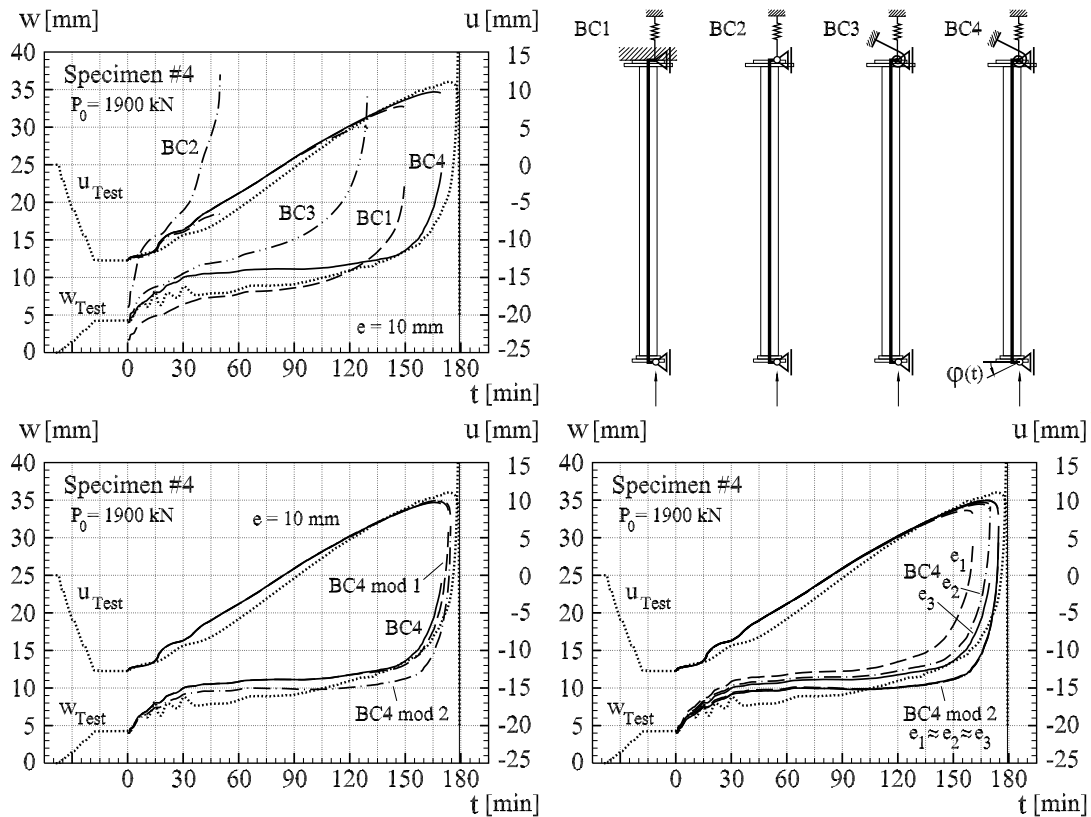


Figure 8. Modelling test-boundary-conditions and variation of load eccentricity.

by the condition that after the application of the pre-load, both the rotation in the hinge at the bottom and the deflection at midspan should match the test measurements. Following this method a rotational stiffness of $k_{rot}=2.75$ kNm/mrad was found. Additionally, the nominally pinned end at the bottom could not be kept up, since the rotations in the hinge of the model with BC3 did not agree well with the measured rotations. As a final enhancement BC4 was developed by imposing the measured rotation in the hinge at the bottom as a time dependent boundary condition. As it can be seen in Figure 8, the model's response with BC4 captured most accurately the test data in terms of both the deformation–time behaviour and the failure time and was therefore used for further numerical sensitivity studies.

Secondly, the impact of a deviation of the nominal value of the load eccentricity was studied. Adjusting the rotational spring stiffness for different values of the eccentricity following the methodology described above, yielded reasonable values of: $e_1=7.5$ mm and $e_2=8.75$ mm besides the nominal value of $e_3=10.0$ mm. Figure 8 (bottom right plot) shows the results obtained with models using BC4 but varying load eccentricities. At first glance it is contradictory that the failure time decreases, the less eccentric the load. However, this is an outcome of the way the rotational spring stiffness was adjusted to match the measurements before the fire starts. If the eccentricity is decreased, then the stiffness of the spring must be lowered in order to meet the measured rotation and midspan deflection after pre-loading. This in turn

leads to an earlier onset of the runaway failure in the last phase of the load-carrying behaviour.

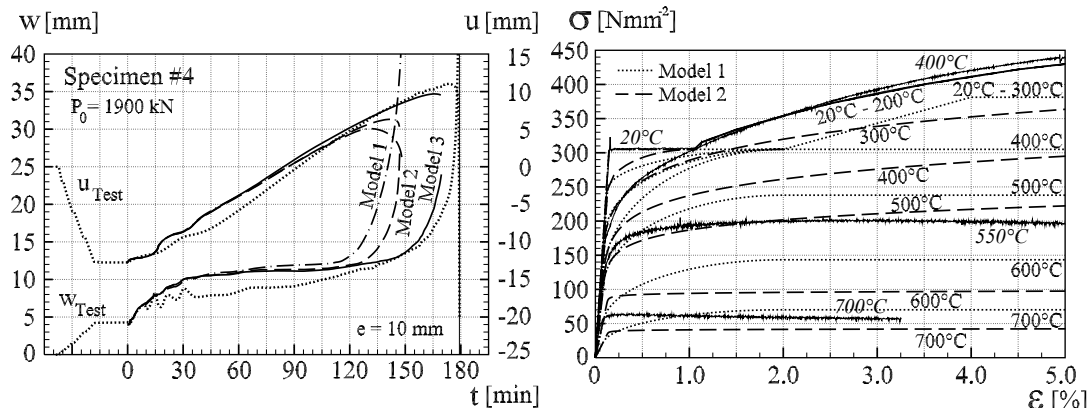


Figure 9. Constitutive models of the steel core.

Thirdly, the influence of the stiffness ratio between the test specimen and the test rig was examined. It changes during a fire exposure since the specimen gradually loses stiffness, whereas the stiffness of the test rig remains constant. Therefore the compliance in the imperfectly fixed upper end tends to diminish with on going fire exposure, which was simulated with two modifications of BC4. The first modification, *BC4 mod1*, consisted of fixing the upper end arbitrarily after 120 minutes and the second modification, *BC4 mod2*, simulated an extremal assumption of fixing the upper end just after the fire started. Figure 8 (lower left plot) shows the results, which follow slightly closer the test with *BC4 mod1*.

Finally, the influence of different constitutive models for the steel core was analysed considering: (1) the Eurocode model, *Model 1*, taking into account only the measured yield strength at ambient temperature, (2) a Ramberg–Osgood based model, *Model 2*, for temperatures above 300°C in combination with the measured stress–strain relationships at ambient temperature and (3) the measured stress–strain relationships, *Model 3*, at ambient temperature, 400°C, 550°C and 700°C. Figure 9 illustrates in the plot on the left the influence of the three different models: *Model 3* captures best the failure time and the deformation–time behaviour, since it implements the actual stiffness and strength of the steel core. On the other hand, *Model 1* underestimates strength and stiffness up to 300°C (Figure 9, plot left) leading to a premature onset of the runaway-failure, whereas its overestimation of the stiffness above 300°C leads to almost the same failure time as with *Model 2*.

CONCLUSIONS

Four ISO-Fire tests were performed with concrete-filled CHS columns with solid steel core. The concept of this type of composite column for their load-carrying behaviour in fire was affirmed: Initially, the steel tube is heated quickly and tends to carry the whole load due to its thermal expansion, leading to its overstressing and consecutive loss of stiffness. Then the load is redistributed mainly to the steel core. Depending on the pre-load level, a stable phase follows, during which the rate of

deflection is bounded and the column expands steadily. Temperature induced loss of stiffness of the core finally triggers runaway failure.

The results of the numerical study illustrate the importance of a suitable implementation of the nominal boundary conditions of the test, as well as the availability of accurate input-data, both in terms of stiffness and strength, for the constitutive model of the steel core.

REFERENCES

- Hanswille G. and Lippes M. (2008), Einsatz von hochfesten Stählen und Betonen bei Hohlprofil-Verbundstützen, *Stahlbau*, Vol. 77, Issue 4, pp. 296-307.
- Hass R., Meyer-Ottens C. and Richter E. (1994), *Stahlbau Brandschutz Handbuch*, Fig. 5-42, p. 125, Wilhelm Ernst & Sohn Verlag für Architektur und technische Wissenschaften GmbH & Co., Berlin, Germany.
- Klingsch W. (1984), Analyse des Tragverhaltens von Geilinger Baustützen bei Normaltemperatur und bei Brandbeanspruchung sowie der zugehörigen Bemessungsverfahren. Gutachten Nr. 84-11, Bergische Universität Wuppertal, Germany.
- Neuenschwander M., Knobloch M. and Fontana M. (2010), Fire Behaviour of Concrete Filled Circular Hollow Section Columns with Massive Steel Core, *SDSS'Rio 2010 - Stability and Ductility of Steel Structures*, E. Batista et al. (Eds.), pp. 473-480, Brazil.
- Neuenschwander M., Knobloch M. and Fontana M. (2011), Numerische Modellierung des Tragverhaltens von betongefüllten Hohlprofilstützen mit Stahlkern unter ISO-Normbrandeinwirkung, *Festschrift Gerhard Hanswille*, Institut für Konstruktiven Ingenieurbau, Bergische Universität Wuppertal, Heft 20, pp. 353-362.
- Neuenschwander M., Knobloch M. and Fontana M. (2012), Numerical Analysis of the Structural Fire Behaviour of Concrete-Filled CHS-Columns with Steel Cores, *ASCCS 2012 - International Conference on Advances in Steel Concrete Composite and Hybrid Structures*, Liew J Y R. and Lee S.C. (Eds.), pp.881-888, Singapore.

An Investigation on the Interface Shear Resistance of Twinwall Units for Tank Structures

J. S. Rana¹; C. Arya¹; J. Stehle²; C. Crook²; A. McFarlane²; and T. Bennett³

¹Dept. of Civil, Environmental and Geomatic Engineering, Univ. College, London WC1E 6BT, U.K. E-mail: j.rana@ucl.ac.uk; c.arya@ucl.ac.uk

²Engineering Excellence Group, Laing O'Rourke, Dartford DA2 6SN, U.K. E-mail: jstehle@laingorourke.com; ccrook@laingorourke.com; amcfarlane@laingorourke.com

³ARUP, Cardiff CF10 4QP, U.K. E-mail: tim.bennett@arup.com

Abstract

Hybrid precast twinwall concrete units, mainly used in basements, core and crosswall construction, are now being adopted in water retaining tank structures. Their use offers many advantages compared with conventional in-situ concrete alternatives. However, the design could be optimised further via a deeper understanding of the unique load transfer mechanisms involved. In the tank application, twinwall units, which consist of two precast concrete biscuits connected by steel lattices and an in situ concrete core, are subject to bending. Uncertainties about the degree of composite action between the precast biscuits and hence flexural performance of the units necessitated laboratory tests to investigate the interface shear resistance. Testing was also required to assess both the leakage performance and buildability of a variety of joint details. This paper describes some aspects of this novel approach to the design/construction of tank structures as well as selected results from some of the tests that were carried out.

INTRODUCTION

In 2009, Tamesis, a joint venture between Laing O'Rourke and Imtech, was awarded the contract to construct extensions to the Beckton Sewage Treatment Works which included a number of large rectangular water-retaining 'aeration' tanks, originally designed with in-situ reinforced concrete.

An alternative hybrid twinwall system (Whittle and Taylor, 2009) combining the benefits of in-situ and precast concrete, including faster construction times, reduced on-site activity, robust continuous jointing, improved quality control, reduced waste and less mess, was developed by Laing O'Rourke (LOR), and proposed to the client via the 'Expanded' site assembly division of LOR. The twinwall system, produced by the 'Explore Manufacturing' division of LOR in a new state-of-the-art facility, has been used before by LOR for water retaining applications but no examples of use for tank applications could be identified anywhere in the world, nor could use at such a large scale in a water-retaining application be found. The proposed use of this system raised a number of questions regarding water tightness and structural performance, which had to be addressed prior to construction. For example, at the outset it was not clear if the twinwall design would be able to

meet the stringent performance criteria demanded by the Civil Engineering Specification for the Water Industry (CESWI, 2004) which requires crack widths to be limited to 0.2mm and also for the rate of leakage to be less than a drop in water level of 10mm in a 7 day period. Moreover, it was unclear if the maximum available wall thickness of units (i.e. 400mm) would be sufficient to resist the forces due to the retained water.

To date, twinwall panels have been commonly used as load bearing elements connected to in-situ or precast lattice slabs (Explore Manufacturing, 2010). A typical twinwall panel essentially consists of two precast reinforced concrete biscuits, which are connected by shear connectors in the form of 3-dimensional triangular steel lattices, partially embedded in the inner faces of the biscuits (Figure 1). The core is filled with concrete and splice bars on site.

The planned use of these units to form the walls of tank structures meant that the units would be subject to magnitudes of flexure not normally applied. Uncertainties about the degree of composite action between the precast biscuits and hence flexural performance of the units meant that laboratory tests were necessary to validate the models used to check the interface shear resistance. Before describing the tests that were undertaken, the following gives more design information on the scheme.

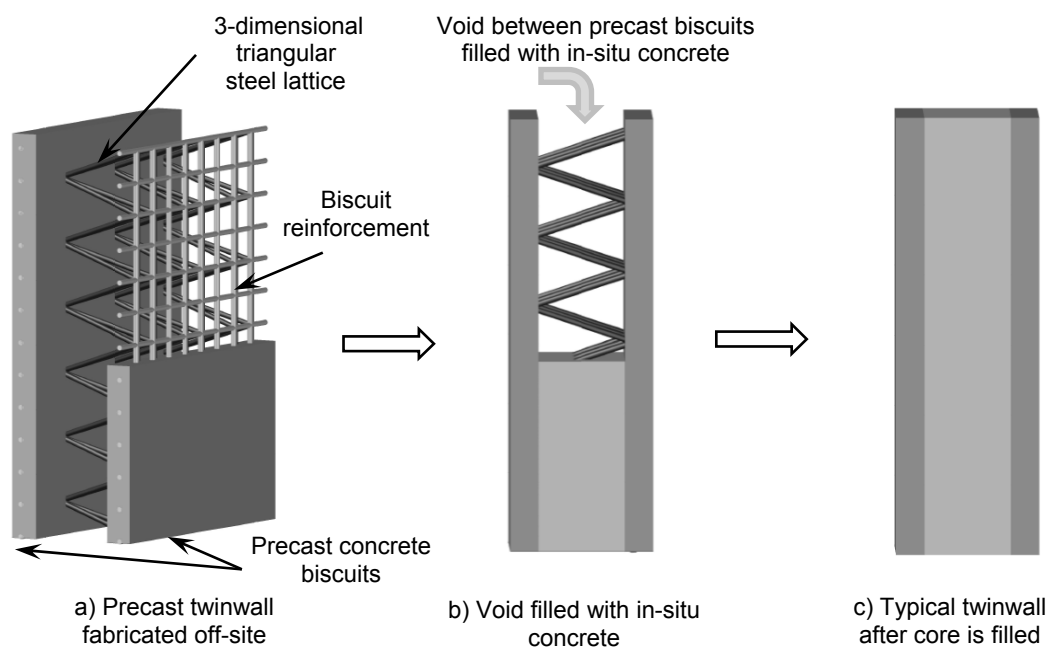


Figure 1 – Components of a typical twinwall

DESIGN

The project requirement was for 2 banks of 3 tanks, as shown in Figure 2. The aeration tank process requires an approximately uniform linear velocity flow, and thus rectangular tanks were deemed necessary, with internal baffle walls provided to effectively lengthen the path of travel within each tank.

Each tank is approximately 80m long, 38m wide and 8m deep. Each bank of tanks has a total width of approximately 113m. Thus the total volume of sewage to be contained is approximately 144,000 m³ or 144 Megalitres.

The original in-situ reinforced concrete tank design required a 700mm thick wall at its base, tapering to 525mm thick at its top. The need for such a thick wall was due to the applied bending moment, which for a cantilever varies according to the water depth cubed.

The maximum overall thickness of twinwall unit available from Explore Manufacturing was 400mm. Clearly such a thin wall would not work in cantilever action; hence, buttresses and tie beams were introduced into the design, not unlike the approach used for walls supporting the lateral thrust of arched cathedral roofs. The structural behaviour was thus modified to one of a ‘propped’ cantilever, which resulted in more than a 50% reduction in the peak bending moment. This approach, which is better suited to precast rather than in-situ construction due to the complexity of the formwork system that would be required due to the presence of buttresses, resulted in approximately 10% savings in the volume of concrete in the structure.

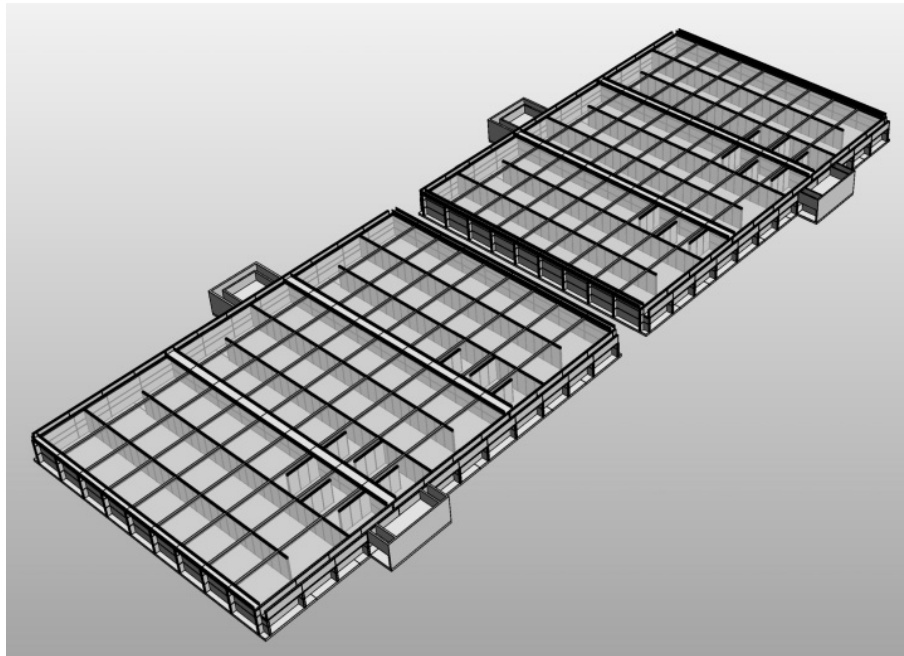


Figure 2 – Digital engineering model of the aeration tanks

TESTING

Due to the innovative nature of the design and construction technique some preliminary testing was necessary. This included building a trial tank as well as carrying out laboratory tests on interface shear resistance as elaborated below.

Trial tank

The internal volume of the trial tank was approximately 9m long by 3m wide by 8m high. The panels on one long face were constructed in a vertical orientation

and on the other side in a horizontal orientation, as shown in Figure 3. The tank was primarily used to assess leakage performance and buildability of a variety of joint details.

To assess leakage, the trial tank was completely filled with water and leakage rates were monitored by recording water levels against a control leak-free contained water volume subject to the same rainfall and evaporation. Some damp patches and cracks were observed, but these were within acceptable criteria. Interestingly, although half the tank was provided with water bars at the base whereas the other half was not, there was no correlation with the extent of the damp patches i.e. the use of water bars did not seem to provide any noticeable benefit. Nevertheless, they were used in the final design.

With regard to the drop in water level, the loss (corrected for rainfall and evaporation) was less than the 10mm criteria required over a 7 day period after the tank had been filled for a month.

A critical feature of the design that was identified at an early stage was the ability of vertical bars and horizontal splice bars to transfer their loads to reinforcement embedded in the precast biscuits of twinwall elements. The magnitude of the bar forces is dependent on the joint location relative to the bending moment diagram, and thus the bar size and bar length are affected. The ease of which splice bars of different sizes and orientation could be installed in the trial, as well as panel handling and manufacture lessons learnt were used to inform the twinwall elementisation in the final design implemented at Beckton.



Figure 3 – Construction of ‘trial’ twinwall water-retaining tank at Laing O’Rourke’s manufacturing facility near Worksop

Interface shear resistance

As previously noted, twinwalls have to date principally been used as wall elements but in water tanks the walls are subject to greater levels of flexure. The bending strength is a function of the degree of composite action between the two outer biscuits, which is in turn a function of the interface shear resistance. Section 6.2.5 of Eurocode 2: Part 1.1 (BSI, 2010), hereafter referred to as EC2, can be used to predict the interface shear capacity, v_{Rdi} , which is given by:

$$v_{Rdi} = c f_{ctd} + \mu \sigma_n + \rho f_{yd} (\mu \sin \alpha + \cos \alpha) \leq 0.5 v f_{cd} \quad \text{-----[Equation 1]}$$

where,

f_{ctd} design tensile strength of concrete

f_{yd} design yield strength of reinforcement

σ_n stress per unit area caused by an external normal force across the interface

$\rho = A_s/A_i$

A_s area of reinforcement crossing the interface, with adequate anchorage at both sides of the interface

A_i area of the joint

α angle between reinforcement and slip surface, and $\alpha \geq \pi/4$

c coefficient of cohesion

μ coefficient of friction

Note that the $\cos \alpha$ term in equation (1) is ignored for $\alpha > \pi/2$ according to section D.2 of BS EN 13747 (BSI, 2005).

The cohesion and friction coefficients depend on the nature/roughness of the finish at the biscuit/in-situ concrete interface. EC2 further implies that the design tensile strength in equation (1) should be based on the 'weaker concrete'. Also, use of equation (1) assumes that the steel is fully anchored on both sides of the interface but EC2 does not directly provide any information on embedment depths and hence it was decided that the relationship between the shear connector embedment depth and interface resistance would be of interest. It should be noted that BS EN 13747: 2005 (BSI, 2005) requires a minimum 10mm of embedment, but it is not clear if this requirement guarantees full strength development.

To investigate some of these issues research, including small scale physical interface shear tests, was instigated at UCL. The key aspects investigated were:

- 1) Surface roughness of the concrete at the core/biscuit interface
- 2) Compressive strength of core and biscuit concrete
- 3) Embedment depth of shear connectors
- 4) Diameter of shear connectors.

A direct way of estimating the interface shear capacity of twinwall is by carrying out push-out tests, which was the approach used in this work. The following gives details of the experimental procedure that was followed.

EXPERIMENTAL PROCEDURE

Figure 4 shows details of the test specimens used in this work. The two outer biscuits (1 and 2) (530 x 100 x 40 mm) were reinforced with 4mm diameter mild steel

bars ($f_{yk} = 250 \text{ N/mm}^2$) placed mid-depth at 40 mm centres in the longitudinal direction and 75 mm and 100 mm centres in the transverse direction. The lattice girder was 80 mm deep overall and the diagonals had a pitch of 39° and 141° . These angles are slightly outside the recommended limits for Equation 1.

The bottom bars were 3mm diameter and the top bar 5 mm diameter, all made of grade 250 steel. The lattice was attached to the reinforcing bars in the biscuits using steel tie wires prior to casting.

The casting procedure for the control specimens (Type “A”, Table 1) involved placing the bottom half of the reinforcement cage supported on spacers in a timber mould and pouring sufficient concrete to form Biscuit 1. In the control specimens, the lattice was embedded 20mm into the concrete biscuit, where the embedment depth refers to the ‘overall’ dimension of the embedment.

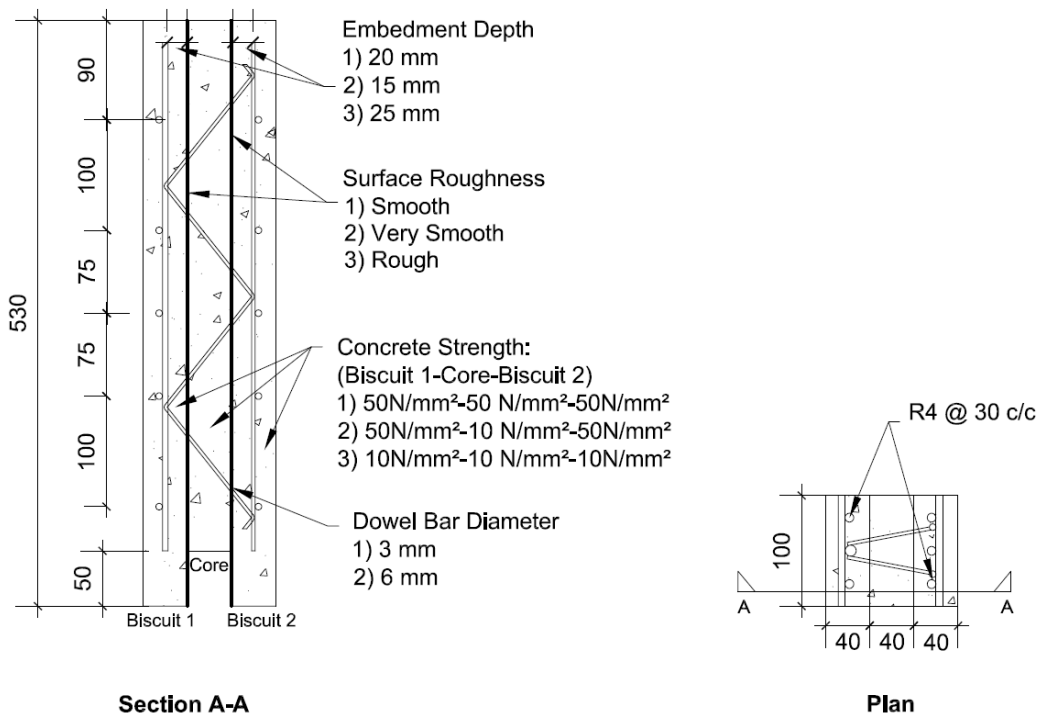


Figure 4 – Details of test specimens

Table 1 - Test details

Type	Surface Roughness	Embedment Depth (mm)	Concrete Cube Strength in Biscuits on Day of Testing (N/mm ²)	Concrete Cube Strength in Core on Day of Testing (N/mm ²)	Dowel Bar Diameter (mm)
A	Smooth	20	35	35	3
B	Very smooth	20	35	35	3
C	Rough	20	35	35	3
D	Smooth	20	35	10	3
E	Smooth	20	10	10	3
F	Smooth	15	35	35	3
G	Smooth	25	35	35	3
H	Smooth	20	35	35	6

After curing for 24 hours the specimens were inverted and the upper half of the cage supported on spacers to achieve an embedment of 20 mm, and positioned in a second timber mould and concreted to form Biscuit 2.

After curing the concrete in Biscuit 2 for 24 hours the two sets of moulds were removed and specimens rotated into the vertical position. Shuttering was then attached to the outside faces and 50mm from the base of each specimen, and the core was cast. The shuttering was removed after 24 hours and specimens air cured for a further four days. It was assumed that this method of preparation would correspond with the 'smooth' surface roughness category in EC2.

Four cubes were also cast from each batch of concrete and cured and conditioned in the same way as the concrete in the test specimen. The target 28-day strength of the concrete used for both biscuits and the core was 50 N/mm². After a total of seven days the specimen was painted white to help monitor crack development during testing.

The other specimens (types B-H) were prepared in a similar fashion except that the surface roughness of the concrete on the inner face of the biscuits, embedment depth of the lattice in the biscuits, the strength of the concrete used for the biscuits and core and the diameter of the diagonal lattice bar (dowel) were varied as summarised in Table 1. Five tests were conducted for each specimen type.

In the case of the type "B" specimen, a 3mm thick neoprene sheet was attached to the inner face of each biscuit prior to casting the core, which was designed to produce a finish corresponding to the "very smooth" category in EC2. The "rough" interface finish in type "C" specimens was achieved by painting the inner face of the biscuits with a retarder and pressure washing in order to remove cement particles prior to casting the core.

Figure 5 shows the test set-up. The push-out tests were carried out generally in accordance with the recommendations in Annex B of Eurocode 4:Part 1-1 (BSI, 2009). Load was applied to the core in 2 kN increments until failure. The deflection at the top and bottom of the core was measured using dial gauges. The lateral displacement of specimens was also measured by means of DEMEC studs but the

results are not discussed in the paper. The results presented are the average of the five tests for each specimen type, and one standard deviation is also shown.

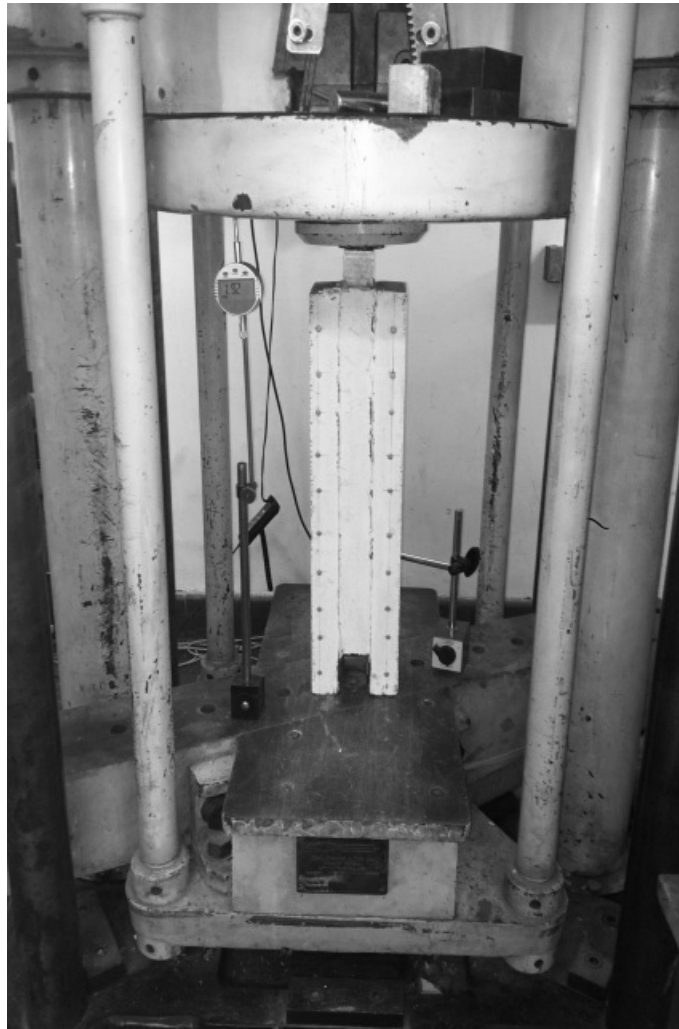


Figure 5 – Test set-up in the laboratory at UCL

RESULTS AND DISCUSSION

Effect of interface surface roughness

Figure 6 shows the effect of interface surface roughness on failure load. It can be seen that the failure load increases with increasing surface roughness.

The design values were determined via equation (1) assuming the c and μ values shown in Table 2, $f_{ctd} = 1.29 \text{ N/mm}^2$, $\sigma_n = 0$, $A_i = 48,000 \text{ mm}^2$ [= 480 mm (lever arm) x 100 (width)] and $f_{yd} = 217 \text{ N/mm}^2$. The area of reinforcement crossing the reinforcement and inclined at 39° to the slip surface, $A_{s1} = 28.3 \text{ mm}^2$ ($= 4 \times \pi 3^2 / 4$). Similarly, the area of reinforcement crossing the reinforcement and inclined at 141° to the slip surface, $A_{s2} = 28.3 \text{ mm}^2$. The design shear resistance of reinforcement inclined at 39° assuming the surface is ‘smooth’ is given by:

$\rho f_{yd} (\mu \sin \alpha + \cos \alpha) = (28.3/48,000) \times 217 (0.6 \times \sin 39^\circ + \cos 39^\circ) = 0.148 \text{ N/mm}^2$
 and for the reinforcement inclined at 141° is given by:
 $\rho f_{yd} (\mu \sin \alpha + \cos \alpha) = (28.3/48,000) \times 217 (0.6 \times \sin 141^\circ + 0) = 0.048 \text{ N/mm}^2$

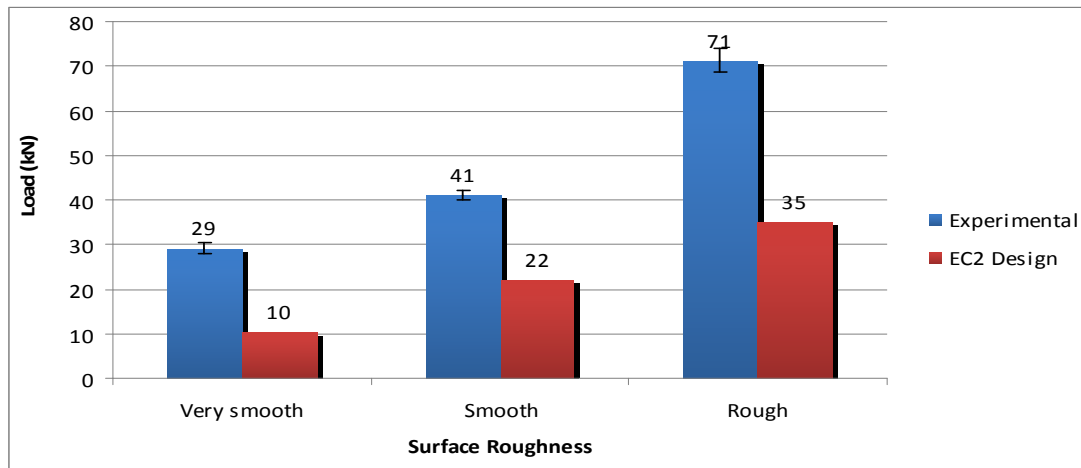


Figure 6 – Effect of surface roughness on failure load

Table 2 – c and μ values for various surface roughness categories (BSI, 2010)

Surface Roughness	c	μ
Very smooth	0.025	0.5
Smooth	0.2	0.6
Rough	0.4	0.7

The results show that EC2 theoretical failure loads are much less than the experimental values for the ‘very smooth’, ‘smooth’ and ‘rough’ surfaces. The EC2 estimate for ‘very smooth’ conditions appears to be the most conservative.

Effect of concrete strength

Figure 7 shows the effect of concrete strength on the experimental and EC2 design failure loads. It can be seen that the EC2 design failure loads are significantly less than the experimental values. The experimental failure loads suggest that the concrete strength in the biscuits is of more importance than the core strength, which may be related to the lattice girder pull-out mechanism.

Effect of embedment depth

Figure 8 shows the effect of embedment depth on experimental and EC2 design failure loads. It can be seen that the EC2 design calculations are not affected by the embedment depth of the lattice, although BS EN 13747: 2005 (BSI, 2005) requires a minimum of 10mm cover to the inside face of the lattice chord. This latter requirement is expressed relative to the base of the lattice triangle, and not the apex. However, the results indicate that the design values are significantly less than the

experimental failure loads for the range of embedment investigated, and thus the 10mm cover requirement appears to be satisfactory. This indicates that EC2 provides satisfactory estimates of the interface shear strength of twinwalls where the lattice embedment is sufficient.

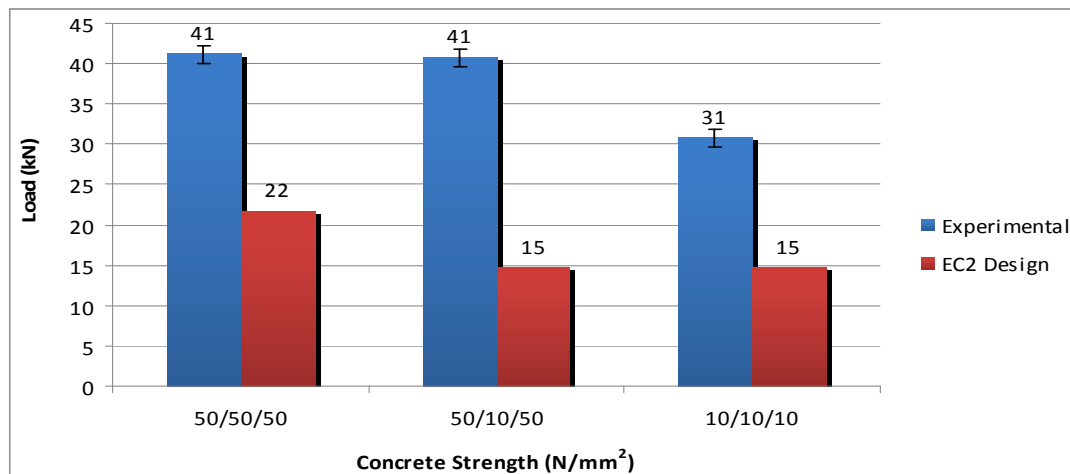


Figure 7 – Effect of concrete strength on failure load

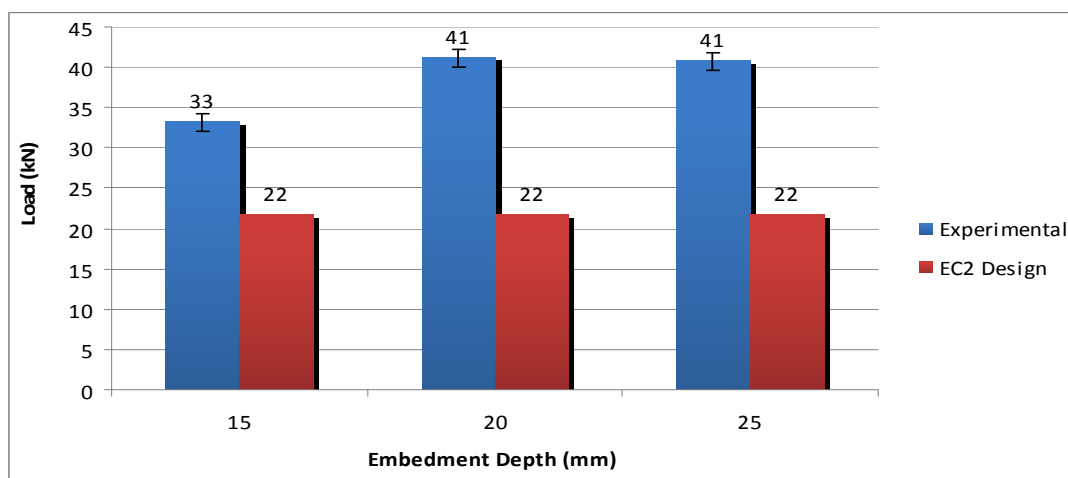


Figure 8 – Effect of embedment depth on failure Load

Effect of dowel bar diameter

Figure 9 shows the effect of dowel bar diameter on failure load. It can be seen that the failure load increases with increasing dowel bar diameter. The EC2 values were again determined via equation (1) assuming $c = 0.20$ and $\mu = 0.6$, $f_{ctd} = 1.29 \text{ N/mm}^2$, $\sigma_n = 0$, $A_i = 48,000 \text{ mm}^2$ [= 480 mm (lever arm) x 100 (width)] and $f_{yd} = 217 \text{ N/mm}^2$. In the case of the specimens with 3mm dowel bars $A_{s1} (\alpha = 39^\circ) = A_{s2} (\alpha = 141^\circ) = 28.3 \text{ mm}^2 (= 4 \times \pi 3^2 / 4)$ and for specimens with 6mm dowel bars $A_{s1} (\alpha = 39^\circ) = A_{s2} (\alpha = 141^\circ) = 113.1 \text{ mm}^2 (= 4 \times \pi 6^2 / 4)$.

In figure 9 it can be seen that the experimental failure loads are greater than the EC2 design loads.

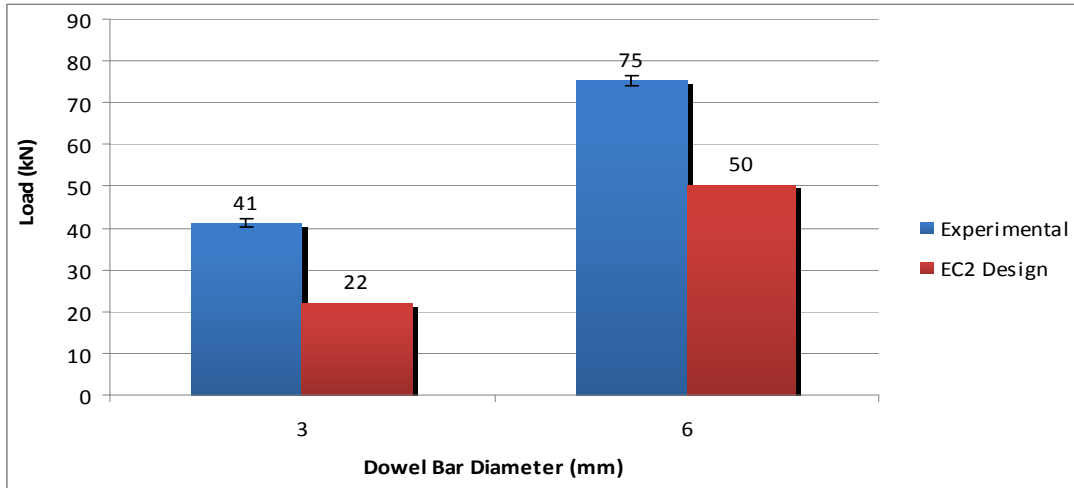


Figure 9 – Effect of dowel bar diameter on failure load

Limitations and further work

One of the limitations of the push-out tests described above is that the base of the test specimen is restrained at the base which causes additional forces to develop normal to the shear interface. More work is required to investigate the effect of the restraints at the base, however it is not believed to be of great significance.

Further work on a broader range of parameters would increase the understanding of the phenomena observed and enable detailed design guidance to be formulated, with the potential result of more cost-effective solutions.

CONSTRUCTION

The tanks at Beckton Sewage Treatment Works were successfully designed and constructed based on the learning of the research programme. A photo of a completed tank is shown in Figure 10. The tank has performed very well to date with conformance to the CESWI leakage criteria proven on site, and the extent of cracking and leakage is observed to be limited to only hairline cracks and no evidence of dampness has been observed.

CONCLUSIONS

- The trial tank built and tested by Laing O'Rourke was successful in demonstrating the buildability and adequacy of the twinwall system when detailed well with respect to the leakage criteria. Project implementation also proved successful.
- The results from the push-out tests demonstrate the effects of surface roughness, concrete strength, embedment depth and dowel bar diameter on the interface shear strength in twinwalls.



Figure 10 – Filled twinwall water tank at Beckton Sewage Treatment Works

- The push-out test results indicate that Eurocode 2 is suitable for making appropriate estimates of the interface shear strength in twinwall elements when lattice girders are embedded sufficiently.

ACKNOWLEDGEMENTS

This work was supported in part by grant EP/G037698/1 for UCL Department of Civil, Environmental and Geomatic Engineering, Centre for Urban Sustainability and Resilience from the UK Engineering and Physical Science Research Council and Laing O’Rourke.

REFERENCES

- BSI, (2005) British Standard. *Precast concrete products – Floor plates for floor systems*. British Standards Institution, Milton Keynes, 2005, BS EN 13747.
- BSI, (2009) British Standard. *Eurocode 4: Design of composite steel and concrete structures — Part 1-1: General rules and rules for buildings*. British Standard Institution, Milton Keynes, 2009, BS EN 1994-1-1:2004.
- BSI, (2010) British Standard. *Eurocode 2: Design of concrete structures – Part 1-1: General rules and rules for buildings*. British Standard Institution, Milton Keynes, 2010, BS EN 1992-1-1: 2004.
- CESWI, (2004) “Civil Engineering Specification for the Water Industry”, 6th edition. Wrc plc, for UK Water Industry Research Ltd, June 2004
- Explore Manufacturing, (2010) *Precast Twinwall Design Guide*. Laing O’Rourke, 2010
- Whittle, R. and Taylor, H., (2009), *Design of Hybrid Concrete Buildings - A guide to the design of buildings combining in-situ and precast concrete*, 2009, Surrey: Concrete Centre.

Seismic Behavior of Steel-Concrete Composite Frame Structures and Design Practice in the United States

Mark D. Denavit¹; Jerome F. Hajjar²; Tiziano Perea³; and Roberto T. Leon⁴

¹Stanley D. Lindsey and Associates, Ltd., 2300 Windy Ridge Parkway SE, Suite 200S, Atlanta, GA 30339. E-mail: mdenavit@sdlal.com

²Dept. of Civil and Environmental Engineering, Northeastern Univ., Boston, MA 02115. E-mail: jf.hajjar@neu.edu

³Universidad Autónoma Metropolitana, Departamento de Materiales, Mexico 02200. E-mail: tperea@azc.uam.mx

⁴Dept. of Civil and Environmental Engineering, Virginia Polytechnic Institute and State Univ., Blacksburg, VA 24061. E-mail: rleon@vt.edu

Abstract

Steel-concrete composite frames have been shown to be a sensible option for use as the primary seismic force resisting system of building structures. However, there remains little data to justify the structural system performance factors (i.e., R , C_d , and Ω_o) that characterize the overstrength and ductility of these systems, which are a vital component of successful design in the United States. Based on a suite of new finite element formulations, this work investigates the behavior of composite moment and braced frames under seismic loading and develops rational system performance factors. A set of archetype frames, selected to be representative of the range of frames seen in practice, were designed according to current design specifications. Nonlinear static pushover and transient dynamic analyses were performed on the frames to generate the statistical data on the seismic response from which the performance factors are quantified. The results from this investigation enable a better understanding of the variability in collapse performance of composite frame systems and will facilitate more effective designs of these systems.

INTRODUCTION

A key component of seismic design in the United States is the allowance for inelasticity in structural elements subjected to severe earthquake ground motions. However, static elastic analysis is prevalent for seismic design in current practice. Because of this, seismic performance factors have been developed. The factors are: the response modification factor, R , used in reducing seismic forces determined through elastic methods; the displacement amplification factor, C_d , used in amplifying displacements determined through elastic methods; and the system overstrength factor, Ω_o , used to estimate the actual strength as compared to the design strength.

These three factors are tabulated for a variety of seismic force resisting systems in national codes (ASCE 2010), however, they have been somewhat arbitrarily assigned. Many R factors were based largely on judgment and qualitative comparisons to the relatively few seismic force resisting systems that had known

response capabilities (FEMA 2009). This is particularly true for composite moment and braced frames where the seismic performance factors were assigned based on comparisons to similar structural steel and reinforced concrete systems.

A methodology has been developed to provide a rational basis for determining seismic performance factors which provide equivalent safety against collapse for buildings with different seismic force resisting systems (FEMA 2009). Equivalent safety is provided through an acceptably low probability of structural collapse common to all systems. Structural collapse in the methodology is defined in the context of incremental dynamic analysis, in which nonlinear time history analyses are performed at increasing magnitudes of seismic loading until the structure achieves its peak strength or predefined displacement limits. In this approach, no explicit modeling of collapse is included. Statistical data is generated from the analyses for a set of archetype models and uncertainty is approximated based on the level of knowledge of the particular system and accuracy of the analysis.

This paper presents a study to investigate the behavior of composite frames under seismic loading and to develop rational seismic performance factors following the methodology given in FEMA P695 Quantification of Building Seismic Performance Factors (FEMA 2009).

SEISMIC FORCE RESISTING SYSTEMS

Two separate seismic force resisting systems are analyzed in this study: composite special moment frames (C-SMF) and composite special concentrically braced frames (C-SCBF). The current seismic performance factors for these two systems are given in Table 1 (ASCE 2010).

Table 1. Current Seismic Performance Factors.

System	Ω_o	R	C_d
C-SMF	3.0	8.0	5.5
C-SCBF	2.0	5.0	4.5

The requirements for composite special moment frames are described in the AISC Seismic Specification (AISC 2010). C-SMFs utilize fully restrained connections and consist of either composite or reinforced concrete columns and either structural steel, concrete-encased composite, or composite beams. They are expected to provide significant inelastic deformation capacity through flexural yielding of the beams and limited yielding of the column panel zones. Columns are designed to be stronger than the fully yielded and strain-hardened beams, although flexural yielding in columns at the base is permitted.

The requirements for composite special concentrically braced frames are described in the AISC Seismic Specification (AISC 2010). C-SCBFs consist of CFT or SRC composite columns, structural steel or composite beams, and structural steel or CFT braces. They are expected to provide significant inelastic deformation capacity primarily through brace buckling and yielding of the brace in tension.

ARCHETYPE FRAMES

To assess the seismic performance factors within the FEMA P695 methodology, it is necessary to have a suite of frames (termed index archetypes) for which the analyses can be performed. Ideally that suite of frames is representative of the entire range of frames seen in practice. However, it is generally recognized within the methodology that a practical number of frames cannot fully represent the permissible range, thus simplifications must be made. The selected frames are described below complete details including the design process are presented in Denavit (2012).

The building layout is the same for each of the index archetype configurations: 3 bays by 5 bays with a bay width of either 6.10 or 9.14 m (20 or 30 ft) (Figure 1). The buildings are 3 or 9 stories tall with a story height of 3.96 m (13 ft). For the moment frames the columns were either RCFTs or SRCs. For the braced frames the columns were CCFTs and the braces were either rectangular HSS or wide flange in a two-story X configuration. A composite floor system was assumed for all configurations, although the beams in the seismic force resisting systems were designed and analyzed assuming bare steel.

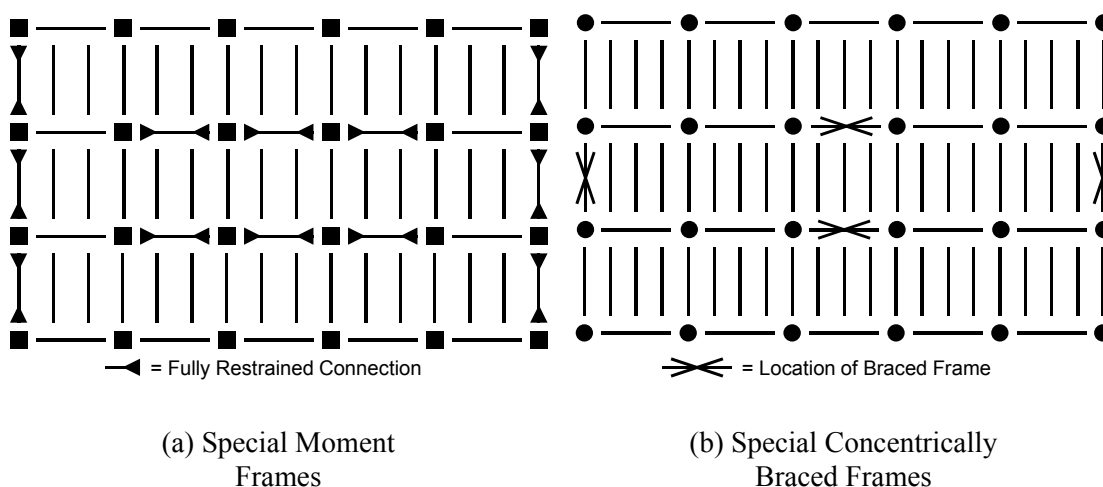


Figure 1. Building Layout.

Two levels of gravity load were selected: “high” which corresponded to warehouse live loading [11.97 kN/m^2 (250 psf)] and the interior frame and “low” which corresponded to office live loading including partitions [3.11 kN/m^2 , (65 psf)] and the exterior frame. Two levels of seismic load were selected corresponding to the levels design earthquake associated with the maximum (D_{\max}) and minimum (D_{\min}) of seismic design category D (ASCE 2010).

The methodology prescribes that $C_d = R$ (FEMA 2009), which is contrary to current practice (ASCE 2010) where C_d is typically less than R (Table 1). For deformation-controlled structures, such as moment frames, this change results in larger member sizes. In this study, most frames were designed assuming $C_d = R$, however, a subset of the moment frames were duplicated and designed with the current value ($C_d = 5.5$) so as to compare to the current state of design practice.

In total, 60 frames were selected and designed for this study. The frames varied in building height (3 and 9 stories), column type (RCFT or SRC for the C-SMFs and CCFT for the C-SCBFs), concrete strength [$f'_c = 25.6$ or 82.7 MPa (4 or 12 ksi)], level of seismic load (SDC D_{max} or D_{min}), level of gravity load (“high” or “low”), and bay width [6.10 or 9.14 m (20 or 30 ft)].

Material Strengths

Two sets of material strengths are used in this study. The first is the nominal strength which is used in the design of the archetypes. The second is the expected strengths which are used in the analyses of the archetypes. The nominal strengths are selected as typical material properties. The expected strengths for the steel materials are defined as described in Section A3.2 of the AISC Seismic Specification (AISC 2010). For lack of a more appropriate definition, the expected strengths for the concrete materials are defined as the required average compressive strength from field strength tests when data are not available to establish a sample standard deviation as described in Section 5.3.2.2 of the ACI Code (ACI 2011).

Seismic Design

The equivalent lateral force method (ASCE 2010) was used for the seismic design. The level of seismic loading is defined in terms of the seismic design category. The frames in this study were designed for seismic design category D at either the maximum (D_{max}) or minimum (D_{min}).

The seismic base shear, V , is defined as the product of the effective seismic weight, W , and the seismic coefficient, C_s , determined based on the fundamental period, T , in accordance with Section 12.8 of ASCE 7 (ASCE 2010). The effective seismic weight of the building is determined in accordance with Section 12.7.2 of ASCE 7 (ASCE 2010).

The effective seismic weight, W , is the sum of the following:

- 100% of the dead load
- 25% of the warehouse floor live load (which is deemed storage)
- 15.4% of the office floor live load [equivalent to 0.48 kN/m² (10 psf) for partitions]

NONLINEAR ANALYSIS MODEL

The nonlinear analysis models consist of beam and zero length elements representing the seismic force resisting frame and nonlinear truss elements representing the destabilizing effect of the remainder of the building that is tributary to the frame. Key details of the model are presented here; full details are presented elsewhere (Denavit 2012).

The beam element used in the model is a distributed plasticity formulation developed specifically for steel-concrete composite frames. The element uses a mixed basis (i.e., using both displacements and forces as primary variables) to allow for accurate modeling of both material and geometric nonlinearities. Fiber sections and

uniaxial cyclic constitutive relations are used to model cross section behavior. The concrete and steel material models account for the salient features of each material, as well as the interaction between the two, including concrete confinement and local buckling.

The connection region of special moment frames is modeled as shown in Figure 2a. Key components are a rigid link parallelogram model with a rotational spring representing the nonlinear panel zone behavior and elastic beam elements which serve to move the beam plastic hinges to specified locations. Nonlinear beam elements for the columns and beams frame into this connection model. The connecting elements (e.g., split tees as shown in Figure 2a) are not explicitly modeled since they are designed to not experience significant deformations, even under large frame deformations.

Connection regions in special concentrically braced frames have large gusset plates that serve to stiffen the connections. Hsiao et al. (2012) developed recommendations for modeling the connection region of steel special concentrically braced frames. A simplified version of the model by Hsiao et al. (2012) is used in this work. The beam-to-column connection region is modeled as shown in Figure 2b. Rigid links are used to model the region where the gusset plate stiffens the beam, brace, and column. The length of the rigid link along the column is equal to the distance from the work point to the top of the gusset plate. The length of the rigid link along the brace is equal to the distance from the work point to the physical brace. The length of the rigid link along the beam is equal to the distance from the work point to column face plus 75% of the distance from the column face to the edge of the gusset plate. The column and beam frame directly into the rigid link whereas a moment release is used between the rigid link and the brace.

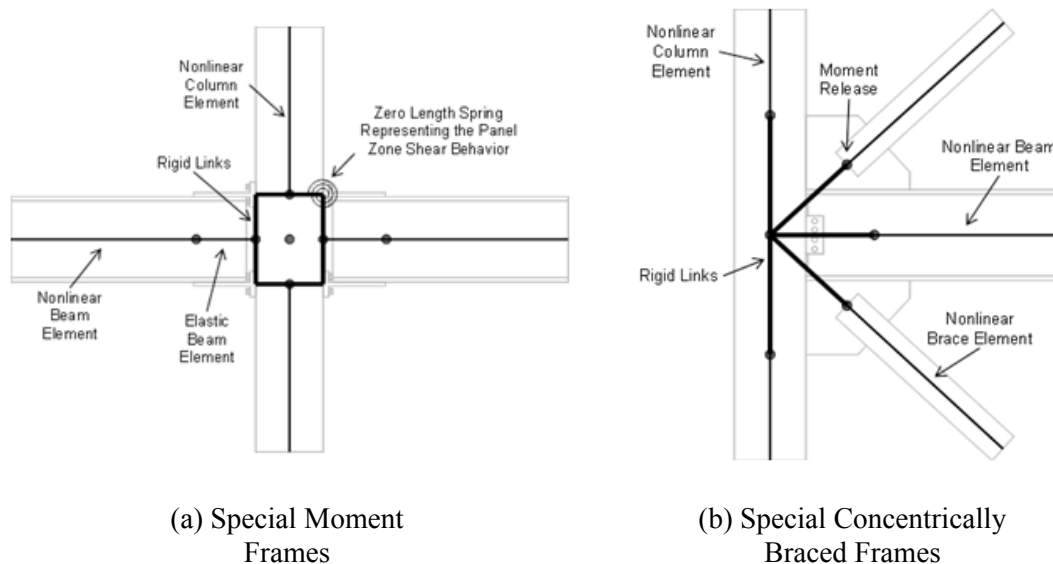


Figure 2. Schematic of the Connection Region Model.

The analyses were performed in two-dimensions. The mesh density was selected such that the model was refined enough to obtain accurate results, but not so

dense as to introduce the ill-effects of localization. The nominal length of the column elements was one-third of the story height. The nominal length of the girder elements was one-third of the bay width for the C-SMFs and one-fourth of the bay width for the C-SCBFs corresponding to the beam spacing (Figure 1). Three integration points were used for all beam elements. Nominal size of the strips in the fiber discretization was $1/20^{\text{th}}$ of the section depth, with the number of fibers in each component defined based on this fixed ratio and rounded up to the nearest integer.

The braces in the C-SCBFs are assumed to be physically oriented such that weak axis buckling is out-of-plane of the frame. However, in the model the brace is oriented such that weak axis buckling is in-plane to allow for the use of a two-dimensional model. Correspondingly, the moment releases at the brace ends represent the relatively weak out-of-plane rotational strength of the gusset plate.

As prescribed in the methodology (FEMA 2009), prior to application of the lateral load (either static or dynamic), gravity load equal to 105% of the dead load plus 25% of the live load and roof live load was applied and held constant for the remainder of the analysis. All gravity loads were applied as nodal loads based on tributary areas.

The methodology (FEMA 2009) does not explicitly define the mass to be used in the analyses. Thus, mass was assigned to the structure based on the effective seismic weight computed for design. For nodes with gravity load, the two translational DOFs were assigned equal masses equivalent to the dead load plus a percentage of the live load. Additionally, for numerical stability, a minimum nominal mass was assigned to all degrees-of-freedom. Also for numerical stability, an additional small elastic stiffness was added to each brace section (e.g., in the event of significant yielding along the full length of the member). Rayleigh damping was used, defined as 2.5% in the 1st and 3rd modes based on recommendations from the methodology (FEMA 2009).

A summary of the gravity load cases and mass used in both the design and the analysis of the archetype frames is presented in Table 2.

Table 2. Gravity Load and Mass in Design and Analysis.

	Design	Analysis
	$1.4 D$	
	$1.2 D + 1.6 L + 0.5 L_r$	
Gravity Load	$1.2 D + 0.5 L + 1.6 L_r$ etc., including live load reduction	$1.05 D + 0.25 L + 0.25 L_r$
	(Section 2.3, ASCE 2010)	(FEMA 2009)
Mass	$D + 25\%$ storage live load $+ 0.48 \text{ kN/m}^2$ (10 psf) for partitions (Section 12.7.2, ASCE 2010)	Same as for design

The model accurately captures member plasticity, local buckling, global buckling, and panel zone behavior as demonstrated through validation studies presented elsewhere (Denavit 2012). However, some aspects of behavior and failure modes have not been modeled.

- Fracture is not included in the model. While fracture is expected during structural collapse, this study is not explicitly modeling collapse. Fracture is not anticipated to control the behavior of well-designed C-SMF, where ductile yielding of the beams in flexure is expected to dominate the response, or C-SCBF, where ductile yielding of the braces and buckling of the braces is expected to dominate the response.
- Connection regions are modeled, however, failure or degradation of the connecting elements is not included in these models. Experimental testing has shown that with proper design and detailing the connecting elements inelasticity can be confined to the member.
- In the design of the frames it was assumed that the beams were provided with lateral bracing sufficient to ensure the full plastic moment capacity could be achieved. Correspondingly, lateral torsional buckling was not included in the model

STATIC PUSHOVER ANALYSES

Static pushover analyses were performed on each frame. Lateral loads were applied at each story in fixed ratios based on the story mass and the mode shape of the structure (FEMA 2009). Thus, an eigenvalue analysis was performed prior to the application of lateral load (but after gravity load was applied). The loading was conducted in displacement control until at least a 20% drop in strength after the peak (V_{80}) was observed. Key results from these analyses include:

- The fundamental period from the model, T_1
- The maximum base shear capacity, V_{max}
- The overstrength factor, $\Omega = V_{max}/V$
- The ultimate roof displacement (i.e., at V_{80}), δ_u
- The effective yield roof drift displacement, $\delta_{y,eff}$, [Equation 1 (FEMA 2009)]
- The period-based ductility, $\mu_T = \delta_u/\delta_{y,eff}$

$$\delta_{y,eff} = C_o \frac{V_{max}}{W} \left(\frac{g}{4\pi^2} \right) (\max(T, T_1))^2 \quad (1)$$

where,

C_o = A coefficient based on the fundamental mode shape (FEMA 2009)

Analysis Results

An example of the results for a three-story C-SMF [RCFT columns, high gravity load, $f'_c = 27.6$ MPa (4 ksi), SDC = D_{max}] is shown in Figure 3. Full results are presented elsewhere (Denavit 2012).

For the C-SMFs, an initially linear response is observed followed by gradual stiffness reduction up to the peak lateral capacity of the frame then near linear post peak degradation until the analysis was stopped after at least a 20% drop in capacity was observed. For the 3 story frames an even distribution of deformation is seen among the stories with the exception of the roof story of some frames where lower deformations were observed at the V80 level. For the 9 story frames, the distribution of deformation was even among the stories at the design base shear level, however, at the maximum base shear and after a 20% drop in capacity, the deformation was concentrated in ranges of 4 to 6 stories forming a multi-story mechanism (Krishnan and Muto 2012). The story groups where the inelasticity was concentrated were either located at the top, middle, or bottom of the structure. No fundamental behavioral differences were observed between the frames with RCFT columns and those with SRC columns owing to the fact that flexural yielding of the beams controlled the response.

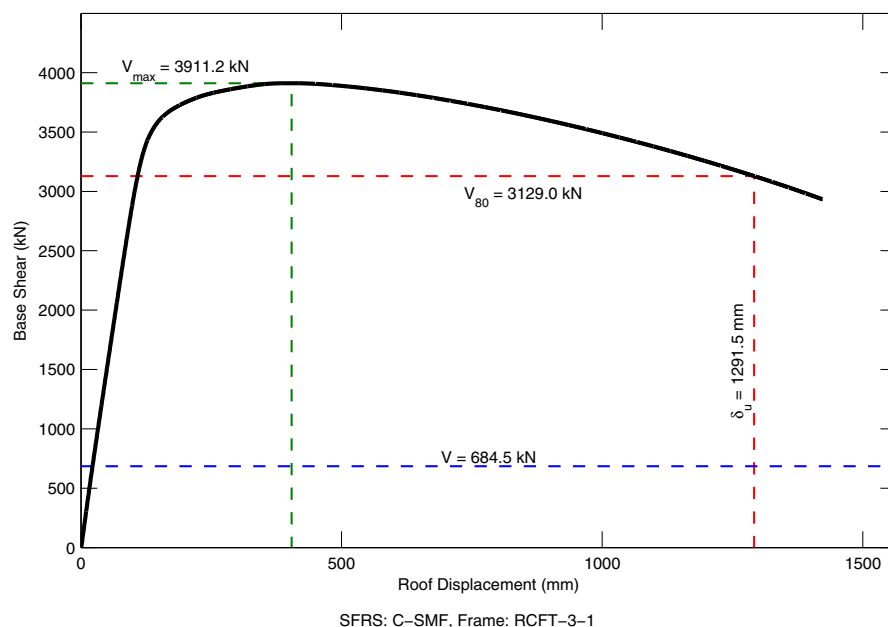


Figure 3. Sample Results of the Static Pushover Analyses.

For the C-SCBFs, the response was initially linear, however, in contrast to the C-SMFs, sharp changes in stiffness including drops in capacity were observed in the response corresponding to yielding and buckling of the individual braces. These jumps are exacerbated by the fact that only one bay of bracing was modeled; had multiple bays been included with slightly different loading or material properties, the response would likely have been smoother. Also in contrast to the C-SMFs, for the 3 story frames the deformation was often concentrated into one story. The 9 story frames showed a similar response to the C-SMFs in that multi-story mechanisms were developed where the deformation was concentrated in 4 to 6 consecutive stories. Conclusions from the results in the context of evaluating the system overstrength factor are given later.

DYNAMIC RESPONSE HISTORY ANALYSES

In the methodology, collapse is assessed in the context of incremental dynamic analyses (IDA) (Vamvatsikos and Cornell 2002). Dynamic response history analyses are performed, subjecting each frame to a suite of ground motions scaled at different intensities. The 44 earthquake ground motions described in the methodology (FEMA 2009) were used for this study.

Explicit modeling of the collapse of structures is a challenging task and the subject of current research (e.g., Khandelwal et al. 2009; McAllister et al. 2012). The FEMA (2009) methodology has avoided the need to explicitly model collapse by defining collapse in the context of incremental dynamic analyses. In incremental dynamic analyses, a frame is analyzed under different ground motions and at different intensities. The resulting curve shows a response value (typically peak story drift) versus an intensity measure. Typical results would show an initially high slope, gradually transitioning to a low slope; however, in practice a wide variety of behavior is seen.

Determination of “collapse” is necessary for the methodology and thus approximate definitions are adopted. In this work, collapse is defined when a prescribed maximum story drift of 10% is observed in the incremental dynamic analysis results. This is an approximate method since collapse is not associated with any particular drift limit (Krawinkler et al. 2003); however, some justification of the 10% limit exists. Generally, little hardening response is seen incremental dynamic analysis results beyond 10% drift. Also, the nonlinear models were not validated for deformations beyond this range and nonlinear effects that are not being modeled directly in this work, such as fracture, lateral torsional buckling, or connection degradation may occur at these higher drift levels.

Key results from the dynamic response history analyses include:

- The median collapse intensity, \hat{S}_{CT} , determined as the intensity, S_T , at which half of the ground motions cause maximum story drifts of greater than 5%
- The collapse margin ratio, $CMR = \hat{S}_{CT}/S_{MT}$ (where S_{MT} is the maximum considered earthquake intensity).

Analysis Results

An example of the results for the same three-story C-SMF highlighted before is shown in Figure 4. Full results are presented elsewhere (Denavit 2012).

For both the C-SMFs and C-SCBFs, the majority of incremental dynamic analysis curves exhibit the typical response with an initial relatively high slope followed by a relatively low slope at higher intensities. The initial slope of the curves for each frame varies, owing to inherent differences between the 44 ground motions. In general, at the maximum considered earthquake intensity (i.e., $S_T = S_{MT}$), the distribution of story drifts is relatively uniform along the height of the building. An exception is the 9 story C-SCBFs where often the top story exhibits deformations several times greater than that of the other stories.

SYSTEM OVERSTRENGTH FACTOR, Ω_o

According to the methodology, the system overstrength factor, (Ω_o , should not be taken as less than the largest average value of overstrength, Ω , from any performance group, however, upper limits of $1.5R$ and 3.0 are applied (FEMA 2009).

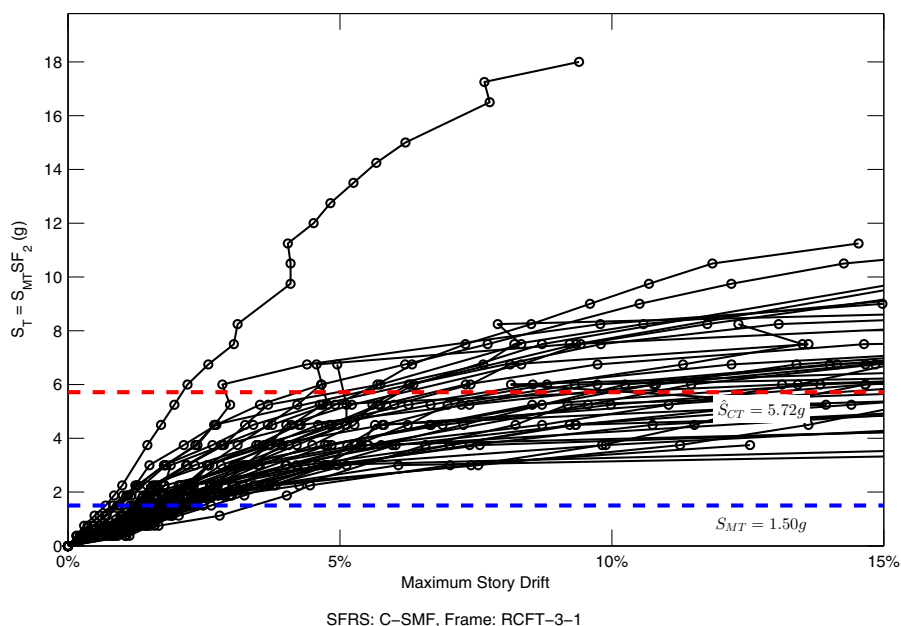


Figure 4. Sample Results of the Dynamic Response History Analyses.

For the C-SMFs, the average overstrength for the performance groups ranges from 5.3 (for the performance group with high gravity load, $SDC = D_{max}$, and long period) to 9.9 (for the performance group with high gravity load, $SDC = D_{min}$, and long period). These values are quite high and reflect the displacement controlled design of these structures. Other studies on steel special moment frames (NIST 2010) have also shown high overstrength. Several factors have led to the particularly high overstrength values seen in this study. The use of $C_d = R$ in the design of the frames reduced the allowable story drifts thus increasing member sizes. In the model, the plastic hinges were forced to a location $2d/3$ away from the column face (where d is the beam section depth). This distance was the assumed length of the connection. Selection of this distance resulted in higher frame strengths as compared to shorter connections. Additionally, reduced beam section connections were not used for these structures; if they had been used, lower overstrength would have been observed. For the results shown, all of the performance groups exceed the practical upper limit of 3.0, so it is recommended that the system overstrength factor remain unchanged from its current value ($\Omega_o = 3.0$).

For the C-SCBFs, the average overstrength for the performance groups ranges from 1.7 (for the performance group with high gravity load, $SDC = D_{min}$, and short period) to 2.8 (for the performance group with low gravity load, $SDC = D_{max}$, and short period). These results are in contrast to the C-SMFs where high overstrength

was observed and reflect the strength controlled design of these structures. Other studies on steel special concentrically frames (NIST 2010) have shown similar overstrength results. In light of these results (some performance groups with overstrength greater than 2.0), an increase the system overstrength factor for C-SCBFs could be warranted, although the current value ($\Omega_o = 2.0$) is likely sufficient.

RESPONSE MODIFICATION FACTOR, R

According to the methodology, the response modification factor that was used to design the archetype frames is acceptable if the probability of collapse for maximum considered earthquake ground motions is approximately 20% or less for each index archetype and 10% or less on average for each performance group (FEMA 2009). To evaluate these conditions, adjusted collapse margin ratios are computed and compared against reference values (Equations 2 and 3).

$$ACMR_i \geq ACMR_{20\%} \quad (2)$$

$$\text{mean}(ACMR_i) \geq ACMR_{10\%} \quad (3)$$

where,

$ACMR_i$ = adjusted collapse margin ratio for each index archetype, i

$ACMR_{20\%}$ = acceptable value of the adjusted collapse margin ratio for 20% collapse probability

$ACMR_{10\%}$ = acceptable value of the adjusted collapse margin ratio for 10% collapse probability

The adjusted collapse margin ratio (Equation 4) is the product of the collapse margin ratio, CMR , as determined from the response history analyses and a spectral shape factor, SSF , given in FEMA P695 (2009). The spectral shape factor depends on the fundamental period, T , and period based ductility, μ_T , and accounts for the frequency content of the selected ground motion record set.

$$ACMR_i = SSF_i CMR_i \quad (4)$$

The acceptable values of the adjusted collapse margin ratio are derived from the lognormal distribution and depend on the desired collapse probability (10% or 20%) and a measure of the total system collapse uncertainty (expressed as β_{total}). Uncertainty in the system collapse assessment comes from a number of sources. Uncertainty due to the variability between ground motions records is characterized by β_{RTR} [Equation 5 (FEMA 2009)]

$$\beta_{RTR} = 0.1 + 0.1\mu_T \leq 0.4 \quad (5)$$

Uncertainty in the design requirements, test data, and nonlinear modeling are characterized by qualitative quality ratings as will be described.

For both of systems, the design requirements have been well-vetted and provide extensive safeguards against unanticipated failure modes. The hierarchy of yielding and failure of components is well established. However, construction practices are comparatively less mature than for either structural steel or reinforced concrete structures. For these reasons, a quality rating of good (B) is given to the design requirements for both C-SMFs and C-SCBFs.

Numerous tests on composite members, connections, and frames have been conducted and reported in the literature. The tests span most of the important parameters which affect design requirements and the behavior is generally well understood. For these reasons, a quality rating of good (B) is given to the test data for both C-SMFs and C-SCBFs.

The nonlinear models directly simulate all predominate inelastic effects and have been extensively validated against experimental results. The sets of archetype frames provide a reasonably broad representation of the design space. However, fracture is not included in the modeling and the frames were assumed to be properly designed to preclude connection deterioration and lateral torsional buckling. For these reasons, a quality rating of good (B) is given to the nonlinear modeling for both C-SMFs and C-SCBFs.

The quality ratings are assigned lognormal standard deviation parameters [Table 3, (FEMA 2009)] and the total system collapse uncertainty is computed with Equation 6 then rounded to the nearest 0.025. The value depends on the period based ductility but is constant for $\mu_T \geq 3$. For both systems the value of β_{total} for $\mu_T \geq 3$ is 0.525.

$$\beta_{total} = \sqrt{\beta_{RTR}^2 + \beta_{DR}^2 + \beta_{TD}^2 + \beta_{MDL}^2} \quad (6)$$

Table 3. Quality Ratings.

System	Quality of Design Requirements	Quality of Test Data	Quality of Nonlinear Modeling
C-SMF	B (Good) $\beta_{DR} = 0.2$	B (Good) $\beta_{TD} = 0.2$	B (Good) $\beta_{MDL} = 0.2$
C-SCBF	B (Good) $\beta_{DR} = 0.2$	B (Good) $\beta_{TD} = 0.2$	B (Good) $\beta_{MDL} = 0.2$

For the C-SMFs, all of the evaluations pass and thus the current response modification factor is deemed acceptable. In fact, all frames pass by a significant margin. Many of the IDA curves retain a significant positive slope even at the high levels of earthquake ground motion used in this study (up to 5-7 times maximum considered earthquake intensity). This is indicative of the excellent performance of C-SMFs subjected to earthquake ground motions. For the C-SCBFs, all of the evaluations pass and thus the current response modification factor is deemed acceptable. The margin of passing is not as great as for the C-SMFs, nonetheless, the C-SCBFs exhibit excellent performance. It should be noted that these results are only strictly applicable to well designed and detailed frames where connection deterioration will not occur and sufficient lateral bracing is provided.

DEFLECTION AMPLIFICATION FACTOR, C_d

According to the methodology, for systems with typical levels of damping, including the systems studied here, the deflection amplification factor, C_d , is equal to the response modification factor (FEMA 2009). For C-SCBFs this represents a minor change as the current difference between R and C_d is small and these structures are typically not displacement controlled. For C-SMFs this represents a significant change. Setting $C_d = R$ results in a 45% increase in C_d from the current value. Additionally, C_d plays a central role in the design of moment frames since they are often displacement controlled.

In this study, four frames were designed with the current C_d value. These frames had smaller members than their counterparts designed with $C_d = R = 8.0$. Some differences in performance were noted. The average overstrength of the frames designed with the current C_d was 4.9 while it was 6.4 for their counterparts. The average adjusted collapse margin ratio of the frames designed with the current C_d was 5.5 while it was 6.2 for their counterparts. These results indicate that the frames designed with the current C_d value have acceptable performance and that setting $C_d = R$ for this system is unnecessary from a safety perspective.

All in all, further study is needed to determine the ramifications of setting $C_d = R$ and whether such a change is necessary. Further study should include the possibility of a corresponding increase in the deformation limits should the C_d factor increase,

CONCLUSIONS

A study was conducted following recommendations in FEMA P695 (2009) to determine the seismic performance factors (i.e., R , C_d , and Ω_o) for composite special moment frames (C-SMF) and composite special concentrically braced frames (C-SCBF). A suite of 60 archetype frames was selected and designed according to current design specifications. Nonlinear static pushover analyses and dynamic response history analyses were performed on the frames to characterize the behavior and generate statistical data to be used in evaluation of the seismic performance factors. Both systems exhibited excellent seismic behavior and current seismic performance factors were found to be acceptable. In particular, it was noted that frames designed with the current deflection amplification factor, C_d , were found to be acceptable and thus a potential change to set $C_d = R$ should be studied further and perhaps accompanied by a corresponding change to the drift limits such that future seismic drift requirements are equivalent to the current seismic drift requirements.

ACKNOWLEDGEMENTS

This material is based upon work supported by the National Science Foundation under Grant Nos. CMMI-0619047 and CMMI-0530756 as part of the George E. Brown, Jr. Network for Earthquake Engineering Simulation (NEES); the American Institute of Steel Construction; the Georgia Institute of Technology; and the University of Illinois at Urbana-Champaign. Computational analyses in this work

were executed in part on the Extreme Science and Engineering Discovery Environment (XSEDE), which is supported by National Science Foundation Grant No. OCI-1053575. Any opinions, findings, and conclusions expressed in this material are those of the authors and do not necessarily reflect the views of the National Science Foundation or other sponsors.

REFERENCES

- ACI (2011). *Building Code Requirements for Structural Concrete and Commentary*. American Concrete Institute, Farmington Hills, MI.
- AISC (2010). *Seismic Provisions for Structural Steel Buildings*. American Institute of Steel Construction, Chicago, Illinois.
- ASCE (2010). *Minimum Design Loads for Buildings and Other Structures*. American Society of Civil Engineers, Reston, Virginia.
- Denavit, M. D. (2012). "Characterization of Behavior of Steel-Concrete Composite Members and Frames with Applications for Design." Ph.D. Dissertation, University of Illinois at Urbana-Champaign, Urbana, Illinois.
- FEMA (2009). *Quantification of Building Seismic Performance Factors*. FEMA P695, Federal Emergency Management Agency, Washington, D.C.
- Hsiao, P.-C., Lehman, D. E., and Roeder, C. W. (2012). "Improved Analytical Model for Special Concentrically Braced Frames." *Journal of Constructional Steel Research*, 73, 80–94.
- Khandelwal, K., El-Tawil, S., and Sadek, F. (2009). "Progressive Collapse Analysis of Seismically Designed Steel Braced Frames." *Journal of Constructional Steel Research*, 65(3), 699–708.
- Krawinkler, H., Medina, R., and Alavi, B. (2003). "Seismic Drift and Ductility Demands and their Dependence on Ground Motions." *Engineering Structures*, 25(5), 637–653.
- Krishnan, S., and Muto, M. (2012). "Mechanism of Collapse of Tall Steel Moment Frame Buildings under Earthquake Excitation." *Journal of Structural Engineering*, ASCE, 138(11), 1361–1387.
- McAllister, T., MacNeill, R., Erbay, O., Sarawit, A., Zarghamee, M., Kirkpatrick, S., and Gross, J. (2012). "Analysis of Structural Response of WTC 7 to Fire and Sequential Failures Leading to Collapse." *Journal of Structural Engineering*, ASCE, 138(1), 109–117.
- NIST (2010). *Evaluation of the FEMA P-695 Methodology for Quantification of Building Seismic Performance Factors*. National Institute of Standards and Technology, Gaithersburg, Maryland.
- Vamvatsikos, D. and Cornell, C. A. (2002). "Incremental Dynamic Analysis." *Earthquake Engineering & Structural Dynamics*, 31(3), 491–514.

Simulated Portfolio for the Seismic Risk Assessment of Composite Structures

A. Mühlhausen¹ and U. E. Dorka²

¹Dept. of Civil and Environmental Engineering, Univ. of Kassel, Kurt-Wolters-Str. 34, 34125 Kassel, Germany. E-mail: axel-muehlhausen@uni-kassel.de

²Dept. of Civil and Environmental Engineering, Univ. of Kassel, Kurt-Wolters-Str. 34, 34125 Kassel, Germany. E-mail: uwe.dorka@uni-kassel.de

Abstract

Assessment of damage costs due to an earthquake is an important issue for the insurance industry, yet it currently lacks real damage data for realistic pricing of individual risks. Sophisticated numerical tools, which are widely used to assess structural behavior in great detail (like FEM), may be used with confidence in modeling damage and therefore, they may be suitable in seismic risk assessment for insurance purposes. To produce a virtual damage database, the “Simulated Building Portfolio”-Tool (SBP-Tool) was developed at the University of Kassel in cooperation with the Munich Re. This paper presents the first virtual portfolio for steel-concrete composite frame structures. The SBP-Tool uses beam elements for the composite columns and steel girders, and shell elements for the concrete slabs. Shear springs are automatically created to model the composite action between concrete slabs and steel beams. Rotational springs model the semi-rigid beam-column connections.

INTRODUCTION

The assessment of damage losses due to an earthquake is an important issue for the insurance and reinsurance industry, but it currently lacks the level of detail that is required for realistic pricing of individual risks.

Once again, the recent earthquakes that struck Chile (Maule, Mw 8.8, February 6, 2010), New Zealand (Darfield, Mw 7.0, September 3, 2010 and Lyttelton, Mw 6.1, February 21, 2011) and Japan (Honshu, Mw 9.0, March 11, 2011) in the last three years proved the strategic importance of this kind of industry and renewed the crucial question of how to develop a resilient concept for society.

Any further advancement in that respect is strictly related to the capabilities of creating reliable models to predict seismic risk. This process implies a better understanding of the hazard, of the vulnerability and of the exposure that is involved.

Even if important on-going projects, like the Global Earthquake Model (GEM), are aiming at sharing and improving our knowledge, the “state-of-the-art” of the empirical data-set regarding earthquake’s economic losses presents a severe non-uniformity. The worldwide information available is extremely different from both the quality and the geographical points of view.

Since earthquakes are rare events, the situation will not likely change significantly in the foreseeable future. It is therefore necessary to further investigate the development of innovative concepts based on consolidated numerical simulation techniques.

This paper presents how to simulate a first portfolio consisting of steel-concrete composite structures, which can be used in combination with detailed wave propagation models to estimate the damage and the resulting damage costs.

[Mazzieri 2013] shows how to describe a spatial variability of strong-ground motions through large-scale 3D simulations of wave propagation in near-surface soils. He developed complex 3D FE-models for a region of 1 km x 1 km and a depth of 50 m. More than 1.000.000 Finite Elements are typically required to simulate the wave propagation in a particular soil system.

Using these complex soil models, Mazzieri assessed the response of buildings due to the simulated wave propagation by modeling them as rigid bodies (Figure 1). This neglects the dynamic characteristics and the non-linear structural behavior of buildings despite being the controlling factors for the response of buildings under seismic actions.

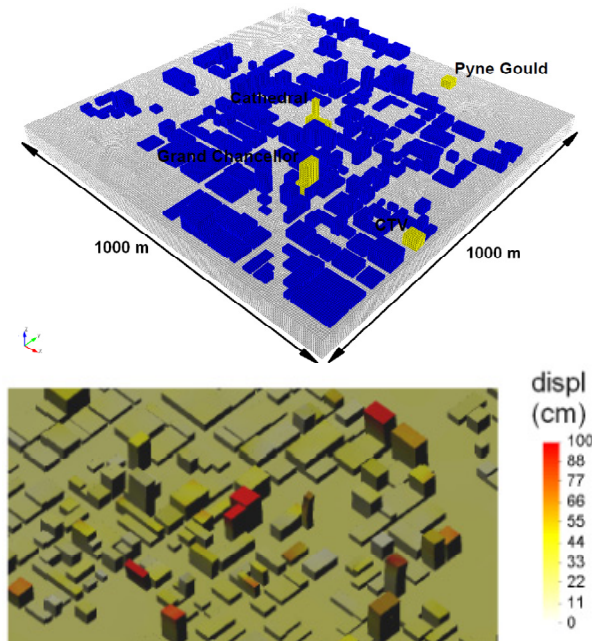


**Figure.1 - Left: 3D-model of the soil and the buildings in Christchurch CBD
Right: Snapshots of the simulated displacement of the buildings of the
Christchurch CBD both from [Mazzieri 2013]**

A combination of such detailed wave propagation models with sophisticated structural models for the buildings in question is required, if reliable data for seismic risk analysis is to be provided.

THE SBP-TOOL FOR GENERATING A VIRTUAL PORTFOLIO

To create this kind of building models, the so-called “Simulated Building Portfolio-Tool” (SBP-Tool) was developed at the University of Kassel in cooperation

with the Munich Re, [Mühlhausen 2011, 2012]. It provides a virtual portfolio of realistic buildings by using a set of global building criteria provided by the user in a configuration file. A statistical process automatically generates each individual building for the portfolio using the given range for each criterion.

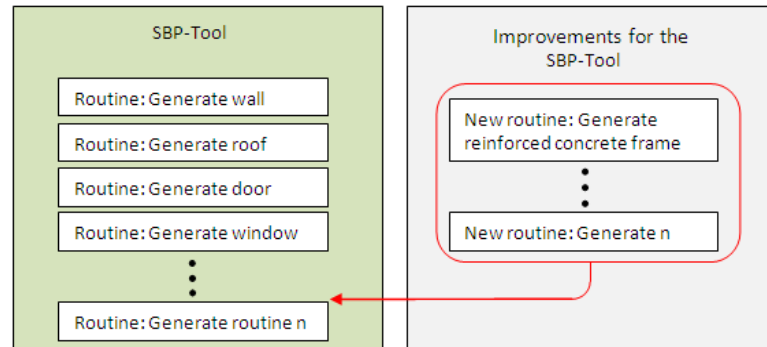


Figure 2. Import new routines to generic SBP-Tool

The program is written in ISO C99 and features a modular design (Figure 2). This allows for easy adaptation to different structures (masonry, steel frames, rc-frames with masonry infill, etc.) and inclusion of additional building features, like stairs or penthouses. Currently, the SBP-Tool is used to generate 3D linear FE-models of masonry buildings (Figure 3) and as a recent addition, steel-concrete composite frame structures. A detailed description of how to generate the sophisticated steel-concrete composite frame structures with the pre-design (static) module is given in the following chapter.



Figure 3. A regional portfolio of 3D FE-models for masonry buildings simulated with the SBP-Tool. This can be combined with any seismic input, e.g. wave propagation models

Whereas the first file (a configuration file) does not depend on any particular FE-software, the second one, the output, must be adapted to its specific commands. This allows the use of other FE-software (Ansys, Open Quake, SLang etc.) without interfering with the initial generation process of the buildings.

SLang imports the ASCII files and, by executing the commands, it creates the mass and stiffness matrices. They are exported as two additional output files. Furthermore, SLang creates a file with all the information associated with each DOF.

Thus, a set of 4 files is created for each building generated containing all the necessary information to perform a dynamic analysis, and in particular a time history analysis.

In general (e.g. non-linear structures) around 500 time histories are required to determine the standard deviation of a local variable with an accuracy of greater than 99 % according to the central limit theorem.

That means for a given portfolio like the one in figure 4 with 65 buildings and approximately 1.700.000 DOFs, 8.500.000 time histories are required. To compute 8.500.000 time histories in a short period of time, the use of an efficient algorithm in combination with parallel computing is necessary.

In the case of linear structures, the use of power spectra provides an efficient way to calculate the required statistical values of local variables, which can be obtained by multiplying the transfer function of the local variable with the power spectrum of the input process (ground motion).

STEEL-CONCRETE COMPOSITE FRAME STRUCTURES WITHIN THE SBP-TOOL

A composite structure combines two or more materials with each other and is a widely used structural system in buildings and bridges.

Nowadays, a wide range of materials can be used in composite structures, like wood and concrete (especially ultra high performance concrete), but the most common way is combining steel and concrete for manufacturing composite columns, composite beams and composite slabs.

The main purpose of combining different materials is to take advantage of the strengths of each material despite the different mechanical properties and their individual weaknesses; for example while one material can be efficient in tension (e.g. steel) the other one (like concrete) would be efficient in compression.

Further advantages of using steel-concrete composite structures are that concrete provides a good protection against corrosion and high temperature (fire). The use of steel-concrete composite structures can result in a more efficient design in comparison with steel or concrete structures alone. Usually, larger spans can be reached when a concrete-steel composite system is chosen [Bode,1998, Huber, 2000].

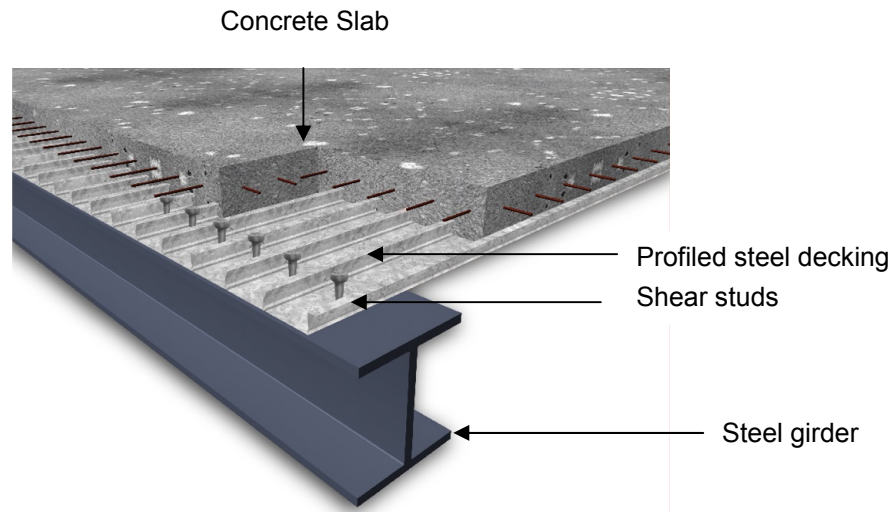


Figure 4. A sketch of a steel-concrete composite slab, [Duowei webpage]

The SBP-Tool is written in a generic way, which allows the addition of new attributes. In its current state, the following SBP-Input parameters are needed to generate similar buildings (from a statistical point of view) for a portfolio (Figure 5):

- number of storeys, approximate building plan,
- types of composite deck and columns,
- year of construction and
- geographic location
-

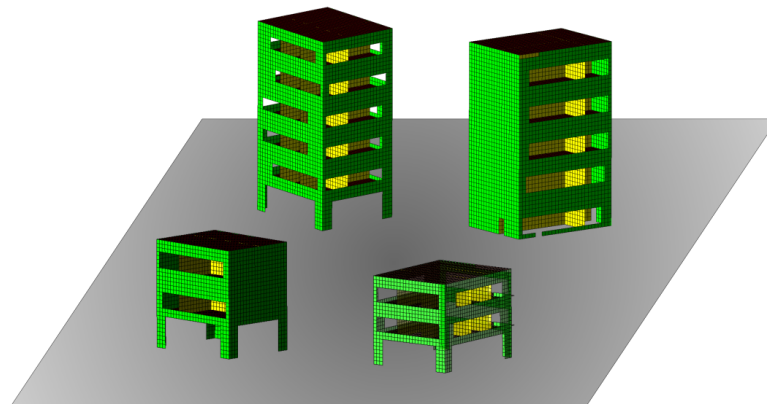


Figure 5. A generated portfolio of steel-concrete composite office buildings using the SBP-Tool

With the knowledge of these SBP-Input parameters, a statistical variation is performed so that hundreds of buildings are generated automatically. The generated buildings with the SBP-Tool have the following components modeled with Finite Elements automatically:

- Steel or steel-concrete composite columns as beam elements,
- steel girders as beam elements,
- reinforced concrete slabs as shell elements,
- semi-rigid beam-column connections as rotational-springs and
- composite beam-slab connections as shear-springs.

A pre-design (static) module is attached to the SBP-Tool to estimate the composite-sections based on codes, which were relevant at the time of construction.

For a given static system (e.g. single span or multi span beams) the maximum bending moment M_{Ed} will be calculated and the necessary steel girder with the needed resistant bending moment M_{Rd} will be chosen from a list of stored profiles automatically. A scheme for the procedure to estimate the necessary steel girder is shown in figure 6.

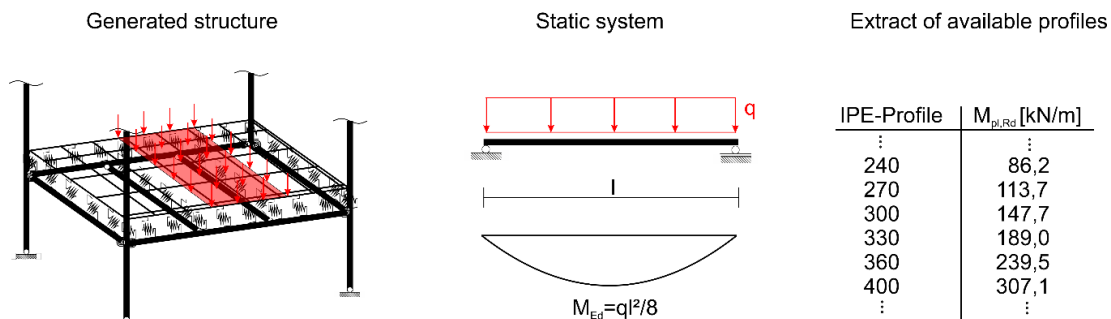


Figure 6. 3D-FE model (left) for a composite frame. Static system of red part is shown in the middle and an extract of the available profiles is shown on the right.

One of the most important aspects of modeling composite structures are the connections between different materials (steel and concrete) and different composite members (beams to columns). To model the beam-slab connections between the steel girder and concrete slab and the semi-rigid beam-column connections, shear springs and rotational springs are used respectively and modeled with the Finite Element software SLang. In figure 7 a three and a four storey frame building is shown.

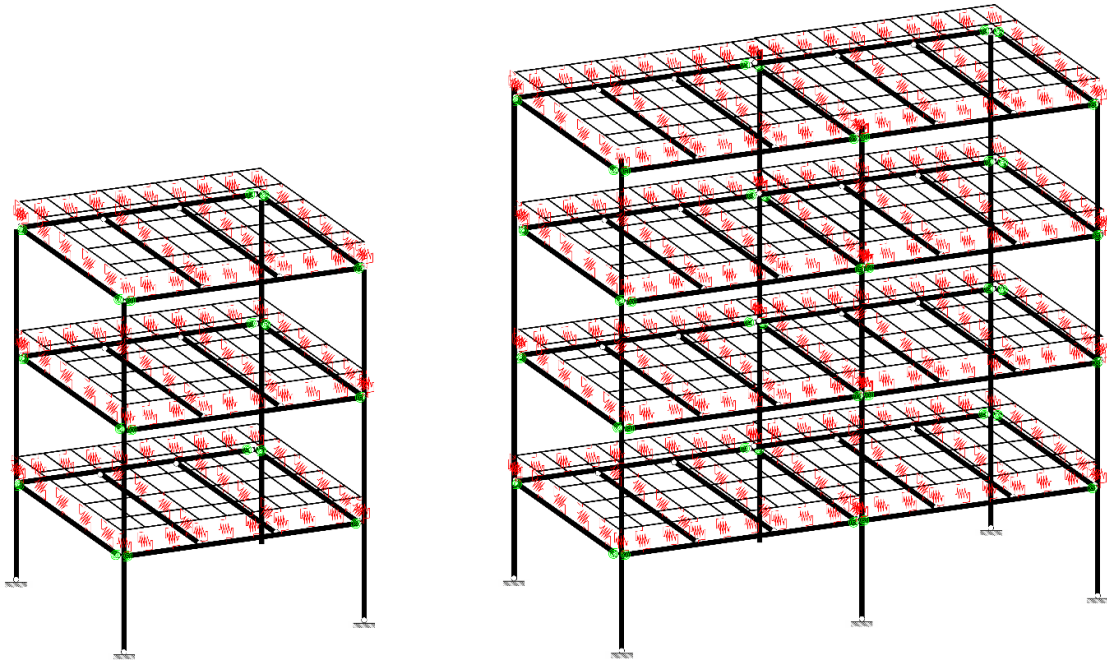


Figure 7. FE-models for a three and four storey steel-concrete composite frame building

THE PORTFOLIO SIMULATION

To perform the time history analysis with the required efficiency and speed, a parallel implementation of Dorka's substructure algorithm [Dorka 1991, 2002], [Bayer et al. 2005] is needed and given in Figure 8 as a flowchart. On the left is shown the linear control mechanism and on the right the flowchart of substructure algorithm.

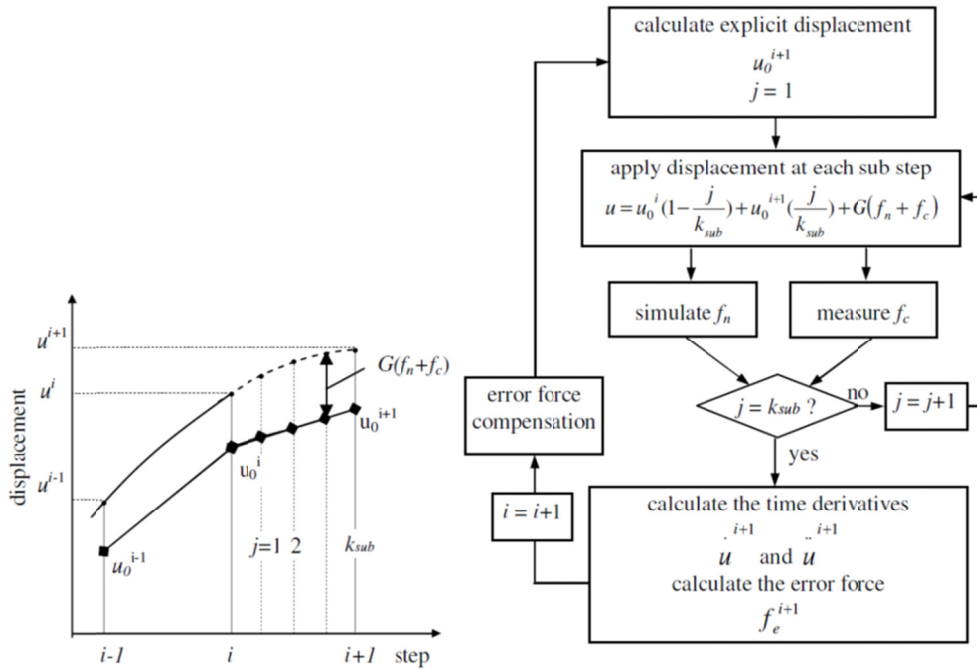


Figure 8. Substructure algorithm with digital feedback and error force compensation, [Dorka 2002].

This algorithm is a discrete formulation of the dynamic equilibrium equation (1):

$$M \frac{d^2u}{dt} + C \frac{du}{dt} + Ku = p(t) + f_r + f_s \quad (1)$$

Its integration constants γ and β are variables. With $\gamma = 0.5$ and $\beta = 0.25$, it becomes the well-known Newmark scheme. It also accommodates experimental and non-linear numerical restoring forces $f_r + f_s$ through a parallel sub-stepping process within each time step, thus avoiding time-consuming matrix inversions and iterations. Therefore, this algorithm, which is called “Open hybrid simulation library” (OpenHySL), can take advantage of multi-core and multi-processor computers using parallel libraries and other optimizations, resulting in solving 10000 DOFs in 43,94 ms per time step on a regular laptop computer [Obón Santacana 2012]. This is because the sub-stepping within each time step does not cause any significant reduction in performance due to its parallel implementation if an adequate number of cores or processors are available.

The time histories are stored in a HDF5 format with all necessary information for the time parameters (date, duration, number of DOF, number of time steps and duration of time step) and for the time integration (acceleration, velocity, displacement and stresses) for further processing, e.g. Matlab.

ILLUSTRATIVE EXAMPLE

To demonstrate this developed approach to estimate economic losses for single risks or whole portfolios, an illustrative example for a 3 storey office building is

chosen. This case study is conducted with a return period of 475 only, but by using several return periods, for example 10, 20, 50, 100, 200, 1000 and 2000 years, a loss curve for a single risk or portfolio can be produced.

Loss curves are the ratio between repair costs and return period and they are an important tool for the insurance and reinsurance industry for calculating the local premium. An economic loss of a single risk is reached much earlier than the mechanical collapse, so it is important to notice that the focus of this study lies on economic aspects not safety aspects.

The following assumptions are made to demonstrate this approach on a 3 storey-office building located in the city centre of Potenza (Italy). To describe the hazard for this building, two parameters are used: the local soil and the peak ground acceleration (PGA). For the region of Potenza, the reference PGA has a value of 0,275g for a return period of 475 years. For this seismic hazard, time histories in x- and y-direction are generated artificially and are shown in Figure 9 with a maximum of ca. 3 m/s².

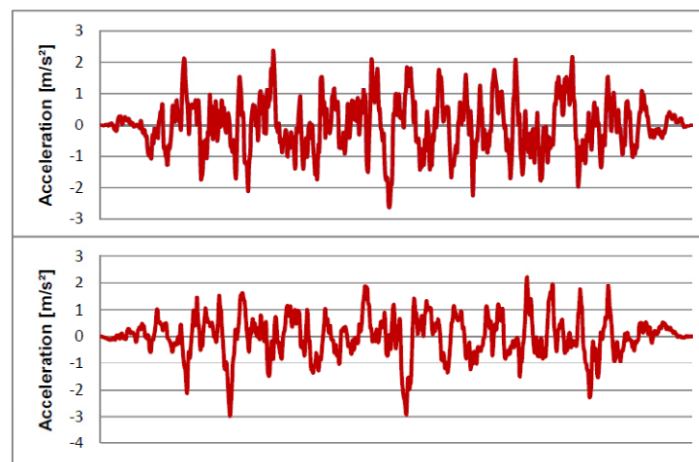


Figure 9. Artificially generated time histories in x- and y-direction for the chosen location (Potenza, Italy) and seismic hazard level

The office building was generated with the SBP-Tool based on the following specific criteria (compare general criteria chapter 5):

- number of storeys: 3 storeys, storey height 4m
- approximate building plan: 21m by 6m,
- types of composite deck: Solid steel-concrete composite deck with steel H-sections
- types of columns: Steel columns
- year of construction: 1972 (This defines the building code to be used by the pre-design (static) module)
- geographic location: Potenza, Italy

The pre-design module of the SBP-tool specifies the columns and beams. For this illustrative example, the profiles are HEA 500 (column) and IPE 400 (beam).

With this information, a FE-model is automatically created with SLang. For this example, the model was ported to SAP2000 manually in order to use this program's advanced visualization capabilities, which Slang is lacking. SAP2000 cannot be used

for a full risk analysis because it cannot utilize the efficient and fast substructure algorithm (Fig. 8), which is required for a risk simulation within a reasonable time frame.

In SAP2000, a typical plastic hinge is color-coded with its elastic limit in purple, its elastic-plastic limit in yellow and its plastic limit in brown (Fig. 10). Additional colors were defined here to describe three damage levels: blue for light damage, light blue for moderate damage and green for total damage. These must refer to different levels of repair costs in order to estimate the total damage cost for the whole structure. In this example, they have been defined close to relevant mechanical states, with a certain need for repair. E.g. the beginning of global yield will require at least minor repairs after an earthquake whereas excessive yield will cause the replacement of the corner.

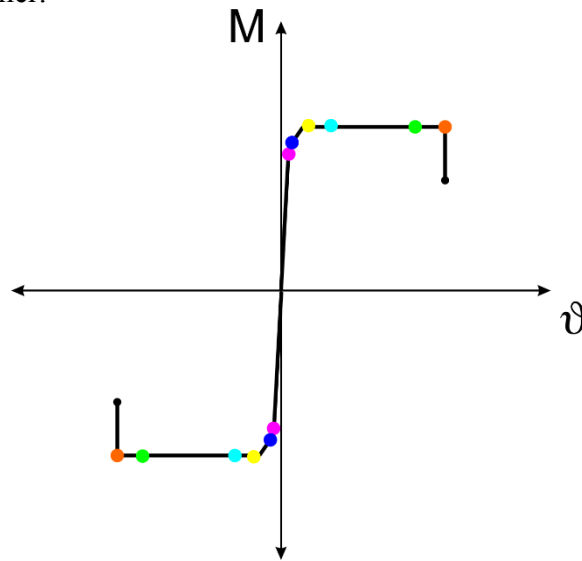


Figure 10. Definition of a plastic hinge with elastic limit (purple), elastic-plastic limit (yellow), plastic limit (brown) and three damage levels (blue, light blue and green).

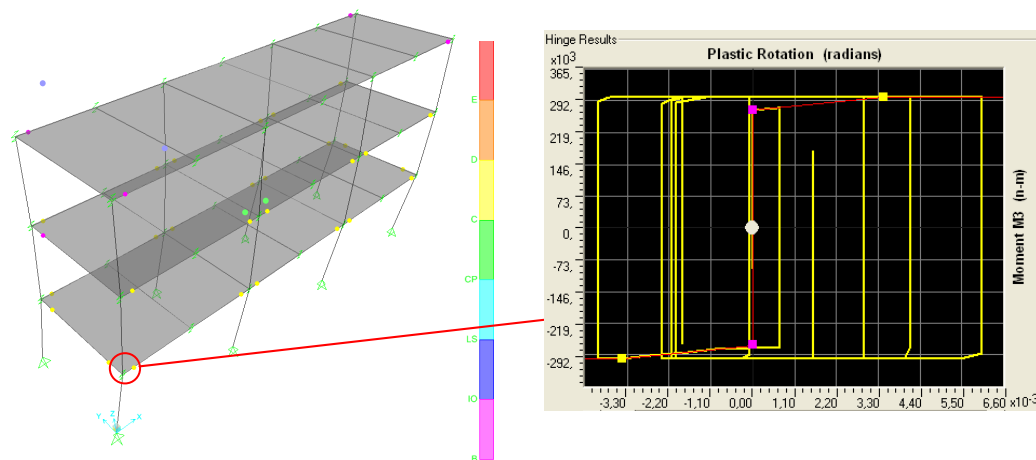


Figure 11. Left: Deformed shape for the sample building from the SAP2000 analysis with color-coded corners according to Figure. 10 showing many corners with moderate to severe damage: This structure is likely to be a total economic loss although it will not collapse.

Obviously the function for the repair cost is not linear and steps are not uncommon. In order to describe the repair function realistically, repair processes must be studied in detail for the different damage levels, which was not done here. Therefore, the results presented in Fig. 11 are only an illustration of the process.

It may be said that most likely this 3-storey office building is a total economic loss for this seismic hazard level although collapse is not to be expected: The hinges in the first floor are completely plasticized and many other hinges are at least moderately damaged. Therefore, the repair costs will most likely exceed the value of the structure.

CONCLUSION

Reliable seismic damage and loss simulation not only requires sophisticated seismological ground models, but foremost detailed structural models, since damage and repair needs depend on the dynamic characteristics and the local non-linear structural behavior. Virtual building portfolios consisting of thousands of FE models can now be generated with the SBP-Tool developed at the University of Kassel. Their seismic risk can be assessed within a reasonable time frame by using an efficient algorithm, which has been developed for hybrid simulations in combination with parallel computing.

In order to validate such sophisticated FE-models, mechanically consistent scaling [Dorka 2013] may be used with advantage since it preserves local behavior in a global analysis without sacrificing computational speed. This has been shown for welded composite beam-column connections under static loading [Amorntipsakul 2013] and further work is under way to extend it to cyclic loading.

This will also enable a realistic analysis of local repair costs as a function of certain local mechanical states that are reached under a certain seismic hazard. This may then lead to a realistic assessment of economic risk for such structures. Then, realistic virtual portfolios can be created for steel-concrete composite frame buildings in order to assess damage costs in regions where no or little event data are available.

REFERENCES

- Amorntipsakul, S., (2013), „Generic Finite Element Model For Mechanically Consistent Scaling Of Composite Beam-to-column Joint With Welded Connection“, Dissertation at the University of Kassel, Kassel, Germany.
- Bayer, V., Dorka, U. E., Füllekrug, U. and Gschwilm J. (2005). „On real-time pseudo-dynamic substructure testing: algorithm, numerical and experimental results”. *Aero. Sc. and Tech*(9): 223-232.
- Bode, H (1998). “Euro-Verbundbau: Konstruktion und Berechnung”, 2. Auflage, Werner Verlag, Düsseldorf, Germany
- Brzev, S., Scawthorn. C., Charleson, A.W., Jaiswal, K. (2012) Interim Overview of GEM Building Taxonomy V2.0, GEM Foundation
- Dorka, U.E., Heiland, D. (1991).“ Fast online earthquake simulation using a novel pc supported measurement and control concept”, *Proc. 4th Int. Conf. Structural Dynamics*, Southhampton: 636-645.
- Dorka, U. E. (2002). “Hybrid experimental - numerical simulation of vibrating structures”, *Proceedings of the International Workshop WAVE 2002*: 183 - 191. Okayama, Japan.
- Dorka, U. E (2013). “Mechanically consistent scaling of composite beam-column joints”, *Advances in Structural Engineering Vol. 15 No. 9, 1609-1618*.
- DUOWEI, Web page:
http://www.duowei.net.cn/en/images/userfiles/1351148949_170.jpg,
 Accessed 27th of June 2013
- GEM, Web page: <http://www.globalquakemodel.org/>, Accessed 27th of February 2013
- HDF5, Web page: <http://www.hdfgroup.org/HDF5/>, Accessed 27th of February 2013
- Huber, G. (2000), “Non-linear calculations of composite sections and semi-continuous joints”, Ernst&Sohn, Berlin, Germany.
- Mazzieri, I., Stupazzini, M., Guidotti, R., Smerzini, C. (2013). “SPEED-Spectral Elements in Elastodynamics with Discontinuous Galerkin: a non-conforming approach for 3D multi-scale problems”, *International Journal for Numerical Methods in Engineering*(2013) ol. 15 No. 9, 1609-1618. itecnico di Milano
- Mühlhausen, A., Dorka, U., Smolka, A. and Stupazzini, M. (2011). Improving Seismic Risk Assessment for the Insurance industry by using 3-D Finite Element Modelling. *The 2011 World Congress on Advances in Structural Engineering and Mechanics*, Seoul, South Korea
- Mühlhausen, A., Dorka, U., Smolka, A. and Stupazzini, M. (2012). Seismic Risk Assessment for Masonry Buildings based on Discriminant Analysis of a Virtual Database. *Proceeding of the 15th World Conference on Earthquake Engineering*, Lisbon, Portugal

- Obón-Santacana, F. and Dorka, U.E. (2012). Effects of Large Numerical Models in Continuous Hybrid Simulation. *Proceeding of the the 15th World Conference on Earthquake Engineering*, September 12-17, 2012, Lisbon, Portugal.
- SLang – The Sturctural Language (2004), Veit Bayer, Maik Brehm, Christian Bucher, et. Al. Documentation. Institute of Structural Mechanics - Bauhaus-University Weimar

Shear-Bond Behaviour of Steel-Fibre Reinforced Concrete (SFRC) Composite Slabs with Deep Trapezoidal Decking: Experimental Study

Fairul Abas¹; Mark A. Bradford²; Stephen J. Foster³; and R. Ian Gilbert⁴

Centre for Infrastructure Engineering & Safety, School of Civil & Environmental Engineering, Univ. of New South Wales, Sydney, NSW 2052, Australia. E-mail: fairul@unsw.edu.au¹; m.bradford@unsw.edu.au²; s.foster@unsw.edu.au³; i.gilbert@unsw.edu.au⁴

Abstract

This paper describes part of an on-going research project within the Centre for Infrastructure Engineering and Safety at UNSW on an investigation of the strength behaviour of SFRC composite slabs having deep steel trapezoidal decking. It describes three groups of short-term load tests on single-span SFRC composite slabs, the test methodology being adopted from Eurocode 4 for the determination of the values of the parameters m and k . The aim of the tests was to study the effect of the presence of steel fibres to the longitudinal shear-bond strength at the interface between the steel profiled sheet and the SFRC concrete slab. The load-deflection responses and the end slips were closely monitored in order to gain a clear insight into the shear-bond behaviour of the test specimens. The concrete properties, including its compressive strength, tensile strength, modulus of elasticity and fracture energy were measured on companion specimens for every test group. The results were used to calculate the longitudinal shear bond strength by using partial interaction theory to provide benchmark experimental results.

Keywords: Composite slabs; Steel-fibre reinforced concrete; Partial shear connection; Trapezoidal profiles; Shear bond.

1. INTRODUCTION

Composite steel-concrete flooring slab systems are used widely in contemporary building construction. The understanding and the application of this structural system have been in place for many years. Composite slabs with deep trapezoidal steel decks are gaining a favourable reputation as economic load carrying members and this system is a very efficient form of construction. In a steel-concrete composite slab, the profiled steel sheet acts as the bottom, tensile reinforcement in the positive moment region of the slab. The strength of the composite slab depends, however, on the longitudinal shear resistance at the interface between the concrete slab and the profiled steel sheeting (Oehlers and Bradford, 1995). Current practice uses plain concrete reinforced with conventional reinforcing mesh for early-age shrinkage control and fire resistance purposes.

The use of steel fibres in concrete as an alternative (or supplement) to conventional reinforcement is now a mature technology, after almost 40 years of

experience and extensive research being devoted to the technology. The variety of fibres being produced and used by the construction industry is growing steadily, and the range of application of steel fibre reinforced concrete (SFRC) is expanding. The inclusion of steel fibres in concrete has been shown to improve the post-cracking behaviour of a reinforced concrete member, both in terms of crack control and ductility. Therefore, the viability of combining composite steel-concrete slabs and steel fibres warrants investigation, and is addressed in the present paper.

However, as with all composite slabs, their strength relies heavily on the resistance to vertical separation and to horizontal slippage between the contact surface of the concrete and the profiled steel sheet. Previous research findings have indicated that the failure of the steel-concrete structure takes place in a horizontal section of the slab close to the support. At failure, the interface of these two materials is disjoined and displaced in relation to each other (Vainiūnas *et al.* 2006). Therefore, it is crucial that this strength aspect of a composite slab system is established prior to its application in practice. An understanding of how the steel fibres affect the longitudinal strength of a composite slab system is much needed.

Specifically, this paper describes three groups of short-term static load tests on single-span composite slabs. The aim of the tests was to study the behaviour and the shear-bond strength of composite slabs with steel fibre dosages of 30 kg/m^3 and 60 kg/m^3 in comparison to a control slab without steel fibres.

2. BACKGROUND

2.1. General

The shear bond and the failure mechanisms related to it are quite complex and difficult to predict (Chen and Shi 2011; Sohel *et al.* 2012). The failure mechanisms of composite slabs are an important aspect in determining the overall behaviour of composite slabs. The fundamental strength characteristic of a composite steel-concrete structural slab is the transfer of forces (or the shear connection) between the two components at the surface of the concrete and the steel sheeting. In steel-concrete composite slabs, the shear connection is in two directions i.e. along the secondary steel beams where it is achieved by headed stud connectors located in the trough of the decking, and along the ribs in the profiled steel sheet orthogonal to the ribs where it is achieved through friction, adhesion and aggregate interlock. The interaction between the concrete and steel generates shear bond between them that dictates their load-carrying capacity.

Composite steel-concrete slabs may fail in different modes depending on the shear span length, the total span length and the effectiveness of the interaction at the interface. For the case of a simply supported slab, the locations of the three modes of failure are shown in Fig. 1. Failure type 1 (flexural) occurs when the bending resistance of the slab is exceeded at the point of maximum applied moment (near mid-span, position 1 in Fig. 1). This is the critical mode of failure, particularly for slabs in excess of 4.5 m long with high degrees of interaction between the concrete and profiled steel sheeting (Lopes and Simões 2008). Failure type 2 (longitudinal shear) occurs when the ultimate longitudinal shear resistance at the interface is exceeded (position 2 in Fig. 1). This failure associated with a significant amount of

slip at the end of the slab. Failure type 3 (shear) occurs near the support (position 3 in Fig. 1) when the applied load is greater than the shear resistance of the slab. This is generally critical for short deep slabs.

Generally in typical composite slab construction using normal plain concrete with slab spans between 2 m to 4.5 m, the failure mode is by longitudinal shear (Johnson 2004, Lopes and Simões 2008) and longer spans are prone to flexural failure. Hitherto, research in the failure of composite slabs has focused on plain concrete, and little guidance is available for slabs with SFRC.

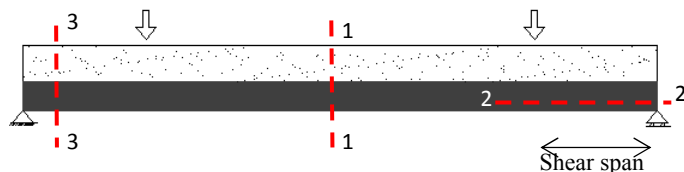


Figure 1: Location of critical section for the failure mode in composite slab.

Eurocode 4 (BSI 2004) prescribes the so-called *m-k* method and the partial shear connection method for determining the strength of composite slabs. These two methods require full-scale laboratory testing. The *m-k* method is the most common method for determining the shear-bond strength of a newly designed profiled steel deck shape and section, giving the strength in terms of the shear capacity of the member under consideration. The partial shear connection method translates the value of the longitudinal shear strength to the limit of bending capacity of the composite slab under consideration.

2.2. Shear bond strength using the m-k method

The evaluation of the longitudinal shear bond resistance by using the *m-k* method was first proposed by Porter and Ekberg (1975), who expressed the relationship between the vertical shear load and the shear span by the equation

$$\frac{V_u s}{bd_p} = m \left(\frac{A_p}{bL_s} \right) + k (f'_c)^{0.5}, \quad (1)$$

where V_u is the maximum shear load (in N); s is the spacing of the shear transferring devices; d_p is the depth of the extreme compression fibre of the slab to the centroid of the profiled sheet (in mm); f'_c is the compressive strength of the concrete (in MPa); A_p is the cross-sectional area of the profiled steel sheet (in mm²) and b is the breadth of the composite slab (in mm). The values of m and k are empirical and are determined experimentally. Because Eq. (1) produces unsatisfactory results when the variation of f'_c is wide, it has been omitted to produce the Eurocode design strength equation

$$V_{1,Rd} = \frac{bd_p}{\gamma_{vs}} \left(m \frac{A_p}{bL_s} + k \right), \quad (2)$$

where the partial factor γ_{vs} is taken as 1.25. Empirically, two different shear spans L_s are tested as in Fig. 2 which is taken from Eurocode 4, and linear regression of the lowest value in the group reduced by 10% produces the line shown in Fig. 2. The longitudinal shear stress at failure is then

$$\tau_u = \frac{V_u}{b \times d_p}. \quad (3)$$

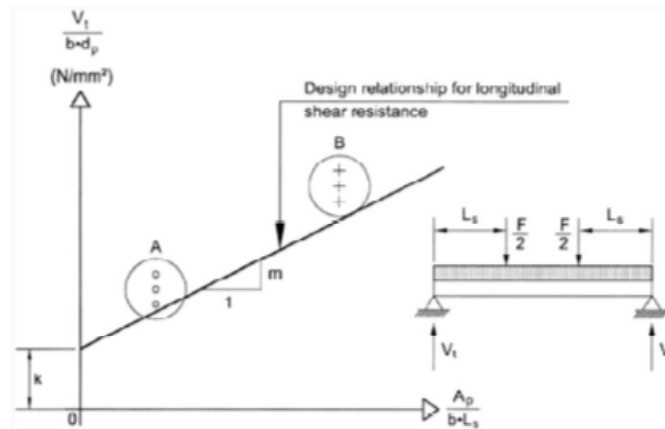


Figure 2: The m-k method as outlined by Eurocode 4.

2.3. Shear bond strength using the partial shear connection method

An alternative method to evaluate the longitudinal shear strength τ_u of a composite slab is the partial shear connection method, which is also in Eurocode 4. Based on rigid plastic analysis (Oehlers and Bradford 1995), the flexural capacity of the composite slab is calculated using a simple stress block for the concrete and the profiled steel sheeting, as shown in Fig. 3. The flexural capacities are calculated at the two extremities of the interaction between the concrete slab and the profiled steel sheeting, and between these two extremities the beam has partial shear connection. As a result, the degree of the shear connection between the concrete slab and the profiled steel sheeting can be assessed, which governs the failure of the beam. The failure load and its corresponding bending moment will determine the degree of interaction from the interaction diagram shown in Fig. 3. It is assumed that before the maximum moment of the member is reached, there is a complete redistribution of longitudinal shear stress at the interface between the concrete and the steel sheeting, and therefore the value of τ_u is calculated.

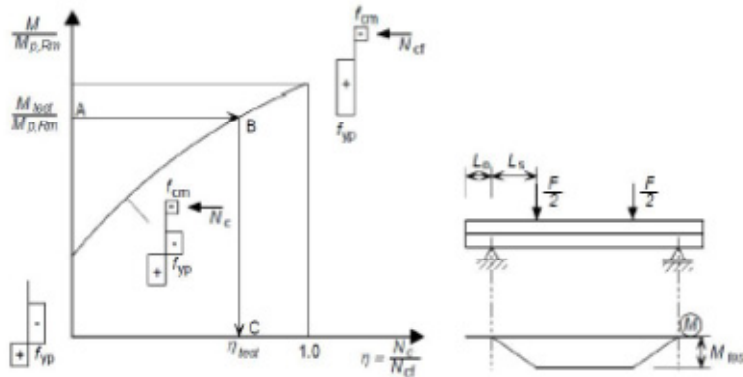


Figure 3: Determining the degree of shear connection from M_{test} as outlined in Eurocode 4.

According to Eurocode 4, this method is only applicable to a slab specimen that exhibits ductile longitudinal shear behaviour, which requires the failure load to exceed the load causing a recorded end slip of 0.1 mm by more than 10%. For any given type of single span composite slab system, a plot of the value of the degree of shear connection η versus the dimensionless bending capacity can be constructed. The degree of shear connection of the test specimen is obtained by interpolating the path of the corresponding flexural capacity obtained experimentally as shown in Fig. 3. Therefore, the longitudinal shear strength τ_u can be calculated from

$$\tau_u = \frac{\eta N_{cf} - \mu P / 2}{b(L_s - L_o)} \tag{4}$$

where η is the degree of shear connection, N_{cf} is the value of compression force in the concrete flange with full shear connection, L_o is the length of the overhang in the specimen and L_s is the shear span of the test specimen. The term $\mu P / 2$ is considered when the friction at support reaction is accounted where P is the total load and μ is the coefficient of friction. If the effect of friction is ignored, then this term can be neglected. Based on rigid plastic theory, the degree of shear connection is also defined by

$$\eta = \frac{N_c}{N_{cf}}, \tag{5}$$

where N_c is the compression force in the concrete and N_{cf} is the compression force in the concrete flange with full shear connection. The strength of the composite slab M_R is derived using the degree of shear connection η from

$$M_R = zN_c + M_{pa}, \tag{6}$$

where z is the lever arm of stress block and M_{pa} is the plastic moment of resistance of the profiled steel sheeting alone.

2.4. Force equilibrium method

The interface behaviour between the sheeting and the concrete slab can also be represented by the shear bond-slip behaviour. The common method to investigate the shear bond-slip behaviour is by conducting a push-out test for the given profiled steel deck specimen. However, the shear bond-slip relationship can also be obtained from full scale testing by using the force equilibrium method. The method was used by An *et al.* (1993) to calculate the relationship of shear bond against the end slips of composite slabs specimen.

Fig. 4 shows a free body diagram of the composite slab at failure and the corresponding strain and internal force acting across the section. For moment equilibrium of this free body diagram,

$$C_c = T_s = \frac{PL_s/2 - M_r}{z} \tag{7}$$

The bending capacity of the sheeting M_r can be determined from the deformed profile shown in Fig. 5. The curvature $1/R$ is related to the moment by

$$\frac{M_r}{E_s I_s} = \frac{1}{R} = \frac{(\delta_1 + \delta_2)}{L_s(L - 2L_s)} \tag{8}$$

where the deformations δ_1 and δ_2 and lengths L and L_s are shown in Fig. 5.

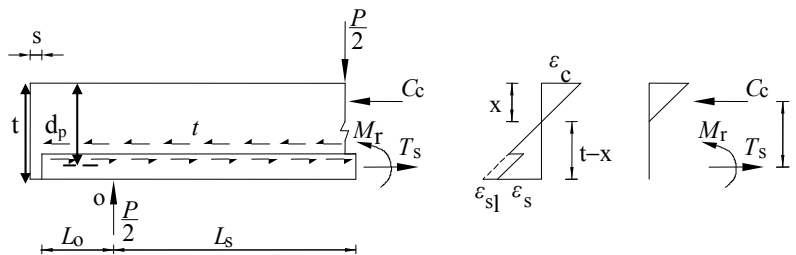


Figure 4: Free body diagram of the shear span, strain variation and internal forces.

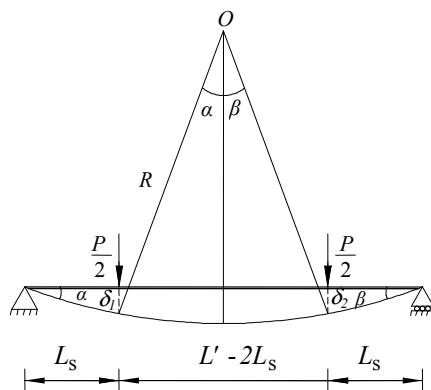


Figure 5: Deflection and curvature of the composite slab test specimen.

The moment lever arm z depends on the location of the neutral axis of the composite slab section, and it can be obtained from the experimentally measured strains. With the measured strain in the steel ε_s and strain in the concrete ε_c and the slip strain ε_{sl} , the lever arm can be calculated from

$$z = d_p - x/3, \quad (9)$$

where

$$x = \left(\frac{\varepsilon_c}{\varepsilon_c + \varepsilon_s + \varepsilon_{sl}} \right) \times t \quad (10)$$

and d_p and t are the distance from the extreme compression fibre to the centroid of the profiled steel sheeting and the overall slab thickness respectively. The longitudinal shear bond stress is assumed to be uniformly distributed along the horizontal shear span contact area, and given by

$$\tau_{avg} = \frac{T_s}{b \times (L_s + L_o)}, \quad (11)$$

while if the support reaction is considered for which the friction coefficient is given by μ , the longitudinal shear stress is given by

$$\tau_{avg} = \frac{F - \mu P/2}{b \times (L_s + L_o)}. \quad (12)$$

3. TEST SETUP

Single-span composite slabs fabricated using deep-trapezoidal steel sheeting (W-deck) of yield strength $f_{yp} = 650 \text{ N/mm}^2$, and steel fibre reinforced concrete were cast and loaded by static and cyclic load patterns up to failure. Three (3) groups of specimens were constructed from a ready-mix concrete containing steel-fibres with dosages of 0 kg/m^3 , 30 kg/m^3 and 60 kg/m^3 of end hooked fibres high strength steel (Dramix RC80/60 BN). In total, 17 single-span composite slab specimens were cast

and moist cured for a period of 28 days and then loaded to failure. The specimens were divided into 3 major groups: 5 slabs in Group 1; 6 in Group 2 and 6 in Group 3, according to the dosage of steel fibres. Each specimen was 3.5 m long (3.3 m between supports) and the average depth of all slabs was 140 mm. The concrete properties, including compressive strength, tensile strength, modulus of elasticity and fracture energy, were measured on companion specimens for every slab tested. An elevation and cross-section of a typical slab is shown in Fig. 6. For each specimen, the deflection at mid-span, the crack widths near the loading points and slip between the decking and the concrete at both ends of the slab were recorded at each load increment from zero to failure of the specimen. Also recorded continuously throughout the tests were the applied loads and the reactions at each support.

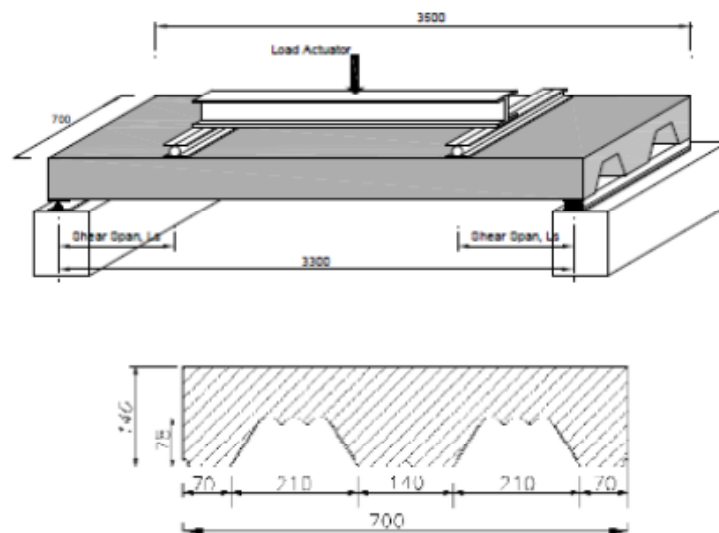


Figure 6: Dimensions and section of slabs.

Figure 7 shows the formwork used in the construction of the specimens. Prior to casting each specimen, the inside surfaces of the timber side and end forms were cleaned and thinly coated with a concrete release agent to prevent adhesion of the concrete and to facilitate removal of the timber forms. The steel decking was continuously supported on the floor and remained there for 28 days. Companion specimens were also cast at the same time as the slab specimens. These were 150 mm diameter cylinders, for measuring the compressive stress-strain relationship and compressive strength, and 150 mm × 150 mm × 600 mm prisms for measuring flexural tensile strength and fracture energy.

Table 1: Details of test specimens.

Slab ID	t (mm)	Shear span (mm)	Fibre dosage (kg/m ³)	Loading	f_c (MPa)
Group 1 – Plain concrete slab					
S1-A-0	145	825	0	static	50
S2-A-0	142	825	0	static + cyclic	50
S1-B-0	143	420	0	static	50
S2-B-0	145	420	0	static + cyclic	50
S3-B-0	143	420	0	static + cyclic	50
Group 2 – 30 kg/m ³ steel fibres					
S1-A-30	142	825	30.67	static	45.3
S2-A-30	146	825	30.67	static + cyclic	45.3
S3-A-30	142	825	30.67	static + cyclic	45.3
S1-B-30	142	420	30.67	static	45.3
S2-B-30	146	420	30.67	static + cyclic	45.3
S2-B-30	148	420	30.67	static + cyclic	45.3
Group 3 – 60 kg/m ³ steel fibres					
S1-A-60	142	825	64.62	static	52.3
S2-A-60	143	825	64.62	static + cyclic	52.3
S3-A-60	145	825	64.62	static + cyclic	52.3
S2-B-60	142	420	64.62	cyclic	52.3
S2-B-60	144	420	64.62	static + cyclic	52.3
S2-B-60	147	420	64.62	static + cyclic	52.3

**Figure 7: Formwork and slab immediately after casting.**

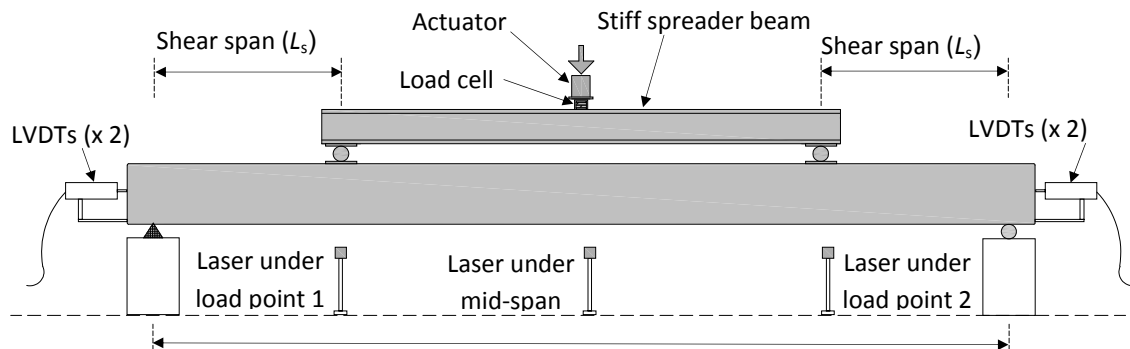


Figure 8: Test setup and loading arrangement.

Fig. 8 shows the spreader beam arrangement. Load was applied at the third-span points in both spans. The initial load, comprising of the self-weight of the slab, the weight of the spreader beams and the weight of all packing used in each test, was measured at the beginning of the test as the sum of the reactions measured by the load cells at each support.

60 mm long hooked end steel fibres (RC80/60BN) were used in the test specimens. The properties of the steel fibres are given in Table 2. The steel fibres were mixed to the required dosages in the back of the concrete truck in the laboratory. The quantities of the measured steel fibre added to the concrete for each test specimen were calculated and the exact dosage was calculated after mixing using standard wash-out tests.

Table 2: Nominal properties of steel fibres.

Steel fibre	Diameter (mm)	Length (mm)	Mean tensile strength (MPa)	Elastic modulus (GPa)
RC80/60BN (L)	0.75	60	1225	200

The instrumentation included: (1) laser transducers, each with an accuracy of 0.01 mm, to measure the deflection of the slabs at the mid-point of each span; (2) load cells to measure the actuator loads (3) LVDTs to measure the slip between the steel deck and the concrete at each end of the slab; (4) surface mounted strain gauges and Demec gauges to measure concrete strain at the top surface of the slab at the loading points.

The test procedure for all groups was identical. Load was applied by a servo-controlled Instron hydraulic actuator via longitudinal and transverse spreader beams based at two different positions for the shear spans. The long shear spans were at $\frac{1}{4}L$ and $\frac{3}{4}L$ of the span length L while the short shear spans were symmetrically at 420 mm measured from the each support. The applied load was measured by using a calibrated load cell that was placed directly under the actuator. The loading procedure was in accordance with the guidelines given in Eurocode 4 with some minor modification of the determination of the range of cyclic loading. One slab from each series of every group was tested with static load only while the other two slabs of the

same series were tested with 5000 cycles of loading for a duration of 3 hours, prior to loading to failure under increasing load. The first slab from each series was tested with static load only in order to determine the level of cyclic load for the other two slabs in the same series. The initial test (cyclic load test) was conducted by applying the cyclic load with the lower and upper limit of 20% and 60% of the failure load respectively obtained from the first slab tested with static load only. The failure load was taken as the load that produced substantial slips causing the load to drop significantly and this value was taken from each of the first slab from each series that was tested with only static load.

4. TEST RESULTS

For each group of test specimens, accompanying material testing was also conducted. A summary of the material test results is given in Table 3.

Table 3: Material test results.

Slab ID	Compressive strength (MPa)	Elastic modulus (MPa)	Direct tensile strength (MPa)	Flexural tensile strength (MPa)	Fracture energy (Nm)
Group 1	50.0	30,900	4.20	4.67	125
Group 2 (30kg/m ³)	45.3	30,100	3.84	6.20	5,300
Group 3 60kg/m ³)	52.3	27,500	4.38	7.57	11,800
Group 3 (S1-A-60)	49.0	24,300	4.28	8.27	19,190

The results for the tests for the long shear span (series A) and short shear span (series B) are shown in Tables 4 and 5 respectively. All specimens behaved in a similar manner. Fig. 9 shows the load versus deflection response of the slab specimen in series A loaded with static load only. The first-crack load occurred at relatively low load: the plain concrete slab cracked at the load of 10 kN; that with a fibre dosage of 60 kg/m³ cracked at slightly higher load of 14 kN. Slab specimens loaded with the short shear span had higher cracking loads compared to the long span series, ranging from 15 kN to 25 kN as well as higher peak loads than the series A slabs as shown in Fig. 10. The loading continued with a reduced stiffness up to the point where the slip between the deck and the concrete occurred. The load dropped as the first slipping occurred.

The end slip was also recorded electronically. Tables 7 and 8 show the key values of load at 0.1 mm slip and the recorded slip at failure for every slab specimen in each series respectively. It can be seen from the tables that significant slip occurred at failure. The ratios of $P_u/P_{0.1}$ are all greater than 1.1 which classify the slab behavior as ductile in accordance with Eurocode 4. The end slip versus applied load for the slab specimens tested with static load from both series A and B are shown in Figs. 11 and 12 respectively. The slab with a long shear span and with a dosage of 60kg/m³ was not instrumented with electronic transducers to measure the

end slips, but rather with mechanical gauges. As such, the reading obtained was deemed considerably inaccurate and omitted from the results.

Slip took place at both ends of the test specimen. It was observed that the slip rates were different between the two ends. As the load increased, the cracked constant moment region became noticeably larger and eventually the slabs failed due to the loss of longitudinal shear strength resulting in significant interface slip at the shear span region as shown in Fig. 13.

Table 4: Test results for Group A (shear span = 825 mm).

Slab ID	Peak load P_u (kN)	Cracking load P_{cr} (kN)	Cracking moment M_{cr} (kNm)	Ultimate moment M_u (kNm)	Moment ratio M_u/M_{cr}	Deflection at failure d_{max} (mm)
S1-A-0	37	10	4.13	15.26	3.700	64
S2-A-0	33	10.75	4.43	13.61	3.070	61
S1-A-30	44.8	12	4.95	18.48	3.733	60
S2-A-30	50	11.75	4.85	20.63	4.255	58
S3-A-30	47	12.75	5.26	19.39	3.686	72
S1-A-60	52.6	14	5.78	21.08	3.650	32
S2-A-60	51	16.75	6.91	21.04	3.045	45
S3-A-60	55.75	15	6.19	23.00	3.717	67

Table 5: Test results for Group B (shear span = 420 mm).

Slab ID	Peak load P_u (kN)	Cracking load P_{cr} (kN)	Cracking moment M_{cr} (kNm)	Ultimate moment M_u (kNm)	Moment ratio M_u/M_{cr}	Deflection at failure d_{max} (mm)
S1-B-0	59	20	4.20	12.39	2.950	26
S2-B-0	59.5	21	4.41	12.45	2.833	48
S3-B-0	57	21.5	4.51	11.97	2.651	42
S1-B-30	91.5	20	4.20	19.21	4.575	57
S2-B-30	90.5	25	5.25	19.00	3.620	44.5
S3-B-30	94	15	3.15	19.74	6.267	43
S1-B-60	100.3	22	4.62	21.06	4.545	36
S2-B-60	108.5	18	3.78	22.78	6.028	52
S3-B-60	111.3	19	4.00	23.37	5.842	55

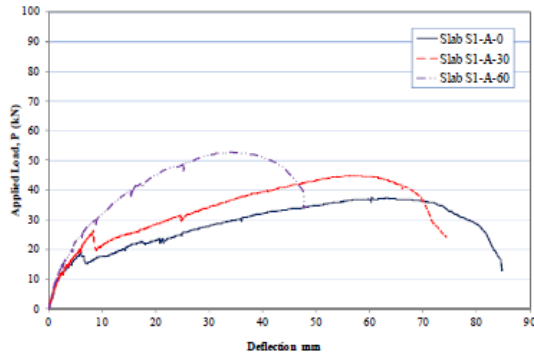


Figure 9: Load-deflection for Series A.

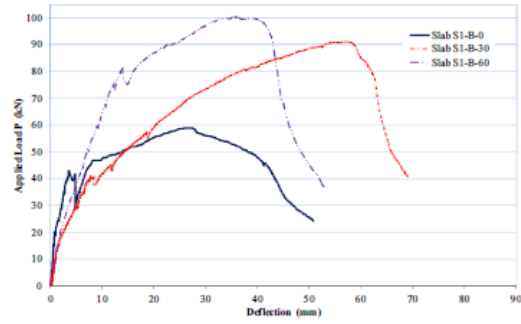


Figure 10: Load-deflection for Series B.

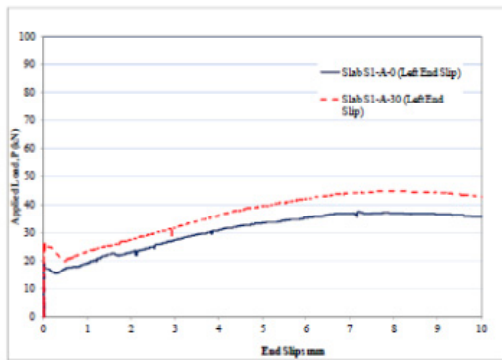


Figure 11: Load-slip for Series A.

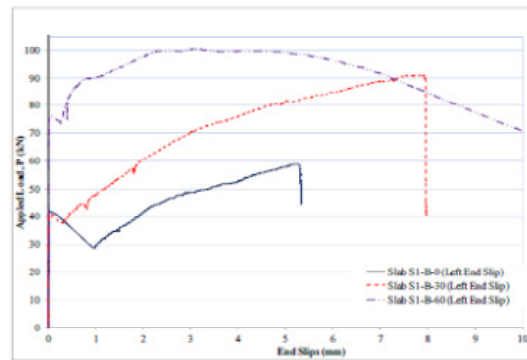


Figure 12: Load-slip for Series B



Figure 13: Typical slab failure.

Table 6: Slip results for Group A (shear span = 825 mm).

Slab ID	Load at 0.1 mm slip. $P_{0.1}$ (kN)	Peak load P_u (kN)	Ratio $P_u/P_{0.1}$	Slip at failure S_f (mm)
S1-A-0	17.5	37	2.1	7.6
S2-A-0	21.0	33	1.6	4.7
S1-A-30	26.2	44.8	1.7	8.1
S2-A-30	32.7	50	1.5	8.1
S3-A-30	17.0	47	2.7	9.8
S1-A-60	-	51.1	-	-
S2-A-60	31.0	51	1.6	6.0
S3-A-60	30.7	55.75	1.8	6.5

Table 7: Slip results for Group B (shear span = 420 mm).

Slab ID	Load at 0.1 mm slip. $P_{0.1}$ (kN)	Peak load P_u (kN)	Ratio $P_u/P_{0.1}$	Slip at failure S_f (mm)
S1-B-0	42.5	59	1.4	5.5
S2-B-0	40	59.5	1.5	7
S3-B-0	40.75	57	1.4	5.8
S1-B-30	41	91.5	2.3	8
S2-B-30	46.5	90.5	1.9	7.5
S3-B-30	34	94	2.8	8.5
S1-B-60	76	100	1.3	4.5
S2-B-60	47.5	108.5	2.3	7.2
S3-B-60	57.7	111	1.9	6.5

5. EVALUATION OF SHEAR BOND STRENGTH

5.1. m-k Procedure

As discussed in Section 2, plots of the type shown in Fig. 2 are needed to obtain m and k . These are given in Figs. 14 to 16.

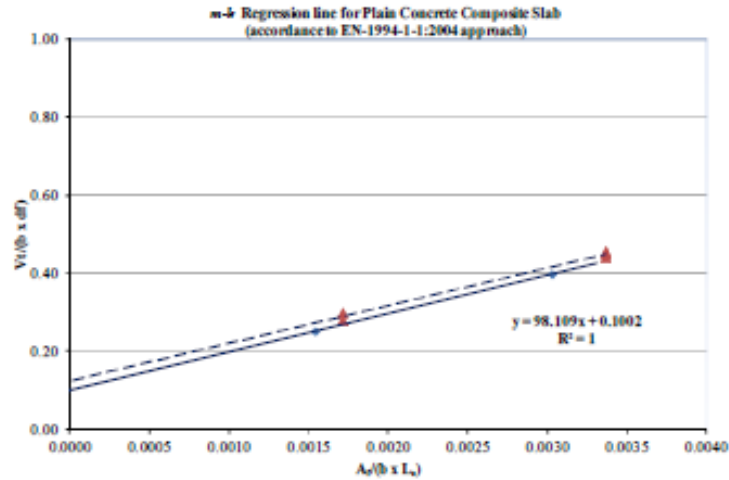


Figure 14: m-k regression for plain concrete slab.

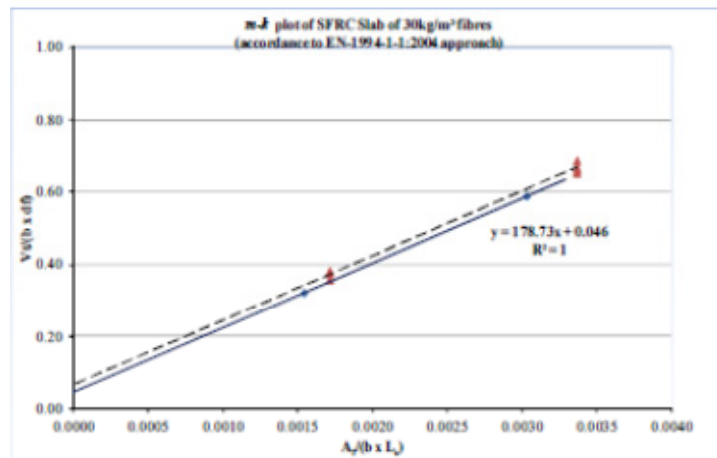


Figure 15: m-k regression for slab with 30 kg/m³ fibre dosage.

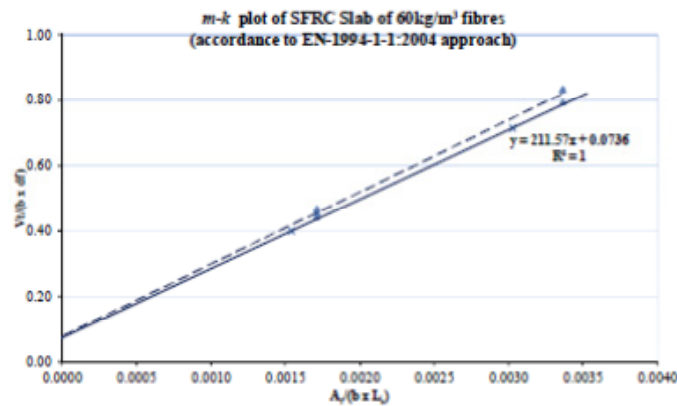


Figure 16: m-k regression for slab with 60 kg/m³ fibre dosage.

Table 8: m-k parameters from tests.

Slab type	m (MPa)	k (MPa)	τ_u (MPa)
Plain concrete composite slab	98	0.100	0.27
Composite slab with 30kg/m ³ steel fibres	179	0.046	0.35
Composite slab with 60kg/m ³ steel fibres	209	0.038	0.40

5.2. Partial Shear Connection Procedure

In order to determine the longitudinal shear strength τ_u in Eq. (4), a plot of the type shown in Fig. 3 and discussed in Section 2 is needed. To simplify the spreadsheet construction of the curve, values of $\eta = 0, 0.2, 0.4, 0.6, 0.8$ and 1 were assumed, and the graph is given in Fig. 17.

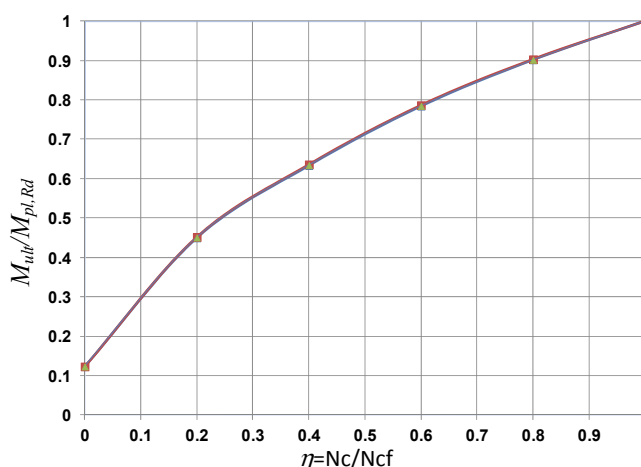


Figure 17: Interaction diagram for Series A (shear span = 825 mm).

In determining the plastic moment of resistance of the composite slab, the plastic moment for the profiled sheeting alone is needed, and this needs an effective area to be calculated to account for local buckling of the thin steel sheeting (Oehlers and Bradford 1995). The effective area can be computed from the effective width b_{eff} , taken as

$$b_{eff} = \frac{857t_s}{\sqrt{f_{yp}}} \left(1 - \frac{857t_s}{b\sqrt{f_{yp}}} \right) \leq \frac{b-15}{2} \text{ mm}, \quad (13)$$

where $f_{yp} = 650$ MPa is the yield strength of the profiled sheeting of thickness $t_s = 1$ mm.

The plastic moment of resistance of the plain concrete composite slabs ($M_{pl,Rd}$) for full interaction is 48.94 kNm while the plastic moment resistance of the profiled sheet alone (M_{pa}) is 5.80 kNm. The degree of interaction for each group was determined based on the ultimate bending moment obtained from the test results. The

values of degree of shear connection and the longitudinal shear resistance for each test group, ignoring the effect of friction at the support reaction, are tabulated in Table 9.

Table 9: Shear bond strengths.

Test Group	Slab ID	$M_{ult}/M_{pl,Rd}$	η	τ_u (MPa)	Average τ_u (MPa)
Plain concrete composite slab	S1-A-0	0.42	0.15	0.100	0.095
	S2-A-0	0.38	0.13	0.089	
SFRC Composite slab with 30kg/m ³ steel fibres	S1-A-30	0.50	0.20	0.138	0.147
	S2-A-30	0.55	0.23	0.158	
	S3-A-30	0.52	0.21	0.145	
SFRC Composite slab with 60kg/m ³ steel fibres	S1-A-60	0.58	0.24	0.165	0.167
	S2-A-60	0.56	0.23	0.158	
	S3-A-60	0.61	0.26	0.179	

5.3. Force Equilibrium Procedure

For the force equilibrium procedure, the moment lever arm is calculated based on strain gauge readings obtained at the top surface of the concrete, the bottom fibre of the profiled sheeting and from slip strains determined from the slip displacements at the end of the shear span. Figs. 18 and 19 show the shear stress versus end slip at both ends for plain concrete and SFRC with a dosage of 30 kg/m³. From these graphs, it can be seen that the slabs with SFRC have higher shear bond stress at the initiation of slip. It can also be seen that the initiation of slip is different at each end of the specimen (this is typical behaviour) and, as a result, different values of the longitudinal shear strength eventuate. The more ductile behaviour at the “high slip” end (Fig. 19) is associated with lower strengths than at the “low slip” end (Fig. 18). Table 10 presents the pertinent values of the longitudinal shear stress, viz. at first slip and at peak load.

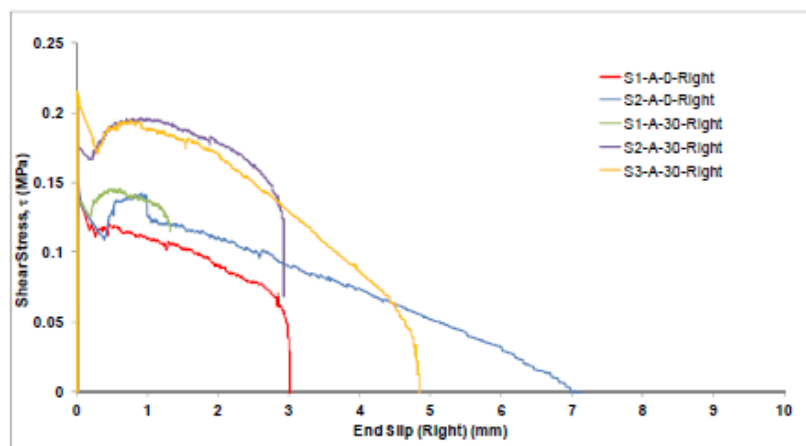


Figure 18: Shear bond stress versus slip at “low-slip” end.

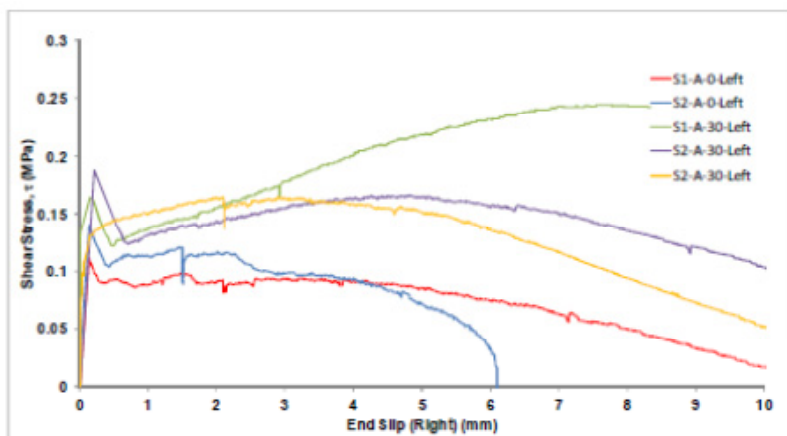


Figure 19: Shear bond stress versus slip at “high-slip” end.

Table 10: Pertinent values of longitudinal shear stress.

Slab specimen	Low-slip shear span			High-slip shear span		
	Shear stress at first slip (MPa)	Max. shear stress (MPa)	Slip at peak load (mm)	Shear stress at first slip (MPa)	Max. shear stress (MPa)	Slip at peak load (mm)
S1-A-0	0.136	0.147	2.84	0.118	0.137	7.60
S2-A-0	0.133	0.142	4.50	0.152	0.157	4.70
S1-A-30	0.134	0.146	1.30	0.165	0.245	8.14
S2-A-30	0.176	0.227	2.82	0.205	0.205	8.02
S3-A-30	0.205	0.218	3.90	0.126	0.215	9.80

The tensile strains in the steel sheeting were recorded electronically, and are given in Figs. 20 and 21, from which it can be seen that the steel strains are less than the yield strain of $3250 \mu\epsilon$ based on $f_{yp} = 650 \text{ MPa}$ and $E = 200 \text{ GPa}$.

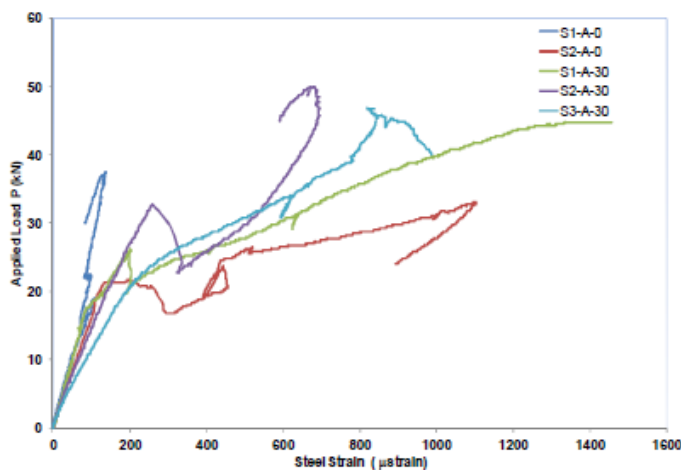


Figure 20: Steel strains in sheeting for load point closest to “low-slip” end

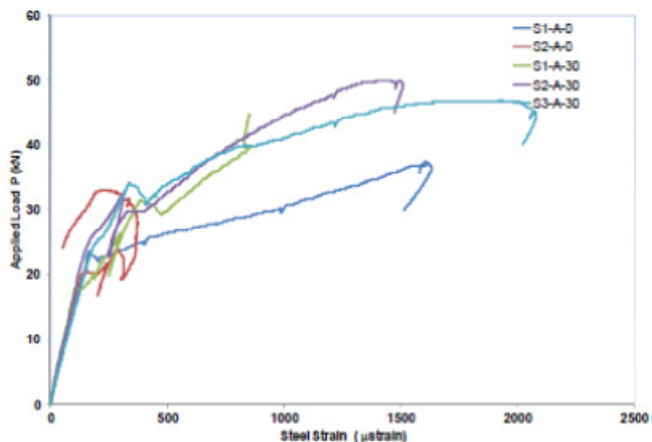


Figure 21: Steel strains in sheeting for load point closest to “high-slip” end

5.4. Discussion of Results

All composite slabs tested showed significant post-cracking moment capacity after first slip, and showed significant ductility prior to failure by longitudinal shear well below their flexural capacity. Table 11 compares the longitudinal shear strength between the plain concrete or SFRC slab and the steel sheeting. The $m-k$ method produces a higher value of the shear bond strength, whilst the results based on the partial shear connection and force equilibrium procedures are in close agreement.

6. CONCLUSIONS

An experimental program involving the full-scale testing of simply supported plain concrete and SFRC composite slabs with profiled steel sheeting were presented and discussed. All slab specimens were tested under four-point bending with shear spans of either 820 mm or 420 mm. The shear bond strength in the test specimens were assessed by $m-k$ procedure, the partial shear connection procedure and the force equilibrium procedure.

All slabs failed by longitudinal shear with substantial end slip displacements being recorded at both ends of the specimens with the sheeting remaining in the elastic range of structural response. Slabs containing steel fibres had higher peak loading and shear bond strengths compared to their plain-concrete counterparts. Additionally, the shear strengths derived from the $m-k$ procedure were higher than those determined from the partial shear connection and force equilibrium procedures, which showed closer agreement.

Table 11: Comparison of longitudinal shear strengths for longer shear spans.

Slab Specimen	Average longitudinal shear bond strength (MPa)		
	$m-k$	Partial interaction	Force-equilibrium
Plain concrete	0.27	0.095	0.152
SFRC with 30kg/m ³	0.35	0.147	0.230
SFRC with 60kg/m ³	0.40	0.167	-

ACKNOWLEDGEMENTS

The work reported in this paper was undertaken with the financial support of the Australian Research Council through Linkage Project LP0991495, BlueScope Lysaght Pty Limited and BOSFA Pty Limited. The second author was also supported by the Australian Research Council through Australian Laureate Fellowship FL100100063. This support is gratefully acknowledged.

REFERENCES

- An L. (1993) Load bearing capacity and behavior of composite slabs with profiled steel sheet. PhD Thesis, Chalmers University of Technology, Sweden.
- British Standards Institution (2004). Eurocode 4. London:BSI.
- Johnson R.P. (2004) Composite Structures of Steel and Concrete. 3rd edn. Oxford: Blackwell Publishing Limited.
- Lopes E. and Simões R. (2008) Experimental and analytical behaviour of composite slabs. *Steel and Composite Structures*, 8: 361-388.
- Oehlers D.J. and Bradford M.A. (1995) Composite Steel and Concrete Structural Members: Fundamental Behaviour. Oxford: Pergamon.
- Porter M., Ekberg C. (1975) Design recommendation for steel deck floor slabs. 3rd *International Specialty Conference on Cold-Formed Structures*, University of Missouri-Rolla, MO, 761-791.
- Chen S. and Shi X (2011) Shear bond mechanism of composite slabs - A universal FE approach. *Journal of Constructional Steel Research*, 67: 1475-1484.
- Sohel K.M.A., Liew J.Y.R, Yan Y.B., Zhang M.H. and Chia K.S. (2012) Behavior of steel-concrete-steel sandwich structures with lightweight cement composite and novel shear connectors. *Composite Structures*, 94: 3500-3509.
- Vainiūnas P., Valivonis J., Marčiukaitis G. and Jonaitis B. (2006) Analysis of longitudinal shear behaviour for composite steel and concrete slabs. *Journal of Constructional Steel Research*, 62: 1264-1269.

Analysis of Near to Free Surface Located Concrete Dowels in Composite Structures

Dipl.-Ing. J. Gajda¹ and Prof. Dr.-Ing. W. Kurz²

¹Institute of Steel Structures, Univ. of Kaiserslautern (TU), 67663 Kaiserslautern, Germany. E-mail: joanna.gajda@bauing.uni-kl.de

²Institute of Steel Structures, Univ. of Kaiserslautern (TU), 67663 Kaiserslautern, Germany. E-mail: wolfgang.kurz@bauing.uni-kl.de

Abstract

Over the last decades, composite structures made of steel and concrete have been developed in order to allow for the economic and competitive construction of buildings and bridges. A main challenge of such structures is the design of the connection between the concrete and steel sections because of high requirements for the load-bearing capacity and ductility. Currently, headed shear studs are the only shear connectors regulated in Eurocode 4 (EN 1994-1-1 2010). In addition to common vertical shear studs, other shear connectors have been tested over the past decades. Concrete dowels, which are novel and versatile shear connectors, have been most extensively investigated. For the application in slender concrete slabs, for example in sandwich constructions (Figure 1), vertical headed studs and concrete dowels are not suitable, as they are limited by their height. In these constructions, it is possible to apply horizontally positioned concrete dowels. This paper deals with the experimental results of horizontally positioned concrete dowels in push-out tests.

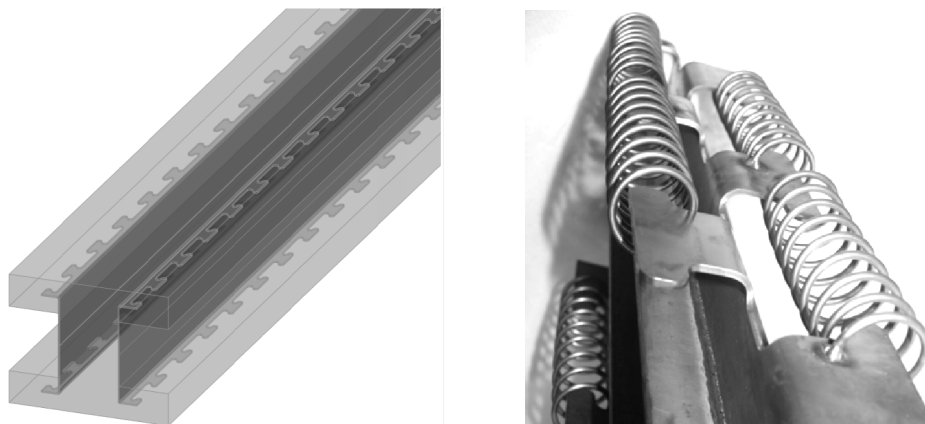


Figure 1. Example of a possible application (left) and spiral reinforcement (right).

INTRODUCTION

Conventionally, shear studs are installed vertically in the concrete slab of a composite structure. However, in some constructions also lying shear studs with a

parallel configuration of the shear connector axis to the plane of the concrete slab are applied. These lying shear studs were already investigated in [Kuhlmann and Breuninger 1998] and [Kürschner 2003] and included in the EC4 [EN 1994-2 2006]. An economical alternative to shear studs are the more frequently used concrete dowels, also known as puzzle strips.

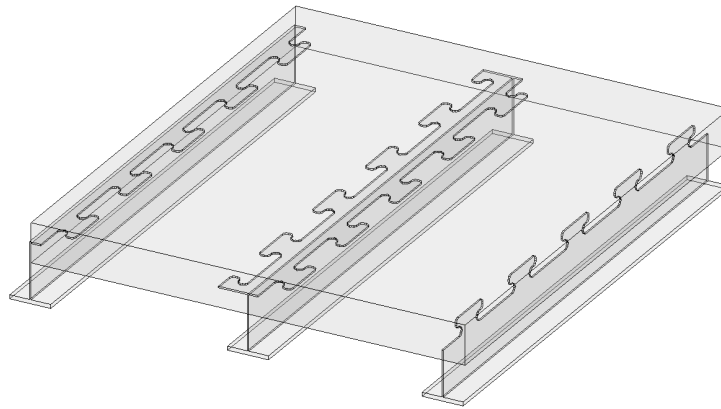


Figure 2. Positions of concrete dowels located close to a free surface.

The interest in the use of concrete dowels in innovative composite structures is increasing. However, normative rules for puzzle strips are still required. Concrete dowels could be used in novel composite concepts in a horizontal or vertical position close to the edge, as shown in Figure 2. Cross-sections are economic as no additional welding work is required. Optimized composite constructions are very effected due to optimal utilization of the material properties.

Examples of those dowel positions are VFT-WIB[®] beams with puzzle shaped openings. Such construction with rolled-steel section as an external reinforcement has already been realized in several projects (see examples in [Seidl and Braun 2009]). The previously investigated beam cross-sections with a short lateral surface distance to the puzzle strip have been primarily developed for the use in bridge constructions. For this reason, the width of the concrete web is 250 mm or more (e.g. [Seidl 2009], [Wagner 2010] and [Burger 2011]). In building construction, in which the composite strip is horizontally lying installed, a significantly lower lateral concrete cover to the concrete dowel may occur.

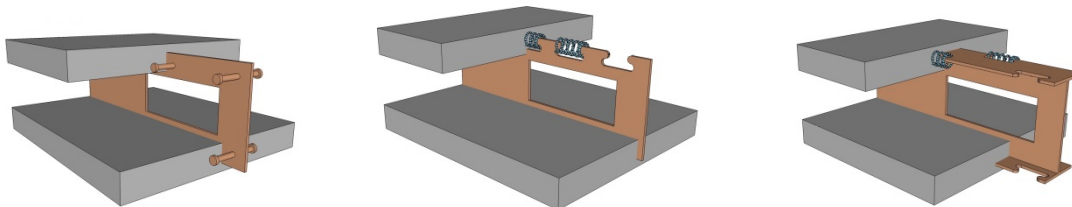


Figure 3. Sandwich constructions by the company Innogration [innogration]

In some modern slim floor constructions and sandwich composite structures concrete dowel strips parallel to the concrete flange plane can be used. Such sandwich composite floors (see Figure 3) have been realized e.g. [Abramski et al. 2010]. Composite cross-sections with lying shear studs as well as with standing concrete dowels were applied. As a next step an alternative solution to the horizontal headed studs, with economic advantage, puzzle shaped concrete dowels were integrated (see [Friedrich 2009] and [Friedrich 2011]).

However, the current design concepts were developed for vertically embedded concrete dowels. Horizontally and vertically close to the edge arranged concrete dowels shown similar influence of the position in the concrete slab. The failure mechanisms of lying or standing close to the edge located concrete dowels have been studied only to some extend.

The results of investigations for concrete dowels with influence will be discussed in this paper. Information about the load carrying behavior in a particularly slender construction with a low lateral concrete cover are displayed.

EXPERIMENTAL INVESTIGATIONS

As observed in the experiments with lying headed studs the specimen failed primarily by splitting of the concrete slab. To describe this failure, the studies on lying headed studs were mainly carried out with push-out tests. Because the shear connectors in composite constructions transmit primarily longitudinal shear, the near-edge concrete dowels were also investigated in push-out tests. These experiments should provide information on the longitudinal shear strength as well as on the ductility. Studies based on a slim concrete slab were conducted on concrete dowels with puzzle and clothoid shape and different concrete strengths and reinforcement designs.

MATERIALS AND CONSTRUCTION

The concrete dowel strips were made of steel sheets with steel grade S235JR and thicknesses of four and six millimeters. For the slender, 10 cm thick concrete slabs one concrete mixtures for a predicted concrete strength class C25/30 were used. The concrete slabs were reinforced with six or eight millimeter stirrups. To compare the influence of the stirrup reinforcement, test specimens without stirrups, or with one, two or three stirrups per dowel were performed. In addition to conventional stirrup reinforcement, tests with spiral reinforced concrete dowels were prepared and carried out. The spiral reinforcement provides a local confinement of the concrete at the zone of highest stresses.

Due to the confinement effect in the core of the spiral a multi-axial stress state is created, which leads to an increased load bearing capacity of the concrete. The positive effect of the spiral reinforcement has already been confirmed by [Abramski et al. 2010] and [Abramski et al. 2011]. The used spirals reinforcement had a diameter of 50 mm and were made of a five mm thick, smooth wire with a determined yield strength of 504-614 MPa. The pitch of the spiral was 25 mm, which

resulted in seven full turns of the spiral per concrete dowel. Figure 4 illustrates the investigated concrete dowel strips with two different cutout geometries and types of described reinforcement.

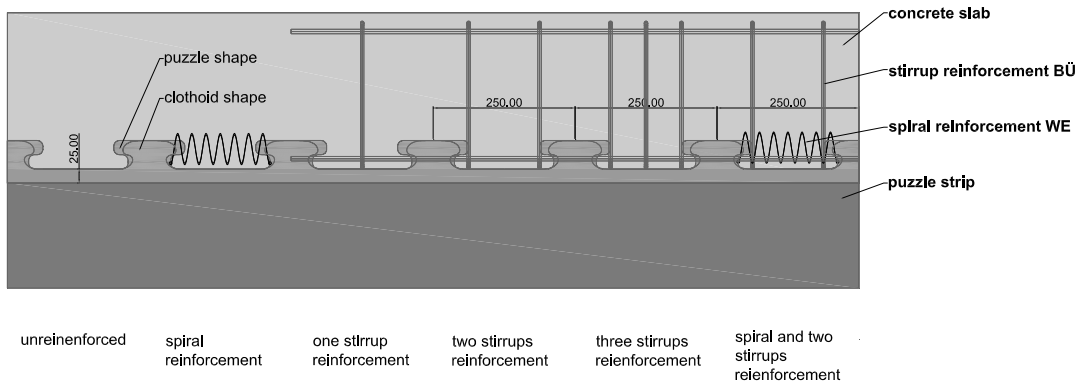


Figure 4. Continuously arranged concrete dowels

CONCRETE DOWELS

The concrete dowels are created by openings in the steel section, which are filled with concrete. Commonly, reinforcement bars are crossing these openings. Two different shapes of the opening of concrete dowel were tested, on the one hand a puzzle strips and on the other hand a clothoid shape of the cut-outs. The cut-outs were created by a corresponding flame-cut of the steel sheet. The axial distance of the concrete dowels was 250 mm. The exact geometry is shown in Figure 5. The composite dowel strip with this geometry is also suitable for designs with beveled teeth puzzle as shown in Figure 1. The height of the steel dowels was 50 millimeters, which were integrated with a concrete cover of 2.5 centimeters into the concrete slab (see Figure 4).

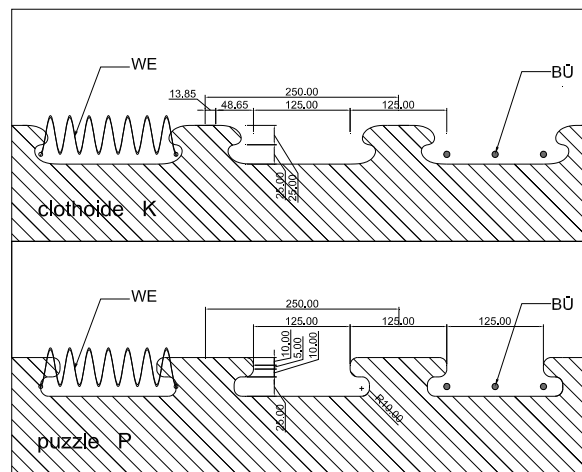


Figure 5. Concrete dowel shapes and types of reinforcement

PUSH-OUT TESTS

In total 38 push-out tests were carried out in several series. Standard push-out tests PO and experiments with beveled dowel strips (labeled POA) were performed. They were designed in accordance with the rules of the Eurocode 4 Annex B [EN 1994-1-1 2010]. For each set of parameters only one test was carried out. In addition to the load bearing capacity, the slip between the steel web and concrete slab in the direction of the applied force was measured in the experiments. The deformation of the concrete slabs perpendicular to the direction of the applied force, the uplift of the concrete slabs was measured. The measurement was made using LVDT's at several points over the height of the specimen.

In some experiments, the widening of the slab thickness was measured perpendicularly to the dowel axis. Information about the splitting cracks along the dowel axis was obtained. The resulting splitting forces in the concrete were transferred to transverse reinforcement. The strains in this reinforcement were measured with strain gauges.

Figure 6 shows an example of the experimental setup of a carried out push-out tests with the measurement equipment.

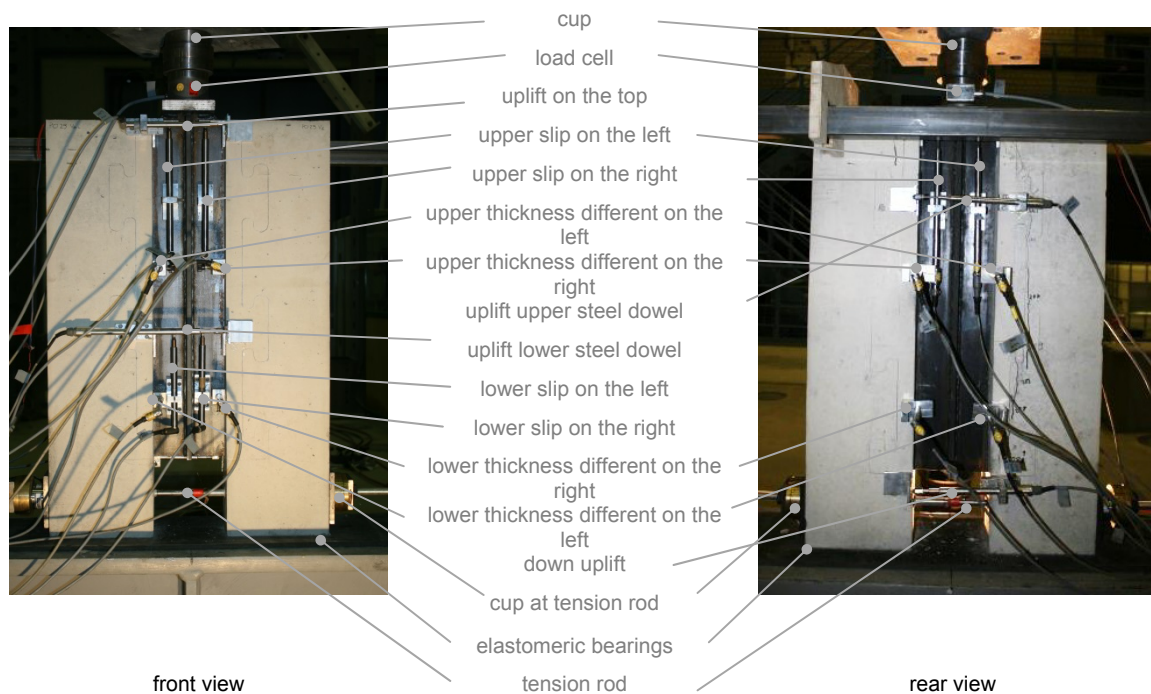


Figure 6. Set-up of the push-out tests

DISCUSSION OF THE TEST RESULTS

The four main parameters that can have influence on the bearing and deformation behavior of the concrete dowels are: material properties, reinforcement type and reinforcement configuration in the influence zone of the dowel and the concrete dowel topology. Therefore, the investigated parameters were primarily the shape of concrete dowel (puzzle and clothoid), the reinforcement type (spiral reinforcement WE and stirrups BÜ) and ratio, the steel web thickness ($t = 6$ mm and $t = 4$ mm) and the concrete strength class (C25/30, C30/37 and C35/45). The thickness of the concrete slab varied from 10 to 15 cm and the width of the concrete slab was varied between 20 and 30 cm (see Figure 10). Thus, the influence of the load introduction on the load bearing capacity could be verified in the experiment. Some typical results will be discussed.

INFLUENCE OF THE CONCRETE DOWEL SHAPE

Two different shapes of concrete dowel were tested in the push-out tests. On the one hand, a puzzle shape was investigated. On the other hand a clothoid shape was tested. The investigations showed that the cut-out shape of the concrete dowels had no significant influence on the structural behavior of concrete dowels (see Table 1). This could be observed in tests. The reason is that the capacity of the transverse reinforcement in the concrete dowel zone is decisive parameter for load capacity of this specimen. The stirrup reinforcement, which is located in the area of concrete dowel, takes the tensile forces after the formation of the first splitting cracks.

Table 1. Comparison of the bearing capacity of the concrete dowel with different geometries

clothoid shape				puzzle shape				ratio of max. load
speciment	reinforcement	series	max. load [kN]	speciment	reinforcement	series	max. load [kN]	
PO1	-	1	228,36	PO8	-	2	214,73	1,06
PO2	spiral	1	367,57	PO9	spiral	2	351,79	1,04
PO6	3Ø6	2	297,71	PO7	3Ø6	2	299,05	1,00
PO17	2Ø6	4	230,08	PO15	2Ø6	4	225,29	1,02

In case of the experiments without reinforcement the load capacities of the specimen with clothoid and puzzle shape differ by six percent. This can be explained by the lower tensile strength of concrete and smaller area of the concrete dowel in the experiments with puzzle shape. Very similar load-slip characteristics and the similar cracking pattern after reaching the maximum load confirms the small influence of the investigated concrete dowel shapes on the load bearing and deformation behavior of the near-edge shear connector.

INFLUENCE OF THE TYPE OF REINFORCEMENT

The load transfer of near-edge concrete dowels is comparable to conventional standing dowel strips (see [Wurzer 1997]). After exceeding the adhesion of the contact interface (static friction), further load increase with rising partly distributed stresses on the soffit surface between steel and concrete dowel. Due to the load application and confined almost hydrostatic stress states, the concrete transfers a stress several times higher than its uniaxial compressive strength.

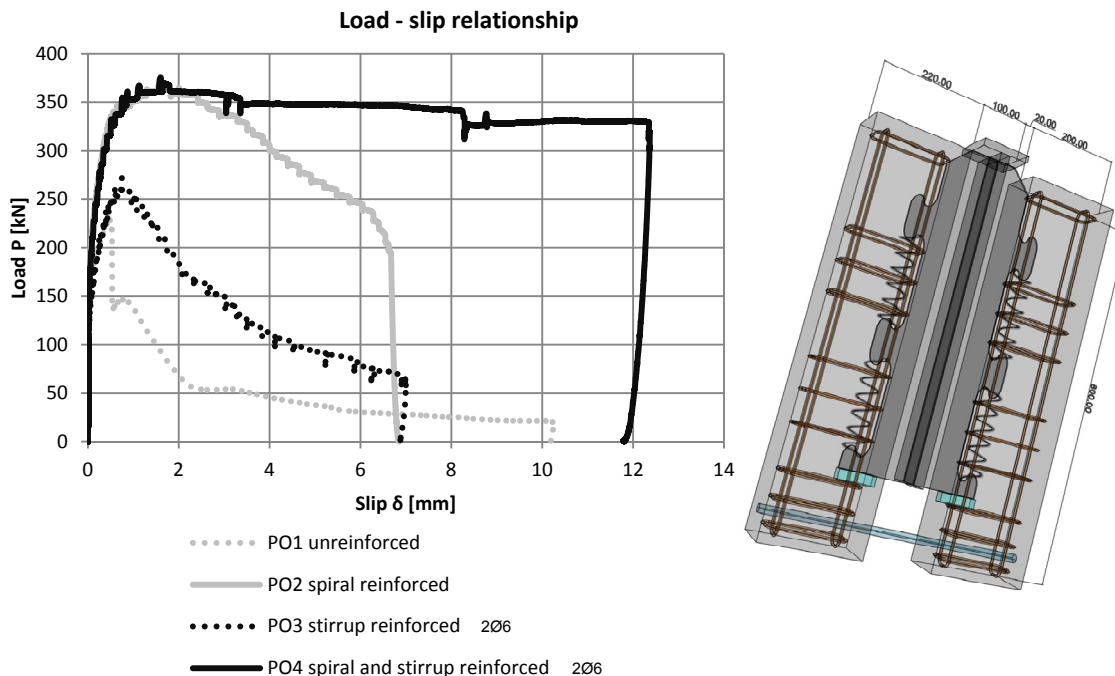


Figure 7. Geometry and load-slip curves of the push-out tests PO

This confinement is enhanced by the spiral reinforcement. The high stresses result in high loads, so that the matrix of the concrete is locally destroyed in the area of the contact surface. As long as the multiaxial state of compression in this area is maintained, a further load increase is possible. Depending on the type of reinforcement, the loads can be increased further through the enhanced concrete confinement correspondingly. The compression-struts spread out and transverse tensile stresses develop perpendicular to the concrete dowel axis. After the formation of cracks, the splitting forces are transferred by the existing transverse reinforcement. This plays a key role in the near-edge concrete dowel not only in terms of the maximum load, but also for its ductility.

Based on the tests and its load-slip characteristics the differences between the types of reinforcement are clearly visible. With reference to the load-slip characteristics of the push-out tests (see Figure 7), it can be seen that the specimen PO1 with unreinforced concrete dowels failed brittle after reaching the maximum load of 228 kN. The stirrup reinforcement in the test PO3 contributes only slightly to the increase of the maximum loads. The increase of the load compared to the

unreinforced test PO1 is about 19% to 272 kN. As a result the ductility of the shear connector is significantly improved. It can be seen that also the spiral reinforcement increases significantly the load bearing capacity of the push-out tests. Compared to test PO1, the load of PO2 was increased by 61% to 368 kN. The ductility was also improved in this case.

The analyses of load-slip curve of PO4 shows a two-fold improvement. Firstly, the combined spiral and stirrup reinforcement is characterized by a high shear load bearing capacity. Secondly, the ductility with combined reinforcement is excellent. Test PO4 shows a distinctive load plateau compared to the rest of the test configurations. Due to the stirrup reinforcement the maximum load at a high level was held until this test was interrupted at a slip value of 12.3 mm. The requirements of Eurocode 4 [EN 1994-1-1,2011] in limiting the deformation perpendicular to the force direction (uplift) were met in all the experiments.

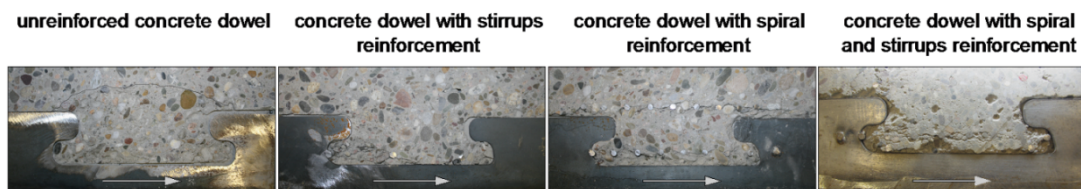


Figure 8. Push-out tests after cutting (first concrete dowel from top).

The block effect of more than one stirrup that has already been described in [Seidl 2009] was also observed. As shown in Figure 8, the confined concrete areas by stirrups or the spiral reinforcement are intact and able to absorb the additional stress. Comparison of the maximum loads of test specimens with one stirrup with a rebar diameter of 8 mm to two stirrups with a rebar diameter of 6 mm shows only a slight increase in load bearing capacity but a significant improvement in ductility. At the high load level, the steel dowels show plastic deformation. In this way the required ductility of the connection is achieved.

INFLUENCE OF CONCRETE STRENGTH

To investigate the influence of the concrete strength on the bearing behavior and ductility of the concrete dowel, experiments with three different concrete compressive strengths were examined. The studies show a significant increase in the stiffness when using a higher concrete strength. In addition, a significant increase in the bearing capacity was achieved. Especially in experiments without spiral reinforcement, the increase of the concrete strength led to an increase of stiffness (see Figure 9). The positive effect observed with the higher concrete strength class, corresponds with the simultaneous improvement of concrete splitting tensile strength (from 3.2 MPa to 4.4 MPa). The experiments with spirals show a smaller influence of the concrete strength. The initial stiffness with a higher concrete strength class is also growing in this case.

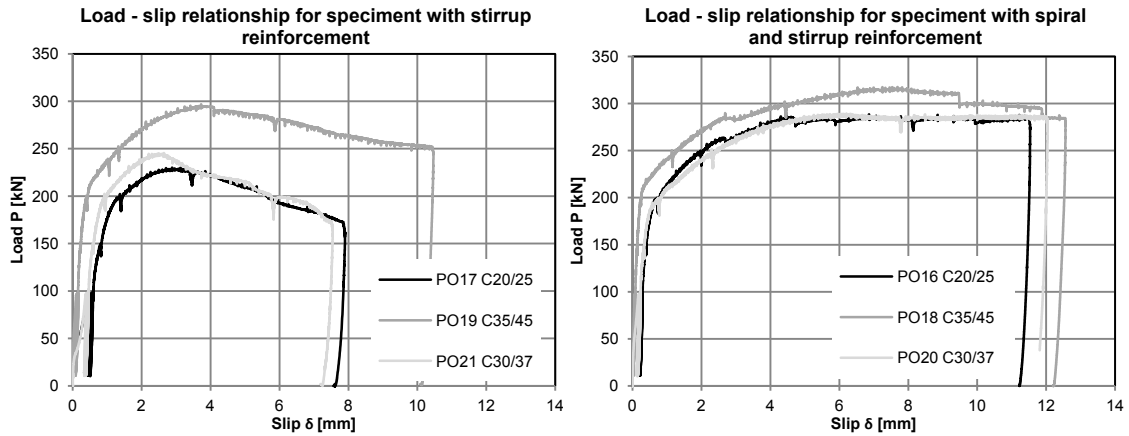


Figure 9. Comparison of load-slip curves for determining the influences of the concrete class.

INFLUENCE OF THE SUPPORT WIDTH

To evaluate the influence of the concrete slab width and the support length which determines the inclination of the compression struts, tests were made with width of 200 mm and 300 mm. The experiments PO26 and PO27 were supported only on the outer half of the support surfaces (see Figure 10). Due to the arrangement of the supports in the outer regions, the concrete struts must prop in these areas so that more horizontal stresses occur.

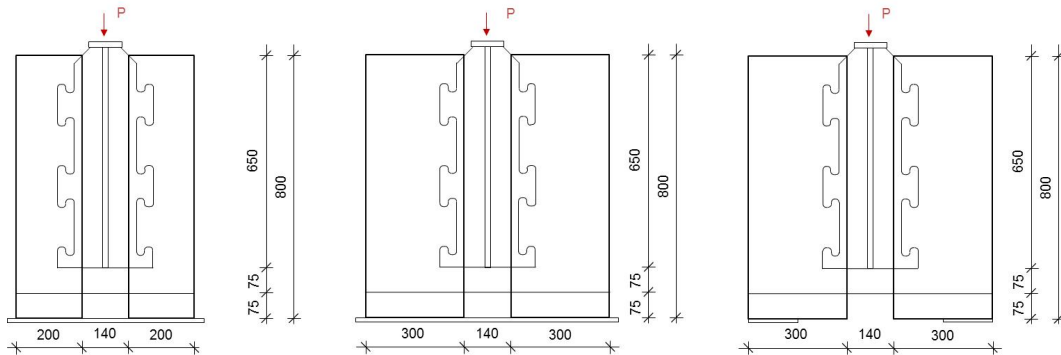


Figure 10. Support of the push-out tests.

As the load-deformation curve in Figure 11 shows, there is no significant effect on the load bearing capacity and ductility. However, the forces in tension rod increased with the increase of the inclination strut. The crack patterns correspond with the inclination of the strut. With increasing load, in the tests the cracks turn in the direction of the strut clearly.

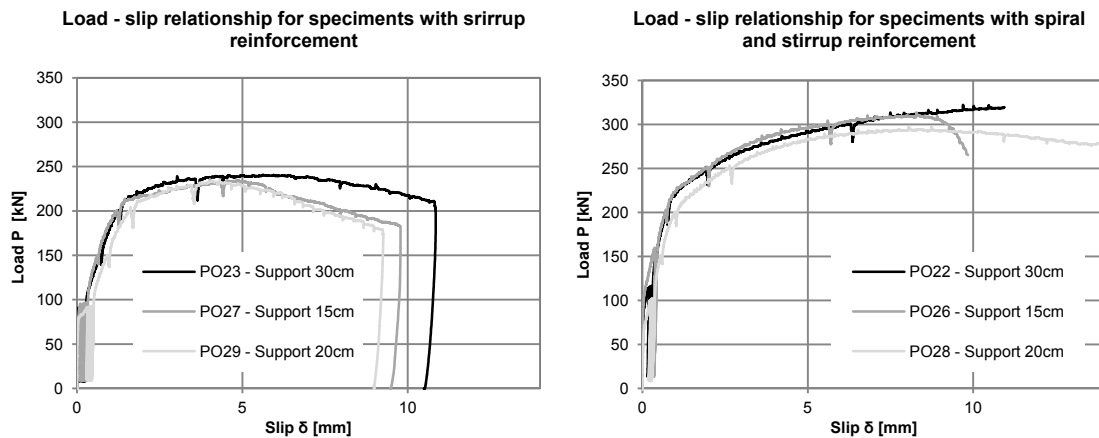


Figure 11. Comparison of Load-slip curves for determining the influences of the test support.

INFLUENCE OF THE PLATE THICKNESS

In further experiments, the thickness of the concrete slab was varied. The width of the slab was 30 cm and supported on the outer edge on a length of 15 cm. The thickness of the plate was chosen to ten and fifteen centimetres. As expected, the tests showed a significant increase of the load capacity at the high slip level (see Figure 12).

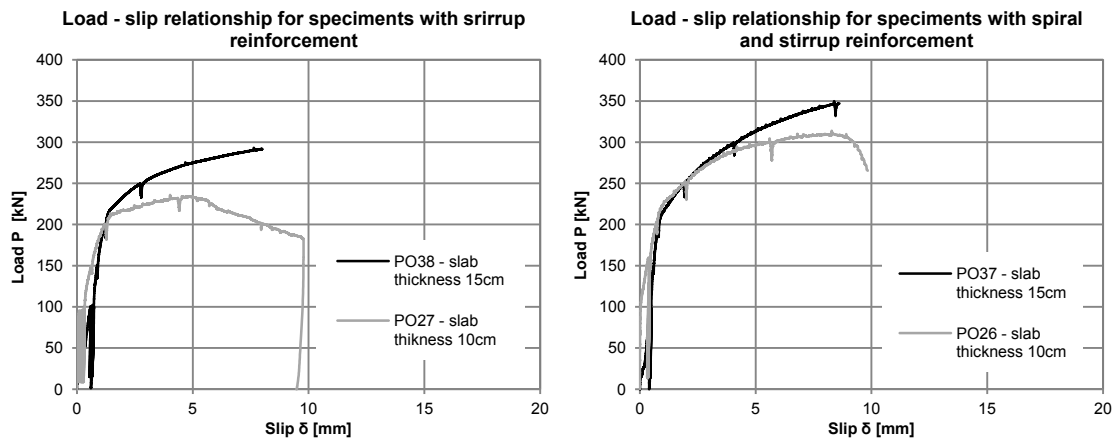


Figure 12. Load-slip curves for determining the influences of the slab thickness.

LOAD TRANSFER MECHANISM OF THE PUSH-OUT TEST

The spread of the stresses is limited by the slab edge for horizontally lying or near-edge located concrete dowels. In this case the high transversal stresses in the

concrete slab can lead to splitting in the slab plane. In all push-out tests, a lifting of the concrete slab perpendicular to the steel web was observed.

The measurement of the widening of the slab thickness at the height of the concrete dowels shows that already at a low load level first splitting cracks occur. The formation of the splitting cracks was confirmed by the results of first FE-simulations. The transverse tensile stresses occurred concentrated at the bottom of the concrete dowels and initiate splitting (see Figure 13).

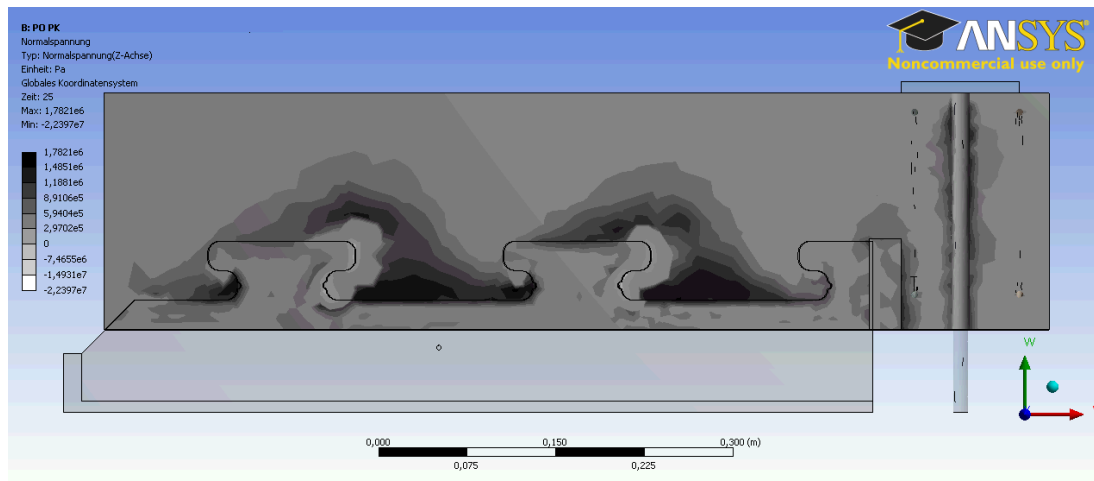


Figure 13. Transverse tensile stresses in the concrete.

SUMMARY

Concrete dowels with influence of the free concrete edge meet the requirements of ductile shear connectors if there are sufficient stirrups. The splitting of the slab was restrained by the arrangement of transverse reinforcement. The required stirrup reinforcement transfers not only the splitting forces and avoids a splitting failure, but favours the load capacity and ductility of the shear connectors. Mainly the arrangement of two transverse reinforcement bars per concrete dowel has a positive effect on the ductility (block effect). The concrete core of the dowel is hold in place by spiral reinforcement. Thereby, higher loads can be transferred. The experiments have shown that a higher concrete strengths and increased slab thickness have a positive impact on both capacity and the deformability of the puzzle strips.

ACKNOWLEDGEMENTS

The research project entitled „Tragwirkung randnaher Betondübel“ (grant number 964-52708-1/81029978) is generously sponsored by the state of Rheinland-Pfalz in the pilot projects InnoProm by means of MBWWK and EFRE.

REFERENCES

- Abramski, M., Friedrich, T., Kurz, W., Schnell, J. (2010). „Tragwirkung von Betondübeln für Sandwich-Verbunddecken mit großen Stegöffnungen“ *Stahlbau* 79, Heft 4, p. 248-258.
- Abramski, M., Schnell, J., Kurz, W. (2011). „Badania experimentalne niekonwencjonalnego zespolenia środnika stalowego z płytą betonową, Inżynieria i Budownictwo”, Warschau, *Fundacja PZITB*, Band 2.
- Burger, S. (2011). „Untersuchungen zum Ermüdungsverhalten von Betondübeln, *dissertation*, Universität der Bundeswehr, München.
- EN 1994-2: 2006-07 (2006). „Bemessung und Konstruktion von Verbundtragwerken aus Stahl und Beton, Teil 2: Allgemeine Bemessungsregeln und Anwendungsregeln für Brücken, Beuth-Verlag, Berlin 2006.
- EN 1994-1-1: 2010-12 (2010). „Bemessung und Konstruktion von Verbundtragwerken aus Stahl und Beton, Teil 1-1: Allgemeine Bemessungsregeln und Anwendungsregeln für den Hochbau“, *Beuth-Verlag*, Berlin.
- Friedrich, T. (2009). „Economical and innovative solutions with precast concrete”, *ICCX Oceania Sydney*, Australia.
- Friedrich, T. (2011) „Bei vorgespannten Betonfertigteildecken ist Haustechnik integriert“, *Allgemeine Bauzeitung* 50/2011, Patzer Verlag, Hannover.
- innogration <http://www.innogration.de/>
- Kuhlmann, U., Breuninger, U. (1998) „Zur Tragfähigkeit von horizontal liegenden Kopfbolzendübeln, *Stahlbau* 67, Heft 7, p. 547-554.
- Kürschner K. (2003). „Trag- und Ermüdungsverhalten liegender Kopfbolzendübel im Verbundbau“, *dissertation*, Universität Stuttgart, Stuttgart.
- Seidl, G. (2009). „Behaviour and bearing capacity of composite dowels in steel-concrete composite girders”, Raport serii PRE nr. 4/2009, *dissertation*, Wrocław University of Technology.
- Seidl, G. and Braun, A. (2009). „VFT-WIB-Brücke bei Vigaun - Verbundbrücke mit externer Bewehrung“, *Stahlbau* 78, Heft 2, p. 86-93.
- Wagner, R. (2010). „Untersuchungen zum Verbundverhalten von Betondübeln in vorwiegend ruhend und nicht ruhend beanspruchten Konstruktionen“, *17. DAST-Kolloquium* Weimar.
- Wurzer, O. (1997). „Zur Tragfähigkeit von Betondübeln“, *dissertation*, Universität der Bundeswehr, München.

Composite Dowels as Shear Connectors for Composite Beams - Background to a New German Technical Approval

Karsten Kathage¹; Markus Feldmann²; Maik Kopp²; Daniel Pak²; Max Gündel³; Josef Hegger⁴; and Joerg Gallwoszus⁵

¹Deutsches Institut für Bautechnik, Kolonnenstr. 30 B, 10829 Berlin, Germany. E-mail: kka@dibt.de

²Institute of Steel Construction, RWTH Aachen Univ., Mies-van-der-Rohe-Str. 1, 52074 Aachen, Germany. E-mail: feldmann@stb.rwth-aachen.de

³Wölfel Beratende Ingenieure GmbH & Co. KG, Max-Planck-Str. 15, 97204 Höchberg, Germany; formerly, Institute of Steel Construction, RWTH Aachen Univ., Mies-van-der-Rohe-Str. 1, 52074 Aachen, Germany. E-mail: guendel@woelfel.de

⁴Institute of Structural Concrete, RWTH Aachen Univ., Mies-van-der-Rohe-Str. 1, 52074 Aachen, Germany. E-mail: jhegger@imb.rwth-aachen.de

⁵Kempen Krause Ingenieure GmbH, Office Euskirchen, Mühlenstraße 5-7, 53879 Euskirchen, Germany; formerly, Institute of Structural Concrete, RWTH Aachen Univ., Mies-van-der-Rohe-Str. 1, 52074 Aachen, Germany. E-mail: joerg.gallwoszus@kempenkrause.de

Abstract

Composite dowels are known as powerful shear connectors in steel-concrete-composite girders. More and more they are used in practice especially for prefabricated composite bridges. Advantages over headed studs are in particular the increased strength, the sufficient deformation capacity even in high strength concrete and the simple application in steel sections without upper flange. However, missing provisions in standards for composite dowels with the economic clothoid and puzzle shape have led to retentions of clients and delays in the approval process. Hence, the aim of the recently finished German research project P804 founded by FOSTA-Research Association for Steel Application was to solve open questions concerning these innovative shear connectors and to prepare a general technical approval available for any design office and construction company. In this paper design concepts for ultimate limit state and fatigue limit state, structural design principles and instructions for production and construction are presented and background information are given.

INTRODUCTION

Composite dowels are shear connectors for composite beams, which consist of openings in steel plates, which are casted with concrete. They are either made of steel plates welded on the upper flange of the steel beam or are fabricated directly out of the web of steel beams. The main advantage against headed studs are the higher bearing capacity and a sufficient deformation capacity even in high strength concrete to be classified as ductile shear connectors acc. to EN 1994-1-1. Furthermore, composite dowels are particularly suitable and economic for composite section made

of steel sections without upper flange, as steel parts next to the neutral axis are reduced (Figure 1 left). Another economic application area is the arrangement of composite dowels in concrete T-beams as external reinforcement (Figure 1 right). In Figure 2 headed studs and composite dowels are compared in view of longitudinal shear capacity as well as composite bending capacity and bending stiffness.

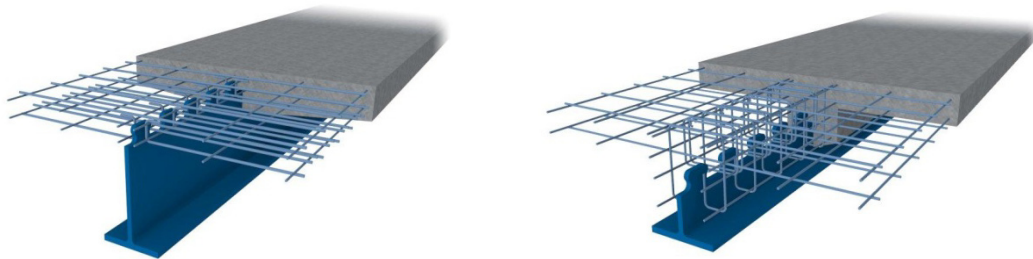


Figure 1. Application examples for composite dowels.

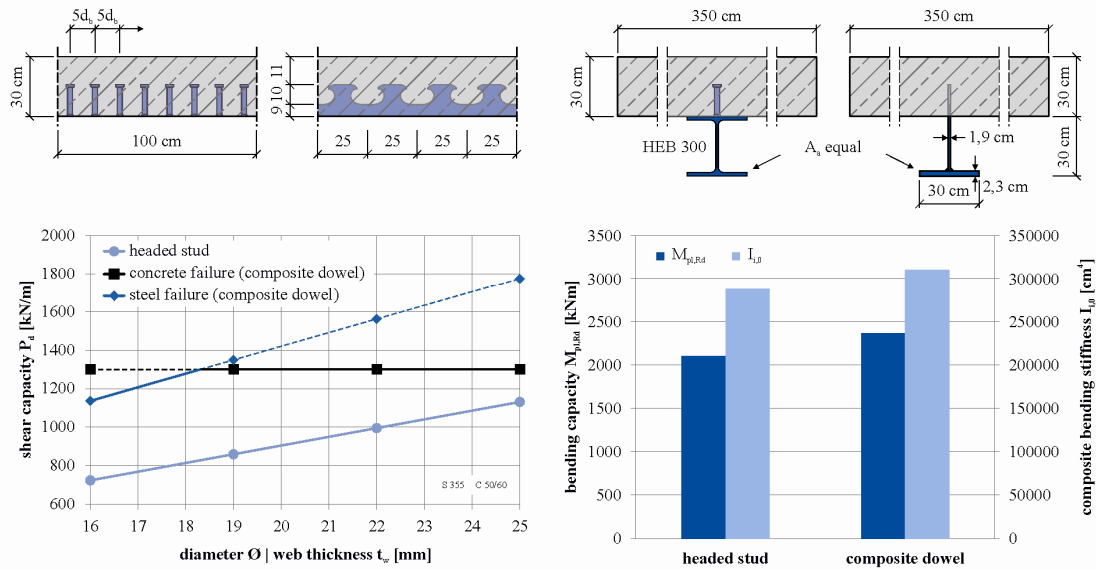


Figure 2. Comparison of longitudinal shear capacity between headed studs and composite dowels (left), comparison of moment capacity and stiffness between conventional composite section with headed studs and upper flange less steel section and composite dowels (right).

Up to now, the lack of technical rules for composite dowels led to delays in the approval process and to retention of clients. However, due to economic and technical advantages in more and more often composite dowels are used for road and railway bridges in Germany with approvals in the individual case. In addition, a specific prefabricated composite bridge type with a composite dowel in clothoid shape is approved by the German railway authority (EBA) and is applied e. g. in the railway bridge Simmerbach, Germany (Figure 3) [Feldmann et al. 2012a].

An extensive description of the main steps in the development of composite dowels can be found in [Feldmann et al. 2012b]. The starting point can be traced back to research of Andrä and Leonhardt, which led to the development of the Perfobond

strip [Leonhardt et al. 1987], [Deutsches Institut für Bautechnik 2007]. At the same time Bode developed the Kombidübel [Bode et al. 1988], [Deutsches Institut für Bautechnik 2000]. Both design concepts are based on the mechanical model for shear failure of the concrete dowel. In the following years important knowledge about the bearing behavior of composite dowels were gained at the University of German Armed Forces [Mangerig et al. 2011], [Mangerig et al. 2012]. From this, mechanical models for the exceedance of the partial area pressure of concrete in the opening and concrete pry-out for composite dowels next to the concrete surface were obtained. The development of composite dowels with puzzle shape were pushed by research projects at RWTH Aachen University [Feldmann et al. 2007], [Heinemeyer et al. 2012] and by HOCHTIEF [Gündel et al. 2009]. They led to a further development of the pry-out model and new models for steel failure. Seidl [Seidl 2009] developed design models for distance effects on concrete pry-out and vertical splitting of composite dowels in concrete T-beams. The beginning of the clothoid shape – an optimization for fatigue loading - can be found in [Berthelley et al. 2011a], [Berthelley et al. 2011b]. This shape was finally used for the prefabricated composite bridge type “VFT-Rail”, which is approved by the German railway authority (EBA) [Eisenbahnbundesamt 2010].



Figure 3. Bridges with composite dowels: road bridge in Pöcking [Seidl 2009] (left) and Simmerbach [Feldmann et al. 2012a] (right).

SCOPE OF THE GENERAL TECHNICAL APPROVAL

The new German general technical approval Z-26.4-56 [Deutsches Institut für Bautechnik 2013] regulates composite dowels in clothoid (CL) and puzzle (PZ) shape (Figure 4). The geometry can be scaled in dependence of the distance of the openings e_x between $150 \leq e_x \leq 500$ mm (notations see Figure 5). The lower bound ensures a sufficient shear area for a ductile behavior in the failure mode concrete shearing. The upper bound limits the maximum distance between composite dowels to prevent an unacceptable curtailment of the dowel capacity. The plate thickness can be between $6 \leq t_w \leq 60$ mm with a ratio of thickness to height between $0.08 \leq t_w / h_D \leq 0.5$. However, in the design formulas only a thickness of up to 40 mm is allowed to be considered. The minimum perpendicular distance of two steel plates is 120 mm to

ensure a sufficient installation of the reinforcement in between. For composite dowels structural steel in grade S235, S355 and S460 acc. to EN 10025 can be applied.

The minimum distance between concrete surface and top edge respectively base of the composite dowel is 20 mm (c_o ; c_u acc. to Figure 5). The distance from the opening to the concrete edge has to be in longitudinal direction more than 2.5 times the concrete pry-out cone h_{po} and in perpendicular direction more than 5.0 times of h_{po} . This ensures the full development of the concrete pry-out cone, if pry-out failure occurs. The minimum distance in perpendicular direction can be neglected, if in beam type sections the concrete reach to the steel flange and confinement stirrups are installed (see section “(iv) Additional verifications for beam-type sections”). This prevents pry-out at the lower concrete surface. The minimum width of beam type sections is 250 mm. The allowed concrete strength of the composite section is – equal to the range of EN 1994-1-1 – from C20/25 to C60/75.

Composite dowels can be used under sagging and hogging moment for static as well as fatigue loading. However, under fatigue loading structural members with centric tension forces perpendicular to the composite dowel are not allowed. For this, unacceptable deterioration of the shear connection can occur.

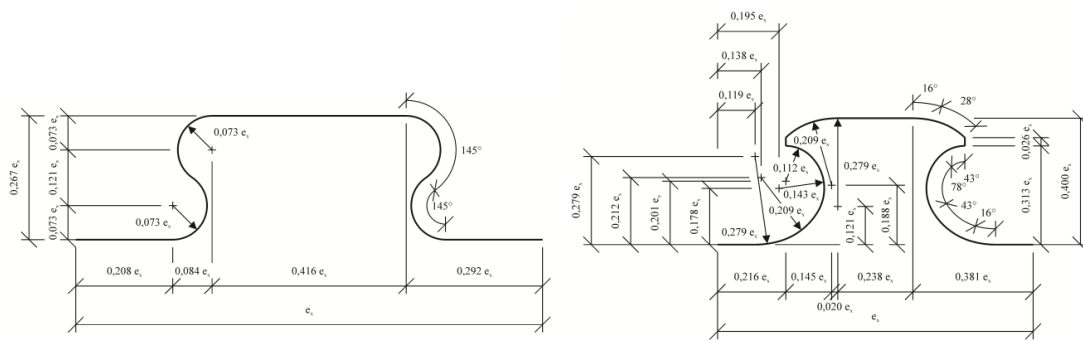


Figure 4. Definition of the composite dowel geometry puzzle shape (left) and clothoid shape (right).

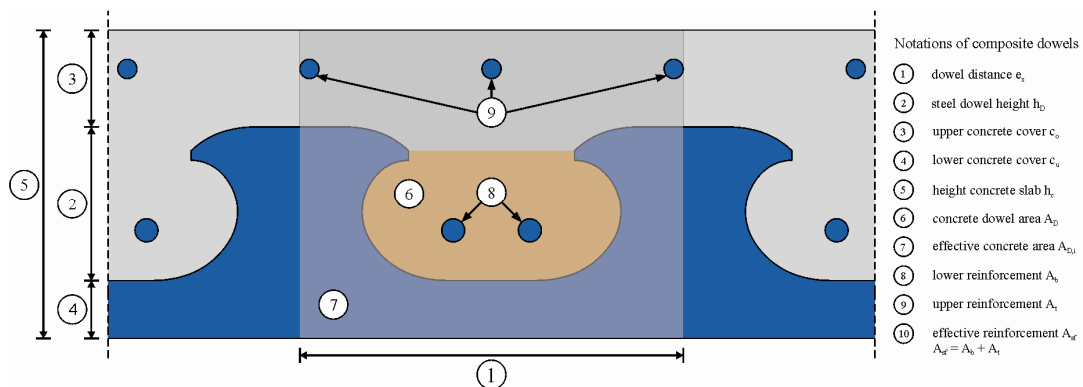


Figure 5. Notations of composite dowels (here: clothoid shape).

DESIGN CONCEPT

The design of composite beams with composite dowels is carried out in accordance with EN 1992, EN 1993 and EN 1994. The German general technical approval regulates only parts, which are not dealt with or are different to the European standards.

Besides the high bearing capacity the major innovation leap of these composite dowels is: the application in upper flange less composite section with equally spaced and partial shear connection; the ductility criterion acc. to EN 1994 is met to utilize plastic redistribution (only for static loading); a complete and consistent design concept for static and fatigue loading is provided for practical application.

LONGITUDINAL SHEAR CAPACITY (STATIC LOADING)

Possible failure modes of composite dowels subjected to static loading are (i) concrete shearing, (ii) concrete pry-out and (iii) steel failure. The characteristic longitudinal shear capacity P_{rk} is determined as the minimum capacity of the aforementioned failure modes. The design value is calculated with the characteristic bearing capacity divided by a partial safety factor of $\gamma_r = 1.25$.

The design formulas for these three failure modes are derived from existing, modified or new developed mechanical models and a statistical evaluation of test results. The quality of different design concepts is compared by the ratio between experimental and theoretical values of a huge test data base [Feldmann 2012b]. Criteria are the shift of mean value and the coefficient of variation. The mechanical models with the highest quality are used to derive design formulas by the statistical evaluation procedure in EN 1990 Annex D.

(i) Concrete shearing

Particularly for small openings and large steel plate thicknesses the dominating failure mode is double shearing of the concrete dowel. Therefore, the main parameters for the bearing capacity are the shear area of the concrete dowel and the shear strength of the concrete. Furthermore, the bearing capacity is affected by the transversal reinforcement within the opening due to an additional dowel effect. In large openings the two shear areas merge together, which is considered by a geometry depended reduction factor η_D ($\eta_{D,CL} = 3 - e_x/180$, $\eta_{D,PZ} = 2 - e_x/400$). For sufficient large openings, which are guaranteed by the application range of the general technical approval, concrete shearing is a ductile failure mode.

$$P_{sh,k} = \eta_D \cdot e_x^2 \cdot \sqrt{f_{ck}} \cdot (1 + \rho_D) \quad \text{in [N/dowel]}$$

$$\text{with } \rho_D = \frac{E_s \cdot A_b}{E_{cm} \cdot A_D}$$

$$A_{D,CL} = 0.20 \cdot e_x^2 \quad \text{and} \quad A_{D,PZ} = 0.13 \cdot e_x^2$$

All notations are shown in Figure 5.

(ii) Concrete pry-out

Low distances between concrete dowel and concrete surface (top or bottom concrete cover) may provoke a failure mode, which is similar to the concrete pry-out of anchors subjected to shear forces. The hydrostatic pressure condition at the load introduction zone generates transversal tension forces, which lead - for insufficient concrete covers - to a cone-shape concrete pry-out (Figure 6). The pry-out can occur for top or bottom concrete cover depending on the position of the concrete dowel. The result is a loss of hydrostatic pressure condition in front of the dowel, which causes a secondary concrete pressure failure. This failure mode is ductile.

$$P_{po,k} = 90 \cdot h_{po}^{1.5} \cdot \sqrt{f_{ck}} \cdot (1 + \rho_{D,i}) \text{ in [N/dowel]}$$

with $h_{po} = \min(c_o + 0.07 \cdot e_x; c_u + 0.13 \cdot e_x)$

$$\rho_{D,i} = \frac{E_s \cdot A_{sf}}{E_{cm} \cdot A_{D,i}}$$

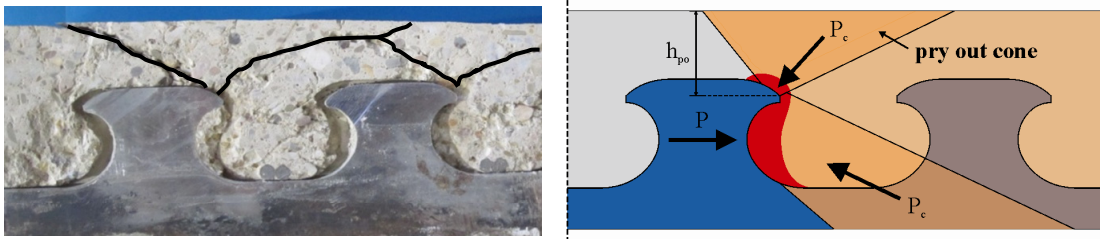


Figure 6. Failure mode pry-out: test specimen (left) and schematic illustration (right).

For composite dowels, where the distance in longitudinal direction is below $e_x < 4.5 \cdot h_{po}$, the bearing capacity is reduced due to an overlapping of the concrete cones. In this case $P_{po,k}$ has to be reduced by χ_x .

$$\chi_x = \frac{e_x}{4.5 \cdot h_{po}} \leq 1$$

The same effect happens by parallel arrangement of composite dowels with a distance smaller than $e_y < 9 \cdot h_{po}$. For this following reduction factor is used:

$$\chi_y = \frac{1}{2} \left(\frac{e_y}{9 \cdot h_{po}} + 1 \right) \leq 1$$

In plate type sections stirrups $\varnothing 8$ mm has to be used for a ductile behavior. The maximum spacing is $4.5 \cdot h_{po}$ and 300 mm to ensure that at least two reinforcing bars are in each concrete cone (Figure 7).

The design against concrete pry-out can be neglected, if the concrete is covered by steel flanges and confinement stirrups are applied (e. g. beam type sections with external reinforcement).

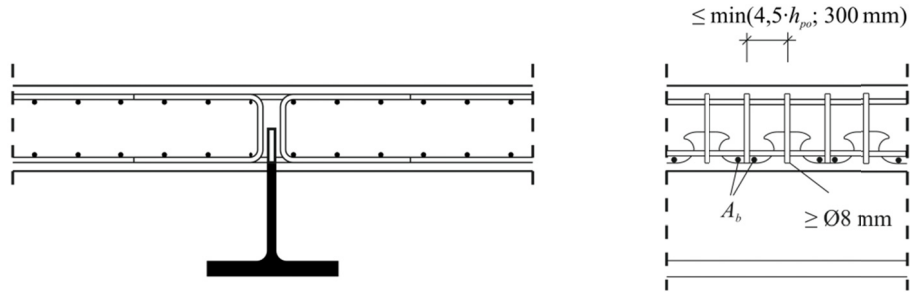


Figure 7. Detailing of reinforcement in composite girder with RC-slab and composite dowels.

(iii) Steel failure

For small plate thickness and low steel strength steel failure can occur. This failure mode is caused by a combined shear-bending mechanism, which leads to a horizontal crack in the steel plate. Due to the ductile behavior of structural steel this failure mode goes along with large plastic deformations and is therefore ductile (Figure 8).

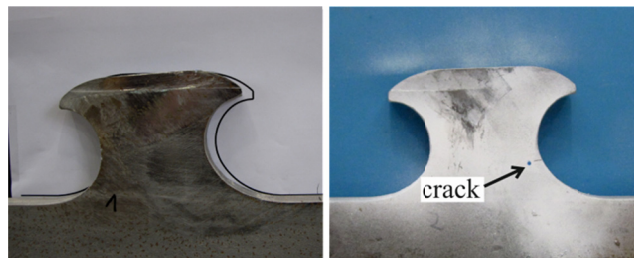


Figure 8. Test specimen with steel failure: plastic deformation (left) and static crack (right).

The basis of the mechanical model is von Mises yielding in a critical section, where stresses due to the shear force P_2 and the bending moment due to $P_2 \cdot z_{p2}$ occur. The position of the critical section is an extremum problem of decreasing cantilever z_{p2} and decreasing load P_2 as well as a decreasing section area (Figure 9).

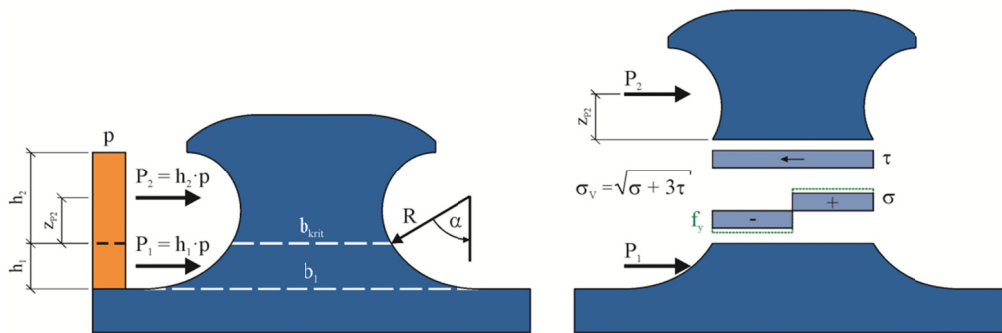


Figure 9. Schematic illustration of failure mode steel failure.

Based on this mechanical model the characteristic bearing capacity is expressed by:

$$P_{pl} = \frac{h_{eff}}{h_{eff} - h_{krit}} \cdot \frac{b_{krit}^2}{\sqrt{16 \cdot h_{s,krit}^2 + 3 \cdot b_{krit}^2}} \cdot t_w \cdot f_y$$

with $h_{krit}(\alpha)$, $h_{s,krit}(\alpha)$, $b_{krit}(\alpha)$, where $\alpha = f(\partial P / \partial \alpha \rightarrow \min)$

Using the specific geometrical parameters for the clothoid and puzzle shape the design formula can be rewritten as a function of e_x :

$$P_{pl,k} = 0.25 \cdot e_x \cdot t_w \cdot f_y$$

(iv) Additional verifications for beam-type sections

In beam-type sections with composite dowels as external reinforcement failure of the concrete web can occur. For thin concrete webs splitting tensile forces can exceed the concrete tensile stress, which results in a horizontal crack at the height of the composite dowel (Figure 10).

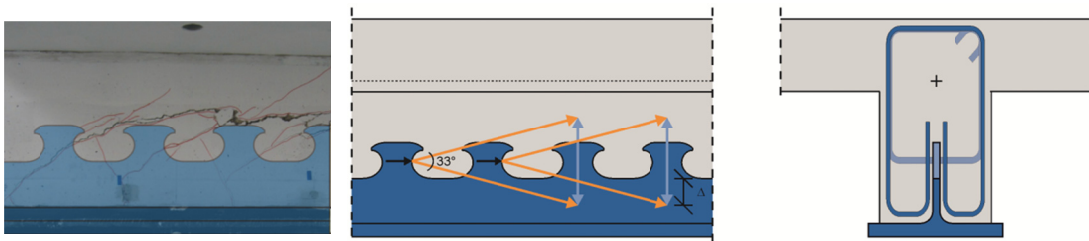


Figure 10. Failure mode vertical splitting: test specimen (left), strut-and-tie model (middle) and required stirrups (right).

This failure mode is non-ductile and has to be prevented by sufficient confinement stirrups. The required reinforcement $A_{s,conf}$ is determined with models for pre-stressed concrete by a strut-and-tie model with an aperture angle of 33°:

$$A_{s,conf} = 0.3 \cdot P / f_{sd}$$

The confining stirrups have to enclose the concrete strut, which is guaranteed by a spacing smaller than e_x and 300 mm (Figure 11).

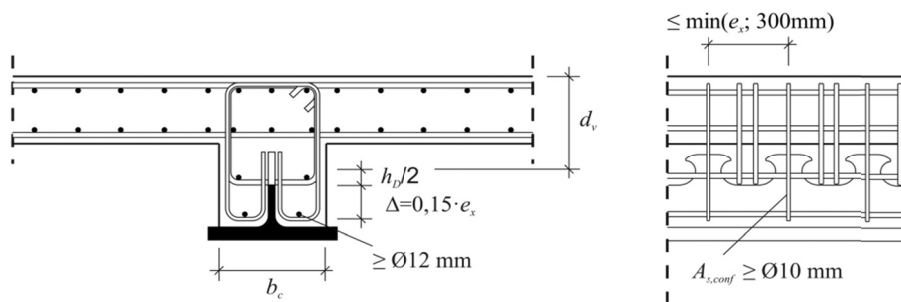


Figure 11. Detailing of reinforcement in composite girder with RC-web and composite dowels.

Furthermore, the stirrup has to reach at least $\Delta = 0.15 \cdot e_x$ below the dowel base. For a ductile behavior a minimum of two stirrups $\varnothing 10$ mm for each opening are required.

Additionally, shear forces in the concrete web have to be verified acc. to EN 1992-1-1. In this design check, the effective depth d_v starts from the half dowel height.

(v) Shear connection

The verification of the longitudinal shear connection has to be proofed in accordance with EN 1994-1-1. The number of required shear connectors is equal to the number of openings in the steel plate. The required transversal reinforcement is determined based on a 45° strut-and-tie model:

$$A_b = 0.5 \cdot P / f_{sd}$$

Equal spacing of shear connectors is allowed for hogging and sagging moment, if the minimum shear connection degree acc. to EN 1994-1-1 is met. In contrast to EN 1994-1-1, equal spacing is also allowed for upper flange less steel sections, if following requirements are met: the shear connection degree is $\eta \geq 0.5$; the span is $L \leq 18$ m; the plastic moment capacity of the composite section must be equal to or smaller than 10-times the plastic moment capacity of the steel profile; the curtailment of the dowel capacity must not incise the design longitudinal shear force more than 25 %. Equally spacing for upper flange less steel sections extend the range of EN 1994-1-1 and opens new interesting application fields for composite dowels.

For fatigue loading the longitudinal shear force has to be determined by elastic theory and the curtailment of the dowel capacity must not incise the design longitudinal shear force. Reason for this is the prevention of unacceptable deterioration of the connection due to plastic force redistribution.

FATIGUE STRENGTH

The fatigue design has to be carried out for the fatigue load model of appropriate standards. The fatigue design concept comprises (i) steel fatigue design, (ii) concrete fatigue design and (iii) securing of a rigid shear joint. In this, the interaction between the fatigue behaviors of different components has to be considered (Figure 12): e. g. degradation of the concrete dowel leads to decrease of the shear connection.

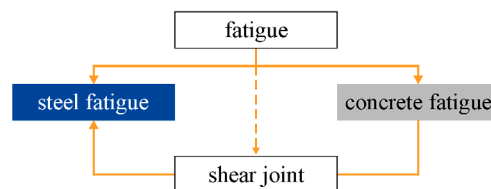


Figure 12. Schematic illustration of the interaction of the fatigue verifications.

This affects the stress distribution over the cross section and therefore the steel fatigue design.

(i) Steel fatigue

The steel fatigue design is based on the geometric stress approach. The stress amplitude at the hot spot is determined for the fatigue load model and compared with the material fatigue strength. The fatigue strength (resistance) is described by the fatigue strength curve of detail category 125 (machine gas cut edges having shallow and regular drag lines) or of detail category 140 (machine gas cut edges with subsequent dressing) in accordance with EN 1993-1-9. The geometric stress amplitude (action) is the sum of stresses coming from longitudinal shear forces (local effects) and from bending of the composite beam (global effects). Both parts are amplified by stress concentration factors depending on the geometry of the composite dowel. The nominal stresses are defined as longitudinal shear stress (local) and normal stress (global) at the dowel base.

$$\Delta\sigma = \left| k_{f,L} \cdot \frac{\Delta V \cdot S_y}{I_y \cdot t_w} \right| + \left| k_{f,G} \cdot \left(\frac{\Delta N}{A} + \frac{\Delta M}{I_y} \cdot z_D \right) \right|$$

$$\text{with } k_{f,L,CL} = 7.3; \quad k_{f,G,CL} = 1.5$$

$$k_{f,L,PZ} = 8.6; \quad k_{f,G,PZ} = 1.9$$

The stress concentration factors $k_{f,L}$ (local) and $k_{f,G}$ (global) for the clothoid and puzzle shape are determined by finite element analysis and verified by strain measurements in cyclic push out and beam tests [Feldmann et al. 2012b] (Figure 13). The stress concentration factors are applicable for steel sections with a lower flange and concrete strength C20/25 and higher. To exclude low cycle fatigue the geometric stress amplitude is limited to $2 \cdot f_y$ and the upper geometric stress is limited to $1.3 \cdot f_y$.

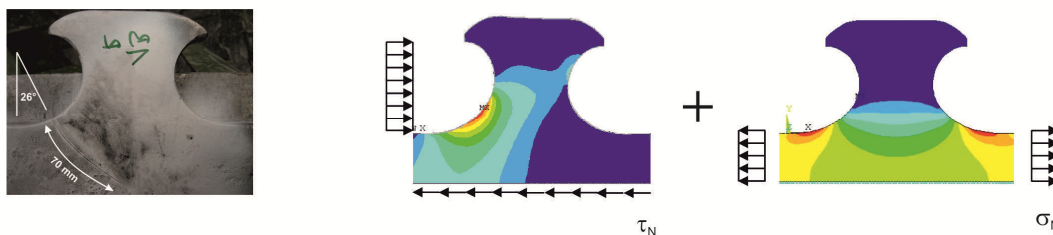


Figure 13. Steel fatigue failure: test specimen (left), FE-analysis of stresses due to local and global loading (middle and right).

In general tension stiffening has to be considered in the stress determination for parts where concrete cracking is expected. On the safe side for the determination of stress due to global bearing behavior the influence of tension stiffening can be neglected (cracked section). For stress due to longitudinal shear transfer the more unfavorable value from calculations with a cracked and an un-cracked section should be used. The design rule in EN 1994-1-1, where it is allowed to determine conservatively the fatigue stress in the composite joint with an un-cracked section, can be unsafe for composite dowels under hogging moment.

(ii) Concrete fatigue

Two types of concrete fatigue failure are known from tests: the loss of bearing capacity due to trickling of crushed concrete out of the composite joint; cyclic concrete pry-out of composite dowels with insufficient concrete cover subjected to high upper loads. The first failure mode can be prevented by a limitation of the crack width to 0.15 mm in parts, where the composite dowel is in the concrete tension zone. This has to be considered for bending action in the concrete chord in longitudinal and perpendicular direction. Cyclic pry-out can be prevented by limitation of the upper load to 70 % of characteristic static bearing capacity acc. to equ. 1 and 2. Up to this load level the bearing behavior is mainly elastic.

(iii) Securing rigid shear connection

The basic requirement for the determination of stresses with a composite section by elastic theory is the assumption of a rigid shear connection between steel and concrete section. However, results of cyclic beam tests show that this assumption is not justified a priori, which can lead to higher geometric stresses in the steel section (Figure 14).

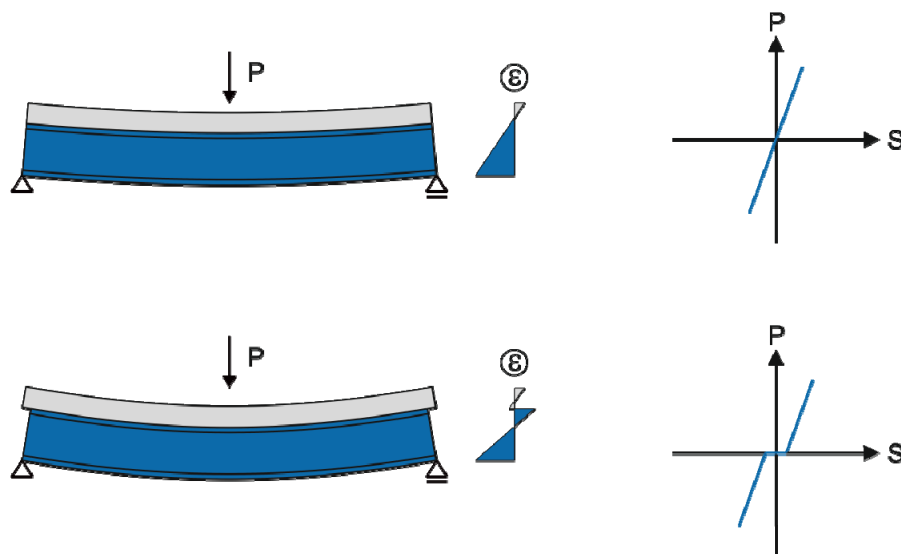


Figure 14. Deformation behavior and strain distribution of composite girder with intact shear connection (top) and damaged shear connection (bottom).

The loss of rigid shear connection is caused by a degradation of the concrete dowel due to cyclic loading. The consequence is a forceless slip before the composite dowel is activated (Figure 14 bottom). This can be avoided by a limitation of the upper force. As criterion for a relevant degradation of the composite joint, the strain shift between steel and concrete section is used. Zero shift is equal to full shear connection; the maximum strain shift corresponds to a composite beam without shear connection. The threshold for an unacceptable degradation is assumed at 90 % shear connection. This criterion is applied to evaluate the condition of the composite joint in cyclic beam test (acceptable or not acceptable). Afterwards the condition of the

composite joint is correlated with the partial area pressure at the concrete dowel. For this, the partial area pressure ratio $E_{cd,3D}$ for upper and lower load from beam tests are plotted into a Goodman diagram, which is often used for concrete fatigue design (Figure 15). Tests with a residual shear connection of more than 90 % are in the green field (acceptable), while tests with an unacceptable degradation are plotted outside. The evaluation of the tests show that the available concrete compressive strength under multi axial stress conditions is up to 7.5 times higher than the uniaxial compressive strength. Based on the assumption that at least 10 % of the total loads are dead loads, the upper load is limited to 55 % of the available multi axial compression strength.

$$P_{cyc} = 3.1 \cdot t_w \cdot h_D \cdot f_{ck}$$

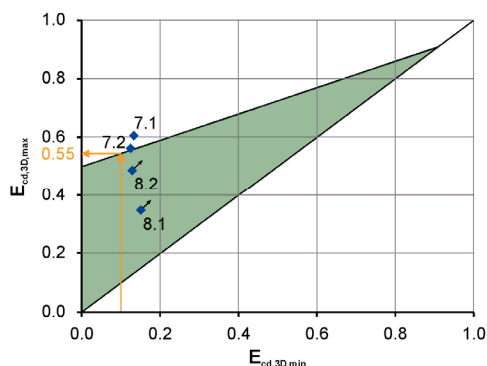


Figure 15. Fatigue strength of cyclic loaded beam tests as a function of partial area pressure ratio $E_{cd,3D}$ for upper and lower load.

FABRICATION AND CONSTRUCTION

Composite dowels have to be fabricated by gas cutting or a cutting-process, which is similar in terms of strength and fatigue. The nominal geometrical values are given in Figure 4, where tolerances of $+2/-4$ mm are acceptable (“+” is an enlargement of the steel shape). The cutting quality has to be in accordance with EN 1090-1 and EN 1090-2 and depends on the execution class. For fatigue loading the quality has to meet the requirements for detail category 125 respectively 140 acc. to EN 1993-1-9. Checking and documentation of the cutting quality is very important as inspection of the shear connector is not possible after casting. To prevent blowholes in the concrete next to the composite dowel the maximum grain size is 16 mm and the consistence of the fresh concrete should be soft to flowable.

CONCLUSION AND OUTLOOK

In this paper the design concept for composite dowels given in the German general technical approval is presented. Design formulas for static and fatigue loading, detailing as well as advices for fabrication and construction are given and augmented by relevant background information.

Due to the regulation in a general technical approval uncertainties in the design and checking process are eliminated. This enables an economic and

timesaving application of these powerful shear connectors. Additional costs for approvals for single cases are omitted.

The general technical approval is a consistent continuation of the development of standardization of composite dowels: it started with approvals for single cases and should become a German steel guideline (DAST) in the future. For this, the presented design concept is a strong basis. Furthermore, it is planned to implement composite dowels in Eurocode 4 as alternative shear connector besides headed studs.

ACKNOWLEDGEMENT

Following research and industrial partners are gratefully acknowledged for their cooperation and support: VDEh, FOSTA, SSF AG, ArcelorMittal, Salzgitter, Max Bögl, Donges Steeltech.

REFERENCES

- Berthelley, J., Lorenc, W., Mensinger, M., Rauscher, S., Seidl, G. (2011a). *Zum Tragverhalten von Verbunddübeln – Teil 1: Tragverhalten unter statischer Belastung*. Stahlbau 80, Issue 3, p. 172–184.
- Berthelley, J., Lorenc, W., Mensinger, M., Ndogmo, J., Seidl, G. (2011b). *Zum Tragverhalten von Verbunddübeln - Teil 2: Ermüdungsverhalten*. Stahlbau 80, Issue 4, p. 256–267.
- Bode, H., Künzel, R. (1988). *Scherversuche zum Tragverhalten eines neuartigen Stahlverbundträgers mit schwalbenschwanzförmigen Stegausehnehmungen als Verbundmittel*. Untersuchungsbericht 2/88, Universität Kaiserslautern.
- Deutsches Institut für Bautechnik (2000). *Allgemeine bauaufsichtliche Zulassung der Kombi-Verdübelung*. Zulassungsnummer Nr. Z-26.4-39, Berlin.
- Deutsches Institut für Bautechnik (2007). *Allgemeine bauaufsichtliche Zulassung der Perfobond-Leiste*. Zulassungsnummer Nr. Z-26.4-38, Berlin.
- Deutsches Institut für Bautechnik (2013). *Allgemeine bauaufsichtliche Zulassung der CL- und PZ-Verbunddübelnleiste*. Zulassungsnummer Nr. Z-26.4-56, Berlin.
- Eisenbahnbundesamt (2010). *Bescheid zur Bauartzulassung des Systems VFT-Rail auf der Grundlage des Bemessungskonzeptes MV-TR*. Bonn.
- Feldmann, M., Hechler, O., Hegger, J., Rauscher, S. (2007). *Neue Untersuchungen zum Ermüdungsverhalten von Verbundträgern aus hochfesten Werkstoffen mit Kopfbolzendübeln und Puzzleleiste*. Stahlbau 76, Issue 11, p. 826–844.
- Feldmann, M., Pak, D., Kopp, M., Schillo, N., Wirth, T., Seidl, G., Mensinger, M., Koch, E. (2012a). *Eisenbahnüberführung Simmerbach - Feldmessungen der Verbunddübel und der Schienenstützpunkte am VFT-Rail®-Träger*. Stahlbau 81, Issue 10, p. 737-747
- Feldmann, M., Gündel, M., Kopp, M., Hegger, J., Gallwoszus, J., Heinemeyer, S., Seidl, G., Hoyer, O. (2012b). *Neue Systeme für Stahlverbundbrücken - Verbundfertigteilträger aus hochfesten Werkstoffen und innovativen Verbundmitteln*. Forschungsbericht, FOSTA P804.

- Gündel, M., Dürr, A., Hauke, B., Hechler, O. (2009). *Zur Bemessung von Lochleisten als duktile Verbundmittel in Verbundträgern aus höherfesten Materialien*. Stahlbau 78, Issue 12, p. 916–924.
- Heinemeyer, S., Gallwoszus, J., Hegger, J. (2012). *Verbundträger mit Puzzleleisten und hochfesten Werkstoffen*. Stahlbau 81, Issue 8, p. 595-603.
- Leonhardt, F., Andrä, W., Andrä, H.-P., Harre, W. (1987). *Neues, vorteilhaftes Verbundmittel für Stahlverbund-Tragwerke mit hoher Dauerfestigkeit*. Beton- und Stahlbetonbau 82, Issue 12, p. 325-331.
- Mangerig, I., Wagner, R., Burger, S., Wurzer, O., Zapfe, C. (2011). *Zum Einsatz von Betondübeln im Verbundbau (Teil 1) – Ruhende Beanspruchung*. Stahlbau 80, Issue 12, p. 885–893.
- Mangerig, I., Wagner, R., Burger, S., Wurzer, O., Zapfe, C. (2012). *Zum Einsatz von Betondübeln im Verbundbau (Teil 2) – Nichtruhende Beanspruchung*. Stahlbau 81, Issue 1, p. 26–31.
- Seidl, G. (2009). *Verhalten und Tragfähigkeit von Verbunddübeln in Stahlbetonverbundträgern*. PhD thesis, Technical University Wrocław.

Adhesives as a Permanent Shear Connection for Composite Beams

Dipl.-Ing. Marcus Kludka¹ and Prof. Dr.-Ing. Wolfgang Kurz²

¹Institute of Steel Structures, Univ. of Kaiserslautern, Paul-Ehrlich-Straße 14, 67663 Kaiserslautern, Germany. E-mail: Marcus.Kludka@bauing.uni-kl.de

²Institute of Steel Structures, Univ. of Kaiserslautern, Paul-Ehrlich-Straße 14, 67663 Kaiserslautern, Germany. E-mail: Wolfgang.Kurz@bauing.uni-kl.de

Abstract

A composite beam is an effective building technique. The shear resistance of such elements is realised by using mechanical components, for example shear studs, which are leading to high local strains in the concrete slab. These local strains can cause high local stress in the steel. The application of adhesive technology avoids these high local stress peaks and enables new designs with the use of novel materials. The durability of adhesive connection is of high importance under climatic and thermal influence. Lack of knowledge of the long-term behavior of bonded joints, especially on long-lasting climatic effects is responsible for the lack of applications in building structures. The project aims to investigate the application of adhesive bonding as an alternative or supplement to mechanical joints in composite structures. The research objective is to obtain knowledge of the structural behavior of shear connection between steel and concrete in dependence of the inherent stress condition and material behavior in the adhesive joint. First, results of small specimen are presented.

INTRODUCTION

Preliminary research on composite beams with an adhesive connection and push-out specimen demonstrate that unaged test specimen have adequate capacity and formability, but limited ductility, in comparison to conventional composite beams with shear studs. Figure 1 shows a typical test beam close to failure. In Figure 2 test results and computed load-deflexion are presented.



Figure 1. composite beam with adhesive connection

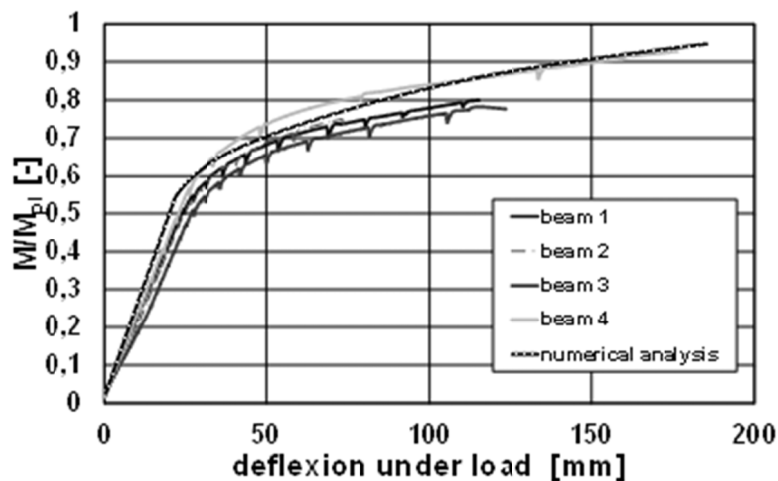


Figure 2. results of the first preliminary adhesive composite beams

Based on these results this project aims to investigate the durability of adhesive joints in composite beams under realistic ageing.

The effects of ageing of adhesive joints shall be investigated by full scale specimens and numerical simulations. Numerical models will be calibrated on small scale tests. By that way the transferability of small scale test results on large components will be checked as well.

After natural and artificial ageing the samples are tested. With the new technical expertise it shall be possible to predicate the maximum capacity and formability of aged composite beams with an adhesive connection.

DESCRIPTION OF THE SMALL SCALE TESTS

All test specimens were produced with the same concrete formulation and steel grade.

This will ensure that the material properties of all specimens are similar in order to transfer the results from small samples to the scale of the large components.

For all tests both surfaces of steel and the concrete are treated by shot blasting. In that case the concrete surface is the decisive on the strength of the connection. To increase the bond stress, a concrete with a bending tensile strength of 10 MPa and compression strength of 70 MPa was developed.

The geometry of the small specimens was chosen according to the maximum grain size.

In the specimen, steel and concrete are bonded by a 3 mm thick adhesive layer (see Figure 4, Figure 5). The substrates have influence on the material behavior of the adhesive. Especially the concrete with its high alkalinity, water content and its permeability has a big influence on the chemical structure of the adhesive in the tension zone.

The small specimen are classified into three groups; Bulk tests to investigate the properties of the adhesive material, Push-Out tests to investigate the shear behavior and Pull-Out tests to investigate the tensile strength of the connection (see Figure 3, Figure 4, Figure 5).

Bulk tests

For the tests two different adhesives were chosen. Each of the adhesives has a specific chemical composition and material behavior. On one hand there is an epoxy adhesive with low deformability but with a high solidity. On the other hand there is a polyurethane adhesive with a relative high deformability and a distinct flow behavior, compared to the epoxy adhesive. But in comparison to the epoxy adhesive the strength of the polyurethane adhesive is significantly lower (see Figure 3).

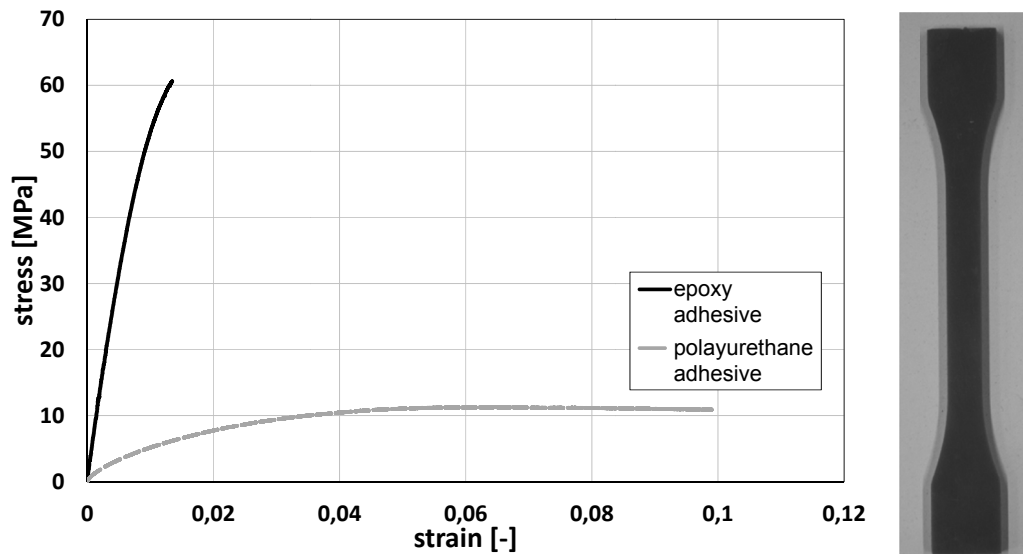


Figure 3. typical results of the bulk tests

The material behavior was determined on bulk samples according to DIN EN ISO 527.

The bulk samples are aged in order to analyze the modification of the material behavior.

Shear tests

The second group of test specimen characterizes the shear strength of adhesive joints. Steel tubes were slotted at the outside of the specimen to minimize the confinement effect of the concrete, which would improve the shear capacity of the concrete surface.

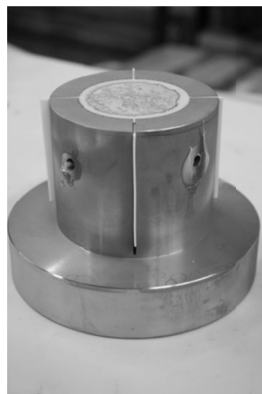


Figure 4. Push-Out specimen

Pull-Out tests

The Pull-Out tests were carried out by connecting steel stamps to the concrete and pulling them off.

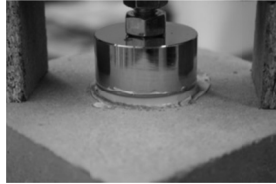


Figure 5. Pull-Out specimen

Ageing

After six months periods under environmental conditions the modification of material properties is tested. The temperature and the air humidity will be measured through the whole time with data loggers.

Accelerate ageing is performed by a temperature of 60°C and 80% humidity and temperature of 60°C and immersion bath, as an artificial ageing process.



Figure 6. natural ageing of the specimens

The full scale specimens will age under the same natural conditions like the small specimens.

TEST RESULTS**Bulk samples**

To gain the material properties of the adhesives, bulk samples according to DIN ISO 527 were tested on their tensile strength and capacity. The unaged and the aged samples were elongated with a constant strain rate of 1%/min.

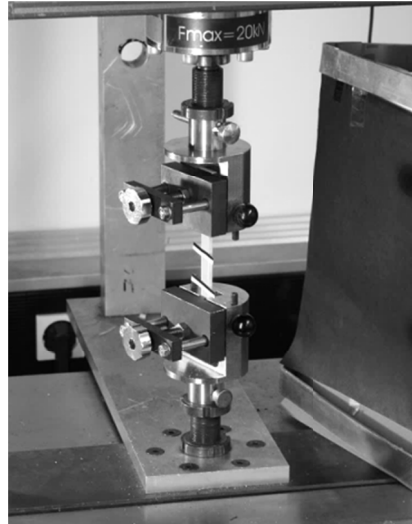


Figure 7. typical experimental set-up of the bulk tests

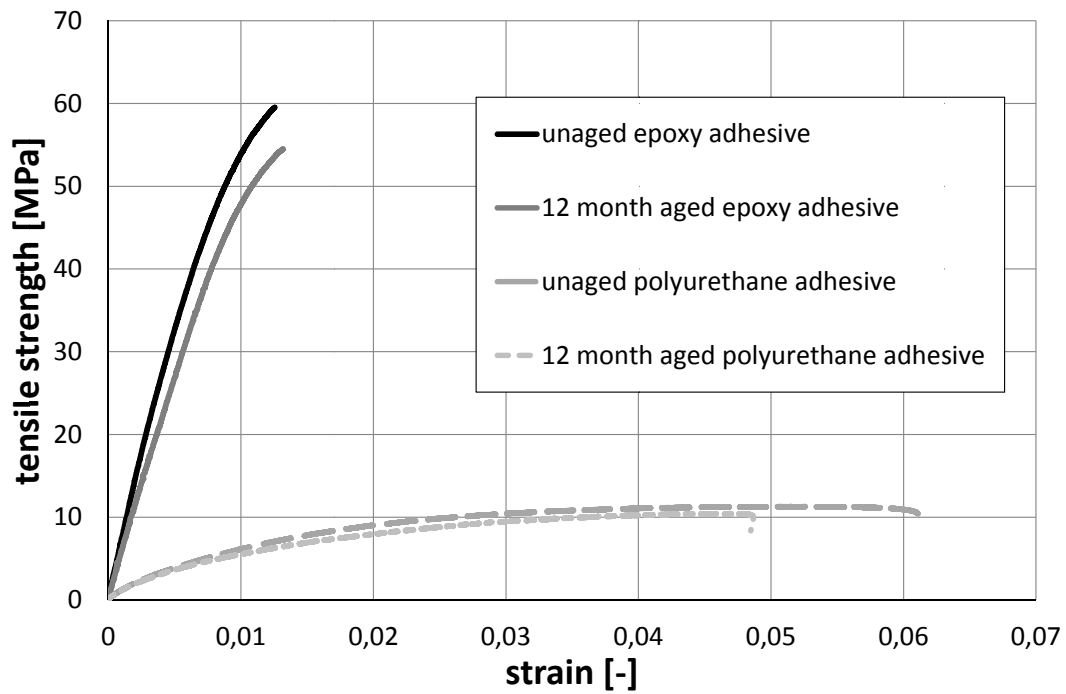


Figure 8. typical test results of the unaged and 12 month aged samples

Shear resistance

The concrete cylinder was pushed out of the steel tube by punching in a steel cylinder on the top side. The testing speed was 0,03 mm/min. The deformation of the adhesive was detected by two LVDT's.

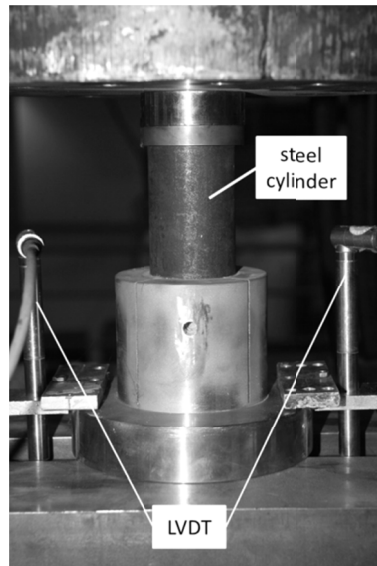


Figure 9. typical experimental set-up of the Push-Out test

The tests were stopped when the maximum load peak was passed. Remarkable slip between steel and concrete was detected in all tests (see Figure 10). A descending branch of the load-slip cannot be detected with this test specimen. After the load peak, friction between steel tube and concrete cylinder is activated, because the relative displacement is strictly restrained after failure (see Figure 13)

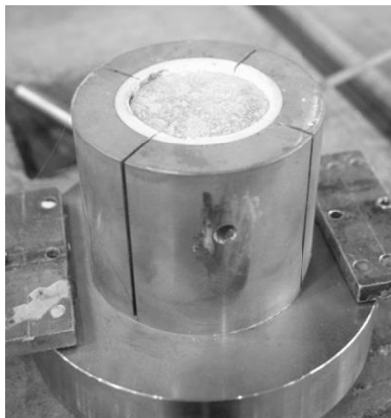


Figure 10. typical results after test run

Comparison of the unaged and naturally aged test specimen

After 12 month under natural weathering conditions specimen were tested to investigate the influence of aging to the shear resistance.

The unaged specimen with epoxy showed a concrete demolition after reaching the load peak. Failure did not occur in the adhesive. After 12 month weathering an adhesive failure was detected. The adhesive detached from the steel after reaching the maximum capacity (see Figure 11).

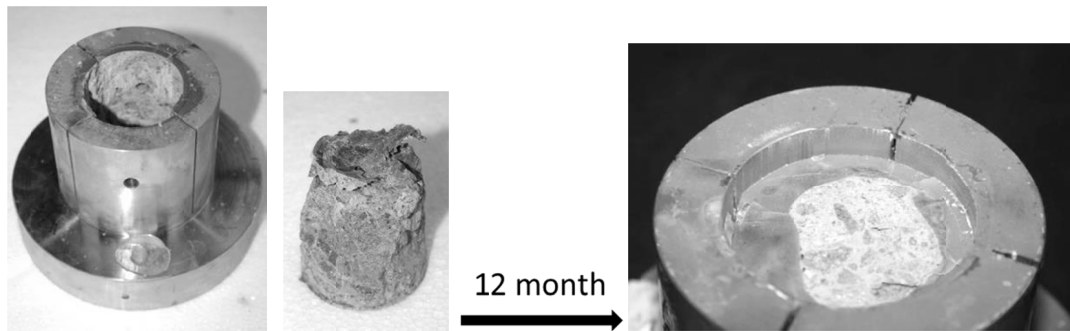


Figure 11. specimen with epoxy

The unaged and the naturally aged specimen with polyurethane adhesive showed an adhesive failure by cohesion fracture (see Figure 12). On the concrete cylinders of polyurethane specimen arrears of the adhesive were visible.

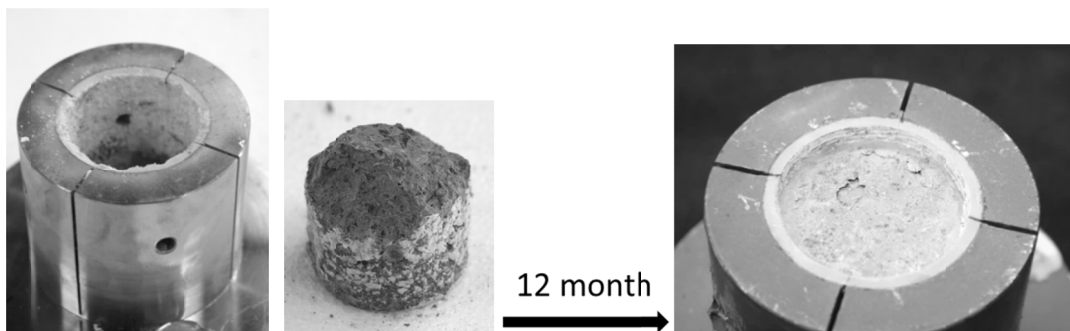


Figure 12. specimen with polyurethane

Typical tests results of both adhesives are shown in Figure 13

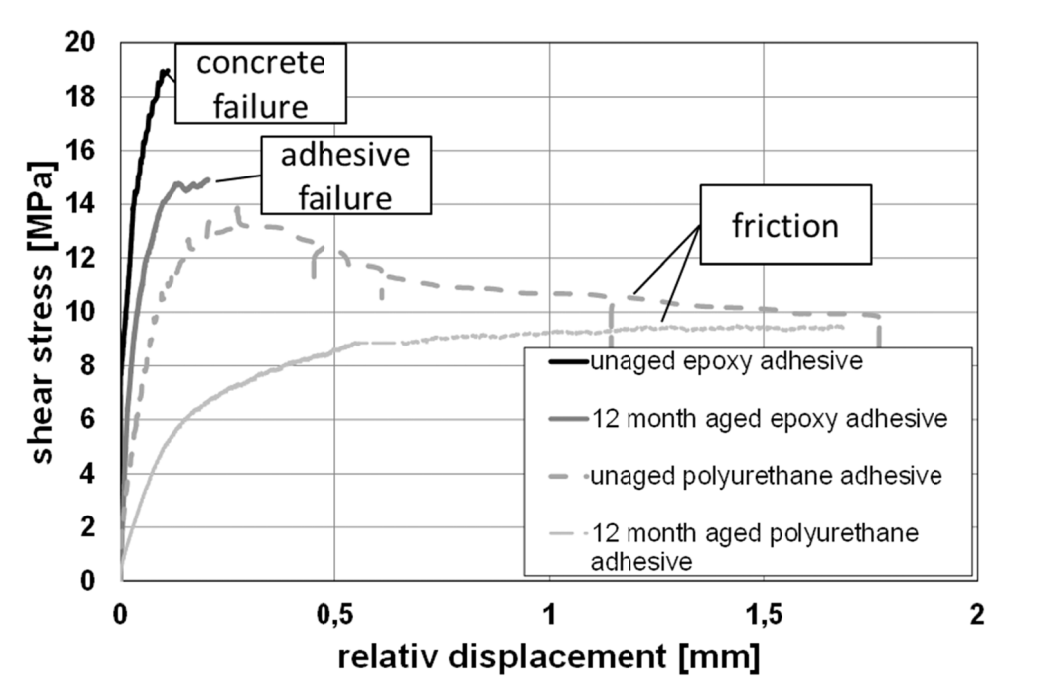


Figure 13. typical test results of the Push-Out specimens

Unaged tensile strength

The affixed steel stamp was pulled off a concrete cube with a constant speed of 0,05 mm/min by a testing cylinder. The strain of the adhesive was detected by two LVDT's, which were attached to the steel stamp. Both, epoxy and polyurethane showed brittle failure. In all cases the concrete surface of the cube failed. So the concrete tensile strength was decisive for the tensile load capacity (see Figure 14).



Figure 14. typical test set-up and results of the unaged Pull-Out tests

The results show that the unaged adhesive has a higher tensile strength than the concrete.

After 12 month natural weathering the tests were repeated. The aged epoxy specimen failed in the same way as the unaged samples.

The polyurethane adhesive failed by separation in the cohesion zone between adhesive and concrete (see Figure 15).



Figure 15. results of an aged polyurethane specimen

Typical results of both unaged and aged adhesives are shown in Figure 16.

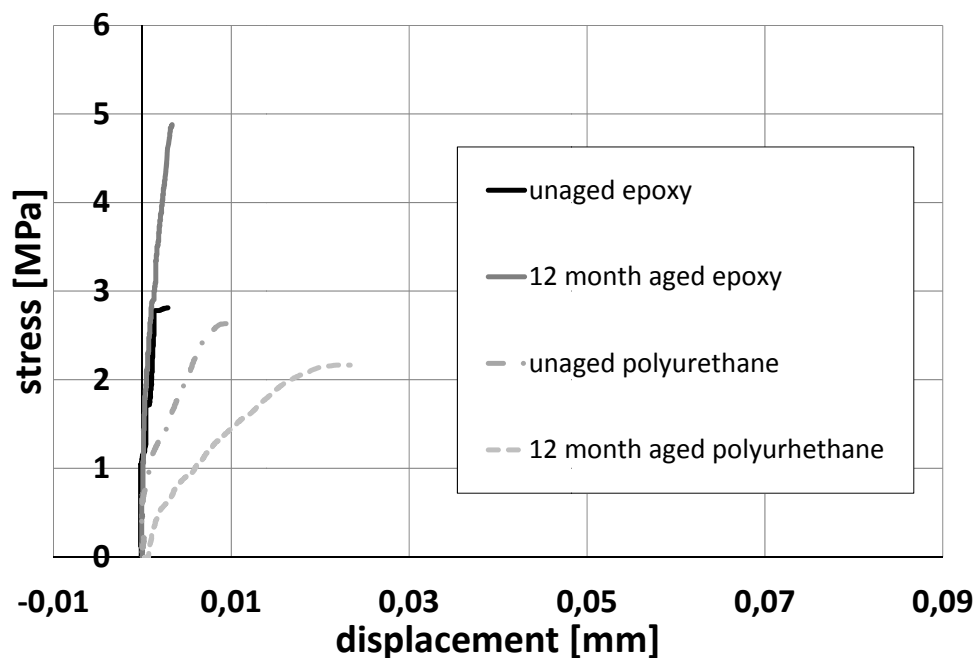


Figure 16. typical results of the Pull-Out specimen

Both types of specimen types show that natural weathering has a significant influence on the material behavior. By comparison the test results of the polyurethane bulk tests and the pull out test it's obvious that the concrete has a huge effect on the chemical structure of the adhesive itself. Especially the tests with polyurethane material show a huge effect of the concrete on the material behavior in the adhesive zone of specimen.

OUTLOOK AND FURTHER PROGRAMM

Large scale test specimens were produced and tested (see Figure 17). After investigating stiffness and deformation at SLS the beams will be aged and tested similar to the small scale specimen.

The behavior of the adhesive joints of the small specimen will be validated by the full scale tests and in addition calculations are performed by using numerical methods. New material laws for the numerical models, which were developed at the University of Kaiserslautern, will be used.



Figure 17. full scale specimen right before and after the connection

ACKNOWLEDGMENTS

The authors are grateful to the AiF German Federation of Industrial Research Associations for the financial support for this project research 17275.

REFERENCES

- Bergmeister, K (2001). "Kleben im Betonbau". *Beton- und Stahlbetonbau* 96, book 10, 625-633
- DIN EN 1994-1-1 (2010). "Design of composite steel and concrete structures-Part 1-1: General rules for buildings, German version", *Beuth-Verlag*, Berlin, Germany
- DIN EN ISO 527 (2010). "Plastics- Determination of tensile properties. German version", *Beuth-Verlag*, Berlin, Germany
- Hartmeyer, S. (2008). "Experimentelle Untersuchung des mechanischen Klebstoff- bzw. Klebschichtverhaltens in der Verbindung Stahl-Beton bei Kurzzeitbeanspruchung". *Assignment at the Institute of Steel Structures*, University of Kaiserslautern, not published.
- Kessler C. (2012). "Dissertation „Experimentelle Untersuchungen und numerische Simulation des nichtlinearen Tragverhaltens geklebter Stahl-Beton-Verbindungen“, *Institute of Steel Structures*, University of Kaiserslautern

Behaviour of Demountable Shear Connectors in Steel-Concrete Composite Beams

Dennis Lam¹; Xianghe Dai²; and Eleonora Saveri³

¹School of Engineering, Faculty of Engineering and Informatics, Univ. of Bradford, Bradford BD7 1DP, U.K. E-mail: d.lam1@bradford.ac.uk

²School of Engineering, Faculty of Engineering and Informatics, Univ. of Bradford, Bradford BD7 1DP, U.K. E-mail: x.dai@bradford.ac.uk

³Facoltà di Ingegneria, Università degli Studi di Perugia, Perugia, Italy. E-mail: ele.saveri@hotmail.it

Abstract

The construction industry in Europe consumes over 70,000 million tonnes of a wide range of materials each year, and generates over 250 million tonnes of constructional waste. Much of the environmental impact of buildings is associated with consumption of resources and generation of waste, therefore reducing waste in construction is becoming a top priority for all the European Governments. Composite structures formed by connecting the concrete slabs to the supporting steel beams have been widely used for many years throughout the world, this cost-effective arrangement for floor system in multi-storey steel frame building structures is responsible for a considerable increase in the load-bearing capacity and stiffness of the steel beams, which has resulted in significant savings in steel weight and construction cost. However, shear connectors are welded through the steel decking and cast into the concrete; this made deconstruction and reuse of the steel components almost impossible. A demountable shear connector is developed to assess its potential and suitability in term of replacing the welded through headed shear studs. Test results shown that these shear connectors can be easily demounted both at working and ultimate load and have a similar capacity to the traditional welded shear connectors. In addition, the new demountable shear connectors possess high ductility in comparison with the welded shear connectors and have similar behaviour to the traditional welded headed stud shear connectors. A finite element is developed to carry out parametric study for this form of shear connector.

INTRODUCTION

Composite steel structures formed by connecting the concrete slabs to the supporting steel beams have been widely used for many years throughout the world. The use of composite action between steel and concrete is well established as a cost-effective arrangement for floor systems in multi-storey steel frame building structures. Composite action between steel beams and concrete slabs through the use of shear connectors is responsible for a considerable increase in the load-bearing capacity and stiffness of the steel beams, which when utilized in design, can result in

significant savings in steel weight and construction cost. However, shear connectors are welded through the steel decking and cast into the concrete; this made deconstruction and reuse of the steel components almost impossible. Another disadvantage associated with welded shear connectors is that the welding very much relies on clean surfaces, free of mill-scale and, above all dryness of the steel surface. These conditions are often difficult to achieve especially when the studs are welded through a galvanised steel sheet; in this case, the weld current is maintained for a sufficient period to burn away the zinc galvanising, which would otherwise cause imperfect welds.

In UK, the Government has set an ambitious and legally binding target to reduce national greenhouse gas emissions by at least 80% by 2050 with an intermediate target of a 34% reduction by 2020, therefore it is important to consider the whole life cycle in composite construction. A demountable shear connector is developed and tested to assess its potential and suitability in term of replacing the traditional welded through headed shear studs. Present knowledge on welded headed stud shear connector in solid slab is well illustrated by (Mottram and Johnson 1990) and (Menzies 1971). This has been the predominance type of shear connectors used in steel – concrete composite construction. These connectors can be classified as flexible connectors, because under small shear forces, there will be relative movement or slip between the concrete slab and the steel beam at the interface. The research in demountable shear connector conducted by (Lam and Saveri 2012) shown in Figure 1 is formed from the standard 19 mm diameter T.W. Nelson headed shear connector with a 16mm threaded end; and with or without a shaft collar, a M16 Gr 8.8 nut is used to fasten the connector to the steel beam. Since the connector is manufactured from the standard headed stud shear connector, it has the same material properties of the standard welded headed shear connectors. Although researches on bolted connectors have been carried out previously by (Dallam 1968) and (Marshall et al. 1971) on bolted connectors, their main emphasis was on the pre-tension behaviour of the shear connectors using high friction-grip bolts. More recently, research by (Kwon et al. 2010) on bolted connectors was focused on the post-installed capacity for strengthening existing structures rather than the sustainable issues. Research on the sustainable issue for demountable shear connectors for composite construction is limited, the only other published research to date is carried out by (Mirza et al. 2010) using blind bolts as shear connectors. Although they performed reasonably adequate as shear connector, some of these blind bolts have a relatively brittle behaviour. The objective of this research is to investigate the behaviour of this form of demountable shear connectors embedded in normal-weight concrete when subjected to a static shear force. The results are used to be compared with those of the welded headed stud shear connectors to help to determine the feasibility of using this form of connectors in composite construction.



Figure 1. Demountable shear connectors

EXPERIMENTAL STUDY

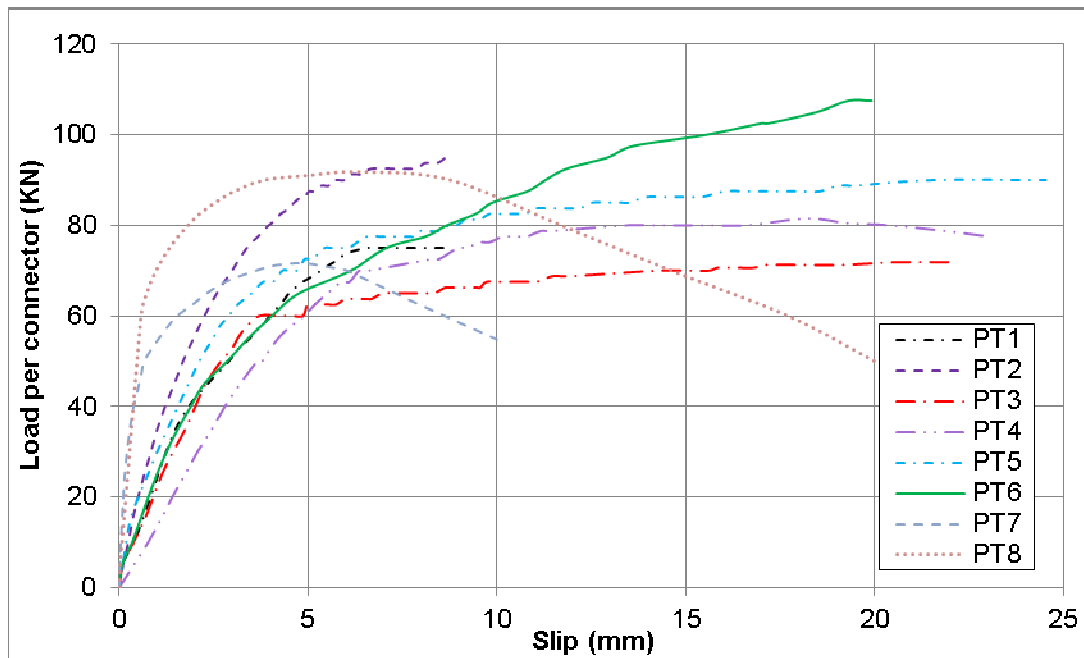
A push off test specimen shown in Figure 2 similar to the one described in (Eurocode 4 2004) was used. The test consisted of a short length of steel beam connected to two concrete slabs $300 \times 300 \times 150$ mm in sizes. 2 pairs of shear connectors were used to connect the concrete slabs to the steel beam, vertical load is applied to the steel beam and slip between the steel beam and the slabs are measured against the load per connector. Both sides of the concrete slabs were cast horizontally using the same mix and poured at the same time. Once the slabs reached their required strength, the slabs were then connected to the steel beam before the test. The test program consisted of eight push off tests. The test parameters included the compressive strength of concrete and the sizes of the headed stud collar. Details of the test series and their results are shown in Table 1 and the load – slip curves are shown in Figure 3.



Figure 2. Push test specimen

Table 1. Push test program and results

Ref.	Concrete Cube Strength, f_{cu} (MPa)	Stud Type	Max. Load per stud (kN)	Slip at Max. Load (mm)	Mode of Failure
PT 1	19.85	16mm	75.0	8.75	Stud fracture
PT 2	21.45	17mm collar	93.5	7.94	Stud fracture
PT 3	20.10	18mm collar	71.9	22.03	Concrete crushing
PT 4	25.20	18mm collar	81.5	18.22	Concrete crushing
PT 5	29.90	18mm collar	90.0	21.25	Concrete crushing
PT 6	61.38	18mm collar	107.5	22.03	Stud fracture
PT 7	20.10	19mm welded	71.6	5.20	Concrete crushing
PT 8	29.90	19mm welded	92.7	9.00	Concrete crushing

**Figure 3. Load – slip curves**

For the demountable headed stud shear connectors, two types of failure mechanism were observed; fracture of the shear connectors near the threaded end or failure by concrete crushing and splitting. The load – slip curves of the two specimens representing these two types of failure are shown in Figure 4.

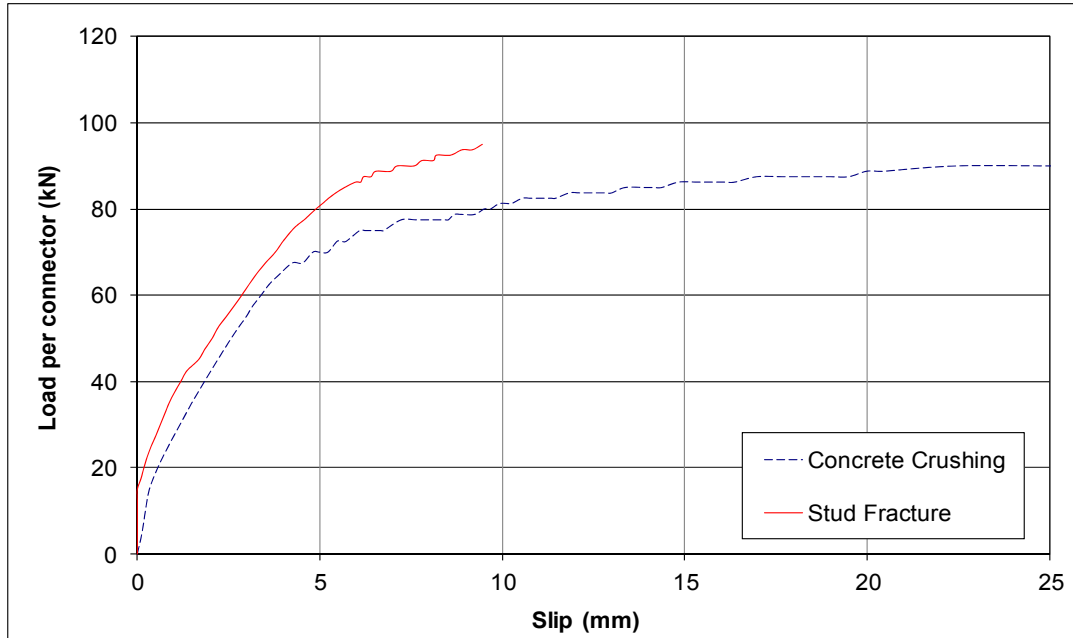


Figure 4. Stud Fracture vs. Concrete Crushing

It can be seen that the load –slip curve associated with stud fracture, although reasonably ductile, end abruptly. Concrete crushing – splitting type of failure provides considerable warning as the load carrying capacity decreases slowly. The fracturing of the shear connectors is shown in Figure 5 while concrete crushing and splitting failure is illustrated in Figure 6. For the specimen failed by concrete crushing, the slabs are demounted from the steel beam and examined carefully, there was no damage occurred to the threaded portion of the shear connectors and the slabs were easily detached from the steel beam.



Figure 5. Shear connector fracture



Figure 6. Concrete crushing

A comparison of load – slip curves of push test with welded headed studs and push test with demountable connectors are shown in Figure 7, the results showed that with similar concrete strength and mode of failure, the demountable connector appears to be more ductile than the welded connector but achieving the similar capacity. However the welded connectors showed a much higher initial stiffness when compared with the demountable studs. In addition, at 6 mm slip, the shear capacity of the demountable connector is 16% lower than the welded connector. However, although these connectors have a lower shear capacity, this might not have significance influence to the ultimate and serviceability limited state of composite beams in bending.

FINITE ELEMENT MODEL

Finite element modelling (FEM) is often used as a complementary tool to provide an efficient alternative to full-scale testing. Figure 8 shows the FE model built for the push test specimen. Due to the symmetry of the specimens (by assuming a symmetry axis along the centre of the steel beam in the direction of the applied shear loading), only half of the push test arrangement with two headed studs was modelled.

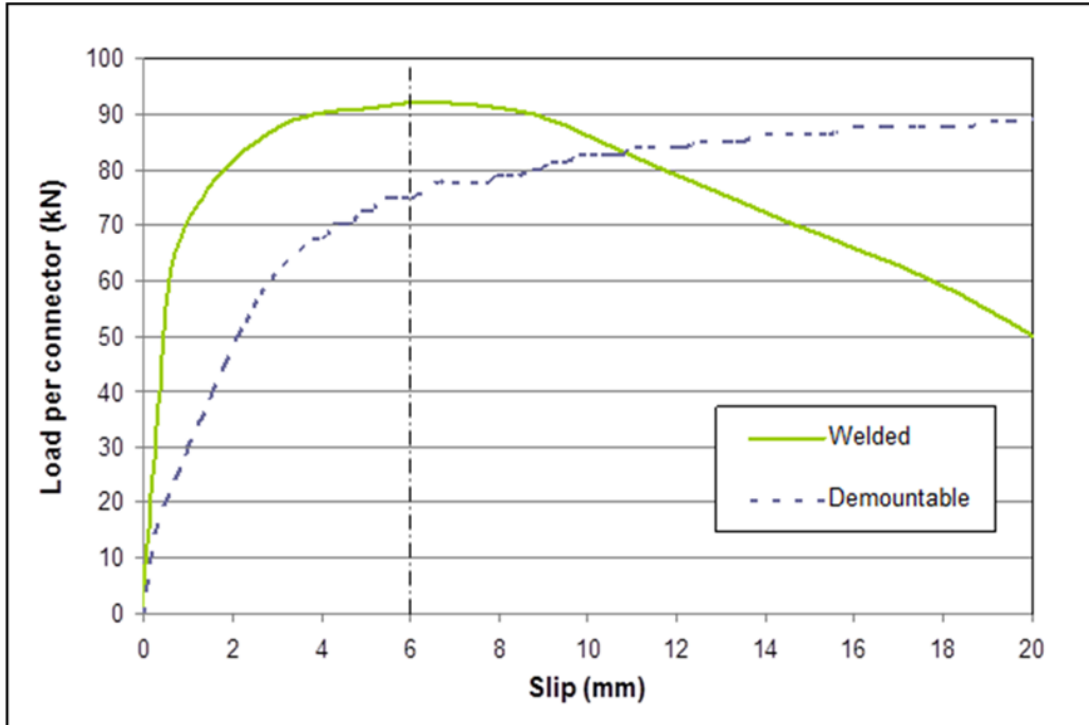


Figure 7. Welded vs. demountable shear connector’s capacity

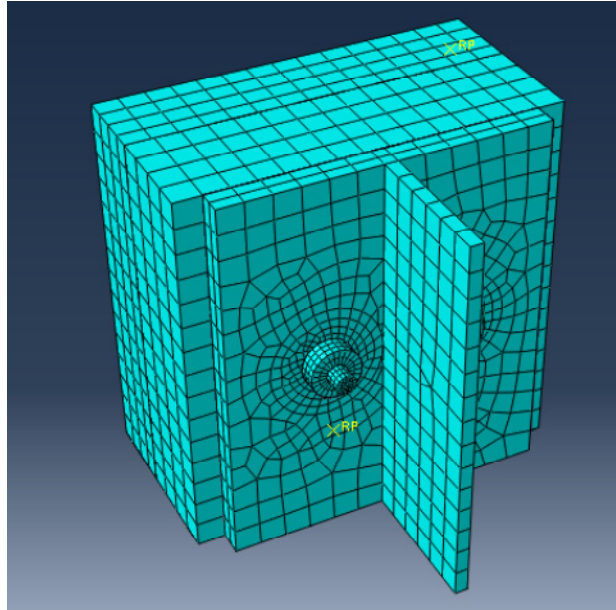


Figure 8. Finite model of push test specimen

Boundaries, Contacts and Loading Condition

For such complicated FE model, many contact surfaces have to be considered. Two types of surface-to-surface contact were created: contact surface and tightening as shown in Figures 9 and 10. Contact surface was implemented for these interfaces: slab to beam; slab to base; beam to nuts; beam to studs shank; slab to studs shanks and slab to studs head. Tightening interface was used to model the tightening behaviour between the stud and the nut.

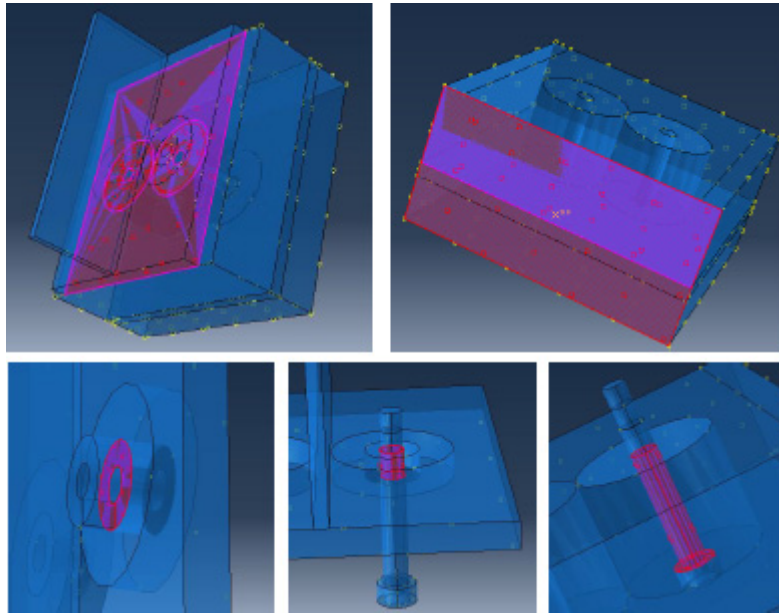


Figure 9. 'Contact' interface

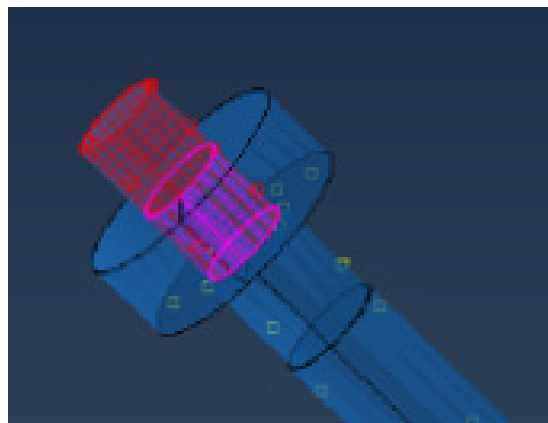


Figure 10. 'Tightening' interface

The steel rebar inside the concrete slab was modelled using the embedded constraint. In this constraint, the translational DOF of the nodes on the rebar elements was constrained to the interpolated values of the corresponding DOF of the concrete elements. The slip and the debonding of the rebar were ignored as they are not of interest to this study. Regarding the loading conditions, this model was analysed with the (ABAQUS 2011) explicit method. In order to obtain a quasi-static solution from the dynamic procedure, it is essential to keep the inertia effects at a minimum level by slow load application. The analysis is similar to the displacement control method used in the tests. Different loading rates were tried and the optimum rate was found to be 0.5 mm/s. Figure 11 shows the loading condition of the push test. The slip was measured as the relative displacement between the nodes on the steel flange and the concrete slab near the shear connector.

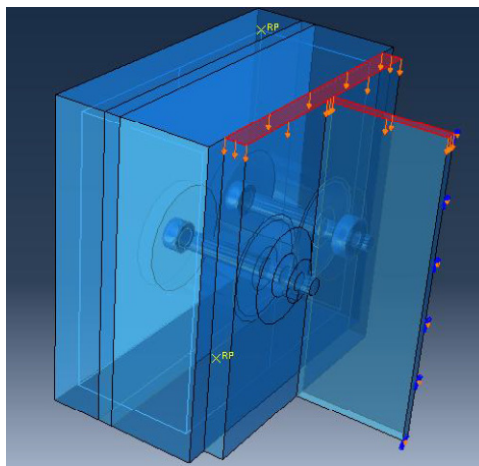


Figure 11. Loading condition

Concrete Model

The Concrete Damaged Plasticity Model (CDP) was used to model the concrete slab: this is based on two main failure mechanisms: tensile splitting and compressive crushing of concrete.

Compressive Behaviour

Concrete Damaged Plasticity response in compression is shown in Figure 12 in according to the ABAQUS concrete material model. The elastic portion of the curve is based on the elastic modulus up to the value of the proportional limit which is taken as $0.4f_{ck}$, where f_{ck} is the compressive cylinder strength of concrete. The second part of the curve is the non-linear parabolic portion which was determined from the relationship given by the (Eurocode 2 2004). This expression is valid for $0 < |\epsilon_c| < |\epsilon_{cu1}|$ where ϵ_{cu1} is the nominal ultimate strain which is taken as 0.0035.

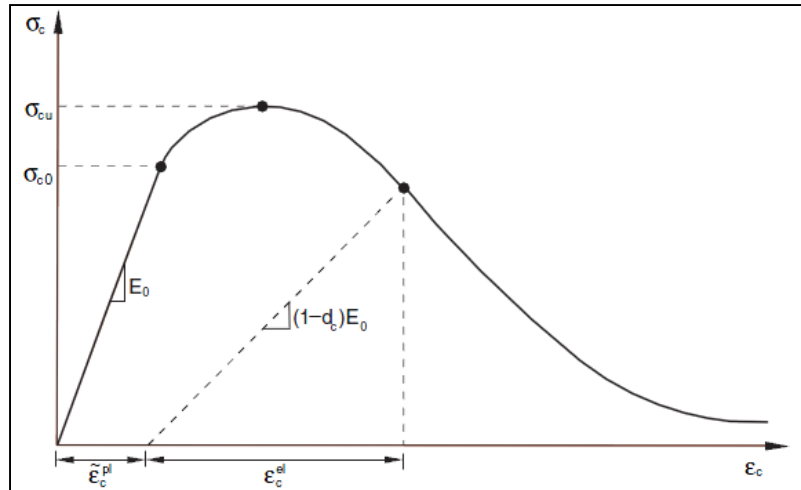


Figure 12. Uniaxial compressive curve of concrete

Tensile Behaviour

For concrete in tension, the tensile stress was assumed to increase linearly with respect to the strain until the concrete crack; after the concrete cracks, tensile stress decreases to zero. The ABAQUS manual suggests that the use of a tension stiffening approach for problems with no or little reinforcement in the significant regions: for unreinforced or lightly reinforced concrete problem as the slabs used for these tests, it is better to express the brittle behaviour of concrete in terms of fracture energy rather than specifying a stress-strain relation in tension. The most realistic model in defining tension softening as a function of fracture energy as experimentally derived by (Cornelissen *et al.* 1986).

Steel Model

The stress–strain behaviour of headed shear stud, steel reinforcement and the steel beam is similar. They behave as linear elastic material until yielding, followed by plastic behaviour. The performance of steel beam is of no particular interest in this study; therefore, it is treated as linear elastic, assuming that its modulus of elasticity is 5 times higher than the usual modulus for structural steel. The shear stud and profiled sheeting were treated as elastic perfectly plastic materials. The modulus of elasticity for shear studs and the rebars was taken as 200 GPa. The yield stress for steel beam, rebars and shear stud was taken to be 350 MPa, 450 MPa and 470 MPa respectively. The density of all steel components was taken as 7900 kg/m³.

COMPARISONS: FE MODEL VS. TEST

The test results obtained from the push tests are compared against the FE results obtained using the ABAQUS. For the shear connector failure of specimen PT2, the load-slip behaviour analyses using the FE model is compared with test result as shown in Figure 13. As it can be seen from Figure 13, the FE model provided a

good prediction of the shear connector capacity, the experimental shear resistance per stud is around 92.5 KN while the maximum load per stud predicted by the finite element model is around 89.0 KN. Likewise, the experimental as well as FE results showed a similar slip at failure (8.95 mm from the experiment and 9.3 mm from the FE model).

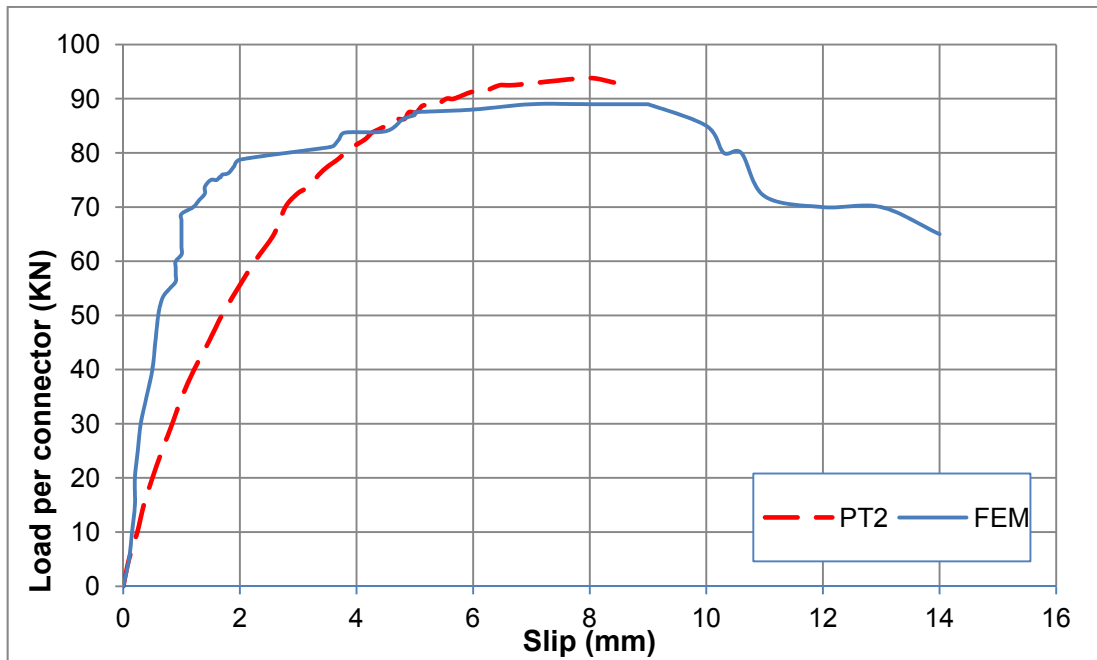


Figure 13. Load vs. slip curves of PT2 vs. FE Model

The biggest difference between the experiment and the FE model is in terms of the initial stiffness. The low stiffness observed during the test was probably due to the demountable connectors are tightened manually which have some initial bolt slip. This phenomenon was not reproduced in the FE analysis. Figure 14 shows the stud failure at the end of the push test, it shows the steel studs failed while the concrete slab is almost undamaged.

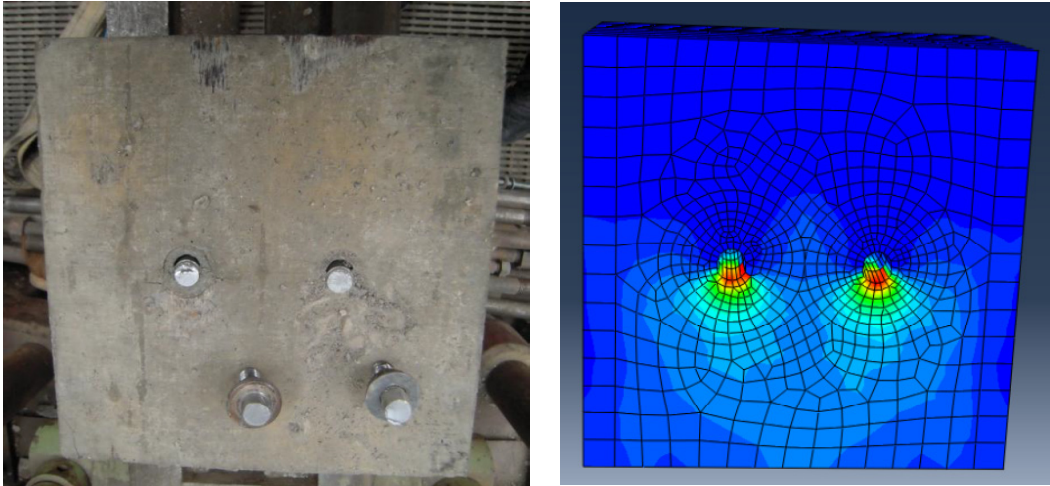


Figure 14. Stud failure: experiment vs. FE model

Specimen PT4 with concrete crushing failure is model using ABAQUS, the experiment result showed excessive concrete crushing at failure and this is observed by the FE model (Figure 15). The load-slip curve of the test vs. FE model is shown in Figure 16, good agreement between the test result and the FE analysis is observed. After the test, the shear connectors were removed and excessive deformation is observed. Once again, as shown in Figure 17, FE model were able to predict the excessive deformation observed in the experimental study, the typical “S shape” of the deformed stud were predicted by the FE model.

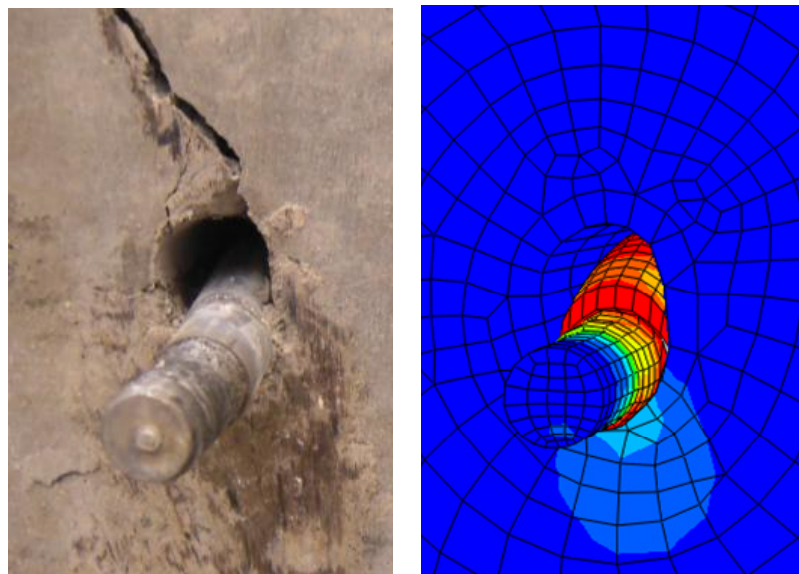


Figure 15. Concrete crushing: experiment vs. FE model

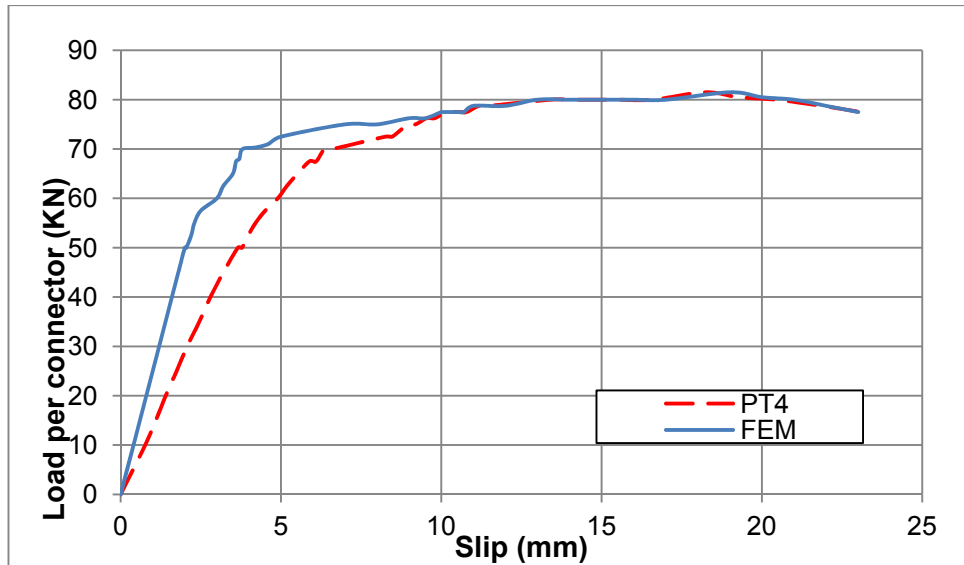


Figure 16. Load vs. slip curves of PT4 vs. FE Model

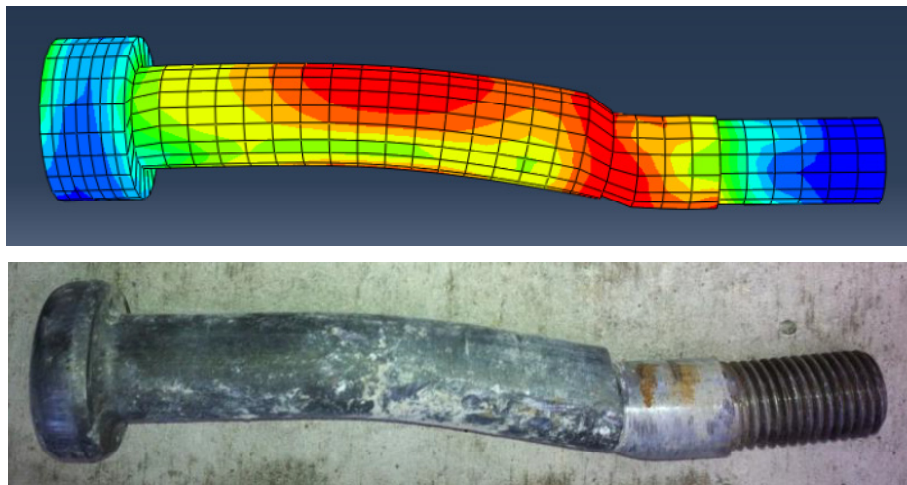


Figure 17. Deformed stud: FE Model vs. experiment

CONCLUSIONS

A demountable shear connector was developed in the form of headed stud shear connector. A series of the push off tests were carried out to assess its potential and suitability. Test results showed that these shear connectors can be easily demounted after test and have a similar capacity and behaviour to the welded headed studs. In addition, test results demonstrated that the new demountable shear connectors process high ductility in comparison with the welded shear connectors, but with a relatively lower initial stiffness due to bolt slip.

A non-linear finite element model of the push test specimen is developed to investigate the capacity of shear connectors embedded in a solid slab. The model took into account the non-linear material properties of the concrete, steel beam,

reinforcement bars and headed stud shear connectors. Results obtained from modelling showed a good prediction of the connector capacity and load-slip behaviour.

Finally, results so far showed that the demountable shear connectors have a similar performance to the welded connectors and would be a big step forward in developing composite beams with this form of shear connectors; which would allow the reuse of steel components after deconstruction.

ACKNOWLEDGEMENTS

The authors would like to thank Nelson Stud Welding UK for supplying the shear connectors used in this research project. The skilled assistance provided by the technical staff in the School of Engineering at the University of Bradford is also greatly appreciated.

REFERENCES

- ABAQUS Standard User's Manual. (2011), Hibbitt, Karlsson and Sorensen, Inc. Version 6.12, USA.
- Cornelissen HAW, Hordijk DA, Reinhardt HW. (1986) 'Experimental determination of crack softening characteristics of normal weight and lightweight concrete'. *Heron*; 31(2): 45-56.
- Dallam, L.N. (1968) 'High Strength Bolt Shear Connectors – Pushout Tests' *ACI Journal*, Vol. 65(9), 767 -769.
- EN1994-1-1. Eurocode 4, (2004) 'Design of Composite Steel and Concrete Structures. Part 1.1, General Rules and Rules for Buildings'. British Standards Institution, London.
- EN1992-1-1. Eurocode 2, (2004) 'Design of Concrete Structures. Part 1.1, General Rules and Rules for Buildings'. British Standards Institution, London.
- Kwon, G., Engelhardt, M.D. and Klingner, R.E. (2010) 'Behavior of post-installed shear connectors under static and fatigue loading' *Journal of Constructional Steel Research*, Vol. 66(4), 532 - 541.
- Lam, D and Saveri, E. (2012), 'Shear capacity of demountable shear connectors', 10th International Conference on Advances in Steel Concrete Composite and Hybrid Structures, Singapore,
- Marshall, W.T., Nelson, H.M. and Banerjee, H.K. (1971), 'An Experimental Study of the Use of High Strength Friction Grip Bolts as Shear Connectors in Composite Beams', *The Structural Engineer*, Vol. 49(4), 171-178.
- Mirza, O., Uy, B. and Patel, N. (2010) 'Behavior and Strength of Shear Connectors Utilising Blind Bolting' *Steel & Composite Structures – Proceedings of the 4th International Conference*, 791 – 796.
- Menzies, J.B. (1971) 'CP 117 and Shear Connectors in Steel-Concrete Composite Beams made with Normal-Density or Lightweight Concrete'. *The Structural Engineer*, Vol. 49(3), 137-153.
- Mottram, J.T. and Johnson, R.P., (1990) 'Push tests on studs welded through profile steel sheeting', *The Structural Engineer*, Vol. 68(10), 187-193.

Steel-Concrete Connections by Adhesion, Interlocking, and Friction for Composite Bridges under Cyclic Loading

Jean-Paul Lebet¹ and Dimitrios Papastergiou²

¹Swiss Federal Institute of Technology Lausanne, EPFL, Steel Structures Laboratory, ICOM, 1015 Lausanne, Switzerland. E-mail: Jean-paul.lebet@epfl.ch

²DIC Engineering, P.O. Box 346, 1860 Aigle, Switzerland. E-mail: dtpapastergiou@gmail.com

Abstract

This paper deals with of a new type of steel-concrete connection for composite beams. The connection is an alternative solution for steel-concrete composite bridges suitable for prefabrication and fast erection. The composite action of the beam is established through an innovative shear connection using adhesion, interlocking, and friction. The resistance of the connection to longitudinal shear is based on the development of shear stresses in the confined interfaces that form the connection. The interfaces include a steel-cement grout interface and a rough concrete-cement grout interface. Confinement is provided by the reinforced concrete slab that encloses the connection. This study applies such a connection to composite bridges and investigates resistance to cyclic loadings using experimental tests. The paper presents the analysis of the test results and a design method to predict the connection fatigue resistance.

INTRODUCTION

In steel-concrete composite bridge construction with prefabricated slab elements, the traditional solution to apply the composite action between the slab elements and the steel girders is concreting the openings (shear pockets) of the slab elements in which shear studs are enclosed. Studs are typically welded on the upper part of the flanges of the girders. However this method presents several disadvantages. The supplementary work in situ for concreting the pockets increases the overall construction time. Due to the development of shrinkage in the concrete of the shear pockets and due to stress concentration, cracks appear at the perimeter and at the corner of the shear pockets. Corrosion agents such as de-icing salt can then enter the cracks therein decreasing the durability of the structure and damaging the connection. Those disadvantages are overcome using a new type of connection by adhesion, interlocking and friction [Thomann and Lebet 2007b, Papastergiou and Lebet 2011c] which are favorable for prefabrication and help guarantee long term durability. The new connection, in comparison with other new innovative solutions such as steel dowels created on the steel web by cutting a steel profile [Feldmann et al. 2008a, Rauscher and Hegger 2008b] or connections with perfobond ribs [Kim and Jeong 2010b], provide an advantage that allow for prefabrication without supplementary cast in place concrete for the deck. Figure 1 presents the new connection. The steel girder is provided with a pair of longitudinal embossed steel

plates welded together and also welded longitudinally to the upper flange of the steel girder. The deck consists of precast reinforced concrete segments fabricated with a rib at the lower part. The surface of the rib is roughened by using a retarding agent during casting, followed by hydro-jetting and sandblasting. The slab segments are positioned over the steel connector and are connected together with epoxy resin and longitudinal prestressing, see Figure 2. The void between the connector and the concrete deck is filled with a high strength cement grout by injection. Once the cement grout is cured the connection is activated and composite action can be achieved.

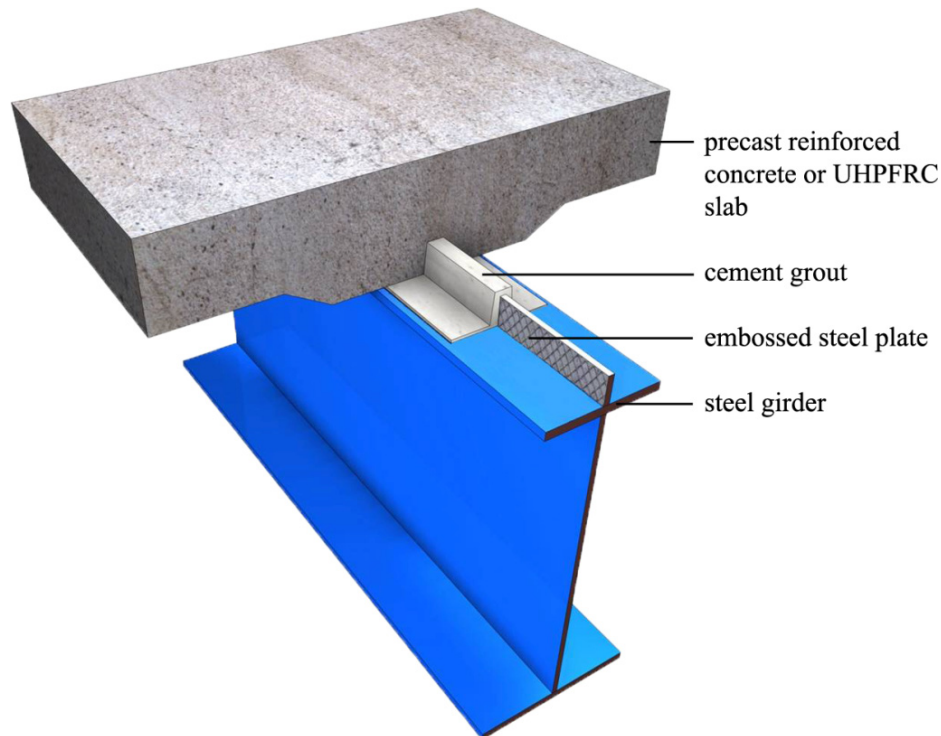


Figure 1. Connection by adhesion, interlocking and friction.

BEHAVIOUR AND RESISTANCE OF THE CONNECTION

Resistance of the connection to longitudinal shear is based on the shear stresses that are developed at two types of interfaces; 1) an interface between the embossed steel and the cement grout, and 2) an interface between cement grout and the concrete deck, as illustrated in Figure 4. Due to the development of the longitudinal shear, τ , in the connection, interfaces tend to slip (see Figure 3). Due to the roughness of the interface, this slip, s , is accompanied by a separation of materials, called uplift, u , at a direction normal to the slip. This uplift is however restrained due to the normal stress (confinement effect), σ , created by the surrounding concrete slab. An equilibrium state is developed with tension in the concrete and in the reinforcement of the concrete slab over the rib and normal compression stresses developed on the interfaces. Figure 4 illustrates the equilibrium state caused by the uplift in the embossed steel-cement grout interface. Equally, uplift between the roughened

concrete and cement grout is also developed but not presented in this Figure. The confinement effect provided by the slab on the interfaces of the connection becomes even more significant if the normal forces resulting from the transversal bending of the slab are considered.

The translational stiffness of the slab is not constant during the development of slip and uplift. Initially the slab is not cracked, as it was observed during cyclic loading push-out tests, and the translational stiffness is large. Once a crack is formed and reinforcement is mobilized the stiffness decreases. Because of its high importance on the connection behaviour and the need for generalization for applications, the confinement effect was studied more in detail through finite element analysis. A typical example of such a confinement effect is the one presented in Figure 5 (a). Initially, before cracking of the concrete the stiffness is high, as expected. Once the crack is formed, point A in Figure 5, the reinforcement steel is submitted to an increasing tension and the normal (confinement) stress continues to increase but with an inferior ratio. At the moment where the middle steel reinforcement yields another change occurs in the curve, point B, and the normal (confinement) stress exhibits a limited increase due to the hardening of the reinforcement and the contribution of the upper reinforcement. At about 2 mm of uplift, point C, the normal stress stops to increase. A model of the confinement effect is shown in Figure 5 (b). Equations associated with this model are given in [Papastergiou, 2012].

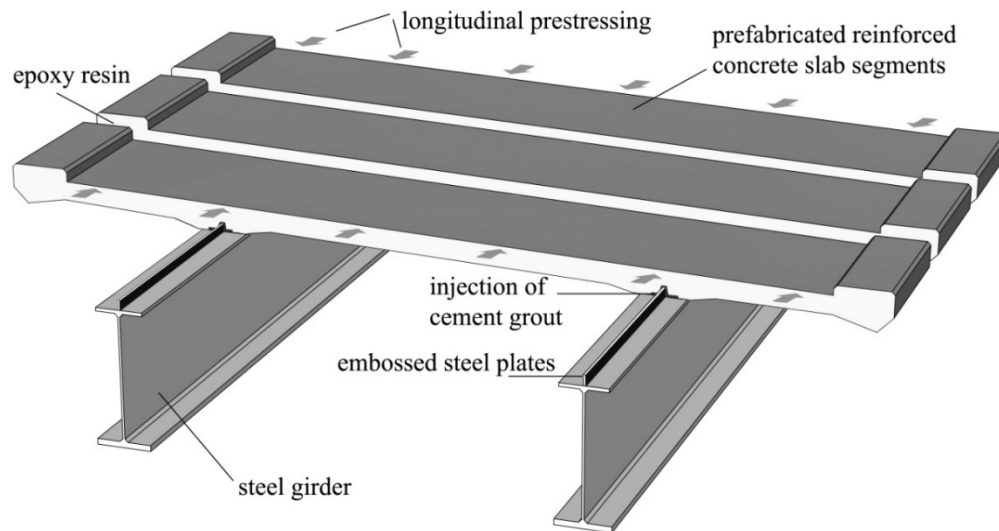


Figure 2. Prefabricated deck segments positioned over steel girders.

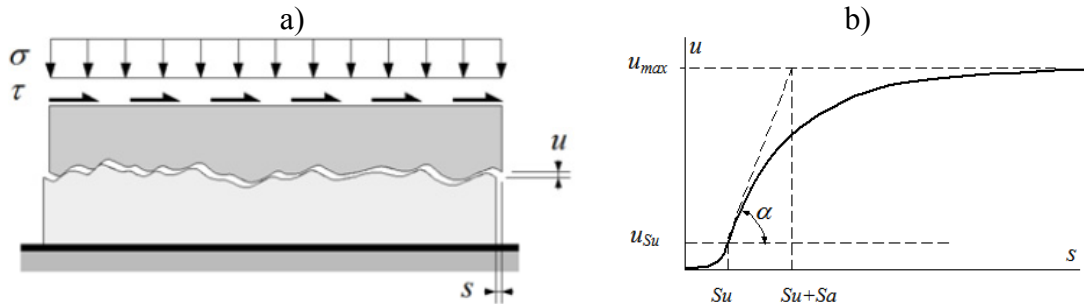


Figure 3. a) Behavior of an interface, and b) definition of the parameters.

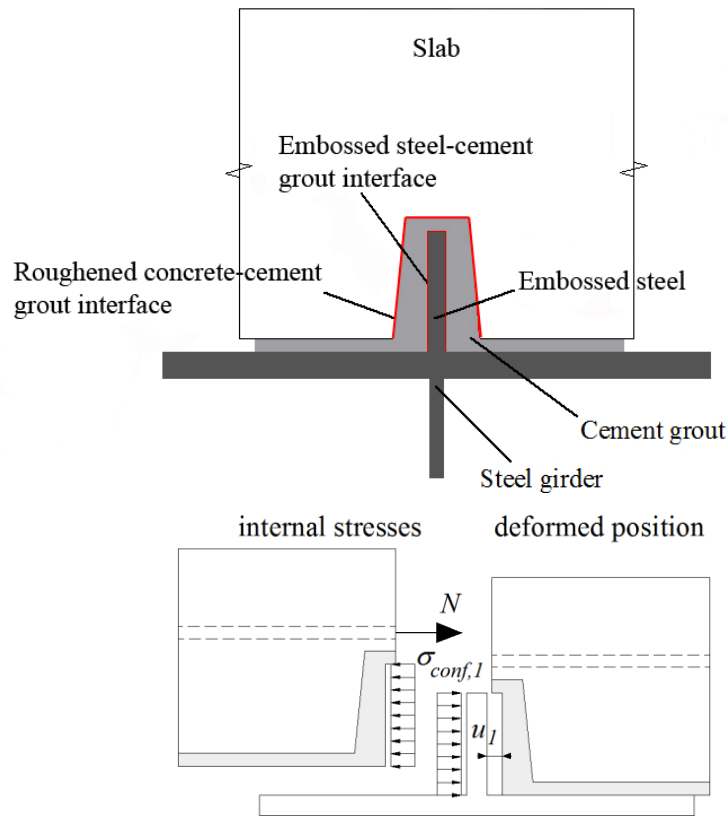


Figure 4. Development of the confinement stresses in the interfaces.

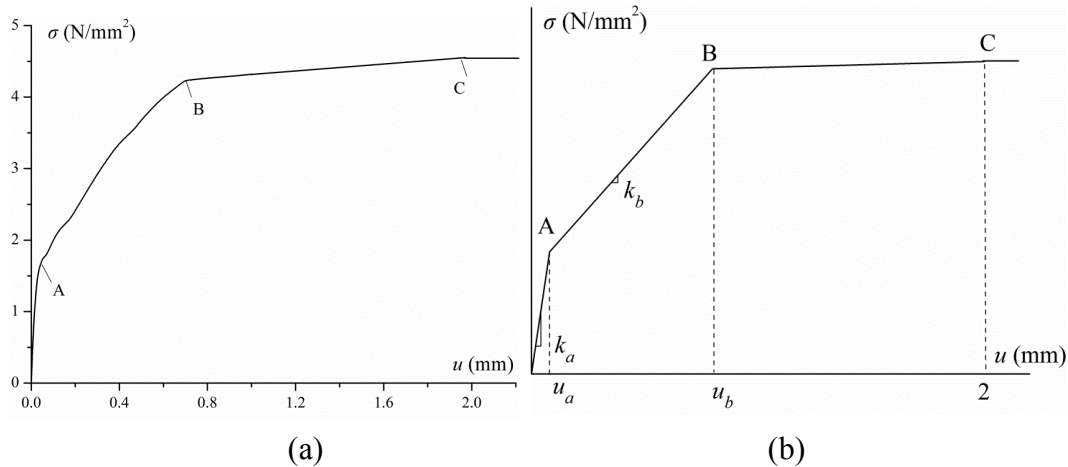


Figure 5. Confinement effect; a) typical FEM result, b) developed model.

This model of the confinement effect is used with the failure criteria, the constitutive law and the kinematic law proposed for each interface behavior. The interaction between them are taken into account in a numerical model of the connection as explained in [Lebet 2008]. The numerical model was validated with numerous push-out tests of the connection. An example of the behavior of the connection (longitudinal shear – slip) resulting from the numerical model is shown in Figure 6.

Point A in Figure 6 corresponds to the end of the elastic behaviour of the connection. Till that point the stiffness of each interface constituting the connection is the elastic stiffness of their constitutive laws. Point B corresponds to the point at which the shear stress at the embossed steel-cement grout interface reaches the ultimate value, for a particular level of confinement. After that point the embossed-steel cement grout interface begins to soften, however the resistance of the connection continues to increase since the normal stress also increases forcing the softening behaviour of the embossed steel-cement grout interface to be developed at higher values. Point C is the first point where the resistance of the connection reaches the ultimate value, V_u , (failure point). For a limited slip, after that point, the different combinations of increasing normal stress and the developed shear stress in the embossed steel interface result practically to maintenance of the ultimate resistance, branch CD in Figure 6. The decrease of the resistance becomes more abrupt at point D, where practically the confinement stress stops to increase significantly.

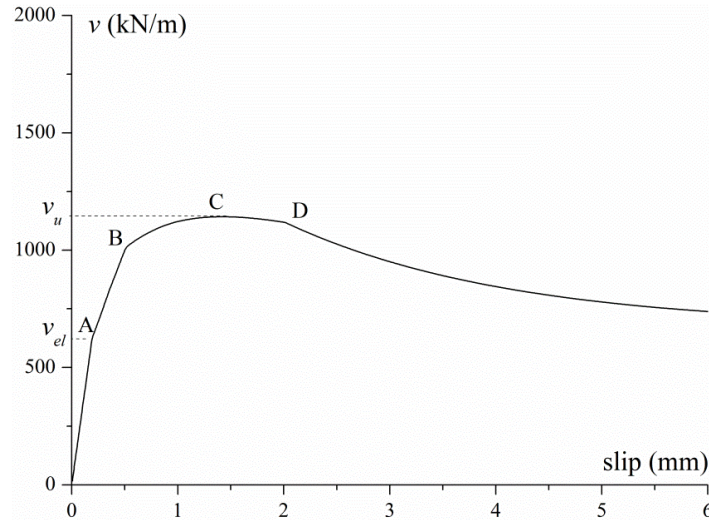


Figure 6. Connection behavior according to the numerical model with characteristic points.

A simplified calculation method for the ultimate resistance of the connection is also given in [Lebet, 2008] where it is shown that this new connection allows full plastic bending resistance of composite beams to be reached.

BEHAVIOUR OF THE CONNECTION UNDER CYCLIC LOADING

To evaluate the behaviour of the new connection under cyclic load, numerous tests were done: i) cyclic tests of the different interfaces, ii) cyclic tests on push-out specimen of the connection, iii) a beam test under cyclic loading followed with a loading up to the ultimate beam resistance. Cyclic loading test results can be found in [Papastergiou, 2012]. In the following, only push-out tests and the test on a composite beam are presented.

Push-out test under cyclic loading

A typical push-out specimen is shown on Figure 7.

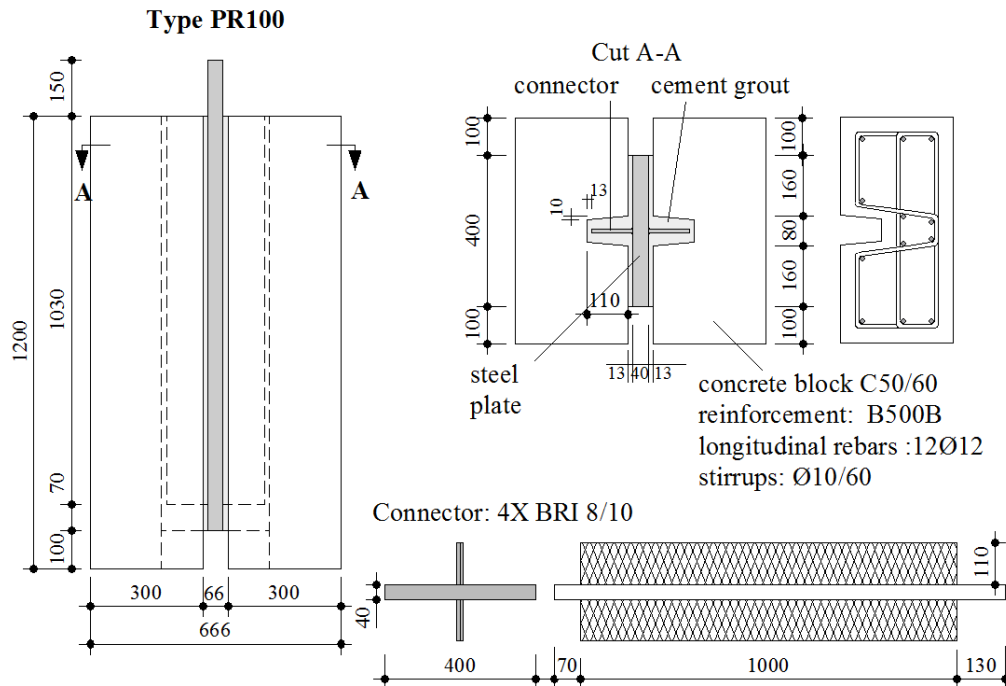


Figure 7. Geometrical characteristics of push-out specimens.

Twelve symmetrical push-out test specimens were fabricated. The blocks for the twelve specimens are made of reinforced concrete-concrete class C50/60 according to [Eurocode 2 (2004)]. Granularity is of maximum diameter 16 mm. The surface of the concrete plates was roughened by sand-blasting. The cement grout was developed by the VSL Company with water to cement ratio varying from 0.29 to 0.32, containing two admixtures (a stabiliser and a plasticizer), the grout resistance at 28 days varies between 76 and 99 MPa.

Cyclic tests were performed under force control with a frequency of 1.5 Hz. During cyclic (pulsar) loading only the shear force is recorded, in order to record the evolution of the force-slip relationship, with the number of cycles, the cyclic loading stops at certain moments, and a complete loading-unloading cycle performed at a loading rate 0.25 mm/min. In addition, the unloading allows registering of the residual slip in the connection, with the number of cycles.

The cyclic loading values correspond to the expected values of the longitudinal shear for this type of connection used to form a twin-I type steel girder-concrete deck composite bridge section, commonly used as illustrated in Figure 2. More precisely the minimum applied load, V_{min} , equal to 260 kN corresponds to longitudinal shear per unit length equal to 130 kN/m. This value is a mean value of the longitudinal shear acting in the connection for long term loads such as dead loads from coating. Verification of connection with respect to the limit of fatigue according to fatigue load model 1 of the Eurocode 1 (2003a) implies for the region of end support of a composite bridge an added variation of the longitudinal shear, Δv_D , of 400 kN/m. Consequently, this verification imposes a maximum load for the push-out tests, V_{max} , equal to 1060 kN. For some tests, this maximum load was increased to 1600 kN to consider ultra high traffic loading. This cyclic loading corresponds to a

variation of 0.41 to 0.55 of V_{max}/V_u , where V_u corresponds to the ultimate load of the push-out test. The push-out specimens were then loaded statically up to their ultimate resistance.

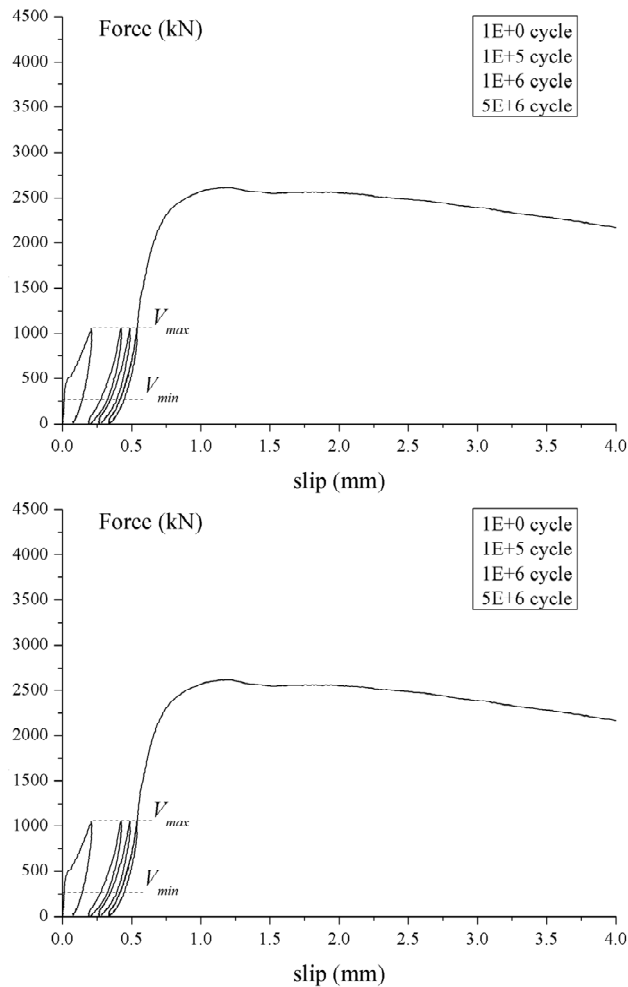


Figure 8. Force-slip relationship for push-out specimens PR100_2 with $V_{max} = 1060$ kN (top) and specimen PR100_8 with $V_{max} = 1600$ kN (bottom).

These fatigue tests run up to 2 million cycles without failure, the tests were generally continued up to 5 million of cycles after which the specimen were loaded statically up to failure. For detailed results see [Papastergiou, 2012]. Figure 8 presents the force-slip relationship of two push-out tests for cyclic loading with two different amplitudes. As seen in those figures an unloading takes place in specific cycles in order to record the residual slip, s_{res} , which is the expression of the damage due to cyclic loading. The graphs include also the final static loading which follows cyclic loading.

The residual slip, s_{res} , and the slip under maximum cyclic shear load, s_{Vmax} , are increasing with repeated loading, however those increases tend to stabilize. This stabilization is more clearly seen in Figure. 9.

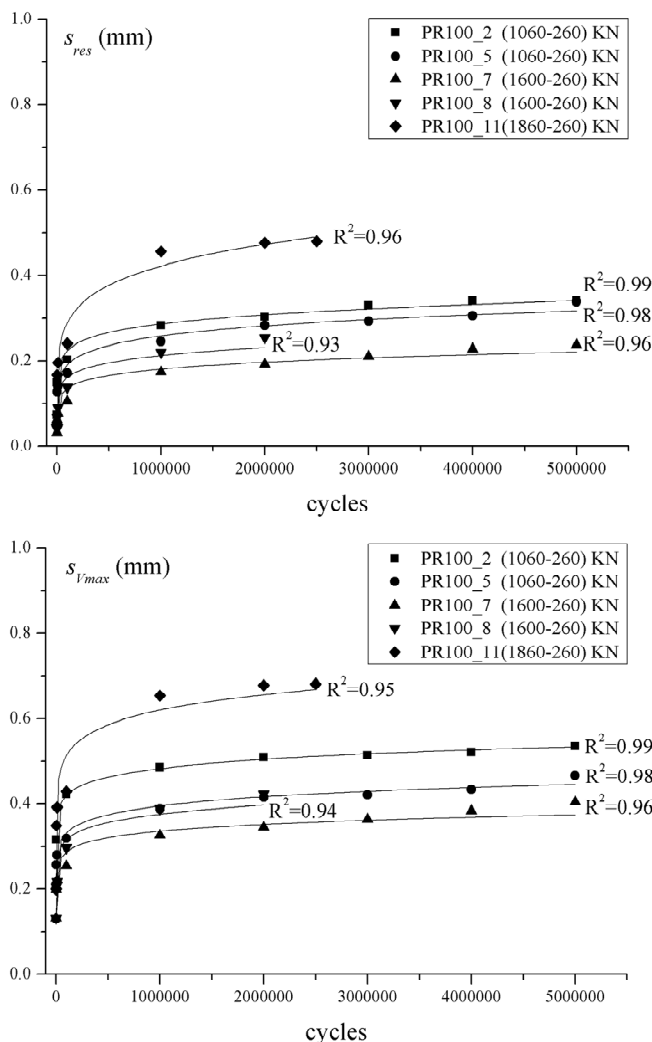


Figure 9. Residual slip, s_{res} , after removal of the load (top) and slip under maximum cyclic shear load, s_{Vmax} (bottom) as a function of the number of cycles N and fitting curves.

For the specimen shown in Figure 9, the stabilization of s_{res} and s_{Vmax} indicates, according to the observed behavior for cyclic loading of interfaces, that the shear stresses developed in the interfaces remain elastic for the corresponding normal stress acting on the interfaces. Consequently, the connection exhibits sufficient resistance to cyclic loading, respected that the maximum applied load does not exceed the value that defines the limit of the elastic domain (domain in which the shear stresses in the interfaces remain elastic). The influence of cyclic loading in this case is limited to the development of a residual slip in the connection which stabilizes with the number of cycles, practically after two million cycles.

For the design, concerning the fatigue limit state, the experimental investigation has shown that the connection is resistant to repeated loading for a ratio of the maximum cyclic shear load versus the ultimate resistance V_{max}/V_u ranging between 0.41 to 0.55. The numerical model provides, as presented in Figure 6, the point A which is the end of the elastic behavior. Up to this point the stiffness of the

interfaces remains constant (elastic stiffness). In other words the shear stresses in the interfaces remain elastic regardless of the increase of the normal stress, since it was found that the elastic stiffness is independent of the normal stress (Papastergiou and Lebet 2011c). Thus based on this experimental verification for no failure during cyclic loading, and based on the fact that the numerical model predicts elastic shear stresses in the interfaces up to point A (shear stress value at point A: v_{el}), it can be assumed that the limit defined by point A, can be considered as a safe limit for cyclic loading of the connection.

For repeated loading with shear stresses remaining elastic, the behaviour of stabilization of the residual slip is guaranteed allowing for use the following equation [Papastergiou, 2012] with application to specimen PR100_6 for example:

$$N_f = \left(\frac{s_u}{s_{V_{max,1}}} \right)^{1/b_{con}} = \left(\frac{1.23}{0.175} \right)^{1/0.072} = 578 \text{ billion cycles}$$

Where N_f is the number of cycles to failure of the connection, $s_{V_{max,1}}$ the slip under maximum shear load for the first cycle, s_u the failure slip corresponding to V_u (Figure 6, point C) and the power indexes b_{con} whose mean statistical values from test fitting curves is 0.072. This number of cycle to failure is far higher than the service life of the bridge.

For the verification at the fatigue limit state of the connection, the characteristic value of the limit of fatigue $v_{Rk,fat}$ is defined as:

$$v_{Rk,fat} = 0.74v_{el}$$

where v_{el} is the longitudinal shear force per unit length at the end of the elastic behavior defined with the numerical model for the specific geometry of the connection; and 0.74 is a conversion factor for the connection longitudinal shear resistance at limit of fatigue based on the 5% fractile of the results of a parametric analysis. For verification, the design longitudinal shear v_{Ed} due to the design value of the permanent load acting on the connection and due to the fatigue model $\gamma_{fat}\Delta v(Q_{fat})$ should verify the relation:

$$v_{Ed} \leq v_{Rk,fat} / \gamma_v$$

where γ_v is the partial factor for the connection equals to 1.25.

Test on a composite beam

The composite beam with the new connection, tested with a cyclic loading up to 5 million cycles followed by a test to failure, is shown in Figure 10 with the details of the instrumentation.

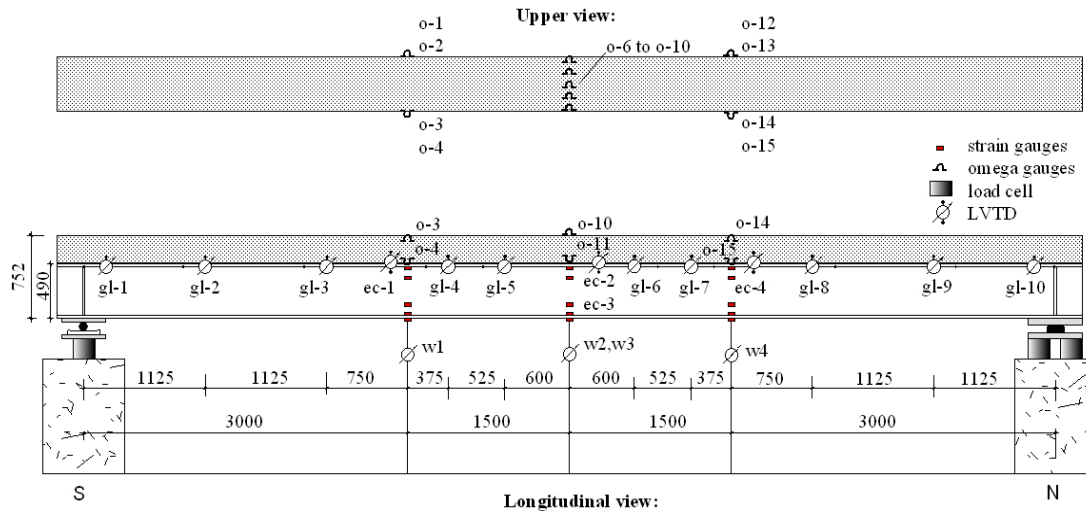


Figure 10. Composite beam geometry and instrumentation for recording.

The steel beam is an HEA 500 of quality S355, the reinforced concrete slab of class C40/50 with a width of 500 mm and a depth of 250 mm. The connector consists of two embossed steel plates of type BRI 8/10 welded together of quality S235 and with a height of 100 mm. The cement grout injected to realize the connection had a compression resistance measured at 75.5 MPa. For the cyclic tests, a vertical cyclic load with constant amplitude and at a frequency of 1 Hz is applied at the first third of the composite beam. The load varies from 140 to 550 kN, resulting to a calculated longitudinal shear per unit length which varies from 137 to 537 kN/m for the first 3 meters of the span, and from 68.5 to 268.5 kN/m for the remaining 6 meters of the span. Unloading of the beam takes place in several characteristic time intervals in order to record the residual slip, s_{res} .

Figure 11 shows the slip under maximum cyclic load s_{Vmax} along the composite beam. The slip under maximum load follows the sign of the longitudinal shear. However it is not uniform along the two parts of the span. An increase of the slip takes place with repeated loading but stabilizes with the number of cycles as shown on Figure 13.

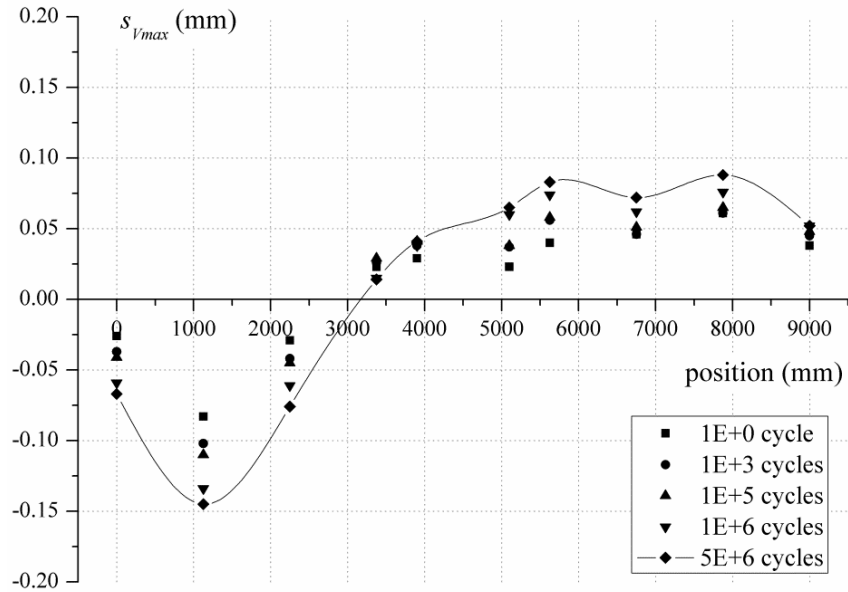


Figure 11. Slip between the steel flange and the slab under maximum cyclic load, s_{Vmax} , along the composite beam.

Figure 12 represents the evolution of the residual slip s_{res} measured after unloading the beam. The residual slip, follows the sign of the longitudinal shear. It increases with repeated loading but it stabilizes within the applied number of cycles.

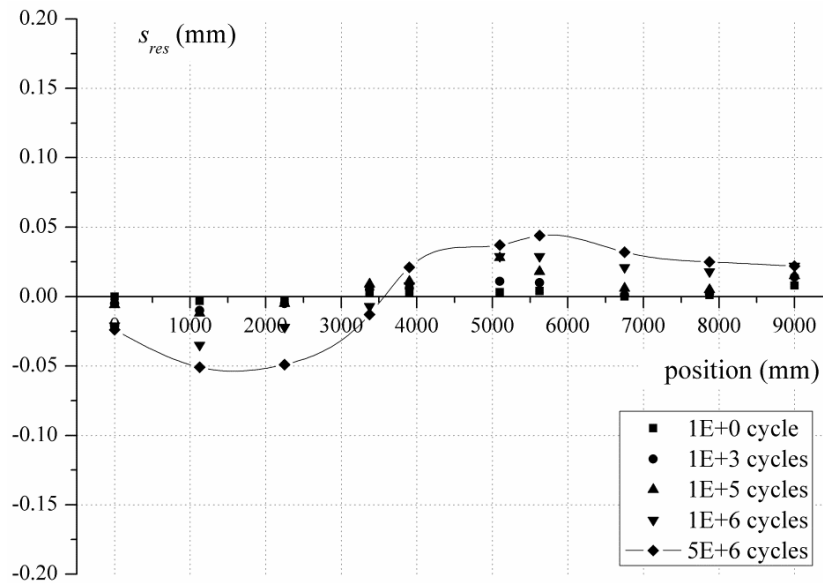


Figure 12. Residual slip, s_{res} , between steel flange and the slab, along the composite beam.

The stabilization is more evident in Figure 13 which shows the residual slip s_{res} and of s_{Vmax} , with the number of cycles, for two sections one at a distance 1125 mm and the second at a distance 5100 mm from the left support of the beam.

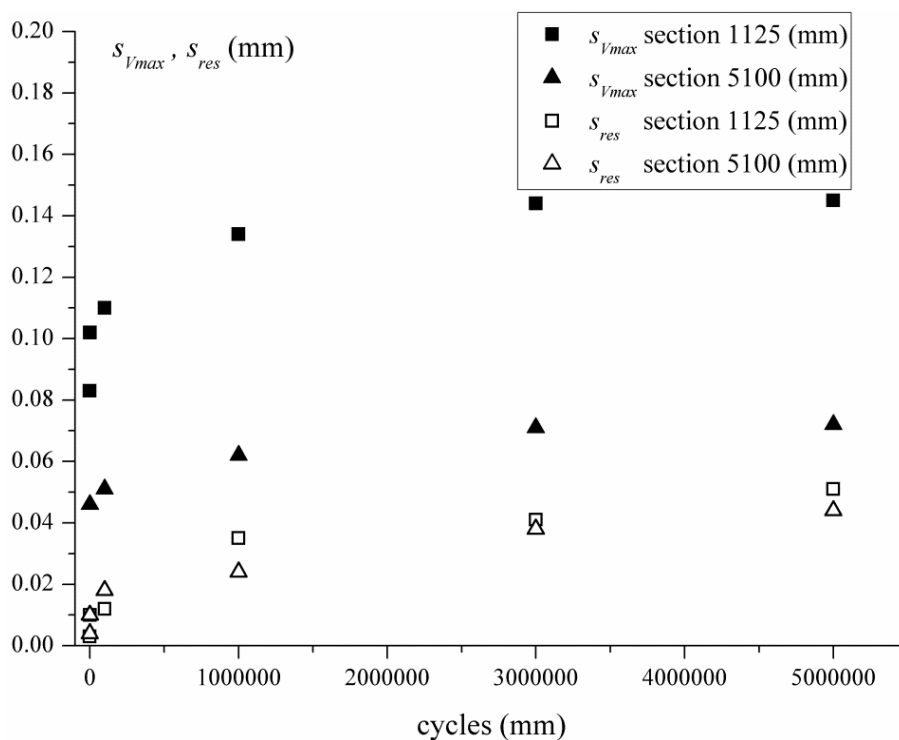


Figure 13. Slip under V_{max} , and residual slip for two sections, as a function of the number of cycles.

After 5 million cycles, there was no failure in the connection and a static test was done up to failure of the composite beam. For the final static test, two hydraulic jacks are used, placed in the middle of the span with a distance of 960 mm between them. The final test is performed under displacement control with a loading velocity equal to 0.1 mm/sec. Figure 14 presents the relationship between the reaction force at the support and the vertical deflection in the middle of the beam. The value of the reaction force due to dead load 22.4 kN is added on that of the measurement to obtain the total value.

The structural performance of the composite beam is significantly ductile. The composite beam starts to fail by plastification of the steel beam at a load of about 470 kN, with increasing bearing capacity as more steel fibers are plastified. For a vertical deflection about 70 mm the first tensile cracks appear in the lower part of the concrete slab, in the middle of the beam, revealing the development of two neutral axes. This is due to the fact that slip, which is kept below 0.2 mm on the elastic domain, starts to increase at this point. The bearing capacity continues to increase. The first point where a small drop of the resistance is noted, for vertical deflection at about 117 mm, corresponds to the initiation of the sprawling of the concrete, outside of the stirrups, in the middle of the span. Plastification of concrete follows. Finally the beam starts to lose bearing capacity when the slip in the north part of the composite beam, increases more than 4 mm for a vertical deflection in the middle of the beam about 193 mm (Figure 15). Further loading results to increase of slip up to the value of 7.7 mm. At that point, with a vertical deflection of 214 mm (Figure 15),

the loading jacks reach their displacement capacity and it was decided to unload the composite beam which develops a permanent deflection of 165 mm.

The plastic resistance of the beam calculated with the measured material values corresponds to 2721 KNm. The design plastic resistance of such a beam is 1870 KNm. Therefore, even after 5 million cycles, the composite beam with the new connection can reach its plastic resistance.

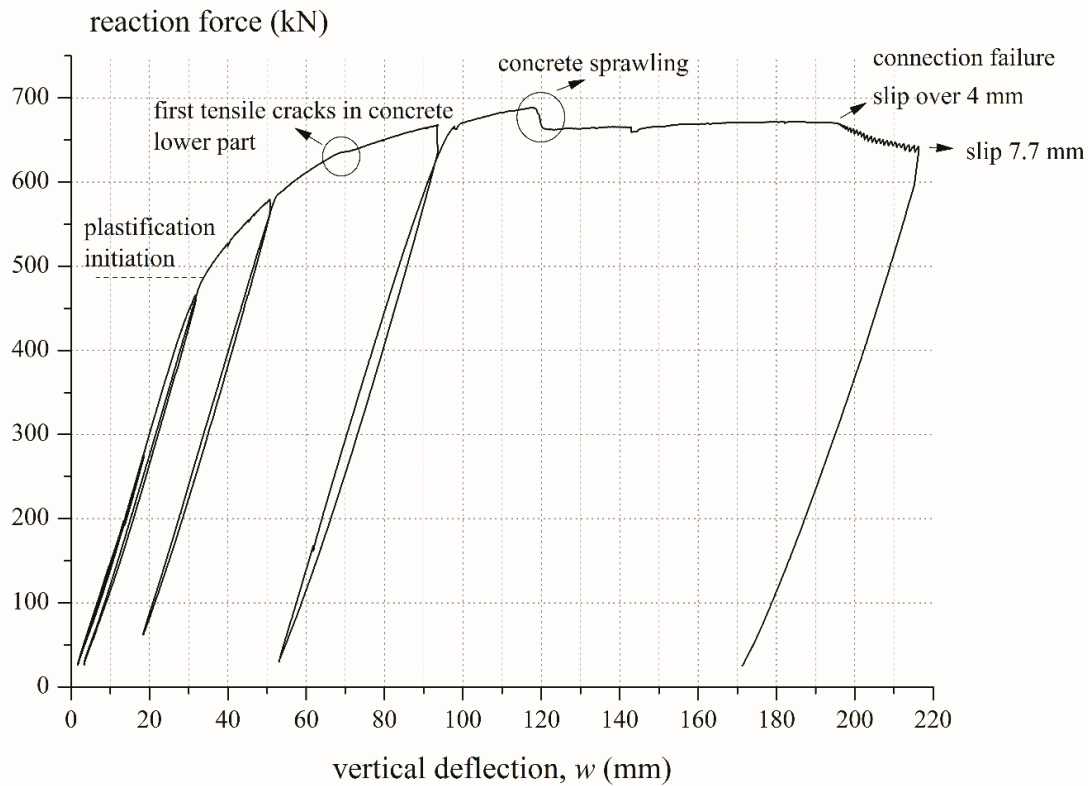


Figure 14. Reaction force at support versus vertical deflection in the middle of the beam.

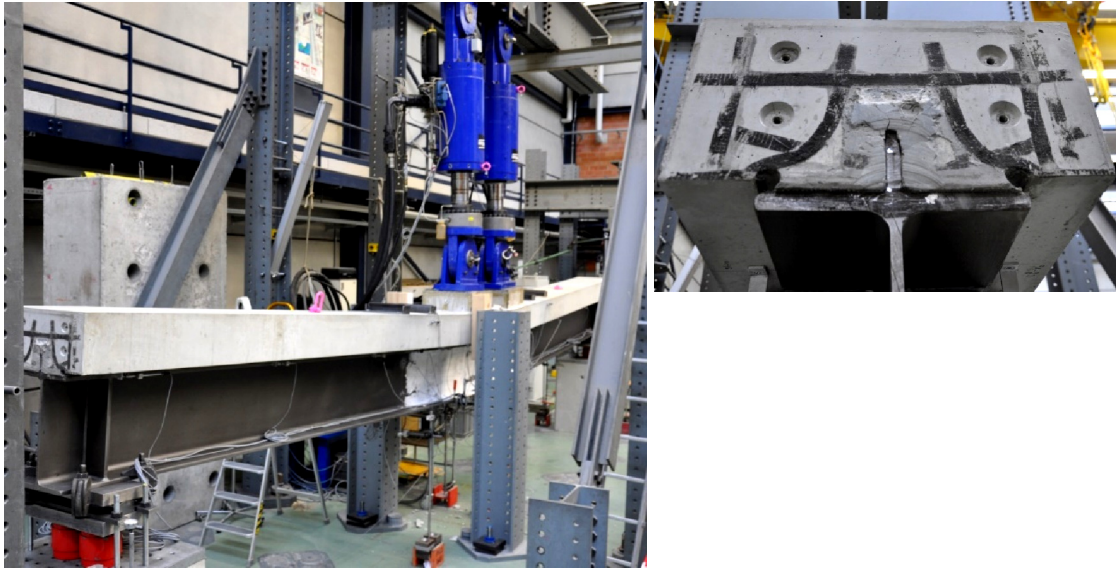


Figure 15. Deformation capacity at the end of test before unloading and slip at the north edge of the beam.

CONCLUSIONS

Connections whose resistance is due to adhesion, interlocking and friction between various interfaces constitute a very promising solution for the fast erection of steel-concrete composite bridges with full-depth precast decks. The results presented in this contribution shows that the fatigue resistance of such a connection is guaranteed as far as the longitudinal shear acting on the connection with the fatigue load remain in the connection's elastic domain. If the connection is designed under this condition, the composite beam can resist the cyclic loading and can reach the full bending plastic resistance.

ACKNOWLEDGEMENTS

This research was supported by the Swiss National Science Foundation, SNSF. The authors wish to express their thanks to the Federal Road office (FEDRO) for financing the specimen fabrication. The two types of cement grout used for the casting of the specimens were provided by the VSL-company and their support was greatly appreciated.

REFERENCES

- Eurocode 1, European Standard (2003), *Actions on structures - Part 2: Traffic loads on bridges*, EN 1991-2.
- Eurocode 2, European Standard (2004), *Design of concrete structures - Part 1-1: General rules and rules for buildings*, EN 1992-1-1.

- Feldmann M., Hechler O., Hegger J. and Rausher S. (2008), "Fatigue behavior of shear connectors in high performance concrete", *Proceedings of the 2008 Composite Construction and in Steel and Concrete Conference VI*, Devil's Thumb Ranch, Tabernash, Co., July, ASCE.
- Kim H.Y. and Jeong Y.J. (2010), "Ultimate strength of a steel-concrete composite bridge deck slab with profiled sheeting", *Eng. Str.*, (32)2, 534-546.
- Lebet J.P. (2008), "New steel concrete shear connection for composite bridges", *Proceedings of the 2008 Composite Construction and in Steel and Concrete Conference VI*, Devil's Thumb Ranch, Tabernash, Co., July, ASCE.
- Papastergiou D. and Lebet J.P. (2011), "New steel-concrete connection for prefabricated composite bridges", *Stahlbau*, 80(12), 894-903.
- Papastergiou D. (2012). "*Connections by adhesion, interlocking and friction for steel-concrete composite bridges under static and cyclic loading*", EPFL Thesis No. 3501.
- Rauscher S. and Hegger J. (2008), "Modern composite structures made of high performance materials", *Proceedings of the 2008 Composite Construction and in Steel and Concrete Conference VI*, Devil's Thumb Ranch, Tabernash, Co., July, ASCE.
- Thomann M. and Lebet J.P. (2007), "Design method for connections by adherence for steel-concrete composite bridges" *Struct. Eng. Inter.*, 17(1), 86-93.

The Effect of Carbon Nanotubes on the Headed Stud Shear Connectors for Composite Steel-Concrete Beams under Elevated Temperatures

Olivia Mirza¹; Kathryn Wilkins¹; Zhong Tao¹; and Brian Uy²

¹School of Computing, Engineering and Mathematics and Institute for Infrastructure Engineering, Univ. of Western Sydney, Locked Bag 1797, Penrith, NSW 2751, Australia. E-mail: o.mirza@uws.edu.au; 16768000@student@uws.edu.au; z.tao@uws.edu.au

²Centre for Infrastructure Engineering and Safety, School of Civil and Environmental Engineering, Univ. of New South Wales Sydney, NSW 2052, Australia. E-mail: b.uy@unsw.edu.au

Abstract

This paper presents a novel experimental and numerical analysis of composite steel-concrete beams at elevated temperatures utilising carbon nanotube. Push tests were conducted as a part of the experimental study to determine the strength of the headed stud shear connectors in both normal concrete and carbon nanotube concrete. The specimens were tested under ambient temperature, 200°C, 400°C, and 600°C, respectively. Results from the experimental study illustrated the reduction of ultimate load and stiffness as temperatures increased. The numerical analysis was in good agreement with the experimental study results. Even though carbon nanotube had no effect on the ultimate load, however, the carbon nanotube reduced concrete spalling and cracking when compared to normal concrete. The carbon nanotube was observed to take effect at temperatures greater than 400°C. As a conclusion, the carbon nanotube concrete material would be an effective choice for reducing concrete spalling and cracking when exposed to elevated temperatures.

INTRODUCTION

Composite steel-concrete beams consist of a concrete slab connected to a steel beam via headed stud shear connectors located at the interface of the components. Composite steel-concrete beams are considered effective due to the high concrete compressive strength complementing the high tensile strength of the steel component [Uy & Liew 2003]. The headed stud shear connectors are used to prevent the vertical separation of the components, and also to transfer the normal and shear loads between the components [Lam & El-Lobody 2005].

The integrity of fire-exposed structures is of high importance to understand. When exposed to elevated temperatures, the concrete and steel mechanical properties decrease with increasing temperature [Mirza and Uy 2009]. Due to the fact that the headed stud shear connectors are indirectly exposed to the elevated temperatures, axial tensions are experienced from the imposed vertical uplift forces [Wang 2005]. Research regarding the integrity of post-fire exposed structures is limited.

Carbon nanotubes are considered as a smart material with research suggesting effective properties to be gained. When added to concrete mixture, the carbon

nanotubes are expected to reduce the concrete from spalling and cracking due to elevated temperatures to overcome concrete durability issues [Potapov et al. 2011]. The experimental investigation of carbon nanotube concrete at elevated temperatures on composite steel-concrete structures has not been explored. This paper herein is to look at the effect of carbon nanotube on headed stud shear connectors for composite steel-concrete beams under elevated temperatures.

EXPERIMENTAL STUDIES

Push test experiments were conducted according to Eurocode 4 [British Standards Institution EC4 2005]. The push test specimens were formed by a reinforced concrete slab standing vertically with two structural steel beams connected via the flanges by welded headed stud shear connectors. Two types of push tests were conducted, including normal concrete material and carbon nanotube concrete material.

Two 400mm long 150UB14.0 Grade 300MPa structural steel beams were used. The reinforced concrete slabs had dimensions of 400mm wide, 400mm long and 200mm deep. The concrete used was nominally 25MPa. The nanotube concrete mixture had an addition of 1% carbon nanotube to concrete material. Three N12 reinforcing bars were spaced at 170mm centre to centre in the concrete slab. 19mm diameters with 100mm long headed stud shear connectors were used. The push test specimen setup for the normal concrete and carbon nanotube concrete materials are shown in Figure 1.

The Eurocode 4 [British Standards Institution EC4 2005] requires push test specimens using concrete to be of 600mm wide, 600mm long and 150mm deep dimensions. However due to the size limitation of the furnace, modifications to the push test specimens have been made. Hence the concrete component is 400mm wide, 400mm long and 200mm deep.

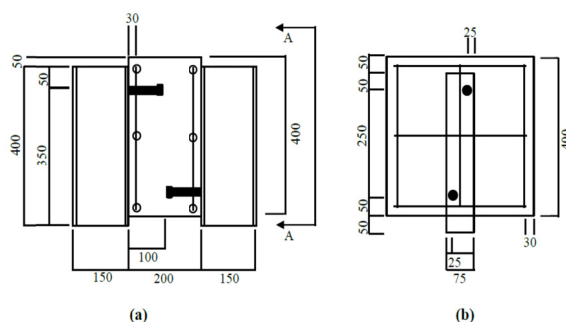


Figure 1. Push test specimens

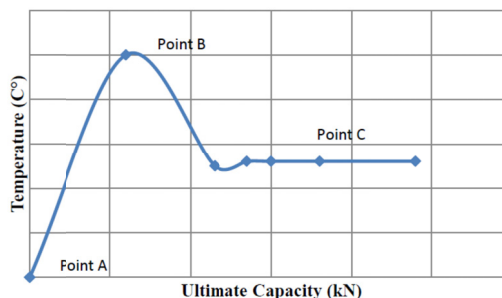


Figure 2. Push test specimens under different conditions

A total of 28 push test specimens were tested. They consist of 14 normal concrete and 14 carbon nanotube concrete materials. The three temperature conditions to be considered include Point A – ambient temperature, Point B – at-fire and Point C – post-fire exposure. The specimens were tested under ambient

temperature, 200°C, post 200°C, 400°C, post 400°C, 600°C and post 600°C. Figure 2 shows the push test experiment details and temperature conditions.

FINITE ELEMENT MODELLING

Material properties

Concrete at ambient temperature

Plain concrete was recommended by [Carreira and Chu 1985], where the stress in compression is assumed to be linear up to a stress of $0.4f'_c$. Beyond this point, the stress is represented as a function of strain according to Equation 1.

$$\sigma_c = \frac{f'_c \gamma (\epsilon_c / \epsilon'_c)}{\gamma - 1 + (\epsilon_c / \epsilon'_c)} \quad (1)$$

where

$$\gamma = \left| \frac{f'_c}{32.4} \right|^3 + 1.55 \text{ and } \epsilon'_c = 0.002$$

For concrete in tension, the tensile stress is assumed to increase linearly relative to strain until the concrete cracks. After the concrete cracks, the tensile stresses decrease linearly to zero. The value of strain at zero stress is usually taken to be 10 times the strain at failure, which is shown in Figure 3.

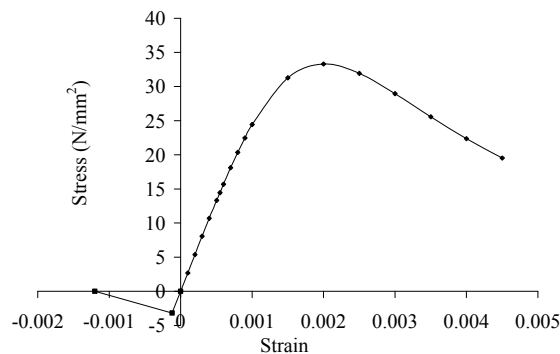


Figure 3. Stress-strain relationship for concrete at ambient temperature, (Carreira and Chu 1985)

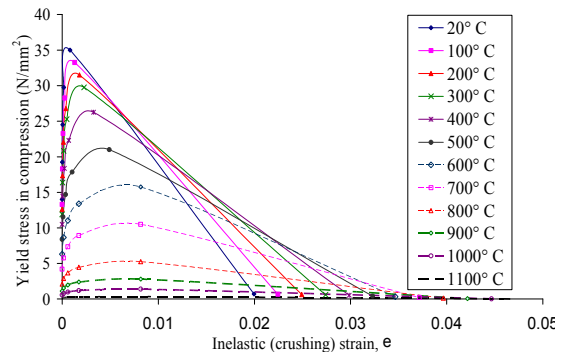


Figure 4. Concrete compressive stress-strain relationship at elevated temperatures, EC2 (British Standards Institution 2004)

Concrete at elevated temperatures

The stress-strain relationship of concrete with siliceous aggregates expressed as a function of the temperature according to Eurocode 2, [British Standards Institution 2004] follows the Equations 2 to 4, and the given distributions in Figures 4 and 5 represent the compressive and tensile stress-strain behaviour of the concrete, respectively.

$$\sigma_c(\theta) = \frac{3\mathcal{E}f_{c,\theta}}{\mathcal{E}_{c1,\theta} \left[2 + \left(\frac{\mathcal{E}}{\mathcal{E}_{c1,\theta}} \right)^3 \right]} \quad \text{for } \mathcal{E} \leq \mathcal{E}_{c1,\theta} \quad (2)$$

$$\sigma_c = 0, \mathcal{E} = \mathcal{E}_{cu1,\theta} \text{ (linear behaviour is adopted)} \quad \text{for } \mathcal{E}_{c1(\theta)} < \mathcal{E} \leq \mathcal{E}_{cu1,\theta} \quad (3)$$

$$\sigma_t(\theta) = k_{c,t}(\theta)\sigma_t \quad (4)$$

where $f_{c,\theta}$ = ultimate stress of concrete, $\mathcal{E}_{c1,\theta}$ = strain at ultimate stress of the concrete, $\mathcal{E}_{cu1,\theta}$ = ultimate strain of the concrete, σ_t = tensile strength of concrete, $k_{c,t}$ = reduction

coefficient for tensile strength of concrete

$$k_{c,t}(\theta) = 1.0 \quad \text{for } 20^\circ\text{C} \leq \theta \leq 100^\circ\text{C}$$

$$k_{c,t}(\theta) = 1.0 - 1.0(\theta - 100)/500 \quad \text{for } 100^\circ\text{C} \leq \theta \leq 600^\circ\text{C}$$

Figure 4 illustrates that the compressive strength of the concrete decreases when temperature increases but the strain of the concrete increases with temperature. The tensile strength of the concrete also decreases with an increase in temperature, as depicted in Figure 5. A tensile stress also can be achieved for temperatures up to 500°C. The modulus of elasticity of the concrete also decreases with an increment in temperature. The reduction of the modulus of elasticity is due to the rupture of bonds in the microstructure of the cement paste when the temperature increases and due to the onset of rapid short-term creep.

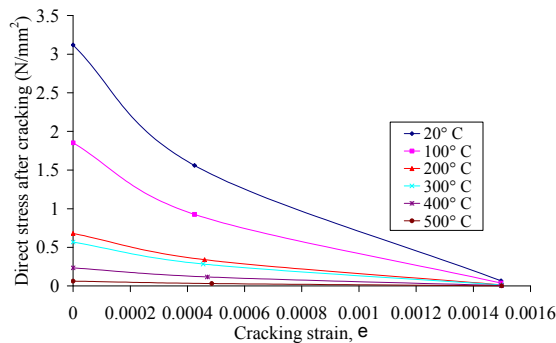


Figure 5. Concrete tensile stress-strain relationship at elevated temperatures, EC2, (British Standards Institution 2004)

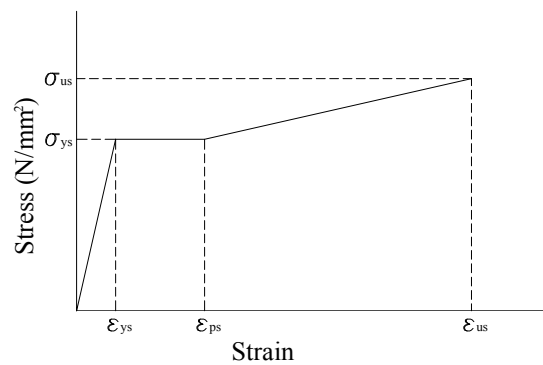


Figure 6. Stress-strain relationship for structural steel at ambient temperature, (Loh, Uy et al. 2003)

Steel material at ambient temperature

The stress-strain characteristics of reinforcing steel and stud shear connectors are essentially similar to structural steel. According to [Loh, et al. 2003], the stress-strain relationship for structural steel is represented as a simple elastic-plastic relationship with strain hardening. The mechanical behaviour for both compression and tension is assumed to be similar. Figure 6 represents the stress-strain relationship for steel and Table 1 indicates the different values of stress-strain for each material.

Table 1. Stress-strain value for structural steel beam, shear connectors, profiled steel sheeting and steel reinforcing

Element	σ_{us}	ϵ_{ps}	ϵ_{us}
Steel beam	$1.28\sigma_{ys}$	$10\epsilon_{ys}$	$30\epsilon_{ys}$
Steel Reinforcing	$1.28\sigma_{ys}$	$9\epsilon_{ys}$	$40\epsilon_{ys}$
Shear Connectors	-	$25\epsilon_{ys}$	-

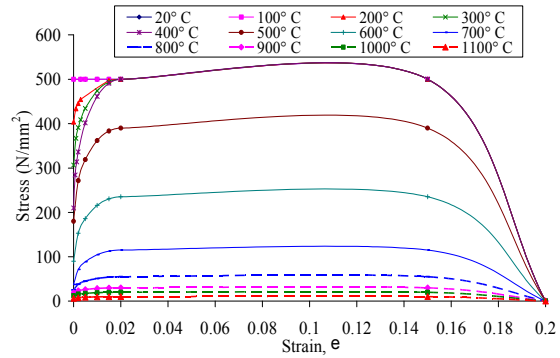


Figure 7. Stress-strain relationship at elevated temperatures for structural steel, EC3 (British Standards Institution 2005)

Steel Material at elevated temperatures

The stress-strain relationship of structural steel as a function of temperature according to Eurocode 3, [British Standards Institution 2005] follows Equations (5) to (9) and the stress-strain relationships are illustrated in Figure 7.

$$\sigma(\theta) = \epsilon E_{a,\theta} \quad \text{for} \quad (5)$$

$$\epsilon \leq \epsilon_{p,\theta}$$

$$\sigma(\theta) = f_{p,\theta} - c + (b/a)[a^2 - (\epsilon_{y,\theta} - \epsilon)^2]^{0.5} \quad \text{for} \quad (6)$$

$$\epsilon_{p,\theta} \leq \epsilon \leq \epsilon_{y,\theta}$$

$$\sigma(\theta) = f_{y,\theta} \quad \text{for} \quad (7)$$

$$\epsilon_{y,\theta} \leq \epsilon \leq \epsilon_{t,\theta}$$

$$\sigma(\theta) = f_{y,\theta} [1 - (\epsilon - \epsilon_{t,\theta}) / (\epsilon_{u,\theta} - \epsilon_{t,\theta})] \quad \text{for} \quad (8)$$

$$\epsilon_{t,\theta} < \epsilon < \epsilon_{u,\theta}$$

$$\sigma(\theta) = 0 \quad \text{for} \quad (9)$$

$$\epsilon = \epsilon_{u,\theta}$$

where $\epsilon_{p,\theta} = f_{p,\theta} / E_{a,\theta}$, $\epsilon_{y,\theta} = 0.02$, $\epsilon_{t,\theta} = 0.15$, $\epsilon_{u,\theta} = 0.20$,

$$a^2 = (\epsilon_{y,\theta} - \epsilon_{p,\theta})(\epsilon_{y,\theta} - \epsilon_{p,\theta} + c / E_{a,\theta}), \quad b^2 = c(\epsilon_{y,\theta} - \epsilon_{p,\theta})E_{a,\theta} + c^2,$$

$$c = \frac{(f_{y,\theta} - f_{p,\theta})^2}{(\epsilon_{y,\theta} - \epsilon_{p,\theta})E_{a,\theta} - 2(f_{y,\theta} - f_{p,\theta})}, \quad f_{y,\theta} = \text{effective yield strength, } f_{p,\theta} =$$

proportional limit

$E_{a,\theta}$ = slope of the linear elastic range, $\epsilon_{p,\theta}$ = strain at the proportional limit, $\epsilon_{y,\theta}$ =

yield strain, $\epsilon_{t,\theta}$ = limiting strain for yield strength. $\epsilon_{u,\theta}$ = ultimate strain

The ultimate strength of the structural steel decreases when the temperature increases, as illustrated in Figure 7. Furthermore, the modulus of elasticity decreases with an increase in temperature.

Finite element type, mesh, boundary conditions and loading conditions

Three-dimensional solid elements were used to model the push off test specimens in order to achieve an accurate result from the finite element analysis. For both the concrete slab and the structural steel beam, a three-dimensional eight node element (C3D8R) was used. A three-dimensional thirty-node quadratic brick element (C3D20R) for shear connectors, a four-node doubly curved thin shell element (S4R) for profiled steel sheeting and a two-node linear three-dimensional truss element (T3D2) for steel reinforcing were used. Figure 8 illustrates the finite element mesh used to represent half of a stud of the push test. The aim of this was to reduce the simulation cost.

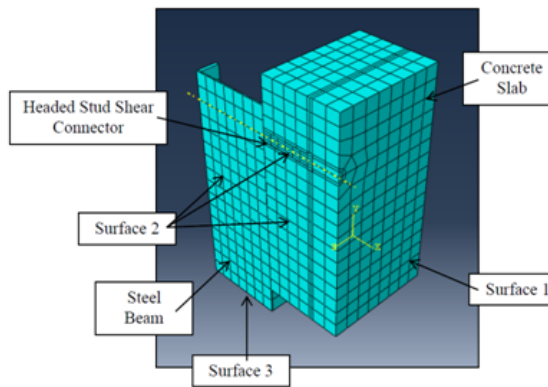


Figure 8. Finite element model for push test specimens

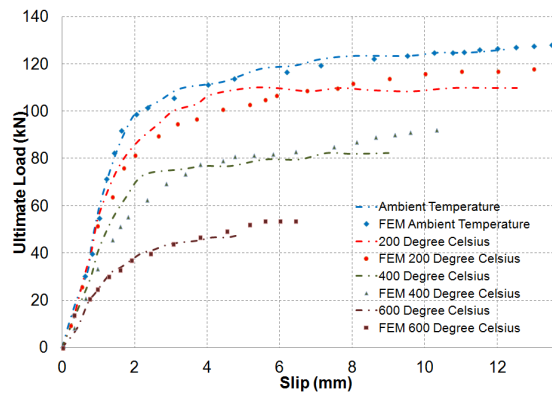


Figure 9. Load versus slip relationships for normal concrete at-fire exposure

In Figure 8, the nodes that lie on the other symmetrical surface (Surface 1) for concrete and steel reinforcing are restricted from moving in the x-direction. All the nodes in the middle of the structural steel beam web, headed stud shear connector, concrete slab and reinforcing steel, which are designated as Surface 2, are restricted

to move in the z-direction. All the nodes of the structural steel beam, which are designated Surface 3, are restricted to move in the y-direction. For the application of load, a static concentrated load was applied to the top of concrete slab employing the modified RIKS method which can be obtained through a series of iterations for each increment for a non-linear structure.

RESULTS AND DISCUSSION

Push test specimens for normal concrete at fire

Generally, the specimens at ambient temperatures, 200°C and 400°C failed due to headed stud shear failure. The failure was signified by a large bang as the stud sheared off the steel flange, separating the concrete slab and steel beam components. For specimens at 600°C, the failure mode was caused by the combination of headed stud failure, concrete cracking and spalling failure. At the same time, it was also observed that the structural steel beam buckled due to the elevated temperatures.

Figure 9 illustrates the comparison of push tests for the normal concrete at-fire exposure. Comparing the stiffness of the normal concrete at ambient temperature to these at 200°C, 400°C and 600°C, a reduction of 8%, 18% and 38% were observed, respectively. Overall, the ambient push test had the greatest stiffness. According to [Mirza and Uy 2009] this is to be expected, as the increase in temperature steadily reduces the stiffness of the steel components. This is also due to the bond failure between concrete and steel surface when subjected to elevated temperatures.

The normal concrete ambient temperature push test achieved an ultimate load of 127kN. The 200°C, 400°C and 600°C normal concrete push tests achieved ultimate loads of 111kN, 78kN and 45kN, respectively. This large reduction illustrates the increased danger of failure of composite steel-concrete beams when subjected to elevated temperatures. Overall the normal concrete ambient temperature specimen achieved the greatest ultimate load. This is due to the increased temperatures decreasing the mechanical properties of the composite steel-concrete specimens; specifically the compressive strength of the concrete component and the rigidity of the steel beam.

The finite element model produced an ultimate shear capacities of 128kN, 118kN, 92kN and 53kN for push test at ambient temperatures, 200°C, 400°C and 600°C, respectively which resulted in less than 10% discrepancy. The push tests compared with the finite element models are shown in Figure 9. The results are in good agreement with the experimental investigation.

Push test specimens for normal concrete at post fire

Similar failure modes were observed for normal concrete at post fire. The specimens at ambient temperatures, post-200°C and post-400°C failed due to headed stud shear failure. The failure was signified by a large bang as the stud sheared off the steel flange, separating the concrete slab and steel beam components. For specimens at post-600°C, the failure mode was caused by the combination of headed stud failure, concrete cracking and spalling failure. However buckling of the steel beam did not occur for the post-600°C specimen.

Figure 10 demonstrates the comparison of push tests for the normal concrete at post fire exposure. The stiffness reduction of 11%, 39% and 45% between the normal concrete ambient temperature and post-200°C, post-400°C and post-600°C was observed. When compared to the normal concrete ambient temperature to at-fire push tests, similar trends of stiffness were observed. However, the normal concrete ambient temperature to at fire push tests achieved a greater stiffness overall when compared to the ambient temperature to post-fire push tests. This suggests that the stiffness of the specimens continues to decrease and is not regained, once exposed to elevated temperatures.

An ultimate shear capacity of 117kN was achieved by the normal concrete ambient temperature. The post-200°C, post-400°C and post-600°C normal concrete achieved ultimate l shear capacities of 110kN, 99kN and 85kN, respectively. This demonstrates ultimate shear capacities reduction of 6%, 10% and 28% compared to the ambient temperature. In comparison to the normal concrete ambient temperature to at-fire push tests, the ambient temperature to post-fire push tests reduced in ultimate load at a significantly lower rate. This suggests that the ultimate shear capacity of the composite steel-concrete beams after exposure to elevated temperatures is greater than exposure during elevated temperatures. According to [Fike and Kodur 2011], this is to be expected as the decreasing temperatures allow for the ultimate strength of the concrete and steel components to be regained.

The greatest ductility was achieved by the ambient temperature. The ductility reduced according to temperatures. Overall the ductility of the normal concrete post-fire push tests is higher when compared to at fire push test. This suggests that greater tensile strength is regained as the specimens cool to ambient temperature. The increasing ductility of the specimens suggests the integrity of the structure also increases. This allows for longer periods of failure to occur, thus increasing safety.

The finite element model produced ultimate loads of 124kN, 114kN, 94kN and 91kN for push test at ambient temperatures, 200°C, 400°C and 600°C. The push tests compared with the finite element models are shown in Figure 10. The results are in good agreement with the experimental investigation.

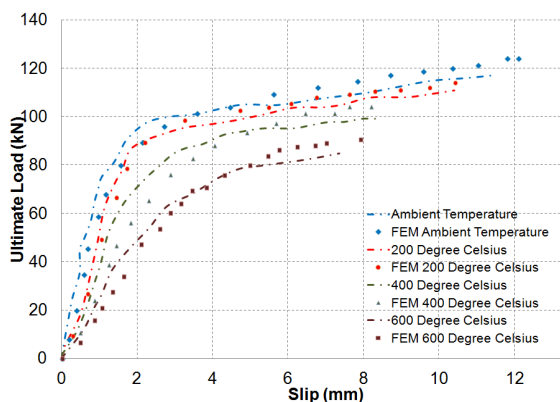


Figure 10. Load versus slip relationships for normal concrete at-post fire exposure

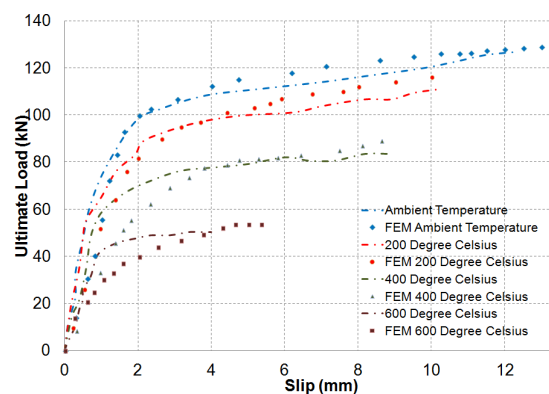


Figure 11. Load versus slip relationships for carbon nanotube concrete at-fire exposure

Push test specimens for carbon nanotube concrete at fire

The failure modes for carbon nanotube are similar to normal concrete. This is due to the carbon nanotube does not have significant affect in increasing the compressive strength of the concrete. However, the reduction of concrete cracking and spalling was observed when compared to the normal concrete at elevated temperatures. This is due to the carbon nanotube concrete being able to prevent nano-cracks from occurring, by requiring a greater amount of energy to form the cracks [Konsta et al. 2010].

Figure 11 demonstrates the comparison of push tests for the carbon nanotube concrete at fire exposure. When compared with ambient temperatures, the stiffness of the nanotube concrete at 200°C, 400°C and 600°C illustrated 4%, 6% and 20% reductions, respectively. When compared to the normal concrete, the stiffnesses are higher.

The nanotube concrete ambient temperature, 200°C, 400°C and 600°C achieved an ultimate shear capacities of 127kN, 111kN, 89kN and 53kN, respectively. When compared to ambient temperature, the ultimate shear capacity reduced 11%, 31% and 58%, respectively. In comparison to the normal concrete ambient temperature to at-fire push tests, the nanotube ambient temperature to at-fire push tests showed a similar trend in ultimate load reduction. More specifically, the nanotube at-fire push tests achieved a slightly higher ultimate load.

Overall the ductility of the at-fire exposure specimens decreased as the temperature increased. This trend in ductility is similar to the ductility trend of the normal concrete ambient temperature to at-fire push tests. The decreasing tensile strength of the headed stud shear connectors means the integrity of the specimen also decreases.

Push test specimens for carbon nanotube concrete at post fire

The specimens at ambient temperature, post-200°C, post-400°C and post-600°C failed due to headed stud shear failure. But there was one improvement to these specimens, i.e. there was no sign of concrete cracking or spalling failure. This is due to the calcium-silicate hydro-crystals decomposing, allowing for the chemically bound water to be released and evaporated.

Figure 12 demonstrates the comparison of push tests for the carbon nanotube concrete at post fire exposure. A 22%, 30% and 63% stiffness reduction was observed between the nanotube concrete ambient temperature and post-200°C, post-400°C and post-600°C, respectively. The normal concrete post-fire push tests achieved a greater stiffness when compared to carbon nanotube concrete post-fire.

An ultimate shear capacity of 120kN was achieved by the nanotube concrete ambient temperature specimens. The post-200°C, post-400°C and post-600°C nanotube concrete demonstrated ultimate loss of 111kN, 99kN and 92kN, respectively. This illustrates ultimate shear capacity reductions of 5%, 19% and 25% when comparing the ambient temperature push test to the post-200°C, post-400°C and post-600°C, respectively. Compared to the nanotube concrete ambient

temperature to at-fire push tests, the ambient temperature to post-fire push tests reduced in ultimate load at a significantly lower rate. This is similar to the ultimate shear capacity trend between the normal concrete at-fire and post-fire push tests.

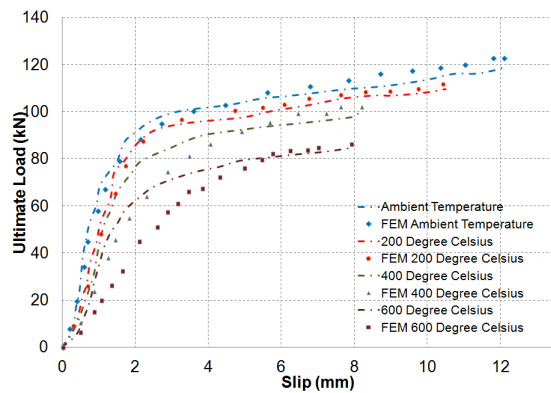


Figure 12. Load versus slip relationships for carbon nanotube concrete at-post fire exposure

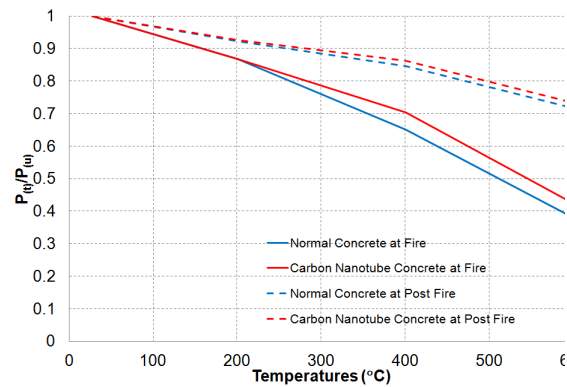


Figure 13. Comparison for ultimate load of headed stud shear connectors according to temperatures

The ductility reduced when temperatures increased. This trend is similar to the carbon nanotube concrete ambient temperature to at-fire push tests, as the at-fire 600°C push test achieved the lowest ductility.

The finite element model produced an ultimate load of 123kN, 112kN, 102kN and 86kN for push tests at ambient temperature, 200°C, 400°C and 600°C. The push tests compared with the finite element models are shown in Figure 10. The results are in good agreement with the experimental investigation.

Comparison of push test specimens for normal and carbon nanotube concrete at fire

In order to measure the shear force resistance of push tests, the loads were measured according to the slip rate of 4mm. Figure 13 illustrates the progression of ultimate load of the push test specimens according to temperatures when carbon nanotube is incorporated. The ultimate shear capacity ratios, $P_{(u)}/P_{(t)}$, related to different temperatures are shown in Figure 13. The figure shows that the carbon nanotube did not show any effect when the temperatures range from ambient to 200°C. When the temperatures reach 400°C and 600°C, the carbon nanotube not only shows the decrease in concrete cracking and spalling, but also 8% and 11% increments in their shear resistance loads, respectively. Therefore, it can be assumed that the carbon nanotube is only useful when temperatures are greater than 200°C.

Comparison of push test specimens for normal and carbon nanotube concrete at post fire

In Figure 13, the ultimate shear capacities for post fire showed similar trend to at fire where the carbon nanotube did not show any effect until the temperature reached 200°C. At temperatures above 200°C, the shear force resistance of carbon nanotube increased when compared to normal concrete. Therefore, it can be assumed that the carbon nanotube is only useful when temperatures are greater than 200°C.

When compared to push test specimens at fire, the post fire push tests illustrated that the shear resistance reduced at a lower rate. This is due to the post-fire specimens regain strength after the specimens cool down to ambient temperature. The carbon nanotube concrete demonstrates a 7% and 8% higher in shear resistance loads for 400°C and 600°C, respectively.

CONCLUSIONS

The experimental studies showed that the failure modes for push tests were generally headed stud shear failure. Even though adding carbon nanotube into the concrete did not significantly increase the compressive strength of the concrete, however, when the specimens were exposed to elevated temperatures, the reduction in concrete cracking and spalling were observed.

When comparing the normal concrete to the carbon nanotube concrete, it was observed that similar ultimate capacities were achieved up to 200°C. After 200°C, the carbon nanotube concrete achieved higher ultimate loads. Furthermore, the carbon nanotube concrete showed that there was a great reduction in spalling and cracking when exposed to elevated temperatures.

It can be concluded that the carbon nanotube material did not have any effect until temperatures reached 200°C or above. This is observed by the change in colour from the carbon nanotube concrete ambient temperature specimen to the 600°C specimen. This suggests that at greater elevated temperatures, the carbon nanotube concrete material would be a more effective choice, particularly with the reduced concrete spalling and cracking achieved.

In comparison of the at-fire exposure results to the post-fire exposure results, it was observed that greater ultimate loads and ductility were achieved by the post-fire exposed specimens, with similar stiffness achieved. This suggests that the strength of the components regains during the cooling process of the post-fire testing.

Accurate finite element models have been developed to investigate the behaviour of shear connection in composite steel-concrete beam at elevated temperatures utilising carbon nanotube. Based on the comparisons between the results obtained from finite element models and available experimental results, it was observed that they are in good correlation. All the failure modes were accurately predicted by finite element model. The maximum discrepancy is 10%.

RECOMMENDATION FOR FURTHER RESEARCH

Composite steel-concrete beam with the inclusion of carbon nanotube showed the improvement in cracking and spalling of concrete under elevated temperatures. Studies considering continuous beams with the inclusion of carbon nanotube to look at the cracking and spalling effects under elevated temperatures will be subjected to future research in this project.

ACKNOWLEDGEMENTS

The authors would like to acknowledge the funding and financial assistance provided by Institute for Infrastructures Engineering, University of Western Sydney. The authors also would like to acknowledge the technical staff at the University laboratory at the University of Western Sydney for their assistance, effort, hard work and overall dedication to the preparation of the experimental study push test specimens and to the conducting of the push test study. Lastly, the authors would like to acknowledge the School of Computing Engineering and Mathematics at the University of Western Sydney for providing an exceptional learning environment, research facilities and materials.

REFERENCES

- British Standards Institution. (2004) *Design of composite steel and concrete structures, Part 1.1 General rules and rules for buildings, British Standard Institute, London*. Vol. ENV 1994-1-1.
- British Standards Institution. (2004) *Design of concrete structures, Part 1.1 General rules and rules for buildings, British Standard Institute, London* Vol. ENV 1992-1-1
- British Standards Institution. (2005) *Design of the steel structures, Part 1.1 General rules and rules for buildings, British Standard Institute, London*. Vol. ENV 1993-1-1.
- Carreira, D. and Chu, K. (1985). "Stress-strain relationship for plain concrete in compression." *Journal of ACI Structural*, 82 (11), 797-804.
- Fike, R. and Kodur, V. (2011). "Enhancing the fire resistance of composite floor assemblies through the use of steel fiber reinforced concrete." *Engineering Structures*, 3, 2870-2878.
- Konsta, G., Metexa, M. and Shah, S., (2010). "Multi-scale mechanical and fracture characteristics and early-age strain capacity of high performance carbon nanotube/cement nanocomposites." *Cement & Concrete Composites*, 32, 110-115.
- Lam, D. and El-Lobody, E. (2005). "Behaviour of headed stud shear connectors in composite beam." *Journal of Structural Engineering-ASCE*, 131(1), 96-107.

- Loh, H.Y., Uy, B. and Bradford, M.A. (2003). "The effects of partial shear connection in the hogging moment region of composite beams Part II - analytical study." *Journal of Constructional Steel Research*, 60(2), 921-962.
- Mirza, O. and Uy, B. (2009). "Behaviour of headed stud shear connectors for composite steel-concrete beams at elevated temperatures." *Journal of Constructional Steel Research*, 65(3), 662-674.
- Potapov, V., Shitikov, E., Trutnev, N., Gorbach, V., and Portnyagin, N. (2011). "Influence of silica nanoparticles on the strength characteristics of cement samples." *Glass Physics and Chemistry*, 37(1), 98-105.
- Uy, B. and Liew, J.Y.R. (2003). *Composite steel-concrete structures*, *The Civil Engineering Handbook*, 2nd edition ed USA: CRC Press LLC
- Wang, Y.C. (2005). "Performance of steel-concrete composite structures in fire." *Progress in Structural Engineering and Materials*, 7(2), 86-102.

Predictive Models for the Stiffness of Vertical Screws as Shear Connection in Timber-Concrete Composite Floors

F. Moshiri¹; R. Shrestha²; and K. Crews³

¹Ph.D. Candidate, Centre for Built Infrastructure, Univ. of Technology Sydney, Building 11, 81 Broadway Ultimo, NSW 2007, Australia. E-mail: Farzad.Moshiri@uts.edu.au

²Lecturer, Centre for Built Infrastructure, Univ. of Technology Sydney, Building 11, 81 Broadway Ultimo, NSW 2007, Australia. E-mail: Rijun.Shrestha-1@uts.edu.au

³Professor, Centre for Built Infrastructure, Univ. of Technology Sydney, Building 11, 81 Broadway Ultimo, NSW 2007, Australia. E-mail: Keith.Crews@uts.edu.au

Abstract

The stiffness, strength, and arrangement of the shear connection play a crucial role in the design of timber-concrete composite (TCC). This paper reviews the available analytical models for prediction of the stiffness of TCC shear connections. The methodology of different analytical models for stiffness of the mechanical fastener TCC connection is discussed and the accuracy of these models is examined based on push out test results for shear connectors. The simplified stiffness models underestimated the experimental data of normal wood screw with an error ranging approximately 10–40%, whereas the models based on Winkler's theory were inaccurate and calculated a much lower stiffness compared to that of experimental test with an error of approximately 60%. The reasons attributed to inaccuracy of the stiffness models are described. This paper recommends further investigation on the prediction of foundation moduli of timber and concrete as the main input parameters of the models based on the Winkler's theory.

Keywords: Timber concrete composite floor (TCC); Stiffness; Foundation modulus; Wood screw.

INTRODUCTION

Timber concrete composites (TCCs) are structural elements that comprises of timber and concrete elements joined together by some form of shear connector. They are most commonly used as floor systems. There are a number of different types of shear connectors that are used in TCCs with varying effectiveness, price and labour requirement. Fasteners include nails, screws, shear keys and proprietary devices.

TCCs benefit from the composite action, resulting in a significant improvement in strength and stiffness compared to the timber and concrete acting independently (Clouston, Bathon, & Schreyer, 2005). The level of this benefit

depends on the stiffness of the connector, and can range from no connection to rigid connection, with the boundaries of structural efficiency determined by these theoretical limits.

The degree of stiffness of the composite is dependent on the stiffness of the connection (Clouston et al., 2005). The connector allows for composite action – that is, for the timber and concrete to act together as one entity, with the timber and concrete acting in tension and compression respectively and due to bending (Branco, Cruz, & Piazza, 2007). This is aligned with the materials' natural properties and behaviours (Moshiri, Crews, et al., 2012; Moshiri, Garven, et al., 2012).

Stiffness of TCC shear connection

The slip between timber and concrete in TCC shear connection and consequently the slip modulus of laterally loaded shear connection has a significant influence on the overall behaviour of composite beams including displacement, stiffness, load carrying capacity and distribution of internal forces. However, Santos, De Jesus, Morais, and Lousada (2010) and Mascia and Santana (2009) reported that the stresses are not so sensible to the behaviour of the shear connection for plywood composite beams. The non-linear load-slip response of a single connection and its stiffness within the linear range of response, which is so called slip modulus, characterises the overall behaviour of composite beams. Furthermore, a connection within the non-linear range results in non-linear behaviour of the TCC system (Mascia & Santana, 2009).

The design of timber composite structure is governed by displacement within serviceability limit state (SLS), hence, the slip at timber connection plays a crucial role on design of timber beams. Furthermore, the linear-elastic approach for design of timber composite systems proposed by Eurocode5 “Gamma method” employs different input parameter such as slip modulus to design the TCC beams whilst inaccurate slip modulus results in unreliable design for the timber composite systems (EN, 2004; Mascia & Santana, 2009). The Gamma method introduced an effective (apparent) bending stiffness of the composite cross-section using the shear bond coefficient, γ as shown in:

$$EI_{eff} = E_c I_c + E_c A_c a_1^2 \gamma + E_t I_t + E_t A_t a_2^2 \quad (1)$$

where, I is moment of inertia; E is modulus of elasticity (MOE) and A is section area. Factor a_1 represents the distance between centroids of concrete floor and effective TCCs whilst a_2 indicates distance between the centroids of timber joist and effective TCCs. The effective bending stiffness is used to check the design resistance of the connector and the stress values in the timber and concrete. The shear bond coefficient is given in Eurocode 5 as:

$$\gamma = \frac{1}{1 + \frac{\pi^2 E_c A_c S}{KL^2}} \quad (2)$$

where, E_c is MOE of the concrete floor, A_c is section area of the concrete floor, S represents spacing of the connectors, K is slip modulus of the connector and L is span length of the beam. Eurocode 5 considers the non-linearity of timber composite connection by different values of slip modulus associated to different level of loading including serviceability and ultimate slip moduli corresponding to $0.4F_{max}$ and $0.6F_{max}$, respectively.

This paper reviews available stiffness models of timber to timber and TCC connections which include both simplified models and models based on the theory of beam on elastic foundation. In case of TCC, the predicted slip modulus can be used as input parameter for the design of composite structure. The experimental aspect of the research consists of push out tests of normal wood screws which is used as shear connection in TCC specimens and aims to examine the accuracy of the available stiffness models of TCC shear connection for their practical application in the design of TCC floor. Due to availability and lower cost, labour requirement and time for fabrication, normal wood screw was selected as shear connection for verification of the models.

ANALYTICAL MODELS

In this section, different available analytical models for the serviceability stiffness of timber composite connections are discussed. Their methodology and required input parameters are also analysed. Lack of appropriate verification of the available models seems to be a major limitation for their practical application in the design of TCC floor. In addition to the stiffness models, the analytical models of the foundation modulus of timber and concrete are presented.

Stiffness model: Eurocode 5

Eurocode 5 proposes an empirical equation to predict the serviceability stiffness, K_s of vertically inserted dowel-type fasteners e.g. dowels, bolts without clearance, screws and nail without pre-drilling in timber-timber connection. In case of TCC, a modification factor of two is taken into account to consider the presence of concrete slab instead of one of the timber components (Dias, 2005; EN, 2004) as:

$$K_s = \rho_m^{1.5} \frac{d}{23} \quad (3)$$

where, ρ_m is the mass per unit volume of timber and d is the diameter of the fastener as defined in EN14592 (2008). The stiffness is approximated based on the diameter of the fastener and density of timber, and is valid for loading parallel to the grain whilst the effect of length of fastener is neglected (Symons. D, Persaud. R, & Stanislaus. H, 2010).

Stiffness model: Zahn (1991)

Zahn (1991) proposed a similar equation to Eurocode 5 to approximate the serviceability stiffness of the single bolt timber-timber connection which was adopted by Forest and Association (1997) as shown in Equation (4). Similar to the model proposed by Eurocode 5, a modification factor of two is adopted by authors to use the model for verification of the experimental data of normal wood screw used in TCC.

$$K_s = 246d^{1.5} \quad (4)$$

Where d is diameter of fastener.

Stiffness model: Turrini G. and Piazza M. (1983) and Ceccotti A. (1995)

Based on the experimental works, Turrini G. and Piazza M. (1983) and Ceccotti A. (1995) proposed Equations (5-6) respectively to approximate the serviceability stiffness of timber composite shear connection as:

$$K_s = 0.08E_t d \quad (5)$$

$$K_s = 0.125E_t d \quad (6)$$

where, d and E_t are diameter of fastener and MOE of timber.

Stiffness model: Kuenzi (1955)

Previous investigations e.g. Hetényi (1946), Kuenzi (1955), Larsen (1975), Patton-Mallory, Pellicane, and Smith (1997) and Gelfi, Giuriani, and Marini (2002) employed generic solutions of an elastic beam on an elastic foundation to approximate the elastic range of overall load-slip response and stiffness of vertically inserted fastener for timber composite joint (Patton-Mallory et al., 1997). The beam on elastic foundation under the acting external loads was investigated first by Winkler (1867).

The Winkler's theory of beam on elastic foundation simulates vertically inserted fastener by a beam with flexural deformation whilst elastic foundations of distributed springs model timber and/or concrete components resisting the deformation of fastener. The Winkler's theory discussed that the design values of timber composite joint with single nail fastener depends on several parameters e.g. material properties of timber and fastener. Moreover, the slip at interface of composite components, slip modulus, internal forces and moments and the deformation profile of fastener along embedded length in timber associated with each stage of loading are approximated.

Kuenzi (1955) first employed the Winkler's theory to introduce a differential equation to approximate the load carrying capacity and the elastic deformations of a single and double planes timber-timber joint by modelling the nail as a linear-elastic beam on an elastic foundation as:

$$EI \frac{d^4 y}{dx^4} + ky = 0 \quad (7)$$

where, k (k_t for timber, k_c for concrete) is the foundation modulus of material whilst E and I are the MOE and second moment of area for the fastener. Equation (7) results in general solution represented in:

$$y_t(x) = (B_{1t} \cos \lambda_t x + B_{2t} \sin \lambda_t x) e^{-\lambda_t x} + (B_{3t} \cos \lambda_t x + B_{4t} \sin \lambda_t x) e^{-\lambda_t x} \quad (8)$$

where,

$$\lambda_t = \sqrt[4]{\frac{k_t}{4E_s I_s}} \quad (9)$$

$$\lambda_c = \sqrt[4]{\frac{k_c}{4E_s I_s}} \quad (10)$$

B_i are constant coefficients based on the compatibility conditions.

Kuenzi (1955) assumed the stiffness of attached springs to be linear elastic whilst later on Foschi (1974) extended the stiffness of spring to non-linear range assuming an ideal elastic-plastic steel for fastener and smooth elastic-plastic for nail. The reaction forces act perpendicular to fastener axis and opposing the deflection of the fastener. Thus, there is compression in the surrounding timber and concrete in front of the fastener. This compressive forces distributed along the fastener are proportional at every point to the deflection of the fastener at this point, $y(x)$ multiply to the foundation modulus, k as shown in Equation (11).

$$P(x) = ky(x) \quad (11)$$

Using compatibility conditions, Kuenzi (1955) approximated the slip at interface of composite by:

$$\Delta = P \left[2(L_1 + L_2) - \frac{(J_1 - J_2)^2}{K_1 + K_2} \right] \quad (12)$$

where, L_1 , L_2 , J_1 , J_2 , K_1 and K_2 are calculated by:

$$L_1 = \frac{\lambda_1}{k_1} \left[\frac{\sinh \lambda_1 t_1 \cosh \lambda_1 t_1 - \sin \lambda_1 t_1 \cos \lambda_1 t_1}{\sinh^2 \lambda_1 t_1 - \sin^2 \lambda_1 t_1} \right] \quad (13)$$

$$L_2 = \frac{\lambda_2}{k_2} \left[\frac{\sinh \lambda_2 t_2 \cosh \lambda_2 t_2 - \sin \lambda_2 t_2 \cos \lambda_2 t_2}{\sinh^2 \lambda_2 t_2 - \sin^2 \lambda_2 t_2} \right] \quad (14)$$

$$J_1 = \frac{\lambda_1^2}{k_1} \left[\frac{\sinh^2 \lambda_1 t_1 + \sin^2 \lambda_1 t_1}{\sinh^2 \lambda_1 t_1 - \sin^2 \lambda_1 t_1} \right] \quad (15)$$

$$J_2 = \frac{\lambda_2^2}{k_2} \left[\frac{\sinh^2 \lambda_2 t_2 + \sin^2 \lambda_2 t_2}{\sinh^2 \lambda_2 t_2 - \sin^2 \lambda_2 t_2} \right] \quad (16)$$

$$K_1 = \frac{\lambda_1^3}{k_1} \left[\frac{\sinh \lambda_1 t_1 \cosh \lambda_1 t_1 + \sin \lambda_1 t_1 \cos \lambda_1 t_1}{\sinh^2 \lambda_1 t_1 - \sin^2 \lambda_1 t_1} \right] \tag{17}$$

$$K_2 = \frac{\lambda_2^3}{k_2} \left[\frac{\sinh \lambda_2 t_2 \cosh \lambda_2 t_2 + \sin \lambda_2 t_2 \cos \lambda_2 t_2}{\sinh^2 \lambda_2 t_2 - \sin^2 \lambda_2 t_2} \right] \tag{18}$$

where, t_i is embedded length of fastener in each component. The serviceability stiffness of the timber composite shear connections is approximated as load capacity divided by slip at interface of composite materials as shown in Equation (19).

$$K = \frac{P}{\Delta} \left[2(L_1 + L_2) - \frac{(J_1 - J_2)^2}{K_1 + K_2} \right]^{-1} \tag{19}$$

In case of TCC joint, the timber and concrete components are assumed to be a Winkler foundation where elements of continuous beam displace perpendicular to the axis of fastener parallel to the compressive force without shear interactions between the adjacent elements. The stiffness of surrounded concrete and timber can be idealised by the springs attached to the fastener embedded in timber and concrete. The deformed shape of fastener in timber and concrete is modelled by a continuous beam which is laid on the springs over its length.

Stiffness model: Gelfi et al. (2002)

Based on The Winkler's theory, Gelfi et al. (2002) proposed a theoretical approach to predict serviceability stiffness of vertically inserted screws in TCC beams. In this model, the Winkler's theory is adopted to take into account the effect of concrete components whilst a timber plank interlayer simulates upgrading of old timber floor by inserting of the fastener into timber plank as permanent formwork and casting a thin concrete slab. The interlayer is simulated as a gap between composite components then the transmitted loads are ignored as shown in Figure 1.

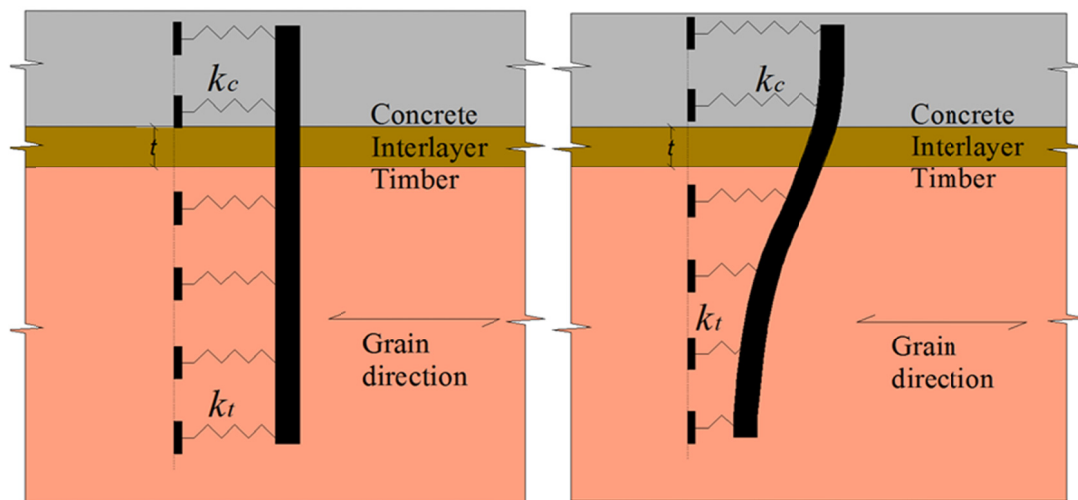


Figure 1. Stiffness model of vertically inserted dowel connection for TCC beam

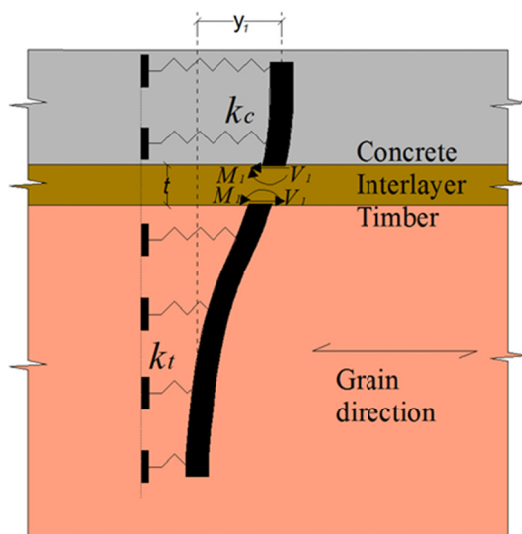


Figure 2. Internal forces of vertically inserted dowel connection for TCC beam

The material properties of concrete and timber are accounted by their foundation moduli whilst the bending stiffness of fastener represents its material properties (Dias, Cruz, Lopes, & van de Kuilen, 2010).

The Winkler's theory of the beam on elastic foundation assumes the following assumptions for simulation of TCC joint (Gabr & Valero, 1995; McLain & Thangjitham, 1983; Patton-Mallory et al., 1997):

- The behaviour of fastener is elastic perfectly plastic
- Winkler foundation (ignores shear strain)
- The connector fits tightly in the hole (no clearance)
- No friction between members or along the fastener
- Small displacement theory is valid
- The governing failure mode is crushing of timber beneath fastener (no splitting)
- Constant material properties through the thickness

The fastener is assumed to behave as a Winkler beam with unlimited length in the concrete and timber. The serviceability stiffness of shear connection is approximated employing the continuity of the flexural deformations for the fastener as shown in Equation (20).

$$K_s = \frac{V_1}{y_{10}} \quad (20)$$

The compatibility equations of fastener are calculated using the flexibility method approach assuming the timber and concrete components as elastic materials as:

$$q_m = f_m Q_m + q_{om} \quad (21)$$

$$\begin{bmatrix} y_{11} & y_{12} \\ \theta_{21} & \theta_{22} \end{bmatrix} \begin{bmatrix} V_1 \\ M_2 \end{bmatrix} + \begin{bmatrix} y_{10} \\ \theta_{20} \end{bmatrix} = 0 \quad (22)$$

where, the flexibility matrix, f_m size (2*2) is determined from the solution of the beam on elastic foundation formula whilst V_1 and M_1 represent the internal loads acting on the free end of the beam as depicted in Figure 2. Moreover, the rotation and deformation of fastener at very end distance from interface are assumed to be zero. The flexibility coefficients of the flexibility matrix are determined by summation of the displacements and rotations of the beam embedded in elastic foundation of concrete, timber and interlayer as given in Equations (23-26).

$$\theta_{20} = 0 \quad (23)$$

$$y_{11} = \frac{2\lambda_c}{k_c} + \frac{2\lambda_t}{k_t} \quad (24)$$

$$\theta_{21} = y_{21} = \frac{2\lambda_c^2}{k_c} - \frac{2\lambda_t^2}{k_t} \quad (25)$$

$$\theta_{22} = \frac{4\lambda_c^3}{k_c} - \frac{4\lambda_t^3}{k_t} \quad (26)$$

Eliminating M_2 in Equation (22), the stiffness of connection is obtained by:

$$K_s = \frac{12\lambda_t\lambda_c E_s I_s}{3(\lambda_t^2 + \lambda_c^2)(\lambda_t + \lambda_c)} \quad (27)$$

Foundation modulus models

Foundation modulus model of timber: Kuenzi (1955)

Kuenzi (1955) approximates the foundation modulus of timber in parallel and perpendicular to the grain directions using:

$$k_t = E_{t,\alpha} \frac{D}{Z} \quad (28)$$

where, d is the diameter of the fastener, Z is the foundation depth, and $E_{t,\alpha}$ is the modulus of elasticity of timber in parallel and perpendicular directions whilst Z is a constant and assumed to be about 25mm.

Foundation modulus model of concrete: Gelfi and Giuriani (1987)

There are few experimental data available for foundation modulus of concrete. Gelfi and Giuriani (1987) estimates the foundation modulus of concrete, k_c by:

$$k_c = \frac{E_c}{\beta} \quad (29)$$

where, E_c is the MOE of concrete and β is a factor as a function of the fastener's diameter to spacing ratio ranging between (2.5-3.3). The foundation modulus of concrete is about four times stiffer than engineered wood products whilst the embedded head of screw in concrete component provides additional interlocking (Symons, Persaud, & Stanislaus, 2010).

EXPERIMENTAL TEST

The experimental data of push out test carried out by Khorsandnia, Valipour, and Crews (2012) is used for verification of the models. The push out test consists of four TCC joint specimens using single normal wood screw, laminated veneer lumber (LVL) and conventional concrete. Typical geometry and details of TCC specimens are depicted in Figure 3. In the push-out tests, the load was applied onto the end of the timber component whilst the concrete slab, fixed on the table of the testing rig, resisted the load. The test aimed to derive the strength and stiffness of the connection. A load cell and linear variable differential transducers (LVDT) were used to measure the load and relative displacement between the timber and concrete (Figure 4). The loading procedure for the push out tests was conducted in accordance with EN26891 (1991) which sets a required loading sequence (Figure 5).

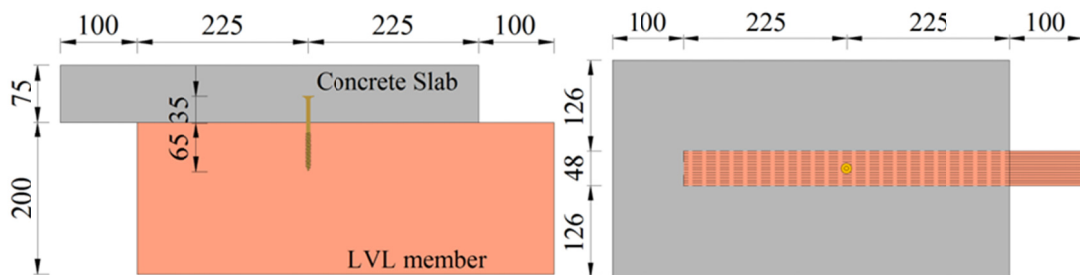


Figure 3. Cross-section- and plan views of specimen in (mm)

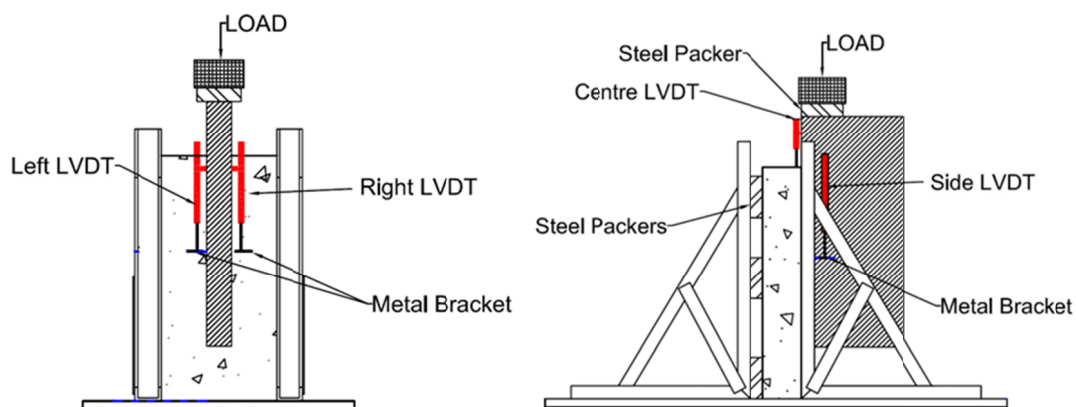


Figure 4. Front and elevation views of push out test set up

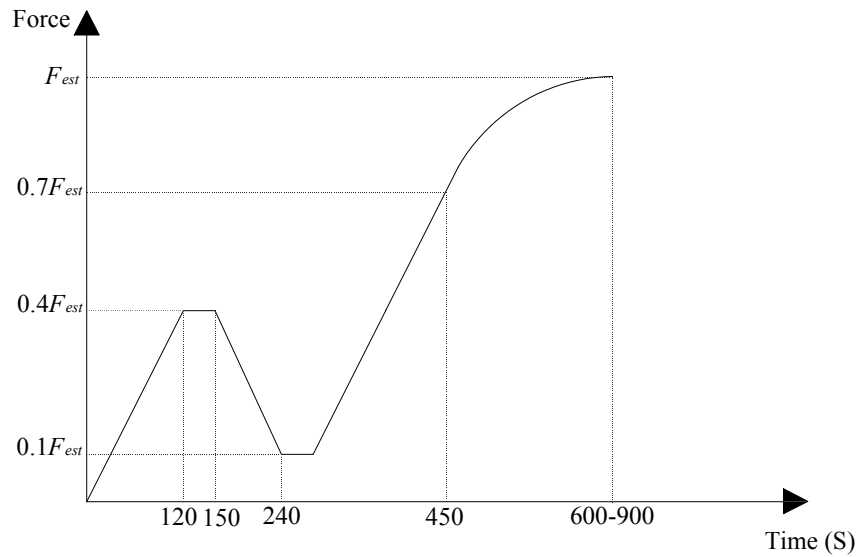


Figure 5. Loading regime in compliance with EN26891 (1991)

The load-slip graphs of TCC joints obtained by push-out test are shown in Figure 6.

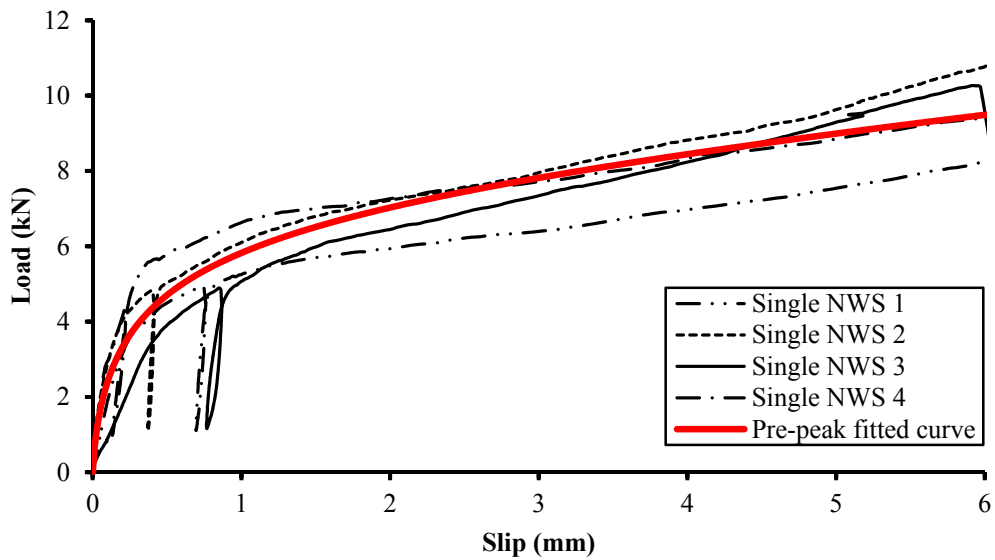


Figure 6. Load-slip diagrams of normal wood screw

Plotting load slip responses of the connections, the serviceability slip modulus, $K_{s,0.4}$ was calculated in compliance with EN26891 (1991) as given in:

$$K_{s,0.4} = \frac{0.4F_{max}}{\frac{4}{3}(v_{04} - v_{01})} \tag{30}$$

where, F_{max} is the load carrying capacity and v_{01} and v_{04} are slip corresponding to $0.1F_{max}$ and $0.4F_{max}$. Table 1 tabulates the serviceability slip modulus of vertically

inserted wood screw shear connection which were calculated in compliance with EN26891 (1991).

Table 1. Serviceability slip modulus of normal wood screw

Specimen	$K_{s,0.4}$ (kN/mm)
NWS1	12.7
NWS2	12
NWS3	6.9
NWS4	17.6
Mean	12.3
σ	4.4
CoV(%)	35.7

COMPARISON OF STIFFNESS MODELS AND EXPERIMENTAL RESULTS

Different available models for serviceability stiffness of timber composite connections using mechanical fastener are discussed in section 2. Table 2 summarises the connection geometry and material properties of normal wood screw connection used in TCC. A summary of the push-out test results and predictions of the available stiffness models of TCC joints using normal wood screw is shown in Table 3.

Table 2. Summary of material properties of TCC joint with normal wood screw

Material properties of TCC joint	Value
Outer diameter of screw, d (mm)	6.6
Shank diameter of screw, d (mm)	5.2
MOE of screw, E_s (MPa)	210000
MOE of LVL, E_t (MPa)	13400
characteristic density of LVL, ρ_k (kg/m ³)	600
embedment depth in timber, t_1 (mm)	65
embedment depth in concrete, t_2 (mm)	35
Foundation modulus of LVL, k_t (MPa)	384
Foundation modulus of concrete, k_c (MPa)	7160

Table 3. Summary of experimental and analytical data of serviceability stiffness

Results	K_{ser} (kN/mm)	% Error
Experiment	12.3	-
Eurocode 5, EN (2004)	8.4	-31.6
Zahn (1991)	8.3	-32.4
Turrini G. and Piazza M. (1983)	7.1	-42.2
Ceccotti A. (1995)	11.1	-9.7
Kuenzi (1955)	4.5	-63.6
Gelfi et al. (2002)	4.5	-63.6

The simplified stiffness models e.g. Eurocode 5, Turrini and Piazza (1983) and Zahn (1991) underestimated the experimental data of normal wood screw with an error ranging approximately 10-40% whereas the models based on Winkler's Theory e.g. Kuenzi (1955) and Gelfi et al. (2002) calculated a much lower stiffness compared to that of experimental test with an error of approximately 60%.

The low foundation moduli of wood screw obtained from the experimental test (Table 2) is attributed to this high underestimation. However, if the foundation modulus value calculated by the foundation modulus model of Kuenzi (1955) (Equation (28)) is employed, a suitable agreement between experimental and analytical stiffness results will be achieved. It is noted that the models based on Winkler's theory are not suitable to calculate the stiffness of TCC connections utilising screw with small diameter.

The accuracy in simplified stiffness models is different where Ceccotti (1995) indicates appropriate agreement with the experimental data whereas other simplified models represent notable difference between analytical and experimental data.

The under estimation error of simplified stiffness models is as expected and agreed with literature. For example Ceccotti, Fragiaco, and Giordano (2006) reported a high difference of 40% for analytical and experimental serviceability stiffness of glued re-bar TCC connections.

The underestimation of simplified stiffness models is due to the fact that these models only consider limited parameters e.g. fastener diameter and MOE of timber whereas, the important parameter such as foundation moduli of timber, slenderness of fastener, its embedding length and MOE are ignored.

The underestimated stiffness and strength lead to the larger resistance but brittle failure of the composite beam whilst an accurate approximation of stiffness and strength by push-out test or some modifications of the predictive models are crucial to have a ductile design.

CONCLUSION

This paper reviews the available models for prediction of the serviceability stiffness of timber composite joint. The analytical results of the models were compared with the experimental results of single normal wood screw shear connection used in TCC specimens.

The simplified stiffness models such as Eurocode 5, Turrini and Piazza (1983) and Zahn (1991) underestimated the experimental data of normal wood screw with an error ranging approximately 10-40% whereas the models based on Winkler's theory such as Kuenzi (1955) and Gelfi et al. (2002) were inaccurate and calculated a much lower stiffness compared to that of experimental test with an error of approximately 60%. The input parameters of the simplified models are limited to diameter of fastener and density or MOE of timber whilst in addition to aforementioned parameters, the effect of the bearing behaviour of concrete and the length of fastener are taken into account in the models based on the Winkler's theory. The reasons attributed to inaccuracy of the stiffness models were discussed.

This paper recommends further investigation on the prediction of foundation moduli of timber and concrete as the main input parameters of the models based on the Winkler's theory. Additionally, further examination of the available stiffness models using experimental data of different types of mechanical fastener with various lengths and diameters is required to propose the models for the design of TCC floor.

It is noteworthy to state that the less input parameters required for the simplified models may be more readily available compared to that for the models based on the Winkler's theory e.g. foundation moduli of timber and concrete, which makes the simplified models more practical for application in design of TCC floor.

ACKNOWLEDGEMENT

The authors wish to acknowledge the financial support of Structural Timber Innovation Company (STIC) for the project.

REFERENCES

- Branco, J. M., Cruz, P. J. S., & Piazza, M. (2007). Experimental analysis of laterally loaded nailed timber-to-concrete connections. *Construction and Building Materials*, 23(1), 400-410. doi: 10.1016/j.conbuildmat.2007.11.011
- Ceccotti, A. (1995). Lecture E13: Timber-concrete composite structures. In H. J. Blass (Ed.), *Step/Eurofortech lecture series. ED*. Netherlands.
- Ceccotti, A., Fragiaco, M., & Giordano, S. (2006). *Behaviour of a Timber-Concrete Composite Beam with Glued Connection at Strength Limit State*. Paper presented at the World Conference on Timber Engineering, USA.
- Ceccotti A. (1995). Lecture E13: Timber-concrete composite structures. In H. J. Blass (Ed.), *Step/Eurofortech lecture series. ED*. Netherlands.
- Clouston, P., Bathon, L. A., & Schreyer, A. (2005). Shear and Bending Performance of a Novel Wood--Concrete Composite System. *Journal of Structural Engineering*, 131(9), 1404-1412. doi: 10.1061/(asce)0733-9445(2005)131:9(1404)
- Dias, A. M. P. G. (2005). *Mechanical behaviour of timber concrete joints*. PhD, university of Delf.
- Dias, A. M. P. G., Cruz, H. M. P., Lopes, S. M. R., & van de Kuilen, J. W. (2010). Stiffness of dowel-type fasteners in timber-concrete joints. *Proceedings of the Institution of Civil Engineers: Structures and Buildings*, 163(4), 257-266.

- EN14592. (2008). Timber structures *Dowel-type fasteners —Requirements*. Brussels, Belgium: European Committee for Standardization.
- EN, B. (2004). Eurocode 5-Design of Timber Structures-Part 1-1 *part 1-1: General rules and rules for buildings*. Brussels, Belgium: European Committee for Standardization.
- Forest, A., & Association, P. (1997). National Design Specification for Wood Construction, (ANSI/NFoPA NDS-1997). *Washington, DC*.
- Foschi, R. (1974). Load-slip characteristics of nails. *Wood science*, 7(1), 69-76.
- Gabr, M., & Valero, S. (1995). Geotechnical properties of municipal solid waste. *ASTM geotechnical testing journal*, 18(2), 241-251.
- Gelfi, P., & Giuriani, E. (1987). Shear force-slip relationship for stud connectors. Studi e Ricerche. *Corso di Perfezionamento per le Costruzioni in Cemento Armato F.lli Pesenti*.
- Gelfi, P., Giuriani, E., & Marini, A. (2002). Stud Shear Connection Design for Composite Concrete Slab and Wood Beams. *Journal of Structural Engineering*, 128(12), 1544-1550. doi: 10.1061/(asce)0733-9445(2002)128:12(1544)
- Hetényi, M. (1946). *Beams on elastic foundation: theory with applications in the fields of civil and mechanical engineering* (Vol. 16).
- Khorsandnia, N., Valipour, H. R., & Crews, K. (2012). Experimental and analytical investigation of short-term behaviour of LVL-concrete composite connections and beams. *Construction and Building Materials*, 37(0), 229-238. doi: 10.1016/j.conbuildmat.2012.07.022
- Kuenzi, E. W. (1955). Theoretical design of a nailed or bolted joint under lateral load. Madison: USDA forest products lab.
- Larsen, H. (1975). Determination of Load-Slip Curves for Bolts and Nails. *Rep. Presented at IUFRO Wood Engrg. Group, 3*.
- Mascia, N. T., & Santana, C. L. d. O. (2009). Remarks on the slip modulus of nailed connections for linear analysis of plywood timber beams. *Construction and Building Materials*, 23(8), 2731-2737. doi: <http://dx.doi.org/10.1016/j.conbuildmat.2009.02.037>
- McLain, T., & Thangjitham, S. (1983). Bolted Wood-Joint Yield Model. *Journal of Structural Engineering*, 109(8), 1820-1835. doi: doi:10.1061/(ASCE)0733-9445(1983)109:8(1820)
- Moshiri, F., Crews, K., Gerber, C., Valipour, H. R., Shrestha, R., & Garven, C. (2012). *The effect of interlayer on the structural behaviour of timber concrete composite joints using light-weight and conventional concrete*. Paper presented at the Diversity in Composites, Leura, New South Wales, Australia.
- Moshiri, F., Garven, C., Gerber, C., Valipour, H. R., Shrestha, R., & Crews, K. (2012). *An investigation on tcc systems using light-weight concrete*. Paper presented at the world conference on timber engineering(WCTE), New Zealand.
- Patton-Mallory, Pellicane, P., & Smith. (1997). Modeling Bolted Connections in Wood: Review. *Journal of Structural Engineering*, 123(8), 1054-1062. doi: doi:10.1061/(ASCE)0733-9445(1997)123:8(1054)

- Santos, C., De Jesus, A., Morais, J., & Lousada, J. (2010). A Comparison Between the EN 383 and ASTM D5764 Test Methods for Dowel-Bearing Strength Assessment of Wood: Experimental and Numerical Investigations. *Strain*, 46(2), 159-174.
- Symons, D., Persaud, R., & Stanislaus, H. (2010). Slip modulus of inclined screws in timber-concrete floor. *Structures and Buildings* 16(4), 245–255.
- Symons, D., Persaud, R., & Stanislaus, H. (2010). Slip modulus of inclined screws in timber-concrete floor. *Structures and Buildings*, 16(4), 245–255.
- Turrini, G., & Piazza, M. (1983). Una tecnica di recupero statico dei solai in legno.
- Turrini G., & Piazza M. (1983). Una tecnica di recupero statico dei solai in legno.
- Winkler, E. (1867). Theory of elasticity and strength. *Dominicus Prague, Czechoslovakia*.
- Zahn, J. J. (1991). Design equation for multiple-fastener wood connections. *Journal of Structural Engineering*, 117(11), 3477-3486.

Numerical Study on the Behaviour of Composite Steel-Concrete Beams Utilising Innovative Blind Bolts

I. S. Wijesiri Pathirana¹; B. Uy¹; O. Mirza²; and X. Q. Zhu²

¹Centre for Infrastructure Engineering and Safety, Univ. of New South Wales, Sydney, NSW 2052, Australia. E-mail: i.wijesiripathirana@unsw.edu.au; b.uy@unsw.edu.au

²Institute for Infrastructure Engineering, Univ. of Western Sydney, Penrith, NSW 2751, Australia. E-mail: O.Mirza@uws.edu.au; xinqun.zhu@uws.edu.au

Abstract

Recent research studies carried out on the condition of the existing infrastructure in Australia have revealed that the percentage of structures reaching the end of their useful life has increased. These structures need alternative structural solutions to extend their useful life to reduce the costs on 'new builds', which are required to replace them. Therefore, methods of strengthening of composite steel-concrete structures have become increasingly important. The flexural behavior of composite steel-concrete beams using blind-bolts was tested using full-scale beam specimens previously. The test results revealed that the ability of these new blind bolts to achieve composite action in composite beams was comparable with that of welded stud shear connectors. In addition, the behavior of the full-scale beam specimen during the flexural test was simulated using three-dimensional non-linear finite element (FE) models developed using ABAQUS. The FE models were validated using the load-deflection curves obtained from the experiment. This paper presents the FE results of composite beam models containing different shear connectors.

1. Introduction

Headed shear studs are the most commonly used connector type in composite steel-concrete beams to achieve composite action. One major problem of retrofitting composite beams with headed stud connectors is their connection. Welded headed studs need to be permanently welded to the top flange of the steel beam of a composite beam. This process requires removing a considerable area of concrete from the concrete slab along the length of a composite beam to allow required space to carry out proper welding around the studs. Blind bolts on the other hand, are a very good solution for this problem as they can be fixed on to the steel beam of a composite steel-concrete beam, from one side, with damaging the concrete slab of the composite beam. Furthermore these new blind bolt types can be utilised to develop demountable composite steel-concrete structures.

It is not until recently that studies have been carried out on structural bolts to be utilised as mechanical connectors to provide the ability of structural rehabilitation. [Kwon et al, 2009] studied the feasibility of rehabilitating existing old non-composite steel girder bridges with concrete decks. The authors concluded that it was both physically and economically possible to rehabilitate existing bridges with the use of post installable shear connectors but no work has been conducted on utilising the removable bolts as shear connectors in composite steel-concrete structures. [Mirza et al, 2010] carried out several push test experiments to evaluate the stiffness, strength, and ductility of blind bolts to compare their properties with conventional welded studs. The experimental results proved those blind bolts are a good option with comparable load capacities to develop demountable shear connector systems. Properly validated finite element models have been used as an efficient tool to study the shear connection behaviour of welded headed shear connections in steel-concrete composite beams. [Mirza and Uy 2009] developed a three dimensional nonlinear finite element model to simulate push test experiments using ABAQUS to study the behaviour of headed shear studs in composite beams, with both solid and profiled sheeting slabs, at elevated temperatures. In other research, [Mirza and Uy 2010] developed three dimensional finite element models using symmetry to simulate push test experiments for welded studs placed at two levels in the specimen to evaluate the structural performance of shear connection in composite beams. In both research the authors carried out parametric studies after validating the finite element models against experimental results.

The main objective of this paper is to present and discuss the results of finite element model simulations of full-scale beam experiments carried out to investigate the capacity of different shear connection systems utilising different shear connector types. Four full-scale beams consist of three composite steel-concrete beams utilising three different connectors, conventional welded studs and innovative blind bolts, and one non-composite beam were tested under static loading. Three dimensional non-linear finite element models (FEM) developed to simulate the four experimental specimens using ABAQUS. The validated finite element models which can accurately predict the load-deflection behaviour of the experimental specimens, are used to assess further the feasibility of using the shear connection systems of these new bolt types in steel-concrete composite beams by carrying out several parametric studies taking key parameters that are concrete strength of the slab, yield strength of the steel beam and the shear connection ratio of composite steel-concrete beams into account. The two blind bolts used in this study are illustrated in Figure 1.



Figure 1. Blind bolt types.

2. Experimental investigation

Four simply supported beams including three composite beams and one non-composite beam were tested. The geometry except the shear connector type of all four beams was identical. The beam specimens were designed to represent an actual secondary beam used in a high rise office building floor in accordance with relevant Australian design standards. Figures 2 and 3 show the typical geometry of the test specimens. The test setup for the beam experiment is illustrated in Figure 5. The load applied on a spreader bar, by a 1000kN hydraulic testing machine, was then transferred on to two steel bars, A & B, placed 500mm away from the centre-line to both sides of the slab. The load was applied as distributed-loads at two points across the full width of the beams. The deflections were measured throughout the test at point, D, the mid span and two points, C & D, 500mm away from the centre to the either sides along the length of the bottom flange of the steel beam. Two linear variable displacement transducers (LVDTs) were used to measure the horizontal displacement at the bottom of the steel beam at both ends. Other values recorded throughout the test were the force and stroke of the hydraulic jack and strains on selected points of the beam via attached strain gauges.

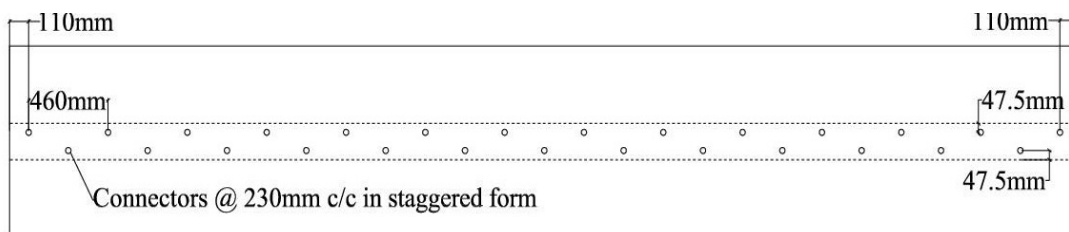


Figure 2. Plan view of the beam.

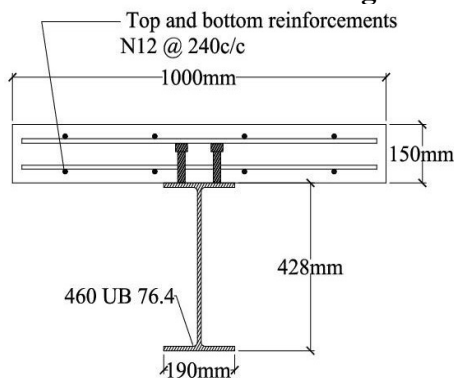


Figure 3. Section view of the beam.

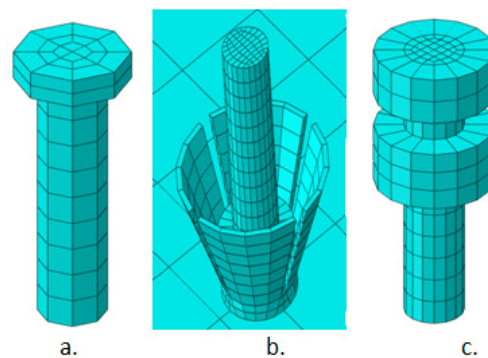


Figure 4. Shear connector models.

3. Finite element modeling

A three dimensional non-linear finite element model was developed to simulate each beam specimen. The finite element models were validated by verifying their load-deflection results against that of the experimental results.

The load-deflection results have been considered in model validation as these results are useful in studying the global behaviour of the beams in relation to their stiffness, ductility and the ultimate strength. The validated models were used in carrying out several parametric studies by considering the effect of some key parameters which are the concrete strength of the slab, yield strength of the steel beam and shear connection ratio of the composite beams. These models were further used to study the behaviour of different components of the composite beams during loading and also to gain further insight into the local behaviour of connectors to evaluate their performance in achieving and maintaining shear connection capacity under flexural loading. The finite element models were developed and run using commercially available software, ABAQUS.

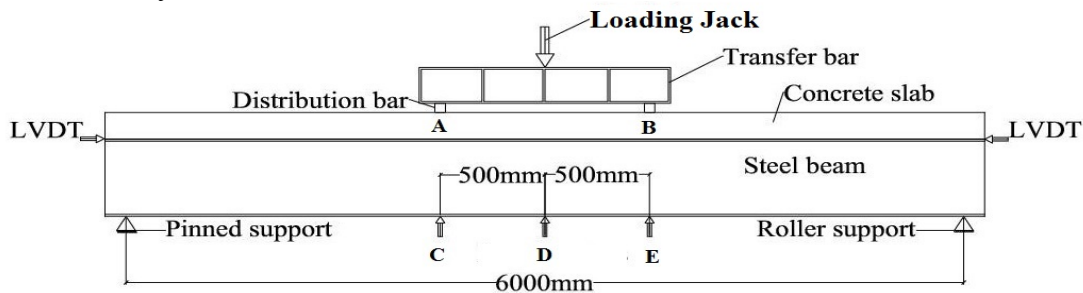


Figure 5. Loading setup.

3.1 Mechanical properties of materials

The mechanical behaviour in relation to the stress-strain characteristics of materials used in finite element modeling in this study including concrete, structural steel, reinforcement steel and shear connectors are represented by constitutive laws and actual material property test data.

3.1.1 Material property of concrete

The concrete damage plasticity model has been utilised to describe the material behaviour for concrete as this model is intended primarily for the analysis of reinforced concrete structures and also designed for applications in which concrete is subjected to monotonic loading under low confining pressure. [Karlsson and Sorensen 2010] describe this as a continuum, plasticity-based, damage model having tensile cracking and compressive crushing of the material as its two main failure mechanisms. The evolution of the yield (or failure) surface is controlled by tensile and compressive equivalent plastic strains linked to failure mechanisms under tension and compression loading. The Concrete Damage Plasticity option must be used in conjunction with Concrete Tension Stiffening and Concrete Compression hardening options in ABAQUS. The flow potential and yield surface parameters have been defined using default values of ABAQUS in the concrete damage plasticity option. The material model introduced by [Carreira and Chu 1985] for normal concrete is used to define the elastic-plastic behaviour of concrete. For the compression region, the model is expressed by the following equations; compression is assumed to be linear elastic up to $0.4 f'_c$. Poisson's ratio of concrete was assumed to be 0.2 and a

normal weight concrete of density 2400 kg/m^3 was assumed for all concrete grades. The characteristic compressive stress was taken as 34 N/mm^2

$$\sigma_c = \frac{f'_c \gamma (\varepsilon_c / \varepsilon'_c)}{\gamma - 1 + (\varepsilon_c / \varepsilon'_c)^\gamma} \quad (1)$$

Where; σ_c = Concrete stress, ε_c = Concrete strain, f'_c = Characteristic compressive strength

$$\gamma = \left[\frac{f'_c}{32.4} \right]^3 + 1.55 \text{ and } \varepsilon'_c = 0.002.$$

In this study the stress-strain relationship of concrete in tension is assumed to be linear. The tensile stress of concrete increases linearly until concrete starts cracking in tension and decreases linearly to zero from that point. The ratio of the uniaxial tensile stress to the uniaxial compressive stress at failure is evaluated as 0.1 [Liang et al. 2004]. Figure 6 illustrates the stress-strain relationship of concrete according to the compression behaviour proposed by [Carreira and Chu 1985] and the uniaxial tensile stress-strain behaviour of concrete.

3.1.2 Material properties of steel beam, reinforcement and connectors

Steel material shows initial elastic behaviour up to the yield point and followed by further yielding or strain hardening before failure. Non-linear behaviour of steel materials in this experiment where loading is monotonic and creep effects are not involved is described with the classical metal plasticity model in ABAQUS.

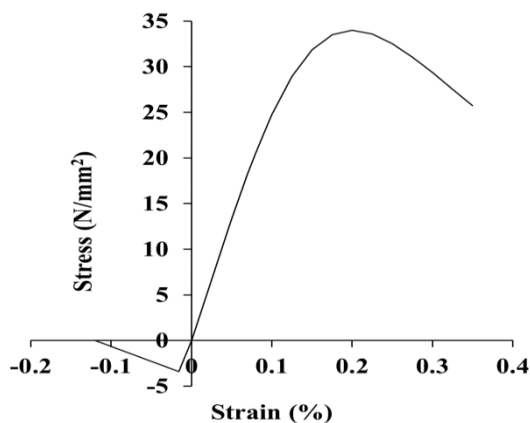


Figure 6. Concrete properties.

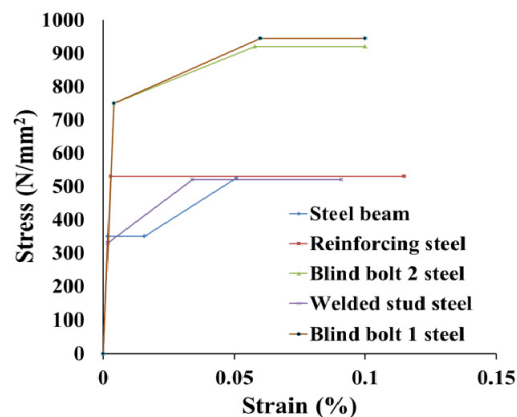


Figure 7. Steel properties.

Perfect plasticity and isotropic hardening definitions are both available in the classical metal plasticity models. Figure 7 illustrates stress-strain relationships converted into piecewise linear curves and used to model the steel beam, reinforcing steel, welded studs, blind bolt 1 and blind bolt 2.

3.2 Geometry, element types and mesh

A half model along the length was considered in the analysis by resulting in a reduction in simulation cost and computational time as specimens are symmetrical along its length. Concrete slabs and steel beams were modeled using eight-node linear hexahedral solid elements with reduced integration and hourglass control (C3D8R) as the main element type. Six-node triangular prism elements (C3D6) were adopted as secondary elements in some areas where geometric shapes are not compatible to be meshed with brick elements. Considering the geometric size of the specimens first order hexahedral solid elements were adopted in modeling long and wide sections of concrete slabs and steel beams. Elements with reduced-integration were adopted as they reduce computer running time. Hourglass control option was used to avoid hourglassing problems with first-order, reduced-integration elements. The elements are incorporated in a reasonably fine mesh in order to further improve the sensitivity of the analysis.

Shear connectors were modeled using second order three-dimensional twenty-node quadratic brick elements with reduced integration (C3D20R) to improve the running time and also the accuracy of the analyses. The connectors were modeled to represent the actual geometric sizes and shapes within the limitations of the application. Figure 4 shows the connector models used in the finite element models. The reinforcement bars were modeled with two-node linear three-dimensional truss elements (T3D2). Figure 8 illustrates the finite element mesh utilised to simulate a half of a composite steel-concrete specimen.

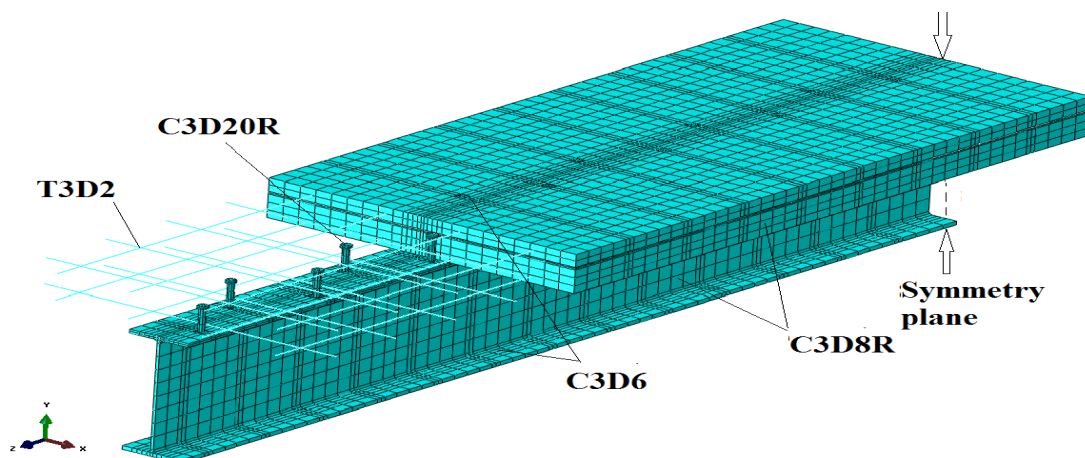


Figure 8. Finite element mesh.

3.3 Contact properties, boundary condition and load application

Contacts between different parts were modeled using interaction and constraint options to represent the actual contact behaviour in the test specimens. Surface to surface interaction was used to model the contact between the steel beam, concrete slab and connector surfaces. The value used for the friction co-efficient was 0.4. The embedded element technique was used to model the contact between

reinforcement bars and concrete. In this technique a perfect bonding between embedded elements and host elements is developed. This bonding will constrain the translational degree of freedom of the embedded nodes and avoid slip between reinforcement bars and concrete. The nodes of the concrete slab, reinforcement bars and steel beam on the plane of symmetry, at the mid-span of the beam were restricted from moving in the z-direction. The plane of symmetry is shown in Figure 8. The load was applied on the model as an imposed displacement of the concrete slab.

4.0 Results and discussion

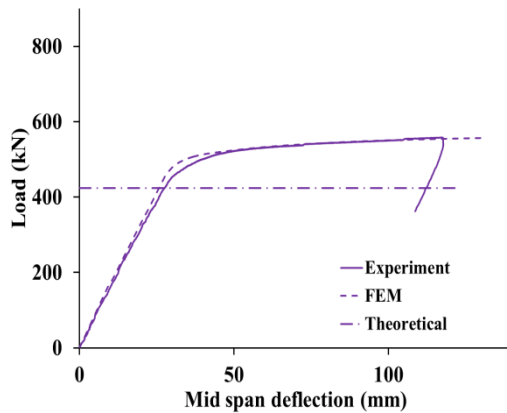


Figure 9. Non composite beam.

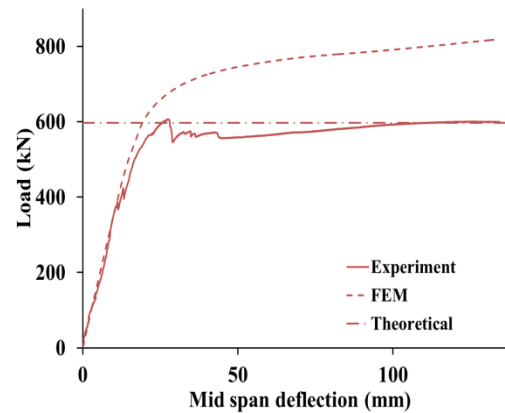


Figure 10. Welded stud beam.

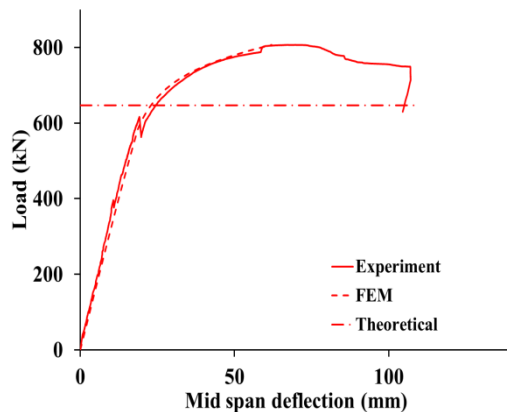


Figure 11. Blind bolt 1 beam.

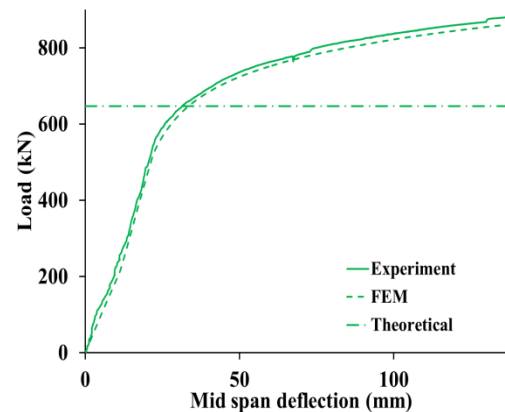


Figure 12. Blind bolt 2 beam.

4.1 Non-composite beam

The load versus mid-span deflection relationships of the finite element model are illustrated in Figure 9. The experimental results and the finite element model results are in good agreement in terms of stiffness, the ductility and the maximum load capacity. These results demonstrate that the finite element model is reasonably accurate and reliable and also valid to be used in further investigations. During the

experiment, cracks were appeared under the concrete slab of the non-composite beam when the loading was reached 40% of the theoretical ultimate flexural capacity of the beam. Figure 13 illustrates the development of tension cracks in the concrete slab under and near the loading points of the non composite FEM model.

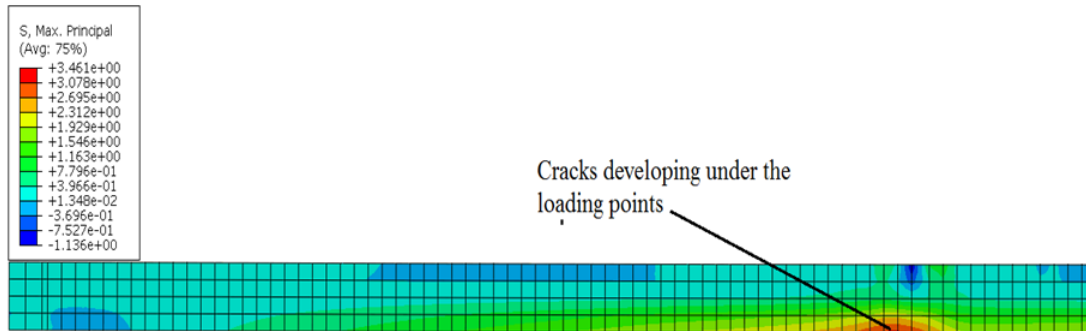


Fig. 13 - Tension cracks in the concrete slab.

4.2 Composite steel-concrete beam with headed stud shear connectors

Figure 10 illustrates the load versus mid-span deflection relationships of the finite element model and the actual beam. The model curve shows good agreement with the experimental curve in terms of the stiffness of the beam. The nearly parallel lines demonstrate equal stiffness of curves until the experimental curve exhibits a sudden drop in load due to initial stud failures at 380 kN. Even after those drops in load in the experimental curve have occurred, the stiffness of both curves does not seem to vary significantly until they have reached 500 kN, where the experimental curve demonstrates yielding. The model curve starts to yield at 600 kN, still suggesting close agreement with the behaviour of the experimental curve. The experimental curve exhibits significant and sudden drops in load after it reaches a maximum load of 606 kN. The difference in ultimate load capacity is quite significant, while the experiment showing 606 kN and the model showing 818 kN, even though the yielding loads of the two curves are in a better agreement. But the curves still demonstrate large ductile regions after reaching the maximum load capacity. The difference in ultimate load capacities of the model and the actual beam can be attributed to the sudden failures of the studs at the welded joints in the beam specimen during loading.

4.3 Composite steel-concrete beams with blind bolt 1

Model results in relation to the load-deflection relationship demonstrated in Figure 11 suggests that the initial stiffness of both model and experimental curves is the same. Further it can be observed that the stiffness of the model curve is fairly similar to that of the experimental curve up to 610 kN, though the experimental curve exhibits permanent deformation and a drop in the stiffness after the first load drop at around 400 kN. Both curves demonstrate yielding at around 610 kN and follow similar stiffness variations beyond that point. The experimental result and the finite

element model results are in good agreement in terms of the stiffness, the ductility and the maximum load capacity. The maximum load reached was 806 kN with a 62 mm deflection and 806 kN with a 64 mm deflection for the experimental result and finite element result respectively. Both experimental and model specimens failed due to concrete failure.

4.4 Composite steel-concrete beam with blind bolt 2

Figure 12 illustrates the load versus mid-span deflection relationships of the finite element model and the actual beam. Both curves show identical behaviour in relation to the stiffness, ductility and the ultimate strength of the actual beam. The beam exhibits a low stiffness at the initial stage of loading and gradually increases the stiffness. This is due to the slight movements of bolts within the gap between the bolt shanks and the over-sized holes in the steel beam flange. Once the bolt shanks have touched the flange, the beam starts to gain its natural stiffness which is similar to the other composite beam specimens. It can be observed that the experimental beam yields at around 550 kN and the model curve shows good agreement with the experimental results. The experimental result and the finite element model result are in good agreement in terms of the stiffness, the ductility and the maximum load capacity. The maximum load reached was 882 kN with a 144 mm deflection and 875 kN with a 154 mm deflection for the experimental result and finite element result respectively.

4.5 Comparison of ultimate flexural capacity results

Table 1 illustrates the comparison of the ultimate strength values obtained from experimental results and analysis results. The theoretical ultimate flexural capacity for a composite steel-concrete beam specimen was calculated using rigid plastic analysis (RPA) by considering its critical, mid-span, cross-section. An equivalent stress block was used in the compressive region of the concrete slab and the area of the concrete slab in tension was ignored in the calculation. The percentage of the difference of the ultimate flexural strength values between the experimental result and the theoretical result for a beam specimen is higher than 25% in all cases except for the welded headed stud beam which has shown the lowest percentage which is 1% between its experimental and theoretical ultimate capacities. The percentage of difference of the ultimate flexural strength values between FEM result and theoretical result for a beam specimen is higher than 25% in all cases. These values further suggest that there could be a premature failure in the welded headed stud beam that resulted the beam to fail well before the expected ultimate flexural capacity calculated by RPA.

5. Conclusions

Four full-scale beam specimens were tested under static loading condition to study the flexural behaviour of three composite steel-concrete beams utilising three different connector types and one non-composite steel concrete beam. Four 3-

dimensional non-linear finite element models (FEM) were developed to simulate the four beam specimens. The load-deflection relationships of the experimental specimens and the FEM models have been analysed to study the global behaviour of the composite steel-concrete beams in relation to stiffness, strength and ductility.

During the experiment all the beams reached a much higher ultimate flexural capacity than their theoretical flexural capacity including the non-composite beam. The headed stud beam showed the minimum increment over the theoretical ultimate load capacity and showed the minimum ultimate load capacity among composite beam specimens. The model results suggest this beam would have exhibited much higher capacity unless there was an unexpected premature failure. The welded headed beam demonstrated the lowest increment in the ultimate load over its theoretical capacity possibly due to sudden weld failures of the connectors. This result supports the argument of difficulty of maintaining the quality of stud welding on steel beams in practice. This problem seems to be easily overcome by utilising these new anchors as shear connectors.

FEM results in relation to the stiffness and maximum load capacity of the beam models are in very good agreement with that of the experimental results. The models have proven to be effective in terms of predicting load-deflection relationships. These models will be used to investigate the effect of key parameters such as shear connection ratio, concrete strength and geometry of the steel beam and the concrete slab of composite steel-concrete beams utilizing blind bolting by carrying out parametric studies.

Table 1. Comparison of ultimate strength results of different analysis methods.

Beam specimen	Ultimate flexural strength values obtained from different analysis methods (kN)			% of Difference of strengths	
	Theoretical result (Fut)	Experimental result (Fue)	FEM result (Fum)	$\frac{[Fue - Fut]}{Fut} \%$	$\frac{[Fum - Fut]}{Fut} \%$
CWS	597	606	818	1%*	37%
CBB1	647	806	806	25%	25%
CBB2	647	882	875	36%	35%
NC	424	558	557	31%	31%

CWS-Welded stud beam, CBB1- Blind bolt 1 beam, CBB2- Blind bolt 2 beam, NC- Non-composite beam.

*: CWS shows the lowest percentage of difference between experimental and theoretical capacity.

6. References

- ABAQUS documentation, version 6.10. USA: Hibbitt, Karlsson and Sorensen; 2010.
- Carreira D, Chu K. Stress-strain relationship for plain concrete in compression. *JACI Struct* 1985; 82(11):797-804.
- Eurocode 4: Design of composite steel and concrete structures, part 1. 1 general rules and rules for buildings, DDENV 1994-1. European Committee for Standardisation (CEN); 1992.
- Kwon G, Engelhardt MD, Klingner RE. Behavior of post-installed shear connectors under static and fatigue loading. *Journal of Constructional Steel Research* 2009; 66(4):532-541.
- Liang QQ, Uy B, Bradford MA, Ronagh HR. Ultimate strength of continuous composite beams in combined bending and shear, *Journal of Constructional Steel Research* 2004; 60(8): 1109-1128.
- Mirza O, Uy B. Behavior of headed stud shear connectors for composite steel-concrete beams at elevated temperatures. *Journal of construction steel research* 2009; 65:662-674.
- Mirza O, Uy B. Effects of strain regimes on the behavior of headed stud shear connectors for composite steel-concrete beams. *Advanced Steel Construction* 2010; 6(1):635-661.
- Mirza O, Uy B, Patel N. Behavior and strength of shear connectors utilising blind bolting. Paper presented to the 4th International conference on steel and composite structures: Sydney 2010, 21-23 July.

Headed Shear Studs versus High-Strength Bolts in Prefabricated Composite Decks

Marko Pavlović¹; Milan Spremić²; Zlatko Marković³; and Milan Veljković⁴

¹Faculty of Civil Engineering, Univ. of Belgrade, Bulevar kralja Aleksandra 73, 11000 Belgrade, Serbia. E-mail: marko@imk.grf.bg.ac.rs

²Faculty of Civil Engineering, Univ. of Belgrade, Bulevar kralja Aleksandra 73, 11000 Belgrade, Serbia. E-mail: spremic@imk.grf.bg.ac.rs

³Faculty of Civil Engineering, Univ. of Belgrade, Bulevar kralja Aleksandra 73, 11000 Belgrade, Serbia. E-mail: zlatko@grf.bg.ac.rs

⁴Dept. of Civil, Environmental and Natural Resources Engineering, Luleå Univ. of Technology, S-97187 Luleå, Sweden. E-mail: milan.veljkovic@ltu.se

Abstract

Prefabricated steel and concrete composite decks are an interesting option to improve competitiveness and sustainability of the composite structures. Longitudinal shear connection is usually established by grouped headed studs, but possible alternative solution is to use bolted shear connectors. Welded headed studs and bolts (grade 8.8) are experimentally examined in the push-out tests (four tests on each). The same arrangement and dimensions of shear connectors (16 mm diameter and 100 mm height above flange) are considered and their resistances and behaviour are compared. Experimental results showed that headed studs and bolted shear connectors have similar shear resistance, while headed studs are more ductile. FEA is performed by ABAQUS/Explicit solver with damage material models to get more insight into behaviour of the specimens. FEA shows rather good agreement with experimental results. Influence of the bolt to hole clearance on the behaviour of specimens with bolted shear connectors is analysed and discussed.

1. INTRODUCTION

Steel and concrete composite beams have been developed for decades to carry out optimal structural system for deck structures. Prefabrication of concrete slab is a good solution to avoid temporary supports and formwork for concrete casting and therefore reduce construction time and minimize traffic disturbance. It is most commonly established by grouting grouped headed studs welded to steel section in envisaged openings (pockets) of prefabricated concrete slabs. An alternative solution is to use bolted shear connectors. Faster erection methods can be developed by casting bolts in prefabricated concrete slabs and on site assembling to predrilled flange of steel section part of composite member, thus eliminating time for grout hardening. The construction costs with use of bolted shear connectors are expected to

be higher when compared to traditional headed studs. Still, the faster erection and life cycle cost analysis may lead, for a certain applications, that the total economy of the precast structures becomes competitive.

Long-term behaviour and durability issues may require replacement of concrete slabs or their parts during maintenance which is complicated and time consuming procedure in case of most commonly used welded shear connectors. With use of bolted shear connectors easier dismantling and replacement of concrete slabs can be achieved. It is also important from sustainability point of view since structure will have to be removed at the end of its lifetime.

Bolt to hole clearance of bolted shear connector should be as small as possible to ensure composite action of a beam. Therefore, low fabrication tolerances of prefabricated elements need to be achieved. As an example, a very good state of the art is provided by [Hällmark 2013] on the requirements, achieved tolerances and costs for a single span $L=28$ m, prefabricated composite road bridge with dry joints between composite slabs,

Welded headed studs, as the most widely used shear connectors, are well covered by design rules in many codes and continuous research on their behaviour in composite structures extends for decades in past. A very good state of the art on the existing experimental results on headed stud from the researches conducted in past few decades, and comparisons to design codes is given by [Pallarés and Hajjar 2010]. [Lam and El-Lobody 2005] conducted parametric FEA by varying headed stud height and concrete strength and compared results of headed studs shear resistance to predictions of design codes. [Gattesco and Giuriani 1996] experimentally examined headed studs behaviour subjected to reverse and monotonic cyclic loading. Grouped behaviour of welded headed studs, for their application in prefabricated slabs in composite beams, have been recently examined by [Okada et al. 2006], [Shim et al. 2008], [Chen et al. 2012] and [Spremić et al. 2013]. There are many other experimental and numerical studies considering various aspects of headed stud behaviour in composite structures, but very limited number of research and analyses of behaviour of bolted shear connectors is available. Also, design and application rules are still not available.

Bolted shear connectors can be used with or without the nuts embedded in concrete, and with or without preloading of bolts. Friction grip bolts (concrete preloaded by bolts) were investigated by [Dallam 1968]. They transfer interface shear forces by friction and are often used in car parks construction [ArcelorMittal 2008]. [Hawkins 1987] conducted the research on non-preloaded anchor bolts without the embedded nut in shear and tension. He showed that such anchors have 80% shear resistance when compared to welded headed studs and only 15% of shear stiffness. Bolted shear connectors with and without embedded nut were partially investigated by [Dedic and Klaiber 1984] and [Kwon et al. 2010] for application in rehabilitation work of strengthening existing non composite bridges. Influence of initial slip in hole of bolted shear connectors on the behaviour of steel and concrete composite beam was partially examined by [Kwon 2008], experimentally and numerically. Conclusion was made that at ultimate load level (failure load), behaviour of a beam with bolted shear connection is similar to the one with headed studs. Some differences in beam behaviour can be noticed in his results at serviceability load level. Detailed analysis

of behaviour and failure modes of bolted shear connectors with single embedded nut, and comparison to headed stud behaviour have been conducted by [Pavlović et al. 2013] using advanced FEA. None of the mentioned researches dealt in detail with initial slip in hole of a bolted shear connector from prefabrication and cyclic loading point of view.

Aim of this paper is to improve competitiveness of bolted shear connectors as advantageous from prefabrication and sustainability point of view by detailed examination of their initial slip behaviour. High strength bolts M16, grade 8.8, as bolted shear connectors with single embedded nut are studied and compared with headed studs of same dimensions. Standard push-out tests [EN1994-1-1 2004] were conducted for both shear connectors as part of the research carried by [Spremić 2013] and [Pavlović 2013]. FE models using damage material models were built and calibrated based on experimental data. Dynamic explicit solver was used to obtain the quasi-static solution. Propagation of initial slip in hole of bolted shear connector for monotonic cyclic loading is closely described by use of FEA results.

2. EXPERIMENTAL WORKS

2.1. Test set-up

Preparation of specimens and testing procedure was done according to EN1994-1-1 – Annex B recommendations [EN1994-1-1 2004]. Four identical specimens were prepared and tested for both shear connector types in the Laboratory for Materials and Structures at Faculty of Civil Engineering in Belgrade. Dimensions are shown in Figure 1.

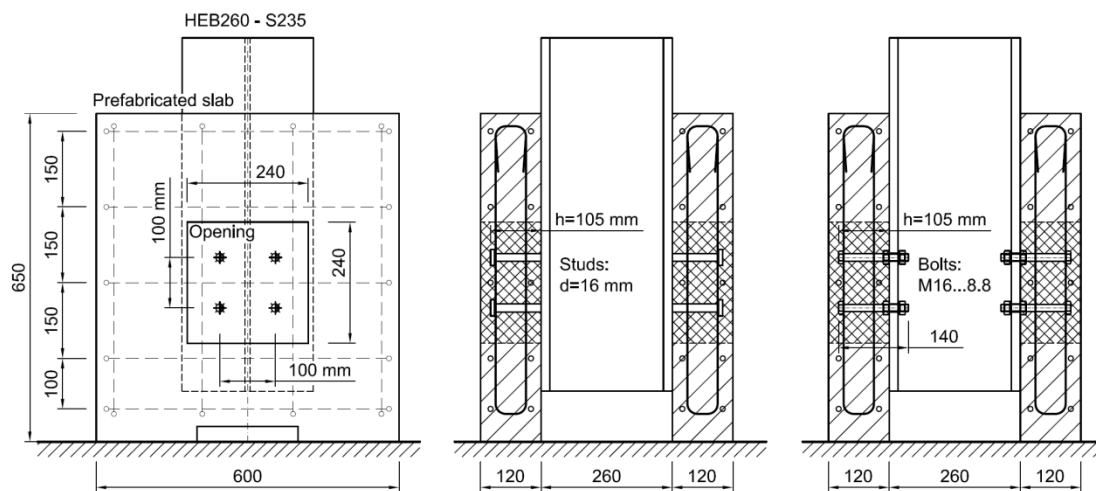


Figure 1. Test specimens layout

Concrete slabs (600x650x120 mm) were prefabricated, with standard reinforcement layout also shown in Figure 1, by casting in horizontal position. Cube compression strength of $f_{ck,cube}=38$ MPa was achieved after 28 days, corresponding to EC2 class C30/37. Openings with dimensions 240x240 mm were left in the middle

for later assembling. Ribbed bars $\phi 10$ mm, class R500 were used for reinforcement. Steel section HEB260, grade S235 had holes with diameter of 17 mm. High strength bolts M16; grade 8.8, with length 140 mm and headed studs $d=16$ mm, $h=100$ mm were used as shear connectors, horizontally and vertically spaced at 100 mm ($>5d$). Bolted shear connectors were clamped to at the steel flange by nut on outer side of the flange and washer and nut on the inner side. Clamping force of 40 kN was applied by torque controlled wrench on inner nut. Headed studs were drawn-arch welded. For both shear connectors, height above steel flange $h_{sc}=105$ mm, was achieved.

Assembling of specimen was done in two phases, one side than another. Steel flanges were greased to avoid bond effects with slab. Openings were filled with three-fraction concrete in horizontal position. To minimize initial shrinkage cracks, specimens were kept in wet condition for three days.

During concreting of openings, concrete cubes and cylinders (minimum four specimens) were made out of the same concrete mixture. Characteristic compressive cube strength $f_{ck,cube}=40$ MPa, and splitting tensile strength $f_{ct,sp}=3.1$ MPa were achieved for concrete in openings. Standard tensile tests for steel section bolt and stud material were conducted to obtain their properties on specimens with 8mm diameters and gauge length of 50mm. Results of standard tensile tests are presented by [Pavlović et al. 2013] and [Sprenić et al. 2013]. Mean engineering tensile strengths of 787 MPa, 530 MPa and 406 MPa were obtained by tests for bolts, headed studs and steel section, respectively.

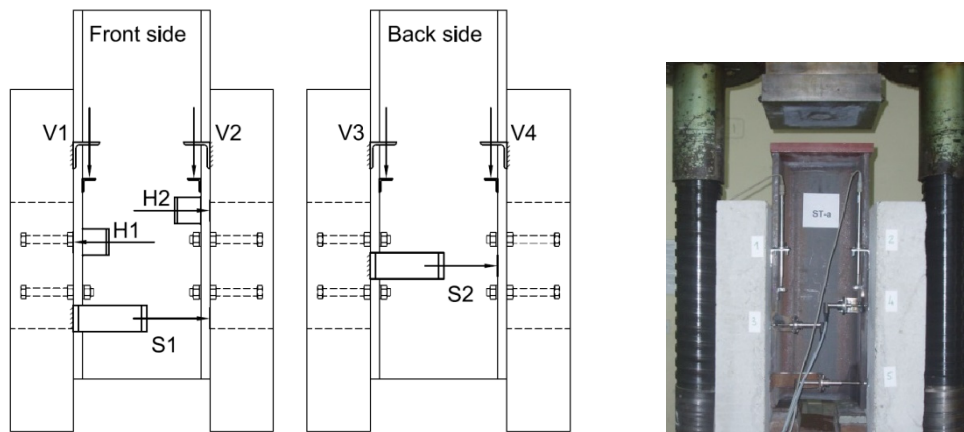


Figure 2. Test set-up

Upon 28 days after specimen preparation, they were equipped with sensors mounts, and put into testing frame with hydraulic jack on fresh gypsum posts to achieve vertical alignment and even bedding. Each specimen was equipped with 8 LVDTs (Linear Variable Displacement Transducer), as shown in Figure 2. Longitudinal slip was measured on both sides of steel section, on both slabs: sensors V1–V4. Transversal separation between steel section and both slabs was measured only on front side, as close as possible to shear connectors: sensors H1 and H2. Separation of slabs was measured on both sides of steel section: sensors S1 and S2. Force was measured by load cell at the top, with capacity of 1000 kN. Data

acquisition and recording for all transducers and load cell was done with 1 Hz frequency by multichannel acquisition device.

Loading regime shown in Figure 3(a) was adopted as specified in [EN1994-1-1 2004]. Force was first applied in 26 cycles as force controlled loading ranging from $F_{\min}=40$ kN to $F_{\max}=280$ kN, corresponding to 5% and 40% of expected failure load. After cyclic loading, failure loading was applied in one step as displacement controlled, such that failure does not appear in less than 15 minutes.

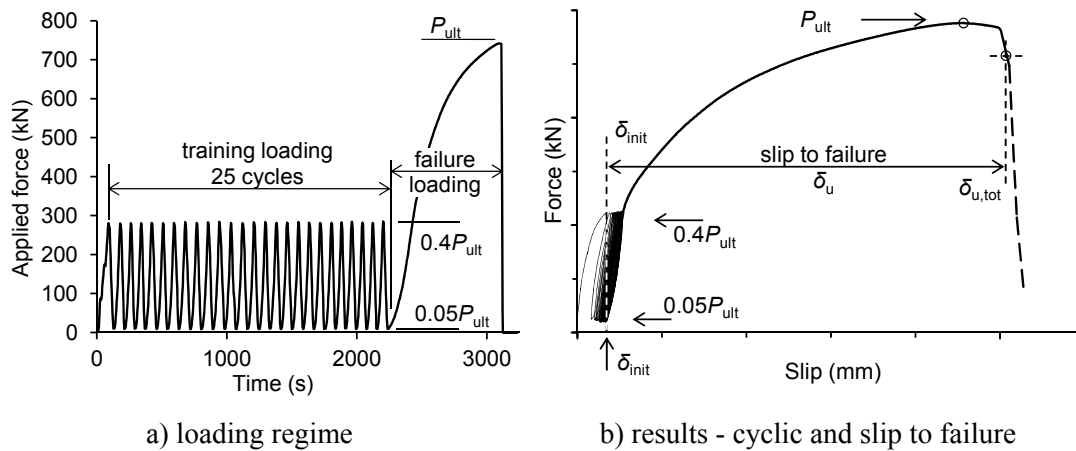


Figure 3. Loading regime and results decomposition

2.2. Experimental results

Results of push-out test for both shear connector types are shown in Table 1. Longitudinal slip is presented as averaged value for sensors V1-V4 divided to the initial accumulated slip during cyclic loading δ_{init} and additional slip to failure δ_u , as defined in Figure 3(b). Total slip $\delta_{u,\text{tot}} = \delta_{\text{init}} + \delta_u$ is also given. Separation of concrete slabs (S1 and S2 from Figure 2) and uplift of the concrete slab from the steel flange (H1 and H2) are given as averaged values.

Table 1. Experimental results for all specimens.

Shear connector type	Specimen (8 shear connectors)	Total force (kN)	Slip - average (mm)			Separation - average (mm)	
		ultimate P_{ult}	initial δ_{init}	to failure δ_u	total $\delta_{u,tot}$	between slabs	steel to concrete
Headed studs	STa	776.8	0.08	7.53	7.61	1.79	1.04
	STb	737.0	0.08	5.79	5.87	1.77	1.15
	STc	770.8	0.07	6.59	6.66	1.91	1.41
	STd	735.6	0.07	8.30	8.37	1.72	0.78
	ST mean	755.0	0.07	7.05	7.12	1.79	1.10
Bolted shear connectors	BT1	720.4	0.34	4.65	4.99	1.78	1.19
	BT2	702.3	1.37	5.01	6.38	1.82	1.19
	BT3	703.5	0.98	4.47	5.45	1.51	1.07
	BT4	741.7	1.12	3.90	5.02	1.23	0.99
	BT mean	717.0	1.00	4.51	5.46	1.59	1.11

Force-slip curves for both shear connector types are shown in Figure 4. Curves are separated in two characteristic parts as designated before in Figure 3(b). Load-slip behaviour of specimens during cyclic loading is shown in Figure 4(a). Only one curve for headed studs is shown to avoid overlapping. Figure 4(b) shows load-slip curves for failure loading for all specimens, referring to additional slip to failure δ_u . Characteristic resistance for headed studs according to [EN1994-1-1 2004], adjusted to measured material properties, is shown as a reference. Initial part is shown as detailed view with curves starting at load of 40 kN since failure loading step starts after the cyclic loading, as shown in Figure 3(b).

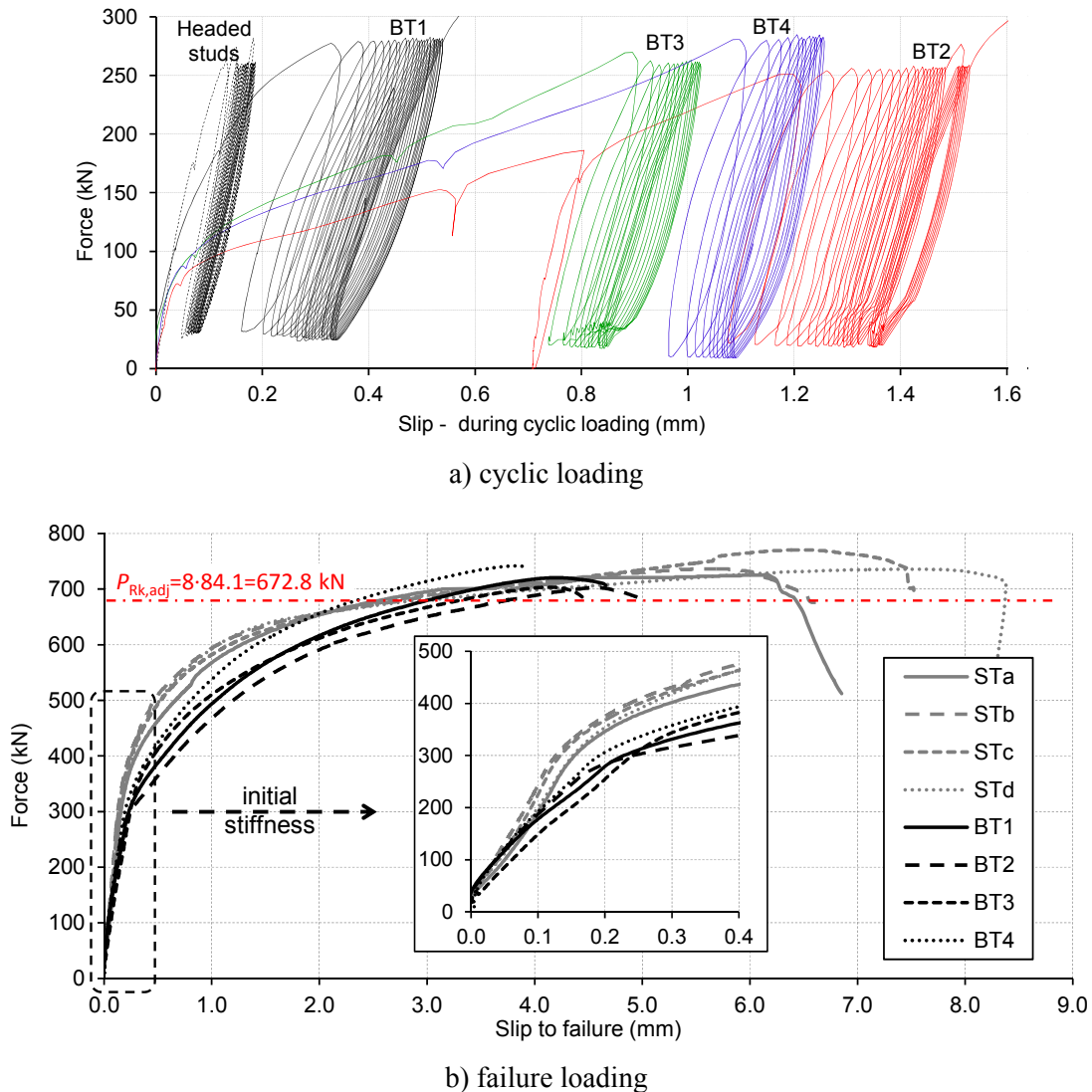


Figure 4. Experimental force-slip curves for all specimens

3. FE ANALYSIS

FE models of push-out tests, for both shear connectors, were built with aim to closely describe their behaviour. Since high strength bolts as shear connectors are used in non-standard connection layout, several important details were considered during modelling and analysis. Bolts were modelled with threads, to account the influence of threads penetration to hole surface on force-slip behaviour. Preloading of bolts was simulated in the numerical analysis, as it was applied in push-out test. Besides failure loading, cyclic load was applied for bolted shear connectors, in order to obtain origin of accumulative initial slip, noticed in experimental test results (see Figure 4(a)).

3.1. Model geometry and boundary conditions

Finite element models for headed studs and bolted shear connectors push-out tests were identical. They consisted of all connection components used in push-out tests.. Figure 5(a) shows complete model for headed studs, while Figure 5(b) shows detailed view around bolts of bolted shear connectors model. Modelling details such as: accurate parts geometry, reinforcement embedment, friction coefficients, etc. were all adopted as presented by [Pavlović et al. 2013]. Double vertical symmetry and fully fixed concrete slab base were used as boundary conditions.

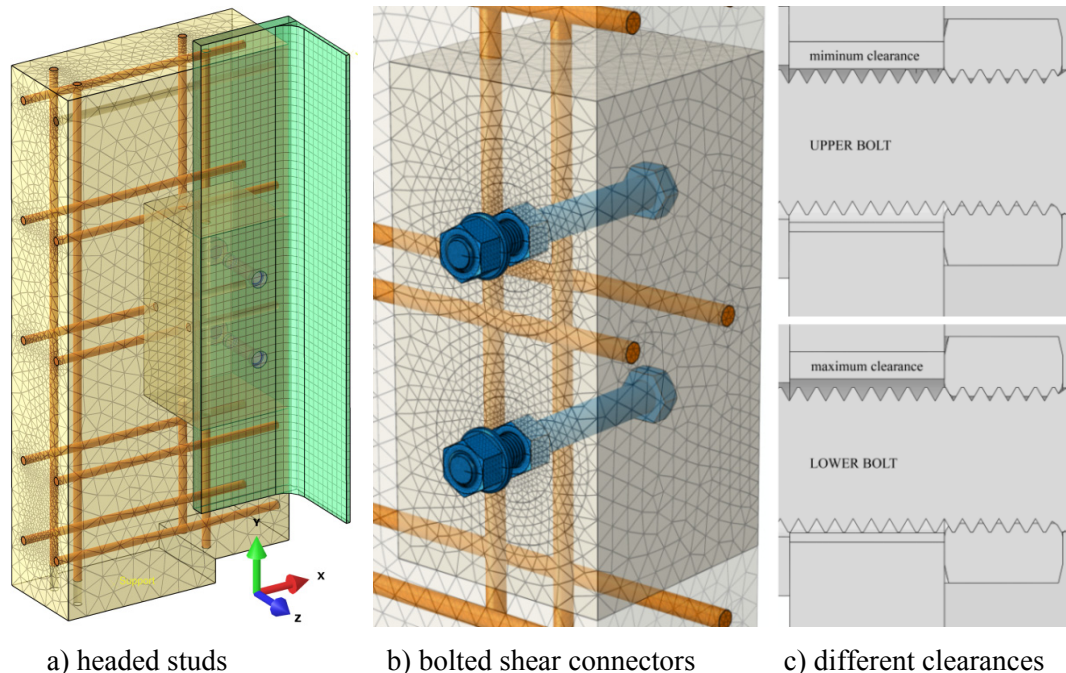


Figure 5. FE models geometry and mesh

Different bolt-to-hole clearances were set for upper and lower bolt in model as shown in Figure 5(c). Upper bolt had minimum clearance of 0.1 mm, while lower bolt had maximum clearance of 0.9 mm. Intention was to simulate equivalent test specimen conditions (random distribution of clearances for 8 bolts of one specimen) and its influence on accumulative initial slip.

3.2. Loading, analysis method and mesh

Loading was defined in three subsequent steps. They correspond to experimental testing: bolt preloading and cyclic loading (only for bolted shear connectors), and failure loading (for both shear connectors types).

Preloading of bolts by turn-of-nut method was introduced as explained by [Pavlović et al. 2013]. Cyclic load was applied as surface stress at top of the steel part to achieve total load of $280/4=70$ kN (double symmetry in model). This loading step is therefore force controlled. Time dependent amplitude function, with values ranging from 0.12 to 1.0 in 26 cycles was defined. In the last step, failure loading was applied as displacement controlled at top surface of the steel profile.

Those FE models exhibit large displacements, high material nonlinearity and complicated contact interactions. According to [Abaqus 2012] best solution is to use explicit dynamic solver (Abaqus/Explicit) to obtain quasi-static solution. Variable, non-uniform mass scaling was used to reduce calculation time. Appropriate smoothing of loading amplitude functions for all loading steps was adopted to avoid large inertia forces in quasi-static analysis.

Complex geometry of model parts (bolts and nuts) required tetrahedron finite elements (C3D4) to be used for most parts (see Figure 5(a) and (b)). Mesh size was varied for different parts in terms of their size and importance. For example, thread area of bolts and nuts were meshed with 1.2 mm elements, while head and shank had a mesh size of 2.4 mm. Hexahedral continuum elements (C3D8R) were used for the steel section as it was possible to generate mesh automatically. High density mesh (0.6 mm) was used in region around bolt holes to include effects of thread-to-hole penetration.

3.3. Material properties

Five different material models have been defined for modelled parts (steel section, concrete, bolt, headed stud and reinforcement.). Special attention has been given to bolt, headed stud and concrete material models since the overall behaviour of shear connection FEA was highly sensitive to their properties. Just short overview of used material models is presented here, while complete data and procedures of material models parameters determination are presented in [Pavlović et al. 2013].

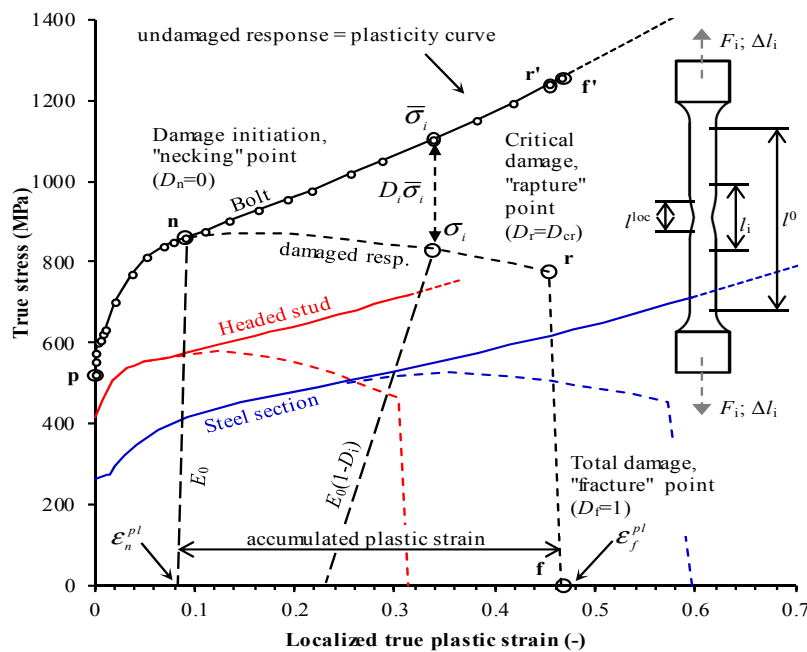


Figure 6. Plasticity curves and damage extraction procedure [Pavlović et al. 2013]

Ductile and shear damage material models were used for bolt and headed stud material to realistically predict their behaviour in push-out tests. Firstly, material

models were calibrated on tensile tests models based on standard tensile test data, as shown in Figure 6(a), for each material used. Later, those material models were used in push-out test with same element type and mesh size to correctly account for damage evolution.

Concrete damaged plasticity (CDP) model in Abaqus was used to describe concrete behaviour. CDP model consists of compressive and tensile behaviour, defined separately in terms of plasticity and damage parameters. Modulus of elasticity $E_{cm}=35.0$ Gpa and mean compressive strength $f_{cm}=40.0$ MPa, as obtained from standard tests results was used to define stress-strain curve shown in Figure 7. Mean tensile strength $f_{ct}=0.9f_{ct,sp}=2.8$ MPa was used. Damage curves for compression and tension were also defined.

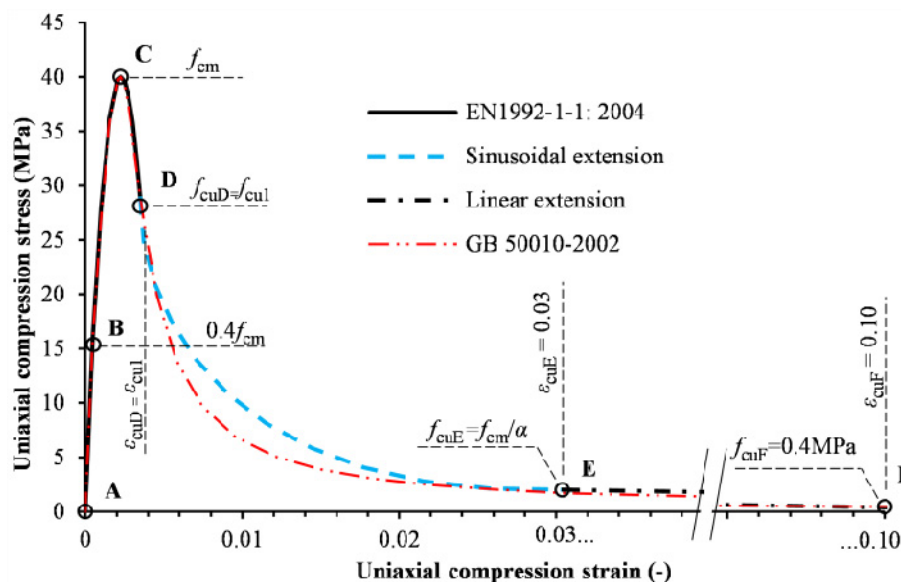


Figure 7. Concrete compression stress-strain behaviour [Pavlović et al. 2013]

3.4. Validation of numerical results

Comparison of experimental and numerical force-slip curves for both shear connectors for failure loading is shown in Figure 8(a). Numerical force-slip curve for initial cyclic loading is compared to experimental curves for bolted shear connectors in Figure 8(b). Deformed shapes of bolted shear connectors, prior to failure, taken out from destroyed concrete slabs, are shown in Figure 9. Comparison is made to FE results at the stage of first (lower in both cases) shear connector failure. Von-Mises stresses in studs and bolts and compression damage variable in concrete are also shown in Figure 9.

Numerical analysis showed good match with experimental results for both shear connector types, even for demanding cyclic loading analysis for bolted shear connectors. Therefore, results of numerical analysis can be used for further investigation shear connectors behaviour.

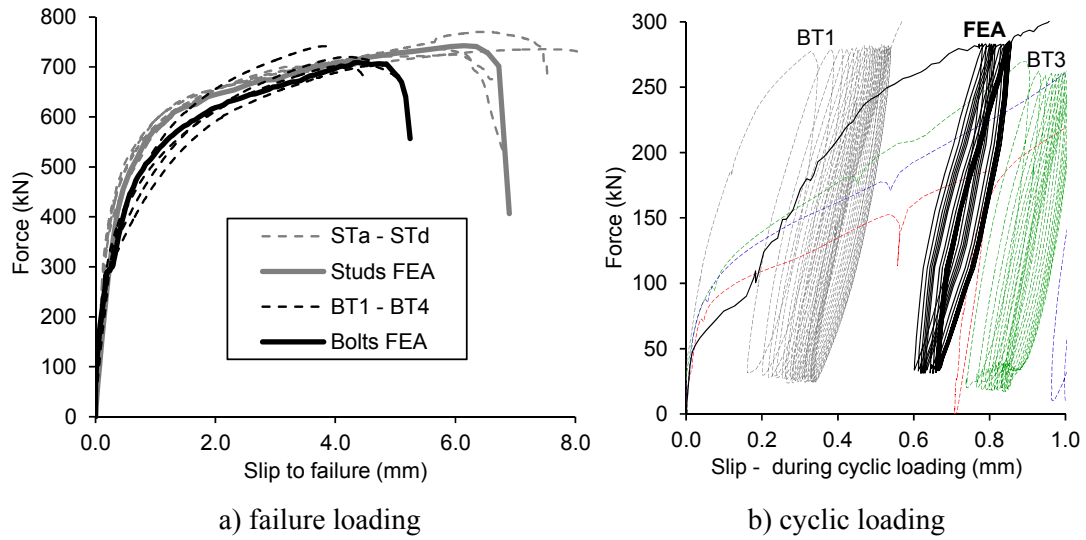


Figure 8. Numerical force-slip curves

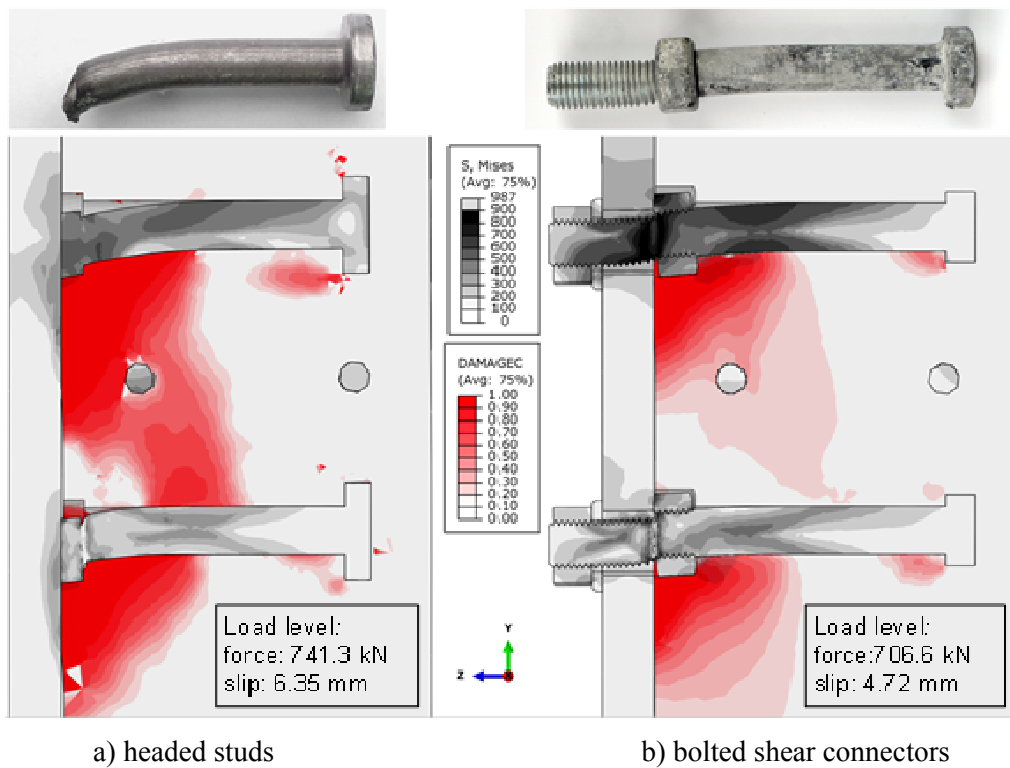


Figure 9. Deformed shear connectors prior to failure – Tests vs. FEA

4. DISCUSSION

4.1. Basic shear connector properties

Shear resistance, stiffness and ductility of headed studs and bolted shear connectors, are compared in details by [Pavlović et al. 2013] based on same experimental results presented here. Detailed analysis of failure modes and load transferring mechanism for both shear connectors is also made with help of similar FE models presented here. Bolted shear connectors have achieved 95% of headed studs shear resistance, but initial tangential stiffness is nearly 50% lower (see detailed view in Figure 4(b)). Bolted shear connectors also exhibited brittle behaviour, according to [EN1994-1-1 2004], with ultimate slip lower than 6.0 mm (see Table 1), while headed studs showed ductile behaviour.

4.2. Initial slip during cyclic loading

Welded headed studs showed practically no initial slip during cyclic loading as it can be seen in Table 1 and Figure 4(a). The reason lies in fact that they are welded to the steel flange. This was also concluded by [Gattesco and Giuriani 1996]. In case of bolted shear connectors, initial slip occur in first load cycle, right after the friction forces due to preloading of bolts are overcome (around 80 kN shear force in Figure 4(a)). Large differences in initial slip for tested specimens of bolted shear connectors, during first load cycle, can be noticed. Those are affected by different clearances between bolts and holes in the steel flange. Moreover, tested specimens consisted of 8 bolts, with randomly distributed clearances, from 0.0 to 1.0 mm. In FE analysis this phenomenon has been simulated by setting maximum and minimum initial clearances for lower and upper bolt, respectively.

Results of cyclic loading FE analysis are shown in Figure 10 as deformed shapes, concrete compressive damage variable contour plots and curves (concrete crushing) and threads penetration curve through loading cycles. After the first load cycle, some bolts void their clearances, but others do not (see Figure 10(b)). Considering further cycles, those bolts transfer shear load by bearing and therefore are subjected to higher shear loads than $P_{tot}/8$, because other bolts are limited to the slipping friction resistance. Their threaded parts penetrate into the hole surface and crushing of concrete occurs in front of them (see Figure 10(b) and (c)). This difference in load transferring mechanism between upper and lower bolt can be seen by comparing Figure 10(a) and (b). Lower bolt have not voided its large initial clearance and practically no crushing of concrete occurs in front of it. In further load cycles, threads of overloaded bolts penetrate deeper into holes surfaces and crushing of concrete propagates leaving noticeable increment of plastic deformation (slip) in each cycle (see Figure 4(a)). During this process, more bolts void their clearances and they start to transfer the shear load by bearing. This leads to the decrease of slip increments. It can be seen in Figure 4(d) and (e) that threads penetration and concrete crushing at different depth points in front of upper bolt are convergent. Also, observing experimental force-slip curves in Figure 4(a), accumulated initial slip during cyclic loading seem to be convergent with number of cycles, possibly ending with all bolts voiding their clearances. It can be observed in Figure 4(a) that specimen BT1 possibly had some bolts with no clearance, and that slip in first loading cycle

(0.32 mm) comes from the their threads penetration. Thread penetration in the first load cycle of FE results, shown in Figure 4(d) is lower (0.23 mm), but this difference is to be expected since in FE analysis 4 of 8 bolts are in bearing due to symmetry conditions. As an opposite example, specimen BT2 had largest initial accumulated slip, possibly having most of bolts with maximum clearance of 1 mm.

Observing experimental results in Table 1 and Figure 4(a) and FE results in Figure 8(b), and considering given analysis of threads penetration, it may be concluded, for the case considered here, that maximum initial slip to be expected is 50% higher than nominal bolt to hole clearance used. This increase factor is expected to be dependent on load range, bolt diameter and steel flange material grade.

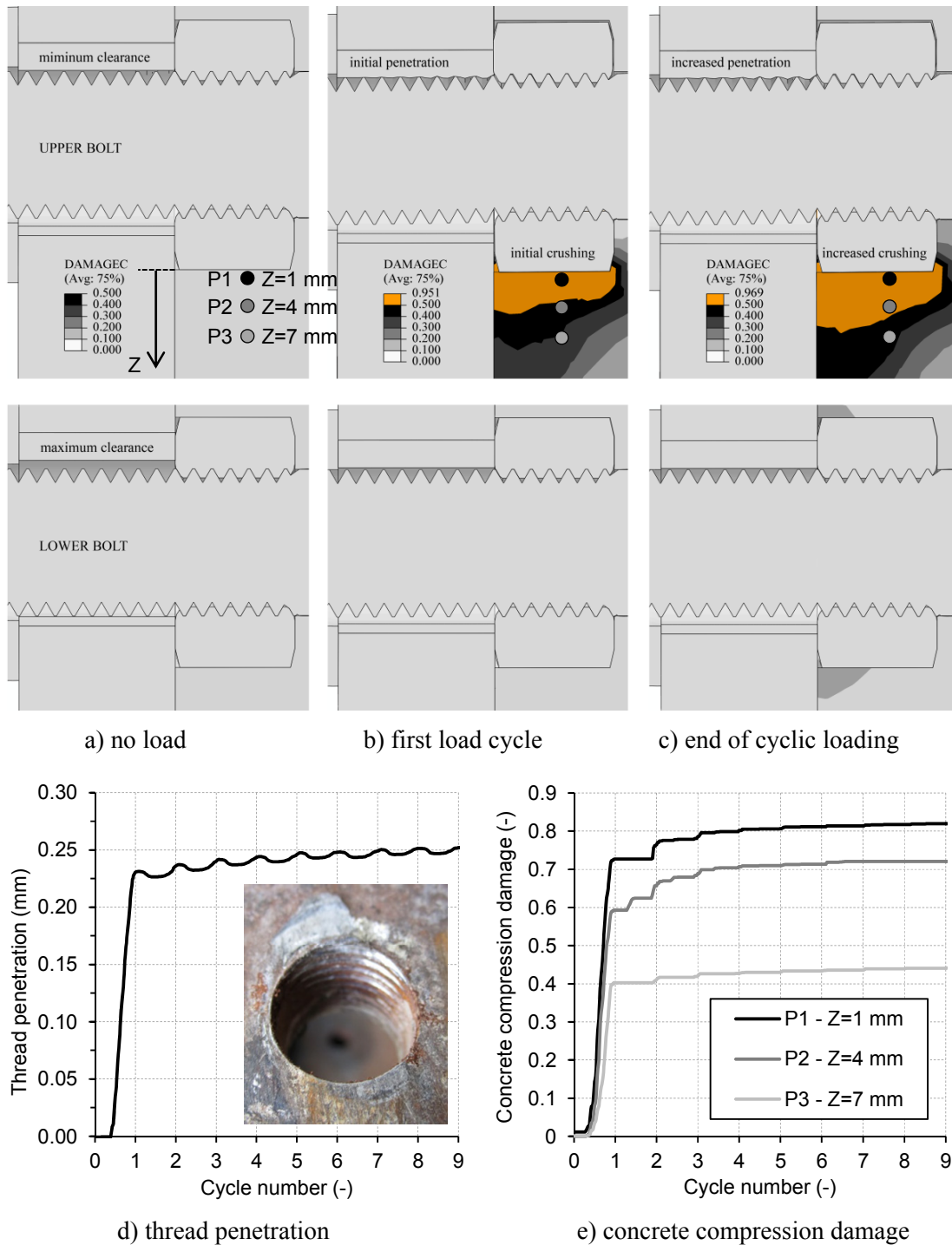


Figure 10. FE results for cyclic loading

5. CONCLUSIONS

Push-out tests using welded headed studs and bolted shear connectors with diameter of 16 mm and 105 mm of height above flange were conducted. Advanced

FE models were analysed to get more insight into specimens' behaviour. Following conclusions have been drawn:

- 1) Bolted shear connectors achieved 95% shear resistance when compared to headed studs. However, bolted shear connectors showed brittle, while headed studs showed ductile behaviour.
- 2) Initial accumulated slip during cyclic loading in case of bolted shear connector is noticeable (from 0.4 mm to 1.5 mm). It is caused by existence of clearance between the bolt and the hole in steel flange. Welded headed studs practically had no initial slip since they are welded to the steel flange.
- 3) Bolted shear connectors tested here (4 specimens), had quite different initial accumulated slips. This is addressed to random distribution of bolt-to-hole clearances.
- 4) Initial slips for bolted shear connectors are up to 50% higher than initial clearances (1mm clearance in this study). The reason for this lies in penetration of bolt threads into the hole surface.
- 5) Ultimate resistance of bolted shear connector is not influenced by initial slip in hole and thread penetration.
- 6) Damage material models paired with dynamic explicit solver can be used to analyse FE models of push-out tests both for cyclic and failure loading.

Even though the initial slip in hole of bolted shear connector does not affect its ultimate shear resistance, behaviour at serviceability load levels of a composite beam with such shear connection may be affected. It should be further investigated for proper application of bolted shear connectors in prefabricated steel and concrete composite decks for possibly required pre-camber design rules.

ACKNOWLEDGMENTS

This work is supported by the Serbian Ministry of Education, Science and Technological Development through the TR-36048 project. The writers would like to acknowledge the support provided by "MB steel" Ltd. and "GEMAX" Concrete production Ltd. from Belgrade for specimen production, as well as the technical staff of the Laboratory of Materials and Structures at Faculty of Civil Engineering in Belgrade.

REFERENCES

- Abaqus (2012) User Manual - Version 6.12. Providence, RI, USA: DS SIMULIA Corp.
- ArcelorMittal (2008) Car Parks in Steel. Luxemburg: ArcelorMittal Corporation.
- Chen X, Kunitomo S, Chong W, Qingtian S. 2012. Parametrical static analysis on group studs with typical push-out tests. *Journal of Constructional Steel Research* 72:84-96.

- Dallam LN. (1968) High Strength Bolts Shear Connectors - Pushout Tests. *ACI Journal Proceeding*(No. 9):767–769.
- Dedic DJ, Klaiber WF. (1984) High-Strength Bolts as Shear Connectors in Rehabilitation Work. *Concrete international* 6(7):41–46.
- EN1994-1-1 (2004) Eurocode 4 - Design of composite steel and concrete structures. Part 1-1: General rules and rules for buildings. Brussels, Belgium: European Committee for Standardization (CEN).
- Gattesco N, Giuriani E. (1996) Experimental study on stud shear connectors subjected to cyclic loading. *Journal of Constructional Steel Research* 38(1):1-21.
- Hällmark R. (2010) Prefabricated Composite Bridges - a Study of Dry Deck Joints. Licentiate thesis. Luleå University of Technology.
- Hawkins N. (1987) Strength in shear and tension of cast-in-place anchor bolts. *Anchorage to Concrete SP-103*:233–255.
- Kwon G. (2008) Strengthening Existing Steel Bridge Girders by the Use of Post-Installed Shear Connectors. PhD thesis. The University of Texas at Austin.
- Kwon G, Engelhardt MD, Klingner RE. (2010) Behavior of post-installed shear connectors under static and fatigue loading. *Journal of Constructional Steel Research* 66(4):532–541.
- Lam D, El-Lobody E. (2005) Behavior of Headed Stud Shear Connectors in Composite Beam. *Journal of Structural Engineering, ASCE* 131(1):96–108.
- Okada J, Teruhiko Y, Lebet JP. (2006) A study of the grouped arrangements of stud connectors on shear strength behaviour. *Structural Eng./Earthquake Eng., JSCE* 23(1):75s-89s.
- Pallarés L, Hajjar JF. (2010) Headed steel stud anchors in composite structures, Part I: Shear. *Journal of Constructional Steel Research* 66(2):198–212.
- Pavlović M. (2014) Resistance of bolted shear connectors in prefabricated steel-concrete composite decks. PhD thesis. University of Belgrade, Faculty of Civil Engineering.
- Pavlović M, Marković Z, Veljković M, Budjevac D. (2013) Bolted shear connectors vs. headed studs behaviour in push-out tests. *Journal of Constructional Steel Research* 88:134-149.
- Shim CS, Lee, PG, Kim DW, Chung CH. (2008) Effects of Group Arrangement on the Ultimate Strength of Stud Shear Connection. *Proceedings of the 2008 Composite Construction in Steel and Concrete Conference VI*.
- Spremić M. (2013) The analysis of headed studs group behavior in composite steel-concrete beam. PhD thesis. University of Belgrade, Faculty of Civil Engineering.
- Spremić M, Marković Z, Veljković M, Budjevac D. (2013) Push-out experiments of headed shear studs in group arrangements. *Advanced Steel Construction* 9(2):170–191.

Design Codes on Stud Shear Connectors for New Details

Chang-Su Shim¹ and Dong-Wook Kim²

¹Dept. of Civil and Environmental Engineering, Chung-Ang Univ., Seoul 156-756, Korea. E-mail: csshim@cau.ac.kr

²Dept. of Civil and Environmental Engineering, Chung-Ang Univ., Seoul 156-756, Korea. E-mail: clearup7@cau.ac.kr

Abstract

Current design codes on stud shear connectors have clear limitations to cover new details of stud shear connection. New trends of stud shear connection are large diameter up to 30mm, clustered studs, different material for bearing, mixed arrangement with lying and vertical studs and confinement details. A research program was started to develop a separate design code on steel-concrete composite structures covering building and bridge structures in Korea. In order to improve current design provisions of stud shear connectors, experimental data on static and fatigue strength were collected, especially for new details. Collected data of experimental results, current design codes on static and fatigue strength of stud shear connection were investigated to expand their application limits. Additional coefficients for static strength are needed to consider new details. For the application of high strength material, shear stress range needs to be limited by 60% of static strength and bearing stress of concrete also need to be limited by 3 times of compressive strength of concrete to use current S-N curves. Shear connectors for precast decks, large studs greater than 27mm and clustered connectors with narrower stud spacing than 5 times of the diameter showed slight decrease of fatigue strength.

Introduction

Headed stud connector is the most common application in composite structures to provide composite action between concrete slab and steel beam. The behavior of stud shear connection in composite beams depends on various factors such as material properties of stud and bearing material, dimensions of studs and reinforcement details. Push-out test is commonly used to evaluate the shear strength of shear connection. As commented by Pallares and Hajjar (2010), the design formula to compute the strength of headed stud connectors need to be reassessed for new design scopes.

In addition, the current provisions (AISC 1995, Eurocode-4 1997) have applicable limitations: limit the strength of steel stud ($f_u < 500\text{MPa}$), limit the small stud diameters ($13\text{mm} < d_s < 25\text{mm}$). Moreover, the current specifications on shear strength do not consider comprehensively on all material properties: confinement effect of concrete, or reinforcement effects, slab dimensions. Current design codes on static strength of shear connection assume two different failure modes. The upper limit of the shear strength is obtained from the stud shank failure. Area of the stud shank and tensile strength of the stud are the main parameters to determine the

strength. In this term, concrete properties are not considered. Combination of damage of bearing concrete and stud failure is considered in the other equation.

Recently, new and high strength materials are more commonly used. However, some new materials could not be applied to the design of shear connection because of the current provisions' limitations. Therefore, the current provisions on shear strength of headed stud need to be more applicable, especially for new requirements of details and materials.

Table 1 summarizes current design codes on static strength of stud shear connection and their range of application. These design provisions can be used for common practices but not for new details and materials, which are not in the range. Therefore, it is necessary to investigate extension of current design equations for new practices as listed in Table 2.

Table 1. Design provisions on static strength of stud shear connection

	EC-4	AASHTO LRFD	JSCE Guidelines
Codes	$P_{Rd(1)} = 0.29\alpha d^2 \sqrt{f_{ck} E_{cm}} / \gamma_v$ $P_{Rd(2)} = 0.8 f_u (\pi d^2 / 4) / \gamma_v$ $P_{Rd} = \min[P_{Rd(1)}, P_{Rd(2)}]$ $\gamma_v = 1.25$	$Q_r = \phi_{sc} Q_n$ $Q_n = 0.5 A_{sc} \sqrt{f_c' E_c} \leq A_{sc} F_u$ $\phi_{sc} = 0.85$	$V_{stud} = \frac{(31 A_{ss} \sqrt{(h_{ss} / d_{ss}) f_{cd}'} + 10000)}{\gamma_b}$ <p style="text-align: center;">or</p> $V_{stud} = A_{ss} f_{stud} / \gamma_b$ $\gamma_c = 1.3, \gamma_s = 1.0, \gamma_b = 1.3$
Range of design parameters	$16 \text{ mm} \leq d_s \leq 25 \text{ mm}$ $f_u \leq 500 \text{ N} / \text{mm}^2$ $f_{ck} : \text{density} \geq 1750 \text{ kg} / \text{m}^3$	minimum yield and tensile strength of 345 MPa and 415 MPa	$13 \leq d_{ss} \leq 32$ $400 \leq f_{stud} \leq 550 \text{ N} / \text{mm}^2$ $14 \leq f_c' \leq 63 \text{ N} / \text{mm}^2$

Table 2. New details and materials for stud shear connection

Detail	Application	References
Large diameter (~31.8mm)	High shear region	Badie et al. 2002 Shim et al. 2004 Wang et al. 2011
Group arrangement with narrow spacing (less than 5ds)	Composite joints Precast decks	Larose 1995 Okada 2004 Shim 2007, 2010 Xue et al. 2011 Xu et al. 2012a, b

Shear connection with additional confinement	Precast decks	Larose 1995 Shim et al. 2007, 2013
Mortar and bedding layer	Precast decks	Shim et al. 2000 2001
High strength material	HPM application	Cederwall and An 1996 Wang et al. 2011 Prakash et al. 2012

In this paper, the effects of the new details and materials on the static and fatigue performance were investigated. Based on database of static and fatigue tests of stud shear connectors from the literature, comparisons were made to the provisions in current design specifications. New equations for static and fatigue strength of stud shear connection to extend the range of design parameters in design codes are proposed. The derived equations will be proposed for new design specification on steel-concrete composite structures in Korea.

Static strength for new details

In previous research works, there were many researchers considered and proposed many new equations of shear strength. From 1920 to 1958, Viest reviewed shear connectors strength. Chapman used to discuss about the behavior of composite sections and shear connectors (1964). Iyengar wrote a comprehensive state of the art up that time (1977). Johnson and Buckby (1979) reported experiments on many specimens in British and in the United States of America.

According to Johnson and Anderson (1993) the constant in Eurocode-4 (1994) was derived from push test results to be 0.26. Because the lateral restraint was usually less stiff than in the concrete slab of a composite beam, it was increased to 0.369 in CEC (1992). The constant according to Ollgaard et al. (1971) is 0.39. Partial safety factor for shear connection is 1.25 without considering materials while Eurocodes use partial safety factors for different materials.

In headed studs particular, Shim (2004, 2010) researched on structure performance of composite joints using bent studs. The interaction in the design provisions for joints under a combination of flexure and shear was checked. New equations to predict strength of stud clusters, and group arrangements of studs were also considered by LaRose (1995) and Okada (2004). In addition, Shim (2004) did 18 experiments to investigate the limitation of current design provisions on shear strength of large studs. Xue (2008) compared the current provisions on shear strength, include of Eurocode-4 (1994), AASHTO LRFD (2007), Chinese code. According to his work, Eurocode-4 is the most conservative prediction on shear strength of headed studs. On the other hand, Cederwall and An (1996) performed experiments on high strength materials and showed the significantly different (6%) in shear prediction between normal strength and new high strength material specimens. All their experimental results are collected in the database.

For shear connection in precast deck bridges, material properties of filling material and bedding height must be considered for the evaluation of structural

performance of stud shear connection (Shim, 2000; Shim, 2001). Large studs up to 31.8mm diameter were experimentally investigated and availability of the current design provisions on stud shear connectors was verified based on the test results (Badie et al., 2002, Shim et al., 2004). The failure modes of shear connection can be categorized into three modes. Mode-1 is defined as stud failure without considerable concrete damage. Mode-3 means the concrete failure without stud failure. When the connectors are failed after considerable concrete damage, it can be defined as Mode-2.

In order to investigate a new prediction on shear strength of headed studs shear connection with new design aspects, 287 data (including test results for common studs by Ollgaard et al. 1971) were selected. As shown in Fig. 1, Eurocode-4 gives conservative prediction while AASHTO LRFD overestimates the shear strength for many cases. Upper limit of the shear strength in AASHTO LRFD need to be changed. Even though Eurocode-4 gives conservative results due to the 0.8 reduction factor, the design equation for Mode-1 showed large scatter for the shear connection with high strength material. The equation for failure Mode-2 shows better variation as shown in Fig.1 (d).

Variation of the prediction mainly comes from two reasons. One is the usage of high strength material and the other is different failure modes in the experiments from the prediction. When the upper limit of the shear strength governs, high strength concrete cannot give better strength. High strength concrete or confinement to the bearing concrete needs to be provided for the prevention of premature failure of concrete slab when large studs or clustered studs are designed. Coefficient for bedding height (Shim et al. 2000), narrow stud spacing (Shim et al. 2013) and confinement effect can be used for better prediction of the shear connection with new details.

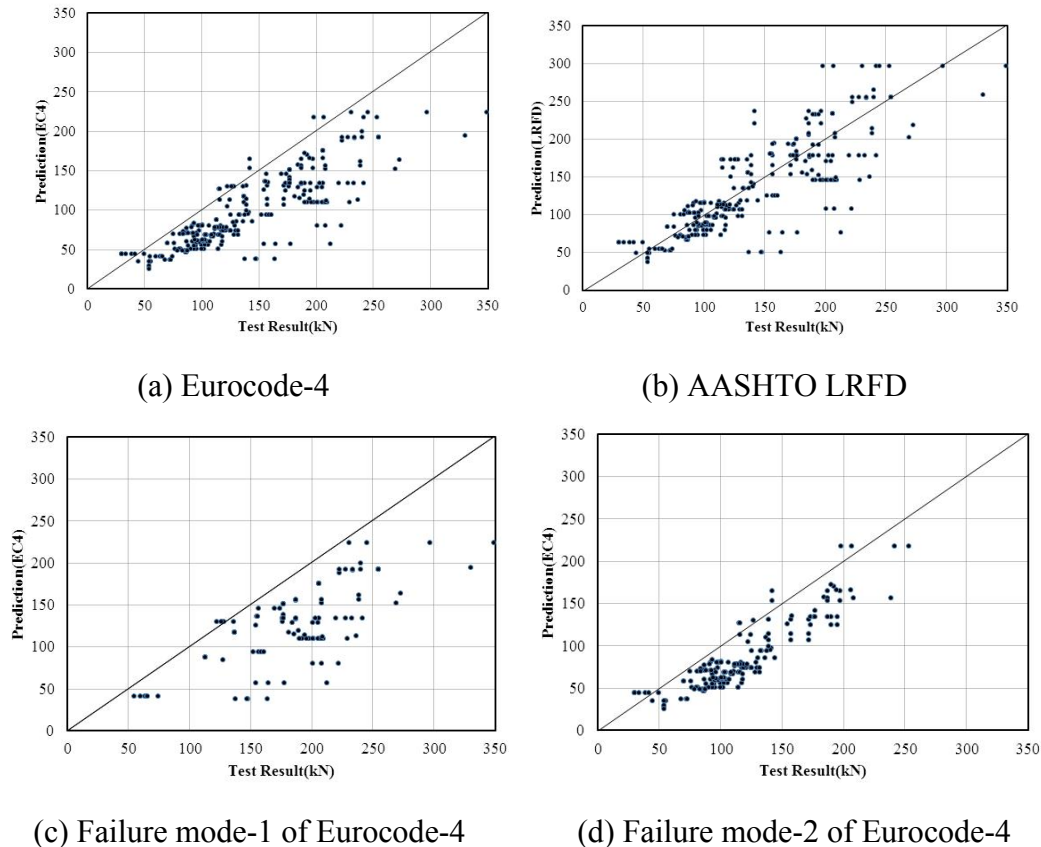


Fig. 1 Comparisons of test data with design codes

Fatigue strength for new details

Stud spacing in bridge structures is normally determined from the fatigue design. For the fatigue design, current S-N curves only consider shear stress range without consideration of maximum stress of stud and bearing concrete. In Eurocode-4, the maximum shear force under the fatigue loading is limited to 0.6 of the static resistance. Lee et al. (2010) compared fatigue design curves from Eurocode-4, BS-5400, JSCE and AASHTO and found that the AASHTO(2007) allows significantly smaller shear stress ranges than the other codes, especially for a common range of bridge design.

Using 160 fatigue test data including the effect of large diameter, precast decks, stud spacing and bearing stress of concrete, current design codes were compared as presented in Fig. 2. Clustered shear studs with closer spacing than 5 times of the stud diameter showed lower fatigue strength than that of normal cases even though AASHTO gives conservative strength. Design of clustered shear studs in prefabricated slabs needs careful consideration because the safety margin of fatigue endurance is decreased significantly.

The fatigue behavior is influenced by the bearing concrete around the stud. When the bearing stress is calculated by dividing shear force to a stud by an area of stud ($2d \times d$), the influence should be considered for the case of bearing stress greater than 3 times of its compressive strength of concrete, as shown in Fig. 2(b).

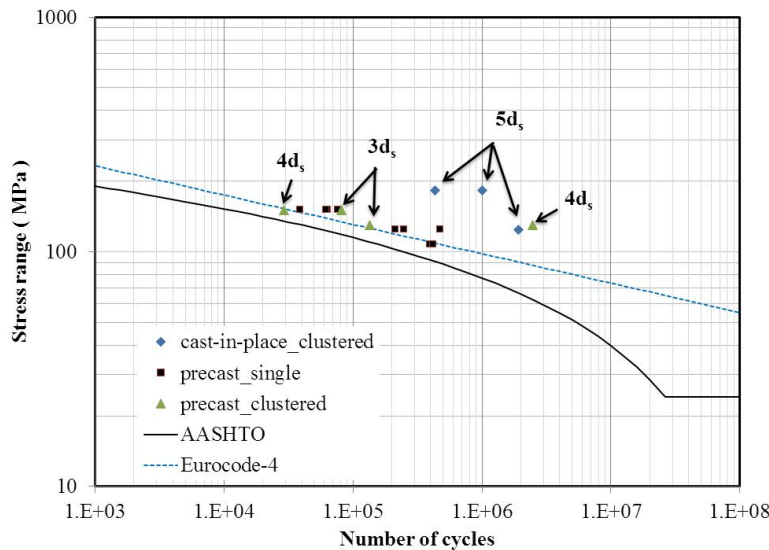
Crushing of bearing concrete near the weld collar increases stud stress resulting in decrease of fatigue strength. This can be avoided by limiting the stress level in design codes.

Large studs with diameter greater than 25mm are increasingly required for clustered arrangement in precast decks and composite joints. As discussed by Shim et al. (2004), quality control of welding of studs is an issue when the automatic welding gun is used. Due to probability of welding defects for large stud connectors, it is necessary to have careful inspection even though test data showed that Eurocode-4 gives a few unconservative estimations, as presented in Fig. 2 (c). AASHTO provision can be used for large stud connectors.

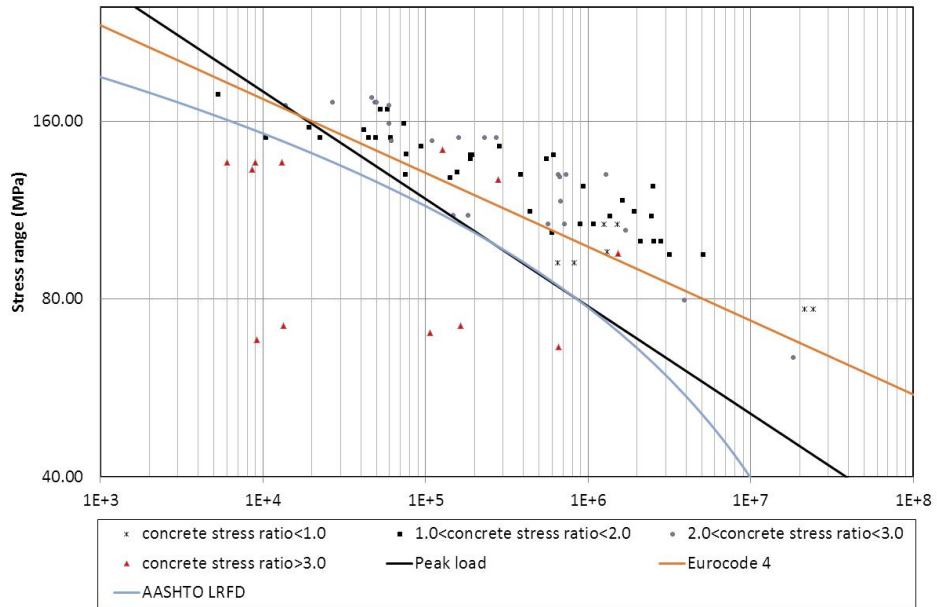
Many attempts to increase shear strength of stud connection using high strength material, large diameter and clustered arrangement have limitation to reduce the required studs in design.

Table 3. Design provisions on fatigue strength of stud shear connection

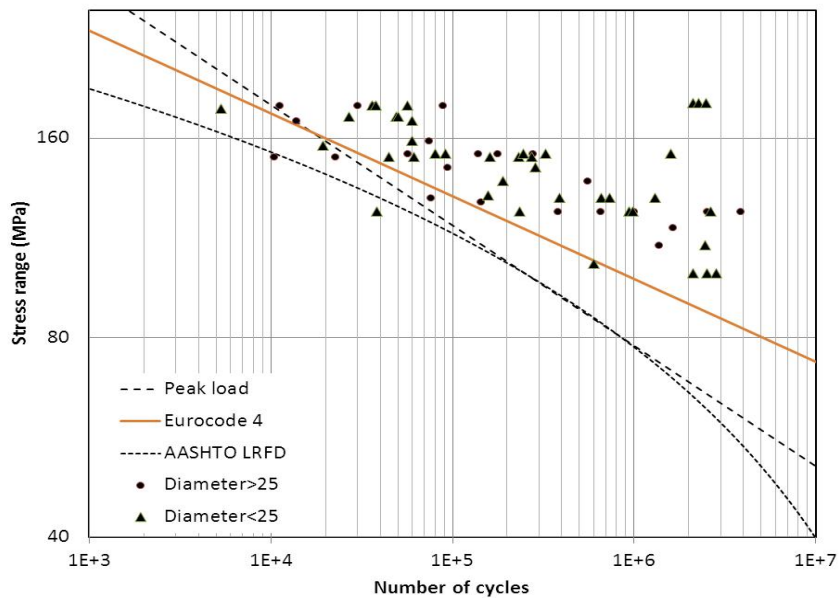
EC-4	AASHTO LRFD	Peak Load by Oehlers(1992)
$\log N + 8 \log(\Delta\tau_k) = 22.12$	$Z_r = \alpha d^2 \geq \frac{38.0}{2} d^2$ $\alpha = 238 - 29.5 \log N$	$N_f (\Delta P / P_R)^m = 10^k$ $N_e = N_f [1 - (P_p / P_R)]$



(a) Effect of stud spacing and precast slab



(b) Effect of concrete bearing stress ratio



(c) Effect of stud diameter

Figure 2. Fatigue strength of stud connectors

CONCLUSION

A new design codes on steel-concrete composite structures is under development considering new details and high performance materials. Database was constructed to investigate the effect of new design aspects on the shear strength and fatigue strength of stud shear connection. For the static strength of the stud connection, Eurocode-4 gives reasonable estimation for new details when appropriate

coefficients are adopted to reduce variation of the strength estimation. AASHTO provisions provide unconservative strength estimation.

For fatigue strength of stud connectors, stud spacing and bearing stress of concrete by the applied shear force should be considered in the design. Even though AASHTO provides conservative estimation of fatigue strength for narrower stud spacing than 5 times of stud diameter, the effect needs to be considered when clustered arrangement is adopted in the design. Bearing stress of concrete should be limited up to 3 times of its compressive strength of concrete. Large studs did not give lower fatigue strength but quality control of welding is essential.

Based on this preliminary study, design equations for static strength and fatigue strength will be developed. Design scope of current design codes on stud shear connection can be expanded to accommodate new design practices.

ACKNOWLEDGMENTS

This research was supported by a grant from the R&D Policy and Infrastructure Development Program (11STANDARD09-01-Development of Performance based design codes on steel-concrete composite structures) funded by the Ministry of Land, Infrastructure and Transport (MOLIT) of the Korean Government.

REFERENCES

- American Association of State Highway and Transportation Officials (AASHTO), (2007). "AASHTO LRFD Bridge Design Specifications".
- American Institute for Steel Construction (AISC) (1993). "Load and Resistance Factor Design Specification for Structural Steel Buildings", *American Institute for Steel Construction, Chicago, Illinois*.
- Badie S.S, Tadros, Kakish M.K, Splittgerber H.F, Baishya D.L. (2002). "Large Shear Studs for Composite Action in Steel Bridge Girders", *J. of Bridge Engineering*, 7(3), 195-203.
- Chapman J.C. (1964). "Composite construction in steel and concrete- the behavior of composite beams", *Structural Engineer*, 42(4), 115-125.
- Cederwall K. and An L. (1996). "Push-out Tests on Studs in High Strength and normal strength concrete", *Journal of Constructional Steel Research*, 36(1), 15-29.
- Eurocode 4, (1997). "Design of composite steel and concrete structures", *Part 2 : composite bridges (ENV 1994-2)*, CEN
- Hanswille G. (2002). "Composite Bridge Design for Small and Medium Spans", *ECSC Report, Univ. of Wuppertal*.
- Iyengar H.S (1977). "State-of-the-art report on composite or mixed steel-concrete construction for buildings", *American society of civil engineers*.
- Johnson R.P. (2000). "Resistance of stud shear connectors to fatigue", *Journal of Constructional Steel Research*. 56, 101-116.
- Johnson R.P. and Anderson, D. (1993), "Designer's handbook to Eurocode-4. Part 1.1: Design of composite steel and concrete structures", *Wiltshire: MHL Typesetting Ltd*.

- Johnson R.P. & Buckby R.J. (1979). "Composite structures of steel and concrete", *Vol. 2: Bridges, Granada, London*.
- Larose K.E., (1995). "Performance of Shear Stud Clusters for Precast Concrete Bridge Deck Panels", *Saskatchewan Institute of Applied Science and Technology, Canada*.
- Lee K.C., Abbas H.H and Ramey G.E. (2010). "Review of Current AASHTO Fatigue Design Specifications for Stud Shear Connectors", *Structures Congress ASCE, 310-321*.
- Okada J., Yoda T., Lebet J.-P. (2004). "A study of the grouped arrangements of stud connections on shear strength behavior", *Journal of Structural Mechanics and Earthquake Engineering, Vol. 23, No. 776/I-68, 81-95*.
- Ollgaard J.G., Slutter R.G., and Fisher J.W. (1971). "Shear strength of stud connectors in lightweight and normal-weight concrete", *AISC Engineering Journal, 8(2), 55-64*.
- Pallares L., Hajjar J.F. (2010). "Headed steel stud anchors in composite structures", Part I: Shear, *Journal of constructional steel research, 66, 198-212*.
- Prakash A., Anandavalli N., Madheswaran C.K., Lakshmanan N. (2012). "Modified Push-out Tests for Determining Shear Strength and Stiffness of HSS Stud Connector – Experimental Study", *Int. J. of Composite Materials, 2(3), 22-31*.
- Shim C.S., Kim J.H., Chung C.H. and Chang S.P. (2000). "The Behavior of Shear Connection in Composite Beam with Full-Depth Precast Slab", *Structures and Buildings, The Institution of Civil Engineers, Jan., Vol. 140, pp. 101-110*.
- Shim C.S, Chang S.P., Lee P.G. (2001). "Design of shear connection in composite steel and concrete bridges with precast decks", *Journal of Constructional Steel Research, 57, pp. 203-219*.
- Shim C.S., Lee P.G., Yoon T.Y. (2004). "Static behavior of large stud shear connectors," *Engineering Structures, 26(12), 1853-1860*.
- Shim C.S., Park J.S., Jeon S.M., Kim D.W. (2007). "Experimental Study on Group Stud Shear Connection", *Proceeding of 5th International Conference on Advances in Steel Structures, 932-937*.
- Shim C.S., Kim D.W. (2010). "Structural Performance of Composite Joints using Bent Stud", *International Journal of Steel Structures 10(1), 1-13*.
- Shim C.S., Kim D.W. Nhan M.X. (2014). "Performance of stud clusters in precast bridge decks", *The Baltic Journal of Road and Bridge Engineering, 9(1), 43-51*.
- Viest I.M. (1960). "Review of research on composite steel concrete beam", *Journal of the Structural Division ASCE. ST6, June, 1-21*.
- Xu C., Sugiura K., Wu C., Su Q. (2012). "Parametrical static analysis on group studs with typical push-out tests", *Journal of constructional steel research, 72, 84-96*.
- Xue D., Liu Y., Yu Z., He J. (2012). "Static behavior of multi-stud shear connectors for steel-concrete composite bridge", *Journal of Constructional Steel Research, 74, 1-7*.

Ultimate Strength of Continuous Composite Concrete Slabs

Alireza Gholamhoseini¹; Ian Gilbert²; and Mark Bradford³

¹Dept. of Civil and Natural Resources Engineering, Univ. of Canterbury, Christchurch, New Zealand. E-mail: alireza.gholamhoseini@canterbury.ac.nz

²Centre for Infrastructure Engineering and Safety, School of Civil and Environmental Engineering, Univ. of New South Wales, Sydney, NSW 2052, Australia. E-mail: i.gilbert@unsw.edu.au

³Centre for Infrastructure Engineering and Safety, School of Civil and Environmental Engineering, Univ. of New South Wales, Sydney, NSW 2052, Australia. E-mail: m.bradford@unsw.edu.au

Abstract

Composite one-way concrete slabs with profiled steel sheeting as permanent formwork are commonly used in the building construction industry. The steel sheeting supports the wet concrete of a cast-in-situ reinforced or post-tensioned concrete slab and, after the concrete sets, acts as external reinforcement. In this type of slab, longitudinal shear failure between the concrete and the steel sheeting is the most common type of failure at the ultimate load stage. Design codes require the experimental evaluation of the longitudinal shear capacity of each type of steel decking using full scale tests in simple-span slabs. There is no procedure in current codes to evaluate the longitudinal strength of continuous composite slabs and this is often assessed by full scale tests. This paper presents the results of three full-scale tests on continuous composite concrete slabs cast with using trapezoidal steel decking profile (KF70) that is widely used in Australia. Slab specimens were tested in four-point bending at each span with shear spans of span/4. The longitudinal shear failure of each slab is evaluated and the measured mid-span deflection, the end slip and the mid-span steel and concrete strains are also presented and discussed. The slabs are modelled in a finite element (FE) software package using interface elements to model the contact between the steel decking and concrete slab.

Keywords: Continuous composite slab; Cracking; Deflection; Longitudinal shear stress; Steel sheeting; Ultimate strength.

1. Introduction

Composite slabs consisting primarily of cold-formed profiled steel sheeting and structural concrete are increasingly used in steel framed buildings worldwide. In this system, the steel sheeting is normally continuous over two-spans between the supporting steel beams and during construction the concrete is poured to form a continuous one-way composite slab.

The steel sheeting has two main roles in this type of floor system; it firstly serves as permanent formwork supporting the wet concrete during construction while secondly, it acts as external reinforcement for the slab, carrying the tension induced by

positive bending moment throughout the life of the structure [1,2]. If the strength provided by the steel sheeting is not adequate, additional reinforcement might be included in the concrete slab, as shown in Fig. 1.

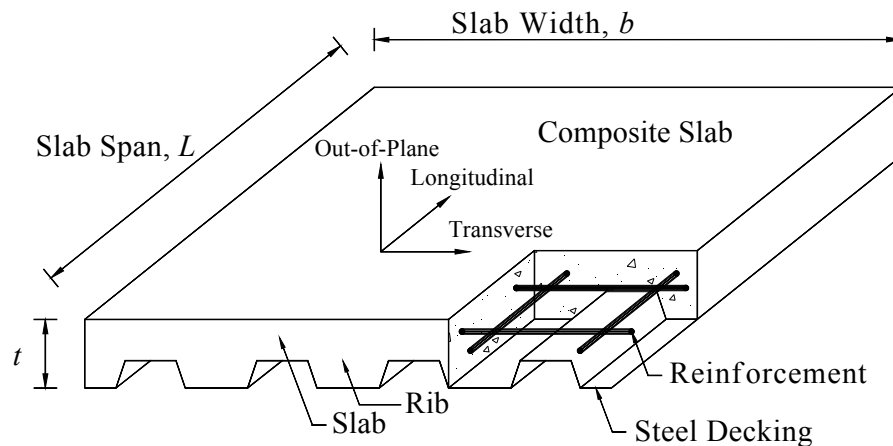


Figure 1. Elements of a composite slab and notation.

The composite action between the steel sheeting and the hardened concrete is dependent on the transmission of horizontal shear stresses acting on the interface between the concrete slab and the steel sheeting. Composite action and the transmission of horizontal shear stresses at the concrete-steel interface are necessary for the steel sheeting to perform its role as the tension reinforcement for the system. The composite action between the concrete and the steel sheeting is achieved, not only by chemical bonding between the sheeting and the concrete, but also by mechanical interlock between the concrete and the embossments on the profiled steel sheeting. Further composite action can be attained by attaching shear studs or similar mechanical shear devices. Resistance against vertical separation is also achieved by the embossments and by adopting a suitable shape for the decking profile [3-5].

A composite slab must be designed to carry the factored design loads at the ultimate limit state. Fig. 2a shows an elevation and a cross-section of a typical composite slab specimen in a four-point bending test. There are three likely failure modes: failure in flexure at the peak moment region (i.e., at section b-b); longitudinal shear failure at section c-c; vertical shear failure at section a-a. Fig. 2b graphs the relationship between the nominal shear stress (V_t/bd_p) and the inverted slenderness of the slab (A_p/bL_s), where V_t is the support reaction; A_p is the cross-sectional area of the steel sheeting; b is the width of the slab cross-section; d_p is the effective depth of the slab and L_s is the shear span. Each of the above failure modes occurs in different parts on the graph, with flexural failure controlling when L_s is large, vertical shear failure when L_s is small and longitudinal shear failure for intermediate values of L_s . The terms of (A_p/bL_s) and (V_t/bd_p) are also used in Eurocode 4 [6] for evaluating of longitudinal shear stress capacity.

Eurocode 4 gives two methods to evaluate the longitudinal shear bond capacity of composite slabs known as the “*m-k*” and “*partial shear connection*” methods. In both methods, the longitudinal shear capacity is assessed by using full scale laboratory tests of simply-supported slabs to measure slab performance as

shown typically in Fig. 2a. Full scale slab specimens are required because the longitudinal shear capacity is dependent on the geometry and flexibility of the particular type of steel sheeting, the size, location and spacing of the embossment on the sheeting, as well as on the slenderness of the slab (i.e. the span-to-depth ratio) [7,8].

Current codes do not present a procedure to evaluate the longitudinal strength of continuous composite slabs and this is often assessed by full scale tests. In some research works [9,10], FE analytical models have been developed for continuous composite slabs based on small scale push out tests. Small scale FE analyses with 3D fully detailed embossments are also suggested to investigate the influence of embossments on longitudinal shear capacity and possibly predicting more accurately input parameters for full scale FE analyses.

In this paper, the results of three full-scale tests on continuous composite concrete slabs cast with using profile decking (KF70) that is widely used in Australia are presented. The slab specimens were tested in four-point bending at each span with shear spans of span/4. The longitudinal shear failure of each slab is evaluated and the measured mid-span deflection, the end slip and the mid-span steel and concrete strains are also presented and discussed. In addition, the slabs are modelled with finite element software using an interface element to model the contact between the slab decking and concrete slab.

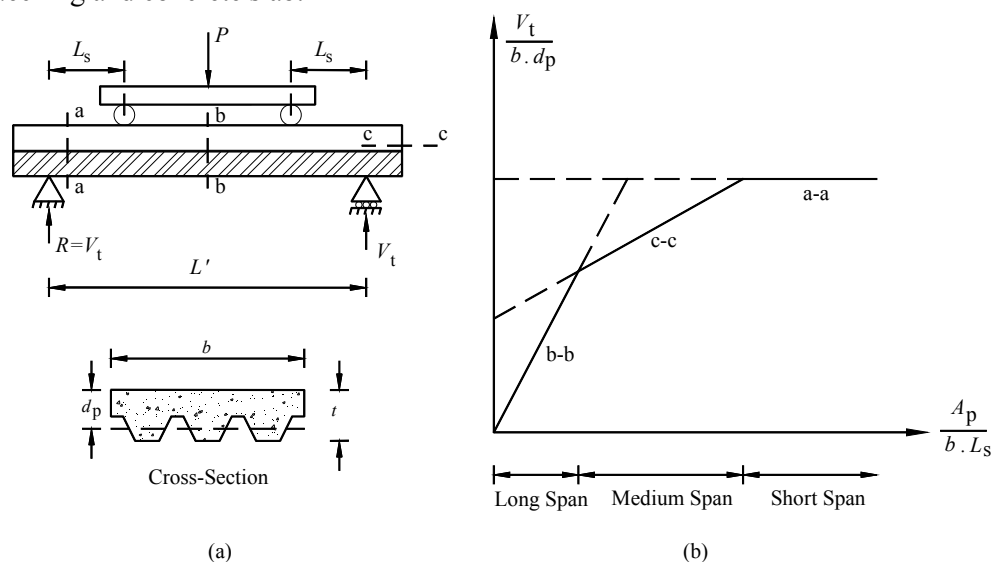


Figure 2. Setup of four-point bending test in a simple composite slab.

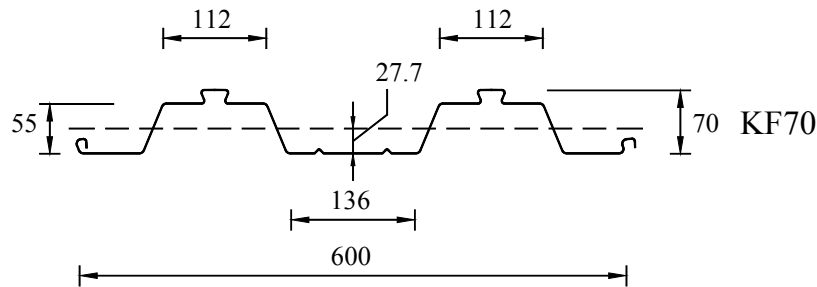
2. Experimental Study

2.1. Overview

The behaviour of composite slabs cast on commonly used trapezoidal decking profile (KF70) manufactured by Fielders Australia Pty Ltd [11] has been studied. The shape and dimensions of the profile are shown in Fig.3. The thickness of the steel sheeting was $t_s = 0.75$ mm. The section properties of the profile are provided in Table 1.

Table 1. Section properties of steel profile used in the experiments.

Deck Profile	Sheet Thickness t_s (mm)	Section Area A_{sh} (mm^2/m)	Height to Centroid y_{sd} (mm)	Mass (kg/m^2)	I_s (mm^4/m)
KF70	0.75	1100	27.7	9.17	584,000

**Figure 3. Dimensions (in mm) of steel decking profile.**

Three identical composite slabs were cast with the profiled steel sheeting as permanent formwork and the concrete was then cured for 7 days under wet hessian. The steel sheets were cleaned thoroughly before placing concrete. The steel decking was completely supported on the laboratory floor during casting of the concrete to minimize initial stress or deformation in the steel sheeting. The slump of the fresh concrete at the time of casting was 90 mm. Each slab was 6900 mm long, with a cross-section 150 mm deep and 1200 mm wide, and contained no bottom reinforcement (other than the external steel decking). Each specimen was continuous over the interior support and simply-supported on a roller at each of the two exterior supports. The centre-to-centre distance between the each exterior roller support and interior hinge support was 3350 mm. Longitudinal and transverse reinforcement was provided in the top of the slabs in the negative moment region over the interior support, as shown in Fig. 4.

2.2. Test Setup and Instrumentation

Each slab was tested with shear span of $L_s = L'/4$ ($3350/4 = 840$ mm). Two load cells were placed underneath each support to measure the support reaction and its variation at any time. The deflection at the mid-spans and the end slip at both exterior supports were measured by using LVDTs. The strains in concrete and steel sheeting were measured at selected sections on the top and bottom surfaces of slabs using 60 mm long strain gauges. The strain in the longitudinal reinforcement at the interior support was measured by using embedded strain gauges. A schematic view of the experimental setup and the measured parameters are shown in Fig. 4. The load was applied in a displacement control manner at a rate of 0.3 mm/min.

compressive stress in the concrete in the top fibres between applied loads, as well as significant increases in slab deflection. Abrupt increases in mid-span deflection and end slip were observed after the loss of composite action.

Without exception, the widest crack occurred at the interior support and in the vicinity of one of the applied loads. After the peak load had been reached, wide cracks at the top surface of the interior support (as shown in Fig. 11) and below the applied line loads eventually divided the concrete. This was typically associated with excessive end slip as exemplified in Fig. 12. Significant post-slip strength was observed in all three slabs. The longitudinal shear failure mode is relevant to post-slip strength and behaviour of composite slabs. According to the Eurocode 4 definition of ductility, the longitudinal shear behaviour is considered to be ductile if the failure load exceeds the load causing a recorded end slip of 0.1 mm by more than 10% and hence, all slabs failed in a ductile manner. Graphs of end slip (S) versus applied load are shown in Fig. 6.

The measured load causing an end slip of 0.1 mm $P_{(0.1\text{mm})}$, the peak load capacity P_{max} and the applied load at the end of the test for each slab are summarised in Table 2. Also given in Table 2 are the deflection at peak load; the deflection at the end of the test; the maximum end slip (at the end of the test); the strain in steel sheeting at mid-span at the peak load and the strain in concrete at mid-span at the peak load. The mid-span deflections in the slabs at the peak load were highly variable, and ranged from $(L'/71)$ for the eastern span to $(L'/176)$ for the western span of slab S2 respectively. Graphs of major measured parameters are shown in Figs. 5 to 10.

The maximum value of the strain in the steel sheeting at mid-span at the peak load was measured at the eastern span of slab S2 and was $\varepsilon_{\text{sm}(\text{max})} = 1290 \mu\epsilon$. The steel yield strain is $\varepsilon_{\text{yp}} = f_{\text{yp}}/E_s = 2620 \mu\epsilon$ and therefore the maximum steel strains reached only 49% of the yield strain. Clearly, the loss of longitudinal shear stress in all slabs prevented the steel sheeting from yielding and the full plastic flexural capacity could not be reached.

Fig.13 shows slab S1 after reaching its peak load and just before termination of the test, and shows the different deflections in either span.

Table 2. Summary of test results.

Slab	$P_{(0.1\text{mm})}$ (kN)	P_{max} (kN)	P_{end} (kN)	Δ_{max} (mm)	Δ_{end} (mm)	S_{max} (mm)	$\varepsilon_{\text{sm}(\text{max})}$ ($\mu\epsilon$)	$\varepsilon_{\text{cm}(\text{max})}$ ($\mu\epsilon$)
S1	120.5	199.8	165.0	E(30.9) W(31.8)	E(66.3) W(36.9)	E(17.5) W(10.8)	E(478) W(440)	E(197) W(138)
S2	133.8	213.0	170.5	E(46.8) W(19.0)	E(92.4) W(17.6)	E(25.0) W(2.4)	E(1290) W(1240)	E(201) W(202)
S3	123.1	208.4	176.6	E(40.4) W(21.0)	E(69.4) W(20.3)	E(19.6) W(3.6)	E(1041) W(787)	E(218) W(233)

Legend: Δ_{max} : deflection at peak load; Δ_{end} : deflection at the end of the test; S_{max} : maximum end slip (at the end of the test); $\varepsilon_{\text{sm}(\text{max})}$: strain in steel at mid-span at peak load; $\varepsilon_{\text{cm}(\text{max})}$: strain in concrete at mid-span at peak load.

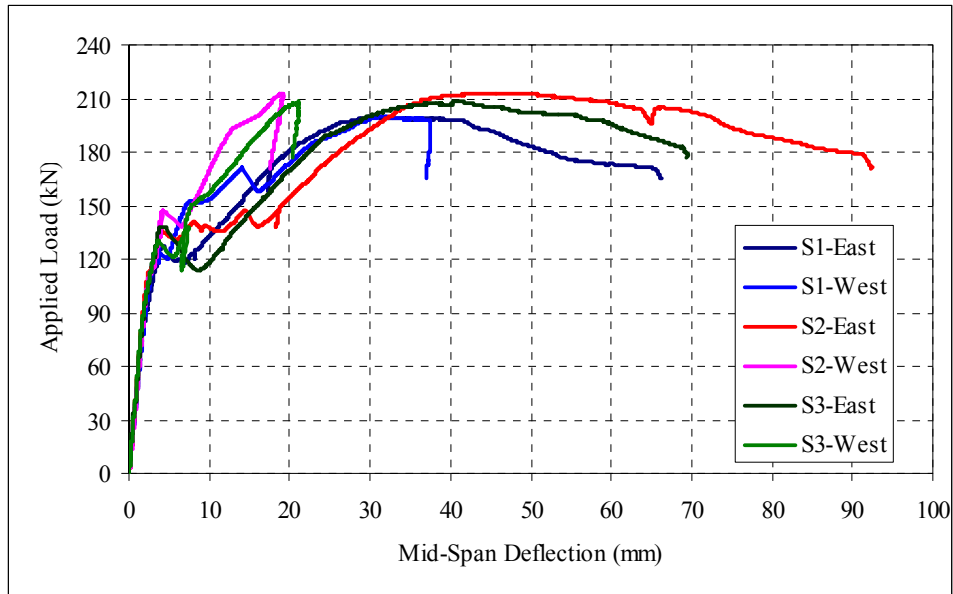


Figure 5. Mid-span deflection versus applied load.

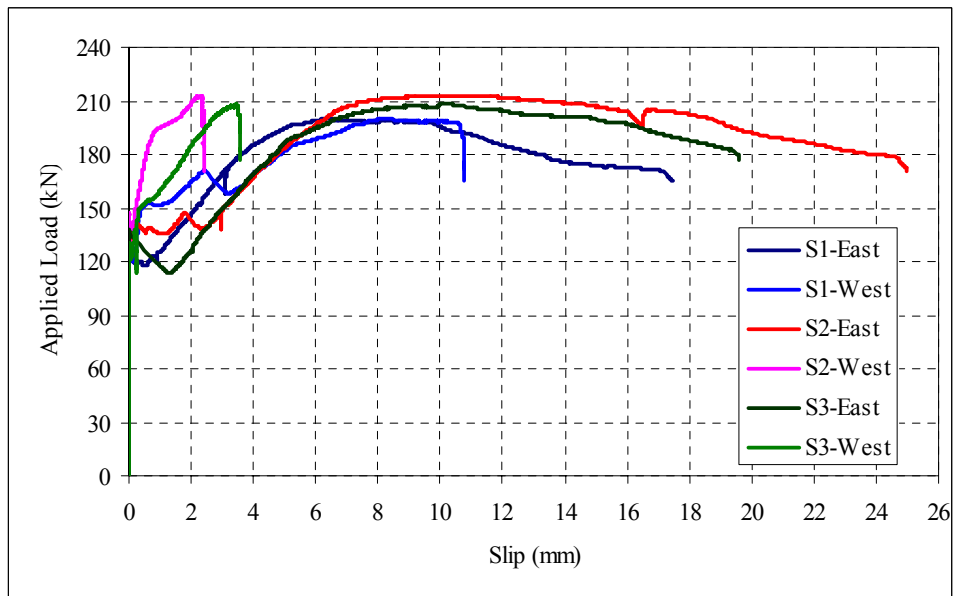


Figure 6. End slip versus applied load.

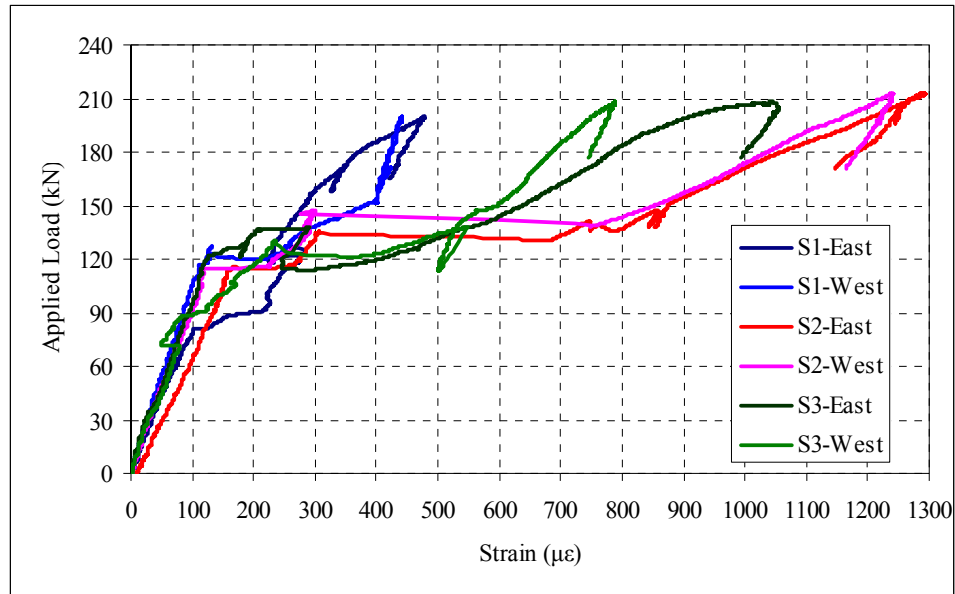


Figure 7. Mid-span strain in steel sheeting versus applied load.

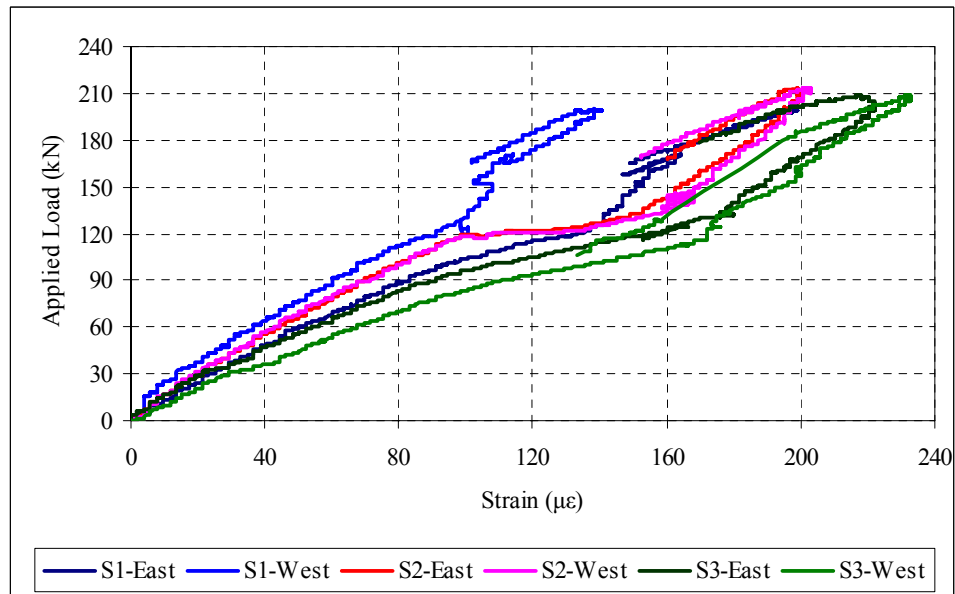


Figure 8. Mid-span strain in concrete versus applied load.

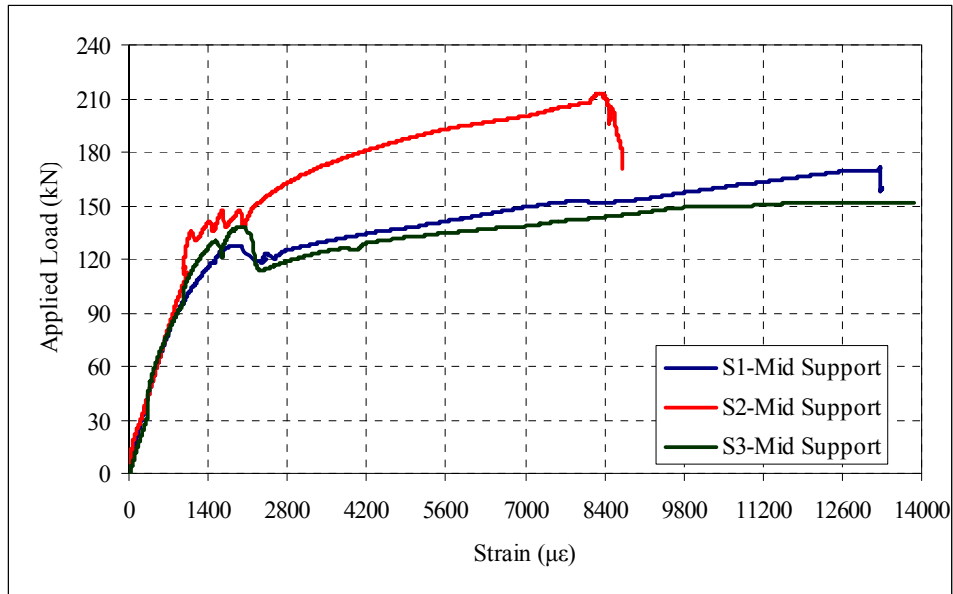


Figure 9. Strain in reinforcement at interior support versus applied load.

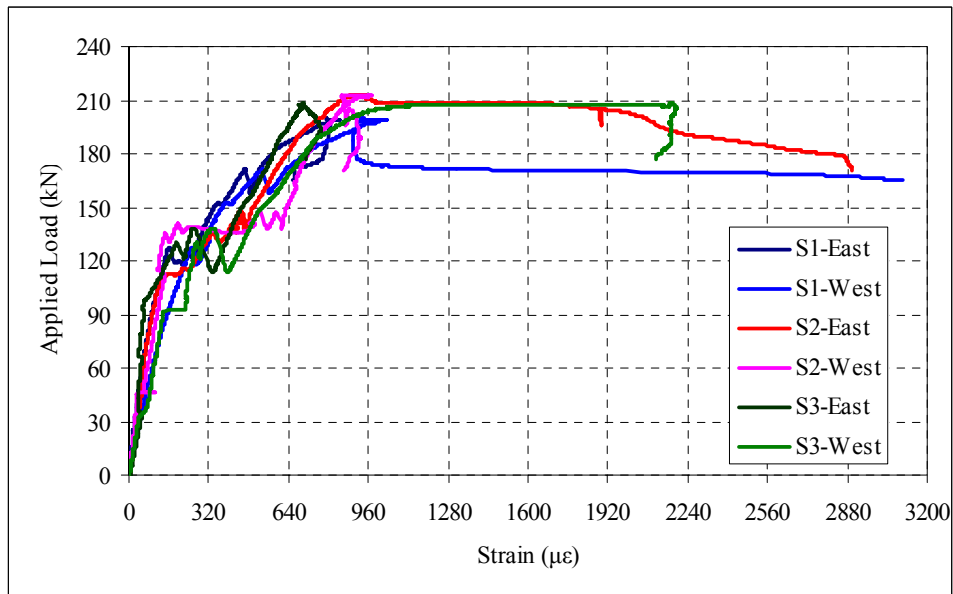


Figure 10. Strain in steel sheeting at interior support versus applied load.



Figure 11. Excessive cracking in concrete surface at interior support in slab S1.



Figure 12. Final end slip at eastern end support of Slab S2 ($S = 25$ mm).



Figure 13. Final deflected shape of slab S1.

4. Finite Element Analysis

4.1. General Structural Modelling

The general purpose finite element software ATENA 3D version 4.2.7 was used in the present study to investigate the ultimate strength of the continuous composite concrete slabs tested in the laboratory. ATENA 3D program is specifically designed for 3D non-linear finite element analysis of solids with rigorous constitutive relationships to model the behaviour of reinforced concrete structures including concrete cracking, concrete crushing and reinforcement yielding.

A three-dimensional (3D) finite element model was developed to account for the material and geometric nonlinearities in the composite slabs. The material properties selected for steel decking, concrete slabs and reinforcing bars were similar to the values obtained from tests on companion specimens as previously summarised in section 2.3.

The Newton-Raphson iterative solution method was chosen. The mid-span deflection of each slab versus the total load was monitored in the analysis. Four monitoring points at the location of the applied line loads and two monitoring points at mid-span were defined to monitor the amount of total load and mid-span deflection, respectively. All of the monitoring points were defined on the top surface of each slab.

Steel plates having 50 mm thickness and 100 mm width were modelled at the load application points to simulate the laboratory experiments and to prevent high stress concentrations at these locations. The partial connection allowing slip to occur between the steel sheeting and concrete slab was considered. Similar to the experimental study, in each analysis the load was applied in a displacement control manner. The finite element model for the analysed slab is shown in Fig. 14.

The concrete slab, steel plates and steel decking were modelled with three dimensional solid linear tetrahedral elements with three translation degrees of freedom per node. Linear tetrahedral elements contain 4 nodes compared to the 10 nodes in quadratic elements, and hence require less computational effort and time to run the analysis. The global element size was limited to 50 mm.

There are two ways that a reinforcing bar can be modelled in ATENA; either as smeared or as discrete bar element. In smeared element modelling, the reinforcement is spread along the macroelement by assigning a reinforcement ratio, whereas in discrete bar element modelling, the reinforcing bar is modelled as one dimensional line element with the assigned bar diameter. The contact between the reinforcing bar and the surrounding concrete macroelement can be assigned either as perfect bond or as specified bond-slip relationship. In this study the reinforcing bars over the interior support were modelled as discrete bars with perfect bond to concrete. The reinforcing bars were modelled using “CC Reinforcement” material type with elastic–fully plastic behaviour without strain hardening.

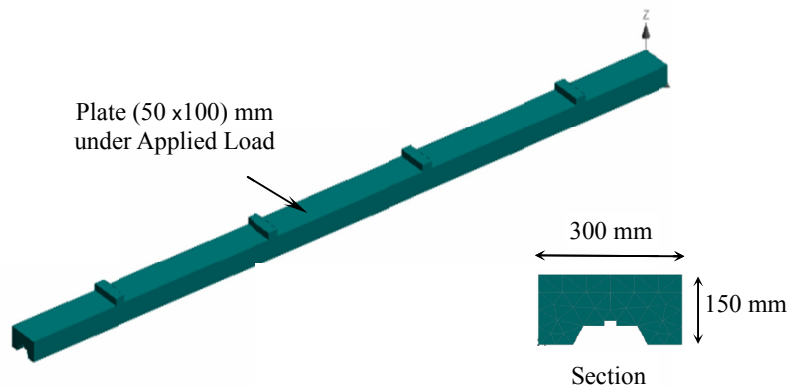


Figure 14. Finite element model.

4.2. Material Modelling

4.2.1. Steel Plate

The steel plates at the load application points were modelled as a linear-elastic material using the “3D Elastic Isotropic” material type with $E_s = 200$ GPa.

4.2.2. Steel Sheeting and Reinforcement

The steel sheeting and reinforcement were modelled as an elastic–fully plastic material without strain hardening using the “3D Bilinear Steel Von Mises” and “CC Reinforcement” material types, respectively. A bilinear stress-strain relationship, as shown in Fig. 15, was used for steel sheeting and reinforcement in both tension and compression. The Von Mises yield criterion was used in the non-linear analysis to treat the plasticity of steel material.

4.2.3. Concrete Slab

The concrete slab was modelled using the “3D Nonlinear Cementitious 2” material, for which its properties in different conditions are presented in the following.

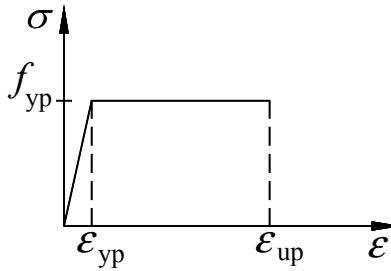


Figure 15. Stress-strain curve for steel sheeting.

(a) Tension Before Cracking

The behaviour of concrete in tension before cracking was assumed to be linear-elastic, i.e. $\sigma = E_c \epsilon$, where σ is the tensile stress in the concrete, E_c is the initial elastic modulus of the concrete and ϵ is the strain in the concrete.

(b) Tension After Cracking

A fictitious model based on a crack-opening law and fracture energy (shown in Fig.16) was used in combination with the crack band theory for modelling concrete tension after cracking using

$$\frac{\sigma}{f_t} = \left\{ 1 + \left(c_1 \frac{w}{w_c} \right)^3 \right\} \exp \left(-c_2 \frac{w}{w_c} \right) - \frac{w}{w_c} (1 + c_1^3) \exp(-c_2) \quad (1)$$

where w is the crack opening, w_c is the crack opening at the complete release of stress, $c_1 = 3$, $c_2 = 6.93$, $w_c = 5.14 G_f / f_t$ and G_f is the fracture energy needed to create a unit area of stress-free crack and was taken as 30 N/m in the numerical model.

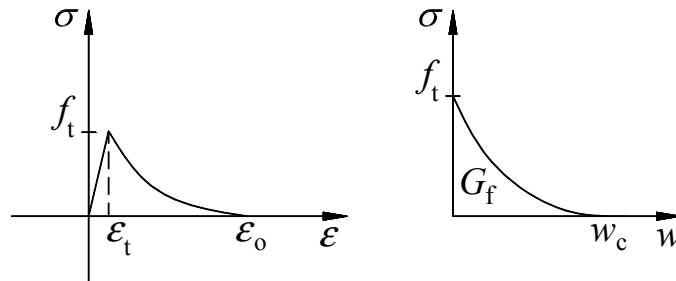


Figure 16. Stress-strain curve for concrete in tension.

(c) Compression Before Peak Stress

The stress-strain curve for concrete in compression is given in Fig. 17. The equation recommended by the CEB-FIP Model Code 1990 [12] was adopted for the ascending branch of the concrete stress-strain law in compression, given as

$$\sigma = f_c \left[\frac{kx - x^2}{1 + (k-2)x} \right], \quad x = \frac{\epsilon}{\epsilon_c}, \quad k = \frac{E_c}{E_{c1}} \quad (2)$$

where σ is the concrete compressive stress; x is a normalised strain; ϵ_c is the strain at peak stress; E_c is the initial elastic modulus and E_{c1} is the secant elastic modulus at the peak stress. The shape parameter k may have any positive value greater than or equal to 1 (e.g. $k = 1$ linear, $k = 2$ parabolic).

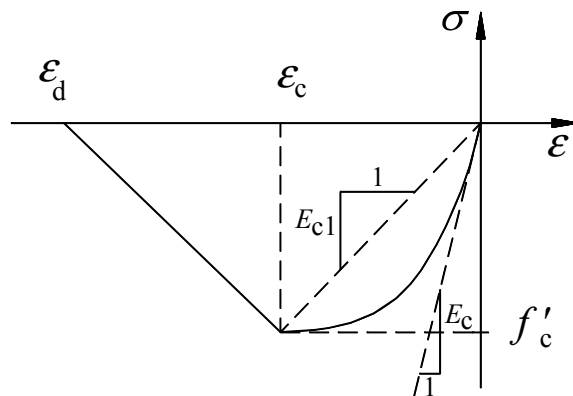


Figure 17. Stress-strain curve for concrete in compression.

(d) Compression after Peak Stress

The softening law in compression is linearly descending. In this study, a fictitious compression model based on dissipated energy was used. The model is based on the assumption that compression failure is localised in a plane normal to the direction of the compressive principal stress. All post-peak compressive displacements and energy dissipation are localised in this plane. It is assumed that this displacement is independent of the size of the member. This hypothesis is supported by experiments conducted by van Mier [13], with the equation being

$$\epsilon_d = \epsilon_c + \frac{w_d}{L'_d} \quad (3)$$

where w_d is the plastic displacement at the end of the softening curve taken as 0.5 mm, ϵ_d is the limiting compressive strain and L'_d is the band size.

4.2.4. Steel Deck-Concrete Slab Interface

The “3D Interface” material type in ATENA 3D was used to model contact between the steel decking and the concrete slab. The interface material is based on the Mohr-Coulomb criterion with a tension cut off. The constitutive relation for a general two-dimensional case is given in terms of tractions on the interface planes and the relative sliding and opening displacements as [14]

$$\begin{Bmatrix} \tau \\ \sigma \end{Bmatrix} = \begin{bmatrix} K_t & 0 \\ 0 & K_n \end{bmatrix} \begin{Bmatrix} \Delta_v \\ \Delta_u \end{Bmatrix} \tag{4}$$

The initial failure surface corresponds to a Mohr-Coulomb condition with an ellipsoid in the tension regime. After the stresses violate this condition, this surface collapses to a residual surface which corresponds to dry friction. The frictional properties of the interface material model in ATENA 3D are defined by the shear cohesion c and the friction coefficient ϕ . The maximum shear stress is limited by the linear relation $\tau = c - \phi\sigma$, where σ is the interface compressive stress. In tension, the failure criterion is replaced by an ellipsoid which intersects the normal stress axis at the value of f_t with the vertical tangent and the shear axis is intersected at the value of c with the tangent equivalent to ϕ as shown in Fig. 18. For this:

$$|\tau| \leq c - \phi\sigma, \quad \sigma \leq 0 \tag{5}$$

$$\tau = \tau_0 \sqrt{1 - \frac{(\sigma - \sigma_c)^2}{(f_t - \sigma_c)^2}}, \quad \tau_0 = \frac{c}{\sqrt{1 - \frac{\sigma_c^2}{(f_t - \sigma_c)^2}}}, \quad \sigma_c = -\frac{\phi f_t^2}{(c - 2\phi f_t)} \quad 0 < \sigma \leq f_t \tag{6}$$

$$\tau = 0, \quad \sigma > f_t \tag{7}$$

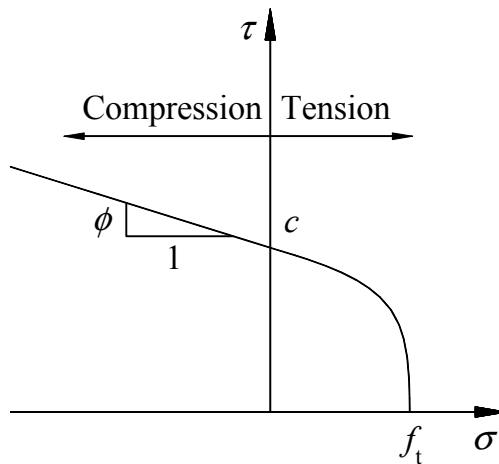


Figure 18. Failure surface for interface element.

The coefficients K_n and K_t in Eq.4 denote the initial elastic normal and shear rigidities respectively. There are two additional rigidity values that need to be specified in the ATENA 3D input [14]. They are denoted in Fig. 19 as $K_{n(\min)}$ and $K_{t(\min)}$. These values are used only for numerical purposes after the failure of the element, in order to preserve the positive definiteness of the global system of equations. Theoretically, after the interface failure the interface rigidity should be zero, which would mean that the global rigidity would become indefinite. These minimal rigidities are recommended to be about 0.001 times of the initial rigidities. The assumed values of $K_n = 1000\text{MN/m}^3$ and $K_t = 60\text{MN/m}^3$ showed the best agreement between the finite element model and

the test results. Of course, these values are deemed to be a function of material properties and rigidities of the steel sheeting and the concrete slab. Vertical separation at the steel-concrete interface was assumed to be negligible, and was achieved by assigning a very large value for the initial elastic normal rigidity K_n in the model. The cohesion stress value of 0.1 MPa and tensile stress value of 0.5 MPa were selected for the interface element properties. A summary of the comparison between the test results and the numerical results obtained from the partial interaction analyses is presented in Fig. 20. In addition, the results of the analysis when yielding occurred in the steel reinforcement and the respective deflection of the slab are shown in Fig. 21.

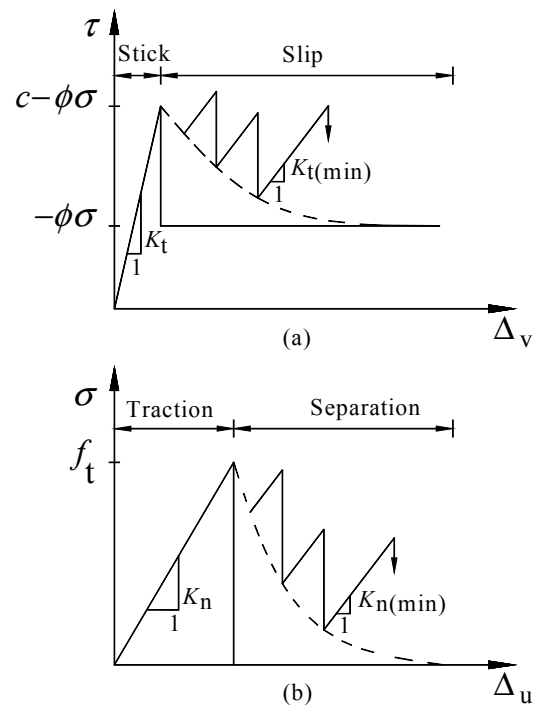


Figure 19. Interface model behaviour in (a) shear and (b) tension.

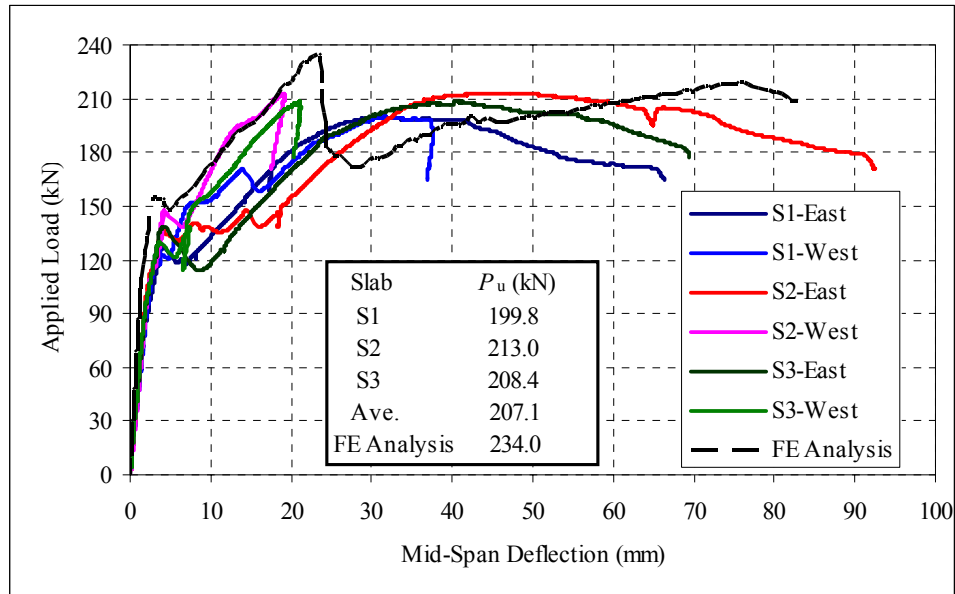


Figure 20. Load versus mid-span deflection comparisons.

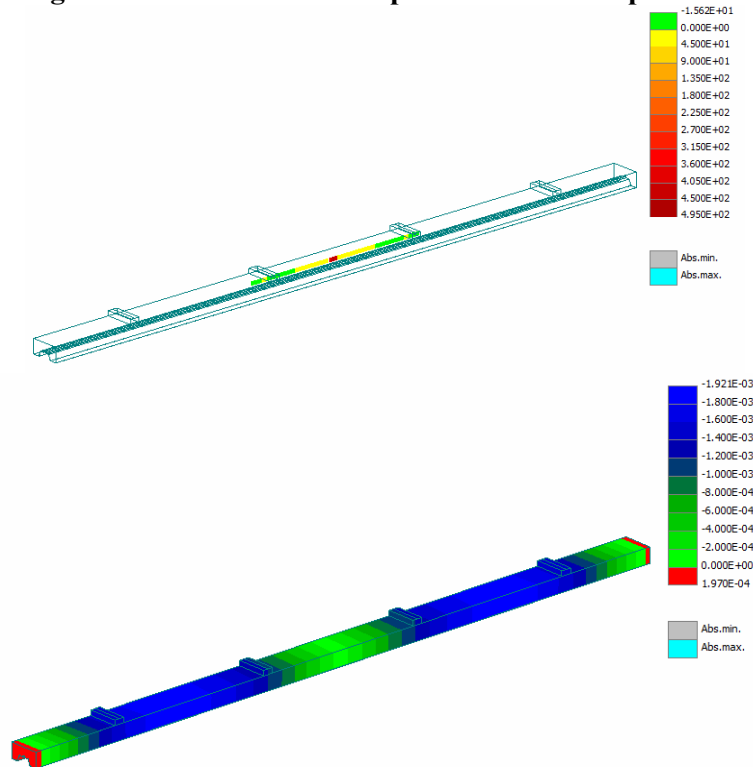


Figure 21. Stress in reinforcement and respective deflection of slab when reinforcement is at yield.

5. CONCLUSIONS

The results of short-term testing to failure of three continuous composite slabs constructed using a profiled steel sheeting section that is widely used in construction industry in Australia have been presented and discussed. The slabs were tested in symmetric four-point bending in each span. The slabs were then modelled in a finite element program and the results were compared with test results. Currently, national design standards do not present guidance for the design of continuous composite slabs, and full-scale testing is needed. In lieu of the expense involved with full-scale testing, the good agreement between the finite element modelling and the test results obtained in the study suggests far less expensive numerical modelling can be used to verify the performance of continuous composite slabs.

For all slabs, the maximum flexural capacity was controlled by yielding of the reinforcement at the interior support with significant slip at the concrete-steel interface in the shear span, well before the fully plastic moment of the composite cross-section could be reached. All slabs satisfied the ductility provisions given in Eurocode 4.

ACKNOWLEDGEMENTS

The work reported in this paper was undertaken with the financial support of the Australian Research Council through Linkage Project LP0991701, decking manufacturer Fielders Australia Pty Limited and Prestressed Concrete Design Consultants Pty Limited. The third author was also supported by the Australian Research Council through Australian Laureate Fellowship FL100100063. This support is gratefully acknowledged.

REFERENCES

- [1] Oehlers D.J. and Bradford M.A. (1995) Composite Steel and Concrete Structural Members: Fundamental Behaviour. Oxford, Pergamon Press.
- [2] Johnson, R.P. (2004) Composite Structures of Steel and Concrete. Oxford, Blackwell Publishing.
- [3] Gholamhoseini A., Gilbert R.I., Bradford M.A. and Chang Z.-T. (2012) Evaluation of Longitudinal Shear Stress and Bond-Slip Relationships in Composite Concrete Slabs using Partial Shear Connection. ACMSM22 Conference, Sydney, Australia, CRC Press/Balkema, 269-274.
- [4] Porter M. and Ekberg C. (1975) Design Recommendations for Steel Deck Floor Slabs. 3rd International Specialty Conference on Cold-Formed Steel Structures, University of Missouri-Rolla, Missouri, 761-791.
- [5] Porter M. and Ekberg C. (1976) Design Recommendations for Steel Deck Floor Slabs. *Journal of the Structural Division, ASCE*, 102: 2121-2136.
- [6] British Standards Institution (2005). EN 1994 Eurocode 4: Design of Composite Steel and Concrete Structures, Part 1.1 General Rules and Rules for Buildings. London, BSI.

- [7] Abdullah, R. (2004) Experimental Evaluation and Analytical Modelling of Shear Bond in Composite Slab. PhD Dissertation, Virginia Polytechnic Institute and State University, Blacksburg, Virginia, USA.
- [8] Baskar, R. (2012). Experimental and Numerical Studies on Composite Deck Slabs. *International Journal of Engineering and Technology*, 2: 1116-1125.
- [9] Daniels, B.J., and Crisinel, M. (1993a). Composite Slab Behavior and Strength Analysis. Part 1: Calculation Procedure. *Journal of Structural Engineering*, 119: 16-35.
- [10] Daniels, B.J., and Crisinel, M. (1993b). Composite Slab Behavior and Strength Analysis. Part 2: Comparison with Test Results and Parametric Analysis. *Journal of Structural Engineering*, 119: 36-49.
- [11] Fielders Australia Pty. Ltd. (2008) Specifying Fielders KingFlor Composite Steel Formwork System. Design Manual.
- [12] CEB (1993) CEB-FIP Model Code 1990. London, Thomas Telford.
- [13] van Mier J.G.M. (1986) Multi-Axial Strain-Softening of Concrete. *Materials and Structures*, 19: 179-200.
- [14] ATENA (2009) Program Documentation, Part 1: ATENA Theory Manual. Prague, Cervenka Consulting.

Evaluation of the Shear Force Behaviour of Composite Slabs

Simon Hartmeyer¹ and Wolfgang Kurz²

¹Voss und Kamb und Partner, Beratende Ingenieure, Europaallee 9-11, 67657 Kaiserslautern, Germany. E-mail: S.Hartmeyer@voka-kl.de

²Univ. of Kaiserslautern (TU), Institute of Steel Structures, 67633 Kaiserslautern, Germany. E-mail: Wolfgang.Kurz@bauing.uni-kl.de

Abstract

The use of composite slabs is common in the international area and is generally used in office and industrial buildings. Especially the advantages in weight support the use of the composite slab in case of refurbishment. The demand of sustainable solutions promotes the exploration of lightweight composite slabs by substitution of the normal weight concrete by concrete with a dry density between 1,400 kg/dm³ and 1600 kg/dm³. First tests have shown an unexpected failure mode due to the specific properties of lightweight aggregate concrete and its combination with composite sheets. In bending tests of composite slabs with lightweight aggregate concrete (LWAC), the failure was initiated by inclined bending cracks with a vertical offset of the crack surfaces and local buckling of the web of the composite sheet in the decisive crack. The known failure mode of specimens with normal weight concrete (NWAC) could not be validated in these tests. By an examination using the European regulations for the dimensioning of shear loaded concrete beams, a safety deficit about 20 % could be detected. Against this background at the University of Kaiserslautern, a new approach was developed to allow a safe determination of the shear capacity. The concept is comparable to different types of concrete and will be shown in this paper.

INTRODUCTION

In addition to an expected reduction of the longitudinal shear capacity by Kurz and Hartmeyer (2011) and Kurz et. al. (2009) in tests of composite slabs with LWAC an unexpected shear failure could be observed.

This problem is intensified by the fact that shear failure cannot be accurately described by the code of composite elements, DIN EN 1994-1-1 (2010). For verification of the shear force capacity of composite slabs, it refers to the regulations for concrete beams without shear reinforcements, DIN EN 1992-1-1 (2011). These empirical rules were not adapted to the specific bearing behaviour of composite slabs and may lead to a safety deficit. A discrete model for composite slabs under shear load is missing.

The specified design equation from DIN EN 1992-1-1 (2011) is a semi-empirical approach to evaluate the shear bearing capacity of slender concrete beams without stirrups. The approach is shown in eq. (1) for NWAC and is adapted to LWAC in eq. (2).

$$(1) \quad V_{Rd,ct} = [C_{Rd,c} \cdot k \cdot (100 \cdot \rho_{sL} \cdot f_{ck})^{1/3}] \cdot b_w \cdot d \quad \text{NWAC} \quad | \quad (2) \quad \text{LWAC} \\ V_{Rd,ct} = [C_{Rd,c} \cdot \eta_1 \cdot k \cdot (100 \cdot \rho_{sL} \cdot f_{lck})^{1/3}] \cdot b_w \cdot d$$

These shear equations have never been adapted to the specific behaviour of composite slabs. Therefore, the empirical design equations are only valid for elements similar to those which have been used in the database for calibration. As a result, there is an inaccuracy of this analytical investigation which increases with decreasing longitudinal reinforcement rate.

The appearing safety deficit by comparing the test results of composite slabs with the expected average shear capacities calculated by the design equation (see eq. (1) and eq. (2)) is shown in Figure 1, left hand. The values of resistance were calculated with average concrete strengths and a mean calibration factor $C_{Rm,c}$ of 0.2 which is confirmed by Reineck (2006).

For a better illustration of the deficit, the safety coefficient referred to the longitudinal reinforcement rate was plotted in the diagram in Figure 1 on the right side. Within the determination of the longitudinal reinforcement rate, the effective anchored reinforcement of the metal sheet is calculated by dividing the anchored tensile force by the mean yield strength of the sheet. By reaching a safety model value greater than 1.0 a safety deficit is given. The safety coefficient γ is equivalent to the division of the mean shear force resistance $V_{Rm,ct}$ with the shear force results of tests $V_{u,Test}$.

A total of 64 experiments with shear force failure were evaluated for illustration in Figure 1.

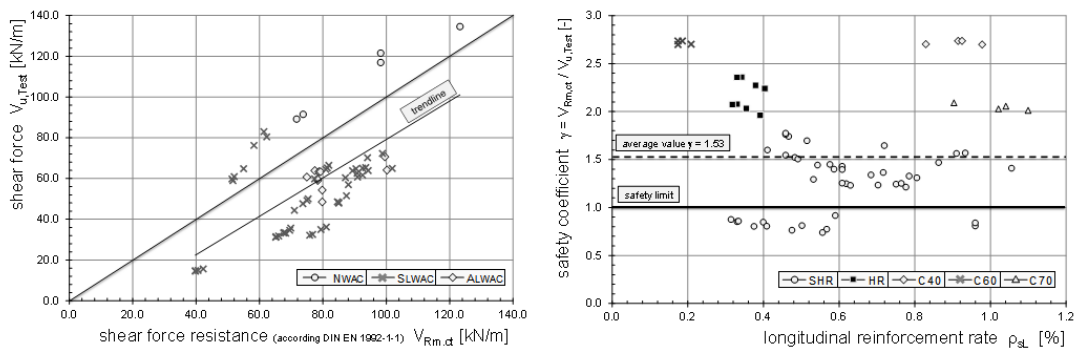


Figure 1. Comparison between mean test results and mean results by design equation $V_{Rm,ct}$.

Against this background a new design model for composite slabs under shear load was developed at the University of Kaiserslautern (TU).

EXPERIMENTAL STUDIES AND RESULTS

Aim of the on-going project is the specific description of the shear bearing behaviour to formulate a discrete model for shear loaded composite slabs made of normal or lightweight aggregate concrete. Therefore the results of former tests with

LWAC were complemented by an investigation at on specimens made of NWAC and LWAC.

The main analyses were made at Four- and Three-Point-Bending tests with metal sheets called SuperHolorib (see Figure 2). The metal sheets were produced and provided by Montana Bausysteme AG. The composite length was variegated between 400 mm and 1000 mm. Overall 42 specimens with LWAC and 6 specimens with NWAC with shear failure could be evaluated.

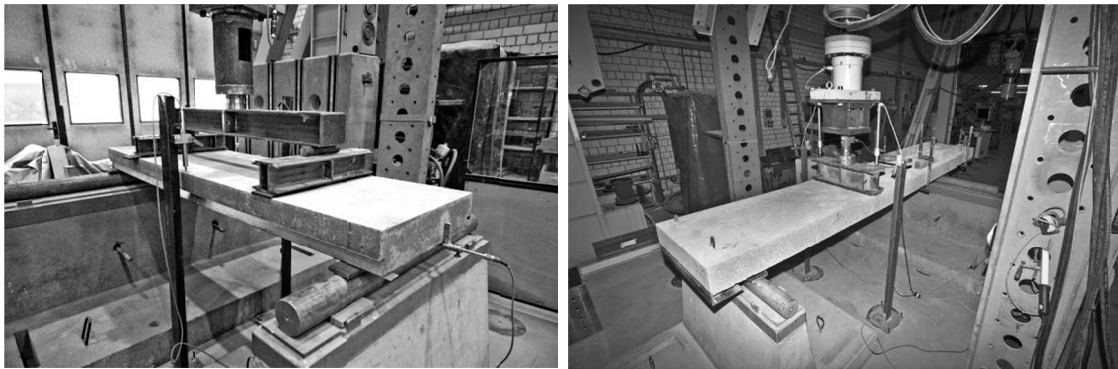


Figure 2. Typical test set-up of the 4-point- (left) and the 3-point-bending test (right).

The typical crack pattern of specimens with a short composite range (left) and with a long composite range (right) are shown in Figure 3.

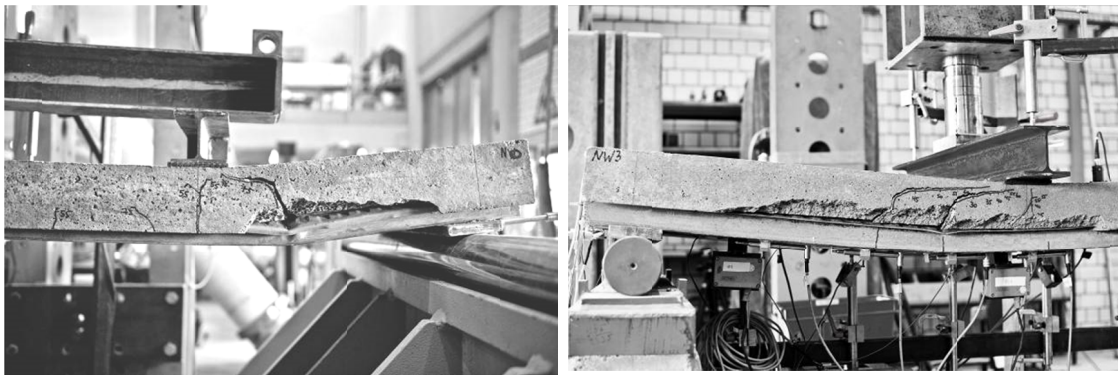


Figure 3. Typical crack pattern of composite slabs with shear failure. The short composite length is shown left and the average composite length right.

A compilation of typical load-deflection-curves and the corresponding load-slip-curves are shown in Figure 4. The dimensions and properties of the described specimens are given in Table 1.

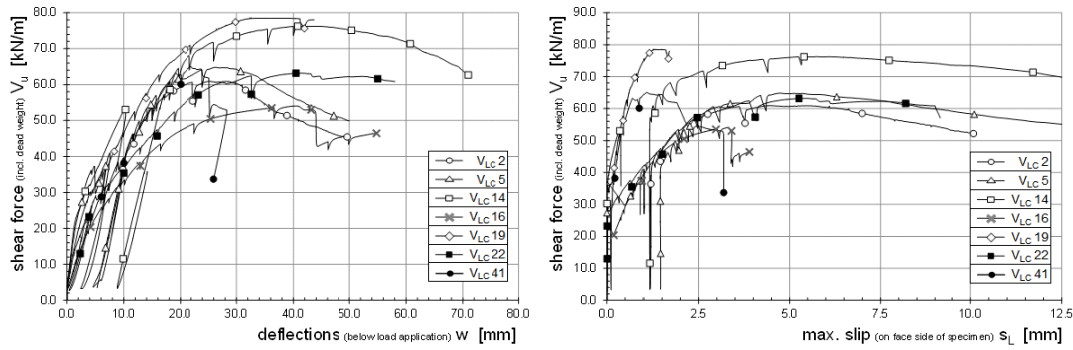


Figure 4. Typical load-deflection-curves (left) and the corresponding load-slip-curves (right).

Most of the tests were executed according to the appendix of DIN EN 1994-1-1 (2010). For the LWAC a bulk density ρ_{dry} between 1.4 kg/dm^3 and 1.6 kg/dm^3 could be assessed. The compressive strength f_{icm} of the used lightweight concrete varied between 15 MPa and 48 MPa. The maximum concrete tensile strength f_{ictm} reached in test was 2.8 MPa. The young’s modulus of the LWAC reached values to the amount of 14000 MPa.

To increase the anchored tensile force of the metal sheet an end-anchoring was used by deforming the metal sheet at both front ends. This kind of anchoring is called forming anchor ‘BVA’. In some of the tests a transverse reinforcement was placed at the ends of the specimens to avoid longitudinal cracking occurring at the face sides of specimen at the edges of the upper chords. All specimens had a height h_t of 140 mm. The metal thickness t_{nom} varied between 0.75 mm and 1.00 mm. The composite length in the tests is denoted by L_s . The length of the metal sheet, overlapping the support was denoted with L_o . The maximum slip $s_{L,u}$ and the maximum deflection w_u corresponding to the ultimate load were also denoted in Table 1.

Table 1. Dimensions and properties of the specimens shown in Figure 4

no-tation	t_{nom} [mm]	L_o / L_s [mm]	h_t [mm]	an-chorage	rein-forcement	f_{icm} [N/mm ²]	f_{ictm} [N/mm ²]	E_{ictm} [N/mm ²]	ρ_{dry} [kg/m ³]	ρ_{sl} [%]	$s_{L,u}$ [mm]	w_u [mm]	V_u [kN/m]
V _{LC} 2	0.75	100 / 500	140	-	transverse	16.5	1.45	12100	1.48	0.27	4.4	25.1	61
V _{LC} 5	0.75	100 / 500	140	-	--	16.1	1.50	11700	1.48	0.40	4.8	26.4	65
V _{LC} 14	0.75	100 / 500	140	BVA	transverse	16.1	1.50	11700	1.48	0.48	5.7	42.3	76
V _{LC} 16	0.75	100 / 800	140	BVA	transverse	22.8	1.66	12700	1.48	0.86	3.3	40.3	54
V _{LC} 19	1.00	100 / 800	140	BVA	transverse	28.8	1.96	13700	1.59	1.21	1.0	25.7	79
V _{LC} 22	1.00	90 / 780	140	-	transverse	22.2	2.05	12300	1.61	0.75	5.4	41.3	63
V _{LC} 41	1.00	100 / 800	140	-	--	46.0	2.35	15300	1.57	0.61	1.1	21.9	65

CONCEPT OF A DESIGN MODEL FOR SHEAR LOADED COMPOSITE SLABS

By increasing the load the inclined bending crack constricted the compression zone until the maximum shear bearing capacity was reached. The shear failure in

composite slabs occurred with considerable endslip and high longitudinal shear stress.

Three bearing components can be identified by examination the shear bearing behaviour of composite slabs. All components are acting in an additive manner. The shear capacity of the metal sheet itself and the shear force bearing capacity in the region of the uncracked compression zone, form a fundamental value of the shear resistance of composite slabs $V_{R,0m}$. Depending on the bonding properties of the composite sheet and the concrete properties, aggregate interlock can additionally improve the total shear capacity.

Across the crack, shear forces can be transferred up to the maximum shear capacity of the metal sheet. By reaching a critical value local buckling in the section of the decisive inclined bending shear crack can be observed (Figure 5).



Figure 5. Buckling of the web at the starting point of the inclined bending crack.

The buckling allows a vertical displacement of the crack surfaces which activates an aggregate interlock. The effectiveness of the aggregate interlock depends on the properties of the concrete and the intensity of the composite action. The crack width already existing at time of the occurring stability failure of the metal sheet further defines the possible aggregate interlock.

The composite action and potentially existing end-anchoring determines the inducible longitudinal shear stress. Only that share of the possible tensile force of the metal sheet is anchored and can be transferred into the concrete. This effective tensile force defines the height of the compression zone. The shear capacity is finally reached, when the inclined bending shear crack cut into the compression zone.

According to these explanations, the shear resistance of composite slabs is determined by the sum of the shear capacity of the metal sheet $V_{p,Rm}$, the transverse force component of the uncracked compression zone $V_{c,cz}$ and the local aggregate interlock $V_{c,ct}$ (see eq. (3)). The interaction of the bearing components is shown schematically in Figure 6.

(3) NWAC / LWAC

$$V_{Rd} = \frac{1}{\gamma_v} \cdot (V_{0,Rk} + V_{c,ct}) = \frac{1}{\gamma_v} \cdot (V_{p,Rk} + V_{c,cz} + V_{c,ct})$$

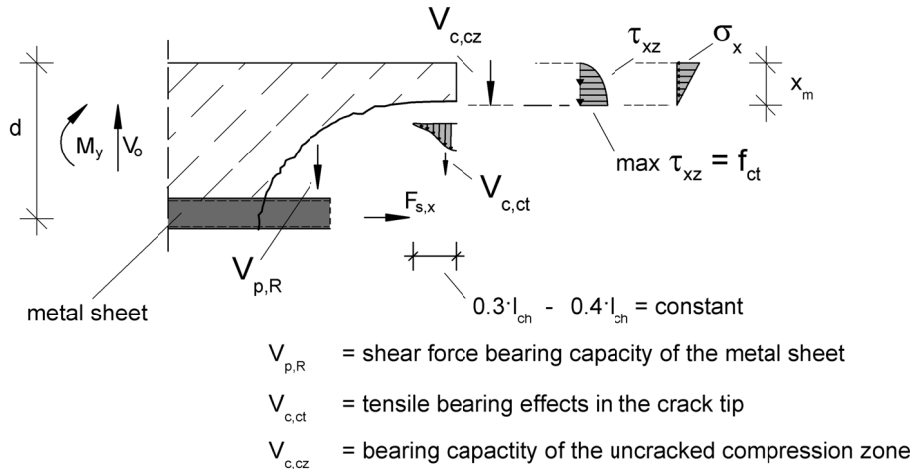


Figure 6. Main influential factors of the shear force bearing behaviour of composite slabs.

The shear capacities of the metal sheets are given by load tables provided by the manufacturer. The values are secured by tests according to DIN EN 1993-1-3 (2010). The used values correspond to the regulations of the technical approval. The ultimate load of the metal sheet called SuperHolorib and Holorib are given in Table 2 (see SuperHolorib (2007) and [SuperHolorib (1994)]).

Table 2. Normalised values of the bearing capacity under pure shear loading.

notation	nom. bearing capacity $\bar{V}_{p,Rk} / \bar{V}_{p,Rm}$		
[-]	0.75 [mm]	0.88 [mm]	1.00 [mm]
Holorib 51	10.6 / 11.4 [kN/m]	14.9 / 15.5 [kN/m]	18.6 / 19.3 [kN/m]
SuperHolorib 51	10.6 / 11.4 [kN/m]	14.9 / 15.5 [kN/m]	18.6 / 19.3 [kN/m]

The calculation of the shear capacity of the non-cracked compression zone significantly depends on the height of the compression zone. The usual assumption of a rigid joint between reinforcement and concrete leads to an overestimation of the height of the compression zone. It is a mistake to calculate the longitudinal reinforcement rate by considering the total cross section of the metal sheet. In partially bonded slabs the resultant longitudinal reinforcement ratios are generally less than 1 % (see Figure. 1).

The empirical approach used in the rules of DIN EN 1992-1-1 (2011), depend on the concrete compressive strength and the degree of longitudinal reinforcement $((100 \cdot \rho_{sL} \cdot f_{ck})^{1/3})$. This is not sufficient for a reliable estimation of the height of the pressure zone. It is even better to calculate the compression zone height x_m by using the partial bond theory for composite slabs.

The height of the compression zone (see eq. (4) and eq. (5)) results by determination the horizontal equilibrium between the anchored tensile force $\eta \cdot A_{pm} \cdot f_{ypm}$ and the resulting concrete compressive force. The rate of partial bond η has to be calculated in accordance with the partial bond theory of DIN EN 1994-1-1 (2010).

$$(4) \quad \text{NWAC} \quad \left| \quad (5) \quad \text{LWAC} \right.$$

$$x_m = \frac{\eta \cdot A_{pm} \cdot f_{ypm}}{b_c \cdot f_{lcm}} \quad \left| \quad x_m = \frac{2 \cdot \eta \cdot A_{pm} \cdot f_{ypm}}{b_c \cdot f_{lcm}}$$

Thereby the height of the compression zone takes a minimum value and is calculated in the section of the maximum bending moment. Due to the investigation on the specific post-cracking behaviour of lightweight aggregate concrete of Faust (2002), it is necessary to assume a triangular stress distribution in the compression zone of LWAC.

By using the derivation of Zink (2000) the shear capacity of the non-cracked compression zone can be calculated according to eq. (6) and eq. (7)

$$(6) \quad \text{NWAC} \quad \left| \quad (7) \quad \text{LWAC} \right.$$

$$V_{c,cz} = \int_0^{x_m} \int_0^{b_w} \tau_{xz}(z) \cdot d_y \cdot d_z = \frac{2}{3} \cdot x_m \cdot b_w \cdot f_{ctm} \quad \left| \quad V_{lc,cz} = \int_0^{x_m} \int_0^{b_w} \tau_{xz}(z) \cdot d_y \cdot d_z = \frac{2}{3} \cdot x_m \cdot b_w \cdot f_{lctm}$$

For description of the shear force bearing capacity of the aggregate interlock $V_{c,ct}$ as a part of the shear model an energetic approach was chosen (eq. (8) and (9)). This approach is based on investigations by Hillerborg, Mod er, Petersson, (1976) and Walraven and Reinhardt (1981) on the fracture process zone at the tip of the crack (see Figure 6).

$$(8) \quad \text{NWAC} \quad \left| \quad (9) \quad \text{LWAC} \right.$$

$$V_{c,ct} = 0.12 \cdot l_{ch} \cdot b_w \cdot f_{ctm} = 0.12 \cdot \frac{G_f \cdot E_{cm}}{f_{ctm}^2} \cdot b_w \cdot f_{ctm} \quad \left| \quad V_{c,ct} = 0.09 \cdot l_{ch} \cdot b_w \cdot f_{lctm} = 0.09 \cdot \frac{G_f \cdot E_{cm}}{f_{lctm}^2} \cdot b_w \cdot f_{lctm}$$

The size of the fracture process zone only depends to the properties of concrete. Due to the fact that the model is limited to the calculation of the tensile forces transmitted within the crack tip, there is no need to describe the crack path of the inclined bending crack. The capable size of the fracture process zone is well documented for different types of concrete in literature (see Hillerborg (1983), Rimmel (1994) and Grimm (1997)).

The aggregate interlock is reduced by the low strength of the aggregates of lightweight concrete. The difference in the roughness of the crack surfaces to NWAC is illustrated in a detailed view on a separated bending shear crack in Figure 7.

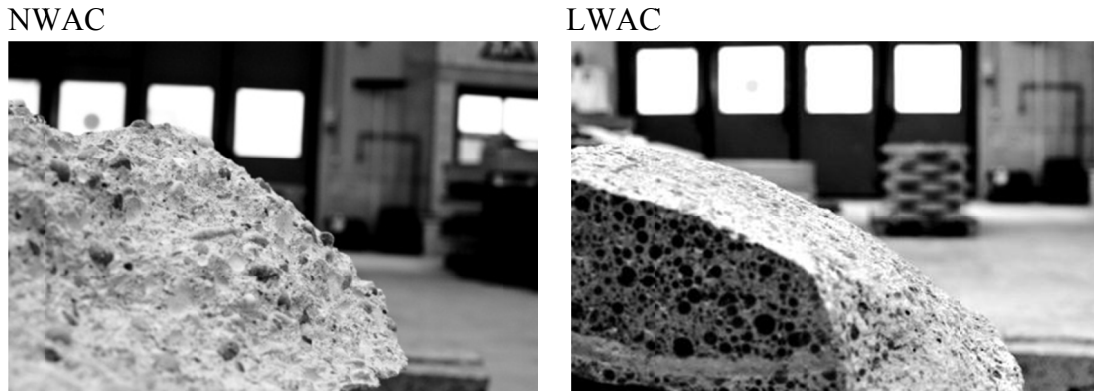


Figure 7. Local roughness of a bending shear crack surface of normal concrete (left) and lightweight concrete (right) at a specimen after testing.

Therefor the embedded pre-factors of 0.12 for NWAC and 0.09 for LWAC are necessary to determine the size of the fracture zone as a percentage share of the fictive length of crack and also to define the volume of the capable stress-crack width-curve within the fracture zone.

With the studies on the local roughness of crack surfaces by Hordijk (1990) and Duda (1991), the length of the fracture process zone can be assumed for NWAC to $0.4 \cdot l_{ch}$ and is sufficiently described for LWAC with $0.3 \cdot l_{ch}$. When calculating the characteristic length l_{ch} of the crack, the energy required for cracking is taken into account. The fracture energy of the concrete G_f [N/m] can be calculated according Hordijk (1990) and Faust (2002) using the empirical equations (10) to (12). Depending on the type of aggregate, the fracture energy is an empirical function of the concrete tensile strength f_{ctm} / f_{lctm} in a unit [MPa].

$$\begin{array}{l} \text{NWAC} \\ G_f = 24 + 26 \cdot f_{ctm} \end{array} \quad (10) \quad \left| \quad \begin{array}{l} \text{SLWAC} \\ G_f = 24 + 16 \cdot f_{lctm} \end{array} \quad (11) \quad \left| \quad \begin{array}{l} \text{ALWAC} \\ G_f = 16 \cdot f_{lctm} \end{array} \quad (12)$$

Differences in the transmission of stress within the crack tip can be detected in good agreement by using an empirical approach, developed by Reinhardt, Cornelissen and Hordijk (1986) (see Figure 8).

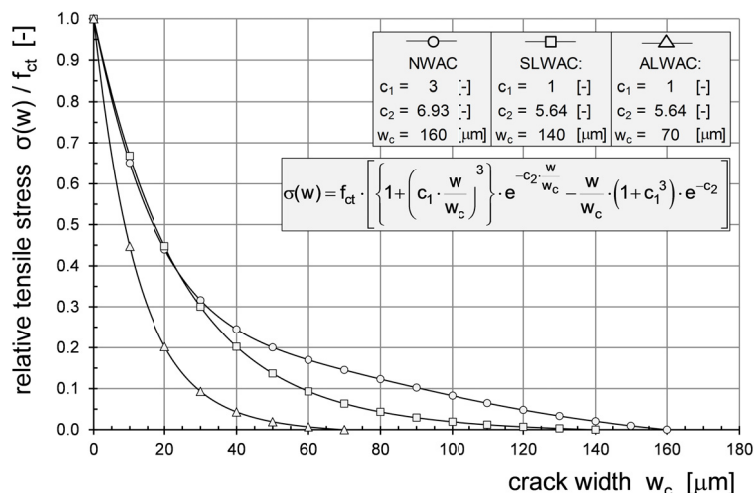


Figure 8. Relative softening behaviour of NWC, SLWAC and ALWAC in accordance to [Reinhardt, Cornelissen and Hordijk 1986].

A block coefficient of 0.3 is sufficiently accurate for the description of the behaviour of normal and lightweight concrete.

In sum, the pre-factor for normal concrete takes a value of 0.12 as the product of the value for the size of the fracture zone and the block coefficient considering the stress-crack-behaviour. Due to the low aggregate interlock, the pre-factor for lightweight concrete is reduced to 0.09.

An important fact is, that the type of aggregate and the used concrete additives such as fly ash or silica fume can have either positive or negative influence on the development of the presented pre-factor. These correlations were illustrated in a number of studies in Faust (2002). In the context of this project a database was established. In that database some distinctly different concrete mixtures were included. This allows a conservative estimation of the pre-factor. Additionally the expected statistical spread of the pre-factor was considered within the statistical analysis of the model.

An opening of the fracture process zone occurred perpendicular to the crack path. A complete activation of the fracture process zone capacity can be assumed by the observable crack path in experiments, which extends always approximately horizontally below the compression zone. Thereby the crack proceeds until the crack propagation reaches the section of maximum moment. Simultaneously the stress at the base of the uncracked compression zone takes its maximum value, which is equal to the concrete tensile strength. The load reserves of the cross section are exhausted and the total shear resistance of the composite slab is reached (see Figure 6).

So the shear resistance of composite slabs with normal weight or lightweight aggregate concrete and metal sheets with an undercut profile and additionally arranged embossments can be determined by equations (13) and (14). Because of the comb-shaped cross section, the compression strut cannot be supported above the raised beads. Therefore the proposal of DIN EN 1992-1-1 (2011) was adopted in the developed model. In the calculation of the bearing parts of the aggregate interlock and the uncracked compression zone, the effective cross-sectional width b_w is used for consideration the necking by the raised beads.

$$\begin{array}{l}
 (13) \qquad \qquad \qquad \text{NWAC} \qquad \qquad \qquad (14) \qquad \qquad \qquad \text{LWAC} \\
 V_{Rm} = \left(V_{p,Rm} + \frac{2}{3} \cdot x_m \cdot b_w \cdot f_{ctm} + 0.12 \cdot l_{ch} \cdot b_w \cdot f_{ctm} \right) \quad V_{Rm} = \left(V_{p,Rm} + \frac{2}{3} \cdot x_m \cdot b_w \cdot f_{lctm} + 0.09 \cdot l_{ch} \cdot b_w \cdot f_{lctm} \right) \\
 = \left(V_{p,Rm} + \left(\frac{2}{3} \cdot x_m + 0.12 \cdot \frac{G_f \cdot E_{cm}}{f_{ctm}^2} \right) \cdot b_w \cdot f_{ctm} \right) \quad = \left(V_{p,Rm} + \left(\frac{2}{3} \cdot x_m + 0.09 \cdot \frac{G_f \cdot E_{lcm}}{f_{lctm}^2} \right) \cdot b_w \cdot f_{lctm} \right)
 \end{array}$$

A comparison of the test loads to the average resistance values according to eq. (13) and eq. (14) is shown in Figure 9. The experimental data used for the comparison includes tests of composite slabs of NWAC or LWAC and metal sheets of the type SuperHolorib as well as Cofrastra 40 with shear failure in a total of 48 specimens. The developed approach for description of shear failure of composite slabs shows a good conformity to the test results.

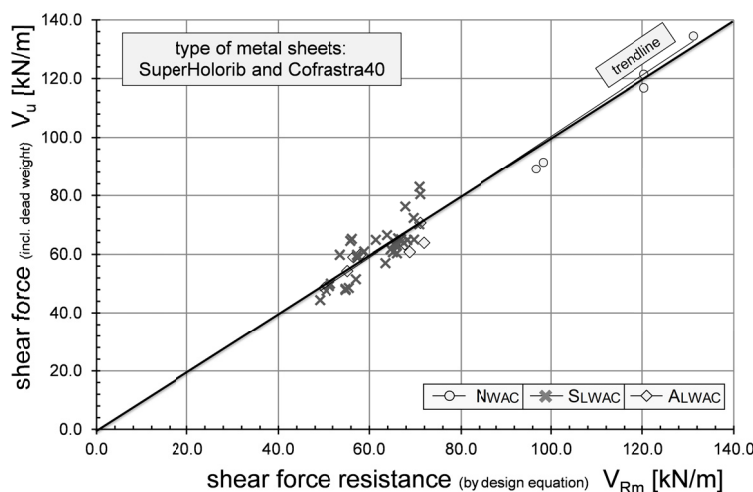


Figure 9. Comparison between mean experimental results V_u and the shear resistance $V_{R,m}$ calculated using eq. (13) and eq. (14).

EMPIRICAL DETERMINATION OF SAFETY FACTOR

The statistical determination of the resistance model was made according to appendix D of DIN EN 1990 (2010). Using the standardized method, the developed resistance model is tested for correlation with all available experimental results. If necessary it has to be empirically improved, so that a safe agreement can be reached between theoretical and experimental values.

The developed model is based on basic variables with statistic spread. These distributions have to be included in a statistical evaluation. That was done by using the progressive method provided by DIN EN 1990 (2010). The scatter of individual parameters was taken from various literatures. Finally it is necessary to transfer the mean values of material strengths to characteristic values. The design equation for shear resistance of composite slabs made of NWAC or LWAC and metal sheets with a combination of a frictional and a mechanical interlock is given by eq. (15) and eq. (16).

(15)

NWAC

$$V_{Rd} = \frac{1}{\gamma_v} \left(\bar{V}_{p,Rk} + \frac{2}{3} \cdot x_k \cdot b_w \cdot f_{ctk} + 0.12 \cdot l_{ch,k} \cdot b_w \cdot f_{ctk} \right)$$

$$= \frac{1}{1.35} \cdot \left[\bar{V}_{p,Rk} + \left(\frac{2}{3} \cdot \frac{\eta \cdot A_p \cdot f_{ypk}}{b_c \cdot f_{ck}} + 0.12 \cdot l_{ch,k} \right) \cdot b_w \cdot f_{ctk} \right]$$

(16)

LWAC

$$V_{Rd} = \frac{1}{\gamma_v} \left(\bar{V}_{p,Rk} + \frac{2}{3} \cdot x_k \cdot b_w \cdot f_{lctk} + 0.09 \cdot l_{ch,k} \cdot b_w \cdot f_{lctk} \right)$$

$$= \frac{1}{1.35} \cdot \left[\bar{V}_{p,Rk} + \left(\frac{4}{3} \cdot \frac{\eta \cdot A_p \cdot f_{ypk}}{b_c \cdot f_{lck}} + 0.09 \cdot l_{ch,k} \right) \cdot b_w \cdot f_{lctk} \right]$$

CONCLUSION / FUTURE PROSPECTS

The presented analytical model is only valid for re-entrant composite sheets in combination with embossments. Examples are the metal sheets of the type SuperHolorib or Cofrastra 40 (see Figure 10).

cross-sectional form	approval number / reference
	SuperHolorib 51@ - undercut Z-26.1-45 / [SuperHolorib 2007]
	Cofrastra 40@ - undercut Z-26.1-22 / [Cofrastra 2007]

Figure 10. Examples of the cross-sectional forms the approach have validity.

Because of the amount of tests performed and the small variations within the failure mode for metal sheets with a combination of mechanical and frictional interlock there are sufficiently reliable results available. The experimental results with normal weight aggregate concrete were added to the basic population for empirical verification. Due to the good conformity to the test results, the presented design approach is sufficiently accurate to be also valid for composite slabs with NWAC. As a result of the statistical analysis by DIN EN 1990 (2010) for the design model a safety factor of $\gamma_v = 1.35$ is necessary.

Compared to metal sheets with an undercut a weaker composite action can be detected for trapezoidal sheets. The open formed metal sheets are usually manufactured with a bigger height of the webs. This results in a higher rigidity of this type of metal sheet and therefore in a higher shear capacity $V_{p,Rm}$. While this allows large spans, the soft composite action leads in combination with lightweight concrete to various cracks with significant crack widths. By exceeding the shear bearing capacity of the metal sheet the crack widths reaches already a critical value, so that

the aggregate interlock cannot be taken into account anymore. The same behaviour could be observed using smooth Holorib-profiles in which the frictional interlock in combination with LWAC is insufficient to activate an effective composite action. However, the fundamental value $V_{0,Rm}$ of the presented shear force equation V_{Rm} describes the shear capacity of the metal sheet itself and the uncracked compression zone and represents thereby a lower limit value of the resistance.

This was confirmed by the good conformity between the calculated fundamental capacities and the experimental average results of tests (see Figure 11). In the comparison a low standard deviation could be documented. Due to the small amount of specimen a statistical evaluation is not reliable.

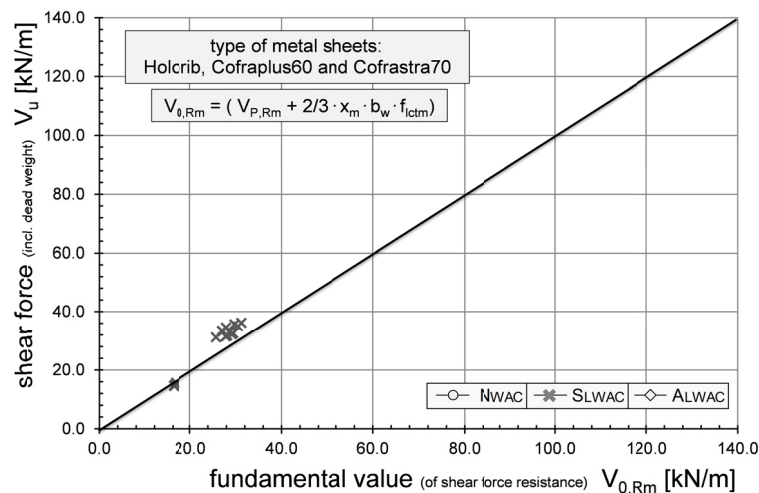


Figure 11. The fundamental value $V_{0,Rm}$ of the presented shear force design equation V_{Rm} compared to test results of trapezoidal metal sheets under shear load.

For further investigation with composite slabs with LWAC and trapezoidal profiles studies on the impact and influence by an additional reinforcement will be of high interest. This should reduce the occurring crack widths. Maybe therefore the aggregate interlock could be activated, which would increase the shear resistance in combination with trapezoidal metal sheets.

Furthermore, it would be desirable to consider the composite joint stiffness in a mechanical manner. This would maybe allow the description of the changeover between the vertical shear failure and the longitudinal shear failure. But this requires meaningful studies on the composite behaviour of metal sheets. The assumption of constant smeared shear stresses within the shear length is not adequate enough.

REFERENCES

- Cofrastra (2007). "Allgemeine bauaufsichtliche Zulassung. Zulassungsbescheid Z-26.1-22: Cofrastra-Verbunddecke, Fa. ArcelorMittal Construction Deutschland GmbH. DIBt, Berlin, 2007.
- DIN EN 1990 (2010). "Eurocode: Basis of structural design. German version, Beuth-Verlag, Berlin, Germany, 2011.

- DIN EN 1992-1-1 (2011). "Design of concrete structures - Part 1-1: General rules and rules for buildings. German version, Beuth-Verlag, Berlin, Germany, 2011.
- DIN EN 1993-1-3 (2010). "Design of steel structures - Part 1-3: General rules - Supplementary rules for cold-formed members and sheeting. Beuth-Verlag, Germany.
- DIN EN 1994-1-1 (2010). "Design of composite steel and concrete structures - Part 1-1: General rules and rules for buildings. German version, Beuth-Verlag, Berlin, Germany, 2010.
- Duda (1991). "Bruchmechanisches Verhalten von Beton unter monotone und zyklischer Zugbeanspruchung. Heft 419 des DAfStb, Berlin, 1991.
- Grimm (1997). „Einfluß bruchmechanischer Kenngrößen auf das Biege- und Schubtragverhalten hochfester Betone. Heft 447 des DAfStb, Berlin, 1997.
- Hillerborg, Modéer, Petersson, (1976). „Analysis of crack formation and crack growth in concrete by means of fracture mechanics and finite elements. In: Cement and Concrete Research 6, pp. 773-782.
- Hillerborg (1983). "Analysis of One Single Crack. In: F.H.Wittmann (Hrsg.): Fracture Mechanics of Concrete, Amsterdam, 1983, pp. 223-249.
- Hordijk (1990). "Deformation Controlled Uniaxial Tensile Tests on Concrete. Stevin-report 25.5.90-7 / VFA, TU Delft, 1990.
- Kurz and Hartmeyer (2011). "Lightweight composite slabs – Research on the shear force behaviour. EUROSTEEL 2011, pp. 2379-2384, Hungary.
- Remmel (1994). "Zum Zug- und Schubtragverhalten von Bauteilen aus hochfestem Beton. Heft 444 des DAfStb, Berlin, 1994.
- Reinhardt, Cornelissen and Hordijk (1986). "Tensile Tests and Failure Analysis of Concrete. In: Journal of Structural Engineering. Vol. 112, No. 11, 1986, pp. 2462-2477.
- Reineck (2006). "Datenbanken für Querkraftversuche als Grundlage der Querkraftbemessung nach DIN 1045-1. 46. DAfStb-Forschungskolloquium, Universität Stuttgart, 2006, S. 253-265.
- SuperHolorib (2007). „Allgemeine bauaufsichtliche Zulassung. Zulassungsbescheid Z 26.1-45: Super-Holorib SHR51-Verbunddecke. Fa. Holorib (Germany) GmbH. DIBt, Berlin, 2007.
- SuperHolorib (1994). „Gutachten Nr. 1.12.1994 - Über die Tragfähigkeit der Stahlblechprofile SuperHolorib 51. Versuchsanstalt für Stahl, Holz, und Steine, Universität (TH) Karlsruhe, 1994.
- Walraven and Reinhardt (1981). "Concrete Mechanics – Theory and Experiments on the Mechanical Behaviour of Cracks in Plain and Reinforced Concrete Subjected to Shear Loading. In: Heron, Vol. 26, Nr. 1, Delft, 1981.
- Zink (2000). "Zum Biegeschubversagen schlanker Bauteile aus Hochleistungsbeton mit und ohne Vorspannung. Universität Leipzig, Fachbereich Bauingenieurwesen, Lehrstuhl für Massivbau und Baustofftechnologie, Dissertation, 2000.

Performance of Composite Slabs with Profiled Sheeting Using High-Strength Steel

Stephen Hicks¹; Audsley Jones²; and Andrew Pennington³

¹General Manager Structural Systems, Heavy Engineering Research Association, P.O. Box 76-134, Manukau, Auckland 2241, New Zealand. E-mail: stephen.hicks@hera.org.nz

²Ph.D. Student (formerly Structural Engineer, Structural Systems, HERA), Civil and Natural Resources Engineering, Univ. of Canterbury, Private Bag 4800, Christchurch 8140, New Zealand. E-mail: audsley.jones@pg.canterbury.ac.nz

³Structural Engineer, Structural Systems, Heavy Engineering Research Association, P.O. Box 76-134, Manukau, Auckland 2241, New Zealand. E-mail: apennington@hera.org.nz

Abstract

Composite slabs using cold-formed profiled steel sheeting have proved popular in multi-storey steel-framed buildings. This paper presents a comprehensive test programme that considers the performance of a modern trapezoidal profiled sheeting using Australasian 550 N/mm² high strength steel, compared to that exhibited by the same profile using European 350 N/mm² steel. Although the ductility of the Australasian steel is low, from composite slab tests it was found that the longitudinal shear behaviour could be considered ductile according to the Eurocode 4 requirements. As a consequence of this, the partial connection method was permitted. However, from the test results presented in this paper, it is shown that the rules given in Eurocode 4, Annex B.3.1 for a reduced investigation lead to unconservative results and should be revised. To remedy this situation, an amendment is proposed.

INTRODUCTION

The rules for testing composite slabs in EN 1994-1-1 (Eurocode 4) (CEN, 2004b) are widely used internationally. Since 2007, the New Zealand steel structures standard NZS 3404.1(SNZ, 1997) has referred to Eurocode 4, and it is expected that the forthcoming joint Australian/New Zealand composite standard AS/NZS 2327 (SA/SNZ, 201X) will implement the European provisions directly. Eurocode 4 provides two options for evaluating the longitudinal shear resistance of composite slabs: a complete investigation of all the relevant variables according to Clause B.3.1(3) (i.e. the thickness and type of steel sheeting, the steel grade, the coating of the steel sheet, the density and grade of the concrete, the slab thickness and the shear span length L_s); or, according to Clause B.3.1(4), a reduced investigation where the results from a smaller test series may be extended to other cases. For a reduced investigation, the results may be applied to the values of the following variables:

- a) For thickness of the steel sheeting t larger than tested.
- b) For concrete with a specified characteristic compressive strength f_{ck} not less than $0.8 f_{cm}$, where f_{cm} is the mean value of the concrete strength in the tests.

- c) For steel sheeting having a yield strength f_{yp} not less than $0.8 f_{ypm}$, where f_{ypm} is the mean value of the yield strength in the tests.

Owing to the fact that interlock is dependent on the local bending of individual plate elements in the sheeting, the limitation in (a) ensures that results are not applied to thinner or weaker sheets, which would be more flexible. As a consequence of this, the manufacturer is encouraged to test the thinnest sheet for a particular profile.

The reason for the limitations given in (b) and (c) is to ensure that the manufacturer does not test a composite slab that has a concrete strength or yield strength of the steel sheeting lower than the 5% characteristic value. According to Eurocode 4, B.3.3(9), the mean concrete strength f_{cm} for each group of slabs that will be tested within 48 hours should be evaluated from a minimum of four concrete cylinder or cube specimens. Whereas, for the steel sheeting, EN 1993-1-3, 3.2.1(2) requires that a minimum of five test coupons should be taken to determine the mean yield strength of the steel f_{ypm} .

It can be deduced from EN 1990, D.8.4 by the use of additional prior knowledge that the limitations given in (b) and (c) imply a maximum coefficient of variation $V_r = 12\%$; according to EN 1992-1-1 (CEN, 2004a), this value is equivalent to a strength class of C35/45 (see Eq. (6)). For the limitation given in (c), the value of V_r is much higher than that normally assumed for the yield strength of steel, where $V_{fy} = 7\%$ is taken for products supplied to EN 10025-1 (JCSS, 2001; CEN, 2004c).

For a manufacturer that produces a profiled sheet in several grades of steel, the rule given by (c) would suggest that tests in a reduced investigation should be undertaken on the lowest grade of steel, which implies that the lowest longitudinal shear resistance in a composite slab will be achieved for this case. However, this was contrary to the first author's view where, keeping other variables equal, it was thought that although the plastic resistance moment of the sheeting would marginally increase, a higher steel grade would reduce the degree of shear connection, thereby suggesting that the longitudinal shear resistance of the composite slab would be lower (see Figure 1).

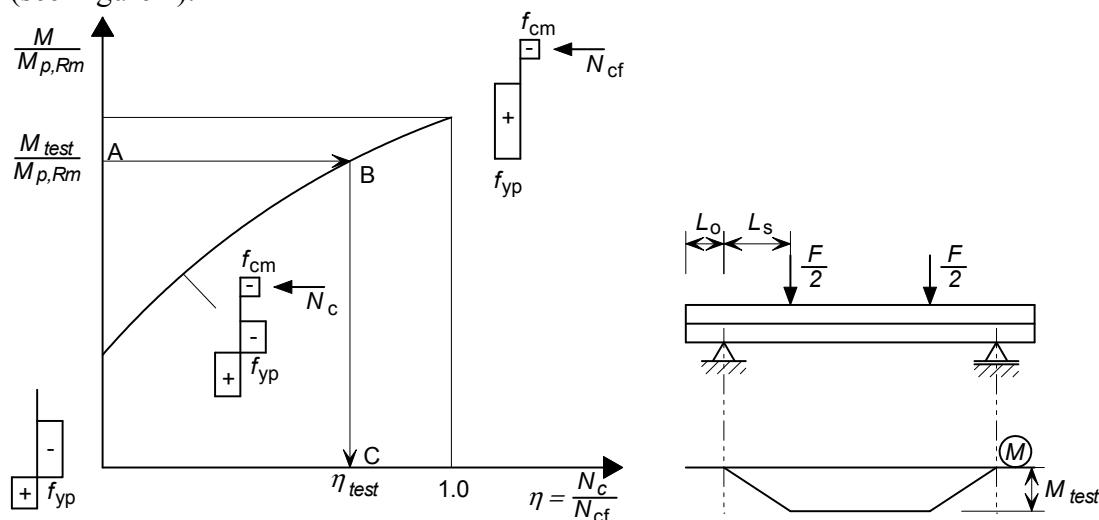


Figure 1 Determination of the degree of shear connection from M_{test} according to Eurocode 4

Composite slab tests were overseen by the first author on a 60 mm deep trapezoidal profile using 0.75 mm thick AS 1397-G550 steel (see Table 1) (SA, 2011). It was subsequently decided by the manufacturer to produce the same profile using a lower grade 0.75 mm thick EN 10134-G350GD steel (see Table 1) (CEN, 2004d). Although an interpretation was requested from the Eurocode 4 Committee (CEN/TC250/SC4), the view of the UK National Mirror Committee (B/525/4) was that (c) requires that tests should be undertaken on the lowest grade of steel in a reduced investigation. Due to this outcome, the composite slab tests were repeated with all variables remaining identical with the exception that the yield strength of the steel was reduced to $f_{yp} = 350 \text{ N/mm}^2$; this enabled the requirement given in (c) to be investigated directly. The remainder of this paper describes this test work and its implications on the design provisions given in Eurocode 4.

Table 1 Nominal material and geometric properties for the steel used in the composite slab tests

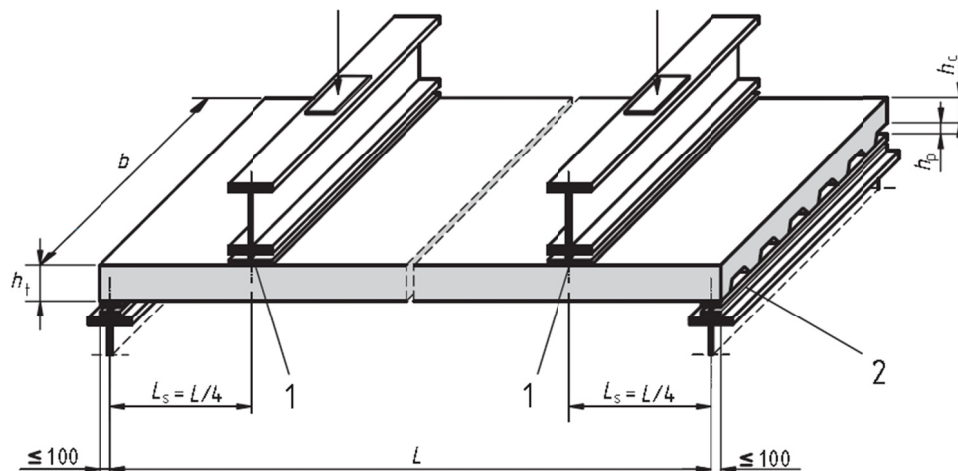
Steel grade designation	Nominal yield strength ^a f_{yp} (N/mm ²)	Tensile strength f_{up} (N/mm ²)	Minimum elongation $A_{80 \text{ mm}}$ ^b (%)	Nominal coated thickness t_{nom} (mm)	Nominal core thickness t_{cor} (mm)	Thickness tolerance for a specified width of $\leq 1200 \text{ mm}^c$ (mm)
AS 1397-G550+Z275	550	550	2	-	0.70	± 0.04
EN 10326-S350GD+Z275	350	420	16	0.75	- ^d	$\pm 0.045^e$

Notes:

- a EN 10326 - if the yield point is pronounced, the values apply to the upper yield point R_{eH}
- AS 1397 - if the yield point is pronounced, the values apply to the lower yield point R_{eL}
- b EN 10326 - for product thicknesses $\leq 0.70 \text{ mm}$ (including coating) the minimum elongation values shall be reduced by 2 units
- AS 1397 - minimum elongation values apply for product thicknesses $\geq 0.60 \text{ mm}$ (bare metal thickness)
- c EN 10143 - the thickness tolerances correspond to the nominal, or 'specified', thickness, which is the whole order thickness of the metallurgically coated product (nominal thickness includes both the substrate and coating).
- AS/NZS 1365 - for coated products, thickness tolerances apply to the base metal only.
- d EN 1993-1-3 - from Clause 3.2.4(3), for Z275 zinc coating $t_{zinc} = 0.04 \text{ mm}$. Therefore, $t_{cor} \approx 0.70 \text{ mm}$
- e EN 10143 - for Special (S) tolerances

COMPOSITE SLAB TESTS

The composite slab specimens conformed to the standard test requirements given in Eurocode 4, B.3 in that, for each test series (defined by the sheeting depth and the steel grade), three nominally identical tests were undertaken on long specimens. To classify the longitudinal shear behaviour, as well as provide data for the $m-k$ method, tests on three nominally identical short specimens were also undertaken. The set-up for the tests is shown in Figure 2 and the corresponding values of the variables considered in each test series are presented in Table 2.

**Key**

- 1 neoprene pad or equivalent $\leq 100 \text{ mm} \times b$
- 2 support bearing plate $\leq 100 \text{ mm} \times b \times 10 \text{ mm}$ (min) (typical for all bearing plates)

Figure 2 Test set-up according to Eurocode 4**Table 2. Nominal material properties and geometric properties used in composite slab tests with the long shear span**

Variable given in Figure 2	Yield strength of sheeting f_{yp} (N/mm ²)	
	350	550
f_{ck} (N/mm ²)	20	
h_t (mm)	130	
b (mm)	600	
L (mm)	3600	
L_s (mm)	900	
L_o (mm)	100	

As can be seen from Table 1, the AS 1397-G550 material does not satisfy the EN 1993-1-1, 3.2.2 (CEN, 2005) ductility requirements where it is recommended that $f_{up}/f_{yp} \geq 1.10$ together with an elongation at failure not less than 15%. As a consequence of this, the non-composite properties of the sheeting was evaluated from design assisted by testing according to EN 1990, Annex D (CEN, 2002) and EN 1993-1-3, Annex A (CEN, 2006a). Nevertheless, although the elongation of the sheeting material with $f_{yp} = 550 \text{ N/mm}^2$ was low, in all cases the failure load in the composite slab tests exceeded the load causing a recorded end slip of 0.1 mm by more than 10%, which meant that the longitudinal shear behaviour was deemed to be

ductile according to Eurocode 4, 9.7.3(3). As a consequence of this, the partial connection method could be used.

The relationship between the mean plastic moment resistance of the composite slabs in the tests and the degree of shear connection is shown in Figure 3. As can be seen from Figure 3, apart from a slight increase in the moment resistance of the profiled sheeting itself, the results clearly show that the degree of shear connection is lower for composite slabs with $f_{yp} = 550 \text{ N/mm}^2$. This indicates that the longitudinal shear strength of the composite slab is lower for sheeting that uses higher grades of steel, which conflicts with the rules given in Eurocode 4, Clause B.3.1(4).

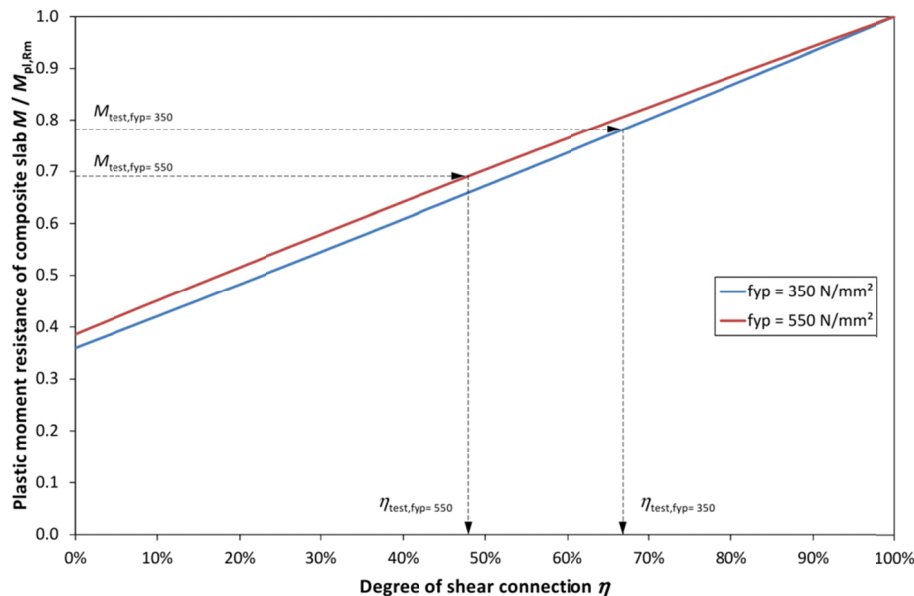


Figure 3 Plastic moment resistance versus degree of shear connection from tests on composite slabs using a 60 mm deep profile

DETERMINATION OF THE CHARACTERISTIC VALUE OF THE LONGITUDINAL SHEAR STRENGTH

The plastic stress distribution for a composite slab in sagging bending is shown in Figure 4. The corresponding equations used to evaluate the design value of the bending resistance moment are given as:

$$M_{Rd} = N_c z + M_{pr} \quad (1)$$

where N_c is the compressive normal force in the slab, given by $N_c = \tau_{u,rd} b L_x \leq N_{c,f}$, $\tau_{u,rd}$ is the design longitudinal shear strength obtained from composite slab tests ($= \tau_{u,rk} / \gamma_{Vs}$), b is the width of the slab, L_x is the distance of the cross-section being considered to the nearest support, $N_{c,f}$ is the design value of the compressive normal force in the slab with full shear connection, z is the lever arm, given by:

$$z = h - 0.5x_{pl} - e_p + (e_p - e) \frac{N_c}{N_{pa}} \quad (2)$$

where h is the overall depth of the slab, x_{pl} is the depth of the plastic neutral axis, e_p is the plastic neutral axis of the profiled steel sheeting, e is the centroidal axis of the profiled steel sheeting, N_{pa} is the design plastic resistance of the profiled sheeting to normal force, given by $N_{pa} = A_{pe} f_{yp,d}$, A_{pe} is the effective cross-section area of the profiled steel sheeting, $f_{yp,d}$ is the design value of the yield strength of the steel sheeting and M_{pr} is the reduced plastic moment resistance of the effective cross-section of the profiled sheeting, given by:

$$M_{pr} = 1.25M_{pa} \left(1 - \frac{N_c}{N_{pa}} \right) \leq M_{pa} \quad (3)$$

where M_{pa} is the design value of plastic moment resistance of the effective cross-section of the profiled sheeting.

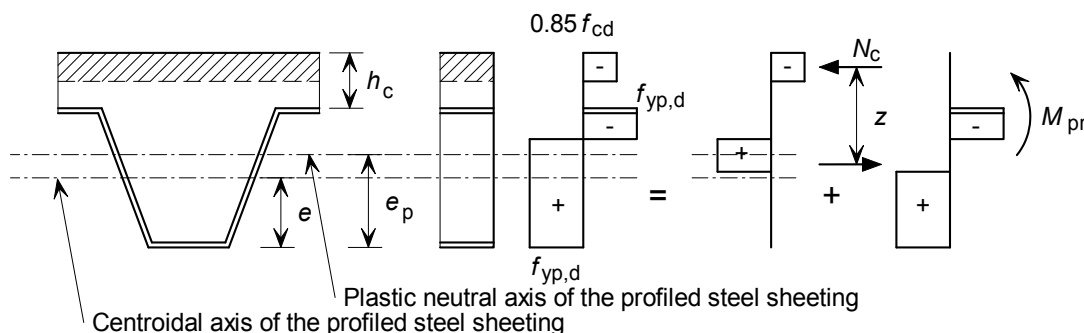


Figure 4 Plastic stress distribution for sagging bending with partial shear connection ($0 \leq \eta < 1.0$)

In accordance with Eurocode 4, B.3.6(4) the characteristic longitudinal shear strength $\tau_{u,Rk}$ was calculated from the test values as the 5% fractile from EN 1990, Annex D. For the statistical analysis according to EN 1990, theoretical values are needed that describe the longitudinal shear strength correctly at the mean. In the analyses presented below, the design model $g_{rt}(\underline{X}_m)$ is given by in Eq. (1), (2) and (3) with the basic variables replaced by the mean measured values \underline{X}_m .

MATERIAL AND GEOMETRIC PROPERTIES

The appropriate coefficients of variation for each basic variable are required in the reliability analysis. The coefficient of variation V_X is calculated from the following equation:

$$V_X = \frac{\sigma_X}{m_x} \quad (4)$$

where σ_x is the standard deviation and m_x is the mean value

The standard deviation for the basic variables was taken from the appropriate design and product Standards (based on the lower 5% fractile value, which corresponds to 1.64 standard deviations when an infinite range of data is considered). For example, the mean compressive cylinder strength is given in EN 1992-1-1 as:

$$f_{ck} = f_{cm} - 8 = f_{cm} - 1.64\sigma_{fc} \quad (5)$$

Re-arranging Eq. (5) the coefficient of variation of the cylinder strength was taken as:

$$V_{fc} = \frac{8}{1.64f_{cm}} \quad (6)$$

The coefficients of variation for other basic variables within the design model are summarised in Table 2 together with their source.

Table 2 Coefficient of variation of the basic variables

Variable	AS 1397-G550 Material	EN 10326-S350GD Material with Special Tolerances (S)
f_y	$= \frac{19}{\sqrt{f_{y,m}}}$ (BlueScope Steel, 2008)	7% (JCSS, 2001)
t	$= \frac{0.08}{\sqrt{12}t_{cor,m}}$ (SA/SNZ, 1996)	$\frac{0.09}{\sqrt{12}t_{cor,m}}$ (CEN, 2006b)
f_{ck}	$= \frac{8}{1.64f_{cm}}$	
h_t	$= \frac{20}{\sqrt{12}h_m} = 4.44\%$ (CEN, 2009)	
b	$= \frac{32.8}{\sqrt{12}b_m} = 1.58\%$ (CEN, 2009)	
L_s	$= \frac{40}{\sqrt{12}L_{sm}} = 1.15\%$ (CEN, 2008)	

EVALUATION OF CHARACTERISTIC VALUE OF LONGITUDINAL SHEAR STRENGTH OF THE COMPOSITE SLABS

It is assumed that the basic variables are statistically independent and have a log-normal distribution (which is desirable as: the resistance function falls to zero at the origin so there are no negative resistances; and it gives a perfect representation of functions that are multiples or divisions of variables). Due to the fact that many of the variables given in Eq. (1), (2) and (3) are correlated (i.e. t is correlated with M_{pa} , e_p , e and A_{pe}), it was considered more efficient to numerically evaluate the coefficient of variation of the theoretical resistance function V_{rt} by generating random values for the basic variables (i.e. a Monte Carlo simulation). Through also considering the coefficient of variation V_{δ} of the error terms δ , the characteristic value was evaluated from the following equation given in EN 1990, Annex D:

$$r_k = b g_{rt}(\underline{X}_m) \exp(-k_{\infty} \alpha_{rt} Q_{rt} - k_n \alpha_{\delta} Q_{\delta} - 0,5 Q^2) \quad (7)$$

where α_{rt} and is the weighting factor for Q_{rt} , Q_{rt} is a coefficient for variation of the variables in the resistance function, α_{δ} is the weighting factor for Q_{δ} , Q_{δ} is a coefficient for variation of the error term δ , Q is a coefficient for variation of the resistance, k_n is the characteristic fractile factor for a number of tests n (with a p fractile = 0.05) and $k_{\infty} = 1.64$ (which is the value of k_n for $n = \infty$).

The results from the reliability analyses are presented in Table 3. To facilitate comparisons, the characteristic longitudinal shear strength is presented non-dimensionally by the correction factor b , given by:

$$b = \frac{\tau_{u,Rk}}{\tau_{u,f_{yp}=350,Rk}} \quad (8)$$

where $\tau_{u,Rk}$ is the characteristic longitudinal shear strength and $\tau_{u,f_{yp}=350,Rk}$ is the characteristic longitudinal shear strength with $f_{yp} = 350 \text{ N/mm}^2$.

Table 3 Comparison of degree of shear connection with steel grade and profiled steel sheeting depth

Yield strength of sheeting f_{yp} (N/mm ²)	Corrected longitudinal shear strength b
350	1.0
550	0.79

As can be seen from Table 3, for the sheet with $f_{yp} = 350 \text{ N/mm}^2$, the shear strength is 26% greater than that achieved with the same sheet with $f_{yp} = 550 \text{ N/mm}^2$. From this comparison, it is clear that the Eurocode 4 rule given by Clause B.3.1(4) for yield strength in a reduced investigation is incorrect. Whilst it could be argued that the test programme reported here is limited in its scope, the present authors are unaware of any other investigation undertaken on composite slabs where the yield

strength was the only parameter to have been varied. As a consequence of this, it is recommended that an amendment to Eurocode 4 is made as follows:

To reduce the number of tests as required for a complete investigation, the results obtained from a test series may be also used for other values of variables as follows:

- a) For thickness of the steel sheeting t larger than tested.*
- b) For concrete with specified characteristic compressive strength f_{ck} not less than $0.8 f_{cm}$, where f_{cm} is the mean value of the concrete strength in the tests.*
- c) For steel sheeting having a yield strength f_{yp} not larger than tested. The yield strength f_{yp} should not be less than $0.8 f_{ypm}$, where f_{ypm} is the mean value of the yield strength in the tests.*

CONCLUSIONS

This paper presents the results from a comprehensive test programme on composite slabs that used a typical modern trapezoidal profiled steel sheet. The tests were unique in that the only parameter that was varied in the test series was the yield strength of the sheeting. In all cases the composite slabs achieved the minimum end slip requirements given by Eurocode 4, which permitted the behaviour to be considered ductile. As a consequence of this, the partial connection method was used. From a structural reliability analysis of the test results according to EN 1990, Annex D it was found that the 5% characteristic value of the longitudinal shear strength was lower in the sheet that possessed the largest yield strength. From this finding an amendment to Eurocode 4 is proposed for composite slab tests in a reduced investigation.

REFERENCES

- BlueScope Steel (2008). Private Communication, BlueScope Steel, Auckland.
- European Committee for Standardization (CEN) (2002). EN 1990+A1 Eurocode — Basis of structural design, Brussels.
- CEN (2004a). EN 1992-1-1 Eurocode 2: Design of concrete structures - Part 1-1: General rules and rules for buildings, Brussels.
- CEN (2005). EN 1993-1-1 Eurocode 3: Design of steel structures - Part 1-1: General rules and rules for buildings, Brussels.
- CEN (2006a). EN 1993-1-3 Eurocode 3 — Design of steel structures - Part 1-3: General rules - Supplementary rules for cold-formed members and sheeting, Brussels.
- CEN (2004b). EN 1994-1-1 Eurocode 4: Design of composite steel and concrete structures – Part 1-1: General rules and rules for buildings, Brussels.
- CEN (2008). EN 1090-2+A1 Execution of steel structures and aluminium structures – Part 2: Technical requirements for steel structures, Brussels.
- CEN (2004c). EN 10025-1 Hot rolled products of structural steels – Part 1: General technical delivery conditions, Brussels.
- CEN (2006b). EN 10143 Continuously hot-dip coated steel sheet and strip - Tolerances on dimensions and shape, Brussels.

- CEN (2004d). EN 10326 Continuously hot-dip coated strip and sheet of structural steels - Technical delivery conditions, Brussels.
- CEN (2009). EN 13670 Execution of concrete structures, CEN, Brussels.
- Joint Committee on Structural Safety (JCSS) (2001). Probabilistic Model Code, <http://www.jcss.byg.dtu.dk/>, Aalborg.
- Standards Australia (SA) (2011). AS 1397 Continuous hot-dip metallic coated steel sheet and strip—Coatings of zinc and zinc alloyed with aluminium and magnesium, Sydney.
- Standards Australia/Standards New Zealand (SA/SNZ) (1996). AS 1365 Tolerances for flat-rolled steel products, Sydney/Wellington.
- SA/SNZ (201X). AS/NZS 2327 Composite steel-concrete construction for buildings, Sydney/Wellington
- Standards New Zealand (SNZ) (1997). NZS 3404 Part 1: Steel Structures Standard, Wellington.

Composite Slab Crack Widths Considering Shrinkage and Gravity Loading

Amir Khanlou¹; Gregory MacRae²; Allan Scott³; Stephen Hicks⁴; Charles Clifton⁵;
Roberto Leon⁶; and Alireza Gholamhoseini⁷

¹Dept. of Civil and Natural Resources Engineering, Univ. of Canterbury, Christchurch, New Zealand. E-mail: amir.khanlou@pg.canterbury.ac.nz

²Dept. of Civil and Natural Resources Engineering, Univ. of Canterbury, Christchurch, New Zealand (corresponding author). E-mail: gregory.macrae@canterbury.ac.nz

³Dept. of Civil and Natural Resources Engineering, Univ. of Canterbury, Christchurch, New Zealand. E-mail: allan.scott@canterbury.ac.nz

⁴Heavy Engineering Research Association, Manukau, New Zealand. E-mail: stephen.hicks@hera.org.nz

⁵Dept. of Civil and Environmental Engineering, Univ. of Auckland, Auckland, New Zealand. E-mail: c.clifton@auckland.ac.nz

⁶Dept. of Civil and Environmental Engineering, Virginia Tech, Blacksburg, VA. E-mail: rleon@vt.edu

⁷Dept. of Civil and Natural Resources Engineering, Univ. of Canterbury, Christchurch, New Zealand. E-mail: alieza.gholamhoseini@canterbury.ac.nz

Abstract

An experimental study was conducted on steel fibre-reinforced concrete (SFRC) composite slabs to quantify crack width resulting from shrinkage and gravity loading. Ten full scale slab specimens were evaluated with different types of bond between the concrete and deck (e.g., greased, unembossed deck, regular deck) and different amounts of concrete reinforcement (e.g., mesh, steel fibre). Concrete shrinkage was measured and monitored over a period of 74 days, and then slabs were tested under increasing load. Each was continuous over two spans and two line loads were applied on each span. Relationships between crack size/distribution were obtained for each slab for different levels of applied load.

Keywords: Continuous composite slab; Cracking; Deflection; Embossment; Shrinkage.

1. INTRODUCTION

Composite flooring systems are widely used in the construction of suspended floors in steel-framed multi-storey buildings around the world because of their relative efficiency compared to many other flooring systems.

In practice, although the concrete is continuous (and typically the steel decks also) over the intermediate supporting beams, usually the slab is designed as a series of simply supported one way slabs [Johnson 2004]. These ‘nominally simply-supported’ slabs require top longitudinal reinforcement at their support, primarily to control the

width of cracks under serviceability actions. Therefore, Standards/Codes introduce a nominal amount of reinforcement in the form of percentage of the cross-section area to be arranged for crack control at the support. Generally, this reinforcement is in the form of mesh or welded wire fabric, and will often be sufficient to cause the shrinkage and temperature stresses to be relieved in small local cracks rather than accumulating over greater distances to form more widely spaced large cracks.

Placing of the mesh reinforcement in the steel-deck composite flooring construction increases the cost, construction complexity, and erection speed. Therefore, the partial or total replacement of the conventional reinforcement (e.g. rebar, mesh) with other forms of crack control has economical benefits, due to eliminating or reducing labour time in construction.

One solution of interest is the of steel fibre reinforced concrete (SFRC), since it may offer structural performance benefits which can be translated into cost savings. However, there are number of outstanding issues related to understanding the behaviour of composite slabs for design, especially considering shrinkage, the effects of different amounts of steel fibre reinforced concrete, the performance under severe inelastic loading demands of fire or earthquake. This research addresses the first two topics.

Previous studies have been conducted on SFRC composite slabs are summarised by Khanlou et al. [2013]. These include those by Ackermann and Schnell [Ackermann 2008] considering different fibre dosages and different steel deck profiles. Abas et al [Abas et al 2013] carried out tests on continuous composite slabs reinforced with SFRC and mesh. Also studies have been conducted on shrinkage in composite slabs by Bradford [Bradford 2010] and Gilbert [Gilbert 2013].

This experimental based research seeks to address a number of issues by developing a better understanding of the behaviour of the steel fibre reinforced concrete composite slabs.

2. EXPERIMENTAL PROGRAM AND TEST SPECIMENS

Ten two span continuous composite slabs were constructed using trapezoidal steel sheet. The slabs were 1.2 m wide by 6.3 m long, with two spans of 3.0 m. Schematic diagrams of the composite slabs are shown in Figure 1. Details of the composite slabs are summarized in Table 1. One type of profiled steel sheeting was used in all the slabs, except for L1 and L2 slabs, which had no embossments and indentations on its surface. Figure 2 shows the cross sectional dimensions of the steel sheet profile. The nominal thickness of the steel decking is 0.9 mm.

L1, L2, L3, and L4 slabs were constructed to study the effect of steel deck in restraining the shrinkage induced stresses and deformations. Conventional plain concrete (without steel fibres or mesh) was used to cast these slabs. Steel deck in L1 and L2 slabs did not have embossments to eliminate mechanical bond. Surface of the steel sheet for L2 and L3 were greased to eliminate the chemical bond (adhesion). In composite slab L4, both mechanical and chemical bond was provided.

In order to study the effect of reinforcement amount and type, different types of reinforcement were used in the slabs. For L5, L6 and L7 composite slabs, SFRC with 20 kg/m³, 40 kg/m³ and 60 kg/m³ were used, respectively. One type of steel fibre, Dramix RC-80/60-BN, was used in the tests. The fibres were high strength, hooked-end cold

drawn produced by Bekaert. The dimensions and material properties of the steel fibres are given in Table 2.

Mesh reinforcement was used in L8, L9, and L10 composite slabs. Brittle mesh with minimum proof stress of 485 MPa and uniform elongation of 1.5% was considered in L8 and L9 slabs. For L10 and L11 slabs, ductile mesh with minimum proof stress of 500 MPa and uniform elongation of 10% was used. Mesh wire diameter, wire spacing, and reinforcement ratio for each slab are given in Table 1.

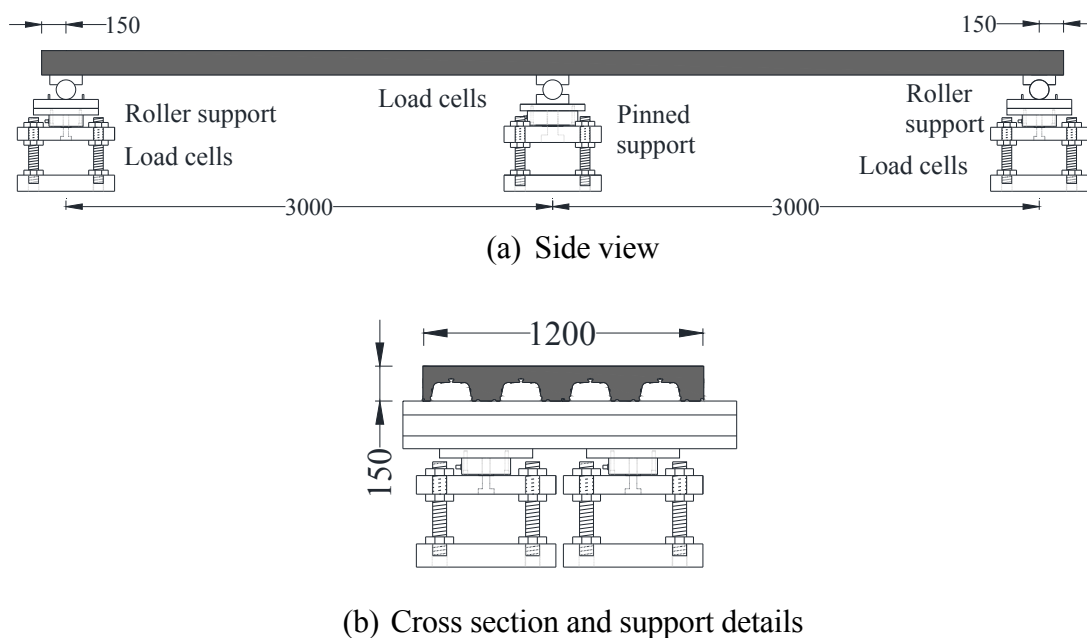


Figure 1. Two span composite slab dimensions and support configuration.

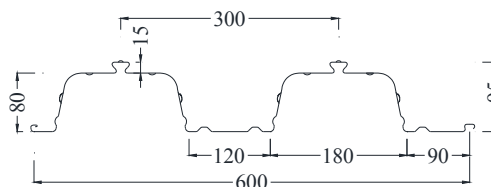


Figure 2. Cross sectional dimensions of the steel sheet profile.

All the slabs were moist cured for 14 days after casting the concrete. In order to measure the drying shrinkage, on the surface of the slabs, Demec points were glued every 500 mm along the length of the slab. Dial gauges were placed at both ends and mid-span of each slab. Concrete shrinkage was measured and monitored over a period of 74 days.

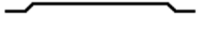
After completion of monitoring concrete shrinkage all test specimens were lifted and positioned in a four point bending loading test setup. Lifting and moving the slabs was done with caution by means of a lifting frame which was specifically designed to avoid or minimize any unexpected damage and to maintain existing geometry and support conditions. A schematic and a photo of the test setup are shown in Figure 3 and Figure 4, respectively.

During the test, slab deflection at both mid spans, deflections under the loading points, and end slip at both ends were measured. Crack widths in the hogging moment region, over the middle support, were measured manually by means of a microscope with an accuracy of 0.01 mm.

Table 1. Details of composite slabs.

Specimen designation	Steel deck surface condition		Reinforcement	Bar diameter (mm)	Reinforcement area per meter width (mm ² /m)	Percentage of cross-sectional area (%)	Fibre content (kg/m ³)
	Embossment	Oiled					
L1	N	N	-	-	-	-	-
L2	N	Y	-	-	-	-	-
L3	Y	Y	-	-	-	-	-
L4	Y	N	-	-	-	-	-
L5	Y	N	Fibre	-	-	-	20
L6	Y	N	Fibre	-	-	-	40
L7	Y	N	Fibre	-	-	-	60
L8	Y	N	665	5.3	147.1	0.21	-
L9	Y	N	661	7.5	294.5	0.42	-
L10	Y	N	SE62	6.1	146	0.21	-

Table 2. Properties of steel fibre.

Length l_f (mm)	Diameter d_f (mm)	Aspect ratio l_f / d_f	Yield stress σ_{fy} (MPa)	Shape
60	0.75	80	1050	

3. TEST RESULTS AND DISCUSSIONS

Shrinkage measurements were taken every seven days over a period of 74 days. Measurements on the surface of the slab were taken using Demec points along the length of the slab. Shrinkage values at the mid-depth of the slab were taken by means of dial gauges at the both ends of the slab. Figure 5 shows shrinkage values over the whole length of slab at 28 days and 74 days for composite slabs L1 to L10. The average strain at the centre of the slab of about 200 $\mu\epsilon$ corresponds to a displacement of about 1.3 mm over the length of 6300 mm. This did not cause separation between the steel decking and concrete slab, but rather bending as shown from the strain profiles. It should be noted that the strains shown are the average over the whole slab length, and they are unlikely to represent the likely profile at any one location.

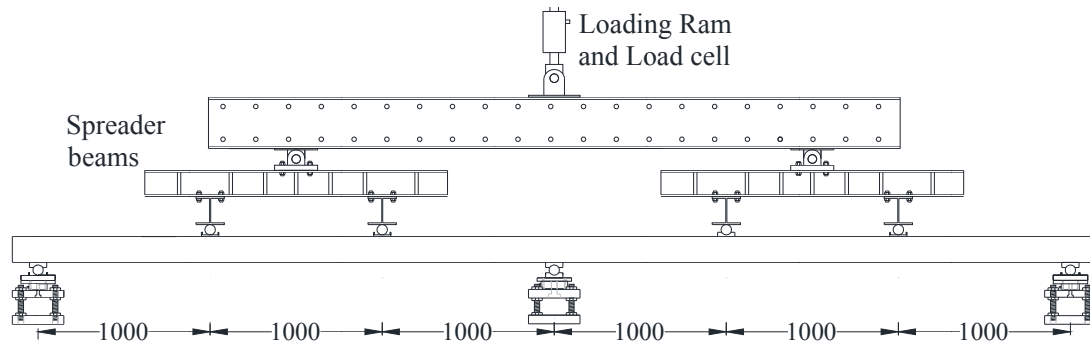


Figure 3. Schematic view of the test setup.



Figure 4. Photo of the test setup.

None of the composite slabs cracked over the middle support except L3. After 28 days a 0.2 mm wide crack was observed in slab L3. This was due to the curling up of the slab at one end, which was about 2.4 mm. Since the surface of the steel deck was greased, only mechanical bond, provided by embossments, was developed and steel deck and concrete curled up together. Sudden loss of mechanical bond between steel deck and concrete caused the concrete to crack. The crack width at 74 days widened up to 0.4 mm.

The restraint provided by the steel deck exerts a tensile strain to the bottom fibre of the concrete in the slab. This restraining effect of the steel deck is observed in Figure 5 from the very low strains at the bottom of the concrete for all slabs, except slab L2 at 74 days. The metal deck in this slab (L2) had no embossment and its surface was greased prior to casting the concrete. Therefore, the steel sheet was acting only as formwork and had no restraining effect at the bottom surface of the concrete.

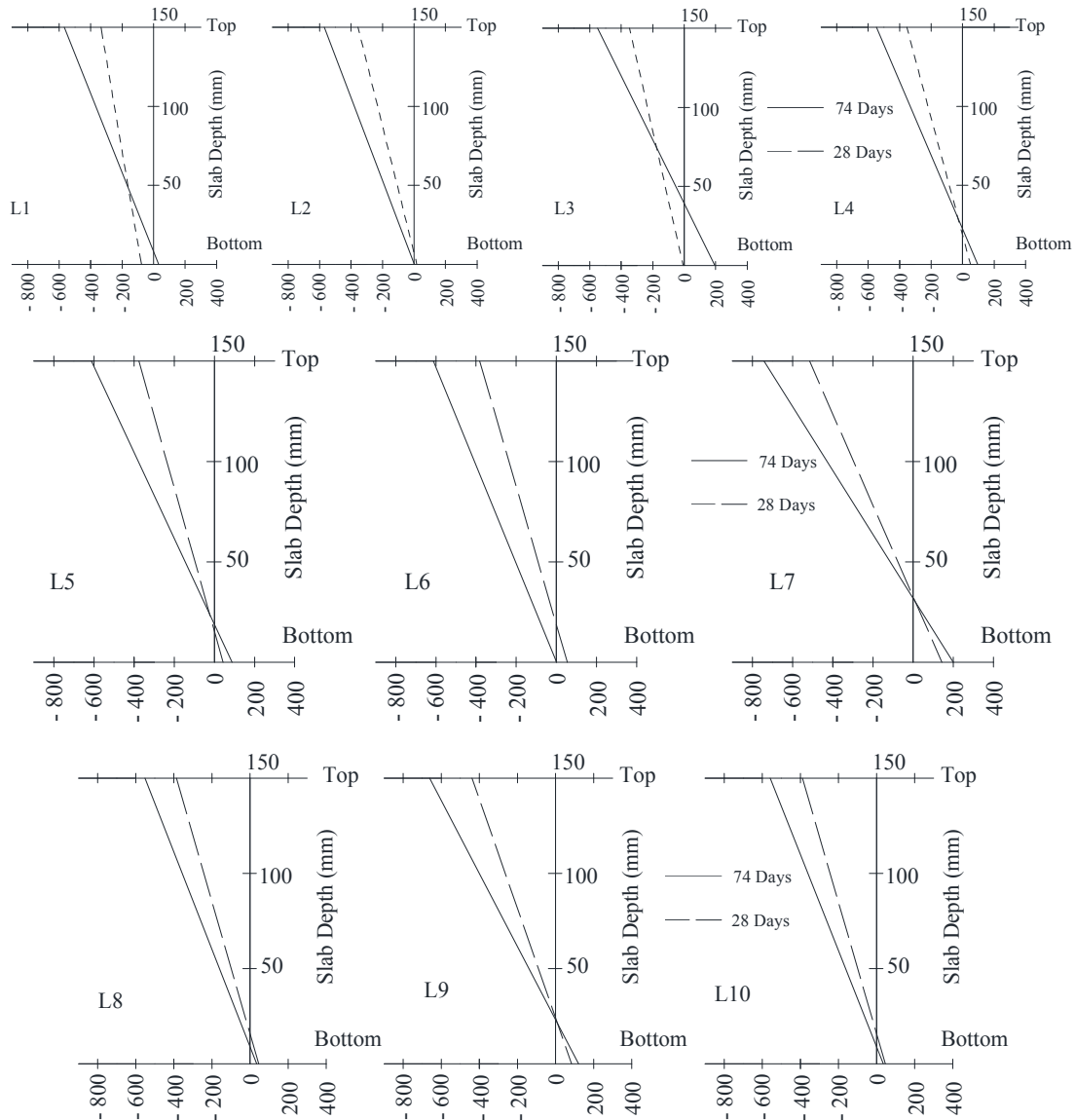


Figure 5. Average shrinkage strain profile (in $\mu\epsilon$) through the composite slab depth.

The shrinkage strains in Figure 5 are the average of the localized shrinkage strains measured along the length of the slab. The maximum localized shrinkage on top of the slab was measured at the ends of the slab, and minimum values were recorded over the middle support.

Figure 6, shows load versus mid-span deflection of the test specimens. The lowest peak load, as expected, was for slab L2, which did not have either chemical or mechanical bond. Slab L4, with normal concrete and deck conditions and no reinforcing, was used as a reference composite slab to evaluate the effect of reinforcement in the other test specimens. The peak load for slab L4 was 299.5 kN.

Composite slabs with different dosages of fibre (i.e. 20, 40 and 60 kg/m³) performed very similarly in terms of strength and displacements. The peak load values for slabs L5, L6 and L7 were 318.9 kN, 319.3 kN, 323.7 kN, respectively. In the mesh

reinforced specimens the peak load increased as the reinforcement ratio was increased. The peak load values for slab L8, L9 and L10 were 290.0 kN, 332.3 kN, 314.6 kN, respectively. Although, slab L8 and L10 had same percentage of reinforcement there was 24.6 kN difference in their peak load. This could be due the cracking sequence during the test.

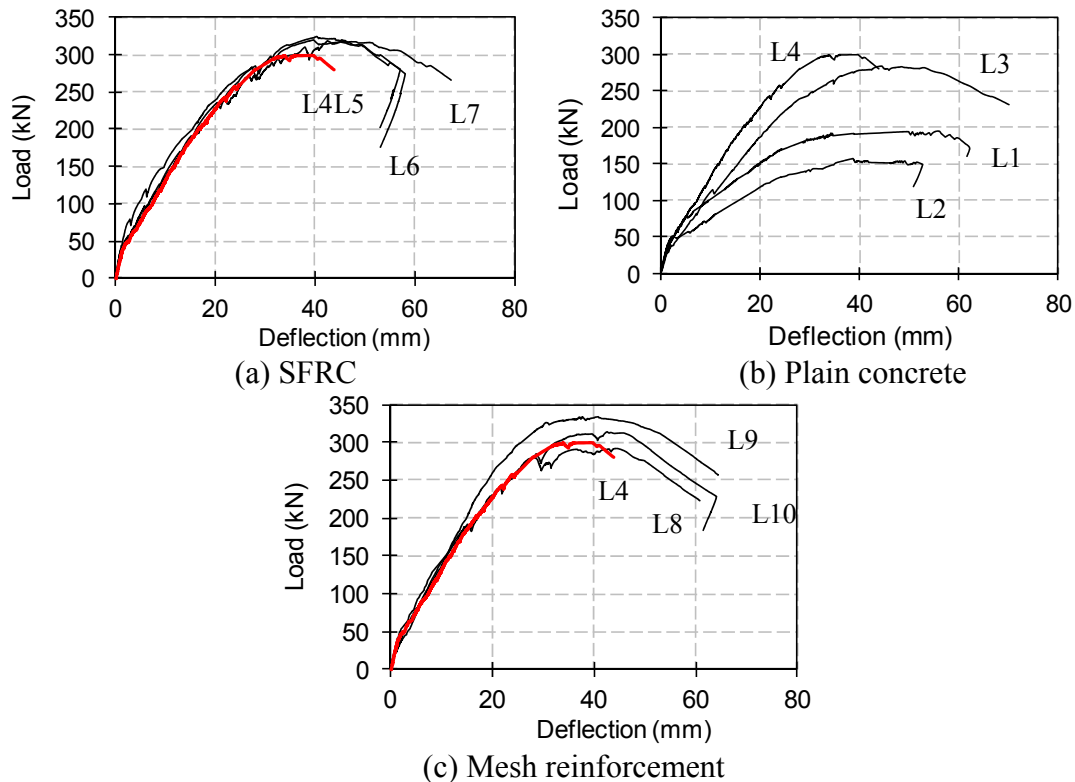


Figure 6. Load versus midspan deflection for composite slabs.

Crack width measurements over the middle support, which were taken during the loading test, are shown in Figure 7. Crack width values for L4, L5 and L6, were almost identical for the same level of loads. In other words, no improvement was gained in terms of crack control by inclusion of steel fibres, compared to the plain concrete. On the other hand, crack width control in slab L7 with 60 kg/m^3 of steel fibres, was significantly improved. In slabs with mesh reinforcement, crack widths were decreased as the steel ratio was increased. The degree of crack control in slab L7, with 60 kg/m^3 of steel fibre, was marginally higher than the best degree of crack control in slabs reinforced with mesh reinforcement. In mesh reinforced composite slabs, slab L9 with 0.42 percentage of cross sectional area of steel had the most effective crack control. Slab L8 cracked at lower load level compared to slab L10 which had the percentage of cross sectional area of steel of 0.21. The crack width values at higher load levels become closer in these slabs (L8 and L10).

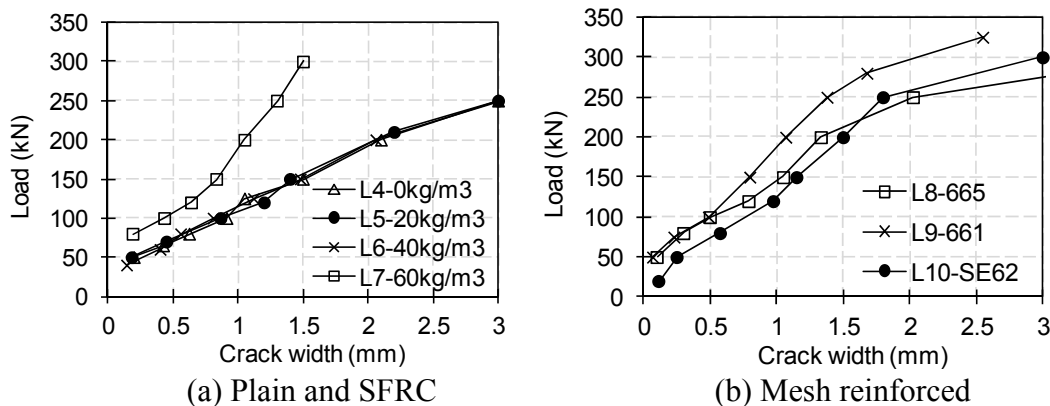


Figure 7. Crack width versus load for composite slabs.

4. CONCLUSIONS

This paper describes ten full-scale continuous two span steel deck composite slab tests. Each slab had different type and amount of reinforcement. Shrinkage measurements over 74 days for this series of the specimens showed:

1- There was no significant difference in both localized and average shrinkage strain values on top surface, for slabs with mesh reinforcement compared to the specimens with steel fibre.

2- Shrinkage strains for specimens with 20 kg/m³ and 40 kg/m³ of steel fibre were in the range of strains measured for conventional reinforcement, while strains for 60 kg/m³ were 10% higher.

3- Cracking due to the shrinkage induced strain was not observed in the mesh-reinforced composite slabs.

From composite slab tests under four point bending, following conclusions were drawn:

1- Composite slabs with SFRC performed very similarly in terms of strength.

2- SFRC composite slabs with dosages of 20 kg/m³ and 40 kg/m³ performed almost identical to the unreinforced composite slab, in terms of crack control in hogging moment region.

3- Application of steel fibre for crack control became effective for slab with SFRC with 60 kg/m³ of fibre, which showed a very significant improvement in crack control. The crack control performance was better than that of the mesh-reinforced slabs.

ACKNOWLEDGMENT

We wish to acknowledge the Heavy Engineering Research Association for initiating this research project together with the Heavy Engineering Education and Research Foundation for providing part of the financial support for the tests. Also, we wish to acknowledge Steve Stickland from Comflor, Dave Anderson of John Jones Steel, and Alan Ross from *BOSEFA* (Bekaert One Steel Fibres Australasia) for generously providing materials.

REFERENCES

- Abas, F. M, Gilbert, R. I., Foster, S. J., and Bradford, M. A. (2013). “Strength and Serviceability of Continuous Composite Slabs with Deep Trapezoidal Steel Decking and Steel Fibre Reinforced Concrete”. *Journal of Engineering Structures*, 49, 866-875.
- Ackermann, F, P and Schnell, J. (2008) “Steel Fibre Reinforced Continuous Composite Slabs”, Composite Construction in steel and Concrete VI – *Proceedings of the 6th International Conference on Composite Construction in Steel and Concrete*, Tabernash, Colorado.
- Bradford, M, A. (2010). “Generic Modelling of Composite Steel-Concrete Slabs Subjected to Shrinkage, Creep and Thermal Strains Including Partial Interaction”. *Journal of Engineering Structures*, 32, 1459-1465.
- Gilbert, R, I. (2013). “Time Dependent Stiffness of Cracked Reinforced and Composite Concrete Slabs”, *Eleventh International Conference on Modern Building Materials, Structures and Techniques, MBMST2013*. Vilnius Gediminas Technical University, pp. 19-34
- Johnson, R. P. (2004). “Composite Structures of Steel and Concrete”, 3rd Edition, Blackwell Scientific Publications.
- Khanlou, A. (2013). “Composite Slabs under Gravity Loading”, PhD Thesis, University of Canterbury. To be submitted.

Longitudinal Shear Capacity of Composite Slabs—In Situ Tests on Slabs in Use for 35 Years and a Historic Review of Design Methods, Research, and Development

Markus Knobloch¹ and Mario Fontana²

¹Institute of Steel, Lightweight and Composite Structures, Ruhr-Universität Bochum, Universitätsstraße 150, 44801 Bochum, Germany. E-mail: markus.knobloch@rub.de

²Institute of Structural Engineering, ETH Zürich, Stefano-Francini-Platz 5, 8093 Zurich, Switzerland. E-mail: mario.fontana@ethz.ch

Abstract

This paper presents an experimental study and an assessment of the test results on composite slabs with profiled steel sheeting performed at Zurich airport in conjunction with the conversion of Terminal B. The structure was built in 1974 with composite floor slabs, a steel frame with stub-girder beams, and hot-rolled steel columns as supporting structure. The experimental investigation focused on the bond behaviour of the composite slabs and the influence of the 35 years service life. Ten large-scale in situ tests were carried out on simple beams with different shear span lengths to evaluate the longitudinal shear capacity. In addition, tests on two-span continuous beams and punching shear tests were performed. The data obtained by the tests enabled the assessment of the slabs. The assessment shows that the profiled steel sheeting after 35 years in use still features good longitudinal shear strength and is fit for reuse as slab of Terminal B of Zurich airport.

INTRODUCTION

Steel deck concrete composite slabs are widely used all over the world since more than 50 years. The use of profiled steel sheets in combination with a concrete layer leads to economic solutions for lightweight building-floors. Composite slabs are cost-efficient and allow fast erection because the profiled steel sheet combines formwork and reinforcement.

The structural behaviour of composite slabs is governed by the longitudinal shear capacity. The semi-empirical *m-k-method* and the *partial connection method* are mainly used for the verification of composite slabs. Most of the available test data on the longitudinal shear behaviour used for verification was established with new slabs especially casted for the laboratory tests. The specimens of these laboratory tests are often first subject to cycles of load (prior to ultimate load testing). However, the test results in particular the experimentally determined longitudinal shear capacities do not consider effects of service life resulting from real usage.

Existing buildings are subjected to change of use, which often requires an assessment of their structure. The assessment of the composite slabs, however, is in many cases difficult due to the lack of knowledge on an eventual loss of longitudinal shear capacity due to vibrations and deformations induced by the service life. In the

past, often profiled steel sheets were used which are often not available on the market any longer and with neither measures to improve the mechanical interlock between the steel deck and the concrete nor special end anchorages. Thus, a large uncertainty concerning the longitudinal shear capacity of such old composite slabs existed.

The reconstruction of Terminal B of Zurich airport allowed to experimentally analysing the longitudinal shear behaviour of composite slabs with profiled steel sheets after 35 years in use. The test results show that the longitudinal shear strength is still (even after 35 years in use) in the range of the initial shear strength found in former laboratory tests on new unused slabs.

DESIGN METHODS, RESEARCH AND DEVELOPMENT

Composite floor slab systems were first developed in the late 1930s for use in high-rise buildings. At that time, the main advantage of this system compared to traditional reinforced concrete slabs was the marked dead load reduction. Composite slabs were soon applied to a wide range of construction projects. At the end of the 1950s the first composite floor slabs appeared in Europe, e.g. Nestlé office building in Vevey, Switzerland. At that time, the composite action was usually provided by pure bond. Mesh wires were welded to the top of the steel sheet corrugations only in cases of significant high load conditions. The first dovetail profiled steel sheeting was used in Europe (introduced from the US) in the middle of the 1960s, e.g. UNO office building, Geneva and Zurich airport, Switzerland (Fig. 1). The introduction of fast-track construction methods brought a new interest in steel design and composite flooring during the late 1980s.



Fig. 1 – Zurich airport, construction site 1974 (Source: *Holorib - la fameuses documentations Holorib bleuses de l'epoque*).

During construction, when the concrete is wet, the decking alone resists the external loading. Due to their high plate slenderness ratios, the thin component plate

elements which make up the decking may buckle prior to yield. The effective widths method is commonly used for considering the decreasing of the load-carrying capacity due to local buckling.

In the final state, steel deck concrete composite slabs show three typical failure modes in function of the shear span lengths. For very short shear spans vertical shear failure may be observed while for very long shear spans bending failure is crucial. However, the capacity of the most end spans of composite slabs in buildings is governed by longitudinal shear failure typical for intermediate shear span lengths. Two design methods, namely the semi-empirical *m-k-method* [Schuster 1972, Porter and Ekberg 1976] and the *partial connection method* [Bode and Sauerborn 1992], are mainly used for the verification of composite slabs. Both methods are based on former investigations, e.g. [Ekberg and Schuster 1968, Porter and Ekberg 1972], that experimentally and numerically analyse the load-carrying behaviour of composite slabs, in particular the longitudinal shear bond behaviour that is often crucial for the capacity of the slabs. Recent studies on the behaviour of composite slabs are performed by e.g. [Crisinel and Marimon 2004, Chen and Shi 2011, Cifuentes and Medina 2013].

TEST SETUP

Test specimens

The longitudinal shear bond behaviour of the steel deck concrete composite slabs was experimentally analysed with destructive in situ tests at Terminal B of Zurich airport. Destructive tests became possible due to the demolishment of the front part of the terminal. The remaining part was undergoing major changes due to new requirements of use.

Terminal B of Zurich airport was built in 1974 as a two-storey steel framed structure with composite slabs. The steel framed structure of the front part of Terminal B is shown in Figure 2. The steel frame consisted of wide-flange HEM 360 columns or HEM 500 corner columns respectively, and vierendeel girders made of two wide-flange HEM 160 profiles as flanges and steel plate with a thickness of $t = 20$ mm as a web. Full strength end plate connections were used to connect secondary IPE 360 beams to the girders.

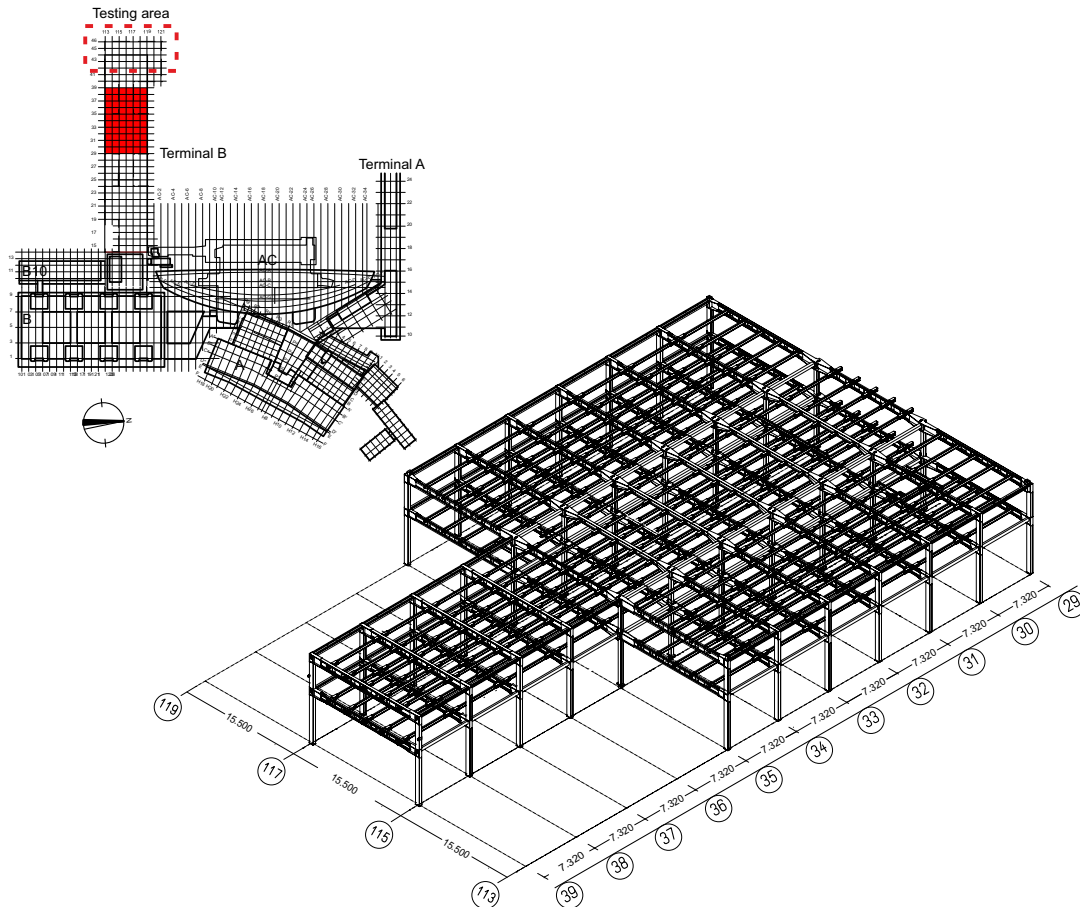


Fig. 2 – Overview of Zurich airport and steel frame structure of Terminal B.

The secondary beams constituted the supports of the composite slab. The profiled steel sheeting was arranged perpendicular to the secondary beams and was fixed to its top flange using powder activated fasteners only. According to the construction plan, two fasteners were used per sheet and support. No additional end anchorages or shear connectors were used. The composite slab consisted of Holorib HR51 re-entrant steel sheeting, a layer of structural concrete with a nominal thickness of 120 mm and a reinforcement mesh $d = 4 \text{ mm}/150 \text{ mm}$. The steel sheeting possessed a nominal thickness of 0.91 mm and a height of the dovetail rib of 51 mm with a spacing of 150 mm. A non-structural screed with a thickness of 120 mm was placed at top separated from the structural concrete by a coated paper foil. The cross section of the composite slab is given in Figure 3.

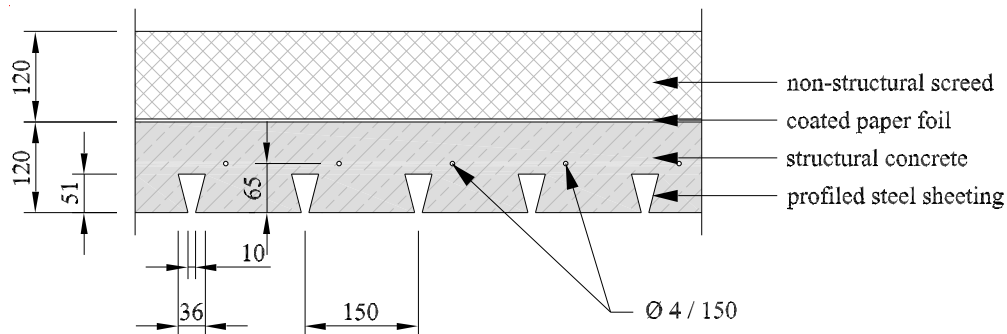


Fig. 3 – Cross section of the composite slab.

The non-structural screed was removed before testing. The same method and construction site equipment intended for the refurbishment of the part of the terminal designated for reuse were used for the removal. The test specimens were produced out of an inner part of the lower floor slab at the airside part of Terminal B. The specimens were diamond cut from the slab and left in situ for testing as simple or continuous beams supported by the secondary beams. A gap of 30 mm was cut around the specimens. The nominal width of the test specimens was 850 mm.

Material properties

The material properties of the profiled steel sheets and the structural concrete used for the composite slabs were determined at the laboratory of the Institute of Structural Engineering and Institute of Building Materials at ETH Zurich. Compressive and tensile strength of the concrete were experimentally investigated with five and four respectively small cylinders bored from the slab with a diamond core drill. The actual mean height of the small cylinders was $h = 112$ mm, the actual mean diameter $d = 44.7$ mm. The mean diameter was less than three times the maximum aggregate size of 16 mm. However, the results of the concrete material property tests did not have a large scatter [Klippel, Knobloch and Fontana 2010]. A universal 4 MN servo hydraulic compressive testing machine was used for the compressive tests. The mean value of the concrete compressive strength was 54.5 N/mm^2 (COV 0.063). A universal 10 kN testing machine was used for the tensile tests. The cylinders were glued between two blocks of aluminum. The mean value of the concrete tensile strength was 3.86 N/mm^2 (COV 0.114).

The yield strength and the ultimate tensile strength of the steel sheet were determined with four tensile material coupon tests according to [EN ISO 6892 2007]. The coupons were cut from the steel sheeting of the composite slab and had a shape according to [DIN 50125 2009]. A universal 100 kN testing machine was used for the tensile tests. The mean value of the lower yield strength was 273.9 N/mm^2 (COV 0.034) (nominal value of elastic limit 2400 kg/cm^2), the mean value of the ultimate tensile strength was 339.1 N/mm^2 (COV 0.012). Details of the material property tests are given in [Klippel, Knobloch and Fontana 2010].

Testing device and measurement

A testing frame was fixed to the secondary beams using high strength steel rods passing through holes with an outside diameter of 50 mm drilled adjacent to the beams. Figure 4 shows the testing frame. The frame mainly consisted of two U-profiles and two wide-flange H-profiles.

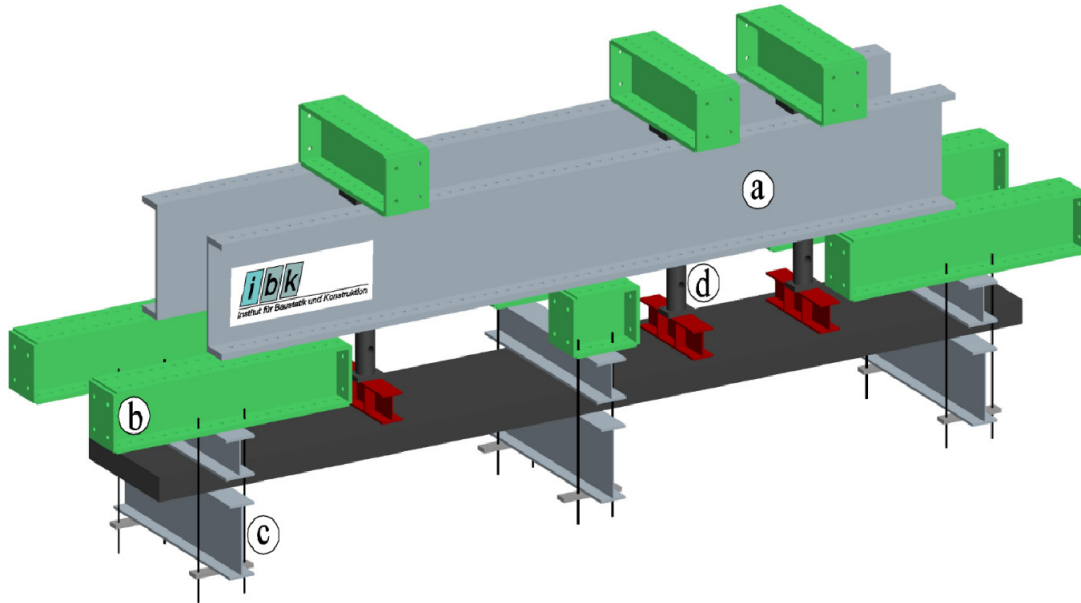


Fig. 4 – Testing frame (a: U-profiles, b: HEB sections, c: IPE 360 secondary beams with tension rods, d: load jacks).

The beam test specimens were tested as four-point and three-point bending tests. The loads were applied by hydraulic load jacks, which could be positioned at different shear spans L_s . The load was applied manually using a hand pump, which allowed adapting the load increase in case of first slip between steel sheeting and concrete. The load was measured using the servo hydraulic pressure. The load was applied to the test specimens using HEA 140 profiles with a length of 800 mm. The mid-span deflection and the deflection close to the jacks were measured using LVDTs (Figure 5). LVDTs were also used to measure the slip at a distance of approximately 400 mm from the supports.

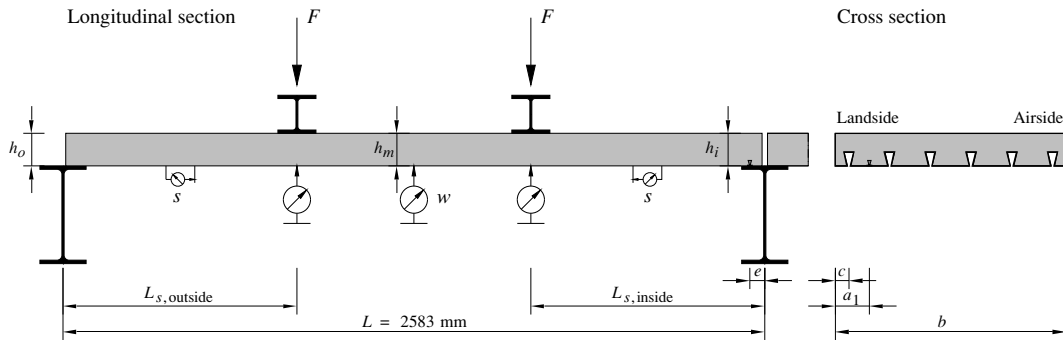


Fig. 5 – Longitudinal section (left) and cross section (right) of the test specimens.

The punching shear capacity of the composite slabs was experimentally determined by two in-situ punching tests. The testing device was slightly modified to apply a concentrated load on an area of 100 x 100 mm² using a massive steel plate (Figure 6). Four LVDTs were used for measuring the deflection of the composite slab close to the loading area. In addition, the load-slip behaviour towards the longitudinal direction of the profiled steel sheeting was measured by two LVDTs below the composite slab. Details of the testing device and measurement of all tests are given in [Klippel, Knobloch and Fontana 2010].

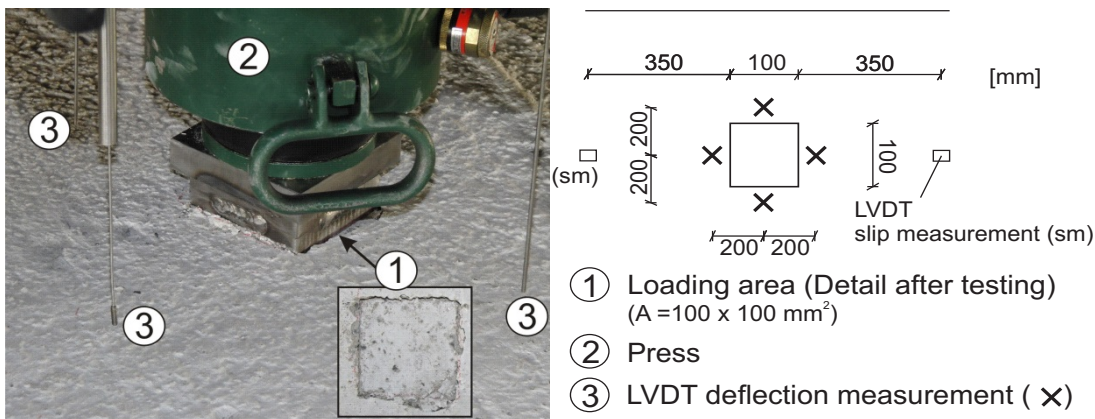


Fig. 6 – Test setup for punching tests including information about installed measurement devices.

Test program

Ten full-scale simple beam tests, labeled sb 1 to 10, (including one pre-test) were carried out as three-point and four-point bending tests with a span between the supports (IPE secondary beams) of 2583 mm. In addition, two continuous beam tests, labeled cb 1 and 2, two punching shear tests, labeled p 1 and 2, two tests on cantilevers, labeled c 1 and 2, and two tests on floor openings, labeled o 1 and 2, were performed. Figure 7 gives the location of the different test specimens within the area used for testing. Details of the continuous beam tests as well as tests on cantilevers and floor openings are given in [Klippel, Knobloch and Fontana 2010].

The distance from the supports to the point loads of the simple beam tests was tantamount to the shear span length L_s of the bending tests. The nominal distance of the three-point bending tests was equal to the half span ($L/2 = 1290$ mm). The four-point bending tests were performed with different shear span lengths. The nominal shear span lengths were $L/3 = 860$ mm, $L/4 = 645$ mm and $L/8 = 322.5$ mm. The shortest shear span length roughly equaled three times the depth of the composite slab. Details of the test specimens and program including shear span lengths are given in Table 1 for the simple beam tests.

Test procedure

The beam test specimens were first subjected to three to five loading cycles with the maximum load value equal to approximately 40 % of the estimated ultimate load. The punching shear test specimens were subjected to five loading cycles with a maximum load of 50 kN. The composite floor slab had already been loaded to many loading cycles during its service life. Thus, it seemed not to be necessary to perform more loading cycles as it is recommended for laboratory tests on composite slabs. After performing several loading cycles, the specimens were loaded until first slip between steel sheeting and concrete. Then, the specimens were loaded either until failure or until large deflections.

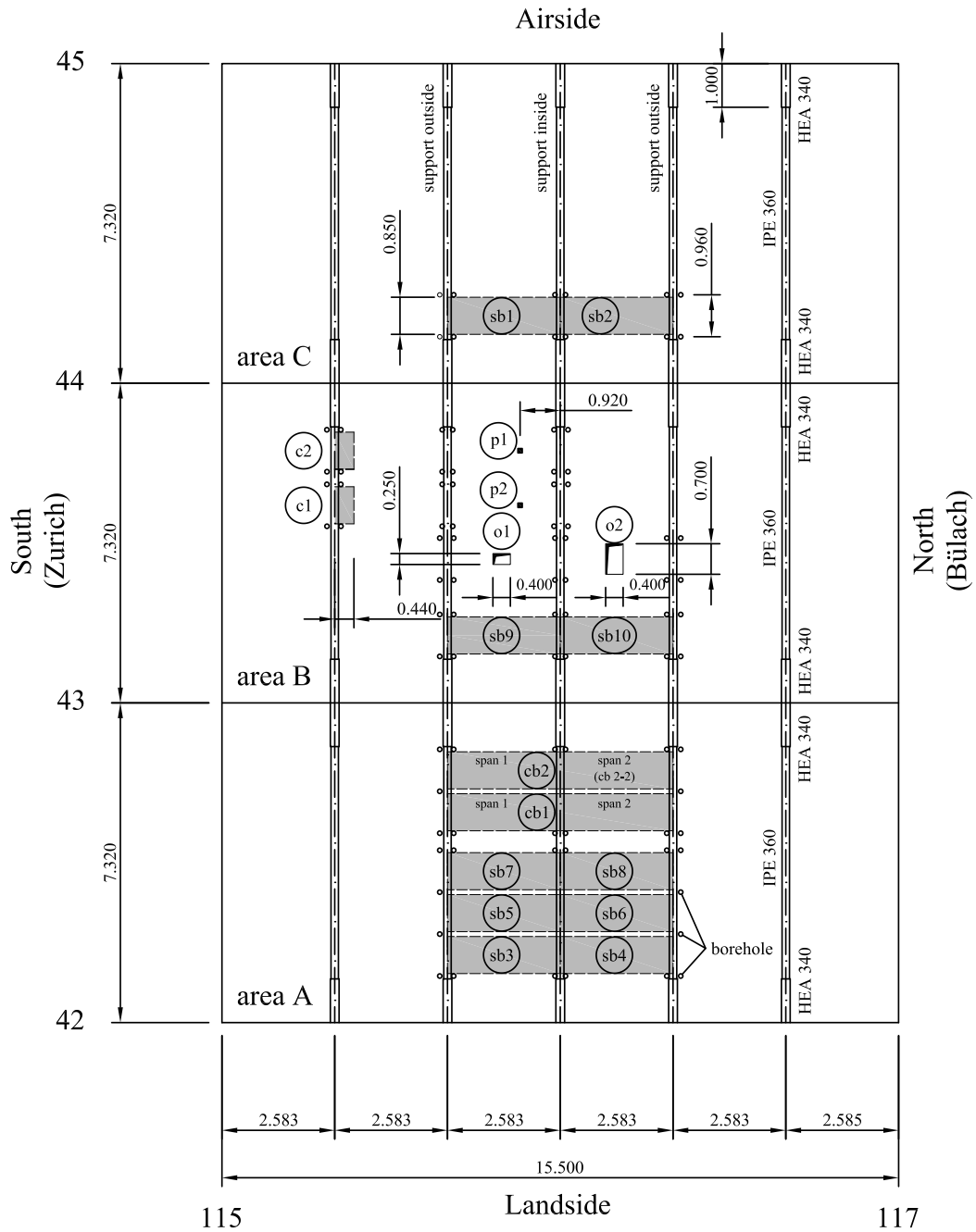


Fig. 7 – Location of the different test specimen within the area used for testing (sb: single beam, cb: continuous beam, c: cantilever, p: punching, o: opening). All dimensions in [m].

TEST RESULTS

Simple beam tests

The failure of all beam test specimens was governed by longitudinal shear failure, even the test specimens with short shear spans. No shear failure was observed. Figure 8 exemplarily shows measured load-deflection (left) and load-slip (right) curves for three- and four-point simple beam bending tests with different shear span lengths. The deflection is given as the vertical deflection at mid-span. The specimens showed almost linear-elastic behaviour until the first distinct slip between the steel sheeting and the concrete was noticed. After the first slip occurred the load dropped down abruptly and increased again for most of the specimens. The behaviour of the specimens was classified ductile if the ratio between the remaining ultimate load F_u (maximum load after load drop caused by slip occurrence) and the load at first slip F_s exceeded 1.1. Otherwise the behaviour of the specimens was classified non-ductile. According to this classification five of nine test specimens showed a ductile behaviour. Table 2 gives the load at first distinct slip, the ultimate load, and the corresponding deflections.

Table 1 – Details of the simple beam tests (see Figure 5 for terms).

Test specimen	Shear span		Width b	Height			No. of dovetails n	Distance dovetail-support c
	Outside $L_{s,outside}$ [mm]	Inside $L_{s,inside}$ [mm]		Outside h_o [mm]	Middle h_m [mm]	Inside h_i [mm]		
sb 2	950	920	843	115	120	107	5	100
sb 3	610	600	847	121	117	105	5	95
sb 4	950	920	845	110	118	105	5.5	70
sb 5	590	600	847	121	128	107	6	30
sb 6	340	365	840	110	116	107	6	150
sb 7	1300	1230	845	121	124	107	5.5	135
sb 8	350	365	844	110	117	107	5.5	100
sb 9	570	595	850	122	130	118	5	100
sb 10	1300	1235	840	133	126	118	5.25	80

Table 2 – Simple beam test results.

L_s	$L/8$		$L/4$		$L/3$		$L/2$		
	sb 6	sb 8	sb 3	sb 5	sb 9	sb 2	sb 4	sb 7	sb 10
Test specimen									
Slip load F_s [kN]*	35.3	42.2	39.4	41.3 ⁱ	41.4	26.5	22.0	21.9	39.9
Ultimate load F_u [kN]	49.8	52.2	48.4	44.9 ⁱ	44.1	31.8	25.0	22.2	31.9 ⁱⁱ
Deflection w_u [mm]	11.1	14.6	21.9	9.2	16.0	42.0	26.2	13.9	35.9
Ratio F_u/F_s	1.41	1.24	1.23	-	1.07	1.20	1.14	1.01	-
Behaviour	ductile	ductile	ductile	brittle	brittle	ductile	ductile	brittle	brittle

* Load at an end slip of 0.1 mm or at first slip respectively

ⁱ Ultimate load reached before end slip of 0.1 mm

ⁱⁱ Residual strength

The load-deflection behaviour was similar for test specimens with equal nominal shear span lengths. However, the ultimate load of the two three-point bending test specimens (sb 7 and sb 10) is highly different. The residual strength of sb 10 is 44% higher than the load of sb 7. For most test specimens powder activated fasteners were only found at the inner support. However, test specimen sb 10 possessed fasteners on both supports which might be the reason for the higher resistance. Details of the test results on simple beams are given in [Klippel, Knobloch and Fontana, 2010].

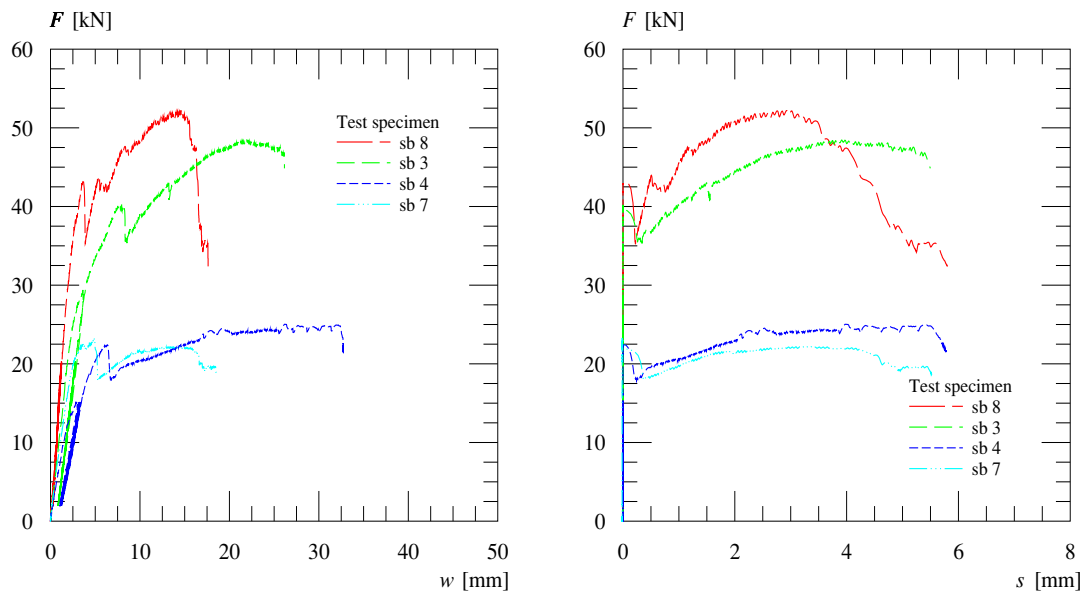


Fig. 8 – Load-deflection (left) and load-slip behaviour (right) of the simple beam tests for different shear span lengths L_s (applied load F is given per jack).

Punching shear tests

Figure 9 shows the load-mean deflection (left) and the load-slip response of the two punching shear test specimens. No visible cracks were observed before failure. After reaching the ultimate loads of 287 kN (p 1) and 268 kN (p 2) both test specimens failed brittle. The difference between the ultimate loads of both tests was small. The ultimate loads were markedly higher than the punching shear resistance according to simplified model given in [EN 1994-1-1, 2004]. The ratio between the punching shear resistance according to the simplified model and the mean value of the ultimate test load was $V_p / F_u = 0.63$.

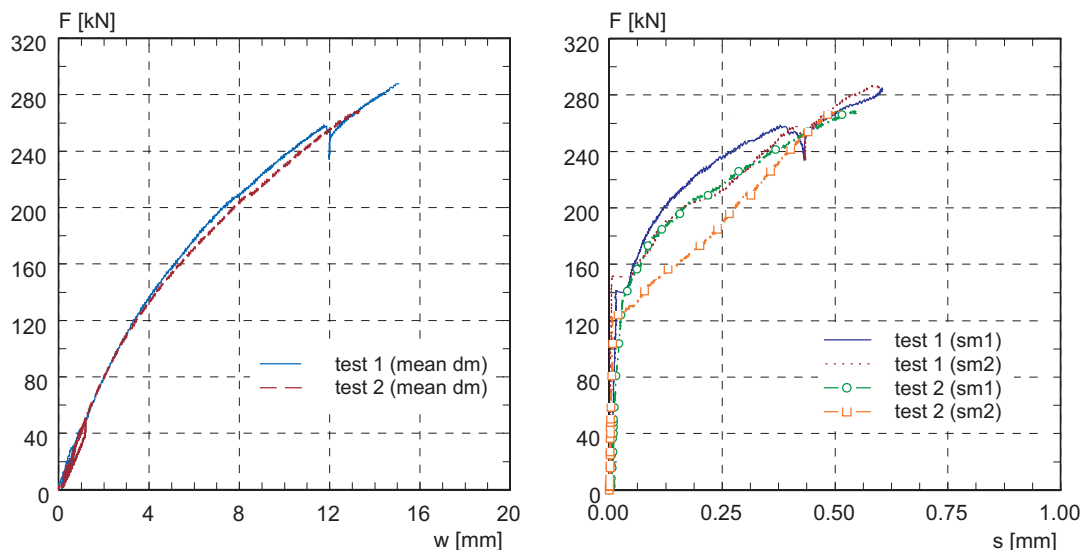


Fig. 9 – Load-deflection behaviour (left) and load-slip response (right) for the performed punching shear tests (slip measurement devices sm 1 and sm 2 placed according to Fig. 6)

ASSESSMENT OF THE TEST RESULTS

The longitudinal shear capacity of composite decks is usually assessed on the basis of simple analytical models, namely the semi-empirical m - k and the partial shear connection method. Both models were used for assessing the test results.

m-k-method

The semi-empirical m - k -method is based on a test program on four-point bending tests with at least six test specimens with two or more different shear span lengths. By means of a linear regression analysis the coefficients m and k are determined considering all tests with longitudinal shear failure and the longitudinal shear resistance is assessed according to Eq. (1).

$$V_{l,Rd} = \frac{b \cdot d}{\gamma_{VS}} \cdot \left(\frac{m \cdot A_p}{b \cdot L_s} + k \right) \quad (1)$$

Figure 10 (left) shows the vertical shear capacity of the simple beam tests $V_{l,Rd}$ (divided by the width b and depth d_p of the slab) as a function of the reciprocal value of the shear span lengths L_s (multiplied by the width b of the slab and divided by the cross section area of the sheeting A_p) considering actual geometrical and material properties. For the assessment of the characteristic values m and k of the method the vertical shear capacity of all test specimens classified as non-ductile were first reduced by 20%. Secondly, the minimum capacity of each group of shear span lengths was reduced by 10% for simplicity [EN 1994-1-1, 2004], and thirdly, a linear regression analysis was performed.

Based on the m - k -method a design value of the longitudinal shear resistance of $V_{l,Rd} = 25.6$ kN was calculated for the composite slab from the results of the

simple beam in situ tests sb 2 to 10 – the results of the pre-test sb 1 was neglected for the assessment.

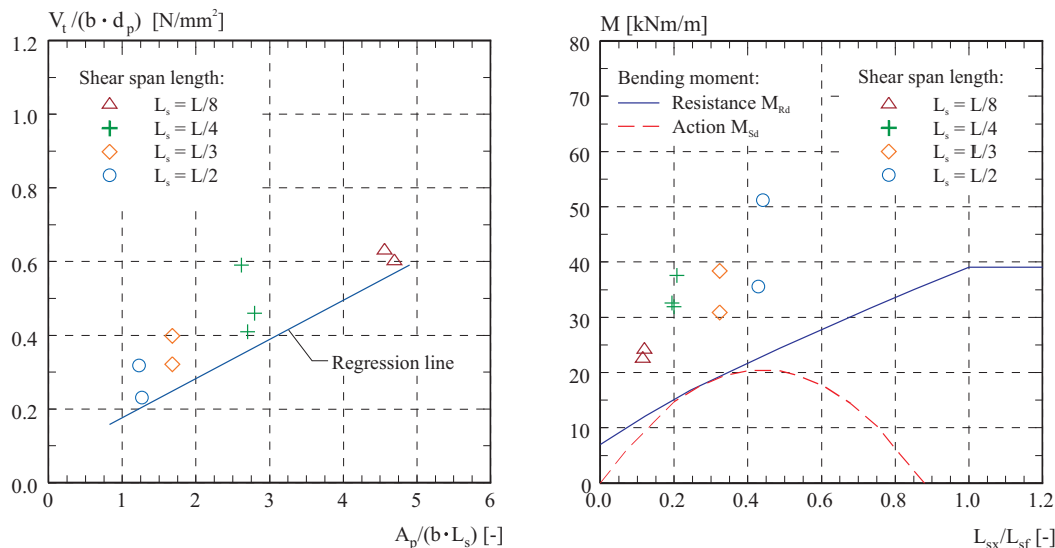


Fig. 10 – Evaluation of the test results with m-k-method (left) and partial shear connection method (right).

Partial shear connection method

As an alternative to the semi-empirical m-k-method the test results were assessed on the basis of the partial shear connection method which is based on the same generic mechanical model as for partial shear connection of composite beams. For no shear connection ($\eta = 0$) the bending resistance corresponds to the pure bending resistance of the steel sheet. The full plastic resistance of the composite slab is reached for full shear connection ($\eta = 1$).

For determining the characteristic value of the bond strength τ_u of the composite floor slab all ultimate loads of tests classified as non-ductile were first reduced by 20%. Then, the minimum value of the tests (considering specimens classified as both ductile and non-ductile) was again reduced by 10% for simplification instead of a rigorous evaluation of the 5% fractile of the test results. The design shear strength $\tau_{u,Rd}$ is calculated by dividing the characteristic value by the partial safety coefficient. The design shear strength $\tau_{u,Rd}$ was 0.164 N/mm². Details are given in [Klippel, Knobloch and Fontana, 2010].

Figure 10 (right) shows the experimentally determined ultimate bending moments (dots) as well as the design bending resistance M_{Rd} calculated with the partial shear connection method (continuous line) as a function of the normalized shear span length L_{sx} / L_{sf} given as the ratio of the actual shear span lengths and the lengths required to reach full plastic bending moment resistance. The bending resistance is based on the design shear strength as well as on the actual material and geometry data considering partial safety factors according to [EN 1994-1-1, 2004].

For the design of the slab with partial shear connection it has to be shown that the design bending moment M_{Ed} does not exceed the design resistance M_{Rd} . Figure 11 (right) shows the bending moment M_{Ed} for a uniformly distributed load (dotted line).

The bending moment for a uniformly distributed load M_{Ed} equals the bending resistance M_{Rd} for a shear resistance $V_{l,Rd} = 27.0$ kN according to the partial shear connection method.

Comparison of the methods and assessment of the composite slab

Table 3 summarizes the results of the assessment of the composite slab with the semi-empirical m-k-method and partial connection method. In addition to the design value of the shear resistance $V_{l,Rd}$ Table 5 gives the design value of the maximum floor load. The shear resistance assessed by the partial shear connection theory was slightly higher compared to the value obtained by the m-k-method. This is in accordance with [Sauerborn, 1995].

Table 3 – Design resistance according to the m-k-method and partial shear connection method.

	$V_{l,Rd}$ [kN]	q_{Rd} [kN/m ²]
m-k-method	25.6	23.3
Partial shear connection method	27.0	24.6

The assessment of the in situ tests show that the longitudinal shear strength of the profiled steel sheeting is even after 35 years in use still in the range of the initial strength found in former laboratory tests on novel unused slabs. Thus, the composite slab is fit for reuse as slab of new Terminal B of Zurich airport.

CONCLUSION

The behaviour of a steel deck concrete composite slab with profiled steel sheeting after 35 years in service has been experimentally investigated by large scale in situ tests. Simple beam and punching shear tests have been performed. In all beam tests, the slabs have shown longitudinal bond shear failure between profiled steel sheeting and concrete. No vertical shear failure has been noticed even for the tests with short shear span length of approximately three times the height of the slab. The actual punching shear capacity was markedly higher than the resistance according to European design rules.

The simple beam tests have been assessed by the semi-empirical m-k- and the partial shear connection method for composite slabs. It was found that the shear resistance obtained by the partial shear connection theory was slightly higher compared to the value obtained by the m-k-method. The results show that the profiled steel sheeting after 35 years in use still features good longitudinal shear strength and is fit for reuse as slab of Terminal B of Zurich airport.

REFERENCES

- Bode H. and Sauerborn I. 1992. "Zur Bemessung von Verbunddecken nach der Teilverbundtheorie." (Partial Shear Connection Design of Composite Slabs) *Stahlbau* 61(8): 241-250. (in German).
- Chen S. and Shi X. 2011. "Shear bond mechanism of composite slabs – A universal FE approach." *Journal of Constructional Steel Research* 67(10): 1475-1484.
- Cifuentes H. and Medina F. 2013. "Experimental study on shear bond behaviour of composite slabs according to Eurocode 4." *Journal of Constructional Steel Research* 82: 99-110.
- Crisinel M. and Marimon F. "A new simplified method for the design of composite slabs." *Journal of Constructional Steel Research* 60(3-5): 481-491.
- DIN 50125. 2009. Prüfung metallischer Werkstoffe – Zugproben. Berlin.
- Ekberg C.E. and Schuster R.M. 1968. "Floor Systems with Composite Form-Reinforced Concrete Slabs." Final Report, 8th Congress of the International Association for Bridge and Structural Engineering, Zurich, pp. 385-394.
- EN ISO 6892. 2007. Metallische Werkstoffe – Zugversuche – Prüfverfahren bei Raumtemperatur, CEN, Brussels.
- EN 1994-1-1. 2004. Design of composite steel and concrete structures – Part 1-1: General rules and rules for buildings. CEN, Brussels.
- Klippel M., Knobloch M. and Fontana M. 2010. Umbau Dock B am Flughafen Zürich – Belastungsversuche an Holorib-Blechverbunddecken Versuchsbericht mit Auswertung. IBK Report No. 325, Institute of Structural Engineering, ETH Zurich, Zurich (in German), <http://e-collection.library.ethz.ch/view/eth:2358>.
- Porter M.L. and Ekberg C.E. 1972. "Summary of Full-Scale Laboratory Tests of Concrete Slabs Reinforced with Cold-Formed Steel Decking." Preliminary Report, 9th Congress of the International Association for Bridge and Structural Engineering, Zurich, pp. 173-183.
- Porter M.L. and Ekberg C.E. 1976. "Design Recommendations for Steel Deck Floor Slabs." *Journal of the Structural Division* 102(11): 2121-2136.
- Sauerborn I. 1995. Zur Grenztragfähigkeit von durchlaufenden Verbunddecken. Universität Kaiserslautern, PhD thesis.
- Schuster R.M. 1972. "Composite Steel-Deck-Reinforced Concrete Systems Failing in Shear-Bond." Preliminary Report, 9th Congress of the International Association for Bridge and Structural Engineering (IABSE), Zurich, Switzerland, pp. 185-191.

A Push Test Study on the Behavior of Post-Tensioned Composite Steel-Concrete Slabs

Mohammad M. Rana¹; Brian Uy¹; and Olivia Mirza²

¹Centre for Infrastructure Engineering and Safety, School of Civil and Environmental Engineering, Univ. of New South Wales, Sydney, NSW 2052, Australia. E-mail: mohammad.rana@student.unsw.edu.au; b.uy@unsw.edu.au

²School of Computing, Engineering and Mathematics, Univ. of Western Sydney, Penrith, NSW 2751, Australia. E-mail: o.mirza@uws.edu.au

Abstract

Post-tensioned composite steel-concrete slabs represent an innovative form of building floor application, which combine the structural advantages of the two most popular flooring systems, comprising post-tensioned slabs in the case of concrete structures and profiled composite slabs in the case of steel structures. The complex interaction between the profiled steel sheets and concrete is usually determined through a push test. A significant step toward understanding the bond behaviour is to generate a local bond stress-slip relationship. In this context, this paper presents results from a preliminary push test study using profiled steel sheets to determine the possible influence of prestress on the bond between the profiled steel sheets and concrete. The variables investigated in the study were (1) level of prestress and (2) height of push specimen. The results of this study indicate that prestress has a negative effect on the bond between the profiled steel sheets and concrete in post-tensioned composite slabs. This is an important finding, which needs to be considered in the ultimate strength of post-tensioned profiled composite slabs.

1. INTRODUCTION

A post-tensioned composite (PTC) slab comprised of concrete, profiled steel sheeting, post-tensioning strands and non-prestressed reinforcement is a very popular form of building floor system at present due to economic and technical advantages of using profiled steel sheets as a substitute for conventional formwork systems and reinforcement in post-tensioned concrete structures. In this system, profiled steel sheets act as permanent formwork during construction and external reinforcement during service. Both post-tensioning and interaction between the profiled steel sheets and concrete enhance the flexural strength and stiffness of PTC slabs compared with post-tensioned concrete slabs and conventional composite slabs. Very limited

research studies into the investigation of the behaviour of PTC slabs have been published to date in the literature. This research has mainly focused on the potential advantages in post-tensioned composite slabs in terms of strength and costs [Schravendeel et al. 1990], the effects of a deep steel sheet on post-tensioned composite slabs [Koukkari 1999], the influence of location of post-tensioning anchors on the transfer length and concrete failure mode [TEKES 2001], development of a long span composite floor through prestressing applied to steel deck [Bailey et al. 2006], influence of various parameters on flexural performance of prestressed composite slabs [Liu et al. 2009], ultimate behaviour and development of design capacity tables for post-tensioned composite slabs [Patrick and Lloyd 2008], ultimate and time dependent behaviour of post-tensioned composite slabs and development of analytical models [Ranzi et al. 2012].

One of the fundamental aspects on which the strength, stiffness and ductility of composite profiled slabs depends to a large extent is the longitudinal shear transfer between the profiled steel sheet and the concrete slab [Oehlers and Bradford 1995]. Evaluation of shear bond in composite slabs has been focussed extensively in research. But no previous studies focussed on the evaluation of bond-slip behaviour of post-tensioned composite slabs. For accurate numerical simulation of post-tensioned composite slabs, a bond stress-slip model that accounts for the effects of prestress is required. Moreover, knowledge of the effects of various levels of prestress on bond-slip behaviour is important to optimise the design of post-tensioned composite slabs.

It is well known that the longitudinal shear is transferred initially by chemical adhesion which is lost as soon as slip occurs. Then the longitudinal shear is transferred by mechanical interlocking and also by frictional forces [Oehlers and Bradford 1995]. It has been recognized that the mechanism of longitudinal shear transfer between the profiled steel sheets and concrete in composite slabs are complex and difficult to model mathematically. Therefore the shear interaction property is usually determined using a push test.

In this context, a series of push tests was conducted to gain an insight into bond-slip behaviour of PTC slabs and to determine possible influences of prestress on this behaviour. This paper uses an exploratory approach to find out an appropriate push test setup from the existing push test studies in composite slabs [Schuster 1970; Stark 1978; Jolly and Zubair 1987; Daniels 1988; Patrick and Poh 1990; An and Cederwall 1992; Veljković 1995; Burnet 1998; Tremblay et al. 2002; Abdullah 2004]. Finally, a similar push test setup as Stark (1978) and Burnet (1998) was adopted with appropriate modification to optimize the ease of testing and accuracy of results although the challenge of handling delamination problem and local buckling at the base of the profiled steel sheets exists. Despite the similarity in the push test setup in [Stark 1978; Burnet 1998] and the one presented in this paper, the objective for this research is quite different.

2. EXPERIMENTAL PROGRAMME

2.1 Test Specimens

Six push test specimens were prepared and tested as a preliminary series of the experimental programme. The push test specimen configuration is shown in Figures 1 & 2.

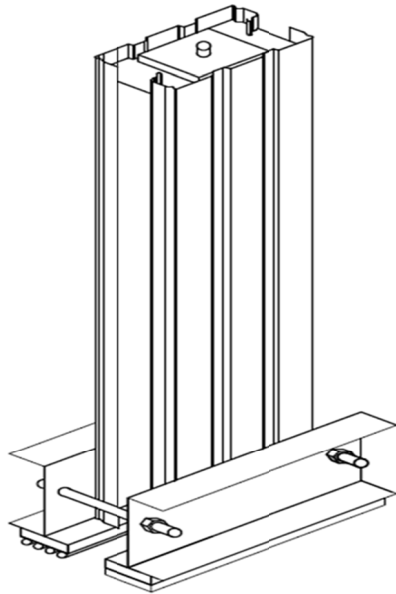


Figure 1. Push specimen configuration

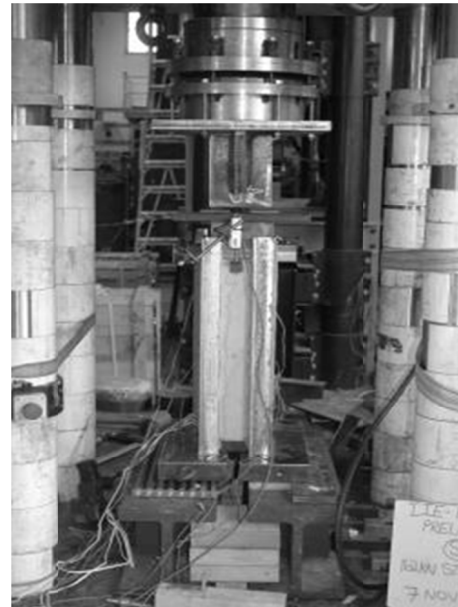


Figure 2. Push specimen ready for testing

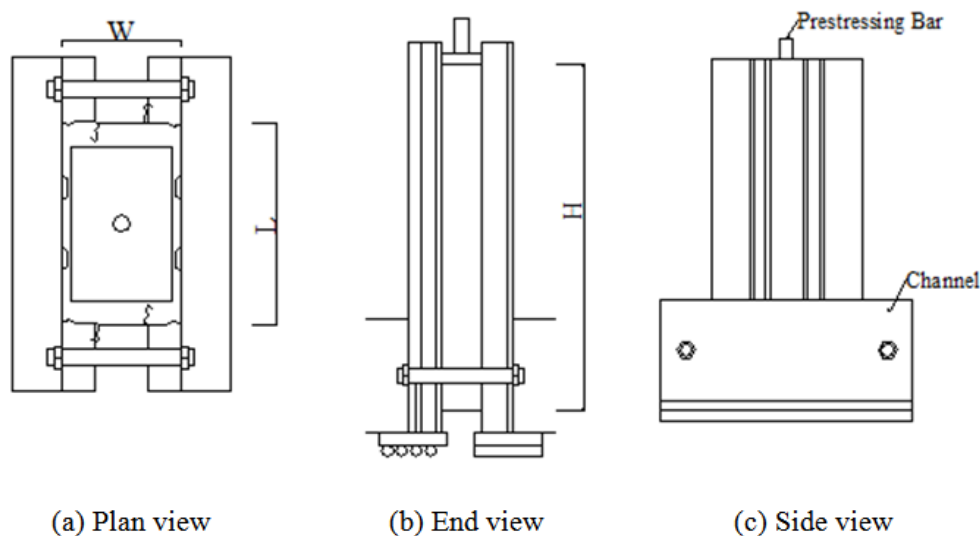
These specimens have been referred to in the following in the form of “PT-i-j” where PT, i and j indicates push test specimen, height of the push specimen (mm) and level of prestress (MPa) respectively. Therefore “PT-500-3” refers to the push test specimen using 500 mm in height and post-tensioned with 3 MPa. In this series, three specimens were post-tensioned. All specimens were constructed using 1.00 mm thick Stramit Condeck HP[®] profiled steel sheets [Stramit 2007]. Each specimen consists of two identical sections of profiled steel sheets which have a concrete block cast in between them. All specimens had identical cross-section with length L and width W of 300 mm and 180 mm respectively. The height of the bonding area H of the push-specimens was varied as 500 mm, 1000 mm and 2000 mm to investigate the variation of bond stress with slab span. The effective bonding area between the concrete and the profiled steel sheets was determined by the height H and the length L of the concrete block. A summary of the push specimens is provided in Table 1.

Two factors are taken into account in determining the minimum and maximum dimension of H. Firstly, the interface area is sufficient to address the effect of the prestress in relation to the variable height. Secondly, the maximum load developed in the sheeting must not cause buckling in the sheeting at the supports, at least prior to obtaining a reasonable slip. Two channels have been fixed at the bottom to maintain the rotational equilibrium of the push specimen and prevent buckling in the sheeting at the base of the push-specimens. The height of the channel has been specified as 200 mm for all the push specimens. The geometry of the push specimen is shown in Figure 3.

Table 1 Details of push specimens

Specimen ID	L (mm)	W (mm)	H (mm)	Effective prestress (kN)	Cross-sectional area (mm ²)	Concrete stress due to prestress (MPa)
PT-500-0	300	180	500	0	54000	0.00
PT-1000-0	300	180	1000	0	54000	0.00
PT-2000-0	300	180	2000	0	54000	0.00
PT-500-3	300	180	500	162	54000	3.00
PT-1000-3	300	180	1000	162	54000	3.00
PT-2000-3	300	180	2000	162	54000	3.00

The length L has been chosen to allow at least one complete width of the sheeting to be tested. Since the width of the Condeck profile is 300 mm, the length of the push specimen has been specified as 300mm to simulate the overall performance. No lateral restraint was required to limit the sheeting distortion. The width W was chosen to be 180 mm to avoid premature splitting of concrete between opposite ribs and to provide enough clearance between the sheets to apply the load uniformly to the concrete block.

**Figure 3. Geometry of the push specimen**

The profiled steel sheets overhang the concrete block by 40 mm at the top and bottom of the push-specimens to accommodate a slip of 10 mm for the concrete block. The base on which the specimen was placed incorporated steel plates of 20 mm in height and one base is placed on a roller so that the profiled steel sheets are free to deform away from the concrete.

2.2 Material Properties

All push specimens were cast on the same day. The details of the constituents of the concrete mix used in the experiments are reported in Table 2.

Table 2 Details of concrete mix

Material	Quantity(per m ³)
Coarse Sand	510 kg
Fine sand	350 kg
10 mm aggregate	343 kg
20 mm aggregate	600 kg
Cement	300 kg
Fly ash	86 kg
Water	105 L
Water reducer	900 ml

The material properties of the concrete were determined from standard cylinder tests as reported in Table 3. The concrete compressive strength at 7, 14, 21, 28 and 34 days was determined as 22.6 MPa, 32.5 MPa, 36.8 MPa, 40.8 MPa and 41.7 MPa respectively. The nominal tensile strength, nominal breaking load and nominal yield load of the prestressing bar, as provided by the supplier, was 1030 MPa, 728 kN and 590 kN respectively. The properties of the profiled steel sheets and prestressing bar were obtained from Standard tensile tests and are presented in Table 3.

2.3 Specimen preparation and post-tensioning

The first step was to cut the profiled steel sheeting to a length of 580 mm, 1080mm, 1580 mm and 2080 mm to allow 40 mm overhang at the top and bottom of the specimen. The sheeting was as received from the manufacturer and no measures were taken to treat the inner surface condition. The formwork ready for pouring is shown in Figure 4.

The formwork was assembled with appropriate dimensions and post-tensioning cable and PVC duct was placed with zero eccentricity. A lifting lug was placed on the sides of the specimen. The specimen was poured along with test cylinders and kept moist for two days. After this period they were left to cure in the air until testing.

The three specimens were post-tensioned at day 10 after casting with a concrete strength measured at day 7 of 23.0 MPa. Post-tensioning was carried out by elongating the 29 mm threaded bar from the live anchor through tightening by a wrench and a load cell was used to measure the applied load to the bars during the post-tensioning while three strain gauges fixed on the bar were used to record the strains within the bar. Push-specimens were clamped well in a strong floor during post-tensioning to minimise any uplift or external disturbance. A single load cell was

used to perform the post-tensioning by calibrating each bar for corresponding strains in that bar. The applied load versus strain recorded by the gauges fixed on the bar for PT-500-3 is illustrated in Figure 5. It was found that the strains recorded by the three gauges are different. The centre strain gauge reading was used for calibration. The full applied design prestressing force was 162 kN and is equal to about 22 % of the nominal breaking load.

Table 3 Material properties of concrete, profiled steel sheets and prestressing bar

Material	Property	Value (MPa)
Concrete	Compressive strength, f'_c	40.8
	Tensile strength, f_{ct}	5.1
	Young's modulus, E_c	35,000
Profiled Steel Sheets	Yield stress, f_y	670
	Ultimate strength, f_u	680
	Young's modulus, E_s	217,000
Prestressing Bar	Yield stress, f_y	1050
	Ultimate strength, f_u	1120
	Young's modulus, E_s	201,000

2.4 Instrumentation

Two linear potentiometers were attached to the sheeting to measure the slip at the interface directly. Three strain gauges (FLA-5-11-3LT) were placed on each outer surface of profiled steel sheeting to observe the strains developed during the debonding process. Three concrete strain gauges (PML-60-3LT) were placed near the centre of the specimen to observe the concrete strains. Concrete strain readings were also taken using DEMEC strain gauges. A data acquisition system was used to record the readings of the load cell, linear potentiometer and strain gauges.



Figure 4. Formwork ready for pouring

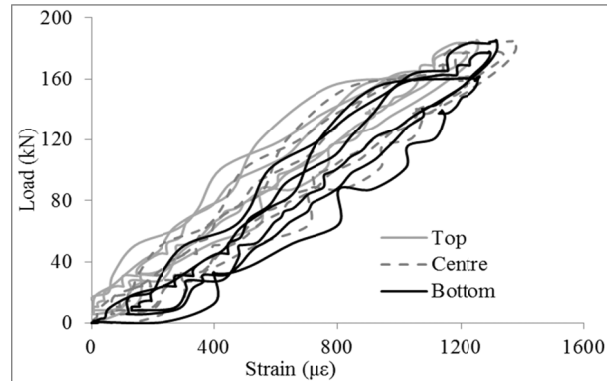


Figure 5. Load versus strain for PT-500-3

2.5 Test setup

Before moving the specimens, clamps are placed on the outer edges to help minimise any disturbances to the sheeting during the test setup. The specimens are then lifted up by the lifting lugs and then placed onto the base of the loading rig. Two channels were fixed and finger tight only at base of the sheeting. The base of one side of the specimen was placed on a roller so that the sheeting is free to move away from the concrete. Two end blocks were placed on the top of the specimen to distribute the load evenly onto the specimen. A push specimen ready for testing is shown in Figure 2.

The load was applied to the specimen very slowly at a rate of 0.005 mm/sec until the chemical bond had completely broken as indicated by the linear potentiometer recording a slip displacement. After failure of the chemical bond, the load was increased gradually. The load and slip were logged continuously. The test was terminated when either the specimen was unable to take any load or the limit of slip had been reached.

3. RESULTS AND DISCUSSION

3.1 Push test specimens PT-500-0 and PT-500-3

The load-slip curves for these two specimens are shown in Figure 6. The failure of the chemical bond was evidenced by a cracking sound, followed by the reduction in load carrying capacity and progression of slip until the limiting slip has been reached to terminate the test. An increase in shear capacity after breakdown of the chemical bond might be due to the increase in roughness of the profile-concrete interface as slip progresses [Burnet 1998].

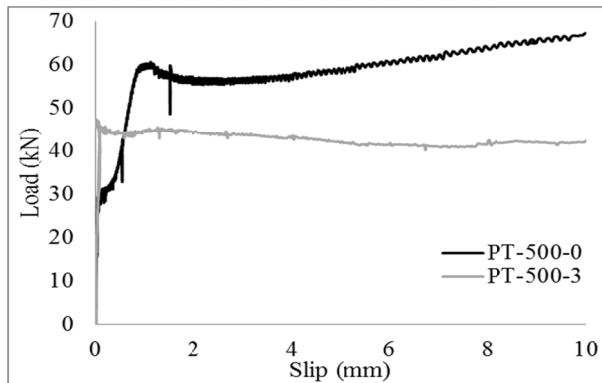


Figure 6. Load-slip curves of PT-500-0 & PT-500-3



Figure 7. Initiation of slip from one side

PT-500-0 specimen carried a maximum load of 60 kN, with one side measuring over 2.5 mm more slip than the other. This resulted from the breakdown of the chemical bond and the initiating slip on one side of the specimen shown in Figure 7, before the chemical bond had fully broken on the other. PT-500-3 specimen recorded a peak load of 47 kN, which results in a 20% reduction in maximum load.

3.2 Push test specimens PT-1000-0 and PT-1000-3

The load-slip curves for these two specimens have been shown in Figure 8. PT-1000-0 specimen suffered pre-delamination before the test at one corner to some extent during handling of the specimen. This specimen recorded a maximum load of 115 kN before failure.

PT-1000-3 specimen recorded a maximum load of 137 kN which is not expected compared with other push specimens. This rise in shear capacity resulted from a buckling at the base of the profiled steel sheets on one side of the specimen that occurred during loading before complete failure of the chemical bond. The deformed shape of the profiled steel sheeting is shown in Figure 9.

3.3 Push test specimens PT-2000-0 and PT-2000-3

These specimens were handled very carefully using some clamps and no delamination was observed before the test. The load-slip curves for these two specimens have been shown in Figure 10. PT-2000-0 specimen recorded a maximum load of 240 kN before failure. One linear potentiometer dropped due to non-uniform distribution of loading at top of the specimen and this is shown in Figure 11. So slip on one side only is reported for analysis purposes.

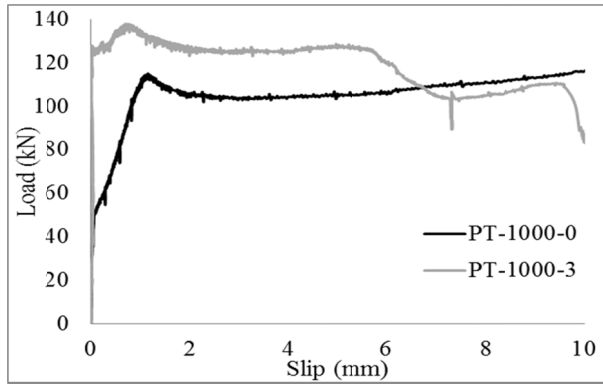


Figure 8. Load-slip curve of PT-1000-0 & PT-1000-3



Figure 9. Local buckling of the sheeting

The PT-2000-3 specimen reached a maximum load of 175 kN before failure which is lower than that of the nonprestressed specimen PT-2000-0. Some local buckling was also observed at the lower portion of the specimen after 5 mm slip occurred. The effect of this local buckling was not considered effective in reducing the chemical bond characteristics as it occurred after a slip of 5 mm had reached.

3.4 Comparison of bond-slip characteristics

Chemical bond is derived from the maximum load at which the chemical bond failed by dividing the load by the entire contact area between the sheeting and the concrete. The residual stress is considered the minimum value after failure of the chemical bond and before the effect of mechanical bond. The average mechanical bond stress is found by dividing the average load between the residual bond and load at 5 mm slip by the entire contact area between the sheeting and the concrete. The chemical bond strength, residual strength and average mechanical bond strength have been reported in Table 4.

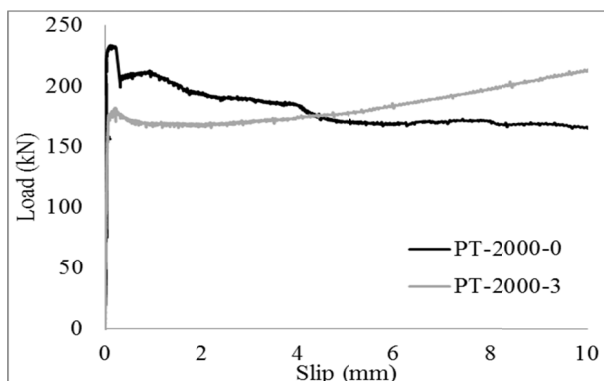


Figure 10. Load-slip curve of PT-2000-0 & PT-2000-3



Figure 11. Linear potentiometer dropped

The comparison of bond stress-slip curves for six different push specimens tested under a static load is shown in Figure 12. It can be seen from both these figures that the chemical bond appears to vary significantly with the prestress. The average chemical bond stress in post-tensioned push specimens is found to be approximately 20% lower than that in push specimens without post-tensioning. Also the residual stress and mechanical bond stress in post-tensioned push specimens is found to be lower than that of push specimens without post-tensioning upto a slip of 5 mm. The reason for the decrease in bond stress may be attributed to the shortening of the concrete block due to prestress.

Table 4 Summary of bond stress of push specimens

Push test specimen	Maximum load before breakdown of chemical bond (kN)	Chemical bond stress (MPa)	Residual Stress (MPa)	Average Mechanical Bond stress upto a slip of 5 mm (MPa)
PT-500-0	60.61	0.26	0.24	0.24
PT-1000-0	115.03	0.25	0.22	0.23
PT-2000-0	233.43	0.25	0.20	0.20
PT-500-3	47.36	0.21	0.19	0.19
PT-1000-3	137.74	0.30	0.27	0.27
PT-2000-3	182.18	0.20	0.18	0.19

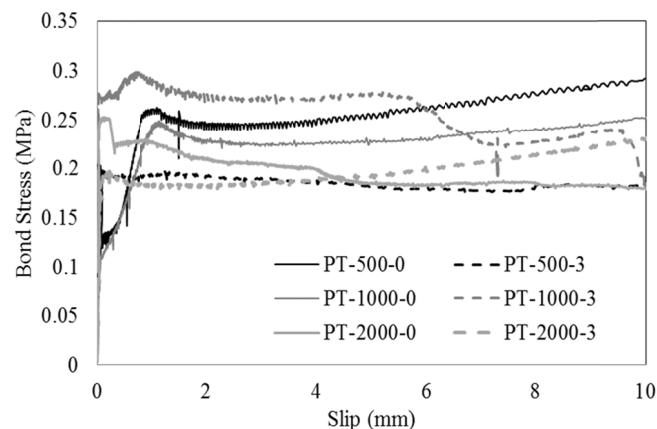


Figure 12. Comparison of bond stress-slip behaviour of push specimens

4. CONCLUSIONS

The bond which must be achieved between the profiled steel sheet and the concrete is very crucial to the composite action of post-tensioned composite slabs. This paper presented the results of a preliminary series of push tests which indicate a negative effect of prestress on local bond stress-slip behaviour. Since this experimental setup is prone to problems of pre-delamination and local buckling at the base of the profiled steel sheets to some extent, further experimental data is required

to properly validate the adequacy of the proposed research and to propose a general local bond stress-slip law for accurate numerical modelling of post-tensioned composite slabs. However, the results of this series will be useful for further study on finite element modelling of shear bond for the full scale slabs. This is expected to be carried out by the authors in near future.

ACKNOWLEDGEMENTS

The experimental work in this paper was conducted at the University of Western Sydney and was funded by the Australian Research Council's Linkage projects (project number LP0990190) and by Stramit Building Products and Arup as Partner Organisations. The authors would like to acknowledge the support and help from the technical staff at The University of Western Sydney in this regard.

REFERENCES

- Abdullah, R. (2004). "Experimental evaluation and analytical modeling of shear bond in composite slabs." PhD Thesis, Virginia Polytechnic Institute and State University, Virginia, USA.
- An, L. and Cederwall, K. (1992). "Composite slabs analysed by block bending test." *Proceedings of the 11th International Specialty Conference on Cold-Formed Steel Structures*, University of Missouri-Rolla, 268-282.
- Bailey, C., Currie, P. and Miller, F. (2006). "Development of a new long span composite floor system." *Struct Eng*, 84(21), 32-39.
- Burnet, M. (1998). "Analysis of composite steel and concrete flexural members that exhibit partial shear connection." PhD Thesis, University of Adelaide, Australia.
- Daniels, B. J. (1988). "Shear bond pull-out tests for cold-formed-steel composite slabs." ICOM- Construction Metallique, Department de Genie Civil, Ecole Polytechnique Federale de Lausanne.
- Jolly, C. K. and Zubair, A. K. (1987). "The efficiency of shear-bond interlock between profiled steel sheeting and concrete." *Proceedings of the International Conference on Steel and Aluminium Structures, Composite Steel Structures - Advances, Design and Construction*, Cardiff, 127-136.
- Koukkari, H. (1999). "Steel sheet in a post-tensioned composite slab." *Proceedings of the Conference Eurosteel '99*, Czech Republic, 199-202.
- Liu, X., Wang, L. and Wang, B. (2009). "Full-range analysis on flexural performance of profiled sheet and prestressed concrete composite slabs." *Journal of Shenyang Jianzhu University (Natural Science)* 5: 25.
- Oehlers, D. J. and Bradford, M. A. (1995). "Composite steel and concrete structural members: fundamental behaviour." Pergamon Press, Oxford.
- Patrick, M. and Lloyde, M. (2008). "Development of moment capacity tables for post-tensioned composite slabs incorporating high-tensile steel decking, validated by test data." *Proceedings of the Australasian Structural Engineering Conference (ASEC)*, Australia, 803.

- Patrick, M. and Poh, K. (1990). "Controlled test for composite slab design parameters." *IABSE Symposium on Mixed Structures including New Materials*, Brussels, Belgium, 227-231.
- Ranzi, G., Al-Deen, S. and Uy, B. (2012). "An experimental study on the service and ultimate behaviour of post-tensioned composite slabs." *IABSE Congress Report*, 701-708.
- Schravendeel, P., de Sitter, W. and Klop, G. (1990). "Prestressed post-tensioned composite floor slabs." *IABSE Symposium on Mixed Structures, including New Materials*, Brussels, 173-178.
- Schuster, R. M. (1970). "Strength and behavior of cold-rolled steel-deck-reinforced concrete floor slabs." PhD Thesis, Iowa State University, Ames, Iowa.
- Stark, J. (1978). "Design of composite floors with profiled steel sheet." *Proceedings of the 4th International Specialty Conference on Cold-Formed Steel Structures*, 893-922.
- Stramit (2007). Stramit Condeck HP: composite slab system: product technical manual, Stramit Building Products, Australia.
- TEKES (2001). Finnsteel Technology Programme 1995-2000: Final Report Technology Programme Report 7/2001, TEKES (National Technology Agent of Finland).
- Tremblay, R., Rogers, C., Gignac, P. and Degrange, G. (2002). "Variables effecting the shear-bond resistance of composite floor deck systems." *Proceedings of the 16th International speciality Conferance on Cold-Formed Steel Structures*, Olando, Florida, 663-676.
- Veljković, M. (1995). "Longitudinal shear capacity of composite slabs." *Nordic Steel Construction Conference '95*, Swedish Institute of Steel Construction and Division of Steel structures, Malmö, Sweden, 547-554.